ACTA METALLURGICA

Board of Governors

Professor Eric Rudberg

Dr. D. J. Carney

Professor R. L. Sproull

Professor D. S. Clark

Professor G. W. Ratheneau

Mr. G. Macdonald Young

Dr. W. Boas

Mr. A. O. Schaefer

Dr. J. H. Hollomon, Secretary-Treasurer

Editor

Professor Bruce Chalmers, Division of Engineering and Applied Physics, Harvard University, Cambridge, Massachusetts, U.S.A.

Associate Editors

Professor N. Petch (Great Britain)

Professor E. Rudberg (Sweden)

Professor P. Laurent (France)

Dr. W. Boas (Australia)

Professor P. Coheur (Belgium)

Professor Antonio Scortecci (Italy)

Professor Seiji Kaya (Japan)

Professor W. G. Burgers (Netherlands)

Professor Väinö Hovi (Finland)

1959

Professor F. R. N. Nabarro (South Africa)

Professor G. H. H. Wasserman (Germany)

Business Manager: Mr. D. J. Raymond

Business Office: Pergamon Press Inc., Acta Metallurgica, 122 East 55th Street, New York 22, N.Y.

The cost of subscription is \$10.00 (U.S.) to members of the Sponsoring Societies, \$15.00 to members of Co-operating Societies, and \$25.00 to individuals who are not members of either. Payment may be made through a sponsoring or co-operating society, or direct to the business office of ACTA METALLURGICA. Changes of address should be sent to the Business Office. Back numbers are available from the Business Manager at the following rates:

All volumes (Vols. 1 through 7, 1953-1959): \$28.00. Agency discount 10%

Single issues: Vols. 1-4 (bi-monthly) \$6.00 per issue

Vols. 5-7 (monthly) \$3.00 per issue

VOLUME 7 1959

VO:

CONTENTS OF VOLUME SEVEN

NUMBER 1			
Propagation of sound in liquid metals: The velocity in lead an Cavity formation in nitrate-doped alkali halides	d tin	R. B. Gordon	1
	ENHOUT-VAN DER	Vorst and W. Dekeyser J. W. Cahn	
	E APPTS S AME	LINCKX and W. DEKEYSER	
Uber die Verfestigung von Aluminium-Einkristallen (99,99% A Orientation of recrystallized grains in strained aluminum single	d) und ihre Deutu	ing W. Staubwasser	
Letters to the Editor:		LIEBMANN and K. LÜCKE	51
		** *	
The temperature dependence of the yield stress in iron Reply to discussion "The temperature dependence of the yiel			57
A general equation prescribing the extent of the austenite-ma	artensite transform		58
alloys and plain carbon steels Shear along grain boundaries of an aluminium-10% zinc allo	y deformed at ro		59
	IAUDHURI, J. E. 1	MAHAFFY and N. J. GRANT	60
Effect of dissolved impurities on grain-boundary migration Knight shift and calorimetric measurements in liquid sodium	alloys R. A	R. A. ORIANI A. ORIANI and M. B. WEBB	62 63
NUMBER 2			
Transformation pseudo-martensitique dans l'hydrure de zirconi		Harry of J. Héannan	0=
		. Huber et J. Hérenguel omas and B. L. Averbach	65
The early stages of plastic deformation in copper Overshooting in quenched aluminium crystals		C. TANNER and R. MADDIN	69 76
Quenching of imperfections in aluminum		ESORBO and D. TURNBULL	83
Self and interdiffusion in aluminum-zinc alloys J. E. Hill			86
Plastizitätsuntersuchungen von Metallkristallen im Ultraschallf			93
The metallography of deformed iron		Brandon and J. Nutting	101
Initial oxidation rate of nickel and effect of the Curie temperat	ure	PICKETT and J. MACNAIRN	111
The formation of surface pits by the condensation of vacancies Contribution à l'étude de la precipitation dans un groupe d'allie	P. E.	Doherty and R. S. Davis	118 124
	ages a base at me	0. 11.11.11.11	121
Letters to the Editor:			
Comments on "Yield strength of metals as a function of grain	n size''	U. F. Kocks	131
An effect of thermal neutrons on Cu ₃ Au		RO and J. B. BURNHAM JR.	131
Yield points in a dilute magnesium-thorium alloy		S. L. COULING	133
Cross slip of extended dislocations		R. L. Fleischer	
	C. Blade, J. W.	H. CLARE and H. J. LAMB	
Carbon damping in manganese alloyed ferrite		G. Lagerberg	
Some observations on intergranular fracture in polycrystallin	e sodium chloride		139
Grain boundary sliding and intercrystalline cracking		TRATER and E. S. MACHLIN	140
Some current papers in other journals	0. 131	RAIDE GIRE L. O. MACHEN	144
NUMBER 3			
Quanahad in vacancies in noble metals. I Theory of decay			
Quenched-in vacancies in noble metals—I. Theory of decay H. Kimura Quenched-in vacancies in noble metals—II. Mechanism of quen		D. Kuhlmann-Wilsdorf	145
		D. KUHLMANN-WILSDORF	154
The kinetics of grain boundary grooving in copper		LLINS and P. G. SHEWMON	163
The dislocation structure of slip bands in iron		R. Low and R. W. GUARD	171
Quenching studies on mechanical properties of pure gold		EHII and J. W. KAUFFMAN	180
Electron irradiation of aluminum-copper alloys		CKER JR. and M. B. WEBB	187
Oxidation of nickel-cobalt alloys in the range of Curie temperat		W. W. SMELTZER	191
On the excess energy of electrolytically deposited silver WE	DYED F SCHOTTE	v and MICHARI B BRUPB	* ***
Double Bragg scattering in cold-worked metals		WEBB and W. B. BEEMAN	203
The cause of the strengthening in quenched beta brass	м. Б.	N. Brown	210
etters to the Editor:			
'omments on "Accommodation strains in martensite formation		LARRY KAUFMAN	216
Discussion of "Comments on accommodation strains in marten	nsite formation ar		
parameter"		J. W. CHRISTIAN	218
parameter" On the equilibrium segregation at a grain boundary	JOHN W. CA	HN and JOHN E. HILLARD	219
Frain boundary segregation		INMAN and H. R. TIPLER	221
lechanism of sintering		W. D. Jones	222
On the effect of static and dynamic preloads on the stress-strain	n curve for a low		
	R.	C. SMITH and I. VIGNESS	223

VOL. 7 1959

Evidence for the surface diffusion mechanism of thermal grooving in copper N. A. Gjostein and F. N. Rhines	224
Ueber die Bedeutung der Versetzungen an den Grenzen der Kristalle des angelassenen Martensits für den mi-	
krophysikalischen Mechanismus der "Anlassprödigkeit" A. Masin Electrical resistivity change from formation of zones in aluminum alloys W. E. Fine Uber Kristallstruktur und Ordnung aus der Schmelze abgeschreckter Legierungen des Systems Kupfer-Zinn	226 228
Etch pits in iron H. J. SEEMAN and H. KNÖDLER R. B. LISS	$\frac{229}{231}$
NUMBER 4	
Work softening in irradiated copper M. J. Makin Partially pinned tilt boundaries T. Vreeland Jr.	$\frac{233}{240}$
Mechanical properties of iron and some iron alloys while undergoing allotropic transformation M. DE JONG and G. W. RATHENAU	246
Room temperature deformation processes in zirconium E. J. RAPPERPORT Vapor pressure measurements over calcium, magnesium and their alloys and the thermodynamics of formation of CaMg, J. F. Smith and R. L. Smythe	254 261
The growth of temper carbon nodules J. Burke	268
Aging in Au-Ni alloys The orientation dependence of etching effects on germanium crystals J. SIVERTSEN and C. WERT P. J. HOLMES	$\frac{275}{283}$
Letters to the Editor:	
On the structure changes produced by ageing of Cu–Ti alloy Sur l'oxydation du manganèse dans l'air température élevées J. Païdassi et A. Echeverría	$\frac{291}{293}$
Sur l'existence d'un processus de germination dans la sulfuration du cuivre aux températures élevées J. Oudar et J. Bénard	295
ANIMADA -	
NUMBER 5 The dynamic yielding of a carbon steel C. J. Maiden	297
Etude par analyse thermique des transformations allotropiques du plutonium Absolute interfacial energies of [001] tilt and twist grain boundaries in copper	305
X. A. GJOSTEIN and F. N. RHINES Oxidation kinetics in the case of ageing oxide films A study of slip lines in α-brass as revealed by the electron microscope	319 331
J. T. FOURIE and H. G. F. WILSDORF Self-diffusion in indium A simplified derivation of the quasichemical approximation in order-disorder theory J. M. Hong	$\frac{339}{350}$ $\frac{354}{354}$
Letters to the Editor:	001
A size effect in plastic bending J. J. GILMAN	357
The mechanism of dispersion hardening Stacking faults in B.V.C.C. metals Errata J. M. SILCOCK	$\frac{357}{359}$ $\frac{360}{360}$
Eirata	900
NUMBER 6	
The mechanical properties of irradiated niobium M. J. Makin and F. J. Minter Forme d'equilibre d'un arc de dislocation coin en presence d'une sursaturation de lacunes G. Saada	361 367
Creep processes in polycrystalline aluminum Theory of order in ternary alloys—II. W. A. Rachinge K. F. Wojciechowski	$\frac{374}{376}$
The hardening and embrittlement of mild steel by cyclic stressing at the fatigue limit Decoration and etching of silver doped rocksalt crystals by surface gas reactions. J. Holder	380
W. Bontinck and W. Dekeyser Appearance of dislocations in metal crystals on evaporation: Twinning dislocations and their relation to	389
annealing twins in copper E. Votava and A. Berghezan The diffusion of carbon during precipitation in α-iron R. H. Doremus	392 399
Observations on regular arrays of etch pits in a titanium-10% molybdenum alloy	999
T. H. Scoffeld and A. E. Bacon	403
A correlation of data on diffusion of solutes in face-centred cubic metals D. Turnbull and R. E. Hoffman Grain growth in zone-refined tin E. L. Holmes and W. C. Winegard Ternary carbides of the transition metals, nickel, cobalt, iron, manganese with zinc and tin	$\frac{407}{411}$
H. H. STADELMAIER and L. J. HUETTER	415
Letters to the Editor: Lattice parameters of solid solutions of phosphorus in iron B. Gale	190
High temperature intercrystalline cracking L. L. SEIGLE	$\frac{420}{421}$
Anomalous increase of resistivity during ageing of aluminium-silver alloys T. Federighi and L. Passari	422
A mechanism for secondary recrystallization in high-purity silicon iron J. L. Walter	424
Expansion coefficient of plastically deformed steel M. J. Hordon and B. L. Averbach Remarques sur l'emploi des repères inertes (<i>Markers</i>) pour les études de diffusion dans les phases plastiques M. Cagnet and J. Moreau	426 427
Erwiderung auf den Brief an den Herausgeber der Herren Cagnet und Moreau F. Wever und H. J. Engell	429
Experimental evidence of boundary migration A. Ferro, C. Sari and G. Venturello	429
	431
Direct observation of sub-structures in martensite Z. Nishiyama and K. Shimizu Kinetics of vacancy precipitation in a silver-zinc solid solution A. S. Nowick and A. E. Roswell	$\frac{432}{433}$
Fractional nucleation in the ageing of an aluminium-4.25 wt. % copper alloy V. B. Ghate and D. R. F. West	436
	438
Erratum	440

VO: 7

NUMBER 7

NUMBER 7		
Zum magnetischen Verhalten von Aluminium und Aluminium-Mischkris		
Effects of torsion on the tensile stress-strain curve of aluminium The flow stress of iron and its dependence on impurities	R. Lingelbach und E. Vogt D. B. Holt G. Schoeck and A. Seeger	44
Electrical resistivity recovery in cold-worked and electron-irradiated nic		
Die Energie und der elektrische Widerstand von Grosswinkelkorngrenze		
Effect of applied tensile stress on phase transformations in steel L	F. PORTER and P. C. ROSENTHAL	
Letters to the Editor:		
Precipitation on dislocations in aluminium—4% copper alloys On the conditions governing the brittle fracture of iron single crystals Au sujet de la fragilité du fer de zone fondue a basse température Some further observations on the growth of copper whiskers from cup Low temperature creep of rock salt single crystals Thermal etching of silver surfaces parallel to {110} planes E. Der Einfluss feindisperser Ausscheidungen auf die Koerzitivkraft von	Simone Besnard et J. Talbot prous iodide S. S. Brenner R. Strumane and W. Dekeyser D. Hondros and A. J. W. Moore Transformatorenblech	51 51 51 52 52
On the pressure of hydrogen in cavities of steel	R. Wagner F. De Kazinczy	
Book review: "Handbook of lattice spacings and structures of metals and alloys"	by W. B. Pearson	
,	T. B. Massalski	523
NUMBER 8		
The cubic-hexagonal transformation in single crystals of cobalt and coba	alt-nickel alloys	
The crystallography of the α-transformation in zirconium and in two tit	P. GAUNT and J. W. CHRISTIAN	529
The crystallography of the x-transformation in zheomuni and in two tits	P. Gaunt and J. W. Christian	53
The dissipation of energy during plastic deformation	J. F. NICHOLAS	
Elimination des lacunes dans les aluminiums très purs Sur le blocage des dislocations par des cavités ou de petits precipites	M. Wintenberger P. Coulomb	
Thermodynamics of liquid Mg-Bi alloys	J. J. Egan	56
The effect of cold work on the electrical resistivity of copper solid solution. The lattice stability of metals—I. Titanium and zirconium	on alloys W. R. Hibbard Jr. L. Kaufman	
NUMBER 9 Untersuchungen über eine neue Art der Sekundärrekristallisation in Fe Lattice defects in a copper-aluminum alloy M. S. Plastic anisotropy of LiF and other rocksalt-type crystals Creep in face-centred cubic metals with special reference to copper Stress induced ordering and strain-ageing in low carbon steels	-3%Si-Legierungen K. Detert . Wechsler and R. H. Kernohan J. J. Gilman P. Feltham and J. D. Meakin D. V. Wilson and B. Russell	599 609 61-
	th an Appendix by J. D. ESHELBY	02
W. C.	LESLIE, R. M. FISHER and N. SEN	63:
Letters to the Editor:	W Assessed and S. E. Drousse	0.43
Twinning in tantalum Some observations on mechanisms of growth of metal whiskers Discussion of "Shear along grain boundaries of an aluminum-10 temperature" On the thermal etching of silicon iron	W. Anderson and S. E. Bronisz W. J. Allan and W. W. Webb sine alloy deformed at room E. C. W. Perryman C. G. Dunn and J. L. Walter	648 648
Radiation-induced precipitation sites in potassium chloride	S. Amelinckx	650
Temperature gradient grain boundary migration Erratum	C. Elbaum	651
NUMBER 10		
The kinetics of the first stage of tempering An internal friction peak due to slow moving dislocations in iron-nitroge		653
Metallographic investigation of precipitation of silicon from aluminum	R. RAWLINGS and P. M. ROBINSON B. ROSENBAUM and D. TURNBULL	659
Letters to the Editor		
	H. MEIKLEJOHN and R. E. SKODA	675
Comments on the recent paper of Clarebrough, Hargreaves and Lorette Further observations on the growth of silver whiskers from silver chlor On the orientation of silicon precipitating from an Al-rich solid solution	o R. O. WILLIAMS ride S. S. Brenner n	676 677
Vacancy precipitation in quenched gold from internal friction measure	URNBULL and E. I. ALESSANDRINI ments R. KAMEL	678 680
Hole model for diffusion in liquids Some observations on the retention of the β -phase in quenched Zr-50 α	R. B. Gordon at.% Ti alloys	681
Mise en évidence d'un microrelief, indice de cisaillement martensitique The effect of impurities on the strength of silver chloride	B. A. HATT and G. I. WILLIAMS H. BIBRING W. J. LUHMAN and A. E. GORUM	682 684 685
The escape of hydrogen from iron	H. B. Wahlin and D. J. Mack	687

VOL. 7 1959

Plastically deformed steel in a weak magnetic field Relation entre la ségrégation des impuretés et l'autodiffusion intergranulaire dans le fer Relation entre la ségrégation des impuretés et l'autodiffusion intergranulaire dans le fer Relation entre la ségrégation des impuretés et l'autodiffusion intergranulaire dans le fer Relation entre la ségrégation des impuretés et l'autodiffusion intergranulaire dans le fer Cracks due to the piling-up of dislocations on two intersecting slip planes in Mg0 crystals A. S. Ker, J. C. M. La and Y. T. Chou A. S. Ker, J. C. M. La and Y. T. Chou B. S. Ker, J. C. M. La and Y. T. Chou A. S. Ker, J. C. M. La and Y. T. Chou A. S. Ker, J. C. M. La and Y. T. Chou B. S. C. Barrett, C. D. Graham, Jr. and J. M. LOMBEL B. C. S. Barrett, C. D. Graham, Jr. and J. M. LOMBEL B. C. S. Barrett, C. D. Graham, Jr. and J. M. LOMBEL B. C. S. Barrett, C. D. Graham, Jr. and J. M. LOMBEL B. C. S. Barrett, C. D. Graham, Jr. and J. M. LOMBEL B. C. S. Barrett, C. D. Graham, Jr. and J. M. LOMBEL B. C. S. Barrett, C. D. Graham, Jr. and J. M. LOMBEL B. C. S. Barrett, C. D. Graham, Jr. and J. M. LOMBEL B. C. S. Barrett, C. D. Graham, Jr. and J. M. LOMBEL B. C. S. Barrett, C. D. Graham, Jr. and J. M. LOMBEL B. C. S. Barrett, C. D. Graham, Jr. and J. M. LOMBEL B. C. S. Barrett, C. D. Graham, Jr. and J. M. LOMBEL B. C. S. Barrett, C. D. Graham, Jr. and Jr. A. Lombel B. S. Berrett, C. D. Graham, Jr. and Jr. A. Lombel B. C. S. Barrett, C. D. Graham, Jr. and Jr. A. Lombel B. C. S. Barrett, C. D. Graham, Jr. and Jr. A. Lombel B. C. S. Barrett, C. D. Graham, Jr. and Jr. A. Lombel B. S. Berrett, C. D. Graham, Jr. and Jr. A. Lombel B. S. Berrett, C. D. Graham, Jr. and Jr. A. Lombel B. S. Berrett, C. D. Graham, Jr. and Jr. A. Lombel B. S. Berrett, C. D. Graham, Jr. and Jr. A. Lombel B. S. Berrett, C. D. Graham, Jr. and Jr. A. Lombel B. S. Berrett, C. D. Graham, Jr. and Jr. A. Lombel B. S. Berrett, C. D. Graham, Jr. and Jr. A. Lombel B. S. Berrett, C. D. Graham, Jr. and Jr. A. Lombel B. S. Berrett, C. D. Graham, Jr. and			
Relation entre la ségrégation des impuretés et l'autodiffusion intergranulaire dans le fer P. CUCIOMN, C. LEYMONE and P. LACOMDE Gracks due to the piling-up of dislocations on two intersecting slip planes in MgO crystals S. M. C. M. Li and Y. T. CHOU GOT THE METERS OF	Plastically deformed steel in a weak magnetic field	A. W. Sleeswyk	689
Cracks due to the piling-up of dislocations on two intersecting slip planes in MgO crystals A. S. Ker, J. C. M. Lt and Y. T. Chou of the mechanism of sulphurization of copper A. S. Ker, J. C. M. Lt and Y. T. Chou of Atxwerfahren für Versetzungen in Fe-Ni-Legierungen S. Mhowec and T. Werbers of S. Mhowec and T. Werbers of S. Marker and T. Werbers of S. C. Barres of S. Marker and T. M. Lommel. The diffusion of venon in silver Effect of hydrogen on the yielding of mild steel "Superhigh plasticity" of commercial iron under cyclic fluctuations of temperature M. G. LOZINSKY and I. S. SIMEONOVA The effect of quenched-in vacancies on the elastic modulus of aluminum The attack of solid alloys by liquid metals and salt metals The three of vacancies in an unusual anelastic modulus of aluminum The role of vacancies in an unusual anelastic phenomenon Letters to the Editor: A simplified treatment of surface melting On surface roughness N. A. Jackson 747 The structure of G.P. zones in Al(Ag) alloys The role of vacancies in allowed phenomenon NUMBER 12 Lattice parameter and resistivity study of order in the alloys CuAu, The plasticity of alkali halide crystals On two dimensional nucleation NUMBER 12 Lattice parameter and resistivity study of order in the alloys CuAu, In the lattice spacings and the stability of close-packed hexagonal Cu-Ga, Cu-Ge and Ag-Al alloys T. B. Massalski and B. Cockayne The effect of plastic deformation on the diffusion of hydrogen in nickel F. D. Walker and M. Markero C. B. Walker and M. Markero S. B. Massalski and B. Cockayne The effect of plastic deformation on the diffusion of hydrogen in nickel H. H. GRIMBER 782 The theory of matrensitic transformations. The generalized lattice invariant shear and the degeneracy of solutions for the cubic to tetragonal transformation. H. H. GRIMBER 782 Letters to the Editor: Existence de plusieurs stades de précipitatio		laire dans le fer	
A. S. Ker, J. C. M. Li and Y. T. Choo. 694 Atzverfahren für Versetzungen in Fe-Ni-Legierungen Discussion of "Orientation of recrystallized grains in strained aluminum single crystals." C. S. Barrett, C. D. Graham, Jr. and J. M. Lommel. Twinning in copper electrodeposits NUMBER 11 The diffusion of xonon in silver Effect of hydrogen on the yielding of mild steel "Superhigh plasticity" of commercial iron under cyclic fluctuations of temperature M. G. LOZINSKY and I. S. SIMEONOVA The effect of quenched-in vacancies on the elastic modulus of aluminum R. C. FOLWEILER and F. R. BROTZEN The attack of solid alloys by liquid metals and salt melts On the theory of self-diffusion in liquid metals The role of vacancies in an unusual anelastic phenomenon Letters to the Editor: A simplified treatment of surface melting On surface roughness The structure of G.P. zones in Al(Ag) alloys The mechanism of crack propagation in ductile metals Studies of copper targets attacked by shaped charges The plasticity of alkali halide crystals NUMBER 12 Lattice parameter and resistivity study of order in the alloys CuAu ₃ The plasticity of alkali halide crystals NUMBER 12 Lattice parameters and zone overlap in solid solutions of lead in magnesium. R. W. W. Mellins A. S. SUSCIBARAJ J. P. Hierti The flect of plastic deformation on the diffusion of hydrogen in nickel Influence de faibles quantités de nickel sur l'oxydation du cuivre Reaction rate and growth forms of reaction product in the system Ag-H ₂ S H. H. GRIDBES The nucleation of nickel whiskers On the theory of martensitic transformations. The generalized lattice invariant shear and the degeneracy of solutions for the cubic to tetragonal transformation N. The effect of plastic deformation on the diffusion of hydrogen in nickel H. H. GRIDBES The nucleation of nickel whiskers On the theory of martensitic transformations. The generalized lattice invariant shear and the degeneracy of solutions for the cubic to tetragonal transformation N. The effect of plastic deformation			691
On the mechanism of sulphurization of copper Atzverfahren für Versetzungen in Fe-Ni-Legierungen Discussion of "Orientation of recrystallized grains in strained aluminum single crystals" C. S. Barrett, C. D. Graham, Jr. and J. M. Lommel. Twinning in copper electrodeposits NUMBER 11 The diffusion of xenon in silver Effect of hydrogen on the yielding of mild steel "Superhigh plasticity" of commercial iron under cyclic fluctuations of temperature Effect of quenched-in vacancies on the elastic modulus of aluminum The effect of quenched-in vacancies on the elastic modulus of aluminum The attack of solid alloys by liquid metals and salt melts On the theory of self-diffusion in liquid metals The role of vacancies in an unusual anclastic phenomenon Eters to the Editor: A simplified treatment of surface melting On surface roughness The structure of G.P. zones in Al(Ag) alloys The structure of G.P. zones in Al(Ag) alloys The structure of G.P. zones in Al(Ag) alloys The plasticity of alkali halide crystals On two dimensional nucleation NUMBER 12 Lattice parameter and resistivity study of order in the alloys CuAu ₁ The lattice spacings and the stability of close-packed hexagonal Cu-Ga, Cu-Ge and Ag-Al alloys The lattice parameters and zone overlap in solid solutions of lead in magnesium C. B. WALKER and M. MAREZIO The effect of plastic deformation on the diffusion of hydrogen in nickel The effect of plastic deformation on the diffusion of hydrogen in nickel The nucleation of nickel whiskers On the theory of martensitic transformations. The generalized lattice invariant shear and the degeneracy of solutions for the cubic to tetragonal transformation Letters to the Editor: Existence de plusieurs stades de précipitation pour les alliages à base de cuivre dureis par le titane J. M. S. WEISLER T. F. BOULLLON EXTENCENS 180 B. W. B. WEISLER T. F. BOULLON EXTENCENS 180 B. W. B. WEISLER T. F. BOULLON EXTENCENS 180 B. J. B. WALKER and M. MAREZIO The defect of plastic deformation of hickel whiskers On the theory of marten			201
Aizverfahren für Versetzungen in Fe-Ni-Légierungen Discussion of "Orientation of recrystallized grains in strained aluminum single crystals." Twinning in copper electrodeposits **NUMBER 11** **Number 10** **Numbe			
Discussion of "Orientation of recrystallized grains in strained aluminum single crystals" C. S. Barrett, C. D. Graham, Jr. and J. M. Lombel. R. C. Barrett, C. D. Graham, Jr. and J. M. Lombel. S. C. Barrett, C. D. Graham, Jr. and J. M. Lombel. R. C. Barrett, C. D. Graham, Jr. and J. M. Lombel. NUMBER 11 The diffusion of xenon in silver Effect of hydrogen on the yielding of mild steel "Superhigh plasticity" of commercial iron under cyclic fluctuations of temperature M. G. Lozinsky and I. S. Simeonova 709 The effect of quenched-in vacancies on the elastic modulus of aluminum R. C. Folweiler and F. R. Brotzen 716 The attack of solid alloys by liquid metals and salt melts On the theory of self-diffusion in liquid metals The role of vacancies in an unusual anclastic phenomenon Letters to the Editor: A simplified treatment of surface melting W. W. W. Mullins 746 On surface roughness M. B. Webb 3 The mechanism of crack propagation in ductile metals Studies of copper targets attacked by shaped charges Studies of copper targets attacked by shaped charges The plasticity of alkali halide crystals On two dimensional nucleation NUMBER 12 Lattice parameter and resistivity study of order in the alloys CuAu ₃ Lattice parameters and zone overlap in solid solutions of lead in magnesium. NUMBER 12 Lattice parameters and zone overlap in solid solutions of lead in magnesium. NUMBER 12 Lattice parameters and zone overlap in solid solutions of lead in magnesium. The effect of plastic deformation on the diffusion of hydrogen in nickel The nucleation of nickel whiskers On the theory of martensitic transformations. The generalized lattice invariant shear and the degeneracy of solutions for the cubic to tetragonal transformation Letters to the Editor: Existence de plusieurs stades de précipitation pour les alliages à base de cuivre dureis par le titane J. Maxence 807 H. B. C. Chamske and G. C. Kuczynski 807 H. B. C. Cran R. S. D. Barrett 809 H. B. O. Barrett 809 H. B. O. Barrett 809 H. B. O. Barrett			
Twinning in copper electrodeposits NUMBER 11 The diffusion of xenon in silver Effect of hydrogen on the yielding of mild steel Superhigh plasticity: 'of commercial iron under cyclic fluctuations of temperature M. G. LOZINSKY and I. S. SIMEONOVA The effect of quenched-in vacancies on the elastic modulus of aluminum R. C. FOLWEILER and F. R. BROTZEN The attack of solid alloys by liquid metals and salt melts On the theory of self-diffusion in liquid metals The role of vacancies in an unusual anclastic phenomenon R. C. FOLWEILER and F. R. BROTZEN The role of vacancies in an unusual anclastic phenomenon R. C. FOLWEILER and C. WAGNER The role of vacancies in an unusual anclastic phenomenon R. C. FOLWEILER and F. R. BROTZEN The role of vacancies in an unusual anclastic phenomenon R. C. FOLWEILER and F. R. BROTZEN The role of vacancies in an unusual anclastic phenomenon R. C. FOLWEILER and F. R. BROTZEN The role of vacancies in an unusual anclastic phenomenon R. C. FOLWEILER and C. WAGNER The role of vacancies in an unusual anclastic phenomenon R. C. FOLWEILER and C. WAGNER The role of vacancies in an unusual anclastic phenomenon R. C. FOLWEILER and C. WAGNER The role of vacancies in an unusual anclastic phenomenon R. C. FOLWEILER and C. WAGNER The role of vacancies in an unusual anclastic phenomenon R. C. FOLWEILER and C. WAGNER The role of vacancies in an unusual anclastic phenomenon R. C. FOLWEILER R. A. SWALIN 736 W. W. W. MULLINS The structure of G.P. zones in Al(Ag) alloys R. A. JACKSON TATA M. B. WEBB 748 N. B. WEBB 748 N. B. WEBB 748 N. B. WEBB 748 N. W. W. MULLINS The hattice parameter and resistivity study of order in the alloys CuAu ₄ The plastic parameters and zone overlap in solid solutions of lead in magnesium NUMBER 12 Lattice parameters and zone overlap in solid solutions of lead in magnesium NUMBER 12 Lattice parameters and zone overlap in solid solutions of lead in magnesium C. B. WALKER and M. MAREZIO T. B. MASSAISKI and B. COCKAYNE T. B. MULLINGER and M. MAREZIO C. B. WALK			037
Twinning in copper electrodeposits NUMBER 11 The diffusion of xenon in silver Fiffect of hydrogen on the yielding of mild steel Superhigh plasticity" of commercial iron under cyclic fluctuations of temperature M. G. Lozinsky and I. S. Simbonova 709 The effect of quenched-in vacancies on the elastic modulus of aluminum R. C. Foldweller and F. R. Brotzen 716 The attack of solid alloys by liquid metals and salt melts On the theory of self-diffusion in liquid metals The role of vacancies in an unusual anelastic phenomenon Letters to the Editor: A simplified treatment of surface melting On surface roughness The structure of G.P. zones in Al(Ag) alloys The mechanism of crack propagation in ductile metals Studies of copper targets attacked by shaped charges The plasticity of alkali halide crystals On two dimensional nucleation NUMBER 12 Lattice parameter and resistivity study of order in the alloys CuAu ₄ P. WRIGHT and K. F. GODDARD The lattice spacings and the stability of close-packed hexagonal Cu-Ga, Cu-Ge and Ag-Al alloys The lattice parameters and zone overlap in solid solutions of lead in magnesium C. B. WALKER and M. MAREZIO Influence de faibles quantités de nickel sur l'oxydation du cuivre Reaction rate and growth forms of reaction product in the system Ag-H ₂ The effect of plastic deformation on the diffusion of hydrogen in nickel H. G. GERP The effect of plastic deformation on the diffusion of hydrogen in nickel Existence de plusieurs stades de précipitation pour les alliages à base de cuivre dureis par le titane. Existence de plusieurs stades de précipitation pour les alliages à base de cuivre dureis par le titane. Existence de plusieurs stades de précipitation pour les alliages à base de cuivre dureis par le titane. Existence de plusieurs stades de précipitation pour les alliages à base de cuivre dureis par le titane. Existence de plusieurs stades de précipitation pour les alliages à base de cuivre dureis par le titane. Existence de plusieurs stades de précipitation pour les alliages à			699
NUMBER 11 The diffusion of xenon in silver Effect of hydrogen on the yielding of mild steel "Superhigh plasticity" of commercial iron under cyclic fluctuations of temperature M. G. Lozinsky and I. S. Simeonova The effect of quenched-in vacancies on the elastic modulus of aluminum R. C. Folweller and F. R. Brotzen 769 The attack of solid alloys by liquid metals and salt melts On the theory of self-diffusion in liquid metals The role of vacancies in an unusual anclastic phenomenon R. C. Folweller and C. Wacker 722 On the theory of self-diffusion in liquid metals The role of vacancies in an unusual anclastic phenomenon R. C. Folweller and C. Wacker 722 On the theory of self-diffusion in liquid metals The role of vacancies in an unusual anclastic phenomenon R. A. Jackson 747 A. Sumulus 746 The structure of G.P. zones in Al(Ag) alloys The structure of G.P. zones in Al(Ag) alloys The structure of G.P. zones in Al(Ag) alloys The plasticity of alkali halide crystals On two dimensional nucleation NUMBER 12 Lattice parameter and resistivity study of order in the alloys CuAu ₃ The plasticity of alkali halide crystals On two dimensional nucleation NUMBER 12 Lattice parameters and zone overlap in solid solutions of lead in magnesium T. B. Massalski and B. Cockayne			
Effect of hydrogen on the yielding of mild steel "Superhigh plasticity" of commercial iron under cyclic fluctuations of temperature M. G. Lozinsky and I. S. Simeonova M. G. Lozinsky and I. S. Simeonova M. G. Lozinsky and I. S. Simeonova The effect of quenched-in vacancies on the clastic modulus of aluminum R. C. Folkweiler and F. R. Brotzen The attack of solid alloys by liquid metals and salt melts On the theory of self-diffusion in liquid metals The role of vacancies in an unusual anelastic phenomenon Letters to the Editor: A simplified treatment of surface melting On surface roughnes The structure of G.P. zones in Al(Ag) alloys The structure of G.P. zones in Al(Ag) alloys The structure of G.P. zones in Al(Ag) alloys The metal-anism of crack propagation in ductile metals Studies of copper targets attacked by shaped charges The plasticity of alkali halide crystals On two dimensional nucleation NUMBER 12 Lattice parameter and resistivity study of order in the alloys CuAu ₄ The lattice spacings and the stability of close-packed hexagonal Cu-Ga. Cu-Ge and Ag-Al alloys T. B. Massatiski and B. Cockayne T. B. Walker and M. Marezio T. B. Walker and M. Marezio T. B. Walker and M. Marezio T. B. Walk	Think in copper the control of the c		
Effect of hydrogen on the yielding of mild steel "Superhigh plasticity" of commercial iron under cyclic fluctuations of temperature M. G. Lozinsky and I. S. Simeonova M. G. Lozinsky and I. S. Simeonova M. G. Lozinsky and I. S. Simeonova The effect of quenched-in vacancies on the clastic modulus of aluminum R. C. Folkweiler and F. R. Brotzen The attack of solid alloys by liquid metals and salt melts On the theory of self-diffusion in liquid metals The role of vacancies in an unusual anelastic phenomenon Letters to the Editor: A simplified treatment of surface melting On surface roughnes The structure of G.P. zones in Al(Ag) alloys The structure of G.P. zones in Al(Ag) alloys The structure of G.P. zones in Al(Ag) alloys The metal-anism of crack propagation in ductile metals Studies of copper targets attacked by shaped charges The plasticity of alkali halide crystals On two dimensional nucleation NUMBER 12 Lattice parameter and resistivity study of order in the alloys CuAu ₄ The lattice spacings and the stability of close-packed hexagonal Cu-Ga. Cu-Ge and Ag-Al alloys T. B. Massatiski and B. Cockayne T. B. Walker and M. Marezio T. B. Walker and M. Marezio T. B. Walker and M. Marezio T. B. Walk			
Effect of hydrogen on the yielding of mild steel "Superhigh plasticity" of commercial iron under cyclic fluctuations of temperature M. G. LOZINSKY and I. S. SIMEONOVA 709 The effect of quenched-in vacancies on the clastic modulus of aluminum R. C. FOLWELER and F. R. BROTZEN 716 The attack of solid alloys by liquid metals and salt melts On the theory of self-diffusion in liquid metals The role of vacancies in an unusual anclastic phenomenon R. C. FOLWELER and F. R. BROTZEN 716 The attack of solid alloys by liquid metals and salt melts On the theory of self-diffusion in liquid metals The role of vacancies in an unusual anclastic phenomenon R. C. FOLWELER and F. R. BROTZEN 716 The attack of solid alloys by liquid metals and salt melts R. A. SWALIN 736 The role of vacancies in an unusual anclastic phenomenon R. C. FOLWELER and F. R. BROTZEN 716 R. A. SWALIN 737 The role of vacancies in an unusual anclastic phenomenon R. C. BOLWELER and F. R. BROTZEN 716 R. A. SWALIN 736 R. A. SWALIN 741 R. A. SWALIN 741 R. A. SWALIN 741 R. A. SWALIN 742 R. A. SWALIN 741 R. A. SWALIN 742 R. A. SWALIN 743 R. A. SWALIN 744 R. A. SWALIN 745 R. A. JACKSON 747 R. A. SOLVDRARA 747 R. A. SOLVDRARA 747 R. A. SOLVDRARA 748 R. C. P. WRIGHT and K. F. GODDARD 747 R. B. MASSALSKI and B. COCKAYNE 748 R. C. C. BRODARD 748 R. A. SWALIN 749 R. C. BODDARD 749 R. WRIGHT and K. F. GODDARD 740 R. B. WALKER and M. MAREJIO 740 R. B. WALKER and M. MAREJIO 740 R. B. WALKER and M. MAREJIO 741 R. B. WALKER and M. MAREJIO 744 R. B. WELLIN 745 R. C. D. BRIEN 746 R. C. D. DAMSK and G. J. D. DENS 741 R. C. D. BRIEN 746 R. C. D. DAMSK and G. J. D. DENS 746 R. C. D. DAMSK and G. J. D. DENS 746 R. C. D. DAMSK and G. J. D. DENS 746 R. C. D. DAMSK and G. J		* ** **	
"Superhigh plasticity" of commercial iron under cyclic fluctuations of temperature M. G. Lozinsky and I. S. Simeonova M. G. Lozinsky and I. S. Simeonova M. G. Lozinsky and I. S. Simeonova The effect of quenched-in vacancies on the elastic modulus of aluminum R. C. Folweller and F. R. Broyzex The role of vacancies in in liquid metals On the theory of self-diffusion in liquid metals The role of vacancies in an unusual anelastic phenomenon Letters to the Editor: A simplified treatment of surface melting On surface roughness The structure of G.P. zones in Al(Ag) alloys The structure of G.P. zones in Al(Ag) alloys The metaphanism of crack propagation in ductile metals Studies of copper targets attacked by shaped charges The plasticity of alkali halide crystals On two dimensional nucleation NUMBER 12 Lattice parameter and resistivity study of order in the alloys CuAu ₄ The lattice spacings and the stability of close-packed hexagonal Cu-Ga, Cu-Ga and Ag-Al alloys The lattice parameters and zone overlap in solid solutions of lead in magnesium NUMBER 12 Lattice parameters and zone overlap in solid solutions of lead in magnesium C. B. Walker and M. Marezio F. BOULLON et J. Stevens The effect of plastic deformation on the diffusion of hydrogen in nickel The nucleation of nickel whiskers On the theory of martensitic transformations. The generalized lattice invariant shear and the degeneracy of solutions for the cubic to tetragonal transformation X-ray study of the kinetics of ordering on AuCu J. L. O'BRIEN and G. C. KUCZYNSKI BOURD RADIO PROPERTIES A. ORDAN BURNENC R. A. ORDAN R. A. ORDAN SON The growth of precipitates from solid solutions Bismuth at low temperature C. B. ARRISSON A. SUCINSEN R. A. C. DAMASK and G. J. DIENS M. H. RICHMAN, D. A. THOMAS and M. COHEN M. H. RICHMAN, D. A. THOMAS and M. C. P. LEISSCHER M. H. RICHMAN, D. A. THOMAS and G. J. DIENS M. H. RICHMAN, D. A. THOMAS and G. J. DIENS The production of vacancy clusters during cold work A. C. DAMASK and G. J. DI			
The effect of quenched-in vacancies on the elastic modulus of aluminum. The effect of quenched-in vacancies on the elastic modulus of aluminum. R. C. FOLWELER and F. R. BROTZEN. The track of solid alloys by liquid metals and salt melts. The role of vacancies in an unusual anelastic phenomenon. R. A. SWALIN. The role of vacancies in an unusual anelastic phenomenon. Esters to the Editor: A simplified treatment of surface melting. On surface roughness. The structure of G.P. zones in Al(Ag) alloys. The mechanism of crack propagation in ductile metals. Studies of copper targets attacked by shaped charges. The plasticity of alkali halide crystals. On two dimensional nucleation. NUMBER 12 Lattice parameter and resistivity study of order in the alloys CuAu ₃ . The lattice spacings and the stability of close-packed hexagonal Cu-Ga. Cu-Ge and Ag-Al alloys. The lattice parameters and zone overlap in solid solutions of lead in magnesium. Lattice parameters and zone overlap in solid solutions of lead in magnesium. Lattice parameters and zone overlap in solid solutions of lead in magnesium. C. B. WALKER and M. MAREZIO. Lattice parameters and zone overlap in solid solutions of lead in magnesium. C. B. WALKER and M. MAREZIO. The effect of plastic deformation on the diffusion of hydrogen in nickel. The effect of plastic deformation on the diffusion of hydrogen in nickel. The theory of martensitic transformations. The generalized lattice invariant shear and the degeneracy of solutions for the eubic to tetragonal transformation. Existence de plusicurs stades de précipitation pour les alliages à base de cuivre durcis par le titane. Existence de plusicurs stades de précipitation pour les alliages à base de cuivre durcis par le titane. Existence de plusicurs stades de précipitation pour les alliages à base de cuivre durcis par le titane. Existence de plusicurs stades de précipitation pour les alliages à base de cuivre durcis par le titane. Existence de plusicurs stades de précipitation pour les alliage			100
The effect of quenched-in vacancies on the elastic modulus of aluminum The attack of solid alloys by liquid metals and salt melts On the theory of self-diffusion in liquid metals The role of vacancies in an unusual anelastic phenomenon R. C. Folweller and F. R. Brotzen R. C. J. D. Harrison and C. Wacner R. C. J. D. Harrison and C. Wacner R. C. J. D. Harrison and C. Wacner R. C. Self-diffusion in liquid metals The role of vacancies in an unusual anelastic phenomenon R. C. Folweller and F. R. Brotzen R. C. J. D. Harrison and C. Wacner R. C. J. Wacner R. C. J. D. Harrison and C. Wacner R. A. Soundaria R. C. J. P. William R. C. L. R. J. J. L. O'Britan and C. Wacner R. C. G. R. Bassert R. C. G. Massalaxia and B. Cockayne R. R. C. Charlison R. A. Soundaria R. C. J. Wacner R. C. J. Wacner R. C. J. Wacner R. C. S. Barrison R. C. J. Wacner R. L. Ceth R. J. Wacner R. C. J. Wacner R. L. Ceth R. J. Wacner R. L. Ceth R. J. Wacner R. R. C. Ceth R. L. Fleischer R. R. Eleischer R. L. Fleischer R. R. L. Eleischer R. L. C. Damask and M. Cohen R. L. Fleischer R. L. C. Damask and G. C. Charasis and R. C. Chara			709
The attack of solid alloys by liquid metals and salt melts On the theory of self-diffusion in liquid metals The role of vacancies in an unusual anelastic phenomenon R. A. SWALIN TABLET STATE A simplified treatment of surface melting On surface roughness The structure of G.P. zones in Al(Ag) alloys The mechanism of crack propagation in ductile metals Studies of copper targets attacked by shaped charges The plasticity of alkali halide crystals On two dimensional nucleation NUMBER 12 Lattice parameter and resistivity study of order in the alloys CuAu ₃ The lattice spacings and the stability of close-packed hexagonal Cu-Ga, Cu-Ge and Ag-Al alloys T.B. MASSALSKI and B. COCKAYNE T.B. MASSALSKI and B. COCK		LOZINSKI and I. S. SIMEONOVA	100
The attack of solid alloys by liquid metals and salt melts On the theory of self-diffusion in liquid metals The role of vacancies in an unusual anelastic phenomenon Letters to the Editor: A simplified treatment of surface melting On surface roughness The structure of G.P. zones in Al(Ag) alloys The mechanism of crack propagation in ductile metals Studies of copper targets attacked by shaped charges The plasticity of alkali halide crystals On two dimensional nucleation NUMBER 12 Lattice parameter and resistivity study of order in the alloys CuAu ₃ The parameters and zone overlap in solid solutions of lead in magnesium C. B. WALKER and M. MAREZIO The effect of plastic deformation on the diffusion of hydrogen in nickel The nucleation of nickel whiskers On the theory of martensitic transformations. The generalized lattice invariant shear and the degeneracy of solutions for the cubic to tetragonal transformation Letters to the Editor: Existence de plusieurs stades de précipitation pour les alliages à base de cuivre dureis par le titane The temperature dependence of surface free energy The role of austenitizing temperature in the nucleation of pearlite M. H. RICHMAN, D. A. THOMAS and M. COHEN M. F. Edischere 81 M. F. RICHMES 81 M. S. Walkere 81 M. S. WECHALER M. H. RICHMAN, D. A. THOMAS and M. COHEN M. F. HEISICHER M. H. RICHMAN, D. A. THOMAS and M. COHEN M. F. HEISICHER M. H. FLEISICHER M. H. FLEISICHER M. H. RICHMAN, D. A. C. DAMASK and G. J. DIENES M. S. BERRY Total Content of the color of the flow stress of an age-hardened alloy On the orientation dependence of surface free energy The role of austenitizing temperature in the nucleation of pearlite M. H. RICHMAN, D. A. THOMAS and M. COHEN M. F. HEISICHER M. H. RICHMAN, D. A. THOMAS and M. COHEN M. F. HEISICHER M. H. RICHMAN, D. A. C. DAMASK and G. J. DIENES M. S. BERRY M. S. DEFERS M. S. BERRY Total Contents of the color of surface free energy M. S. C. DAMASK and G. J. DIENES M. S. BERRY The role of austenitizing temperature coloper M. C. DAMASK and G. J. D		OLWEILER and F. R. BROTZEN	716
On the theory of self-diffusion in liquid metals The role of vacancies in an unusual anelastic phenomenon R. A. Swalin 736 B. S. Berry 741 Letters to the Editor: A simplified treatment of surface melting On surface roughness The structure of G.P. zones in Al(Ag) alloys The mechanism of crack propagation in ductile metals Studies of copper targets attacked by shaped charges The plasticity of alkali halide crystals On two dimensional nucleation NUMBER 12 Lattice parameter and resistivity study of order in the alloys CuAu ₃ The lattice spacings and the stability of close-packed hexagonal Cu-Ga, Cu-Ge and Ag-Al alloys T. B. Massalski and B. Cockayne T. B. Massa			
Letters to the Editor: A simplified treatment of surface melting On surface roughness The structure of G.P. zones in Al(Ag) alloys The mechanism of crack propagation in ductile metals Studies of copper targets attacked by shaped charges The planticity of Idaki halide crystals On two dimensional nucleation NUMBER 12 Lattice parameter and resistivity study of order in the alloys CuAu ₃ The lattice spacings and the stability of close-packed hexagonal Cu-Ga, Cu-Ge and Ag-Al alloys T.B. Massalski and B. Cockayne T.B. The deependence of the flow stress of an age-hardened alloy On the orientation dependence of surface free energy T.B. Cocker and Ag-Al alloys T.B. Massalski and B. Cockayne T.B. Cocker and Ag-Al al			
A simplified treatment of surface melting On surface roughness The structure of G.P. zones in Al(Ag) alloys The structure of G.P. zones in Al(Ag) alloys The mechanism of crack propagation in ductile metals Studies of copper targets attacked by shaped charges The plasticity of alkali halide crystals On two dimensional nucleation NUMBER 12 Lattice parameter and resistivity study of order in the alloys CuAu ₃ The lattice spacings and the stability of close-packed hexagonal Cu-Ga, Cu-Ge and Ag-Al alloys T.B. MASSALSKI and B. COCKAYNE T.B. MASSALSKI and B. COCKAYNE T.B. MASSALSKI and B. COCKAYNE T.B. MASSALSKI and M. MAREZIO F. BOULLON et J. STEVENS T.B. CL. WALKER and M. MAREZIO F. BOULLON et J. STEVENS T.B. MASSALSKI and B. COCKAYNE T.B. CL. WALKER and M. MAREZIO T.B. C. B. WALKER T.B. C. C. B. WALKER T.B. C. C. C. T.		B. S. Berry	741
A simplified treatment of surface melting On surface roughness The structure of G.P. zones in Al(Ag) alloys The structure of G.P. zones in Al(Ag) alloys The mechanism of crack propagation in ductile metals Studies of copper targets attacked by shaped charges The plasticity of alkali halide crystals On two dimensional nucleation NUMBER 12 Lattice parameter and resistivity study of order in the alloys CuAu ₃ The lattice spacings and the stability of close-packed hexagonal Cu-Ga, Cu-Ge and Ag-Al alloys T.B. MASSALSKI and B. COCKAYNE T.B. MASSALSKI and B. COCKAYNE T.B. MASSALSKI and B. COCKAYNE T.B. MASSALSKI and M. MAREZIO F. BOULLON et J. STEVENS T.B. CL. WALKER and M. MAREZIO F. BOULLON et J. STEVENS T.B. MASSALSKI and B. COCKAYNE T.B. CL. WALKER and M. MAREZIO T.B. C. B. WALKER T.B. C. C. B. WALKER T.B. C. C. C. T.	I t- the Editor		
The structure of G.P. zones in Al(Ag) alloys The mechanism of crack propagation in ductile metals Studies of copper targets attacked by shaped charges The plasticity of alkali halide crystals On two dimensional nucleation NUMBER 12 Lattice parameter and resistivity study of order in the alloys CuAu ₃ The plasticity of alkali halide crystals On two dimensional nucleation NUMBER 12 Lattice parameter and resistivity study of order in the alloys CuAu ₃ The lattice spacings and the stability of close-packed hexagonal Cu-Ga, Cu-Ge and Ag-Al alloys T. B. Massalski and B. Cockayne T. B. Massalski and B. Cockayne T. B. Walker and M. Marezio			
The structure of G.P. zones in Al(Ag) alloys The mechanism of crack propagation in ductile metals Studies of copper targets attacked by shaped charges The plasticity of alkali halide crystals On two dimensional nucleation NUMBER 12 Lattice parameter and resistivity study of order in the alloys CuAu ₃ The lattice spacings and the stability of close-packed hexagonal Cu-Ga, Cu-Ge and Ag-Al alloys The lattice spacings and the stability of close-packed hexagonal Cu-Ga, Cu-Ge and Ag-Al alloys The lattice parameters and zone overlap in solid solutions of lead in magnesium C. B. WALKER and M. MAREZIO Influence de faibles quantités de nickel sur l'oxydation du cuivre Reaction rate and growth forms of reaction product in the system Ag-H ₂ S Reaction rate and growth forms of reaction product in the system Ag-H ₂ S The nucleation of nickel whiskers Cn. the theory of martensitic transformations. The generalized lattice invariant shear and the degeneracy of solutions for the cubic to tetragonal transformation M. S. Wechsler S. T. B. MASSALSKI and B. COCKAYNE The effect of plastic deformation on the diffusion of hydrogen in nickel H. FISCHMEISTER et J. DROIT The effect of plastic deformation on the diffusion of hydrogen in nickel The nucleation of nickel whiskers R. E. Cech To the theory of martensitic transformations. The generalized lattice invariant shear and the degeneracy of solutions for the cubic to tetragonal transformation M. S. Wechsler The production of liquid Na-Cs alloys The growth of precipitates from solid solutions Bismuth at low temperature The temperature dependence of the flow stress of an age-hardened alloy On the orientation dependence of surface free energy The role of austenitizing temperature in the nucleation of pearlite M. H. RICHMAN, D. A. THOMAS and M. COHEN M. H. RICHMAN, D. A. THOMAS and M. COHEN M. H. RICHMAN, D. A. C. DAMASK and G. J. DENES 181			
The mechanism of crack propagation in ductile metals Studies of copper targets attacked by shaped charges attacked by shaped charges and copper targets attacked by shaped charges and place the plasticity of alkali halide crystals and the degeneration on two dimensional nucleation and place the parameter and resistivity study of order in the alloys CuAu ₃ P. Wright and K. F. Goddard The lattice parameter and resistivity study of order in the alloys CuAu ₃ P. Wright and K. F. Goddard The lattice parameters and zone overlap in solid solutions of lead in magnesium Influence de faibles quantités de nickel sur l'oxydation du cuivre Reaction rate and growth forms of reaction product in the system Ag-H ₂ S The effect of plastic deformation on the diffusion of hydrogen in nickel H. H. Grimes R. E. Cech R. E.			
Studies of copper targets attacked by shaped charges The plasticity of alkali halide crystals On two dimensional nucleation NUMBER 12 Lattice parameter and resistivity study of order in the alloys CuAu ₃ The lattice spacings and the stability of close-packed hexagonal Cu-Ga, Cu-Ge and Ag-Al alloys T. B. Massalski and B. Cockayne T. B. Massalski and B. Cockayne T. B. Massalski and B. Cockayne T. B. Mussalski and B. Cockayne T. B. Musler T. B. Mussalski and B. Cockayne T. B. Musler T. D. Boutleon et J. Stevens T. B. Musler T. B. Musler T. D. William Musler T. D. William M. Musler T. D. Musler T. C. D. Musler T. C. D.			
The plasticity of alkali halide crystals On two dimensional nucleation NUMBER 12 Lattice parameter and resistivity study of order in the alloys CuAu ₃ P. WRIGHT and K. F. GODDARD T. B. MASSALSKI and B. COCKAYNE T. B. WALKER and M. MAREZIO F. BOUILLON et J. STEVENS T. B. WALKER and M. MAREZIO F. BOUILLON et J. STEVENS T. B. WALKER and M. MAREZIO F. BOUILLON et J. STEVENS T. B. WALKER and M. MAREZIO F. BOUILLON et J. STEVENS T. B. WILLIAM T. H. H. GRIMES R. E. C. Ed. T. H. H. GRIMES R. E. C. Ed. T. H. H. GRIMES R. E. C. Ed. T.			
NUMBER 12 Lattice parameter and resistivity study of order in the alloys CuAu ₃ P. Wright and K. F. Goddard The lattice spacings and the stability of close-packed hexagonal Cu-Ga, Cu-Ge and Ag-Al alloys T. B. Massalski and B. Cockayne 762 Lattice parameters and zone overlap in solid solutions of lead in magnesium C. B. Walker and M. Marezio T. B. Wassalski and B. Cockayne 762 Lattice parameters and zone overlap in solid solutions of lead in magnesium C. B. Walker and M. Marezio T. B. Wassalski and B. Cockayne 762 Lattice parameters and zone overlap in solid solutions of lead in magnesium C. B. Walker and M. Marezio 769 Influence de faibles quantités de nickel sur l'oxydation du cuivre Reaction rate and growth forms of reaction product in the system Ag-H ₂ S H. Fischmeister et J. Droit 777 The effect of plastic deformation on the diffusion of hydrogen in nickel H. H. Grimss 782 The nucleation of nickel whiskers R. E. Cech 787 On the theory of martensitic transformations. The generalized lattice invariant shear and the degeneracy of solutions for the cubic to tetragonal transformation M. S. Wechsler 793 X-ray study of the kinetics of ordering on AuCu J. L. O'Brien and G. C. Kuczynski 803 Letters to the Editor: Existence de plusieurs stades de précipitation pour les alliages à base de cuivre durcis par le titane J. Burker 807 Heats of formation of liquid Na-Cs alloys R. A. Oriansi 808 The growth of precipitates from solid solutions J. Burker 809 Bismuth at low temperature C. S. Barrett 810 The temperature dependence of the flow stress of an age-hardened alloy A. Kelly 811 On the orientation dependence of surface free energy N. A. Gjostein 812 The role of austenitizing temperature in the nucleation of pearlite M. H. Richman, D. A. Thomas and M. Cohen 814 Dislocation barriers and cross slip W. F. Hosford and R. L. Fleischer 817 The production of vacancy clusters during cold work A. C. Damask and G. J. Diexes 818			
NUMBER 12 Lattice parameter and resistivity study of order in the alloys CuAu ₃ P. Wright and K. F. Goddard 757 The lattice spacings and the stability of close-packed hexagonal Cu-Ga, Cu-Ge and Ag-Al alloys T. B. Massalski and B. Cockayne 762 Lattice parameters and zone overlap in solid solutions of lead in magnesium C. B. Walker and M. Marezio 769 Influence de faibles quantités de nickel sur l'oxydation du cuivre Reaction rate and growth forms of reaction product in the system Ag-H ₂ S H. Fischmeister et J. Droit 777 The effect of plastic deformation on the diffusion of hydrogen in nickel H. H. Grimes The nucleation of nickel whiskers The nucleation of nickel whiskers The nucleation of nickel whiskers The teory of martensitic transformations. The generalized lattice invariant shear and the degeneracy of solutions for the cubic to tetragonal transformation M. S. Wechsler X-ray study of the kinetics of ordering on AuCu J. L. O'Brien and G. C. Kuczynski 803 Letters to the Editor: Existence de plusieurs stades de précipitation pour les alliages à base de cuivre durcis par le titane J. Manenc Heats of formation of liquid Na-Cs alloys T. B. Massalski and B. Cockayne 762 Boy A. C. B. Walker and M. Marezio 769 The production of vacancy clusters of na age-hardened alloy A. Kelly 803 M. H. Richman, D. A. Thomas and M. Cohen 814 Absolute grain boundary energies in copper The production of vacancy clusters during cold work A. C. Damask and G. J. Dienes 818			
Lattice parameter and resistivity study of order in the alloys CuAu ₃ P. Wright and K. F. Goddard 757 The lattice spacings and the stability of close-packed hexagonal Cu-Ga, Cu-Ge and Ag-Al alloys T. B. Massalski and B. Cockayne 762 Lattice parameters and zone overlap in solid solutions of lead in magnesium C. B. Walker and M. Marezio 769 Influence de faibles quantités de nickel sur l'oxydation du cuivre Reaction rate and growth forms of reaction product in the system Ag-H ₂ S H. Fischmeister et J. Droit 777 The effect of plastic deformation on the diffusion of hydrogen in nickel H. H. Grimes 782 The nucleation of nickel whiskers On the theory of martensitic transformations. The generalized lattice invariant shear and the degeneracy of solutions for the cubic to tetragonal transformation M. S. Wechsler 793 X-ray study of the kinetics of ordering on AuCu J. L. O'Brien and G. C. Kuczynski 803 Letters to the Editor: Existence de plusieurs stades de précipitation pour les alliages à base de cuivre durcis par le titane Heats of formation of liquid Na-Cs alloys The growth of precipitates from solid solutions Bismuth at low temperature The temperature dependence of the flow stress of an age-hardened alloy On the orientation dependence of surface free energy The role of austenitizing temperature in the nucleation of pearlite M. H. Richman, D. A. Thomas and M. Cohen 814 Dislocation barriers and cross slip W. F. Hosford and R. L. Fleischer 817 The production of vacancy clusters during cold work A. C. Damask and G. J. Dienses 818			
The lattice spacings and the stability of close-packed hexagonal Cu–Ga, Cu–Ge and Ag–Al alloys T. B. Massalski and B. Cockayne The B. Malker and M. Marezio The F. Bouillon et J. Stevens The growth forms of reaction product in the system Ag–H ₂ S The role of plastic deformation on the diffusion of hydrogen in nickel The space of plastic deformation of hydrogen in nickel The space of plastic deformation on the diffusion of hydrogen in nickel The space of plastic deformation on the diffusion of hydrogen in nickel The space of plastic deformation on the diffusion of hydrogen in nickel The space of plastic deformation on the diffusion of hydrogen in nickel The space of plastic deformation on the diffusion of hydrogen in nickel The space of plastic deformation on the diffusion of hydrogen in nickel The space of plastic deformation on the diffusion of hydrogen in nickel The space of plastic deformation on the defendence The H. H. Grimes The Boulllon et J. Droit The space of plastic deformation on the defendence The Boulllon et J. Droit The space of plastic deformation on the defendence The H. H. Grimes The B	NUMBER 12		
The lattice spacings and the stability of close-packed hexagonal Cu–Ga, Cu–Ge and Ag–Al alloys T. B. Massalski and B. Cockayne The B. Malker and M. Marezio The F. Bouillon et J. Stevens The growth forms of reaction product in the system Ag–H ₂ S The role of plastic deformation on the diffusion of hydrogen in nickel The space of plastic deformation of hydrogen in nickel The space of plastic deformation on the diffusion of hydrogen in nickel The space of plastic deformation on the diffusion of hydrogen in nickel The space of plastic deformation on the diffusion of hydrogen in nickel The space of plastic deformation on the diffusion of hydrogen in nickel The space of plastic deformation on the diffusion of hydrogen in nickel The space of plastic deformation on the diffusion of hydrogen in nickel The space of plastic deformation on the diffusion of hydrogen in nickel The space of plastic deformation on the defendence The H. H. Grimes The Boulllon et J. Droit The space of plastic deformation on the defendence The Boulllon et J. Droit The space of plastic deformation on the defendence The H. H. Grimes The B	Lattice parameter and resistivity study of order in the alloys CuAu.	P. WRIGHT and K. F. GODDARD	757
Lattice parameters and zone overlap in solid solutions of lead in magnesium C. B. Walker and M. Marezio The limited and growth forms of reaction product in the system Ag—H ₂ S H. Fischmeister et J. Droit The effect of plastic deformation on the diffusion of hydrogen in nickel The nucleation of nickel whiskers The nucleation of nickel whiskers The nucleation of nickel whiskers The effect of plastic deformation on the diffusion of hydrogen in nickel The nucleation of nickel whiskers The nucleation of nickel whiskers The nucleation of nickel whiskers The effect of plastic deformation on the diffusion of hydrogen in nickel The nucleation of nickel whiskers The nucleation of nickel whiskers The growth of the cubic to tetragonal transformation The generalized lattice invariant shear and the degeneracy of solutions for the cubic to tetragonal transformation The generalized lattice invariant shear and the degeneracy of solutions of the cubic to tetragonal transformation The generalized lattice invariant shear and the degeneracy of solutions of the cubic to tetragonal transformation The generalized lattice invariant shear and the degeneracy of solutions of the cubic to tetragonal transformation The generalized lattice invariant shear and the degeneracy of solutions of the cubic to tetragonal transformation The generalized lattice invariant shear and the degeneracy of solutions of the cubic to tetragonal transformation The generalized lattice invariant shear and the degeneracy of solutions of the cubic to tetragonal transformation The generalized lattice invariant shear and the degeneracy of solutions for the cubic transformation The generalized lattice invariant shear and the degeneracy of solutions for the cubic transformation The generalized lattice invariant shear and the degeneracy of solutions for the cubic transformation The generalized lattice invariant shear and the degeneracy of solutions for the cubic transformation The generalized lattice invariant shear and the degeneracy The formation of lattice invariant			
Influence de faibles quantités de nickel sur l'oxydation du cuivre Reaction rate and growth forms of reaction product in the system Ag-H ₂ S H. FISCHMEISTER et J. DROIT The effect of plastic deformation on the diffusion of hydrogen in nickel The nucleation of nickel whiskers On the theory of martensitic transformations. The generalized lattice invariant shear and the degeneracy of solutions for the cubic to tetragonal transformation M. S. Wechsler 793 X-ray study of the kinetics of ordering on AuCu Letters to the Editor: Existence de plusieurs stades de précipitation pour les alliages à base de cuivre durcis par le titane J. Manenc Heats of formation of liquid Na-Cs alloys The growth of precipitates from solid solutions Bismuth at low temperature The temperature dependence of the flow stress of an age-hardened alloy On the orientation dependence of surface free energy The role of austenitizing temperature in the nucleation of pearlite M. H. RICHMAN, D. A. THOMAS and M. COHEN W. F. HOSFORD and R. L. FLEISCHER BIG M. H. FISCHMEISTER et J. DROIT 777 H. FISCHMEISTER et J. DROIT 778 H. FISCHMEISTER et J. DROIT 777 H. H. GRIMES R. E. CECH R. E. CECH R. J. DROIT 777 R. D. C. B. WALKER and M. MAREZIO 769 F. BOUILLON et J. STEVENS 782 H. FISCHMEISTER et J. DROIT 777 782 H. FISCHMEISTER et J. DROIT 782 H. H. GRIMES R. C. E. Malen 178 189 180 181 181 181 181 181 181 181 181 181			762
Influence de faibles quantités de nickel sur l'oxydation du cuivre Reaction rate and growth forms of reaction product in the system Ag-H ₂ S H. FISCHMEISTER et J. DROIT The effect of plastic deformation on the diffusion of hydrogen in nickel The nucleation of nickel whiskers On the theory of martensitic transformations. The generalized lattice invariant shear and the degeneracy of solutions for the cubic to tetragonal transformation X-ray study of the kinetics of ordering on AuCu Letters to the Editor: Existence de plusieurs stades de précipitation pour les alliages à base de cuivre durcis par le titane Heats of formation of liquid Na-Cs alloys The growth of precipitates from solid solutions Bismuth at low temperature The temperature dependence of the flow stress of an age-hardened alloy On the orientation dependence of surface free energy The role of austenitizing temperature in the nucleation of pearlite M. H. RICHMAN, D. A. THOMAS and M. COHEN W. F. HOSFORD and R. L. FLEISCHER A. C. DAMASK and G. J. DIENES 818	Lattice parameters and zone overlap in solid solutions of lead in magnesiur	n	
Reaction rate and growth forms of reaction product in the system Ag-H ₂ S H. FISCHMEISTER et J. DROIT The effect of plastic deformation on the diffusion of hydrogen in nickel The nucleation of nickel whiskers On the theory of martensitic transformations. The generalized lattice invariant shear and the degeneracy of solutions for the cubic to tetragonal transformation M. S. Wechsler The action of the kinetics of ordering on AuCu Letters to the Editor: Existence de plusieurs stades de précipitation pour les alliages à base de cuivre durcis par le titane Letters of formation of liquid Na-Cs alloys The growth of precipitates from solid solutions The temperature dependence of the flow stress of an age-hardened alloy On the orientation dependence of surface free energy The role of austenitizing temperature in the nucleation of pearlite M. H. RICHMAN, D. A. THOMAS and M. COHEN W. F. HOSFORD and R. L. FLEISCHER Absolute grain boundary energies in copper The production of vacancy clusters during cold work A. C. Damask and G. J. DIENES 818			
The effect of plastic deformation on the diffusion of hydrogen in nickel The nucleation of nickel whiskers On the theory of martensitic transformations. The generalized lattice invariant shear and the degeneracy of solutions for the cubic to tetragonal transformation X-ray study of the kinetics of ordering on AuCu Letters to the Editor: Existence de plusieurs stades de précipitation pour les alliages à base de cuivre durcis par le titane Letters to the Editor: Existence de plusieurs stades de précipitation pour les alliages à base de cuivre durcis par le titane J. Mannenc J. Mannenc R. A. Oriani Bismuth at low temperature The temperature dependence of the flow stress of an age-hardened alloy On the orientation dependence of surface free energy The role of austenitizing temperature in the nucleation of pearlite M. H. Richman, D. A. Thomas and M. Cohen M. F. Hosford and R. L. Fleischer A. C. Damask and G. J. Diexes			774
The effect of plastic deformation on the diffusion of hydrogen in nickel The nucleation of nickel whiskers On the theory of martensitic transformations. The generalized lattice invariant shear and the degeneracy of solutions for the cubic to tetragonal transformation M. S. Wechsler 793 X-ray study of the kinetics of ordering on AuCu J. L. O'Brien and G. C. Kuczynski 803 Letters to the Editor: Existence de plusieurs stades de précipitation pour les alliages à base de cuivre durcis par le titane J. Manenc J. Manenc R. A. Orlansi 807 Heats of formation of liquid Na-Cs alloys The growth of precipitates from solid solutions Bismuth at low temperature The temperature dependence of the flow stress of an age-hardened alloy On the orientation dependence of surface free energy The role of austenitizing temperature in the nucleation of pearlite M. H. Richman, D. A. Thomas and M. Cohen Dislocation barriers and cross slip Absolute grain boundary energies in copper R. L. Fleischer R. Bernard R. E. Cech R. E. Fleischer R. L. Fleischer R. E. Fleischer R. E. Cech R. E. Gen R. E. Fleischer R	Reaction rate and growth forms of reaction product in the system Ag-H ₂ S		
The nucleation of nickel whiskers On the theory of martensitic transformations. The generalized lattice invariant shear and the degeneracy of solutions for the cubic to tetragonal transformation X-ray study of the kinetics of ordering on AuCu Letters to the Editor: Existence de plusieurs stades de précipitation pour les alliages à base de cuivre durcis par le titane J. Manenc J. Manenc J. Manenc J. Manenc R. A. Oriani 803 Letters to the Editor: Existence de plusieurs stades de précipitation pour les alliages à base de cuivre durcis par le titane J. Manenc J. Manenc R. A. Oriani 803 Letters to the Editor: Existence de plusieurs stades de précipitation pour les alliages à base de cuivre durcis par le titane J. Manenc R. A. Oriani 803 Letters to the Editor: Existence de plusieurs stades de précipitation pour les alliages à base de cuivre durcis par le titane J. Manenc R. A. Oriani 806 R. A. Oriani 807 R. A. Oriani 808 Bismuth at low temperature The temperature dependence of the flow stress of an age-hardened alloy On the orientation dependence of surface free energy The role of austenitizing temperature in the nucleation of pearlite M. H. Richman, D. A. Thomas and M. Cohen W. F. Hosford and R. L. Fleischer R. L. Fleischer 814 816 M. H. Richman, D. A. C. Damask and G. J. Diexes 817 The production of vacancy clusters during cold work A. C. Damask and G. J. Diexes			
On the theory of martensitic transformations. The generalized lattice invariant shear and the degeneracy of solutions for the cubic to tetragonal transformation M. S. Wechsler 793 X-ray study of the kinetics of ordering on AuCu J. L. O'Brien and G. C. Kuczynski 803 Letters to the Editor: Existence de plusieurs stades de précipitation pour les alliages à base de cuivre durcis par le titane J. Manenc 807 Heats of formation of liquid Na-Cs alloys R. A. Orlani 808 The growth of precipitates from solid solutions J. Burke 809 Bismuth at low temperature The temperature dependence of the flow stress of an age-hardened alloy A. Kelly 811 On the orientation dependence of surface free energy N. A. Gjostein 812 The role of austenitizing temperature in the nucleation of pearlite M. H. Richman, D. A. Thomas and M. Cohen 814 Dislocation barriers and cross slip W. F. Hosford and R. L. Fleischer 816 Absolute grain boundary energies in copper R. L. Fleischer 817 The production of vacancy clusters during cold work A. C. Damask and G. J. Dienes 818			
of solutions for the cubic to tetragonal transformation X-ray study of the kinetics of ordering on AuCu J. L. O'BRIEN and G. C. KUCZYNSKI Letters to the Editor: Existence de plusieurs stades de précipitation pour les alliages à base de cuivre durcis par le titane J. MANENC J. MANENC R. A. ORIANI Bismuth at low temperature The temperature dependence of the flow stress of an age-hardened alloy On the orientation dependence of surface free energy The role of austenitizing temperature in the nucleation of pearlite M. H. RICHMAN, D. A. THOMAS and M. COHEN Dislocation barriers and cross slip Absolute grain boundary energies in copper The production of vacancy clusters during cold work A. C. Damask and G. J. DIENES M. S. WECHSLER 793 M. S. WECHSLER 809 J. L. Hather 809 A. KELLY N. A. GJOSTEIN 812 M. H. RICHMAN, D. A. THOMAS and M. COHEN W. F. HOSFORD and R. L. FLEISCHER 816 R. L. FLEISCHER 817 A. C. DAMASK and G. J. DIENES			101
X-ray study of the kinetics of ordering on AuCu Letters to the Editor: Existence de plusieurs stades de précipitation pour les alliages à base de cuivre durcis par le titane J. Manenc J. Manenc J. Manenc J. Manenc R. A. Orlani Sor The growth of precipitates from solid solutions Bismuth at low temperature The temperature dependence of the flow stress of an age-hardened alloy On the orientation dependence of surface free energy The role of austenitizing temperature in the nucleation of pearlite M. H. RICHMAN, D. A. THOMAS and M. COHEN Dislocation barriers and cross slip Absolute grain boundary energies in copper The production of vacancy clusters during cold work J. Manenc J. Manenc R. A. Orlani 808 C. S. Barrett C. S. Barrett N. A. GJOSTEIN 812 M. H. RICHMAN, D. A. THOMAS and M. COHEN W. F. HOSFORD and R. L. FLEISCHER R. L. FLEISCHER 816 A. C. Damask and G. J. DIENES			793
Letters to the Editor: Existence de plusieurs stades de précipitation pour les alliages à base de cuivre durcis par le titane J. Manenc J. Manenc Bora R. A. Oriani R. A. Oriani Bora Bismuth at low temperature The temperature dependence of the flow stress of an age-hardened alloy On the orientation dependence of surface free energy The role of austenitizing temperature in the nucleation of pearlite M. H. Richman, D. A. Thomas and M. Cohen M. F. Hosford and R. L. Fleischer Absolute grain boundary energies in copper The production of vacancy clusters during cold work A. C. Damask and G. J. Dienes 818			
Existence de plusieurs stades de précipitation pour les alliages à base de cuivre durcis par le titane J. Manenc J. Manenc J. Manenc J. Manenc R. A. Oriani Regrowth of precipitates from solid solutions J. Burke Bismuth at low temperature The temperature dependence of the flow stress of an age-hardened alloy On the orientation dependence of surface free energy The role of austenitizing temperature in the nucleation of pearlite M. H. Richman, D. A. Thomas and M. Cohen Dislocation barriers and cross slip Absolute grain boundary energies in copper The production of vacancy clusters during cold work A. C. Damask and G. J. DIENES 817			
Heats of formation of liquid Na–Cs alloys The growth of precipitates from solid solutions Bismuth at low temperature The temperature dependence of the flow stress of an age-hardened alloy On the orientation dependence of surface free energy The role of austenitizing temperature in the nucleation of pearlite M. H. RICHMAN, D. A. THOMAS and M. COHEN Dislocation barriers and cross slip Absolute grain boundary energies in copper The production of vacancy clusters during cold work A. C. Damask and G. J. DIENES 818	Letters to the Editor:		
Heats of formation of liquid Na-Cs alloys The growth of precipitates from solid solutions Bismuth at low temperature The temperature dependence of the flow stress of an age-hardened alloy On the orientation dependence of surface free energy The role of austenitizing temperature in the nucleation of pearlite M. H. RICHMAN, D. A. THOMAS and M. COHEN Dislocation barriers and cross slip Absolute grain boundary energies in copper The production of vacancy clusters during cold work A. C. Damask and G. J. Dienes 808 R. A. ORIANI SOR HOTHANDIANI SOR HOTHANDIA	Existence de plusieurs stades de précipitation pour les alliages à base de		
The growth of precipitates from solid solutions Bismuth at low temperature The temperature dependence of the flow stress of an age-hardened alloy On the orientation dependence of surface free energy The role of austenitizing temperature in the nucleation of pearlite M. H. RICHMAN, D. A. THOMAS and M. COHEN Dislocation barriers and cross slip Absolute grain boundary energies in copper The production of vacancy clusters during cold work A. C. Damask and G. J. Dienes 310 W. F. Hosford and R. L. Fleischer R. L. Fleischer 817 A. C. Damask and G. J. Dienes			
Bismuth at low temperature The temperature dependence of the flow stress of an age-hardened alloy On the orientation dependence of surface free energy The role of austenitizing temperature in the nucleation of pearlite M. H. RICHMAN, D. A. THOMAS and M. COHEN Dislocation barriers and cross slip Absolute grain boundary energies in copper The production of vacancy clusters during cold work W. F. HOSFORD and R. L. FLEISCHER R. L. FLEISCHER A. C. DAMASK and G. J. DIENES 818			
The temperature dependence of the flow stress of an age-hardened alloy On the orientation dependence of surface free energy The role of austenitizing temperature in the nucleation of pearlite M. H. RICHMAN, D. A. THOMAS and M. COHEN Dislocation barriers and cross slip Absolute grain boundary energies in copper The production of vacancy clusters during cold work A. C. Damask and G. J. Dienes 818			
On the orientation dependence of surface free energy The role of austenitizing temperature in the nucleation of pearlite M. H. RICHMAN, D. A. THOMAS and M. COHEN Dislocation barriers and cross slip Absolute grain boundary energies in copper The production of vacancy clusters during cold work N. A. GJOSTEIN 812 W. F. HOSFORD and R. L. FLEISCHER 816 817 A. C. DAMASK and G. J. DIENES 818			-
The role of austenitizing temperature in the nucleation of pearlite M. H. Richman, D. A. Thomas and M. Cohen Bislocation barriers and cross slip Absolute grain boundary energies in copper The production of vacancy clusters during cold work W. F. Hosford and R. L. Fleischer R. L. Fleischer 817 A. C. Damask and G. J. Dienes			
Dislocation barriers and cross slip Absolute grain boundary energies in copper The production of vacancy clusters during cold work M. H. RICHMAN, D. A. THOMAS and M. COHEN W. F. HOSFORD and R. L. FLEISCHER R. L. FLEISCHER 817 A. C. DAMASK and G. J. DIENES 818		N. A. GJOSTEIN	012
Dislocation barriers and cross slip Absolute grain boundary energies in copper The production of vacancy clusters during cold work W. F. Hosford and R. L. Fleischer 816 R. L. Fleischer 817 A. C. Damask and G. J. Dienes 818		E. D. A. THOMAS and M. COHEN	814
Absolute grain boundary energies in copper The production of vacancy clusters during cold work A. C. Damask and G. J. Dienes 818			
The production of vacancy clusters during cold work A. C. Damask and G. J. Dienes 818			
			818
			819

VOI

Brandon, D. G. 101 Brenner, S. S. 519, 677 Brinkman, J. A. 47 Bronisz, S. E. 645 478 Bronisz, S. E. Brown, N. 210 Burke, J. 268, 809 BURNHAM, J. B., JR. 131 CAGNET, M. 427 CAHN, J. W. 18, 219 CECH, R. E. 787 Chaudhuri, A. B.
Chou, V. T. 694
Christian, J. W. 218, 529, 534
Clare, J. W. H. 136
CLARE, J. W. H. 136
CLARE, B. 762
CLARE, B. 762 COHEN, M. 86, 814, 819 Cohen, M. 86, 814, 819
Couling, S. L. 133
Coulomb, P. 556, 691
Damask, A. C. 818
Davis, R. S. 118
Dekeyser, W. 8, 29, 389, 520
Descript K. 83 VOL. 7 1959 DETERT, K. 589 DICKEY, J. E. 350 DIENES, G. J. 818 DOHERTY, P. E. 118 **Doi**, Тояню 291 Doremus, R. H. 339 DROTT, J. 777 DUNN, C. G. 6 648 Echeverria, A. 293 EGAN, J. J. 560 ELBAUM, C. 651 ENGELL, H. J. 429 ERICKSON, J. S. 58 ESHELBY, J. D. 628 FEDERIGHI, T. 422 ESHELBY, J. FEDERIGHI, T. 422 FELTHAM, P. 614 FERRO, A. 429 FINE, M. E. 228 FISCHMEISTER, H. FISHER, R. M. 632 FLEISCHER, R. L. 134, 816, 817

AERTS, E. 29

ALLAN, W. J. 646 AMELINCKX, S. 8,

BACON, A. E. 403

BARNES, S. C. BARRETT, C. S. BEEMAN, W. W.

Bénard, J. 295

BENARD, 3. 293 BENARD, A. 392 BESNARD, S. 517 BEVER, M. B. 199 BIBRING, H. 684 BIRNBAUM, H. K. 516

BLADE, J. C. 136 BLAHA, F. 93 BOTINCK, W. 389 BOULLON, F. 774

FODERARO, A. 131 FORTY, A. J. 139 FOURIE, J. T. 339

GALE, B. 420 GAUNT, P. 529, 534

GHATE, V. B. 436 GILMAN, J. J. 357, 608

Graham, J. D., Jr. 699 Graht, N. J. 60 Gray, D. L. 431 Grimes, H. H. 782 Guard, R. W. 171

GJOSTEIN, N. A. 224, 319, 812 GODDARD, K. F. 757 GORDON, R. B. 1, 681 GORUM, A. E. 685

Alessandrini, E. I. 678

AMELINCKX, S. 8, 29, 650 ANDERSON, R. W. 645 AVERBACH, B. L. 69, 86, 426

700

699, 810 203

HANNIBAL, W. D. 697 HATT, B. A. 682 HÉRINGUEL, J. 65 HIBBARD, W. R., JR. 565 HILLERT, M. 653 HILLERT, M. 955 HILLIARD, J. E. 86, 219 HOFFMAN, R. E. 407 HOFFMAN, R. E. HOLDEN, J. 380 HOLMES, E. L. 411 P. J. 283 HOLMES, P. J. 283 D. B. 446 HOLT, D. B. 446 HONDROS, E. D. 5 HONIG, J. M. 354 521 426 HORDEN, M. J. HOSFORD, W. F. HUBER, M. A. 65 816 HUETTER, L. J. 415 HUGGINS, R. A. 3: INMAN, M. C. 221 INTRATER, J. 140 JONES, W. D. 222 JONG, M. DE 246 357 680 KAMEL, R. KAUFFMAN, J. W. 180 KAUFMAN, L. 216, 575 KAZINCZY, F. DE 525 KEH, A. S. 694 KELLY, A. 811 KERNOHAN, R. H. 599 KIMURA, H. 145, 154 KNÖDLER, H. 229 KOCKS, U. F. 131 KOISTINEN, D. P. 59 KUCZYNSKI, G. C. 803 Kuhlman-Wilsdorf, D. 145, 154 LACOMBE, P. 691 LAGERBERG, G. 137 LAMB, H. J. 136 93 Langenecker, B. LESLIE, W. C. 69 LEYMONIE, C. 694 LESLIE, W. C. 632 LEYMONIE, C. 691 Li, J. C. M. 694 Liebmann, B. 51 LINGELBACH, R. 441 LISS, R. B. 231 LOMMEL, J. M. 699 LOUAT, N. 57 Low, J. R. JR. 58, 171 LÜCKE, K. 51 LUHMAN, W. J. 685 MACHLIN, E. S. 140 MACHLIN, E. S. Mack, D. J. 687 McLean, D. 438 Macnairn, J. 111 Maddin, R. 76, 145, 154 MAENHOUT-VAN DER VOORST, W. 8 MAHAFFY, J. E. 60 MAIDEN, C. J. 297 MAKIN, M. J. 233, 361 MANENC, J. 124, 807 MABBURGER, R. E. 59 Marezio, M. 769 Mǎsín, A. 226 Massalski, T. B. 528(B), 762 MEAKIN, J. D. 614 MEIJERING, J. L. 33 331 MEIKLEJOHN, W. H. 675 MESHII, M. 180 MINTER, F. J. 361 MOORE, A. J. W. 521 Moreau, J. 427 Mrowec, S. 696 MICHOLAS, J. F. 163 MULLINS, W. W. 163 NICHOLAS, J. F. 544 NISHIYAMA, Z. 432 NOWICK, A. S. 433 Nowick, A. S. 433 NUTTING, J. 101, 515 O'BRIEN, J. L. 803 OMANI, R. A. 62, 63, 808

OUDAR, J. 295 Païdassi, J. 293 Pascard, R. 305 Passari, L. 422 Passari, L. 422 Pearson, W. B. 528(B) Perryman, E. C. W. 64 PICKETT, J. 111 PORTER, L. F. 504 RACHINGER, W. A. 374 RAPPERPORT, E. J. 254 RATHENAU, G. W. 246 RATHENAU, G. W. RATHENAU, G. W. 246
RAWLINGS, R. 659
RHINES, F. N. 224, 319
RICHMAN, M. H. 814, 819
ROBINSON, P. M. 659
ROSENBAUM, H. S. 664, 678
ROSENTHAL, P. C. 504
ROSWELL, A. E. 433
RUSSELL R. 628 RUSSELL, B. 628 SAADA, G. 367 SARI, C. 429 SCHOET, G. 469 628 SCHOFIELD, T. H. Schottky, G. 495 Schottky, W. F. 199 Seeger, A. 469, 495 SEEMAN, H. J. SEIGLE, L. 421 SEN, N. 632 SHEWMON, P. G. 421 SHUMIZU, K. 432 SILCOCK, J. M. 359 SIVERTSEN, J. 275 SKODA, R. E. 675 SLEESWAY SLEESWYK, A. W. 689 SMELTZER, W. W. 191 SMITH, J. F. 261 SMITH, R. C. 223 261 SMYTHE, R. L. Sosin, A. 478 STADELMAIER, H. H. STAUBWASSER, W. 43 STEVENS, J. 774 STRUMANE, R. 520 TALBOT, J. 517 TANNER, L. E. Thomas, D. A. 69 THOMAS, G. 515, 814 TIPLER, H. R. 221 TUCKER, C. W. JR. Turnbull, D. 83, 407, 664, 678 UHLIG, H. 111 VENTURELLO, G. VERHEIJKE, M. L. 331 VIGNESS, I. VOGT, E. 441 VOTAVO, E. 392 VREELAND, T. JR. 240 Wagner, R. 523 Wahlin, H. B. 687 Walker, C. B. 769 Walter, J. L. 424, 648 Webb, M. B. 63, 187, 203 Webb, W. W. 646 WECHSLER, M. S. 599, 793 WERBER, WERT, C. 275 WEST, D. R. F. WEST, D. R. F. 429 WERBER, T. 696 WERT, C. 275 WHITWHAM, D. 65 WILLIAMS, G. I. 682 WILLIAMS, R. O. 676 WILSDORF, H. G. F. WILSON, D. V. 628 339, 819 WILSON, D. V. 628
WINEGARD, W. C. 411
WINTERBERGER, M. 549
WRIGHT, P. 757
YOSHIDA, H. 51

PROPAGATION OF SOUND IN LIQUID METALS: THE VELOCITY IN LEAD AND TIN*

R. B. GORDON+

The velocity of propagation of longitudinal sound waves in liquid lead and tin has been measured over a temperature interval upward from the freezing point. A constant linear decrease of the sonic velocity with increasing temperature is found in both metals. The acoustic data are used to evaluate the parameters in a simple hole theory of the liquid state, which is then compared with data for diffusion in liquid metals.

PROPAGATION DU SON DANS LES METAUX A L'ETAT LIQUIDE LA VITESSE DANS LE PLOMB ET L'ETAIN

La vitesse de propagation d'ondes sonores longitudinales dans le plomb et l'étain liquides a été mesurée pour une gamme de température débutant au point de solidification. Pour les deux métaux, on a observé une diminution constante et linéaire de cette vitesse lorsque la température s'accroît. Les valeurs de grandeurs acoustiques permettent d'évaluer les paramètres d'une théorie du "simple trou" de l'état liquide. Celle-ci peut alors être comparée avec les données expérimentales relatives à la diffusion dans les métaux liquides.

SCHALLAUSBREITUNG IN FLÜSSIGEN METALLEN: DIE SCHALLGESCHWINDIGKEIT IN BLEI UND ZINN

Die Ausbreitungsgeschwindigkeit longitudinaler Schallwellen in flüssigem Blei und Zinn wurde in an den Schmelzpunkt anschliessenden Temperturbereichen gemessen. Bei beiden Metallen wurde eine konstante lineare Abnahme der Schallgeschwindigkeit mit zunehmender Temperatur gefunden. Die Ergebnisse der akustischen Messungen werden zur Bestimmung der Parameter einer einfachen Löcher (hole)-Theorie des flüssigen Zustands verwendet, die dann mit Daten über die Diffusion in flüssigen Metallen verglichen wird.

Knowledge of the propagation constants for sound waves has often been of value in the study of the structure of non-metallic liquids. Presumably such acoustic data could be equally useful in the case of metallic liquids, for although there is no rigorous theory relating the velocity and attenuation of sound to atomic structure in the liquid state, acoustic data can be compared in a number of ways with the various approximate theories of liquids. A series of experiments has been undertaken to determine the sonic velocity and attenuation in a representative selection of liquid metals and alloys, and in this paper the results of velocity measurements on pure Pb and Sn are reported.

EXPERIMENTAL METHOD

In the ultrasonic pulse technique, (1) which is a convenient method for making rapid and accurate measurements of the velocity of sound in liquids, the time required for a short pulse of sound to traverse a path of known length in the liquid is measured. In the apparatus used in our experiments

a sound pulse is generated by an X-cut quartz crystal transducer which is in direct contact with the liquid metal. After travelling a known distance in the liquid, the pulse is reflected back to the quartz crystal where it generates an electric signal which is in turn amplified and applied to the vertical deflection plates of a cathode ray oscilloscope. The oscilloscope sweep is triggered to start at the moment of pulse generation, and with suitable adjustment of the sweep speed a set of signals corresponding to the repeated reflection of the pulse in the liquid is seen on the oscilloscope face. All of the electronic circuits to accomplish this are commercially available in the Sperry Ultrasonic Reflectoscope and this instrument was employed in our experiments. The need for additional electronic equipment to measure the time interval between successive reflections is avoided by the use of a comparison method:

A mercury delay line of variable length is connected in parallel with the unknown, as shown in Fig. 1, and adjusted until the leading edges of the two sets of reflections so produced are just in coincidence. Since the velocity of sound in mercury is accurately known, the sonic velocity in the unknown liquid can be calculated from the ratio of the transducer to reflector distances in the mercury and the unknown.

VOL.

1959

^{*} This research was supported by the USAEC. Received March 28, 1958.

[†] Hammond Laboratory, Yale University, New Haven,

ACTA METALLURGICA, VOL. 7, JANUARY 1959



VO

19

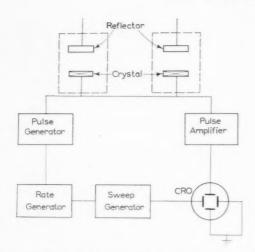


Fig. 1. Circuit used for ultrasonic measurements on liquid metals. The tank for the liquid of unknown velocity and a mercury delay line, each containing a crystal transducer and a reflector, are connected in parallel to the pulse generator and amplifier.

Used in this way the Reflectoscope is essentially a "null" indicator and the velocity so measured is independent of the exact values of any of the circuit components in the instrument.

The liquid metal is contained in a steel tank set up with the quartz crystal in the bottom and the steel reflector at the top. The reflector can be moved in translation by means of a micrometer screw, while additional adjustments allow the reflector surface to be set accurately parallel to the surface of the quartz crystal, a condition indicated by a maximum in the amplitude of the reflected signals. Temperature is measured at a number of points along the acoustic path by means of thermocouples and, in order to avoid refraction effects, is kept uniform to better than 0.1°C. The thermocouples were calibrated at the freezing points of Sn, the Sn-Pb eutectic, and water. No attempt was made to isolate the surface of the melt from the atmosphere.

Since the transducer to reflector distances, which are of the order of 4 in., are known to within ± 0.005 in. from measurements with a vernier height gage corrected for thermal expansion, the velocity of sound in the unknown liquid relative to that in mercury can be determined to within ± 0.1 per cent. Small changes in the velocity of sound resulting from temperature changes can also be measured with good precision since the displacement of either reflector, once the apparatus is set up, can be determined to ± 0.0001 in. In practice it was found possible to determine the sonic velocity at any temperature, relative to that in the same liquid at some given temperature, to within ± 0.01 per cent.

Thus the linearity of the dependence of velocity on temperature could be tested and the temperature coefficient of velocity found with one per cent accuracy through measurements made in a temperature interval of about $50^{\circ}\mathrm{C}$ or less.

The most critical part in the apparatus is the mount for the quartz transducer. The crystal must be supported against the hydrostatic pressure of the liquid while, at the same time, acoustic noise arising from reflections in the backing materials must be kept very low. At ordinary temperatures these requirements are met by cementing the crystal to some insulating material which readily absorbs sound. At higher temperatures it has been found necessary to use an "air backed" crystal: the crystal is supported at its edges by a shoulder on a lavite block and the electrode area is confined to the central, unsupported region. Using this mounting, good quality signals with no appreciable background noise have been attained at temperatures in excess of 350°C.

EXPERIMENTAL RESULTS

An acoustic frequency of 5 Mc/s was used for all of the velocity measurements reported here. This frequency is high enough so that diffraction effects are not troublesome and low enough to allow the use of a quartz transducer of reasonable thickness vibrating in its first harmonic—it is generally difficult to attain sufficient acoustic energy output from crystals operating on higher harmonics. The lead and tin used, together with a sample of the tin taken after completion of the velocity measurements, were spectrographically analyzed with the results reported in Table 1; there is no evidence

Table 1. Spectrographic estimates of metals for ultrasonic measurement

T	in:				
	Virgin	Used		Virgin	Used
Sn Pb As Bi Fe	major 0.X—low 0.0X—low 0.0X—low 0.0X	major 0.X—low 0.0X—low 0.0X—low 0.0X	Cu Ni Sb Ag Mn	0.0X 0.00X 0.00X 0.000X not found	0.0X 0.00X—high 0.00X 0.000X 0.000X

Elements checked but not found: Co, Cr, Mo, V, Zn, Cd, In, Al, Ti, Mg, Si.

Lead:			
Pb	major	Fe	0.00X
Bi	0.X—low	Cu	0.00X-low
Sn	0.0X	Ag	0.00X—low

Elements checked but not found: Co, Cr, Mo, V, Zn, Cd, In, Al, Li, Mg, Si, As, Ni, Mn.

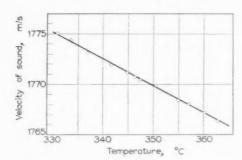


Fig. 2. A typical set of ultrasonic velocity data, in this case for liquid lead.

of contamination of the melts by the steel containing vessel during the measurements.

In both liquid Pb and Sn the velocity of sound, v_{ν} is found to decrease linearly with temperature as is shown, for example, by the data in Fig. 2. The method of least squares was used to calculate the straight line which best represents the velocity-temperature data for each metal; the results are summarized in Table 2.

The velocity of sound in liquid Pb and Sn has been measured by O. J. Kleppa $^{(2)}$ who found values of 1790 ± 15 and 2270 ± 20 m/sec, respectively, at the freezing points. No explanation for the discrepancy in the case of Sn is known, but it may be observed that the sonic velocity obtained for liquid Na by Kleppa is about 200 m/sec lower than that found by Pochapsky. While all of these various measurements have been made at different acoustic frequencies, the acoustic dispersion in liquid metals is probably very small.

1959

DISCUSSION

Temperature variation of velocity. From time to time investigators have observed marked changes in the physical properties of liquid metals in the immediate vicinity of the freezing temperature. For example a marked increase in the viscosity, η , of tin near the freezing point has been reported. (4) Now the viscosity of liquid metals is usually described in terms of the relaxation time for atomic jump, τ , and at moderately high temperatures viscosity, like diffusion, is presumably due to the

Table 2. Velocity of sound in liquid lead and tin

	Number of Measure- ments	Temperature Interval (°C)	$T = T_{\text{melt}}$ (m/sec)	$\frac{-dv_l}{dT}$ (m/sec/°C)
Pb Sn	48	328-370 230-335		$0.277 \pm .006$ $0.236 \pm .001$

occurrence of jumps over a distance of about one atom spacing, with a relaxation time of the order of $10^{-10}\,\mathrm{sec.^{(5)}}\,$ A liquid acts like a fluid—has no shear modulus-because for even the most rapidly alternating stresses which can be generated in the laboratory, $\omega \tau \ll 1$, ω being the circular frequency. The occurrence of a sharp increase in a plot of $\ln \eta$ vs. 1/T, as T approaches the freezing point, implies the existence of a second relaxation time in the liquid that decreases very rapidly with temperature. On the basis of the data obtained by Yao and Kondic⁽⁴⁾ it may be estimated that for this second relaxation time $\omega \tau$ would approach the order of magnitude of unity near the freezing temperature when $\omega \approx$ 107 sec-1. Near its freezing point, then, liquid Sn would be expected to appear somewhat rigid to 5 Mc/s elastic waves. The velocity of longitudinal sound waves v_i , in an isotropic medium is given by

$$v_l^2 = rac{rac{1}{eta} + rac{4}{3}\,\mu}{
ho}$$

where β is the compressibility, μ the shear modulus, and ρ the density. Any rigidity of the liquid due to incomplete relaxation will therefore influence v_l , and a departure from a linear relation between v_l and T should then occur near the freezing point. As shown in Fig. 3 such a departure from linearity is not observed in tin, even when the temperature is carried below the freezing temperature.

Equation of state for liquid metals. If an equation of state for a material giving the volume as a function of temperature and pressure is available, expressions for the coefficient of thermal expansion, α , and the isothermal compressibility, β_I , can be calculated. A particularly simple model of liquid structure leading to such an equation of state has been devised by Frenkel: (6) it is assumed that the thermal expansion and compressibility of the liquid are due entirely to the presence of a certain concentration of "holes" in the liquid structure, each hole having a definite

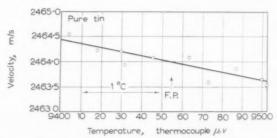


Fig. 3. The velocity of sound in liquid tin obtained during slow cooling through the freezing temperature.

volume, v. Let $u=u_o+Pv$ be the work required to form a hole of volume v by expanding the liquid against a constant pressure. The number of holes among the N atoms of a mole of liquid is then assumed by Frenkel to be

$$N_H = N \exp\left(-u/kT\right) = N \exp\left(-U/RT\right) \quad (1)$$

where U is the work required to form N holes in a very large volume of the liquid. Thus the energy required to form additional holes as the temperature is raised increases the specific heat of the liquid by an amount

$$\begin{split} \Delta C_P &= \left(\frac{\partial}{\partial T} u N_H\right)_P = u N \bigg[\frac{\partial}{\partial T} \exp\left(-u/kT\right)\bigg] \\ &= \frac{u^2}{kT^2} v \exp\left(-u/kT\right) \ (2) \end{split}$$

above that of the liquid without holes. The equation of state follows from the assumption that all the thermal expansion of the liquid is due to hole formation, i.e., $V-V_o=N_Hv$ where V_o is the "incompressible volume" corresponding to a close packed array of atoms. Using equation 1, then,

$$V = V_o \left[1 + \frac{N}{V_o} v \exp\left(-\frac{u_o + Pv}{kT}\right) \right]$$
 (3)

This equation is used to calculate the isothermal compressibility

$$\beta_I = -\frac{1}{V} \left(\frac{\partial V}{\partial P} \right)_T = \frac{V - V_o}{V_o} \frac{v}{kT} \tag{4}$$

and thermal expansion

$$\alpha = \frac{1}{V} \left(\frac{\partial V}{\partial T} \right)_{P} = \frac{V - V_{o}}{V_{o}} \frac{u}{kT^{2}}$$
 (5)

If for a given liquid the quantities V, β_I and α are measured, then the characteristic parameters u, V_o , and v can be found by solving equations 3, 4, and 5 simultaneously. Upon solving for U in this

Table 3. Properties of metals needed to determine parameters in the equation of state

	(°K)	$V \ ({ m cm^3/mole})$	$(^{\circ}\mathrm{C}^{-1} \overset{\alpha}{\times} 10^{-5})$	$ ho_I^{eta_I} imes 10^{-12} ho$
Pb	600	19.41 ^(a)	$9.35^{(a)}$	3.350
Sn	505	$17.02^{(a)}$	$9.04^{(a)}$	2.600
Na	371	24.7(b)	$27.8^{(b)}$	19.11
Hg	300	14.82(c)	17.99	4.040

Sources:

(a) H. J. FISHER and A. PHILLIPS, Trans. Amer. Inst. Min. (Metall.) Engrs. 202, 1060 (1954).

(a) Handbook of Chem. and Phys., Cleveland (1947).

way it is found that

$$[AN \exp{(-U/RT)}]U^2 + [ABN \exp{(-U/RT)}]U$$

$$- B^2V = 0$$
 (6)

where $A = \beta_I kT$ and $B = \alpha RT^2$.

This equation, which may be solved most conveniently by a graphical method, always has two roots and the choice between the two sets of values for u, V_o and v so obtained must be made on the basis of additional physical evidence.

The isothermal compressibilities of liquid Pb and Sn can be calculated from the ultrasonic velocity data reported in Table 2 by using the relations

19

$$eta_a = rac{1}{{v_{\scriptscriptstyle I}}^2
ho} \qquad eta_I = eta_a + rac{T lpha^2}{
ho C_P}$$

where β_a is the adiabatic compressibility of the liquid. Precise ultrasonic velocity measurements have also been made for liquid Na⁽³⁾ and Hg⁽¹⁾ and calculations for these two metals are made for purposes of comparison. The remaining input data required to solve equation 6 are available in the literature and are summarized in Table 3. The two sets of solutions obtained with this set of data are reported in Table 4.

Table 4. Parameters for equation of state

	$U \ ({ m cal/mole})$	$({ m cm^3/mole})$	$(\mathrm{cm^3} \times 10^{-24})$	ΔC_P (cal/mole deg.
Pb Solution I Solution II	1115 4250	18.31 19.13	4.62 17.61	$0.685 \\ 0.715$
Sn Solution I Solution II	840 3850	$16.14 \\ 16.72$	$\frac{3.32}{15.22}$	$0.612 \\ 0.634$
Na Solution I Solution II	$\frac{830}{2230}$	$\frac{22.65}{23.90}$	10.70 28.7	$0.813 \\ 0.858$
Hg Solution I Solution II	650 1890	14.13 14.56	3.38 9.83	$0.810 \\ 0.834$

⁽b) E. A. GRIFFITHS and E. GRIFFITHS, Proc. Roy. Soc. A27, 477 (1915).

Table 5. Atomic radii calculated from the incompressible volume of the liquid (Å)

	1-1				
		Pb	Sn	Na	Hg
Radius from U	Solution I	1.75	1.68	1.88	1.61
	Solution II r CN = 12	1.78 1.75	$\frac{1.70}{1.62}$	1.91 1.89	1.62 1.57
Radius from V_a Pauling radius fo	Solution II	1.78	1.70	1.91	

In order to decide whether solution I or solution II is the physically significant one for each of the metals considered, the parameters of the equation of state may be compared with other known properties of these metals. For example, the incompressible volume, V_o , should be the same as the volume occupied by a close-packed array of metal atoms. Assuming, since most liquid metals have a coordination number of nearly 12, that this close-packed structure corresponding to V_o is a f.c.c. one, the radii of the atoms may be computed from the values of V_a given in Table 4. The radii so obtained are displayed in Table 5.

It is seen that in each case solution I lies closer to the Pauling radius for coordination number 12 than does solution II, and that the agreement with the Pauling radii is quite good in the case of the metals which crystallize in cubic crystal structures. It may be observed in passing that the quantity $V-V_o$ is not the same as the volume change which occurs upon melting, as has been sometimes claimed in the literature. The latter quantity should be smaller, as is the case with the metals considered here, because of the thermal expansion of the solid.

1959

The other quantity in Table 4 which may be compared directly with known properties of the liquid metals is the specific heat increment ΔC_P . In the approximation used in Frenkel's model, the total specific heat of the liquid, $C_{P}(l)$, should be the sum of the contributions due to: (1) the thermal vibration of a close packed array of atoms held at constant

volume, (2) the thermal excitation of the conduction electrons and, (3) the work required to expand the liquid to its actual molar volume by the formation of holes, ΔC_{P} . As a first approximation, at least, the thermal vibration contribution to C_P might be taken to be the Debye specific heat of a fully excited isotropic elastic continuum, viz., 5.97 cal/mole deg. Alternatively, the sum of the first two contributions to $C_{\mathcal{P}}(l)$ could be assumed to be the specific heat of the solid metal at constant volume measured near the freezing temperature, $C_{\nu}(s)$. Values of $C_{\nu}(l)$ calculated according to these two approximations are displayed in Table 6. Only the ΔC_P values from solution I are used here, since this appears to be the physically significant case; the specific heat data generally are not sufficiently precise to be of any help in distinguishing between the two possible solutions.

In the Debye approximation the elastic anisotropy of the close packed array of atoms is neglected, as is the possibility of anharmonic atomic vibration at high temperature. Furthermore, the reliability of the assumption that the electronic specific heat of a liquid metal is given by γT , where γ is obtained from low temperature data, is not known. It might be, then, that really close agreement between $C_P(l)$ calculated as $5.97 + C_{
m elec} + \Delta C_P$, and experiment, could not be expected. On the other hand, the approximation $C_P(l) = C_V(s) + \Delta C_P$ should be best for those metals where the structure of the solid is most nearly similar to the cubic close packed structure assumed to correspond to V_o ; this is seen from Table 6 to be the case.*

The other two parameters in Table 4, U and v, cannot be compared directly with any known

Table 6. Calculated and observed molar specific heats of liquid metals (cal/mole deg.)

	Pb	Sn	Na	Hg
$C_P(l) = 5.97 + C_{ ext{elec}}^{(a)} + \Delta C_P \ C_P(l) = C_{_{m{P}}}(s)^{(b)} + \Delta C_P \ C_P(l) ext{ observed}$	7.17 6.78 6.80 ^(c)	$\substack{6.80 \\ 7.66 \\ 6.78^{(d)} - 7.30^{(e)}}$	6.94 7.67 $7.603^{(e)}$	6.92

Notes: a Celec = γT where γ is obtained from low temperature specific heat data. Numerical values of γ are from Handbuch der Physik. Vol. 14. Berlin (1956).

b Calculated from $C_P(s)$ by the relation $C_P - C_V = \alpha T^2 V \beta$. Values of $C_P(s)$ are from K. K. Kelly, Bull. Bur. Mines No. 476; except for that of Na which is from Marshall Sittig, Sodium. New York (1956).

c K. K. Kelly, Bull. Bur. Mines No. 476. d Liquid Metals Handbook (2nd Ed.). Washington (1952). e Marshall Sittig, Sodium. New York (1956).

f Handbook of Chem. and Phys. (30th Ed.). Cleveland (1946).

^{*} The specific heat $C_p(l)$ of both Na and Hg decreases with increasing temperature above the freezing point, goes through a minimum and then increases. The cause of this decrease is not known; it is responsible for the low $C_p(l)$ of Hg in Table 6 but it is not known whether or not it influences the specific heat at the freezing temperature.

7 19

properties of the metals considered, but they do enter in a discussion of diffusion in terms of the hole model. According to this model diffusion in liquids proceeds in a manner similar to that in solids: the atoms of the liquid occupy sites on a more or less regular lattice with each lattice site in every 50 or 100 being vacant. The presence of this relatively large number of holes leads to a "vacancy" mechanism of diffusion in the liquid and to a large atomic mobility which, for shear stresses of sufficiently long duration, is equivalent to fluidity. Now in solids the activation energy for self diffusion is the sum of the energy required to form a vacancy and the activation energy for an atomic jump, these two energies usually being of about the same order of magnitude. Measurements of the activation energy for diffusion in liquid metals have been made for Na, (7) Hg(8) and Pb.(12) In the case of Sn the activation energy for self diffusion can be estimated from data giving the viscosity of these metals as a function of temperature⁽⁹⁾ through the Stokes-Einstein relation.†

These data are summarized in Table 7. They verify the conclusion that for the metals considered, solution I of equation 6 is the physically significant one: the activation energy for self diffusion must be at least as great as U and in the case of solution II this is not so for Pb, Sn and Hg by substantial amounts.

The values of v from solution I correspond to holes having a radius about two thirds that of an unrelaxed vacancy in the liquid. It might therefore be expected that in *liquid* metals the energy for hole formation would be a smaller part of the total activation energy for self diffusion than is the energy for vacancy formation in the case of solid metals.

With the exception of Hg, Table 7 shows that the energy for hole formation is about a third of the total energy for diffusion; in solids this ratio is of the order of one half.

Comparison with other hole or free volume theories. The assumptions used in the simple hole theory of liquids represent only a first approximation. In particular, the distribution of hole sizes which would exist in a real liquid is neglected. Since the dependence of u on hole size is not known—and it is probably not just proportional to $v^{2/3}$ for holes of atomic size—the sharpness of this distribution cannot be specified. Perhaps the distribution is much sharper in liquid metals than in liquids having complex molecules; certainly very large holes would not be expected in the metallic case.

In other free volume theories of liquids the problem of the distribution of hole sizes does not arise, because the free volume is not thought of being localized in holes but rather is considered to be distributed uniformly among all the atoms present. Because the analogy with the solid state is not so close and the mathematical complexity is substantially greater in the case of these "distributed free volume theories." only the simplest of them yield results that can be directly compared with experiment. One such theory is that due to Eyring and Hirschfelder (10) in which each atom is regarded as being confined within a "cage" which is larger than the space available to it in a close packed structure by an amount equal to the free volume of the liquid, $V - V_o$. The potential energy of the atom is considered to be a constant so long as it is in its cage; otherwise it is infinite. Under these conditions the partition function, and hence the free energy, of the liquid can be calculated at once. Collins⁽¹¹⁾ has shown how the free volume appearing in the Evring-Hirschfelder theory can be determined in a simple way from the velocity of sound, the coefficient of thermal expansion, and the specific heat of the liquid. He finds that

$$\left(\frac{V_o}{V}\right)^{1/3} = 1 - \frac{RT\alpha^2 M v_l^2 + RC_P(l)}{\alpha C_P(l) M v_l^2} \ . \tag{7}$$

† The Stokes–Einstein relation is that $D=kT/\eta\lambda$ where η is the coefficient of viscosity and λ is an appropriate interatomic distance. If it is assumed that $D=D_0\exp(-Q/RT)$, then the viscosity must depend on temperature through the relation $\eta=AT\exp(Q/RT)$, where A is a constant, and Q must be found from a plot of $\ln\eta/T$ vs. 1/T. The viscosity and diffusion data for liquid metals are as yet not sufficiently accurate to allow the determination of the correct power of T in the pre-exponential parts of the equations above for D and η , but the assumption that $D=D_0\exp(-Q/RT)$ is consistent with the hole model of liquid diffusion used here.

Table 7. Activation energies for self diffusion in liquid metals

Pb Sn Na					
Q for self diffusion (cal/mole)	2400 ^(a) -3680 ^(b) -4450 ^(c)	$2500^{(a)}$	2430	1160	
U/Q	0.47 - 0.31 - 0.25	0.34	0.34	0.56	

Notes: a From viscosity data, reference 9.

e Self diffusion measurement.

b From viscosity data of Bienias and Sauerwald, Z. anorg. u. allgem. Chem. 161, 51 (1927).

Table 8. Incompressible volume and atomic radius from Eyring-Hirschfelder theory

	Pb	Sn	Na	Hg
V_o (cm³/mole)	11.89	10.80	11.27	9.91
r (calc. from V_o) (Å)	1.51	1.47	1.49	1.43
r (Pauling, CN = 12) (Å)	1.75	1.62	1.89	1.57

where M is the atomic weight and v_i^2 is expressed in units of cal/g. Values of V_o and the corresponding atomic radii calculated by means of equation 7 are displayed in Table 8. In each case the incompressible volume obtained is smaller than that found in the simple hole theory, while the atomic radii are much smaller than the Pauling radii for coordination number 12: in fact, with the exception of Sn, the calculated radii are smaller than the single bond radii of these metals. It would appear to be difficult, then, to apply the Eyring-Hirschfelder free volume theory to liquid metals, but it is not known whether this is a result of the assumption of a distributed free volume or of the simple pairwise potential function that is used.

CONCLUSIONS

To the extent that the four metals considered here, Pb, Sn, Na, and Hg are typical of metallic liquids in general, the following conclusions about the structure of liquid metals are suggested by the velocity of sound data:

1959

1. The sonic velocity is a linear function of temperature down to, and below, the freezing point. It reveals no evidence of pre-solidification phenomena.

2. The ultrasonic data can be satisfactorily fitted to a simple hole model of the liquid state due to

3. This hole model describes diffusion in liquid

metals by a mechanism analogous to the vacancy mechanism in solid metals.

4. The activation energy for atomic jump is a greater part of the total activation energy of diffusion in liquid than in solid metals, apparently because of the small size of a "vacancy" in the liquid.

5. The Eyring-Hirschfelder free volume theory is not applicable to liquid metals.

ACKNOWLEDGMENTS

The writer is indebted to Messrs M. I. Green and M. Gell for assistance in making the ultrasonic measurements and reducing the resulting data, and to Sperry Products, Inc., for the loan of an Ultrasonic Reflectoscope.

REFERENCES

- 1. L. Bergmann, Der Ultraschall. Zürich (1949). O. J. Kleppa, J. Chem. Phys. 18, 1331 (1950).
- T. E. POCHAPSKY, Phys. Rev. 84, 553 (1951).
 T. P. YAO and V. J. KONDIC, J. Inst. Met. 81, 17 (1952). 5. J. FRENKEL, Kinetic Theory of Liquids, p. 188 ff. Oxford
- 6. J. FRENKEL, Kinetic Theory of Liquids. p. 174 ff. Oxford (1956).
- 7. R. E. MEYER and N. H. NACHTRIEB, J. Chem. Phys. 23, 1851 (1955).
- R. E. Hoffman, J. Chem. Phys. 20, 1567 (1952).
- 9. H. J. FISHER and A. PHILLIPS, Trans. Amer. Inst. Min. (Metall.) Engrs. 202, 1060 (1954).
- 10. H. Eyring and J. O. Hirschfelder, J. Phys. Chem. 41, 249 (1937).
- 11. F. C. Collins, J. Chem. Phys. 25, 581 (1956).
- 12. S. J. ROTHMAN and L. D. HALL, Trans. Amer. Inst. Min. (Metall.) Engrs. 206, 199 (1956).

CAVITY FORMATION IN NITRATE-DOPED ALKALI HALIDES*

S. AMELINCKX, W. MAENHOUT-VAN DER VORST, and W. DEKEYSER†

Cavities filled with a gaseous product were formed in nitrate-doped alkali halide crystals after anneal in a hydrogen atmosphere.

These experiments show that the gaseous products of a chemical reaction in a solid, precipitate along dislocations if enough activation is present to allow diffusion.

Diffusion is facilitated by the formation of small agglomerates consisting of a few gas molecules and a number of vacancies.

LA FORMATION DE CAVITES DANS LES HALOGENURES ALCALINS DOPES AU NITRATE

Des cavités, renfermant un produit gazeux, ont été formées dans des cristaux d'halogénures alcalins dopés au nitrate après un recuit en atmosphère d'hydrogène.

Ces expériences montrent que les produits gazeux résultant d'une réaction chimique dans un solide, précipitent le long des dislocations si l'activation existante est suffisante pour permettre la diffusion.

La diffusion est facilitée par la formation de petits agglomérés composés de quelques molécules de gaz et d'un certain nombre de lacunes.

HOHLRAUMBILDUNG IN ALKALI-HALOGENIDEN MIT NITRATZUSATZ

In Alkalihalogenid-Kristallen mit zugesetztem Nitrat werden nach Glühen in einer Wasserstoff-atmosphäre gasgefüllte Hohlräume gebildet.

Die Experimente zeigen, dass die gasförmigen Reaktionsprodukte einer chemischen Reaktion in einem Festkörper sich entlang von Versetzungen ausscheiden, wenen genügend Aktivierung vorhanden ist, um Diffusion zu ermöglichen.

Die Diffusion wird erleichtert durch die Bildung von kleinen Agglomeraten aus einigen Gasmolekülen und einer Anzahl von Leerstellen.

It has been shown in this laboratory that dislocations can be decorated in silver activated alkalihalide crystals by annealing them in hydrogen. The decorating particles are silver, but, in a few cases, it was observed that cavities also developed along the dislocation lines. This could be traced back to a contamination of the silver salt with the corresponding nitrate. A systematic study of this phenomenon was made, and the following crystals were studied:

- (a) KCl + 0.75% AgCl containing traces of AgNO₃.
- (b) KBr + 0.75% AgBr containing traces of AgNO $_3$.
- (e) KCl + 0.75% Ag₂O.
- (d) KCl + 0.90% AgNO₃.
- (e) KCl + 0.70% KNO₃.

The crystals were grown in the laboratory by the Czochralski method. The indicated additions are weight percentages added to the melt; they are chosen to correspond to an addition of 0.75% AgCl.

DECORATION EFFECTS

19!

(i) After hydrogen anneal

Cleavage parallelepipeds of all crystals were annealed for 2 hr at some 750°C in oxygen-free hydrogen and then cooled slowly. After this treatment the dislocations were decorated in crystals a, b, c and d by silver particles, visible by ultramicroscopy. In a, b, dand e, cubic cavities, centered on the dislocation lines and bounded by (100) faces or sometimes by a combination of (100) and (110) faces, were found. In most cases (crystal e excepted) a silver speck can be observed in them. The cavities can be observed as well in transmission as in ultramicroscopy. Fig. 1, taken in ultra microscopy, reproduces an example from which it is evident that they are on dislocations. With a sufficient concentration of cavities, one obtains a decoration consisting of a quasi-continuous channel, as visible in Fig. 2. This was practically always so for crystal e.

Although the silver decoration is of course absent in the latter case, it is evident that the cavities are on dislocations. They are very often elongated in the direction of the dislocation line, which of course favours the formation of channels; their surfaces are sometimes visibly stepped. The concentration of

† Laboratorium voor Kristalkunde, Rozier, 6, Gent/Belgium.

^{*} This work is part of a research program (C. E. S.) sponsored by I.R.S.I.A. (Brussels) and Gevaert N. V. (Antwerp). Received April 1, 1958.

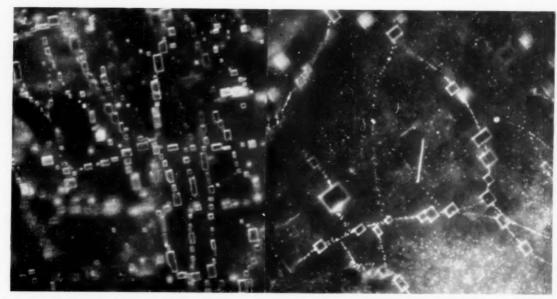


Fig. 1. Cavities along dislocation lines in silver nutrate doped KCl crystals, after thermal treatment in hydrogen. ×675.

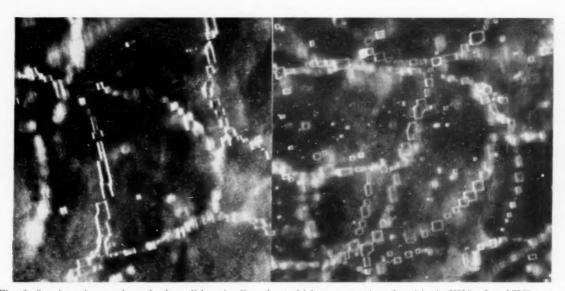


Fig. 2. Quasi-continuous channels along dislocation lines due to high concentration of cavities in KNO₃-doped KCl. ×600.

cavities is largest in the neighbourhood of the surface which has been in contact with the hydrogen; the central part of the crystal remains practically clear.

To study the nature of these cavities, a crystal fragment was dissolved in water under the microscope. Every time the dissolution front reached a cavity, a gas bubble two or three times larger than the cavity escaped. This means that the cavities are filled with gas under a pressure of a few atmospheres. The gas is practically insoluble in water. Quenching the crystal

results in a higher pressure, but a somewhat smaller cavity size. A very long anneal of 24 hr, produced larger cavities containing gas under a lower pressure; the zone containing a large concentration of cavities extends further in the crystal.

(ii) After additive coloration

In order to obtain indications of the role of the hydrogen in the process described in the previous paragraph, the crystals were coloured additively with

VOL. 7 1959

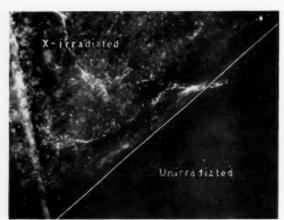


Fig. 3. Boundary zone between the non-irradiated and irradiated parts of a silver nitrate doped KCl crystal.

potassium metal by the Rexer method. The same results were obtained. This indicates that the hydrogen probably plays the same role as the potassium metal, i.e. supplies electrons and forms HCl at the surface, just as KCl is formed when potassium is used. As no closed vessel is needed for the Rexer method, this excludes the possibility that the small amount of hydrogen which could be dissolved in the potassium has played a role in the process.

(iii) After irradiation and anneal

It has been reported that specks can be observed in silver activated alkalihalide crystals after an intense X-ray irradiation. (2) Although experiments were performed under variable circumstances, we never could reproduce this effect when pure silver chloride was added to the melt. The effect of temperature, of irradiation time and of silver concentration was tried out, all with negative results.

On the other hand, it is known that NaNO_3 decomposes partially when it is irradiated with ionizing radiation of sufficient energy, and that gas pockets are formed on subsequent anneal.⁽³⁾ It was therefore worthwhile to try to see if similar treatments of silver nitrate doped crystals would produce specks, release gas, or both; and, if so, whether the pockets would develop along dislocation lines. Both X- and γ -rays were used in these experiments.

When the added silver chloride was contaminated with AgNO₃, or when the crystals were doped with AgNO₃, the as-grown crystals contained already very small silver specks. Their size and number is markedly affected by an X-ray irradiation (copper tube, 40 kV, 20 mA) followed by an anneal. Fig. 3 illustrates this effect. It shows the boundary zone between the non-irradiated and irradiated parts of such a crystal

which was X-rayed partly covered by a lead screen. The crystal was heated to 600° C immediately after irradiation. An anneal prior to irradiation, even at higher temperatures, has no effect at all. The decoration in this case is also due to cavities filled with gas and covered with silver. Crystals irradiated in the pile at Mol ($\sim 10^{17}$ neutrons/cm²), are heavily coloured. The F-bands are bleached when they are exposed to daylight and after an anneal at 600° C the decoration is extremely dense. This decoration is also due to cavities filled with gas and some small silver specks. Crystals irradiated with high energy γ -rays produced by fission products are not coloured and show no special decoration when they are annealed.

ABSORPTION MEASUREMENTS

(i) Infra-red

As AgNO₃ decomposes in air at temperatures (+450°C) well below the melting point of KCl, it is important to know which groups are incorporated into the crystals. Therefore, absorption measurements were performed in the infra-red region. A Beckman recording spectrophotometer was used. Similar measurements have already been performed by Maslakowez⁽⁴⁾ who examined alkalihalide crystals doped with the corresponding alkalinitrite and nitrate, and found two absorption peaks respectively at 1420 cm⁻¹ (7.22-7.26 μ) and 1250 cm⁻¹ (7.85–8 μ). The first one was attributed to the nitrate group, the other to nitrite ions. The relative intensities of the peaks depends on the melting point of the alkalihalide. Maslakowez therefore postulated that an equilibrium was formed in the melt between nitrite and nitrate groups through oxygen release of the latter ion. Our measurements of the untreated crystals are shown in Fig. 4. More than two peaks were observed, specimens doped with AgNO₃ and KNO₃ having the same absorption spectrum. The absorption maxima shift to shorter wavelength as the lattice parameter decreases. This is shown in Table 1 for the two most intense peaks.

Slices taken from the surface region and from the central part of hydrogen treated specimens were also examined. In the first, which contain a high concentration of cavities the NO₃ and NO₂ peaks are no longer present; in the second, containing far less

TABLE 1.

Crystal	Lattice parameter (Å)	max 1 (μ)	$\max 2 (\mu)$
KBr	6.59	7.80	7.22
KCl	6.28	7.77	7.14
NaCl	5.63	7.66	6.99

VOI 7 195

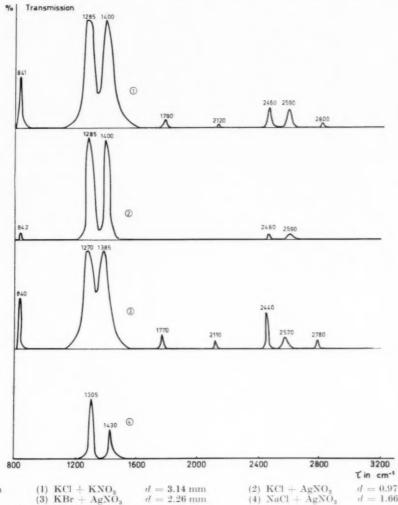


Fig. 4. i-r spectra

VOL.

1959



$$\begin{array}{l} \text{(2) } \text{KCl} + \text{AgNO}_3 \\ \text{(4) } \text{NaCl} + \text{AgNO}_3 \end{array}$$

$$d = 0.97 \text{ mm}$$

$$d = 1.66 \text{ mm}$$

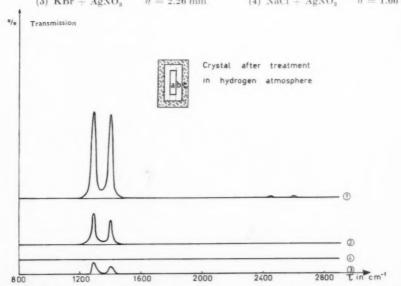


Fig. 5. i-r spectra from a KCl + $AgNO_3$ crystal: (1) untreated specimen; (2) (3) (4) After treatment in hydrogen atmosphere. The curves correspond respectively to sections a, b, and c of the crystal.

cavities, they are strongly reduced as shown in Fig. 5.

This indicates that the oxygen-nitrogen groups are at the origin of the gaseous products which fill the cavities after the indicated treatment. The latter however do not show up in the infra-red diagrams.

(ii) Visible and u-v absorption measurements

The absorption spectra of irradiated and uncoloured alkali halide crystals doped with $\mathrm{Ag^+}$, $\mathrm{NO_2^-}$ and $\mathrm{NO_3^-}$ have been extensively studied by several authors. $^{(5,6,7)}$ In order to follow the evolution occurring during the hydrogen treatment of such crystals, we have extended such measurements to crystals doped with nitrate-contaminated silver chloride, silver nitrate, silver oxide and potassium nitrate. The quantities of these impurities added to the melt was calculated to correspond to 0.75 wt. % of pure silver chloride, which allows comparison with crystals doped with the same amount of AgCl.

The absorption measurements were performed with

a Beckman spectrophotometer D.U. The specimens were coloured by X-rays originating from a tube with a copper target operating at 40 kV and 20 mA. In all experiments the crystals were at a distance of 6 cm from the window. X-rayed crystals were measured immediately after irradiation.

(a) Untreated crystals. Table 2 summarizes the relative intensities of the different absorption bands. In accordance with earlier investigations the silver ion bands are found in all crystals containing this ion. This 2150 band is more pronounced when the AgCl is contaminated with AgNO₃, owing to overlapping of a nitrate ion band. KCl crystals containing 0.75% of KNO₃ show a small peak at 3600 Å and a very intense one at 2150 Å, whilst the band at 2900 Å observed by Maslakowez does not seem to be present. The same bands were also observed in KBr and KCl crystals containing 0.75% AgNO₃, whilst NaCl doped with AgNO₃ only has the intense band at 2150 Å (Fig. 6).

The bands at 2150 Å and 3600 Å in KBr-AgNO₃

195

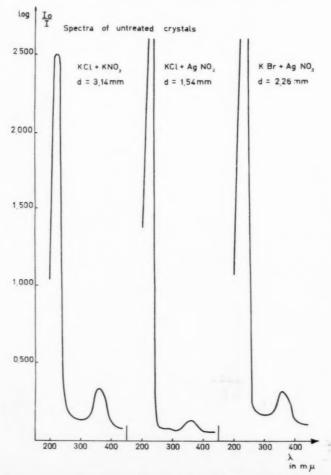


Fig. 6. u-v spectra of untreated nitrate-doped KCl and KBr crystals.

TABLE 2

		TABLE				
	λ in Å	Half width (Å)	$\log I_0/I$	$\overset{\lambda \text{ in }}{{A}}$	Half width	$log I_0/I$
KCl + AgCl pure	2150	25	1.6		_	
KCl + AgCl imp.	2150	30	1.9	-		
$KCl + Ag_{\circ}O$	2150	25	1.7	-		
$KCl + AgNO_3$	2150	35	2.6	3600	50	0.11
$KBr + AgNO_3$	2150	50	2.6	3600	50	0.2
NaCl + AgNO ₃	2150	30	2.6	_	_	_
$KCl + KNO_3$	2150	30	2.6	3600	50	0.17

crystals are more intense and very broad in comparison with those observed in KCl–AgNO $_3$ and KCl–KNO $_3$ samples.

The KCl-Ag₂O crystals only have a small band at 2150 Å which must be ascribed to the silver ions.

(b) Coloured crystals. In all the irradiated silver activated crystals the characteristic X-ray induced A, B, C, D, E-bands are present. Their relative intensity was affected by the different added negative ions: the F-band is reduced in comparison with the others: the A-band is more intense. This is illustrated in Fig. 7 and Table 3 in which the absorption peaks of two specimens, one containing AgCl contaminated with AgNO₃, the other pure AgCl, are compared. Both specimens were irradiated for 7 hr in identical conditions, and have nearly the same thickness d. The B-band is very intense with respect to the others in crystals doped with pure AgNO3. In the early stages of the irradiation, the E-band is prominent and grows more rapidly than the A, B, C and D-bands. This is reversed after a certain time, E reaches a saturation value while B, being the most intense, and also C and D continue to grow steadily (Fig. 8). The E-band is always less intense in nitrate doped crystals than in those to which pure silver chloride was added.

VOL.

1959

When the coloured crystals are irradiated in the F-band, the B and A-bands increase. Even when kept in the dark for several hours, the F-band decreases while the A and B-bands become more intense (Fig. 9).

All crystals, except those of KCl doped with pure AgNO₃, are fully bleached thermally when heated up

TABLE 3

TABLE 6.					
$\begin{array}{l} \mathrm{KCl} + \mathrm{AgCl_{pure}} \\ d = 1.14 \ \mathrm{mm} \end{array}$	$rac{ ext{KCl} + ext{AgCl}_{ ext{AgNO}}}{d = 1.16 ext{ mm}}$				
$\logI_{\scriptscriptstyle 0}/I$					
1.65	2.6				
0.69	0.88				
0.56	0.61				
0.64	0.59				
1.66 1.13					
	$d = 1.14 \text{ mm}$ $\log \lambda$ $\frac{1.65}{0.69}$ $\frac{0.56}{0.64}$				

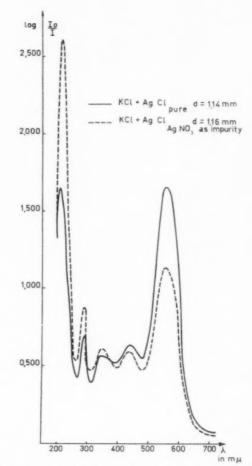


Fig. 7. Spectra of different silver-activated KCl crystals, respectively doped with pure AgCl, and AgCl with ${\rm AgNO_3}$ as impurity.

to 600°C. In the latter the A-band is unaltered, the B and D-bands are partly bleached and an intense colloid band at 4350 Å which overlaps the E-band is present. The same colloid band is also present in hydrogen-treated silver-activated halides, and its maximum shifts somewhat according to the duration of the anneal and rate of cooling (Fig. 10). The coloured crystals doped with KNO3 showed some special features. Next to the F-band, strong bands at 2100 Å and 3600 Å are present as well, and a shoulder at 2750 Å is observed. When the irradiation is prolonged a broad band develops overlapping those originally situated at 3250 and 3600 Å (Fig. 11). The 3250 Å absorption is also found in specimens treated in a hydrogen atmosphere, and in this case no trace is found of the absorption at 3600 Å.

THE NATURE OF THE GASEOUS PRODUCT

Attempts were made to determine the nature of the

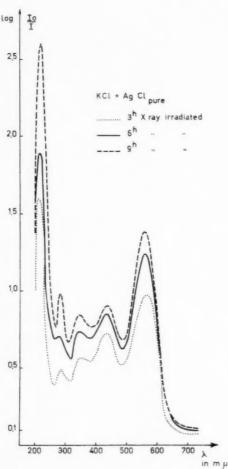


Fig. 8. Relative intensity of the absorption bands in KCl + pure AgCl after different irradiation times.

gaseous product which was found to be a mixture of oxygen and nitrogen. This conclusion is based on the following experiments:

- (i) the gas results from the decomposition of NO_3^- and NO_9^- groups.
- (ii) as already stated no reaction between the gas and water could be detected.
- (iii) when a quantity of crystals containing cavities are dissolved in gas-free distilled water, the escaping bubbles can be trapped in a test tube where they assemble to a volume of several cm³. When white phosphorus is brought under water into contact with this gas, white fumes soluble in water develop, but only part of the gas reacts.
- (iv) when a crystal doped with AgNO₃ is sealed in an evacuated tube and irradiated, it was proved by mass spectroscopy that oxygen and nitrogen were formed. Attempts to examine by mass spectroscopy a bubble captured from dissolved crystals failed.

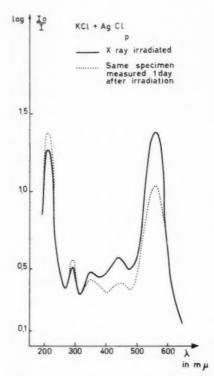


Fig. 9. Influence of bleaching of the F-band in the dark, on the A and B-bands.

195

If we consider the starting and end products we can write the reaction chemically as follows:

$$2Ag^{+} + 2NO_{3}^{-} \rightarrow 2Ag^{0} + N_{2} + 3O_{2}$$

It is however clear that some intermediate stage occurs: as written the reaction only involves a transfer of the electron of the $\mathrm{NO_3}^-$ group to the $\mathrm{Ag^+}$. Experimentally it is found that no cavities are formed by a heat treatment alone, even if silver specks are already present; it is necessary to heat the crystals in hydrogen or alkali metal vapour. This means that the surface reaction

$$[H_2 + 2KCl \rightarrow 2HCl + 2K^+ + 2e + 2\Box^-]$$

i.e. the electron, the vacancy or both, are essential for the decomposition of the $\mathrm{NO_3}^-$ groups and subsequent cavity formation. As the information so far available only permits highly speculative considerations about the details of this reaction, we will not attempt to go into further details. Two points may be noted. First it looks as if clustering of the $\mathrm{NO_3}^-$ is also necessary, because the formation of single oxygen atoms does not seem very probable. Secondly volume considerations equally favour such a hypothesis. A $\mathrm{NO_3}^-$ group can

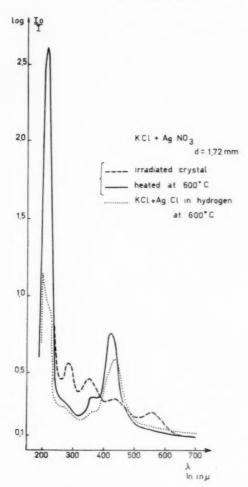
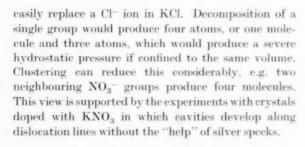


Fig. 10. Formation of the silver colloid band after heat treatment.



MECHANISM FOR THE FORMATION AND GROWTH OF THE CAVITIES

Ultramicroscopic examination of the as-grown crystals of the type a, b, c, d revealed that they already contained small specks, resulting from the thermal decomposition of the silver nitrate during the growth process. As it was found that most of the cavities contained a silver speck, we must consider the possibility that they are preferentially nucleated

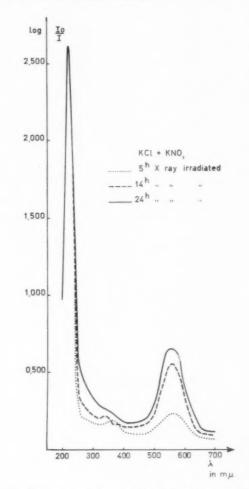


Fig. 11. Absorption spectra of KNO₃-doped KCl crystals after different irradiation times.

around them. This would lower considerably the activation energy for the formation of a cavity. This idea was already put forward by Seitz⁽⁸⁾ in an attempt to explain the formation of porosity in Kirkendall experiments. It was suggested on that occasion that small impurity particles were responsible for the nucleation of pores, as this would considerably diminish the required degree of supersaturation of vacancies with respect to a perfect crystal.

To see whether this was the case, or whether the cavities nucleated directly at dislocations, the following experiments were performed.

A crystal was bent, slightly annealed and then treated in hydrogen. It was found that although the newly formed dislocations were decorated with silver, cavities had only developed along "old" dislocation lines, i.e. on pre-existing specks.

When the bent crystal was well annealed at a temperature close to the melting point, and allowed to cool slowly, specks were present along the polygonisation boundaries, and cavities developed around them when the crystals were hydrogen treated.

These experiments indicate that the silver precipitates more readily than the $\mathrm{NO_3}^-$ reduction products. This is due, in our view, to the greater mobility of the $\mathrm{Ag^+}$ ion. In the first experiments no cavities were formed along the newly formed dislocation lines because the temperature and time of anneal had not been sufficient to allow movement of a sufficient number of $\mathrm{NO_3}^-$ groups towards them.

We imagine the process of the formation and growth of a cavity in the following way. As soon as a small number of gas molecules succeed in agglomerating, they form a center of hydrostatic vacancies. The resulting small agglomerate (let us call it a "microcavity") of gas and vacancies has now the ability of rapid diffusion, as this implies only transfer of material from one wall of the "micro-cavity" to the other. As a consequence these micro-cavities will agglomerate, the larger ones growing at the expense of the smaller ones. Agglomeration will mainly take place at the dislocation lines as there is also elastic interaction between the stress field of the micro-cavity and that of the dislocation. This results in the formation of the larger cavities along dislocations.

The gas in this cavity may still be under high pressure, and it will then as a consequence attract vacancies, which will allow the cavity to expand and release the pressure. More gas can now be accommodated. There is then a balance between gas pressure and flow of vacancies towards the cavity.

The growth of a cavity centered on a dislocation probably takes place according to a mechanism similar to that considered by Frank for the growth of dislocated crystals. Consider the cavity centered on a dislocation with screw character, as represented in very schematic fashion in Fig. 12.

It is now clear that growth of the cavity i.e. removal of material from the crystal, will occur preferentially

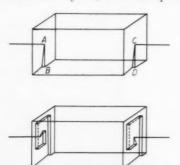


Fig. 12. Schematic view of the cavity formation along screw dislocations.

along the steps AB and CD. Stated in another, equivalent way: vacancies will precipitate along the steps AB and CD (this process will even be favoured by diffusion along the dislocation line). As a result the steps AB and CD wind up into a spiral and the situation shown in Fig. 9 follows. The side faces, in which no dislocations emerge, will either grow slowly or not at all at the final stage of the growth process.

This explains why the cavities are very often elongated in the direction of the dislocation line, and why faces of the cavity are stepped.

As a consequence of its line tension, the dislocation line will in many cases end at a corner of the cavity.

It is clear that as soon as vacancies precipitate, new vacancies will be produced to maintain the equilibrium concentration. The density of the crystal will be considerably lower in the regions containing cavities. In order to verify this, Dr. Spaepen of the C.S.K. at Mol (Belgium) kindly performed density measurements. The following results were obtained:

Specimen	Density at 15.26 °C (g/ml)		
Pure KCl	1.98970 ± 0.00002		
$KCl + AgNO_3 + H_2$ (bulk)	1.98935 ± 0.00002		
KCl + AgNO ₃ + H ₂ (near surface)	1.97610 ± 0.00005		
KCl + AgCl + AgNO ₃ as impu-			
rity + H ₂ (bulk)	1.98971 ± 0.00002		
KCl + AgCl + AgNO ₃ as impu-			
rity + H, (near surface)	1.98948 ± 0.00002		
KCl + AgCl + AgNO ₃ as impurity	1.99013 ± 0.00002		
KCl + KNO ₃	1.98931 ± 0.00002		
$KCl + Ag_{2}O$	1.98959 ± 0.00002		

195

This proves beyond doubt that a considerable expansion of the crystals takes place.

DISCUSSION

These experiments illustrate that the gaseous products of a chemical reaction in a solid precipitate along dislocations, if enough thermal activation is present to allow diffusion. The precipitation is made easier still at already existing specks.

One can draw a close analogy between the phenomena described here and the process of hydrogen embrittlement observed in copper (containing copper oxide) for instance. In both cases, a gaseous product is formed (in the latter case water vapour). From our observations it is reasonable to assume that in copper also the cavities will form on dislocations and pin them, thus causing the observed embrittlement. Also, in the case of copper the presence of particles of oxide or of another impurity will certainly favour the formation of cavities.

ACKNOWLEDGMENTS

We are very much indebted to Dr. Spaepen of the C.S.K. at Mol (Belgium) who kindly performed the density measurements and provided facilities for the irradiation of some crystals in the pile and with fission products. We also thank Dr. G. Vanderkelen for the mass spectrographic analyses and Mr. P. De Bièvre for recording the i-r spectra.

REFERENCES

- I. W. VAN DER VORST and W. DEKEYSER, Phil. Mag. 1, 882 (1956).
- J. H. SCHULMAN, J. Phys. Chem. 57, 759 (1953).
 G. HENNING, R. LEES and M. S. MATHESON, J. Chem. Phys. 21, 664 (1953).
- I. Maslakowez, Z. Phys. 51, 696 (1928).
 H. Etzel and J. H. Schulman, J. Chem. Phys. 22, 1549 (1954).
- A. SMAKULA, Z. Phys. 45, 1 (1927).
 E. HUTCHISON and P. PRINGSHEIM, J. Chem. Phys. 23, 1113 (1955).
- 8. F. Seitz, Acta Cryst. 3, 355 (1950).

2

THE KINETICS OF CELLULAR SEGREGATION REACTIONS*

J. W. CAHN†

Cellular segregation reactions, such as discontinuous precipitation and pearlite formation, often accomplish the segregation solely by diffusion along the cell boundary as it sweeps through the original unsegregated phase. Previous theories, which have assumed that the reaction is diffusion controlled, have been inadequate in describing many of its quantitative aspects.

If the diffusion is limited to the advancing cell boundary, the lamellae of the cells or nodules cannot reach equilibrium composition at any non-zero growth rate and for this reason the growth rate of the cells can no longer be determined by the diffusion rates alone. It is concluded that at least two controlling kinetic processes are required to describe such a complex reaction.

A simple model, which, in addition to diffusion control, assumes that the cell boundary moves with a velocity proportional to the net free energy decrease (taking into account the incompleteness of the segregation as well as the creation of lamellae surfaces), reproduces many of the observed features of these processes. Among these are the incompleteness of the segregation and the interlamellar spacing.

LA CINETIQUE DES REACTIONS DE SEGREGATION CELLULAIRE

Souvent les réactions de ségrégation cellulaire, telles que la précipitation des carbures et la formation de perlite, se produisent uniquement par diffusion le long de la frontière de la cellule lorsque celle-ci traverse la phase non ségrégée.

Les théories antérieures, qui admettaient que la réaction est contrôlée par la diffusion, sont incapables d'interpréter quantitativement de nombreux aspects de cette réaction.

Si la diffusion n'intéresse que la frontière de la cellule en mouvement, les lamelles des cellules ou nodules ne peuvent atteindre la composition d'équilibre pour toute vitesse de croissance non-nulle. Pour cette raison, la vitesse de croissance des cellules ne peut être déterminée en s'appuyant uniquement sur les vitesses de diffusion. Une telle réaction complexe ne peut donc être décrite que par l'intervention d'un minimum de deux mécanismes cinétiques.

Un modèle simple permet de reproduire la plupart des aspects observés et attribués à ces mécanismes. Ce modèle admet, outre l'action de la diffusion, que la frontière de la cellule se meut à une vitesse proportionnélle à la diminution d'énergie libre du réseau. On tient compte également de la formation de surfaces lamellaires ainsi que de l'état d'achèvement de la ségrégation.

DIE REAKTIONSKINETIK DER AUSSCHEIDUNG VON ZELLARTIGEN GEFÜGEN

Ausscheidungsreaktionen von zellartigen Gefügen, wie die inhomogene Ausscheidung und die Perlitbildung, laufen oft allein durch Diffusion entlang der Zellgrenze ab, während sich diese durch die ursprüngliche übersättigte Phase bewegt. Frühere Theorien, die angenommen hatten, dass die Reaktion durch die Diffusion bestimmt wird, reichen zur Beschreibung von vielen quantitativen Zügen nicht aus.

Wenn die Diffusion auf die vorrückende Zellgrenze beschränkt ist, können die Lamellen des Ausscheidungsgefüges bei einer endlichen Wachstumsgeschwindigkeit nicht die Gleichgewichtszusammensetzung erreichen, aus diesem Grund kann die Wachstumsgeschwindigkeit der Zellen nicht mehr allein durch die Diffusionsgeschwindigkeiten bestimmt sein. Daraus folgt, dass mindestens zwei bestimmende kinetische Vorgänge nötig sind, um solch eine komplexe Reaktion zu beschreiben.

Ein einfaches Modell, dem zugrunde liegt, dass die Reaktion durch die Diffusion bestimmt wird, und dass sich zusätzlich die Zellgrenze mit einer Geschwindigkeit proportional zur Abnahme der freien Energie bewegt (wobei sowohl die Unvollständigkeit der Ausscheidung als auch die Bildung von Lamellenoberflächen in Rechnung gesetzt wird) gibt viele der bei diesen Prozessen beobachteten Züge wieder. Unter diesen sind die Unvollständigkeit der Ausscheidung und die Abstände zwischen den Lamellen.

INTRODUCTION

VOI

195

Many solid state segregation reactions such as precipitation and eutectoid decomposition, result in a lamellar structure in which parallel plates of the final phases are grouped in nodules or cells. Most of the segregation occurs as the boundary of the growing nodules moves through the sample leaving behind the

^{*} Received April 11, 1958.

[†] General Electric Research Laboratory, Schenectady, New York.

[‡] The distinction between eutectoid decompositions and precipitations is as follows. In eutectoid decomposition two new phases form alternate lamellae in a cell or nodule growing from the parent phase. In precipitation one of the two phases forming the cell lamellae has the same structure as the parent phase but differs in composition and orientation. Otherwise the morphology is the same.

segregated structure. In recent years it has become apparent that diffusion along the moving nodule boundary is often the only way that this mode of segregation can occur, and that little diffusion occurs in the lattice ahead of the boundary or in the lamellae after they have formed. Often the new phases in the nodules are formed at compositions which differ from the final equilibrium composition and can only approach equilibrium by means of slow lattice diffusion.

This method of segregation has been called a pearlite reaction for eutectoid decompositions. For precipitations it has been known as cellular or discontinuous precipitation and occasionally as the recrystallization reaction. The mechanism for this type of process has been the subject of many papers. The approach of Zener⁽⁴⁾ for pearlite, which has been modified by Turnbull⁽⁵⁾ for precipitation, seems to have been the only one which has attempted to treat some of the quantitative relationships describing this process. It has been quite unsuccessful in predicting the spacing between lamellae of the same phase, since the predicted spacing is reported to be smaller than that observed by a factor which ranges^(4,6) from 3 to 100.

For the iron-carbon eutectoid (pearlite) Zener assumed that carbon diffusion through the lattice, rather than along the pearlite boundary, controls the growth of pearlite. (The extrapolated carbon diffusion data are sufficiently high to account for the carbon segregation.⁽⁷⁾) Much evidence exists, however, to indicate that the rate of growth is not controlled by the carbon diffusion rate. For example, it is known that pearlite nucleates on a grain boundary but grows only into one of the adjoining grains. This cannot be consistent with the assumption that carbon diffusion through the lattice controls the rate, for then the pearlite would grow into both grains. Furthermore, alloy elements exert a strong influence on the growth rate without having a corresponding effect on the carbon diffusion rate. There is strong evidence that the alloy elements diffuse along the boundary, (8) and it may be this diffusion which is important in controlling the growth rate.

Turnbull's modification (for precipitation) of Zener's treatment included the assumption that the process was grain boundary diffusion controlled. However, not all of Zener's original relations were consistently modified and there are some which still apply only to lattice diffusion.

The present paper is an attempt to develop a

model for these processes on the assumption that lattice diffusion is negligible compared with grain boundary diffusion. Two important modifications result. The first is that the cell can not segregate to equilibrium composition for any non-zero growth rate. This decreases the overall free energy change and places an upper limit to the growth rate for a given spacing. This upper limit results from the fact that at sufficiently high growth rates the segregation would be insufficient to give the thermodynamically required decrease in free energy accompanying cell formation.

The second important modification results from the fact that any growth rate smaller than the above mentioned upper limit is now possible and consistent with the diffusion rate. Another kinetic parameter is, therefore, needed to specify the process. In this paper, a model which assumed that the boundary moves with a velocity proportional to the net free energy decrease will be developed. It will be shown that the behavior of the cellular segregation reaction depends on the ratio of the mobility of the boundary to the diffusion coefficient along the boundary. Two simple systems will be treated; precipitation from dilute solution, and a symmetric eutectoid.

THEORY

Zener's model⁽⁴⁾ for pearlite assumed that carbon diffusion ahead of the interface controlled the rate of growth. The rate of this diffusion to the tips of the carbide lamellae (per unit area of the lamellae tip) is proportional to a driving force and inversely proportional to the spacing. This driving force was assumed to be proportional to the net free energy change ΔF accompanying the formation of carbide and ferrite of equilibrium composition, including the surface energy of the ferrite-carbide interfaces. Thus, per mole alloy

$$\Delta F = \Delta F_0 + \frac{2\sigma V}{S} \tag{1}$$

where ΔF_0 is the free energy change for the formation of a mole of equilibrium composition pearlite, σ is the carbide–ferrite surface free energy, V the molar volume of pearlite and S the interlamellar spacing. The growth rate, which is proportional to the flux to lamellae tips and hence also to $\Delta F/S$, is small for large spacings because of the large distance over which diffusion takes place. It is also small for small spacings because $-\Delta F$ becomes small as more energy is converted to surface free energy. ΔF and hence also the growth rate vanish for a critically small

VOL.

1959

[§] See later section on ΔF_0 .

spacing S_0 given by

$$S_0 = -\frac{2\sigma V}{\Delta F_0} \tag{2}$$

The maximum growth rate is obtained for a maximum in $-\Delta F/S$ and occurs for a spacing equal to twice S_0 . Zener assumed that this spacing would be the observed spacing, but this prediction has not been verified. In view of this last assumption, this is not surprising, for the spacing could easily be governed not by the desire to maximize growth, but by any one of a number of quantities which the system might want to maximize, e.g. the rate of entropy production. Alternatively the ability of the cell to create new platelets might be the limiting factor. To eliminate this latter point the experiments on thermal cycling were carried out, and are reported later in this article.

When we now consider how Zener's model must be modified to take into account the assumption that all segregation occurs by diffusion along the advancing cell boundary we come to the following conclusions:

- 1. The system cannot reach equilibrium segregation. This has been shown experimentally for several systems⁽⁶⁾ and is a direct consequence of the diffusion assumption. The degree of segregation will be a function of the growth rate, spacing and diffusion coefficient.
- 2. Only a fraction, P, of ΔF_0 is realized if segregation is incomplete. The minimum possible spacings from purely thermodynamic reasons would correspondingly be larger by 1/P. This fraction P is a function of growth rate, spacing, and diffusion coefficient and for precipitation has a form quite different from that for eutectoid decompositions. An examination of Fig. 1 shows that, for any small amount of precipitation, P is positive as long as the precipitate does not differ too drastically from the equilibrium composition. Hence a small amount of segregation, leaving the original phase only slightly changed in composition, will make P positive. For eutectoids, however, both new phases have to be reasonably close to the final composition for P to be positive, and hence a large amount of segregation must be accomplished.
- 3. The growth rate is no longer inversely proportional to S. The gradients are still inversely proportional to S, and so is the total flux to the lamellae, but the flux per unit area of lamellae tip, which is the quantity that determines its growth, is inversely proportional to both S and I (the thickness of the lamellae). If the degree of segregation is constant, I is proportional to S and we obtain the relationship derived by Turnbull⁽⁵⁾ that the growth rate is inversely

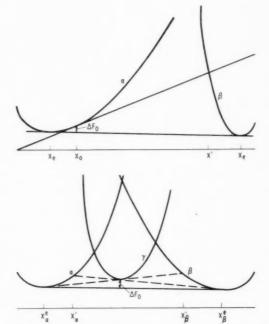


Fig. 1. Schematic free energy curves for a precipitating and eutectoid system. The chemical part of the free energy will decrease in a precipitating system as long as precipitate of a composition exceeding X' is formed, regardless of how little precipitates, and, therefore, of how little the α phase change in composition. For a eutectoid system none of the new phases can approximate the original phase in composition, and segregation to at least $X_{\alpha'}$ and $X_{\beta'}$ must occur.

proportional to S^2 . But if the degree of segregation is not constant no such relationship will be obtained.

19

4. For a given spacing a range of growth rates is possible, resulting in different degrees of segregation. Therefore, another quantity must be specified. In Zener's treatment the spacing fixed the growth rate by the diffusion equation. Actually the diffusion equation provides only a relationship between spacing. growth rate, and the degree of segregation, and permits a range of growth rates for a given spacing within the limits imposed by thermodynamics. Another physical principle which relates these three quantities, growth, spacing and segregation is needed. Since within the limits imposed by thermodynamics, the boundary is free to move at any velocity, one can assume that it moves as an ordinary boundary under an applied pressure. The average pressure in this case is $\Delta F/V$ where ΔF now takes into account the fraction P of ΔF_0 realized due to incomplete segregation, as well as the retarding forces of the interlamellar surfaces.

$$\Delta F = P\Delta F_0 + \frac{2\sigma V}{S} \tag{3}$$

Any periodic variation in both driving pressure and boundary mobility will be smoothed out by a curving of the cell boundary if the surface tension of the boundary is a sufficiently large fraction of $-P\Delta F_0 S/V$. Thus we can use the ΔF defined above and write for the growth rate G,

$$G = -M\Delta F \tag{4}$$

where M is an average mobility of the boundary.

Since the growth rate in turn influences the degree of segregation through the diffusion equation and hence P, we have two simultaneous equations in the three unknowns. Thus, for a given spacing we can then determine the corresponding growth rate and degree of segregation.

What then determines the spacing? From the thermal cycling experiments we have good reason to believe that it is not the inability to create new lamellae, for a colony or nodule which had a spacing smaller than that usually observed for a given temperature rapidly changed over to the characteristic spacing. Let us assume that the spacing which the system chooses is that which maximizes the decrease in the free energy ΔF . Because of equation 4 this is also the spacing which maximizes both the growth rate, G, and the rate of decrease in free energy per unit area of cell boundary $G\Delta F_0/V$. It should be possible and would be desirable to justify this assumption on more basic grounds, but how this should be done has so far eluded the author.

For comparison it is interesting to note that in Zener's treatment the maxima in $-\Delta F$, G and $-G\Delta F/V$ do not coincide and give respectively for S/S_0 the values ∞ , 2 and 3 for bulk diffusion and ∞ , 3/2 and 2 for cell boundary diffusion. Zener and Turnbull both chose a maximum in G.

The diffusion equation

Of the available free energy change ΔF_0 , only the fraction P is realized during the segregation. P is related to the growth rate and the spacing by the diffusion equation which we will solve for two highly idealized cases. These illustrate some of the features of precipitation and eutectoid decomposition.

We will make the following simplifying assumptions:

- (1) That the advancing boundary is plane. This will underestimate the effect of spacing, and result in a higher value of P.
- (2) That no diffusion occurs except in the boundary and that the boundary can be represented by a slab of thickness δ , of material of concentration X_B having a diffusion coefficient D_B . D_B will be assumed independent of concentration and δ will be considered sufficiently small for there to be no concentration variation across the thickness.

(3) That the system has reached steady state, i.e. that the concentration in the advancing slab is stationary. We can then write the diffusion equation

$$D_B \delta \frac{d^2 X_B}{dZ^2} + G(X_0 - X_P) = 0 \tag{5}$$

where X_0 , X_P are the concentrations of the matrix and lamellae respectively and Z is the distance along the boundary normal to the lamellae. X_B and X_P are functions of Z, in other words the lamellae are allowed to vary in composition across their thickness.

- (4) That X_B and X_P are related by some simple equation. This means that the local lamellae composition is related to the composition of the boundary ahead of it.
- (5) That the phases are of equilibrium composition along the interface between lamellae.

Precipitation from dilute solution

Here we shall assume that X_P for the depleted parent phase is proportional to X_B where the X values represent the minor component. The diffusion equation is then easily integrated to give for the depleted parent phase

$$X_P = X_0 + A \cosh \left(\frac{kGS^2}{D_R\delta}\right)^{1/2} \frac{Z}{S} \tag{6}$$

where $k = X_P/X_B$, A is an integration constant, and Z is measured from the center of the lamella of the parent phase.

For precipitation from dilute solution the precipitate lamellae will be thin compared to the spacing. Hence in view of the fifth assumption we can set $X_P = X_c$ at Z = S/2 and thus evaluate A to obtain for the depleted parent phase lamellae

$$\frac{X-X_0}{X_e-X_0} = \frac{\cosh\left(\frac{kGS^2}{D_B\delta}\right)^{1/2}\frac{Z}{S}}{\cosh\frac{1}{2}\left(\frac{kGS^2}{D_B\delta}\right)^{1/2}} = \frac{\cosh\sqrt{\alpha}\cdot\frac{Z}{S}}{\cosh\frac{\sqrt{\alpha}}{2}} \quad (7)$$

The important parameter describing this process is

$$\alpha = \frac{kGS^2}{D_B\delta}\,.$$

The fraction of minor component precipitated is

$$Q = \frac{2}{(X_0 - X_c)} \int_0^{1/2} (X_0 - X) \, d(Z/S)$$

which upon integration becomes

$$Q = \frac{2}{\sqrt{\alpha}} \tanh \frac{\sqrt{\alpha}}{2} \tag{8}$$

VOL. 7 1959

19

For precipitation from slightly supersaturated solution the free energy curve can be approximated by a parabola, and we obtain as the fraction of the total free energy change released by cellular precipitation

$$P(\mathbf{x}) = 1 - \frac{2}{(X_0 - X_e)^2} \int_0^{1/2} (X - X_e)^2 \, d(Z/S)$$

which gives

$$P(\alpha) = \frac{3}{\sqrt{\alpha}} \tanh \frac{\sqrt{\alpha}}{2} - \frac{1}{2} \operatorname{sech}^2 \frac{\sqrt{\alpha}}{2}$$
 (9)

If P is a function of α alone, the basic assumption that

$$-\Delta F = -P\Delta F_0 - \frac{2\sigma V}{S}$$

be maximized results in the following equation for α in terms of a new dimensionless parameter β

$$\beta = -\frac{kM\sigma^2V^2}{D_B\delta\Delta F_0} = \frac{\alpha^3P'}{P+2\alpha P'}$$
 (10)

where $P' = dP/d\alpha$. Equation 10 gives α as a function of the important parameter β which contains only terms that can be evaluated by independent measurement. Figure 2 gives the various quantities of interest in a precipitation process. P and Q are defined above as respectively the fraction of the available free

energy change released by precipitation, and the fraction of excess solute precipitated. $R = -2\sigma V/$ $S\Delta F_0 = S_0/S = 2\alpha P'$ is the fraction of ΔF_0 converted to surface free energy, and can have any value from 0 (infinite spacing) to 0.49 which corresponds to a spacing slightly larger than Zener's predicted spacing. (P-R) is the fraction of ΔF_0 available to exert pressure on the boundary and hence is equal to $G/(-M\Delta F_0)$.

The prediction is that, for a highly mobile boundary with a low diffusion constant, the precipitation is almost reversible in that all of the chemical energy released is converted to surface energy and the boundary goes as fast as is thermodynamically possible. At the other extreme of small β , the boundary is sluggish compared to its ability to accomplish segregation. The spacing can now be large and the segregation will still be sufficiently complete. Furthermore, a large spacing will reduce the drag due to surface tension on the sluggish boundary, permitting the full pressure of ΔF_0 to bear on it.

Decomposition of the symmetric eutectoid

Let us consider a symmetric eutectoid system with the eutectoid composition at $X_0 = 1/2$, the two new phases at $X_{\alpha}^{\ e} = X_e$ and at $X_{\beta}^{\ e} = 1 - X_e$ where $X_e < 1/2$. We will assume that the concentration of the minor constituent in either phase is proportional to its concentration in the boundary, i.e. $X_P/X_B=k$ for the alpha phase, and $(1 - X_P)/(1 - X_B) = k$ for the

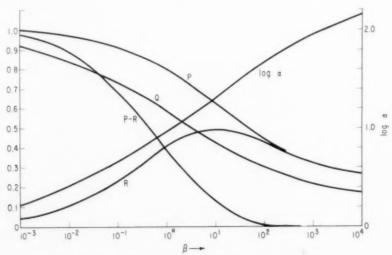


Fig. 2. Precipitation from dilute solution as a function of the parameter $\beta =$ $-MV^2\sigma^2/D_R\delta\Delta F_0$

P the fraction of ΔF_0 realized.

Q the fraction of material precipitated.

R the fraction of ΔF_0 expended on surface energy. P-R the fraction of ΔF_0 exerting a pressure on the cell boundary $\beta=kGS^2/D_B\delta$

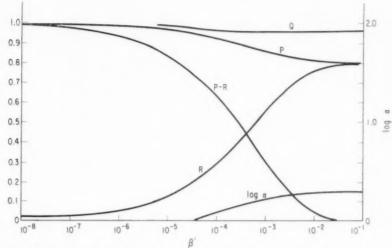


Fig. 3. Decomposition of the symmetric eutectoid as a function of the parameter $\beta' = M V^2 \sigma^2 / D_B \delta C$ for $\Delta F_0 = -0.010$.

 β phase, where k is a constant. Then for the α phase

$$\frac{\frac{1}{2} - X}{\frac{1}{2} - X_e} = \frac{\cosh\left(\frac{kGS^2}{D_B\delta}\right)^{1/2} \frac{Z}{S}}{\cosh\frac{1}{4}\left(\frac{kGS^2}{D_B\delta}\right)^{1/2}} \tag{11}$$

and for the β phase

$$\frac{X - \frac{1}{2}}{X_e - \frac{1}{2}} = -\frac{\cosh\left(\frac{kGS^2}{D_B\delta}\right)^{1/2} \frac{(S/2 - Z)}{S}}{\cosh\frac{1}{4} \left(\frac{kGS^2}{D_B\delta}\right)^{1/2}}$$
(12)

From assumption (5) we obtain $k=2X_e$. We can define Q again as follows

$$Q = \frac{4}{(\frac{1}{2} - X_e)} \int_0^{1/4} (\frac{1}{2} - X) \, d(Z/S)$$

$$= \frac{4}{\sqrt{2}} \tanh \frac{\sqrt{\alpha}}{4}$$
(13)

which is quite similar to the expression derived before (equation 8). In order to evaluate P we again assume a parabolic free energy curve for the two new phases. Hence the free energy ΔF of each phase relative to α and β in equilibrium with each other is

$$\Delta F = \frac{C}{(\frac{1}{2} - X_e)^2} (X - X_e)^2 \text{ for } \alpha$$

$$\Delta F = \frac{C}{(\frac{1}{2} - X_e)^2} (X + X_e - 1)^2 \text{ for } \beta$$
(14)

C is approximately temperature independent and is very much larger than $-\Delta F_0$. The ratio $-\Delta F_0/C$ varies approximately as the undercooling from the eutectoid temperature.

Using equation (14) we can write as before

$$\begin{split} P &= 1 + \frac{4C}{\Delta F_0 \left(\frac{1}{2} - X_e\right)^2} \int_0^{1/4} (X - X_e)^2 \, d(Z/S) \\ &= \left(1 + \frac{C}{\Delta F_0}\right) - \frac{C}{\Delta F_0} \left(\frac{6}{\sqrt{\alpha}} \tanh \frac{\sqrt{\alpha}}{4} \right) \\ &\qquad \qquad - \frac{1}{2} \operatorname{sech}^2 \frac{\sqrt{\alpha}}{4} \right) \quad (15) \end{split}$$

Again it is worth noting that, because $-C/\Delta F_0$ is large, α must be small in order that P be positive. This was mentioned before in connection with Fig. 1 and is apparent from the form of equation 15.

Since we are only interested in the region of positive P and hence small α , we can expand P in powers of α :—

$$P(\alpha) = 1 + \frac{2C}{15\Delta F_0} \left(\frac{\alpha}{16}\right)^2 + \cdots$$

Since P is again a function of α alone, we can apply equation 10 and obtain, by multiplying by $-\Delta F_0/C$,

$$\beta' = \frac{kM\sigma^2V^2}{D_B\delta C} = -\frac{\frac{64}{225} \left(\frac{\alpha}{16}\right)^5}{\frac{\Delta F_0}{C} + \frac{2}{3} \left(\frac{\alpha}{16}\right)^2}$$
(16)

where $\beta' = -\beta \Delta F_0/C$ and has the advantage that it is approximately temperature independent for small undercooling. Similarly we obtain

$$R = -\frac{8C}{15\Delta F_0} \left(\frac{\alpha}{16}\right)^2 \tag{17}$$

In Fig. 3 the values of P, Q and R are plotted for

VOL. 7 1959



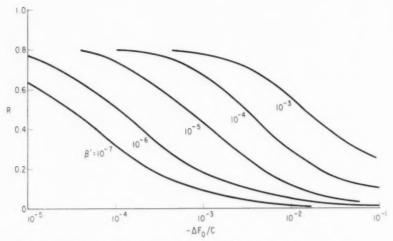


Fig. 4. The fraction R for a symmetric eutectoid as a function of ΔF_0 for various values of β' .

eutectoids with $\Delta F_0/C = -10^{-2}$ for comparison with Fig. 2. For small values of β' and β the behavior is quite similar, but for large values the behavior is different. For large β' equation (7) gives

$$\frac{\alpha}{16} = \left(-\frac{3\Delta F_0}{2C}\right)^{1/2}$$

and P=R=0.8 for all values of $\Delta F_0/C$ for a symmetric eutectoid. Thus for large β' the eutectoid differs markedly from the precipitate. This is because in order to accomplish the thermodynamically required amount of segregation, a fine spacing is required. This fine spacing, in the limit, requires 0.8 of the available free energy.

In order to examine the behavior of the spacing with temperature for various systems, R is plotted against $\Delta F_0/C$ for various values of β' (Fig. 4).

The iron-carbon eutectoid

The iron–carbon eutectoid is of great practical interest. Unfortunately, the pure binary has never been systematically studied, and it is well known that small quantities of impurities or alloying elements exert a profound influence on the growth rate $G^{(7)}$. The high temperature carbon diffusion data can be extrapolated to the region in which pearlite occurs, and this gives a bulk diffusion coefficient which, within experimental error, could account for the observed growth rate. The fact that pearlite invariably grows into only one of the two grains must indicate that carbon diffusion through the bulk is not the rate determining step. Furthermore, the alloying elements which cannot diffuse rapidly through the bulk appear to segregate to a large extent and influence

the growth rate markedly without affecting the spacing by more than a factor of 2.⁽⁷⁾

Zener⁽⁴⁾ has pointed out that the impurities or alloy elements can not affect ΔF_0 markedly because of their low concentration. However, if the distribution coefficient between the boundary and the ferrite or cementite is small, they can be swept along by the boundary and thus reach a very high concentration. In this respect their effect on the driving pressure may not be negligible. If this is so a large degree of segregation of the alloy elements will be accomplished.

A more significant factor in the alloy effect might be in the marked dependence of grain boundary mobility on impurities. To a first approximation it seems that this would manifest itself mainly in the growth rate, since effects due to changes in the parameter β' could well be independent of impurity content. Even if β' changes, the ratios P,Q and R are relatively insensitive to β' and the more significant change in

$$G = -(P - R)M \Delta F_0$$

would come from changes in M. Since the spacing is given by

$$S = -\frac{2\sigma V}{R\Delta F_0}$$

it contains no quantities which would depend drastically on impurities.

The calculation of ΔF_0

The value of ΔF_0 is clearly defined here as the maximum available free energy change when one mole of alloy is decomposed to the ultimately stable phases. Some confusion exists because Zener introduced into his discussion both the free energy change ΔF_0 , and the chemical potential change $\Delta \mu$ of the minor

component (carbon). For his computation of the minimum possible spacing he correctly used ΔF_0 .

The chemical potential change is related by the Gibbs-Thompson equation to the minimum permissible radius of curvature at the tip of the lamellae. The free energy change is related to the minimum permissible spacing. It is possible from a knowledge of the various surface tensions, and the $\Delta\mu$ values for both components, to arrive at the minimum spacing by considering the curvatures of the cell boundary and the triangle of forces at the junction of two lamellae with this boundary. This gives an expression for the minimum spacing identical with equation (2).

When we are considering precipitation from a dilute solution, $\Delta \mu$, which is equal to $RT \ln{(X_c/X_0)}$, differs from ΔF_0 by a factor of $1/2(X_0-X_e)$. The former varies as (X_0-X_e) whereas the latter varies as $(X_0-X_e)^2$. Turnbull^(5,6) wrongly uses $\Delta \mu$ instead of ΔF_0 to compute his spacing.

 $\Delta\mu$ is related to the minimum precipitate thickness, ΔF_0 to the minimum spacing. That this is self consistent may be seen as follows: If the supersaturation (X_0-X_e) is doubled, $\Delta\mu$ is doubled and the platelets may be half as thin. But twice as much will precipitate on these thinner platelets. Hence four times as many platelets are possible, resulting in a reduction in the minimum spacing by a factor of 4.

1959

Turnbull and Treaftis⁽⁶⁾ report a spacing 100 times coarser than Zener's predicted spacing. This is however the result of confusing $\Delta\mu$ with ΔF_0 . In fact the Zener spacing as calculated by Turnbull would result in the thermodynamically impossible situation (in equation 1) where the surface energy term would be ten times the available free energy. Figure 5 is a plot, from their data, of $-S\Delta F_0/2V$ i.e. σ/R ($-S\Delta F_0/2V=2\sigma$ if the Zener spacing exists). In order to evaluate ΔF_0 Henry's and Rauolt's laws were assumed.

$$\Delta F_0 = NkT \Big(X \log \frac{X_e}{X} + (1-X) \log \frac{1-X_e}{1-X} \Big)$$

 X_c was taken from Stockdale's solubility data.⁽⁹⁾ The more recent solubility data of Borelius $et\ al.^{(10)}$ was not used because its temperature dependence seemed inconsistent with recent calorimetric measurements of the heat of formation of the alloys.⁽¹¹⁾ Indeed preliminary results⁽¹²⁾ on the redetermination of the tin solubility, by observing resistometrically the temperature at which it is completely dissolved, indicates that Borelius' phase boundary is too high at the lower tin concentrations. The difference between Stockdale's and Borelius' data amounts to a factor of 2 in ΔF_0 in the region of interest for Fig. 5.

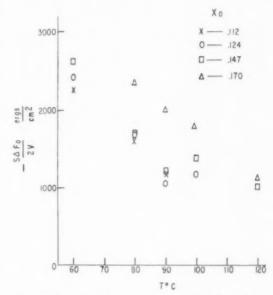


Fig. 5. The spacing data of Turnbull and Treaftis. (6)

Using a value of σ of 150 ergs/cm² we obtain a value of R ranging from 0.06 to 0.15, and thus the spacing is coarser than the Zener prediction by a factor ranging from 3 to 8 instead of the reported factor of 100.

Thermal cycling experiments

A plausible explanation for the failure to observe the spacing predicted by Zener is that it is difficult to nucleate or create the additional lamellae. It then becomes hard to understand the rapid creation, during a quench, of a band of fine pearlite so often observed on specimens of partially transformed isothermal pearlite. Similar observations exist for Pb-Sn precipitate nodules which continue growing, at room temperature, with the characteristic room temperature spacing with no discernable transition region. Down-quench observations like these could still be explained by rapid nucleation or multiplication of plates to within a certain factor of the Zener spacing. Up-quenches on the other hand force the specimen to start with a finer spacing than it normally would have, that is, a spacing closer to the Zener spacing. This should be a more nearly ideal spacing according to Zener, but not according to the present model. Accordingly two alloys, an SAE 1080 plain carbon eutectoid steel and a Pb-6.5 wt. % Sn, were partially transformed at a lower temperature to establish a fine spacing, and then permitted to grow at a higher temperature. In all cases the spacing coarsened within a short distance. Figures 6 and 7 are representative micrographs of the observed spacing change. The spacing predicted by Zener is therefore

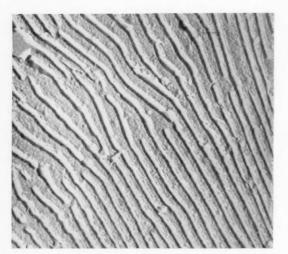


Fig. 6. Spacing change in a SAE 1080 plain carbon eutectoid steel during an up-quench from 660°C to 700°C. $\times 7812.$

not "an ideal but otherwise unattainable" spacing. The system will approach its characteristic spacing from perturbations in either direction.

DISCUSSION

It has been found necessary to describe the growth of a cellular segregation reaction by at least two independent rate processes: the diffusion along the cell boundary, and the mobility of the cell boundary in response to the driving pressure which results from the decrease in free energy when the boundary moves and accomplishes segregation. The model was evaluated for two highly idealized cases; precipitation from dilute solution and a symmetric eutectoid. It was found that for each case, two extremes occurred. The low-mobility high-diffusivity extreme resulted in a coarse interlamellar spacing and complete segregation. This is because, when the boundary is sluggish compared to the diffusion coefficient, much segregation can be accomplished even at large spacings.

The high-mobility low diffusivity extreme resulted in just enough segregation so that the free energy change was negative. The boundary rushed ahead as fast as it could within the limits imposed by the thermodynamics of the model. For eutectoids this resulted in an even finer spacing than that predicted by Zener, because much segregation must be accomplished before ΔF is negative. For precipitation this resulted again in a coarse spacing, and this time in little segregation.

Unfortunately none of the important kinetic parameters for a cell boundary is known. We are therefore limited to estimates and checks for internal consistency.

For instance there should be a relationship between spacing and degree of segregation which we can read off Fig. 2. From Turnbull's and Treaftis' spacings data we estimate $R \sim 0.05-0.15$, which means a β of the order of 10⁻², which in turn should go along with a degree of segregation Q of 85-90%. From their resistance data Turnbull and Treaftis(3) estimate Q = 0.6. A recent calorimetric determination of the heat of formation of the alloy(11) can be combined with the reported heat of precipitation(13) to give Q = 0.6. Both these estimates of Q are for room temperature, whereas the spacing was measured at higher temperatures. Since there is a large uncertainty in the estimation of R, owing to the estimation of ΔF_0 from an extrapolated phase boundary, the comparison is inconclusive. It would be useful to have simultaneous knowledge of the heat and free energy of formation, the heat of precipitation, the surface tension and spacing.

Another comparison with data comes from measured growth rates. Let us consider the case when β is small, that is, the low-mobility high-diffusivity extreme. Then (P-R) is approximately constant and the growth rate is then proportional to ΔF_0 or the



Fig. 7. Spacing change in a Pb-6.5% Sn colony started at 60°C, continued first at 80°C and then at room temperature.

VOI 7 195 square of the supersaturation for small supersaturation. This is quite different from Turnbull's prediction that

 $G = \frac{X_0 - X_e}{X_0} \left(\frac{D_B \delta}{S^2} \right)$

which, together with the spacing prediction, results in a fifth power dependence of growth on supersaturation. Table 1 gives a summary of growth data⁽⁴⁾ for Au–Ni in the small supersaturation region. The data seems to fit a square dependence, for which $(X_{500}-X_e)/(X_{100}-X_e)=5^{1/2}=2.2$, better than a fifth power dependence $5^{1/5}=1.38$. This therefore permits a checking of the basic assumption of this paper.

The value of β of 10^{-2} estimated for Pb–Sn is smaller by a factor of 10^{-3} than would be estimated from the slab model of a boundary, if we assume isotropic mobilities in the slab and no barrier to the incorporation or removal of atoms into or from the crystal lattices. That β and M appear to be small by this factor is not therefore surprising. In an actual boundary the atomic mobilities may vary over a wide spectrum as one traverses normal to the boundary. The atomic mobilities which enter into the diffusion coefficient are heavily weighted in favor of the largest, while the reverse is true for the boundary mobility which will reflect the lower atomic mobility of the atoms which are in process of leaving or entering the boundary.

Most of the experimental observations of spacing fall in a very narrow range of undercooling, ΔT (a factor of 10), or supersaturation (a factor of 2). Over these ranges β and ΔF_0 would hardly change sufficiently to cause much variation in R, the fraction of free energy expended on lamellae surfaces. Indeed R appears to vary only slightly. The trend in R, as well as its value, are predicted by this model but require data on D_R and M.

1959

Experiments on cellular precipitation in bicrystals, to determine growth rate, spacing and fraction precipitated as a function of misorientation, would be extremely useful, since the variations of M and Dwith θ can be estimated, and ΔF_0 remains constant. The one experimental observation available on growth rate only has been interpreted(15) according to the Zener-Turnbull model. This keeps the spacing constant and therefore makes the growth rate proportional to D_B . Identical results would be obtained for the present model if the ratio of mobility to diffusion constant is independent of orientation. Then β is constant, resulting in a constant spacing and degree of segregation as well as a growth rate proportional to boundary mobility. Conversely, if the spacing is found not to be constant, one can predict

the change in β and hence in M/D_B . This, together with a knowledge of the angle of dependence of D_B , would enable one to predict M, G and Q.

In the case of the iron-carbon eutectoid, pearlite, it would be useful to examine the high purity alloy to see if spherical instead of hemispherical nodules begin to form, and in addition to assess the complete role of the impurities which have hitherto always been present.

Often general intragranular precipitation competes at higher temperatures with the cells, giving rise to what has been called the recrystallization reaction. By this term it has been implied that the general precipitation strains the grain, and that the cellular reaction has for its driving force the strain energy due to the general precipitation. That this is not so can be seen from the observations that the so-called recrystallization reaction often stops before it has consumed its grain. This can only mean that the driving force has disappeared. This would seem to rule out strain energy, and is strong support for a chemical driving force which has been diminsished by general precipitation.

In summary the author would like to stress that the basic point of this paper is the need for at least two kinetic parameters to describe cellular segregation processes. The choice of the grain boundary diffusion coefficient and the grain boundary mobility was made here and is capable of experimental check. The assumption that the system chooses to maximize the free energy decrease proved to be useful, and it is felt that such an assumption should be derivable from more basic kinetic assumptions.

ACKNOWLEDGMENTS

Thanks are due to D. Turnbull for his continued stimulation; to H. N. Treaftis and M. Ruoff for their assistance in the thermal cycling experiments, to J. C. Fisher, W. C. Hagel, J. E. Hilliard, G. W. Sears and D. A. Vermilyea for their valuable criticism, and to E. E. Underwood for permission to quote unpublished data from his thesis.

Table 1. Composition (at % Ni) at which growth rate of 100 Å/sec and 500Å/sec are observed in Au-Ni alloys (E. E. Underwood)

T (°C)	X_{σ}	X_{100}	X_{500}	$\frac{X_{500} - X_{60}}{X_{100} - X_{60}}$
700	6.40	9.75	17.75	4.1
	66.75	58.5	50.25	2.0
600	$\left(\begin{array}{c} 4.25 \\ 77.0 \end{array}\right)$	5.90 71.1	8.50 66.5	2.6 1.8
500	2.5	7.6	19.5	3.3
	84.0	77.5	64.5	3.0

REFERENCES

- 1. C. S. Smith, Trans. Amer. Soc. Metals. 45, 533-75 (1953).
- D. TURNBULL, Diffusion Short Circuits and Their Role in Precipitation, 1954 Bristol Conf. p. 203-211.
 D. TURNBULL and H. N. TREAFTIS, Acta Met. 3, 43-54

- D. Turnbull and H. S. Tabada.
 (1955).
 C. Zener, Trans. Amer. Inst. Min. (Metall.) Engrs. 167, 550 (1956).
 D. Turnbull, Acta Met. 3, 55-63 (1955).
 D. Turnbull and H. N. Treaftis, Trans. Amer. Inst. Min. (Metall.) Engrs. 212, 33-8 (1958).
 R. F. Mehl and W. C. Hagel, Progress in Metal Physics Vol. 6, pp. 74-134. Pergamon Press, London (1956).
- 8. J. W. Cahn, Trans Amer. Inst. Min. (Metall.) Engrs.
- 209, 140-4 (1957).
 D. Stockdale, J. Inst. Met. 49, 267 (1932).
 G. Borelius, F. Larris and E. Ohlsson, Arkiv für Mat.
- G. Boreltus, F. Larris and E. Ohlsson, Arrive far Mar. Astr. och Fys. 31A, No. 10 (1944).
 W. K. Murphy and R. A. Oriani, Acta Met. 6, 556 (1958).
 H. N. Treaftis and J. W. Cahn, to be published.
 W. Desorbo and D. Turnbull, Acta Met. 4, 495-509 (1956).
- (1956).
 14. E. E. Underwood, Precipitation in Gold Nickel Alloys, D.Sc, Thesis, MIT, Fig. 35, (1954).
 15. J. W. Cahn, Acta Met. 4, 217 (1956).

THE SURFACE HARDENING OF X-IRRADIATED NaC1*

E. AERTS, S. AMELINCKX and W. DEKEYSER†

The increase in Vickers hardness due to exposure of NaCl single crystals to $40~\rm kV$ unfiltered X-rays is studied both as a function of irradiation time and of depth, i.e. the distance from the surface facing the beam. The optical absorption was also measured, as a function of these variables, on the same crystals in order to find a possible correlation between hardness increase and colour centre concentration. The effect of optical and thermal bleaching was also followed.

It is found that the hardness near to the surface is influenced by the presence of a free surface; when thin specimens are used an increase in hardness is found on both surfaces.

All observations can satisfactorily be explained if the surface hardening is assumed to be due to the formation of small colloids. The hardening is then quite similar to precipitation hardening in an alloy. The formation of the colloids is analogous to the "printing-out" process in silver bromide exposed to light.

LE DURCISSEMENT SUPERFICIEL DE NaCI IRRADIÉE PAR RAYONS X

La variation de la dureté de monocristaux de NaCl, provoqué par leur exposition à des rayons-X a été mesureé en fonction de la dureté d'irradiation et de la profondeur, c.à.d. de la distance à la face perpendiculaire au faisceau incident. Les spectres d'absorption ont été mesurés sur les mêmes échantillons utilisés pour les mesures de la dureté afin de déceler une corrélation possible entre la dureté, la nature et la densité des centres de couleur. L'effet de la décoloration optique et thermique a été suivi.

Il a été trouvé que la surface joue un rôle important dans le durcissement observé. Si des échantillons très minces sont utilisés on observe un durcissement des deux côtés du specimen.

Toutes les observations peuvent s'expliquer logiquement en admettant que le durcissement superficiel est dû à la formation de colloïdes. Le phénomène est de ce fait similaire au durcissement structural qu'on observe dans les alliages. La formation des colloïdes est similaire à l'effet "print out" des halogénures d'argent exposés à la lumière.

DIE OBER FLÄCHENAUSHÄRTUNG VON BESTRAHLTEN NaCI-MONOKRISTALLEN

Die durch Röntgenbestrahlung hervorgerufene Variation der Vickershärte von NaCl-Monokristallen wurde gemessen als Funktion der Bestrahlungs dauer sowie der Fiefe-d.h. der Entfernung zu der Fläche, die senkrecht zum einfallenden Strahlungsbündel liegt. Die Absorptions-spektren wurden an den gleichen Proben gemessen, um den Zusammenhang zwischen Härte, Natur u. Dichte der Farbenzentren festzustellen. Der Effekt einer optischen u. thermischen Entfärbung wurde studiert.

Es wurde festgestellt, dass die Oberfläche eine wichtige Rolle bei der Härtezunahme spielt. Bei sehr dünnen Proben, wurde ein Härkanstieg an beiden Flächen festgestellt.

Alle diese Beobachtungen können logisch erklärt werden, wenn man annimmt dass, der Härteanstieg der Oberfläche durch die Bildung von kolloiden herrorgerufen wird. Er ähnelt dann der Aushärtung, die bei Metall-Legierungen stattfindet. Die Bildung von Kolloïden ist mit dem "Print Out" Prozess von belichteten silbersalzen verwandt.

1. INTRODUCTION

VOL.

It is now well established that alkalihalide crystals "harden" on irradiation with X-rays. The effect was first found by Podachewsky⁽¹⁵⁾ and studied by two different methods:

- (i) Elastic damping (Frankl and Read⁽⁴⁾, Gordon and Nowick⁽⁷⁾).
- (ii) Hardness measurements by means of indentations on the X-rayed face (Li⁽²⁾, Westervelt⁽³⁾). It appears however, from the experimental results, that the two methods reveal effects which are probably due to somewhat different causes.

The hardness increase measured by means of the indentation method is confined to a surface layer (see Fig. 5) whereas the damping is a volume effect which persists even after removal of the surface layer.

An explanation of the bulk effect has been given by Gordon and Nowick⁽⁷⁾. To our knowledge, no adequate explanation has been given for the surface effect. In order to obtain more information on the surface hardening, we followed its variation as a function of distance from the exposed surface and of time of irradiation. Measurements of optical absorption also as a function of depth, were performed on the specimens used for the hardness tests to establish whether some correlation existed between the hardening and the centres produced by irradiation.

^{*} This work is part of a Research Scheme supported by I.R.S.I.A. Received April 4, 1958.

[†] Laboratorium voor Kristalkunde, Rozier, 6, Gent, Belgium.

2. EXPERIMENTAL TECHNIQUES

The measurements were carried out on melt-grown crystals, made in this laboratory by the Czochralski method, from pro analysis NaCl obtained from U.C.B. The specimens were all cleaved from the same crystal: their dimensions were approx. $7 \times 6 \times 15$ mm. They were placed in a frame at a reproducible distance (1.5 cm) from the window of an X-ray tube with a copper target, operated at 40 kV and 20 mA. The distance was chosen in such a way that the divergence of that part of the beam intercepted by the crystal was negligible. In some experiments the crystal was placed immediately in front of the beryllium window. The crystals were wrapped in black photographic paper, always of the same thickness, in order to prevent optical bleaching during irradiation and for transfer from X-ray unit to spectrometer.

The absorption measurements were made on a thin slice, cleaved after irradiation along a plane parallel to the incident beam. Use was made of a Beckmann D.U. type spectrophotometer, adapted for scanning the crystal in depth. For this purpose a slit was placed in front of the crystal, in order to limit the incident beam to a width of 0.25 mm. Readings were taken every 0.10 mm. All the absorption measurements were made at room temperature, immediately following irradiation.

As the hardness is practically unaffected by partial or total bleaching, the same precaution was not necessary for the hardness measurements, which were made on a fresh cleavage slice similar to that used for the absorption measurements. The hardness was measured with a Leitz "Durimet" Vickers micro hardness tester. All V.H. values are mean values of five measurements. The indentation diagonals were oriented approximately in [100] directions when not otherwise mentioned. Finally, in order to measure in a more direct way the effect of irradiation on the mobility of dislocations, the indented surfaces were etched. Measurements of the distance travelled by

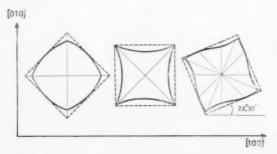


Fig. 1. Indentation patterns. In all cases the dimensions in the $\langle 110 \rangle$ directions are unaltered. The dotted line represents the original outline of the indentation mark.



Fig. 2. Indentation on cube face of NaCl with the diagonals of the pyramid forming an angle of $22\frac{1}{2}^{\circ}$ with the cube directions. $\times 400$.

the leading dislocation, for a given load, could then be carried out. We established that this distance was independent of the orientation of the indentation figure.

3. OBSERVATIONS

(a) Shape of indentation figure

(i) Microscopic observations. It was found that the hardness depended somewhat on the orientation of the diagonals of the indentation figures with respect to the lattice. When parallel to [100] reproducible results of $21.9 \pm 0.3 \,\mathrm{kg} \,\mathrm{mm}^{-2}$ were found on an irradiated surface; this value was lowered to $29.0 \pm 0.3 \,\mathrm{kg} \,\mathrm{mm}^{-2}$ when the diagonals were parallel to [110]. This is due to the shape of the indentation figure which alters from a perfect square to the forms represented in Fig. 1 and Fig. 2, immediately after releasing the load. The diagonals shorten, in one orientation, and as this length is used to calculate the hardness, a higher V.H. value results in that case. The shape of the hardness profiles is however as demonstrated by Fig. 3, curves 4 and 5.

The alteration in shape of the indentation figure is of course due to crystal anisotropy and can be understood by considering the geometry of the slip pr cess. As has been shown previously, (8) slip occurs on a number of glide planes during the indentation process.

The peculiar shape of the figures can now be explained by assuming that edge dislocations present a larger "after effect" than screws i.e. they can move backward more easily than screw dislocations. The same effect is responsible for the non-circular shape of the indentation figure when a spherical indenter is used.⁽⁸⁾

(ii) Interferometry. Multiple beam interferograms of indentation figures using a spherical indenter have been published by Votava et $al.^{(8)}$ The prominent features were the occurrence of small hills, due to the piling up of dislocations, in the [110] and [1 $\overline{10}$] directions. The results are not essentially different in the

VOI 7 19

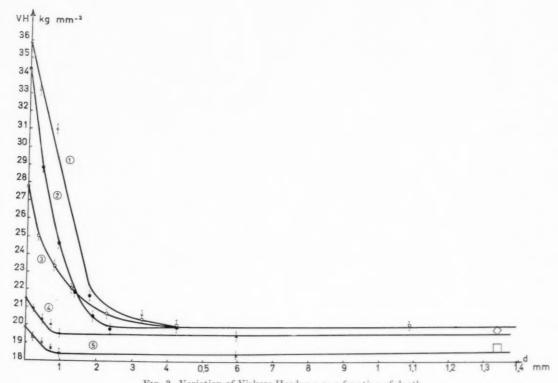


Fig. 3. Variation of Vickers Hardness as a function of depth. Curve 1: After anneal in hydrogen for $4\frac{3}{4}$ hr and subsequent irradiation during 9 hr. 2: After anneal in hydrogen for $4\frac{3}{4}$ hr without irradiation.

2. After anneal in hydrogen for 44 hr without irra

3: After 9 hr irradiation.

4: Hardness measured with diagonals of the indenter parallel to [100]

5: Hardness measured with diagonals of the indenter parallel to [110].

case of a square indenter as shown by the interferograms (Fig. 4(a) and (b)). Several indentations with different orientations were made, and the silvered crystal was matched against an optical flat, also silvered. The resulting interferogram, using monochromatic light filtered from a mercury arc, shows the characteristic hills.

VOL.

(b) Hardness measurements as a function of depth

(i) Thick specimens. In these experiments the crystals were carefully cleaved in the direction parallel to the incident X-ray beam. The hardness was measured on a fresh cleavage plane, since it was found that measurements on "old" surfaces are not reliable. From the same specimen, a lamella was cleaved for use in the optical measurements.

Gordon and Nowick⁽⁷⁾ performed such measurements for one exposure time; we have extended this as a function of irradiation time.

Fig. 5 is a plot of hardness vs. depth in the crystal. The first point is taken on the exposed surface itself. It is clear from this plot that the region where hardening occurs is limited to a layer some 0.6 mm thick,

even after 36 hr irradiation. The point where hardening could no longer be observed shifts inwards with increasing exposure time. As this point cannot be determined very accurately, we have plotted the half-value of the hardening as a function of exposure time, in Fig. 6.

A plot of the hardening (V.H. after irradiation

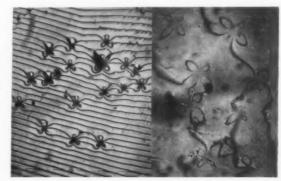


Fig. 4. Interferograms of indented cube faces of NaCl. Note the occurrence of four hillocks around every indentation square (a) at small magnification. ×37.5.
(b) at higher magnification and larger dispersion. ×75.

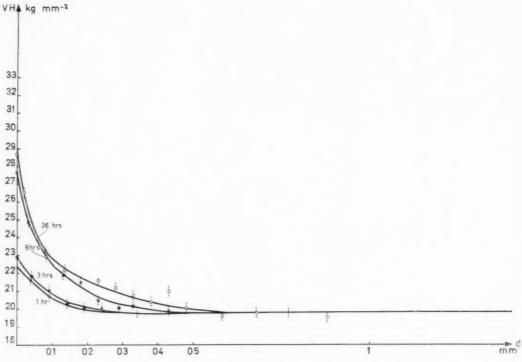


Fig. 5. Vickers Hardness as a function of depth for various irradiation times.

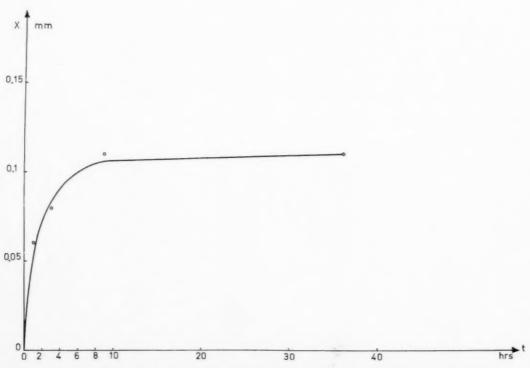


Fig. 6. Shift of the half-value of the hardening as a function of irradiation time.

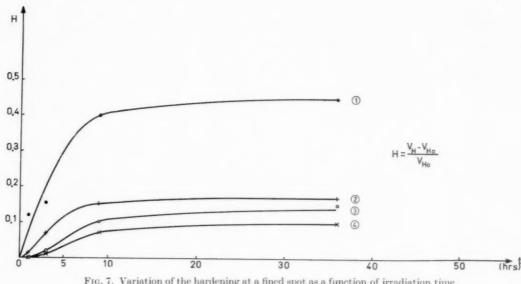


Fig. 7. Variation of the hardening at a fined spot as a function of irradiation time.

Curve 1: surface.

3: at 0.14 mm from the surface.

4: at 0.19 mm from the surface.

minus original V.H. divided by original V.H.) at a given depth approaches a saturation value. This is virtually achieved for the exposed surface after some 20 hr (Fig. 7).

It was found that indenting the crystals in the dark, without previous exposure to light, gave no measurable difference from crystals that were partly or even completely bleached optically. It was therefore concluded that if colloids are responsible for the hardening, they do not result from optical coagulation of F-centres, but should form already during irradiation.

(ii) Thin specimens. To see whether the vicinity of a surface has any influence on the hardening, the following experiment was performed. A thin crystal (0.37 mm) was exposed to X-rays under the same conditions as those of Fig. 5, the exposure time being chosen in such a way that some hardening should occur over the whole depth. The hardness profile, on a cleavage face parallel to the incident beam, has the shape shown in Fig. 8. The rise in hardness towards the back surface clearly demonstrates the influence of the vicinity of a free surface.

(iii) Hydrogen annealed specimens. In order to verify whether colloid formation could give rise to hardening, the following experiment was carried out. It had been found in this laboratory (II) that an anneal in hydrogen of NaCl containing even traces of silver will result in the formation of silver colloid along the dislocation lines. The colloid is first formed at the surface and after prolonged treatment the decorated region moves

inward. NaCl containing traces of Ag (no silver was added deliberately) was therefore annealed for about 5 hr at 750°C in hydrogen and then cooled slowly. It was observed in the ultra microscope that, in the surface region, very small particles had been formed along the dislocation lines. The hardening measured as a function of depth is plotted in Fig. 3, curve 1. It is now evident that the colloids have hardened the crystal quite markedly.

It is clear that the hardening is much greater than can be obtained by means of X-irradiation. If the same crystal is irradiated for 9 hr the hardness

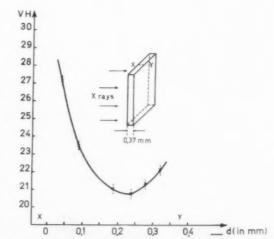
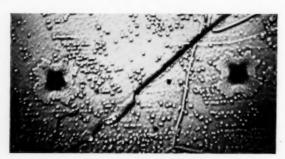


Fig. 8. Vickers Hardness as a function of depth for a thin lamella. Irradiation time $6\frac{1}{2}$ hr; crystal immediately above the window of the X-ray tube.

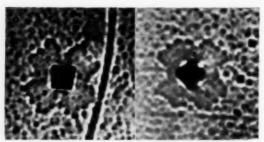
VOL.

1959

Fig. 9. Etched indentation patterns on cube face of NaCl. (a) In the non-hardened regions. Two different loads were used



(b) On the irradiated surface. Note the difference in development of the wings, compared with the previous patterns, although the load was the same as the larger load in (a).



(c) On the irradiated surface. Indentation in two different

increases still further (curve 3). For comparison the hardness profile of a crystal irradiated also for 9 hr but not treated in hydrogen is shown (curve 2).

(iv) Etching. Fig. 9(a) shows the etch pattern of the deformation zone around the indentation before irradiation, and Fig. 9(b) and 9(c) after 4 hr irradiation on the window. The indentations were made under the same conditions, using a 15 g load. It is clear that a marked difference exists in the development of the "wings" which correspond to the hills in the interferogram. The deformed region in the irradiated crystal is much more restricted than in the non-irradiated one. This shows that not only the nucleation of dislocations, but also dislocation movement, is hampered in the irradiated regions.

Indentations made at different depths d behind the irradiated face were etched, and the distance D over which the leading dislocation moved was measured. The plots of Fig. 10 were obtained in this way. The variation of 2D with depth d is similar to the variation in V.H., but proves to be more sensitive. It was found that in the hardened region the following relation holds:

$$D = a \log d + b$$

where a=1.18 and b=2.42 (D and d are measured in mm).

(c) Optical absorption as a function of depth

Mador et al. (1) have published curves relating F and M absorption to depth in the crystal; depth vs. log I_0/I is plotted on a semi-logarithmic scale. A broken line consisting of straight segments results. Near the surface the absorption is enhanced. This result is interpreted as due to the production of vacancies near the irradiated surface, and their subsequent conversion to F-centres, so called "hard F-centres." It is attractive to attempt a correlation between the production of "hard F-centres" and the surface hardening: the production of vacancies might for instance induce the dislocations to climb out of their glide planes, and so produce hardening.

Our measurements were therefore plotted in the same way as those of Mador *et al.*, (1) and to clarify the discussion we first compare the conditions under which both series of experiments were performed.

19

Although the conditions are slightly different, we believe that they are not sufficiently so to explain the absence in the present work of the essential feature i.e. the break in the curves.

Our curves are represented in Figs. 11 and 12 and should be compared with those of Mador $et\ al.$ (their figure 7). Most of our curves were taken several times in order to ensure that they were reproducible. A feature of significance is the larger increase in M-absorption, near to the surface, as compared with F-absorption.

These plots should be compared with those of Fig. 5.

This indicates that no direct correlation exists, either

	X-rays	Specimen
Mador et al.	50 kV 15 mA	Thin crystals mounted be- tween two thick crystals during irradiation
Present measurements '	40 kV 20 mA	Thin crystals cleaved from large irradiated crystals.

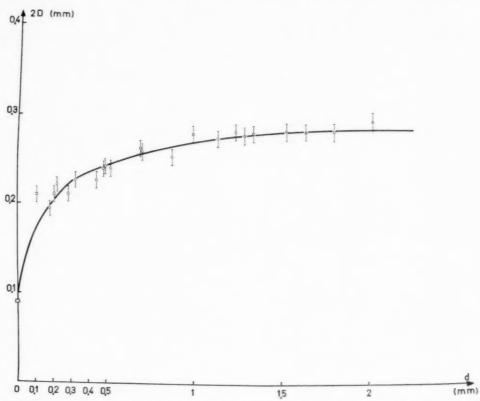
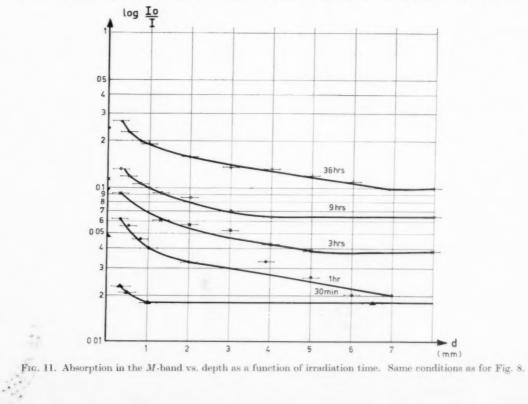


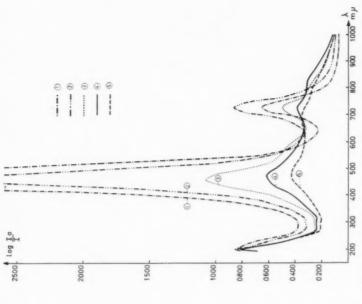
Fig. 10. Variation of the diameter 2D of the etching wings as a function of depth d; the different markings take into account the difference in orientation of the indentation figures (the coordinate lines represent the $\langle 100 \rangle$ directions).

VOL.

1959



109 IO



14

30 min

99 9

36 hr

50

Fig. 13. Evolution of the absorption spectrum of an irradiated crystal submitted successively to various optical bleaching treatments.

8 (mm)

Fro. 12. Absorption in the F-band vs. depth as a function of irradiation time. Measurements performed on different specimen but all values reduced to a thickness of 1 mm.

90

0 0 1

Curve 1: immediately after 6½ hr irradiation.
2: After 6 min bleaching.
3: After an additional 30 min bleaching.
4: After an additional 150 min bleaching.
5: After an additional 9 hr bleaching.

VOI 7 19

for the F or the M-band. One can, for example, deduce from these curves that the same F-centre or M-centre concentration does not correspond to the same increase in hardness.

We therefore looked for a correlation with some other centre, and found that the heavily irradiated crystals could not be fully bleached optically in the region immediately adjacent to the X-rayed surface. Some absorption in the visible region shown in Fig. 13 remained. The absorption has a maximum at about $820~\mathrm{m}\,\mu$. We therefore scanned a freshly irradiated crystal in depth for this wavelength and found that the absorption was confined to a layer of about the same thickness as that in which hardening occurs. This is shown in Fig. 14. It seems not unreasonable to consider this as an indication that the centres causing this absorption are also at least partly responsible for the surface hardening.

A very rough estimate of the depth over which this absorption extends was also made by microscopic examination of the crystal, in transmission, along a direction parallel to the exposed face. Darkening was observable up to 0.2 mm behind the exposed face. This corresponds closely to the distance over which hardening is observed for the same exposure time.

(d) Annealing experiments

1959

(i) Annealing of freshly irradiated crystals. To test the validity of this hypothesis the thermal annealing

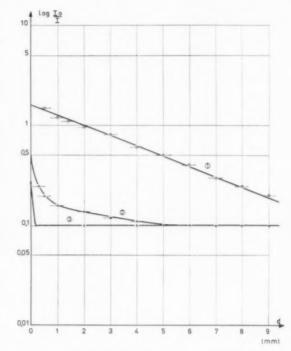


Fig. 14. Absorption in various bands vs. depth for the same crystal (irradiation time 9 hr, thickness 0.84 mm; results not reduced to a thickness of 1 mm).

- 1: absorption curve for $\lambda = 464 \text{ m}\mu$.
- 2: absorption curve for $\lambda = 725 \text{ m}\mu$ 3: absorption curve for $\lambda = 820 \text{ m}\mu$.
- Note the increasingly better correlation with increasing complexity of the center.

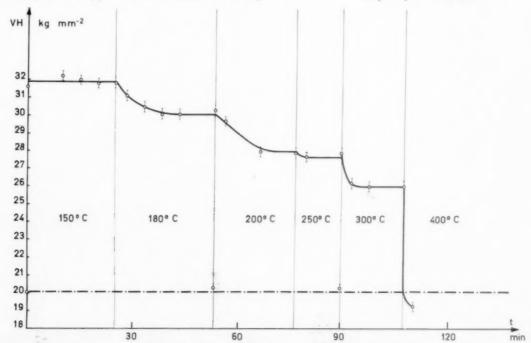


Fig. 15. Effect of thermal bleaching. The dash-dot line represents the variation of the hardness of non-irradiated crystal submitted to the same thermal treatment as the irradiated one.

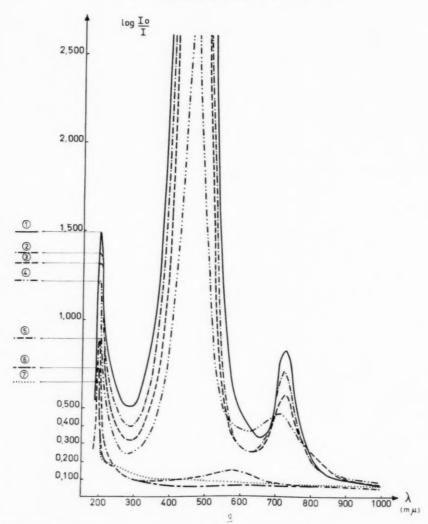


Fig. 16. Evolution of the absorption spectrum of an irradiated crystal submitted successively to various heat treatments. curve 1: immediately after 6½ hr irradiation. 2: after 5 min at 150°C. 3: after an additional 15 min treatment, at 150°C. 4: after an additional 20 min treatment, at 180°C. 5: after an additional 20 min treatment, at 200°C. 6: after an additional 10 min treatment, at 300°C. 7: after an additional 3 min treatment, at 400°C.

of the hardness (Fig. 15) and the thermal bleaching of the absorption (Fig. 16) were followed simultaneously on a crystal irradiated by X-rays for $6\frac{1}{2}$ hr at room temperature, placed immediately before the window of the X-ray tube.

For the hardness measurements the crystal was successively heated in a small furnace for the indicated time intervals at the given temperatures, then cooled quite moderately in a reproducible way and the hardness measured again at room temperature. The temperature was increased after a plateau was reached. The measurements were always made in the same region of the irradiated face but separated sufficiently to avoid interference. The resulting curve (Fig. 15) is similar to that obtained by Westervelt⁽³⁾ in the case of KCl.

The front slice, parallel to the irradiated face of the same crystal, was used for the absorption measurements, which were all made at room temperature. The evolution of the absorption spectrum after the indicated heat treatments is represented in Fig. 16.

19!

(ii) Annealing of optically bleached crystals. In these experiments, all crystals were placed at the minimum distance from the window of the tube, irradiated for $6\frac{1}{2}$ hr and fully bleached afterwards except for a small zone, which, as already stated, resists such treatment. The remaining absorption is reproducible for the same irradiation time, and is shown in Fig. 17. A small F-band, next to two other bands, one at 670 m μ and another at 820 m μ , are present. The successive curves of Fig. 17 show the evolution of these bands after the indicated heat treatments: the peak at

 $820~\mathrm{m}\mu$ disappears first, the band at $670~\mathrm{m}\mu$ shifts somewhat to the longer wavelengths and diminishes in intensity as the anneal proceeds. The crystal has finally the typical blue colour of NaCl containing colloids.

Hardness vs. annealing measurements of such crystals are not essentially different from those of freshly irradiated crystals. A small difference was however found at the beginning of the heat treatment. Whereas no decrease of hardness was found at $150^{\circ}\mathrm{C}$ in freshly irradiated crystals, there was now a small decrease, about one unit V.H. after 1 min.

(iii) Hardness anneal measurements on quenched crystals. In order to see whether vacancies were responsible for the hardening, measurements were made on quenched crystals. The crystal was heated to about 700°C and then quenched to room temperature. The hardness was then $22.7\pm0.3~\mathrm{kg~mm^{-2}}$, whereas it was $19.2\pm0.2~\mathrm{kg~mm^{-2}}$ before the quench. After a 3 min anneal at $400^\circ\mathrm{C}$ and very slow cooling a residual hardness of $21.2\pm0.3~\mathrm{kg~mm^{-2}}$ was found, The hardness increase due to vacancies is thus not removed at $400^\circ\mathrm{C}$ whereas this was the case for the hardening of irradiated crystals. The significance of this experiment may be questionable in view of the possibility of plastic deformation during puenching.

(e) Experiments on partly irradiated crystals

1959

(i) Hardness profiles. Some crystals were irradiated only on one half, the other being covered by a screen having a sharp re-entrant edge, so as to be able to compare directly the difference in hardness between the irradiated and non-irradiated parts; and also to follow the behaviour at the transition region. When the hardness was measured across the transition region the striking result of Fig. 18 was obtained. The curve was not a simple step function as one would expect; instead there was some "overshoot" which, in one measured case, was almost as large as the hardening in the irradiated region. The effect is too large to be accounted for by some scattering of X-rays by the edge of the screen. Diffusion of defects, generated in the irradiated region, into the other part of the crystal would suppress the hardening in the transition region. The result would be simply a broadening of that transition region. It was found moreover that the peak hardness varied considerably along the line parallel to the edge of the shadow (as represented by the different peaks in Fig. 18).

We therefore feel that the explanation is probably that the material in the transition region is stressed and possibly strained. It has been shown by Estermann *et al.*⁽⁵⁾ that NaCl expands when it is irradiated.

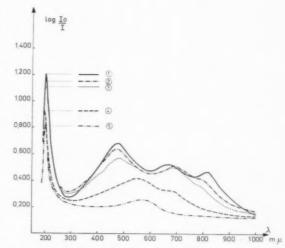


Fig. 17 Evolution of the absorption spectrum of an optically bleached crystal, as a consequence of various heat treatments. The crystal was irradiated for 6½ hr.

curve 1: after optical bleaching.

2: after 5 min at 150°C.

3: after an additional 10 min at 150°C.

4: after an additional 5 min at 200°C.

5: after an additional 15 min at 200°C.

It is therefore reasonable to assume that the material in the transition region is subject to high stress, resulting in some local hardening. The scatter on the peak value would be in accordance with the hypothesis that locally some glide has taken place.

(ii) Etching. In an attempt to detect eventual plastic deformation or strain in the transition region, partly irradiated crystals were etched using the methyl alcohol etch described previously. (13) A striking result was obtained when the face exposed to X-rays was etched. The irradiated part etched much more heavily than the non-irradiated one, as is seen in Fig. 19. The pits due to grown-in dislocations can be clearly distinguished in both parts. They are however consistently smaller in the irradiated part, which exhibits a pronounced "background" etching. The latter consists in its major part of flat-bottomed pits, suggesting that these are revealing not dislocations but, most probably, agglomerates of point defectsnot necessarily situated on dislocations, but very near to the surface. Eventually small colloidal particles formed at the surface may be responsible for their formation. Small dislocation loops might also lead to the same result. This accelerates the overall dissolution rate of the surface, which in turn explains why the dislocation pits become smaller in the irradiated

If the thin front layer is cleaved away and the crystal etched again, no difference can be detected between the two parts. The background etching is

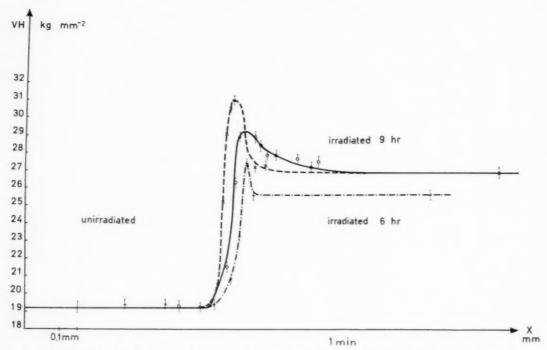


Fig. 18. Hardness in the transition region between irradiated and non-irradiated parts of a crystal.

absent now. This suggests that the damage which can be revealed by etching is confined to the layer which also exhibits hardening.

Fig. 19 shows some traces of deformation in the form of short slip lines in the region adjacent to the boundary. It is difficult to decide whether these were introduced during cleavage, or as a consequence of the irradiation. The double etching technique which has been used for lithium fluoride⁽⁴⁾ would allow us to decide this point. This was however not possible here.

We believe nevertheless that the etched slip traces

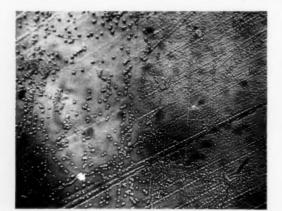


Fig. 19. Etched front face of irradiated crystal. Note the difference in etching characteristics of the left (non-irradiated) and the right (irradiated) half. A few short slip traces are visible in the transition region.

are due to plastic deformation as a consequence of differential expansion during irradiation. Evidence for this has been found previously by Smith et al. (6) by means of interferometry. It is clear that a good part of the background etching is along surface steps. Some of the larger steps are also slightly attacked in the non-irradiated region, and can thus be traced further in the irradiated part. The etching along steps could mean that the colloidal particles form preferentially at some specific sites of the steps; possibly kink sites.

(f) Hardness measurements on electron-bombarded crystals

Crystals have been subjected to bombardment with $50~\rm kV$ electrons for $30~\rm min$. The observed change in hardness on the surface exceeded that due to X-irradiation. The observed value was $52~\rm kg~mm^{-2}$. Hardness change could also no longer be detected at depth $0.5~\rm mm$ but the decrease with depth was much steeper, as could be seen by comparing Fig. $20~\rm with$ Fig. $5.~\rm mass could$

4. DISCUSSION

We believe that the observed phenomena can be explained on the hypothesis that the surface hardening is caused by the formation of small colloidals. In this discussion we call "colloid" every agglomerate of point defects, with or without captured electrons.

This point of view is supported by the following arguments:

- (1) The hardening is not due to F- or M-centres because in regions where the same concentration of F- or M-centres exists, the hardening differs considerably. After optical bleaching the hardening subsists.
- (2) The hardening is not due to a direct by-product of the F-centre production. If the hardening were due for instance to the cation vacancies liberated from vacancy pairs by the production of F-centres, one would still expect to find some proportionality between the concentration of F-centres in a given region and the hardening. This may well be the case for the bulk hardening, revealed by damping, but again this does not seem to be the case for the surface hardening.
- (3) The hardened region seems to be correlated geometrically with the region where the absorption resisting optical bleaching is found. This absorption is now regarded as most probably due to small colloids which cannot be resolved in the ultramicroscope. This follows from measurements of the absorption after optical bleaching. The pronounced increase of M-absorption at the surface points also to coagulation in that region.

VOL.

1959

- (4) The annealing experiments indicate that there is parallelism in the evolution of the band corresponding to the colloid absorption and the evolution of the hardening. Both disappear at about the same temperature, 400°C. The gradual decrease in hardness is accompanied by a gradual shift in the absorption maximum. This may be explained by a softening caused by over-aging, as observed in precipitation hardening. The growth of the colloidal particles, which can be followed even by visual inspection as a colour change, diminishes their pinning power as their number decreases and, as a consequence, the distance between pinning or movement hampering points increases.
- (5) The hardening observed at the back face of a thin specimen has to be explained by assuming that some entity responsible for the hardening diffuses in or out at the free surface. For the formation of an excess of sodium the escape of chlorine is necessary. The diffusing entity therefore may well be chlorine (or anion vacancies).
- (6) The overall etching in the irradiated part can also be explained on the same basis. Etching would be caused by the agglomeration of point defects i.e. small colloidal particles. The reason why hardening is confined to the surface region is twofold:
 - (i) possibility of escape of chlorine,

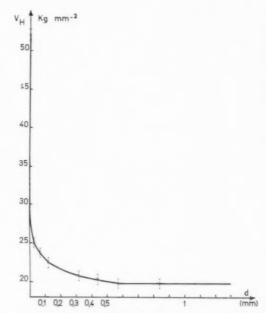


Fig. 20. Variation of Vickers Hardness as a function of depth for a crystal irradiated for 30 min with electrons of $50\,\mathrm{kV}.$

- (ii) a high supersaturation of F-centres has to build up, to give rise to colloids.
- (7) Annealing of quenched crystals shows that the hardening is not caused by the formation of vacancies. The mechanism of hardening can now be visualized in the following way. The holes and electrons created by the X-rays would be respectively trapped in V- and F-type centres. The anion vacancies are rather immobile, whilst the cation vacancies may on the other hand move as such or incorporated in a V-type centre. When these reach the surface the hole may be used to convert the Cl- into Clo, and finally the Clo may form Cl2 molecules which can now escape. The escape of the cation vacancy on the other hand means that a sodium ion has migrated inwards, establishing in this way the excess of sodium. The electron of the F-centre, or an electron created by the X-irradiation, may now be captured by the excess sodium ion which is thus converted to Na.

The presence of excess sodium in the heavily irradiated regions could be proved more directly by dissolving a thin layer of such a crystal in distilled water. Under the microscope the production of gas bubbles could be observed: this was not the case in the non-irradiated part. The gas can now be either hydrogen produced by the reaction of free sodium with water, or free chlorine which was occluded in the crystal. In both cases the crystal should contain free sodium. In the heavily irradiated region the crystal has, by analogy with the silver halides, been subjected

to the print-out process. A similar effect was observed when NaCl crystals were bombarded with electrons. (12)

It is clear that, in the absence of a free surface, no free chlorine will escape and, if sufficient activation is supplied, the whole crystal will again return to normal.

In the surface layer however, the excess sodium can agglomerate and form colloids capable of pinning the dislocations. Eventually colloids may also nucleate at sites other than dislocations, owing to their high supersaturation and small mobility.

This would imply that even newly created dislocations would be more difficult to move through the "forest" of colloid centres. This is what we believe to be the case. The plastic deformation associated with the indentation probably takes place by means of new dislocations, since "old" dislocations are probably firmly pinned by impurities. From the dimensions of the dislocation-free regions (as revealed by decoration techniques) on the one hand, and the dimensions of the region occupied by an indentation on the other hand, one expects moreover that some of the indentations will be located in a dislocation-free region.

The gradual softening during anneal and the existence of plateaus can now also be understood. At a given temperature a certain particle size is in equilibrium; with increasing particle size the pinning becomes less effective i.e. the distance between pinning points increases, and the crystal softens. At the temperature where the colloids "evaporate" the hardening disappears completely. If these assumptions are correct the radiation-induced surface hardening is, in fact, fully comparable to precipitation hardening in alloys. The experiments with the partially

irradiated crystals indicate that stress and some strain can also play a role in the process, as is possible in precipitation hardening. Experiments with soft and hard X-rays are taken into consideration to ascertain whether or not the differential expansion at different depths plays a role.

Note added in proof

After this paper was submitted for publication, we were informed that somewhat similar results as those reported here were obtained by J. J. Gilman (private comm.) in neutron irradiated LiF.

ACKNOWLEDGMENT

We are grateful to Prof. De Sy and the members of his staff for the facilities they provided in using the Durimet.

REFERENCES

- J. C. Mador, R. J. Wallis, M. C. Williams and R. C. Herman, Phys. Rev. 96, 617 (1954).
- 2. YIN-YUAN LI, Acta Met. 1, 455 (1953).
- 3. D. R. Westervelt, Acta Met. 1, 755 (1953).
- 4. D. R. Frankl and T. Read, Phys. Rev. 89, 663 (1953).
- 5. ESTERMANN, LEIVO and STERN, Phys. Rev. 75, 627 (1949).
- W. J. SMITH, W. J. LEIVO and R. SMOLUCHOWSKI, Phys. Rev. 105, 37 (1956).
- 7. R. B. GORDON and A. S. NOWICK, Acta Met. 4, 514 (1956).
- 8. E. VOTAVA, S. AMELINCKX and W. DEKEYSER, Acta Met. 3, 89 (1955).

VOI

- St (1935).
 P. L. Pratt, Report of 1954 Bristol Conference p. 402.
 Physical Society, London (1955).
- 10. M. E. CASPERI and LAN-YING-LIN, Colour Centre Sym-
- posium. Argonne (1956).
 W. Van der Vorst and W. Dekeyser, Phil. Mag. Ser. 8,
 1, 882 (1956).
- 1, 882 (1950). 12. D. E. McLennan, Canad. J. Phys. 29, 122 (1951).
- 13. S. AMELINCKX, Acta Met. 2, 848 (1954).
- 14. J. J. GILMAN and W. G. JOHNSTON, G. E. Research Rep.
- 15. M. N. Podachewsky, Phys. Z. Sowjet. 8, 81 (1935).

ÜBER DIE VERFESTIGUNG VON ALUMINIUM EINKRISTALLEN (99,99% AI) UND IHRE DEUTUNG*

W. STAUBWASSER†

Die Aufgabe dieser Arbeit war, ein möglichst vollständiges Bild der Verfestigung von Einkristallen aus Reinstaluminium zu erhalten. Hierzu wurde die Orientierungsabhängigkeit der Verfestigung und ihre Temperaturabhängigkeit untersucht. Bei der letzteren hat man sich auf die Temperaturen von $\pm 21^{\circ}\mathrm{C}$ und $\pm 195^{\circ}\mathrm{C}$ beschränkt. Gleichzeitig mit diesen Untersuchungen wurde jeweils die Oberflächenerscheinungen und der Asterismus beobachtet. Dabei wurden folgende Ergebnisse erhalten:

Die Orientierungsabhängigkeit der Verfestigung wie auch die des Oberflächenbildes hängt von dem Ausmass der Betätigung zusätzlicher Gleitsysteme ab. Auf Grund der ausgedehnten Asterismusuntersuchungen kann ein Modell über die Knickbandbildung beschrieben werden. Es beruht auf einer Stauung von Versetzungen vor Hindernissen und deren Stabilisation durch eine Mikrogleitung nach einem zweiten Gleitsystem. Bei der Verformung der Einkristalle bei —195°C wurde festgestellt, dass die Verfestigung bei anfänglicher Abgleitung im Gebiet des easy-glide nabezu temperaturunabhängig ist im Gegensatz zur Verfestigung bei weiterer Verformung. Die Gleitbanddichte ist bei der tieferen Temperatur wesentlich grösser als bei höherer nach gleicher Abgleitung. Dafür sind die Gleitbänder entsprechend feiner ausgebildet. Der Asterismus ist ebenfalls im easy-glide-Gebiet temperaturunabhängig. Nach grösseren Abgleitungen jedoch ist er bei der tieferen Temperatur kleiner als bei der höheren.

ON WORK-HARDENING OF ALUMINIUM-SINGLE CRYSTALS (99.99%) AND ITS INTERPRETATION

To obtain a more complete survey of the work-hardening of high purity aluminium single crystals the orientation- and temperature-dependence of work-hardening was investigated. The study of the temperature dependence was limited to two temperatures ($+21^{\circ}\text{C}$ and -195°C). With the measurements of stress–strain curves observations of the surface patterns and X-ray asterism were combined. The results are as follows:

The orientation dependence of work-hardening as well as that of the surface patterns depends on the amount of slip in additional glide-systems. By reason of an extensive study of the asterism a model for kink-band formation can be described. This is due to a piling up of dislocations at obstacles and their stabilization by micro-slip in a second glide-system. The deformation at $-195^{\circ}\mathrm{C}$ showed the work-hardening of easy glide to be nearly independent on temperature in contrast to the further stages of deformation. After equal shear-strains the density of slip-bands is essentially greater at the lower temperature than at the higher one but they have a finer appearance. In the easy glide-stage asterism was found to be temperature independent as well. After larger deformations it is, however, smaller at the lower temperature than at the higher one.

SUR LA CONSOLIDATION DES MONOCRISTAUX D'ALUMINIUM (99,99% AI) ET SUR SON INTERPRETATION

Le but de ce travail est de donner une vue aussi complète que possible de la consolidation de monocristaux d'aluminium pur. L'auteur étudie à effet, l'influence de l'orientation et de la température sur la consolidation. Il s'est limité à des températures variant entre $+21^{\circ}$ C et -195° C. En même temps, il observe dans chaque cas, les phénomènes de surface et l'astérisme. Il a obtenu les résultats suivants: L'influence de l'orientation sur la consolidation ainsi que sur les figures de surface dépend de la mise en action de systèmes de glissement supplémentaires. L'auteur décrit sur la base d'investigations approfondies sur l'astérisme, un modèle de formation de bandes de pliage. Ce modèle consiste en une accumulation de dislocations devant des obstacles et leur stabilisation au moyen d'un micro-glissement suivant un second système de glissement. On constate au cours de la déformation des monocristaux à · 195°C, que la consolidation au cours du début de glissement dans le domaine du glissement facile est indépendante de la température, contrairement à la consolidation au cours d'une déformation subséquente. La densité des bandes de glissement est pour des basses températures sensiblement plus grande que celle pour des températures plus élevées après le même glissement. Pour cette raison, les bandes de glissement sont plus fines. L'astérisme est également dans le domaine du glissement facile, indépendant de la température. Après des glissements élevés, il est cependant plus faible pour les basses températures que pour les températures plus élevées.

1. EINLEITUNG

Eine Reihe von Autoren^(1 bis 6) hat nachgewiesen, dass die Verfestigung von Reinst-Aluminiumeinkristallen nicht allein eine Funktion der Schubspannung des begünstigsten Gleitsystems ist, sondern dass andere Faktoren, wie die Mitbetätigung weiterer Gleitsysteme, welche Störquellen für die Gleitung erzeugt, massgebend für diese sind. Die vorliegende Arbeit gibt eine vollständige Übersicht der Orientierungsabhängigkeit bei Raumtemperatur, sowie Messungen bei -195° C. Bei allen Kristallen wurde das Oberflächenbild während der Dehnung beobachtet.

^{*} Mitteilungen aus dem Institut für Metallkunde in Göttingen. Received October 21, 1957; revised version April 17, 1958.

[†] Interatom, Duisburg.

sowie an extrem orientierten Kristallen mit einer besonders empfindlichen Röntgenmethode^(7,8) der Asterismus festgestellt.

Die Einkristalle hatten einen Durchmesser von 1,5 mm und waren etwa 40–50 cm lang. Sie wurden nach dem Rekristallisationsverfahren für vorgegebene Orientierungen hergestellt. Der Reinheitsgrad der Kristalle betrug 99,99% Al mit 0,008% Si als Hauptverunreinigung. Apparative Einzelheiten können den Arbeiten von Lange und Lücke^(1,2,3) sowie der Originalarbeit des Autors⁽⁹⁾ entnommen werden. Die Verformung erfolgte durch Dehnung in einem Apparat nach M. Polanyi und E. Schmid.

2. DIE VERFESTIGUNG VON EINKRISTALLEN VERSCHIEDENER ORIENTIERUNG BEI $+20\,^{\circ}\text{C}$ UND $-195\,^{\circ}\text{C}$

In den Fig. 1 bis 4 sind die Verfestigungskurven für die verschiedenen Orientierungen dargestellt. Die Werte sind alle auf Schubspannung τ und Abgleitung a umgerechnet, wobei das Einsetzen der Doppelgleitung durch Rechnungen nach V. Göler und Sachs (10) berücksichtigt wurde. Bei Mehrfachgleitung, wie sie bei den Eckkristallen (111) und (100) auftritt, wurde die Orientierungsänderung im Verlauf der Dehnung röntgenographisch kontrolliert und entsprechend berücksichtigt. So wurde z.B. gefunden, dass sich die Orientierung des (111) Kristalles während der Dehnung praktisch gar nicht ändert, während beim (100) Kristall die Orientierungsänderung mit dem Beginn des flachen Teiles der Verfestigungskurve einsetzt.

Die drei Eckkristalle, sowie als vierter ein Kristall, dessen Winkel zwischen Zugachse und Gleitebene, sowie Gleitrichtung 45° betragen (sin $\chi \cdot \cos \lambda \approx$ 0.5 = max. "(0.5)-Orientierung") zeigen extreme Verfestigungskurven. Für Kristalle, deren Orientierungen zwischen den vier genannten liegen, geht die Verfestigungskurve kontinuierlich von dem einen Typ zum anderen über. Die Ausbildung des flachen linearen Anfangsteiles der Verfestigungskurve (easyglide) hat bei der (0,5) Orientierung sein Maximum und verschwindet bei den Eckkristallen vollständig (siehe auch⁽¹¹⁾). Sehr deutlich wird dies aus Fig. 5, wo die Verfestigung nach 10% Abgleitung über dem Orientierungsdreieck aufgetragen wurde. Die kritische Schubspannung τ_0 ist fast orientierungsunabhängig.

Bei der Verformung in flüssiger Luft (-195°C) zeigte es sich, dass die kritische Schubspannung kaum temperaturabhängig ist. Dies gilt in gleichem Masse für das easy-glide-Gebiet für mittlere Orientierungen

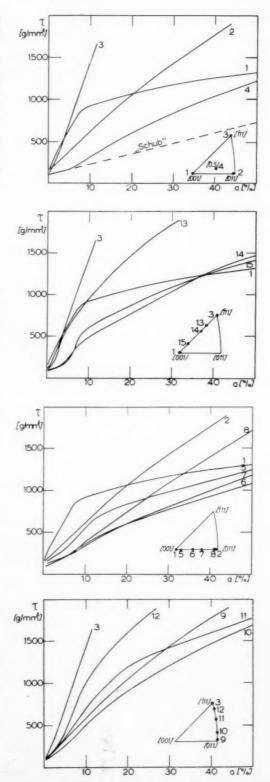


Fig. 1 bis Fig. 4. Verfestigungskurven von Kristallen verschiedener Orientierung (Schubspannung τ , Abgleitung a).

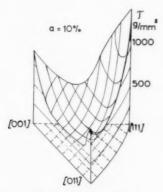


Fig. 5. Die Verfestigung in Abhängigkeit von der Orientierung nach einer Abgleitung von 10%.

(Fig. 6). Die weitere Verfestigung ist stark temperaturabhängig (Fig. 7). Versuche, bei denen nach einer gewissen Dehnung bei $+20^{\circ}\mathrm{C}$ oder $-195^{\circ}\mathrm{C}$ bei $-195^{\circ}\mathrm{C}$ oder $+20^{\circ}\mathrm{C}$ weiterverformt wurde, erbrachten eine stark temperaturabhängige Streckgrenze der vorverformten Kristalle. Dies ist aus der Fig. 8 ersichtlich. Der gleiche Effekt wurde auch bei Änderung der Verformungsgeschwindigkeiten gefunden, wie aus den Fig. 9 und 10 ersichtlich ist.

3. DER ASTERISMUS BEI VERSCHIEDENEN ORIENTIERUNGEN UND TEMPERATUREN

(a) Gesamtverlauf des Asterismus mit wachsender Abgleitung

1959

Für die Untersuchungen wurden Kristalle mit extremen Orientierungen ausgesucht ($\langle 0,5 \rangle$, $\langle 111 \rangle$, $\langle 100 \rangle$). Beim $\langle 0,5 \rangle$ –Kristall mit nur einem bevorzugten Gleitsystem bestätigte sich, dass sich die betätigte $\{111\}$ Ebene nur um die $\langle 112 \rangle$ Achse verbiegt, die senkrecht zur Gleitrichtung $\langle 110 \rangle$ steht und in der Gleitebene liegt. Dies gilt auch für die Kristalle der $\langle 111 \rangle$ und $\langle 100 \rangle$ Orientierung, bei denen sich

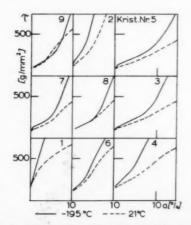


Fig. 6. Die Abhängigkeit der Anfangsverfestigung von der Temperatur. Orientierungen s. Fig. 7.

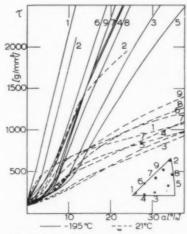


Fig. 7. Die Abhängigkeit der Gesamtverfestigung von der Temperatur.

gleichzeitig 6 bzw. 8 Gleitsysteme betätigen können. Bei letzteren wurden alle Systeme untersucht. Da der Asterismus örtlich verschieden war, was besonders für die $\langle 0,5 \rangle$ Orientierung gilt, wurden die Mittelwerte über eine Kristallänge von 20 mm, was etwa 20–30 Laue aufnahmen entspricht, für die Darstellung der Asterismuskurven in Fig. 11 errechnet. Die Gitterverbiegung beträgt die Hälfte des Asterismuswinkels.

Wie aus der Fig. 11 ersichtlich ist, gehören zu den drei extrem orientierten Kristallen typische Asterismuskurven. Zunächst ist auffallend, dass je steiler die Verfestigungskurve verläuft, desto flacher die Asterismuskurve ist. Es ist bemerkenswert, dass eine deutliche Korrelation zwischen den Verfestigungsund Asterismuskurven besteht. Eine Verbreiterung der Reflexe setzte sofort mit beginnender Verformung ein.

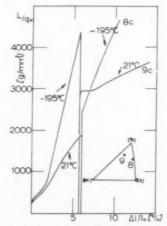


Fig. 8. Verfestigungskurven unter dem Einfluss von Temperaturwechseln.

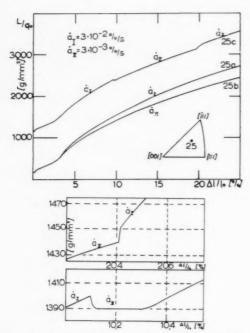


Fig. 9 und 10. Verfestigungskurven mit verschiedener Dehngeschwindigkeit und unter dem Einfluss von Geschwindigkeitswechseln.

In Fig. 11 sind ebenfalls die Asterismuskurven für die in flüssiger Luft gedehnten Kristalle gezeigt. Die Kurve für den $\langle 0,5 \rangle$ Kristall verläuft wieder bis zu 6% Abgleitung sehr flach, von da ab jedoch nicht mehr so steil wie die Kurve für die bei 21°C verformten Kristalle. Die Kurven für die $\langle 100 \rangle$ - und $\langle 111 \rangle$ -Kristalle können nicht ohne weiteres mit denen für 21°C verglichen werden, da die Orientierungen nicht

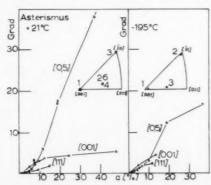


Fig. 11. Der Asterismus der $\langle 100 \rangle, \langle 111 \rangle$ und $\langle 0,5 \rangle$ Orientierungen in Abhängigkeit von der Abgleitung bei 21°C und -195°C.

genau übereinstimmen, und gerade die $\langle 111 \rangle$ und $\langle 100 \rangle$ Ecken in allen orientierungsabhängigen Grössen gegen kleine Änderungen der Orientierung sehr empfindlich sind. So darf es nicht verwundern, dass die beiden Kurven etwas höher als die bei 21°C gefundenen liegen. Aber auch hier sind die Werte für den $\langle 111 \rangle$ Kristall niedriger als die des $\langle 100 \rangle$ Kristalls.

(b) Feinstruktur der Lauereflexe

(i) $\langle 0,5 \rangle$ Orientierung. Mit beginnender Verformung spalten sich die strichförmigen Lauereflexe sofort auf. Die Aufspaltung erfolgt um eine $\langle 112 \rangle$ Achse, die senkrecht zur Gleitrichtung $\langle 110 \rangle$ steht. In Fig. 12 sind einige solcher Aufnahmen gebracht,



Fig. 13. Lage der Versetzungswände auf Grund der Aufspaltung der Lauereflexe in Abb. 12. Massstab 1 : 5

195

die in 0,5 mm Abstand der Reihe nach von einem Kristallstück nach 4% Abgleitung aufgenommen wurden. Die nebenstehende Skizze (Fig. 13) gibt für diesen einfachen Fall die geometrischen Verhältnisse im Kristall wieder. Im allgemeinen ist die Aufspaltung sehr viel feiner und komplizierter als in diesem Beispiel. Die Fig. 14 gibt solche Reflexe einer bestimmten Stelle nach verschiedenen Abgleitungen wieder. Bis zu 7% Abgleitung ist die Aufspaltung der Reflexe noch scharf. Ab dann verschmieren die Reflexe zusehends und zwar so, dass sie an einem Ende scharf begrenzt sind, am anderen Ende aber allmählich auslaufen. Innerhalb der Reflexe sind noch grobe Strukturen zu erkennen. Eine solche Reflexausbildung ist den sich in diesem Bereich ausbildenden Knickbändern zuzuschreiben. In Fig. 15 sind diese Verhältnisse an einem gemessenen Kristall dargestellt. Nach etwa 5-6% Abgleitung, also kurz vor Beginn

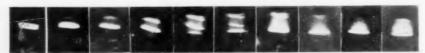
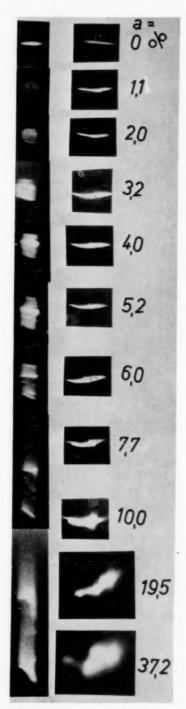


Fig. 12. Aufspaltung der Lauereflexe nach 4% Abgleitung. Die Aufnahmen wurden in $0.5 \,\mathrm{mm}$ Abstand entlang eines $\langle 0.5 \rangle$ Kristalls gemacht. Einstrahlung in Richtung $\langle 110 \rangle$. V=2-fach



VOL.

1959

Fig. 14. Aufspaltung der Lauereflexe einer Stelle eines $\langle 0,5 \rangle$ Kristalls nach verschiedenen Abgleitungen. Links Einstrahlung parallel zu $\langle 110 \rangle$, rechts senkrecht zu $\langle 110 \rangle$ in $\langle 112 \rangle$ Richtung. V=2-fach.

der Verschmierung der Reflexe, erreicht man einen Abstand der feinen Knickgrenzen von durchschnittlich 200–300 μ . In Richtung $\langle 112 \rangle$, also der Biege-

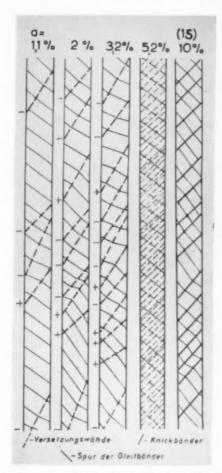


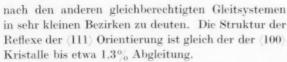
Fig. 15. Lage der Versetzungswände und Knickbänder nach verschiedenen Abgleitungen auf Grund der Aufspaltung der Lauereflexe eines 20 mm langen Kristallstückes der $\langle 0.5 \rangle$ Orientierung. Massstab 1:5

achse, konnte bis etwa 8% Abgleitung kein Asterismus festgestellt werden. Ab dann löst sich dre strichförmige Reflex in einzelne verwaschene Knoten auf, von denen kleine Stacheln ausgehen. Letztere Bürften die Folge von Gitterverbiegungen in kleinen dezirken nach anderen Gleitsystemen sein.

(ii) \(\lambda \) und \(\lambda \) 111\) Orientierung. Bei der \(\lambda \) 100\) Orientierung erfolgt die Aufspaltung der Reflexe nicht in der einfachen Art wie im vorigen Beispiel. Sie sind sowohl aufgespalten, wie auch in sich geknickt. Ab etwa 1,3% Abgleitung sind zusätzliche schmale stachelartige Streifen zu erkennen, die von den ursprünglichen Reflexen ausgehen. Diese Stacheln werden mit wachsender Verformung immer ausgeprägter, bis letztlich der gesamte Reflex nur noch aus diesen besteht (Fig. 16). Diese Erscheinung ist die gleiche wie beim \((0,5) \) Kristall nach grösseren Abgleitungen und ist ebenfalls durch Gitterverbiegungen



Fig. 16. Lauereflex eines $\langle 100 \rangle$ Kristalls, der nach 7,5% Abgleitung nur noch aus sehr schmalen Streifen besteht. $V=2\text{-}\mathrm{fach}.$



Für die drei extremen Orientierungen war eine Abhängigkeit der Reflexstruktur von der Verformungstemperatur nicht erkennbar.

4. OBERFLÄCHENERSCHEINUNGEN

Die ersten unter dem Mikroskop sichtbaren Gleitbänder treten nach etwa 3-4% Abgleitungauf und zwar zunächst in Gleitbandgruppen. (3,12,13,14) Diese gehören bei den mittleren Orientierunge nur einem Gleitsystem an, und verbreitern sich im Verlauf der Dehnung allmählich über den gesamten Kristall. Die Gleitbandgruppen an den Symmetralen (100)-(111) und (111)-(110) werden jeweils von einem der gleichberechtigten Gleitsystemen gebildet. Man findet bei geringen Dehnungen auch Gebiete, wo beide Gleitsysteme sich gleichzeitig durchzusetzen versuchten. Es werden dabei keine gut ausgebildeten Gleitbänder gebildet, sondern nur Gleitbandfragmente in Form eines schwach gitterförmigen Musters auf der Kristalloberfläche. Dies kann durch eine Mikrogleitung nach gleichzeitig zwei Systemen gedeutet werden. Nach etwa 10% Abgleitung durchkreuzen sich die gleichberechtigten Systeme in den Bändern, sowie auch an den Stellen mit Mikrogleitung, sodass das gewohnte Bild der Doppelgleitung entsteht. Dies gilt auch für die (111) und (100) Kristalle in analoger Weise, bei denen 6 bzw. 8 Gleitsysteme gleichberechtigt sind (s. Fig. 17). Bekanntlich bewegen sich die Orientierungen im Verlauf der Dehnung auf die Symmetrale (100)-(111) hin. Es wurde hierbei beobachtet, dass bei mittleren Orientierungen nach einer vorhergegangenen Bandbildung nach einem System das Doppelgleitsystem bereits vor Erreichen der Symmetralen einsetzt. Auf der Symmetralen (100)-(110) werden Gleitbänder über grössere Strekken entweder nach dem einen oder nach dem anderen



Fig. 17. Oberfläche eines (100) Kristalls nach 20% Abgleitung.
 V=160 fach.

der beiden gleichberechtigten Systeme gebildet. Überschneidungen finden praktisch nicht statt.

Eine echte Quergleitung (cross-slip) unter der man eine Verbindung zweier Gleitbänder durch eine Gleitung nach einem anderen System versteht, $^{(3,5,16)}$ wurde nur sehr selten beobachtet. Die Quergleitung kann unter spitzen (Z) oder stumpfen (Z) Winkeln auftreten. Eine Orientierungsabhängigkeit dieser Erscheinung konnte nicht beobachtet werden. Die letztere überwog stark. Es wurden sogar in einigen Fällen an einem Gleitband beide Arten beobachtet.

Unter Knickbändern (kinkbands, deformation bands) versteht man eine S-förmige Verkrümmung der Gleitbänder, die sich in einer Zone etwa entlang der {110} Ebene erstrecken, zu der die Gleitrichtung die Normale ist. (1.2,3,15,16,17,18) Besonders kräftig sind die Knickbänder um die (0,5) Lage ausgebildet. Sie verlaufen dort gerade und in verhältnismässig weiten Abständen von 0,5-1,0 mm. Nach 40% Abgleitung wird in den Knickbändern eine Gleitung nach einem anderne Gleitsystem beobachtet (s. Fig. 18). Gegen die Symmetrale (100)-(111) wird die Zahl der Knickbänder geringer und sie sind weniger ausgeprägt, bis sie auf der Symmetralen selbst sehr selten werden. Gegen die Symmetrale (111)-(110) hin werden die Knickbänder ebenfalls feiner, ihre Zahl nimmt jedoch zu. Ihr Verlauf ist sehr unregelmässig,



Fig. 18. Gleitung nach einem zusätzlichen Gleitsystem in einem Knickband nach 40% Abgleitung. V=160 fach.

wobei auch Verzweigungen vorkommen können. In Gebieten mit ausgeprägt bandartiger Anordnung der Gleitbänder treten die Knickbänder nur in Bändern mit ausgeprägter Gleitung nach einem System auf. Im engen Bereich der (111)- und (100)-Ecken finden sich keine Knickbänder mehr.

Bei der Verformung in flüssiger Luft liegen die Gleitbänder viel dichter als bei der Verformung bei $21^{\circ}\mathrm{C}$. Dafür sind sie schwächer ausgebildet. Dieser Vergleich gilt bei gleicher Abgleitung. Die Knickbänder sind ebenfalls häufiger, aber feiner und unregelmässiger ausgebildet. Das Oberflächenbild der $\langle 111 \rangle$ und $\langle 100 \rangle$ Kristalle ist etwa dasselbe wie bei den bei $21^{\circ}\mathrm{C}$ gedehnten Kristallen gleicher Orientierung.

5. DISKUSSION

Die vorliegende Arbeit wurde bereits 1954 abgeschlossen. (9) Es sind daher eine Reihe der vorliegenden Messergebnisse im Hinblick auf die theoretischen Ansichten zur Verfestigung bereits von einigen Autoren, (19-20) denen die Originalunterlagen zur Verfügung gestellt wurden, eingehend diskutiert worden. In den folgenden Ausführungen wird daher auf die theoretische Deutung der Verfestigung nur wenig eingegangen, sondern im wesentlichen auf die verschiedenen Arbeiten hingewiesen.

Betrachtet man rein geometrisch die Schubspannungsverhälnisse aller Gleitsysteme innerhalb des Orientierungsdreieckes, (21) so erkennt man leicht, dass nach Erreichen einer gewissen Verfestigung durch das Hauptgleitsystem die kritische Schubspannung für ein Nachbarsystem bereits innerhalb des Orientierungsdreieckes erreicht werden kann, und somit dieses zur Gleitung angeregt wird. Dies stellt die Grundlage für die Diskussion der Orientierungsabhängigkeit dar. Die Verfestigungskurven mittlerer Orientierungen, bei denen anfänglich sich nur ein Gleitsystem betätigt, werden vor allem durch den flachen linearen Anfangsteil (easy-glide), der nahezu temperaturunabhängig ist, charakterisiert. Der Beginn des wiederansteigenden Teils der Verfestigungskurve sowie ihr wieder flacherer Endverlauf sind stark temperaturund orientierungsabhängig. Für die Ausbildung des flachen linearen Anfangsteiles der Verfestigungskurven ist offenbar die Betätigung nur eines Gleitsystemes Bedingung.

Die Ergebnisse aller oben angeführten Untersuchungen lassen sich zwanglos in ein zunächst qualitatives Bild über den Verfestigungsmechanismus einfügen. Im folgenden sei nur noch ausser den bereits zitierten Arbeiten^(19,20) auf eine Reihe von Veröffentlichungen hingewiesen, die sich mit quantitativen Aussagen über Verfestigung beschäftigen.^(4,5,6,22,23,24,25)

Letztlich soll noch ein Modell über die Knickbandbildung wie es sich aus den sehr umfangreichen Asterismusmessungen ergibt, gegeben werden. Es wird hierbei angenommen, dass sich von vornherein im Kristall Orte befinden, an denen Versetzungen auf gehalten werden können, deren Natur später noch erörtert werden soll. Vor diesen zunächst wenigen Hindernissen stauen sich mit beginnender Verformung die laufenden Versetzungen. Solche auf benachbarten Ebenen können von den ersteren festgehalten werden. (26) Es entsteht folglich eine Versetzungswand, die sich senkrecht zur Gleitebene durch den ganzen Kristall erstreckt und eine leichte Desorientierung erzeugt. Die Wände bestehen aus Versetzungen nur eines Vorzeichens, also entweder aus + oder - Versetzungen. Die örtliche Anordnung, das Vorzeichen der Wände, sowie die Zahl der Versetzungen in ihnen sind mehr oder wenigen zufällig. Es muss aber weiter angenommen werden, dass die Wände "durchlässig" sind, d.h. dass sie nur eine bestimmte Anzahl von Versetzungen aufhalten können Wären die Wände starr und undurchlässig, so würden sich keine über den ganzen Kristall erstreckende Gleitbänder bilden, und die Grenzen müssten schon nach wenigen % Abgleitung sichtbar werden. Sie bilden also keine ernsthaften Gleithindernisse, wie auch aus der Verfestigungskurve hervorgeht. Mit wachsender Verformung nimmt die Zahlder Wände auf Grund neu gebildeter Hindernisse zu, bis eine gleichmässige Verteilung mit einem Abstand von 200-300 µ und eine Anzahl der aufgestauten Versetzungen von etwa 20-40 erreicht wird, wie durch Ausmessen der aufgespaltenen Lauereflexe ermittelt wurde. Eine Wanderung der Wände bei fortschreitender Verformung wurde nicht beobachtet. Gegen Ende des flachen Anfangsteils der Verfestigungskurve wird in der Umgebung der Versetzungswände ein Spannungszustand erreicht. der eine Gleitung nach einem anderen Gleitsystem anregt, welche nach etwa 40% Abgleitung sichtbar wird (s. Fig. 18). Hierdurch können durch Versetzungsreaktionen unbewegliche Hindernisse gebildet werden, die die Wände undurchlässig machen. Es stauen sich nun alle Versetzungen vor den Wänden, und zwar die positiven auf der einen und die negativen auf der anderen Seite, wodurch eine S-förmige Krümmung der Gleitebenen bewirkt wird. Die Zahl der Versetzungen auf beiden Seiten der Wände ist im allgemeinnen ungleich. Mit wachsender Verformung wächst auch das Krümmungsgebiet, bis es makroskopisch sichtbar wird, wobei auch weitere eng benachbarte Versetzungswände in das Krümmungsgebiet mit einbezogen werden. Neu

VOL.

entstehende Gleitbänder können die Voll entwickelten Knickbänder mehr durchdringen: Diese stellen in diesem Stadium ein ernsthaftes Gleithindernis dar. (3,15)

Nach Honeycombe(17) nimmt der Knickbandabstand mit steigender Temperatur durch Überwindung der Hindernisse infolge thermisch aktivierter Prozesse und zunehmendem Reinheitsgrad zu. Die Deutung hierfür liegt in obigem Modell in der ad hoc Annahme von Hindernissen als Knickbandkeime begründet. Da die Zahl der Knickbänder mit sinkender Temperatur zunimmt, muss aber bei gleicher Abgleitung die Zahl der in ihnen gestauten Versetzungen kleiner sein, was dann eine geringere Krümmung bewirkt. Diese Temperaturabhängigkeit wurde durch das Experiment bestätigt.

In gleichem Sinne wie Verunreinigungen Knickbandkeime bilden können, können Gleitungen nach zweiten Gleitsystemen durch Bildung von unbeweglichen Hindernissen denselben Einfluss ausüben. Die vielbeachtete Abhängigkeit der Knickbandbildung vom Windel λ ergibt sich in einfacher Weise aus der Orientierungsabhängkeit der störenden Gleitsysteme.

Aus den Asterismusmessungen der (100) und (111) Kristalle geht hervor, dass sich für jede der möglichen Gleitebenen Versetzungswände bilden. Insgesamt erhätl man eine Anordnung, die man als eine Art Zellstruktur bezeichenen kann. Es kann angenommen werden dass auf Grund der Stabilität der Zellwände eine Gleitung im wesentlichen innerhalb der Zellen stattfindet, was sich sowohl im Oberflächenbild durch Mikrogleitung (s Fig. 17) äussert, als auch zu starken Gitterverzerrungen innerhalb der Zellen führt (vgl. Stachelbildung bei den Lauereflexen). Eine Knickbandbildung als zweite Entwicklungsstufe kann wegen der hohen Dichte der Zellwände nicht mehr erfolgen. Wenn die Knickbandbildung bei einer gleichzeitigen Betätigung mehrerer Gleitsysteme unterdrückt wird, so ist das für das nacheinander Betätigen nur noch begrenzt der Fall. Bis nämlich das zweite Gleitsystem einsetzt, können sich die Knickbänder, nach dem erstenschonsoweitentwickelt haben, dass sie bereits sichtbar werden. Gegen die Symmetrale (100)-(111) hin müssen die Knickbänder zwangsläufig seltener werden. In der Nähe der Symmetralen (111)-(110) wird ein anderes Verhalten beobachtet.

Die Knickbandhäufigkeit nimmt zu, und der Verlauf der Bänder ist erheblich gekrümmt. Dies hängt wahrscheinlich damit zusammen, dass hier die Gleitung nur auf einer Ebene in aber zwei Richtungen erfolgt. Diese Art der Doppelgleitung wirkt sich also anders auf die Knickbandbildung aus als bei einer Gleitung auf verschiedenen Ebenen.

Die vorliegende Arbeit wurde 1952-54 im Institut für allgemeine Metallkunde der Universität Göttingen durchgeführt. In erster Linie möchte ich besonders Herrn Prof. Dr. phil. Dr. ing e.h. G. Massing für die Ermöglichung dieser Arbeit, sowie für seine wohlwollende Unterstützung danken. Für Anrengungen zu verschiedenen Versuchen, insbesondere zu denen bei tiefer Temperatur bin ich Herrn Prof. Dr. Lücke und für zahlreiche wertvolle Diskussionen Herrn Dr. P. Hassen zu großem Dank verpflichtet. Herrn Dr. J. Diehl gilt mein Dank für die Durchsicht der vorliegenden Arbeit. Für die zur Verfügung gestellten verschieden Apparaturen sei der Deutschen Forschungsgemeinschaft gedankt.

LITERATURVERZEICHNIS

- 1. H. LANGE, and K. LÜCKE Z. Metallk. 43, 55 (1952).
- 2. H. Lange, and K. Lücke Z. Metallk. 44, 183 (1953).
- 3. H. LANGE, and K. LÜCKE Z. Metallk. 44, 514 (1953).
- Haasen and G. Leibfried, Z. Phys. 131, 538 (1952).
- 5. P. Haasen, Z. Phys 136, 26 (1953).
- 6. F. RÖHM and J. DIEHL, Z. Metallk. 43, 126 (1952).
- 7. A. GUINIER and J. TENNEVIN, Acta Cryst. 2, 133 (1949).

- H. SEEMANN and BOHLIN, Ann. Phys., Lpz. 59, 455 (1919).
- 9. W. Staubwasser, Dissertation, Göttingen (1954). 10. F. V. GÖLER and G. SACHS, Z. Phys. 41, 103 (1927).
- 11. R. S. Davis, R. L. Fleischer, J. D. Livingston and
- B. CHALMERS, J. Metals, N.Y. 136 (1957). 12. R. BECKER and P. HAASEN, Acta Met. 1, 325 (1953).
- 13. B. JAOUL and Ch. CRUSSARD, C.R. Acad. Sci., Paris 234,
- 700 (1952).
- 14. H. MÜLLER and G. LEIBFRIED, Z. Phys. 142, 87 (1955).
- R. W. CAHN, J. Inst. Met. 79, 129 (1951).
- 16. H. Wilsdorf and D. Kuhlmann Wilsdorf, Z. angew.
- Phys. 4, 361, 409, 418 (1952). 17. R. W. HONEYCOMBE, J. Inst. Met. 80, 49 (1951-52).
- 18. N. K. CHEN and C. H. MATHEWSON, J. Metals, N. Y. 653
- 19. A. SEEGER, Z. Naturf. 9a, 758, 856, 870 (1954).
- 20. P. Haasen and G. Leibfried, Fortschr. Phys. 2, 73 (1954).
- 21. J. DIEHL, M. KRAUSE, W. OFFENHÄUSER, and W. STAUB-
- Wasser, Z. Metallk. 45, 489 (1954). 22. J. Diehl, Dissertation, Stuttgart (1955).
- G. Leibfried and P. Haasen, Z. Phys. 136, (1953).
 J. Diehl, S. Mader and A. Seeger, Z. Metallk. 46, 650 (1955).
- 25. J. DIEHL, Z. Metallk. 47, 331 (1956).
- 26. F. C. Frank and A. N. Stroh, Proc. Phys. Soc. B65, 811 (1952).

ORIENTATION OF RECRYSTALLIZED GRAINS IN STRAINED ALUMINUM SINGLE CRYSTALS*

H. YOSHIDA, B. LIEBMANN, and K. LÜCKE†

Artificially nucleated crystals were grown in strained aluminum single crystals by cutting them at one end with pliers and then subjecting them to recrystallization heating. An overwhelming majority of the new crystals showed an orientation characterized by a 40° rotation around the [111] axis relative to the old matrix.

Recrystallization always started at the cut end with many fine grains. After further heating most of these fine grains disappeared and only a few large crystals were left. They grew further into the deformed matrix and one of them finally occupied the full diameter of the wire.

Laue and Debye–Scherrer X-ray photographs showed that in the early stage of recrystallization the orientation of the many fine grains were distributed at random, while the crystal finally obtained usually was characterized by a 40° [111] rotation. This indicates that the preferred orientation of the final crystals originates in growth selection.

The preference for [111] rather than the other $\langle 111 \rangle$ axes may be caused either by the plastic deformation of the old matrix, or by the fact that the boundary between the two crystals is a pure tilt boundary if both have a common [111] axis.

ORIENTATION DES GRAINS RECRISTALLISES DANS LES MONOCRISTAUX D'ALUMINIUM DEFORMES

Les auteurs provoquent la croissance de cristaux formés par germination artificielle dans des monocristaux déformés d'aluminium en les sectionnant à une extrêmité et en les soumettant à un traitement de recristallisation. La grande majorité des nouveaux cristaux montrent une orientation caractérisée par une rotation de 40° autour de l'axe [111] relatif à l'ancienne matrice.

La recristallisation commence toujours à l'extrémité sectionnée avec de nombreux grains fins. Après chauffage ultérieur, la plupart de ces grains fins disparaissent et il ne reste plus que quelques gros cristaux. Ceux-ci continuent à croître dans la matrice déformée et finalement l'un d'eux occupe tout le diamètre du fil.

Les photographies de rayons X par les méthodes de Laue et de Debye–Scherrer montrent qu'au début de la recristallisation, l'orientation de nombreux grains fins est destribuée au hasard, tandis que le cristal finalement obtenu est caractérisé d'habitude par une rotation de 46° autour de [111]. Ceci indique que l'orientation préférentielle des cristaux finaux a son origine dan une sélection au cours de la croissance.

La préférence pour l'axe [111] plutôt que pour les autres axes (111) peut être causée soit par la déformation plastique de l'ancienne matrice, soit par le fait que le joint entre les deux cristaux est un joint de torsion si les deux cristaux ont un axe [111] commun.

DIE ORIENTIERUNG VON REKRISTALLISIERTEN KÖRNERN IN GEDEHNTEN ALUMINIUM-EINKRISTALLEN

In gedehnten Aluminium-Einkristallen wurde die Keimbildung von Kristallen durch das Abschneiden eines Endes mit einer Drahtzange und eine nachfolgende Rekristallisierungsglühung erzwungen. Eine überwältigende Mehrheit der neuen Kristalle besassen eine Orientierung, die durch eine 40°-Drehung um die [111]-Achse relativ zur alten Matrix gekennzeichnet ist.

Die Rekristallisation begann stets am Schnittende mit vielen feinen Körnern. Nach längerem Glühen verschwanden diese und nur einige grosse Kristalle blieben übrig. Sie wuchsen weiter in die verformte Matrix hinein und einer davon nahm schliesslich den ganzen Drahtdurchmesser ein.

Laue- und Debye-Scherrer-Aufnahmen zeigten, dass im Anfangs-stadium der Rekristallisation die Orientierung der vielen feinen Körner statistisch verteilt war, während der zum Schluss vorhandene Kristall in der Regel durch eine 40°-Drehung um die [111]-Achse gekennzeichnet war. Dies zeigt, dass die Vorzugsorientierung der endgültigen Kristalle auf Wachstumsauslese beruht.

Der Vorzug der [111]-Achse vor den anderen (111)-Achsen kann entweder durch die plastische Verformung der alten Matrix verursacht sein, oder durch die Tatsache, dass als Grenze zwischen den beiden Kristallen eine reine "Neigungskorngrenze" (beide Kristalle sind um eine Achse in der Korngrenze gegeneinander gedreht) auftritt, wenn beide eine gemeinsame [111]-Achse haben.

1. INTRODUCTION

To explain the generation of recrystallization textures in metals two theories have been proposed: that of oriented growth⁽¹⁾ and that of oriented nucleation.⁽²⁾ It has been difficult, however, to prove either of the theories, since mostly indirect evidence

^{*} The work described in this paper was supported by the Office of Naval Research under Contract No. nr-562(12) and the Air Force Office of Scientific Research of the Air Research and Development Command, under Contract AF 49(638)–75. Reproduction in whole or in part is permitted for any purpose of the United States Government. Received September 5, 1957; revised version April 18, 1958.

[†] Metals Research Laboratory and Department of Physics, Brown University, Providence, Rhode Island.

for their validity has been presented. In order to check these theories directly, experiments were carried out simultaneously and independently by Graham and Cahn, (3) and Liebmann, Lücke, and Masing. (4) Both groups of workers studied the orientation of recrystallization nuclei and their rate of growth in strained aluminum single crystals. However, the results obtained by the two groups showed many differences and contradictions in spite of their close similarity both in experimental methods and in materials used. The reasons for these discrepancies are not understood at present. Therefore, a reexamination of the results is desirable,

It was the purpose of the present work to recheck and supplement some of the previous work of Liebmann et al. The investigation of the orientations of recrystallized grains in strained wire-shaped aluminum single crystals has been extended to different orientations of the deformed single crystals, different degrees of deformation, different purities and different conditions of nucleation and of growth. The results verified those of Liebmann and co-workers. Moreover, the results gave additional proof of the validity of the theory of oriented growth for the case described in this paper.

2. EXPERIMENTAL PROCEDURES

In most of the experiments commercially pure aluminum wire 1.5 mm diameter of the same composition as in the previous work was used. Some experiments were carried out with wires of high purity aluminum (99.995%). Using the strain anneal method, crystals of 12 ft lengths were grown from the wires. By cutting these long crystals into small pieces many single crystals of exactly the same orientation could be obtained. The orientations of the single crystals used are shown in Fig. 1. P gives the orientation of the high purity crystal; A, B, C and D are crystals of commercial purity. The commercially pure crystal used in the previous work⁽⁴⁾ is indicated by the number 0.

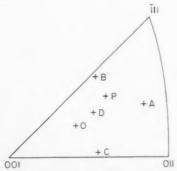


Fig. 1. Orientation of the wire axes of the single crystals.

Most of the single crystals were extended 20 per cent and some 10, 30 or 50 per cent. They usually were cut at one end by diagonal pliers, but in some cases the cut ends were also strongly squeezed by needle-nosed pliers. These specimens will be characterized by the word "squeezed" whereas the non-squeezed crystals are referred to by the word "cut". The strained and either cut or cut-and-squeezed crystals were then subjected to a recrystallization heating. Furnaces with a temperature gradient were used and the crystal was always placed with its cut end at the point of highest temperature. The overall extension of the crystal was generally not large enough to cause spontaneous nucleation during this heat treatment and recrystallization started only at the cut end.

For this recrystallization heating two different furnaces were available. The first was an ordinary electrical furnace as used previously. (4) It has a medium high temperature-gradient with its highest temperature slightly below the melting point of aluminum. The second was a special furnace with an extremely high temperature-gradient of approximately 350°C/cm. In the latter (Fig. 2) the flame of a fisher burner fed with propane gas under constant pressure touches a running water surface. The single crystal wire can be moved with various velocities upward out of the running water into the flame. At the gas pressure normally used, the tip of the crystal melted down when it reached a position about 17 mm above the water surface. Most of the experiments have been carried out in the special high gradient furnace, for in this way recovery of the rest of the deformed crystal could be avoided. The specimen was moved with speeds of 1.5 mm/min (referred to as

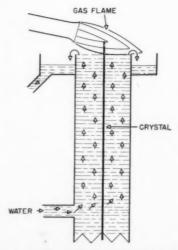


Fig. 2. Schematic drawing of the high temperature-gradient furnace.

"high") or 0.3 mm/min ("low"), or was kept in one position with the top 15 mm above the water surface ("zero-speed"). The last method gave the clearest results and therefore was most frequently adopted.

Under all of these different conditions new crystals grew from the cut end. Most frequently they occupied the full diameter of the wire. In some cases, however, parallel-growing bi-crystals were obtained over a considerable length and in others, polycrystalline recrystallization occurred near the cut end of the specimen. When single and bi-crystals were obtained the orientation relationship between those crystals and the deformed matrix were determined by means of Laue photographs.

In order to elarify certain implications additional experiments, to be described later, were carried out.

3. EXPERIMENTAL RESULTS

The orientations of the new crystals artificially nucleated at the ends of the deformed crystals are given in Table 1. 83 experiments were performed: in 53 cases single crystals were obtained; in 22 cases bi-crystals, and only in 8 cases poly-crystals. The Table shows that orientations of the new crystals which are characterized approximately by a rotation of 40° around the [111] axis of the deformed matrix (as shown for two crystals in Fig. 3) are very much preferred. This can be seen from the diagram of Fig. 4 in which the orientations of all the new single and bi-crystals listed in Table 1 are plotted.

The preference of such an orientation relationship is proved most convincingly by the fact that in 15 of the 17 analyzed bi-crystals at least one of the two crystals, and in 11 cases even both, had such an orientation. In the latter cases, the 40° rotations of the two crystals

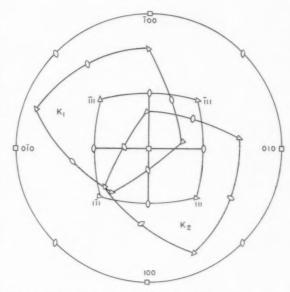


Fig. 3. Orientation relation of an artificially nucleated bi-crystal to the deformed matrix. The matrix is plotted in standard projection. K_1 and K_2 represent the orientations of the two parts of the bi-crystal.

were either in directions opposite to each other (as shown for example in Fig. 3), or in the same direction leading then to a pair of crystals of quite similar orientation. To a minor extent some other orientation relationships were preferred. In 8 single crystals rotations of nearly 40° around the [III] axis were found.

Especially clear results have been found by considering only the specimens with 20 per cent deformation characterized by the word "cut". 34 experiments resulted in 25 single crystals, 7 bi-crystals and 2 poly-crystals. All of the bi-crystals had orientations

TABLE 1

							Single	Crystals]	Bi-Crystal	8	
Specimen	Extension (° ₀)	Temp. gradient of furnace	Speed of crystal move- ment	Type of defor- mation	Number of experi- ments	Total number	Nearly 40° rotation around [111] axis	Nearly 40° rotation around [III] axis	tions rotation rotation o	Other orienta- tions	Poly- crystals			
		Normal	0	Cut	3	3	3	ō	0	0	0	0	0	0
A	20	High	Low	Cut squeezed	8 7	6 3	6 2	0	0	1 4	1 0	0 3	0 1	1 0
		nign	High	Cut squeezed	8 18	3 11	$\frac{2}{5}$	0 2	1 4	5 5	5 ne	0 ot analyze	o d	0 2
В	20	High	0	Cut squeezed	5 9	4 5	4 3	0	0 2	1 2	1 2	0	0	0 2
C	20	High	0	Cut squeezed	10 5	9 2	5 0	4	0 1	0	0	0 0	0 1	1 2
D	50	High	Low	Cut	5	2	2	0	0	3	2	1	0	0
P	30	High	0	Cut	5	5	5	0	0	0	0	0	0	0
_92	-		Total N	ımber:	83	53	37	-8	8	22	11	4	2	8

VOL. 7 1959

characterized by a 40° rotation of both crystals around the [111] axis. 20 single crystals showed this same orientation relationship. In 4 single crystals, the rotation of 40° was around [III] and in only one specimen was a different orientation obtained. Fig. 5 gives the orientation of all 20 per cent deformed "cut" specimens (single and bi-crystals). The "squeezing" and the growing at "high" speed obviously diminishes somewhat the preference for $40^{\circ}~\langle111\rangle$ rotations. But even then, this orientation relationship is proved to be present much more often than would be expected statistically.

The experiments on crystals extended 10 per cent are not included in Table 1 or Fig. 4. With commercially pure aluminum (crystal D) 6 trials were made,

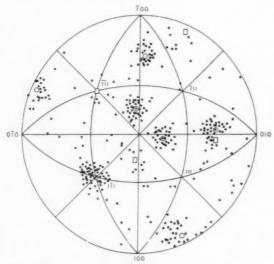


Fig. 4. Orientation relation of all artificially nucleated grains to the deformed matrix. The matrix is plotted in standard projection.

- Orientation of the {111} poles of the new crystals. Ideal situation of the {III} poles after clockwise or counter-clockwise 40° [111] rotation.
- ☐ Ideal situation of the {111} poles after counter-clockwise 40° [111] rotation.

but no recrystallization occurred except for the very tip of the cut end. In the case of high purity aluminum (crystal P) 6 trials were made and only in two of them did recrystallization occur. In both cases single crystals were obtained but showed none of the orientations mentioned above.

A special set of experiments was performed to investigate the origin of the new crystals. A deformed crystal was put into the high temperature-gradient furnace with its cut end 14 mm above the water surface. It was heated for different periods of time, and between successive heating periods Laue photographs of different parts of the crystal were taken. Fig. 6 shows the results schematically.

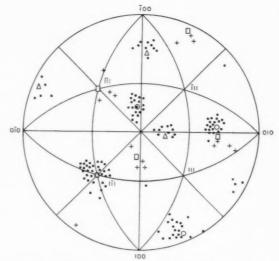


Fig. 5. Orientation relation between artificially nucleated grains and deformed matrix in cases where the matrix was extended 20 per cent and the nucleation was caused by cutting

only. The matrix is plotted in standard projection. Orientation of the {111} poles of new crystals characterized by 40° [1117] rotations.
 Orientation of the {111} poles of new crystals characterized by 40° [111] rotations.

○ Ideal situation of {111} poles after clockwise 40° [111]

Ideal situation of {111} poles after counter-clockwise 40° [III] rotation.

☐ Ideal situation of the {111} poles after counter-clockwise 40° [III] rotation.

19

Before the heating only the Laue spots of the deformed matrix were found, except for the very end of the crystal where the heavy deformation due to cutting caused a strong smearing out of the spots. (Stage a, Fig. 6.) After less than 1 min of heating, photographs of the tip showed a very large number of Laue spots indicating the presence of many small recrystallized grains. The length of this recrystallized zone was less than 1 mm; in distances larger than 1 mm from the end, only the deformed matrix was found (stage b). After further heating most of the Laue-spots had

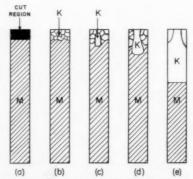


Fig. 6. Different stages of growth selection after artificial nucleation shown schematically.

disappeared. This means that most of the new grains had ceased to exist and only a few large crystals were left. At the same time recrystallized grains grew further into the deformed matrix (stages c and d) until one of them (K) finally occupied the full diameter of the wire (stage e). A careful check showed that the Laue spots of the crystal K finally obtained were present already in the Laue photographs of the very first stage of recrystallization (stage b, Fig. 6).

In addition to the Laue photographs, Debye–Scherrer patterns from the tip were obtained in stage b, Fig. 6, while the specimen was rotating around the wire axis. Fig. 7 gives the results: there is no sign of a preferred orientation in this early stage of recrystallization.

In some cases spontaneous nucleation over the whole length of the specimen was brought about by putting the specimen into a furnace without a temperature gradient. The distance between the nuclei was, however, so large that practically all of them could grow to occupy the whole cross section until the nuclei touched each other. Also their orientation has been determined, but for the two crystals investigated no preferred orientation could be detected

It should be mentioned that after the deformation of 20 per cent, crystal B showed double slip. No second slip system, however, could be detected microscopically in crystal A or C.

VOL.

1959

4. DISCUSSION

Orientation relationships approximately given by a 40° rotation around a common (111) axis have been frequently reported in the recrystallization of polycrystalline and single-crystal aluminum. (1,4,5,6,7) Similar orientation relationships are observed for other cubic face-centered metals with only the angle of rotation being somewhat different. For instance in copper the rotation is normally found to be 30°. The fact that the angles are different for different metals indicates that they are not determined merely by crystallographic factors, in contrast to the assumptions of Kronberg and Wilson. (8)

Since in some cases the scatter of the observed orientations around the ideal one was rather large⁽²⁾ and since in other cases orientations of this kind were not found at all,⁽³⁾ certain doubts arose about the significance of such an orientation relationship. However, the experiments described in this paper show clearly that under proper conditions an overwhelming majority of the recrystallized crystals exhibit such an orientation.

Moreover, a clarification of the mechanism responsible for the preference of this orientation is obtained.

There is now good evidence that, at least in the case described in this paper, it is a growth selection. As shown in the preceding section the final grain characterized by a 40° [111] orientation was already present in the tip of the cut crystal after the first stage of recrystallization (Fig. 6b), but in this stage grains of such orientations are not more numerous than grains of any other orientations as indicated by Fig. 7. Therefore, the preferred orientation of the crystals finally obtained can originate only by preferred growth.

This conclusion is supported by two other facts. First, the preferred orientation is only found if there is really a growth competition between many crystals. For this reason one obtains a random orientation in the spontaneous nucleation experiments. Because of the large distances between the different nuclei in this case, every nucleus has the opportunity to grow without interference by neighboring nuclei. Second, in direct measurements of the rate of the boundary

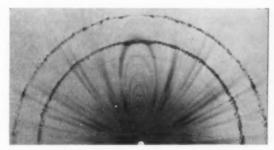


Fig. 7. Debye–Scherrer photograph of the top of a cut crystal in the first stage of recrystallization. The four heavy spots originate from the deformed matrix.

movement during recrystallization, the crystals related to the deformed matrix by a 40° [111] rotation showed the highest values. This result originally published by Liebmann *et al.* has been confirmed in the meantime by Green.⁽⁹⁾

Figs. 4 and 5 show that new crystals related to the matrix crystal by 40° rotations around [111] are much more numerous than crystals with rotations around any other $\langle 111 \rangle$ axis. At first sight there appear two possible reasons for the non-equality of the four $\langle 111 \rangle$ axes in the matrix. The first is due to the plastic deformation of the wire; different amounts of slip have occurred in the different $\{111\}$ planes. From this point of view the preferred [111] axis can be described as the normal to the cross slip plane.

The second possible reason concerns the nature of the grain boundary. As indicated by work of Beck and co-workers the grain boundary mobility during recrystallization of aluminum depends strongly on the

orientation of the boundary itself. (10) In the present investigation the four (111) axes form different angles with the wire axis, while for energy reasons the boundary is always normal to the latter. This leads to a different structure of the boundary in each of the four cases. From this point of view the preferred axis turns out to be that one of the four which is most nearly perpendicular to the wire axis. If the axis of rotation were exactly normal to the wire axis the boundary would be a pure tilt boundary. If both axes were parallel a pure twist boundary would be obtained. Of the four (111) axes, [111] is the most nearly parallel to the wire axis and new crystals characterized by rotations around this axis are never obtained or show extremely small growth rates. Therefore the results can be described from this point of view by saving that pure tilt boundaries show highest mobility and pure twist boundaries show lowest mobility, which is in agreement with the results of Beck et al.

From the authors' experiments described here it is difficult to decide whether the preference for (1111) is an exclusive result of the orientation of the boundary, or if the different history of the {111} planes during deformation still has some influence since in the wireshaped crystals the wire axis is also the axis of deformation. For example, for a crystal with an orientation exactly on the line (001) (011) (Figs. 1 and 5), both (III) and (III) would be cross slip planes. Therefore 40° rotations around the [III] and [III] axes would be expected from the first point of view (deformation) mentioned above. According to Table 1 and Fig. 5, [III] rotations have indeed been found for crystal C. the orientation of which is very close to this line (Fig. 1). But this supports not only the idea of the normal of the cross slip plane being the preferred axis, but also the idea of the importance of the structure of the boundary. This structure is the same for rotations about the two axes [111] and [1111], which form the same angle with the wire axis. Further investigation of the two principles might be possible by applying non-tensile deformations or by using sheet-shaped crystals. Such experiments are in preparation.

The question remains why crystals with the 40° [111] orientation relationship show faster growth than other orientations, and why eventually tilt boundaries

move faster than twist boundaries. The theory of the orientation dependence of grain boundary mobility is still in a very unsatisfactory state. It is hoped that direct measurements of the rate of grain boundary motion as a function of orientation, and of the nature of the boundary, will contribute to the solution of this problem. Measurements of this type are in progress.

It may be mentioned that some of the apparent contradictions between the results of Graham and Cahn, (3) and of Liebmann et al. (4) are probably caused by differences in the state of impurities. These differences may be a result of the different techniques used to grow the initial single crystals. Both groups used the strain-anneal method, but while Graham and Cahn grew their crystals by lowering aluminum strips (99.6%) into a salt bath, Liebmann and co-workers pulled aluminum wire (99.8%) through a short air furnace. In the present investigation no preferred orientations of the recrystallized grains were obtained if the single crystal wires used (99.8%) had been annealed for 1 hr at temperatures near 600°C prior to deformation. The salt bath furnace used by Graham and Cahn automatically involves a longer heating of the crystals, in contrast to the short air furnace used by Liebmann et al., where each point of the crystal reaches 600°C only for a few minutes. Since annealing prior to deformation does not diminish the preferred orientations of recrystallized grains in high purity aluminum (99.99%), the effect seems to be caused by dissolved impurities.

REFERENCES

VOI 7

19

- P. A. Beck, Advanc. Phys. 3, 306 (1954); Acta Met. 1, 230 (1953)
- W. G. Burgers and T. J. Tiedema, Acta Met. 1, 234 (1953).
- C. D. Graham Jr. and R. W. Cahn, J. Metals, N.Y. 504, 517 (1956).
- B. LIEBMANN, K. LÜCKE and G. MASING, Z. Metallk. 47, 57 (1956).
- N. K. Chen and G. H. Mathewson, Trans. Amer. Inst. Min. (Metall.) Engrs. 194, 501 (1952).
- Y. C. Liu and W. R. Hibbard Jr., J. Metals, N.Y. 672 (1953).
 Y. C. Liu and W. R. Hibbard Jr., J. Metals, N.Y. 1249
- (1955).
 8. M. L. Kronberg and H. F. Wilson, Trans. Amer. Inst.
- M. L. Kronberg and H. F. Wilson, Trans. Amer. Inst. Min. (Metall.) Engrs. 185, 501 (1949).
 R. E. Green Jr., Brown University, unpublished work.
- R. E. Green Jr., Brown University, unpublished work.
 S. Kohara, M. Parthasarathi and P. A. Beck, J. Appl.

Phys., in press.

The temperature dependence of the yield stress in iron*

Erickson and Low⁽¹⁾ have recently suggested that the observed flattening of the yield-stress vs. temperature curve for iron at low temperatures may be due to the occurrence of twinning rather than to the effect of atmosphere density which is taken into account in Louat's modification⁽²⁾ of the theory of Cottrell locking. It is the purpose of the present note to indicate that this suggestion is not necessarily at variance with the modified theory.

We suppose that twinning occurs by the process suggested by Cottrell and Bilby(3) but with the additional condition that the source dislocation (Burgers vector a/2[111] be solute locked. Remembering that only a dissociated part (Burgers vector a/6[111]) of the twinning source moves away from the atmosphere, it may be shown that the zero-temperature restraint offered to a dislocation by a solute atom (δ_0) will be less for twinning than for slip (Burgers vector a/2[111]). Furthermore, in order to move the twinning dislocation, a comparatively temperatureindependent stress (τ) , necessary to dissociate the dislocation, must be supplied in addition to that required to overcome the restraint offered by the atmosphere. Since the behaviour of a twinning source differs from that of a slip source only in these particulars (i.e. δ_0 and τ) which do not basically affect the activation of yielding, the theory should be applicable to both cases. On these grounds a plot of $\sigma - (1/T)$ ($T^{\circ}K = \text{test temperature}$) for twinning should show relative to slip behaviour: (a) a lower value of $d\sigma/d(1/T)$ since this is proportional to σ_0 , (b) the existence of a positive constant stress (τ) .

1959

Erickson and Low have suggested that the experimentally obtained $\sigma-T$ relation may be broken up into three sections in which the modes of deformation are: (a) slip at temperatures above $125^{\circ}\mathrm{K}$, (b) slip followed by twinning in the range $78\text{--}125^{\circ}\mathrm{K}$, and (c) twinning below $78^{\circ}\mathrm{K}$. Whilst the evidence supporting these contentions is adequate for regions (a) and (c) there is some doubt as to whether or not the original deformation in region (b) is twinning or slip. If Erickson and Low's results are plotted, as shown, against 1/T, the scheme of best fit is essentially three straight lines, and the transitions from one line to the next occur at temperatures which approximate to those at which the authors indicate changes in the

mode of deformation. Referring to the figure it may be seen that the occurrence of transitions follows naturally from our remarks above, as indicated by the construction lines. Here the transition at $T=140\,^{\circ}\mathrm{K}$ is supposed to be due to the intervention of twiuning as the initiator of deformation, whilst that at 87 $^{\circ}\mathrm{K}$ follows from the modified theory⁽²⁾ and is thus determined by the atmosphere density. It should be noted that relations of the type D–A are common in the literature whilst those like D–B are not.

In conclusion we observe that:

- (a) The difference in intercepts at 1/T=0 of the relations C–B and D–A which should approximate to τ , is $\sim 2.5 \times 10^9$ dyn cm⁻²; a stress which is of the same order as that ($\sim 1 \times 10^9$ dyn cm⁻²) suggested by Cottrell and Bilby⁽³⁾ to be necessary for the initial motion of the twinning dislocation.
- (b) As remarked above, the slope $(d\sigma/d(1/T))$ is proportional to σ_0 which is, according to Cottrell, $^{(4)}$ proportional to the change in the solute-atom dislocation interaction energy when the dislocation and atmosphere separate. These considerations suggest a method of estimating the ratio of slopes for slip and twinning. On this basis we find a slope ratio (slip to twinning) of 2.9 which is in agreement with the measured value, namely 2.5.
- (e) Factors which tend to increase the slope, such as increased rates of loading, will tend to increase the temperature at which twinning becomes apparent.
- (d) It is reasonable that an original twinning deformation can be followed by an extensive amount of slip. Thus it is apparent from a consideration of the Burgers vectors involved that a pile-up of twinning dislocations will interact with a suitable secondary source to the same degree independently of whether the motion of this source gives slip or twinning. The same is not true of arrays of slip dislocations where slip-slip interactions will be greater than (~3 times) those of slip-twinning. This suggests that if slip does occur at all after the original twinning deformation, it will tend to continue.
- (e) Erickson and Low's observation, that twinning becomes progressively more general as the temperature is lowered, would seem to follow if the difference between the stresses necessary for slip and twinning increases with decreasing temperature. This condition

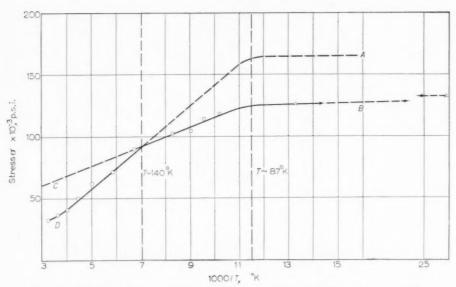


Fig. 1. Yield stress vs. reciprocal temperature. D—A, predicted form for case of slip only.
D—B, after Erickson and Low. C—B, predicted form for case of twinning only. Observations:
○— slip only; ⊙— twinning, then slip; or slip, then twinning; △— twinning, then slip.

may be seen to be satisfied by inspection of the figure. Furthermore, it must be borne in mind that we are here interested in the propagation of deformation and hence with the behaviour of a few sources near the end of dislocation arrays, rather than that of the whole assemblage of sources in the material, which determines the yield point. This restriction implies a greater (2 or 3 times) slope than appears in Fig. 1, and hence a similar factor in the rate of increase of difference in critical stresses, since according to the theory this slope varies inversely with the logarithm of the number of atomic lengths of dislocation under stress.

Taking this result in conjunction with that of (d) above, we see that slip should be rare if the ratio of the critical stresses for slip and twinning approaches 3:1.

Thanks are due to the Chief Scientist, Department of Supply, for permission to publish this note.

Aeronautical Research Laboratories N. LOUAT Bex 4331, G.P.O.
Melbourne

References

- 1. J. S. ERICKSON and J. R. Low, Acta Met. 5, 405 (1957).
- 2. N. LOUAT, Proc. Phys. Soc. B 69, 454 (1956).
- 3. A. H. COTTRELL and B. A. BILBY, Phil. Mag. 42, 573
- A. H. COTTRELL, Report on the Strength of Solids p. 30. Physical Society, London (1948).
 - * Received March 20, 1958.

Reply to discussion "The temperature dependence of the yield stress in iron" by N. Louat*

On the basis of our observations we cannot agree with Louat's suggestion that deformation is initiated by twinning in the temperature range 140°K to 78°K.

19!

In this range of temperature a drop in load at the upper yield point is observed, a Luder's band appears at one end of the specimen and propagates along the gage length. However, before the Luder's band spreads over the whole gage length, necking and fracture take place within the Luder's band. The gage length of the broken specimen is then made up of two regions: the Luder's band region and a region which is undeformed, except for pre-yield microstrains. If such a partially deformed specimen is examined microscopically, twins are observed only in the Luder's band. Twins are not observed in the region outside the Luder's band, even though the whole of the gage length had been loaded to the upper yield point stress. Our reason for qualifying this statement for the tests at 78°K was the observation of a few small discontinuities in the load-extension curve, similar to those of the twinning discontinuities at 20°K, just before the drop in load at the upper yield point.

Incidentally, the observation that twinning, without a yield-point, occurs at 20°K has been confirmed by compression tests at this temperature. In these tests no drop in load, or flow at constant load, was

observed for strains up to 3 or 4% in compression. Compression tests at 78%K sometimes exhibited twinning discontinuities just preceding the flow at constant load corresponding to the yield point.

J. S. Erickson J. R. Low, Jr.

General Electric Research Laboratory Schenectady, N.Y.

* Received April 28, 1958.

1959

A general equation prescribing the extent of the austenite-martensite transformation in pure iron-carbon alloys and plain carbon steels*

During cooling, the austenite–martensite transformation in carbon steels begins at a certain temperature designated the M_s temperature and proceeds only upon continuous cooling below this temperature.

In order to understand more completely the kinetics of this transformation, it is necessary to know quantitatively how the transformation proceeds upon cooling. Previous studies have been made using light micrographic, dilatometric and magnetometric techniques. Because these methods suffer certain limitations, the extent of transformation was determined by making precise X-ray diffraction measurements of volume per cent retained austenite after quenching to known temperatures as low as -80°C. The X-ray method used, first proposed by Averbach and Cohen⁽¹⁾ and later modified by Beu,⁽²⁾ is described in detail elsewhere. (3) This method has a limit of detectability of less than 0.5% retained austenite and the accuracy has been shown to be within 0.3% austenite at the 5% level and within 1% austenite at the 50% level.(3)

The pure iron-carbon alloys used for this investigation were prepared by vacuum melting. All samples were copper-plated before being given the heat treatment and the surface layers of the sample were removed by electropolishing before the X-ray measurements were made. These precautions were taken to insure that the phase composition measurements were truly representative of the bulk material.

Table 1 lists the results of the retained austenite measurements made on pure iron–carbon alloys. The M_s data quoted in the table has been derived from the work of Digges (4) and Greninger. (5) The data of Table 1 are presented graphically in Fig. 1. In this figure, volume per cent retained austenite is plotted logarithmically against the difference between M_s and T_q in degrees centigrade. Also plotted in Fig. 1 are data for some plain carbon steels as well as three data points for SAE 52100 steel. The retained austenite values for these steels were determined by the authors while the M_s values are those reported in the literature for these steels. (4–6)

The straight line in Fig. 1 fitted to the data points from the pure iron-carbon alloys satisfies the equation

$$\begin{split} V_{\gamma} &= \exp{[-1.10\times 10^{-2}(M_s-T_q)]}; \\ M_s &> T_q > -80^{\circ} \mathrm{C} \end{split}$$

where V_{γ} represents the volume fraction retained austenite and T_q represents the lowest temperature reached during quenching.

The fit of all the data plotted to the straight line indicates that this equation prescribes the extent of transformation not only in pure iron-carbon alloys, but in the plain carbon steels as well.

It is apparent that the straight line through the pure iron-carbon data points extrapolates naturally to the required intercept of 100% austenite at

TABLE 1

Sample No.	Austenitizing treatment	Quenching temp. (T_q)	Tempering treatment (after quench)	% Retained austenite (measured)	% C	M_s*	$(M_s - T_q)$
1 2 3 4	20 min, 960°C	24°C	30 min, $150^{\circ}\mathrm{C}$	0.8 1.9 8.5 18.0	0.37 0.50 0.81 1.10	415 380 250 188	391 256 226 164
1 2 3 4		. −24°C		0.6 1.4 5.0 10.0	0.37 0.50 0.81 1.10	415 380 250 188	439 404 274 212
1 2 3 4		−79°C	4	1.1 2.3 5.3	0.37 0.50 0.81 1.10	415 380 250 188	459 329 267

^{*} M_s was obtained from a smooth curve connecting data points of $\mathrm{Digges}^{(4)}$ and $\mathrm{Greninger}^{(5)}$

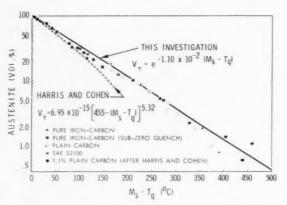


Fig. 1. Experimental data plotted on semi-logarithmic coordinates and the empirical equation derived by fitting a straight line to these points. Also shown are data obtained, and the equation proposed, by Harris and Cohen.⁽⁶⁾

 $M_s - T_o = 0$. It is from this plot that the parameter of the equation has been determined. Although the equation is well established by the data obtained in the present work, and by the intercept at $M_s - T_q = 0$, the data obtained previously by Harris and Cohen⁽⁶⁾ on a 1.1% carbon steel are also plotted in Fig. 1. Their data in the 30-100% retained austenite range also fit the equation. In addition to the data of Harris and Cohen, an empirical equation due to these investigators is also shown in Fig. 1. This equation was derived from studies of the extent of transformation in a variety of steels. It will be noted that their equation, while fitting the data well at high retained austenite values, predicts too little retained austenite at temperatures more than 100°C below M_s . This is probably due to the fact that Cohen and his colleagues determined the extent of transformation by light microscopic examination and, hence, a considerable amount of retained austenite could go undetected.

Thus $V_{\gamma}=\exp{\left[-1.10\times10^{-2}(M_s-T_q)\right]}$ represents a new general equation describing quantitatively the progress of transformation from austenite to martensite in carbon steels. The fit of this equation to the data confirms Cohen's conclusion⁽⁷⁾ that such variables as chemical composition and austenitizing temperature affect the amount of retained austenite only by their effect upon M_s .

An interesting feature of this equation is its similarity in form to equations describing other decay systems (e.g. radioactive decay). Hence, at any temperature below M_s , a constant fraction of the austenite remaining will be transformed by a given additional temperature decrement. Specifically, cooling an additional 63°C transforms one-half of the austenite remaining at any temperature below

the M_s . Furthermore, the equation prescribes that the transformation cannot be brought to completion by cooling and hence an M_f , i.e. the temperature at which transformation is complete, does not exist.

Besides being of theoretical importance, the new general relationship is of wide practical application. For example, the M_s of a particular steel can be determined simply by measuring the retained austenite content of a specimen of the steel quenched to a known temperature. This avoids the tedious task of quenching several specimens of the steel to temperatures in the neighborhood of an estimated M_s and then looking for the first traces of martensite under the microscope.

Finally, the equation can be used to assist in the solution of dimensional stability problems in hardened steel. Since there is a volume growth associated with the transformation of the metastable austenite that is retained, it is important, where dimensional stability is needed, that the amount of austenite retained be controlled to a certain tolerable limit. After the M_s temperature of a steel has been determined as described above, the equation may be used to calculate the quenching temperature necessary to reduce the amount of austenite present to a desirable level.

The authors wish to thank Mr. D. N. Callahan who made the retained austenite measurements and Messrs. F. Webbere and H. Rezeau who prepared the pure iron-earbon alloys.

D. P. Koistinen

195

 $Research\ Staff$

R. E. MARBURGER

General Motors Corporation Detroit 2, Michigan

References

- B. L. AVERBACH and M. COHEN, Trans. Amer. Inst. Min. (Metall.) Engrs. 176, 401 (1948).
- K. E. Beu, Trans. Amer. Inst. Min. (Metall.) Engrs. 194, 1327 (1952).
- 3. K. E. Beu, Proc. ASTM, 55, 630 (1955).
- 4. T. G. Digges, Trans. Amer. Soc. Metals, 28, 575 (1940).
- A. B. Greninger, Trans. Amer. Soc. Metals, 30, 1 (1942).
 W. J. Harris and M. Cohen, Trans. Amer. Inst. Min.
- W. J. HARRIS and M. COHEN, Trans. Amer. Inst. Min (Metall.) Engrs. 180, 447 (1949).
- M. COHEN, Phase Transformations in Solids, p. 608. Wiley, New York (1951).
 - * Received January 8, 1958; revised version April 25, 1958.

Shear along grain boundaries of an aluminum-10% zinc alloy deformed at room temperature*

Grain boundary shear is generally supposed to occur to a measurable extent only under conditions of creep deformation at moderately high temperatures. Evidence is presented in this note of grain boundary shearing which occurred in an aluminum-10% zinc

alloy at room temperature during tensile deformation (i.e. under a rather rapid rate of strain).

A more effective type of marker line than hither to used was utilized to study the non-homogeneous deformation that resulted from the straining. These marker lines consisted of the grooves that are left on the specimen surface after machining. An example of these lines on an undeformed specimen surface is shown in Fig. 1 at $\times 1000$. It is apparent that although the depth of the lines varies due to the microscopic irregularities in the cutting tool, yet the resolvable spacing between them is 1 μ or less. The spacing between the marker lines, by the present technique, gives a closer spacing between the lines than is apparent in the published photographs of Moore et al.⁽¹⁾

An aluminum-10% zinc alloy was used in these

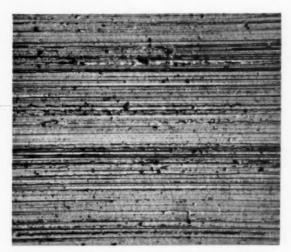


Fig. 1. Machining grooves on specimen surface after annealing. ×1000.

experiments. The specimens were annealed for 1 min at 784°F after machining; the resulting grain size was 0.05 mm. The specimens were not electropolished after the anneal so that the machining grooves could be utilized as markers. Two specimens were deformed under rapid loading conditions at room temperature, immediately after they had been annealed, so that for practical purposes they were in a solid solution condition. The final elongations of the specimens were respectively 4.85 per cent and 10.5 per cent. The results described below relate to the specimen having an elongation of 4.85 per cent, but these results were confirmed by the specimen having the 10.5 per cent elongation.

Figure 2 shows an example of the distortion of the marker lines that resulted from the elongation. It is

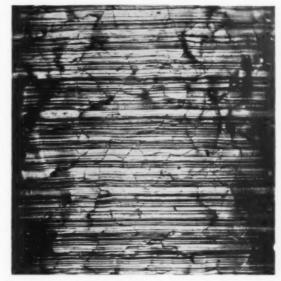


Fig. 2. General distortion of the machining grooves after straining at room temperature. ×150.

apparent that the marker lines which were continuous across grain boundaries prior to the deformation were distorted as a result of the room temperature deformation in essentially one of the two following ways:

1. The marker lines still remained continuous across grain boundaries, but were bent, either smoothly or sharply, at interfaces within the grains, these interfaces frequently being very close to grain boundaries. Figure 3 shows an example of this type of distortion of the marker lines, and is due to the presence of subgrains, as was confirmed from a comparison of the Laue back reflection photograms taken from the undeformed and deformed specimens, respectively.

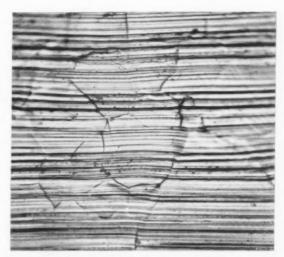


Fig. 3. Distortion of machining grooves at interfaces within grains. ×500.

VOL. 7 1959



Fig. 4. Displacement of machining grooves as a result of grain boundary sliding. ×1000.

2. The marker lines were very clearly displaced at the grain boundaries. Such a displacement could occur only if grain boundary shear took place during deformation. Many instances of the displacement of the marker lines at grain boundaries will be noted in Figs. 2 and 3: in addition, Fig. 4 shows a very obvious example of such an effect. The distortion of the marker lines that is to be expected in the regions of the grains near grain boundary junctures, where plastic deformation occurs to accommodate grain boundary shearing, was also very clearly observable (see Fig. 5).

The conclusion from the present work is not so much that grain boundary sliding occurs during the room temperature deformation of an aluminum-zinc alloy, but that it occurs at a temperature which is

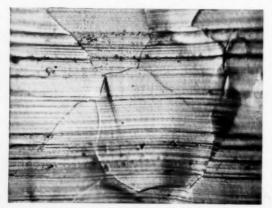


Fig. 5. Distortion of machining grooves in the neighborhood of a grain boundary juncture. (Same as Fig. 3). ×1000.

0.33 of the absolute solidus temperature⁽²⁾ of the alloy. In this connection, grain boundary sliding has also been reported to occur during the room temperature deformation of magnesium(3) and of high purity aluminum. (4) However, the present observations are superior for two reasons. First, the marker lines are both regular and closely spaced, and second, as shown in Fig. 5, the necessary plastic deformation near grain boundary junctures was clearly observed.

According to Ke, internal friction measurements are interpreted to show that the viscosity of grain boundaries in aluminum is too high at room temperature to permit sliding to occur on deformation. However, the observations presented above for the aluminum-zinc alloy and the results noted for magnesium(3) and for aluminum,(4) demonstrate that grain boundary sliding does occur during the room temperature deformation of these materials. This being the case, it appears that perhaps internal friction measurements are not adequate in predicting the temperature range over which the much larger amounts of shear that are observed in grain boundary sliding can take place under conventional tensile or creep conditions. The present work further suggests that if there is a temperature below which grain boundary sliding does not occur during the deformation of aluminum, then that temperature must be less than 0.33 of the absolute solidus temperature, or of the melting temperature.

A. R. CHAUDHURI J. E. MAHAFFY N. J. GRANT

191

Department of Metallurgy Massachusetts Institute of Technology Cambridge, Massachusetts

References

1. H. F. Moore, B. B. Betty and C. F. Dollins, Univ. Illinois Bull. 72 (1935).
2. C. J. SMITHELLS (Ed.), Metals Reference Book Vol. 1, p. 323.

Butterworths, London (1955).

- F. E. HAUSER, C. D. STARR, L. TIETZ and J. E. DORN, Trans. Amer. Soc. Metals 47, 102 (1955).
- 4. F. B. Cuff Jr. and N. J. Grant, Amer. Inst. Min. (Metall.) Engrs., to be published.
 - * Received April 29, 1958.

Effect of dissolved impurities on grainboundary migration*

Lücke and Detert(1) have attempted to explain the strikingly large repressing effect of very small concentrations of dissolved impurities upon the rate of recrystallization, by attraction forces between the grain boundary and the impurity atoms left behind by the moving boundary. An alternative mechanism, in terms only of what goes on within the boundary, is here suggested.†

Consider a general high-angle grain boundary between two grains, one having a larger free energy than the other because of a higher dislocation density. Assume a homogeneous distribution of solute atoms at a very low concentration, c, in the bulk of the two grains. In obedience to the Gibbs adsorption isotherm, the grain boundary will have a different concentration, c'. As the temperature is raised, a temperature is attained that is high enough for detachment of atoms from both grains into the boundary. There will then be transfer of atoms from the grain of higher free energy to the other, through the boundary layer or "phase", and the boundary will move. However, both because the free energy of the vanishing grain is larger and because of the more disturbed nature of the lattice of that grain, detachment of atoms from the vanishing grain should be easier than the attachment of atoms to the growing grain. Hence, the assumption will be made that the rate-controlling step in boundary migration is the organization of atoms into the lattice at the advancing contact between the growing grain and the boundary phase.

It is now suggested that the strong effect of dissolved impurities upon grain-boundary migration is due to an "adsorption" of the solute atoms at the advancing edge of the growing grain. The rate of accretion of solvent atoms, which is to say the rate of advance of the boundary, is impeded by the solute atoms occupying sites which the solvent atoms must occupy in order to permit the grain to grow. The grain can grow only if solvent atoms forcibly cover up such "adsorbed" solute atoms, or if the temperature is high enough so that the "adsorbed" solute atoms may be shaken off into the boundary. In the latter case, the grain-boundary migration will be analogous to the process of zone melting, in that the grain boundary will increase in solute concentration to some other steady-state value as it sweeps into new regions of the vanishing grain. At higher temperatures, higher solute concentrations will be necessary to slow down grain-boundary migration than at lower temperatures. In direct opposition to the hypothesis of Lücke and Detert, (1) the present model entails either an unchanged solute concentration, c', in the boundary, or an enrichment therein at higher temperatures.

1959

The present mechanism envisages the general grain boundary as having some thickness, a magnitude of only a few lattice spacings being sufficient for the boundary to be regarded as a "phase" functioning simply as the medium for transfer of atoms from one grain to another. The considerations of Cahn and Hilliard⁽²⁾ support the concept of a finite thickness of a grain boundary, and Inman and Tipler(3) find evidence for very thick grain boundaries. However, a twin boundary, or a boundary between two grains in special crystallographic relationship, probably has no boundary "phase", and the motion of such a boundary should be very little affected by dissolved impurities. The suggested mechanism for the advance of a general grain boundary offers the possibility of understanding the orientation dependence of boundary motion, (4) since the nature of the growth sites of the advancing edge of the growing grain will depend on the orientational relationship between the boundary and the lattice of the growing grain.

The writer is grateful to Karl T. Aust for bringing the problem to his attention, and for helpful conversations.

R. A. ORIANI

General Electric Research Laboratory Schenectady, New York

References

- 1. K. Lücke and K. Detert, Acta Met. 5, 628 (1957).
- J. W. Cahn and J. E. Hilliard, J. Chem. Phys. 28, 258 (1958).
- M. C. Inman and H. R. Tipler, Acta Met. 6, 73 (1958).
 P. A. Beck, Metal Interfaces, p. 208. Amer. Soc. Metals
 - * Received May 12, 1958.

(1952).

Knight shift and calorimetric measurements in liquid sodium alloys*

Measurements of the Knight shift of the nuclear magnetic resonance frequency of a nuclear species in a metal or alloy may lead to information about the conduction electrons. We have measured the sodium Knight shift in dilute liquid alloys Na(Hg) and Na(Au).

The alloys were prepared under vacuum and dispersed ultrasonically at $130^{\circ}\mathrm{C}$ in mineral oil. The particle size in the resonance samples was less than 15μ . Resonance measurements were made at $130^{\circ}\mathrm{C}$ and 6.75 k oersteds using a Varian 6 in. magnet and a Numar spectrometer. The Na line width was approximately 500 c/s, determined by magnetic field inhomogeneities. The sodium resonance frequencies in the alloys were compared to measurements on similar dispersions of pure metallic sodium at the same temperature.

[†] The writer became aware after these thoughts had been expressed that a similar view was being independently developed by G. W. Sears of this Laboratory.

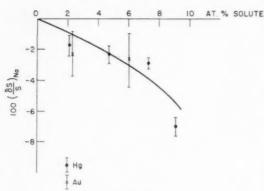


Fig. 1.

The results for Na(Hg) and Na(Au) alloys are plotted in Fig. 1. The indicated uncertainties are estimated from the reproducibility of many measurements. The Na(Au) data represent earlier work with larger uncertainties.

The observed changes in the Knight shift on alloving are not in accord, even as to sign, with either the rigid band(1) or the Friedel model(2) of terminal solid solutions. Clearly valence differences alone cannot explain the results and undoubtedly, a more elaborate treatment, giving electronic wave functions in some detail, is required.

The enthalpy of formation of the liquid alloys was measured in a simple calorimeter consisting of the reaction vessel, calibration heater, stirrer, and thermocouple immersed in a volume of mineral oil contained in a dewar. The heat of mixing of the two components could be calculated from the recorded thermocouple e.m.f.-time curve and the calibration factor of the calorimeter as measured electrically. The reaction vessel was a device that permitted holding the two separated components in vacuum at 130°C within the calorimeter before the mixing. The mixing was accomplished by electromagnetically lifting a stainless steel valve from its seat, thereby

Table 1. Heats of formation of liquid Na-Hg and Na-Au solutions from the liquid components, 130°C

Alloy	$\frac{\Delta H}{(\mathrm{cal/g.\ atom})}$		
Na,995Hg,005	-33		
Na _{.979} Hg _{.021}	-230		
Na.954Hg.046	-560		
Na,927 Hg,073	-835		
Na.913Hg.087	-1030		
Na.967 Au.033	-100†		

† This is calculated from the heat of mixing of liquid Na with solid Au by the assumption that the heat of fusion of Au is independent of temperature.

permitting the liquid sodium to drop onto the weighed amount of either liquid mercury or solid gold. Table 1 presents the results obtained; the accuracy is estimated at +5 per cent. The present values for Na(Hg) solutions are about 30 per cent larger negative numbers than those that would be obtained by extrapolation of the values derived by Kubaschewski and Catterall.(3)

To round out the thermodynamic information and to aid in future understanding of the Knight shift data, it is pointed out that liquid Na-Hg solutions are characterized by considerable negative volumes of formation.(4)

Acknowledgment

The authors are happy to acknowledge the experimental aid rendered by John Bujake and E. McCliment.

R. A. ORIANI

19

M. B. WEBB General Electric Research Laboratory Schenectady, New York

References

- H. Jones, Proc. Roy. Soc. A144, 255 (1934).
 J. FRIEDEL, Adv. in Physics 3, 446 (1954); J. Phys. Radium 16, 444 (1955).
- 3. O. Kubaschewski and J. A. Catterall, Thermochemical Data of Alloys. Pergamon Press, London (1956).
- 4. E. Vanstone, Trans. Faraday Soc. 7, 42 (1911).
 - * Received May 21, 1958.

TRANSFORMATION PSEUDO-MARTENSITIQUE DANS L'HYDRURE DE ZIRCONIUM*

D. WHITWHAM, MELLE A. HUBER et J. HÉRENGUEL†

L'examen micrographique des alliages zirconium-hydrogène permet de distinguer l'hydrure sous deux phases différentes. Celle qui correspond au métal saturé en hydrogène (pression: 1 atm.) possède un réseau tétragonal (c/a < 1), fait déjà signalé par plusieurs auteurs. La texture tout à fait particulière de cette phase indique qu'elle se forme par la transformation pseudo-martensitique d'une phase cubique.

PSEUDO-MARTENSITIC TRANSFORMATION IN ZIRCONIUM HYDRIDE

Metallographic examination of a series of zirconium-hydrogen alloys reveals the existence of two different hydride phases. The hydride corresponding to full saturation of the metal with hydrogen (1 atm. pressure) has a tetragonal lattice (c/a < 1), as shown by various authors. The metallographic structure of this phase has certain particularities which indicate that its formation depends on a pseudo-martensitic transformation of a cubic phase.

EINE PSEUDO-MARTENSITISCHE UMWANDLUNG IN DER ZIRCONIUM-WASSERSTOFFVERBINDUNG

Die mikrographische Untersuchung der Zirconium-Wasserstoff Legierungen ermöglicht zwei verschiedene Phasen in der Wasserstoffverbindung zu unterscheiden. Die dem mit Wasserstoff gesättigtem Metal entschprechende Phase (Druck:1 atm.) hat eine tetragonale Struktur (c/a < 1)—wass schon von mehreren Autoren hingedeutet wurde. Die ganz besondere Struktur dieser Phase weist hin dass sie durch pseudo-martensitische Umwandlung einer kubischen Phase gebildet wird.

Au cours d'une étude sur la microstructure des alliages Zirconium-Hydrogène, nous avons observé une structure tout à fait particulière rappelant celles qui ont déjà été décrites pour certains alliages Indium—Thallium⁽¹⁾ et Manganèse-Cuivre.⁽²⁾ Comme on le voit sur la Fig. 1, chaque grain est subdivisé en bandes parallèles. De plus certaines bandes contiennent à l'intérieur une famille de stries parallèles et, assez souvent, on peut remarquer dans un seul grain deux familles de bandes principales qui s'entrecroisent (Fig. 2). Toutes ces particularités sont communes à l'alliage d'indium + 21,75% de thallium étudié par L. Guttman⁽¹⁾ qui les a associées à une transformation du réseau sans diffusion, du système cubique à faces centrées au système tétragonal.

Le zirconium déhafnié employé contenait comme impuretés principales: 1000 ppm Fe; 850 ppm O_2 et 450 ppm Si (le titre en Zr était de 99,7%, par différence).‡

Les alliages zirconium-hydrogène ont été préparés par absorption à chaud d'une quantité connue d'hydrogène. Celui-ci était introduit à la pression atmosphérique dans un tube en pyrex de volume connu dans lequel était également placée une plaquette de métal de 0,6 mm d'épaisseur, et de poids connu,

préalablement dégazée sous vide (pression $< 1 \mu$ Hg) pendant 3 hr à 1000°C, puis polie chimiquement (45% NO₃H, 10% HF et 45% H₂O en volume). Après remplissage le tube était scellé puis porté à 500° ou 600°C pendant 12 hr, temps vérifié suffisant pour atteindre l'équilibre (absorption totale et répartition régulière de l'hydrogène dans le métal). Toutes précautions étaient prises concernant la pureté de l'hydrogène (purification par passage successivement sur un catalyseur d'oxydation et sur de l'alumine activée) et le balayage du tube avant scellement (balayage par l'hydrogène sec du tube porté à 120°-160°C). Malgré ces précautions un mince film d'oxyde se produit à la surface, donnant des teintes d'interférence jaunes ou bleues. Ce film n'a pas du tout empêché l'absorption de l'hydrogène, jusqu'à la saturation qui s'est montrée dans nos essais de 65,8 at. H₂ à la pression atmosphérique.

L'hydrogène absorbé a été dosé par dissolution complète d'un échantillon dans l'acide fluorhydrique à 20%. Cette méthode est reproductible à $\pm 0.5\%$ du volume total d'hydrogène libéré; compte tenu de l'hydrogène produit par dissolution du métal (Zr + 4 HF = ZrF₄ + 2H₂), ce chiffre se transforme en $\pm 0.4\%$ at. H₂ sur l'alliage saturé à 65.8% at. H₂.

Dans tous les cas nous avons obtenu une confirmation approximative de cette analyse:

—soit par mesure de l'hydrogène non absorbé au cours de l'essai, en cassant le bout du tube sous l'eau

^{*} Received March 25, 1958.

[†] Centre de Recherches d'Antony, Seine.

[‡] Cet échantillon, avec son analyse, nous a été remis par le Centre d'Etudes Nucléaires de Saclay; nous l'en remercions bien vivement.

et en mesurant le volume d'hydrogène résiduel;
—soit par estimation du volume intérieur du tube
scellé déduit de ses dimensions externes et de
l'épaisseur du verre.

(Cette deuxième méthode, moins précise, a dû être employée dans le cas des traitements à 600°C parce que le tube s'est aplati sous l'action combinée de la température et du vide créé par l'absorption de l'hydrogène).

Les examens micrographiques nous ont permis de distinguer facilement les trois phases principales annoncées α , β et δ du diagramme d'équilibre:^(3,4)



Fig. 1. Alliage de zirconium à 64% at. H_2 . Phase ϵ . Subdivision des grains en bandes parallèles. G=1000.

- —Solution solide α , contenant des bâtonnets d'hydrure en structure de Widmanstätten (alliage à 2% at. H₂ refroidi lentement) (Fig. 3);
- —Solution solide β -structure typiquement martensitique après trempe (alliage à 30% at. H₂) (Fig. 4);
- —Phase δ sur un alliage à 60,4% at. H_2 refroidi lentement (Fig. 5).

La sous-structure orientée que l'on voit dans les grains de la phase δ (Fig. 5) se développe plus ou moins clairement dans différents échantillons: toutefois cette structure n'est pas à confondre avec celle de la phase ε (Fig. 1 et 2).

Seul le diagramme d'équilibre (Fig. 6), établi par D. A. Vaughan et J. R. Bridge, (4) montre des alliages



Fig. 2. Alliage de zirconium à 65,8% at. $\rm H_2$. Phase ε . Croisement des bandes. G=1500.



F16. 3. Alliage de zirconium à 2% at H $_2$. Phase $\alpha+$ bátonnets d'hydrure, G=1000.

saturés d'hydrogène et ces auteurs ne signalent qu'une seule phase pour l'hydrure: $\delta.*$

Par contre E. A. Gulbransen et K. F. Andrews⁽⁵⁾ avaient déjà signalé l'existence de deux phases différentes:

Structure	Paramètres (Å)	Composition at. H ₂ (%)	
δ: cubique à faces centrées	a = 4,78	59 à 60,9	
ε: tétragonal à faces centrées	a = 4.97 $c = 4.48$	62,1 à 66,3	

Des diagrammes de Debye–Scherrer nous ont montré sur la structure des Fig. 1 et 2 le même réseau tétragonal avec a=4.97 Å et c=4.45 Å: il s'agit donc de la phase ε différente de δ .



Fig. 4. Alliage de zirconium à 30% at. $\rm H_2.$ Phase β martensitique. (Trempé à $650\% \rm C.)~~G=1000.$

L'étude aux rayons X, de Vaughan et Bridge, $^{(4)}$ confirme bien les résultants de Gulbransen et Andrews $^{(5)}$ mais les premiers auteurs nient l'existence d'une autre phase ε —attribuant à la phase δ tous les alliages de 55 à 65% at. H₂ (à la température ambiante). Leur conclusion était basée sur deux observations :



Fig. 5. Alliage de zirconium à 60,4% at. H₂. Phase δ (Refroidissement lent). G=1000.

- (a) le rapport c/a varie d'une façon continue de 1,08 à 0,90 pour les alliages de 55 à 65% at. H₂: le réseau cubique serait alors simplement un cas particulier des variations continues de paramètres.
- (b) en chauffant l'alliage à 65% at. $\rm H_2$, le réseau tétragonal (c/a=0.90) se rapproche de plus en plus du réseau cubique, vers 720%C.

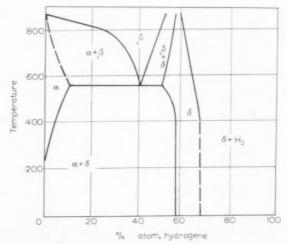


Fig. 6. Diagramme d'équilibre zirconium-hydrogène établi par Vaughan et Bridge⁽⁴⁾ par étude sur diagrammes de poudre en fonction de la composition et de la température.

^{*} Nous avons reproduit le diagramme d'équilibre de Vaughan et Bridge⁽⁴⁾ en changeant l'appellation de la phase γ en δ. Ceci concorde avec les symboles employés par Gulbransèn et Andrews.⁽⁵⁾

Ce deuxième résultat était interprété comme étant dû à une diminution de la teneur en hydrogène, par suite d'une dissociation pendant l'essai. Par contre, dans nos propres essais, le tube de pyrex s'est aplati complètement pour tout alliage préparé à $650^{\circ}\mathrm{C}$, indiquant ainsi la présence d'un vide ou d'une pression réduite.

Les observations micrographiques établissent sans ambiguité l'existence de deux phases différentes, ce qui laisse donc prévoir une discontinuité (quoique faible) dans la courbe c/a pour les compositions comprises entre 55 et 65% at. H_2 . Nous avons, par ailleurs, trouvé la même structure "en zèbre" aussi bien après refroidissement lent qu'après trempe à l'eau —aussi bien après une saturation du métal à 600°C qu'a 500°C (au-dessus et au-dessous de la température de transformation de l'eutectoïde). Il s'agit donc sûrement d'une transformation pseudo-martensitique du type cubique à faces centrées en type tétragonal à faces centrées. La phase cubique pourrait très bien exister à haute température, mais il est intéressant de remarquer que la transformation pourrait également se produire en saturant la phase cubique avec de l'hydrogène.

La saturation maximum en hydrogène à $600^{\circ}\mathrm{C}$, au cours de nos essais, n'est que de 65.8 ± 0.4 at. H_2 alors que les chiffres de Gulbransen et Andrews étaient de 66.3%. Cet écart peut être attribué à des différences de composition du métal ainsi qu'au degré de purification de l'hydrogène.

Enfin il faut noter que l'alliage saturé d'hydrogène est très fragile (et facilement pulvérisé); un réseau de criques superficielles se développe toujours à l'échelle de quelques grains sans doute par suite de dilatations anisotropes. Toutefois on retrouve une très bonne ductilité après dégazage complet de l'hydrure, compte tenu des criques superficielles qui évidemment ne se ressoudent pas.

La densité de l'hydrure à 65.8% at. H_2 , mesurée par simple pesée à l'air et dans l'eau, est égale à 5.62 ± 0.02 ; ce chiffre est à comparer à 6.53 pour le zirconium pur.

REFERENCES

- L. GUTTMAN, J. Metals N.Y. 3, (12) 1472 (1950).
- 2. F. T. WORRELL, J. Appl. Phys. 19, 929 (1948)
- 3. C. E. Ells et A. D. McQuillan, J. Inst. Met. 85, 89 (1956).
- D. A. VAUGHAN et J. R. BRIDGE, J. Metals N.Y. 8, (5) 528 (1956).
- E. A. Gulbransen et K. F. Andrews, J. Electrochem. Soc. 101, 474 (1954).

THE EARLY STAGES OF PLASTIC DEFORMATION IN COPPER*

D. A. THOMAS† and B. L. AVERBACH†

Small plastic strains in the range $1-500 \times 10^{-6}$ were measured with electrical resistance strain gages for high-purity polycrystalline copper tensile specimens. Plastic extension was observed at stresses above about 1000 lb/in^2 , and the plastic strain at a given stress was shown to depend on the third power of the grain size.

A deformation mechanism is proposed in which the movement of the dislocations produced at small strains is blocked by grain boundaries. This picture predicts the observed grain size dependence and also accounts for the shape of the stress–plastic strain curve and for the magnitude of the plastic strain. Creep was observed in all specimens at stresses slightly above those required for the first observable plastic deformation. The creep rate at constant stress was greater the larger the grain size.

LES PREMIERS STADES DE LA DEFORMATION PLASTIQUE DU CUIVRE

Sur des éprouvettes de traction de cuivre polycristallin de haute pureté, les auteurs ont mesuré de petites déformations plastiques, de l'ordre de $1-500\times10^{-6}$, à l'aide de jauges de contrainte à résistivité électrique. L'allongement plastique a été observé pour des tensions supérieures à $1000~\rm lb/in^2$ et on a trouvé que la déformation plastique à une tension donnée, variait comme la troisième puissance de la grosseur du grain.

Les auteurs proposent un mécanisme de déformation au cours duquel les dislocations naissant pour des déformations faibles sont bloquées aux joints des grains. Ce modèle permet de prévoir l'influence de la grosseur du grain et en outre explique la forme de la courbe de traction et l'amplitude de la déformation plastique.

Pour tous les échantillons, un fluage a été observé pour des tensions légèrement supérieures à celles nécessaires pour produire la première déformation plastique détectable. Plus le grain est gros, plus est grande la vitesse de fluage sous tension constante.

DIE ANFANGSSTADIEN DER PLASTISCHEN VERFORMUNG VON KUPFER

An Zugstäben aus hochreinem, polykristallinem Kupfer wurden mit Hilfe von Dehnungsmessstreifen kleine plastische Dehnungen im Bereich $1-500\times 10^{-6}$ gemessen. Plastische Verformung wurde bei Spannungen oberhalb von etwa 1000 lb/in² beobachtet; bei fester Spannung variiert die plastische Dehnung mit der dritten Potenz der Korngrösse.

Es wird ein Verformungsmechanismus vorgeschlagen, bei dem die Bewegung der Versetzungen bei kleiner Verformung durch die Korngrenzen blockiert wird. Dieses Bild führt zu der beobachteten Korngrössenanhängigkeit und erklärt auch die Gestalt der Spannungs- (plastische) Dehnungskurve sowie die absolute Grösse der plastischen Dehnung. An allen Proben wurde bei etwasgrösseren Spannungen, als sie zur Erzeugung der ersten beobachtbaren plastischen Deformation notwendig sind, Kriechen beobachtet. Die Kriechgeschwindigkeit bei konstanter Spannung ist um so höher, je grösser die Korngrösse ist.

1. INTRODUCTION

Strain measurements at small strains have been made by several investigators. Smith⁽¹⁾ and Smith and Van Wagner⁽²⁾ determined stress–strain curves for a number of copper-base alloys using an optical extensometer with a strain sensitivity of 1×10^{-6} . Permanent departures from Hooke's Law were observed at stresses well below the usual yield strength. For annealed tough pitch copper the stress required to give a plastic strain of 2×10^{-6} was only 1150 lb/in² compared to the yield strength (stress for 0.5 percent extension) of 5500 lb/in². For a very finegrained 70–30 brass, the corresponding stresses were 23,000 lb/in² and 29,000 lb/in². Small plastic strains

were also determined for steels by Roberts *et al.*,⁽³⁾ by Muir *et al.*,⁽⁴⁾ and less extensively by Vreeland *et al.*,⁽⁵⁾

Metallographic evidence that plastic deformation occurs at low stresses in polycrystalline alpha brass containing 35.4% zinc has been presented by Jacquet. (6) Small electropolished tensile specimens were stressed in the range 1-4 kg/mm² (1420 to 5700 lb/in2) and "measurable elongation" was detected at about 3.6 to 3.8 kg/mm² (5100 to 5400 lb/in²). Slip lines on the polished surfaces were observed, and arrays of etch pits produced by a sensitive electroetching technique corresponded to the slip observed on the surface and were also found in the bulk of the specimen after deep electropolishing. Samuels⁽⁷⁾ and Samuels and Hatherly(8) have used the same techniques for cartridge brass and their work supports the conclusion that plastic deformation is detectable at a very early stage.

Technology, Cambridge, Massachusetts.

This paper is taken from a thesis submitted by D. A.
 Thomas in partial fulfillment of the requirements of the Sc.D. degree in Metallurgy at M.I.T. Received April 4, 1958.
 † Department of Metallurgy, Massachusetts Institute of

VOI 7 195

Although there is strong evidence that plastic deformation occurs at relatively low stresses, there has been relatively little work on the variables which affect this initial deformation. This research was undertaken in an effort to obtain experimental data which could clarify the phenomena that occur during the early stages of plastic deformation.

2. EXPERIMENTAL METHODS AND RESULTS

Copper with a purity of 99.999% * was obtained in the form of a large-grained continuously cast rod of ³ in. diameter. The preparation, purity and some of its properties have been described by Smart et al. (9) Flat strips 0.030 and 0.060 in, thick were prepared by a sequence of cold rolling and annealing procedures. and sheet tensile specimens with a gage section 0.36 in. wide and 1.25 in. long were machined. Several factors were considered in determining the sequence of reduction and annealing steps. The number of reductions and anneals had to be large enough to produce a uniform grain size in the tensile specimens. An attempt was made to minimize the resultant preferred orientation and the processing was carried out in accord with the general principles developed by Cook and Richards for copper. (10-12) The final as-recrystallized grain size depended primarily on the final cold reduction, being smaller the greater the final reduction. All intermediate and final annealing operations were carried out in an atmosphere of dry hydrogen. Discontinuous grain growth was observed for specimens which had final reductions of 60 per cent and 40 per cent but was not observed for specimens with a final reduction of 20 per cent. Metallographic observations† indicated an increasing number of grains with the cube texture orientation as the final reduction was increased. This type of preferred orientation was the probable cause for the discontinuous grain growth observed for specimens with large final reductions. Only material with a uniform grain size was used. The grain size was difficult to measure because of the large number of irregular annealing twins present, and it was determined by a comparison at 75× with the ASTM non-ferrous grain size stan-

A simple dead load tensile machine was used. Axial loading was obtained by applying a small load to the specimen (corresponding to a stress of approximately

410 lb/in²) and then adjusting the points of application of the load until the strain gages on each side of the gage section indicated the same strain. The stress on either side of the specimen differed by less than 8 per cent from the average stress. SR-4 electrical resistance strain gages, with a gage length of $\frac{3}{8}$ in. were mounted on both sides of the gage section of the tensile specimen. The strain in each gage was determined and the test results were plotted as average stress vs. the average of the strains indicated by the independent strain gages. The strain sensitivity was of the order of 1×10^{-6} .

A typical plot of the results is shown in Fig. 1. The region up to a strain of 200×10^{-6} is plotted on an expanded strain scale that is still consistent with the accuracy of the strain measurement. The results were obtained by a load–unload technique, with the load being increased after each load–unload cycle. Each point on the "total strain" curve shows the strain measured while the specimen was under stress. Each point on the "plastic strain" curve shows the strain measured after removal of the indicated stress. Most of the specimens underwent a very small apparent contraction in length before plastic extension began at a stress of about 1000 lb/in². The

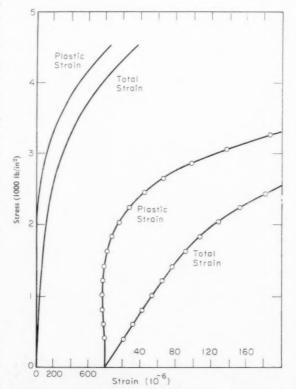


Fig. 1. Stress–strain curves for specimen with grain size of $0.04~\mathrm{mm}$.

^{*} This material was kindly supplied by the American Smelting and Refining Company.

[†] The specimens were electropolished at 2.0 V in a solution of two parts orthophosphoric acid and one part water. They were etched by reducing the voltage to about 0.9 V for 90 sec. Etch pits developed preferentially on cube faces, and the cube faces also showed a characteristic luster.

negative strain never exceeded 3×10^{-6} , and it was assumed that at least a part of this effect was associated with the bonding of the strain gage to the specimen.

The pronounced effect of grain size on the tensile curves is illustrated in Fig. 2 by the plastic strain curves for specimens of the smallest grain size tested. 0.025 mm, an intermediate grain size, and the largest grain size tested, 0.08 mm. The reproducibility of the curves was indicated by tests of three identically treated specimens. For stresses of 1250, 1500 and

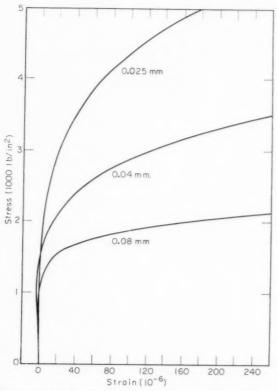


Fig. 2. Plastic strain curves for specimens with grain sizes of 0.025, 0.04 and 0.08 mm.

2500 lb/in², the plastic strains were in the ranges 2-4, 7-10, and $84-91 \times 10^{-6}$ respectively. Another group of three specimens was given identical annealing treatments followed by different cooling rates from the annealing temperature, and the results are shown by the plastic strain curves of Fig. 3. One specimen was furnace cooled to 250°F in about 10 hr and then air cooled. The intermediate cooling rate was achieved by taking the muffle tube from the furnace and cooling it to room temperature in about 40 min with a flow of hydrogen passing through the tube. The rapid cooling rate was achieved by playing a stream of nitrogen gas on the specimen as it

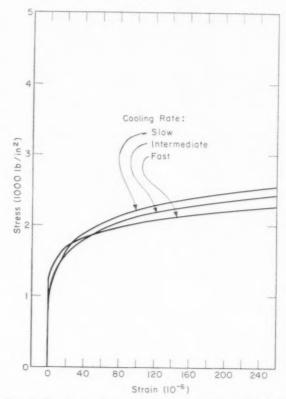


Fig. 3. Plastic strain curves for specimens annealed at 565°C for 120 min and cooled at different rates. Grain size 0.07 mm.

was taken from the tube, and this resulted in a cooling time of about 6 min. The intermediate cooling rate procedure was used for all of the other specimens reported in this paper. Fig. 3 shows that the effect of cooling rate was appreciable at high strains, the strain at a given stress being greater the faster the cooling rate. The anomalous behaviour of the rapidly

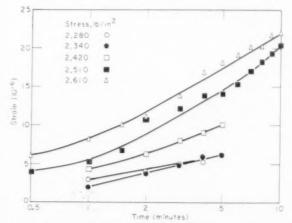


Fig. 4. Creep at various stresses for specimen with grain size of 0.055 mm.

VOL. 7 1959 cooled specimen at small strains probably resulted from slight accidental deformation during the handling of the specimen after annealing.

At stresses somewhat above those at which the first plastic strain was observed it appeared that the total strain increased with time in all specimens, indicating that creep was taking place. Some creep results are shown in Fig. 4, with creep measurements starting 15 sec after the application of the load. Creep was first observable when the strain increased $1\text{--}3\times10^{-6}$ in a loading time of 2 or 3 min. The stress at which creep was first detected was difficult to determine precisely, but there was an unmistakable trend with grain size. Fig. 5 shows the approximate stress

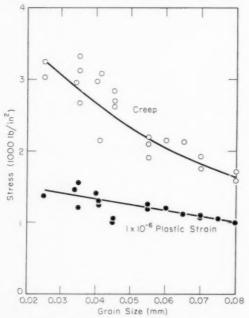


Fig. 5. Stress for detection of creep and of 1 \times 10⁻⁶ plastic strain.

for the first observation of creep along with the stress required to give 1×10^{-6} plastic strain. Grain size also influenced the extent of creep at higher stresses. For example, a specimen with a grain size of 0.08 mm had a higher creep rate for any given stress than did the specimen of Fig. 4, with a grain size of 0.055 mm. At a stress of about 2500 lb/in² the larger grained specimen extended 15×10^{-6} in the 4 min period from 1 to 5 min after creep measurement began, compared to an extension of 9×10^{-6} for the smaller grained specimen.

3. MECHANISM FOR THE EARLY STAGES OF PLASTIC DEFORMATION

In the very early stages of plastic deformation some of the complexities resulting from the presence

of large numbers of dislocations may be minimized. It is assumed that dislocation generators are activated on the application of a sufficiently high stress, and that the resultant dislocations are piled up at grain boundaries and other obstacles. At the beginning of plastic deformation each generator is considered to be independent of the others, and complications arising from the break-through of piled-up dislocations do not occur. Dislocation generators, which may have the form of Frank-Read sources, (13) are presumed to be present initially in the material, probably as dislocation segments between nodes of a three-dimensional dislocation network of the type suggested by Mott. (14) Cottrell(15) has summarized the evidence for the existence of dislocations in such networks. A source becomes active when the resolved shear stress exceeds Gb/l, where G is the shear modulus, b is the Burgers vector of the dislocation, and l is the length of the dislocation segment. As the dislocations approach a grain boundary they pile up against it, and the source ceases to be active when the back-stresses of the piled-up dislocations reduce the stress at the source to a critical value. The principal effect of the grain boundary is thus to impose a definite limitation on the number of dilocations that can be created by a source at a given stress.

This picture is very similar to that proposed by Vreeland, Wood and Clark⁽¹⁶⁾ (subsequently referred to as VWC) to account for the preyield strain in mild steel. VWC considered that the dislocations were pinned by interaction with carbon atoms, but the development of their theory considered only the stress activation of the sources and did not consider the effect of carbon pinning. Accordingly their mechanism should apply more specifically to plastic deformation in pure metals.

VOI

195

The correct shape of the plastic strain curves at small strains is predicted from these considerations. The final equation of VWC gives the plastic strain in the tensile specimens as a function of the stress, the number and the length distribution of sources, and the distance (or area on a slip plane) between obstacles. The essential factor needed to account for the observed shape of the stress-strain curves is that sources of various lengths be initially present, the shorter sources being more numerous. At small stresses this results in very small plastic strains, since only the long sources become active, but at larger stresses more and more sources become active and the plastic strain from each successive stress increment increases with increasing stress. Koehler(17) has used a qualitatively similar source length distribution in attempting to account for the initial shape of

the plastic strain curves of single crystals. This mechanism can also be used to predict the grain size dependence of the plastic strain curves. VWC and Cottrell⁽¹⁸⁾ both give expressions for the number of dislocations that can be produced by a source before the back-stress from the dislocations

piled up at an obstacle halts the operation of the source. According to VWC: $n = \frac{2\pi L \left(\tau_r^{~2} - \tau_{~c}^{~2}\right)}{Gb\tau_-}$

where n is the number of dislocations piled up against the obstacle, L is the half-distance from source to obstacle, τ_r is the applied resolved shear stress at the source, and $\tau_e = Gb/l$ is the critical stress required to operate the source. If τ_r is not much greater than τ_c , and the source is considered to be at the center of a grain of diameter D, so that dislocations piled up at opposite boundaries contribute equally to the decrease of the stress at the source,

$$n \cong \frac{\pi D(\tau_r - \tau_c)}{2Gb} \tag{2}$$

For comparison, Cottrell(18) gives

VOL.

1959

$$n \cong \frac{2D(\tau_r - \tau_i)}{Gb} \tag{3}$$

where n is the number of dislocations that must pile up at the boundary of a grain of diameter D in order to reduce the applied stress to some lower stress τ_i , which is here identified with the stress below which a source will no longer operate. Both of these equations indicate that the slip, nb, from a source is directly proportional to D.

The contribution to the tensile strain from one slip source in a polycrystalline metal depends on (1) the amount of slip from the source (2) the angular relationship of the operative slip plane and slip direction to the tensile axis and (3), the ratio of the area of the slipped grain to the area of the specimen along the slip plane. The amount of slip is proportional to D and the area of the grain is proportional to D^2 ; hence the tensile strain is proportional to D^3 . Since the total strain ε_{σ} at a stress σ is the sum of the strains from the individual sources, each of which depends on D^3 ,

$$\varepsilon_{\sigma} = KD^3 \tag{4}$$

where K is a factor which includes the stress, the number and length distribution of dislocation sources, and geometrical factors. Thus, at a given stress, specimens of different grain size that are otherwise identical should have tensile strains which depend upon (grain diameter)3.

This mechanism also predicts the correct magnitude of the plastic strain. Equation (2) can be used to estimate the number of dislocations produced by a Frank-Read source. D is taken as a medium grain size of 0.05 mm. If the dislocation density ρ is assumed to be $10^7/\text{cm}^2$, the mean source length \bar{l} is then approximately $\rho^{-1/2} = 3.2 \times 10^{-4}$ cm. For copper, G is 6×10^6 lb/in² and b is 2.55×10^{-8} cm, so that the critical stress to operate the mean source, $\tau_c = Gb/l = 480 \text{ lb/in}^2$. Appreciable plastic strain was always observed at a tensile stress of 2000 lb/in2, for which $\tau_r = 1000$ lb/in². From equation (2), n = 27.

The contribution of each active source to the total strain is nb (A_a/A_p) , where A_a is the area of the grain and A_p the area of the specimen along the slip plane. For a specimen of unit cross-section, A_n is approximately $\sqrt{2}$. Assuming that an average of one Frank-Read source has been active in each grain, and that there are about D^{-3} grains in a unit volume of the specimen, the total plastic strain is given by the strain per source multiplied by the number of active sources

$$\varepsilon_{\sigma} \cong nb \frac{A_{\sigma}}{A_{p}} D^{-3} = 95 \times 10^{-6} \tag{5}$$

A large number of Frank-Read sources has thus acted to produce a small strain of about 0.01 per cent. At lower stresses where fewer sources would be active. still smaller strains would result. This calculated strain is approximate but the order of magnitude is correct. It is similar to the strains found in the exprimental results reported here.

4. DISCUSSION

The suggested mechanism for the early stages of plastic deformation readily accounts for the observed shape of the stress-plastic strain curves and for the order of magnitude of the plastic strain. Equation (4) for the grain size dependence of the plastic strain predicts that a plot of log ε_{σ} vs. log D should have a slope of three. The data for all specimens cooled at the intermediate rate after annealing are plotted in Figs. 6 and 7 for tensile stresses ranging from 1500 to 2250 lb/in². A line of slope three is drawn on each graph and is consistent with the grain size dependence in each case, although there is considerable scatter in the data. There is no doubt that grain size is a major factor in determining the amount of plastic strain that can occur at a given stress.

Scatter in the results could arise from errors in measuring ε_a , from the fact that K of equation (4) may not be the same for all specimens, and from errors in measuring the grain size. The largest relative

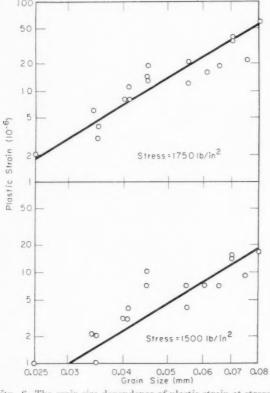


Fig. 6. The grain size dependence of plastic strain at stresses of 1500 and 1750 lb/in².

experimental errors in strain measurement were at small strains, where the measured strain was comparable to the sensitivity of measurement, and where the small apparent negative strains would introduce the greatest uncertainty.

The results of Fig. 3 show that ε_{σ} depended on cooling rate for specimens of constant grain size, and the factor K thus must be affected by cooling rate. Maddin and Cottrell(19) have shown an effect of quenching rate, and of annealing temperature before quenching, on the plastic properties of aluminum single crystals; rapid cooling markedly increased the critical resolved shear stress of aluminum crystals of various degrees of purity. The effect of cooling rate in the present work was the opposite, but the complexity of the phenomena at play may account for such differences. Annealing temperatures from 260 to 620°C were required to obtain the range of grain sizes tested. Since impurity distribution and vacancy concentration depend on annealing temperature itself, as well as on cooling rate, all specimens were subject to variations in these factors.

Dunn and Koch⁽²⁰⁾ have recently found that the dislocation etch pit density in silicon–iron decreases during secondary recrystallization from about 2×10^7

cm⁻² for the primary grains to about 2×10^6 cm⁻² for the secondaries. Differences in crystal perfection could also result from changes in the growth conditions required for the production of specimens with various grain sizes. Hence the number and length distribution of Frank–Read sources may change as the grain size is varied.

A distribution of grain sizes exists about the mean grain size D^* . Since slip from a source in a grain of diameter D gives a tensile strain proportional to D^3 . grains larger than the average grain size will contribute relatively large strains. The total strain for the same number of active sources would thus be greater for such a specimen than for a specimen containing only grains of dimension D^* . Feltham⁽²¹⁾ has pointed out, however, that the results of Hu and Beck(22) for the grain size distributions of high-purity aluminum specimens at three stages of grain growth show that the normalized distributions are identical if grain size is plotted logarithmically. This means that if $D_2^* = cD_1^*$, grains of size D_2 in the large grain size specimen have the same relative frequency of occurrence as grains of size D_2/c in the small grain size specimen. Thus the ratio of strains of corresponding grain sizes in the new distribution and in the old

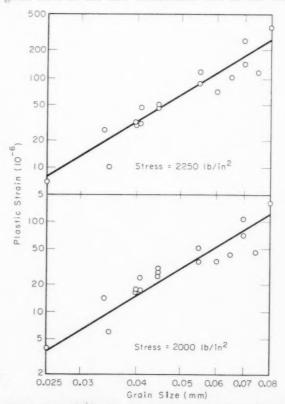


Fig. 7. The grain size dependence of plastic strain at stresses of 2000 and 2250 lb/in².

distribution is $D_2^3/(D_2/c)^3 = c^3$. But $c^3 = (D_2^*)^3/c^3$ $(D_1^*)^3$, so that the total strains in the two specimens will be in the ratio $(D_2^*)^3/(D_1^*)^3$.

In light of the mechanism for early deformation presented here, it is interesting to consider the stress necessary to activate the first Frank-Read source. If the longest source present, of length l_m , is on the plane of maximum resolved shear stress, $\tau_e = \sigma/2 =$ Gb/l_m . As before, the mean source length is taken to be about 0.003 mm; a large number of sources would exist in a single grain, even for the smallest grain size of 0.025 mm. It is improbable that the longest source would be longer than about half the grain diameter, or approximately 0.01 mm. Then $\sigma \simeq 300$ lb/in². The important feature of this result is that Frank-Read sources can be expected to be active at stresses well below those at which plastic strain was first observed in this work. Additional plastic strain occurs as the stress is increased, until it becomes observable at approximately 1000 lb/in².

Creep at the small stresses and strains found here has not previously been reported for polycrystalline metals, although the experiments of Chalmers (23) with tin single crystals demonstrated creep at very small strains. Wyatt(24) conducted experiments on polycrystalline high-conductivity copper over a range of stresses and temperatures, but the lowest stress for which creep was reported near room temperature (27°C) was 6 kg/mm² (8540 lb/in²), where a total strain of 10×10^{-3} occurred 2 sec after load application, and an additional strain of about 1×10^{-3} occurred after 2000 sec at constant stress.

1959

The characteristics of the creep observed in the present work parallel those of the stress-plastic strain curves in most respects. Fig. 5 shows that the grain size dependence of the stress for detection of creep was similar to the grain size dependence for the detection of plastic strain. The creep rate and the total creep in a given time period generally increased with increasing stress and grain size, as did the plastic strain in the tensile tests. These similarities support the intuitive expectation that the mechanism of the creep deformation should be closely related to the mechanism of the time-independent deformation. One possible way of accounting for the creep would be

to consider that the dislocation loops moving away from an active Frank-Read source toward a grain boundary may be held up locally by lesser obstacles, probably other dislocations that intersect the active slip plane. As Schoeck(25) has summarized, the energies necessary to surmount these obstacles are of the order of 1 eV. This value is sufficiently small so that kT at room temperature, which is 1/40 eV, can be expected to aid in overcoming it. A mechanism can then be visualized in which the dislocation loops reach their ultimate obstacle, the grain boundary, only with the help of thermal fluctuations in overcoming other obstacles along the way. Creep would be the observed summation of the local advances of all the held-up dislocations.

5. ACKNOWLEDGMENTS

The authors are pleased to acknowledge the support of the United States Atomic Energy Commission. One of the authors (D. A. T.) was the holder of a fellowship from Horizons, Inc.

REFERENCES

- C. S. SMITH, Proc. Amer. Soc. Test. Mater. 40, 864 (1940).
 C. S. SMITH and R. W. VAN WAGNER, Proc. Amer. Soc. Test. Mater. 41, 825 (1941).
- C. S. Roberts, R. C. Carruthers and B. L. Averbach, Trans. Amer. Soc. Metals. 44, 1150 (1952).
- 4. Hugh Muir, B. L. Averbach and Morris Cohen, Trans. Amer. Soc. Metals, 47, 380 (1955).
- T. VREELAND Jr., D. S. WOOD and D. S. CLARK, Trans. Amer. Soc. Metals. 45, 620 (1953).
- P. A. JACQUET, Acta Met. 2, 752 770 (1954). L. E. Samuels, J. Inst. Met. 83, 359 (1955).
- 8. L. E. Samuels and M. Hatherly, J. Inst. Met. 84, 1660
- 9. J. S. SMART JR., A. A. SMITH JR. and A. J. PHILLIPS, Trans. Amer. Inst. Min. (Metall.) Engrs. 143, 272 (1941).
- M. Cook and T. Ll. RICHARDS, J. Inst. Met. 66, 1 (1940). 11. M. COOK and T. Ll. RICHARDS, J. Inst. Met. 67, 203 (1941).
- M. COOK and T. Ll. RICHARDS, J. Inst. Met. 69, 201 (1943).
- 13. F. C. Frank and W. T. Read, Phys. Rev. 79, 722 (1950). 14. N. F. Mott, Proc. Phys. Soc. B64, 729 (1951).
- 15. A. H. Cottrell in Deformation and Flow of Solids. Springer Verlag, Berlin (1956). 16. T. Vreeland Jr. D. S. Wood and D. S. Clark, Acta
- Met. 1, 414 (1953).
- 17. J. S. Koehler, Phys. Rev. 86, 52 (1952)
- A. H. COTTRELL, Dislocations and Plastic Flow in Crystals, p. 111. Oxford University Press (1953).
- R. MADDIN and A. H. COTTRELL, Phil. Mag. 46, 735 (1955)
 C. G. DUNN and E. F. KOCH, Acta Met. 5, 548 (1957).
- P. Feltham, Acta Met. 5, 97 (1957).
- 22. P. A. Beck, Advances Phys. 3, 245 (1954).
- 23. B. Chalmers, Proc. Roy. Soc. A156, 427 (1936).
- O. H. WYATT, Proc. Phys. Soc. B66, 459 (1953)
- 25. G. Schoeck in Creep and Recovery. Amer. Soc. Metals, (1957).

OVERSHOOTING IN QUENCHED ALUMINUM CRYSTALS*

L. E. TANNER*† and R. MADDIN;

Single crystals of 99.8 and 99.993% pure aluminum which were quenched from annealing treatments at 600°C and strained in tension exhibited marked effects in their deformation process. It was shown in this investigation that the stress axis "overshoots" the [100]–[111] symmetry line and that conjugate slip does not begin until "overshooting" reaches a maximum. Slip lines were found to be long, sharp, and straight with cross-slip in evidence. Stress–strain curves showed low rates of work hardening, and very little asterism was observed in Laue X-ray photograms as compared to those of furnace-cooled crystals, indicating that quenched crystals deform in a much less turbulent manner than do slowly cooled crystals. It is felt that the quenching operation involves the pinning of dislocations by quenched-in vacancies and that the "overshooting" behavior is due to latent hardening of the conjugate slip system as proposed for alpha-brass by Piercy, Cahn and Cottrell. (141)

MODIFICATION DU MODE DE DEFORMATION DE CRISTAUX D'ALUMINIUM TREMPES

Des monocristaux d'aluminium de pureté 99,8 et 99,993% ont révélé un comportement particulier au cours de leur déformation par traction après un recuit à 600°C suivi d'une trempe.

Les auteurs montrent dans cette étude que l'axe des tensions dépasse la ligne de symétrie [100]–[111] et qu'un glissement conjugué ne commence pas avant que cet effet ait atteint un maximum. Les lignes de glissement sont longues, effilées et étroites et le glissement croisé apparaît bien. Les courbes tension-déformation montrent de faibles vitesses de durcissement et peu d'astérisme se marque aux rayons X, par comparaison avec celui observé pour des cristaux refroidis au four. Ceci indique que les cristaux trempés se déforment d'une manière beaucoup moins désordonnée que des cristaux refroidis lentement. Les auteurs pensent que la trempe conduit au blocage des dislocations, suite au gel des lacunes, et que l'effet de dépassement de l'axe des tensions ci-dessus mentionné (overshooting) est provoqué par un durcissement latent du système de glissement conjugué. Cette dernière hypothèse a déjà été proposée pour le laiton α par Piercy, Cahn et Cottrell.

ÜBERSCHIESSEN BEI ABGESCHRECKTEN ALUMINIUMKRISTALLEN

Aluminium-Einkristalle mit 99.8 bzw. 99.993% Aluminium, die nach einer Glühbehandlung bei 600°C abgeschreckt wurden, zeigten bei Zugversuchen ausgeprägte Abweichungen in ihrem Deformationsverhalten. Es ergab sich, dass die Stabachse die [100]–[111]-Symmetrale "überschiesst" und dass Gleitung im konjugierten Gleitsystem erst einsetzt, wenn das "Überschiessen" ein Maximum erreicht hat. Die Gleitlinien waren lang, scharf und gerade mit Anzeichen für Quergleitung. Im Vergleich zu Kristallen, die im Ofen abgekühlt waren, zeigte sich in den Spannungs-Dehnungs-Kurven nur geringer Verfestigungsanstieg und bei Laue-Aufnahmen nur geringer Asterismus. Die Verformung von abgeschreckten Kristallen verläuft also erheblich weniger turbulent als die von langsam abgekühlten. Es wird vermutet, dass infolge des Abschreckens die Versetzungen an eingefrorenen Leerstellen Gleitsystems beruht, wie es für z-Messing von Piercy, Cahn und Cottrell⁽¹⁴⁾ vorgeschlagen wurde.

INTRODUCTION

Recently there has been much interest in the effect of quenching on the mechanical properties of pure metals. (1-5) Maddin and Cottrell (2) found that the critical resolved shear stress of aluminum single crystals could be raised considerably by rapid cooling rates after annealing. It has also been observed that

the mode of deformation of aluminum crystals can be greatly altered by such heat treatment. (6) In this investigation the changes in the primary and conjugate slip processes were studied. Of particular interest was the determination of whether the stress axis of a quenched crystal tested in tension would "overshoot" the [100]–[111] symmetry line during straining.

195

The usual theory of deformation of single crystals in tension⁽⁷⁾ predicts that slip should take place on the primary system accompanied by the rotation of the stress axis to the symmetry line. At this point double slip begins and the stress axis rotation follows the symmetry line toward [112]. This has been observed in crystals of copper⁽⁸⁾ and aluminum.^(7,9) Alloy crystals, however, have been found to "overshoot" the symmetry line.⁽¹⁰⁻¹⁴⁾ Piercy, Cahn and Cottrell⁽¹⁴⁾

^{*} This paper is part of a thesis presented by L. E. Tanner to the Graduate School of Engineering, University of Pennsylvania, in partial fulfillment of the requirements for the degree of Master of Science of Metallurgical Engineering. The investigation was made possible by the Barium Steel Foundation Fellowship, the Office of Naval Research, and Armour Research Foundation of Illinois Institute of Technology. Received April 10, 1958.

[†] Metals Research Department, Armour Research Foundation of Illinois Institute of Technology, Chicago, Illinois.

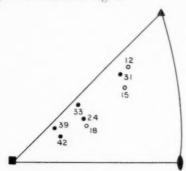
^{*} School of Metallurgical Engineering, University of Pennsylvania, Philadelphia, Pennsylvania.

studied overshooting in alpha-brass and concluded that it was probably caused by latent hardening of the conjugate slip system, thus agreeing with the earlier viewpoint. (15)

In this investigation a number of single crystals of aluminum of two purities were annealed and quenched or furnace-cooled. They were tested in tension and the critical resolved shear stresses were determined; the stress axis rotations were followed by Laue backreflection techniques; and slip lines were observed.

EXPERIMENTAL METHODS

Single crystals of 99.8%* purity aluminum (0.078 in. diameter) were produced by the strain-anneal method⁽¹⁷⁾ while the crystals of 99.993%* purity were grown from the melt in the Bridgman manner⁽¹⁸⁾ utilizing the "soft" mold technique of Noggle.⁽¹⁹⁾ The resulting crystals could be cut into two or three specimens of approximately 1.25 in. length. The orientations of the crystals, determined in the usual manner.⁽²⁰⁾ are found in Fig. 1.



VOL.

1959

Fig. 1. Initial orientation of the stress axes of single crystals of 99.8% (○) and 99.993% (●) purity aluminum.

Specimens were heat treated at $600^{\circ} \pm 2^{\circ}\mathrm{C}$ for 1 hr by being suspended in a vertical tube furnace. Quenching was accomplished by allowing the specimens to fall freely into an ice water bath onto a soft support. A specimen of identical orientation to each specimen quenched was cooled very slowly by shutting off the furnace, allowing 12 hr to reach room temperature. All samples were electropolished in the usual manner using an electrolyte of nitric acid and methyl alcohol.

The small size of the specimens was chosen in order to maximize the effect of the quench while introducing a minimum of quenching strains. Electropolishing removed an average of 0.002 in. from the crystal surface and was considered sufficient to remove effectively any strain-hardened surface layer. It

should be noted that Roswell and Nowick⁽⁵⁾ eliminated quenching strains by air-cooling gold and found an appreciable quench hardening. This confirms earlier suggestions⁽²⁾ that this effect is independent of quenching stresses.

The quenched specimens were allowed to remain at room temperature for at least one day prior to mechanical testing in order to ensure the maximum quench hardening. Crystals whose orientations were within 10° of the [100]-[111] symmetry line were chosen for the overshooting study since the asterism expected as a result of straining would not become so great as to make accurate orientation measurement prohibitive. The investigation was made by plotting their lattice reorientation obtained from Laue backreflection photograms after each increment of strain. Specimens of 99.8% purity were strained on an Instron tensile tester at strain rates of the order of 5×10^{-3} to 1×10^{-2} min⁻¹. The higher purity crystals were tested in a specially designed tensile jig in which load was applied by a slow speed motor. Slip line formation was observed during testing through a ×100 telescope. Two additional sets of crystals were used for a closer study of slip lines. These surfaces were observed at higher magnifications after small increments of strain.

Calculations of the resolved shear stress and resolved shear strain were made in the usual manner. In the case where single slip was in operation the resolved shear strain is given by:⁽²¹⁾

$$a_i = \frac{\cos \lambda_i}{\sin X_i} - \frac{\cos \lambda_o}{\sin X_o}$$

where λ_o is the initial angle between the stress axis and the slip direction, λ_i is this angle after the *i*th strain; X_o is the initial angle between the stress axis and the slip plane, and X_i is this angle after the *i*th strain. The tensile elongation, ε_i , is found in the following manner:⁽²²⁾

$$arepsilon_i = rac{l_i}{l_o} = rac{\sin \lambda_o}{\sin \lambda_i} = rac{\sin X_o}{\sin X_i}$$

where l_o is the initial gauge length and l_i is the gauge length after the *i*th strain. The resolved shear stress, σ_i , was calculated from the formula:⁽²²⁾

$$\sigma_i = \frac{\text{Load}}{\text{Initial Area}} \sin X_i \cos \lambda_i$$

In the case of double slip when the stress axis has rotated to the symmetry line, the following relationship was used for calculating resolved shear strain: (9.23)

$$a_i = \left[\frac{\cos\lambda_s}{\sin X_s} - \frac{\cos\lambda_o}{\sin X_o}\right] + 2.45 \ln\left[\frac{1+2\,\cot\,\delta_i}{1+2\,\cot\,\delta_o}\right]$$

^{*} The purities referred to in this work are those provided with the material by the producer. The 99.993% pure aluminum was supplied by Alcoa Research Laboratories.

The angle δ_a is the angle between the stress axis at the point it initially reaches the symmetry position and the (112) plane. The angle δ_i is given by

$$\varepsilon_{i}' = \frac{\sin \delta_{o}}{\sin \delta_{i}}$$

where the tensile strain ε_i is given by

$$\varepsilon_{i}^{'} = \varepsilon_{i}/\varepsilon_{s}$$

 ε_s being the tensile strain at which the stress axis first reaches the symmetry line. Resolved shear stress for double slip was found from the following: (9.23)

$$\sigma_i = \frac{\text{Load}}{\text{Initial Area}} \; \varepsilon_i \sin X' \! \cos \lambda', \label{eq:sigma}$$

where the angles X' and λ' are given by

$$\sin X' = \cos 54^{\circ}44' \cos (35^{\circ}16' - \delta_i)$$
$$\cos \lambda' = \cos 30^{\circ} \cos \delta.$$

RESULTS

Figs. 2 and 3 show the maximum rotation of the stress axis beyond the symmetry line of samples of 99.8 and 99.993% purity, respectively. For comparisons, the orientations of the furnace-cooled crystals are shown at the identical strains of their quenched mates. Additional data relating to these results are summarized in Table 1. In general, calculated rotations agreed with observed rotations during the initial stages of deformation. The rotation beyond the symmetry line by quenched crystals was associated with greater strains than would be expected assuming single slip to continue on the primary system. However, we were unable to correlate amounts of strain with the degree of overshooting. The stress axes of the furnace-cooled crystals remained within 1° of the symmetry line after the line had been reached.

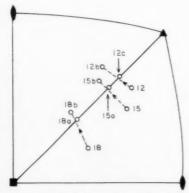


Fig. 2. Lattice re-orientation during tensile straining of furnace-cooled crystals (nos. 12c, 15a and 18a) and quenched crystals (nos. 12b, 15b and 18b).

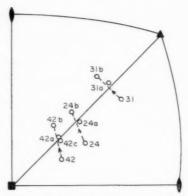


Fig. 3. Lattice re-orientation during tensile straining of furnace-cooled crystals (nos. 24a, 31a, 42a and 42c) and quenched crystals (nos. 24b, 31b and 42b).

Consistent with the results of Maddin and Cottrell(2) the critical resolved shear stress of aluminum crystals is greatly increased by quenching. The values for both purities are found in Table 2. The 99.993% pure crystals showed a consistent yield increase of the order of four times. The values of furnace-cooled samples seemed higher than would be expected, since Maddin and Cottrell⁽²⁾ reported 80 lb/in² for crystals of comparable purity. This could have been due to contamination during growth of the crystals from the melt. Specimen 42a seemed to be work hardened prior to testing, as indicated by asterism in its X-ray photogram and its high yield stress. Increases in the lower purity crystals appear to be of the order of 2 to 2\frac{1}{3}. times the furnace-cooled values, but in other tests not reported here the increases were as high as 5 times and values for furnace-cooled samples were not regular.

19

Stress-strain curves for furnace-cooled and quenched specimens of crystals 18, 24 and 42 are presented in Fig. 4, 5 and 6, respectively. In general, the curves of furnace-cooled samples exhibited a normal high rate of work hardening; however, it was observed that the slope of curve 42c (Fig. 6) is not as steep as one might expect from a crystal of such orientation. There seemed to be no apparent reason why it behaved in this manner.

The curve of the quenched crystals had a lower slope after a sharp, but not discontinuous, yield point. It was assumed that single slip took place on the primary system predominantly during the initial stages of deformation of both furnace-cooled and quenched crystals. Double slip, involving the primary and conjugate systems, was assumed to be the mode of deformation in furnace-cooled samples after their lattice rotation to the symmetry position. Since overshooting was observed in the quenched crystals, the primary system was considered to remain active up to

Table 1. Lattice rotation data for single crystals of aluminum of 99.8 and 99.993% purity*

Specimen No.	Condition (heat treatment 600°C for 1 hr)	Angle between stress axis and sym- metry line	Tensile elongation necessary for rotation to symmetry line (%)	Resolved shear strain necessary for rotation to symmetry line	Overshoot; maximum rotation beyond symmetry line	Tensile elongation for rotation from symmetry line to maximum overshoot (%)	Resolved shear strain for rotation from symmetry line to maximum overshoot
$\frac{12b}{12c}$	quenched furnace-cooled	6	11.8 11.8	$0.24 \\ 0.24$	5° none	14.8	0.48
$15a \\ 15b \\ 18a$	furnace-cooled quenched furnace-cooled	8° 8°	20.4 20.4 21.5	0.54 0.54 0.40	none 4° 1°	15.4	0.29
$\frac{18b}{24a}$	quenched furnace-cooled	8° 6	21.5 11.6	$0.40 \\ 0.32$	3°	16.6	0.35
$\frac{24b}{31a}$	quenched furnace-cooled	6° 5	11.6 11.5	$0.32 \\ 0.36$	3° 0°30′	16.6	0.29
$\frac{31b}{42a}$	quenched furnace-cooled	5° 5°30′	11.5 11.5	$0.36 \\ 0.39$	4°30′ 1°	13.4	0.26
$\frac{42b}{42c}$	quenched furnace-cooled	$5^{\circ}30'$ $5^{\circ}30'$	11.5 11.5	$0.39 \\ 0.39$	4 none	17.6	0.38

^{*} Specimens 12, 15 and 18 are 99.8% pure; specimens 24, 31 and 42 are 99,993% pure.

the point of maximum rotation beyond the symmetry line. It was then assumed that single slip takes over on the conjugate system. The S denotes the strain at which it was observed that the symmetry orientation was reached. The C denotes the strain at which it was observed that conjugate slip began in the quenched crystal.

VOL.

1959

The difference in the degree of asterism in Laue

Table 2. Yield strength of single crystals of aluminum of 99.8 and 99.993% purity*

Specimen No.	Condition (heat treatment 600°C for 1 hr)	Critical resolved shear stress (lb/in²
12b	quenched	1600.0
12c	furnace-cooled	834.0
15a	furnace-cooled	514.0
15b	quenched	1305.0
18a	furnace-cooled	586.0
186	quenched	1100.0
24a	furnace-cooled	184.1
24b	quenched	751.9
31a	furnace-cooled	176.4
316	quenched	769.1
33a	furnace-cooled	192.0
33b	quenched	815.1
39a	furnace-cooled	205.0
39b	quenched	802.4
42a	furnace-cooled	290.2
42b	quenched	790.2
42c	furnace-cooled	188.0

^{*} Specimens 12, 15 and 18 are 99.8% pure; specimens 24, 31, 33, 39 and 42 are 99.993% pure.

X-ray photograms of furnace-cooled and quenched specimens is quite striking. The Laue spots of quenched crystals are much less disturbed for a major part of the straining operation as compared to the effect on the spots of furnace-cooled samples for identical strains. This is seen in photograms of 42b and 42c at 0.080 shear strain (Fig. 7 and 8, respectively).

The appearance of the slip lines also indicated the pronounced change brought about by quenching. The

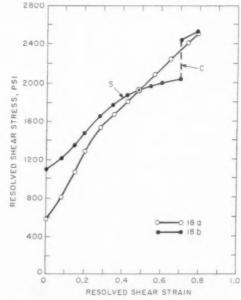


Fig. 4. Resolved shear stress vs. resolved shear strain curves of crystals nos. 18a (furnace-cooled) and 18b (quenched).

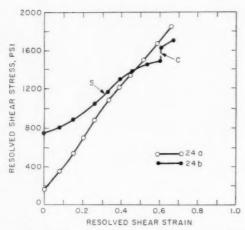


Fig. 5. Resolved shear stress vs. resolved shear strain curves of crystals nos. 24a (furnace-cooled) and 24b (quenched).

slip lines of furnace-cooled samples are characteristically short and wavy, while those of quenched crystals are long, sharp, and straight with cross-slip in evidence, quite reminiscent of slip lines seen in alpha-brass crystals. In general, conjugate slip appeared before the stress axis reached the symmetry line in furnace-cooled samples, but did not appear in quenched samples until the maximum overshooting had been reached. This is illustrated in Figs. 9 and 10. In the case of crystal No. 33 the symmetry orientation is reached at 5 per cent elongation and, as can be seen, double slip has taken place in the furnace-cooled sample (Fig. 9), while the quenched sample has only primary and cross-slip lines (Fig. 10).

DISCUSSION

This investigation has shown that quenching affects the mode of deformation of aluminum crystals considerably and seems to be independent of purity.

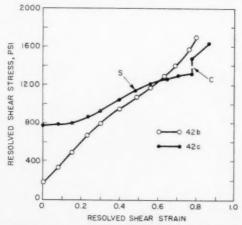


Fig. 6. Resolved shear stress vs. resolved shear strain curves of crystals nos. 42c (furnace-cooled) and 42b (quenched).



Fig. 7. Laue back-reflection X-ray photogram of crystal no. 42c (furnace-cooled) at 0.080 shear strain.

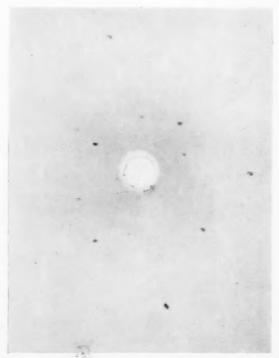


Fig. 8. Laue back-reflection X-ray photogram of crystal no. 42b (quenched) at 0.080 shear strain.

The lower rate of work hardening and the small degree of asterism in Laue photograms indicate a much less turbulent deformation process than is observed in furnace-cooled crystals. In addition to the above, the high stress necessary to nucleate slip, the character of the slip lines, and the presence of overshooting indicate a great similarity in the behavior of quenched aluminum to that of alpha-brass.(10-14) In studying overshooting in alpha-brass crystals Piercy, Cahn and Cottrell(14) concluded that this behavior was typical of metals in which slip lines, formed in the initial stages of deformation, grow more readily than new ones can be nucleated. This has been attributed to the pinning of dislocations. Besides alpha-brass, (24) work-softened aluminum(14,25) experiences this phenomenon. As in alpha-brass, pinning produces a localized latent hardening such that slip on the active system provides a local barrier to slip on an intersecting system. Thus, the barriers formed in the early stages of deformation on the primary system continue to be effective as deformation proceeds. This in turn becomes an over-all latent hardening when the stress axis rotates to the symmetry line. At this point there is an unequal distribution of slip between the primary and conjugate systems, such that the mean free path between the obstructing slip lines of the other system are appreciably longer in the primary slip planes than in the conjugate ones. Therefore, single slip continues on the primary system: i.e., the stress axis overshoots the symmetry line.



Fig. 9. Crystal no. 33a (furnace-cooled) after 5 per cent elongation. $\times 250$.



Fig. 10. Crystal no. 33b (quenched) after 5 per cent elongation.

Though the details of the quenching mechanism are still a matter of discussion, it is generally accepted to involve the pinning of dislocations by quenched-in defects.(1-5) Thus, the behavior of quenched aluminum is considered to be consistent with the above explanation.

ACKNOWLEDGMENTS

The authors wish to thank Drs. D. W. Levinson, W. Rostoker, J. W. Kauffman, and H. Kimura for their helpful discussions during the course of the work.

REFERENCES

- 1. C. H. LI, J. WASHBURN and E. R. PARKER, Trans.
- Amer. Inst. Min. (Metall.) Engrs. 197, 1223 (1953).
 2. R. Maddin and A. H. Cottrell, Phil. Mag. 46, 735 (July 1955).
- 3. M. LEVY and M. METZGER, Phil. Mag. 46, 1021 (Sept. 1955).
- 4. J. W. KAUFFMAN and M. MESHII, Bull. Amer. Phys. Soc., Series II, 2, 3, RA 11, 145 (March 1957).
- 5. A. E. ROSWELL and A. S. NOWICK, Acta Met. 5, 228 (April 1957). 6. R. Maddin, private communication.
- 7. G. I. TAYLOR and C. F. ELAM, Proc. Roy. Soc. 123 (A102),
- 643 (1923). 8. F. von Göler and G. Sachs, Z. Phys. 55, 581 (1929).
- 9. R. KARNOP and G. SACHS, Z. Phys. 41, 116 (1927).
- M. Masima and G. Sachs, Z. Phys. 50, 161 (1927)
- 11. G. Sachs and J. Weerts, Z. Phys. 62, 473 (1930).
- E. OSSWALD, Z. Phys. 83, 55 (1933)
- C. F. Elam, Proc. Roy. Soc. A116, 694 (1927).
- 14. G. R. PIERCY, R. W. CAHN and A. H. COTTRELL, Acta Met. 3, 331 (July 1955)
- 15. E. SCHMID and W. Boas, Crystal Plasticity, pp. 142-3. Hughes, London (1950).
- 16. E. Schmid and W. Boas, Crystal Plasticity, pp. 22-24. Hughes, London (1950).
- 17. G. K. WILLIAMSON and R. E. SMALLMAN, Acta Met. 1, 487 (Sept. 1953).

VOL.

- 6, 305 (1925).
- T. S. Noggle, Rev. Sci. Instr. 24, 184 (1953).
 A. B. Greninger, Trans, Amer. Inst. Min. (Metall.) Engrs. 117, 61 (1935).
 E. Schmid and W. Boas, Crystal Plasticity, p. 59. Hughes,
- London (1950).
- 18. P. W. Bridgman, Proc. Amer. Acad. Arts and Sci. 60, 22. E. Schmid and W. Boas, Crystal Plasticity, p. 105. Hughes, London (1950).

 - T. H. Blewitt, Phys. Rev. 91, 1115 (1953).
 G. W. Ardley and A. H. Cottrell, Proc. Roy. Soc. A219, 328 (1953).
 - 25. R. J. STOKES and A. H. COTTRELL, Acta Met. 2, 341 (March 1954).

QUENCHING OF IMPERFECTIONS IN ALUMINUM*

W. DeSORBO and D. TURNBULL+

The formation and annealing-out of point defects in high purity aluminum was investigated resistometrically. E_f , the energy of formation of the defects, was found to be $0.79\pm0.04~{
m eV}$. The annealing behavior is complex but the temperature variation is well described by an activation energy for the motion of defects, $E_{\rm m}=0.52\pm0.04$ eV. This is near the activation energy for the clustering of solute atoms at low temperature in aluminum-rich Al-Cu and Al-Ag alloys.

TREMPE DES IMPERFECTIONS DANS L'ALUMINIUM

Les auteurs ont étudié, par mesure de la résistivité électrique, la formation ainsi que l'annulation par recuit des défauts ponetuels dans l'aluminium de haute pureté. Ils ont trouvé que l'énergie de formation des défauts était $E_t = 0.79 \pm 0.04 \, \mathrm{eV}$.

Le comportement au recuit est complexe, mais la variation de température est en accord avec une énergie d'activation pour le mouvement des défauts, $E_m=0.52\pm0.04\,\mathrm{eV}$. Cette valeur est proche de l'énergie d'activation pour la formation à basse température d'amas d'atomes dissous dans les alliages Al-Cu et Al-Ag riches en aluminium.

ABSCHRECKEN VON GITTERFEHLERN IN ALUMINIUM.

Mit Hilfe von Widerstandsmessungen wurde Bildung und Erholung von punktförmigen Fehlstellen in Reinst-Aluminium untersucht. Für die Bildungsenergie E_t der Fehlstellen wurden $0.79\,\pm\,0.04$ eV gefunden. Das Verhalten bei Erholung ist unübersichtlich, aber die Änderung mit der Temperatur lässt sich gut durch eine Wanderungsenergie der Fehlstellen beschreiben, $E_\pi=0.52\,\pm\,0.04$ eV. Das entspricht etwa der Aktivierungsenergie für die Zusammenlagerung der gelösten Atome in aluminiumreichen Al-Cu und Al-Ag Legierungen bei tiefer Temperatur.

Recently several investigations concerning quenching of imperfections in aluminum by resistometric techniques have been reported.(1.2.3.4) The increase in resistivity, $\Delta \rho_o$, immediately after quench, is describable by the equation:

$$\Delta \rho_o = A \exp\left(-E_f/kT_O\right) \tag{1}$$

where A is a constant, T_Q the absolute temperature before quench and E_f is considered to be the energy of formation of defects responsible for the resistivity increase. Bradshaw and Pearson⁽²⁾ reported $E_t = 0.76$ \pm 0.04 eV and $A=1240, \ddagger$ Federighi and Gatto⁽⁴⁾ obtain a value of 0.74 ± 0.03 eV.

Our measurements⁽³⁾ give a value of 0.79 ± 0.04 eV and A = 3055.* The specimens, consisting of wires (6-9 ft length) and prepared from zone-refined§ aluminum were mounted, non-inductively and strain free, on a thin mica cross 2 in. high and about 1 in. cross section. The assembly was heated in a furnace and, by a plunger technique, quenched into an alcoholwater mixture at -50° C. The temperature, T_{o} ,

before quench varied from 260 to 330°C. Rapid cooling from these lower values of T_Q seems to result in the introduction of fewer extraneous structural or chemical impurities. This is indicated by the complete recoverability of the excess resistivity upon quenching from these temperatures. The resistivity measurements were all made at 20.000 + 0.002°K in order to obtain high sensitivity. That is, at this lower temperature there is a relative enhancement of the resistivity component due to the 'quenched-in' imperfections in their disturbance of the periodicity of the lattice over that caused by the thermal motion of the lattice.

In Fig. 1 is shown a plot of the logarithm of the resistivity component, $\Delta \rho_o$, due to the 'quenched-in' imperfections, as a function of reciprocal T_Q . Below 330°C the results are described by equation (1). In each point determination, $\Delta \rho_o$ completely disappears upon isothermal holds at 273 or 300°K—a result in agreement with that of Wintenberger (5) reported for slower air quenches.

The activation energy for motion, E_m , of the defects may be evaluated from annealing experiments carried out isothermally, Some typical isothermal annealing curves at 0 and 22°C are presented in Fig. 2(a) where $\Delta \rho / \Delta \rho_o$, the fractional part of 'quenched-in' resistance remaining at time t, is plotted against time. The shape of the isotherms is rather complex. In the initial stages it is best described by a second-order rate

^{*} Received April 21, 1958

[†] General Electric Research Laboratory, Schenectady, New York.

[‡] When $\Delta \rho_o$ is expressed in μ -ohm cm. § Spectroscopic analysis by L. Bronk revealed: 'trace' of Cu, but not detected were Fe, Pb, Sn, Mg, Si, Bi, Ag, Pt, Ni, Co,

Mn, Zn, In, Ca, Sb, Ti, Li, Tl.

¶ To study the effect of geometry of wire assembly on quenching rates, we also tested shorter wire specimens again arranged noninductively but in a flat horizontal helix (Table 1).

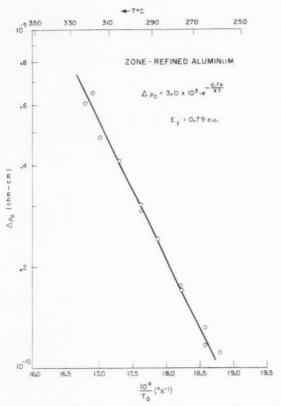


Fig. 1. Logarithm of the resistivity component, $\Delta \rho_o$, due to the 'quenched-in' imperfections, as a function of reciprocal temperature, T_Q , immediately before quench.

equation but in the later stages of annealing there are deviations from this. However, within experimental error the different isotherms could be superimposed completely if operated on by suitable time scale factors. Thus E_m apparently is independent

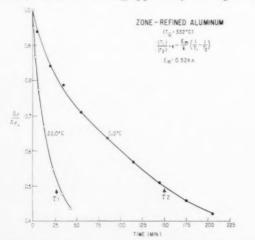


Fig. 2(a). Annealing behavior of the fractional part of 'quenched-in' resistance remaining at time t, plotted as a function of time.

of the extent of the reaction. Fig. 2(b) shows the agreement of the data at two temperatures with the second-order rate law. Table 1 summarizes the activation energy for motion, E_m , obtained for different wire specimens by substitution of the 'half-time' of the anneal in the simple rate equation. These values of activation energy for defect motion are in good agreement with the average value of $E_m \simeq 0.52$ eV obtained by evaluating the ratio of the slopes of $\ln{(\Delta \rho/\Delta \rho_o)}$ vs. t at identical concentration (Fig. 3). Bradshaw and Pearson'(2) report $E_m = 0.44 \pm 0.03$ eV for specimens quenched from higher temperatures. For the lower (and also small) temperature interval of T_Q reported here, E_m is approximately constant* and independent of T_Q .

It has been pointed out that these E_m values are similar to the activation energy for low temperature clustering in Al–Cu⁽⁶⁾ and Al–Ag.⁽⁷⁾ A discussion on the possible influence of quenched-in vacancies on the rate of clustering of solute atoms in Al-base alloys has been given.⁽⁸⁾ Similar conclusions arrived at independently by Federighi⁽⁹⁾ have since come to our attention.

More recently we have conducted some experiments on the change in length (l) of aluminum wires during the isothermal anneal of quenched-in imperfections. The preliminary results indicate that \mathcal{T} decreases

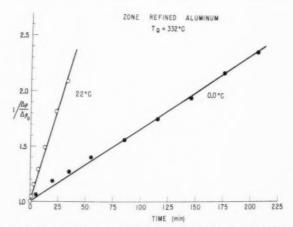


Fig. 2(b). Annealing data and a second-order kinetic relationship.

^{*} Reference 3 referred to a preliminary value of activation energy for defect motion in Al as 0.37 eV, which value had been obtained in quench from a higher temperature (500°C) and effectively air quenched in manually transferring the sample from the furnace to a dry ice–acetone mixture. Subsequent experiments in quenching from these higher temperatures, where, with our plunger technique, we are not retaining all the imperfections generated, also tend to lead to lower E_m values. The range of values thus obtained are similar to a range of E_m values (0.25–0.5 eV) reported by Federighi and Gatto (4).

Table 1. Activation energy for annealing of imperfections in aluminum

Specimen	Diameter (in.)	T_Q (°C)	$T_{ m annealed}$ (°C)	$\frac{E_m}{(\mathrm{eV})}$
1 (V)*	0.020	275.5 275.5	$\begin{array}{c} 0.0_{\scriptscriptstyle{0}} \\ 22.4_{\scriptscriptstyle{0}} \end{array}$	0.51
2 (V)	0.020	331.7	0.0_{0}	0.53
3 (H)†	0.020	331.7 331.7	$\frac{22.0_{0}}{0.0_{0}}$	0.52
		331.7	22.0_{0}	
4 (V)	0.010	$332.0 \\ 332.0$	$\begin{array}{c} 0.0_{\scriptscriptstyle 0} \\ 22.0_{\scriptscriptstyle 0} \end{array}$	0.55
5 (H)	0.010	332.0	$0.0_{\scriptscriptstyle 0}$	0.55
6 (H)	0.0075	$332.0 \\ 332.0$	22.00	0.51
0 (II)	0.0075	332.0	$\begin{array}{c} 0.0_{\mathfrak{g}} \\ 22.0_{\mathfrak{g}} \end{array}$	0.01
7 (V)	0.0075	$\frac{332.0}{332.0}$	$0.0^{\circ}_{22.0_{0}}$	0.52

(V)* 6-9 ft of wire wound non-inductively around a thin mica cross, diameter 1 in. vertical height of spiral ~2 in. (H)† 15-18 in. of wire wound non-inductively in a horizontal

helix, ∼l in. diameter.

1959

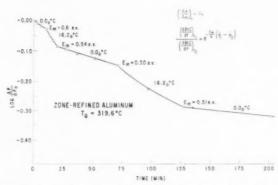


Fig. 3. Activation energy of motion of 'quenched-in' defects determined from the ratio of slopes of log $\Delta \rho / \Delta \rho_o$ vs. t at identical concentrations.

during annealing in agreement with some earlier work of Takamura.(10)

As yet we have no clear explanation for the shape of the annealing isotherm. If the annealing process consisted simply in the movement of unassociated defects to dislocations and their annihilation there, first-order kinetics would be expected. (11) Therefore, we can perhaps only conclude that the activation energy for motion of unassociated defects equals or exceeds 0.52 eV and that the activation energy for self-diffusion in aluminium,

$$Q=E_{\rm f}+E_{\rm m}\geqslant 1.3\pm 0.08~{\rm eV}$$

This is a fair agreement with $Q=1.4\pm0.1\,\mathrm{eV}$ obtained by Spokas(12) from nuclear magnetic resonance measurements and Nowick's (13) estimate of 1.43 + 0.09 eV.

The authors thank G. E. Nichols for his assistance in the experimental work.

REFERENCES

- I. C. Panseri, F. Gatto and T. Federighi, Acta Met. 5, 50
- 2. F. J. Bradshaw and S. Pearson, Phil. Mag. 2, 570 (1957). W. DeSorbo and D. Turnbull, Bull. Amer. Phys. Soc.
- II 2, 262 (1957) F. Federighi and F. Gatto, La Tempra Delle Vacanze Reticolari Nell'Alluminio, Presented at the XLIII Congress of the Italian Physical Society, Padova (Sept. 23,
- W. WINTENBERGER, C.R. Acad. Sci., Paris 242, 128 (1956).
- D. TURNBULL and H. N. TREAFTIS, Bull. Amer. Phys. Soc. 1, 334 (1956).
- D. TURNBULL and H. N. TREAFTIS, Acta Met. 5, 534 (1957).
- W. DESORBO, H. N. TREAFTIS and D. TURNBULL, Acta Met. 6, 401 (1958).

- F. Federighi, private communication.
 J. Takamura, Metal Phys. 2, (3), 112 (1956).
 J. S. Koehler, F. Seitz and J. E. Bauerle, Phys. Rev. 107, (6), 1499 (1957)
- J. SPOKAS, Thesis, University of Illinois (1957) unpub-
- 13. A. S. Nowick, J. Appl. Phys. 22, 1182 (1951).

SELF AND INTERDIFFUSION IN ALUMINUM-ZINC ALLOYS†

J. E. HILLIARD, B. L. AVERBACH§ and MORRIS COHEN§

The self-diffusion rates of radioactive Zn^{65} and the interdiffusion rates have been determined in f.c.c. aluminum—zinc alloys. The self-diffusivity of zinc D_{Zn^*} increases as the zinc content is increased, while the thermodynamic driving force decreases with increasing zinc content until a minimum is reached at about 38 at. $^{0}_{0}$ Zn, just above the miscibility gap. As a result of these two opposing trends, the interdiffusion coefficient \tilde{D} changes only slightly with variation in composition. The values of \tilde{D} follow the relationship: $\tilde{D} = X_{\rm Al}D_{\rm Zn}^*(1+d\ln f_{\rm Zn}/dl\ln X_{\rm Zn})$, where $X_{\rm Al}$ and $X_{\rm Zn}$ are the respective atomic fractions, and $f_{\rm Zn}$ is the thermodynamic activity coefficient of zinc. The lack of an observable contribution of $D_{\rm Al}^*$ to the interdiffusion coefficient indicates that the self-diffusivity of aluminum is considerably smaller than that of zinc over the ranges of temperature and composition studied.

AUTO ET INTER-DIFFUSION DANS LES ALLIAGES ALUMINIUM-ZINC

Les vitesses d'auto-diffusion de l'isotope Zn^{65} et les vitesses d'interdiffusion ont été déterminées dans des alliages de zinc-aluminium cubique f.c.

L'autodiffusibilité du zinc $D_{\rm zinc}$ augmente quand le pourcentage de zinc s'accroît, tandis que la force de déplacement décroît avec l'augmentation du pourcentage de zinc jusqu'à un minimum d'environ 38% at, juste au-dessus de la lacune de miscibilité.

Il résulte de ces deux tendances opposées que le coefficient d'interdiffusion \tilde{D} change seulement faiblement avec la variation de la composition. Les valeurs de \tilde{D} suivent la relation $\tilde{D} = X_{A1}D_{\rm Zn}$ (1 + $d \ln f_{\rm Zn}/dl$. $\ln X_{\rm Zn}$) où $X_{\rm A1}$ et $X_{\rm Zn}$ sont les fractions atomiques respectives et $f_{\rm Zn}$ est le coefficient d'activité thermodynamique du zinc. L'absence d'une contribution observable du $P_{\rm A1}$ au coefficient d'interdiffusion indique que l'auto-diffusion de l'aluminium est considérablement plus faible que celle du zinc, pour la gamme de température et de composition étudiée.

SELBST- UND INTERDIFFUSION IN ALUMINIUM-ZINK-LEGIERUNGEN.

In kubisch flächenzentrierten Aluminium-Zink-Legierungen wurden die Selbstdiffusionsgeschwindigkeiten von radioaktivem Zn. die Interdiffusionsgeschwindigkeiten bestimmt. Der Selbstdiffusionskoeffizient von Zink $D_{\rm Zn}^*$ nimmt mit steigendem Zinkgehalt zu, während die thermodynamische treibende Kraft mit steigendem Zinkgehalt abnimmt und bei etwa 38 at. O_0^* Zn, der Konzentration der Mischungslücke, ein Minimum erreicht. Der Interdiffusionskoeffizient \tilde{D} ändert sich infolge dieser gegenläufigen Einflüsse bei Veränderung der Zusammensetzung nur wenig. Die Werte von \tilde{D} folgen der Beziehung: $\tilde{D} = X_{\rm Al} D_{\rm Zn}^*$ ($1 + d \ln f_{\rm Zn}/dl \ln X_{\rm Zn}$), wobei $X_{\rm Al}$ und $X_{\rm Al}$ die jeweiligen Atomkonzentrationen sind und $f_{\rm Zn}$ der thermodynamische Aktivitätskoeffizient von Zink ist. $D_{\rm Al}^*$ trägt nicht in beobachtbarem Mass zum Interdiffusionskoeffizienten bei. Dies zeigt, dass der Selbstdiffusionskoeffizient von Aluminium in dem untersuchten Temperatur- und Konzentrationsbereich beträchtlich kleiner ist als der von Zink.

1. INTRODUCTION

The self-diffusion of zinc and the interdiffusion coefficients in aluminum-zinc alloys have been measured as a first step in a study of the effects of plastic deformation on diffusion in these alloys. In addition, it had been hoped that the aluminum self-diffusivities could be derived from a combination of these data and the previously measured thermodynamic activities⁽¹⁾ through the Darken equation⁽²⁾ which had been verified experimentally for the gold-nickel system.⁽³⁾ Unfortunately, the self-diffusivity of zinc was so much greater than that of aluminum for the

temperatures and compositions investigated that the interdiffusion coefficient was fixed almost completely by the zinc self-diffusivity and the thermodynamic driving force. Although the self-diffusivity of aluminum cannot be determined from the data, these findings do serve as another experimental verification of the Darken equation.

2. EXPERIMENTAL PROCEDURE

a. Self-diffusion

Alloys containing 16.7, 36.9, 49.4 and 62.9 at. % zinc were melted and chill east under a blanket of dried argon. The resulting billets were extruded to \$\frac{5}{8}\$ in. diameter rods. Lower zinc alloys, 4.3 and 9.2 at. %, were obtained as rods. Specimens were

[†] This work was sponsored by the Aeronautical Research Laboratory, Wright Air Development Center under Contract No. AF 33(616)–3264 at the Massachusetts Institute of Technology, Cambridge, Massachusetts. Received April 30, 1958.

^{*} Present address: General Electric Research Laboratory, Schenectady, New York.

[§] Department of Metallurgy, Massachusetts Institute of Technology.

 $[\]parallel$ 99.99+ Al, Aluminum Company of America and 99.999+ Zn, New Jersey Zinc Company. $_{\pm}$

[¶] Provided by Prof. N. J. Grant (MIT) from rods produced by the Aluminum Company of America.

examined for segregation and other defects, and then homogenized for several days at temperatures within a few degrees of the melting points. Discs $\frac{1}{2}$ in, diameter by $\frac{3}{8}$ in, thick were machined from the annealed alloys, and similar specimens were hot pressed from the pure metals. The end faces were surface ground or milled and then lapped to a flatness of 1 μ on a glass plate. The final grain size was of the order of 2 mm or larger.

About 1 μc of Zn⁶⁵ (corresponding to a layer thickness of approximately 5×10^{-5} cm) was deposited electrolytically on the ground face of each specimen from a bath prepared by adding 10 mc of Zn⁶⁵ to 50 ml of the following solution: 108 g ZnSO₄·7H₂O, 9 ml of 48% HF, and water to make 250 ml.⁽⁴⁾ Good electrodeposits were obtained at a

Table 1. Self-diffusion coefficient of zinc in aluminum-zinc alloys

At. o Zn	Temperature (°C)	$\begin{array}{c} \text{Diffusion time, } t \\ (10^4 \text{ sec}) \end{array}$	D^* (cm ² /sec)
0.00	654	1.44	6.87 × 10-
0.00	650	3.04	$5.34 \times 10^{-}$
0.00	650	2.16	
0.00	610	2.88	2.58×10^{-1}
0.00	579	8.64	$1.29 \times 10^{-}$
0.00	525	4.32	3.85×10^{-1}
0.00	510	7.14	$3.10 \times 10^{-}$
0.00	450	17.6	5.99×10^{-1}
0.00	405	75.2	$1.47 \times 10^{-}$
4.33	610	2.88	3.95×10^{-1}
4.33	570	2.88	$1.41 \times 10^{-}$
4.33	510	7.14	4.41×10^{-1}
4.33	450	17.6	$9.72 \times 10^{-}$
4.33	405	77.5	$2.53 imes 10^{-1}$
4.33	360	207.4	6.13×10^{-1}
9.23	575	2.70	$2.45 \times 10^{-}$
9.23	525	4.32	$6.87 \times 10^{-}$
9.23	510	7.14	$6.88 \times 10^{-}$
9.23	450	17.6	$1.45 \times 10^{-}$
9.23	405	77.5	$3.63 \times 10^{-}$
9.23	360	207.4	$1.06 \times 10^{-}$
16.7	525	4.32	$1.42 \times 10^{-}$
16.7	510	10.9	$1.12 \times 10^{-}$
16.7	450	17.4	$3.01 \times 10^{-}$
16.7	405	77.5	$7.76 \times 10^{-}$
16.7	360	172.7	$2.42 \times 10^{-}$
36.9	450	17.4	8.53 × 10-
36.9	440	8.91	$6.28 \times 10^{-}$
36.9	405	51.1	2.55×10^{-1}
36.9	380	43.2	1.44×10^{-1}
36.9	360	172.7	7.34×10^{-1}
49.4	440	8.58	9.29×10^{-1}
49.4	405	51.1	3.81×10^{-1}
49.4	380	43.2	2.16×10^{-1}
49.4	360	172.7	1.29×10^{-1}
49.4	325†	95.1	
62.9			
62.9	405	51.1	4.26×10^{-1}
	380	43.2	2.47×10^{-9}
62.9 62.9	360	78.1	1.48×10^{-6}
	325†	103.4	4.28×10^{-1}
100	405	51.1	7.71×10^{-9}
100	380	26.0	4.05×10^{-6}
100	360	78.1	2.82×10^{-9}
100	325	103.4	9.78×10^{-1}

1959

current density of about 50 mA per cm² with a platinum wire anode. Immediately prior to plating, the specimens were cleaned by gentle rubbing on a wet filter paper charged with detergent and fine alumina, and this was followed by successive quick dips in 30% HNO₃ and in dilute HF.

The gamma activities were measured with a scintillation counter, and the specimens were then sealed off in individual Vycor tubes under a partial pressure of argon. Diffusion anneals were carried out by placing the tubes in cylindrical aluminum or steel blocks in horizontal muffle furnaces controlled at the winding to 1°C. The position of each block in the furnace was adjusted so that there was no difference between the readings of two thermocouples placed 3.5 in. apart inside the block. Measurements of total activity before and after annealing indicated that the average loss of zinc by volatilization was less than 1 %.

About 0.02 in, was removed from the circumference of each diffused specimen, and twelve parallel sections of equal thickness were machined from the radioactive face. The section thickness for different specimens varied from 0.001 to 0.006 in, and the thickness of each section was checked by weight measurements. The relative gamma activity of each section was measured by means of a scintillation counter using a thallium activated sodium iodide well-type detector. The overall resolving time of the system was measured at 5.4 $\mu{\rm sec}$. The counting loss of the system was 0.9 percent per 100,000 epm and the sensitivity 20,000 epm for 0.1 $\mu{\rm c}$ of Zn⁶⁵ with a background of 650 epm.

The values of D^* were evaluated from the equation:

$$C = C_0/(4\pi D^*t)^{1/2} \exp(-y^2/4Dt) \tag{1}$$

where: $D^* = \text{self-diffusion coefficient}$.

C= concentration of tracer element (proportional to the specific activity) at a distance y from the surface after a time t

 $C_0 = \text{initial quantity of tracer element per}$ unit area.

 D^* was calculated in the usual manner from the slope of a plot of $\log c$ vs. y^2 , with the penetration depth y being taken as the distance to the midplane of the section. Good straight lines were obtained in all cases. The measured values of $D_{\rm Zn}^*$ are listed in Table 1 and the temperature dependence is shown in Table 2. The activation energies $Q_{\rm Zn}^*$ and the frequency factors $D_{o,{\rm Zn}}^*$ were calculated from a least-squares analysis of the self-diffusivities, and the dependence

[†] These temperatures are in a two-phase region.

VOI 7 19

Table 2. Activation energies and frequency factors for self-diffusion of zine in aluminum-zine alloys

At. % Zn	Q^* (kcal/mole)	D_0^* $(\mathrm{cm^2/sec})$
0.00	30.9 - 0.6	1.1 ± 0.4
4.33	28.3 ± 0.7	$(3.5 \pm 1.6) \times 10^{-1}$
9.23	27.0 ± 1.0	$(2.0 \pm 1.4) \times 10^{-1}$
16.7	25.0 ± 1.1	$(1.0 \pm 0.5) \times 10^{-1}$
36.9	24.1 + 0.9	$(1.6 \pm 0.9) \times 10^{-1}$
49.4	21.9 + 1.0	$(4.8 \pm 3.1) \times 10^{-3}$
62.9	20.0 ± 0.9	$(1.2 \pm 0.7) \times 10^{-5}$
100.0	$20.5 \ \widetilde{+} \ 1.8$	$(3.1 \pm 4.5) \times 10^{-3}$

of these quantities on composition are shown in Figs. 1 and 2. The vertical bars indicate the probable errors.

b. Interdiffusion

Interdiffusion couples were prepared by extrusion,† with the following analyzed compositions in at. %: 0.0–9.0, 9.1–18.1, 18.2–37.1, 37.6–48.5 and 48.5–72.0. The alloy billet forming the zinc-rich side of the couple was machined to a cylinder 5 in. long \times 1 $\frac{3}{4}$ in. diameter and inserted in a well of the same size drilled from the center of a 6 in. long \times 3 $\frac{1}{2}$ in. diameter billet of the second alloy. The two billets were then extruded together at 100°C through a 1 \times $\frac{1}{2}$ in. rectangular die to form a bar containing a zinc-rich core having the shape of a flattened ellipse of $\frac{1}{4}$ \times $\frac{5}{8}$ in. cross-section. There was negligible diffusion across the interface during the extrusion. Porosity was detected in the two bars containing 37.6–48.5 and

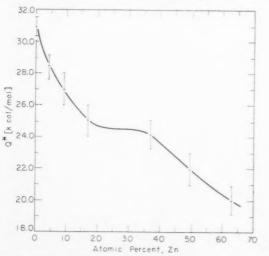


Fig. 1. Activation energy Q* for self-diffusion of zinc in aluminum-zinc alloys.

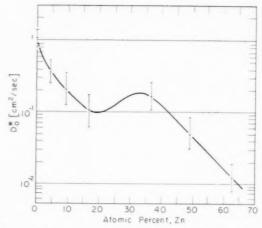


Fig. 2. Frequency factor D_0^* for self-diffusion of zinc in aluminum-zinc alloys.

48.5--62.0 at. $^{0/}_{0}$ zine, and all of these data were discarded.

A strip with a $\frac{1}{4} \times \frac{1}{2}$ in. cross-section arranged so that there was a $\frac{1}{4}$ in. layer of the zinc-rich alloy sandwiched between two $\frac{1}{8}$ in. thick layers of the other alloy was machined from each extruded bar. This strip was cut into $\frac{1}{2}$ in. lengths which were then sealed in individual Vycor tubes under a partial pressure of argon. The Vycor tubes were placed in stainless steel or aluminum cylinders, and the diffusion anneals were carried out for periods of one day to five weeks.

The penetration curves were determined by an X-ray absorption method described by Ogilvie. (6) A section 0.02–0.04 in. thick was cut normal to the diffusion interface and parallel to the diffusion direction. The surfaces of the section were ground, and in some cases hand lapped to keep the faces parallel to within 0.0001 in. The specimen was then lightly etched in HF vapor to reveal the diffusion zone.

The diffusion specimen was placed at the receiving slit of a Geiger counter spectrometer that was arranged to diffract $MoK\alpha$ radiation from a plane silicon crystal cut to the (111) face. The specimen was traversed past the receiving slit, which was normally set at a width of 0.001 in. and a height of 0.275 in. by means of a micrometer screw graduated to 0.0001 in. The intensity I of the beam transmitted by a two component phase is given by:

$$\ln I = \ln I_0 - L\rho_{(A+B)} [w_A(\mu/\rho)_A + w_B(\mu/\rho)_B]$$
 (2)

where I_0 is the incident intensity, L the specimen thickness, w the weight fraction, μ the linear absorption coefficient and ρ the density. If it is assumed that $\rho_{(A+B)} = X_A \rho_A + X_B \rho_B$ and that the densities of

[†] The authors are grateful to Dr. Paul Lowenstein of Nuclear Metals, Inc., Cambridge, Mass. for suggesting and carrying out this procedure.

A and B are in the same ratio as their atomic weights, then equation (2) becomes:

$$\ln I = \ln I_0 - L(X_A \mu_A + X_B \mu_B) \tag{3}$$

Because of the restricted composition range of the couples, the foregoing assumptions introduce an absolute error of less than 0.4 per cent in the determination of the composition. Thus, the composition parameter, $X'=(X-X_1)/(X_2-X_1)$, which appears in the solution of the diffusion equation can be replaced by the parameter,

$$I' = (\ln I - \ln I_1)/(\ln I_2 - \ln I_1),$$

where X is the atomic fraction at distance y, X_1 and X_2 are the terminal compositions of the couple, and I, I_1 and I_2 are the corresponding intensities.

The observed intensities were corrected experimentally for Geiger tube counting losses, and I' was plotted vs. y on probability paper. If \tilde{D} is independent of composition such a plot should give a straight line for the appropriate solution of Fick's Law which has the form

$$X' = \frac{1}{2}[1 - \text{erf}[y/2(\tilde{D}t)^{1/2}]$$
 (4)

where erf
$$(u) = \frac{2}{\sqrt{\pi}} \int_{o}^{u} \exp(-z^2) dz$$

1959

Some of the couples yielded straight line plots on probability paper and a single value of \tilde{D} was calculated from the slope. However, the remaining couples gave two approximately linear branches of slightly different slope as shown in Fig. 3.

A mathematical analysis of plots of this type has been reported by Hall⁽⁸⁾ who derived the following expression:

$$D(X) = \frac{1}{4h^2} + \frac{k\pi^{1/2}}{2h^2} \exp{(h\lambda + k)^2} \operatorname{erfc}{(h\lambda + k)}$$
 (5)

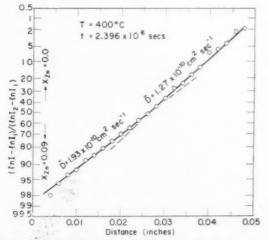


Fig. 3. Probability plot of $(\ln I - \ln I_1)/(\ln I_2 - \ln I_1)$ for 0–9.1 at. % zinc couple.

in which h is the slope of one of the linear segments of a plot of X' vs. $y/t^{1/2}$, k is the value of the composition function at the intercept of this linear segment (or its extrapolation) with the Matano interface, $\lambda = y/t^{1/2}$, and erfe $u = \pi^{-1/2} \int_0^{\sigma} \exp(-z^2) dz$. This

expression is valid only over the linear portions of the probability plot, and for this reason Hall intended it to be used as a supplement to the regular Matano analysis. However, for most of these couples the variation in \tilde{D} was of the same order as the computational error in the graphical Matano method. Accordingly, it was considered satisfactory to determine only the terminal values, which could be obtained directly from the probability plot since as y approaches $-\infty$:

$$\begin{split} \tilde{D}(X_1) &= 1/4 h_{X_1}^{}{}^2 \\ \tilde{D}(X_2) &= 1/4 h_{X_2}^{}{}^2 \end{split}$$
 and

where h_{X_1} and h_{X_2} are the slopes of the linear branches of the plot in the composition regions denoted by the subscripts. Interdiffusion coefficients calculated in this manner are listed in Table 3. Where duplicate runs were made, both values are tabulated.

3. DISCUSSION

Darken⁽²⁾ has proposed the following relationship for a binary system:

$$\begin{split} \tilde{D}(X) &= (X_A D_B * + X_B D_A *) (1 + d \ln f_A / d \ln X_A) \\ &= (X_A D_B * + X_B D_A *) m \end{split} \tag{6}$$

in which X_A , X_B are the atomic fractions, D_A^* , D_B^* the self-diffusivities and f_A the activity coefficient, with the subscripts referring to the components. The thermodynamic factor m has been calculated from the unsmoothed thermodynamic data⁽¹⁾ and is plotted as a function of composition in Fig. 4. The obvious method of computing this factor by graphical differentiation of an activity coefficient plot is unsatisfactory because of the large errors introduced. The following procedure was therefore adopted. From well-known thermodynamic relationships:

$$\begin{split} RT & (d \ln f_A/d \ln X_A) = X_A (1 - X_A) \\ & \times \left\{ (1 - X_A) \frac{d}{dX_A} \left[F_A{}^E/(1 - X_A)^2 \right] \right. \\ & \left. - 2 F_A{}^E/(1 - X_A)^2 \right\} \end{split} \tag{7}$$

in which $F_A{}^B$ is the partial molar excess free energy of component A. Though this expression is seemingly complicated, it has two advantages. First, the variation of $F_A{}^B/(1-X_A)^2$ with composition is usually small and approximately linear for many systems;

Table 3. Interdiffusion coefficients in aluminum-zine alloys (cm² sec⁻¹)

Temp.	Atomic ^o , Zinc							
	0.0	9.0	9.1	18.1	18.2	37.6		
540	$6.12 imes 10^{-9} \ 6.08 imes 10^{-9}$	$6.12 imes 10^{-9} \ 6.08 imes 10^{-9}$	_	_	_	_		
485	1.49×10^{-9}	1.74×10^{-9}	$\begin{array}{c} 2.21 \times 10^{-9} \\ 2.03 \times 10^{-9} \end{array}$	$\begin{array}{c} 2.21 \times 10^{-9} \\ 2.03 \times 10^{-9} \end{array}$	-	-		
440	$4.92 imes 10^{-10}$	$6.96 imes 10^{-10}$	6.92×10^{-10}	$7.48 imes 10^{-10}$	7.08×10^{-10}	5.11 × 10 ⁻¹		
400	1.27×10^{-1}	1.93×10^{-10}	$2.15 \times 10^{-10} \ 1.97 \times 10^{-10} \ 2.37 \times 10^{-10}$	$egin{array}{l} 2.15 imes 10^{-10} \ 1.97 imes 10^{-10} \ 1.88 imes 10^{-10} \end{array}$	_	-		
360	$3.48 \times 10^{-11} \ 4.49 \times 10^{-11}$	$\begin{array}{c} 5.22 \times 10^{-11} \\ 4.49 \times 10^{-11} \end{array}$	$6.12 imes 10^{-11}$	6.12×10^{-11}	6.66×10^{-11}	1.10×10^{-1}		
330	$1.92 \times 10^{-11} \\ 1.76 \times 10^{-11}$	$1.92 imes 10^{-11} \ 1.99 imes 10^{-11}$	3.64×10^{-11}	3.64×10^{-11}	_	_		

hence its derivative can be accurately estimated. Secondly, if (as is the case with aluminum–zinc alloys) the configurational entropy is approximately ideal then, to the same degree, $F_{\mathcal{A}}^{E}$ is temperature independent so that the right-hand side of equation (7) is a function only of composition.

Because of the positive deviation from ideality in these alloys, the thermodynamic factor m is less than unity over the whole alpha solid-solution region. The minimum value occurs at $X_{\rm Zn}=0.375$ corresponding to the top of the miscibility gap.

If we assume that the self-diffusivities can be expressed in the form: $D_o^* \exp(-Q^*/RT)$ where the

0.9 0.8 0.7 m = (1+d Infzn/d In Xzn) 0.6 0.5 0.4 0.3 0.2 0.1 0 0.2 0.3 0.4 0.5 0.6 Xzn

Fig. 4. Thermodynamic factor (1 $+ d \ln f_{\rm Zn}/d \ln X_{\rm Zn}$) for aluminum-zinc alloys.

frequency factor D_0^* and the activation energy Q are constants for a given composition, then equation (6) can be written:

$$\tilde{D} = m[X_A D_{0,B}^* \exp(-Q_B^*/RT) + X_B D_{0,A}^* \exp(-Q_A^*/RT)]$$
(8)

An analysis^(3a) of this equation shows that a plot of $\ln D \text{ vs. } 1/T$ will not necessarily be linear, and that its instantaneous slope is given by:⁽³⁾

$$\begin{split} d\; (\ln\,\tilde{D})/d(1/T) &= -pQ_A */R - (1-p)Q_B */R \\ &+ T(m-1)/m \quad [\text{for } S^E = 0] \quad (9) \end{split}$$

in which

$$p = 1/(1 + X_A D_B^* / X_B D_A^*)$$

The required condition that the excess configurational entropy S^E should be nil is satisfied by aluminum—zine alloys⁽¹⁾ within the accuracy necessary for the present purposes.

It can be demonstrated that deviations from linearity in the $\ln \bar{D}$ vs. 1/T plot may be particularly pronounced in alloys, such as those of aluminumzinc, for which m < 1. To obviate this difficulty the procedure of plotting the measurements in the form of $\ln (\bar{D}/m) = \ln (X_A D_B^* + X_B D_A^*)$ vs. 1/T was adopted (Fig. 5). The first two terms on the right-hand side of equation (9) should have a negligible temperature dependence and the plots in Fig. 5 should thus be linear.

For the diffusivities in the pure components, equation (6) predicts $\tilde{D}(X_{\rm Zn}=0)=D_{\rm Zn}\,(X_{\rm Zn}=0)$. It will be seen from Fig. 5 that, except for the low-temperature points, the observed values of $\tilde{D}(X_{\rm Zn}=0)$ are in fact adequately fitted by the line previously

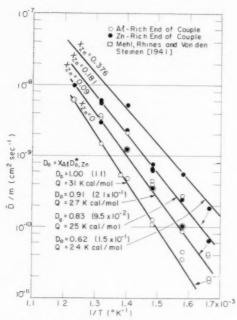


Fig. 5. \widetilde{D}/m vs. 1/T for aluminum-zinc alloys. $m = 1 + d \ln f z_0/d \ln X z_0$

determined for the self-diffusion of zinc in pure aluminum. The abnormally high values of \tilde{D} at 330° and 360°C may be caused by the contribution of grain-boundary diffusion at these low temperatures. Values of \tilde{D} obtained from an extrapolation to $X_{\rm Zn}=0$ of measurements at 400° and 449°C by Mehl et al. (10) are in good agreement with these data. Earlier results obtained by Beerwald (11) from incremental couples between pure aluminum and a 0.84 at. % zinc alloy display considerable scatter and, on the average, are about 15 percent lower than the data obtained here. This discrepancy may be due to the fact that Beerwald's couples were not welded but merely held together under pressure during the diffusion anneal.

1959

At compositions other than $X_{\rm Zn}=0$, a contribution to \bar{D} is to be expected from the self-diffusion of aluminum since, according to equation (6), $\bar{D}/m=X_{\rm Al}D_{\rm Zn}^*+X_{\rm Zn}D_{\rm Al}^*$. However, as indicated by the lines drawn for $X_{\rm Zn}=0.09,~0.181,~{\rm and}~0.376,~{\rm the}$ results can be quite adequately accounted for by the single term $X_{\rm Al}D_{\rm Zn}^*$. This correlation is further demonstrated by the compositional variation at 440°C depicted in Fig. 6. The lower curve is for the observed values of \bar{D} which, it will be noted, are approximately independent of composition; the upper series of points are for \bar{D}/m and the dotted curve represents $(X_{\rm Al}D_{\rm Zn}^*)$.

The observation that D/m is apparently identical

in value to $X_{\rm Al}D_{\rm Zn}^*$ implies that, over the composition and temperature range of the measurements, $X_{\rm Zn}D_{\rm Al}^* \ll X_{\rm Al}D_{\rm Zn}^*$ and therefore that $D_{\rm Al} < D_{\rm Zn}^*$. In other words, the self-diffusivity of aluminum is not a rate-determining factor for interdiffusion in aluminum–zinc alloys.

A conventional measurement of the self-diffusivity of aluminum appears to be unfeasible because of the lack of a suitable isotope. However, from changes in the electrical resistivity of quenched samples annealed at low temperatures, it has been estimated and low that $Q_{\rm Al}$ in pure aluminum is about 30 kcal/mole. This is only slightly less than the value $Q_{\rm Zn}=30.9~(\pm0.6)$ kcal/mole obtained here for the self-diffusivity of zinc in aluminum; however, $Q_{\rm Zn}$ drops rapidly on alloying so that at $X_{\rm Zn}=0.167, Q_{\rm Zn}=25.0~(\pm1.1)$ kcal/mole. If it is assumed that the ratio of the frequency factors for the two self-diffusivities is independent of composition, then the condition $D_{\rm Al}^* < D_{\rm Zn}^*$ can be satisfied if $Q_{\rm Al}^*$ decreases slightly less rapidly than $Q_{\rm Zn}^*$.

Concerning the temperature dependence of self-diffusion in zinc, Jaumot and Smith⁽⁵⁾ give values of 22.7–23.5 kcal/mole for $Q_{\rm Zn}^*$ in polycrystalline zinc over the temperature range 200–415°C. The same investigators indicated that grain boundary diffusion is not important at temperatures above 200°C. In addition, they reported 22.0 kcal/mole for $Q_{\rm Zn}^*$ parallel to the hexagonal axis and 23.5 perpendicular to the axis. Shirn et al.⁽¹³⁾ found 21.8 kcal/mole parallel and 24.3 perpendicular, while Liu and Drickamer⁽¹⁴⁾ obtained 19.6 kcal/mole parallel and 25.9 perpendicular. The present investigation resulted in a value of 20.5 \pm 1.8 kcal/mole for polycrystalline zinc (Table 2). Despite these variations in temperature dependence, the self-diffusivities for polycrystalline

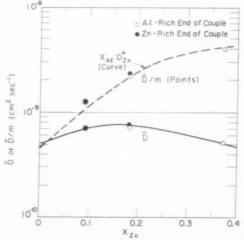
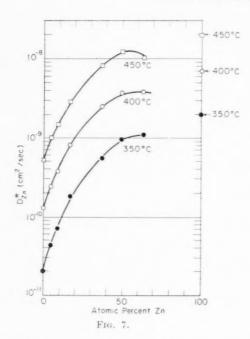


Fig. 6. \widetilde{D} and \widetilde{D}/m for aluminum—zine alloys at 440°C $(m=1+d\ln f_{\rm Zn}/d\ln X_{\rm Zn})$.



zinc at a given temperature are in rather good agree-

The peak of the $(\alpha + \alpha')$ miscibility gap lies at about 360°C and 40 at. % zinc, and the minimum in the thermodynamic driving force function for interdiffusion should occur at this composition. There is no obvious effect of the miscibility gap on the diffusivities, activation energies, or frequency factors for self-diffusion. This was also demonstrated in the case of gold-nickel alloys. (3) Both the activation energies and the frequency factors (Figs. 1 and 2) decrease significantly with increasing zinc content in the aluminum-zinc alloys; the overall trend appears to follow the lowering of the solidus temperature in the phase diagram. (1) The self-diffusivities also vary markedly with composition, as shown in Fig. 7; here again, the rise in self-diffusivity with increasing zinc content follows the trend of the falling solidus temperature. The correlation of diffusivities and activation energies with melting temperature is inherent in many of the recent interpretations of self-diffusion data. (15.16.17) However, these interpretations are not sufficiently refined to account for the shape of the Q^* and D_0^* curves in Fig. 1 and 2, especially since the inflections shown are almost within the experimental error.

The mobilities may be obtained from the relationship $D^* = B^*kT$, where B^* is the mobility, k is Boltzmann's constant, and T is the absolute temperature. It is evident that the mobilities must have the same concentration dependence as shown in Fig. 7 for the self-diffusivities. Since the relative values for the factor kT are 1.00:0.93:0.85 for the three temperatures shown (723:673:623°K), the mobilities have almost the same temperature dependence as the self-diffusivities.

In conclusion, it should be emphasized that the satisfactory interpretation of these measurements by Darken's equation⁽⁶⁾ provides strong circumstantial evidence for the validity of this equation.

ACKNOWLEDGMENTS

Much of the experimental work for this investigation was carried out by G. Pishenin. The authors are also grateful for the sponsorship of the Wright Air Development Center.

REFERENCES

- 1. J. E. HILLIARD, B. L. AVERBACH and MORRIS COHEN, Acta Met. 2, 621 (1954).
- 2. L. S. Darken, Trans. Amer. Inst. Min. (Metall.) Engrs. 175, 184 (1948).

- 3. J. E. REYNOLDS, B. L. AVERBACH and MORRIS COHEN, Acta Met. 5, 29 (1957); 3a. J. E. HILLIARD, Appendix.
 S. HEIMAN, J. Electrochem. Soc. 95, 205 (1949).
- 5. F. E. JAUMOT and R. L. SMITH, J. Metals, N.Y. 8, 137 (1956) and 8, 164 (1956).
- 6. R. E. OGILVIE, Sc. D. Thesis. Department of Metallurgy, M.I.T. (1955).
- 7. E. C. Ellwood, J. Inst. Met. 80, 217 (1952).
- 8. L. D. Hall, J. Chem. Phys. 21, 87 (1953).
- 9. C. Matano, Jap. J. Phys. 8, 109 (1933).
- 10. R. F. Mehl, F. N. Rhines, and K. A. von den Steinen, Metals and Alloys 13, 41 (1941)
- 11. A. BEERWALD, Z. Elektrochem. 45, 789 (1939).
- 12. W. DeSorbo and D. Turnbull. Private communication. G. A. Shirn, E. S. Wajda and H. B. Huntington, Acta Met. 1, 513 (1953).
- 14. T. LIU and H. G. DRICKAMER, J. Chem. Phys. 22, 312 (1954).
- 15. C. Zener, Imperfections in Nearly Perfect Crystals, Chap. 2. John Wiley, New York (1952).
- A. D. LeClaire, Acta Met. 1, 438 (1953). F. S. BUFFINGTON and MORRIS COHEN, Acta Met. 2, 660 (1954).

PLASTIZITÄTSUNTERSUCHUNGEN VON METALLKRISTALLEN IN ULTRASCHALLFELD*

F. BLAHA† und B. LANGENECKER†

Dehnungsversuche an aus der Schmelze gezogenen Metallkristallen einer Länge von 11–19 mm bei einem Durchmesser von 0,4–0,5 mm zeigten, dass die zur Aufrechterhaltung der Translation notwendige Schubspannung durch eine überlagerte Schalleinwirkung beträchtlich vermindert werden kann. Die solcherart verursachte Spannungsverminderung setzt unmittelbar nach Einschalten des Schallfeldes ein. Nach dessen Abschalten nimmt die Verfestigung rassch wieder zu, bis schliesslich derselbe Verfestigungskoeffizient erreicht wird, wie er dem unbeschallten Kristall zukommt.

Dem Betrage nach lagen die durch Schallabstrahlung von 2W/cm² verursachten Spannungsverminderungen bei plastisch verformten Al-, Cd- und Zn-Kristallen alle in ein und derselben Grössenordnung (50–100 g/mm²), konstante Temperatur vorausgesetzt.

Eine ganz ähnliche Spannungsverminderung bewirkten auch in bestimmter Form gegen die Grundplatte der Dehnungsapparatur ausgeführte elastische Stösse, die sich auf den Kristall übertrugen.

Aus den gemessenen und überschlägig berechneten Zustandsgrössen des Ultraschallfeldes sowie aus den bei Schalleinwirkung beobachteten Verminderungen der Schubspannung wurde eine Deutung dieser Spannungsverminderung in dem Sinne versucht, dass es sich hiebei vorwiegend um eine Aktivierung von festgelaufenen Versetzungen handelt.

ULTRASONIC INVESTIGATION OF THE PLASTICITY OF METAL CRYSTALS.

Using tensile tests of metal crystals drawn from the melt (length 11–19 mm, diameter 0.4–0.5 mm) it is shown that the shearing stress necessary for continued translation is decreased markedly by superimposed ultrasonic vibrations. The stress drops immediately after turn-on of the vibration field. After turn-off work-hardening increases rapidly, until finally the rate of hardening arrives at values as measured with crystals that had not been subjected to ultrasonic vibration.

The decrease in shearing stress caused by $2W/cm^2$ ultrasonic irradiation was found to be about the same order of magnitude (50–100 g/mm²) for plastic deformation of Al, Cd, and Zn crystals, the temperature being constant,

Elastic percussions of the base of the tensile-testing machine, which propagated to the crystal, had a similar effect on the stress. Starting from the parameters of the ultrasonic field (which have been measured or estimated) and from the observed decrease in shearing stress a theory is proposed basing on the idea that the underlying process is the activation of anchored dislocations.

PHENOMENES DE PLASTICITÉ DE CRISTAUX METALLIQUES SOUS CHAMPS D'ULTRASONS

Les auteurs effectuent des essais de traction sur des cristaux métalliques de 11–19 mm de largeur et 0,4–0,5 mm de diamètre. Ils montrent que la tension de cisaillement nécessaire pour le maintien du glissement peut être considérablement diminuée par l'action du son. La diminution de tensions ainsi provoquée a lieu immédiatement après l'application sonore. Dès que celui-ci cesse d'être appliqué, la restauration augmente de nouveau rapidement jusqu'à ce que finalement le coefficient de restauration atteigne la même valeur que pour un cristal qui n'est pas soumis aux ultrasons.

Suivant le cas et pour une densité d'ultrasons de 2W/cm², les diminutions de tension obtenues pour des cristaux d'aluminium, cadmium et zinc déformés plastiquement sont du même ordre de grandeur (50–100 g/mm²), la température restant constante.

Une diminution de tension analogue est obtenue par des impulsions élastiques exercées sur la plaque de base de l'appareil de traction qui se transmettent au cristal.

Les auteurs donnent à partie des grandeurs caractéristiques, mesurées ou calculées, des charges des ultrasons et des diminutions des tensions observées une explication des phénomènes en admettant qu'il s'agit d'une activation des dislocations.

1. EINLEITUNG

1959

Bei zunehmenden plastischen Verformungen erfahren Metallkristalle im allgemeinen eine Verfestigung. Zu den Ausnahmen, d.h. entfestigenden Effekten, gehören beispielsweise die Spannungsverminderung nach der Bildung von Deformationszwillingen, (14) ferner die Entfestigung durch Betätigung eines ursprünglich latenten Gleitsystems, (10) wie sie sich ähnlich auch nach Bestrahlung mit schweren Teilchen zeigt, der Bauschingereffekt in verschiedenen Vari-

anten,⁽⁸⁾ sowie Fälle, in welchen Verunreinigungen die Ursache dafür sind, dass nach hinreichenden plastischen Verformungen eine Entfestigung im wirksamen Gleitsystem⁽⁵⁾ erfolgt. Hinzu kommt die in letzter Zeit bekanntgewordene Bearbeitungserholung oder Verformungsentfestigung,⁽¹⁸⁾ die bei reinen Metallkristallen in einer Entfestigung ein und desselben, vom Anfang der plastischen Verformung an wirksamen Translationssystems besteht⁽⁶⁾ und jeweils nach Übergängen zu höheren Temperaturen in Erscheinung tritt.

In der vorliegenden Arbeit wird nun gezeigt, dass

ACTA METALLURGICA, VOL. 7, FEBRUARY 1959

^{*} Received April 11, 1958; revised version May 13, 1958.

[†] II. Physikal. Institut der Universität Wien.

Metallkristalle auch dann eine Entfestigung erfahren, wenn sie wägrend des Dehnungsvorganges einem Schallwellenfeld (oder Stosseinwirkungen) ausgesetzt werden.

2. APPARATUR UND PROBENMATERIAL

Der Versuchsaufbau bestand im wesentlichen aus einem modifizierten polanyi-Dehnungsapparat auf Dehnungsmeßstreifen-Basis wie er in⁽³⁾ ausführlich beschrieben wurde. Zur Erzeugung von Ultraschall wurde ein Gerät verwendet, welches bei 800 kHz eine Gesamtabgabeleistung von maximal 25 W aufweist (2 W/cm²).

Der Quarzschwinger dieses Gerätes befindet sich in einem durch Umlaufwasesr gekühlten Schallkopf S (Abb. 1), auf welchen ein zylindrisches Glasgefäss G von 30 mm ϕ und 150 mm Höhe aufgesetzt wurde. In dieses Glasgefäss wurde ${\rm CCl_4}$, der sich wegen seines verhältnismässig günstigen Schallwiderstandes für alle derartigen Untersuchungen gut geeignet erwies, eingefüllt, der auch den Ultraschall auf den Metallkristall übertrug.

Der Schallkopf konnte samt dem aufgesetzten Glasgefäss mittels einer Hebebühne so weit angehoben werden, dass der zu untersuchende Metallkristall zur Gänze in die Flüssigkeit eintauchte, so dass diese gleich zeitig auch als Temperaturbad wirkte. Ein aus einem Kupferröhrehen von 4 mm Durchmesser und

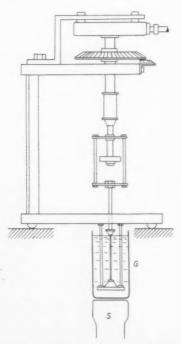


Abb. 1. Schema des Dehnungsapparates mit Ultraschallkopf.

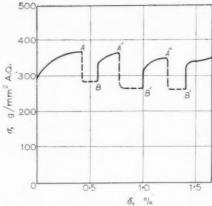


Abb. 2. Spannungs-Dehnungskurve eines Zink-Kristalles bei wiederholter Ultraschalleinwirkung.

150 mm Länge, mit einem in den Boden eingelöteten 0,2 mm starken Konstantandraht bestehendes Thermoelement gab die Badtemperatur auf $\pm 0,05^{\circ}\mathrm{C}$ an; die Temperatur konnte auf $\pm 0,3^{\circ}\mathrm{C}$ konstant gehalten werden. Kupfer-Kanstantan war nicht nur wegen der grossen Thermokraft, sondern auch deshalb gewählt worden, weil sich Kupfer im Gegensatz zu Eisen gegen Kavitation⁽¹⁾ recht beständig erwies.

Die vorliegenden Plastizitätsuntersuchungen wurden an Proben folgenden Reinheitsgrades durchgeführt: Al 99,996 %; Cd 99,95 %; Zn 99,995 %. Aus den nach einem Czochralski-Verfahren $^{(7)}$ durch Ziehen aus der Schmelze hergestellten drahtförmigen Einkristallen wurden 14-19 mm lange Teilstücke ausgewählt, deren mikroskopisch ermittelter Durchmesser 0,4-0,5 mm betrug. Die kristallographische Orientierung wurde mittels Röntgen-Drehkristallaufnahmen bestimmt; der Winkel χ_0 zwischen Probenlängsachse und Translationsebene lag bei sämtlichen Proben zwischen 26° und 28° .

19

Bei allen Dehnungsversuchen betrug die Dehnungsgeschwindigkeit 25 μ/Minute , was einer Abgleitgeschwindigkeit von etwa $5\cdot 10^{-5}\,\text{sec}^{-1}$ entsprach.

Um Druckspannungen oder Knickungen der Kristalle bei manchmal zwischendurch ausgeführten Entlastungen der Proben mit Sicherheit auszuschliessen wurden diese stets in den Halterungen des Dehnungsapparates belassen und nur auf etwa 1/7 der Streckgrenze entspannt.

Die im folgenden gebrachten Beobachtungsergebnisse stellen eine Auswahl charakteristischer Beispiele aus zahlreichen Versuchen dar, wobei sich die strichlierten Kurventeile stets auf Dehnungen mit gleichzeitiger Ultraschalleinwirkung, durchlaufend gezogene auf solche ohne Ultraschall beziehen.

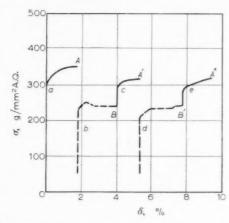


Abb. 3. Spannungs-Dehnungskurve von Zn bei zeitweiser Ultraschalleinwirkung

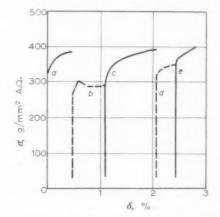


Abb. 5. Spannungs-Dehnungskurve eines Zinkkristalles bei Schalleinwirkung von 2 W/cm² (b) und 1 W/cm² (d).

3. PLASTIZITÄT VON AI-, Cd- UND Zn-KRISTALLEN IM SCHALLFELD

Schaltet man während der plastischen Verformung eines Zn-Kristalles das Ultraschallfeld ein (ein Beispiel hiezu bringt Punkt A, Abb. 2), so sinkt die Spannung σ zunächst schroff ab; mit fortschreitender Dehnung δ lenkt sie dann auf einen Wert ein, der während der Schalleinwirkung angenähert beibehalten wird. Unmittelbar nach dem Abschalten des Schallfeldes (Punkt B) steigt die Spannung bis zum Erreichen des plastischen Bereiches steil an. Ein abermaliges Einschalten des Ultraschallfeldes (A') hat wiederum einen Spannungsrückgang zur Folge usw.; dieser Vorgang kann bis zur Zerreissgrenze mehrmals wiederholt werden. (2) In dem in Abb. 2 wiedergegebenen Falle betrug die Spannungsverminderung durch Ultraschalleinwirkung im Mittel etwa 90 g/mm² A.Q., das sind etwa 25% der Ausgangsspanning in A, A' usw.

1959

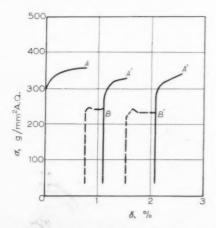


Abb. 4. Spannungs-Dehnungskurven von Zink.

Abb. 2 stellt im übrigen eine Messreihe dar, bei welcher ausnahmsweise die Umlaufwasserkühlung des Schallgebers abgeschaltet war, wodurch jede Beschallungsperiode eine Erhöhung der Badtemperatur um ~2°C verursachte: Während der Dehnung ohne Ultraschalleinwirkung sank sie wieder um etwa 1°C ab, so dass mit fortschreitender Versuchsdauer allmählich eine Temperaturerhöhung stattfand. Aus diesem Grunde weisen die Werte A, A' usf., sowie B, B' usf. eine abnehmende Tendenz auf. Zusätzlich zu der durch Ultraschalleinwirkung verursachten Spannungsverminderung um 90 g/mm² A.Q. hatte mithin die erhöhte Temperatur nach drei Beschallungsperioden eine Spannungsverminderung um etwa 20 g/mm² A.Q. zur Folge. Alle übrigen, nachstehend beschriebenen Untersuchungen im Ultraschallfeld wurden bei konstanter Temperatur (Umlaufkühlung eingeschaltet) durchgeführt.

Um den Einfluss einer vorangehenden etwas stärkeren plastischen Verformung auf die Ausbildung

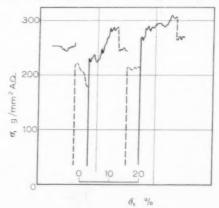


Abb. 6. Ausschnitt aus einer Spannungs-Dehnungskurve für einen Cd-Kristall bei zeitweiser Ultraschalleinwirkung.

des Effektes zu sehen, wurde—wie Abb. 3 wiederbigt—ein Kristall zuerst ohne Ultraschall um angenähert 2% gedehnt, dann in A entlastet und neuerlich, jedoch bei gleichzeitiger Schalleinwirkung gedehnt (bis B). Schaltete man das Schallfeld in B ab, so stieg die Spannung mit fortschreitender Verformung ebenso wie in dem in Abb. 2 beschriebenen Versuch bis A' auch hier wieder an (Kurventeil c). Der weitere Kurvenverlauf in Abb. 3 stellt eine Wiederholung des eben beschriebenen Versuchsablaufes dar. Die Werte in B und B' liegen in Abb. 3 um etwa 110 g/mm² unter A und um etwa 75 g/mm² unter A' und A".

Wenn in teilweiser Abänderung der eben beschriebenen Versuchsbedingungen nach den Dehnungen bei Schalleinwirkung ebenfalls entlastet und dann neuerlich gedehnt wurde, ergaben sich ganz ähnliche Resultate, wofür Abb. 4 ein Beispiel liefert. Die Spannungswerte von B und B' liegen hier wieder um etwa 100, bzw. 85 g/mm² A.Q. unter denen von A bzw. A'.

Wenn die zweite Dehnung im Ultraschallfeld bie nur I W/cm² aufgenommen wurde, wie Kurve d in Abb. 5 zeigt, fiel hiebei die Spannungsverminderung nur ungefähr halb so gross (ca 45 g/mm² A.Q.) wie bei der Beschallung mit 2 W/cm² für Kurve b aus, d.h. die Spannungsverminderung war der Intensität des Ultraschallfeldes angenähert proportional.

Bei allen Plastizitätsuntersuchungen waren die Kristallproben longitudinal beschallt worden. Im Falle einer versuchsweise zur Probenlängsachse senkrechten Beschallung betrug der Spannungsrückgang bei Zn nur etwa 1/3 des Betrages im longitudinalen Schallfeld.

Aus orientierenden Untersuchungen des plastischen Verhaltens von Zn-Kristallen unter Schalleinwirkung

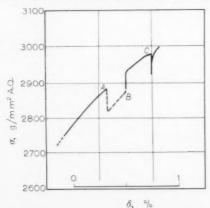


Abb. 7. Ausschnitt aus einer Spannungs-Dehnungskurve für einen Al-Kristall mit Ultraschalleinwirkung von A bis B sowie nach einem Stoss bei C.

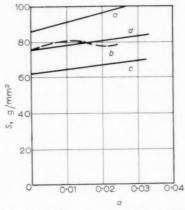


Abb. 8. Verestigungskurven von Zink bei 19°C(a), 93°C(c), 58°C(d) sowie bei 19°C und gleichzeitiger Ultraschalleinwirkung (b). (Ordinate = Schubspannung S, Abszisse = Abglietung a)

im Hörbereich (15–10.000 Hz) scheint hervorzugehen, dass sich die Kristalle hiebei ebenso wie bei der Einwirkung von Ultraschall verhalten.

Der Schallabstrahler bestand bei diesen Versuchen aus einem umgebauten elektrodynamischen Lautsprecher, dessen Schwingspule mit einer Kuststoffmembran in Verbindung stand. Diese Membran bildete den Boden des Gefässes, in welchem sich die Übertragungsflüssigkeit befand, in die der Kristall samt Halterungen eintauchte. Ein mit Hilfe eines regulierbaren Tongenerators gesteuerter Kraftverstärker besorgte die Erregung des Schallabstrahlers.

19

Al- und Cd-Kristalle zeigten bei einer plastischen Verformung im Schallfeld grundsätzlich dasselbe Verhalten wie Zn. Die Spannungsverminderungen lagen bei gleichen Versuchsbedingungen in derselben Grössenordnung (50–100 g/mm² A.Q.). Hiezu bringen die Abb. 6 und 7 mit Ausschnitten aus Spannungs-Dehnungskurven je ein Beispiel.

Der infolge Schalleinwirkung veränderte Verlauf der Spannungs-Dehnungskurve legte as nahe, das plastische Verhalten im Ultraschallfeld einerseits und bei höheren Temperaturen andererseits zu vergleichen. Ein Zn-Kristall, der bei einer bestimmten Temperatur T_1 (19°C) gedehnt wurde, lieferte die Verfestigungskurve a in Abb. 8. Dehnte man eine zweite Probe gleicher Beschaffenheit bei derselben Temperatur und liess gleichzeitig Ultraschall einwirken, so erhielt man Kurve b, deren Werte unter Kurve a liegen. Ohne Ultraschall ergibt sich bei einer höheren Temperatur T₂ (93°C) eine noch tiefer liegende Kurve c. Es lässt sich aber auch eine Temperatur T_2 (58°C) angeben, deren zugehörige Verfestigungskurve d weitgehend mit Kurve b zusammenfällt. Man kann aus Abb. 8 ersehen, dass

die zu den einzelnen Verfestigungskurven gehörigen kritischen Schubspannungen mit zunehmenden Temperaturen abnehmen (aber in einer Grossenordnung bleiben); ebenso entspricht auch die kritische Schubspannung bei Schalleinwirkung der Schubspannung bei entsprechend höherer Temperatur.

Hinsichtlich der Energien, die durch Wärmezufuhr bzw. durch Beschallung auf den Kristall übertragen wurden, besteht jedoch für die beiden Verfestigungskurven b und d ein beträchtlicher Unterschied: (1) Um die Temperatur des in Abb. 8 charakterisierten Zn-Kristalles (Volumen V=0.0028 cm³; spez. Gewicht s=7,1 g/cm³; spez. Wärme $c=9.2\cdot 10^{-2}$ cal/g.grad; $T_2-T_1=T=39^{\circ}\mathrm{C}$) von T_1 (19°C) auf T_2 (58°C) zu erhöhen, ist eine Wärmemenge von c.s. $V\cdot T=9.2\cdot 10^{-2}\cdot 7.1\cdot 2.8\cdot 10^{-3}\cdot 39=7\cdot 10^{-2}$ cal nötig, bzw. umgerechnet $\sim 2\cdot 10^{18}$ eV.

(2) Unter Berücksichtigung der teilweisen Reflexion der Schallwellen an den Begrenzungen (Übertragungsflüssigkeit/Metallhalterung/Kristall) erhält man nach Abschätzungen, deren Wiedergabe hier unterdrückt sei, in obigem Zn-Kristall Schubspannungsamplituden von etwa 2–3 g/mm² und als mittlere Schalldichte $\sim 10^{-8}$ Wsec/cm³ $\approx 6 \cdot 10^{12}$ eV/cm³ und somit im Zn-Kristall vom Volumen V=0.0028 cm³, $\sim 1.7 \cdot 10^{10}$ eV.

Auf eine Diskussion dieser Abschätzungsergebnisse wird weiter unter eingegangen.

Es sei noch darauf hingewiesen, dass auch die normale Kristallerholung im Ultraschallfeld untersucht wurde. Dabei stellte sich heraus, dass der Ultraschall genannter Energiedichte zu einer merklichen Beschleunigung der Kristallerholung, bei welcher der Kristall in entspanntem Zustand einige Zeit ruht, nicht beitrug.

4. PLASTIZITÄT VON Zn- UND AI-KRISTALLEN BEI EINWIRKUNG VON STOSSEN

Es wurde schon darauf hingewiesen, dass die von einem unter Last befindlichen Kristall getragene Spannung unmittelbar nach dem Einschalten des Schallfeldes schroff absank und zwar so weit, dass dabei im allgemeinen bereits mehr als etwa 3/4 der endgültigen, für die im Ultraschallfeld typische Entfestigung in Erscheinung trat. Nähere Untersuchungen dieser schlagartigen Entfestigung, vor allem unter Anwendung eines Impulsgenerators, stehen noch aus. Hingegen wurde schon die Auswirkung kurzdauernder Schwingungen auf Kristalle verfolgt, wie sie bei einem elastischen Stoss im vorliegenden Falle gegen die Grundplatte des Dehnungsapparates, zustandekamen und die sich auf den im Dehnungsapparat fixierten Kristall fortpflanzten. Man

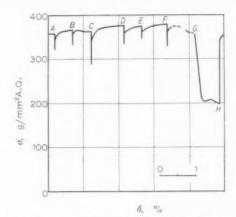


Abb. 9. Spannungs-Dehnungskurve eines Zinkkristalles bei Einwirkung von Stössen.

kann sich die durch einen Stoss verursachten zusammengesetzten Schwingungen in nach der Fourier-Analyse gekoppelte Schwingungen n-facher Frequenz einer Grundfrequenz zerlegt denken.

Die Versuche an Zn und Al wurden solcherart durchgeführt, dass während der Dehnung der Kristalle ein Gummiball (17 g Gewicht, $\phi = 4.5 \text{ cm}$) aus verschiedenen Höhen frei auf die Grandplatte des Denungsapparates fallen gelassen und beim Zurückspringen abgefangen wurde. Durch die reproduzierbaren Aufschläge wurde jeweils ein Stoss ausgeübt, der in allen Fällen einen plötzlichen Spannungsrückgang am Kristall zur Folge hatte (A, B, ..., F, in Abb. 9). Nach dem jähen Spannungsabfall stieg die Spannung stets sogleich wieder steil an und nahm sodann bei gleichzeitigem ausgiebigem plastischen Fliessen nur mehr allmählich zu. Über die Fallhöhen und die dadurch verursachten Spannungsverminderungen bringt Tabelle I eine Zusammenstellung. Diese durch Abb. 9 beschriebene Versuchsreihe wurde so ausgeführt, dass sich die Probe in Luft befand: war sie in ein Flüssigkeitsbad eingetaucht, so ergaben sich ganz ähnliche Resultate.

Tabelle 1

Kristall	Fallhöhe des Balles (cm)	in Abb. 9	Spannungsver- minderung $\Delta \sigma$ (° ₀) g/mm ² A.Q.		$\Delta \sigma$ durch Ultraschall (2W/cm ²) g/mm ² A.Q
Zn	25 25 25	A B E	10,0 9,5 7,5	35 33 27	
	50 50 75	D F C	13.5 14.5 20.0	47 50 70	75-110
Al	80		2,0	60	60- 70

Ab G wurden 500 unmittelbar aufeinanderfolgende Aufschläge des 2 mal pro Sekunde aus einer Höhe von 25 cm herabfallenden Gummiballes ausgeübt, wodurch die Spannung zunächst binnen 5 Aufschlägen um ca 50% vermindert wurde. Sodann sank sie im weiteren Verlauf nur noch allmählich ab und begann unmittelbar nach dem letzten Aufschlag (ab Punkt H) wieder anzusteigen.

Der Verlauf der Kurven war also bei Einwirkung von Stössen ähnlich wie bei den oben beschriebenen Versuchen im Ultraschallfeld.

5. DISKUSSION

Nimmt man hinsichtlich der plötzlichen Spannungsverminderung vereinfachend an, dass der einwirkende Schall zunächst einmal die während der vorangegangenen Dehnung ohne Schalleinwirkung festgellaufenen Versetzungen plötzlich aktiviert, d.h. dem Gleitprozess wieder zu führt, so kann man einen grössenordnungsmässigen Abschätzungsversuch hinsichtlich der Versetzungsdichte in den benützten Zn-Kristallen anstellen.

Um in Zn eine Versetzung zu aktivieren, ist eine Energie von ungefähr 1 eV erforderlich. Bei reinen hexagonalen Kristallen werden die Abstände 1 der Gleichgewichtslagen der in der Basisebene liegenden Versetzungslinien hauptsächlich durch den Abstand von Hindernissen bestimmt, welche durch die zur Basisebene querorientierten Versetzungen gebildet werden (Versetzungen in Richtung der c-Achse). Die Wanderung dieser querorientierten Versetzungen würde erst unter Spannungen erfolgen, welche um 2 bis 3 Grössenordnungen über den im Experiment aufgetretenen liegen. Mithin sind also die Querversetzungen praktisch unbeweglich, und der Abstand Ihrer Durchstosspunkte in der Basisebene ist zugleich der Abstand 1. Bei Verfestigung wird eine immer grösser werdende Anzahl von Versetzungen auf diese Hindernisse auflaufen und ihrerseits die noch aktiven Versetzungen in der Wanderung behindern. Es wird also die freie Fläche, zwischen aufeinanderfolgenden Hindernissen, die von den wirksam Verbliebenen Versetzungen überstrichen werden kann, zusehends verkleinert.

Versucht man in Anlehnung an Seeger⁽¹⁵⁾ aus den gemessenen Schubspannungen mit und ohne Schalleinwirkung auf die mittleren Abstände der Versetzungslinien zu Beginn der plastischen Verformung sowie von querorientierten und aufgestauten Versetzungen, durch welche die freien Flächen zwischen aufeinanderfolgenden Hindernissen begrenzt werden, zu schliessen, so erhält man grössenordnungsmässig eine Versetzungsdichte, die mit anderweitigen

Abschätzungsergebnissen gut übereinstimmt: Aus der Röntgen-Kleinwinkelstreuung⁽¹⁵⁾ ergibt sich eine mittlere Dichte von 10⁸ bis 10⁹ Versetzungen/cm² und auch das Impuls-Echo-Verfahren (Messung der Dämpfung von Ultraschallwellen^(4,11,13)) liefert etwa die gleichen Werte.

Den Abschätzungsversuchen lag die Annahme zugrunde, dass die plötzliche Spannungsverminderung, die bei allen Kristallen im Moment des Einschaltens des Schallfeldes beobachtet werden konnte und für Al, Cd und Zn in der gleichen Grössenordnung lag, auf die Aktivierung von Versetzungen, die während der vorangegangenen Verfestigung auf Hindernisse aufgelaufen und dadurch blockiert worden waren, zurückzuführen ist.

Diese Annahme stellt eine nicht ganz einwandfreie Vereinfachung dar, denn die einem verfestigten Kristall zugeführte Energie-sei es nun thermische oder Schallenergie-bewirkt eine Herabsetzung der Fließspannung, die nicht allein durch Aktivierung von Versetzungen (Überwindung von Hindernissen), sondern auch infolge Verminderung der Versetzungsdichte (Beseitigung von Hindernissen) zustandekommt. Während die letztere Art irreversibel ist, stellt das Überwinden von Hindernissen einen reversiblen Prozess dar, d.h. es geht hier nach Aufhören der Energiezufuhr die Fließspannung auf den alten Wert zurück. Von Zink ist bekannt, dass die Temperatur-abhängigkeit der Verfestigungskurve bei Raumtemperatur von den beiden genannten Komponenten herrührt⁽¹⁵⁾. In den Abb. 3 und 4 lässt sich auch deutlich erkennen, dass A höher als A' und A" liegt, da ja in den beiden letzten Fällen der irreversible Anteil in der Spannung nicht mehr aufscheint. Dieser ist jedoch wesentlich kleiner als der reversible Anteil.

19!

Stellt man die Lage einer Versetzung als Potentialfunktion des Weges dar-wie dies in ähnlicher Form für Versetzungsschleifen von Mason⁽¹¹⁾ angegeben wurde—so kommt bei einer Gleichgewichtslage (Ruhe) die Versetzung an die Stelle 0 in Abb. 9 zu liegen, während nach beiden Richtungen Potentialberge der Höhe h sie an der Fortbewegung hindern. Wird nun am Kristall eine Schubspannung S aufgewendet, so bewirkt dies eine Verlagerung der benachbarten Potentialberge um einen Betrag 8, der von der Grösse der äusseren Schubspannung abhängt. Ist diese genügend gross, so wird die Potentialschwelle bei der ersten ausreichenden thermischen Schwankung überschritten und die Versetzung bewegt sich fort: die Richtung des Lagewechsels ist eindeutig durch die in der Gleitebene wirksame Schubspannung bestimmt.

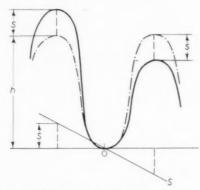


Abb. 10. Modell des Potentialverlaufes für Versetzungen sowie dessen Änderung infolge einer angelegten Schubspannung,

Nimmt man an, dass die Dämpfung von Schallwellen vornehmlich an Gitterfehlstellen (Versetzungslinien) erfolgt, was durch Experimmente^(1,13) gesichert erscheint, so wirkt der Schalldurchgang durch den Kristall wie ein Anheben der Gleichgewichtslagen der absorbierenden Versetzungen oder in einem anderen Bilde: die Überlagerung der äusseren Schubspannung mit der Wechselspannungsamplitude einer ebenen, elastischen Welle verursacht während eines Teils des Schwingungszyklus eine Gesamtspannung, die ausreicht, um Versetzungen aus ihren Potentialmulden herauszuheben, was der Einleitung plastischen Fliessens gleichkommt.

Im entlasteten Zustand, wenn also im Translationssystem keine gerichtete Schubspannung herrscht, werden die Versetzungslinien durch die beim Schalldurchgang durch den Festkörper auftretenden oszillierenden Druck- und Zugspannungen lediglich periodisch ausgeweitet und wieder rückgebildet, (11) was zu keinem äusserlich hervortretenden Effekt führt, sofern die Schallenergie nicht zu hoch ist. Daher konnte wohl auch bei der Beschallung von entlasteten Kristallen kein messbarer Effekt, d.h. keine merkliche Beschleunigung der normalen Kristallerholung beobachtet werden.

Fur die Annahme, dass die plötzliche Spannungsverminderung beim Einschalten des Schallfeldes hauptsächlich auf eine Aktivierung von latenten Versetzungen zuruckzuführen ist, spricht auch noch folgendes: In der Versetzungstheorie gilt, (16) dass stets derjenige Vorgang ausschlaggebend ist, welcher bei ungefähr glichem Energiebedarf den geringeren Zeitaufwand erfordert. Wenn nun während einer plastischen Verformung die äussere Spannung plötzlich abfällt, dann hat die Abgleitgeschwindigkeit eben plötzlich zugenommen. Nun hängt die Abgleitgeschwindigkeit vom mittleren Zeitbedart für die Aktivierung von Versetzungen vor Hindernissen

sowie von der mittleren Laufzeit bis zum nächsten Hindernis ab. Falls Versetzungen erst erzeugt werden müssen, so kommt der hiefür erforderliche Zeitaufwand noch hinzu. Da die Aktivierungsenergie für die Erzeugung von Versetzungen etwa ebenso gross wie für deren Wanderung ist, darf man wohl annehmen, dass der raschere Vorgang, d.i. die blosse Aktivierung vorhandener Versetzungen zunächst anspricht.

Wenn während einer plastischen Verformung anhaltend beschallt wird, so kann neben der Aktivierung von auf Hindernisse aufgetroffenen Versetzungen mit zunehmender Beschallungsdauer auch eine gesteigerte Erzeugung von Versetzung enin Erscheinung treten. Deren Bildung ist hiebei allerdings lediglich innerhalb von vorhandenen Spannungshöfen (Versetzungsquellen), hingegen nicht im ungestörten Kristallbereich möglich. Für den letzteren Fall wären nämlich Spannungen erforderlich, die um mehrere Grössenordnungen über den im Experiment aufgetretenen liegen. Die vermehrte Erzeugung von Versetzungen kann allmählich zu einem Gleichgewichtszustand hinsichtlich Verbrauch und Neubildung von Versetzungen führen. Damit wäre das Einlenken der Spannungskurve nach dem zunächst schroffen Spannungsabfall beim Einschalten des Schallfeldes (gegen B in Abb. 2 hin) verständlich.

Nach den bisherigen informatorischen Versuchen scheint für die Frequenzen von 15 bis 10.000 Hz und 0,8 sowie 1 MHz keine ausgeprägte Frequenzabhängigkeit zu bestehen, was insoferne nicht weiter überraschend ist, als die natürliche Frequenz einer Versetzungsschleife in der Grössenordnung $10^9\,\mathrm{sec}^{-1}$ liegt. Hingegen war die Spannungsverminderung der Intensität der Schalleinwirkung angenähert proportional.

Im Sinne der dargelegten Auffassungen kann man auch die Spannungsverminderungen, die durch Stösse verursacht werden deuten; es ist dann lediglich anzunehmen, dass die beim elastischen Stoss übertragene Energie in Form von Schwingungen zum Kristall gelangt und in diesem ebenfalls eine Aktivierung der Versetzungen bewirkt. Mti den obigen Deutungsversuchen steht die Beobachtung im Einklang, dass die Spannung nach einem ausgeübten stoss sowohl schroff absinkt als auch sogleich wieder steil ansteigt.

Es wurde schon darauf hingewiesen, dass infolge der bevorzugten Däm-fung von Schallwellen an Versetzungen die potentielle Energie in diesen Fehlbereichen wesentolich stärker angehoben wird als in der ungestörten Umgebung. Im Gegensatz dazu nehmen bei einer Temperaturerhöhung die Schwingungsamplituden der Atome sowohl in Potentialmulden als auch im ganzen übrigen ungestörten Bereich des Kristalls zu; dadurch wird u.a. auch die Peierls-Spannung auf dem mit wesentlich grösseren Energieaufwand verbundenen Umweg über die Temperaturabhängigkeit der interatomaren Wechselwirkungskräfte verringert. Dies mag der Grund dafür sein, dass in einem Kristall (vgl. Abschn. 3) eine Schallenergie von etwa 10¹⁰ eV eine ganz ähnliche Verlagerung der Verfestigungskurve ergab wie eine Wärmemenge, die etwa 10¹⁸ eV entsprach.

Hinsichtlich Auswirkung eines Oberflächeneffektes konnte kein entscheidender Einfluss bei den durchgeführten Experimenten festgestellt werden. Die Proben verhielten sich, ob sie nun in CCl₄, H₂O eingetaucht waren oder sich einfach in Luft befanden, in prinzipiell gleicher Weise.

Wir danken Herrn Prof. DDr. E. Schmid für sein stets förderndes Interesse und Herrn Doz. Dr. A. Seeger für Lesen und Kritik des Manuskriptes.

QUELLENANGABE

- L. Bergmann, Der Ultraschall. S. Hierzel, Zürich (1949).
 F. Blaha und B. Langenecker, Naturwiss. 20, 556
- (1955).
 3. F. Blaha und B. Langenecker, Österr. Philips Zeitschr.
 2, 137 (1956).
- 4. P. G. BORDONI, J. Acoust. Soc. Amer. 26, 495 (1954).
- 5. A. H. COTTRELL und D. F. GIBBONS, Nature 162, 488 (1948).
- A. H. COTTRELL und R. J. STOKES, Proc. Roy. Soc. A 233, 17 (1955).
- J. CZOCHRALSKI, Z. Phys. Chem. 92, 219 (1917).
- E. H. EDWARDS und J. WASHBURN, J. Metals 6, 1239 (1954).
- A. GRANATO und K. LÜCKE, J. Appl. Phys. 27, 583 (1956).
- 10. M. Masima und G. Sachs, Z. Phys. 50, 161 (1928).
- W. Mason, Bell. Syst. Tech. J. 34, No. 5, 903 (1955).
 T. A. Read, Trans. Amer. Inst. Min. (Metall.) Engrs.
- 33, 30 (1941).
 R. L. Roderick und R. Truell, J. Appl. Phys. 23, 267
- (1952).14. E. Schmid und W. Boas, Kristallplastizität. Springer,
- Berlin (1935). 15. A. SEEGER, Z. Naturf. **9**ä, 758 u. 870 (1954); **11**ä, 985
- (1956).
 16. A. SEEGER, Handb, d. Physik (S. Flugge) VII/1, 383.
 Springer, Berlin (1955).
- 17. A. SEEGER, Acta Met. 5, 24 (1957).
- 18. R. J. STOKES und A. H. COTTRELL, Acta Met. 2, 341 (1954).

VOI

THE METALLOGRAPHY OF DEFORMED IRON*

D. G. BRANDON and J. NUTTING†

The slip lines produced on the surface of polycrystalline iron, after deformation of 20–30 per cent, have been examined with the aid of carbon replicas and the electron microscope. Different types of slip traces have been observed but the most common was that of diffuse wavy bands. From the attenuation of an etch structure it has been possible to estimate the total slip displacement in the slip band and the band width.

On electro-polished and etched surfaces prepared after deformation, markings were found which indicated the slipped regions. It is thought that the passage of dislocations disperses small segregated regions and so changes the rate of chemical attack. By direct examination of thin iron films in the electron microscope the dislocations present in the deformed material have been observed. It is concluded that the wavy slip bands form by intimate cross slip of the dislocations from the original slip plane on which they were generated; whilst dislocations on different systems interact to produce tangled networks rather than piled up groups. From the observed interactions of slip lines and grain boundaries a modification of Taylor's theory on the deformation of polycrystalline aggregates is proposed.

LA METALLOGRAPHIE DU FER DEFORME

Les auteurs ont examiné au microscope électronique, par la méthode de l'empreints au carbone, les lignes de glissement qui apparaissent à la surface du fer polycristallin, après une déformation de 20–30%. Ils observent différents types de traces de glissement, bien que le plus souvent on n'aperçoive que des bandes diffuses et ondulées. Sur la base de l'atténuation de la structure d'attaque, il a été possible d'estimer le déplacement total de glissement dans la bande de glissement, ainsi que la largeur de celle-ci.

Les régions où se produisent les glissements sont identifiables sur des surfaces polies électrolytiquement et attaquées après déformation. Il est possible que le passage des dislocations disperse de petites zones de ségrégation et qu'ainsi la vitesse d'attaque soit modifiée. Les dislocations présentes dans le fer déformé ont été mises en évidence par l'examen direct de lames métalliques minces au microscope électronique. Les auteurs en concluent que les bandes de glissement ondulées se forment par glissement croisé des dislocations du plan de glissement original sur lequel elles ont été créées; par contre, les dislocations de différents systèmes interfèrent pour produire des réseaux entrelacés plutôt que des emplements. Sur la base des interactions observées entre lignes de glissement et joints de grains, les auteurs proposent une modification de la théorie de Taylor sur la déformation des agrégats polycristallins.

DIE METALLOGRAPHIE VON VERFORMTEM EISEN

Die Gleitlinien, die nach Verformungen von 20–30% auf der Oberfläche von vielkristallinem Eisen auftreten, wurden mittels Kohleabdrücken elektronenmikroskopisch untersucht. Verschiedene Arten von Gleitspuren wurden beobachtet, am häufigsten traten diffuse wellige Bänder auf. Aus der Schwächung einer Ätzstruktur konnte die gesamte Gleitverschiebung und die Bandweite eines Gleitbandes abgeschätzt werden.

Oberflächen, die nach der Verformung elektrolytisch poliert und geätzt worden waren, wiesen in den geglittenen Gebieten Markierungen auf. Vermutlich werden Anhäufungen von C-Atomen in kleinen Gebieten von durchgewanderten Versetzungen wieder aufgelöst, auf diese Weise ändert sich die Geschwindigkeit des chemischen Angriffs. Durch direkte elektronenmikroskopische Untersuchung von dünnen Eisenfilmen wurden die im verformten Material vorhandenen Versetzungen beobachtet. Es ergab sich der Schluss, dass sich die welligen Gleitbänder durch kurze Quergleitung der Versetzungen aus ihren ursprünglichen Gleitebenen heraus bilden; während die Wechselwirkung von Versetzungen verschiedener Systeme häufiger zur Bildung von verwickelten Netzwerken führt, als zu aufgestauten Gruppen. Aus Beobachtungen über die Wechselwirkung von Gleitlinien und Korngrenzen ergibt sich ein Vorschlag zur Verbesserung der Taylor'schen Verformungstheorie von vielkristallinem Haufwerk.

INTRODUCTION

The electron microscope has been used extensively to study the surface markings accompanying the deformation of many face-centred cubic metals, and the results of these investigations have proved of great value in formulating and testing the dislocation theory of plastic deformation for these metals. (1, 2, 3) Similar information on body-centred cubic metals is not available, although some work on the effect of surface finish on deformation has been published. (4) To supplement the extensive work that has already

1959

^{*} Received April 14, 1958

[†] Department of Metallurgy, Cambridge University,

been done on the factors affecting the stress-strain curve of pure iron, and to clarify some of the results obtained on the crystallography of the slip lines, it seemed desirable that the detailed structure of the deformation markings occurring should be investigated.

The crystallography of the slip process in iron has been studied by many workers with varying conclusions. Barrett et al. (5) investigated the slip traces occurring under different conditions of stress and temperature in iron and silicon ferrite, concluding that slip was on {110} {112} or {123} planes operating in the (111) direction; but that slip on {110} was that most favoured. Chen and Maddin⁽⁶⁾ have proposed that slip in body-centred cubic metals is made up of short units of slip on {110} planes; in this way the mean slip plane may be {112} {123} or a more complex plane, and the waviness of the slip lines can then be explained. Vogel and Brick, (7) in a very complete study on a-iron, and Steijn and Brick,(8) in work on high purity iron under different temperature and stress conditions, conclude that "corrugated" slip of the Chen-Maddin type is unlikely and propose that slip occurs on non-crystallographic planes intermediate between the plane of maximum resolved shear stress and the nearest {110} plane to it. In addition, Steijn and Brick propose a slip mechanism in terms of atom movements to account for the wavy slip traces of body-centred cubic metals.

Allen et al. (9) have investigated the tensile behaviour of single crystals of iron and have determined the orientation relationships for slip, twinning and cleavage at different temperatures; they found straight slip lines at low strains and wavy slip lines at high strains.

Paxton et al.⁽⁴⁾ have obtained electron micrographs showing coarse localized slip lines on mechanically polished surfaces, whereas diffuse closely spaced slip lines were observed on electropolished surfaces. Campbell et al.⁽¹⁰⁾ have studied the deformation of pearlite using perspex–carbon replicas and have observed corrugated structures on some slip lines which they relate to the corrugated slip proposed by Chen and Maddin.

EXPERIMENTAL METHOD

A 99.8% Swedish iron and a 99.97% high purity iron manufactured from it were supplied for this investigation by the British Iron and Steel Research Association. The analyses are given in Table 1.

After cold rolling to 1 mm thick, strip specimens $7 \text{ cm} \times 1 \text{ cm}$ were cut. These were annealed in vacuo and furnace cooled, cooled outside the furnace but within the vacuum tube, or water-quenched by removing from the vacuum tube and plunging into cold water.

The strip specimens were electropolished in perchloric acid – acetic acid solution (1:4), and then elongated in a hand-operated Hounsfield tensometer. After optical examination, direct carbon replicas were wet-stripped from the central portion of each specimen and examined in a Siemens Elmiskop 1 or Elmiskop 2 electron microscope. The specimens were then abraded to remove the slip traces and after further electropolishing to remove at least 20 μ of metal they were etched in 1% nital and examined for deformation etch structures.

19

Table 1. Analyses of materials used

Designation	B.I.S.R.A. reference No.	C	Si	Mn	s	Р	Ni	Cr	Мо	W	V	Ti	Co	Cu	Al
Swedish iron 99.8%	AA05	0.02	0.02	< 0.005	0.015	0.001	0.01	< 0.01	< 0.01	< 0.02	< 0.01	< 0.02	< 0.01	< 0.01	< 0.003
High purity iron 99.97%	AHP19	0.0024	< 0.001	0.004	0.005	< 0.001	0.01	0.001			_	_	-	0.004 -0.007	< 0.00
Des	signation		B.I.8	S.R.A. refe	erence n	0.		Sn		0		N		Н	
Swedish	iron 99.8%	r		AAO	5		<	0.02	-						
High puri	ty iron 99.97	0/0		AHPI	19				i	0.0022		0.0013		0.000	005

To investigate the dislocation arrangements existing in deformed iron, a technique was developed for preparing thin metal films from tensile specimens of iron foil. A sample of the 99.97% iron was rolled down to 70 μ thickness and small tensile specimens cut from the cold rolled foil. These were annealed in vacuo at 750°C for 1 hr and furnace cooled. They were then electropolished to different thicknesses and deformed to fracture in the Hounsfield tensometer.

After optical examination the fractured test pieces were further electropolished until they had been perforated in several places. Specimens were then cut from the perforated regions with a razor blade, and mounted for direct examination by transmission in the electron microscope.



Fig. 1. 99.8% Iron. Furnace cooled, etched 1% nital, elongated 30 per cent. Showing diffuse wavy slip bands. ×5000.

RESULTS

The varied nature of the deformation structures observed, and the limited field of view in the electron microscope, prevented any useful comparison of the effects of impurity content or grain size upon the slip patterns.

Similarly, apart from the appearance of some "corrugated" slip lines, the effects seen on etched surfaces appeared very little different from those observed on specimens tested as electropolished. The rate of cooling also had little effect on the deformation structures, though etch structures were less prevalent on quenched specimens.

Replica technique

Both the thickness of the carbon replicas and the angle between direction of evaporation and specimen surface had a profound influence on the contrast obtained and the apparent surface contours. Thin

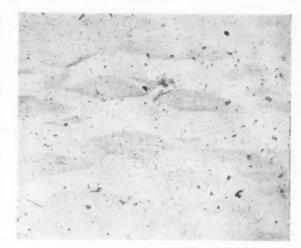


Fig. 2. Same specimen as Fig. 1. Showing "slug structure". ×5000.

replicas showed high resolution of fine surface detail, in particular the early stages in the formation of etch structures, but were incapable of showing up broad diffuse slip bands. This is thought to be due to the very pliable nature of the carbon replica which enables it to withstand rough treatment but makes it difficult to obtain accurate replicas of wavy surfaces. In order to observe the broad bands thick carbon replicas having greater rigidity than the thin ones had to be used.

Metallography of the slip lines

The most commonly observed structure was one of a series of diffuse, wavy, low contrast bands (Fig. 1). The bands frequently split and recombined with no apparent change in slip direction. A related structure,

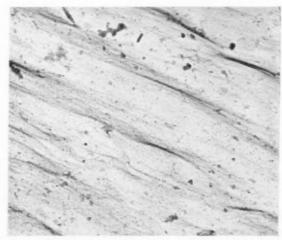


Fig. 3. Same specimen as Fig. 1. Showing lamellated slip lines. ×25,000.

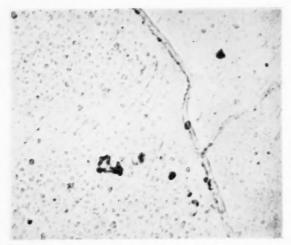


Fig. 4. Same material and treatment as Fig. I. Showing attenuated etch structure in slipped region and deformed grain boundary. ×25,000.

observed by Fujita and Nishiyama⁽¹¹⁾ on aluminium at high deformations and called "slug structure", was also seen (Fig. 2). Sharp slip steps were observed less frequently, and occasionally lamellated slip lines similar to those seen by Brown⁽¹⁾ on aluminium were found (Fig. 3).

On many specimens, especially those which had been slowly cooled, etch markings were observed. These were small regions, about 200 Å in diameter, of which there were 10^{10} – 10^{11} cm⁻² of specimen surface. These etch markings were useful in investigating the nature of the slip patterns, for it was observed that on deforming specimens which had been etched previously, the etch structure became attenuated (Fig. 4). This attenuation indicates that the new surface formed by

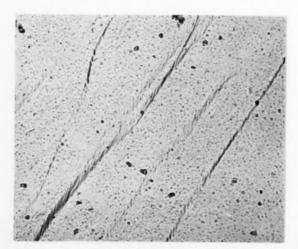


Fig. 5. Same material and treatment as Fig. 1. Showing corrugated slip markings. ×16,000.

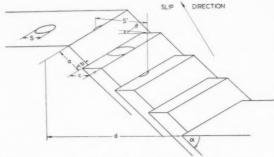


Fig. 6. Relationship between the slip plane, slip direction and the attenuated etch structure.

the deformation process is not confined to a few neighbouring slip planes, and hence the slip process must itself be distributed over many closely spaced planes.

Elsewhere on specimens containing etch structure the slip lines show markings similar to the corrugations observed by Campbell *et al.*⁽¹⁰⁾ (Fig. 5). It is difficult to believe that the high contrast of these markings results from simple attenuation of the etch structure.

From a consideration of Fig. 6 the geometrical relationship between slip planes, slip direction, and attenuation of etch structure can be determined. The direction of attenuation is a function of the slip direction, and for replicas which do not retain the macroscopic waviness of the surface, the angle which the direction of attenuation makes with the slip traces can be measured from the micrographs, thus indicating the position of the surface examined relative to the glide ellipse of the operative slip system. Rough values of slip distance S, and slip band thickness B, can then be evaluated by measuring the attenuation of the

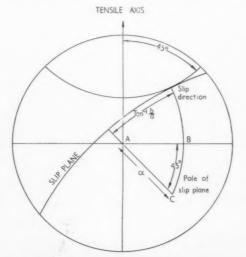


Fig. 7. Stereographic projection of the slip plane and slip direction in the plane of the specimen surface,

VOI 7 19 etch structure and by assuming that the slip direction is at 45° to the tensile axis along the major axis of the glide ellipse, as shown in Fig. 7.

a = slip perpendicular to slip line per slip step

b = slip parallel to slip line per slip step

c =spacing of slip steps on surface

n = number of steps per band

 α = angle slip plane makes with surface

d = measured width of slip band

 $\theta = \text{angle elongated structure makes with normal}$ to slip band on surface of replica

s =width of surface structure

s' = projected length of elongated structure

Then
$$\tan \theta = b/(a \cos \alpha + c)$$
$$d = n(a \cos \alpha + c)$$
$$\therefore \tan \theta = nb/d$$

If
$$s = n'c$$

 $s' = n'[(d/n)^2 + b^2]^{1/2}$
 $= n'd/n (1 + \tan^2 \theta)^{1/2}$
 $\therefore s/s' = n(c/d) \sec \theta$

But slip band width =
$$nc \sin \alpha = B$$

 $\therefore B = s/s'd \sec \theta \sin \alpha$

Also
$$na \cos \alpha = d - nc$$

 $\therefore a/b = (d - nc)/d \tan \theta \cdot \cos \alpha$
 $= (\cos \theta - s/s')/\sin \theta \cos \alpha$

1959

Total amount of slip =
$$n(a^2 + b^2)^{1/2} = S$$

If the slip direction is along the major axis of the glide ellipse α can be eliminated. In the stereographic triangle ABC in Fig. 7:

$$\cot \alpha = \cos (\tan^{-1} b/a)$$

$$= 1/[1 + (b/a)^2]^{1/2}$$
Let
$$(\cos \theta - s/s')/\sin \theta = x$$
Then
$$a/b = x/\cos \alpha$$

$$\therefore \cot^2 \alpha (1 + \cos^2 \alpha/x^2) = 1$$

$$\therefore \cos^4 \alpha/x^2 + 2\cos^2 \alpha - 1 = 0$$

$$\therefore \cos^2 \alpha = x [(1 + x^2)^{1/2} - x]$$

Results obtained using this analysis gave slip distances of about 0.15–1 μ , with slip band widths up to 0.4 μ after 20–30 per cent elongation.

Duplex slip and grain boundary interactions

Duplex slip involving the intersection of two slip systems operating in different slip directions was not frequently observed and when it occurred it seemed to be associated with the formation of lamellar markings (Fig. 8). More often the two systems of slip lines would not intersect but would fade out.

Slip lines were frequently observed to "cross" grain



Fig. 8. Same material and treatment as Fig. 1. Showing duplex slip and lamellated slip bands. ×12,500.

boundaries in a manner similar to that found by Ogilvie⁽¹²⁾ in aluminium and α-brass. The profile of the slip line, obtained by examining the grain boundary kinks formed and their relation to the slip trace, again indicated that slip occurred on a large number of closely spaced planes (Fig. 4). The grain boundary kinks were also observed when the surface was polished and etched after deformation and then were usually more clearly delineated. In addition, the length of boundary at the kink was frequently not etched (Fig. 9).

Where the slip lines did not "cross" the boundary they either faded out or bent round becoming parallel to the boundary (Fig. 10). The effect of slip adjacent to the grain boundary is to depress one grain with

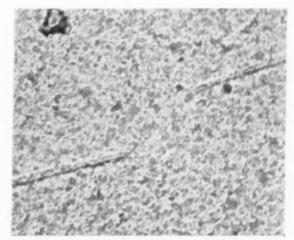


Fig. 9, 99.8% Fe. Furnace-cooled, elongated 20 per cent, polished and etched in 1% nital. Showing grain boundary kink and absence of boundary etching at the kink. ×35,000.

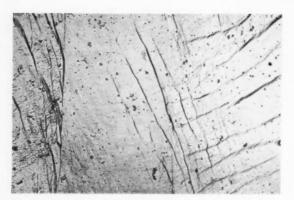


Fig. 10. Same material and treatment as Fig. 1. Composite micrograph showing interaction of slip and grain boundary. Note the absence of slip on one side of the boundary and the short localized slip lines faulted by duplex slip. ×11,333.

respect to its neighbour, and optical examination of many specimens suggests that this accounts for much of the surface rumpling observed during deformation. Similar effects have been observed by Kawada $^{(13)}$ on aluminium tested at $350\,^{\circ}\mathrm{C}$. The strain in the boundary region produced by the deflected slip lines in Fig. 10 is accommodated in the neighbouring grain by short slip lines confined to the neighbourhood of the boundary.

Etch structures

Optical examination of specimens polished and heavily etched after deforming more than about 15 per cent revealed striations very similar in appearance to slip lines (Fig. 11). Electron microscopical examination of the structures showed them to be poor in contrast, but quite clearly indicated the contrast to be due to the etch structure being less



Fig. 11. 99.97% Iron. Deformed to fracture, polished and etched in 1% nital. Showing wavy etch bands. Optical photomicrograph. $\times 2,500$.

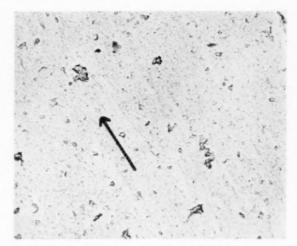


Fig. 12. Same specimen as Fig. 11. The etch bands are not clearly marked but run in the direction of the arrow. ×12,500.

highly developed in these bands than elsewhere (Fig. 12).

Etch structures on iron similar to that in Figs. 4. 5, 9 and 12 have been reported previously, (10.14) and have been attributed either to differential etching at the carbon or nitrogen atmospheres which are believed to surround dislocations, (14) or to small carbide precipitates. (10) As the thin metal films examined in this investigation show no evidence of precipitation and no diffraction effects attributable to precipitates, it is thought that these markings are a result of segregation rather than precipitation. Dislocation atmospheres of interstitial atoms would be expected to produce the observed bump structures, but the density would not be expected to exceed 108-109 cm⁻² of specimen surface. Zener(15) has pointed out that the lattice distortion energy of the iron lattice will be substantially reduced if clustering of interstitial atoms occurs, because if two carbon atoms occupy neighbouring positions in the lattice each will produce some of the distortion which the other would have produced on its own. Zener calculates the binding energy of two carbon atoms occupying neighbouring lattice positions to be 2 kcal/mole of carbon. It is therefore likely that platelets due to Zener clustering will be found, and these may account for the discrepancy between the dislocation density expected in annealed iron and the density of etch structure observed. In addition substitutional impurity atoms will be expected to segregate to edge dislocations and if these segregates are cathodic to the matrix, on etching they will also form bump structures. The major cathodic impurities in the material used in this investigation are 0.01 at. % nickel and 0.005 at. % copper. The electrode potentials of these elements referred to iron as

standard are +0.19 and +0.775 V respectively. It is highly likely therefore that segregates of copper, at least, will show strong etching effects similar to those observed. It can be concluded that the etching effects observed can be accounted for in terms of segregation, both in the form of dislocation atmospheres and in Zener platelets.

While no direct evidence of the nature of the etch bands is yet available it is reasonable to assume that they represent regions in which impurity is more homogeneously distributed than elsewhere. Two reasons can be given for homogeneous etching in banded regions in the deformed material. If the dislocations remaining in the slip bands have no segregate associated with them, and the Zener platelets have been dispersed by slip, then the slip band would be expected to be more readily attacked than the matrix and would etch as a shallow trough. If ageing has occurred and atmospheres have reformed at the dislocations, then the slip band would be less readily attacked than the matrix and a ridge or region of high density should be found.

The poor contrast in the etch bands made it difficult to determine whether or not they were ridges or troughs. However a specimen deformed at 87°C, when ageing should occur, showed much sharper etch bands, some of which were ridges. It is thought therefore that the etch bands produced after deforming at room temperature are due to the absence of impurity segregation in the regions in which slip has occurred. If this is correct then the formation of the etch structure provides a means of comparing the width of the slip bands within the metal with those observed on the surface.

From the specimens examined it is clear that these etch bands normally have thicknesses of the same order of magnitude as the slip bands observed on the surface, and hence it can be concluded that the phenomenon of homogeneous slip is not confined to the surface layers, but occurs in the bulk material.

The examination of thin foils

The surface structures and stress–strain curves found for foils thicker than 50 μ showed the same features as those observed for bulk specimens, but the foils failed after about 10 per cent elongation. Thinner foils failed at successively lower elongations and a 15 μ foil failed intergranularly with no perceptible signs of plastic deformation. Therefore only the results obtained by thinning the 50 μ foil will be described, as this was the thinnest foil whose properties were substantially the same as those of the bulk material.

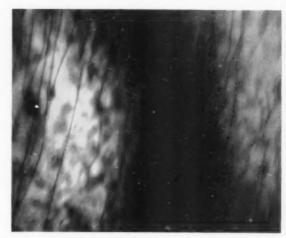


Fig. 13. 99.97% iron rolled to thin foil and polished to 50 μ thick, elongated 10 per cent in tension and thinned for direct examination in electron microscope. Showing a band of dislocations running parallel to an extinction contour. \times 80.000,

The dislocations in the thin films frequently lay in bands whose orientation could be determined by selected area diffraction. Fig. 13 shows a band of dislocations lying in a {111} plane. These bands have been associated with the residual dislocations generated by the original active slip sources, and it is thought that Fig. 13 represents a section perpendicular to the active slip direction. The dislocations have cross-slipped out of the plane in which they were generated and, in the original specimen, would have travelled on numerous slip planes lying perpendicular to the plane of the micrograph to form a diffuse slip band on the surface.

Where bands of dislocations intersect, the resulting structure is a complex, tangled network. Fig. 14 shows such a network formed at the intersection of

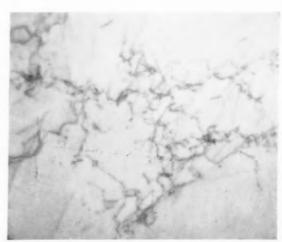


Fig. 14. Same specimen as Fig. 13. Showing complex tangled dislocation network. ×50,000.

dislocations lying on two slip systems. Several dislocations not locked in the network can be seen lying in their original slip planes approximately parallel to the bands. It is easy to see that networks such as this will form obstacles to slip and may therefore be responsible for work hardening. No piled up groups of dislocations similar to those found by Hirsch *et al.*⁽¹⁶⁾ and Whelan *et al.*⁽¹⁷⁾ in face-centred cubic metals have been found in the iron films.

DISCUSSION

Bilby (18) has discussed the operation of "cone" sources of slip, and Suzuki and Fujita(19) have invoked this type of slip source to explain observations on aluminium indicating that some slip bands were "homogeneous"; that is, slip within the bands was distributed over a large number of adjacent slip planes. Diehl et al. (20) have explained the formation of the lamellated slip bands, also observed in aluminium, by assuming that elements of dislocations which have cross slipped and which do not lie in the original slip plane provide locks for the remaining part of the dislocation loop to act as a subsidiary source. Although cross slip of the individual dislocations occurs readily in iron and therefore lamellar slip produced by the mechanism of Diehl and co-workers might be expected, it is not usually found. In the very broad slip bands shown in Fig. 1 there is no evidence of lamellae, and as the resolving power of the replica technique used is better than 30 Å, it seems unlikely that the mechanism postulated by Diehl et al. is operating. A more likely premise is that the dislocations are relatively free to move on whichever plane they lie, and that either cross slip of individual dislocations out of the plane in which they were generated, or the operation of cone sources, leads to the formation of slip bands within which the slip is evenly distributed over many adjacent slip planes.

The wavy dislocation lines in Fig. 13 provide direct confirmation for both the ease of cross slip of the individual dislocations and the occurrence of slip in broad bands. The frequency with which tangled networks of dislocations are observed can also be explained in terms of groups of dislocations travelling in broad bands. A greater volume of the metal is traversed by the moving dislocations than would be the case if many dislocations moved on the same plane, and therefore the chances of forming a network are greatly enhanced. However, if the above deductions are correct the anomalous observations of corrugated slip and of the occasional formation of resolvable slip lamellae remain to be explained.

It is now possible to formulate a qualitative theory of the deformation of polycrystalline iron. Within the grains, slip on single slip systems occurs with ease once the dislocation sources have been torn from their Cottrell atmospheres and are operating freely. Individual dislocations can cross slip readily and the formation of piled up groups of dislocations at barriers to slip does not occur. However the formation of dislocation networks is easier than in face-centred cubic metals and these networks rapidly grow, forming obstacles to slip. In overcoming these obstacles, dislocations either bend round them, to form wavy slip lines, or subsidiary sources may in rare instances come into operation at the obstacles themselves, forming lamellated slip bands on the surface.

At the grain boundaries the dislocations pile up in an irregular array, and therefore the slip lines on the surface appear to fade out as they approach the boundary. Alternatively the dislocations may either be deflected by the boundary or be absorbed into it, then generating more dislocations on the other side of the boundary. In the first case the slip lines are observed to bend round parallel to the boundary as they approach it, so forming a step, while in the second case the slip lines apparently cross the boundary, continuing in much the same direction in the neighbouring grain. Where crossing of the grain boundaries occurs the boundaries are kinked by several thousand Angstroms. This may mean that a high barrier energy has to be overcome, but once slip is initiated in the neighbouring grain it can continue at a reduced stress. The etching effects at boundary kinks (Fig. 9) suggest that this barrier is in part due to segregated impurity in addition to the normal barrier effect due to change in lattice orientation across the boundary.

19

The frequency with which slip lines are observed to be deflected by the boundary is a consequence of the low stress required to make the dislocations cross slip, compared with the stress required to activate new sources in the neighbouring grain. Whether the boundary blocks the dislocations, deflects them, or allows them to continue into the next grain will depend on the relative orientations of the two grains, the angle the operative slip system makes with the boundary and the number of dislocations arriving at the boundary. The severe local strain produced by these interactions between the slip bands and the grain boundaries frequently results in the activation of secondary slip systems only operative in the neighbourhood of the boundary.

Effects similar to the interactions noted here have been observed on face-centred cubic metals. (12.13.21.22.23) These have led Hargreaves (24) to

suggest that the grains of a polycrystalline metal could be subdivided into small regions in which slip is uniform, separated by regions in which slip is not uniformly distributed. Any complete theory of the deformation of polycrystalline aggregates must take into account the continuity of both the stresses and the strains at the grain boundaries. Taylor's theory (25) has taken into account the strain continuity condition, but he has simplified the problem by assuming that the strain is uniform throughout the specimen and this involves discontinuities of stress. Bishop and Hill (26) rigidly adhered to both continuity conditions, but no metallographic predictions can be made from their treatment of the deformation of polycrystals.

More recently Kocks⁽²⁷⁾ has greatly refined Taylor's theory, firstly by assuming that the operative slip systems in polycrystalline specimens are the same as those found on deforming single crystals of certain specific orientations, and secondly by using some of the assumptions made by Bishop and Hill. From the results obtained when deforming single crystals of aluminium under conditions leading to multiple slip, Kocks has been able to calculate the stress-strain curve for polycrystalline aluminium, and the curve he obtained agreed well with that determined by experiment. From the methods used by Kocks no metallographic predictions can be made and in particular no differentiation is made between the properties of the grain boundary regions and the grain interior.

VOL.

1959

The results obtained in this investigation have shown that the influence of the grain boundary may extend over regions of the order of $10~\mu$ across, and may be more if the activation of local slip sources, to produce short localized slip lines, is involved. It is suggested that instead of the sharp stress discontinuity and uniform strain proposed by Taylor and shown in Fig. 15(A), the stress and strain may both be hetero-

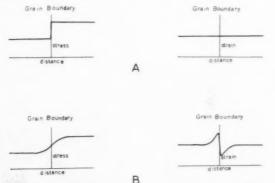


Fig., 15. Stress and strain distributions at a grain boundary.
(A) According to Taylor's theory.

(B) In agreement with the results shown in Fig. 10.

geneous as shown in Fig. 15(B). Such strain distributions are frequently observed and an example is shown in Fig. 10.

CONCLUSIONS

- Slip in iron is, in general, homogeneously distributed over wide bands of material.
- (2) The bands of slip in the interior of the bulk metal can be made visible under certain conditions by etching. The effect is associated with segregation present before deformation, but disturbed during the deformation process.
- (3) Observations on thin films of metal have revealed the dislocation arrangements existing in slip bands, and have confirmed deductions made from surface structures and etch bands.
- (4) Effects observed at grain boundaries have been explained in terms of the behaviour of dislocations as deduced from observations of thin films and surface slip structures.
- (5) A qualitative theory of deformation of polycrystalline iron based on a simple modification of Taylor's theory has been proposed.

ACKNOWLEDGMENTS

The authors would like to thank Professor G. W. Austin for his interest and encouragement and the provision of laboratory facilities.

One of us (D. G. B.) would like to thank the Department of Scientific and Industrial Research for a maintenance allowance during the tenure of which this research was carried out.

REFERENCES

 A. F. Brown, Symp. Metallurgical Applications of the Electron Microscope, p. 103. Institute of Metals, London (1949).
 D. Kuhlman-Wilsdorf and H. Wilsdorf, Acta Met. 1,

394 (1953).

- 3. H. Wilsdorf and J. T. Fourie, Acta Met. 4, 271 (1956).
- H. W. PAXTON, M. A. ADAMS and T. B. MASSALSKI, Phil. Mag. 43, 257 (1952).
- C. S. Barrett, G. Ansel and R. F. Mehl, Trans. Amer. Soc. Metals 25, 702 (1937).
- N. K. CHEN and R. MADDIN, Trans. Amer. Inst. Min. (Metall.) Engrs. 191, 937 (1951).
- F. L. Vogel and R. M. Brick, Trans. Amer. Inst. Min. (Metall.) Engrs. 197, 700 (1953).
- R. P. STEIJN and R. M. BRICK, Trans. Amer. Soc. Metals 46, 1406 (1954).
- N. P. Allen, B. E. Hopkins and J. E. McLennan, Proc. Roy. Soc. A234, 221 (1956).
- J. D. Campbell, J. Duby and K. E. Puttick, *Phil. Mag.* 48, 548 (1957).
- H. FUJITA and Z. NISHIYAMA, Mem. Inst. Soc. Ind. Res. 14, 91 (1957).
- G. J. OGILVIE, J. Inst. Met. 81, 491 (1953).
- 13. T. KAWADA, J. Phys. Soc. Japan 7, 240 (1952).
- 14. F. VAN WIJK, Rev. Univ. des Mines 12, 555 (1956).
- 15. C. ZENER, Phys. Rev. 74, 639 (1948).
- P. B. HIRSCH, R. W. HORNE and M. J. WHELAN, Phil. Mag. 1, 677 (1956).

- M. J. WHELAN, P. B. HIRSCH, R. W. HORNE and W. BOLLMAN, Proc. Roy. Soc. A240, 524 (1957).
 B. A. BILBY, Rep. Conf. Deformation in Solids, p. 124. Physical Society, London (1955).
 H. SUZUKI and F. E. FUJITA, J. Phys. Soc. Japan 9, 531 (1954).
- (1954).
- 20. J. Diehl, S. Mader and A. Seeger, Z. Metallk. 46, 650 (1955).
- 21. K. T. Aust and N. K. Chen, Acta Met. 2, 632 (1954).
- 22. W. Boas and G. I. OGILVIE, Acta Met. 2, 655 (1954).
- 23. J. D. LIVINGSTONE and B. CHALMERS, Acta Met. 5, 322 (1957)

- M. E. Hargreaves, J. Aust. Inst. Met. 1, 125 (1956).
 G. I. Taylor, J. Inst. Met. 62, 307 (1938).
 J. F. W. Bishop and R. Hill, Phil. Mag. 42, 414 and 1298 (1951).
- 27. U. F. Kocks, Acta Met. 6, 85 (1958).

INITIAL OXIDATION RATE OF NICKEL AND EFFECT OF THE CURIE TEMPERATURE*

H. UHLIG,† J PICKETT†‡ and J. MACNAIRN†§

Nickel foil was oxidized for 24 hr periods within the temperature range 307° to 442°C producing NiO films up to 3400 Å thick maximum. A discontinuity in oxide growth is observed at the Curie temperature (353°C). Data obtained at 390°, 394° and 405°C as a function of time show that a two-stage oxide growth rate occurs, a higher rate following an initially lower rate. Both stages are represented by a linear relation between oxide thickness and logarithm of time. Many initial oxidation rate data obtained by other investigators, for Ni and a variety of metals, also follow the two-stage logarithmic equation.

Based on control of the initial oxidation rate by electron transfer from metal to oxide, the discontinuity of oxide thickness at the Curie temperature is explained by an observed work function of nickel slightly higher above the Curie temperature than below. The change of work function also explains a slightly higher activation energy for oxidation above the Curie temperature than below. Calculations show that the density of trapped electrons in a constant density space charge next to the metal surface is 1.3×10^{15} at $390^{\circ}\mathrm{C}$. Density of available sites for trapped charge in a diffuse charge layer, which grows on top of the constant density layer, is the same order of magnitude (5.5×10^{15}) . A higher density of sites for NiO than for Cu₂O, plus a higher work function for Ni than for Cu, are in line with a lower oxidation rate of Ni compared to Cu. It is calculated that contact of oxide with Ni or Cu lowers the work function at the metal-oxide interface by about 0.6 V. This value agrees, in the case of Cu₂O, with the energy required to excite an electron from the filled band to the conduction band.

VITESSE INITIALE D'OXYDATION DU NICKEL ET EFFET DE LA TEMPERATURE DE CURIE

Des feuilles de nickel sont oxydées pendant 24 heures à des températures comprises entre 307 et 442°C. Il se produit un film de NiO d'une épaisseur de 3.400 Å au maximum. Les auteurs observent une discontinuité dans la croissance de l'oxyde à la température du point Curie (353°C). Les résultats obtenus à 390, 394 et 405°C montrent que la vitesse de croissance du film en fonction du temps présente deux stades. Les deux stades peuvent être représentés par une relation linéaire entre l'épaisseur de l'oxyde et le logarithme du temps. Des données sur l'oxydation du nickel et d'autres métaux rapportées par d'autres chercheurs, s'accordent également à la loi logarithmique en deux stades.

La discontinuité de l'épaisseur de l'oxyde à la température de Curie est expliquée, sur la base du contrôle de la vitesse initiale d'oxydation par le transfert d'électrons du métal à l'oxyde, par l'énergie libre du nickel qui est plus élevée au-dessus du point Curie. La variation d'énergie libre explique également une énergie d'activation pour l'oxydation légèrement supérieure au-dessus de la température de Curie. Les calculs montrent que la densité des électrons emprisonnés dans une charge spaciale de densité constante au voisinage de la surface du métal, est de 1,3 × 10¹⁵ à 390°C. La densité des sites disponibles pour la charge emprisonnée dans une couche de charge diffuse, qui croît au sommet de la courbe à densité constante, est du même ordre de grandeur (5,5 × 10¹⁵). Une densité plus élevée des sites pour Ni que pour Cu₂O ainsi qu'une énergie libre plus élevée pour le Ni que pour le Cu, sont en concordance avec la vitesse d'oxydation plus faible de Ni comparée à celle du cuivre. On peut calculer que le contact d'oxyde avec le Ni ou le Cu abaisse l'énergie libre à l'interface métal-oxyde d'environ 0,6 V. Cette valeur est en accord avec l'énergie nécessaire pour exciter un électron de la couche complète à la couche conductrice.

DIE ANFÄNGLICHE OXYDATIONSGESCHWINDIGKEIT VON NICKEL UND DER EINFLUSS DER CURIE-TEMPERATUR

Nickelfolien wurden im Temperaturbereich zwischen 307° und 442°C Oxydationsbehandlungen von jeweils 24 Stunden unterworfen, dabei bildeten sich NiO Filme mit einer maximalen Dicke von 3400 Å. Bei der Curie-Temperatur (353°C) wurde eine Unstetigkeit des Oxydwachstums beobachtet. Messungen des Anlaufverhaltens bei 390°, 394° und 405°C als Funktion der Zeit zeigen, dass das Oxyd in 2 Stufen wächst; auf eine anfänglich geringere Oxydationsgeschwindigkeit folgt eine höhere Geschwindigkeit. Beide Stufen lassen sich durch eine lineare Beziehung zwischen der Oxydaticke und dem Logarithmus der Zeit darstellen. Viele Ergebnisse anderer Autoren über die anfängliche Oxydationsgeschwindigkeit von Ni und einer Anzahl anderer Metalle folgen ebenfalls der zweistufigen logarithmischen Gleichung.

1959

^{*} Received April 28, 1958. This research was jointly supported by the Office of Naval Research and by the Shell Oil Companies in the United States.

[†] Corrosion Laboratory, Department of Metallurgy, Massachusetts Institute of Technology, Cambridge, Massachusetts.

[‡] Present address: Nuclear Metals, Inc., Cambridge, Massachusetts.

[§] Present address: Chrysler Corporation, Detroit, Michigan.

Auf Grund der Annahme, dass der Elektronenübergang vom Metall zum Oxyd die anfängliche Oxydationsgeschwindigkeit bestimmt, wird die Unstetigkeit der Oxyddicke bei der Curie-Temperatur erklärt durch die Austrittsarbeit, die bei Nickel oberhalb der Curie-Temperatur erwiesenermassen etwas grösser ist als unterhalb derselben. Die Änderung der Austrittsarbeit erklärt auch die Tatsache, dass die Aktivierungsenergie der Oxydation oberhalb der Curie-Temperatur etwas grösser ist als unterhalb derselben. Berechnungen zeigen, dass bei 390°C die Dichte der eingefangenen Elektronen in einem Gebiet konstanter Raumladungsdichte in der Nähe der Metalloberfläche 1.3×10^{15} beträgt. Die Dichte der zum Einfangen von Ladungen zur Verfügung stehenden Plätze in einer diffusen Ladungsschicht, die auf der Schicht konstanter Ladungsdichte aufwächst, ist von derselben Grössenordnung (5.5×10^{15}) . Eine grössere Dichte solcher Plätze in NiO als in Cu $_2$ O und die Tatsache, dass bei Ni die Austrittsarbeit grösser ist als bei Cu, sind im Einklang mit der im Vergleich zu Cu geringeren Oxydationsgeschwindigkeit von Ni. Die Rechnung ergibt, dass der Kontakt von Oxyd auf Ni oder Cu die Austrittsarbeit auf der Metall-Oxyd-Grenzfläche um etwa 0.6 V verringert. Im Fall von Cu $_2$ O stimmt dieser Wert überein mit der Energie, die notwendig ist, um ein Elektron aus dem gefüllten Band in das Leitfähigkeitsband anzuheben.

In view of its general applicability to the initial oxidation behavior of many metals, there has been considerable interest in understanding the fundamental basis for the logarithmic oxidation equation:

$$y = k_0 \ln \left(\frac{t}{\tau} + 1\right) \tag{1}$$

where y is the oxide film thickness, t is time, and k_0 and τ are constants. It is significant to the mechanism involved that, under conditions of thin-film formation, the oxidation rate is affected by properties of the base metal itself, such as grain orientation, lattice transformation and Curie temperature. A suitable derivation of the logarithmic equation, therefore, must take these effects into account. When the oxide becomes relatively thick and the rate is controlled by ion diffusion or electric charge migration proportional to oxide thickness, it is well known that the parabolic equation holds instead. Under these conditions, an effect of grain orientation, lattice transformation or Curie temperature is no longer observed.

Data showing that the initial oxidation rates undergo a discontinuity at the Curie temperature were first presented by Tammann and Siebel for Ni-Fe(1) alloys, and later by Uhlig and Brasunas for Cr-Fe alloys. (2) Anomalies at the Curie temperature for the oxidation rate of magnetite, iron, and nickel using a continuous weighing method were reported by Seigneurin and Forestier. (3) They also found anomalies at both the Curie temperatures of 10% Al-Fe and of Fe when this alloy was oxidized, and at the Curie temperature of Fe for non-magnetic 12% Mn-Fe and 14% Mn-Fe alloys. The anomalies for Ni tended to disappear as the heating time was increased, indicating, the authors stated, that diffusion processes through the oxide were apparently not influenced by the Curie temperature of the metal.

Quantitative oxidation rate measurements are presented herewith for nickel, which undergoes a magnetic transformation at 353°C⁽⁴⁾ to 358°C⁽⁵⁾ (Curie temperature). The significance of these data is discussed in relation to a plausible mechanism of thin film formation, and, in addition, factors are discussed bearing on the inherently greater oxidation resistance of nickel as compared, for example, with copper.

PROCEDURE

Oxidation tests were carried out in a silica tube inserted into a horizontal furnace maintained at $\pm 1.5^{\circ}\mathrm{C}$. Specimens of nickel foil 0.025 cm thick, measuring 15.2×10.2 cm were coiled into a spiral. The coil rested on a semi-cylindrical cradle of nickel sheet fitted with spot-welded Chromel wire supports at both ends. The nickel specimens made contact with the wire only. Oxygen gas, dried by towers of anhydrous calcium sulfate and phosphorus pentoxide passed at the rate of 200 ml/min through a small diameter glass tube into the rear or closed end of the silica tube, thereby becoming pre-heated before reversing direction and passing over the nickel.

19

Before weighing, specimens were degreased in hot benzene, pickled in 1 vol. conc. HNO₃ to 1.5 vol. H₂O at 80°C, washed, then immersed respectively in acetone and benzene. They were then heated in wet hydrogen for a minimum of 41 hr at 1000°C. This was an important step in the procedure because it removed traces of oxidizable impurities, probably carbon, which when present oxidize at low temperatures in preference to nickel and account for either little or no weight gain as compared with the hydrogentreated samples. Specimens were then heated in vacuum at 1000°C for 1½ hr to remove hydrogen. They were subsequently pickled in 15 vol. % HNO3-5 vol. % HF at 80°C to remove superficial oxide, washed, and immersed in acetone, then benzene. It was important to handle the specimens with tongs during and after pickling. Possible spalling of oxide was observed by lining the nickel cradle with aluminum

foil and weighing any material that collected there during the tests. In general, spalling was not found to be a problem, within the temperatures and times studied, for oxide films the maximum thickness of which was about 3400 Å.

Two sources of nickel were employed. The first was a commercially pure Type A nickel foil containing deoxidizers such as magnesium and small amounts of cobalt and other impurities normal to such material The second was a limited amount of high purity nickel foil* which had been produced by electroplating from purified nickel chloride solution. This was reported as better than 99.99% Ni exclusive of O_2 (about 0.01%) and H_2 . It was also subjected to a preliminary wet H_2 treatment. Oxidation tests were carried out at various temperatures for a total time of 24 hr at each temperature. In addition, a number of isothermal oxidation tests were carried out as a function of time within the temperature range $390^\circ-405^\circ\mathrm{C}$.

RESULTS

The logarithm of weight gain as a function of reciprocal absolute temperature is plotted in Fig. 1. Since NiO seems to be the only oxide that forms within the presently considered temperature range, (6) the corresponding density of 7.45 gives a conversion factor, uncorrected for roughness factor of the metal surface, of 626 by which mg/dm² should be multiplied in order to convert to oxide thickness in Angstrom units (Å).

VOL.

1959

It will be observed that a definite discontinuity occurs between points at 345° and 357°C. This region corresponds to the Curie temperature of nickel.

A second discontinuity occurs at about 395°C for commercial nickel. The cause of this discontinuity is not known, but it is probably related to the presence of impurities normal to commercial nickel. High purity nickel does not show a similar break in oxidation behavior at this temperature.

The logarithmic oxidation equation is obeyed in the region of 400°C as data of Fig. 2 show. Each point represents one specimen oxidized from zero time to the recorded time. It will be observed that two slopes characterize the weight-gain/time dependence, a higher rate following an initially lower rate.

The discontinuous jump from the lower to the upper slope for data obtained at 394° and 405°C suggests that a few points on the lower slope may actually occupy either of two positions beyond the intersection of the two slopes; that is they can follow the lower slope for a limited time beyond the intersection, or follow instead the upper slope, depending on accidental factors of oxide growth. The specific time at which the oxidation rate changes from the 1st slope to the 2nd slope is not particularly reproducible either for Ni or for our data on Cu obtained earlier, although the observed time at which the break occurs is consistently much longer for Ni than for Cu.

There is little question but that the logarithmic equation holds similarly within the temperature range encompassed by data of Fig. 1. Tammann and Köster⁽⁷⁾ were the first to show that this equation applies to nickel oxidized in the temperature range 485°-645°C. Campbell and Thomas⁽⁸⁾ showed that oxidation of Ni follows the logarithmic equation up to 302°C. Replotted data of Gulbransen and Andrew⁽⁹⁾ indicate that the logarithmic equation

^{*} Supplied by courtesy of W. A. Wesley, International Nickel Company.

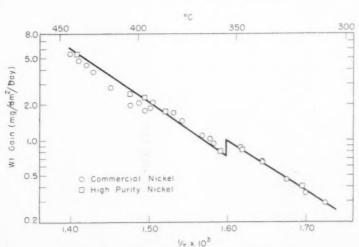


Fig. 1. Weight gain of nickel in oxygen, 24 hr exposure.

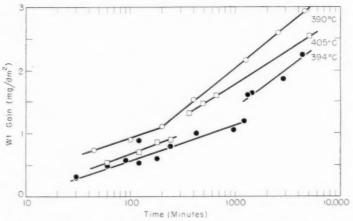


Fig. 2. Weight gain of commercial H₂-treated nickel at elevated temperatures in oxygen as a function of time.

applies up to 500°C ;⁽¹⁰⁾ at higher temperatures the parabolic equation holds.

The replotted data of Gulbransen and Andrew (Fig. 3) also exhibit a two-stage logarithmic oxidation behavior; the change in oxidation rate at 475°C, for example, occurs after about 12 hr. Data of Campbell and Thomas show a break after 50 min at 302°C. Similarly data of Engell et al., (11) who measured the oxidation rate of Ni at 400°C, at 30 to 240 mm Hg oxygen pressure, show a higher rate after 7.5 to 20 hr. They expressed their results in accord with the cubic oxidation equation, but their data can also be represented adequately by a two-stage logarithmic relation as replotted in Fig. 3. Considering the facts that (1) various data for Ni reported so far were obtained at differing pressures, and (2) the inherent difficulty of reproducing initial oxidation

rates because of variable surface roughness factor and surface impurities, data of Figs. 1 and 2 are reasonably consistent with reported weight gain or oxide thickness values by other investigators.

The two-stage logarithmic behavior is characteristic of the thin film behavior not only of Ni, but of several other metals, including copper, (7,8,12,13,14) iron (7,15) and zinc. (16) For example, data of Gulbransen and Andrew (17) on cobalt, replotted in Fig. 3, show an increased rate after 20 min oxidation at 500°C, and after 40 min at 400°C, within which temperature range the logarithmic equation is valid.

19

Because the logarithmic equation is obeyed, plotting log wt gain is equivalent to plotting log reaction rate constant vs. 1/T. This makes it possible to calculate activation energies from data of Fig. 1. Above the Curie temperature, favoring data for the

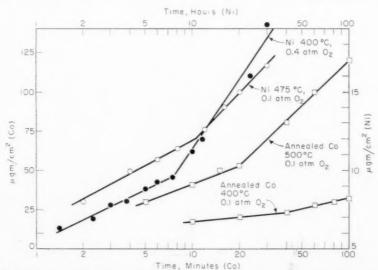


Fig. 3. Weight of oxygen reacting with Ni or Co as a function of time at elevated temperatures. $\Box \bigcirc$ Gulbransen and Andrew⁽⁹⁾⁽¹⁷⁾ \bullet Engell, Hauffe and Illschner⁽¹¹⁾

higher purity nickel, the activation energy is found to be 21,000 cal/mole. Below the Curie temperature, the activation energy is lower, namely 19,900 cal/mole.

DISCUSSION

By assuming a drift velocity of ions in the oxide proportional to an exponential power of the electric field within the oxide, and assuming a constant potential difference across the oxide, Cabrera and Mott⁽¹⁸⁾ derived the inverse logarithmic equation $1/y = A - \ln t$. This equation was shown by Young et al. to be applicable to some but not all of their oxidation rate data on Cu at 70° and 159° C. (19) Rhodin⁽²⁰⁾ stated that his data on oxidation of copper were also in accord, but plots of his data for the cubic face showed conformance as well to the logarithmic equation up to 50° C and to the cubic equation at 80° C, the latter data also being represented adequately by a two-stage logarithmic equation.*

Mott and Cabrera also discussed conditions of ion diffusion which lead to the cubic equation. Earlier, Mott⁽²¹⁾ derived the logarithmic equation based on the quantum mechanical tunnel effect for electrons, but this model applies only to very thin films and not to the extent of observable film thickness for which the logarithmic equation is valid. In addition, the correct temperature dependence of the oxidation rate was not obtained.

1959

Grimley and Trapnell,⁽²²⁾ by assuming a constant field instead of constant potential difference across the oxide, derived the logarithmic equation for a *p*-type oxide when transport of metal ions in the oxide is rate-determining, and the linear equation when a surface reaction is rate-determining. For an *n*-type oxide, the linear equation only was obtained for either control by ion transport or surface reaction. In practice, however, the logarithmic equation may also apply to an *n*-type oxide, as for example in the oxidation of zinc. They also discussed growth equations when ion drift velocity is proportional to the field, leading, under specific conditions, to derivation of the cubic equation.

Derivations of Cabrera and Mott, and of Grimley and Trapnell fall short of explaining a change in activation energy for oxidation at the Curie temperature. It is also difficult to reconcile their proposed mechanisms of oxidation with the appreciable effect of grain orientation and transformation of metal lattice. These particular effects were discussed in a fundamental analysis of the initial oxidation rate by one of us. (14) According to this analysis, electron transfer from metal to oxide at the metal-oxide interface is an important controlling step in the process. Since the work function of a metal varies with crystal face and lattice type, and is higher above than below the Curie temperature, for Ni at least, an explanation for the effect of the base metal on oxidation behavior is made clear. It is also clear that there may be circumstances under which the controlling reaction differs, as perhaps in the case of copper below 150°C where very thin films are formed. A change in the activation energy for the initial oxidation rate of Cu is indicated, for example, by data of Lustman and Mehl(12) between about 105° and 130°C which suggests that the oxidation mechanism may change in this region. But above 150°C up to the temperature where diffusion and migration processes in the oxide become controlling and lead to the parabolic equation, the rate-controlling step appears to be electron transfer. This is also apparently the case for nickel in the range of temperatures presently considered.

Electron transfer control of the initial oxidation rate is dependent on an increasing space charge in the oxide accompanying oxide growth. Measured Volta potentials confirm a more negative (or less positive) total space charge as oxidation proceeds. Trapped electrons saturate impurity and imperfection sites resulting first in a constant density space charge. After the oxide reaches a given thickness, sites are no longer saturated and a diffuse space charge layer forms instead, similar to the diffuse double layer adjacent to a metal surface in an aqueous electrolyte. Both space charge layers induce potentials at the metal-oxide interface which slow down the ratecontrolling electron transfer step in the oxidation process, but the diffuse layer is less effective in this regard per unit film thickness, than is the constant density layer. Hence oxidation proceeds in two stages, an initial rate being followed by a higher rate as is observed. The positive potential accounting for electron transfer from metal to oxide is approximated by the electron affinity of atomic oxygen (3.4 eV) chemisorbed on the oxide at the oxide-O, interface. This model of thin film oxidation behavior leads to the logarithmic equation described earlier for which k_0 and τ can be calculated in terms of certain fundamental properties of metal and oxide.

According to electron transfer control, the activation energy for initial oxidation is equal to $e(\phi-v)$ during formation of the constant charge density oxide, and to $4\pi ne^2lL/\varepsilon + e(\phi-v)$ for the diffuse charge layer, where ϕ is the work function of the

^{*} It appears to be general that reported initial oxidation rate data can be fitted in some degree and equally well either to the cubic equation or to the two-stage logarithmic equation.

metal as modified by contact with the oxide, v is the positive potential at the metal-oxide interface approximated by the electron affinity of oxygen, e is the electron charge $(4.80 \times 10^{-10}~{\rm e.s.u})$, ε is the dielectric constant of the oxide, n is the density of sites for trapped electrons in the constant density space-charge layer, L is the maximum observed thickness of the constant density space-charge layer, and l is the theoretical maximum thickness to which the constant density space-charge layer can grow in absence of a diffuse layer. In other words, the total space charge per unit area of oxide equivalent to thickness l and electron density n would induce a potential at the metal surface equal and opposite to v.

If ϕ_0 is the work function of the metal, it can be considered that $\phi = \phi_0 - \chi$, where χ is a constant equal to the amount ϕ_0 is modified by contact of oxide with metal. Furthermore, l, L, n, v and ε are independent of ϕ_0 . On this basis, if there is a change of work function $\Delta\phi_0$ at the Curie temperature, as has been reported, (23,24) the activation energy above and below the Curie temperature should differ by $e\Delta\phi_0$. The observed difference of activation energies (Fig. 1) equal to 21,000 - 19,900 =1.100 cal/mole is equivalent to 0.048 eV, or a change in work function $\Delta\phi_0$ of about 0.05 V. This change is consistent with the limited quantitative data on the discontinuous change in work function for nickel at the Curie temperature reported by Cardwell. (23)

The discontinuous decrease of oxide thickness just above the Curie temperature is also predicted on the basis of a change in work function. Since the 24 hr oxidation times of Fig. 1 correspond to times beyond the first stage of oxidation, or to formation of the diffuse charge density layer, the oxidation equation becomes:

$$y = k_0' \ln \left(\frac{t}{\tau'} + 1 \right) \tag{2}$$

where τ' is the time at which the diffuse charge density oxide layer begins to form, and k_0' corresponds to the second higher slope on plotting y vs. $\ln t$. At constant time t,

$$dy = \frac{k_0' d\tau'}{t + \tau'} - \frac{k_0'}{\tau'} d\tau' \tag{3}$$

where, as derived formerly, (14)

$$\tau' = \frac{k_0'}{A} \exp \frac{-C_0 e}{kT} \tag{4}$$

A is a constant, and C_0 has the value $-4\pi nelL/\varepsilon - (\phi - v)$. Because all terms are independent of the

work function ϕ , it follows that:

$$d\tau' = \frac{\tau'e}{kT} d\phi \tag{5}$$

and
$$-dy = \frac{k_0'e}{kT} \left[\frac{t}{t+\tau'} \right] d\phi \tag{6}$$

The above equation predicts that if oxidation is carried out to time t, an increase of work function $\Delta \phi$ (or $\Delta \phi_0$) at t will be accompanied by a decrease of oxide thickness Δy . From Fig. 1, Δy at the Curie temperature is equal to 0.26 mg/dm² or 163 Å. The value τ' from Fig. 2, which is the time at which the higher slope begins, is not readily reproducible experimentally, but averages about 250 min. Correspondingly, t = 1440 - 250 = 1190 min measured from the beginning of the higher rate. If $\Delta \phi_0$ is taken as 0.05 V at 353°C , k_0' is calculated equal to 210 Å. From Fig. 2, the average of slopes for the second stage of oxidation, equal to $2.303k_0$, is 1.20 mg/dm². This is equivalent to a value of k_0 of 325 Å at approximately 400°C, which compared to 210 Å at 353°C is the right order of magnitude. In other words, the quantitative agreement of equation (6) with experiment is reasonably good.

From the relation described in the earlier reference $^{(14)}k_0=\varepsilon kT/4\pi ne^2l$, it is possible to calculate nl, where n is the density of sites for trapped charge in the constant density space charge layer. Accordingly, from data at 390°C in Fig. 2, $k_0=152\,\text{Å}$, and assuming that $\varepsilon=12$, it is found that $nl=2.5\times10^{11}$. Furthermore, it was shown that

19

$$v = 2\pi nel^2/\varepsilon$$
,

hence taking an average empirical value: $v=3.6~{\rm eV}$ based on data for several metals and carbon, $^{(14)}$ $l=1.9\times 10^{-4}~{\rm cm}$ and $n=(2.5\times 10^{11})/(1.9\times 10^{-4})=1.3\times 10^{15}$. This value for the density of trapped charge in the constant density layer at 390°C is larger than the corresponding value 0.6×10^{14} calculated previously for copper at $250^{\circ}{\rm C}$, $^{(14)}$ and which value extrapolated to 390°C is still smaller, namely 1.0×10^{13} .

The value for the density n_o of available sites for trapped charge in the diffuse layer, all of which are not filled, can be calculated from the relation:

$$k_0{'} = \frac{x_0}{2} \left(\frac{kT}{-C_0 e} \right) \quad \text{where} \quad x_0 = \left(\frac{\varepsilon kT}{2\pi n_0 e^2} \right)^{1/2}$$

From Fig. 2, $k_0{}'$ at 390°C = 365 Å, and from Fig. 1, $-C_0e=0.91$ eV (21,000 cal/mole); therefore $n_0=5.5\times10^{15}$. Hence n and n_0 are the same order of magnitude. This value for n_0 at 390°C is also appreciably higher than the corresponding value 1×10^{11}

obtained by extrapolation of data for Cu₂O to the same temperature. It should be noted that values for n_0 , and also for n, would be somewhat smaller if corrected for the roughness factor of the metal surface.

From the activation energy $-C_0e$, the following relation holds:

$$\frac{4\pi ne^2lL}{\varepsilon} + e(\phi - v) = \frac{0.91}{300}$$

where L is thickness of oxide at the beginning of the second oxidation stage (L = 690 Å at 390°C). The first term is calculated equal to 0.26 eV, and hence $(\phi - v) = 0.65 \,\mathrm{V}$. Taking the averaged work function ϕ_0 for nickel = 4.8 V, (25) the value of

$$\phi_0 - (\phi - v) = K = 4.1 \text{ V}.$$

This value is more nearly correct than the value 3.6 eV given in the earlier reference(14) where the observed activation energy was assumed to correspond to the first stage of oxidation, rather than to the second stage which actually applies, as seen from data of Fig. 2. The corresponding value of $\phi_0 - (\phi - v)$ calculated for copper is 4.2 V.

It is apparent that since k_0 is inversely proportional to nl, the lower value of k_0 for nickel compared to copper is due in part to a higher density of trapped electrons in the constant density space charge of NiO than in Cu₂O. Furthermore, since the dominant term for τ is exp $e(\phi - v)/kT$, the larger value of τ for Ni is the result of a higher value for $e(\phi - v)$. namely 0.65 relative to 0.28 eV for Cu. Both factors account for a lower initial oxidation rate of nickel compared to copper.

VOL.

1959

Similarly in the diffuse charge density layer, k_0 is inversely proportional to $n_0^{1/2}$, where n_0 is orders of magnitude larger for NiO than for Cu₂O. Furthermore, k_0' is also inversely proportional to $-C_0e$, but since $-C_6e = 0.91 \text{ eV}$ for Ni and 0.42 eV for Cu, the ratio is only 0.91/0.42 = 2.2. Hence the smaller ko' value for Ni is accounted for largely by the increased density of available sites for trapped charge in NiO. The value of τ' is determined largely by the value of $\exp{-C_0e/kT}$ and hence is larger for Ni than for Cu. Both smaller k_0' and larger τ' account for the lower oxidation rate of Ni compared to Cu in the second stage of the logarithmic oxidation process.

The larger value of $(\phi - v)$ for Ni than for Cu is apparently due to the larger work function for Ni. If reasonable weight can be placed on reported average values for work functions, it is possible to calculate the contribution χ of the oxide to the work function of the metal covered by oxide, from the relation mentioned earlier: $\phi = \phi_0 - \chi$. Calculated values for γ are listed as follows:

$$\begin{array}{ccccc} (\phi-v) & \phi & \phi_0^{(25)} & \chi \\ & (v=3.6~{\rm V}) & \\ {\rm Ni} & 0.65{\rm V} & 4.25~{\rm V} & 4.84~{\rm V} & 0.59~{\rm V} \\ {\rm Cu} & 0.28 & 3.88 & 4.47 & 0.59 \end{array}$$

The coincidence of values of χ for Cu₂O and NiO is probably fortuitous, but the equality of y to the energy necessary to excite an electron from the filled band of Cu₂O to the conduction band, reported as equal to 0.6-0.7 V, (26) may be significant.

REFERENCES

- 1. G. Tammann and G. Siebel, Z. anorg. Chem., 148, 297
- 2. H. Uhlig and A. des. Brasunas, J. Electrochem. Soc., 97, 448 (1950).
- 3. L. Seigneurin and H. Forestier, C. R. Acad Sci., Paris 243, 2053 (1956).
- 4. Metals Hawlbook, Amer. Soc. Metals, Cleveland, Ohio (1948).
- Amer, Institute of Physics Handbook, p. 5–208, McGraw-Hill, New York (1957).
- E. Gulbransen and J. Hickman, Trans. Amer. Inst. Min. (Metall.) Engrs. (Inst. Metals Div.) 171, 306 (1947).
 G. Tammann and W. Köster, Z. anorg. Chem., 123,
- 196 (1922).
- W. Campbell and U. Thomas, Trans. Electrochem. Soc., 91, 623 (1947).
- E. GULBRANSEN and K. Andrew, J. Electrochem. Soc., 101, 128 (1954).
- P. Landsberg, J. Chem. Phys. 23, 1079 (1955).
- 11. H. ENGELL, K. HAUFFE and B. Illschner, Z. Electrochem., 58, 478 (1954).
- 12. B. LUSTMAN and R. MEHL, Trans. Amer. Inst. Min. (Metall.) Engrs. (Inst. Metals Div.) 143, 246 (1941).
- R. TYLECOTE, J. Inst. Met., 78, 327 (1950).
- H. H. Uhlig, Acta Met., 4, 541 (1956).
- B. Lustman, Truns. Electrochem. Soc., 81, 359 (1942).
 W. Vernon, E. Akeroyd and E. Stroud, J. Inst. Met., 65, 301 (1939).
- 17. E. Gulbransen and K. Andrew, J. Electrochem. Soc., 98, 241 (1951).
- N. Cabrera and N. Mott, Rep. Progr. Phys., 12, 163 (1949).
- 19. F. Young, J. Cathcart and A. Gwathmey, Acta
- Met., 4, 145 (1956). 20. T. RHODIN, J.A.C.S., 72, 5102 (1950); Ibid. 73, 3143 (1951)
- 21. N. F. Mott, Trans. Faraday Soc., 35, 1175 (1939).
- 22. T. GRIMLEY and B. TRAPNELL, Proc. Roy. Soc., A 234, 405 (1956).
- A. B. Cardwell, Phys. Rev., 76, 125 (1949).
 G. Spivak and A. Gel'berg, Doklady Akad. Nauk, SSSR, 94, 455 (1954).
- 25. H. Michaelson, J. App. Phys., 21, 536 (1950).
- 26. N. MOTT and R. GURNEY, Electronic Processes in Ionic Crystals, p. 163-4, 189. Oxford Press (1940).

THE FORMATION OF SURFACE PITS BY THE CONDENSATION OF VACANCIES*

P. E. DOHERTY and R. S. DAVIS+

Small surface pits were observed to form on electropolished surfaces of aluminum single crystals during cooling from elevated temperatures. The amount of cooling required before the pits began to form increased exponentially as the holding temperature decreased. Pits did not form in the vicinity of sub-boundaries or grain boundaries. The width of the pit-free region at the boundary increased with decreasing cooling rates. The formation of pits during cooling is attributed to the condensation of vacancies at the specific location of the free surface. Apparently a definite and constant supersaturation of vacancies is required before condensation begins.

LA FORMATION DE PIQURES DE SURFACE PAR LA CONDENSATION DE LACUNES

Les auteurs observent de petites piqûres de surface sur la surface polie électrolytiquement de monocristaux d'aluminium, pendant le refroidissement à partir de températures élevées. L'importance du refroidissement nécessaire avant la formation de piqûres augmente d'une manière exponentielle lorsque la température de diminue. Les piqûres ne se forment pas au voisinage des sous-joints ou des joints. La largeur de la région aux joints des grains exempte de piqûres augmente lorsque la vitesse de refroidissement diminue. La formation de piqûres pendant le refroidissement est attribuée à la condensation des lacunes à des endroits spécifiques de la surface libre. Apparemment, une sursaturation définie et constante des lacunes est nécessaire avant que la condensation ne commence.

DIE BILDUNG VON OBERFLÄCHENGRÜBCHEN DURCH DIE KONDENSATION VON LEERSTELLEN

Auf den Oberflächen von elektrolytisch polierten Aluminium-Einkristallen wurde die Bildung von kleinen Oberflächengrübehen während des Abkühlens von erhöhten Temperaturen beobachtet. Der Betrag der Abkühlung, der zur Einleitung der Grübehenbildung notwendig war, nahm mit abnehmender Haltetemperatur exponentiell zu. In der Umgebung von Subgrenzen oder Korngrenzen bildeten sich keine Grübehen. Die Ausdehnung der grübehenfreien Bereiche an den Grenzen nahm mit abnehmender Kühlgeschwindigkeit zu. Die Bildung der Grübehen während der Abkühlung wird der Kondensation von Leerstellen an bestimmten Stellen der freien Oberfläche zugeschrieben. Zur Einleitung der Kondensation ist offensichtlich eine bestimmte und konstante Übersättigung an Leerstellen notwendig.

INTRODUCTION

Vogel et al.⁽¹⁾ have shown that the intersection of edge dislocations with the free surface of germanium single crystals may be revealed by chemical etching. Subsequent work has shown that screw dislocations may be revealed by the same technique but the type of dislocation affects the size of the etch pit.⁽²⁾ Similar direct observations have been reported for many materials.

Hendrickson and Machlin⁽³⁾ have thermally etched silver single crystals and observed etch pits which they associated with dislocations. However, Hirth and Vassamillet⁽⁴⁾ concluded from a direct comparison of etch pit densities and dislocation densities measured by a double crystal spectrometer technique that an unequivocal correlation between thermal etch pits and dislocations does not exist in silver. Although a reliable etch pit technique has not been developed for aluminum the formation of

dislocation etch pits in this material by chemical etching $^{(5)}$ and thermal etching $^{(6)}$ has been reported.

This investigation is an outgrowth of an attempt to develop a reliable thermal etch pit technique for aluminum.

EXPERIMENTAL

The single crystals were prepared by seeded horizontal growth from the melt. (7) The initial specimen size was $\frac{7}{8} \times \frac{7}{8} \times 8$ in. The specimens were annealed for an extended period at 640°C and furnace cooled. The Schultz (8) back reflection technique was used to determine the perfection of the crystals. Only those specimens whose sub-grain size exceeded about 2 mm were used. The specimens were subsequently electropolished in a solution of 5 parts methanol to 1 part perchloric acid; the current density was approximately 16 A/dm² with the solution temperature maintained below -10° C.

Observations of the individual pits were made by standard optical techniques. A special furnace was constructed so that the surface of the specimen could

^{*} Received May 2, 1958.

[†] Division of Engineering and Applied Physics, Harvard University.

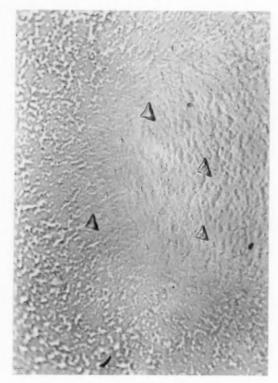


Fig. 1. Typical pits (bounded by $\{111\}$ planes). $\times 1137.5$

be observed during heating and cooling. With suitable lighting the presence of pits only $0.5~\mu$ in diameter could be detected without optical aid. This is presumably due to their strong crystallographic morphology as illustrated in Fig. 1 (the pits are bounded by (111) planes).

OBSERVATIONS AND DISCUSSION

Pits were observed on the electropolished surface of aluminum single crystals as the result of heating to an elevated temperature and cooling. Pits typical of a region remote from sub-boundaries are shown in Fig. 1. Fig. 2 shows pits that have formed along a very small angle boundary (less than 1'). The density of pits observed in regions free from sub-boundaries was approximately $2\times 10^7\,\mathrm{cm}^{-2}$.

These pits are formed only during cooling from an elevated temperature and not during heating or while the specimen is held at a constant temperature. A definite temperature drop, ΔT , is required before the first pits are observed. The value of ΔT for a particular specimen increased with decreasing holding temperature, T_h as shown in Fig. 3a. The data are plotted in Fig. 3b as $\ln \Delta T$ vs. $1/T_{\rm abs}$. In general, new pits form and existing pits grow on cooling below $T_h - \Delta T$.

The formation of pits on cooling a specimen from an elevated temperature suggests the condensation of vacancies (Schottky defects) at particular points on the surface. If a finite and constant value of supersaturation of vacancies is required before pits will nucleate and grow, the results in Fig. 3 may be understood qualitatively.

The concentration of vacancies in a crystal, N_e , as a function of holding temperature, T_h has the form

$$N_v = N \exp\left(-Q_F/RT_{h(abs)}\right) \tag{1}$$

where N is the total number of atoms per unit volume in the crystal, Q_F is the activation energy for formation of a vacancy in cal/g atom, and R is the gas constant. The supersaturation of vacancies required for nucleation, of the pits in terms of ΔN_v , the excess concentration of vacancies above the equilibrium value, is given by

$$\begin{split} N \exp{(-Q_F/RT_h)} - N \exp{[-Q_F/R(T_h - \Delta T)]} \\ = \Delta N_v \quad (2) \end{split}$$

This may take the form:

$$\begin{split} \exp\left(-Q_F/RT_h\right) &= \exp\left[-Q_F/R(T_h - \Delta T)\right] \\ &= \text{a constant} \quad (3) \end{split}$$

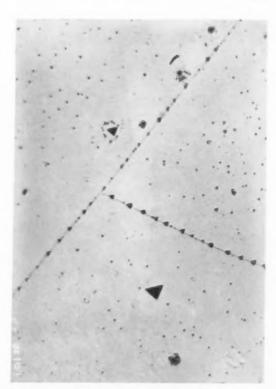


Fig. 2. Pits as formed on sub-boundaries with a misorientation less than 1'. \times 1137.5

VOL. 7 1959

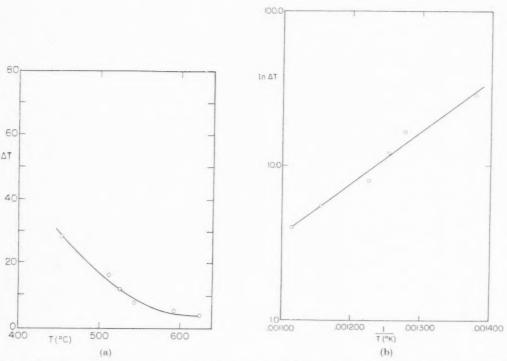


Fig. 3. The decrease in temperature required to form pits, ΔT , as a function of holding temperature T_h is plotted in (a). In (b) the results are plotted as $\ln \Delta T$ vs. $1/T_h(abs)$.

A value for Q_F of 17,500 cal/g atom was obtained by Bradshaw and Pearson⁽⁹⁾ from resistivity measurements on aluminum after quenching. Table 1 contains the values of the constant in equation (3) for the six holding temperatures and their respective values for ΔT (reported in Fig. 3) when $Q_F=17,500$ cal/g atom.

TABLE 1					
T_h	$\frac{\Delta T}{(^{\circ}\mathrm{C})}$	Constant ($\times 10^{-6}$)			
453	28.5	2.3			
511	16.5	3.0			
525	12.0	2.7			
543	8.0	2.2			
592	5.5	2.6			
625	4.0	2.5			

The hypothesis that the pits form by the condensation of vacancies at particular points on the surface, and that nucleation is required, gains additional support from the following observations:

(1) Pits do not form in the vicinity of small or large angle grain boundaries. Fig. 4a is a photomicrograph of the surface of a single crystal that

has been heated to an elevated temperature and air cooled. Fig. 4b is a photomicrograph taken in the vicinity of one of the lines that appear in Fig. 4a. The lines appear dark due to the absence of pits in this region. Fig. 4c is a single spot of a Laue backreflection photograph, taken by the Schultz technique, in the same area as 4a. There is a one-to-one correspondence between the lines in 4a and the boundaries revealed in 4c. Apparently a boundary acts as a sink for vacancies. The width of the region affected increases with decreasing cooling rate from a particular holding temperature. A value for Q_M , the activation energy for the movement of vacancies, may in principle be obtained from a quantitative investigation of this phenomenon or of the rate of growth of individual pits. The appropriate measurements are being made. If a reasonable value for Q_M is assumed (12,000 cal/g atom⁽⁹⁾) and if D_0 is assumed to equal unity, the value for D, which defines the rate of flow of vacancies in the lattice, is approximately 10^{-4} cm² sec⁻¹, at 600°C. A point 0.1 mm from the boundary will, after a drop in temperature to 600°C, nearly reach the equilibrium concentration of vacancies in 0.1 sec. The observed region that is affected by the boundary is, therefore, not unreasonable.

19

(2) The growth process of pits is, to some extent,



Fig. 4a. A photomicrograph of the electropolished surface of an aluminum crystal after heating to 600°C and air cooling. ×4.4

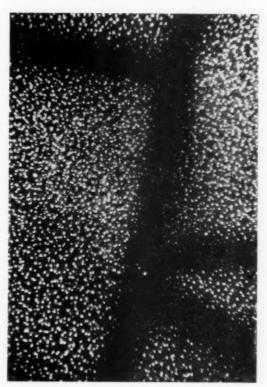


Fig. 4b. A photomicrograph taken in the vicinity of a few of the dark lines visible in 4(a). ×231.25.

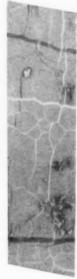


Fig. 4c. A Laue back-reflection spot taken by the Schultz technique in the same region as 4(a). The misfit of the sub-boundaries range between 10' and 1°. × 3.5 approx.

reversible. If a specimen is heated to an elevated temperature T_h and cooled to just below $T_h - \Delta T$, so that a few small pits are formed, and then reheated to T_h the pits disappear. On further cooling the ΔT required for formation of pits is negligibly small. If the specimen is heated to T_h and cooled considerably below $T_h - \Delta T$, on reheating to T_h they do not completely disappear. If this latter case is repeated several times, a few pits will grow. It is suggested that the pits act as sources of vacancies during heating; although this "filling in" process does not return the surface to its original (as electropolished) condition.

- (3) Repeated thermal cycling over a temperature range slightly less than ΔT , will not produce pits. This confirms the hypothesis that there is a minimum supersaturation of vacancies required before the pits will nucleate.
- (4) If a few pits are produced on the surface by chemical etching and the specimen is thermally cycled, new pits will not form in a considerable area around

each previously existing pit. Apparently an existing pit, even if formed chemically, acts as a sink for vacancies, and, therefore, the supersaturation of vacancies in a local volume does not reach the level required for nucleation of new pits. Fig. 5 illustrates this effect in the case of a surface imperfection that was present after electropolishing.

(5) If a specimen is deformed plastically and then thermally cycled the ΔT required for the formation of pits is markedly increased over that required before deformation. This is reasonable if the excess vacancies produced during the cooling part of the cycle were used up in dislocation climb which would allow dislocations to leave their high energy position on a slip plane. Attempts to "quench in" the vacancies were apparently successful in that water quenching from an elevated temperature did not produce observable pits. However, a specimen of the size and shape used in this investigation deformed to a considerable extent during water quenching. Pits did not form on subsequent heating; the excess

VOL. 7 1959

Fig. 5. The large pit near the center of this photomic rograph was present before the smaller pits were formed by air cooling from 600 °C. $\times\,231.25.$

vacancies were presumably used up in dislocation climb.

(6) For the case of a specimen heated to 450° C and air cooled the estimated number of vacancies required to produce a pit was about 6×10^{8} . The observed pit density was 10^{6} cm⁻². If one assumes that the depth of material that contributes vacancies to pits is approximately half the thickness of the region at the boundary that was free of pits (0.005 cm).

$$\Delta N_{vp}/N^*=6\times 10^{-5}$$

where ΔN_{ep} is the total number of vacancies that condense in the pits and N^* is the total number of atoms in the estimated volume drained by a pit. This calculation is for a case where the measured temperature drop for formation of pits was 125°C. If it is assumed that the pits did not grow below this temperature

$$\Delta N_{v\,p}/N^*=5\times 10^{-6}$$

from equation (2).

(7) Although it has not been definitely established that each pit corresponds to a point of emergence of a dislocation at the surface, the experimental results strongly suggest that such a correlation exists.

It has been established that a one-to-one correlation between dislocations and pits does not always occur. For example, the density of pits decreases somewhat with a decreasing holding temperature or a decreasing cooling rate from a particular temperature. These observations suggest a difference in the nucleating power of the various sites on the surface rather than a difference in the rate of growth of the pits.

CONCLUSIONS

The condensation of vacancies at particular points on carefully electropolished surfaces of aluminum single crystals accounts for the observed pit formation on cooling from elevated temperatures. A definite supersaturation of vacancies is required for the nucleation of pits.

It may be concluded that:

- (a) The surfaces of these specimens are not sufficiently active sources and sinks for vacancies for equilibrium to be maintained. This may be a direct result of the thin, and presumably coherent, oxide film that is always present on aluminum.
- (b) Dislocations in a mechanically metastable, but disordered, array are not effective sources or sinks for vacancies whereas dislocations in subboundaries are. A similar conclusion might be drawn from the results of Cottrell on the formation of holes in irradiated copper. Chalmers⁽¹⁰⁾ has suggested that this may be due to the relative difficulty of forming jogs in dissociated dislocations which is not present for the undissociated dislocations that make up the sub-boundaries.
- (e) The points of emergence of dislocations at the surface act as sites for the heterogeneous nucleation of pits. The energy of a dislocation is several electron volts per atomic spacing. The reduction in line length on formation of a pit could significantly reduce the supersaturation required for nucleation.
- (d) Frank has discussed the equilibrium configuration of the surface at a dislocation. Atom movements take place to establish a mechanical balance between the surface tension and the line tension of a dislocation to form a slight depression at a surface. It may be concluded from the reversibility results reported here that the depression formed in the presence of an oxide is of subcritical size whereas the depression that is formed on filling in a pit during heating is larger and supercritical.
- (e) When accurate and reproducable measurements are available of the temperature drop required to nucleate pits for a wide range of holding temperatures, a value for Q_F , the energy of formation of vacancies, may be obtained.

ACKNOWLEDGMENTS

The authors wish to thank the members of the Division of Engineering and Applied Physics who contributed to this work with valuable discussion and other assistance. The financial assistance received from the Office of Naval Research is gratefully acknowledged.

REFERENCES

1. F. L. VOGEL, W. G. PFANN, H. E. COREY and E. E. THOMAS, Phys. Rev. 90, 489 (1953).

- 2. S. G. Ellis, J. Appl. Phys. 26, 1140 (1955).
- 3. A. A. HENDRICKSON and E. S. MACHLIN, Acta Met. 3, 64
- (1955).
 4. J. P. Hirth and L. Vassamillet, J. Appl. Phys. 29,
- 5. G. WYON and J. M. MARCHIN, Phil. Mag. 46, 1119
- (1955). 6. S. KITAJIMA, J. Japan Inst. Metals, 18, 592 (1954).

 Proc. Roy. Soc. A196, 64 (1949).

- B. CHALMERS, Proc. Roy. Soc. A196, 64 (1949).
 L. G. SCHULTZ, J. Metals, N.Y. 6, 1082 (1954).
 F. J. BRADSHAW and S. PEARSON, Phil. Mag. 2, 570 (1957).
- 10. B. Chalmers. Private Communication.

CONTRIBUTION A L'ETUDE DE LA PRECIPITATION DANS UN GROUPE D'ALLIAGES A BASE DE NICKEL*

J. MANENC†

L'étude d'un phénomène de préprécipitation dans un alliage Ni–Cr 80–20 durci avec de l'aluminium et du titane a conduit à explorer la précipitation dans les alliages de base Ni–Al, Ni–Al–Ti, Ni–Cu–Al, Ni–Si, Ni–Cu–Si, Ni–Mo–Si. Tous ces alliages ont la même structure, c'est-à-dire, qu'une phase cubique à faces centrées ordonnée précipite dans une matrice cubique à faces centrées. L'évolution est la même pour tous: stade de préprécipitation pour des revenus courts avec diffusion anormale des rayons X, sous forme de noeuds satellites au voisinage des noeuds de la matrice; structures intermédiaires légèrement quadratiques par suite de la cohérence; précipités visibles de structure cubique.

Il existe deux catégories d'alliages: ceux qui forment des précipités en plaquettes et ceux qui les forment en cubes. Ces derniers existent pour les teneurs donnant une différence de paramètres entre matrice et précipité de l'ordre de 0,01 Å.

STUDY OF PRECIPITATION IN SEVERAL NICKEL-BASE ALLOYS

The investigation of the pre-precipitation phenomenon in the alloy Ni-80%-Cr 20%, hardened with aluminum and titanium, has led to the study of precipitation in the following nickel-base alloys: Ni-Al, Ni-Al-Ti, Ni-Cu-Al, Ni-Si, Ni-Cu-Si and Ni-Mo-Si. All these alloys precipitate an ordered face-centred-cubic phase in a f.c.c. matrix. The ageing sequence, identical for all the alloys, is as follows: pre-precipitation stage after short ageing periods there is the presence of anomalous X-ray scattering in the form of satellites near the matrix Bragg spots; intermediate phase—slightly quadratic as a result of its coherency with the matrix; the visible stable precipitate processing a f.c.c. structure.

Two classes of alloys exist: those in which the precipitates form platelets and those which form cubic particles. The second category appears when the concentration provokes a difference in parameters between the matrix and the precipitate of the order of 0.01 Å.

BEITRAG ZUM STUDIUM DER AUSSCHEIDUNG BEI EINER GRUPPE VON LEGIERUNGEN AUF NICKELBASIS

Das Studium der "Vor-Ausscheidung" bei einer 80–20 Ni-Cr Legierung, die durch Aluminium- und Titanzusatz gehärtet worden war, führte zur Untersuchung der Ausscheidung bei Legierungen auf der Basis Ni-Al, Ni-Al-Ti, Ni-Cu-Al, Ni-Si, Ni-Cu-Si, Ni-Mo-Si. All diese Legierungen haben die gleiche Struktur, d. h. in einer kubisch-flächenzentrierten Matrix scheidet sich eine geordnete kubisch-flächenzentrierte Phase aus. Der Verlauf ist bei allen der gleiche. Nach kurzem Anlassen ein Stadium der "Vor-Ausscheidung" (Zonenbildung), verbunden mit anomaler Röntgenstreuung in Form von "Satelliten", die den Reflexen der Matrix benachbart sind; Übergangsstrukturen, die infolge der Kohärenz leicht tetragonal verzerrt sind; schliesslich siehtbare Ausscheidungen kubischer Struktur.

Zwei Gruppen von Legierungen wurden gefunden: Bei der einen haben die Ausscheidungen die Form von Plättehen, bei der anderen die von Würfeln. Diese letzteren treten dann auf, wenn der Gehalt an Zusatz eine Differenz der Gitterkonstanten (zwischen Matrix und Ausscheidung) der Grössenordnung 0.01 Å verursacht.

Ce travail a eu pour base de départ l'étude de la précipitation lors du vieillissement des alliages Ni-Cr 80-20 durcissables et tenaces à chaud.

Les propriétés réfractaires de la solution solide nickel chrome ont été améliorées par l'incorporation d'aluminium et de titane, susceptibles de former des précipités par revenu après trempe. (1–6) Par la détermination des diagrammes d'équilibre correspondants Taylor et Floyd (7) ont montré que le

précipité dérivait de la phase Ni₃Al cubique à faces centrées de maille ordonnée type Cu₃Au.

19

Pour notre part, nous avons suivi par la diffraction des rayons X l'évolution de la précipitation et nous avons pu constater trois stades. Un stade dit de préprécipitation, un stade avec structures intermédiaires où matrice et précipités sont encore cohérents, enfin le stade où les structures sont celles d'équilibre. (8,9)

Ceci nous a conduit comme Bagariatsky et Tiapkine^(10,11,12) et indépendamment, à l'étude d'alliages

^{*} Received March 25, 1958.

[†] O.N.E.R.A. Chatillon sous Bagneux, France.

plus simples de base, tels que Ni–Al, $^{(13)}$ Ni–Al–Ti, $^{(14)}$ Ni–Ti $^{(15)}$ et à d'autres alliages de structure cristallographique sembable $^{(16)}$ à partir desquels nous avons généralisé nos premiers résultats.

Méthodes expérimentales

L'alliage Ni–Cr 80–20 est un alliage industriel de composition Cr 19,5%, Al 1,5%, Ti 2,4%.

Les autres alliages ont les compositions suivantes:

$$Ni + 7\% Ti + 2\% Al; Ni + 20\% Cu + 6\% Al;$$

Ces derniers ont été élaborés spécialement à partir de métaux raffinés et comportaient moins de 0.3% d'impuretés.

Les teneurs en éléments durcissants ne sont pas critiques, elles ont été choisies de manière à avoir un pourcentage élevé de phase précipitée tout en conservant une température de début de solution solide comprise entre 900° et 1050°C. Le Titane, le Chrome, le Cuivre, le Molybdène accentuent, ou réduisent, la différence de paramètre entre la maille de la matrice appauvrie et celle du précipité d'équilibre (nous aurions pu utiliser vraisemblablement d'autres éléments tels que le tungstène ou le tantale par exemple).

Echantillons

VOL.

1959

A partir des lingots nous avons fait découper des bandes de 5×5 mm de section, homogénéisées 65 heures à $1080^{\circ}\mathrm{C}$, trempées à l'eau puis laminées. Certains alliages trop fragiles aux joints des grains ont été portés sous vide à une température de 50° inférieure à la température de début de fusion, (après découpage). Les gros grains ainsi obtenus ont donné, après laminage, des éprouvettes de 1 à 1,5 mm d'épaisseur, exemptes ou presque de fissures.

Examens aux rayons X.

Les méthodes exposées ailleurs $^{(9)}$ sont les suivantes:

Diagrammes Debye–Scherrer en rayonnement monochromatique Cu et Cr. (18)

Diffusion au voisinage des taches de Bragg pour les gros cristaux par montage à double focalisation. (19)

Diffusion centrale—Méthode Guinier avec monochromateur et chambre à vide, $^{(20)}$ rayonnement $CuK\alpha$.

Les Micrographies sont dues à Madame Ch. Bückle et G. Lenoir et ont été réalisées à l'aide d'attaques mises au point pour les nimonics⁽³⁾

RESULTATS EXPERIMENTAUX

Tous les alliages mentionnés plus haut ont les structures successives suivantes:

Après remise en solution et trempe à l'eau ils se composent d'une seule phase cubique à faces centrées: la solution solide sursaturée. Après revenu isotherme à des températures variables suivant la composition, cette phase se transforme en passant par un stade de préprécipitation. Ce stade est caractérisé par un accroissement des propriétés mécaniques, en particulier, la dureté Fig. 1, et par la diffusion anormale des rayons X au voisinage des raies et des noeuds de diffraction de la matrice.

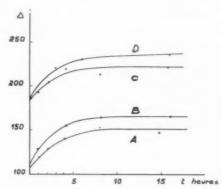


Fig. 1. Courbes de dureté: Vickers 30 kg. Courbe A $\text{Ni} + 7^{0}_{0} \text{Al}; 524^{\circ}\text{C}$ Courbe B $\text{Ni} + 7^{0}_{0} \text{Al}; 550^{\circ}\text{C}$ Courbe C $\text{Ni} + 7.8^{\circ}_{0} \text{Al}; 550^{\circ}\text{C}$ Courbe D $\text{Ni} + 7.8^{\circ}_{0} \text{Al}; 650^{\circ}\text{C}$

Il existe alors deux formes de diffusion anormale:

1. Pour les alliages Ni + 7,8% Al, Ni + 7% Al, Ni + 2% Ti + 5% Al, Ni + 7% Ti + 2% Al, Ni + 30% Cu + 5% Si, Ni + 7,5% Mo + 5% Si, la diffusion se présente sous la forme de noeuds bien résolus situés au voisinage des noeuds du réseau réciproque de la matrice et sur les rangées (100) exactement comme pour les alliages Cu–Fe–Ni⁽²¹⁾ et Ni–Cr–Cu. (17) Les noeuds (h,0,0,) ne comportent qu'une seule paire de tels noeuds, (h,k,0) deux paires, enfin (h,k,k) 3 paires. La Fig. 2 montre les taches de Bragg (111) et (200) obtenues à l'aide du montage à double focalisation pour un échantillon polycristallin à gros grains de Ni + 30% Cu + 5% Si vieilli.

La Fig. 3 donne les raies DS (220), (311), (222) avec leurs satellites pour le Ni + 7,5% Mo + 5% Si revenu 2 hr à 650°C.

Les alliages énuméres ci-dessus ont des différences de paramètres relatives entre précipités et matrice à 700° C, supérieures à 0.5° ₀.

2. Pour les alliages de la catégorie du Ni-Cr



Fig. 2. Ni + 30% Cu + 5% Si; 16 hr 500 C après trempe

80–20 Nimonic tels que Ni + 7% Si et Ni + 20% Cu + 6% Al la diffusion satellite pour les noeuds (h.0.0) est dans la direction du centre (0.0.0) mais élargie en cone de meme axe.

Pour les noeuds (111) et (222) elle prend la forme de calottes sphériques avec légers renforcements au voisinage des rangées (100) mais qui ne sont pas résolus. Sur les diagrammes l'intensité diffusée est nulle sur le plan perpendiculaire à la direction du

La Fig. 4 montre un diagramme obtenu dans les mêmes conditions que pour la fig. 2 sur du Ni-Cr 80-20 vieilli 16 hr 700°C après trempe à l'eau.

Pour les deux familles les maxima des satellites se rapprochent des raies principales au fur et à mesure que le vieillissement se poursuit. La diffusion se transforme en diffraction correspondant aux domaines des précipités et de la matrice appauvrie de dimensions suffisantes comme nous l'expliquerons plus loin. A ce stade les structures ne sont pas cubiques, mais quadratiques⁽¹⁴⁾ surtout pour les alliages à grand Δa où pour maintenir la cohérence les réseaux se déforment dans le plan des plaquettes. Les précipités

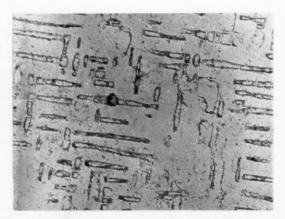


Fig. 3. Ni + 7,5% Mo + 5% Si; 4 hr 650°C après trempe Fig. 5. Ni + 7,8% Al, micrographie électronique 300 hr



Fig. 4. Ni-Cr, 80-20, tâches de Bragg (111) et (200), 16 hr

sont en effet visibles après attaque anodique et se présentent sous forme de plaquettes dont les grandes faces sont parallèles aux plans (100) du réseau de la matrice. Elles paraissent constituées en réalité par la juxtaposition de parallèlépipèdes élémentaires séparés par d'étroites bandes de composition différente et que l'on peut supposer voisine de la matrice appauvrie.



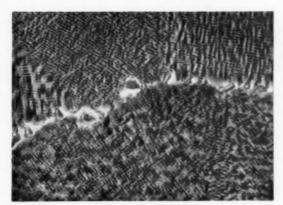


Fig. 6. Ni + 30% Cu + 5% Si, micrographie optique 116 hr 640 C + 75 hr 700 C $\times 2.000.$

Pour les alliages à Δa plus petit que 0,01 Å, les micrographies montrent des précipités en forme de cubes dont les arètes sont parallèles aux directions {100} du réseau de la matrice; après des revenus suffisamment longs tels que par exemple 1000 heures à 800°C, ils sont placés en files suivant les axes $\langle 100 \rangle$ et parfois groupés dans les plans {100}.

La Fig. 5 montre les plaquettes pour le Ni + 7,8% Al grossissement 30.000, la Fig. 6, les plaquettes dans le Ni + 30% Cu + 5% Si.

VOL.

1959

La Fig. 7 est une micrographie montrant les précipités dans le Ni + 7% Si—La Fig. 8 dans le Ni + 20% Cu + 6% Al.

Les résultats précédents peuvent être résumés par le tableau suivant où nous avons marqué pour chaque alliage la différence de paramètre entre matrice et précipité et la forme des diffusions anormales ainsi que des précipités visibles par la suite.

Nous avons signalé⁽¹⁴⁾ que certains alliages précipitant des plaquettes après trempe à l'eau et revenu, donnaient de la diffusion anormale identique à celle du deuxième groupe pour un refroidissement relativement lent. Les précipités visibles sont aussi cubiques.

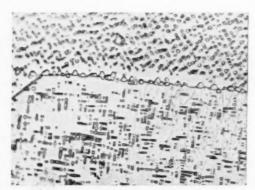


Fig. 7. Ni + 7% Si, 64 hr 850°C ×1875.

DISCUSSION

A l'état trempé comme à l'état d'équilibre, ces alliages ont même structure et ne diffèrent que par les valeurs des paramètres des mailles. Après revenu, les réseaux des précipités et de la matrice restent parallèles, les plans de précipitation et de cohérence sont les plans {100}. Le précipité a une structure ordonnée basée sur Ni₃Al ou Ni₃ Si. Ils passent par les trois stades de précipitation.

Avant d'envisager ces trois stades, il est un fait important à examiner c'est l'état trempé.

Bagariatsky et Tiapkine⁽¹¹⁾ ont signalé qu'après trempe les diagrammes de rayons X comportaient déjà des taches de diffraction correspondant aux noeuds de structure ordonnée des précipités. Nous les avons trouvé aussi pour les échantillons épais de Ni + 7.8% Al pour lesquels la vitesse de trempe était relativement lente. Pour voir l'influence exacte de la vitesse, nous avons examiné des échantillons



Fig. 8.

d'épaisseur 3/100 de mm de cet alliage et de Ni +30% Cu +5% Si. Nous n'avons pas trouvé de taches sur les diagrammes Debye Scherrer pas plus que de diffusion centrale alors qu'il en apparaît comme nous le verrons plus loin au cours du vieillissement. Il semble que les conditions de trempe jouent un grand rôle en cette affaire surtout pour les alliages à forte teneur en éléments durcissants.

Nous allons considérer le premier groupe d'alliages au stade de préprécipitation; il donne des effets comparables à ceux donnés par les alliages ternaires Cu–Ni–Fe, et Al–Ni–Co qui ont fait l'objet d'études théoriques. (21,22,23) Voyons laquelle parmi ces théories peut la mieux rendre compte de nos résultats.

Soit une perturbation de la régularité du réseau se traduisant par une modulation du facteur de structure et par un déplacement périodique des atomes dans une direction (100), ceci suivant des ondes planes de grandes dimensions par rapport à la longueur d'onde.

Le calcul permet de trouver une diffusion en forme de satellites équidistants des noeuds du réseau réciproque et dont l'écartement dépend de la période. Du fait de l'équivalence des trois directions (100) il y a une paire de satellites pour les noeuds (h,0,0), deux pour (h,k,0) et trois pour (h,k,l). Ces calculs ont été repris récemment par Tiedema, Bouman et Burgers (24) pour les alliages Au-Pt. (Il est possible dans la plupart des cas de négliger les effets de variation de densité électronique). La théorie prévoit une largeur égale des satellites et de la raie principale ce qui n'est pas vrai expérimentalement. Il faut donc faire appel à une variation de la longueur d'onde de modulation en différents points du réseau. Autre difficulté: le rapprochement des satellites du noeud principal qui devrait correspondre à une augmentation de la longueur d'onde en fonction du temps de revenu; ce fait est physiquement difficile à admettre.

MODULATION PERIODIQUE DU RESEAU

Théorie des Germes Isolés. Développée par Guinier, elle est plus près des thèories de la précipitation exprimées pour les alliages légers à durcissement structural. Les germes sont répartis au hasard. Ils sont formés d'une plaque centrale de quelques plans atomiques; on peut supposer sa composition voisine de celle du précipité d'équilibre (raies de structure ordonnée). Le plan de précipitation est (100). Ce noyau est bordé de deux zones de même forme dont la composition est celle de la matrice appauvrie. Les distances réticulaires varient uniquement dans la direction (100) perpendiculaire à la grande base de la plaquette ainsi formée. La variation d'écartement dans la zone centrale est exactement compensée par celle des zones extérieures: la distance réticulaire moyenne est ainsi celle de la matrice sursaturée. La diffusion des rayons X n'a lieu que dans la direction correspondante de l'espace réciproque.

Le calcul précédent faisait appel à des approximations qui conduisaient à des satellites d'égale intensité de part et d'autre du noeud principal; expérimentalement cette intensité n'est pas égale mais par un calcul plus rigoureux on peut rendre compte de ce résultat. Il est vrai qu'une modulation simultanée du facteur de structure atomique et de la distance réticulaire peut donner le même effet. Pour nos alliages, il y a lieu de tenir compte de l'incidence des variations de densité électronique sur l'intensité des satellites. Quoique faiblement, ces variations sont décelables aux petits angles. La Fig. 9 montre les anneaux de diffusion au voisinage du centre, obtenus avec Ni + 30% Cu + 5% Si polycristallin pour différents revenus. On remarquera en faveur de la

deuxième théorie, la diminution du diamètre en fonction du temps de vieillissement comme pour les satellites aux grands angles. On peut noter aussi, dans le même sens, l'existence sur certains de nos diagrammes DS d'un "deuxième ordre" de diffusion du côté de la matrice appauvrie.

Ce deuxième ordre apparaît avant ou pendant le passage de la diffusion anormale à la diffraction. On peut l'expliquer de la manière suivante: pour un

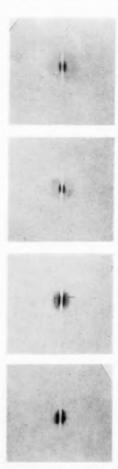


Fig. 9. Diffusion centrale Ni + 30% Cu + 5% Si: (a) 110 hr 400°C (b) 1 hr 500°C (c) 64 hr 500°C

1 hr 540°C

complexe de grande taille mais encore cohérent avec la matrice sursaturée chacune des trois parties donnerait si elle était seule une image de diffraction centrée sur le point de l'espace réciproque correspondant à la valeur moyenne du paramètre de sa maille. Celles des deux plaques extérieures de matrice appauvrie se superposent mais la différence de phase introduite par le noyau central donne une interférence

avec modulation. Cette modulation peut donner lieu à deux pies de diffraction voisins et inscrits dans l'image que donnerait une seule d'entre elles. Il v a en plus interférence faible entre le centre et les parties extérieures de la zone. Au contraire, si nous avions une périodicité, le deuxième ordre devrait apparaitre plus tôt; il correspondrait d'après le modèle de Hargreaves à l'existence d'une région de matrice sursaturée entre le précipité et la partie de matrice appauvrie relative au suivant. Nous devrions alors le trouver pour un modèle tel que celui de Tiedema, dissymétrique, du côte du précipité dont l'épaisseur est la plus faible. Pour l'autre catégorie d'alliages à faible différence de paramètres la forme de diffusion peut être difficilement interprétée par une modulation du réseau à trois dimensions. La forme des précipités visibles permet d'imaginer l'apparition au début du revenu de germes cubiques ou de forme voisine. Ces germes pourraient comporter un novau central de structure voisine de celle du précipité d'équilibre. Ce noyau serait entouré d'une coquille de matrice appauvrie. La forme cubique explique qualitativement la disposition de la diffusion dans l'espace réciproque.

On peut faire le rapprochement avec les résultats de Guinier et Walker sur l'aluminium argent⁽²⁵⁾ et avec les calculs de Huang⁽²⁶⁾ et Cochrane⁽²⁷⁾ pour des modèles à symétrie sphérique.

Les derniers auteurs ont considéré la diffusion causée par le déplacement des atomes et ils ont montré que la diffusion devait être nulle dans l'espace réciproque sur le plan perpendiculaire à la direction qui joint le noeud au centre.

Expérimentalement pour nos alliages l'intensité diffusée est très faible dans ce plan pour les noeuds (111).

Dans l'état actuel de nos recherches nous pensons que la théorie des zones ou complexes isolés rend mieux compte de nos résultats expérimentaux. Il nous reste à comparer le comportement des deux catégories d'alliages pour les deux stades suivants. Pour le premier groupe la cohérence entre matrice et précipité provoque des déformations des réseaux le long du plan de précipitation. Les réseaux sont quadratiques tant que la relaxation n'intervient pas, mais elle ne peut intervenir que lorsque les précipités sont suffisamment espacés. Ceci ne se produira qu'après une coalescence poussée qui réduira les zones de cristal perturbé et permettra au réseau de prendre sa structure d'équilibre cubique à faces centrées.

Pour les autres alliages la deformation du réseau du précipité apparaît moindre que pour celui de la matrice. On peut penser que le noyau est soumis à une compression quasi hydrostatique tandis que la matrice est en extension sur les faces des petits cubes.

Cette déformation de la matrice peut être à l'origine du groupement des précipités en files. L'existence d'une bande étroite de matrice appauvrie entre deux précipités pourrait réduire l'énergie libre de déformation due à la différence de volume.

Composition	Matrice- précipité a en A	Matrice en A°			
Ni + 7.8% Al. Ni + 5% Al + 2% Ti Ni + 2% Al + 7% Ti Ni + 2% Al + 7% Ti Ni + 30% Cu + 5% Si Ni + 7.5% Mo + 5% Si	+0.017 $+0.027$ $+0.036$ $+0.038$ $+0.023$	3,539 3,539 3,544 3,540 3,533 Satellites résolus Plaquettes			
Ni + 7% Si 80% Ni + 20% Cr Ni + 20% Cu + 6% Al	$-0,008 \\ +0,01 \\ +0,009$	3,510 Satellites 3,56 non résolus 3,555 Cubes			

Echantillons laminés $50\,^{\rm o}_{\rm o}$ recuits 3 heures 800 C revenus 70 heures 700 C.

Nous venons de montrer pour ces alliages de structure très voisine une évolution semblable de la précipitation. Nous avons rencontré deux formes de diffusion anormale au stade de la préprécipitation en correlation certaine avec la forme des germes extrapolée à partir de celle des précipités visibles. Il semble se dégager de ces résultats une très grande influence des facteurs géométriques sur la forme des précipités. Cette influence avait été prévue par Nabarro (28) qui avait montré par le calcul que la forme en plaquette était d'autant plus probable que la différence de volume entre matrice et précipité était plus grande. L'énergie libre interfaciale qui apparaissait était largement compensée par la réduction de l'énergie de déformation en passant du précipité spherique de même volume au précipité 'aciculaire".

BIBLIOGRAPHIE

- P. Chevenard et X. Wache Schweizer, Schweizer Archiv. 127 (Avril 1952).
- L. B. Pfell, H. P. Allen et C. G. Convay, Special Report no. 43. Iron and Steel Institute, London (1951).
- C. BÜCKLE et J. POULIGNIER, Rev. Met. 53, No. 3, 1233 (1956).
- 4. Y. Baillie et J. Poulignier, Rev. Met. 51, No. 3, (1952).
- W. Betteridge et A. W. Franklin, J. Inst. Met. 85, part II, 473 (1957).
- R. NORDHEIM et N. J. GRANT, J. Metals N.Y. 6, 211 (1954).
- A. TAYLOR et R. W. FLOYD, J. Inst. Met. 52, No. 80, 577 (1951); Ibid. 53, No. 81, 25 (1952); Ibid. 53, No. 81, 451 (1952).
- J. Manenc, C.R. Acad. Sci., Paris. 238, 1817 (1954);
 Ibid. 240, 2413 (1955).
- 9. J. Manenc, Rev. Metall. 54, No. 3, 161 (1957)
- A. Bagariatsky et N. D. Tiapkine, Dokl. Akad. Nauk. SSSR 108, No. 3, 451 (1950).

1959

- A. Bagariatsky et N. D. Tiapkine, Dokl. Akad. Nauk. SSSR Cristallographie 2, No. 3, 419 (1957).
 A. Bagariatsky et N. D. Tiapkine, Dokl. Akad. Nauk.

- A. Bagariatsky et A. D. Hapkine, Dokt. Aran. Mank. SSSR 115, No. 6, 419 (1957).
 J. Manenc, C.R. Acad. Sci., Paris. 242, 2344 (1956).
 J. Manenc, C.R. Acad. Sci., Paris. 243, 1119 (1956).
 Ch. Bückle et J. Manenc, C.R. Acad. Sci., Paris 244, 1027.
- 1643 (1957). J. Manenc, Rev. Métall. 54, No. 11, 867 (1957).
 J. Manenc, Act. Met. à paraître.
 F. Sebilleau, Rech. Aéronautique No. 59, 33 (1957).

- 19. J. Manene, Acta Cryst. 259 4, (1951).

- 20. A. GUINIER, Théorie et Technique de la Radiocristallographique, édit. DUNOD.

 21. V. DANIEL et H. LIPSON, Proc. Roy. Soc. A181, 368 (1943).
- M. F. Hargereaves, Acta Cryst. 4, No. 4, 301 (1951).
 A. Guinier, Acta Met. 3, 300 (1955).
- 24. T. J. Tiedema, J. Bouman et W. G. Burgers, Acta Tub.
- 5, 310 (1957). 25. C. B. Walker et A. Guinier, Acta Met. 1, 568 (1953).
- K. Huang, Proc. Roy. Soc. A190, 102 (1947).
 W. Cochran, Acta Cryst. 9, No. 3, 259 (1956).
- 28. F. R. N. NABARRO, Proc. Phys. Soc. 52, 90 (1940).

LETTERS TO THE EDITOR

Comments on "Yield strength of metals as a function of grain size"*

W. M. Baldwin Jr.⁽¹⁾ points out the interesting and quite significant fact that most data on the dependence of yield stress on grain size can be equally well represented as straight lines in plots of σ_y vs. D^{-1} , $D^{-1/2}$, or also $D^{-1/3}$ (D= grain diameter). The fact that apparently on a plot of σ_y vs. $D^{-1/3}$ the lines for many materials go through zero is taken by Baldwin to be significant and to suggest a physical law. It should be noted, however, that if σ_y is represented by an equation of the form:

$$\sigma_y = aD^{-1/n} + b \tag{1}$$

with varying $n, b \approx 0$ is to be expected for some values of n, by mere mathematical reasoning. Supposing that

$$\sigma_u = a_2 D^{-1/2} + b_2 \tag{2}$$

is the correct law (where a_2 and b_2 are chosen roughly to correspond to Baldwin's figure 1) and plotting this

1959

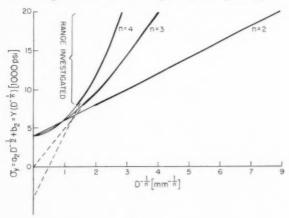


Fig. 1

in coordinates σ_y vs. $D^{-1/3}$ (see figure) we see that, in the range measured, this curve can well be mistaken for a straight line. This line, however, would necessarily cut the ordinate at a value b_3 lower than b_2 , and on each plot of σ vs. $D^{-1/n}$ for increasing n, this intercept would be lower. For one value of n it will be at about $b \approx 0$, and for each higher n value it will then give negative yield stresses for finite grain diameters, if the law were to hold for all grain sizes. So from the data as represented by Baldwin, a dependence on $D^{-1/4}$ would be physically impossible,

 $D^{-1/2}$ definitely possible, and $D^{-1/3}$ a borderline case. It may be surprising that n for the borderline case, which depends not only on a_{λ} and b_{λ} but also on the range of grain sizes yet investigated, should be 3 for all materials. It must be pointed out however that, although the experimental data can be represented by Baldwin's lines which go exactly through zero. the best fitting straight lines would show some spread around zero, which is apparently substantial in about 40 per cent of the cases (e.g. Ti and Mo), and both positive and negative. † Admittedly the spread could be interpreted as experimental error if there were any other reason to suspect an inverse cube root law. However it does seem large enough not to "suggest" any physical law, if indeed a law of the form (1) is found to be less natural than one with b=0. The fact, however, that an inverse cube root law would give negative yield stresses at finite grain sizes for many materials precludes general conclusions of the kind drawn by Baldwin and suggests n=2 as the highest possible value for all materials over the total range of grain diameters.

U. F. Kocks

Gordon McKay Laboratory Harvard University

References

- W. M. Baldwin, Jr., Acta Met. 6, 139 (1958).
- * Received March 24, 1958.

† The case of the steels at 78°K, which Baldwin exempts from generality by the incorrect argument that the Cottrell effect would be important at that temperature but not at room temperature, must be counted as an instance from those materials for which the best fitted straight lines in a plot of σ_y vs. $D^{-1/3}$ give an intercept $b_3 \neq 0$.

An effect of thermal neutrons on Cu3Au;

Several investigators have reported that slow neutrons seem capable of changing some macroscopic properties of metallic solids. (1,2,3) Cook and Cushing (1) ascribed the differences in ordering of copper—gold samples when reactor irradiated in and out of cadmium shields to the effect of the ¹⁹⁸Hg impurity which results from the decay of slow neutron induced radioactive gold. Blewitt and Coltman (4) rejected this hypothesis both on the grounds that only minute amounts of mercury were formed and that electron irradiation, which is essentially unable to form

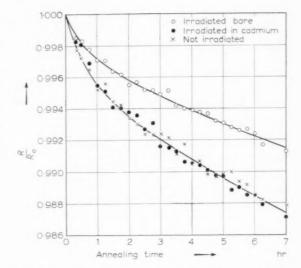
impurity atoms, will also give rise to ordering in $\mathrm{Cu_3Au}$. They argued that since the principal effect of electron bombardment was the creation of Frenkel defects, those defects must play a role in ordering. They then proposed a mechanism of radiation ordering in a reactor neutron flux based entirely on the effect of the fast flux. Although it seems clear that Frenkel defects do assist the ordering of coppergold alloys, it is by no means obvious that thermal neutrons have no role in the creation of these defects.

Thermal neutrons are capable of displacing atoms from their lattice positions in solids. When a slow neutron is captured by a nucleus, the excess binding energy of the new nucleus, about 8 MeV in most nuclei, is usually emitted immediately (within approximately 10^{-14} sec) in the form of one or more capture gamma rays. The nucleus recoils so as to conserve momentum. If the energy acquired by the recoil atom is greater than its threshold displacement energy, about 25 eV in most tightly-packed solids, a vacancy–interstitial pair will be created. Upon emission of a single photon, the recoil atom will acquire a kinetic energy given by $E = E_g^2/2Mc^2$, where E_g is the gamma energy, M is the mass of the recoil atom, and c is the velocity of light.

A preliminary experiment, designed to explore the effect of thermal neutrons on the electrical resistivity of Cu₃Au, has been completed. Cu₃Au wires, 10 cm long by 0.015 in. diameter, were heat treated so as to produce a highly disordered state ($\rho = 11.2 \,\mu\Omega\text{-cm}$). Two of these wires were irradiated close together in one of the isotope holes of the ANL CP-5 reactor. This hole is almost completely free of neutrons having energies high enough to produce direct lattice displacements of copper or gold atoms in Cu₂Au. As a further control, one of the two irradiated wires was wrapped in a cadmium foil thick enough to shield out 98 per cent of the thermal neutrons. Gamma dosimetry measurements made several days after the experiment indicated that the fraction of the gold atoms in the unshielded sample that had absorbed neutrons during the irradiation was 3.7×10^{-6} whereas the fraction in the shielded sample was only 6×10^{-8} .

After a 6 hr irradiation at 30°C, the wires were removed from the reactor and immediately mounted along with an unirradiated wire in a bath whose temperature was maintained at 130.0 ± 0.1 °C. The resistances of the three wires were then recorded as functions of time, with the results shown in the figure.

Within the accuracy of the experiment (± 0.0005 in R/R_o) the wire shielded from thermal neutrons behaved the same as the unirradiated wire. They



both showed the normal isothermal resistivity decrease consistently found in a series of pre-irradiation experiments on wires given the same heat treatment. However, the resistivity of the unshielded irradiated wire decreased at a slower rate, presumably because its degree of order had been increased during the irradiation.

The average energy acquired by recoil gold atoms following emission of their capture gammas is approximately 50 eV; the maximum is 114 eV. These low energy recoils have been shown by electron experiments to be capable of creating measurable resistance effects in Cu₃Au in concentrations of less than six parts per million. This experiment indicates that at least some of the defects produced by these low energy recoils are mobile at room temperature. Possibly these are multi-vacancies which we expect to be created by a large fraction of the gold recoils and which, according to theory, (6) move readily at room temperature.

195

In reactor irradiated metals other than those having neutron absorption cross sections which are much larger than their scattering cross sections, capture recoil atoms are not likely to contribute appreciably to the over-all radiation damage. The significance of the slow neutron process may lie, rather, in its usefulness as a solid state research tool. Slow neutron irradiations of certain materials in the absence of fast neutrons will produce recoil atoms of rather well defined numbers and energies without the contamination of thermal spikes and/or displacement spikes. By irradiating isotopes whose daughters are stable or have sufficiently long half lives, one can minimize the complexities associated with impurity atoms and with recoil atoms resulting from decay betas, gammas, and neutrinos.

The authors wish to express their thanks to W. J. Mayer, W. Richards, and S. T. Staehnik of the Research Staff, and the members of the Argonne National Laboratory's CP-5 staff, for their kind help.

Research Staff
A. Foderaro
General Motors Corporation
J. B. Burnham jr
Detroit 2. Michigan

References

 L. G. Cook and R. L. Cushing, Acta Met. 1, 539, 549 (1953).

2. R. E. Davis et al., Phys. Rev. 74, 1255 (1948).

- W. E. JOHNSON and K. LARK-HOROVITZ, Phys. Rev. 76, 442 (1949).
- T. H. BLEWITT and R. R. COLTMAN, Acta Met. 2, 549 (1954).
 J. ADAMS, A. GREEN and R. A. DUGDALE, Phil. Mag. 43, 1217 (1952).
- 6. H. B. Huntington, Phys. Rev. 91, 1092 (1953).

Received May 5, 1958.

1959

Yield points in a dilute magnesium-thorium alloy*

Although yield points have not been reported previously in magnesium alloys, they have recently been observed during tensile testing of several magnesium alloys containing thorium or rare earth additions. A typical example, to be discussed here, is a polycrystalline binary alloy containing 0.5 wt.%

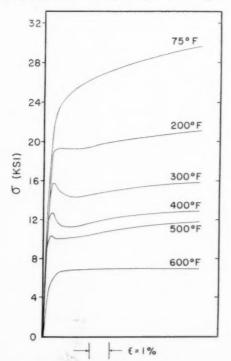


Fig. 1. Tensile stress–strain curves at various temperatures for Mg + 0.5% Th alloy.

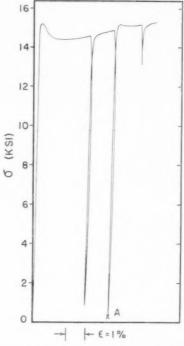


Fig. 2. Strain-aging results for a test temperature of 300 F. Point A: aged 2 min at 400 F.

thorium. The yield points are present when the material is tested at elevated temperature but, surprisingly, disappear when testing is performed at room temperature. To the author's knowledge, such behavior has not been found in other metals where, as a rule, yield points associated with solute-atom pinning become more pronounced as the test temperature is lowered. Speculation on the reason for this anomalous effect is given.

The alloy studied was the same material as that used in another investigation:(1) it consisted of electrolytic magnesium plus 0.52% thorium. Tensile specimens 7 in. long with a 1 in. reduced section were prepared from 0.064 in. thick cold-rolled sheet. Prior to testing, the samples were annealed 4 hr at 650°F (giving a fine-grained recrystallized structure) and air cooled. The solubility of thorium in magnesium at 650°F is 1%, (2) so that the anneal at 650°F was a solution heat treatment and slight aging might have occurred during the air cool. Specimens were strained on a gear-driven 12,000 lb Baldwin Model P.T.E. testing machine. A microformer extensometer was used to measure strain and the strain rate was about 0.01 min⁻¹. Samples were heated to test temperature in about 15 sec and held at temperature during straining by passing a high-amperage alternating current through them.

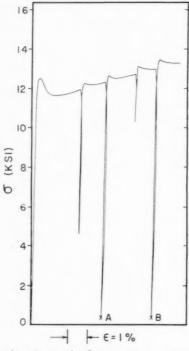


Fig. 3. Strain-aging results for a test temperature of 400 F. Point A: held 1.5 min at 400 F; point B: held 3 min at 400 F.

Stress-strain curves for samples tested at 75, 200, 300, 400, 500 and 600°F are presented in Fig. 1. Yield points are quite pronounced for tests at 300, 400 and 500°F, faintly visible for the test at 200°F and absent for tests at 75 and 600°F. Results from strain-aging experiments are shown in Fig. 2 and 3. There is no yield point when the sample is unloaded and reloaded at 300°F, but the yield point reappears when the specimen is unloaded, aged at 400°F and retested at 300°F. The yield point is always present on retesting when the test temperature is 400°F (Fig. 3), presumably because aging is very rapid at this temperature. Slight strain aging effects were also found when the test temperature was 200°F (aging temperature 400°F) but none could be detected for room temperature testing.

For a yield point to be present during tensile testing, a Lüders band must initiate at the upper yield point and propagate, at lower stress, through the reduced section of the sample during the yield point elongation. Now if a Lüders band is to propagate, a somewhat homogeneous strain must be transmitted, grain to grain, along the specimen; this can occur only if the individual grains possess sufficient modes of plastic deformation to assume arbitrary (but small) changes in shape. It is suggested that this condition is not met for magnesium at room

temperature because essentially the only operative deformation mechanisms are basal slip and, to a lesser extent, {1012} twinning. With increasing temperatures, however, the critical resolved shear stresses for slip on non-basal planes ({1011} and {10\overline{10}}) fall sharply; it is believed that the extra deformation modes available when non-basal slip is a contributive mechanism are sufficient to allow the propagation of homogeneous strain, and thus yield points are observed. (Using the recent results of Reed-Hill and Robertson, (3) it may be shown that the ratio of the critical resolved shear stress for nonbasal slip to that for basal slip is about 60: 1 at 75°F but only about 2:1 at 550°F.) If the above considerations are correct, then single crystals of Mg + 0.5% Th would show a yield point when tested at room temperature; this has not as yet been checked.

S. L. COULING

The Dow Chemical Company Metallurgical Laboratory Midland, Michigan

References

- S. L. COULING, J. F. PASHAK and L. STURKEY. Amer. Soc. Metals Preprint No. 59, Volume 51, 1959.
- A. S. Yamamoto and W. Rostoker, Trans. Amer. Soc. Metals 50, 1090 (1958).
- 3. R. E. REED-HILL and W. D. ROBERTSON, Trans. Amer. Inst. Min. (Metall.) Engrs. 209, 496 (1957).
 - * Received May 6, 1958.

Cross slip of extended dislocations*

According to the current theory for deformation of face-centered-cubic metals, the end of Stage II hardening is caused by thermally activated cross slip.⁽¹⁾ An activation energy has been estimated on the assumption that cross slip requires the two partial dislocations on the primary plane to combine before the dislocation may cross slip.⁽²⁾

Letting (111) and (111) be the primary and cross slip planes, the dislocation reactions may be the following:

(1)
$$\frac{a}{6}[112] + \frac{a}{6}[2\overline{1}1] \rightarrow \frac{a}{2}[101]$$
 and

(2)
$$\frac{a}{2}[101] \rightarrow \frac{a}{6}[1\overline{1}2] + \frac{a}{6}[211].$$

The energy of activation is closely related to the energy required to produce the first reaction over some length of the dislocation.

It is here noted that there exists an alternative cross slip process and that this alternative process should have a lower activation energy and hence is VOI 7 19

more likely to occur. Cross slip may occur when a leading partial dislocation, say $\frac{a}{6}[2\overline{1}1]$, dissociates into two partials, one of which, $\frac{a}{a}$ [211], glides on the cross slip plane and the other of which, $\frac{a}{3}$ [010], is sessile at the intersection of the two planes involved. Written as a reaction this is

(3)
$$\frac{a}{6}[2\overline{1}1] \rightarrow \frac{a}{6}[211] + \frac{a}{3}[0\overline{1}0].$$

Subsequently the second of the partials originally on the primary plane is attracted to the sessile partial, combines with it to give $\frac{a}{6}[1\overline{1}2]$, which is the second partial needed on the cross slip plane.

(4)
$$\frac{a}{6}[112] + \frac{a}{3}[0\overline{1}0] \rightarrow \frac{a}{6}[1\overline{1}2].$$

Just after (3) has occurred one has a "stair-rod" dislocation identical to that envisaged by Thompson as part of an extended edge dislocation crossing from the primary to the cross slip plane. (3) Thompson later (4) discussed the possibility of a screw dislocation of the type considered here, but noted that it may not be a stable configuration. It is because of this instability that thermal activation is required.

As an indication of the relative energies involved in the reactions (1) and (2) vs. (3) and (4), the differences of the squares of the Burger's vectors may be considered. (5) For equation (1) one obtains $a^2/6$, and for equation (3) $a^2/9$ —a ratio of 3:2. Equations (2) and (4) need not be considered since both involve a decrease in the energy. The above result indicates that as a first approximation the energy for cross slip by the process suggested above is 2/3 of that for the total recombination of partials.

The above discussion assumed cross slip onto the portion of the cross-slip plane making an obtuse angle with the portion of the primary already traversed. If the dislocation moves in the opposite direction (through an acute angle), the reactions are these:

(5)
$$\frac{a}{6}[2\overline{1}1] \rightarrow \frac{a}{6}[10\overline{1}] + \frac{a}{6}[1\overline{1}2]$$
 and

(6)
$$\frac{a}{6}[112] + \frac{a}{6}[10\overline{1}] \rightarrow \frac{a}{6}[211].$$

The difference in the Burger's vectors gives an activation energy that is 1/3 that for full recombination of dislocations.

An approximate configuration just after reaction (3) is indicated in Fig. 1. Here the force of attraction between the first partial and the sessile is opposed by the sum of the contributions by the other partial, other dislocations, the stacking fault, and the applied stress.

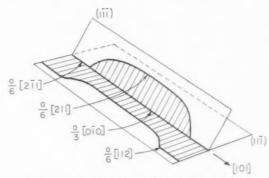


Fig. 1. Cross slip of an extended dislocation.

Friedel⁽⁶⁾ has noted that cross slip by Seeger's mechanism may be facilitated by the prior presence of a jog. Since cross slip involving a "stair-rod" dislocation would be eased also, the above discussion should still give proper relative energies, at least approximately. It appears that a jog of more than one atomic distance, since the dislocation making up the jog may be dissociated, would assist the stairrod configuration, while single-step jogs would favor the total recombination process.

Detailed calculations are clearly needed to decide rigorously between the processes discussed here: this note seeks to point out that the stair-rod process should be considered.

The author is pleased to acknowledge the financial support of the Atomic Energy Commission.

Note added in proof-Calculations using the factor $1/1 - \nu$ ($\nu = \text{Poisson's ratio}$) appropriate for the energy of edge dislocations confirm that cross slip of extended dislocations is highly preferred in the acute sense, but indicate that cross slip by a recombined dislocation is slightly preferred in the obtuse sense.

R. L. Fleischer

Massachusetts Institute of Technology Cambridge, Massachusetts

References

- 1. A. SEEGER, J. DIEHL, S. MADER and R. REBSTOCK, Phil. Mag. 2, 323 (1957)
- 2. G. Schoeck and A. Seeger, Report of a Conf. on Defects in Crystalline Solids, p. 340. Phys. Soc., London (1955).
 3. N. Thompson, Proc. Phys. Soc. B**66**, 481 (1953).
- 4. N. Thompson, Conference on Defects in Crystalline Solids,
- p. 153, Phys. Soc., London (1955). A. H. COTTRELL, Dislocations and Plastic Flow in Crystals,
- p. 38, Oxford Univ. Press, Oxford (1953). J. Friedel, Les Dislocations. Gauthier-Villars, Paris (1956).
 - * Received May 16, 1958.

1959

Recrystallization of zone-refined aluminium*

During the past few years a number of investigators (1.2.3.4) have demonstrated a remarkable decrease in the recrystallization temperature of cold worked aluminium due to the decrease in the impurity content resulting from zone refining.

In our experiments we have commenced with a bar of 99.99% aluminium, 50 cm long and 1 cm² in cross-section, contained in a graphite boat. A molten zone 3 cm long was maintained using a Radyne high-frequency induction heater whilst the molten zone was traversed at 1 cm/hr. Duplicate bars were prepared after one, two, four and eight passes in this apparatus and the purified sections from each bar were used for the recrystallization studies.

Preliminary experiments on material given eight passes in the zone refining apparatus indicated that recrystallization at room temperature could be obtained if the material was given more than 85 per cent cold reduction at room temperature. In consequence, further studies were carried out on material given 40 per cent cold reduction at room temperature. To achieve this, the zone-refined bars were cold-rolled to 0.090 in. sheet, recrystallized at 200°C and finally cold-rolled to 0.054 in. (40 per cent cold work). Samples approximately $3~\rm cm \times 1~cm$ were then annealed for 30 min at various temperatures in the range $100^\circ -320^\circ C$. The extent of recrystallization was assessed by an examination under polarized light of electropolished and anodized specimens.

The temperatures of anneal necessary for recrystallization to begin, and for complete recrystal-

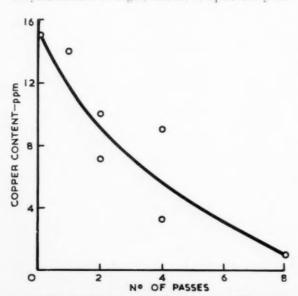


Fig. 1. Relationship between purity (as measured by copper content) and number of passes.

- O BEGINNING OF RECRYSTALLISATION.
- COMPLETE RECRYSTALLISATION.

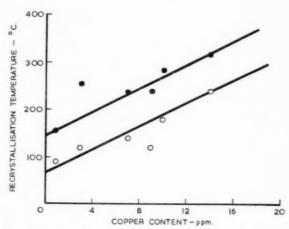


Fig. 2. Relationship between purity (as measured by copper content) and recrystallization temperatures.

lization in 30 min, are given in Table 1. It will be seen that there was a progressive decrease in the recrystallization temperature as the number of passes given in the zone-refining apparatus was increased. Reasonable agreement was obtained between measurements on samples rolled from different bars given the same zone-refining treatment.

195

Radiochemical analysis was carried out for copper on some of the samples, to obtain an indication of the general level of purity obtained, and Figs. 1 and 2 show the relationship between the copper content and the number of passes, and recrystallization temperatures respectively. Taking the copper content as a measure of the purity of the material, the results show that increasing the number of passes—and hence the purity—produces a marked decrease in the recrystallization temperature, thus confirming the observations of previous workers. It is hoped to produce material

Table 1. Recrystallization temperature of zone-refined aluminium cold worked 40 per cent

No. of passes	Temperature for beginning of recrystallization (°C)	Temperature for complete recrystallization (°C)
1	275	320
1	240	320
2	140	240
2	180	280
1 2 2 4 4 8	120	240
4	120	255
8	<100, approx. 90	155
8	<100, approx. 90	208

capable of recrystallizing at even lower temperatures by using aluminium of higher initial purity before zone-refining.

J. C. BLADE

Aluminium Laboratories Limited. Banbury, Oxon.

J. W. H. CLARE H. J. LAMB

References

I. G. CHAUDRON, Nature 197, 923 (1954).

ALBERT and J. LE HERICY, C. R. Acad. Sci., Paris 242, 1612 (1956).

A. W. Demmler, J. Metals N.Y. 8, 558 (1956).

P. Albert and O. Dimitrov, C. R. Acad. Sci., Paris 245,

* Received May 19, 1958.

1959

Carbon damping in manganese alloyed ferrite*

It was shown by Dijkstra and Sladek(1) that the internal friction resulting from strain induced diffusion of nitrogen in ferrite is influenced considerably by the presence of metallic solutes. At a frequency of vibration of about 1 s⁻¹ the internal friction vs. temperature curve of a binary Fe-N alloy exhibits a peak at 22°C the shape of which corresponds to a single relaxation time. In ferrite containing 0.5% of a solute metal as well as nitrogen a secondary peak appears in addition to that at 22°C. The temperature for the secondary peak is characteristic of the pertinent alloying element, being 32° for Mn, 45° for Cr, 75° for Mo, and 87°C for V at the frequency cited. Hence a metallic solute introduces at least one extra relaxation time in the nitrogen diffusion process. These results could be explained by assuming the dissolved metal atoms to create interstices in which the nitrogen atoms have lower energies than in normal sites between iron atoms. The 22°C peak should then be due to nitrogen atoms jumping between the normal sites and the secondary peak to jumps from the low energy sites.

One would expect the damping due to carbon in ferrite to be similarly influenced by solute metals. However, Wert⁽²⁾ demonstrated that carbon damping curves in the presence of any of the solutes Ni, Mo, Cr, Mn or V all displayed only one peak (at 40°C, 0.9 s⁻¹) corresponding to a single relaxation time as in unalloyed ferrite. On the other hand wires from the different alloys that were carburized and quenched from 710°C to give a Q_{max}^{-1} value of 0.015 had widely different carbon contents, the extremes being 0.015% for unalloyed ferrite and 0.065% for ferrite with 0.5% manganese. Since the numerical value of the carbon content as given in % C is roughly the same as the pure Q_{max}^{-1} for Fe-C ferrite⁽³⁾ the carbon in excess of 0.015% in the ternary alloys could be assumed either

	Table 1					
Test material (%)	C	Mn	P	s	N	0
P	0.001	0.001	0.001	0.001	< 0.001	0.005
A	0.29	0.52	0.003	0.016	0.005	0.012
В	0.10	0.83	0.005	0.023	0.003	0.007

to have formed carbide or to be trapped near solute metal atoms in the ferrite. The latter situation probably presupposes the existence of a secondary peak but if this were located at a comparatively high temperature it could have been masked by the rapid precipitation of carbon during the measurement. By measuring the peak height as a function of carbon concentration in alloyed as well as in pure ferrite it would be possible to decide whether there is an interaction between carbon and solute metal atoms. Such experiments for the case of manganese as the alloying element are reported in this note. As in the papers referred to above the internal friction measurements were carried out according to Kê.(4)

The compositions of the test materials used are given in Table 1. The pure iron P was obtained from Philips Research Laboratories in Eindhoven. Alloys A and B with manganese were vacuum melts with electrolytic iron, electrolytic manganese, and graphite as starting materials.

The specimens had the shape of wires 0.7 mm in diameter and 320 mm in length. As a first treatment they were purified from carbon and nitrogen by annealing in wet hydrogen at 700°C. Since the height of the damping peak does not solely depend on the carbon content but also on grain size and texture(5.6.7.8) these two factors should not vary appreciably for different specimens and test materials. A fairly large grain size was desired as then the disturbing effect of grain boundaries is small. Texture should be avoided. Both conditions could be realized by furnace cooling the decarburized wires in evacuated quartz tubes from the γ -range. The temperatures from which cooling was performed and the resulting grain sizes are listed in Table 2. (Iron P had to be

Table 2

Test material	Furnace cooled from	Grain size ASTM
P	1025°C	3
A	1100°C	3.5
В	1100°C	3.5

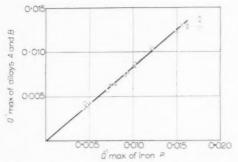
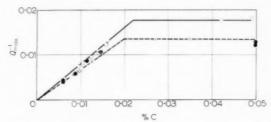


Fig. 1. $Q_{\rm max}^{-1}$ of alloys A and B vs. $Q_{\rm max}^{-1}$ for iron P after carbon equilibration and quenching from 710°C. \times A=0.52% Mn \bigcirc B=-0.83% Mn

cooled from a lower temperature than alloys A and B in order to avoid an extremely coarse grain size.) As could be judged by X-ray diffraction applying the method described in (7) the wires were free from texture.

It was first attempted to carburize simultaneously wires from different test materials to a given carbon activity by exposing them at 710°C to a gas mixture of CO and CO, of controlled composition. The time of treatment was 2 hr which is sufficient to allow for equilibrium provided that carbon diffusion controls the process as is likely. The method has the inherent disadvantage that gas mixtures with more than about 40°, CO, will oxidize iron at this temperature. Hence, carbon contents below about 0.011% (in pure ferrite) cannot be obtained in practice without oxidation which is to be avoided. The carburized wires were solution treated at 710°C for 10 min in an argon atmosphere and quenched before measuring. In spite of a rigorous control of gas composition and temperature during carburisation there was a wide scatter in the $Q_{\rm max}^{-1}$ values. Therefore, wires carburized in the same run were sealed into an evacuated quartz tube and soaked for 24 hrs at 715°C. The damping peaks obtained upon subsequent solution treatment indicated that the earbon had become evenly distributed between the different wires. It was found that complete equilibration could be achieved in this way also when the initial carbon contents of the wires were widely different (within the solubility range). Thus by properly selecting the specimens put into the tube homogeneous carbon contents covering the whole solubility range could be obtained. Fig. 1 shows Q_{max}^{-1} values of alloys A and B as a function of the corresponding Q_{max}^{-1} of iron P after carbon equilibration. As could be expected the carbon damping peak in manganese alloyed ferrite varies linearly with carbon activity as is known to be the case for pure ferrite. The fact that the slope of the



curve is less than unity might in part be a consequence of the difference in grain size between the test materials (cf Table 2) and possibly also of undetected differences in texture. However, it is felt that manganese will lower the slope although this effect cannot be considered as definitely established.

Some wires were analyzed for carbon by an electrolytic titration method. There was no systematic deviation in carbon contents within a set of wires from different test materials that had been equilibrated together. The $Q_{\rm max}^{-1}$ values are plotted as a function of carbon content in Fig. 2. Also in this case the curves are straight lines. In view of the limited accuracy of the chemical analysis $(\pm 0.001\%)$ the slopes have been adjusted to agree with the results of Fig. 1. Carbon contents above the solubility limit were obtained by carburizing in hydrogen saturated with n-heptane as ${\rm CO/CO_2}$ mixtures with carbon activities considerably higher than that of cementite for some reason seemed to be incapable of forming this phase.

19

Interaction between carbon and manganese in the ferrite would imply a decrease in the carbon activity and a corresponding increase in the solubility. According to Fig. 2 this is not the case. On the contrary the solubility is possibly somewhat lowered in the presence of manganese. This might be due to a decrease in the carbon activity of cementite which is to be expected since Fe₃C and Mn₃C are isomorphous and mutually soluble⁽¹⁰⁾ and the carbon activity of Mn₃C is very much lower than that of Fe₃C.⁽¹¹⁾

The present results show that within the accuracy of the measurements there is no interaction between carbon and manganese in the ferrite. The high carbon content of 0.065°_{0} at a $Q_{\rm max}^{-1}$ of 0.015 in the Fe–Mn–C alloy as reported by Wert⁽²⁾ was probably due to carbide formation, possibly as a cementite film at the surface. It remains to be explained why carbon and nitrogen behave differently in alloyed ferrite.

The author is indebted to the Stora Kopparbergs Bergslags AB for permission to publish this note and wishes to thank Mr. Åke Josefsson for his interest and valuable comments during the investigation.

G. Lagerberg†

Research Department Stora Kopparbergs Bergslags Aktiebolag Domnarvet Sweden

REFERENCES

- 1. L. J. DIJKSTRA and R. J. SLADEK, J. Metals N.Y. 5, 69 (1953).
- C. A. Wert, J. Metals, N.Y. 4, 602 (1952).
 L. J. Dijkstra, J. Metals, N.Y. 1, 252 (1949).
- T. S. KÉ, Phys. Rev. 71, 533 (1947).
 G. Lagerberg and A. Josefsson, Acta Met. 3, 236 (1955)
- 6. H. J. SEEMAN and W. DICKENSCHEID, Acta Met. 6, 62 (1958).
- 7. G. LAGERBERG and E. G. WOLFF, Acta Met. 6, 136 (1958).
- 8. P. Stark, B. L. Averbach and Morris Cohen, Acta Met. 6, 149 (1958)
- 9. W. Oelsen, H. Haase and G. Graue, Arch. Eisenhüttenw. 22, 225 (1951).
- 10. K. Kuo and L. E. Persson, J. Iron St. Inst. 178, 39 (1954). 11. L. S. Darken and R. W. Gurry, Physical Chemistry of Metals, p. 363. McGraw-Hill, New York (1953).
 - * Received June 23, 1958.
 - † Now at AB Atomenergi, Stockholm, Sweden.

Some observations on intergranular fracture in polycrystalline sodium chloride*

Polycrystalline sodium chloride can be cleaved in a transgranular manner only when the rotation of the cleavage plane across the grain boundaries is small.(1) For large misorientations and where the grain boundary lies obliquely across the advancing cleavage crack, the fracture becomes intergranular. An analysis of these observations has suggested that grain boundaries in sodium chloride are weak, having about half the strength of the cleavage plane in a single grain. This weakness might be expected simply from consideration of the large degree of geometrical and ionic misfit occurring at a boundary, but might also be considered likely from the segregation or precipitation of impurities in this region. The micrographs accompanying this note illustrate the occurrence of grain boundary precipitation particularly well, but also indicate that some caution must be exercised in attributing weakness to all forms of precipitate.

Fig. 1 shows the typical appearance of an intergranular fracture surface. The oblique illumination used here reveals the generally smooth nature of the surface, broken only by a number of sharply defined tilts. These tilts are probably the traces of subboundaries in the crystal structure. Usually two sets of traces can be distinguished; one set at which there



Fig. 1. Grain boundary fracture surface, showing boundary traces and precipitation of impurities.

is simply a sharp tilt of the surface (as at A in Fig. 1) and another marked by tilt together with a dense clustering of foreign particles (B in Fig. 1). The particles are thought to have arisen from impurities which have been concentrated in the melt in the boundary region during growth of the individual grains and have finally precipitated, preferentially along sub-boundaries. It is suggested here that one set of traces corresponds to sub-boundaries in the grain below the surface being examined, whilst the other set is simply the impression of sub-boundaries from the adjacent grain. The crack appears to be truly intergranular and, moreover, the boundary followed is that which was frozen-in during solidification; the cracking therefore provides a fairly good indication of the form of the surfaces of the individual grains as they finally solidified from the melt.

Although precipitation in the neighbourhood of a grain boundary can undoubtedly lead to weakness, a number of observations suggest that, in some cases at least, it can also lead to strengthening. For example, Figs. 2 (a), (b) show the opposite faces of an intergranular fracture in a specimen which contained particularly large precipitates. The high degree of correspondence between the patterns of particles in the two surfaces indicates that these too must have been fractured during cracking. It is possible therefore for a particle to interfere sufficiently with the propagation of a crack to increase the resistance to parting of the grains. This possibility is further demonstrated by Fig. 3. This is an internal interferogram of a crack arrested inside a grain boundary. Although the uniformity in intensity of the background reflection indicates that the two surfaces of the crack are almost parallel, the secondary patterns of interference fringes encircling large precipitates can be considered to represent a residual cohesion at these points, which must be removed before the grains are

Fig. 2. (a) Pattern of precipitates in one surface of intergranular fracture.

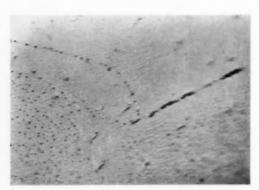


Fig. 2. (b) Pattern in opposite surface of fracture. ×52.5.

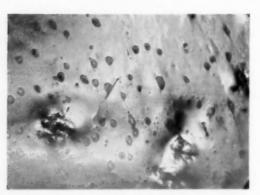


Fig. 3. Internal interferogram of intergranular fracture just prior to failure. ×52.5.

finally parted. An examination of the order of colours in the fringe patterns, when unfiltered mercury light is used, verifies that the surfaces are in fact pinned together by the precipitates and not strained apart.

A real pinning effect implies not only a high internal strength within the precipitates themselves, but also extremely good adhesion with the two grains of the matrix, since considerable stress must have been concentrated here by the main crack. The secondary interference patterns show how this stress has been relieved, by extensive strain of the surrounding matrix rather than by fracture at the interfaces with the precipitates. Good adhesion between a precipitate and its parent grain can of course be expected, since epitaxial growth is likely, but it is difficult to understand how the strong junction with the other grain is established.

This note is published by permission of the Chairman of Tube Investments Limited.

A. J. Forty†

19

Tube Investments Research Laboratories nr. Cambridge, England

References

1. A. J. Forty, 1958. To be published.

* Received April 23, 1958.

† Now at H. H. Wills Physical Laboratory, University of Bristol.

Grain boundary sliding and intercrystalline cracking*†

During a study of the phenomenon of grain boundary sliding in 99.999°_{\circ} Cu bi-crystals, it was found that voids were formed along the grain boundaries of the bi-crystals. This observation is in agreement with that of Chen and Machlin.⁽¹⁾ A quantitative study was

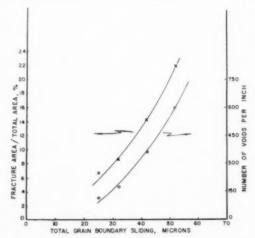


Fig. 1. Fracture area per total area as a function of total grain boundary sliding. Hydrogen atmosphere.

^{*} This research was supported by the United States Air Force, through the Office of Scientific Research of the Air Research and Development Command. Received June 10, 1958.

made of the relation between void formation and boundary sliding. Bi-crystals of copper were stressed in pure shear parallel to the common boundary. The resolved shear stress was $300 \, \mathrm{lb/in^2}$ and tests were conducted in hydrogen and in a vacuum of 5×10^{-4} mm Hg over the range of temperature from $650^{\circ}\mathrm{C}$ to $900^{\circ}\mathrm{C}$. The results of this investigation are shown in Figs. 1–4.

1959

For the crystals tested in hydrogen, isolated voids were produced by boundary sliding as shown in Fig. 2. Those tested in a vacuum of 5×10^{-4} mm Hg developed grain boundary cracks rather than isolated voids as illustrated in Fig. 4. In both cases, the grain boundary area occupied by cracks or voids increased with increasing amounts of grain boundary sliding. This increase in crack or void area was accomplished,



2a. 300 lb/in², 850°C, displacement 52 μ .

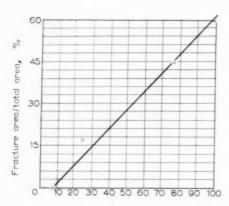


2b. 300 lb/in2, 800°C, displacement 42 u.



2c. 300 lb/in², 680°C, displacement 25 μ .

Fig. 2 a.-e. Voids after sliding along grain boundary. Hydrogen atmosphere. Stress, temperature and displacement indicated. Polished with diamond dust. Unetched. $\times 75$.



Total grain boundary sliding, μ

Fig. 3. Fracture area per total area as a function of total grain boundary sliding. Vacuum $5 \times 10^{-4} \, \mathrm{mm}$ Hg.

at least for the specimens tested in hydrogen, by an increase in the number of voids that developed with increasing amounts of sliding. A significant observation is that the number of voids and the void area produced for a given amount of grain boundary sliding is independent of the temperature (from 650°C to 900°C) at which the sliding was carried out. This observation leads to the conclusion that vacancy condensation has no connection with either void nucleation or growth in these experiments.

Because the crystal orientation in these experiments was chosen to minimize slip, and because the spacing between the slip lines that did develop was larger than the spacing between voids, it may be concluded that Gifkins' mechanism(2) does not operate exclusively. In his mechanism voids are nucleated as a consequence of the stress developed at the edge of a slip plane that

is blocked by a grain boundary.

The mechanism that is in best agreement with our data is that of Chen and Machlin. (1) However, even this mechansim must be modified to allow plastic deformation to occur at the jogs prior to fracture there. The fact that new voids are continually being produced during the grain boundary sliding can be explained either by the continual production of grain boundary jogs, as for example by slip, or by distribution in the stresses developed at jogs, or both. In any case, the jog regions must deform concomitantly with grain boundary sliding. Otherwise, all the jogs would produce voids at about the same small amount of grain boundary sliding.

An experiment was devised in an attempt deliberately to increase the number of jogs present in the

boundary. A specimen was plastically deformed at room temperature to produce a large number of slip plane intersections with the grain boundary, then subjected to grain boundary sliding conditions at elevated temperature. The number of voids produced by grain boundary sliding in this specimen is many times that found in "as grown" boundaries. Compare Fig. 5 with Figs. 2 a-c.

The effect of atmosphere on intercrystalline cracking is revealed by a comparison of Figs. 1 and 3 and Figs. 2 and 4. The tendency of a partial pressure of oxygen $(5 \times 10^{-4} \, \mathrm{mm \; Hg})$ to elongate the voids into cracks, and thereby increase the fracture area per unit amount of boundary sliding, is apparent. It is probable that the oxygen acts to lower the fracture strength of grain boundary jogs as well as to prevent rewelding together of submicroscopic areas of decohesion produced by the fracture of jogs and their subsequent sliding apart, after Chen and Machlin.(1)

It may be concluded on the basis of our experimental results that

- (1) Grain boundary sliding along stationary; grain boundaries will lead to the formation of voids situated along these grain boundaries.
- (2) The number of voids produced increases monotonically with the amount of grain boundary sliding independent of the temperature.
- (3) Vacancy condensation and any other thermally activated process, as a mechanism for the primary nucleation and growth of voids, is unimportant under our experimental conditions.
- (4) Upon testing in hydrogen the voids are isolated. With a vacuum of 5×10^{-4} mm Hg the voids are better described as cracks.
- (5) The number of voids produced per unit of grain boundary area is sensitive to the grain boundary morphology and jog population.

J. INTRATER E. S. MACHLIN

19

Materials Research Corporation Yonkers, New York. Department of Metallurgy Columbia University, N.Y.

References

- 1. C. W. CHEN and E. S. MACHLIN, Acta Met. 4, 666 (1956). R. C. GIFKINS, Acta Met. 4, 98 (1956).
 - Received June 10, 1958.
- Stationary grain boundaries are defined as non-migrating grain boundaries.



4a. 1200 lb/in², 700°C, displacement 100 $\mu.$



4b. 300 lb/in², 800°C, displacement 76 $\mu.$



4c. 300 lb/in², 700°C, displacement 23 $\mu.$

Fig. 4 a–c. Voids and cracks after sliding along grain boundary. Vacuum 5×10^{-4} mm Hg. Stress, temperature and displacement indicated. Polished with diamond dust. Unetched. $\times 75$.



Fig. 5. Voids along grain boundary. Specimen pre-strained 2100 lb/in², room temperature, 2 hr; subsequently 300 lb/in², 900°C, 5 hr, hydrogen atmosphere. Displacement 20 μ . Polished with diamond dust. \times 75.

SOME CURRENT PAPERS IN OTHER JOURNALS

Journal of the Institute of Metals, Vol. 87

Part 1, September 1958:

The fatigue properties of zinc. D. M. Fegredo and G. B. Greenough.

The behaviour of cold-worked copper in fatigue. D. S. Kemsley.

The supercooling of gold as affected by some catalysts. F. J. Bradshaw, Margaret E. Gasper, and S. Pearson. Direct study of eutectic alloys by means of electron microscopy. N. Takahashi and K. Ashinuma.

The upper temperature limit of stability of G.P. zones in ternary aluminium-zinc-magnesium alloys. I. J. Polmear. A method of assessing the die-filling characteristics of powders. J. Oakley.

An X-ray survey of certain transition-metal systems for sigma phases. A. G. KNAPTON,

Part 2, October 1958

The effect of particle size on the sintering of copper powder.

A. Duffield and P. Grootenhuis,

The properties of extruded chromium. E. A. Brandes and H. E. N. Stone.

The constitution of cadmium-tin-zinc alloys. H. J. Bray. Metallic impurities in the silver coinage trial plates (1279 to 1900). J. S. Borbes and D. B. Dalladay.

The pseudo-binary systems of uranium carbide with zirconium carbide, tantalum carbide, and niobium carbide. L. D. Brownlee.

The molybdenum-rhenium system. A. G. Knapton.

Part 3, October 1958

The ageing characteristics of two commercial alloys based on the aluminium-zinc-magnesium system. I. J. Polmear and P. Scott-Young.

The kinetics of morphology of the allotropic transformation of cobalt. Hervé Bibring, François Sebilleau, and Charlotte Bückle.

Preliminary investigations on the properties of chromium and chromium alloys at elevated temperatures. G. R. Wilms and T. W. Rea.

Cleavage fracture in cast chromium of high purity. J. F. McNeil and H. R. Limb.

Solid solutions of mercury in silver and gold. H. W. RAYSON and L. D. CALVERT.

The solid solutions of gallium in lead. J. Neill Greenwood. The uranium-thorium system and some aspects of the uranium-thorium-zirconium system. (Miss) J. R. Murray.

Archiv für das Eisenhüttenwesen

Heft 10, Oktober 1958:

Über die Geschwindigkeit der Reduktion von Eisenoxyd mit

Wasserstoff. Von Ludwig Von Bogdandy in Oberhausen und Hans-Günter Riecke.

Gleichgewichtsuntersuchungen zwischen Dolomit, Eisen(II)-oxydschlacken und Eisenschmelzen. Von Wilhelm Anton Fischer und Horst Spitzer.

Übergrosse Spektralgeräte und ihre Anwendung bei der Untersuchung von Eisen und Stahl. Von Georg Graue, Siegfried Eckhard, und Robert Marotz.

Untersuchung an durch Warmwalzen verformbaren Oxydeinschlüssen in unberuhigten Weichstählen. Von Heinz Lessing und Hanns Malissa.

Zur Entschwefelung und Desoxydation von Reinsteisen nach dem Vakuumschmelzverfahren. Von Walter Jäniche und Herbert Beck.

Sauerstoff und die Reckalterung von Reinsteisen. Von Walter Jäniche und Herbert Beck .

Einfluss der Temperatur bis 1000°C auf die Mikrohärte von Eisen und Eisenlegierungen. Von Hermann Schenck, Eugen Schmidtmann, Helmut Brandis und Karl Winkler.

Temperaturabhängigkeit der Hystereseschleife einer Eisen-Chrom-Legierung mit 24% Cr. Von Albrecht v. Kienlin. Zur thermodynamischen Analyse. X—Kalorimetrie und Thermodynamik der Blei-Wismut-Legierungen. Von Willy Oelsen und Ruth Bennewitz.

Acta Crystallographica

Part 11. November 1958:

Phase determination for colemanite, $\rm CaB_3O_4(OH)_3.H_2O.$ J. Karle, H. Hauptman and C. L. Christ.

Studies of borate minerals (III): The crystal structure of colemanite, CaB₃O₄(OH)₃,H₂O. C. L. Christ, Joan R. Clark and H. T. Evans, Jr.

Structure du Cyanure de sodium hydraté. Marie-Thérèse le Bihan.

VO

19

Die Kristallstruktur von $\mathrm{Na_2Zn}(\mathrm{SO_4})_24\mathrm{H_2O}(\mathrm{Zn\text{-}Bl\ddot{o}dit})$. Von M. Giglio,

M. GIGLIO.
The least-squares refinement of the crystal structure of Ce(IO₃)₄.H₂O ceric iodate monohydrate. James A. Ibers and Don T. Cromer.

A single crystal neutron diffraction study of Diaspore, AlO(OH). WILLIAM R. BUSING and HENRI A. LEVY.

Short Communications:

A polynomial approximation to atomic scattering factor curves. H. C. Freemann and J. E. W. L. Smith.

Atomic scattering factors for wolfram. Edgar L. Eichhorn. Zur Structur des Kupfernitrates Cu(NO₃)₂·1,5H₂O. K. Dornberger-Schiff und Janusz Leciejewicz.

QUENCHED-IN VACANCIES IN NOBLE METALS—I THEORY OF DECAY*

H. KIMURA,† R. MADDIN‡ and D. KUHLMANN-WILSDORF‡

The decay laws for quenched-in vacancies in metals are calculated using two types of sink for the vacancies, i.e. stray or network dislocations and sessile rings formed by the condensation of vacancies. Annihilation at these two types of sink results in entirely different decay curves. The decay of the quenched-in resistivity in Au observed by Bauerle and Koehler is analyzed on the basis of the present theory assuming a repulsive force between two vacancies separated from each other by a few atomic distances. For quenching from above a critical temperature, it is concluded that most of the vacancies disappear at the sessile rings as divacancies; for quenching from below the critical temperature, most of the vacancies disappear at stray dislocations or dislocations in the network as single vacancies.

TREMPE DES LACUNES DANS LES METAUX NOBLES—I THEORIE DE L'EVOLUTION

Les lois de l'évolution pour les lacunes maintenues par trempe dans des métaux sont calculées en employant deux types de puits pour les lacunes: dislocations vagabondes ou dislocations en réseau et anneaux sessiles formés par la condensation de lacunes. L'annulation de ces deux types de puits conduit à des courbes d'évolution entièrement différentes. La chute de la résistivité après trempe dans l'or observée par Bauerle et Koehler est analysée sur la base de la théorie présentée ici en partant d'une force répulsive entre deux lacunes séparées l'une de l'autre par quelques distances atomiques.

Pour une trempe au-dessus d'une température critique, on conclut que la plupart des lacunes évoluent aux anneaux sessiles comme "paire de lacunes"; pour les températures en-dessous de la température critique, la plupart des lacunes disparaissent aux dislocations vagabondes ou aux dislocations de réseau comme lacunes simples.

ABGESCHRECKTE LEERSTELLEN IN EDELMETALLEN—I THEORIE DES AUSHEILENS

Die Gesetze für das Ausheilen abgeschreckter Leerstellen in Metallen werden berechnet mit Hilfe zweier Typen von Senken für die Leerstellen, nämlich vereinzelten Versetzungen oder solchen des Versetzungsnetzwerks und nichtgleitfähigen Ringen, die durch Kondensation von Leerstellen entstehen. Das Verschwinden an diesen beiden Typen von Senken ergibt völlig verschiedene Ausheilkurven. Das Ausheilen der von Bauerle und Koehler beobachteten Widerstandserhöhung von abgeschrecktem Gold wird auf Grund der hier vorgelegten Theorie analysiert unter der Annahme einer abstossenden Kraft zwischen zwei Leerstellen, die einige Atomabstände voneinander entfernt sind. Für das Abschrecken von oberhalb einer kritischen Temperatur ergibt sich die Folgerung, dass die meisten Leerstellen als Doppelleerstellen an den nicht gleitfähigen Ringen verschwinden, während beim Abschrecken von unterhalb der kritischen Temperatur die meisten Leerstellen an vereinzelten Versetzungen oder an solchen des Netzwerks als einfache Leerstellen verschwinden.

1. INTRODUCTION

1959

The investigation of Maddin and Cottrell⁽¹⁾ in 1955 on quenching of super purity aluminum single crystals showed that the yield point of these crystals could be increased markedly by rapid quenching and that the maximum hardening was attained on aging. They concluded that the yield increase was produced by the migration of vacancies quenched into the crystal and annihilation of these vacancies at dislocations in such a manner as to jog the dislocations,

thus making them harder to move. It was also shown by Kauffman and Koehler that the presence of non-equilibrium numbers of vacancies quenched into metals could be detected by electrical resistivity measurements. In the past few years there have been a number of investigations on quenching as it affects both electrical resistivity⁽²⁾ and mechanical properties⁽³⁾ of pure metals. In particular Bauerle and Koehler⁽⁴⁾ have carefully followed the resistivity changes on aging after quenching of Au wires from various temperatures.

The results obtained by Bauerle and Koehler can be summarized briefly as follows:

- (1) The formation energy of defects was 0.98 eV.
- (2)† The quenched wires of Au contracted on

of Tokyo,

† Contractions in quenched and aged Al, Ni and Au have been reported by J. Takamura⁽⁵⁾ and are being studied more extensively at present.⁽⁶⁾

^{*} Part of a thesis submitted 11 April 1958 to the Faculty of the Graduate School of Arts and Sciences, University of Pennsylvania, by H. Kimura, in partial fulfillment of the requirements for the Ph.D. degree. Sponsored by the Office of Naval Research. Received April 25, 1958.

[†] Formerly, School of Metallurgy, University of Pennsylvania; now Department of Metallurgy, University of Tokyo, Japan.

School of Metallurgy, University of Pennsylvania.

annealing after quenching, with the rate of contraction always proportional to the rate of the decay of resistivity.

- (3) On quenching from below 750°C, the activation energy for defect migration was about 0.82 eV and decay of quenched-in resistance occurred at a low rate which could be described as an exponential decay (except for the very beginning). More than 99 per cent of the resistivity was annealed out below 60°C.
- (4) On quenching Au from temperatures above 800°C, the activation energy for the recovery of quenched-in resistivity, i.e. the activation energy for defect migration is about 0.63 eV with a fast decay rate and a complicated decay curve. About 10 per cent of the quenched-in resistivity remains after a low temperature anneal, and is recovered only on annealing above 500°C for prolonged periods.

It appears quite certain from investigations to date that the defects quenched into metals which are responsible for the increased resistivity are vacancies. It is considered that the analysis of the kinetics of vacancy decay to two different types of sinks explains the complicated observations noted above.

2. THE EFFECT OF QUENCHING TEMPERATURE ON VACANCY DECAY—QUALITATIVE CONSIDERATIONS

Several models for quench hardening, which are closely related to the nature of sinks for quenched-in vacancies, have been proposed, i.e. formation of jogs on dislocations, (1) formation of spherical voids on dislocations, (7) etc. None of them, however, consider the relation between the nature of the sinks and the decay of quenched-in vacancies. Existing investigations on the quenched-in resistivity, while concerned mainly with measurements on the formation and migration energies of vacancies, fail to explain the reason for the complexities present in the decay curve and for the residual resistivity remaining after low temperature annealing following a high temperature quench.

The experimental results briefly reviewed above suggest that there are at least two different kinds of sinks for vacancies. Therefore, it is important to examine the various possible sinks for vacancies. Although surfaces and grain boundaries can act as sinks and, theoretically, could absorb all of the non-equilibrium vacancies, this process cannot explain the observed hardening or resistivity remaining after annealing. The formation of spherical voids⁽⁷⁾ on dislocations, on the other hand, cannot explain the observed contraction of the specimens and hence voids formed through the condensation of vacancies must be ruled out as predominant or even frequent

sinks. Network or random dislocations, however, can act as sinks and a detailed mechanism of the geometry of the annihilation will be proposed in Part II of this report. Finally, vacancies themselves can generate vacancy sinks by aggregating into small vacancy clusters in the form of single layers which collapse and thereby form sessile dislocation rings. (8)

In the case of f.c.c. metals (only Au and Cu are discussed in this paper), the resultant dislocation rings will lie in {111} planes and surround a stacking fault. Since such sessile dislocations cannot dissociate into other partial dislocations, absorption of vacancies at the periphery of the sessile ring causes it to grow in diameter while remaining in its original plane.

The periphery of the sessile rings can be considered as an aggregate of sinks for vacancies, whereby the number of sinks increases as the sessile ring grows through the absorption of vacancies. Therefore, the decay curve, which is related to the number of sinks, becomes complicated whenever substantial proportions of such sessile rings are formed. On the other hand, there is reason to believe that the number of sinks stays materially constant if the complete dislocations thought to be present at random or in the form of a network act as the main sinks. A constant number of sinks yields a simple decay law, namely, exponential decay.

The introduction of various types of sinks, however, cannot explain the variation of the activation energy for migration of defects with quenching temperature. In this connection, Koehler et al. (9) recently suggested that during annealing, vacancies spend part of their lifetime as single vacancies and the remaining part as divacancies. The time which a vacancy spends as a single vacancy can be considered to be inversely proportional to the concentration of single vacancies, and thus the higher the quenching temperature, the shorter a time the average vacancy will exist as a single vacancy. Since theoretical considerations⁽¹⁰⁾ lead to the conclusion that divacancies move with a lower activation energy than single vacancies, this yields an explanation for the lower activation energies found for higher quenching temperature and on this basis, Koehler et al. (9) explained the variations in the observed activation energy of recovery after quenching. Calculations which are given in Appendix III. however, show that the observed variation in the activation energy is too large to be explained by this principle. Moreover, if the above principle were correct, the activation energy for the decay should have changed gradually with the concentration of single vacancies; consequently an energy between 0.8 eV and 0.7 eV should have been observed.

VOI 7 19

To remove these difficulties we suggest that during the annealing chemical equilibrium between single- and di-vacancies is not achieved, but that substantially, the ratio of single vacancies to divacancies remains as it is established during the quench. At low quenching temperatures, the concentration of thermal equilibrium vacancies is too low to cause the formation of an appreciable number of divacancies or larger vacancy clusters during quenching. Consequently, vacancies are quenched-in primarily as single vacancies and decay out as single vacancies on subsequent annealing. In that case stray dislocations or dislocations existing in the network constitute the predominant sinks because vacancy clusters, necessary for the nucleation of sessile dislocations, are absent. When the quenching temperature is high, a high thermal equilibrium concentration of vacancies allows for the formation of a larger number of divacancies and larger vacancy clusters during quenching. Then the main migrating defects during annealing are divacancies with a small amount of single vacancies, triple vacancies or even bigger clusters. Particularly large vacancy clusters collapse to form large numbers of sessile rings during quenching or at the very beginning of annealing. Therefore, after quenching from a high temperature, the predominant types of sinks are sessile rings. A complex decay curve results. The presence of these sessile rings with their enclosed stacking faults then explains why a high temperature is required to completely anneal out the hardening and the quenched-in residual resistivity remaining after high temperature quenching followed by low temperature annealing.

VOL.

1959

3. DECAY LAWS OF QUENCHED-IN VACANCIES

Koehler *et al.* have recently given solutions to the diffusion equation for the decay of vacancies⁽⁹⁾ at stationary dislocations which show that the decay can be represented as an exponential decay, except at the very beginning of the annealing. Except at the beginning of annealing, the decay can be represented by the equation,

$$-dN/dt = \alpha n_s N \tag{1}$$

where N is the number of vacancies remaining after annealing time t, α is a constant and n_s is the number of sinks. When, instead, sessile dislocation rings serve as sinks, they move by absorption of vacancies, but since this motion is very slow, the Koehler $et\ al.$ solution can also be applied to the case of sessile rings.

This solution due to Koehler and co-workers presupposes that the stress field around the dislocations does not disturb appreciably the random motion of vacancies. This is entirely reasonable for an interaction energy (attraction) between vacancies and dislocations not larger than about 0.3 eV and for vacancies which are more than about 10 atomic distances away from the dislocation. As the fraction of their lifetime which average vacancies spend inside the region of appreciable attraction is less than 1 per cent for vacancies initially located more than 100 atomic distances away from dislocations, any error introduced by neglecting the stress field of the dislocations is surely negligible.*

(a) Fixed sink decay

When stray dislocations or dislocations in the form of a network constitute the sinks, n_s in equation (1) is constant and equation (1) is integrated to give an exponential relation.

The constant αn_s in equation (1) may be given by

$$\alpha n_s = Azv(\rho_d/n_0) \exp\left(-E_M/kT\right) \tag{2}$$

where A is the entropy factor for migration of vacancies, z is the coordination number, v is the atomic vibration frequency, ρ_d is the density of dislocations per :m², n_0 is the number of atoms per cm² and E_M is the migration activation energy. This expression implies that a vacancy meets a sink after making c^{-1} jumps, where c is the concentration of sinks and uses the expression for the number of jumps, m, a vacancy makes during time t, as given by Cottrell:(13)

$$m = Azvt \exp\left(-E_{M}/kT\right) \tag{3}$$

Thus the simple exponential decay can be understood as the result of the absorption of vacancies at stationary dislocations.

(b) Variable sink decay

When sessile rings constitute the majority of sinks, n_s is no longer constant. For mathematical convenience, it is assumed that the number of sessile rings, N_s , remains constant during the annealing, i.e. that all nuclei for sessile rings are present at t=0. This is no undue simplification since the great majority of nuclei will be formed during quenching. As shown in the appendix, calculations for this case give

$$n_s = 2K \tanh \alpha Kt$$
 (4)

and

$$N = N_0 \left(\cosh \alpha K t\right)^{-2} \tag{5}$$

where N_0 is the initial number of vacancies and K

^{*} Roswell and Nowick⁽¹¹⁾ showed that the decay of vacancies in Ag–Zn alloys followed a $t^{2/3}$ law. However, the Cottrell–Bilby⁽¹²⁾ law applied in that calculation considers the accumulation of impurity atoms around dislocations, whereas the present case involves the *disappearance* of vacancies at dislocations in pure metals.

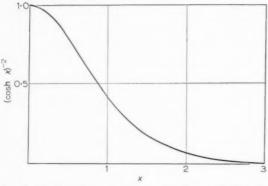


Fig. 1. $(\cosh x)^{-2}$ vs. x, representing the qualitative decay curve for quenched-in resistivity if vacancies are either all single or all double and are absorbed at sessile dislocations only.

equals $(\pi/2)(N_sN_0)^{\frac{1}{2}}$ and $\pi(N_sN_0/2)^{\frac{1}{2}}$ for single vacancies and divacancies, respectively. Fig. 1 shows the curve of $(\cosh x)^{-2}$, i.e. gives the expected form of the curve for the recovery of quenched-in resistivity if all vacancies were absorbed at sessile rings.

(c) Combination decay*

If dislocations and sessile rings act as sinks concurrently, the differential equation for decay contains two terms corresponding to the two types of sinks. If n_F and n_V are the number of fixed sinks and variable sinks, respectively, equation (1) becomes

$$-dN/dt = \alpha(n_1 + n_2)N \tag{6}$$

As shown in the Appendix, if N_F and N_V are the number of vacancies which have disappeared at fixed sinks and at variable sinks, respectively,

$$N_F = \frac{(B^2 + q)\{\exp{[(-q)^{\frac{1}{2}}t]} - 1\}}{2C[B + (-q)^{\frac{1}{2}}] - 2C[B - (-q)^{\frac{1}{2}}]\exp{[(-q)^{\frac{1}{2}}t]}}$$

$$N_{\Gamma} = N_F^{\ 2}/4M^2$$
 (8)

where

 $M=n_F/\pi N_s^{\frac{1}{2}}$ for single vacancies $M=n_F/2\pi N_s^{\frac{1}{2}}$ for divacancies

 $A = \alpha n_1 n_0, B = -\alpha n_1, C = \alpha n_1 / 4M^2$

and

$$q = 4AC - B^2$$

4. QUANTITATIVE INTERPRETATION OF BAUERLE AND KOEHLER'S EXPERIMENTS ON THE RECOVERY OF QUENCHED-IN RESISTANCE IN AU

(a)
$$T_O^{\dagger} < 750^{\circ}C$$

Since the decay law in this case was found to be exponential, the fixed sink decay law can be applied. In order to find quantitative results, consider that a single vacancy meets another vacancy after making c^{-1} jumps, where c is the concentration of vacancies.* The mean free time of a vacancy, t_1 , then, is given by

$$1/t_1 = Azvc \exp\left(-E_M/kT\right) \tag{9}$$

For single vacancies, $A \simeq 10^{(15)}$, z = 12, and $v \simeq 10^{13}$ sec⁻¹. For $T_0 = 700$ °C, c is about 3×10^{-5} . From these values t_1 is calculated to be about 70 sec at 60°C, $(E_M$ is taken as 0.82 eV). However, the annealing period at 60° C for $T_{o} = 700^{\circ}$ C was found experimentally to be very much longer, namely, about 80 hr. Therefore, a mechanism must operate in order to make the combination of vacancies difficult whenever they meet. It is suggested that any two vacancies are subject to a short range repulsive force limited to distances of several atomic spacings. This repulsion is strongest when they are separated from each other by, say, two atomic distances. Hence, in order to form divacancies or vacancy elusters, vacancies must overcome a potential barrier in addition to the lattice potential in a perfect region. While Eshelby (16) showed that an elastic repulsion between two single vacancies is to be considered as small, Seeger (17) estimates that a vacancy can be considered to be negatively charged, and hence, a noticeable repulsive force can reasonably be assumed to exist. Then equation (9) is modified to

$$1/t_1 = Azvc \exp \left[-(E_M + E_R)/kT \right]$$
 (10)

19!

where E_R is the additional potential. To make t_1 as long as 80 hr at 60°C, E_R is calculated to be about 0.24 eV.

From the experimental decay curve ρ_d in equation (2), the density of pre-existing dislocations is calculated to be 3×10^7 cm⁻². If, on the other hand, the density of sinks is calculated from the number of jumps made by a vacancy during annealing, ρ_d is 0.85×10^7 cm⁻².

(b)
$$T_{O} > 850^{\circ}C$$

It is shown in Appendix IV that, for $T_Q>850^{\circ}\mathrm{C}$, more than half of the vacancies form divacancies during quenching. During recovery then, due to the activation energy for vacancy combination, single vacancies decay out as singles. Divacancies, on the other hand, cannot dissociate during low temperature annealing if the binding energy of a divacancy is more

^{*} We are indebted to G. Schoeck⁽¹⁴⁾ for suggesting this treatment of the combination decay.

[†] T_Q is referred to as the quenching temperature.

^{*} Collision probability on a three dimensional random walk consideration is a more rigorous treatment of the problem; however, the solution is not available. It is considered, nevertheless, that the above approximation is quite reasonable.

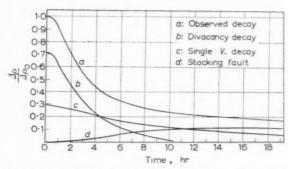


Fig. 2. Reproduction of Fig. 11 due to Bauerle and Koehler, representing the decay of quenched-in resistivity after quenching from 900°C and annealing at 40°C. (Component b, c, and d derived through the present theory.)

than $0.2~{\rm eV},^*$ which it most likely is. This can be seen from the numerical answer to the equation

$$1/t_2 = Azv \exp\left[-(E_M + E_R + B)/kT\right]$$
 (11)

where B is the binding energy of a divacancy and z the coordination number which, here, equals 14.

The similarity between the $(\cosh \alpha Kt)^{-2}$ curve in Fig. 1 and the observed curve in Fig. 2 implies that the decay consists of a combination decay with sessile rings as the predominant sinks. Since single vacancies and divacancies† decay out independently of each other to common sinks, i.e. dislocations in the network and the sessile rings, the decay is governed by four simultaneous differential equations. The analysis of the decay curve ($T_Q = 900^{\circ}\text{C}$, annealed at 40°C) is not rigidly possible because the full solution of the problem (equations 7 and 8) is too involved to allow the evaluation of all constants from the experimental curve. Instead the curve is considered to be composed of additive parts as will be discussed below, Fig. 2, namely the curves representing the resistivity due to single vacancies, due to divacancies and due to the stacking faults bordered by newly formed sessile dislocations. Since the mobility of single vacancies, $E_{M1} = 0.82 \text{ eV}$, is much less than that of divacancies, $E_{M2} = 0.63$ eV at 40°C, the tail of the decay curve is due, solely, to the migration and annihilation of single vacancies. Since the remaining decay was

1959

found experimentally to be exponential, the number of sinks can be considered to be effectively constant after 12 hr. The stacking fault area enclosed by the sessile rings, together with the sessile rings themselves. is considered to be responsible for the resistivity remaining after the annealing, whereby the latter contribute far less than the stacking faults. The curve of resistivity due to the stacking fault area, c, is approximated by 0.117 $\{\eta - (\cosh \alpha Kt)^{-2}\}\$ where η is the fraction of vacancies which are absorbed at sessile rings. ρ_d is calculated to be 3.5×10^8 cm⁻² from the curves a, c in Fig. 2 with aid of equation (2) with the selected values of A, z and E_{M} . Hence, the increase in the total dislocation density due to formation of sessile rings is calculated to be a factor of about 10, since from exponential decay after a quench from 750°C the dislocation density was determined as $\rho_d = 3 \times 10^7 \text{ cm}^{-2}$

The central part of the curve b may be approximated by a variable sink decay of divacancies. Assuming η in the above equation to be 0.9 and 75 per cent of the initial quenched-in resistivity to be due to the annihilation of divacancies (which results from a reasonable extension of the tail of the decay), the decay is given by

$$(\Delta \rho / \Delta \rho_0) = (\cosh \alpha K t)^{-2} + 0.133 \{ \eta - (\cosh \alpha K t)^{-2} \}$$
(12)

From the value at t=6 hr, αK is calculated to be $8.05 \times 10^{-5}~{\rm sec^{-1}}$. α is given by

$$\alpha = (A_2 Z_2 v/n_0) \exp{(-E_M/kT)} \quad \text{with} \quad A_2 \simeq 1.$$

 $Z_2=8,\; n_0=6 imes 10^{22}\; \mathrm{cm^{-3}}$ and $E_{M2}=0.63\; \mathrm{eV},$ and is evaluated as $\alpha = 1.07 \times 10^{-19}/\text{sec cm}^3$; K is found to be $7.8 \times 10^{14} \, \mathrm{cm}^{-3}$. The initial concentration of vacancies is about 1.6 \times 10⁻⁴ for $T_{O} = 900^{\circ}\mathrm{C}$ and N_{\star} is found to be 3.7×10^{10} cm⁻³. The radius of the average sessile ring is then calculated to be 2.2×10^{-4} cm. The number of sessile rings was calculated assuming that divacancies and vacancies can be annihilated at any place along the periphery of an assumed circular ring. Since it is likely, however, that they may not be annihilated with equal facility at all positions on the ring, the number of rings so calculated can be considered to be the lower limit and hence, the size so calculated an upper limit to the size of the ring. The density of sessile dislocations is calculated as 5×10^7 cm⁻², which is in fairly good agreement with the value estimated from the tail of the decay considering the many simplified assumptions. Bauerle and Koehler's observation showed the remaining resistivity after annealing as about $0.35 \times 10^{-8} \,\Omega$ -cm. Our calculations show the total stacking fault area

^{*} Although Koehler *et al.* consider the binding energy to be less than 0.3 eV (probably 0.1 eV), calculations (Kimura Thesis) show that a binding energy of 0.4 eV is equally reasonable as suggested from the measurements of Okkerse⁽¹⁸⁾ on self-diffusion in Au. Theoretical estimates by Bartlett and Dienes⁽¹⁹⁾ as well as by Seeger and Bross⁽¹⁹⁾ show the binding energy to be between 0.3 and 0.5 eV.

[†]Triple vacancies can also move with an activation free energy about equal to that of divacancies, and hence we cannot differentiate between the motion of these two. Since the number of triple vacancies and larger vacancy clusters are small compared to the number of divacancies, we neglect

enclosed by sessile rings to be 0.57×10^4 cm²/cm³. Assuming that one-third of the total area contributed to the resistivity, the resistivity due to stacking fault of unit area is estimated to be $0.2 \times 10^{-11}~\Omega$ -cm/cm². From this the resistivity due to stacking faults associated with extended dislocations (10 atomic distances) of density N cm² would be $0.6 \times 10^{-18}N$ Ω -cm, which is about 60 times larger than the calculated value of resistivity due to unextended dislocations (20) and is in good agreement with Seeger's estimate of 40, (21)

(c) Explanations of other results in the Bauerle and Koehler experiments

The slow decay rate at the beginning of annealing for $T_Q=800^{\circ}\mathrm{C}$ can be considered as a period during which vacancy clusters collapse. Slight deformation after quenching but before annealing can increase the dislocation density and hence increase the rate of decay at the beginning of the annealing, and also vacancies created by deformation may facilitate the nucleation of sessile dislocations.

Since for high quenching temperatures, the predominant sinks after the nucleation period are sessile rings, the decay rate at later stages in the recovery is not affected by deformation.

Impurity atoms can act as trapping centers for vacancies. (22) These traps can reduce the repulsive force between two separated vacancies and result in more easily created nuclei for sessile rings. A fast decay rate and a large residual resistivity may be explained in this way.

5. CONCLUSIONS

The complicated features of decay of quenched-in vacancies in Au can be explained by introducing two types of sinks, namely random dislocations or dislocations forming a network on the one hand, sessile dislocation rings formed by aggregation and condensation of vacancies on the other. Nucleation of sessile rings is accomplished for the most part during quenching if the specimen is quenched from above a critical temperature, 800°C in Au, and is practically absent if the quenching temperature is lower than 750°C. More than half the vacancies form divacancies and vacancy clusters during quenching from about 800°C. For quenching from below the critical temperature, most of the vacancies are quenched-in as single vacancies.

During low temperature annealing, single vacancies anneal out as single vacancies with a correspondingly high activation energy of motion, and dissociation of divacancies does not occur. Therefore, for low quenching temperatures, stray dislocations or dislocations in the network are the only sinks and the decay is exponential with a high activation energy for vacancy migration; for high quenching temperatures the decay is a combination decay with low activation energy due to the motion of the predominant divacancies mainly to sessile dislocations. To explain the experimental results, a repulsive force of about 0.24 eV has to be assumed between any two vacancies separated from each other by a few atomic distances. The binding energy of a divacancy is taken as 0.4 eV.

Calculations based upon experimental results and the present theory show that the increase in the total density of dislocation due to the formation of sessile rings is about 10 times.

Note added in proof

While the present paper was in press, a substantial part of the predictions and conclusions in it, as well as in the previous paper by D. Kuhlmann-Wilsdorf⁽⁸⁾ have been shown to be correct in a series of experiments initiated following discussions and lectures by one of us (RM).

We should like to thank Drs. Hirsch, Silcox, Smallman and Westmacott for informing us of their recent success in observing sessile rings, using electron transmission microscopy in aluminum foils, and to Drs. Hirsch and Silcox for informing us of their observations of dislocation tetrahedra in quenched gold.

APPENDIX I

Derivation of Variable Sink Decay

The number of sinks, n_s , is given by

$$n_{\circ} = (2\pi r/D)N_{\circ} \tag{I-1}$$

where r is the radius of a sessile ring, N_s is the number of sessile rings and D is the diameter of the atom. Differentiating equation (I-1).

$$dn_s/dt = 2(\pi N_s/D)(dr/dt) \tag{I-2}$$

If N_V^{-1} is the number of vacancies disappearing to form N_s number of sessiles with radius r, then

$$N_V^{-1} = (4\pi r^2/\pi D^2) N_s = (4r^2/D^2) N_s \qquad {\rm (I-3)}$$

If N is the number of vacancies remaining after time t, then

$$N = N_0 - N_V^{-1} = N_0 - (4r^2/D^2)N_s$$
 (I-4)

and

$$dN/dt = (4N_s/D^2)2r(dr/dt)$$
 (I-5)

Substituting (I-4) in (1), we have

$$-(dN/dt) = \alpha n_s [N_0 - (4r^2/D^2)N_s]$$
 (I-6)

From (I-1), (I-2), (I-5) and (I-6), we have

$$dn_s/dt = (\pi^2/2)N_sN_0\alpha - \alpha n_s^2/2$$
 (I-7)

Putting

$$(\pi^2/2)N_sN_0\alpha \equiv \beta^2/2$$

and integrating (I-7), we have

$$egin{aligned} n_s &= \pi \sqrt{(N_s N_0)} [\exp{\{lpha \pi (N_s N_0)^{rac{1}{2}}t\}} - 1]/\ &[\exp{\{lpha \pi (N_s N_0)^{rac{1}{2}}t\}} + 1] \end{aligned}$$

putting $K = (\pi/2)(N_s N_0)^{\frac{1}{2}}$, we have

$$n_s = 2K \tanh \alpha Kt$$
 (4)

Integrating (1) with (4), we have

$$N = N_0(\cosh \alpha Kt)^{-2} \tag{5}$$

For divacancies, equation (I-1) is changed into

$$n_s = (2\pi r/D)N_s$$

and equation (I-3) into

$$N_V^{-1} = (2r^2/D^2)N_s$$

Consequently, K becomes $K = \pi (N_s N_0/2)^{\frac{1}{2}}$.

APPENDIX II

Derivation of Combination Decay

If N_F and N_V are the number of vacancies which have disappeared at fixed sinks and at variable sinks, respectively, and N_0 is the initial number of vacancies, $N=N_0-N_F-N_V$. Equation (6) is written as

$$dN_F/dt + dN_V/dt = \alpha (n_F + n_V)(N_0 - N_F - N_V) \eqno(\Pi - 1)$$

Since N_F is independent of n_F as is N_F of n_F , equation (II–1) can be separated as

$$dN_E/dt = n_E(N_0 - N_E - N_V)$$
 (II-2)

and

1959

$$dN_V/dt = n_V(N_0-N_F-N_V) \qquad {\rm (II-3)} \label{eq:NV}$$

The quantity n_V is given by

$$n_s=\pi (N_V N_S)^{\frac{1}{2}}$$
 for single vacancies, and $n_s=\sqrt{2\pi (N_V N_S)^{\frac{1}{2}}}$ for divacancies.

Dividing equation (II-2) by equation (II-3), we have

$$dN_F/dN_V = (n_1/\pi N_s^{\frac{1}{2}})N_V^{-\frac{1}{2}}$$
 for single vacancies.

Since $n_1/\pi N_s$ is constant with time, N_F and N_V , this expression may be represented by M. Hence we have

$$dN_F/dN_V = MN^{-\frac{1}{2}} \tag{II-4}$$

Integrating (II-4) we have

$$N_F = 2MN_V^{\frac{1}{2}}$$

(the integration constant is evaluated as zero), and

$$N_V = N_V^2 / 4M^2$$
 (II-5)

Substituting equation (II–5) into equation (II–2), and integrating

$$N_F = \frac{(B^2 + q)\{\exp{[(-q)^{\frac{1}{2}}t]} - 1\}}{2C[B + (-q)^{\frac{1}{2}}] - 2C[B - (-q)^{\frac{1}{2}}]\exp{[(-q)^{\frac{1}{2}}t]}}$$
(7

where $A=\alpha n_1N_0,\ B=-\alpha n_1,\ C=-\alpha n_1/4M^2$ and $q=4AC-B^2.$

APPENDIX III

Koehler et al. (9) suggest for the vacancy–divacancy complex an effective diffusion coefficient, D_e , as

$$D_e = (\tau_1 D + \tau_2 D_2)/(\tau_1 + \tau_2)$$
 (III-1)

where τ_1 and τ_2 are the time a vacancy spends as a single vacancy and as a part of a divacancy, respectively, D and D_2 are the diffusion coefficients of a single and divacancy, respectively. These four quantities are given as follows:

$$\begin{split} 1/\tau_1 &= 8\nu \exp{(-E_{M1}/kT)c} \\ 1/\tau_2 &= \nu \exp{[-(E_{M1}+B)/kT]} \\ D &= (\nu a^2/6) \exp{(-E_{M1}/kT)} \end{split}$$

and

$$D_2 = (\nu_2 a^2/24) \exp(-E_{M2}/kT)$$

where ν and ν_2 are the frequency factors of singleand di-vacancies, respectively, E_{M1} and E_{M2} are the activation energies for migration of single- and divacancies, c is the concentration of single vacancies, B is the binding energy of a divacancy and a is the nearest neighbor atomic distance. With values given by them for these quantities, D_c can be written as

$$D_e = D \, \frac{1 + 0.9 c \, \exp{[(E_{M1} + B - E_{M2})/kT]}}{1 + 8 c \exp{(B/kT)}}$$

 $D_e=33D$ for $T_Q=1000^\circ\mathrm{C}$ and $D_e=3D$ for $T_Q=700^\circ\mathrm{C}$. Therefore, the half decay time for $T_Q=700^\circ\mathrm{C}$

Table 1. Number of jumps made by a single vacancy during quenching

T_1	(°C)	18 - 9 5		18 - 5	m × 10⁴°C/sec
(0)	(0)	$(p = 2.0 \times$	To C/sec)	$\psi = a$	× 10 C/sec
1000	900	2 ×	10^{9}	1	$\times~10^{9}$
900	800	1 ×	109	5	$\times 10^{8}$
800	700	4.5 ×	108	2.2	$\times 10^{8}$
700	600	1.6 ×	10 ⁸	8	$\times 10^7$
600	500	5 ×	107	2.4	$\times 10^7$
500	400	0.9 ×	107	5	$\times 10^a$
400	300	1.2 ×	10 ⁶	6	\times 10 ⁵
300	200	6 ×	104	3.2	$\times 10^4$
200	100	9 ×	102	4	$\times 10^2$
100	0	10		5	

VO1 7 19

should be about 11 times greater than the half decay time for $T_Q=1000^\circ\mathrm{C},$ if both decays are approximated as exponential. The actual observations, however, show that the half decay time at $60^\circ\mathrm{C}$ for $T_Q=700^\circ\mathrm{C}$ is 19 hr, which corresponds to about 114 hr at $40^\circ\mathrm{C};$ and at $40^\circ\mathrm{C}$ for $T_Q=1000^\circ\mathrm{C}$ the half decay time is 0.5 hr. This difference appears to be too great to be explained by the Koehler et~al. analysis.

APPENDIX IV

Formation of Divacancies and Vacancy Clusters During Quenching

Numerical values as to the percentage of divacancies etc., have been used several times already in this paper. They were gained by the following considerations: The number of jumps a vacancy makes during a period in which the temperature of the specimen falls from T_1 to T_2 is given by

$$m = \int_{T_{-}}^{T_{2}} Azv \exp\left(\frac{E_{M}}{kT}\right) dt$$
 (IV-1)

where T is a function of the time t. Experimentally, T is found to be $T = T_O - \beta t$ where β , the quenching rate, is $2.5 \sim 5 \times 10^{4}$ °C/sec. Equation (IV-1) is integrated numerically for temperature intervals of 100°C and shown in Table 1. We may also calculate the number of jumps the average vacancy has to make in order to establish chemical equilibrium between single- and di-vacancies at temperature T. The results are shown in Table 2. From these two calculations we can estimate for each quenching temperature, a temperature whose corresponding chemical equilibrium between single- and di-vacancies is established during quenching. These temperatures, T_{eq} , are given in Table 3. The ratio of the concentrations, c_1 and c_2 , of single- and di-vacancies, respectively, in chemical equilibrium is given by

$$c_2/c_1 = 0.858c_1 \exp(B/kT)$$

Assuming that the concentration of vacant sites, n, is constant during quenching, i.e. $n=c_1+2c_2$. The ratio at T_{eq} for each quenching temperature is

Table 2. Number of jumps, m^1 , a vacancy is required to make in order to establish chemical equilibrium between single- and di-vacancies

$_{(^{\circ}\mathrm{C})}^{T_{Q}}$	$(T = {}^{m^1}400^{\circ}\text{C})$	$(T=\overset{m^1}{300^{\circ}\text{C}})$	$(T=rac{m^1}{200^{\circ} ext{C}}$
60°	1.2×10^7	$2.5 imes10^7$	6.8×10^7
700	3×10^6	6.2×10^{6}	1.7×10^{7}
80°	1.1×10^{6}	$2.1 imes 10^6$	$5.8 imes 10^6$
90°	$4 imes 10^5$	8.2×10^5	$2.3 imes 10^6$
100°	1.9×10^{5}	$3.9 imes 10^5$	1.1×10^{6}

calculated and shown in Table 3, along with n, and c_1 and c_2 . Here B is taken as 0.4 eV.

For $T_Q>850\,^{\circ}\mathrm{C}$, large vacancy clusters form and collapse to sessile rings during quenching, although the number of such clusters is very small compared to the number of divacancies.* Moreover, if it is assumed that the contribution of a divacancy to the resistivity is 1.6 times that of a single vacancy, the formation of divacancies does not change appreciably the exponential relationship between quenched-in resistivity and quenching temperature below $950\,^{\circ}\mathrm{C}$.

It must be noted that the number of jumps during quenching, ~10⁹, is larger than the number of jumps during annealing, ~10⁸. The fact that vacancies can be quenched into metals means that sinks for vacancies are not effective at high temperatures, i.e. above about 400°C.† The reason for this is the comparatively low binding energy between vacancies and dislocations which, for high temperatures, prevent the establishment of vacancy concentrations on dislocations sufficiently high to cause climbing of dislocations or formation of small sessile rings on dislocations (these mechanisms will be discussed in Part II).

REFERENCES

- R. Maddin and A. H. Cottrell, Phil. Mag. 46, 735 (1955).
- J. W. Kauffman and J. S. Koehler, Phys. Rev. 88, 149 (1952); Ibid. 97, 555 (1955).
 B. G. Larazev and O. N. Ovcharenko, Dokl. Akad. Nauk SSSR 100, 875 (1955).

Table 3. T_{eq} and concentrations, c_1 and c_2 , of single- and di-vacancies after quenching

T_Q (°C)	$T_{eq} \ (^{\circ}C)$	n	c_1	c_2	c_2/c_1
600	400	$0.52 imes 10^{-5}$	0.52×10^{-5}	0	0
700	350	0.21×10^{-4}	0.20×10^{-4}	0.5×10^{-6}	2.5×10^{-2}
800	300	0.63×10^{-4}	0.5×10^{-4}	0.07×10^{-4}	0.14
900	250	1.6×10^{-4}	0.82×10^{-4}	0.4×10^{-4}	0.49
1000	250	0.34×10^{-3}	0.134×10^{-4}	0.1×10^{-4}	0.75

Initial concentration of vacant site, n, is calculated using an entropy factor of 3. Quenching rate, β , is 2.5×10^{4} °C/sec.

^{*}The maximum size of a cluster before collapsing is estimated to be about 10 vacancies if the surface tension minus the stacking fault energy is taken as 1000 ergs/cm².(8) † Kimura, Ph.D. Thesis

- F. J. Bradshaw and S. Pearson, Phil. Mag. 1, 812 (1956); Ibid. 2, 379, 570 (1957). C. Panseri, F. Gatto
- and T. Federight, Acta Met. 5, 50 (1957).
 3. C. H. Li, J. Washburn and E. R. Parker, Trans. Amer. Inst. Min. (Metall.) Engrs. 197, 1223 (1953). M. Levy and M. Metzger, Phil. Mag. 46 (vii) 1021 (1955). E. Roswell and A. S. Nowick, Acta Met. 5, 228 (1957). J. W. KAUFF-MAN and M. MESHII, Bull. Amer. Phys. Soc. 2, 145 (1957). L. TANNER and R. MADDIN, Tanner M.S. Thesis, Univ. of Penn. (1958). J. TAKAMURA, Private Communication.
- 4. J. E. BAUERLE and J. S. KOEHLER, Phys. Rev. 107, 1493
- 5. J. TAKAMURA, Kinzoku-Butsuri (Metal Physics) 2, 112 (1956).
- 6. J. TAKAMURA, Private Communication.
- 7. J. Friedel, Les Dislocation. Gauthier-Villars, Paris (1956).
- 8. D. KUHLMANN-WILSDORF, Phil. Mag. 3, 125 (1958).
- 9. J. S. Koehler, F. Seitz and J. E. Bauerle, Phys. Rev. 107, 1499 (1957).
- 10. J. H. BARTLETT and G. J. DIENES, Phys. Rev. 89, 848 (1953).

- 11. A. E. Roswell and A. S. Nowick, Bull. Amer. Phys. Soc. 2, 122 (1957).
- 12. A. H. COTTRELL and B. A. BILBY, Proc. Phys. Soc. A62, 49 (1949).
- 13. A. H. COTTRELL, Vacancies and other Point Defects in Metals and Alloys 1. Inst Metals Mono. and Report Ser. No. 23. Institute of Metals, London (to be published).
- 14. G. Schoeck, Private Communication.
- 15. H. Brooks, Impurities and Imperfections (Edited by O. T. Marzke) p. 1. American Society for Metals, Cleveland (1955).

- J. D. ESHELBY, Acta Met. 3, 487 (1955).
 A. SEEGER, Phil. Mag. 46, 1194 (1955).
 B. OKKERSE, Phys. Rev. 103, 1246 (1956).
 A. SEEGER and H. BROSS, Z. Phys. 145, 161 (1956).
- 20. For example, A. Seeger and H. Stehle, Z. Phys. 146, 242 (1956).
- 21. A. SEEGER, Canad. J. Phys. 34, 1219 (1956).
- 22. W. M. LOMER and A. H. COTTRELL, Phil. Mag. 46 (vii) 711 (1955).

QUENCHED-IN VACANCIES IN NOBLE METALS—II MECHANISM OF QUENCH HARDENING*

H. KIMURA† R. MADDIN‡ and D. KUHLMANN-WILSDORF‡

Two types of hardening were observed on ageing after quenching Cu wire, depending on the quenching temperature.

A comparison of the observed quench hardening in Cu and Au with the decay of quenched-in resistivity in Au shows that the two types of hardening can be explained assuming two types of sinks for vacancies as discussed in Part I. For high quenching temperatures, the hardening is considered to be due to the formation of sessile rings; for low quenching temperatures, to the annihilation of vacancies at pre-existing dislocations. Detailed mechanisms for the annihilation of vacancies are discussed.

The activation energies for migration of single- and di-vacancies in Cu are found to be about 0.7 eV and about 0.6 eV, respectively.

TREMPE DES LACUNES DANS LES METAUX NOBLES-II

Deux types de durcissement ont été observés au cours du vieillissement après trempe de fils de cuivre. Ceux-ci dépendent de la température de trempe. La comparaison du durcissement de trempe observé dans le cuivre et dans l'or avec l'évolution de la résistivité après trempe dans l'or, montre que les deux types de durcissement peuvent être expliqués sur la base de deux types de puits pour les lacunes (cfr partie I). Pour des températures de trempe élevées, le durcissement semble dû à la formation d'anneaux sessiles. Pour des températures de trempe plus basses, ce durcissement semble dû à l'annulation des lacunes aux dislocations préexistantes. Les auteurs discutent en détail de mécanismes permettant l'annulation des lacunes.

Les énergies d'activation pour le déplacement de lacunes simples et de paires de lacunes dans le cuivre sont de l'ordre de $0.7~{\rm eV}$ et $0.6~{\rm eV}$, respectivement.

ABSCHRECKEN VON LEERSTELLEN IN EDELMETALLEN—II MECHANISMUS DER ABSCHRECKVERFESTIGUNG

Beim Altern abgeschreckter Cu-Drähte wurden je nach der Abschrecktemperatur zwei Typen von Verfestigung beobachtet.

Ein Vergleich der beobachteten Abschreck-Verfestigung von Cu und Au mit der Abnahme des eingefrorenen Widerstands von Au zeigt, dass sich die beiden Verfestigungstypen durch die Annahme zweier Arten von Leerstellensenken erklären lassen, wie bereits in Teil I diskutiert. Bei hohen Abschrecktemperaturen wird als Ursache der Verfestigung die Bildung von unbeweglichen Ringen angesehen, bei niedrigen Abschrecktemperaturen das Verschwinden der Leerstellen an den von vornherein vorhandenen Versetzungen. Mechanismen für das Verschwinden der Leerstellen werden im einzelnen diskutiert.

Für die Aktivierungsenergie der Wanderung von Einzelund Doppelleerstellen in Cu wurden etwa 0,7 eV bzw. 0,6 eV gefunden.

1. INTRODUCTION

In Part I of this report, in which the recovery of quenched-in resistivity in Au was analyzed, we concluded that the most probable sinks for quenched-in vacancies are sessile dislocation rings formed by the condensation of vacancies and stray dislocations or dislocations in the form of a network.

The mechanism for the annihilation of vacancies at sessile rings simply consists in the removal of atoms from the edges of the enclosed stacking fault. It

appears likely that the sessile dislocations will tend to be hexagonal, following $\langle 110 \rangle$ directions, and that vacancies will be added, preferentially, at sites where they are jogged. The mechanism for the annihilation of vacancies at extended dislocations, on the other hand, is probably quite complicated. Some of the details of these processes might be clarified through the simultaneous study of the electrical conductivity and of the change in mechanical properties of pure f.c.c. metals after quenching.

19

Quench hardening in Au has been investigated extensively by Kauffman and Meshii, $^{(1)}$ but little is known about the various aspects of quench hardening in Cu, except that Makin $^{(2)}$ found that Cu crystals became harder by quenching from 900° C to -70° C and also by subsequent ageing. Since Cu and Au can be expected to show closely similar behavior, and

^{*} Part of a thesis submitted 11 April 1958 to the Faculty of the Graduate School of Arts and Sciences, University of Pennsylvania, by H. Kimura in partial fulfillment of the requirements for the Ph.D. degree. Sponsored by the Office of Naval Research. Received May 5, 1958.

[†] Formerly, School of Metallurgy, University of Pennsylvania; now, Department of Metallurgy, University of Tokyo, Tokyo, Japan.

^{*} School of Metallurgy, University of Pennsylvania.

since no detailed resistivity measurements on quenched Cu are as yet available, extensive investigations on the quench hardening in Cu, due to the authors, and the results on Au due to Kauffman and Meshii are discussed in conjunction with the experiments of Bauerle and Koehler⁽³⁾ on the recovery of quenched-in resistivity in pure Au.

2. EXPERIMENTAL PROCEDURE

Copper wire specimens, 99.999% pure and 0.25 mm in diameter, were heated by passing an electric current through them. Argon gas, containing a small amount of alcohol vapor, was used to protect the specimens from oxidation (the amount of hydrogen resulting from the dissociation of the alcohol was negligibly small). The temperature of the specimens was obtained, from measurements of their electrical resistance, to an accuracy of $\pm 15^{\circ}\mathrm{C}$. The specimens were then quenched into ice water by either of two different methods:

In one quenching method the heating current was cut off by means of a mercury switch immediately after immersing the specimen into the quenching medium. This method will be referred to as a "water quench". In another method, the current was cut off before the specimen was immersed in the quenching medium. This will be referred to as an "air-quench", mainly because the specimen in fact cooled to some extent even before it entered the ice water.

VOL.

1959

Larger specimens, 0.64 mm in diameter, were also used. They were heated in a vertical furnace, through which argon gas flowed, and were quenched into water, held at 4°C, by allowing the specimen to fall into the water. No measurable bending or change of yield point were caused by the fall of the specimens into water, as was ascertained through experiments with

dummy specimens. This quenching method will be referred to as a "large specimen quench".

After quenching, the 0.25 mm specimens were aged in boiling water or water baths of different temperatures, and the 0.64 mm specimens in oil baths. The temperature of the baths was controlled to within $\pm 1^{\circ}$ C. Tensile tests were performed with a tensile testing apparatus designed for the testing of thin wires. The apparatus was somewhat soft but yielded good reproducibility, as was found from measurements on several Cu single crystal wires, as well as on annealed polycrystalline wires. The accuracy of measurement was determined as ± 3 per cent for the 0.64 mm specimens and ± 5 per cent for the 0.25 mm specimens.

In the 0.64 mm specimens, the grain size was measured after the tensile test. Results from specimens with grain sizes outside of the range, 20 ± 10 grains/mm², were not recorded. The observed yield stress for specimens with different grain sizes were standardized using an empirical relationship between grain size and yield stress (30 g/mm² per 10 grains/mm²). The grain size was not individually determined in the 0.25 mm wire, since many specimens chosen at random all had about the same grain size of $100 \, \text{grains/mm}^2$.

Kauffman and Meshii used the same quenching technique as the "water quench" described above; the diameter of the Au wire they used was 0.40 mm.

3. RESULTS

(1) Water quenching of 0.25 mm wire

As is apparent from Fig. 1, which shows the ageing curves at 100°C for various quenching temperatures, two different types of hardening are observed depending on the quenching temperature. With a quenching

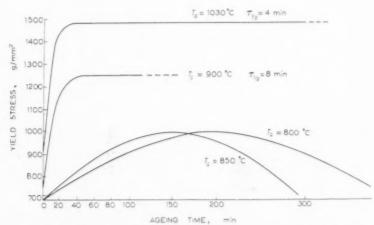


Fig. 1. Change in yield stress of $0.25\,\mathrm{mm}$ specimens after water quench, as dependent on ageing time with the ageing temperature of $100\,^{\circ}\mathrm{C}$.

temperature, T_Q , higher than 900°C, a small initial increase in the yield stress (less than about 30 per cent) was observed.* Immediately after immersal in the temperature bath the yield stress increased rapidly then leveled off, and maintained the increased value for prolonged ageing periods. The half time, i.e., the time at which the specimens attained one-half of the total increase in the yield stress, was about 4 min for $T_{Q} = 1030^{\circ}$ C and about 8 min for $T_{Q} = 900^{\circ}$ C. The amount of hardening was a function of the quenching temperature; with the yield stress at saturation equal to $1480~\mathrm{g/mm^2}$ for $T_Q=1030^\circ\mathrm{C}$ and to $1240~\mathrm{g/mm^2}$ for $T_o = 900$ °C. (This may be compared with 670 g/mm², the yield stress of annealed specimens.) Fig. 2 shows the actual measurements of the age hardening curve at 100° C for $T_{Q} = 1030^{\circ}$ C.

When the quenching temperature was lower than 850°C, there was no observable initial hardening; the yield stress increased rather slowly with ageing after quenching, and decreased on further ageing. The amount of the increase was almost independent of the quenching temperature, the maximum yield stress being 1000 g/mm², but the time to reach the maximum hardening, $t_{\rm m}$, depended upon the quenching temperature, and was $t_{\rm m}=150~{\rm min}$ for $T_Q=850^{\circ}{\rm C}$ and $t_{\rm m}=200~{\rm min}$ for $T_Q=800^{\circ}{\rm C}$.

The activation energy for the hardening process in specimens quenched from $T_Q = 1030^{\circ}\text{C}$ was calculated from the ageing curves at 100° , 84° , 72° and 61°C by plotting the logarithm of the time for particular values of the yield stress against $1/T_A$, where T_A is the

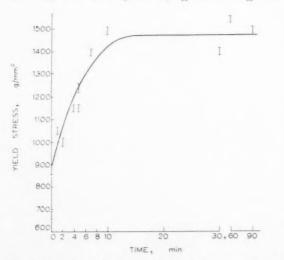


Fig. 2. Experimental points and interpolation curve of change in yield stress of water quenched 0.25 mm Cu specimen with quenching temperature $T_{\varrho}=1030^{\circ}\mathrm{C}$, aged at 100°C.

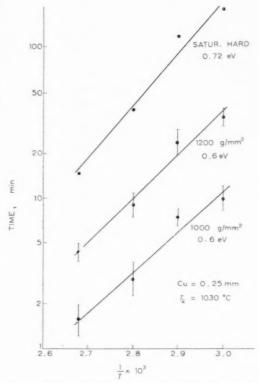


Fig. 3. Plot for the determination of the activation energy for hardening after water quenching. Ageing temperature; 100°, 84°, 72° and 61°C.

VO

19

ageing temperature. These data are shown in Fig. 3. The activation energy using this method was found to be $0.6\pm0.05\,\mathrm{eV}$. The activation energy as determined from the time to reach saturation hardening, on the other hand, was about $0.7\,\mathrm{eV}$, but a considerable error is involved in estimating the time at which maximum hardening is reached.

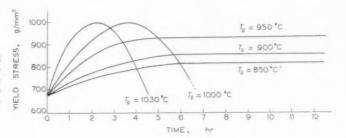
The described characteristics of hardening for $T_Q \ge 900^{\circ}\mathrm{C}$ are very similar to those for the hardening of quenched Au observed by Kauffman and Meshii, i.e. the increase in yield stress is about 2 to 5 times and depends on the quenching temperature; no resoftening is observed on low temperature ageing; the half time is 2 min at $100^{\circ}\mathrm{C}$.

(2) Air quenching of 0.25 mm wire

Fig. 4 shows the curves obtained for ageing at 100°C for various quenching temperatures. The features of the hardening curves with $T_Q \geq 1000$ °C are essentially those noted for low temperature water quenching. This is not at all surprising, since the actual quenching temperature was undoubtedly much lower than the recorded quenching temperature. Again, the maximum hardeness is almost independent of the recorded quenching temperature. For recorded quenching

^{*} The cause of any initial hardening has not been investigated in this paper.

Fig. 4. Ageing curves for air-quenched 0.25 mm Cu specimen. Ageing temperature 100°C. The recorded temperature, in this case, is rather higher than the effective quenching temperature.



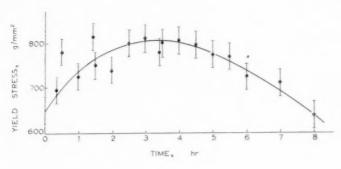
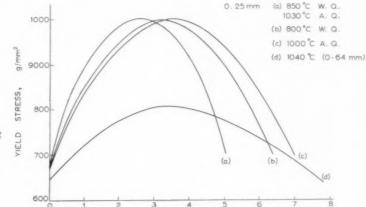


Fig. 5. Change in yield stress of Cu wire (0.64 mm) with ageing time (T_Q = 1040°C, T_A = 100°C).



TIME ,

Fig. 6. Comparison of three quenching methods.

1959

temperatures of 950°, 900° and 850°C, no overageing effect was observed. The greatest hardening achieved was lower for lower quenching temperatures. It would seem that these curves correspond to actual quenching temperatures lower than the lowest water quenching temperatures examined.

(3) Water quenching of 0.64 mm wire

With a quenching temperature of 1040°C, there was a small amount of initial hardening, namely to 650 g/mm² from an initial value of 550 g/mm². Qualitatively, the age hardening curve here is the same as for the low temperature water quenching. This, again, is not surprising since (i) the specimen was exposed to a cooler atmosphere before reaching the quenching bath, and (ii) a thicker specimen causes a slower rate of quenching. Fig. 5 shows an ageing

curve at 100°C for $T_Q=1040$ °C. A comparison of the three different quenching methods is given in Fig. 6. Although the time to reach maximum hardening depended upon both quenching temperatures and method, the fractional increase in yield stress was the same in all cases.* Overageing followed at about the same rate as hardening. This comparison can thus be interpreted as follows: Quenching from the same recorded quenching temperature by the different methods results in different effective quenching temperatures and, correspondingly, different concentrations of quenched-in vacancies. Therefore, an activation energy calculated for the hardening and

^{*} The apparently smaller increase in 0.64 mm wire was due to initial hardening. The maximum increase above the value for the annealed specimen, in reality, was also about 50 per cent, namely to $800\,\mathrm{g/mm^2}$ from a yield stress of the annealed specimen of $550\,\mathrm{g/mm^2}$.

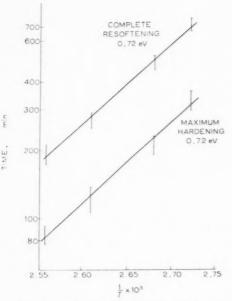


Fig. 7. Calculation of the activation energies for the hardening and the resoftening, using 0.64 mm Cu wire quenched from 1040°C and aged at temperatures between 95°C and 117°C.

resoftening processes from the results of one of the three quenching methods can be considered also to be representative of the other two quenching methods as long as the same type of hardening curve is observed.

Ageing curves at 117°, 110°, 100° and 95°C for the 0.64 mm wire quenched from 1040°C were used to calculate the activation energy for the type of hardening curve exhibiting an overageing effect, Fig. 7. The logarithm of the times for both maximum hardening and complete resoftening were plotted against $1/T_A$. The activation energy for both methods was found to be equal to 0.72 ± 0.10 eV. This value should be compared with the activation energy of about 0.6 eV determined for the hardening after a high-temperature water quench of the 0.25 mm specimen (Fig. 3).

4. DISCUSSION

(1) Comparison of Hardening with Resistivity Decay

The kinetics of the hardening after quenching from high temperatures are quite similar to those observed by Kauffman and Meshii in Au and to the resistivity decay in Au quenched from above $850^{\circ}\mathrm{C.^{(3)}}$

The half time for hardening is 4 min at 100°C in Cu quenched from 1030°C, and 2 min at 100°C in Au quenched from about 1000°C. (1) In Au, according to Bauerle and Koehler, (3) the half decay time of the quenched-in resistivity is 30 min at 40°C for $T_O =$

1000°C, which would correspond to about 1 min at 100°C. Following the arguments in Part I of this report, and since the activation energies after rapid water quenching are almost the same for the two metals, i.e., 0.6 eV in Cu and 0.63 eV in Au,⁽³⁾ we may conclude that (i) the hardening in the 0.25 mm Cu specimens, water quenched from above 900°C, (ii) the hardening in Au observed by Kauffman and Meshii, and (iii) the resistivity decay in Au quenched from above 850°C are predominantly due to the migration to sessile rings of divacancies with a small amount of single, trivacancies, or larger clusters. It is, therefore, concluded that in the high temperature water quenching of the 0.25 mm specimens the hardening is due to these sessile rings.

Conversely, although Kauffman and Meshii did not determine detailed ageing curves for $T_o \sim 740^{\circ} \text{C}$ in Au, they reported that the hardening fell to zero with decreasing quenching temperature down to 740°C. We consider, then, that the quenching of Au from below 750°C corresponds to the water quenching of Cu from below 850°C as well as to all air quenching experiments and all results obtained with the thicker specimens. This conclusion appears reasonable not only in view of the larger formation energy of vacancies in Cu, 1.3 eV,* compared to 0.98 eV in Au, but also because, for the quenching of Cu under the conditions named, the features of hardening are similar to the decay in Au. For example, the half decay time in Au is 19 hr at 60° C for $T_{o} = 700^{\circ}$ C, which corresponds to about 1 hr at 100°C, whereas the time for maximum hardening is ~2.5 hr at 100°C for Cu quenched from 850°C. Therefore, we consider that this latter type of hardening and overageing is due to the annihilation of single vacancies at stray or network dislocations originally present in the material. Using equation (10) in Part I of this report, the excess potential energy, E_R , which two single vacancies must overcome in order to form a divacancy is evaluated as 0.23 eV for Cu as compared to 0.24 eV in Au. (Part I)

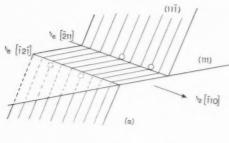
19

(2) Mechanism of Quench Hardening

(a) Fast water-quenches from below 900°C, air-quenches and quenches of 0.64 mm specimens

The mechanism of hardening due to the annihilation of vacancies at dislocations must explain the ageing as well as overageing, and be consistent with the constancy of the number of sinks deduced in Part I of this paper. First we shall examine how vacancies may condense at dislocation sites, aside from the

^{*} The value 1.3 eV is deduced from the difference in the self-diffusion energy, $2.0~{\rm eV}$, $^{(4)}$ and the migration energy for single vacancies, $0.7~{\rm eV}$, observed in the present investigation.



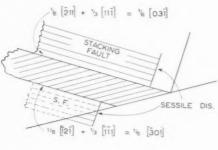


Fig. 8. Formation of sessile rings on an extended screw dislocation.

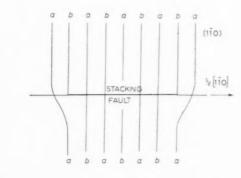
generally accepted possibility that dislocations may form voids⁽⁵⁾ or jogs at places where, statistically, the two partials had combined for a brief instance in the course of thermal motion.⁽⁶⁾ Three particular orientations of dislocations will be considered:

VOL.

1959

 (i) Serew dislocations, with Burgers vector ½[110], on a (111) plane.

Vacancies close to the dislocation could form



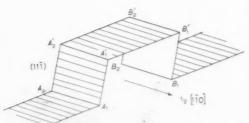


Fig. 9. Climbing of an edge dislocation (after Barnes).

vacancy clusters which collapse to form sessile rings on (111) planes, Fig. 8.* Those segments of the sessile rings which are in contact with the original partial dislocations of the screw dislocation react with them to form sessile dislocations by the reactions

$$\frac{1}{6}[\bar{1}2\bar{1}] + \frac{1}{3}[\bar{1}11] = \frac{1}{6}[\bar{3}01]$$

$$\frac{1}{6}[\bar{2}11] + \frac{1}{3}[11\bar{1}] = \frac{1}{6}[03\bar{1}]$$

In this way screw dislocations can be pinned by the absorption of vacancies.

(ii) Edge dislocations, with Burgers vector $\frac{1}{2}[1\overline{1}0]$, on a (111) plane.

As Barnes pointed out, $^{(7)}$ an extended edge dislocation can climb through the addition of vacancies without first forming constrictions. Vacancies can simply condense on the two (1 $\overline{10}$) inserted planes thereby eliminating them, Fig. 9. However, it is necessary for the block of crystal between these two inserted planes to shift a small distance, namely $\frac{1}{12}[11\overline{2}]$, in order to establish the correct sequence of the (110) planes. This behavior causes the climbing of a segment of the extended dislocation, A_1 , A_2 , B_1 , B_2 to A_1^1 , A_2^1 , B_1^1 , B_2^1 .

(iii) Dislocation parallel to a (110) direction.

When a dislocation, with Burgers vector $\frac{1}{6}[1\overline{1}0]$, on the (111) plane is parallel to, say, [101], i.e., the intersection between the (111) plane and the (111) plane, again condensation of vacancies may take place as discussed in (i) but, this time, on the (111) plane, Fig. 10. The segment of the so formed sessile dislocation, with Burgers vector $\frac{1}{3}[\bar{1}1\bar{1}]$ in contact with the $\frac{1}{6}[1\overline{2}1]$ partial, reacts with it to form a $\frac{1}{6}[\overline{101}]$ partial, which further reacts with the [211] partial which moves towards it, thereby removing the stacking fault of the original extended dislocation. This reaction, i.e. $\frac{1}{6}[101] + \frac{1}{6}[211] = \frac{1}{6}[112]$, results in a partial which then traverses the stacking fault on the (111) plane, eliminating it, and further reacts with the $\frac{1}{3}[1\overline{1}1]$ sessile on the opposite side of the stacking fault according to $\frac{1}{3}[1\overline{1}1] + \frac{1}{6}[1\overline{1}2] = \frac{1}{3}[1\overline{1}0]$. Now the original Burgers vector is restored and the climbed section will again dissociate into partials. (8) The corresponding complete reaction is also possible when a glide dislocation is parallel to [01I] as well as when the reaction begins with the other partial. Because of the tendency of stacking faults to be bounded by (110) directions, the connecting segments, i.e., those sections

^{*} The strain field of a dislocation, on the one hand, causes a greatly increased vacancy concentration close to its core, and on the other hand may, in favorable directions, reduce or eliminate the repulsive force between vacancies. Therefore, the nucleation of stacking faults close to a dislocation is probably much facilitated.

Fig. 10. Climbing of an extended dislocation lying parallel to the intersection between its own slip plane and another {111} plane (not cross slip plane).

of the dislocation which connect the climbing segment and the parent dislocation will, preferentially, belong to the cross slip plane or the other possible {111} plane.

With these mechanisms (as well as with the conventional idea of dislocation climb), hardening and resoftening can be explained as schematically represented in Fig. 11. Obviously, the pinning of screw dislocations causes hardening, but it cannot explain resoftening, and we have to examine the consequences of dislocation jogging in general. At the beginning of ageing, the density of the jogs* and their average size are small. They then grow in number and width until they finally coalesce. The presence of jogs should cause hardening for three fairly obvious reasons:

(1) Any connecting segment which does not lie in the cross slip plane must be difficult to move because its slip plane, defined as the plane common to the Burgers vector and the axis of the connecting segment, cannot be a {111} plane. Thus a dislocation line will be pinned by every connecting segment not lying in the cross slip plane. However, we could argue that the great

(3) Moreover, even the connecting segments on the cross slip plane forming an obtuse angle with the main dislocation line would give rise to some hardening. During motion, this type of connecting segment would, on the average, meet obstacles with about the same probability per unit length of dislocation line as the parent dislocation. However, since the resolved shear stress on the cross slip plane is smaller than that on the main slip plane, those obstacles could not be easily overcome.

19

Thus we expect that the yield stress will first increase as the number of jogs increases and then

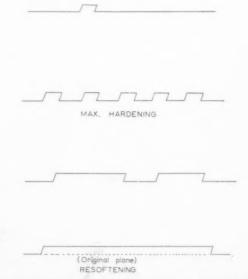


Fig. 11. Hardening and resoftening due to climbing of extended dislocations, schematically.

majority of connecting segments would in fact lie in the cross slip plane, because only in this position can they reduce their energy by dissociating into partials.

⁽²⁾ If this should be so, then, as can be seen from Figs. 9, 10 and 11, about 50 per cent of the connecting segments would form an acute angle with the main dislocation line. Such segments would be subject to a resolved shear stress which has, with regard to the Burgers vector, the opposite direction from the parent dislocation line as well as the climbing parts of it and the other connecting segments, i.e. they would be driven in the opposite direction from the rest of the dislocation. Any hardening due to this effect would be at a maximum where the calculated resolved shear stress is at its maximum and would be absent for orientations for which the resolved shear stress on the cross slip plane is zero. Therefore, in general, jogs containing only easily mobile dislocation parts-on the main slip plane and the cross slip plane-would also pin the dislocation.

^{*} The word "jog" refers to a configuration consisting of a climbing segment and connecting segments. The height of a jog is not restricted to one atomic distance.

decrease again as the jogs coalesce. Moreover, hardening can be expected not to exceed some critical value which will be reached when the width of the jogs is about equal to the distances between them. Hence, maximum hardening should be almost independent of the quenching temperature, but the time to form the critical number and size of jogs should be the larger the smaller is the number of quenched-in vacancies, i.e. the lower is the quenching temperature. The critical number of vacancies to cause maximum hardness may be estimated from the data obtained on air-quenching from 950°C, since this apparently just fails to yield maximum hardening due to jogs. As seen from Fig. 6, the effective quenching temperature for air quenching may be considered to be about 200°C lower than the recorded quenching temperature. The critical number of vacancies (resulting from airquenching from 950°C) therefore, is estimated to be about 10^{17} cm⁻³. If the dislocation density is taken as $5 \times 10^7 \, \mathrm{cm}^{-2}$, $10^{17} \, \mathrm{vacancies/cm}^3$ can create jogs of 50 atomic distances in height and width separated by sections of the parent dislocation 50 atoms long.

(b) Very fast water-quenches from high temperatures

A quantitative theory of the relation between quenching temperature and the hardening curves would require a detailed knowledge of the nucleation of stacking faults as well as of the interaction between moving dislocations and sessile rings, both of which are not yet available. However, we can make a semi-quantitative estimate, following an idea due to Seeger (9) which says that the yield stress of a metal is proportional to the square root of the dislocation density. As was derived in Part I of this report, the dislocation density in Au, due to the growth of the sessile rings, rises by at least a factor of 10, and this, then, would be in good agreement with an increase of 2 to 5 in the yield stress, (1) and with the observed rise in saturation hardness with increasing quenching temperature.

Another possible explanation for the steady value of hardness after some ageing could be that the absorption of vacancies at complete dislocations leaves them jogged and, therefore, difficult to move. The sessile dislocations, on the other hand, presumably get much less jogged and may be readily converted into, and act as, dislocation sources as soon as the stress reaches the value which is necessary to activate them, depending on their size and the density and distribution of dislocations in the metal. (10)

For high temperature quenches, the hardening due to sessile rings is rather stronger than that due to maximum jogging as observed after quenches from lower temperatures. Although in specimens quenched from above the critical temperature the jogging of random or network dislocations presumably occurs in just the same manner as in the less severely quenched specimens, no resoftening is observed even after prolonged ageing. However, since maximum hardness due to jogging would occur before the final hardness value is reached, any superimposed overageing effect would be difficult to discover.

(c) On the constancy of sinks after low temperature quenches

Since single vacancies can move along dislocation lines with a high mobility.(11) the time a vacancy spends between attaching itself to a dislocation and finding a true sink is much shorter than the time it spends in diffusing to the dislocation. Therefore, a narrow cylindrical region, the axis of which is the dislocation line itself, can be considered as the actual vacancy sink (see also Part I of this paper). Depending on the estimate one makes of the effective diameter of this cylindrical region in relation to the length of the connecting segments, jogging will increase the length of a dislocation to a greater or lesser extent. In any event, the increase in the effective length of a dislocation by jogging is probably small, and, in the most extreme case for maximum hardening estimated above, will still be below the factor of 2. Therefore, to a first approximation, the number of sinks may be considered to remain constant during ageing. Still, the increase in the number of sinks at maximum hardening might be noticeable and, hence, in very accurate measurements of the decay of quenched-in

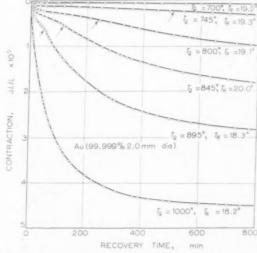


Fig. 12. Contraction of quenched Au wire on annealing at or near room temperature. ($T_{\it Q}$ is the quenching temperature, $T_{\it R}$ is the annealing temperature.) Arrows show the change in the recovery rate (after Takamura).

vacancies, a deviation of the decay curves from the simple exponential law should be observed. Such a deviation has quite recently been observed by Takamura⁽¹²⁾ in the contraction of the specimens quenched from various temperatures (Fig. 12). The time before the deviation becomes noticeable should increase with decreasing quenching temperatures, which is in agreement with the experimental result (Fig. 12). (The recorded quenching temperatures in Fig. 12, however, may be higher than the effective quenching temperatures because of the size of the specimens and the quenching technique used.)

A final remark should be made here. The guiding idea in the two parts of the present report is that Au and Cu, if quenched sufficiently rapidly from a high temperature, contain large numbers of nuclei for sessile dislocation rings, but do not contain such nuclei if quenched more slowly or from a lower temperature. This must, however, not be construed to mean that no sessile rings would be formed in slowly cooled specimens. On the contrary, it is probable that such sessile rings, due to the condensation of vacancies, are formed under almost any circumstances. However, with the techniques discussed in the present paper, these could not easily be discovered for two reasons. On slow cooling or milder quenching than was discussed in the present report, the rings (i) would have considerable diameters before reaching room temperature, and (ii) would, to a great extent, already have been converted to ordinary dislocation rings through the thermal nucleation of suitable half dislocations in the enclosed stacking fault. (10) Both effects would cause a rather slower increase of dislocation length (i.e. number of vacancy sinks) with number of absorbed vacancies, and thus make the rings indistinguishable from any other kind of glide dislocations. Therefore,

in the whole of this paper, the term "random" or "stray" dislocations is meant to include converted dislocation rings.

5. CONCLUSIONS

The two types of decay of quenched-in resistivity in Au correspond to the two types of quench hardening observed in Cu. For a very fast quench with a quenching temperature higher than about 900°C, hardening is caused principally by the formation of sessile rings. The migrating defects are mainly divacancies with an activation energy for migration of $0.60 \pm 0.05 \,\mathrm{eV}$. When the quenching temperatures are lower than 850°C, hardening is caused by condensation and annihilation of vacancies at dislocations in the network. The migrating defects are single vacancies and move with an activation energy of $0.72 \pm 0.10 \, \mathrm{eV}$. A repulsion between two vacancies separated from each other by a few atomic distances is estimated as 0.23 eV in Cu.

REFERENCES

- 1. J. W. Kauffman and M. Meshii, Bull. Amer. Phys. Soc. 2, 145 (1957).
- 2. M. J. Makin, U.K. AERE Report (to be published).
- 3. J. E. Bauerle and J. S. Koehler, Phys. Rev. 107, 1943 (1957)

VOI

- 4. M. S. MAIER and H. R. NELSON, Trans. Amer. Inst. Min. (Metall.) Engrs. 147, 39 (1942).
- 5. J. FRIEDEL, Les Dislocations. Gauthier-Villars, Paris (1956).
- 6. A. N. Stroh, Proc. Phys. Soc. B67, 427 (1954). See also A. Seeger, Defects in Crystalline Solids, p. 391. Physical Society, London (1955).
- 7. R. S. BARNES, Acta Met. 2, 380 (1954).
- 8. H. Suzuki, Private Communication.
- 9. A. Seeger, for example, Dislocations and Mechanical Properties of Crystals, p. 243. Wiley, New York (1957).
 10. D. Kuhlmann-Wilsdorf, Phil. Mag. 3 125 (1958).
- 11. D. Turnbull, Defects in Crystalline Solids, p. 203.
- Physical Society, London (1955). 12. J. TAKAMURA, J. Phys. Soc. Japan (to be published) Private Communication.

THE KINETICS OF GRAIN BOUNDARY GROOVING IN COPPER*

W. W. MULLINS† and P. G. SHEWMON±

In an earlier paper the diffusion equation associated with grain boundary grooving was solved and it was concluded that surface diffusion was the dominant transport mechanism for copper. For this mechanism the theory predicts that the shape of the groove profile has a time independent form and that the groove width and depth increase linearly with $t^{1/4}$. These two predictions have been tested by studying the grooving of tilt boundaries in copper annealed in dry hydrogen at 930°C and 1035°C. Both predictions agree with the experimental results. The validity of the theory allows one to calculate the surface diffusion coefficient, D_s . The advantages of this method of determining D_s are discussed.

LA CINETIQUE DU "CREUSEMENT" DE FRONTIERES DE GRAINS DANS LE CUIVRE

Dans un article précédent, l'équation de diffusion associée au "creusement" d'une frontière de grain a été résolue et on a conclu que la surface de diffusion était le mécanisme dominant de transport pour le cuivre. Pour ce mécanisme, la théorie prédit que la forme du profil du sillon est indépendante du temps et que la largeur et la profondeur s'accroissent linéairement suivant $t^{1/4}$. Ces deux prévisions ont été vérifiées en étudiant le creusement de frontières diversement orientées dans du cuivre recuit dans de l'hydrogène sec à 930°C et 1035°C.

Ces deux prédictions sont en accord avec les résultats expérimentaux. La validité de la théorie permet de calculer les coefficients de diffusion superficielle, D_s . Les auteurs discutent enfin les avantages de cette méthode pour la détermination de D_s .

DIE KINETIK DER FURCHENBILDUNG AN KORNGRENZEN VON KUPFER

In einer früheren Arbeit wurde die Diffusionsgleichung, die mit der Furchenbildung an Korngrenzen verknüpft ist, gelöst und der Schluss gezogen, dass bei Kupfer die Oberflächendiffusion der vorherrschende Transportmechanismus ist. Für diesen Mechanismus sagt die Theorie voraus, dass die Gestalt des Furchenprofils nicht von der Zeit abhängt und dass die Breite und die Tiefe der Furchen linear mit $t^{1/4}$ anwächst. Beide Voraussagen wurden geprüft durch eine Untersuchung der Furchenbildung an Neigungskorngrenzen von Kupfer, welches bei 930°C und 1035°C in trockenem Wasserstoff geglüht worden war. Beide Voraussagen stimmen mit den experimentellen Befunden überein. Die Richtigkeit der Theorie ermöglicht die Berechnung des Oberflächendiffusionskoeffizienten D_z . Die Vorteile dieser Bestimmungsmethode für D_z werden erörtert.

1. INTRODUCTION

The previous experimental studies that have been made of thermal grooving at grain boundaries have focused attention on the measurement of the equilibrium angles with which the interfaces intersect. (1) From these data, the ratio of grain boundary free energy (γ_B) to surface free energy (γ_s) has been calculated (usually assuming the γ 's to be independent of interface orientation).

In the following study, attention is focused on the kinetics of groove enlargement in copper bicrystals. The purpose of the investigation is twofold: first, to test the predictions of a recent theory of thermal grooving $^{(2)}$ with regard to both the shape of the groove profile and the time dependence of its size, and secondly, to combine the experimental measurements with a relation obtained from the theory to calculate the surface diffusion coefficient D_s .

2. DESCRIPTION OF THE THEORY

The processes by which a groove may enlarge are surface diffusion, evaporation, and volume diffusion. (Herring⁽³⁾ has reviewed the evidence that plastic flow is inoperative as a transport mechanism when surface free energy is the motivation.) The summary of the analysis of these processes that follows will emphasize surface diffusion, since the theory predicts and experiment shows this mechanism to be dominant in copper. Results for the other processes will be mentioned for purposes of comparison.

The theory is based upon the assumption that γ_s and D_s are constant for the range of crystallographic orientations exposed by the groove surfaces. The Gibbs–Thompson formula is used to relate the chemical potential of an atom on the groove surface to the local curvature. The transport of matter induced by differences in chemical potential, and the concomitant development of groove topography, are calculated for the mechanisms of surface diffusion and evaporation. An approximation is used that depends upon the small slope of the groove surface.

^{*} Received April 30, 1958.

[†] Westinghouse Research Laboratories, Pittsburgh 35, Pa. ‡ Carnegie Inst. Technology, Pgh. 13, Pa., formerly Westinghouse Res. Lab.

Fig. 1. Section showing idealized profile of stationary thermal groove (Vertical exaggeration $\times 2.18$).

The grain boundary enters the theory simply as a mathematical boundary condition requiring a fixed discontinuity of slope at the groove root.

To understand the results for the case of surface diffusion, consider a plane grain boundary that intersects an initially plane surface at right angles. Take a cross-section normal to both planes, and choose cartesian coordinates so that the x-axis coincides with the trace of the initial surface, and the negative y-axis coincides with the trace of the grain boundary (Fig. 1). Then after a time t, the groove profile is given by the expression

$$y(x, t) = m(Bt)^{1/4}Z[x/(Bt)^{1/4}]$$
 (1)

where Z is a function defined by a certain power series, $m = \gamma_B/2\gamma_s$ is the slope at the root, and $B = D_{s''s'} v \Omega^2/kT$ in which v denotes the number of atoms/cm² of surface, Ω denotes the atomic volume, and kT has its usual meaning.

Two consequences of equation (1) are evident: (1) The shape of the profile y(x, t) is independent of the time. The solid curve of Fig. 2 shows this shape, normalized to have a unit slope at the groove root.

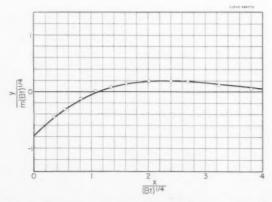


Fig. 2. Solid curve is theoretical shape of profile (normalized); circles are experimental values.

(2) All linear dimensions are proportional to $t^{1/4}$. In particular the width, w, between the two maxima on either side of the groove root, and the vertical depth, d, from the groove root to the maxima are given by the expressions

$$w = 4.6(Bt)^{1/4}, (2a)$$

$$d = 0.973m(Bt)^{1/4} \tag{2b}$$

Although the development of a groove by the action of volume diffusion has not been discussed in detail, it follows from an analysis of similitude given by Herring, $^{(4)}$ that the linear dimensions of the profile are proportional to $t^{1/3}$ provided the groove shape remains fixed. (The constancy of the shape seems very likely from a preliminary examination of the equations.) Assuming the similitude results to be applicable, a discussion is given in the Appendix of the development of a groove under the concomitant action of surface diffusion and volume diffusion. It is concluded that volume diffusion may be ignored as a contributing process when evaluating the results of this study.

The effect of evaporation in the experimental system studied (mean path of gas atoms \ll groove widths) is formally similar to the effect of volume diffusion discussed in the Appendix. Because of the low equilibrium vapor pressure of copper, however, it is easily shown that evaporation is at least two orders of magnitude less important than volume diffusion which in turn is negligible.

3. EXPERIMENTAL PROCEDURE

The bicrystals were made from vacuum melted commercial cathode sheet (99.99% Cu) in the split AUC graphite mold shown in Fig. 3. Seeds which had the [100] within less than 1° of their cylindrical axis were initially obtained by using the technique of Couling. (5) The [011] was determined by using an X-ray back reflection technique and was marked on

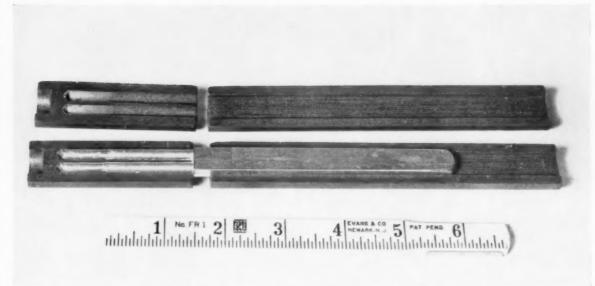


Fig. 3. Split graphite mold and bicrystal grown in it.

the sides of the seeds, which were then placed in the bottom half of the split mold. The desired relative orientation was obtained with a small protractor. The boundaries used can be completely characterized by giving the angle θ between the two [011] directions, and the angle ϕ between one of these and the studied face of the specimen. These angles were determined by using a Geiger tube spectrometer. For the three orientations used, $\theta=12^\circ,~\phi=2.5^\circ;~\theta=25^\circ,~\phi=12^\circ;~\theta=55^\circ,~\phi=32^\circ.$

VOI.

1959

The bicrystals were grown in a furnace with a four section Kanthal-A winding. The crucible was held inside a McDanel Porecelain tube evacuated to <10⁻⁴ mm Hg, and a temperature gradient was obtained (a) by shunting the lower section of the windings, and (b) by supporting the mold with an 18 in. long copper bar whose lower end was water cooled. This established a gradient of 10°C/in. in the molten copper. The temperature of the furnace was raised until all of the copper charge and part of the seeds were molten. A uniformly increasing d.c. voltage was then added to the control thermocouple output, thereby decreasing the temperature at 10°C/hr (a growth rate of about 1 in./hr). This procedure invariably gave a bicrystal of the same orientation as the seeds and, in nearly all runs, the grain boundary remained in the center of the specimen for its entire length (~6 in.).

Before cutting and polishing, the bicrystal was centered in a $\frac{3}{4}$ in. diameter glass tube, and "Cold-Mount," a room temperature polymerizing plastic, was poured around it. After this the crystal was

lightly clamped in a vise and $\frac{1}{2}$ in, lengths of the bicrystal cut off with a jeweler's saw, or an abrasive cut off wheel. The cold worked layer was removed by alternately etching in an aqueous solution of HNO_3 and grinding on coarse paper until 0.030 in, had been removed from each cut surface. The plastic was easily removed by heating to $170^{\circ}\mathrm{C}$ in cil.

The final specimen preparation consisted of mechanically polishing the surface through 4/0 paper and electropolishing in a solution of 55% orthophosphoric acid and water. Upon removal from the bath, the specimen was immediately rinsed in running distilled water, then alternately rinsed in 10% orthophosphoric acid and in distilled water, and finally dried with acetone. During this operation it was essential that the surface be kept wet until the acetone rinse. This rinsing procedure was to minimize the adsorption of phosphorous from the polishing solution. (6) After a satisfactory polish the grain boundary was not detectable under the interference microscope; that is, if there was a groove at the grain boundary it was less than a few hundred angstroms deep.

The specimens were annealed in a vycor tube with a flowing atmosphere of dry hydrogen or a dry mixture of 93% nitrogen and 7% hydrogen.* They were supported in a slotted piece of previously outgassed AUC graphite with the grain boundary horizontal. When the grain boundary was not oriented in this

^{*} The gases were dried by passing them over copper screen at $600^{\circ}\mathrm{C}$ and then through a magnesium perchlorate drying tower.

manner, the small shear stresses resulting from uneven support were adequate to cause a shear of several thousand angstroms at the grain boundary. A shear of 1000 Å was enough to destroy the symmetry of the grain boundary groove and ruin the run.

The most difficult experimental problem was maintaining microscopically smooth, clean surfaces during the anneal. The procedure adopted for the lower temperatures was to obtain a vacuum tight system, place the specimens in a cold portion of the vycor tube, close and flush the tube with dry gas, and pull a furnace controlled at the desired temperature over the specimens. For the higher temperature anneals, an OFHC copper tube extending almost the length of the furnace was placed between the samples and the vycor. The anneal was terminated by pulling the furnace from the specimens. The temperature of the specimens during the run was determined with a thermocouple inside the graphite specimen holder or by placing a thermocouple inside the equilibrated furnace before inserting the specimens.

The depth, width, and shape of the grain boundary grooves were determined with a Zeiss interferometric microscope. This instrument is of the Linnik type (7) which compares the observed surface with a reference flat in another part of the system, instead of inserting a reference surface between the objective and the surface to be observed. The pictures were taken on 35 mm Kodak Plus-X film at a magnification on the film of \times 91. These were then enlarged to \times 765 in printing. The interference technique produces a vertical exaggeration of about \times 50. Thus a groove 10 μ wide and $\frac{1}{4}$ μ deep appears 7.65 mm wide and 9.5 mm deep on the enlarged print.

4. RESULTS

The theory to be tested assumes symmetry across the grain boundary plane and a clean metal surface with γ_s independent of surface orientation. Therefore data are not included for samples that show the following: (1) An asymmetric groove (arising from grain boundary shear or presumably from failure of the boundary to meet the surface plane at right angles). (2) Pits or particles of a second phase (arising presumably by reaction of the sample with atmospheric impurities). (3) Faceting (as indicated by fine scale irregularities in fringes). Satisfactory groove patterns are shown in the sequence of Fig. 4 which illustrates the increasing size of the groove profile with increasing annealing time.

The first test of the theory was to compare the observed and predicted groove shapes. Accurate determination of the shape of a profile is most easily



Fig. 4. Growth of grain boundary groove at 930°C. ×334.7.

19

accomplished for large grooves whose photographs show fringes that are equally spaced and perpendicular to the groove. In four such cases, a curve running along the center of a given fringe was traced onto coordinate paper. The profile was normalized to unit slope at the root by multiplying selected abscissas by the root slope m. To test for geometrical similarity to the theoretical curve, the coordinates of the selected points were then multiplied by the scale factor required to make the depth, d, equal for the measured and theoretical curves. Typical are the experimental points shown in Fig. 2, which are obtained from the largest profile shown in Fig. 4; the agreement is quite satisfactory. It should be added that samples rejected because of one of the three points listed above often showed profiles differing appreciably from the theoretical ones, especially in that the maxima were often small and occasionally absent.

To determine the time dependence of the groove size, measurements of the width, w, were selected, as they were found to be more reproducible than measurements of the depth. The reason for this is twofold: the determination of the groove bottom is somewhat arbitrary and especially difficult for small grooves; the width is much less sensitive than the depth to changes in $\gamma_s = \gamma_B/2m$ (see equations 2a and 2b) and is therefore liable to be less affected by adsorption, etc. The data for width as a function of

TABLE 1

	IABLE I	
Specimen*	Time (hr)	Width (µ)
	Temp. 930°C	
Г12-24	0.9	6.55
25-33	0.9	5.5
55-33	0.9	5.9
55-25	4.0	8.0
12-21	4.5	8.3
T12-20†	16	12.4
25-31†	16	11.75
25-33	81	19.0
12-23	81	17
	Temp. 1035 C	
□12-23	0.8	6.9
25-33	0.8	7.5
_55-13	0.8	7.9
T12-23	6	12.7
25-33	6	14.2
_25-25	6	13.9
55-1	16	17.3
55-13	16	16.4
25-33	81	26.1
55-13	81	26.8

* Specimens may have been interchanged.

† The first number in the designation denotes the total misorientation, θ .

time and type of grain boundary are given in Table 1 for 930°C and 1035°C. Anneals at 830°C did not give reproducible results and are omitted. The brackets to the left of a set of specimen designations indicate these specimens were annealed together. Thus the time-temperature history of the bracketed specimens is exactly the same. For all anneals, the temperatures are within ± 5 °C of the indicated value.

Inspection of Table 1 shows no consistent variation of groove width with θ . Also the spread in the data for each time and temperature falls within the uncertainty in the measurement of the corresponding width. This uncertainty is about 1 μ for the 16 and 81 hr anneals and slightly less for shorter anneals. Thus for a plot of width vs. time, the data for each

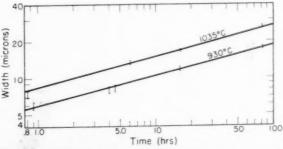


Fig. 5. Width as a function of time for grain boundary grooves in copper. The lines are of slope 1/4.

time and temperature were averaged and the points plotted as the average $\pm 0.5 \mu$. In Fig. 5, the best straight line of slope 1/4 is placed through the points.

5. DISCUSSION

From the agreement of the experimental data with the theoretical prediction of both the profile shape and the relation $w \sim t^{1/4}$, we draw the following conclusions for the conditions under which the runs were made: (1) The dominant process responsible for groove enlargement is surface diffusion. (2) The assumption that the surface parameters are constant over the range of orientation exposed on the groove surface is a good approximation.

The only parameter in equation (2a) which is not known is the surface diffusion coefficient, D_s . Thus from the values of B obtained from Fig. 5 above, one can calculate values of D_s . Using the following values

$$\begin{split} \Omega &= 1.18 \times 10^{-23} \, \mathrm{cm^3/atom} \\ \nu &= \Omega^{-2/3} = 1.93 \times 10^{15} \, \mathrm{atoms/cm^2} \\ \gamma_s &= 1670 \, \mathrm{ergs/cm^2} \, (\mathrm{ref.~8}), \end{split}$$

the values of D_s are 13.5×10^{-5} cm²/sec at 1035° C, and 3.0×10^{-5} at 930° C. The uncertainty in D_s stems from three sources: error in the measured widths, w, error in γ_s , and the value assumed for v. The values of w are read to ± 4 per cent so the error in B due to this is ± 16 per cent (from equation 2a). Thus the two values of D_s given above have relative errors of ± 16 per cent. The absolute values would appear to be good to within ± 25 per cent. These values are for diffusion normal to the [100] on surfaces whose normals range from 0° to 40° from the [011] direction. From the symmetry of the grooves on the asymmetric tilt boundaries and from the lack of variation of w with θ , it would seem that D_s varies less than ± 25 per cent in this family of planes.

These values of D_s agree with those obtained by Gjostein⁽⁹⁾ in his study of the grain boundary surface tension of copper. By fitting equation (1) to the base of the groove, he obtained his values 14.3×10^{-5} at 1065°C and 3.4×10^{-5} cm²/sec at 930°C .

There have been only two other studies of surface diffusion on copper and silver in the higher temperature range. Hackerman and Simpson (10) studied the spreading of Cu⁶⁴ on copper at 750°C and reported $D_s=4\times10^{-5}$ cm²/sec, while Frauenfelder, (11) studied the spreading of Cu⁶⁴ on silver at 750°C and reported $D_s\times8\times10^{-7}$ cm²/sec. These workers neglected the loss of Cu⁶⁴ into the bulk of the metal. If loss to the interior is included, it can be estimated from Fisher's analysis of the grain boundary diffusion

problem⁽¹²⁾ that the true values of D_s are at least 100 times greater than those reported. However the resulting value of D_s are not of sufficient accuracy to give a separate check on the values of D_s obtained in this study.

The determination of D_s from grooving kinetics appears to be a very promising technique. In cases where the assumptions of the theory are validated by experimental agreement, the procedure has three advantages over existing methods for determining D_{\circ} : (1) It is free from the difficulty that arises in tracer work of assessing the flux of atoms that leave the surface to enter the bulk. (2) It is most easily used at temperatures near the melting point where surface contamination is minimized—at these temperatures tracer methods suffer from a serious loss of tracer atoms to the bulk. (3) It has the advantage over other morphological methods of being based on a rigorous geometrical analysis. Existing estimates of D_{ϵ} , from morphological measurements, suffer from the use of oversimplifications of complicated geometries.(13)

Its shortcomings with respect to a tracer study using the Fisher–Whipple solution⁽¹²⁾ are as follows: (1) It measures a mean D_s over a small range of orientations, and requires that D_s and γ_s are independent of orientation. (2) It is applicable only for self-diffusion work, in a one component system.

ACKNOWLEDGMENTS

Gratitude is expressed to Mr. Leon Adams and Mr. George McGraw for their valuable assistance in all phases of the experimental work.

APPENDIX

The Effect of Volume Diffusion on Groove Development

The calculation is divided into two parts: in part **A**, a potential theory problem is solved that represents the instantaneous contribution to groove development made by volume diffusion; in part **B** this contribution is added to that of surface diffusion and an equation is obtained that represents the cumulative groove development by the concomitant action of both processes. From this equation the overall effect of volume diffusion is determined to be small.

A. The volume diffusion will be assumed to be divergenceless and quasi-steady state, and to be maintained by the boundary condition of an impressed curvature at the surface. Because of the small slope of the groove profile, two approximations are used: the curvature K is approximated as $-\partial^2 y/\partial x^2$; the values that the concentration and its derivatives assume on the surface and on the plane y=0 are identified. The grain boundary is ignored since the experimental profile shapes indicate the boundary is inoperative as a vacancy source or sink; otherwise it should have only a slight effect on the diffusion flux.

VO

19

For mathematical simplicity, the actual curvature K(x) of the experimental profiles will be approximated by a Gaussian expression $K(x) \simeq f(x) = h \exp{(-bx^2)}$ (plotted for $x \ge 0$ and h = 1 as the solid line of Fig. 6). This should be a good approximation since both K(x) and f(x) have the same qualitative shape and they share the properties of a

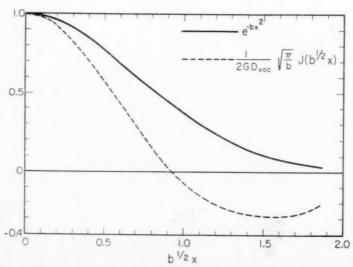


Fig. 6. Solid curve is the assumed profile curvature; dotted curve is the resulting diffusion flux.

maximum at x=0, and a point of inflection. The parameter h is chosen to make K(O)=f(O)=h. Using equations (1) and (2a) to evaluate K(O) one finds $h=2.65\ m/w$. The value of b may be chosen to make the inflection points of K(x) and f(x) coincide, but it does not affect the final result and need not concern us.

Denoting by c(x, y) the concentration of vacancies, and by c_o the equilibrium value of c in the interior, we have the following equations:

$$\nabla^2 c = 0,$$
 A1

$$c(x,O) = c_o - G \exp{(-bx^2)} \label{eq:condition} \qquad \qquad \mathbf{A2}$$

$$c(x, -\infty) = c_o.$$
 A3

Equation A2 is the Gibbs–Thompson formula for our case with $G=c_o\gamma\Omega h/kT$

The solution of equations A1 through A3, obtained by a Fourier method, may be expressed as the integral

$$\begin{split} c(x,y) &= c_o - \frac{G}{\pi} \int_o^\infty \! dw \exp{(wy)} \int_{-\infty}^\infty \exp{(-b\varepsilon^2)} \\ &\quad \times \cos{w(x-\varepsilon)} \, d\varepsilon \quad \text{A4} \end{split}$$

The integrals over ε and w may be evaluated from a table of Fourier transforms.⁽¹⁴⁾ The result is

$$\begin{split} c(x,y) &= c_o - (G/2) \{ e^{b(y\,+\,ix)^2} \, \mathrm{Erfc} \, [-b^{1/2} (y\,+\,ix)] \\ &+ e^{b(y-ix)^2} \, \mathrm{Erfc} \, [-b^{1/2} (y\,-\,ix)] \} \quad \mathrm{A5} \end{split}$$

where

VOL.

1959

Erf.
$$u = 1 - \frac{2}{\sqrt{\pi}} \int_{0}^{u} \exp(-t^2) dt$$
.

Using A5, one finds the current of atoms J(x) leaving each element of surface to be

$$\begin{split} J(x) &= -D_{\text{vac}} \left(\partial c / \partial y \right)_{y=0} \\ &= 2 \sqrt{(b/\pi)} \, G D_{\text{vac}} [1 - 2b^{1/2} x \Phi(b^{1/2} x) \exp{(-b x^2)}] \end{split}$$

where

$$\Phi(u) = \int_{a}^{u} \exp(t^2) dt.$$
 A6

The dashed line of Fig. 6 is a plot of

$$[\sqrt{\pi/(2\sqrt{b\cdot GD_{\mathrm{vac}}})}]J(b^{1/2}x)$$

for $x \geqslant 0$ (since J is an even function). One sees that current leaves the central region and flows to the outer regions. (The integrated current vanishes.) The rate of transfer of atoms by volume diffusion r_v (per unit length of the groove) is given by the integral of the current between its two zero's $\pm x_o = \pm 0.925/b^{1/2}$, namely

$$egin{align} r_v &= \int_{-x_o}^{x_o} J(x) \ dx = D_{ ext{vac}} \int_{-x_o}^{x_o} \left(rac{\partial c}{\partial y}
ight)_{y=0} dx \ &= 1.38 G D_{ ext{vac}} = rac{3.7 D_v \gamma m}{w k T} \end{split}$$

In the last step we have substituted for G, assigned h its value, and used the relation $D_v = D_{\rm vac}\Omega c_o$. The integral is evaluated by noting that expression A5 is of the form

$$\begin{split} c(x,y) &= c_o + \sigma(y+ix) + \sigma(y-ix) \\ &= c_o + \sigma_+(x,y) + \sigma_-(x,y) \end{split}$$

so that

$$\left(\frac{\partial c}{\partial y}\right)_{y=0} = -i\left(\frac{\partial \sigma_+}{\partial x}\right)_{y=0} + i\left(\frac{\partial \sigma_-}{\partial x}\right)_{y=0}.$$

Substitution of this expression into the second integral of A7 permits immediate evaluation. The effect of using the correct K(x) in place of our approximation f(x) would be a slight adjustment in the numerical coefficient of A7.

B. To calculate the groove development when both volume diffusion and surface diffusion occur, we will make the approximation that both volume diffusion and surface diffusion, when acting alone, develop the same fixed shape (Fig. 2). This should be a good approximation since the boundary conditions⁽²⁾ for both curves may be shown to be the same.

Corresponding to r_v (Appendix **A**) let r_s be the rate of transport of atoms due to surface diffusion. It may be shown from the theory of groove development by surface diffusion⁽²⁾ that

$$r_s = K_s/w^2$$
 A8

where

$$K_s = 9.0 D_s \gamma \Omega v m / kT$$
.

Furthermore from A7 we have

$$r_v = K_v/w$$

where

$$K_v = 3.7 D_v \gamma m/kT$$
 A9

Finally denote by V(t) the volume of material transported (per unit groove length) to form the groove. Then $V=gw^2$ where g is a geometrical factor given by g=0.042m. It now follows from the approximation stated at the outset that

$$dV/dt = 2gw(dw/dt) = \Omega(r_s + r_v)$$

= $(\Omega K_s/w^2) + (\Omega K_v/w)$ A10

This is a differential equation for w(t). Separation of variables and a simple integration⁽¹⁵⁾ gives the solution

$$\alpha w - (\alpha w)^2/2 + (\alpha w)^3/3 - \ln(1 + \alpha w)$$

= $(\alpha^4 K_*/2g)t = (\alpha w_*)^4/4$ A11

where we have introduced the notation $\alpha = K_v/K_s = D_v/2.4D_s\Omega^{1/3}$ and where w_s in the last step is the width that would be developed by surface diffusion alone ($\alpha = 0$).

For a known D_a and a given experimental w(t), equation A11 could be solved for D_s . Instead, we will show that the difference between w and w_s is less than experimental error for values of D_{s} calculated in the text by ignoring volume diffusion. Taking $D_s = 1.43 \times 10^{-4}, \, D_v = 2 \times 10^{-9} \, \, \mathrm{cm^2/sec^{(16)}}$ and $w_s = 16 \,\mu$ (16 hr width at 1035°C) gives $\alpha w_s =$ 0.45. Substitution of this value into All followed by simple rearrangement gives $(w - w_s)/w = 0.06$. This falls within the 8 per cent experimental error. For shorter times the error is less; for longer times it is greater.

REFERENCES

- 1. G. BAILEY and H. WATKINS, Proc. Phys. Soc. B 63, 350 (1950); A. Greenough and R. King, J. Inst. Met. 79, 415 (1951); F. BUTLNER, H. UDIN, and J. WULFF, Trans. Amer. Inst. Min. (Metall.) Engrs. 197, 313 (1953).
- 2. W. W. Mullins, J. Appl. Phys. 28, 333 (1957).

- 3. C. Herring, Chapter in Structure and Properties of Solid Surfaces, edited by R. Gomer and C. S. Smith,
- University of Chicago Press (1952).
 4. C. Herring, J. Appl. Phys. 21, 301 (1950).
 5. L. Couling, Ph.D. Thesis, Metallurgy, Carnegie Institute Technology (1953).
- P. JACQUET and M. JEAT, Rev. Mét. 118, 537 (1951).
 H. MYKURA, Proc. Phys. Soc. B 67, 281 (1954).
- 8. H. Udin, Metal Interfaces p. 114. American Society for
- Metals, Cleveland (1952). 9. N. GJOSTEIN, Ph.D. Thesis, Metallurgy, Carnegie Inst.
- Technology (1958). 10. N. HACKERMAN and N. SIMPSON, Trans. Faraday Soc.
- 52, 638 (1956). 11. H. FRAUENFELDER, Helvet. Phys. Acta 23, 371 (1950). 12. J. Fisher, J. Appl. Phys. 22, 74 (1951); A more rigorous solution is given by R. Whipple, A.E.R.E. R/R. 1026
- (Harwell, England). 13. G. C. Kuczynski, Trans. Amer. Inst. Min. (Metall.)
- Engrs. 185, 169 (1949). 14. Bateman Manuscript Project, Tables of Integral Trans-
- forms, V. p. 1. McGraw-Hill, New York (1954).
- 15. B. O. Peirce, A Short Table of Integrals. Ginn (1929). 16. A. Kuper, H. Letaw, Jr., L. Slifkin, E. Sonder, and C. Tomizuka, Phys. Rev. 96, 1224 (1954).

THE DISLOCATION STRUCTURE OF SLIP BANDS IN IRON*

J. R. LOW Jr. and R. W. GUARD†

The dislocation structure of slip lines in silicon iron has been examined by an etch-pit technique. It has been observed that the arrays when viewed normal to the edge component are straight but not coplanar over long distances while the arrays where the screw component emerges from the surface show much curvature. In bend specimens the increase in strain from the neutral plane toward the surface is accomplished mainly by the lateral growth of the first bands formed rather than by the formation of new slip bands.

Observations made in the slip plane itself demonstrate that the motion of the screw components is considerably more limited than that of the edges. Evidence is presented for the existence of interaction between the edges and screw components of adjacent loops in agreement with the theoretical predictions.

The observations can be most adequately explained by the double cross-slip model of the formation of a slip band. Evidence is presented for the transfer of portions of a loop from one plane to another as this model requires.

LA DISTRIBUTION DES DISLOCATIONS DANS LES BANDES DE GLISSEMENT DU FER

La distribution des dislocations dans les lignes de glissement de fer-silicium ont été examinées par une technique de piqures de corrosion. Les réseaux de dislocation sont droits mais non coplanaires sur de longues distances lorsqu'ils sont observés normalement à la composante coin. Ils montrent une plus grande courbure lorsque la composante vis est perpendiculaire à la surface examinée. Dans les échantillons fléchis, l'accroissement de déformation de la fibre neutre à la fibre externe est obtenu principalement par la croissance latérale des premières bandes formées plutôt que par la formation de nouvelles bandes de glissement.

L'examen sur le plan de glissement démontre que le déplacement des composantes-vis est notablement plus limité que celui des composantes-coin. En accord avec les prédictions théoriques, les auteurs confirment l'existence d'une interaction entre les composantes-vis et coin des anneaux de dislocation adjacents.

Ces observations peuvent s'interpréter le plus aisément par un modèle de double glissement croisé pour la formation de la bande de glissement. Conformément à ce modèle, les auteurs mettent en évidence certains transferts de portions d'anneaux de dislocation d'un plan à un autre plan.

DIE VERSETZUNGSSTRUKTUR DER GLEITBÄNDER VON EISEN

Die Versetzungsstruktur der Gleitlinien von Silizium-Eisen wurde mit einer Ätzgrübchen-Methode untersucht. Dabei ergaben sich folgende Beobachtungen: Senkrecht zu den Stufenkomponenten sind die Anordnungen geradlinig aber über grosse Entfernungen nicht koplanar, während die Anordnungen an den Austrittspunkten der Schraubenkomponenten auf der Oberfläche stark gekrümmt sind. In gebogenen Proben erfolgt die Zunahme der Dehnung von der neutralen Ebene zum Rand hin hauptsächlich durch Breitenwachstum der zuerst gebildeten Bänder und weniger durch die Bildung neuer Gleitbänder.

Beobachtungen in der Gleitebene selbst zeigen, dass die Bewegung der Schraubenkomponenten beträchtlich mehr eingeschränkt ist, als die der Stufenkomponenten. Beweise für das Auftreten einer Wechselwirkung zwischen Stufen- und Schraubenkomponenten von unmittelbar benachbarten Ringen werden aufgezeigt in Übereinstimmung mit theoretischen Voraussagen.

Die Beobachtungen lassen sich am besten durch das Modell der doppelten Quergleitung für die Bildung eines Gleitbandes erklären. Beweise für die Übertragung von Teilen eines Ringes von einer Ebene zu einer anderen, die dieses Modell erfordert, werden erbracht.

INTRODUCTION

In studying the deformation of body-centered cubic metals it is often observed that the slip lines are wavy and irregular. This causes some difficulty in interpreting the slip process by the usual dislocation models although several models have been proposed to account for these observations together with the

other observations of asterisms, lattice rotations, and the orientation variations of the critical resolved shear stress which occur during deformation (see Maddin and Chen⁽¹⁾). The evidence on which these models are based is, in many cases, contradictory. In addition, most of the models of the slip process are based on indirect observations of slip bands and slip lines. The present work presents observations on the dislocation structure of the slip bands in Fe–3 $\frac{1}{4}$ % Si single crystals which provide information on which a

^{*} Received May 14, 1958

[†] General Electric Co. Research Laboratory Schenectady,

model of the slip process can be based. A model for the formation of macroscopic slip lines is proposed which accounts for the observations. The present results together with similar experiments of Gilman and Johnston⁽²⁾ on LiF, indicate some of the serious deficiencies in the present concepts of dislocation multiplication and generation during the formation of the slip band.

The technique used in the experiments depends on the revelation of the dislocations by etch pits. (3) This technique has the advantage that the slip process can be studied at a very early stage (strains of less than 1 per cent) compared to the usual observations. The resolution is still, however, on a gross scale compared to the scale of the usual dislocation interaction distances as will be shown later. It will be shown below that the technique is reliable in that it shows both edge and screw dislocations. In addition, dislocations are continuously decorated so that any section through a crystal reveals all of the dislocations cut by the plane of the section.

EXPERIMENTAL TECHNIQUE AND OBSERVATIONS

Single crystal specimens of a 3.2% silicon-iron containing approximately 0.005 wt. % carbon, about 1 mm thick and having the orientation shown in Fig. 1, were bent about an axis normal to the (112) face. This orientation is such that, for small deformations, only a single (110) slip system is active. (3) Before bending, the crystals were hand ground on all faces using metallographic polishing papers, aged 15 min at 150°C and electropolished and etched. If any etch pit evidence of localized deformation due to grinding was observed, the crystals were again electropolished until they were free of all etchs pits except those in small-angle boundaries and the normal random distribution of about 106 cm⁻². (3) Bending was accomplished by pressing the crystals between steel dies of the desired radius of curvature or by means of a four-point bending fixture. After bending, the specimens were aged at 150°C for up to 18 hr to produce carbon decoration of the dislocations introduced by the deformation.(4) They were then electropolished and electroetched in the Morris⁽⁵⁾ chromic-acetic acid electropolishing solution used by



Fig. 1. Orientation of single crystals used. Bending was carried out around an axis normal to the (112) plane. Tensile specimens were extended parallel to the (112) plane.

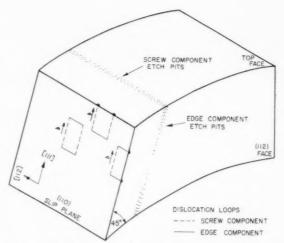


Fig. 2. View of crystal showing the relation of (110) dislocation loops to different faces on which etch pits or grooves were observed.

Dunn and Hibbard⁽³⁾ in their studies of polygonization and by Suits and Low⁽⁴⁾ in their studies of carbon decoration of dislocations in silicon iron.

19

The orientation of these bend specimens was such that the dislocation pattern in the slip plane would be that shown schematically in Fig. 2. In crystals of this orientation slip will cause no visible surface offset on the (112) faces since there is no displacement normal to this surface. The top face, however, showed the "wavy" slip lines typical of iron. Dislocations lying in the [112] direction would be pure edge. While those in the [11I] direction would be pure screw, dislocation lines in other directions in the slip plane would be of mixed character. Thus, etch pits on the (112) face represent points of intersection of edge components with the plane of polish while etch pits on the top face represent the intersection of screw components with the plane of polish. Occasionally, after some metal was removed by polishing, short shallow grooves were observed on these two faces, and these represent short segments of screws or edges lying close enough to the plane of observation to produce localized attack by the etchant.

In addition to the above-mentioned planes of observation, the crystals were sectioned parallel to the slip plane and polished and etched to reveal dislocation loops. In this section the dislocation lines appear as grooves.

EDGE DISLOCATION PATTERNS

Fig. 3 shows a typical etch pit pattern extending from the neutral plane to the tension surface on the (112) face of a 1 mm thick crystal bent to a 5 cm

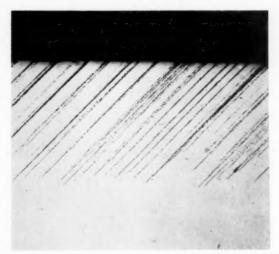


Fig. 3. Etch pits observed on the (112) face of a bent crystal near the neutral axis. $\times 166.7$.

radius of curvature (1 per cent elongation at the surface). The top of the photograph is toward the outer fibers of the bend specimen, and the bottom of the photograph is the neutral plane.

It is characteristic of the edge dislocation arrays that at low magnifications they appear to follow substantially straight lines over large distances. These lines are traces of a $(1\overline{10})$ plane on the surface. However, at higher magnifications, Fig. 4, it is found that the pits scatter about the slip plane trace and are apparently collinear only for very short distances. Furthermore, the distribution of etch pits along the slip line is not uniform, nor does it vary uniformly in

1959

going from the region of low strain to the region of higher strain. The pits often appear in groups of five to ten fairly closely spaced pits lying along a single line (see arrows in Fig. 4), each group separated from the next by a short distance. As the strain increases in going from the region of low strain near the neutral axis toward the outer fiber of the bend specimen, the slip lines* broaden into bands* by the appearance of new lines of pits immediately adjacent to the central line of pits and the density of pits along a given slip line increases somewhat. This results in a slip band, broad at the outer edge of the bend specimen and tapering down to a single line of pits as the neutral axis is approached.

That the straightness of the edge dislocation arrays in the slip lines and bands is real is illustrated in Figs. 5 and 6. These photomicrographs are taken of the (112) face of a tension specimen. The specimen was 10 mm wide and 1 mm thick, the broad face being the (112) face. Both the single straight arrays and broad bands of parallel arrays are visible. The spacing between bands is irregular but the average is about $10~\mu$.

SCREW DISLOCATION PATTERNS

As illustrated schematically in Fig. 2, the etch pit pattern observed on the top face of the bend specimens used in this investigation will be due to screw dislocations intersecting this surface at 45°. The pattern

^{*} The term "line" will be used to refer to single rows of pits not necessarily collinear, while the term "band" will be used to refer to clusters of several parallel lines of etch pits.

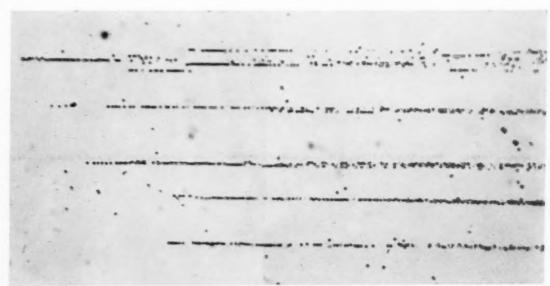


Fig. 4. The nature of slip lines near the neutral axis showing the non-collinear nature of the arrays and the lateral spreading at higher strain. $\times 1000$.

Fig. 5. Straight slip lines and bands on the (112) face of a tension specimen. The arrays of edge dislocation etch pits remain straight. ×66.7.



Fig. 6. Higher magnification picture of the same field as Fig. 5 to show the nature of the clustering to form bands of slip. $\times 562.5$.



Fig. 7. Straight slip lines on top face of a bend specimen caused by screw component etch pits at very small strain top surface of bend specimen after I per cent strain. Note (0.1 per cent). $\times 133.3$.

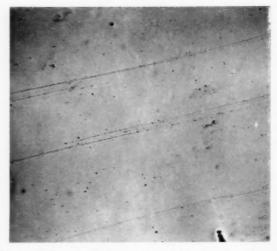


Fig. 8. Higher magnification view of same area showing interference and branching of adjacent slip lines.

here is quite different from that for the edge components. In a lightly bent specimen (0.1 per cent elongation at the outer fiber) the slip lines appear reasonably straight over large distances, see Fig. 7; however, where two adjacent slip lines overlap there is a tendency for the screw components to move out of the original plane and for the slip lines to show branching as in Fig. 8. This type of non-crystallographic motion of the screw components becomes a common feature of the slip pattern at higher deformations, and is illustrated in Figs. 9 and 10, for the specimen bent to a maximum strain of 1.0 per cent. This is not cross slip of the kind observed in facecentered cubic metals since the screw dislocations do not move in conjugate slip planes; rather, their

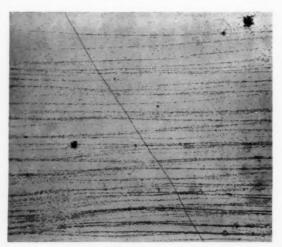


Fig. 9. Wavy "non-crystallographie" slip bands on the tendency for bands to cluster. ×140.6.

175

motion is governed by the direction of the shear stress locally. Thus, the screw dislocations appear to be able to move in any direction in the crystal without regard to specific slip planes. This aspect of the motion of screw dislocations is much more strikingly illustrated in Fig. 11, which shows a typical etch pit pattern for a polycrystalline specimen. The markedly curved set of lines at the left center presumably arises from the behavior of the screw

Fig. 10. Same field as Fig. 9 showing nature of clusters of slip lines and wavy character of bands. ×750.

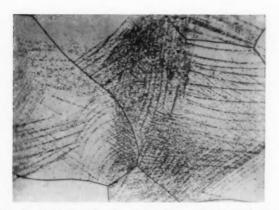


Fig. 11. Typical etch pit pattern in weakly strained polycrystalline specimen showing sharply curved slip lines. \times 109.4.

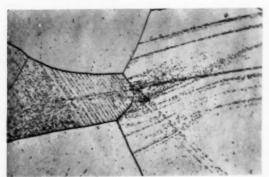


Fig. 12. Etch pit pattern in polycrystalline specimen showing straight arrays presumed to be edge dislocations. \times 125.

segments of loops under the action of the complex local stresses.

These observations agree with the frequently made proposal that the "wavy" nature of the slip lines in iron results from the ability of the screw segments of dislocation loops to move off the glide plane easily. However, as Fig. 12 shows, certain arrays remain confined to a straight line even under the complex stress pattern which must exist in polycrystalline material. These dislocations are presumably edge character.

DISLOCATION PATTERNS IN THE SLIP PLANE

When a crystal bent to a surface elongation of 1 per cent was sectioned parallel to the slip plane, it was found possible to reveal dislocation loops as continuous grooves on the surface of polish. Experiment has shown that the dislocations revealed will be within 200 Å of the surface etched. While these grooves are visible optically, the best observations are from electron microscope photomicrographs using carbon replicas. The replica reveals both the grooves and also the pits corresponding to other dislocation segments intersecting the surface. The patterns of grooves are similar to those observed by Wilsdorf and Kuhlman-Wilsdorf in Al-4% Cu. (6)

A typical dislocation loop pattern is shown in Fig. 13. In this section the straight vertical lines are screw dislocations and the irregular horizontal lines are edge or mixed dislocations. It will be noted that there is a strong tendency for the screw components of these loops to align themselves with the (111) direction over large distances while the edge components are severely distorted.

The edge segments are not only curved in the direction of the shear stress but also show local distortions. This distortion results from the torque exerted on the edge component by the screw components of other loops in adjacent, parallel planes. This torque tends to rotate the line of the edge loop into a direction that is more nearly perpendicular to the adjacent screw segment. (7) In virtually every case where a reversal of curvature in the edge component is observed, a screw component from another dislocation loop on an adjacent plane can be found at the region of distortion in the edge component. This effect is illustrated in greater detail in Fig. 14. In the region of lower strain approaching the neutral axis of the bend specimen, more nearly isolated loops are observed and here the edge components remain more nearly straight, Fig. 15.

Another striking feature of these dislocation loops is their dimensions as determined by the relative

VOL. 7 1959

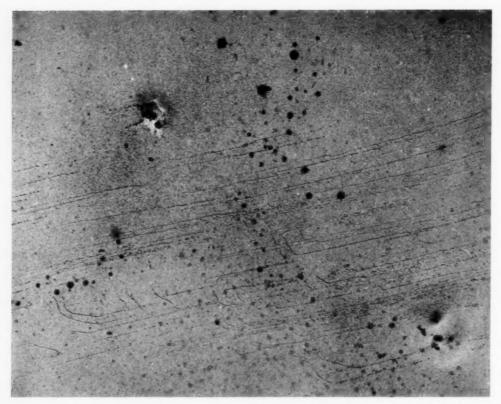


Fig. 13. Typical pattern of dislocation loops revealed as grooves on the slip plane. The long comparatively straight segments line in a [111] direction. Two-step carbon replica. $\times 4500$.



Fig. 14. Patterns observed on the slip plane which show the interaction of edge and screw components of loops on adjacent planes. Two-step carbon replica. $\times 10,000$.



Fig. 15. Pattern of edge loops near the neutral axis. \times 1031.3. motion of the screw and edge components. In these bend specimens the loops are much longer than they are wide and have a "U" shape with the open end of the "U" toward the top surface of the bend specimen. The loop dimensions where both screw components may be seen, indicate that the screw components on the average, move about 3.0–5.0 μ with a maximum of 20 μ . On the other hand, the edge components, since only those of one sign are



Fig. 16. A series of edge components having some screw components not lying in the plane of polish. Two-step carbon replica. $\times 7500$.

found, must move distances comparable to the full depth to which slip is observed, i.e., from 50 to 100 μ .

The tendency of the screw components to move out of their original glide plane, mentioned above, in connection with "wavy" slip lines, is evident on a finer scale in (110) section photographs. Frequently, in a given section, an array of edge components, all in one plane, will be observed with one or both of the screw components missing, Fig. 16. When this occurs the edge component grooves often terminate in an etch pit, indicating that a dislocation line lying oblique to the plane of observation exists at these terminal points. This is interpreted to mean that the screw component of a loop has moved out of the plane of the edge components generating a short dislocation segment oblique to the slip plane. This feature of the dislocation loops is particularly well illustrated in Fig. 17.

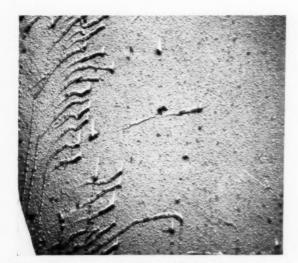


Fig. 17. An array of edge loops with the screw component lying below the plane of polish so that they terminate in an etch pit. Two-step carbon replica. × 6000.

One further point needs to be made with respect to the (110) section photographs. In all cases where dislocation loops or segments of loops are visible (Figs. 13–17), the dislocations appear to be continuously decorated judging from the fact that they etch as grooves rather than as arrays of pits. This point is of considerable importance in the interpretation of etch pit patterns on other polished sections, since it means that any section through the crystal, when properly etched, reveals all of the dislocations cut by plane of the section. This would not be true, for example, if the decoration consisted of separated precipitate particles along the dislocation line.

DISCUSSION

Dynamic generation from Frank-Read sources

The present study was not directed at the nature of dislocation sources in metals but the results indicate certain possibilities. In no case has a slip line been observed to originate from a sub-boundary in the annealed crystal, probably since these dislocations are bound in place by solutes. In any slip line the number of dislocations is too large to have come from pre-existing sources without some multiplication mechanism.

The number of slip lines observed in a tensile specimen at strains of about 0.01 per cent is between 5 and 10 per 100 μ distance normal to the slip plane. As is evident from the bend tests (Fig. 3) the increase in strain as the stress increases away from the neutral plane is accomplished primarily by an increase in the strain per band with only rarely other widely separated slip lines becoming active. This observation suggests again the importance of having some multiplication process. Because the displacement of adjacent loops involved is small and a single loop moves only a short distance, the present observations show that the slip process within a band differs from the observations of Wilsdorf and Fourie⁽¹⁶⁾ on electron micrographic examination of alpha brass. The reasons for this are not known, but may be related to the difference in crystal structure.

The present observation of the distribution of dislocations indicate that the slip bands in Fe-3% Si are not formed by the dynamic generation of large numbers of dislocation loops from a single source, but that the process takes place by the formation of sources on adjacent planes at a fairly early stage. Since we rarely observed more than 10 coplanar loops it is not possible to reconcile the observations with the theoretical predictions for the dynamic generation process. (9,10) The existing models of this

kind must be modified to permit lateral growth even during single slip and to stop generation after a smaller number of loops have been produced.

Interaction models

On the basis of their observations on LiF, Gilman and Johnston⁽²⁾ have described the multiplication in which a moving dislocation loop leaves behind it a number of dislocation sources. Presumably this results from the interaction of the stress field of the moving dislocation with defects on adjacent planes, although these defects have not been detected by etch pitting. In this manner the slip line can grow laterally but only at a slow rate, since the stresses are high only at small distances from the dislocation which is moving. For the case of a single loop moving through the lattice, one can calculate the distance over which interaction is possible. For reasonable values of the shear stress (G/500) the distance is of the order of 50b. For the case of piled-up arrays the shear stress ahead of the array is raised to a value of $n\pi$ to $n\pi/2$ depending on their spacing. The interaction distance is then increased by a factor of n/2to n. Since the number of coplanar loops observed in the present work is at most 10, the width of the region over which new sources could be activated by these piled up arrays is less than 0.1 μ . This distance is smaller than the observed values as shown by the slip lines in Fig. 6.

However, even in this model it becomes difficult to explain the nature of the curved slip lines on faces where screw dislocations are observed, unless there are an almost indefinite number of defects of very fine spacing (1 μ or less). For the curved slip lines in Figs. 9 and 10 the separation is somewhat larger than could be accounted for by the collision model.

Double cross-slip model

In this model the transfer of dislocation loops from plane to plane takes place by double cross-slip of screw segments as shown in Fig. 18.⁽¹¹⁾ This results in lateral growth as well as length-wise development of the slip line. In the absence of the generation of a large number of loops from a single source, cross slip of this kind is required to produce the amount of offset observed along a slip line. The loops given off by a single source move through the lattice and the edge segments are restrained to a single plane. When a segment of a loop in the screw orientation encounters an unfavorable local stress, it can move off into another plane until it reaches a position where the local stress allows it to move in a plane parallel to the original plane. The segment lying in the new

slip plane can now operate as a Frank-Read source and generate new loops. After this process is repeated several times the loops are no longer simple but have a complex shape. These variations in local stress causing cross slip can arise from other dislocations, impurity particles, or changes in the external stress such as notches, fillets, etc. In polycrystalline material the local stresses vary because of the presence of grain boundaries.

An obstacle preventing the growth of loops from the original source is the presence of loops in adjacent planes from the cross-slipped sources. As shown in Fig. 18 the new segment of the loop which generates loops on adjacent planes produces dislocation segments of opposite sign which will stop the loops from the original source. The process of generation of the slip band then occurs by the repetition of that shown in Fig. 18. The lateral interference can be one of the reasons for the difference in the motion of edges and screws, since the former are always moving into regions relatively free of new dislocation loops.

With an observed density of 10^6 dislocations per cm² in the undeformed crystal and an observed average movement of the screw components of approximately 10μ , jogs due to intersections with the existing network would be spaced about 10μ

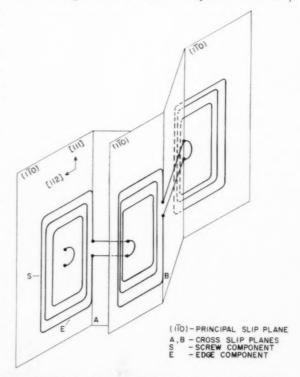


Fig. 18. Schematic representation of the process of formation and lateral growth of a slip band by the process of successive cross slip.

apart. Such a density of jogs in the screw components would not be expected to stop the motion of the latter. Rather, it appears that they are stopped by interaction with other screw components on closely adjacent planes arising from the cross-slip mechanism of dislocation multiplication.

Once the screw components of the leading dislocation loop are stopped, those of succeeding loops then pile upon the stopped dislocations or glide out of the slip plane. Thus, straight collinear arrays of large numbers of screw dislocations are rarely seen in comparison with those for the case of the edge segment. This effect can be seen plainly by comparing Fig. 5 with Fig. 9. For a given loop the edge and screw components will not be coplanar and the loop cannot collapse easily when the stress is removed. By counting the number of edge segments in a single plane of polish, it can be seen that no more than 20-30 loops can result from the operation of a single source and that the number is usually less than 10. The elementary slip process is then the formation and motion of these loops in the glide plane.

The motion of dislocations can be very rapid, but because of the short distance of motion of a single line the lengthwise growth of an optically visible slip band, during constant-rate tensile test, is not a direct measure of dislocation velocity but is related to the rate of formation of the arrays by the rate at which the amount of double cross-slip increases the breadth as the stress increases. For this reason measurements of the growth rate made by microscopic examination will not necessarily give true values of the dislocation mobility.

ACKNOWLEDGMENTS

The authors wish to acknowledge the assistance of J. Erickson and J. P. Smith in carrying out the experiments. The electron micrographs were made by Miss Anna M. Turkalo who made many helpful suggestions in their preparation. The results and their interpretation have been discussed with J. J. Gilman W. G. Johnston. We would particularly like to acknowledge the help of C. G. Dunn who has always been willing to supply us with the various crystals required for the investigation.

REFERENCES

- 1. R. MADDIN and N. K. CHEN, Progress in Metal Physics
- Vol. 5, pp 66-67. Pergamon Press, London (1954).
 2. J. J. Gilman and W. G. Johnston, Dislocations and Mechanical Properties of Crystals. John Wiley, New York, 1977. York (1957).
- 3. C. G. DUNN and W. R. HIBBARD JR., Acta Met. 3, 409-411 (1955).
- 4. J. C. Suits and J. R. Low Jr., Acta Met. 5, 285-289
- C. E. Morris, Metal. Progr. 56, 696 (1949).
- 6. H. Wilsdorf and D. Kuhlman-Wilsdorf, Report on a Conference on Defects in Crystalline Solids, p. 175. Physical Society, London (1954).
- W. T. READ JR., Dislocations in Crystals, p. 135. McGraw-Hill, New York (1953).
- H. WILSDORF and J. T. FOURIE, Acta Met. 4, 271 (1956).
 J. C. FISHER, E. W. HART and R. H. PRY, Phys. Rev. 87,
- 958-961 (1952).
- 10. N. F. MOTT, Phil. Mag. 43, 1151-1178 (1952).
- 11. J. S. Koehler, Phys. Rev. 86, 52-56 (1952).

QUENCHING STUDIES ON MECHANICAL PROPERTIES OF PURE GOLD*

M. MESHII and J. W. KAUFFMAN†

The effect of quenching from temperatures in the range $500^{\circ}\text{C}-1050^{\circ}\text{C}$ on the mechanical properties of 99.999% gold wires was studied over the range of cooling rates from 1000° to $60,000^{\circ}\text{C/sec}$. The specimens were deformed in tension at various temperatures from liquid nitrogen to 250°C . Upon aging at temperatures of 25° , 60° and 100°C subsequent to quenching, the yield stress was found to increase markedly, depending on the cooling rate and the quenching temperature. No effect was found for a rate of cooling of 1000°C/sec . An increase of the yield stress of six fold occurred upon quenching from 1030°C with a rate of cooling of $60,000^{\circ}\text{C/sec}$.

The activation energy corresponding to the rate of increase in yield stress was $0.7 \, \mathrm{eV}$ upon aging at $25-100\,^{\circ}\mathrm{C}$. Variation of the testing temperature from $-196\,^{\circ}\mathrm{C}$ to $150\,^{\circ}\mathrm{C}$ had no effect on the increase in yield stress resulting from quenching and aging. However, a considerable decrease in the yield stress of quenched samples was observed for tests at $250\,^{\circ}\mathrm{C}$. No resoftening was caused by annealing at $250\,^{\circ}\mathrm{C}$ for as long as $6 \, \mathrm{hr}$. Appreciable softening was observed above $600\,^{\circ}\mathrm{C}$ for anneals of $1 \, \mathrm{hr}$.

The effect of quenching temperature can be divided into three temperature regions when the complication of quenching strains are not present. Region I depends strongly on quenching speed and lies from about 930°C to the melting temperature for a $30,000^{\circ}$ C/sec cooling rate; region II lies just below and extends down to 740° C, and region III below 740°C. The dependence of yield stress on quenching temperature in region II gives an activation energy of 1.1 eV.

ETUDES DE LA TREMPE ET DES PROPRIETES MECANIQUES DE L'OR PUR

Les auteurs ont étudié les effets de la trempe à partir de températures comprises entre 500° C et 1050° C, sur les propriétés mécaniques de fils d'or pur à $99,999^{\circ}$. Les vitesses de refroidissement utilisées varient de 1000° à 60000° /sec.

Les échantillons ont été déformés par traction à des températures allant de celle de l'azote liquide à $250^{\circ}\mathrm{C}$. Au cours du vieillissement après trempe aux températures de 25° , 60° et $100^{\circ}\mathrm{C}$, la limite élastique croît fortement. Elle dépend de la vitesse de refroidissement et de la température de trempe car si aucune variation n'a été observée pour une vitesse de refroidissement de $1000^{\circ}/\mathrm{sec.}$, par contre un accroissement considérable de l'ordre de six fois apparaît après une trempe à partir de $1030^{\circ}\mathrm{C}$ avec une vitesse de refroidissement de $60000^{\circ}\mathrm{C}/\mathrm{sec.}$

VO!

19

L'énergie d'activation correspondant à l'augmentation de la limite élastique au cours des vieillissements à 25– $100\,^{\circ}$ C, est de 0.7 eV. Une variation de la température d'essai de $-196\,^{\circ}$ C à $150\,^{\circ}$ C n'a pas d'effet sur l'accroissement de la limite élastique résultant de la trempe et du vieillissement. Cependant, une diminution considérable de la limite élastique s'observe pour les essais à $250\,^{\circ}$ C. Aucun adoucissement ne résulte d'un traitement à $250\,^{\circ}$ C pendant 6 heures. Un adoucissement cependant s'observe après traitement au dessus de $600\,^{\circ}$ C pendant 1 heure.

Si il n'intervient pas de complication due aux tensions de trempe, l'effet de la température de trempe peut être précisé en fonction de trois gammes de température. La première gamme s'étend du point de fusion à 930°C environ pour une vitesse de refroidissement de 30000°C/sec. L'effet de la température est fortement dépendant de la vitesse de trempe.

La seconde région intéresse les températures comprises entre 930°C et 740°C et la troisième région les températures inférieures à 740°C. Dans la deuxième gamme, l'influence de la température de trempe sur la limite élastique donne une énergie d'activation de 1,1 eV.

EINFLUSS DES ABSCHRECKENS AUF DIE MECHANISCHEN EIGENSCHAFTEN VON REINEM GOLD

Gegenstand der Untersuchung ist die Beeinflussung der mechanischen Eigenschaften von Drähten aus 99999% Gold durch Abschrecken, wobei die Abschrecktemperaturen zwischen $500^{\circ}\mathrm{C}$ und $1050^{\circ}\mathrm{C}$, die Abschreckgeschwindigkeiten zwischen 1000° und $60000^{\circ}\mathrm{C}/\mathrm{see}$ lagen. Die Proben wurden bei Temperaturen zwischen der des flüssigen Stickstoffs und $250^{\circ}\mathrm{C}$ zugverformt. Altern bei 25° , 60° und $100^{\circ}\mathrm{C}$ im Anschluss an das Abschrecken bewirkte eine erhebliche Vergrösserung der Fliessspannung, die noch von Abschreckgeschwindigkeit und "Temperatur abhing. Eine Abkühlungsgeschwindigkeit von $1000^{\circ}\mathrm{C}/\mathrm{see}$ blieb ohne Einfluss, Abschrecken von $1030^{\circ}\mathrm{C}$ mit einer Geschwindigkeit von $60000^{\circ}\mathrm{C}/\mathrm{see}$ führte dagegen zu einer Erhöhung der Fliessspannung auf das Sechsfache.

Die Geschwindigkeit, mit der die Fliessspannung während des Alterns bei 25°–100°C zunahm, führt auf eine Aktivierungsenergie von 0,7 eV. Änderung der Verformungstemperatur zwischen —196°C und 150°C war ohne Einfluss auf die durch Abschrecken und Altern hervorgerufene Vergrösserung der Fliessspannung, Verformung bei 250°C ergab dagegen eine beträchtliche Abnahme der Fliessspannung abgeschreckter Proben. Selbst sechsstündiges Glühen bei 250°C bewirkte keine Entfestigung, nach einstündigem Glühen oberhalb 600°C wurde dagegen weitgehende Entfestigung beobachtet.

^{*} This work was partially supported by the U.S. Atomic Energy Commission. Received February 20, 1958; revised version

[†] Department of Metallurgy, Northwestern University, Evanston, Illinois.

Sieht man von der Komplikation durch Temperaturspannungen beim Abschrecken ab, so lässt die Abhängigkeit von der Abschrecktemperatur drie Temperaturbereiche unterscheiden: Bereich I hängt stark von der Abschreckgeschwindigkeit ab und erstreckt sich bei einer Abkühlgeschwindigkeit von 30000°C/see von der Schmelztemperatur herab bis etwa 930°C; Bereich II schliesst unmittelbar an und endet bei 740°C, Bereich III liegt unterhalb 740°C. Die Abhängigkeit der Fliessspannung von der Abschrecktemperatur im Bereich II ergibt eine Aktivierungsenergie von 1,1 eV.

INTRODUCTION

Previous investigators have noted an increase in yield stress in zinc⁽¹⁾ and aluminum^(2,3) accompanying cooling from high temperatures, which they explained as due to quenched-in vacancies. Other work has involved electrical resistivity^(4,5,6,7) and volume changes^(7,8,6) resulting from quenching. Still other workers⁽¹⁰⁾ have investigated changes in internal friction of pure gold due to cooling the specimens at a rate of about 4°C/minute. Recent studies have been made on quench hardening in copper⁽¹¹⁾ and hardening induced by additive coloration in KCl crystals.⁽¹²⁾

The purpose of the present investigation is to study systematically the mechanical effects resulting from quenching over a wide range of cooling rates and quenching temperatures. The previous quantitative work in metals has involved mainly the changes in electrical resistivity and also some volume change determinations. This work has yielded considerable information on the kinetics of quenched-in defect migration. However, little knowledge was acquired in regard to the nature of the configuration formed as a result of this migration. A study of this end result is better carried out by an investigation of the effects of quenching on mechanical properties, since the mechanical effects are related to such configurations, and also the increase in yield stress reaches a maximum when electrical resistivity and volume changes have nearly disappeared.

1959

The samples chosen were 99.999% pure gold polyerystalline wires of 0.016 in. diameter. Gold is an ideal metal for quenching studies because of its resistance to high temperature gaseous contamination. This choice also allows direct comparisons to be made with other electrical resistivity studies which have been carried out on similar samples.

EXPERIMENTAL PROCEDURE

99.999% pure gold polyerystal wire of 0.016 in. diameter was used. Specimens were heated by passing current through them in an argon atmosphere. About 11 A was required for a temperature of 1030°C. Temperatures were measured with a calibrated optical pyrometer and also by determining the electrical resistivity. Two inches of the center part of a 9 in. overall length was used for tensile tests; over this gage length the temperature was constant to within 1 per cent.

The specimens were supported horizontally and were quenched by moving them through a cool liquid. Variation of quenching speed was obtained; (1) by using various liquids, (2) by controlling the temperature of the liquid and (3) by the speed of specimen's motion through the quenching liquid. For very slow quenches carbon tetrachloride was used; the fastest rates were obtained with cold water. In this way we obtained a range of quenching rates of 1000°C/sec to 60,000°C/sec averaged over the entire quench. Quenching rates were measured with an oscilloscope, which gave the specimen voltage and hence its relative change of resistance as a function of time during the quench.

Tensile tests were performed with an Instron testing machine. A constant cross head motion of 0.01 in./min was maintained to rupture. The tests were carried out in liquid nitrogen, boiling water, paraffin baths, and at room temperature. The yield stress was taken to be the point of deviation from linearity of the initial portion of the stress-elongation curve obtained; this point is easily definable to within 5 per cent.

Metallographic examination showed that usually there were a few grains within the cross section, Local deformation was apparent after a few per cent extension.

RESULTS

1. General behavior

The effect of rapid quenching and of subsequent aging is shown in Fig. 1. For no aging no mechanical effect was found, provided that internal stresses were not generated during the quenching process. A rate of quenching of 70,000°C/sec produced an increase in yield stress without aging as shown by curve C. Upon aging at 0°C–100°C after rapid quenching the yield stress increased to a saturated value, which depended on the rate of quenching. Besides an increase in yield stress accompanying aging, the shape of the stress–elongation curves changed. For the more rapid quenches the ductility was found to decrease as seen by A.

2. Effect of quenching rate

The rate of cooling is of major importance in quenching studies of metals. The effect of stresses generated during the quench can be seen from curves C and D of Fig. 1. The time-temperature curves

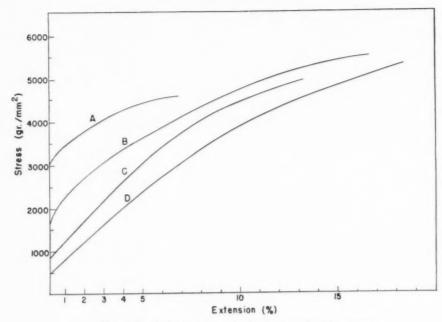


Fig. 1. Typical stress vs. extension curves of gold specimens.

(A) Quenched from 1030°C with an average rate of cooling of 60,000°C/sec and aged to saturation.

(B) Quenched from 1030°C with an average rate of cooling of 30,000°C/sec and aged to saturation.

(C) Quenched from 1030°C with the maximum rate of cooling of 70,000°C/sec and not aged.

(D) Quenched from 1030°C with the maximum rate of cooling below 30,000°C/sec and not aged; also a slow cooled specimen.

obtained during the quench usually show roughly a linear decrease of temperature with time. The maximum quenching rate usually was about 10–20 per cent higher than the average over the complete quench. It was found that the initial increase in yield stress depends on the maximum cooling rate rather than the average during the quench; this dependence is shown in Fig. 2. Calculations of the radial stresses generated by the temperature gradients due to cooling agree roughly with these results. The yield stress of samples quenched from 1030°C and

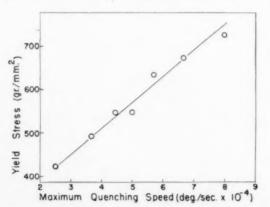


Fig. 2. The effect of the maximum quenching speed on the yield stress of the specimen immediately after quenching. All specimens were quenched from 1030° C.

aged to give maximum hardening was measured as a function of average quenching rate from 1000°C/sec to 60,000°C/sec; these results are given in Fig. 3. The value of the yield stress for specimens quenched at 2000°C/sec and aged shows no appreciable increase over those annealed and slow cooled. At higher quenching rates the yield stress continually increases and no saturation of the effect appears up to the fastest quenches obtained. The increase of yield stress corresponding to aging to maximum effect, for quenches from 1030°C of 60,000°C/sec average quenching rate, is larger than the initial effect due to quenching stresses by roughly a factor of five. Therefore, still faster quenches are required to trap nearly all of the vacancies present at 1030°C at which these quenches were initiated. Specimens quenched at rates giving large initial increases in the yield stress exhibit different aging kinetics for those for which no plastic strains were produced. Increased aging rates are found for the strained samples but no quantitative study was carried out in this matter.

19

3. Aging

Isothermal aging at 25°, 60° and 100°C was performed for various time intervals with specimens quenched from 1030°C to 2°C with an average cooling rate of 30,000°C/sec; this quenching rate does not

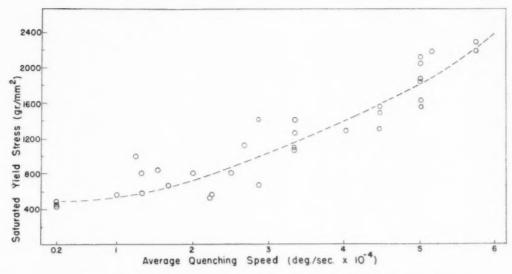


Fig. 3. The effect of average quenching speed on the saturated yield stress after aging. All specimens were quenched from 1030 C.

plastically deform the specimens. These results are given in Figs. 4, 5 and 6. The increase in yield stress resulting from quenching starts from zero for no aging and increases monotonically with aging to a saturated value, which does not vary with the aging temperature. These data give an activating energy of $0.7~{\rm eV}$.

4. Quenching temperatures

The effect of quenching temperature, i.e. the temperature from which the quench was begun, was studied over the range 600°C–1050°C for quenching rates of 30,000°C/sec and 60,000°C/sec. The logarithm of the increase in yield stress for fully aged specimens

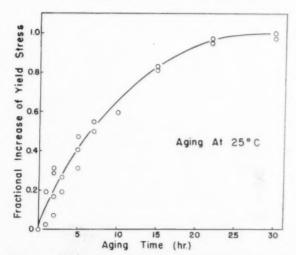


Fig. 4. Increase of yield stress in the course of aging at 25 C after quenching from 1030 C with an average cooling rate of 30,000 C/sec.

as a function of the reciprocal of absolute temperature is shown in Fig. 7. First, consider the quenches made at a speed of 30,000°C/sec; three temperature regions were found: Region I above 930°C where little temperature dependence was found, region II a linear relationship extending from 930°C down to 740°C and region III below 740°C where a more rapid fall-off to no effect occurred. For the more rapid quenches the added complexity strains are present. This results in the plateau region for low temperature quenches where this effect becomes large compared to that of aging. The linear region is displaced to a higher level for the 60,000°C/sec quenches and extends to a higher temperature close to the melting point; hence region I is considerably reduced by the more rapid quench. Surprisingly, for both speeds of quenching the linear portions in Fig. 7 are parallel. The activation energy given by this slope is 1.1 eV, which roughly agrees with the value obtained from the initial quench-in electrical resistivity as a function of quenching temperature. (5,6)

5. Testing temperature and resoftening

The range of temperatures of the tensile tests extended from -196°C to 250°C . The results are given in Fig. 8. The lower curve, annealed and slow cooled samples, is nearly straight over the whole range; the upper curve, quenched at $30,000^{\circ}\text{C/sec}$ from 1030°C and aged to saturation, is parallel to the lower curve below 150°C but shows a drop-off of yield stress approaching the unquenched behavior at temperatures above about 200°C .

VOL. 7 1959

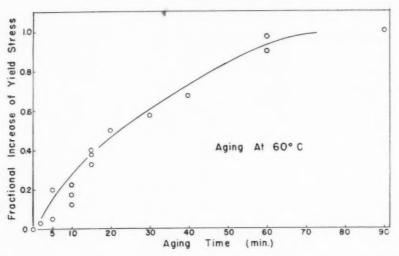


Fig. 5. Increase of yield stress in the course of aging at 60°C after quenching from 1030°C with an average cooling rate of 30,000°C/sec.

The fall-off behavior with increasing temperature of the quenched samples described above is in surprising contrast to the results of Fig. 9 where specimens were annealed in the range $100^{\circ}\text{C}-700^{\circ}\text{C}$ for 1 hr subsequent to the quench and aging process, and then tested at room temperature. No resoftening was found in the range of the drop-off of Fig. 9; rather resoftening begins above 500°C . Anneals up to 6 hr at 250°C produced no detectable resoftening.

6. Effect of plastic deformation

Specimens were given the following treatments:

(1) Quenched from 1030°C at 30,000°C/sec, (2) deformed in tension immediately following the quench, (3) aged at 100°C for 1 hr, (4) measured for yield stress. Therefore, the yield stress is increased by two controlled factors, the tensile deformation and the

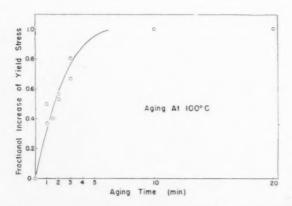


Fig. 6. Increase of yield stress in the course of aging at 100° C after quenching from 1030° C with an average cooling rate of $30,000^{\circ}$ C/sec.

subsequent aging. For deformations up to 1 per cent extension these two effects were found to be additive but were less than additive for larger extensions.

DISCUSSION

The present state of knowledge of quench hardening is not sufficiently developed to justify the acceptance

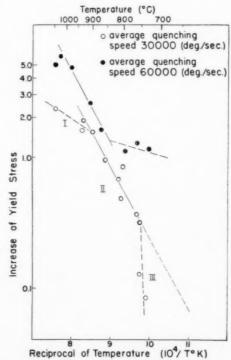


Fig. 7. The increase of yield stress due to quenching and subsequent aging, as a function of quenching temperature. Most data taken in region III show no increase in yield stress and therefore cannot be shown in this plot.

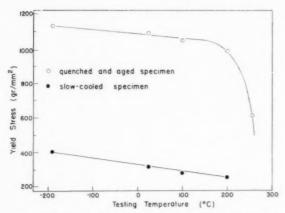


Fig. 8. Effect of testing temperature on the yield stress of quenched and subsequently aged specimens and of slowly cooled specimens.

of definite detailed mechanisms for the hardening process. However, certain conclusions can be drawn from the present results, as listed below, and various possible hardening mechanisms can be discussed in the light of these results.

1. No appreciable increase in yield stress is observed immediately after quenching when plastic deformation does not occur during the quench. Therefore, quenched-in defects, since they are dispersed immediately after quenching, do not harden the samples to an extent sufficient to detect.

2. The rate controlling process is the same for the increase of yield stress as for the recovery of electrical resistivity. This is apparent from a comparison of the present results with those of electrical resistivity measurements⁽⁷⁾ which were carried out on the same type of specimens and with comparable quenching rates. The rates for both processes are equal within experimental error, and the activation energies coincide, i.e. 0.7 eV for quenches made from above 850°C. This process has been interpreted by Koehler et al.⁽¹⁴⁾ to be the migration of vacancies and divacancies, mainly the latter, to dislocations.

3. The configuration producing hardening must be very stable because of the high temperature necessary for resoftening. Complete recovery of mechanical properties, and of that part of the electrical resistivity which remains after room temperature recovery has been completed, takes place within the same annealing temperature range. This indicates that the same stable configuration resulting from quenched-in defects is responsible for both the residual electrical resistivity and mechanical properties after room temperature aging.

4. The hardening produced by quenching and aging can possibly occur either by defects migrating to

dislocations and forming certain stable configurations which lock dislocations, or by a precipitation type hardening, i.e. random stable clusters of vacancies which act as barriers to dislocation motion. These clusters might collapse forming sessile ring dislocations. Several stable configurations which are considered to give the hardening effect may be pointed out in the former case. Coulomb and Friedel (16) have proposed void formation on the dislocation lines. If a number of vacancies coagulate, they may be able to produce a new constriction jog on the extended dislocation. Also, sessile ring type of configurations on the extended dislocations is a possible mechanism. Of course, isolated vacancies along the dislocation line cannot produce any of the above configurations: the energy for a jog in the noble metals(13) being too great to allow single vacancies to produce jogs. Rather, single vacancies can travel rapidly along dislocation lines until joining with the already existing stable form, or disappearing at a sink.

5. The dependence of the yield stress on quenching temperature for a cooling rate of 30,000°C/sec is seen to divide into three temperature regions in Fig. 7. In the intermediate region the increase in yield stress is approximately proportional to the quenched-in electrical resistivity found by other workers (6,7) as is seen by the comparison of activation energies, 1.1 eV for hardening and about 1.0 eV for electrical resistivity. The linear region in Fig. 7 falls off above 900°C (region I) for a quenching speed of 30,000°C/sec. The linear region for the 60,000°C/sec quenching rate extends to higher temperatures: therefore, the falling off in region I is due to insufficient quenching speed at the higher temperatures. Since no significant initial hardening is observed for quenches from temperatures in region I, the defects not trapped during the quench must have escaped via a mechanism not resulting in hardening. The surprising behavior is

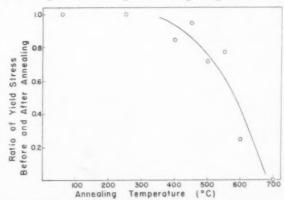


Fig. 9. Resoftening at elevated temperatures. Annealing time 1 hr.

VOL. 7 1959 that of region III where a marked decrease in yield stress is found below quenching temperatures of about 740°C. This can be explained in terms of the difference both in the form and in the concentration of quenched-in defects as the quenching temperature varies.

6. The rapid fall off to no measurable effect for quench temperatures below about 740°C can be understood from the difference in behavior between single vacancies and divacancies and also from their relative change in concentration with quenching temperature. Koehler and co-workers, (14) taking 0.2 eV for the binding energy of a divacancy and a quenching speed of 30,000°C/sec, calculated that the quenched-in concentration of divacancies increases by a factor of 6 as the quenching temperature is increased from 700°C to 800°C. However, for this same increase in quenching temperature the calculated single vacancy concentration after quenching shows no appreciable increase because of the formation of divacancies from single vacancies during the quench.

The single vacancy is free to migrate rapidly along the dislocation line. It is presumed from Turnbull and Hoffman's work⁽¹⁵⁾ that single vacancies, in fact, travel much more rapidly along the dislocation line than in the undistorted lattice. The situation is reversed for the case of divacancy. The divacancy becomes relatively immobile when attached to a dislocation because it has to tumble or break up to two single vacancies for motion. When the divacancy is parallel to the dislocation line, the force of attraction acts so as to prevent the divacancy from tumbling, and it becomes less mobile than in the perfect lattice. Therefore, divacancies are expected to be much more effective than single vacancies as nucleating sites along dislocations.

This model is consistent with the results of electrical resistivity measurements on quenched specimens, although electrical resistivity does not show region III behavior. In this region single vacancies predominate and contribute to electrical resistivity immediately after quench, but they rapidly escape along the dislocation line without forming stable configurations when there are not enough slow-moving divacancies to impede their transportation. Seeger⁽¹⁷⁾ has shown that the resistivity contribution of a divacancy ought to be about the same as that for two single vacancies. Thus, the results are not conflicting.

REFERENCES

- Choh Hsien Li, J. Washburn, and Earl R. Parker, J. Metals, N.Y. 5, 1223 (1953).
- R. MADDIN and A. H. COTTRELL, Phil. Mag. 46, 735 (1955).
- J. Takamura and S. Miura, Bulletin, Spring Meeting, Japan Inst. of Metals 38, 20 (1956).
- J. W. Kauffman and J. S. Koehler, Phys. Rev. 97, 555 (1955).
- J. E. BAUERLE, C. E. KLABUNDE, and J. S. KOEHLER, Phys. Rev. 102, 1182 (1956).
- Frys. Rev. 102, 1182 (1956).
 F. J. Bradshaw and S. Pearson, Phil. Mag. 2, 379
- J. E. Bauerle and J. S. Koehler, Phys. Rev. 107, 1493 (1957).

VO:

- 8. J. TAKAMURA. Private communication.
- 9. J. Takamura, Metal Physics 2, 112 (1956).
- 10. A. E. Roswell and A. S. Nowick, Acta Met. 5, 228 (1957).
- 11. H. KIMURA and R. MADDIN. Private communication.
- 12. T. Suzuki. Private communication.
- A. SEEGER, Defects in Crystalline Solids, p. 391. Physical Society, London (1955).
- J. S. KOEHLER, F. SEITZ, and J. E. BAUERLE, Phys. Rev. 107, 1499 (1957).
- 15. D. TURNBULL and R. E. HOFFMAN, Acta Met. 2, 419 (1954)
- P. COULOMB and J. FRIEDEL, Lake Placid Conference on Dislocations and Mechanical Properties of Crystals, p. 555 (1956).
- H. Bross and A. Seeger, J. Phys Chem. Solids, To be published.

ELECTRON IRRADIATION OF ALUMINUM-COPPER ALLOYS*

C. W. TUCKER, Jr. and M. B. WEBB†

Irradiation of quenched Al–2 at.% Cu alloys with 1.4 MeV electrons to integrated fluxes of 8×10^{16} electrons/cm² at $-60^{\circ}\mathrm{C}$ has shown that mobile irradiation defects can promote the low-temperature clustering of copper atoms at this temperature. Estimates assuming a vacancy-like irradiation defect indicate that it is reasonable to expect the formation of very small clusters with these irradiations. These results imply that the thermally activated low-temperature clustering of copper proceeds by an excess vacancy mechanism rather than a dislocation mechanism.

IRRADIATION D'ALLIAGES Al-Cu PAR FLUX D'ELECTRONS

Les auteurs ont fait irradier à $-60^{\circ}\mathrm{C}$ des alliages Al-Cu (2% at) trempés par des électrons de 1,4 MeV jusqu'à un flux intégré de 8.10^{16} électrons/cm². Cette irradiation a montré que les défauts mobiles qu'elle crée peuvent provoquer des amas d'atomes de cuivre à basse température. L'hypothèse de l'existence de défauts d'irradiation du type lacune permet de s'attendre raisonnablement à la formation de très petits amas en conséquence de l'irradiation. Ces résultats indiquent que cette formation d'amas de cuivre à basse température, qui est thermiquement activée, est due à des lacunes en excès plutôt qu'à un mécanisme faisant intervenir des dislocations.

ELEKTRONENBESTRAHLUNG VON ALUMINIUM-KUPFER-LEGIERUNGEN

Die Bestrahlung abgeschreckter Al–2At.% Cu Legierungen mit 1,4 MeV Elektronen bei $-60^{\circ}\mathrm{C}$ bis zu einem integrierten Fluss von 8 \times 10^{16} Elektronen/cm² zeigte, dass bewegliche Bestrahlungsfehler die bei tiefer Temperatur stattfindende Zusammenlagerung von Kupferatomen (Bildung von G. P. Zonen) bei dieser Temperatur unterstützen können. Unter der Annahme eines leerstellenähnlichen Bestrahlungsfehlers ergeben Abschätzungen, dass man vernünftigerweise die Bildung sehr kleiner G. P. Zonen bei dieser Bestrahlung erwartet. Diese Befunde besagen, dass die thermisch aktivierte Bildung von G. P. Zonen bei tiefen Temperaturen durch einen Mechanismus mit überschüssigen Leerstellen und nicht durch einen Versetzungsmechanismus vor sich geht.

INTRODUCTION

The formation of the various metastable phases from super-saturated solutions of copper in aluminum is, of course, a very old and much studied problem. (1) Recently attention has been devoted to the so-called cold-hardening reaction which occurs at temperatures as low as $-60^{\circ}\mathrm{C}$ and during which clusters or Guinier–Preston zones form. This process is of interest because it proceeds with an activation energy of only $0.5~\mathrm{eV}$, (2) whereas the activation energy for diffusion of copper in aluminum is $1.4~\mathrm{eV}$. (3) Some mechanism other than normal diffusion is, therefore, required to account for the cold-hardening reaction.

The two mechanisms most frequently proposed are an excess vacancy mechanism and a dislocation mechanism. (2) According to the excess vacancy mechanism the act of quenching retains a large fraction of the vacancies present at the high temperature, and these vacancies permit diffusion of the copper at low temperatures. Since the activation energy for the formation of these vacancies need not

be supplied thermally, one expects the activation energy for the motion of copper to be in the neighborhood of 0.5 eV. On the other hand the dislocation mechanism is based on the reasonable assumption that diffusion of copper along a dislocation pipe proceeds with a much lower activation energy than in the matrix. One expects the activation energy for diffusion along a dislocation pipe to be approximately 0.5 eV. While difficulties arise with both mechanisms and various means of surmounting them have been suggested, it was felt that electron irradiation, as a means of introducing point defects independently, might be helpful in distinguishing the two proposed mechanisms.

There are, of course, uncertainties concerning the nature of the defects in electron irradiated Al–Cu at the temperatures of the cold-hardening reaction, even as there may be uncertainties concerning the nature of the quenched defects. However, from the neutron work on aluminum $^{(5,6)}$ it is likely that in Al–Cu there is a defect mobile in the temperature range -80° to -40° C. In the upper part of this range, -60° to -40° C, the cold-hardening reaction will just proceed thermally. The situation was,

VOL.

^{*} Received May 21, 1958.

[†] General Electric Research Laboratory, Schenectady, New York.

therefore, hopeful since it has been known for some time now that precipitation and ordering phenomena are most likely to be promoted by irradiation if some irradiation defect is mobile in a temperature range at or just below temperatures at which the reaction will go slowly thermally. It was, therefore, decided to study any effect which electron irradiation might have on the very early stages of the cold-hardening reaction. Electrical resistance measurements were chosen to follow the course of the reaction because of their sensitivity to the reaction in the early stages.

EXPERIMENTAL

Samples of the alloy (Al-2 at.% Cu) were prepared from ribbon 4 mils thick and 0.09 in. wide by splitting 40 in. lengths down to a 1 in. gauge length at the center. Thus current and potential leads were available for the resistance measurements. Samples were homogenized by annealing for 1 hr at 540°C, quenched into a cutectic mixture of calcium chloride and water at -45°C, and then quickly placed in liquid nitrogen for storage.

Mounting of the samples in an irradiation holder was accomplished in an alcohol bath which was kept at temperatures below -80°C. The holder was drained while the samples were kept cold with jets of cold dry nitrogen gas which also were used for sample temperature regulation during irradiation. Electrons with an energy of 1.4 ± 0.1 MeV at the sample were supplied by a commercial model General Electric resonant transformer. Most irradiations lasted 4 hr and were made with an accelerator current of 50 μ A. This gave an electron flux of approximately 5.6×10^{12} electrons/cm²/sec at the sample and an integrated flux of about 8.1×10^{16} electrons/cm². Resistance measurements were made by up-quenching samples from the liquid nitrogen, in which they were stored after irradiation, to either -20° or 0°C. Resistance was recorded continuously as a function of time by the method of Turnbull and Treaftis, (7) starting in the most favorable cases about 5 sec after the upquench.

First a blank run was made at $-70^{\circ}\mathrm{C}$ for 4 hr to establish that no thermal excursions occurred at any point in the procedure. Next, irradiation runs were made at $-70^{\circ}\mathrm{C}$ for integrated fluxes of 4×10^{16} and 8×10^{16} electrons/cm². Small but detectable slowing of the rate of resistance change in the first few minutes of the resistance–time curves at $-20^{\circ}\mathrm{C}$ were noted due to these irradiations. Following this, a run was made at $-145^{\circ}\mathrm{C}$ for an integrated flux of 8×10^{16} electrons/cm². No detectable change in the resistance–time curves run at $-20^{\circ}\mathrm{C}$ was observed in this case.

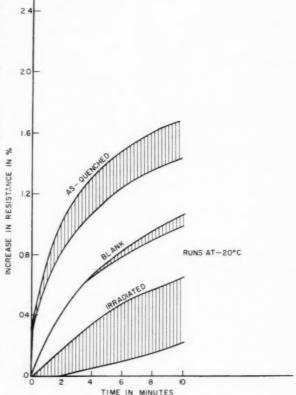


Fig. 1. Change in resistance vs. time curves run at -20° C.

19

At this point it seemed clear that the effect of electron irradiation was probably due to the defect mobile in pure aluminum around -60°C. Consequently a series of irradiations for integrated fluxes of 8×10^{16} electrons/cm² were made at -60° C with subsequent resistance-time curves being made at -20° and 0°C. Here the effect of irradiation on the course of the resistance-time curves was particularly strong during the first few minutes. It was realized that part of this effect, however, might be due to thermal activation of the reaction during the irradiation, so blank runs (runs identical except for the absence of irradiation) were made. The results of these and other experiments are shown in Figs. 1 and 2.* Since there was a certain amount of scatter amongst samples with supposedly identical treatment, the results are presented as scatter bands to illustrate the deviations encountered.

The difference between the as-quenched and blank curves in Figs. 1 and 2 shows that a portion of the reaction proceeded thermally during the hold at

^{*} Data are only shown for the first 10 min, but runs out to times as long as a few hours showed that all curves are essentially parallel after the first 10 min.

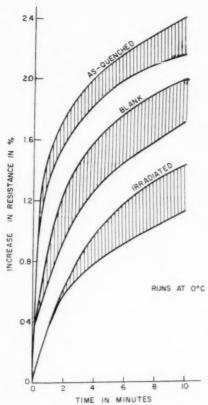


Fig. 2. Change in resistance vs. time curves run at 0°C,

1959

 -60° C. The difference between the blank and irradiated curves shows that the reaction has been affected by the irradiation. The subsequent thermal reaction in the irradiated samples is obviously slower than that in the blank specimens.

The question which arises, however, is whether this difference between the blank and irradiated curves is a true irradiation effect or whether it might be due to electron beam heating or to thermal spikes. The data of DeSorbo et al. (2) show that a temperature rise of 7°C would be required to produce the observed difference between the blank and irradiated curves. That the temperature rise due to beam heating was less than 1°C was shown by all of the following methods: substituting resistive heating comparable to beam heating; measuring sample temperature changes in beam accelerator "beam on-beam off" experiments; and rough heat flow calculations. In addition an irradiation at double the accelerator current gave no evidence for beam heating. Thermal effects due to spikes can also be shown to be negligible since the energy transferred in an average electron-atom encounter is only 150 eV. In the short time of 10⁻¹⁰ sec the spike reaches its optimum size

for affecting the reaction and then the temperature rise is only 3°-4°C. But the size and intensity of the spike are such rapid functions of time that shortening the spike duration very quickly constricts the volume affected to insignificant amounts, while increasing the spike duration rapidly drops the temperature rise so that no effects could possibly be produced by spikes. It can also be shown that the low temperature tail of the spikes discussed by Chang⁽⁸⁾ cannot produce effects in the present case.

The next question which naturally arises is whether the difference between the blank and irradiated curves is due to a portion of the reaction which proceeds during the irradiation, presumably caused by the migration of irradiation defects, or whether it is due to a slowing of the subsequent thermal reaction by some action of the irradiation defects. The resistances of two samples were, therefore, carefully measured at 20°K before and after an irradiation at -60°C. Resistance increases of 1.4 and 1.9 per cent were found. Comparison of the as-quenched and blank curves of Figs. 1 and 2 shows that an increase of 0.6 per cent is to be expected due to thermal activation of the reaction during the irradiation. The remainder of the resistance increase in the samples, 0.8 and 1.3 per cent, represents that portion of the reaction which is promoted by and during the irradiation. Thus it is clear that the irradiation defects promote the cold-hardening reaction during the irradiation rather than slowing the subsequent thermal reaction.

This conclusion is also supported by the fact that the difference between the total relative change in resistance of the blank and irradiated curves corresponds roughly to that occurring in 6 min at $-20^{\circ}\mathrm{C}$ and in 1–2 min at $0^{\circ}\mathrm{C}$ in the blank samples.

DISCUSSION OF RESULTS AND CONCLUSIONS

The main result of the present work is that irradiation can promote the cold-hardening reaction. This is most easily understood in terms of a vacancy or point defect mechanism. To show that one might expect these irradiations to produce significant clustering, estimates for diffusion caused by a vacancy-like irradiation defect were made. These order of magnitude calculations indicate that a fractional number of defects of about 10^{-5} is produced during the irradiations, that each defect makes roughly 10^5 jumps in its average lifetime of about $200 \sec^{(5)}$ and, therefore, that each atom in the sample jumps once. It can then be shown that this number of jumps could lead to a major fraction of the copper atoms forming pairs and triplets during the irradiation. These

estimates are, of course, very approximate and are subject to many uncertainties; for example, the interaction of the irradiation defects with the higher concentration of quenched-in defects is unknown. The estimates are presented simply to show that it is not unreasonable that the present irradiation doses could produce defects capable of causing the observed effects.

The present results and their interpretation are similar to those reported for the effect of irradiation on ordering in partially ordered Cu₃Au^(9,10) and in α-brass.(11)

In conclusion, it can be stated that electron irradiation point defects can promote the cold-hardening reaction. This is presumed to occur by migration of a vacancy-like irradiation defect through the lattice, thus permitting the formation of clusters of a small number of copper atoms. This mechanism is, of course, the same as the excess vacancy mechanism except that the defect is formed by irradiation.

This conclusion is not entirely unequivocal since it may be possible to devise a means by which point defects could affect a dislocation mechanism. These experiments show that if indeed the mechanism involves dislocations, it is promoted by point defects. This situation is difficult to imagine.

ACKNOWLEDGMENTS

It is a pleasure to thank Dr. D. Turnbull who suggested this problem and to thank a number of people who assisted in the work: H. N. Treaftis for the resistance-time curves, Dr. W. DeSorbo and G. E. Nichols for the 20°K resistance measurements, and J. W. Corbett, R. M. Walker, and R. B. Smith for help with the irradiation facilities and the irradiations.

REFERENCES

- 1. No attempt will be made to document this work. The survey by H. K. HARDY and T. J. HEAL, Progress in Metal Physics Vol. 5, p. 143. Pergamon Press, London (1954), gives an excellent review.
- 2. This has been determined by a variety of methods. The results of W. DeSorbo, H. N. TREAFTIS and D. TURNBULL, Acta Met. (1958) accepted for publication are recent and typical.
- 3. R. M. BRICK and A. PHILLIPS, Trans. Amer. Inst. Min. (Metall.) Engrs. 124, 331 (1937)
- 4. J. S. Koehler, F. Seitz and J. E. Bauerle, Phys. Rev.
- 107, 1499 (1957). 5. A. W. McReynolds, W. Augustiniak, M. McKewon,
- and D. Rosenblatt, *Phys. Rev.* **98**, 418 (1955).
 6. J. K. Redmann, T. S. Noggle, R. R. Coltman, and T. H. Blewitt, Bull. Amer. Phys. Soc. Ser. II, 1, 130 (1956).
- D. Turnbull and H. N. Treaftis, Acta Met. 3, 43 (1955).
- R. Chang, Acta Met. 5, 275 (1957)
- 9. R. A. DUGDALE and A. GREEN, Phil. Mag. 45, 163 (1954).
- 10. T. H. BLEWITT and R. R. COLTMAN, Acta Met. 2, 549

19

11. A. C. Damask, J. Phys. Chem. Solids 4, 177 (1958).

OXIDATION OF NICKEL-COBALT ALLOYS IN THE RANGE OF CURIE TEMPERATURES*†

W. W. SMELTZER:

The surface oxidation kinetics of metallographically polished nickel–cobalt alloys, 10.5 and 25.1% cobalt, have been studied in the temperature range 400° to 800° C using a vacuum microbalance technique. The alloy of largest cobalt concentration oxidized most rapidly. The oxidation rates have been represented, to a first approximation, by cubic and parabolic time laws. In the temperature range of the second order magnetic transformation below the Curie temperature, the Arrhenius temperature coefficients of the rate constants demonstrate continuous variations. It is proposed, with results for nickel oxidation as datum, that these variations are caused by electronic properties of the metal substrate, which influence the rate determining reaction step of metal ion diffusion through the surface oxide layer.

OXYDATION D'ALLIAGES NICKEL-COBALT DANS LE DOMAINE DES TEMPERATURES DES POINTS CURIE

L'auteur étudie au moyen d'une microbalance sous vide la cinétique de l'oxydation entre 400 et 800 °C d'alliages nickel—cobalt (10,5 et 25,1% Co) polis métallographiquement. L'alliage avec la teneur la plus élevée en cobalt s'oxyde le plus rapidement. Les vitesses d'oxydation peuvent être représentées, en première approximation, par des lois cubiques et paraboliques. Dans le domaine des températures de la transformation magnétique de second ordre au-dessous du point Curie, les coefficients d'Arrhenius des constantes de vitesse varient d'une mainière continuelle. L'auteur propose sur la base de données sur l'oxydation du nickel l'interprétation suivante: les variations observées sont dues aux propriétés électroniques du substrat métallique qui influencent l'étape déterminant la vitesse de réaction, à savoir la diffusion de l'ion métallique au travers de la couche d'oxyde superficielle.

OXYDATION VON NICKEL-KOBALT-LEGIERUNGEN IN DER UMGEBUNG DER CURIE-TEMPERATUR

Mit Hilfe von Mikrowägungen im Vakuum wurde die Kinetik der Oberflächenoxydation von metallographisch polierten Nickel—Kobalt-Legierungen (10,5%) und 25,1% Kobalt) untersucht. Am schnellsten oxydierte die Legierung mit dem grössten Kobaltgehalt. Die Geschwindigkeit der Oxydation liess sich in erster Näherung durch kubische bzw. parabolische Zeitgesetze darstellen. Versucht man, die Temperaturabhängigkeit der Koeffizienten dieser Gesetze durch eine Arrhenius-Gleichung zu beschreiben, so zeigt die "Aktivierungsenergie" in der Nähe der magnetischen Umwandlung 2. Ordnung unterhalb der Curie-Temperatur systematische Veränderungen. Als Ursache für diese Veränderungen—bestimmt als Abweichung von den entsprechenden Grössen bei der Oxydation von Nickel—werden die elektronischen Eigenschaften des zugrundeliegenden Metalles vorgeschlagen; sie beeinflussen den geschwindigkeitsbestimmenden Reaktionsschritt, nämlich die Diffusion der Metallionen durch die Oxydschicht an der Oberfläche.

INTRODUCTION

1959

There is considerable experimental evidence to support the view that the kinetics of metal oxidation are altered by variation of metal substrate properties. This evidence has been summarized by Lustman⁽¹⁾ and Uhlig,⁽²⁾ and measurements of different oxidation rates of metal surfaces of different crystal orientation, discontinuities in oxidation rates at metal lattice transformation temperatures and variations in oxidation characteristics of metals and alloys above and below Curie temperatures have been quoted. This

investigation on the oxidation of nickel-cobalt alloys deals with the latter effect.

In 1925, Tammann and Siebel⁽³⁾ found that magnetic transitions in iron–nickel and iron–vanadium alloys at the Curie temperatures influenced oxidation rates. Uhlig⁽²⁾ has postulated that these findings show the important role of electron emission from the metal in its initial oxidation stages. If it be assumed that the electron work function is of different value and relatively temperature independent above and below the Curie temperature, the temperature coefficient of oxidation rate constants may show a discontinuity. This effect has been found for iron–chromium alloys⁽⁴⁾ and nickel;⁽⁵⁾ the activation energies for oxidation, determined from plots of the logarithms of the oxidation rates vs. the reciprocal

^{*} This work forms part of a research project sponsored by the Air Force Office of Scientific Research, Air Research and Development Command.

[†] Received May 6, 1957; revised version June 2, 1958. ‡ Metals Research Laboratory, Carnegie Institute of Technology, Pittsburgh, Pennsylvania.

of the absolute temperatures, were larger above the Curie temperatures. Seigneurin and Forestier⁽⁶⁾ have determined the velocity of air oxidation at various temperatures for magnetite, iron and nickel by a continuous weighing technique. In each case, curves of relative weight change, as a function of temperature at which oxidation was accomplished, showed positive anomalies without discontinuities in the neighborhood of the Curie temperature. The oxidation of an iron alloy containing 10% aluminum showed two such anomalies, one at the Curie temperature of the alloy and the second at the Curie temperature of iron. The nonferromagnetic 12% manganese—iron alloy also showed anomalous behavior at the Curie temperature of iron.

In an attempt to gain further knowledge of the oxidation characteristics of metals in the range of Curie temperatures, the oxidation of nickel-cobalt alloys has been studied in this investigation. This alloy system possesses specific advantages since nickel and cobalt form a continuous series of solid solutions. Hence, the Curie temperatures, which range from 353° to 1115°C, are only associated with second order electronic transitions without changes in lattice structure. To determine the influence of the magnetic state of the metal substrate on the oxidation rates, alloys containing 11 and 25% cobalt have been oxidized in temperature ranges above and below Curie temperatures. Moreover, the oxidation rates have been continuously determined by a precise experimental technique for evaluations of different oxidation rate constants. This has been done because previous investigations on the influence of magnetic properties on oxidation behavior have been based upon weight gains of specimens for given periods of exposure, and on application of an assumed oxidation rate law.

EXPERIMENTAL

The nickel-cobalt alloys, which were prepared by vacuum fusion of high purity nickel and cobalt, were supplied through the courtesy of the Westinghouse Electric Corporation. These alloys contained 10.5 and 25.1% cobalt. Analysis of the 25.1% cobalt alloy showed the following major impurities expressed in %: 0.001 aluminum, 0.005 calcium, 0.02 copper, 0.01 iron, 0.002 manganese, 0.20 silicon, 0.02 carbon and 0.003 sulfur. Sixteen other metallic elements were not detected by spectrographic analysis. Ingots were cold rolled by multiple passes to sheet 0.02 in. thick. Specimens, 0.01 in. thick, were prepared for oxidation from this sheet by abrasion with metallographic papers to 4/0 fineness.

A vacuum microbalance assembly, similar to that

described by Gulbransen, $^{(7)}$ was used to determine the oxidation rates of these alloys in oxygen. Weight gains of a specimen were continuously determined by observing the displacement of pointers on the balance beam and frame of the quartz microbalance with a sliding microscope. The balance sensitivity was 1 division $(0.001~{\rm cm})$ of the micrometer slide per $2.1~{\rm \mu g}$ for a sample and counterweight of $0.6900~{\rm g}$. Electrolytic cylinder oxygen was purified of hydrogen, water, carbon oxides and residual condensible vapors by passage through a train consisting of platinized asbestos, ascarite, activated alumina and a trap at liquid air temperature. The furnace temperature in the region for suspension of a metal specimen from the microbalance was controlled to $+2^{\circ}{\rm C}$.

Oxide formation on the alloy was studied as a function of time and temperature at a constant oxygen pressure. Before oxidation, a specimen was degassed in a vacuum of 10^{-5} – 10^{-6} mm during the furnace heating period of 2 hr and an anneal of 1 hr at the oxidation test temperature.

RESULTS

VO:

19

Both alloys exhibited similar initial rapid rates of oxidation which decreased with time for exposures of approximately 24 hr in the temperature range 400°–800°C. This is illustrated by the rectilinear plots of the weight gain of the specimens, μg oxygen/cm², vs. time at constant oxygen pressures and temperatures in Figs. 1 to 3. In Fig. 1, oxidation curves are illustrated for the Ni–11% Co alloy above its Curie temperature of 490°C and in the temperature range 500°–800°C at 760 mm oxygen pressure. The experimental reproducibility of three test runs at 700°C was within 10 per cent. As illustrated in Fig. 2, the oxidation rate at this temperature was unaltered, within the experimental precision, by oxygen pressures

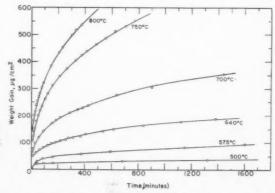


Fig. 1. Oxidation of nickel–11% cobalt alloy specimens in the temperature range $500^{\circ}-800^{\circ}\mathrm{C}$ at $760~\mathrm{mm}$ oxygen pressure.

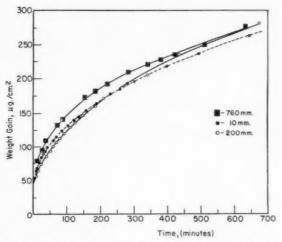


Fig. 2. Oxidation of nickel–11% cobalt alloy specimens at $700^{\circ}\mathrm{C}$ in the oxygen pressure range $10\text{--}760\,\mathrm{mm}.$

ranging from 10 to 760 mm. Oxidation curves for the Ni–25% Co alloy in the temperature range $400^\circ{-}800^\circ\mathrm{C}$ at 200 mm oxygen pressure are illustrated in Fig. 3. For this alloy, the Curie temperature was $635^\circ\mathrm{C}$; thus, six of the ten investigated temperatures are less than the Curie value. Triplicate and duplicate test runs at 700° and $560^\circ\mathrm{C}$ respectively were reproducible within 10 per cent.

DISCUSSION

The oxidation of nickel-cobalt alloys has not been intensively investigated. (8) In this paper, an analysis is carried out to show the effect of the magnetic state of the metal substrate on oxidation rates, by means of time laws with results for nickel oxidation as datum. The equations of parabolic and cubic oxidation applied in this analysis are,

$$x^2 = K_2 t + a(T) \tag{1}$$

$$x^3 = K_3 t + b(T) \tag{2}$$

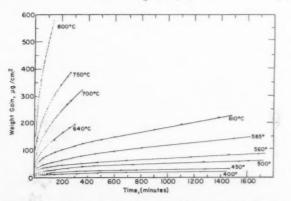


Fig. 3. Oxidation of nickel–25% cobalt alloy specimens in the temperature range $400^\circ{-}800^\circ\mathrm{C}$ at 200 mm oxygen pressure.

where x is the oxide thickness, K_2 and K_3 are the parabolic and cubic rate constants respectively, t is the time, and a(T) and b(T) are constants dependent upon the temperature and oxygen pressure.

Frederick and Cornet(8) have found that nickel and a series of nickel-cobalt alloys oxidized according to a parabolic law in the temperature range 800°-1400°C. Also, the oxidation of nickel in a lower temperature range, 400°-750°C, has been carried out by Gulbransen and Andrew⁽⁷⁾ using a vacuum microbalance technique. The results were interpreted by a parabolic law, although large deviations were found during the initial stages of oxidation and smaller deviations over long time periods. At the low temperature of 400°C, the oxidation of nickel for exposures of 9 hr has been approximated to a cubic law by Engell et al.(9) These investigators have suggested that the cubic relationship transforms to a parabolic law for larger oxide thicknesses at longer times or higher temperatures. In Fig. 4, some results from the investigation of Gulbransen and Andrew are represented by a cubic law. This relationship gives an excellent approximation to the initial oxidation rates.

It is advantageous to compare the oxidation of the alloys with niekel, since parabolic and cubic rate laws give a good first approximation to these results. This is illustrated by parabolic and cubic plots for the

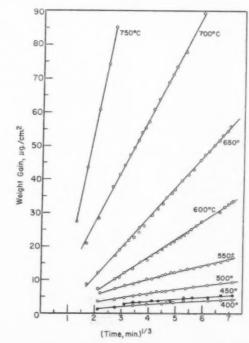


Fig. 4. Cubic time law plot of oxidation data for nickel.

alloys containing 25 and 11% cobalt in Figs. 5 and 6 respectively. Because these laws represent the results for relatively long periods of time, the parabolic and cubic rate constants have been determined at each temperature and plotted to the Arrhenius relation,

$$K = A \exp\left(-E/RT\right) \tag{3}$$

where A is the frequency factor, E is the energy of activation, R is the gas constant, and T is the absolute temperature.

Figs. 7 and 8 show Arrhenius plots of the parabolic and cubic rate constants for nickel and the alloys in the temperature range 400° to 800°C. For nickel, the parabolic constants are those determined by Gulbransen and Andrew⁽⁷⁾ from tangents to the parabolic plots: the values at temperatures greater than 550°C are for exposures of 4-6 hr and at lower temperatures for exposures of 24-30 hr. The cubic constants were determined from the slopes of the linear curves shown in Fig. 4. Since the curves were not linear at the lowest temperature of 400° and 450°C, the constants were determined from tangents to the curves at 4-6 hr of exposure. For the alloy containing 11% cobalt, the parabolic constants were determined from tangents to parabolic plots at the final stages of exposure. The cubic constants were determined from slopes of the linear sections of the curves shown in Fig. 6. The parabolic constants for the alloy containing 25% cobalt were determined from the linear

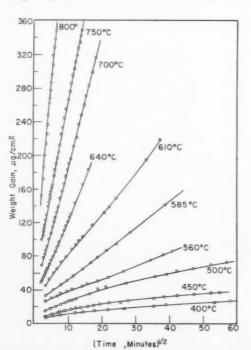


Fig. 5. Parabolic time law plot of oxidation data for nickel- 25% cobalt alloy.

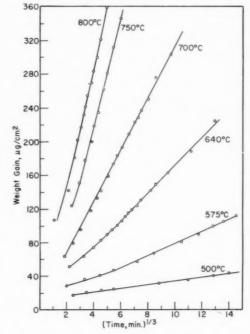


Fig. 6. Cubic time law plot of oxidation data for nickel-11% cobalt alloy.

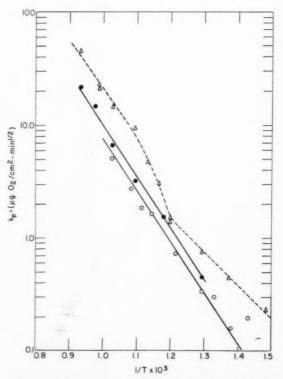


Fig. 7. Arrhenius plots of parabolic rate constants: \bigcirc —nickel-11% cobalt; \triangle —nickel-25% cobalt.

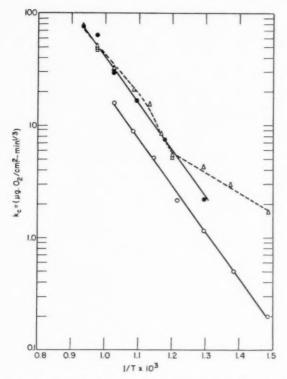


Fig. 8. Arrhenius plots of cubic rate constants: \bigcirc —nickel-11% cobalt; \triangle —nickel-25% cobalt.

1959

sections of the curves illustrated in Fig. 5 at temperatures greater than 500°C and from tangents to the curves at exposures of 24 hr at lower temperatures. To determine the cubic constants, the results were plotted in cubic form and constants evaluated for initial oxidation rates. These curves were linear for the experimental exposures at 400° and 450°C, and the slopes were used for rate constant evaluations. At higher temperatures, the curves were convex to the time co-ordinate. Tangents to these curves, which correspond to initial linear sections, were used to evaluate the constants. For example, the tangent for the highest temperature of 800°C was the line drawn through the initial point of 152 µg/cm2 at 5 min to the fifth determined point of 214 µg/cm² at 13 min.

The Arrhenius plots illustrate an oxidation anomaly in the range of the Curie temperature. The plots are linear for parabolic and cubic oxidation of nickel and the 11% cobalt alloy above their Curie temperatures. On the other hand, the plots for the alloy containing 25% cobalt are distinctly different: linear sections of the curves at low temperatures continuously change in a temperature range commencing approximately 80° below the Curie value of 635°C to other linear sections above this latter temperature. Since

nickel and nickel–cobalt alloys transform from the ferromagnetic to the paramagnetic state over such a temperature range by a co-operative electronic process of the second order, $^{(10)}$ this anomalous oxidation behavior may be associated with the metal substrate. It could be suggested that the carbon impurity may have caused the anomalous behavior of the 25% cobalt alloy. However, this behavior is probably associated with the magnetic properties of nickel and cobalt, because nickel and two alloys containing carbon impurity have been oxidized in the same temperature range and only the alloy which undergoes a magnetic transformation exhibits anomalous behavior.

The variation in the temperature coefficients of the rate constants may be shown to be associated with the electronic property of the metal substrate. The most rapid transformation from cubic to parabolic oxidation for the alloy of largest cobalt concentration is consistent with a proposal of Frederick and Cornet⁽⁸⁾ that substitutional solution of trivalent cobalt ions in the oxide at temperatures less than 900°C increases the concentration of nickel vacancies. If, as it is generally assumed, electrical space charge has a negligible effect on oxidation rates represented by a parabolic law, the variation in the Arrhenius temperature coefficient in the temperature range of the magnetic transformation may be caused by the activities of the metal components. This second order electronic co-operative process may alter the partial molar free energies of the metal components at the metal/oxide interface and, therefore, the gradient of metal vacancies in the oxide, to the extent that the logarithms of the parabolic oxidation constants do not vary exponentially with the reciprocal of the absolute temperature. This behavior may be represented by the following reaction mechanism:

$$\begin{split} \operatorname{Ni}_{(\text{alloy solid solution})} + \operatorname{Ni} \stackrel{+}{\square}_{(i)} + 2 \oplus_{(i)} &\rightleftharpoons \operatorname{Null} \quad (4) \\ 2\operatorname{Co}_{(\text{alloy solid solution})} + 2 \oplus_{(i)} &\rightleftharpoons 2\operatorname{Co}(\operatorname{Ni})_{(\text{oxide lattice})} \\ &+ \operatorname{Ni} \stackrel{+}{\square}_{(i)} + 3\operatorname{NiO} \quad (5) \end{split}$$

where the concentrations of nickel vacancies and positive holes in the oxide at the metal/oxide interface are denoted by the subscripts (i). These reactions show that the concentration of nickel vacancies at this interface is dependent upon the activities of the metal components in the alloy.

The range of cubic oxidation is probably caused by the effect of a surface electrical field in the oxide. With the assumption that electrons migrate more readily than metal ions through the oxide to form a dipole layer, Cabrera and Mott⁽¹¹⁾ and Grimley⁽¹²⁾ have derived an expression for metal-deficit oxides which may be approximated to a cubic law. Hauffe and Ilschner⁽¹³⁾ have derived, in a somewhat similar manner, a cubic law for the condition of a diffuse charge density. Because the metal substrate influences parabolic oxidation of the alloys, it appears reasonable to assume that a mechanism of cation vacancy migration under the influence of an electrical field determines the cubic oxidation rates.

According to the theory of Cabrera and Mott, and Grimley for cubic oxidation, electrons escape from the metal into electron levels of adsorbed oxygen. These levels are filled to the Fermi level of the metal and the rate determining reaction step is the migration of metal vacancies under the direct influence of the electrostatic field across the dipole layer. For nickel, vacancies are formed at the oxide/oxygen interface by reaction of nickel from oxide lattice positions with absorbed oxygen ions. This mechanism may be represented by the following reactions:

$$2e_{\text{(metal)}} + 0_{\text{(ads)}} \rightleftharpoons 0_{\text{(ads)}}^{=} \tag{6}$$

$$O_{(ads)}^{=} \rightleftharpoons NiO + Ni \square$$
 (7)

where 2e represents two electrons transferred from the metal through the oxide to adsorbed oxygen. If the concentration of oxygen ions is related to the electrostatic potential by the Poisson relation, it may be shown that the cubic rate constant is

$$K_3 = (3D_oV^2\chi kT\Omega/8\pi e^2)\exp\left[-(\Delta F^\circ + W)/kT\right] \eqno(8)$$

In this expression, D_o is the frequency factor of the diffusivity of vacancies, ΔF° is the standard free energy of reaction (7), W is the potential barrier between diffusion states in the oxide, V is the electrostatic potential across the dipole layer, χ is the dielectric constant, Ω is the volume of oxide per metal ion, k is Boltzmann's constant, T is the absolute temperature and e is the electronic charge.

If the electrostatic potential and the free energy of activation are largely independent of temperature, the expression for the cubic oxidation constant is to a first approximation of Arrhenius form. The plots of log K_3 vs. 1/T for nickel and the alloys above Curie temperatures illustrate typical linear curves. However, the plot for the alloy containing 25% cobalt has shown that the energy of activation and the frequency factor transform in a temperature range below its Curie value. Consequently, the electrostatic potential and the standard free energy for formation of cation vacancies cannot be regarded as

independent of temperature if the electronic properties of the alloy are altered by the magnetic transformation. A quantitative analysis cannot be attempted, to verify this conclusion, because there is insufficient information on metallic and oxidation properties of the nickel–cobalt system. In spite of this limitation, qualitative information may be advanced to support the essential correctness of this belief.

Cardwell(14) has shown that the values of the electron work function for nickel are 5.05 and 5.2 eV for the ferromagnetic and paramagnetic states respectively. This alteration will decrease correspondingly the electrostatic potential of the surface dipole layer, because the electronic levels of adsorbed oxygen are filled to the Fermi level of the metal (equation 6). Therefore, the frequency factor of the cubic oxidation constant, which is dependent upon this potential, will be smaller above the Curie temperature. The finding that the cubic oxidation rate is largely independent of oxygen pressure in the range 10-760 mm, Fig. 2, indicates that a steady state surface concentration of oxygen ions has been attained. According to the proposed oxidation mechanism (equations 6 and 7), the steady state concentration of cation vacancies at the oxide/oxygen interface is dependent upon the free energy change for chemisorption because of its dependence upon the concentration of oxygen ions. A continuous but anomalous temperature dependence of this free energy term in the magnetic second order transformation range, due to an alteration of the Fermi level in the metal, will influence the standard free energy of vacancy formation, ΔF° , at the oxide/oxygen interface. Consequently, metal substrate electronic properties may cause a larger activation energy of cubic oxidation above Curie temperatures. The smaller extrapolated intercept and larger slope of the Arrhenius plot for cubic oxidation of the 25% cobalt alloy, above the Curie temperature, tend to substantiate these considerations.

19

The results for the initial oxidation rates of nickel^(7,9) may be represented equally well in comparison to the cubic equation by a logarithmic law. If the results are plotted as weight gain of oxygen vs. log. time, the curves are convex to the time co-ordinate. It has been demonstrated^(15,16) that such curves may be transformed to linear curves by a unique value of the parameter t_o at each temperature in the logarithmic equation,

$$x = k \ln \left(1 + t/t_{\rm o}\right) \tag{9}$$

Despite this limitation of data presentation, the cubic equation has been applied for film thicknesses

analyzed in this investigation because $\log{-\log}$ plots of the equation

$$x^n = kt \tag{10}$$

show that values of n approximate to values of 3 and 2 for cubic and parabolic over different regions of film thickness. Also, the cubic law has served as a limiting formulation to describe vacancy diffusion under the direct influence of an electrical field in a p-type oxide. (12)

This investigation has illustrated that a second order magnetic transformation causes a variation but not a discontinuity in the temperature coefficient of oxidation constants. Generalization of this phenomenon to other metals does not follow, since previous investigations have shown oxidation discontinuities at both first order phase changes and second order magnetic transformations in the ranges of Curie temperatures.(2) It has been proposed in this paper that a variation in the electronic properties of a metal in the magnetic transformation range influences the rate-determining reaction step of metal ion migration through the surface oxide layer. However, direct experimental verification for this conclusion is lacking. The oxidation rates, after the transition from a cubic to a parabolic law, are probably not influenced by electrical space charge, because Gulbransen and Andrew⁽⁷⁾ have found good agreement between experiment and predictions of transition state theory for the parabolic oxidation of nickel. The interpretation of cubic oxidation based upon the assumption of a surface electrical dipole layer is a valid assumption, because Grimley⁽¹²⁾ has shown that the distance of electrical space charge in nickel oxide at the metal/oxide interface is 640 Å at 1200°C and to the order of 1 cm at room temperature.

VOL.

1959

Significance is not attached to evaluations of frequency factors and activation energies from the Arrhenius plots of this investigation as an aid to the interpretation of the reaction mechanism, because tangents to the different time law plots have been used for evaluations of rate constants and because theories of the electronic factor differ. Uhlig and Brasunas⁽⁴⁾ and Uhlig⁽²⁾ have assumed that electron escape from the metal to oxide may determine the rates of logarithmic and cubic oxidation. The characteristics of logarithmic oxidation of nickel and iron-chromium alloys have been advanced as confirmation of this theory. The activation energy for nickel oxidation was 0.05 eV greater than the value below the Curie temperature, which is attributed to the difference of 0.15 eV in the electron work

function for the paramagnetic and ferromagnetic states. For iron-chromium alloys of different compositions, a much larger difference of 0.9 eV was found in the magnitudes of the activation energies above and below Curie temperatures. Here, the theory cannot be tested as values are not available for electron work functions. The two different concepts of either the rate of ion diffusion through the oxide under the influence of a surface electrical field, or electron emission from the metal determining the growth rates of oxide films, cannot be presently distinguished from available experimental results.

SUMMARY

Reactions of nickel-cobalt alloys containing 10.5 and 25.1% cobalt with oxygen have been studied over the temperature range 400°-800°C. The oxidation rates of nickel were increased by cobalt additions. For the investigated film thicknesses, the oxidation rates approximated initially to a cubic law and to a parabolic law at longer times. The Arrhenius temperature coefficients of the cubic and parabolic constants for nickel and the alloys were linear above the Curie temperatures. An anomalous oxidation characteristic was illustrated by the 25.1% cobalt alloy; namely, the temperature coefficients of the oxidation constants changed continuously in a temperature range extending approximately 80°C below and to the Curie temperature. It has been proposed that these variations are associated with the magnetic transformation from the ferromagnetic to paramagnetic state, and that electronic properties of the metal substrate influence the rate determining reaction step of metal ion diffusion through vacancies in the surface oxide laver.

ACKNOWLEDGMENTS

The author wishes to express his thanks to Mrs. Mary W. Thomas and Mr. J. M. Gazica for technical assistance, and to Dr. M. Simnad, General Dynamics Corporation, San Diego, California, for discussions which led to initiation of the presented investigation.

REFERENCES

- 1. B. Lustman, Trans. Electrochem. Soc. 81, 359 (1942).
- 2. H. H. Uhlig, Acta Met. 4, 541 (1956).
- G. TAMMANN and G. SIEBEL, Z. anorg. Chem. 148, 297 (1925).
- H. H. Uhlig and A. S. Brasunas, J. Electrochem. Soc. 97, 448 (1950).
- 5. H. H. Uhlig and J. J. Pickett, unpublished data, reference 2.
- L. SEIGNEURIN and H. FORESTIER, C. R. Acad. Sci., Paris 243, 2052 (1956).
- E. A. Gulbransen and K. F. Andrew, J. Electrochem. Soc. 101, 128 (1954).

- S. F. FREDERICK and I. CORNET, J. Electrochem. Soc. 102, 285 (1955).
 H. J. ENGELL, K. HAUFFE and B. ILSCHNER, Z. Elektrochem. 58, 478 (1954).
 C. ZWIKKER, Physical Properties of Solid Materials. p. 170. Interscience Publishers, New York (1954).
 N. CABBERA and N. F. MOTT, Rept. Progr. Phys. 12, 163 (1949).
 W. W. SMELTZER and M. T. SIMNAD, Acta Met. 5, 328 (1957).
- 163 (1949).

- A. CARDWELL, Phys. Rev. 76, 125 (1949).
 P. T. LANDSBERG, J. Chem. Phys. 23, 1079 (1955).
 W. W. SMELTZER and M. T. SIMNAD, Acta Met. 5, 328 (1957).

VO:

ON THE EXCESS ENERGY OF ELECTROLYTICALLY DEPOSITED SILVER*

WERNER F. SCHOTTKY† and MICHAEL B. BEVERT

Silver was deposited from cyanide solution. The excess of its energy over that of annealed silver was measured by tin solution calorimetry. This quantity was related to the mechanism of crystal growth. The stored energy of cold work in silver was also measured.

L'ENERGIE D'EXCES DE L'ARGENT DEPOSE ELECTROLYTIQUEMENT

Les auteurs ont procédé au dépôt électrolytique d'argent au départ d'une solution de cyanure. L'excès de son énergie par rapport à celle de l'argent recuit, a été mesuré par calorimétrie en solution d'étain. Cette quantité est en rapport avec le mécanisme de croissance des cristaux.

Les auteurs ont également mesuré l'énergie accumulée dans l'argent par déformation à froid.

ÜBER DIE ÜBERSCHÜSSIGE ENERGIE VON ELEKTROLYTISCH ABGESCHIEDENEM SILBER

Aus einer Cyanidlösung wurde Silber abgeschieden. Der Überschuss seiner Energie über die von ausgeglühtem Silber wurde kalorimetrisch mit Hilfe der Lösungswärme in flüssigem Zinn gemessen. Diese Grösse wurde mit dem Mechanismus des Kristallwachstums in Verbindung gebracht. Die bei Kaltverformung in Silber gespeicherte Energie wurde ebenfalls gemessen.

Experiments and theoretical considerations point to the important role which imperfections play in the mechanism of crystal growth. Since excess energy is associated with such imperfections, grown crystals can be expected to have a higher energy content than annealed crystals.

1959

Various experiments have provided evidence for the presence of crystal imperfections in electrolytically deposited silver. Kohlschütter and Torricelli (3) showed that the shape of a single crystal grown from silver nitrate solution becomes less well defined during electrodeposition until the growth of the single crystal ceases in favor of the formation of new crystals. This indicates that nucleation of new crystals has become energetically preferred. (4) Raub (5) found that the hardness of silver deposited from evanide solutions was higher than that of annealed silver. He attributed this difference to the existence of a strained condition, which makes the electrodeposited metal comparable to cold-worked metal. In this he followed a suggestion made by Tammann and Jaacks. (6) Wyllie (7) demonstrated that electrodeposition of silver generated internal stresses in the deposit. Kaischew et al. (8) observed screw dislocations in surfaces of electroplated single crystals of silver.

In the investigation reported here the amount of excess energy of electrodeposited silver was measured. For comparison the energy of cold work stored by silver was also measured. These energy measurements were carried out by tin solution calorimetry.⁽⁹⁾ Resistance measurements were made on specimens of electrodeposited and annealed silver.

1. EXPERIMENTAL PROCEDURES

(1) Crystal growth

Aqueous solutions containing 0.4 mole of silver cyanide and 1.2–1.6 mole of potassium cyanide per liter were used as electrolyte. Two plates of pure silver served as anodes. The cathode was a sheet of silver, which had been annealed in vacuum. It was 3×10^{-3} cm thick and its area was 10×6 cm².

Silver was deposited on both sides of the cathode until an average thickness of about 3×10^{-2} cm was reached. The temperature of the solution was usually 25°C. A current of about 0.3 A was used corresponding to a current density of $5\times 10^{-3}\,\mathrm{A/cm^2}$. The polarization of the cathode was measured by a Luggin capillary.

The concentration of potassium cyanide was varied within the limits stated above. In some experiments 2 mg/l. of carbon disulfide was added to the solution. The current density was varied within small limits.

(2) Annealing treatments

The electrodeposited silver was cleaned and cut into chips of about 0.2×0.05 cm². After mixing, half of the chips were placed in a "Vycor" tube having a

‡ Professor of Metallurgy, Massachusetts Institute of Technology, Cambridge, Massachusetts.

^{*}This investigation was supported by the U.S. Atomic Energy Commission under Contract No. At(30-1)-1002. Received October 15, 1957; revised version June 3, 1958.

[†] Staff member, Division of Sponsored Research, Massachusetts Institute of Technology, Cambridge, Massachusetts. Present address: Fritz-Haber-Institut der Max-Planck-Gesellschaft, Berlin, Germany.

volume of 5–10 cm³, which was evacuated and heated for several hours at 550°C. After this treatment the vacuum was checked by a spark tester in every run; no appreciable change in its quality was found. Also, no condensate was detected. These observations indicated that the silver sample had not released significant amounts of foreign substances during annealing. It may be concluded that the differences in the heat effects caused by the addition of electrodeposited and annealed samples to the calorimeter are substantially due to differences in their structure rather than their composition.

(3) Calorimetric measurements

Electrodeposited and annealed samples were added to liquid tin and the associated heat effect was measured. (9) In order to increase the accuracy of the measurements the method of thermal compensation (10) was used. This method takes advantage of the fact that gold dissolves in liquid tin with the evolution, and silver with the absorption, of heat. The heat effect of additions containing twice as much gold as silver is small, if the additions are made from 0°C to the tin bath at 240°C. Differences in the heat effects accompanying the addition of electrodeposited and annealed samples of silver could thus be measured with increased accuracy. These differences, after the effects of changing concentration in the tin solution are taken into account, represent the excess energy due to electrolytic deposition.

From each plated sheet eight to ten additions of 1 g could be prepared. Half of them were annealed. In order to reduce possible self-annealing effects, usually no more than 18 hr were allowed to elapse between the termination of electrodeposition and the beginning of the calorimetric determinations.

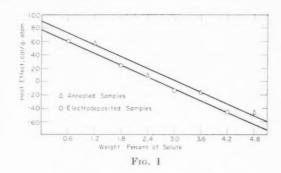
In general, successive additions to the calorimeter consisted of deposited and annealed samples. The time required for dissolution at 240°C was about 2 min, but depended slightly on the size of the chips of silver. The calorimeter was calibrated at the end of each run by additions of tin.

Fig. 1 illustrates a calorimetric run by presenting a plot of the heat effect of electrodeposited and annealed additions vs. concentration.

The final value of the excess energy was found by adding 10 per cent of the measured value in order to correct for the presence of the annealed base plate.

(4) Experiments with cold-worked silver

Silver wire of 99.9% purity was annealed and cold worked by drawing through several dies. The total reduction of the cross-section was 87 per cent, corresponding to a true strain of 2.05.



The energy of cold work stored by the wire was measured by tin solution calorimetry as described in Section 3. Wire annealed in vacuum served as standard.

(5) Resistance measurements

The resistance of specimens prepared from electrodeposited silver was measured by means of a Kelvin bridge. Two potential and two current leads of silver were welded to the specimen. After measurements on silver in the deposited state, the specimen with the leads attached was annealed in vacuum. Another set of resistance measurements was then made.

2. EXPERIMENTAL RESULTS

19

(1) Electrodeposited silver

Eighteen experiments of the type shown in Fig. 1 were performed with electrodeposited silver. They yielded an average value of the excess energy of 12 ± 5 cal/g atom of the deposited metal. The uncertainty in this value is mainly due to the limitations of the calorimetric method as applied to this particular problem.

The electrodeposited samples probably contained a small amount of energy which was introduced when the sheet was cut into strips. This was included in the measured excess energy since the standards were annealed after cutting. In estimating the importance of this effect the energy stored in silver wire deformed by drawing is of interest. As reported in the next section, wire deformed rather severely to a true strain of 2.05 stored less energy than the electrodeposit. Since the cutting operation affected only a narrow region near the cut face, its effect on the measured excess energy of the electrodeposited samples may be considered negligible.

Changes in the current density during c: ; stal growth within the limits of 4 to 6×10^{-3} A/cm² did not change the measured value of the excess energy appreciably. Similarly, the variations in the concentrations of cyanide and the addition of carbon disulfide mentioned in Part 1 did not change the measured

excess energy. In interpreting these findings the lack of sensitivity of the method should be kept in mind.

The measured values of the polarization of the cathode ranged from 0.2 to 0.4 V. The variations within this range depended in part on the amount of free cyanide in the electrolyte. Experiments in which the effects of concentration polarization were reduced by stirring produced a drop by one third of the polarization.

The electrical resistance of the electrodeposited specimens decreased about 1 per cent upon annealing. However, the sensitivity of the measuring method was low, and these results should be considered only as exploratory.

(2) Cold-worked silver

VOL.

1959

Five measurements of the energy of cold work stored by silver during wire drawing were made. They yielded a value of 10 ± 4 cal/g-atom. This is not inconsistent with values of the stored energy for gold—silver wires drawn to the same strain, (11) if an extrapolation for composition to pure silver is made. (10)

3. DISCUSSION

The excess energy of electrolytically deposited silver and the energy stored by cold-worked silver measured in this investigation are of the same order of magnitude. This is consistent with other known similarities of electrodeposited and cold-worked metals. (5,6,7) It should not be concluded, however, that the detailed characteristics of the two states are identical. The discussion which follows will be concerned with problems involved in the electrolytic deposition of silver.

Silver deposited from a cyanide bath is known to have a small grain size. In the growth process, after individual crystals have reached a critical size, they cease to grow and new nuclei form. These in turn grow to a certain critical size. The repeated sequence of growth and nucleation is a general phenomenon. It is clearly illustrated for electrolytic growth by the experiments with single crystals of silver by Kohlschütter and Torricelli. (3)

According to the Gibbs-Thomson equation the local chemical potential at the surface of a small crystal acting as a nucleus is greater than that of the underlying larger crystal. Thus, the formation of a nucleus on the surface of a large growing crystal seems to be impossible, if the local chemical potential is exclusively a function of crystal size. Therefore, if nuclei form on the surface of larger crystals, the local chemical potential must be determined, not only by crystal size, but also by other factors, such as the local density of imperfections.

For the special case of dislocations it may be assumed that they have the same probability of formation on each new crystal layer that is deposited. Also existing dislocations persist during further growth of the crystal. Accordingly, the density of dislocations in the direction of growth is proportional to the distance from the base. In view of this increase in the density of imperfections with the size of a growing crystal, the local chemical potential increases correspondingly and finally may reach a value sufficiently high for the formation of a new nucleus.

An excess chemical potential of a growing crystal is in accord with an observation reported by Kohlschütter and Torricelli. (3) They deposited small silver crystals cathodically from a silver nitrate solution and observed that when the current was interrupted a portion of the deposited silver redissolved, apparently by local cell action. This indicates a slightly less noble electrode potential of the deposit which, however, may be due in part to concentration polarization.

As the model implies, a polycrystalline deposit must have a certain excess energy referred to an equilibrated metal, which is approximated by a well annealed specimen.

The excess energy measured by tin solution calorimetry is due not only to the presence of the imperfections mentioned but also to the interfacial energy associated with grain and subgrain boundaries present in the electrode in excess of those in annealed specimens. Thus

average imperfection energy

= measured excess energy

- interfacial energy (1)

or

average imperfection energy

< measured excess energy (2)

If the local density of imperfections is proportional to the distance from the base of each growing crystal, the average density is equal to half the maximum value attained when the crystal ceases to grow. The same relation holds for the associated energies. Consequently, the maximum local imperfection energy per gram-atom is twice the average imperfection energy per gram-atom. In accordance with equation (2)

maximum local imperfection energy per gram-atom < 2 imes measured excess

energy per gram-atom (3)

If the value of the excess energy measured in this investigation is used, it follows that

maximum local imperfection energy $< 24 \, \mathrm{cal/g\text{-}atom}$

(4)

The maximum local imperfection energy may be assumed to be of the same order of magnitude as the corresponding excess of the chemical potential. This is equivalent to a contribution of 1 mV or less to the polarization. This value is much lower than values found to be necessary for nucleation of silver on other metals, such as gold or platinum, which range between 20 and 28 mV corresponding to a supersaturation of 2.3 to 3.2 in the surface concentration of adsorbed atoms according to Erdey-Gruz and Volmer. (12) These authors also mention that for nucleation on a substrate of the same composition a lower excess of the chemical potential is sufficient. This is in accord with the low value of the imperfection energy. To supplement available qualitative observations, measurements on the magnitude of polarization required for the nucleation of silver on silver are desirable so that the consequences of the model proposed here for the repeated sequence of nucleation and growth of electrodeposits may be pursued.

ACKNOWLEDGMENTS

The authors are greatly indebted to Professor C. Wagner for discussions which led to this investigation and for further contributions. Mr. Benjamin Howell gave valuable assistance in the experimental work. Mr. Barton Roessler carried out the resistance measurements.

REFERENCES

- 1. W. K. Burton, N. Cabrera and F. C. Frank, Nature, Lond. 163, 398 (1949).
- L. J. Griffin, Phil. Mag. (7) 41, 196 (1950). V. Kohlschütter and A. Torricelli, Z. Elektrochem. 38, 213 (1932).
- 4. C. Wagner, unpublished memorandum.
- E. Raub, Z. Metallk. 38, 87 (1947).
- 6. G. Tammann and H. Jaacks, Z. anorg. Chem. 227, 249 (1936).
- M. R. J. WYLLIE, J. Chem. Phys. 16, 52 (1948).
- 8. R. Kaischew, E. Budewski and J. Malinowski, Z. Phys. Chem. 204, 348 (1955)
- 9. L. B. TICKNOR and M. B. BEVER, Trans. Amer. Inst. Min. (Metall.) Engrs. 194, 941 (1952).
- 10. P. GREENFIELD and M. B. BEVER, Acta Met. 5, 125 (1957).
- 11. A. L. TITCHENER and M. B. BEVER, Trans. Amer. Inst.
- Min. (Metall.) Engrs. (in press).
 12. T. Erdey-Gruz and M. Volmer, Z. Phys. Chem. A157, 182 (1931).

DOUBLE BRAGG SCATTERING IN COLD-WORKED METALS*

M. B. WEBB† and W. W. BEEMAN+

The small-angle X-ray scattering from cold-worked metals is examined in terms of a double Bragg scattering mechanism. The intensity and angular distribution of the scattering expected from this mechanism are calculated and found to be in accord with experiment. It is shown that this mechanism should give a strongly polarized scattered flux at small angles and that the strong electric vector should be radial in the detecting plane. The polarization of the scattered flux was measured and found in agreement with these predictions.

It is concluded that the double Bragg process and not density fluctuation scattering is responsible for most of the observed small-angle scattering.

DOUBLE DIFFRACTION DE BRAGG DANS LES METAUX DEFORMES A FROID

La diffraction des rayons X sous faible angle des métaux déformés à froid est examinée en fonction d'un mécanisme de double diffraction de Bragg. Les auteurs calculent l'intensité et la distribution angulaire de la diffraction résultant de ce mécanisme et ils les trouvent en accord avec l'expérience.

Ils montrent que ce mécanisme pourrait donner un flux diffracté très polarisé aux faibles angles et que le vecteur électrique interne devrait être radial dans le plan de détection. La polarisation du flux diffracté a été mesurée. Elle est en accord avec ces hypothèses.

Les auteurs concluent que c'est la double diffraction de Bragg et non la variation de densité de la diffraction qui est responsable de la plupart des diffractions à faible angle observées.

DIE DOPPELTE BRAGG-STREUUNG IN KALTVERFORMTEN METALLEN

Die Kleinwinkelstreuung von Röntgenstrahlen in kaltverformten Metallen wird untersucht, indem ein Mechanismus von doppelter Bragg-Reflexion zugrunde gelegt wird. Die nach diesem Mechanismus zu erwartende Intensität und Winkelverteilung der Streuung werden berechnet; man findet, dass sie mit dem Experiment übereinstimmen. Weiterhin wird gezeigt, dass dieser Mechanismus eine starke Polarisation der um kleine Winkel gestreuten Strahlung ergeben sollte, und dass die starke Komponente des elektrischen Vektors in der Beobachtungsebene radial liegen sollte. Die Polarisation der gestreuten Strahlung wurde gemessen, sie stimmt mit diesen Voraussagen überein.

Es ergibt sich der Schluss, dass die doppelte Bragg-Reflexion und nicht die Streuung an Dichteschwankungen für den Hauptanteil der beobachteten Kleinwinkelstreuung verantwortlich ist.

INTRODUCTION

1959

Guinier⁽¹⁾ first observed that thin, cold-worked Cu foils, used in transmission, scatter far more X-ray intensity at small angles than annealed foils. This scattering has since been investigated by several authors.^(2,3,4) Foils, both stretched and rolled, of Cu, Ni, Al and Zn have been used. The scattering is qualitatively the same in all cases.

Various interpretations of this scattering have been suggested. Blin and Guinier, (2) Dexter, (5) and Beeman and Neynaber (6) have considered the scattering from a collection of cavities or voids formed by the condensation of vacancies produced during the deformation. Dexter, (5) Blin, (7) and Seeger (8) have considered the

small-angle X-ray scattering that would arise from the density variations around dislocations.

An alternative scattering mechanism has been proposed and investigated by Neynaber $et\ al.^{(3)}$ and Webb and Beeman. They have pointed out that a ray may leave the sample making a small angle with the transmitted beam if it has been successively Bragg reflected from equivalent sets of planes by two slightly misoriented grains or sub-grains. The mechanism is simply illustrated in Fig. 1. A ray of the incident beam, a, strikes a grain of the polycrystalline sample, s, and may be Bragg reflected anywhere into the cone I. A once reflected ray b, for example, may pass through another grain and be reflected a second time anywhere into the cone II. A possible doubly reflected ray making a small angle with the transmitted beam is labelled c.

Elementary considerations lead to the following conclusions. A ray, such as c, which is scattered in an almost horizontal plane must result from two

† General Electric Research Laboratory, Schenectady, New York

^{*} This research was supported in part by the UNITED STATES AIR FORCE, under Contract No. AF 18(600)-698 monitored by the Office of Scientific Research, Air Research and Development Command. Received June 2, 1958.

[†] University of Wisconsin, Madison, Wisconsin.

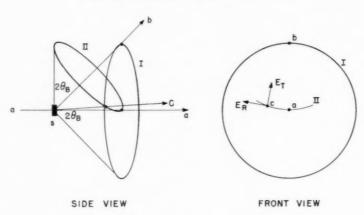


Fig. 1. Double Bragg scattering process. a, incident beam; I cone containing once-reflected rays; b, a particular once-reflected ray; II cone containing twice-reflected rays arising from b; c, twice-scattered ray; s, sample; E_R and E_T , radial and tangential components of the electric vector of ray c.

Bragg reflections in an almost vertical plane. If c makes a small angle ϕ with the forward beam, it has been reflected from two grains the normals to whose reflecting planes make a small angle α where

$$\phi = (2\sin\theta_B)\alpha = (n\lambda/d)\alpha \tag{1}$$

Finally, if the grains and sub-grains of the sample are randomly oriented, the number of doubly reflected rays per unit solid angle (at small angles) is proportional to ϕ^{-1} .

It was proposed^(3,4) that the observed small-angle scattering from cold-worked metals is the unresolved sum of a large number of double scatterings from pairs of sub-grains. These are very probable in a cold-worked material because of the large number of sub-grains and because the sub-grains from an original annealed grain are misoriented only by small angles. Neynaber et al.⁽³⁾ point out that the reversible temperature dependence of the scattering, and the immediate appearance of the scattering following cold work at liquid-air temperatures, are easily understood in terms of the double scattering mechanism.

The present paper will show that the observed scattered intensity and angular distribution are reasonable and will report measurements of the polarization of the small-angle scattering which cannot be explained except by double Bragg scattering.

TOTAL SCATTERED FLUX

The scattering geometry consists of four vertical slits, each 6 mm high and a few tenths of a millimeter wide placed in an evacuated chamber. The first two slits are 10 cm apart and define the incident beam. The sample foil is placed 5 cm beyond the second slit. The third and fourth slits are also 10 cm apart. They

are on an arm which can rotate about a vertical axis through the sample position. The third slit is 5 cm beyond the sample.

The X-ray source is a rotating iron anode tube run at 80 mA, and 30 kV. With slits 0.4 mm wide, about $10^9 \, \mathrm{Fe} K \alpha$ photons strike the sample per second. Backgrounds are less than one count per second. A characteristic absorber of iron is placed between the third and fourth slits to remove the K fluorescence of the copper or nickel sample, and a proportional counter with pulse height discrimination serves as detector.

VO

19

We now proceed to estimate the total double scattered flux passing through the detection plane using the following model of the cold-worked sample. The sample is assumed to be composed of randomly oriented grains of average linear dimension g. Each grain consists of sub-grains, of average linear dimension l, whose crystallographic normals are clustered in a small solid angle, ω . Each sub-grain reflects X-rays as a perfect crystal. We assign an angular width, δ , and a reflectivity, r, to the single crystal diffraction pattern of the sub-grains, but only the integrated reflecting power, $R = r\delta$, occurs in the final formula. Several different sets of reflecting planes may contribute to the scattering. For $FeK\alpha$ radiation on Ni the possible reflections are (200), (111), (222), (220) and (311). The total multiplicity associated with these planes, counting oppositely directed normals separately, is b = 58. The total double scattered flux is not a function of the divergence and area of the incident beam as long as a good statistical sample of double reflections is excited. We therefore assume, for convenience, that all the incident photons are parallel to the slit axis and illuminate the sample

uniformly over a small area, A. The thickness of the foil is t.

We now write for the total double scattered flux through the detection plane

$$F = F_0 P_1 n_1 P_2 n_2 f_1 f_2 \tag{2}$$

In this equation P_1 is the probability that a sub-grain, illuminated by the incident beam, is so oriented as to give a Bragg reflection and is equal to $(b\delta \cos \theta_B)/2$. The number of sub-grains illuminated is $n_1 = At/l^3$. P_2 is the probability that a sub-grain, lying in a once reflected beam, is so oriented as to give a second Bragg reflection, and is equal to $\delta/\sqrt{\omega}$. Since ω is small the same set of Bragg planes (but of different sub-grains) must be used in the first and second reflections. P_2 cannot be greater than unity and $P_2 = \delta/\sqrt{\omega}$ is correct only if $\delta \ll \sqrt{\omega}$. If $\delta \gg \sqrt{\omega}$ the original grains become the reflecting units in the double scattering process and the sub-grains enter only as they influence $r\delta$ (for the original grain) via the mosaic structure. Isolated double reflection peaks from the large grains of annealed samples have indeed been observed. (3) The number of sub-grains illuminated by a once reflected beam is $n_2 = g/2l$. Since g > t we have used the value of t rather than g in the numerical evaluation. It is assumed that the only probable double reflection processes are those involving sub-grains of the same original grain. f_1 , the fraction of the incident flux reflected by a sub-grain (so oriented as to reflect), is equal to rl^2/A and $f_2 = r$ is the fraction of the once reflected flux which is second reflected. F_{α} is the incident flux.

Substituting into equation (2) gives

$$F = F_o \left(\frac{b\delta}{2} \frac{\cos \theta_B}{2} \right) \left(\frac{At}{l^3} \right) \left(\frac{\delta}{\sqrt{\omega}} \right) \left(\frac{g}{2l} \right) \left(\frac{rl^2}{A} \right) (r) \quad (3)$$

Simplifying

$$F = F_o \frac{b(r\delta)^2 tg \cos \theta_B}{4l^2 \sqrt{\omega}} \tag{4}$$

In Table I we give the parameters used in evaluating equation (4).

We finally obtain for the total flux through the detecting plane

$$F = 1.5 \times 10^5 \text{ ets/sec} \tag{5}$$

The total number of double reflections excited is $N = P_1 n_1 P_2 n_2$. It is not separately needed in our comparison with experiment and is difficult to estimate since it involves explicitly the shape and divergence of the incident beam and the angular width of the sub-grain diffraction pattern. However, is is desirable to know that it is large. For the sample of Table 1 and the slit geometry used, N is between 10^6 and 10^7 .

We defer the experimental results until after a discussion of the shape of the small-angle scattering curve.

THE DISTRIBUTION OF SUB-GRAIN TILT ANGLES

We remark in the introduction that an assembly of randomly oriented sub-grains gives a doubly scattered flux density which, at small angles, varies as the reciprocal of the scattering angle. A more detailed treatment of the angular dependence of the scattering must be based on equation (1). Assume that a part of the incident beam has been once reflected, by a representative sub-grain, from a set of planes with spacing d(hkl). In order that a second sub-grain again reflect this beam, and that the final beam emerge at a small angle ϕ with the forward direction. two conditions must be satisfied. The normal to the hkl planes of the second sub-grain must make an angle $90^{\circ} - \theta_{R}$ (to within the accuracy δ) with the first reflected beam and the normal must also make an angle a with the normal of the first reflecting sub-grain. ϕ , α and d(hkl) are related by equation (1). In Fig. 2 we illustrate the process; b is the first reflected beam and n_1 is the normal of the first reflecting sub-grain. The number of sub-grains giving a second reflection at an angle ϕ is proportional to $P(\alpha) d\alpha$, the number of sub-grains per unit solid angle (of the distribution of normals) which are tilted by an angle between α and $\alpha + d\alpha$ with respect to the first reflecting sub-grain. Averaging over all first reflecting sub-grains it is seen that

$$P(\alpha) = K\phi F(\phi) \tag{6}$$

In this equation K is a function of the parameters of Table 1 but not of ϕ nor of α , and $\phi F(\phi)$ is the

TABLE 1

$\cos \theta_B$	Average cosine of Bragg angle	0.5
1	Average dimension of sub-grains	10^{-4} cm
co co	Solid angle of misorientation of sub-grains	2.5×10^{-3} steradians
b	Total multiplicity of reflecting planes	58
g	Average dimension of original grains	$2.5 imes 10^{-3} ext{ cm}$
$r\delta = R$	Integrated reflecting power of sub-grains	10-4
t	Thickness of sample	10^{-3} cm
F_o	Incident flux (with 0.4 mm × 6.0 mm slits)	10° cts/sec

VOL. 7 1959

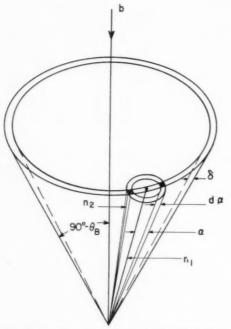


Fig. 2. Conditions on the normal n_2 of a subgrain which may reflect the once-reflected ray, b, so that it emerges at an angle $\phi = (n\lambda/d)\alpha$ with the transmitted beam. n_1 , is the normal of the first reflecting sub-grain and δ is the width of a sub-grain diffraction curve.

double scattered flux making an angle ϕ with the forward direction. The quantity directly observed in the experiments is $F(\phi)$, the double scattered flux, per unit solid angle, at the angle ϕ . K is also a function of d(hkl). The quantity $n\lambda/d(hkl)$ in equation (1) is of order unity and varies by a factor of less

than two for the several Bragg reflections which are excited by $FeK\alpha$ radiation on nickel. Thus the curves of $\phi F(\phi)$, which we give in Fig. 3, are qualitatively similar to $P(\alpha)$ but are somewhat smeared out because of the different Bragg reflections which contribute to the double scattered flux.

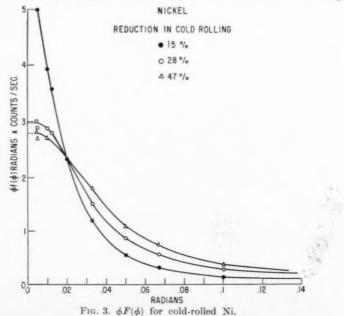
COMPARISON WITH EXPERIMENT

The curves of Fig. 3 are taken from experiments of Brammer. (9) Several slit widths were used in obtaining the data over the angular range $15' \leqslant \phi \leqslant 6^{\circ}$. Curves were matched in overlapping angles and the data reduced to the counting rates observed with slits $6 \text{ mm} \times 0.4 \text{ mm}$.

The total scattered flux through the observation plane for our spectrometer is given experimentally by

$$F = \frac{(1.5a)^2 2\pi}{hd} \int_0^\infty \phi F(\phi) \, d\phi \tag{7}$$

In this equation a is the slit separation of 10 cm, the slit height h=6.0 mm and the slit width d=0.4 mm. The integration has been performed graphically from Fig. 3 assuming that it falls off at ϕ^{-3} at large angles. The extrapolations at large and very small angles make a total contribution of less than 20 per cent to the integral. The integrated observed flux, determined in this way, is 7×10^3 cts/sec, to within about 20 per cent for each of the three reductions in rolling. To compare with the calculations, this flux must be divided by the transmission of the sample itself and of the fluorescence absorber. These together transmit ten or twelve per cent of the beam.



Thus neglecting absorption in both cases we calculate a total double scattered flux of 1.5×10^5 cts/sec and observe 6.5×10^4 cts/sec. This agreement is well within the combined uncertainties of the measurement and the calculation. It establishes the point that a double scattering mechanism may be expected to give fluxes of the order of those observed. The fact that the scattered flux is nearly independent of the deformation for rolling reductions between 15 and 50 per cent is probably due to the fact that in this region the sub-grain size, l, and the misorientation $\sqrt{\omega}$ are both changing slowly and in opposite directions.

As mentioned above, plots of $\phi F(\phi)$ vs. ϕ are qualitatively similar to the distribution of tilt angles between sub-grain normals within a single deformed grain. Such plots, Fig. 3, have half widths of one or two degrees and show observable intensity to 10° or more. They are broader for the greater reductions in rolling. Both observations are in agreement with the microbeam experiments of Gay et al.⁽¹⁰⁾

POLARIZATION OF THE SCATTERED FLUX

1959

A much more direct proof of double reflection is obtained from observation of the polarization of the scattered flux. We have mentioned that a double scattered ray emerging at a small angle, and in nearly the horizontal plane, has been twice Bragg reflected through large angles in nearly the vertical plane. It should, therefore, be strongly polarized. We define a polarization ratio as the square of the radial component of the electric vector divided by the square of the tangential component. (Radial and tangential refer to the directions in the detecting plane with the transmitted beam as center as illustrated in Fig. 1.) This ratio should be $\cos^{-4} 2\theta_B$ for a doubly scattered ray where θ_B is the Bragg angle. For the possible $FeK\alpha$ reflections from Ni the ratio lies between 1.8 and 40. Calculation of the appropriate average over the various possible Bragg reflections predicts a polarization ratio of 6.7. The stronger component of the electric vector is radial in the detection plane.

A single scattering process, such as scattering by cavities or density fluctuations near dislocations, can provide only a very small polarization at small angles, only about a 1 per cent deviation of the polarization ratio from unity at our angles of observation. In addition the slightly stronger electric vector is tangential in the detection plane.

The polarization of the flux scattered by coldworked Ni was measured by again reflecting the scattered beam, first in the horizontal and then in the vertical plane using an auxiliary crystal. The

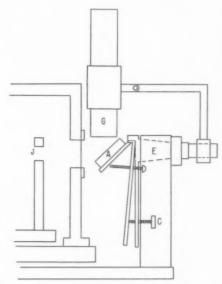


Fig. 4. Auxiliary crystal mount. A, rock salt crystal; C, fine adjustment screw; E, cone bearing coaxial with 3rd and 4th slits; G, geiger counter; J, 4th slit of spectrometer.

apparatus is shown in Fig. 4. Radiation which has been scattered through about 1° in nearly the horizontal plane is selected by the third and fourth vertical slits. J represents the last slit in the symmetrical four slit spectrometer. This radiation is reflected by a rock salt crystal, A, into a Geiger counter, G. Rock salt gives a strong (400) Fe $K\alpha$ reflection at 87° and is thus an efficient analyzer for polarization. The crystal is rocked, by means of the screw, C, through the whole angular range within which it reflects rays of the scattered beam. We shall call a plot of reflected flux vs. angular position of the auxiliary crystal the vertical rocking curve. Since the crystal reflection is through nearly 90°, the area under this curve is a measure of the total flux through the slit which has its electric vector in the horizontal plane. The crystal mount and the Geiger tube are then rotated through 90° around the cone bearing E, and a horizontal rocking curve is determined. The axis of the bearing E is coincident with the scattered beam defined by the slits J. The ratio of the areas under the vertical and horizontal rocking curves is then the observed polarization ratio. A pair of such rocking curves are shown in Fig. 5. The width of the rocking curves are different because the vertical and horizontal divergences of the scattered beam are different.

Variations in reflectivity across the face of the auxiliary crystal could lead to a systematic error since a different region of the crystal surface is illuminated in the two positions. To eliminate this error, before and after each sample rocking curve, a



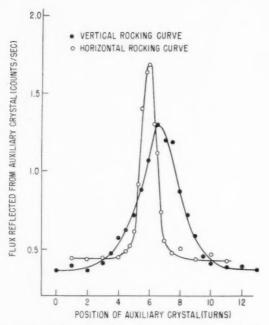


Fig. 5. Horizontal and vertical rocking curve for a Ni foil rolled 6%. The rolling direction was vertical and the scattering angle was 1°30′.

similar curve was taken with a reference carbon black scatterer in the sample position. The observed polarization of the Ni scattering was multiplied by the reciprocal of the apparent polarization of the carbon black scattering. This correction to the polarization was less than 10 per cent.

The error in the polarization ratio from the counting statistics was approximately 3.5 per cent. For each of five rolled Ni samples, the polarization was measured twice and the average relative difference between the two measurements was 4.5 per cent.

As a check on the experimental method, the polarization of the (111) reflection of $FeK\alpha$ radiation from Ni was measured, yielding the correct value within experimental error. As a further check the scattering from carbon paper, which is expected to be unpolarized and which gives approximately the same (weak) scattered intensity as cold-worked metals, was measured. This scattering was unpolarized within experimental error showing that there was no spurious background, different in the two positions of the auxiliary crystal, which may have been too small to detect in the rocking curves from the intensely scattering carbon black.

The use of relatively high slits was necessary for intensity considerations. Owing to their finite height, the analysing slits of the spectrometer accept rays which have been scattered in other than the horizontal plane. This has the effect of reducing the observed

polarization. From an approximate analysis of this effect for the geometry of these experiments, the expected polarization ratio of flux scattered by the double reflection mechanism in Ni is 3.40 instead of the perfect collimation value of 6.75.

The result of many experiments is that the flux scattered by cold-worked Ni at small angles is polarized with the strong electric vector radial in the detecting plane and that the polarization ratio, for small deformations in cold work, is about that calculated. The measured polarization ratio is a function of the amount of deformation, being greater for small deformations. Table 2 gives representative

Table 2				
No.	Per cent deformation	Polarization ratio of Ni scattering at 1°30′		
1	6	2.11		
2a	6	1.82		
2b	6	1.73		
3a	6.25	3.02		
3b	6.25	3.15		
4	15	1.97		
5a	35	1.60		
5b	35	1.70		
6	48	0.948		
7	50	1.12		

data. 2a and b and 5a and b refer to two independent measurements on the same samples. 3a and b are measurements on two pieces of the same sample cut in half after rolling. The agreement between two determinations on the same sample is considerably better than for different samples having had supposedly identical treatments. To determine the polarization ratio as a function of deformation, it was measured during a sequence of cold working on the same sample. The data for two such sequences are plotted in Fig. 6 as curves A and B. For all the data cited above the rolling direction was vertical in the spectrometer. Curve C of Fig. 6 gives the results for the same sequences as curve B but with the rolling direction horizontal, and shows that the polarization is radial in the detecting plane.

The result that the small-angle scattering is polarized leads, without reference to the details of the scattering mechanism, to the general result that the scattered beam has been multiply scattered through large angles. Only large-angle processes lead to appreciable polarization, and then only multiple processes will bring the beam back to small angles.* Since the Bragg reflections are the only

^{*} One minor exception is the case where a strong anisotropic large-angle process leaves the transmitted beam polarized. This is certainly not the case in these experiments since all processes remove only a small fraction of the incident beam and since the Debye-Scherrer rings are nearly uniform.

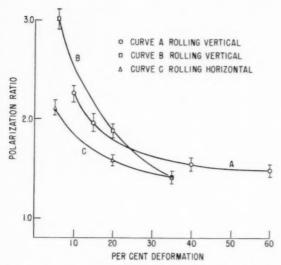


Fig. 6. Polarization ratio for Ni samples as a function of deformation through rolling sequences. Curves B and C are for the same sample with the direction of rolling horizontal and vertical, respectively.

important large-angle processes, we conclude that the double reflection mechanism makes an important contribution to the small-angle scattering from coldworked metals.

1959

The interchange of energy between a Bragg reflection and the forward beam within a single coherent domain (a sub-grain) gives a multiply scattered flux in the forward direction. Physical broadening in such a case could perhaps give scattered intensity in the angular range observed. Such a process is, however. inconsistent with the polarization results. Flux so derived from a single sub-grain would be polarized: however, when summed over all reflecting sub-grains, the resulting polarization would be small. Any residual polarization, due to non-random sub-grain orientations and strains, would be in the same direction throughout the detecting plane, and not radial as observed.

Only at the smallest deformations is the polarization ratio near that predicted. The loss of measured

polarization may be caused by the physical broadening of the Bragg reflections. Such a broadening would reduce the polarization in the same way as the finite slit height, for flux from a broadened double reflection which is centered in nearly the vertical plane, and is vertically polarized, will be accepted by the slit. This effect will be important when the physical broadening is the same order as the scattering angle, which is reasonable for the large deformations. The measurement of polarization as a function of scattering angle would help verify this explanation. but such experiments were precluded by intensity considerations.

Further evidence against a major contribution to the observed flux from single scattering processes at either large or small deformations has recently been presented by Atkinson and Lowde. (11) They found that cold neutrons of too long a wavelength to be Bragg reflected were not appreciably scattered by cold-worked copper. Still more recently Atkinson⁽¹²⁾ has measured photographically the small-angle X-ray scattering from copper and aluminum. Using samples with strong preferred orientation, he of course, found large deviations from circular symmetry in both the Debye-Scherrer rings and the small-angle scattering pattern. The latter could be deduced, in detail, from the former on the basis of the double scattering mechanism.

REFERENCES

- A. GUINIER, C. R. Acad. Sci., Paris 208, 894 (1939).
- 2. J. Blin and A. Guinier, C. R. Acad. Sci., Paris 233, 1288 (1951)
- 3. R. H. NEYNABER, W. G. BRAMMER and W. W. BEEMAN, Phys. Rev. 99, 615 (1955) A.
- 4. M. B. Webb and W. W. Beeman, Bull. Amer. Phys. Soc. 1, 138 (1956).
- L. Dexter, Phys. Rev. 90, 1007 (1953).
- 6. W. W. BEEMAN and R. H. NEYNABER, Phys. Rev. 95, 617 (1954) A.
- 7. J. Blin, Ph.D. Thesis, University of Paris (1954).
- A. SEEGER, Acta Met. 5, 24 (1957).
 W. G. BRAMMER, Ph.D. Thesis, University of Wisconsin
- 10. P. GAY, P. B. HIRSCH and A. KELLEY, Acta Met. 1, 315 (1953).
- 11. H. H. ATKINSON and R. D. LOWDE, Phil. Mag. 2, 589
- 12. H. H. Atkinson, Phil. Mag. (1958) (In press).

THE CAUSE OF THE STRENGTHENING IN QUENCHED BETA BRASS*

N. BROWN†

Quenched CuZn is strengthened by vacancies which are generated by the rapid disorder-to-order transformation. The quenching temperature which produces maximum strength is a function of quenching rate. The strength immediately after quenching depends on the number of trapped imperfections, where the number is proportional to the amount of ordering during the quench minus the amount of decay during the quench. The vacancies probably originate from the strong interaction between dislocations in the presence of long range order. Density change, effect of cooling rate, activation energy for decay, electrical resistivity and Clarebrough's work on internal friction support the idea that the strength of quenched beta brass is associated with vacancies rather than anti-phase domains.

LA CAUSE DU DURCISSEMENT DANS LE LAITON β TREMPE

Le laiton β trempé est rendu plus résistant par les lacunes qui sont créées lors de la transformation rapide ordre-désordre. La température de trempe qui produit le maximum de résistance est une fonction de la vitesse de trempe. La résistance directement après trempe dépend du nombre d'imperfections piégées. Ce nombre est proportionnel au degré d'ordre atteint au cours de la trempe diminué de l'effet de trempe.

Les lacunes ont comme origine probable la forte interaction entre les dislocations en présence d'ordre à grande distance.

La variation de densité, l'effet de la vitesse de refroidissement, l'énergie d'activation du processus, la résistivité électsique ainsi que le travail de Clarebrough sur la friction interne sont en accord avec l'idée que la résistance du laiton β trempé est associée aux lacunes plutôt qu'aux domaines antiphases.

DIE URSACHE DES FESTIGKEITSANSTIEGS VON ABGESCHRECKTEM BETA-MESSING

Die Festigkeit von abgeschrecktem CuZn wird durch Leerstellen erhöht, die bei der raschen Ordnungsumwandlung erzeugt werden. Die Abschrecktemperatur, die zu der höchsten Festigkeit führt, ist eine Funktion der Abschreckgeschwindigkeit. Die unmittelbar nach dem Abschrecken erreichte Festigkeit hängt von der Zahl der festgehaltenen Fehlstellen ab, diese Zahl ist proportional dem Betrag der Ordnungseinstellung während des Abschreckens minus dem während des Abschreckens ausgeheilten Betrag. Die Leerstellen entstehen wahrscheinlich durch die starke Wechselwirkung zwischen Versetzungen im ferngeordneten Zustand. Die Dichteänderung, der Einfluss der Abkühlgeschwindigkeit, die Aktivierungsenergie des Ausheilens, der elektrische Widerstand und die Befunde von Clarebrough über die innere Reibung unterstützen die Annahme, dass die Festigkeit von abgeschrecktem Beta-Messing mit Leerstellen und nicht mit Antiphasen-Domänen verknüpft ist.

1. INTRODUCTION

The effects of quenching beta brass have been studied by many investigators. Smith⁽¹⁾ studied the effect of quenching on electrical resistivity and hardness, and concluded that beta brass always has essentially complete long range order after quenching and that the effects of quenching are associated with the size of anti-phase domains. Chipman and Warren⁽²⁾ measured the superlattice lines of quenched and slowly cooled beta brass, and concluded that the quenched state had the same amount of long range order as the equilibrium state. Thus, it is generally concluded that beta brass orders so rapidly that even

a water quench cannot freeze-in an appreciable amount of disorder. Green and Brown⁽³⁾ further investigated the effect of quenching beta brass (Fig. 1) and also studied the kinetics of the decay process which occurs after quenching (Fig. 2). The result of Green and Brown (Fig. 1) has since received two different interpretations both of which are believed to be wrong in the light of the present investigation. Ardley(4) suggested that Fig. 1 represents strength as a function of various amounts long range order. In other words, Ardley stated that the quenched state has the degree of long range order which corresponds to its quenching temperature. However, Smith, (1) and Chipman and Warren (2) have shown that water quenching does not freeze-in an appreciable amount of disorder; therefore, Ardley's interpretation is wrong.

19

^{*} This work was supported by the Office of Ordnance Research, United States Army, and the Atomic Energy Commission. Received April 14, 1958.

[†] School of Metallurgical Engineering, University of Pennsylvania, Philadelphia, Pennsylvania.

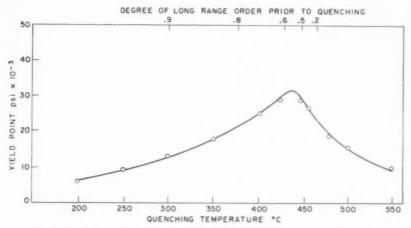


Fig. 1. Yield point immediately after quenching vs. quenching temperature.

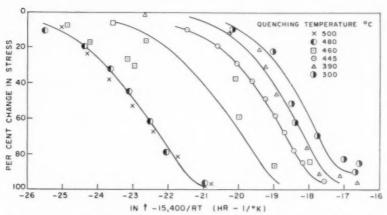


Fig. 2. Decay of the strength after quenching as a function of time and annealing temperature. Each curve corresponds to a different quenching temperature.

Cottrell⁽⁵⁾ interpreted Fig. 1 differently in that he attributed the maximum to an effect of the size of anti-phase domains. According to Cottrell the strengthening by anti-phase domains is given by

$$\tau = \frac{\gamma}{l} \left(1 - \frac{\alpha b}{l} \right)$$

where γ is energy of the anti-phase domain boundary, l is the size of the anti-phase domains, α is a factor depending on the shape of the anti-phase domains and b is the interatomic distance. The Cottrell theory predicts that the function of strength vs. anti-phase domain size passes through a maximum at a domain size of about 10 atomic distances; therefore, the maximum strength in Fig. 1 was associated with this critical domain size. If Cottrell's theory were correct, then a specimen quenched from above T_c should show a maximum in strength during the decay process. However, the softening curves (Fig. 2) continuously decrease with time. This behavior is in

contrast to $\mathrm{Cu_3Au}$ whose strength goes through a maximum during the annealing of a specimen quenched from above T_c . Additional data will be given which shows that the Cottrell theory does not fit beta brass.

More recently Clarebrough $^{(6)}$ detected an internal friction peak in quenched CuZn. The kinetics of the decay in the internal friction peak were identical with the kinetics of decay in strength as determined by Green and Brown. Clarebrough associated the quenching effect with an excess of vacancies, but he did not explain why a quenching temperature below T_c produces the maximum effect. The present investigation suports Clarebrough's view that quenching beta brass produces an excess of vacancies beyond the usual type of vacancy production. It turns out that Fig. 1 is a general type curve for beta brass in that the ordinate could be yield point, internal friction, density electrical resistivity or concentration of vacancies.

VOL. 7 1959

2. EXPERIMENTAL DATA

a. Density measurements

The CuZn contained 51.4 wt.% Cu. Grain size was 1-2 mm and the sample was from the same heat of metal as used in the prior investigation. (3) Metallographic examinations showed the alloy to be single phase at all temperatures. Density measurements were made by the displacement method⁽⁷⁾ which detects changes in density of +0.0002 g/cm³. These measurements were carried out on 3/8 in. diameter specimens water quenched from different temperatures, and were repeated on the same specimens after a low temperature anneal for a time which completed the decay. The change in density during decay was plotted against quenching temperature (Fig. 3). A maximum occurs at about 450° and the curve has the same general shape as that in Fig. 1. Thus, the strengthening is associated with a density change. This change cannot be attributed to residual strains which

are expected to behave monotonically with quenching temperature. If the density change were associated with the disappearance of anti-phase domains, then it is expected that the change would vary inversely with the size of those domains.

b. Effect of quenching rate

The rate of decay as measured isothermally (Fig. 2) suggested that an appreciable amount of decay could occur during the water quenching of the 3/8 in. specimens on which Fig. 1 is based. In order to minimize the amount of decay which might occur during the quench, the quenching rate was increased by using 0.03 in. thick specimens. With the thin specimen the maximum strength is produced by quenching from the critical temperature. Specimens were quenched at slower cooling rates. Slower cooling not only reduces the maximum strength attainable, but also shifts the quenching temperature which produces the maximum (Fig. 4).

19

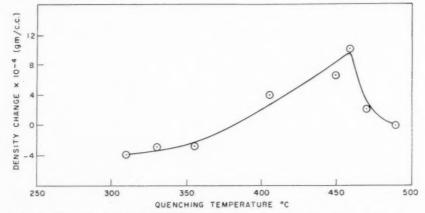


Fig. 3. Change in density after complete decay as a function of quenching temperature.

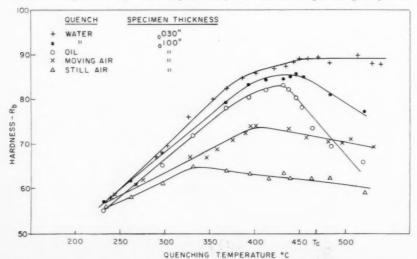


Fig. 4. Effect of quenching rate on the yield point immediately after quenching.

The shift in the maximum with cooling rate is inconsistent with Cottrell's view that the maximum strength is associated with a critical domain size of about 10 atomic distances. Such an interpretation of Fig. 4 leads to the conclusion that water quenching from above 450°C and cooling in still air from about 340°C both produce this same critical domain size. This conclusion is not consistent with the way in which anti-phase domains grow.

c. Electrical resistivity

The electrical resistivity of quenched beta brass was measured as a function of quenching temperature. The resistivity curves have the same form as those for strength vs. quenching temperature. Since resistivity varies monatomically with anti-phase domain size, (4) the maxima in Fig. 4 cannot be attributed to the critical size of anti-phase domain demanded by the Cottrell theory.

3. ANALYSIS

The data in Fig. 4 indicate that strength is not simply a function of temperature prior to quenching. but that something significant is taking place during the quench. Quenching strains and ordinary vacancy production are eliminated as primary factors, since quenching strains continuously increase quenching temperature and the ordinary vacancy concentration varies exponentially with temperature. The strength could only be related to the ordering that is known to take place during the quench. It must be concluded that the greater the amount of ordering that occurs during the quench, the greater is the resultant increase in strength. (Top curve in Fig. 4). However, some of the generated strength may decay during the quench.

After quenching to room temperature all specimens have essentially complete long range order. (1,2) Therefore, the less a specimen is ordered prior to quenching, the stronger it is after quenching provided no decay occurs during the quenching. However, the rate of decay as described by Fig. 2 and the cooling rate, as determined by quenching medium and size of specimen, will affect the amount of decay that occurs during this treatment. Although specimens quenched from the critical temperature and above generate the highest strength, this strength may not be the maximum because decay is large. A specimen quenched from an intermediate temperature will generate less strength in comparison, but will retain maximum strength because it decays more slowly. Specimens quenched from lower temperatures increase in strength even less and the retained strength is lower even though their rate of decay is very slow.

It is now possible to reproduce Fig. 1 by a calculation based on the following assumptions:

- (1) Strength is proportional to the amount of ordering during quench.
- (2) At all temperature the strength decays in accordance with the data in Fig. 2.

The following differential equation describes the change in strength during the quench:

$$dN = \frac{\partial N}{\partial S} \cdot dS + \frac{\partial N}{\partial t} \cdot dt \tag{1}$$

where N is strength, S is degree of long range order, and t is the time. $\partial N/\partial S$ is constant, and is that part of the equation associated with strengthening. $\partial N/\partial t$ is the rate of decay. The empirical equation⁽³⁾ (Fig. 2) describing the rate of decay is given by

$$d(\ln N)/dt = -5300 \exp{[5.6(1-S_o) - 15,400/RT]}$$
 (sec⁻¹) (2)

where S_o is the equilibrium degree of long range order at the quenching temperature T_o , and T is the temperature at any time t.

The relationship between time and temperature is obtained from heat transfer considerations. Assuming Newton's Law of cooling, the following relationship is obtained for water quenching to 300°K.

$$dT/dt = -6K(T - 300)/\rho CD$$
 (3)

where K is the heat transfer coefficient, ρ is density, C is specific heat, and D is both height and diameter of the specimen. Combining equations (1), (2) and (3)

$$dN = dS + \frac{5300 \exp \left[5.6(1 - S_o) - 15400/RT\right]}{\left[6K(T - 300)/\rho CD\right]}$$
(4)

Since the specimen is at equilibrium prior to quenching, the initial conditions are

$$N=0$$
 at $t=0$ and $T=T_o$

The following physical constants were used to solve equation (4)

$$K=0.08$$
 and 0.16 cal cm⁻² sec⁻¹ °C⁻¹

$$C=0.09$$
 cal g $^{-1}$ °C $^{-1}$

$$\rho = 8.3 \text{ g cm}^{-3}$$

$$D = 0.94 \text{ cm}$$

$$T = 738^{\circ}$$
C (critical temperature)

The relationship between S_o and T_o was obtained from X-ray data. A numerical method of solution was used. The results of the calculation are given in Figs. 5 and 6, which show the strength that existed during the quench for different quenching rates. Some curves show a maximum near the critical temperature because order changes very rapidly in

7 1959

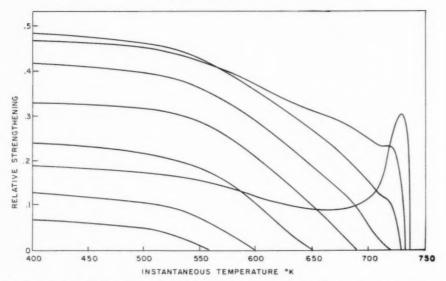


Fig. 5. The strength that existed during the quench as a function of the specimen temperature. The intersection of each curve with the abscissa determines the quenching temperature.

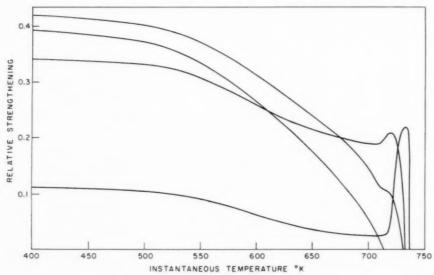


Fig. 6. Same as Fig. 5 for a different quenching rate.

that region. The intersection of the curves with the ordinate gives the strength retained at room temperature. In Fig. 7 the strength retained after quenching is plotted against quenching temperature. The two quenching rates were chosen so as to encompass the uncertainty in the heat transfer coefficient. The curve in Fig. 7 is a calculated version of Fig. 1. The agreement between the calculated and experimental curves is surprisingly good. The assumptions on which the calculation was made appear to be justified in the light of the variety of independent data used to make the calculation.

4. DISCUSSION

19

The analysis and experiments substantiate the argument that rapid ordering, which occurs by quenching, strengthens beta brass. It refutes the viewpoint that the as-quenched strength is only a function of the initial state. The experimental evidence does not indicate that the size of anti-phase domains is the primary cause of strengthening. Vacancies are probably involved because the activation energy for the decay process is 15,400 cal/mole (3,6) compared to about 36,000 cal/mole for self-diffusion in the ordered region, (8) and because there is an

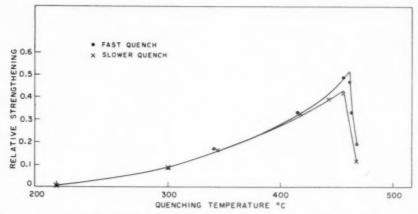


Fig. 7. Calculated strength retained after quenching as a function of quenching temperature. The curves are derived from Figs. 5 and 6 by plotting the intersection with ordinate vs. the intersection with abscissa.

increase in density during the decay process. The internal friction peak observed by Clarebrough was explained by an excess of vacancies. Anti-phase domain boundaries do not seem to be primarily responsible for the strengthening because Cottrell's theory indicates that a critical intermediate domain size has a maximum strength and it is difficult to imagine that this critical size is shifted to lower quenching temperatures by decreasing the quenching rate. The variation in electrical resistivity with quenching temperature is not consistent with antiphase domains.

959

There is a possible mechanism whereby vacanices could be generated by ordering. It is a geometric necessity that anti-phase domain boundaries terminate on a dislocation. (9) Thus, dislocation pairs of like sign are jointed by an anti-phase boundary. As the degree of order increases the dislocations come closer together so as to minimize the energy of disorder in the boundary. The interaction is so strong that at complete order the dislocations should be about fifteen atom distances apart. (9) Thus, ordering would cause dislocation movement which could produce vacancies both by dislocations cutting dislocations and by climb. The dislocations are more

uniformly distributed in the disordered than in the ordered state, and this may explain the variation in rate of decay with initial state of order (Fig. 2) if dislocations act as sinks during the decay process. Thus, the strength generated would be associated with the jogs formed on dislocations which had moved during the ordering process, and the decay process would be the annihilation of jogs by the excess vacancies produced during the rapid ordering.

The author would like to thank John D. Corrie for making the density measurements.

REFERENCES

- 1. C. S. Smith, Trans Amer. Inst. Min. (Metall.) Engrs. 152, 144 (1943).
- D. CHIPMAN and C. WARREN, J. Appl. Phys. 21, 696 (1950). 3. H. Green and N. Brown, Trans. Amer. Inst. Min (Metall.) Engrs. 197, 1240 (1953).
- G. W. Ardley, Acta Met. 3, 525 (1955).
- 5. A. H. Cottrell, Monograph: Relations of Properties to Micro-structure. Amercian Society for Metals, Cleveland (1954)
- L. M. Clarebrough, Acta Met. 5, 413 (1957).
 J. D. Corrie, M.S. Thesis. University of Pennsylvania (1958).
- A. B. KUPET, D. LAZARUS, J. R. MANNING and C. T.
- Tomizuka, Phys. Rev. 104, 1536 (1956). N. Brown and M. Herman, Trans Amer. Inst. Min. (Metall.) Engrs. 206, 1353 (1956).

LETTERS TO THE EDITOR

Comments on "Accommodation strains in martensite formation and the use of a dilatation parameter"(1)*

Christian⁽¹⁾ has applied Eshelby's strain energy calculations to the nucleation problem of a thin oblate spheroid of martensite in order to investigate the dependence of the shear strain energy (per unit volume) E_2 , and the dilatational strain energy, E_1 , on the following quantities:

- a. The uniform dilatation, Δ
- b. The expansion normal to the habit plane, ξ
- c. The homogeneous shear strain, s
- d. The semi-thickness/radius ratio of the embryo, c/r.

The purpose of the present note is to compare the results of the above mentioned analysis with earlier calculations of (E_1+E_2) , and to comment on the nucleation considerations advanced by Christian.⁽¹⁾

The total strain energy⁽¹⁾ is defined as:

$$E_{(S)} = E_1 + E_2 \quad \text{ergs/cm}^3$$
 (1)

where

$$\begin{split} E_1 = & \frac{G}{(1-\mu)} \left[\frac{\pi}{4} \, \xi^2 + \frac{\pi (1+\mu)}{3} \, \xi \Delta \right] \frac{c}{r} \\ & + \frac{2G(1+\mu)}{9(1-\mu)} \, \Delta^2 \; \, \text{ergs/cm}^3 \end{split} \tag{2}$$

and

$$E_2 = \frac{G\pi(2-\mu)}{8(1-\mu)} s^2 \frac{c}{r} \quad \text{ergs/em}^3$$
 (3)

while G is the shear modulus, and μ is Poisson's ratio. The overall energy change attending the formation of a thin oblate spheroidal embryo of martensite, $\Delta W^{\gamma \to \alpha'}$ has been formulated as follows:⁽²⁾

$$\Delta W^{\gamma o lpha'} = 2\pi r^2 \sigma + rac{4}{3}\pi r^2 \left(rac{c}{r}A
ight) + rac{4}{3}\pi r^2 c \Delta f^{\gamma o lpha'}$$
 ergs/embryo (4)

where σ is the interfacial energy in ergs/cm² (which arises from the dislocations present in the austenite-martensite interface), $\Delta f^{\gamma \to \alpha'}$ is the change in chemical free energy per unit volume attending the transformation, and (c/r)A is the strain energy per unit volume. The value of $A \cong 2.09 \times 10^{10}$ ergs/cm³ \sim G/38 has been calculated by Knapp and Dehlinger⁽³⁾ for the (225), habit in iron base alloys.

If equation (4) is now modified to encompass Christian's results then:

$$\Delta W^{\gamma \to \alpha'} = 2\pi r^2 \sigma + \frac{4}{3} \pi r c^2 A' + \frac{4}{3} \pi r^2 c (\Delta f^{\gamma \to \alpha'} + \varepsilon)$$

ergs/embryo (5)

VO

7

19

...ban

$$A' = G \left[\frac{\pi(2-\mu)}{8(1-\mu)} s^2 + \frac{\pi\xi^2}{4(1-\mu)} + \frac{\pi(1+\mu)}{3(1-\mu)} \Delta\xi \right]$$

$$\frac{d\text{vn/cm}^2}{4} (6)$$

and

$$\varepsilon = \frac{2G(1+\mu)}{9(1-\mu)} \Delta^2 \quad \text{dyn/em}^2 \tag{7}$$

Equation (5) is thus seen to be very similar to equation (4) with the following modifications: A has been replaced by A' (which may or may not have the same numerical value as A), and an additional volume free energy term, ε in dyn/cm² or ergs/cm³, has been added. This seems quite logical since Δ is defined as a uniform dilatation which would shift T_0 by changing $\Delta f^{\gamma \to z'}$ in a manner similar to the effect of adding a γ stabilizing element. (2)

On this basis, the relationship between c and r which minimizes the restraining stress, opposing the transformation (for a given volume of embryo) $_{is}^{(2)}$

$$\frac{c^2}{r} = \frac{\sigma}{A'} \,, \tag{8}$$

According to Christian⁽¹⁾ the uniform strain Δ and the normal strain ξ are related to the microscopic dilatation characteristic of the transformation, δV , as follows:

$$\Delta + \xi = \delta V \tag{9}$$

Christian⁽¹⁾ further states that Δ need not have the same sign as δV . For steels $\delta V \sim 0.04$ (the latter value has been adopted⁽⁴⁾ in preference to Christian's value of 0.05) while $s \sim 1/\sqrt{32}$.

In order to derive suitable values for ξ and Δ in the martensite problem in steels, consider the following approach: Let

$$\Delta w^{\gamma \to \alpha'} = \frac{3\Delta W^{\gamma \to \alpha'}}{4\pi r^2 c} \quad \text{ergs/cm}^3$$
 (10)

$$\Delta w = \Delta g + \Delta f \text{ ergs/cm}^3$$
 (11)

(dropping the superscripts for convenience).

where the "back stress" retarding the transformation is given by

$$\Delta g = \frac{3\sigma}{2c} + A' \frac{c}{r} + \varepsilon \quad \text{dyn/em}^2$$
 (12)

The minimum restraining stress can be attained if the c/r ratio is such that equation (8) is obeyed. Hence

$$\Delta g_{\min} = A' \left(\frac{3}{2} + 1\right) \frac{c}{r} + \varepsilon \quad \text{dyn/em}^2$$
 (13)

where the "strain energy" contributes a factor of 1 and the "surface energy" contributes a factor of 3/2 to the first term in equation (13). If $\mu=1/3$, and $\delta V=\Delta+\xi$, then Δg_{\min} can be further minimized with respect to ξ at constant c/r, δV , σ , and s. when

$$\xi = \delta V \frac{\left(\frac{8}{9} - \frac{5\pi c}{3r}\right)}{\left(\frac{8}{9} - \frac{35\pi c}{24r}\right)} \tag{14}$$

since c/r < 1/20 in the nucleation size range⁽²⁾

$$\xi \sim \delta V(0.95) \tag{15}$$

or

VOL.

1959

$$\xi \sim 0.038$$
 and $\Delta \sim 0.002$ (16)

(the results of equation (14) are $\xi \sim 0.039$, $\Delta \sim 0.001$; and $\xi \sim 0.034$, $\Delta \sim 0.006$ for c/r = 1/10 and 1/40 respectively so that the actual value of c/r is not too critical as long as c/r is small.) This minimization procedure also indicates that Δ has the same sign as δV , since $\xi < \delta V$, in contrast to Christian's statement that Δ and δV need not have the same sign.

However, equation (13) has been derived by keeping s and σ fixed, while Christian indicates that there may be an interaction between ξ , s and σ . A more general minimization procedure might eliminate the condition imposed by equation (14) on the sign of Δ in relation to δV . Such a procedure would require prior knowledge of the ξ -s- σ "interactions" which are not presently available.

Taking the values of ξ and Δ estimated in equation (16), A' and ε can be calculated as follows:

$$\varepsilon = \frac{2G(1 + \mu)}{9(1 - \mu)} \Delta^2 \sim 1.4 \times 10^6$$

$$ergs/em^3 \sim 0.3 \quad eal/mole \quad (17)$$

$$A' = \frac{G}{38}(1.17 + 0.07 + 0.001) = \frac{1.24G}{\text{dyn/cm}^2}$$
(18

where $G=8\times 10^{11}\,\mathrm{dyn/cm^2}$ and the molar volume is $\sim 7.2\,\mathrm{cm^3}$. Hence $A'\sim 1.24\,A$, where the biggest

contribution to the difference between A' and A comes from the shear strain component. At present, it is not clear why the Eshelby–Christian and Knapp–Dehlinger calculations yield different results. Part of the discrepancy may be due to the fact that Eshelby's equations refer to a coherent interface, while the austenite–martensite interface is only semi-coherent because of the interface dislocations.†

Equation (16) indicates that the additional volume energy ε is negligibly small when compared with the magnitude of $\Delta f^{\gamma \to \alpha'}$ which is about 1.75×10^9 ergs/cm³ = 300 cal/mole at M_{\odot} .

In order to estimate Christian's E_s , which is equal to $A'(c/r) + \varepsilon$ for embryos within the nucleation range of sizes, we may set $\Delta g_{\min} \simeq -\Delta f$. It has been shown⁽²⁾ that there are in fact two types of critical embryo size, the smaller size corresponding to a minimum r for spontaneous growth (with the aid of thermal fluctuations) while the larger one corresponds to the minimum size for athermal cataclysmic growth. It turns out that the r for which $\Delta w = 0$ lies between these two embryo sizes.

Consequently setting

300 cal/mole =
$$\frac{5}{2}A'\left(\frac{c}{r}\right) + 0.3$$
 cal/mole (19)

and $A'\sim 2.3\times 10^{10}~\rm dyn/cm^2\sim 3950~cal/mole$ (as a compromise between the E–C and K–D values) we find

$$c/r \sim 1/33$$
 (20)

or

$$E_s \sim 120 \text{ cal/mole}$$
 (21)

Thus in the embryo stage 60 per cent of the restraining energy is surface energy and 40 per cent is strain energy. These estimates apply only in the embryonic stage. Once cataclysmic growth begins the martensite plate meets various obstacles which result in departures from the $c^2/r = \sigma/A'$ condition, and hence a cessation of growth due to a rising $\Delta g^{(2)}$ (i.e. an increasing back stress). For a full grown plate E_s has been estimated as ~ 60 cal/mole⁽⁶⁾ and the surface energy as ~ 5 cal/mole.⁽⁶⁾ The value of E_s given by equation 21 is considerably smaller than the value of 290 cal/mole suggested by Christian.⁽¹⁾

LARRY KAUFMAN

Manufacturing Laboratories, Inc. Cambridge, Massachusetts

 $[\]dagger$ In the original calculation of $A^{(3)}$ two different methods were used. The first method yielded $A \sim G/38$ and the second resulted in a value of $A \sim 1.2~G/38$, which is much closer to the result of equation (18). However in subsequent calculations Knapp and Dehlinger used the former value.

References

1. J. W. Christian, Acta Met. 6, 377 (1958).

 L. KAUFMAN and M. COHEN, Progress in Metal Physics Vol. 7. Pergamon Press, London; M. COHEN Trans. Amer. Inst. Min. (Metall.) Engrs. 212, 171 (1958).

H. Knapp and U. Dehlinger, Acta Met. 4, 289 (1956).
 J. R. Patel and M. Cohen, Acta Met. 1, 531 (1953).

5. F. C. Frank, Acta Met. 1, 15 (1953).

 M. COHEN, E. S. MACHLIN and V. J. PARANJPE, Thermodynamics in Metallurgy p. 242. American Society for Metals, Cleveland, Ohio (1950).

* Received July 18, 1958.

Discussion of "Comments on accommodation strains in martensite formation and the use of a dilatation parameter"*

My views on the nucleation of martensite are closely similar to those of Dr. Kaufman, and I am indebted to him for an advance copy of his excellent review article, written in collaboration with Professor Cohen.(1) I should like to add a few brief comments in reply to his interesting note. The purpose of my original letter was to attempt a physical explanation of the dilatation parameter which Bowles and Mackenzie have introduced into their theory of the crystallography of martensite transformations. (2) I agree, of course, that if E_{\circ} (or Δg) is minimised at constant σ and s, Δ and δV have the same sign, and $|\Delta| \leq |\delta V|$; the value of Δ which minimises E_1 in this way is very small, as pointed out in my letter and confirmed by Kaufman. However, we have the interesting result that the empirical Δ values chosen to fit the erystallography may be opposite in sign to δV (as in steels), or larger in absolute magnitude (as in titanium and zirconium). It is not quite correct to state that knowledge of the Δ -s- σ interactions is not available. An equation connecting s and δ (and hence s and Δ) was given in my letter, and as emphasised there, this shows that minimum E_s for steels will correspond to $\Delta < 0$, although δV is positive.

Using Kaufman's notation (which differs in some respects from that in my letter), his equation (5) may be generalised to:

$$\Delta W = 2\pi r^2 \sigma(\Delta) + (4/3)\pi r c^2 A'(\Delta) + (4/3)\pi r^2 c \{\Delta f + \varepsilon(\Delta)\}$$
(1)

Minimising ΔW , or Δg at constant volume of martensite, then requires

$$(\partial \Delta W/\partial c) = (\partial \Delta W/\partial r) = (\partial \Delta W/\partial \Delta) = 0$$

giving:

$$\frac{c^2}{r} = \frac{\sigma(\Delta)}{A'(\Delta)} = -\frac{\left\{3(\partial \sigma/\partial \Delta) + 2c(\partial \varepsilon/\partial \Delta)\right\}}{2(\partial A'/\partial \Delta)}$$
(2)

When the variation of σ and s with Δ is ignored, there

is an optimum value of Δ intermediate between 0 and δV , and a relation

$$c/r = -(\partial \varepsilon/\partial \Delta)/(\partial A'/\partial \Delta)$$

This equation, however, does not reduce to Kaufman's equation (14), since differentiation of his equation (13) introduces an extra factor 2/5 on the right hand side. This difference apparently arises because he first minimises the 'opposing stress' at constant volume, treating A' as constant, and then minimises with respect to Δ at constant c/r. This does not seem logical, and I think the above procedure is the correct way of minimising Δg at constant volume of the martensite embryo.

The crystallographic conditions for a real solution define a range of values of Δ . (3) If both surface and strain energies change monotonously in the same sense across this range, equation (2) has no real solution, and the preferred Δ will be at that limit of the range at which both energies are least. However, if the right hand side of (2) is positive, a minimum value of ΔW may correspond to an intermediate Δ . The crystallographic results for steels suggest that A'decreases and σ increases as Δ becomes increasingly negative. For low carbon steels, the Bowles-Mackenzie theory implies that the variation of A'with Δ is the important factor, and the empirical Δ is close to the smallest permissible value. For alloy and high carbon steels, a value of Δ near to zero is apparently preferred, presumably indicating a greater relative influence of the surface energy term.

19

In principle, a solution to equation (2) can be obtained. The variation of A' with Δ follows from the definition of A', together with the expression for s^2 in my letter and the condition $\Delta + \xi = \delta V$. The variation of σ with Δ depends on the variation of the lattice invariant shear, given by substituting $\delta \eta_i$ for η_i in equation (5) of reference (3), and this could be calculated by Knapp and Dehlinger's method. In practice, the uncertainties are too great for the formidable algebra to be worthwhile. However, I cannot see any advantage in using the values in Kaufman's equation (16), since the neglected variation of s^2 is almost certainly the most important part of $(\partial A'/\partial \Delta)$.

The discrepancy between A and A' does not seem to me to be very serious, but it cannot arise because the interface is only semi-coherent. It is evident from Knapp and Dehlinger's outline description of their calculation⁽⁴⁾ that they use an elastic model closely similar to Eshelby's, and the strain energy depends only on the macroscopic ('shape') deformation. As they give only final numerical values, it is

difficult to compare the results, but they state that their methods, which gave two alternative answers, are approximate. The only assumptions in Eshelby's calculations are that matrix and martensite have identical, isotropic elastic constants, and that $r \gg c$. It is not quite clear that the same value of s is used in estimating A and A', although if Knapp and Dehlinger used Frank's shear of $1/\sqrt{32}$, (5) this is negligibly different from the value $s \approx 0.18$ which I assumed.

I am grateful to Dr. Kaufman for pointing out that E_s cannot be almost equal to the total driving force at M_s if the shape at constant volume is adjusted to minimise the opposing stress. Provided that ε is negligible, his result that 60 per cent of the restraining energy is surface energy depends only on the assumption that the form of the embryo is determined by a minimum of ΔW (Δg at constant volume), and remains true when the more general equation (1) above is taken for ΔW .

Finally, it is interesting to note that Kaufman's equation (8) may also be applicable to mechanical twins, particularly elastic twins in equilibrium with the matrix. Since $\Delta = \xi = 0$, and s is known exactly, it should be possible to calculate A' rather accurately. Measurements of c and r in such twins might thus enable the twin interface energy σ to be estimated; experimental results certainly confirm that c/r is small when s is large.

J. W. CHRISTIAN

Department of Metallurgy The University Museum Parks Road, Oxford

VOL.

1959

References

- L. Kaufman and M. Cohen, Progress in Metal Physics Vol. 7. Pergamon Press, London (1959).
- J. S. Bowles and J. K. Mackenzie, Acta Met. 2, 129, 138, 224 (1954); Ibid. 5, 137 (1957).
- 3. J. W. CHRISTIAN, J. Inst. Met. 84, 394 (1955-6).
- 4. H. KNAPP and U. DEHLINGER, Acta Met. 4, 289 (1956).
- 5. F. C. Frank, Ibid. 1, 15 (1953).
 - * Received August 18, 1958.

On the equilibrium segregation at a grain boundary*

Inman and Tipler have recently reported⁽¹⁾ finding an appreciable excess of phosphorus at the grain boundaries of a dilute iron–phosphorus alloy. In some specimens the excess was equivalent to a layer of pure phosphorus more than 60 Å thick. In discussing their results, the authors rejected the possibility that a phosphorus-rich phase is precipitated at the boundaries and, instead, attribute the excess to an equilibrium segregation.

We find this and similar explanations of data for other systems somewhat disturbing, since, subject to some reasonable assumptions, an equilibrium between the observed degree of segregation and the grain interior would constitute a violation of the second law of thermodynamics. To demonstrate this we will derive an expression giving an upper limit for the allowable excess of a component at the grain boundary.

We start with the well-known Gibbs equation⁽²⁾ for the variation of boundary tension (σ) at constant temperature

$$d\sigma = -\Sigma \Gamma_i \, d\mu_i,\tag{1}$$

in which μ_i is the chemical potential of the *i*th component and Γ_i the excess amount of this component per unit area. The excess quantity Γ is defined† as the difference between the actual amount of the component in the system and that which would have been present in the same volume if the phases were homogeneous right up to an imaginary dividing surface. For a grain boundary between two identical phases, the Γ 's are independent of the position assigned to the dividing surface. This is not true if the two phases differ in composition or density. It is also to be noted that the derivation of (1) is independent of the boundary thickness or of the manner in which the composition or density varies across the boundary.

For a two-component system (1) gives

$$-\frac{d\sigma}{dx} = \Gamma_1 \frac{d\mu_1}{dx} + \Gamma_2 \frac{d\mu_2}{dx} \tag{2}$$

where x is the atomic fraction of component 2 which we will take as the solute. Since the μ 's cannot vary independently, but are related by the Gibbs–Duhem equation

$$x\frac{d\mu_2}{dx}+(1-x)\frac{d\mu_1}{dx}=0$$

we can rewrite (2)

$$-\frac{d\sigma}{dx} = \Gamma_{2(1)} \frac{d\mu_2}{dx} \tag{3} .$$

where $\Gamma_{2(1)}$ is defined by

$$\Gamma_{2(1)} = \left(\Gamma_2 - \frac{x}{1-x}\Gamma_1\right).$$
 (4)

The advantage of (3) over (2) is not in the elimination of $d\mu_1/dx$, but in the fact that $\Gamma_{2(1)}$ can be calculated,

[†] This definition is that used by Gibbs. In Guggenheim's⁽³⁾ treatment two dividing surfaces are introduced, one on each side of the boundary, and the Γ 's are defined as the *total* number of moles per unit area in the material between the two dividing surfaces. Because of the Gibbs-Duhem relation, equation (1) holds true for either definition.

as shown later, from experimental measurements; whereas Γ_1 and Γ_2 cannot be derived individually without knowing the variation of the molar volumes across the boundary.

If
$$\frac{d\sigma}{dx}$$
, $\frac{d\mu_2}{dx}$ and $\Gamma_{2(1)}$ are all known for a particular composition, application of (3) immediately determines whether the observed excess is consistent

mines whether the observed excess is consistent with an equilibrium segregation. Up to the present time, a complete set of such measurements is not available for any metallic system. We can however estimate the maximum value that $\Gamma_{2(1)}$ can attain.

We first note that if there is an excess of component 2 at the boundary, $\Gamma_{2(1)}$ is positive and σ decreases with increasing x. However, the total decrease in σ between x=0 and the solubility limit $x=x_e$ obviously cannot exceed σ_1 , the boundary tension in pure component 1. Equation (3) thus yields the condition

$$0 < \sigma\left(x_{\epsilon}\right) = \sigma_{1} - \int_{0}^{x_{\epsilon}} \Gamma_{2(1)} \left(\frac{d\mu_{2}}{dx}\right) dx. \tag{5}$$

If we restrict ourselves to the case where $x_e \ll 1$, Henry's law can be applied to the solute (x) to give

$$\frac{d\mu_2}{dx} = \frac{kT}{x} \tag{6}$$

Before we can perform the integration of (5) an assumption has to be made about the variation of $\Gamma_{2(1)}$ with composition. Let us denote the measured value of $\Gamma_{2(1)}$ at an atomic fraction x_0 by $\Gamma^0_{2(1)}$. We will suppose that

$$\Gamma_{2(1)} \geqslant \frac{x_1}{x_0} \Gamma_{2(1)}^0 \text{ for } 0 \leqslant x \leqslant x_0$$
 (7)

and

$$\Gamma_{2(1)} \geqslant {\Gamma^0}_{2(1)} \quad \text{for} \quad x_0 \leqslant x \leqslant x_e \,. \tag{8}$$

From (3) and (6) it is evident that (7) is equivalent to

the condition $d\sigma/dx\geqslant -\frac{kT}{x_0}\left.\Gamma^0_{~2(1)}\right.$ for the range 0 to

 x_e . In other words, we are assuming that in the terminal solution σ will decrease with increasing x with an ever decreasing rate. So far as we know, this is observed to be true in practice. For the range x_0 to x_e we are merely assuming in (8) that the adsorption of component 2 at the boundary does not decrease with increasing x. This again appears to be, if anything, a conservative assumption. Substituting (6), (7) and (8) in (5) and performing the integration, we obtain

$$\Gamma^{0}_{2(1)}kT[1 + \ln(x_e/x_0)] < \sigma_1$$
 (9a)

O

$$\Gamma_{2(1)}^0 < \sigma_1/kT[1 + \ln(x_e/x_0)].$$
 (9b)

To relate this expression to the experimentally measured quantities, let us denote by N_1 and N_2 the number of atoms of the two components removed from an area A of boundary. If sufficient thickness has been removed from the boundary so that the remaining material is of the bulk composition, then by definition

$$A\Gamma_2 = N_2 - x_0 \alpha, \tag{10}$$

and

$$A\Gamma_{1} = N_{1} - (1 - x_{0})\alpha, \tag{11}$$

where α is the total number of atoms which would have been removed if the interior composition and density had remained constant up to the imaginary dividing surface. If (10) and (11) are substituted in (4) α is eliminated leaving

$$\Gamma^{0}_{\ 2(1)} = \frac{1}{A} \left(N_{2} - \frac{x_{0}}{(1 - x_{0})} N_{1} \right). \tag{12}$$

Since the right-hand side of (12) vanishes at the composition (x_0) of the grain interior, its value is independent of the depth of material removed for analysis providing the depth exceeds the boundary thickness.

Table 1. Calculation of \(\Gamma^0 P(Fe)\) from data of Inman and Tipler (1)

1, 5,000								
Specimens	Grain boundary area, A(cm²)	$N_{ m P}(imes 10^{-16})$ (b)	$N_{ m Fe}(imes 10^{-16})$ (b)	$\Gamma^0_{ m P(Fe)} = rac{N_{ m P}}{A} - rac{x_{ m P}}{1 - x_{ m P}} rac{N_{ m Fe}}{A} \ (imes 10^{-16}) \ ({ m for} \ x_{ m P} = 0 \cdot 002)$	Equilibration temperature (°K)	Minimum value for $\sigma_{\rm Fe}$ (erg cm ⁻²		
4P8(A+B)	0.48	0.58	178	0.46	1423.	3,000		
4P5(C+D)	0.67	2.716	794.3	1.69	1423.	10,900		
4P4(A+B)	0.67	5.379	786.7	5.68	973	25,200		

(a) From authors' table 5.

(b) The figures in this column are the sum of the number of P or Fe atoms for each pair of fracture surfaces, denoted A and B, or C and D in the authors' tables 3 and 4.

(c) From authors' table 2.

(d) Calculated from our inequality (9a) using $x_0 = 0.02$.

The inequality (9) does not, of course, apply when the excess is present in a second phase at the boundary, providing the alloy is saturated with respect to a bulk quantity of this phase. The latter qualification is required to exclude the case in which a phase, because of a low interfacial energy, is stable at the grain boundary but not elsewhere. Such a phase is thermodynamically indistinguishable from a segregate and the maximum excess of a component that it can contain is likewise limited by (9).

Let us now consider the application of (9) to the data of Inman and Tipler for a 0.17 atomic per cent phosphorus-iron alloy. Substituting as reasonable values: $x_0 = 0.002$, $x_e = 0.02$, T = 1000°K and $\sigma_{\rm Fe} = 850 \ {\rm erg \ cm^{-2}}$ (σ for ferrite is not known; 850 erg cm-2 is the measured(4) grain-boundary tension of austenite) in (9b), we find $\Gamma^0_{P(Fe)} < 0.19 \times 10^{16}$ atoms cm⁻², which is roughly equivalent to a layer of pure phosphorus 3 Å thick at the boundary. This limit is by a factor of 2 to 25 smaller than the excess observed (Table 1) in three specimens which we selected as representing approximately the minimum, average and maximum amount of excess phosphorus in the specimens analysed by the investigators. Alternatively, (9a) can be used to calculate the minimum values of σ_{Fe} that would be required if the excess phosphorus was due to an equilibrium segregation. As will be seen from the final column of the table, these minimum values greatly exceed any reasonable value that could be attributed to the grainboundary tension of pure austenite or ferrite.

We must therefore disagree with the opinion held by the investigators, and instead conclude that most (if not all) of the excess phosphorus was present either in a precipitate or a non-equilibrium segregate.

> John W. Cahn John E. Hilliard

General Electric Research Laboratory. Schenectady New York

1959

References

- M. C. Inman and H. R. Tipler, Acta Met. 6, 73 (1958).
- J. W. Gibbs, Collected Works, Vol. I, p. 230. Yale University Press, New Haven (1948).
- E. A. Guggenheim, Trans Faraday Soc. 36, 397 (1940).
 J. H. Van Vlack, Trans. Amer. Inst. Min. (Metall.) Engrs.
 - * Received May 27, 1958.

191, 251 (1951).

Grain boundary segregation*

Our recent observation⁽¹⁾ that phosphorus segregates at the grain boundaries of an iron–phosphorus alloy in amounts equivalent to some 20 monolayers of pure



Fig. 1. Carbon replica impression of precipitate type (a). Seen in profile. $\times 5600$.

phosphorus, has been of some concern to us, for as Cahn and Hilliard⁽²⁾ point out, it is difficult to justify an "equilibrium segregation" of more than about one monolayer of solute on reasonable thermodynamic grounds.

For some time past, in order to clarify the position, we have been searching for phosphorus-bearing precipitates at the grain boundary fracture surfaces of iron-phosphorus alloys, using the electron microscope in conjunction with a carbon extraction replica technique. This work, which we hope soon to report in detail, has provided evidence of three precipitate forms (which we designate types (a), (b) and (c)), at the grain boundary surfaces. Of the type (a) precipitate only the impression has so far been observed upon the carbon replicas, attempts to extract the precipitate itself having proved unsuccessful. The precipitate forms types (b) and (c) have been extracted, however, and photographs of all three forms are reproduced in Figs. 1, 2 and 3. The density of the precipitates type (a) and (b) upon the replicas appears to be sufficiently great to account for the previously observed phosphorus segregation(1) in terms of a phosphorus-bearing precipitate.

However, it is not clear that any of the precipitates do in fact contain phosphorus, for although electron diffraction patterns have been obtained, a positive identification has not yet proved possible. It is of interest that the d_{hkl} spacings which have been measured do not correspond with those of the iron phosphides. This is a not unexpected result, for recent work at this laboratory⁽³⁾ shows the solid solubility of phosphorus in iron at 950°C to be not less than 0.9 wt. per cent, and since the alloys we have examined contain not more than 0.09 wt. per

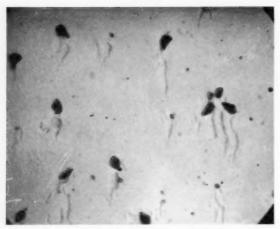


Fig. 2. Precipitate type (b). ×28000.

cent of phosphorus, they are likely to be unsaturated with respect to this element at the quenching temperatures (700–900°C). Under these conditions one would not therefore expect to find at equilibrium precipitates of the simple iron phosphide type (in particular Fe_3P), at the grain boundaries.

To conclude, our present view is that a large part of the segregated phosphorus probably exists in the form of a precipitate at the grain boundaries, and we believe that this precipitate may arise because of the presence of other solute impurities in the iron. The phase diagram which is of importance here in considerations of the equilibrium state of the alloy, is then not that which refers to iron and phosphorus alone, but that which includes also other remaining impurities in the alloy. We do not however exclude the possibility of the existence of a segregated monolayer of phosphorus at the grain boundaries, since the marked degree of grain boundary weakness



Fig. 3. Precipitate type (c). ×5600.

in these alloys which can be caused by small phosphorus additions would seem to imply a drastic reduction of the grain boundary energy as a consequence of a substantially complete coverage of the grain boundary surfaces by phosphorus. However it will obviously be very difficult to detect such a monolayer experimentally when phosphorus-bearing precipitates are also present at the grain boundaries.

M. C. INMAN H. R. TIPLER

VO

19

National Physical Laboratory Teddington England

References

- M. C. Inman and H. R. Tipler, Acta Met. 6, 73 (1958).
 J. W. Cahn and J. E. Hilliard, Acta Met. 7, 219 (1959).
 B. Gale, Acta Met. To be published.
 - * Received July 28, 1958.

Mechanism of sintering*

Two currently favoured theories for describing the densification during sintering of cubic metals are, (a) lattice diffusion from surfaces or boundaries towards pores, and (b) plastic deformation of the mass. Of these (a) fails to account quantitatively for the initial very high rates of densification and (b) does not explain observed increases in sizes of pores with time.

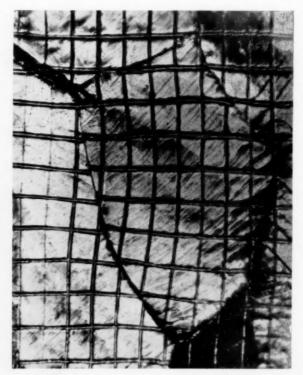


Fig. 1. Photomicrograph of deformed grain in aluminium,

Because of this latter phenomena most authorities now appear to favour a lattice diffusion mechanism.

It appears, however, that the difficulty concerning the initial very high rates of densification can be resolved if we assume extensive grain boundary shearing movements. It is known that extensive grain boundary sliding occurs in most metals during deformation. See for example Fig. 1 showing relative movements of crystals (as revealed by a marker grid) in polycrystalline solid aluminium under creep stress at 500°F.(1) In normal polycrystalline metals such movements are very limited because of blocking of neighbouring grains. In a compact of compressed metal powder however, neighbouring grains are welded to each other at relatively few points, and in the early stages of sintering considerable rearrangement of the relative disposition of the powder particles under surface tension forces is possible by this mechanism, and would appear to be quite adequate to account for the densification observed.

It would be very desirable to have quantitative work correlating initial rates of densification with internal surface areas of compacts prepared under varying pressures.

W. D. Jones

Berk House, Portman Square London, W.1

VOL.

1959

References

- Hans Brunner and Nicholas J. Grant. Metallurgy Reports February 1958, 9 (1).
 - * Received June 26, 1958.

On the effect of static and dynamic preloads on the stress-strain curve for a low carbon steel*

It has been widely observed that the upper yield point in a low-carbon steel is eliminated by the first cycle of loading beyond the yield stress, and only recovers a sharp yield point after an aging treatment. The purpose of this communication is to point out that the disappearance of the yield point will not occur if the subsequent stress—strain curve is obtained at a considerably higher strain rate than the first cycle of loading, and that generally the strain rate of the first load cycle has significant effects on subsequent stress—strain cycles.

Experiments were performed in which specimens were subjected to either static or dynamic loads which were of sufficient magnitude to initiate yield and cause a permanent elongation of approximately 0.5 per cent to occur in all cases. The static tests were performed in a universal testing machine and the dynamic tests in a rapid load testing machine fully described elsewhere.⁽¹⁾ The specimens were re-tested

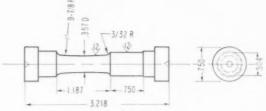


Fig. 1. Test specimen.

in either dynamic or static tension and the resulting stress-strain curves were compared. The rate of elongation of the 1 in. test length specimens (Fig. 1) was about 10 sec^{-1} and 10^{-5} sec^{-1} for the dynamic and static tests respectively. The specimens were of a low-carbon steel with the composition (wt. %):

C Mn Si Ni Cr S P 0.10 0.32 0.16 0.11 0.07 0.031 0.011 The material had been normalized; a description of the heat treatment and instrumentation is given in reference 2.

Fig. 2 is a typical result for two specimens, one of which had been previously yielded in dynamic tension and the other in static tension, and immediately reloaded in dynamic tension. For the curves in Fig. 3, the initial loadings were the same as Fig. 2, but the reloadings were in static tension.

As indicated in Fig. 2, the dynamic retest of a dynamically preloaded specimen shows the characteristic absence of a sharp yield point. However, after static yielding, a dynamic test reveals the presence of a pronounced upper yield phenomenon, and in fact the stress–strain curve is almost identical to that obtained for a similar dynamic test of a virgin specimen. In the case of static reloading, the magnitude of the stress–strain curve for the dynamically preloaded material is lower than that for the statically

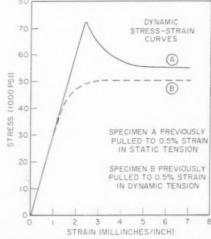


Fig. 2. Dynamic retest of previously yielded specimens.

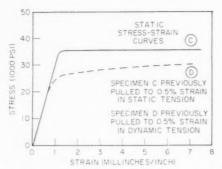


Fig. 3. Static retest of previously yielded specimens.

pre-loaded material. It was observed in all cases that the level of the stress-strain curve was less for specimens that had been pre-loaded dynamically.

The observed behaviour follows a pattern which is consistent with the following explanation: For static loading, flow occurs relatively slowly and the deformation can be accomplished by a large amount of flow in relatively few slip regions. As the rate of loading is increased the flow rate must also increase, but there is a dislocation immobility effect (or viscosity effect) such that a greater stress is required to increase the flow rate of a given slip region. The greater value of stress will cause other sources of dislocations to become activated. Flow will therefore occur along many more slip planes under dynamic conditions than under static. It is reasonably apparent, from the reapparance of the yield point for the dynamic test following the static test, that only a partial unlocking of such dislocation sources had occurred under the static test, and that the dynamic test raised the stress level to a magnitude sufficient to bring additional sources into action.

The lowering of the level of the subsequent flowstress curve by dynamic pre-strain, as compared with static pre-strain, can be considered as a result of having activated many dislocation sources. It is quite probable that for relatively large values of flow, the materials may work harden at different rates such that the curves may intersect.

The flow mechanism described is in agreement with microscopic flow patterns in which coarse patterns were observed under static and fine patterns under dynamic tests.(3)

It has been brought to the authors' attention that the strain may not be uniform throughout the 3/8 in. gage length and that the distribution and magnitude of local strain values may be different for the dynamic and static cases. It is possible that the strain under gage could attain local maximum values up to about 2 per cent, which is the value of strain after which

appreciable work-hardening begins. Possible differences in cross-sectional area resulting from this local strain for the different tests would result in negligible changes of stress as compared with those calculated on the basis of original area. While the qualitative conclusions previously given are not affected by considerations of nonuniform strain (in fact such conditions are presupposed), quantitative results may be dependent upon the gage length. R. C. SMITH

Mechanics Division U.S. Naval Research Laboratory Washington, D.C.

References

I. VIGNESS

19

- 1. I. VIGNESS, J. M. KRAFFT and R. C. SMITH, Proc. Conf. on Properties of Materials at High Rates of Strain. Institution of Mechanical Engineers (1956).
- 2. R. C. SMITH, T. E. PARDUE, and I. VIGNESS, Proc. Soc.
- Exp. Stress Anal. 13, (No. 2), 183 (1956).
 J. D. Campbell and J. Duby, Proc. Roy. Soc. A236, 24 (1956).
- * Received May 7, 1958; revised version June 23, 1958.

Evidence for the surface diffusion mechanism of thermal grooving in copper*†

It has been proposed^(1,2) that thermal grooves, which are known to appear at grain boundaries when polished metal surfaces are heated to high temperatures, form by a surface diffusion mechanism. Recently, Mullins(3) has given a quantitative treatment of the kinetics of groove formation. From a consideration of the surface diffusion and evaporationcondensation transport mechanism, Mullins is able to show that the shape of the groove profile for either mechanism should be independent of the time. A basic difference in the shape of the profile for the two transport mechanisms also is predicted. If matter is transported primarily by surface diffusion, small humps of material will build up outside the groove; this should not be true when evaporation-condensation is the primary mode of transport. The formation of humps alongside of a grain boundary groove has been observed; (1.2,4-6) a typical example of this type of profile for copper is shown in the interferogram in Fig. 1.

During the course of measuring some absolute grain boundary energies in copper, (6) it was possible to determine the depth and width of grooves which formed at [001] tilt boundaries of varying misorientation. In addition to this, the shape of the

[†] Abstracted from a thesis presented by the Aluminum Company of America Fellow, N. A. GJOSTEIN, to the faculty of the School of Engineering and Science, Carnegie Institute of Technology, in partial fulfillment of the requirements for the Degree of Doctor of Philosophy in Metallurgical Engineering.

profile was determined, for high energy boundaries, from the type of interferogram shown in Fig. 2. It is the purpose of this note to report an analysis of these results based on Mullins treatment of the thermal grooving process.

According to Mullins, the depth d of the groove, as measured along the normal to the surface, from the maximum of the surface to the vertex of the groove, can be expressed as

$$d = 0.973m(Bt)^{1/4} \tag{1}$$

where
$$B = \frac{D_{s \hat{\gamma}' s} \Omega^2 v}{kT}$$
 and $m = \cot \alpha$ or $\cot \beta$.

The constant B is expressed in terms of D_s , the surface diffusion coefficient; γ_s the surface-free energy per unit area; Ω , the atomic volume; r, the number of atoms per unit area; and kT, which has its usual meaning. The angles α and β may be defined as those that each side of the groove vertex makes with normal to the surface; they are determined from the perpendicular-type fringe pattern, Fig. 1, by using techniques described elsewhere. $^{(6\cdot7)}$

The semiwidth s of the groove, as measured along the surface, from the vertex to either of the maxima is given by $s = 2.3(Bt)^{1/4}.$ (2)

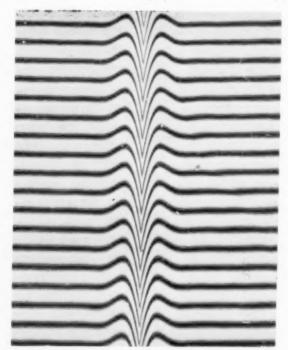


Fig. 1. Interferogram showing the perpendicular-type fringe pattern of a thermal groove which formed at a 32° symmetrical [001] tilt boundary; the plane of the surface shown is parallel to the common [001] direction and normal to the grain boundary; contour interval, 0.27 μ. ×571.5.

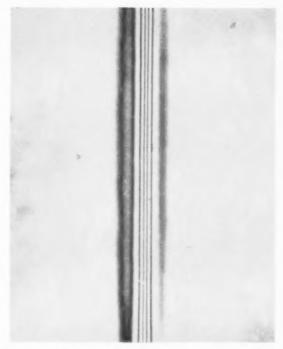


Fig. 2. Interferogram showing the parallel-type fringe pattern of a thermal groove which formed at a 37° symmetrical [001] tilt boundary; the plane of the surface shown is parallel to the common [001] direction and normal to the grain boundary; contour interval, 0.27 μ . ×571.5.

Equation (2) predicts that s should be independent of m. After annealing specimens for 37 hr at 1065°C , the average value of s was found to be $6.5 \pm 0.5 \; \mu$, there being no significant trend in s as m varied from 0.04 to 0.20. At 930°C (60 hr), s was $7.5 \pm 0.5 \; \mu$ with again no significant variation with m.

Further predictions may be made by combining equations (1) and (2) to find d/s, hence

$$d/s = 0.423m. (3)$$

It is clear that the ratio d/s should be time independent, and that a plot of d/s vs. m should be linear and have the slope 0.423, regardless of the time or temperature of annealing. Such a plot is shown in Fig. 3, and it can be seen that the data for both temperatures are in reasonably good agreement with the theoretical straight line.

Mullins' theory also suggests a possible method of determining D_s from the shape of the groove profile, which is given approximately by

$$y(x, t) = m(Bt)^{1/4} [-0.780 + U - 0.288U^2]$$
 (4)

for
$$0 < U < 1$$
, where $U = \frac{x}{(Bt)^{1/4}}$, and the y and x

axes are arranged normal and parallel to the surface, respectively, with their origin at the vertex of the

1959

Fig. 3. Comparison of experimental data for d/s and m at 1065°C and 930°C with the relationship predicted by Mullins. (3)

groove. Following a method suggested by Hilliard, (5) it was found that for copper the shape of the groove profile, as taken from a parallel fringe pattern, Fig. 2, can be represented empirically by the equation

$$y = ax + bx^2 \tag{5}$$

where a and b are evaluated from a plot of y/x vs. x. By comparing coefficients in expressions (4) and (5), it is possible to deduce that

$$D_s = \frac{kT}{\gamma_s \Omega^2 vt} \left[\frac{-0.288m}{b} \right]^4. \tag{6}$$

Taking the following values for the constants for copper:

$$\begin{split} k &= 1.38 \times 10^{-16} \ \rm ergs/deg, \\ \Omega &= 1.18 \times 10^{-23} \ \rm cm^3/atom \\ v &= \Omega^{-2/3} = 1.93 \times 10^{15} \ \rm atoms/cm^2 \\ \gamma_s &= 1670 \ \rm ergs/cm^{2*} \end{split}$$

 D_s was calculated from measured values of m and b, using equation (6). Table 1 gives the D_{\circ} values for 1065°C and 930°C; the value listed for 1065°C represents an average taken from six different profiles. while at 930°C only one profile was used. For comparison, the result of Hackerman and Simpson (8) at 750°C has been included.

It is clear that the interferometric method gives results which are not in agreement, except in order to magnitude, with those obtained by using radioactive tracers. Moreover, the data are insufficiently complete

Table 1. Surface diffusion coefficient of copper

$D_s ({ m cm^2/sec})$	
$(12.5\pm 1.2) imes 10^{-4}$	
$2.7 imes 10^{-5}$	
$4.2 imes10^{-5}$ †	

to permit a meaningful evaluation of the activation energy for surface diffusion. With more accurate determinations of the shape of the groove profile, however, this method may provide a useful way of measuring D_s .

> N. A. GJOSTEIN† F. N. RHINES‡

> > 19

†Staff Research and Development Laboratory Thompson-Ramo-Wooldridge, Inc. Cleveland, Ohio

Department of Metallurgical Engineering Carnegie Institute of Technology Pittsburgh, Penn.

References

- 1. B. Chalmers, R. King and R. Shuttleworth, Proc. Roy. Soc. A193, 465 (1948).
- 2. J. B. Hess, Metal Interfaces, 134, ASM monograph (1952). 3. W. W. Mullins, J. Appl. Phys., 28 (3), 333 (1957)
- 4. H. Udin, A. J. Shaler and J. Wulff J. Metals, N. Y. 1, 186 (1949).
- 5. J. E. HILLIARD, Research to be published.
- 6. N. A. GJOSTEIN and F. N. RHINES, Acta Meta. To be published. N. A. GJOSTEIN, Ph D. Thesis, Carnegie Institute of
- Technology (February 1958)
- 8. N. HACKERMAN and N. H. SIMPSON, Trans. Faraday Soc. 52, 628 (1956).
 - * Received July 22, 1958.

Ueber die Bedeutung der Versetzungen an den Grenzen der Kristalle des angelassenen Martensits für den mikrophysikalischen Mechanismus der "Anlassprödigkeit"

In der vorangehenden Arbeit⁽¹⁾ haben wir das Sammeln der Atome der Verunreinigungen beim Entstehen der "Anlassprödigkeit" um die Versetzungen an den Grenzen der Kristalle des angelassenen Martensits herum zur Identifikation dieser Versetzungen benützt. In der gegenwärtigen Arbeit wollen wir umgekehrt über die Bedeutung dieser Versetzungen für die Lösung der "Anlassprödigkeit" selbst, für die Lösung des mikrophysikalischen Mechanismus dieses Vorganges abhandeln.

Die "Anlassprödigkeit" (weiter bloss "A.S.") entsteht, wie bekannt, in Cr-Mn, Cr-Ni und auch in Fe-C Stählen im kritischen Interval der Temperaturen von 450°C ÷ 600°C. Für diese Versprödung ist charakteristisch, dass ihr Entstehen durch keine bemerkbaren Veränderungen der magnetischen und elektrischen Eigenschaften, der Härte oder spezifischen Dichte, wie z.B. beim Altern, sondern bloss durch eine Aenderung des Verlaufes des Bruches beim Schlag (der transkristallische Bruch ändert sich in einen interkristallischen) und durch das

[†] Data of Hackerman and Simpson; (8) represents an average of values for different crystallographic planes and directions.

Sinken der Kerbschlagzähigkeit begleitet wird. Beim Studium mittels eines Elektronenmikroskops gelang es nicht, eine wie immer geartete Ausscheidung, die für die Versprödung verantwortlich wäre, (2,3) festzustellen. Es wurde bloss entdeckt, dass beim Aetzen mit einer Wasserlösung der Pikriersäure an den Grenzen der ursprünglichen y-Körner und längs der Grenzen der Kristalle des angelassenen Martensits (α-Körner) feine Rinnen ausgeätzt werden. (2) Das beweist, dass die Aenderungen welche beim Entstehen der "A.S." verlaufen, nicht bloss an die Grenzen der ursprünglichen y-Körner, wie allgemein die derzeitigen Theorien erwägen, lokalisiert werden, sondern verlaufen auch an den Grenzen der Kristalle des angelassenen Martensits und so also in Gebieten, die dem Inneren der y-Körner entsprechen. Aus der Tatsache, dass es in der Arbeit⁽¹⁾ gelang, durch Hervorrufen der "A.S." die Versetzungen an den Kristallgrenzen des angelassenen Martensits sichtbar zu machen, geht dann hervor, (1,4) dass diese Veränderungen eigentlich die Segregation der Atome der Unreinigkeiten zu diesen Versetzungen sein wird.

Wenn wir nun diese Segregation in die Lösung des Mechanismus der "A.S." einbeziehen, bekommen wir folgenden mikrophysikalischen Mechanismus dieser Versprödung.

1959

Die Anwesenheit der Atome der Unreinigkeiten bei den Versetzungen an den Kristallgrenzen des angelassenen Martensits ruft der Versetzungstheorie nach⁽⁵⁾ das Abbremsen der Bewegung dieser Versetzungen bei plastischer Verformung hervor und verhindert dadurch die plastische Verformung dieser Kristalle bei der Kerbschlagprüfung. Da der Kontakt zwischen den einzelnen Kristallen des angelassenen Martensits in den Gebieten der ursprünglichen y-Körner, in denen diese enstanden sind, direkt ist, ohne Uebergangsgebiete mit unvollkommenem Anknüpfen des Kristallgitters, werden die Kristalle untereinander im Inneren dieser Gebiete einen bestimmten Zusammenhang aufrecht erhalten, der auch auf die Existenz der Versetzungen an ihren Grenzen gebunden ist. Das Blockieren der Versetzungen beim Entstehen der "A.S." wird daher die Bildung grösserer Komplexe durch die einzelnen Kristalle des angelassenen Martensits im Augenblick der Verformung, die den ursprünglichen y-Körnern entsprechen, zur Folge haben; diese werden dann auf einmal als ganze Einheiten der plastischen Verformung durch Schlag widerstehen.

Um die auf diese Weise gebildeten Einheiten herum werden dann die normalen Grenzen der ursprünglichen γ -Körner existieren, die hier auch nach der Umwandlung des Austenits in Martensit zufolge des

diffusionslosen Charakters der martensitischen Transformation erhalten blieben.

In diesen Grenzen, im Gegensatz zum Inneren der ursprünglichen γ-Körner, wird aber die plastische Verformung als ein von Versetzungen unabhängiger Mechanismus, durch individuelle Bewegungen der einzelnen Atome verlaufen (sei es schon nach (6) oder(7) u.ä.), denn hier werden Gebiete mit ungeordneter Verteilung der Atome existieren, welche dadurch hervorgerufen wurde, dass der Kontakt der Kristallgitter der y-Körner vor dem Härten nicht nur auf einen Winkel unter 20°* beschränkt war, sondern hat sich auch auf grössere Winkel erstreckt. Bei der Zerstörung des Musters bei der Schlagprüfung, welcher eine intensive plastische Verformung vorangeht, (8,9) wird daher der Bruch in diesen Grenzen verlaufen, denn diese werden im Augenblick des Schlags bei gleichzeitigem Blockieren der Versetzungen im Gitter die einzigen Gebiete sein. welche der plastischen Verformung fähig sein werden.

Im Einklang damit scheint deswegen der Bruch des Stahls mit "A.S." als ein zu den γ -Körnern interkristallischer Bruch, obgleich in Wirklichkeit hier diese Körner nicht mehr existieren. Durch das Herabsetzen der Temperatur bei der Kerbschlagprüfung auf—78°C oder—193°C ändert sich nichts an diesem Verlauf, denn durch das Herabsetzen der Temperatur wird nicht das Blockieren der Versetzungen beseitigt. Umgekert aber wird durch das Anwärmen oberhalb des Intervals von 450°–600°C, wodurch die Atome der Unreinigkeiten aus der festen Lösung ausgeschieden werden, der Bruch wieder transkristallisch verlaufen, ebenso wie bei nichtversprödeten Stählen. (10)

Wenn beim Prüfen die Verformungskraft ruhig, statisch wie z.B. bei der Festigkeitsprüfung, Härteprüfung u.ä., wirken wird, dann wird es möglich sein, dass sich die Versetzungen von den Atomen der Unreinigkeiten lösen und infolgedessen wird die plastische Verformung der einzelnen Kristalle möglich sein. Bei diesen Prüfungen kann das Entstehen der "A.S." nicht zum Vorschein kommen, was auch mit den bisher durchgeführten Experimenten im Einklang ist.

Beim Entstehen der "A.S." kommt es ebenfalls zur Seigerung der Atome der Verunreinigungen in die Gebiete der ursprünglichen γ -Körner. (1) Ihr Einfluss an diesen Stellen muss aber im Vergleich mit jenem bei den Versetzungen viel kleiner sein, denn da können sie bloss die Bewegung der einzelnen Fe-Atome bremsen, im Falle der Versetzungen dagegen

^{*} Für den das Versetzungsmodell gilt.

wird durch das "Verankern" irgendeines Atomes der Atomkette der Versetzung die Bewegung einer ganzen Atomreihe unmöglich gemacht.

Nach dem oben angeführten Mechanismus muss sich aber ihre Anwesenheit markant in der Empfindlichkeit der Kerbschlagprüfung auf das Entstehen der "A.S." äussern. Wenn nämlich die plastische Verformung beim Schlag bloss an den Grenzen der ursprünglichen y-Körner verlaufen wird, und zwar durch Diffusionsbewegung der Fe-Atome, dann muss alles, was die Diffusion der Eisenatome bremst, zum Heranwachsen des Widerstandes gegen die plastische Verformung im Augenblick des Schlages, d.i. zur Vergrösserung des Sprödigkeitsgrades führen. Und solchen Einfluss hat das Herabsetzen der Temperatur unter 0°C, die Anwesenheit der Atome der Unreinigkeiten (für Kohlenstoff siehe(11)) und der legierenden Elemente wie Cr. Mn (für Chrom siehe z.B.(12) in diesen Grenzen und infolgedessen auch die hohe Temperatur und lange Dauer der Austenisation, welche die Seigerung dieser Atome zu den Grenzen der y-Körner unterstützen, u.ä.

Die Anwesenheit von Elementen, welche umgekehrt die Diffusionsbewegung der Atome der Unreinigkeiten unterdrücken, wird eindeutig zur Unterdrückung des Entstehens der "A.S." führen, denn sie verhindert die Segregation dieser Atome zu den Versetzungen an den Kristallgrenzen des angelassenen Martensits und dadurch auch ihr Blockieren. Ihre Wirkung wird allerdings nur soweit gelten, inwiefern sie ebenfalls im Gitter des α-Eisens aufgelöst sein werden. Wenn sie wie z.B. bei langfristigem Glühen bei höheren Temperaturen als Karbide, Nitride u.ä. ausscheiden, dann verschwindet ihre beschrenkende Wirkung und auch diese Stähle werden am Ende spröde werden. Dies gilt für Mo und W.

Die ausführliche Lösung des mikrophysikalischen Mechanismus der "A.S." und der eigentliche Mechanismus des Blockierens der Versetzungen werden später veröffentlicht.

A. Masín

Physikalisches Laboratorium des Forschungsinstitutes für Verkehrswesen, Resortanstalt des Verkehrsministeriums, Prag, Tschechoslowakei

References

1. A. Masin, Naturwiss. 45, 207 (1958).

- B. Woodfine, J. Iron St. Inst. 173, 240 (1953).
 J. Nutting, P. Plateau, G. Henry et C. Crussard, Revue universelle des Mines 99, 512, 543 (1956).
- 4. A. Masín and V. Havel, Acta Phys. Hung. (im Druck). 5. A. H. COTTRELL, Dislocations and Plastic Flow in Crystals.
- Oxford Press, London (1953).
 6. N. F. Mott, Proc. Phys. Soc. **60**, 391 (1948).
 7. Ting-Sui-Kê, J. Appl. Phys. **19**, 285 (1948).

8. R. GREEN, Phys. Rev. 102, 376 (1956).

9. B. S. Kasatkin, Dokl. Akad. Nauk. SSSR 101, 665 (1956). 10. S. F. Jurev and Z. I. Kuznicina, Fiz. metal. metalloved.

3, 282 (1956).

11. P. L. GRUZIN, JU. V. KORNEV und G. V. KURDJUMOV, Dokl. Akad. Nauk SSSR 80, 49 (1951)

12. P. L. GRUZIN, Dokl. Akad. Nauk SSSR 100, 65 (1955).

* Received July 22, 1958.

Electrical resistivity change from formation of zones in aluminum alloys*

In Al-rich-Ag alloys the electrical resistivity decreases during cold hardening, that is, while zones are forming from the supersaturated solid solution.(1) This is the normal behavior on precipitation from solid solution. In Al-Cu alloys containing about 2 at. % Cu the resistivity during cold hardening at room temperature initially increases, (2.3) reaches a maximum at about three hours and then decreases. (2) After 200 hr the resistivity is the same as 10 min after quenching.(2) If the aging is carried out at a higher temperature so that the stable precipitate θ forms, then the normal decrease in resistivity is observed.(4)

VO

19

One then concludes that during zone aging of Al-Cu alloys, two main resistivity effects are occurring: A decrease in resistivity due to a reduction in Cu concentration in the solid solution, and an increase due to the presence of the zones. Geisler (5) suggested that the resistivity increase is due to coherency strains between the precipitate and matrix. Large coherency strains need not be assumed for zones in the Al-Ag case since the Al and Ag atoms are nearly of the same size; the zones are thought to be nearly ideal. (6) The zones in the Al-Cu case are not ideal. The structure and composition of the zones is not known with certainty but according to Gerold(7) consists of Cu sheets up to about 50 atoms in diameter and one atom thick oriented parallel to 100 type planes in the matrix with the surrounding lattice distorted elastically.

The atomic diameters of Al and Cu are 2.856 Å and 2.551 Å, respectively and thus differ by about 12%. If the mismatch in the region of the zone is taken up by elastic strains, the strain energy in this region would be extremely large. In the case of nucleation eatalysis (8) for crystallization of solids if the mismatch in lattice spacing of the crystal and catalyst are more than a few per cent, it is probably energetically more favorable for the mismatch to be taken up mainly by a grid of edge dislocations rather than by lattice strains. Similar considerations should hold for

formation of zones Al in–Cu alloys. It therefore seems reasonable to suggest that the zones contain extra rows of copper atoms. These rows would lie in 110 type directions. Each extra row of atoms may be thought of as a pair of edge dislocations of opposite sign in the matrix, one above and one below the zone, spaced apart a distance equivalent to the thickness of the zone. The Burgers vectors would be of the type and magnitude $\frac{1}{2}\langle 110 \rangle$. The increase in resistivity according to this model would be due to scattering of electrons by the extra rows of atoms as well as the lattice strains in the matrix. The following rough calculation indicates that this suggestion is quite reasonable.

According to Barer and Bever⁽⁴⁾ the resistivity of an Al–2 at.% Cu alloy decreases about 20% due to precipitation at 250°C where the stable precipate forms. This is due to removing copper from solid solution. According to Fink and Smith, (2) the resistivity decreases about 1.5% during aging for a long time at room temperature. Thus, in a specimen well-aged at room temperature the resistivity at room temperature is roughly 18.5% higher than the resistivity of the matrix alone. The resistivity is about 4 $\mu\Omega$ -cm and thus about 0.7 $\mu\Omega$ -cm is attributable to scattering of conduction electrons by zones.

1959

The resistivity from the extra rows of copper atoms and the lattice strains should be comparable to that from the imagined grid of edge dislocations in the zone-matrix interfaces. Since the mismatch is roughly 12%, a grid of edge dislocations spaced about 8 atom diameters apart would be required. The number of dislocations per cm2 of zone-matrix interface would equal 2.3×10^{13} . In a 2 at.% Cu alloy, assuming all of the copper atoms to be in zones one atom thick, there would be roughly 1.5×10^{13} dislocation lines threading each cm2 of alloy. According to the experimental determination of Wintenberger, (9) in pure aluminum the resistivity per dislocation line per cm² is $2.2 \times 10^{-14} \,\mu\Omega$ -cm. Using this figure, a resistivity of 0.33 $\mu\Omega$ -cm is estimated for the extra resistivity or about half of the experimental value. The agreement between the two values indicates that there may be some validity in our assumption of extra rows of copper atoms in the zones.

If these extra rows of copper atoms do exist, they could also contribute to the hardening since cutting of zones during plastic deformation would necessitate creation of jogs in these extra rows. This would be analagous to the case of the necessity for cutting dislocations which thread the slip plane.

Acknowledgments

I am grateful to Dr. Anthony Kelly for helpful discussion.

M. E. FINE

Department of Metallurgy Northwestern University Evanston, Illinois

References

- D. Turnbull and H. N. Treaftis, Acta Met. 5, 534 (1957).
 W. L. Fink and D. W. Smith, Trans. Amer. Inst. Min. (Metall.) Engrs. 137, 107 (1940).
- W. DeSorbo, H. N. Treaftis and D. Turnbull, Acta Met. 6, 402, (1958).
- R. D. Baher and M. B. Bever, Trans Amer. Inst. Min. (Metall.) Engrs. 185, 544 (1949).
- A. H. Geisler, Trans. Amer. Inst. Min. (Metall.) Engrs. 180, 230 (1949); Precipitation from Solid Solutions in Metals, Phase Transfermations in Solids, p. 458. John Wiley and Sons, New York (1951).
- A. Guinier, J. Metals, N.Y. 8, 673 (1956).
 V. Gerold, Z. Metallk. 45, 599 (1954).
- D. Turnbull and B. Vonnegut, Industr. Engrg. Chem. 44, 1202 (1952).
- 9. M. WINTENBERGER, C.R. Acad. Sci., Paris 244, 2800 (1957).

This research was sponsored by the United States Air Force through the Air Force Office of Scientific Research of the Air Research and Development Command under Contract AF 18(600)1468.

* Received August 8, 1958.

Über Kristallstruktur und Ordnung aus der Schmelze abgeschreckter Legierungen des Systems Kupfer-Zinn*

Bornemann und Sauerwald,(1) Bienias Sauerwald, (2) Gebhardt, Becker und Schäfer (3) und Bornemann und Wagemann, (4) Matsuyama, (5) Roll und Motz⁽⁶⁾ haben festgestellt, dass flüssige Kupfer-Zinn-Legierungen im Zusammensetzungsbereich der intermetallischen Phasen Cu₃Sn und Cu₃₁Sn₈ (ε- und δ-Phase) relative Extremwerte der Dichte, der Viskosität und der Leitfähigkeit besitzen. Für die Abweichung dieser physikalischen Eigenschaften vom monotonen Verlauf, wie er nach der Mischungsregel in Abhängigkeit von der Zusammensetzung zu erwarten wäre, werden zwischenatomare Bindungskräfte verantwortlich gemacht,†(7) die insbesondere bei intermetallischen Phasen auch noch in der Flüssigkeit wirksam sind und mit ansteigender Temperatur abnehmen.

Im Zustandsdiagramm des Systems Cu–S
n liegt zwischen dem Flüssigkeitsgebiet und den beiden geordneten Phasen ε und δ die γ -Phase. Wie gezeigt

[†] Yao⁽⁷⁾ z.B. gibt eine zusammenfassende und vergleichende Darstellung der Eigenschaften flüssiger Legierungen von Zweistoffsystemen mit intermetallischen Phasen, mit lückenloser Mischkristallbildung und von eutektischen Systemen.

wurde, $^{(8,9)}$ ist die γ -Phase im ganzen Existenzgebiet kubisch und, nahezu unabhängig von der Temperatur, bis zum Übergang ins $(\gamma+L)$ -Gebiet geordnet. Bei der Zusammensetzung Cu_3Sn enthält das kubische γ -Gitter (12Cu + 4Sn) Atome je Einheitszelle in einer Anordnung analog zur Überstruktur im Fe_3Al-Gitter. Mit steigendem Kupferanteil sind die fehlenden Zinnatome in statistischer Verteilung durch Kupferatome ersetzt.

Werden Proben mit 25,0 und 20,5 At. % Sn z.B. von 700°C aus dem γ-Zustand in Wasser von 20°C oder in flüssiger Luft abgeschreckt, so erhält man die beiden geordneten Phasen ε' und δ durch diffusionslose Transformation. (9.10) Die geordnete ε' -Phase der Zusammensetzung Cu₃Sn hat eine orthorhombische Einheitszelle mit (6Cu + 2Sn) Atomen in nahezu hexagonal dichter Packung und ist bis auf die fehlende, von Schubert, Kiefer, Wilkens und Haufler(11) gedeutete "Verwerfungsüberperiode" der stabilen geordneten & Phase gleich. Die durch Abschrecken aus dem y-Gebiet gewonnene geordnete kubische δ-Phase unterscheidet sich im Debve-Scherrer-Diagramm nicht von der durch Abschrecken aus dem δ-Gebiet entstehenden Phase, deren Pulveraufnahme wiederum übereinstimmt mit dem Hochtemperaturdiagramm der geordneten stabilen δ -Phase selber.

Die beschriebenen Beobachtungen und Zusammenhänge gaben den Anlass dazu, Proben dieser beiden Legierungen vom Flüssigkeitszustand auf tiefe Temperatur abzuschrecken und röntgenographisch zu untersuchen.

In Quarz-Mark-Röhrchen (0,3 bis 0,5 mm Durchmesser, unter 10⁻⁴ Torr Druck zugeschmolzen) wurden zuvor bereits legierte Präparate mit 25,00 und 20,53 At. % Sn je 30 min lang bei 700°C (fest, γ-Phase), 755, 800, 900, 1000 und 1100°C geglüht und in Wasser bzw. in flüssiger Luft abgeschreckt. Unabhängig von der Ausgangstemperatur war bei 25,00% Sn die geordnete ε' -Phase und bei 20,53At. % Sn die geordnete δ-Phase auf den mit Co-Kα-Strahlung angefertigten Debye-Scherrer-Diagrammen zu beobachten und visuell bei beiden Legierungen keine Abnahme der Überstrukturintensität oder Verbreiterung der Linien mit zunehmender Temperatur im Flüssigkeitszustand bemerkbar. Für Röntgenaufnahmen zur photometrischen Auswertung wurden anschliessend die ε' -Proben im Achatmörser zerstossen. In Fig. 1 ist das Verhältnis $V_T=$ $(\Sigma I_{t}/\Sigma I_{G})_{T}$ der gesamten Intensität aller Überstrukturlinien zur gesamten Intensität aller Grundstrukturlinien in Abhängigkeit von der Ausgangstemperatur aufgetragen, bezogen auf den Wert $V_{700} = (\Sigma I_{\mathcal{U}}/\Sigma I_G)_{700}$ der von 700°C aus dem festen

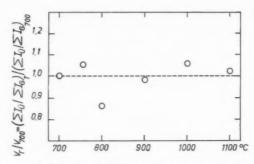


Fig. 1. Verlauf des Intensitätsverhältnisses zwischen den Überstrukturlinien und den Grundstrukturlinien der ε' -Phase mit der Ausgangstemperatur, bezogen auf den Wert bei 700°C.

y-Zustand abgeschreckten Proben. Die Grösse V kann direkt als ein Mass für den Fernordnungsgrad angesehen werden. Im Rahmen der Messgenauigkeit besagt Fig. 1, dass der Ordnungsgrad aus dem flüssigen Zustand abgeschreckter Legierungen nicht von der Ausgangstemperatur abhängig ist und dem der festen γ-Phase (700°C) entspricht. Eine Abnahme der Ordnung mit ansteigender Ausgangstemperatur liesse nach den oben zitierten Eigenschaften flüssiger Cu-Sn-Schmelzen den Schluss zu, dass ein anomaler Ordnungszustand von zunächst noch unbekanntem Grad schon in der flüssigen Phase in der Umgebung der beiden Zusammensetzungen besteht. Da eine Abnahme der Fernordnung im abgeschreckten Zustand jedoch nicht festgestellt wurde, kann mit Sicherheit nur gesagt werden, dass sich die Ordnung in der γ-Phase überaus schnell und, in Übereinstimmung mit den Hochtemperaturaufnahmen im y-Gebiet selbst, sehr stabil ausbilden muss.

VO

19

Die Ordnung wird sich ausserdem unmittelbar beim Übergang von der Schmelze in die γ-Phase einstellen. Schreckt man nämlich Proben mit 20.53 At. % Sn vom flüssigen Zustand in Wasser ab, so sind auf der Oberfläche der erstarrten Probe Wachstumslamellen zu beobachten parallel zur (111)-Ebene der δ-Phase (nachgewiesen durch Laue-Aufnahmen senkrecht zur Lamellenfläche), in der Art, wie sie Graf (12) z.B. bei Kupfer gefunden hat. Abgesehen von der Ordnung lässt sich die δ-Phase, der y-Phase annähernd gleich, als eine kubisch raumzentrierte Phase auffassen. Die Transformation $\gamma \rightarrow \delta$ ist zudem homogen über makroskopische Kristallbereiche. (9) Es kann deshalb angenommen werden, dass die kubischen Achsen des δ -Gitters bei der Transformation die Richtung der kubischen Achsen des y-Gitters beibehalten. Die Lamellenflächen müssen nach dieser Voraussetzung folglich auch parallel zur (111)-Ebene des γ-Gitters gewesen sein. Lamellenwachstum tritt nach Graf in erster

Linie parallel zur dichtest gepackten Netzebene eines Gitters auf. Die Ebene (111) kann aber nicht die dichtest gepackte Ebene eines als ungeordnet vorausgesetzten kubisch raumzentrierten Gitters sein. Andererseits besteht das Gitter der geordneten y-Phase aus vier ineinandergestellten kubisch flächenzentrierten Teilgittern mit jeweils einer Atomart (3Cu-, 1Sn-Gitter), deren dichtest gepackte Ebenen (111)-Ebenen sind. Demnach ist die y-Phase vom Beginn des Kristallisationsvorganges an in der beschriebenen Art als geordnet anzusehen.

H. J. SEEMANN

Institut für Metallphysik und H. KNÖDLER Metallkunde an der Universität des Saarlandes, Saarbrücken

References

- 1. K. Bornemann und F. Sauerwald, Z. Metallk. 14, 145 (1922).
- A. BIENIAS und F. SAUERWALD, Z. anorg. allgem. Chem. 161, 51 (1927)
- 3. E. Gebhardt, M. Becker und S. Schäfer, Z. Metallk, 43, 292 (1952). BORNEMANN und G. WAGEMANN, Ferrum 11, 276
- Y. Matsuyama, Sci. Rep. Tohoku Univ. 16, 447 (1927).
 A. Roll und H. Motz, Z. Metallk. 48, 435 (1957).
- T. P. YAO, Neue Giesserei Techn. Wissenschaftl. Beih. 17, 897 (1957).
- 8. H. HENDUS und H. KNÖDLER, Acta Cryst. 9, 1036 (1956). 9. H. Knödler, Dissertation, Univ. Saarbrücken (1958).
- H. Knödler, Acta. Cryst. 10, 86 (1957).
- 11. K. Schubert, B. Kiefer, M. Wilkens und R. Haufler, Z. Metallk. 46, 692 (1955).
- 12. L. Graf, Z. Metallk. 42, 336, 401 (1951); Ibid. 45, 36 (1954).
 - * Received August 18, 1958.

1959

Etch pits in iron*

It has been shown by Suits and Low(1) that a necessary prerequisite to the formation of etch pits in slip bands in silicon iron is an aging treatment at 160°C. More recently Boswell(2) has shown etch pits in high purity iron but states that the pits have been observed at dislocations only in specimens slowly cooled from between 750°C and 850°C. Both articles indicate that the segregation of solute (carbon) to dislocation sites is necessary before the selective etching will occur.

We have developed etch pits in iron in what appears to be glide bands without any pre-treatment. The formation of etch pits was very sensitive to orientation and crystals whose (100) plane was very near parallel to the surface showed the greatest concentration of etch pits. The material used in this work was SAE 1010 steel that had been decarburized in wet hydrogen. The large crystals, up to 2 in. in diameter, were

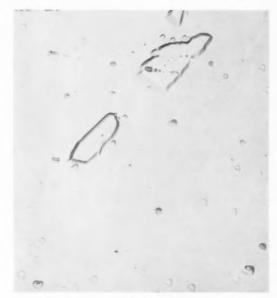


Fig. 1. As annealed and polished, $\times 406.3$.

developed in 1/8 in. thick specimens by the strain anneal method utilizing a nitrogen atmosphere.

Fig. 1 shows an area in a large crystal of a polycrystalline sample prior to deformation and Fig. 2 the same area after plastic deformation. Etch pits developed in line formation only after plastic deformation, indicating that what we are observing is due to the deformation. The small grains in Figs. I and 2 are remains of the fine layer of grains that coat the specimen after the strain anneal process and are



Fig. 2. Plastically deformed. $\times 406.3$.

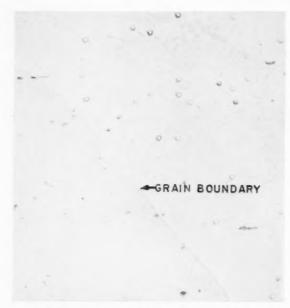


Fig. 3. As annealed and polished. ×406.3.

utilized as "landmarks" in re-photographing an area. Figs. 3 and 4 show another set of photographs of an area before and after deformation. The glide band shown in Fig. 4 is blocked on one end by the grain boundary and the other by an inclusion. Fig. 5 is an area after fairly severe plastic deformation. The bands

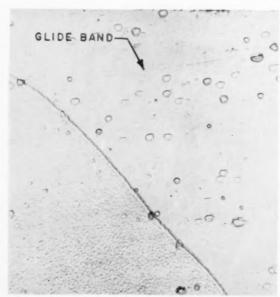


Fig. 4. Plastically deformed. ×406.3.

are usually approximately 45° to the direction of loading and parallel.

The etch pits shown in the photographs were developed by a technique similar to that employed by Boswell and consisted of electropolishing in chromic-acetic acid and etching in 1 per cent nital for 1 min and 0.5 per cent picric acid in ethyl alcohol for 5 min. The deformation was by bending and the specimens were etched immediately after straining.

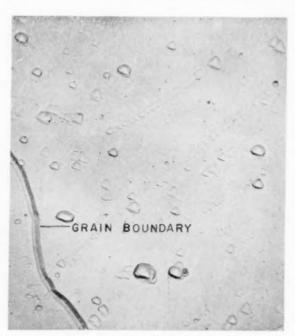


Fig. 5. Plastically deformed. ×437.5.

The reason for the development of etch pits in glide bands in the decarburized SAE 1010 steel without a pre-treatment is not apparent at present. However, the material used is relatively impure when compared with high purity vacuum melted iron. These impurities, the hydrogen remaining from the decarburizing process or nitrogen introduced in growing the crystals may be the contributing factors.

Caterpillar Tractor Co. Peoria, Illinois

R. B. Liss

19

References

- J. C. Suits and J. R. Low Jr., Acta Met. 5, 285 (1957).
 F. W. C. Boswell, Metal Progress, 72, No. 6, 92 (1957).
- * Received September 8, 1958.

WORK SOFTENING IN IRRADIATED COPPER*

M. J. MAKIN†

The temperature dependence of the flow stress of polycrystalline copper, both unirradiated and after neutron irradiation, has been investigated by repeated tensile testing first at temperature T_1 and then at temperature T_2 . In this way reversible and irreversible temperature effects can be separated. In irradiated copper the temperature sensitivity of the flow stress is very large during the early stages of the deformation, and irreversible effects occur when the temperature of the deformation is changed. A sharp yield drop, accompanied by a Lüders band, appears when an irradiated specimen is strained at a high temperature (e.g. 20°C) after being deformed at a low temperature (e.g. -195°C). This phenomenon is not sensitive to the temperature range over which the experiments are carried out but occurs only during the early stages of the deformation. After about 15 per cent extension the flow stress becomes entirely reversible on changing the temperature, and the temperature dependence is only slightly greater than in unirradiated material. The effect is not observed in alpha brass and is removed from irradiated copper by mild annealing treatments. The phenomenon is believed to be associated with the high temperature sensitivity of the lattice hardening produced on irradiation. An explanation is proposed in which groups of dislocations piled up during low temperature deformation behind the obstacles responsible for the lattice hardening collapse on subsequent higher temperature deformation either by by-passing the obstacles or by actually removing the smaller obstacles.

ADOUCISSEMENT DU CUIVRE IRRADIE

L'auteur a déterminé, par des essais successifs de traction à deux températures T_1 et T_2 , l'effet de la température sur la tension de glissement du cuivre polycristallin, normal ou irradié aux neutrons.

De cette manière, on peut distinguer les effets réversibles et irréversibles de la température. Pour le cuivre irradié, l'effet de la température sur la tension de glissement est très important au début de la déformation. Des effets irréversibles apparaissent si l'on modifie la température d'essai.

Une chute brusque à la limite élastique, accompagnée de la formation de bandes de Lüders, apparaît lorsque l'échantillon irradié est étiré à une température élevée (p. ex. 20° C) après avoir été déformé à basse température (p. ex. -195° C).

Ce phénomène ne dépend pas de l'écart de température entre les essais successifs mais ne se marque que pour les premiers stades de la déformation. Après un allongement de l'ordre de $15\,\%$, la tension de glissement devient entièrement réversible au cours de variation de la température. L'influence de la température n'est que très légèrement plus marquée que pour un échantillon non irradié. Un effet identique ne s'observe pas pour le laiton α . Dans le cas du cuivre irradié, on peut d'ailleurs l'éliminer par un recuit. L'auteur propose une explication faisant intervenir des groupes de dislocations formées près des joints de grains. L'importance des empilements dépend de la tension requise pour rendre actives les sources de dislocation; dans le cuivre irradié, cette tension est très influencée par la température. Les résultats indiquent que le durcissement d'irradiation résulte à la fois d'un durcissement dû aux sources de dislocation, très influencée par la température, et d'un durcissement réticulaire indépendant de la température.

VERFORMUNGSENTFESTIGUNG VON BESTRAHLTEM KUPFER

Die Temperaturabhängigkeit der Fließspannung von vielkristallinem Kupfer wurde sowohl im unbestrahlten Zustand als auch nach Neutronenbestrahlung untersucht durch wiederholte Zugvresuche, die zuerst bei der Temperature T_1 und danach bei der Temperatur T_2 durchgeführt wurden. Auf diese Weise lassen sich reversible und irreversible Temperatureffekte trennen. Bei bestrahltem Kupfer ist die Temperaturempfindlichkeit der Fließspannung während der ersten Verformungsstadien sehr gross und bei einer Änderung der Verformungstemperatur treten irreversible Effekte auf. Eine scharfe obere Streckgrenze, begleitet von einem Lüdersband, erscheint bei der Dehnung einer Probe bei hoher Temperatur (z.B. 20°C), nachdem sie bei einer tiefen Temperatur (z.B. -195°C) verformt worden war. Diese Erscheinung ist nicht empfindlich gegenüber dem Temperaturbereich, über welchem die Versuche ausgeführt werden, sie tritt jedoch nur während der frühen Verformungsstadien auf. Nach etwa 15% Dehnung wird die Fließspannung bei Temperaturänderungen vollkommen reversibel und die Temperaturabhängigkeit ist nur wenig grösser als bei unbestrahltem Material. Dieser Effekt wird bei Alpha-Messing nicht beobachtet und er verschwindet bei bestrahltem Kupfer nach einer sanften Glühbehandlung. Eine Erklärung wird vorgeschlagen, bei der Versetzungsgruppen hinter Korngrenzen gebildet werden; die Grösse der Aufstauungen wird dabei durch die Spannung bestimmt, die notwendig ist um Versetzungsquellen zu betätigen, diese ist bei bestrahltem Kupfer sehr temperaturempfindlich. Die Ergebnisse zeigen, dass die Bestrahlungsverfestigung sowohl von der Verfestigung der Versetzungsquellen, die sehr temperaturempfindlich ist, herrührt, als auch von einer temperaturunempfindlichen Verfestigung des Gitters.

1

1959

^{*} Received May 20, 1958. Revised January 19, 1959.

[†] Metallurgy Division, A.E.R.E., Harwell, Berks, England.

INTRODUCTION

Previous experiments by the author⁽¹⁾ have shown that the tensile properties of irradiated metals are much more dependent upon the temperature of testing than are those of unirradiated metals. This is particularly true of copper and nickel, where after a neutron dose of 5×10^{19} thermal neutrons/cm² (plus the associated fast neutrons) the yield strength increased by 77 per cent on lowering the temperature from 200°C to -195°C, whereas in unirradiated copper the equivalent increase was only about 5 per cent.

The present experiments were designed to investigate this temperature dependence not only at the yield point, as in the previous experiments, but also as a function of deformation, and to see if any irreversible effects were introduced when the testing temperature was changed.

A method of testing capable of separating reversible from irreversible effects is to strain first at temperature T_1 and then, at a particular deformation, to unload the specimen and continue the test at tempperature T_2 . If the dislocation arrangement is unaltered during the unloading then the change in flow stress as a function of testing temperature for a particular dislocation arrangement is measured. Repeated testing in this way enables the change in flow stress with temperature to be determined over a wide range of dislocation densities. Irreversible effects usually appear in the form of a yield point, as in the case of work softening in aluminium crystals studied by Cottrell and Stokes (2) and the author's work(3) on the yield point effect introduced by unloading in copper crystals.

EXPERIMENTAL DETAILS

The copper was an "oxygen-free high conductivity" grade, Table 1, and was supplied in the form of an-

Table 1. Purity of the copper

Impurity	% in copper	Impurity	% in copper
Iron	0.0003	Magnesium	0.0001
Silver	0.005	Bismuth	0.0005
Lead	0.002	Zine	0.001
Tin	0.0002	Cadmium	0.0001
Nickel	0.005	Silicon	0.0001
Cobalt	not detected	Manganese	not detected
Aluminium	not detected	Chromium	not detected
Calcium	0.0005		

nealed wire 0.080 in. diameter. The specimens were prepared by drawing to 0.048 in. diameter followed by annealing at 450° C for 60 min. The average grain diameter of the specimens was 0.010 to 0.015 mm,

thus avoiding the complicating effects which arise when specimen and grain sizes become comparable.

The specimens were irradiated for 9 months at about $100^{\circ}\mathrm{C}$ in a flux of 6×10^{12} slow n/cm²/sec. and the total dose of slow neutrons was 1×10^{20} n/cm². The ratio of fast to slow flux is not accurately known but is estimated to be about unity for the positions used. To prevent damage during handling the specimens were mounted in a robust aluminium jig and enclosed in an argon atmosphere. An equal number of control specimens were stored at the same temperature for the same time as the irradiated specimens.

Tensile tests were made with a hard beam machine at a strain rate of $1\times 10^{-4}\,\mathrm{sec^{-1}}$. The specimens were gripped in pin vices which were attached in a special jig designed to prevent damage to the specimen during mounting. The tensile machine was arranged so that the specimen could be enclosed in a readily interchangeable bath enabling rapid temperature changes to be made during a test.

$Temperature~^{\circ}C$	Bath	Fixed Point	
-195	liquid nitrogen	boiling point	
-160	iso-pentane	melting point	
-110	alcohol	melting point	
-78	dry ice and acetone	sublimation point	
-40 -10	calcium chloride solution	freezing point	
20	air	room temp- erature	
100	silicone oil	controlled to $\pm 1^{\circ}\mathrm{C}$	

The method of testing was to strain a specimen by repeated increments of about 1.5 per cent, alternately at -195° C and at a higher temperature, the load being completely removed between increments. The effect of temperature on the deformation was determined by comparing the flow stress at the end of one increment with that at the beginning of the next.

RESULTS

Two series of stress-elongation curves for unirradiated and irradiated copper are shown in Figs. 1 and 2 respectively. The curve for unirradiated metal indicates a completely reversible change in flow stress each time the temperature is changed. Irradiated metal, however, shows irreversible effects at low extensions. A large yield drop occurs on testing at the higher temperature after deformation at the lower, and there is an abnormally high initial rate of work hardening on subsequent retesting at the lower

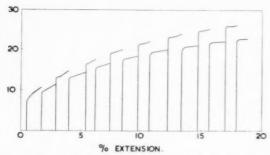


Fig. 1. Stress–strain curve of an unirradiated polycrystalline copper specimen tested alternately at -195° and 20°C.

temperature. These effects diminish as the deformation proceeds, and after about 15 per cent extension the change in flow stress is reversible.

(a) Reversible changes in flow stress

1959

The ratio of flow stresses during temperature cycles between -195°C and 20°C for unirradiated and irradiated specimens are shown in Fig. 3, where the ratios on changing from low to high temperature and vice versa are plotted separately. After between 10 and 15 per cent extension the ratio of flow stresses is almost independent of strain and the same values are obtained from low to high temperature transitions as from those in the reverse direction. This constant value of the ratio of the flow stresses was taken to be the reversible change in flow stress with temperature, and was measured in a series of experiments between -195°C and a number of temperatures between -160°C and 100°C, for both irradiated and unirradiated specimens. Fig. 4 reveals that the flow stress of irradiated copper is only very slightly more temperature dependent than that of unirradiated metal.

After irradiation, however, the temperature dependence of the flow stress determined in this way is considerably less than the temperature dependence

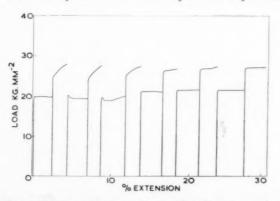


Fig. 2. Stress–strain curve of an irradiated copper specimen tested alternately at 20° and $-195^\circ\mathrm{C}$ showing the work softening phenomenon.

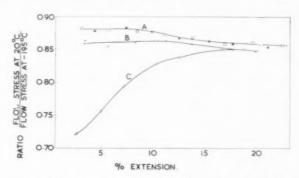


Fig. 3. The ratio (flow stress at 20° C)/(flow stress at -195° C) obtained on repeated testing of; A, unirradiated copper cycled from 20° to -195° C; B, irradiated copper, cycled from 20° to -195° C; and C, irradiated copper, cycled from -195° to 20° C.

of the yield stress, curve c, Fig. 4, as measured in normal tensile tests. This is discussed more fully later.

(b) Irreversible changes in flow stress

Non-reversible effects occur in the early stages of the deformation of irradiated specimens. After preliminary deformation at $-195^{\circ}\mathrm{C}$ there is a large yield point on re-testing at higher temperatures (Fig. 2). The effect appears to be largely independent of the temperature of the second deformation, provided it is higher than about $-100^{\circ}\mathrm{C}$. On retesting at $-195^{\circ}\mathrm{C}$ yield occurred at a lower stress than that reached at the end of the previous deformation at $-195^{\circ}\mathrm{C}$. After the yield the rate of work hardening was rapid until the original stress level had

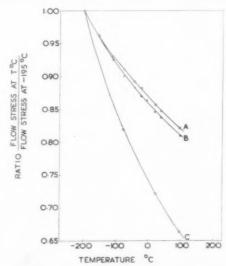


Fig. 4. Temperature dependence of flow stress in; A, unir-radiated copper; B, irradiated copper after large deformation (>20 per cent ext.); and C, the yield stress of irradiated copper.

been reached, when a fairly abrupt change in slope occurred to the "normal" rate of work hardening. These effects were observable only during the early stages of the deformation; after $10{\text -}15$ per cent extension the behaviour on changing the temperature became entirely reversible. Yield drop phenomena were also observed on temperature cycling tests between $-78\,^{\circ}\text{C}$ and $20\,^{\circ}\text{C}$, and also between $20\,^{\circ}\text{C}$ and $114\,^{\circ}\text{C}$.

Experiments were made to determine whether the deformation during the vield drop was distributed uniformly throughout the specimen, or was concentrated in one or two regions, as in a Lüders band. A specimen with scribed markings every 2 mm along the gauge length was tested at -195°C; the extension was fairly uniformly distributed along the specimen. Subsequent testing at room temperature produced a large vield drop and measurements on the specimen revealed that the deformation was localized into two regions, Fig. 5. The stress-strain curve was then taken at -195°C, and the specimen re-measured. The results, Fig. 5, show that the subsequent extension at -195°C was entirely in the work softened parts of the specimen. If the short length of the "active" region is allowed for, the rate of work hardening becomes normal. Hence the apparently rapid rate of hardening on re-testing at -195°C is due entirely to the short length of the specimen undergoing elongation.

The further experiment was made of re-testing the specimen at -195° C during the normal hardening and re-measuring. The deformation occurred uniformly through the specimen.

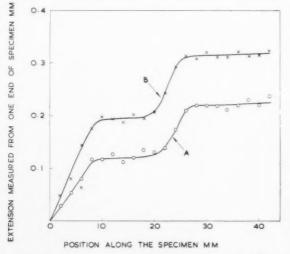


Fig. 5. The extension as a function of the distance along the specimen; A, after work softening at $20^{\circ}\mathrm{C}$ following deformation at $-195^{\circ}\mathrm{C}$; and B, after subsequent deformation at $-195^{\circ}\mathrm{C}$.

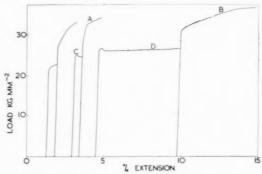


Fig. 6. Stress–strain curve of an irradiated specimen cycled between 20° and -195° C, showing the effect of the amount of deformation at 20° C on the subsequent curve at -195° C.

The slope of the rapid hardening region on retesting at -195°C, after preliminary deformation at a higher temperature, is controlled by the amount of deformation at the high temperature. This is demonstrated in Fig. 6 during cycles between 20°C and -195°C. Curve A following a short deformation (0.5 per cent) at 20°C shows a very rapid actual rate of hardening whereas in curve B, taken after a large extension (5.3 per cent) at 20°C, the rate of hardening is much smaller. This behaviour is a consequence of the localised nature of the deformation at the higher temperature; after a small extension only a small region has been softened and consequently on retesting at -195°C the active gauge length is very short during the initial period. A large extension, however, produces a long softened region which deforms on subsequent testing at -195°C. The ratio of the amount of extension in curves D and C in Fig. 6 is 10: 1 and the ratio of the slopes of the rapid work hardening regions in curves A and B is in excellent agreement at 9.4:1.

19

All experiments in which the specimen was first tested at temperatures above $-100^{\circ}\mathrm{C}$ and then retested at $-195^{\circ}\mathrm{C}$ showed the same initial region of rapid work hardening at $-195^{\circ}\mathrm{C}$; followed by a lower, normal rate of hardening. Microscopic examination revealed that both the initial high temperature deformation and the subsequent deformation at $-195^{\circ}\mathrm{C}$ were distributed uniformly throughout the specimen, in marked contrast to the localized deformation at the higher temperature which occurs during work softening. The yield stress on first deformation at the high temperature is also lower than the stress at which work softening occurs at this temperature after preliminary deformation at $-195^{\circ}\mathrm{C}$, Fig. 7.

The effect of irradiation on the properties of metals has sometimes been compared with that of solid solution alloying, and the analogy between irradiated

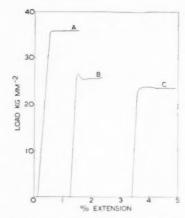


Fig. 7. Stress–strain curves of irradiated specimens; A, at $-195\,^{\circ}\mathrm{C};$ B, on subsequent deformation at $20\,^{\circ}\mathrm{C};$ and C, on initial testing at $20\,^{\circ}\mathrm{C}.$

copper and alpha brass has been quoted. Some tests were made, therefore, on 70/30 alpha brass wires to determine whether this also showed the work softening effects found in irradiated copper. The results, Fig. 8, are essentially similar to those of unirradiated copper, no yield phenomena being observed near the start of the deformation. In this respect, therefore, the properties of irradiated copper and alpha brass are quite different.

(c) Annealing behaviour

VOL.

1959

The effect of various annealing treatments on the irreversible yield phenomena has been measured. Fig. 9 shows a series of tests at 20°C and -195°C on an irradiated specimen after annealing at 330°C for 60 min. Two features are immediately apparent; firstly all signs of yield phenomena have disappeared, and secondly the yield stress is still high (24.4 kg mm²; cf. 7.0 kg mm² for unirradiated specimens). The annealing treatment has removed the strongly tem-

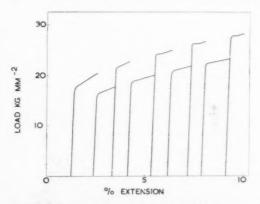


Fig. 8. Stress-strain curve of 70/30 alpha brass cycled between -195° and 20° C.

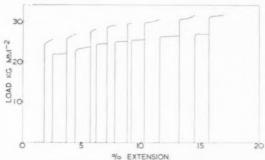


Fig. 9. Stress–strain curve of irradiated copper cycled between -195° and 20° after annealing at $330^\circ\mathrm{C}$ for 60 min.

perature dependent process responsible for the yield drop effects, but has not removed the majority of the irradiation hardening. The effect of other annealing treatments on the ratio of flow stresses on re-testing at $20^{\circ}\mathrm{C}$, after initial deformation at $-195^{\circ}\mathrm{C}$, is plotted against the yield stress at $-195^{\circ}\mathrm{C}$ in Fig. 10. The results indicate that the large temperature sensitivity of the yield stress is almost completely removed by mild annealing treatments which do not greatly affect the general level of the stress–strain curve. The majority of the hardening is removed during 60 min anneals only at temperatures near $400^{\circ}\mathrm{C}$.

(d) Behaviour of single crystal specimens

To determine if these effects were confined to polycrystalline specimens, temperature cycling tests were made on irradiated copper single crystals between —195°C and 20°C after different amounts of irradiation. No yield points were observed on re-testing at 20°C until after about 10¹⁹ neutrons/cm². The characteristics of the yield drop are the same as in polycrystalline specimens, but the effect is smaller in magnitude than in polycrystalline material.

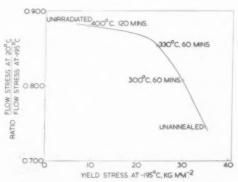


Fig. 10. Ratio (flow stress at 20°C)/(flow stress at -195°C) as a function of the yield stress after various annealing treatments.

DISCUSSION

The characteristics of the irreversible phenomena in irradiated polycrystalline copper when the temperature of deformation is changed are similar to those of "work softening" observed in aluminium by Cottrell and Stokes(2) and in copper by Adams and Cottrell. (4) The effect occurs only when the specimen is re-tested at a higher temperature and is accompanied by a Lüders band type of deformation in both cases. On re-testing at a lower temperature after work softening, an apparently high rate of work hardening is obtained initially due to the extension being confined to the work softened region. In general characteristics, therefore, work softening in irradiated copper and heavily cold worked aluminium are similar. They differ, however, in that in aluminium the effect occurs only after heavy plastic deformation, whereas in irradiated copper it is observed only in the early stages of deformation (up to ~12 per cent extension). The arguments of Cottrell and Stokes to demonstrate that work softening is not due to strain ageing phenomena, or to geometrical softening, apply with equal force in the case of irradiated copper, and it is concluded that a real softening of the material occurs.

The phenomenological cause of the effect is that the dislocation pattern produced on initial testing at —195°C is unstable on further deformation at higher temperatures and collapses with the formation of a yield point. The important problems are to decide what are the essential features of the low temperature deformation, and what is the nature of the collapse of the low temperature dislocation pattern. In the case of aluminium the obstacles are thought to be Lomer-Cottrell sessile dislocations, which hold up groups of glide dislocations, and Cottrell and Stokes attributed work softening to the dissociation of these obstacles. Recently, however, Seeger et al. (5) have shown that collapse of the dislocation pattern occurs by the glide dislocations bypassing the obstacles at the higher temperature, rather than by the dissociation of the latter. Work softening in aluminium occurs, therefore, only during the parabolic hardening stage of single crystals, when the steady pile-up of dislocations during linear hardening is being relieved by escape from the pile-up by slip on a second system.

This explanation cannot be immediately transferred to irradiated copper, since the mechanism of irradiation hardening is quite different from that of work hardening. Analysis of the shape of the stress–strain curve after irradiation (6,7) indicates that there are two main causes of irradiation hardening, dislocation hardening and lattice hardening. Dislocation harden-

ing is a measure of the difficulty of generating new dislocations and lattice hardening is a measure of the difficulty of continuing dislocation motion through the crystal lattice. With the grain size used in the present experiments the majority of the hardening is lattice hardening⁽⁷⁾ (~95%) and is very temperature dependent, (7) being much less at high temperatures than at low. Mild annealing treatments greatly reduce this high temperature sensitivity of the lattice hardening in copper(7) by producing a very much greater reduction at low testing temperatures than at high. It is considered that the lattice hardening must be due to obstacles of some kind introduced by the irradiation into the crystal lattice and that the passage of dislocations through or past these obstacles is a thermally activated process giving rise to a temperature dependent lattice hardening. For the present discussion it is not necessary to specify the nature of these obstacles.

During initial deformation at −195°C the obstacles offer a high resistance to dislocation movement and consequently dislocations will tend to pile up behind obstacles. This effect can be directly seen in lithium fluoride crystals(8) where the position of the dislocations can be revealed by etching. On releasing the load there is little reverse plasticity indicating that large scale running back of the dislocations does not occur. Similar behaviour is observed on unloading unirradiated copper single crystals(3) and the formation of short lengths of sessile dislocation during unloading has been suggested as the reason why the dislocation pile-ups do not relax. In the case of irradiated copper, however, the obstacles due to irradiation will prevent large scale relaxation. On retesting at 20°C deformation recommences when the stress is large enough to overcome the back stress due to the high density of dislocations built up at -195°C. Since the resistance offered by the obstacles is much less at 20°C than at -195°C, the dislocation distribution built up at -195°C will not be stable at 20°C and will collapse with the formation of a yield drop and the start of a Lüders band. In order to account for the low yield stress on subsequent retesting at -195°C, however, it is necessary to postulate a real softening of the metal during the high temperature deformation. This may occur by the by-passing of obstacles during the high temperature deformation as in the case of heavily deformed unirradiated metals, dislocations escaping from pile-ups in front of obstacles by crossslip on to neighbouring glide planes. Alternatively the softening may occur by the removal of some of the obstacles during the high temperature deformation. This is suggested by the observation that work

19

softening is associated with the high temperature sensitivity of the lattice hardening in that both are removed by mild annealing treatments which would remove only the smallest obstacles. The temperature sensitivity on retesting at -195°C after work softening at 20°C is also low suggesting that the smallest obstacles are not operating in this case either.

An electron microscope study of the slip line appearance after various deformation treatments would, in principle at least, determine which of these two mechanisms is operating.

ACKNOWLEDGMENTS

It is a pleasure to thank Dr. A. H. Cottrell and

Dr. H. M. Finniston for their interest and encouragement, and Mr. F. J. Minter for assistance with the experimental work.

REFERENCES

- M. J. Makin, J. Inst. Met. 86, 449, (1957-8).
- 2. A. H. COTTRELL and R. J. STOKES, Proc. Roy. Soc. A233, 17 (1955).
- M. J. Makin, Phil. Mag. 3, 287 (1958).
 M. A. Adams and A. H. Cottrell, Phil. Mag. 46, 1187 (1955).
- 5. A. SEEGER, J. DIEHL, S. MADER and M. REBSTOCK, Phil. Mag. 2, 323 (1957).
 6. M. A. Adams—private communication.
- 7. M. J. Makin-unpublished work.
- 8. A. D. Whapham-private communication.

PARTIALLY PINNED TILT BOUNDARIES*

T. VREELAND Jr.+

This paper presents the results of a theoretical study of the conditions under which small angle tilt boundaries in a crystal can be moved when subjected to a stress which does not produce general slip. The dislocations in the boundary are assumed to be partially pinned by Cottrell atmospheres, intersecting substructure, or precipitates along the dislocation lines. The results show that partially pinned dislocation boundaries may move at lower stresses than similarly pinned isolated dislocations if the density of pinned segments is sufficiently low. Stress concentrations at pinned segments on a small angle boundary are discussed. A "yield condition" for motion of certain partially pinned boundaries is described in which pinned dislocations are left behind when the boundary is moved.

JOINTS DE FLEXION PARTIELLEMENT ANCRES

L'auteur présente les résultats d'une étude théorique des conditions sous lesquelles des joints de flexion entre grains d'orientations voisines dans un cristal peuvent être déplacés lorsqu'ils sont soumis à une tension qui ne produit pas un glissement général. Il suppose que les dislocations dans les joints sont partiellement ancrées par des atmosphères de Cottrell interceptant les sous-structures ou les précipités le long des lignes de dislocation. Les résultats montrent que les limites de dislocations partiellement ancrées peuvent se déplacer à des tensions inférieures à celles des dislocations isolées fixées d'une manière similaire, si la densité des segments fixées sur un joint à angle faible. L'auteur discute les concentrations de tension sur des segments fixées ur un joint à angle faible. Il décrit une condition pour le mouvement de certaines limites partiellement fixées dans lesquelles les dislocations ancrées restent en arrière lorsque le joint se déplace.

TEILWEISE FESTGEHALTENE NEIGUNGSKORNGRENZEN

In dieser Arbeit wird untersucht, unter welchen Bedingungen eine Spannung, die noch kein allgemeines Fliessen hervorruft, zur Bewegung von Kleinwinkel-Neigungskorngrenzen führt. Es wird dabei angenommen, dass die Versetzungen in der Korngrenze durch Cottrell-Atmosphären, Schnittpunkte mit der Substruktur oder Ausscheidungen längs der Versetzungslinien teilweise festgehalten werden. Wie sich zeigt, können Korngrenzen aus teilweise festgehaltenen Versetzungen schon bei geringeren Spannungen wandern, als ähnlich festgehaltene isolierte Versetzungen, vorausgesetzt, dass die Dichte der festgehaltenen Segmente genügend gering ist. Die Spannungskonzentrationen an festgehaltenen Segmenten einer Kleinwinkelkorngrenze werden diskutiert. Für die Bewegung bestimmter teilweise festgehaltener Korngrenzen, bei der festgehaltene Versetzungen zurückgelassen werden, wird eine "Fliessbedingung" angegeben.

INTRODUCTION

Small angle tilt boundaries have been observed in many crystals. These boundaries are known to be made up of an array of dislocations which lie on different slip planes. In its simplest form, a tilt boundary is made up of edge dislocations, all of the same sign, as shown schematically in Fig. 1. The angle of tilt associated with this boundary is given by $\theta = |\mathbf{b}|/h_m$ where \mathbf{b} is the Burgers vector of the dislocations and h_m is their average spacing. The energy of a simple tilt boundary is minimum if the dislocations lie in a planar array and are equi-spaced. There is an abrupt change in the slope of the slip plane at the small angle boundary. This change in slope may be observed readily in zinc where a boundary intersects the cleavage (or slip) plane.

Tilt boundaries are observed in some crystals in the

as-grown condition. These boundaries may also be introduced into a crystal lattice by plastic deformation. One method of introducing boundaries by plastic

VO!

19

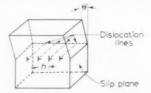


Fig. 1. Schematic drawing of a small angle tilt boundary.

deformation is to bend the crystal and then anneal it. Bending introduces an excess of dislocations of one sign, and annealing allows the dislocations to climb and move to the minimum energy configuration.

Small angle tilt boundaries in zinc single crystals have been observed to move through the crystal when an appropriate shear stress is applied. (1,2) The movement of a tilt boundary under the action of a shear stress, τ , is schematically illustrated in Fig. 2. The boundary moves in a direction which causes the applied

^{*} This research was supported by the Solid State Sciences Division, Air Force Office of Scientific Research, ARDC, Washington 25, D.C. under Contract No. AF18(600)-490 Project Designation R-335-10-6. Received May 5, 1958; revised version July 21, 1958.

[†] California Institute of Technology, Pasadena, California.

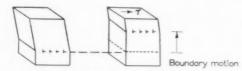


Fig. 2. Schematic drawing of a tilt boundary moved by an applied shear-stress.

stress to do positive work, i.e. the surface where τ is applied moves in the direction of the shear-stress. Bainbridge et al. (2) found that a thermal activation process is a major controlling feature of boundary motion in zine at temperatures in the range of $300^\circ - 400^\circ \text{C}$. An erratic, jerky boundary motion, frequently accompanied by a decrease in the angle of the boundary, has been observed at room temperature. (2) The boundaries occasionally refuse to move even though the load is continuously increased.

Experiments on crystals of C.P. zinc (99.999+% purity) performed at the California Institute of Technology have shown that:

(a) The shear stress required to move a small angle tilt boundary ($\theta=0.4$ to 2°) at room temperature is equal to or greater than the stress required to cause general slip in the crystal. Boundaries have been observed to remain stationary while as much as 30 per cent slip took place in the crystal.

1959

(b) Boundaries in annealed crystals are anchored where the dislocations intersect a free surface. In many cases the central portion of the tilt boundary moves while the ends remain fixed at the free surface. Removal of the surface material to a depth of approximately 200 μ eliminates the free surface anchoring. This effect may be caused by the anchoring action of impurities which segregate to the region where the boundary dislocations intersect the free surface. Such segregation has been observed by Maroun et al. (3)

(c) Microscopic observation of etched crystals of C.P. zinc indicate that precipitate particles lie along dislocation lines. These particles are believed to be a lead–zinc phase. (4) Such particles act as effective obstructions to the motion of dislocations.

These observations may be interpreted as follows: obstacles to the motion of dislocations exist in addition to the Peierls forces which resist the motion of a dislocation through a perfect lattice. Thermally activated atomic diffusion (at temperatures substantially above room temperature) permits the boundary dislocations to climb and pass obstacles, or to carry the obstacles with the boundary, so that boundaries remain intact as they are moved. When sufficient time is not available for substantial atomic diffusion to take place (at lower temperatures) dislocations cannot climb and obstacles cannot move with the boundary.

Therefore dislocations will be left behind as the boundary moves on, assuming that they cannot slip past or through the obstacles. When dislocations are left behind, i.e. removed from the boundary, the average dislocation spacing in the boundary is increased, so the boundary angle is decreased.

The theoretical work presented in this paper was stimulated by a desire to find the conditions under which a simple tilt boundary in a crystal can be moved at stress levels which do not produce general slip. The paper considers boundaries which are subjected to an applied stress, but are restrained from moving because some of the boundary dislocations are anchored or pinned. The pinning may result from precipitates along the dislocation lines, Cottrell atmospheres on the dislocations, intersecting substructure, or sessile dislocations. The boundary is assumed to consist of straight dislocations of infinite length when no external stress is acting.

Two types of pinned boundary are considered. First are those in which some of the dislocations are pinned along their entire length and the remainder of the dislocations are unpinned. The other type of pinned boundary contains dislocations which are pinned at discrete segments along their length. The conditions for the motion of such boundaries without the aid of atomic diffusion is investigated.

BOUNDARIES WITH FREE AND COMPLETELY PINNED DISLOCATIONS

The pinning of the dislocations in the boundary is assumed to be periodic such that every nth dislocation is pinned. This assumption is made for the purpose of simplifying the mathematical analysis, but the results may be extended to boundaries with completely pinned dislocations randomly distributed in the boundary. The dislocation spacing is designed as h, and the distance between pinned dislocations is denoted by d, as shown in Fig. 3. Thus d=nh. All of the dislocations lie in the xz plane when no external stress is acting. An applied shear stress, τ_a , causes the unpinned dislocations to move out of the plane as shown.

Equations are obtained which give the equilibrium shape of the boundary in an isotropic crystal under an applied stress. The total stress on the pinned dislocations is found. The coordinate system is taken

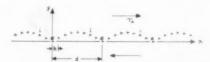


Fig. 3. Boundary of free and completely pinned dislocations with an applied stress acting.

as shown in Fig. 3 with the origin at one of the pinned dislocations. The equilibrium displacement, y_j , of an unpinned dislocation at x_j is determined by the condition that the stress at (x_j, y_j) , produced by all other dislocations, the applied stress, and the Peierls stress which opposes the motion of an unpinned dislocation through the lattice, must be equal to zero. The stress at (x_j, y_j) , due to the planar array of dislocations at $y = y_i$, $x = x_i \pm md$, $m = 1, 2, \ldots$, has been shown by Burgers⁽⁵⁾ to be

$$\begin{split} \tau_{x_i y_j} &= \frac{Gb}{2\pi(1-v)} \frac{\pi^2}{d^2} (y_j - y_i) \\ &\times \frac{\cosh \frac{2\pi(y_j - y_i)}{d} \cos \frac{2\pi(x_j - x_i)}{d} - 1}{2 \left\{ \sinh^2 \frac{\pi(y_j - y_i)}{d} + \sin^2 \frac{\pi(x_j - x_i)}{d} \right\}^2} \end{split}$$

where G = shear modulus, $\nu =$ Poisson's ratio, and b = magnitude of the Burgers vector.

The half angle relationships for the hyperbolic sine and the sine terms in the above equation may be used, giving the more convenient form

$$\tau_{x_{j}y_{j}} = \frac{\pi G b}{4(1-\nu)} \frac{y_{j}-y_{i}}{d^{2}} (-a_{ij}), \tag{1}$$

where

$$a_{ij} = 4\frac{1-\cosh\frac{2\pi(y_j-y_i)}{d}\cos\frac{2\pi}{n}\left(j-i\right)}{\left[\cosh\frac{2\pi(y_j-y_i)}{d}-\cos\frac{2\pi}{n}\left(j-i\right)\right]^2}$$

and $x_i = ih$

The stress at (x_j, y_j) , due to the planar array of dislocations at $y_j, x_j \pm md, m = 1, 2, \ldots$, is zero, by equation 1. The equilibrium equation for the jth dislocation $(j \neq 0)$ then becomes

$$(au_a - au_c) + \sum\limits_{\substack{i=0\ i \neq j}}^{n-1} rac{\pi G b}{4(1-
u)} rac{y_i - y_i}{d^2} (-a_{ij}) = 0,$$

OF

$$1 = A \sum_{i=0}^{n-1} \frac{y_i - y_i}{d} a_{ij} = \sum_{i=0}^{n-1} (z_i - z_i) a_{ij}, \quad (2)$$

where

$$A = \frac{\pi G b}{4(1-\nu)\left(\tau_a - \tau_c\right) d}\,, \quad z = A\,\frac{y}{d},$$

and τ_e = the stress opposing the motion of an unpinned dislocation through the lattice.

The stress required to hold a pinned dislocation, τ_0 , appears in the equilibrium equation for the dis-

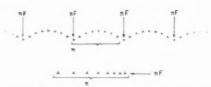


Fig. 4. Equal stress concentrations at obstructions in a partially pinned boundary and at the head of a pile-up of n dislocations. F = force acting on each dislocation.

location j = 0, which may be written as follows:

$$\frac{\tau_0}{\tau_a - \tau_c} = 1 + \sum_{i=1}^{n-1} z_i a_{ij}.$$
 (3)

The stress ratio $\tau_0/(\tau_a - \tau_c)$ may be evaluated by writing equation (2) in the form

$$1 = z_{i}a_{0j} + \sum_{\substack{i=1\\i \neq i}}^{n-1} (z_{i} - z_{i})a_{ij}$$

and summing this equation over j, which gives the following relation:

$$n-1 = \sum_{j=1}^{n} z_j a_{0j}, \tag{4}$$

since $a_{ij} = a_{ji}$. Combining equations (3) and (4) gives

$$\tau_0/(\tau_a - \tau_c) = n = d/h. \tag{5}$$

Equation (5) is valid for non-isotropic as well as isotropic crystals.

The pinned dislocations are therefore subjected to a stress n times $(\tau_a - \tau_c)$. This result is analogous to the stress concentration at the head of an array of n dislocations on one slip plane obstructed by a pinned dislocation, where $\tau_0/(\tau_a - \tau_c) = n$, as shown in Fig. 4.

The equilibrium shape of the boundary may be obtained by solving for the values of z_j , in equation (2), and by using the appropriate values of A and d to give y_i . For displacements of the boundary such that

$$\left| \frac{y_{j\pm 1} - y_j}{h} \right| \ll 1,$$

$$a_{ij} \simeq \frac{4}{1 - \cos\frac{2\pi}{n}(j-i)} \tag{6}$$

and equation (2) reduces to a set of linear equations when all possible values of j are taken. These equations have been solved for various values of n. The results are plotted in Fig. 5 which shows values of $z \operatorname{vs} x/d$.

The displacements, y_j , of the dislocations increase as τ_a is increased. When they become sufficiently large that $|(y_{j+1}-y_j)/h|$ approaches unity, the

approximation given by equation (6) breaks down. For a given value of the applied stress the largest value of $|(y_{j\pm 1}-y_j)/h|$ occurs for j=0 and is $y_i/h=y_{n-1}/h$. A second order approximation for the shape of the displaced boundary may be obtained by employing the exact expression, equation (2), for the coefficient $a_{1,0}=a_{n-1,0}$ while retaining the approximate values of the remainder of the coefficients

This may be done in the following manner, and equation (2) for the case j = 1 is rewritten in the form

$$1 + \sum_{i=2}^{n-1} (z_i - z_1) a_{i1} = A \left(\frac{y_1}{d} \right) a_{10}. \tag{7}$$

The first term on the left of equation (7) represents the force which the applied stress exerts on the dislocations j = 1. The sum comprising the second term

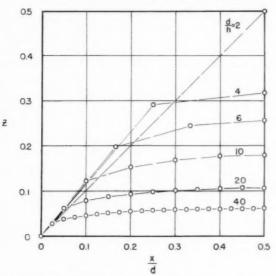


Fig. 5. Dimensionless dislocation displacement, Z, for various values of n=d/h.

represents the force which the dislocations j=2, 3, . . . , n-2, exert on the dislocations j=1. This is evaluated by employing the values of (z_i-z_1) given in Fig. 5 which were obtained from the first order approximate solution.

The two forces represented by the terms on the left side of equation (7) both tend to move the dislocations j=1 away from the pinned dislocations, j=0. They are balanced by the attractive force between the pinned dislocations, j=0 and the dislocations j=1 represented by the term on the right side of equation (7). When the exact expression for a_{10} is employed it may be seen that this attractive force exhibits a maximum value at some critical value of y_1/h . That is the quantity $(y_1/h)a_{10}$ exhibits a maximum value. Since the left side of equation (7)

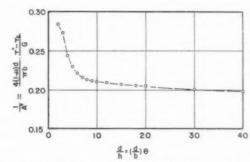


Fig. 6. Critical stress as a function of the boundary angle for a boundary with a given spacing between pinned dislocations.

is known, the equation may be solved for the critical value of $A=A^*$ corresponding to the maximum value of $(y_1/h)a_{10}$. The associated critical applied stress

$$\tau^* = \tau_c + \frac{\pi G b}{4(1-v)d} \frac{1}{A^*} \tag{8}$$

is the stress which will cause the tilt boundary to move away from the pinned dislocations.

The critical values of $1/A^*$ and h/A^*d are plotted in Figs. 6 and 7 as a function of d/h=n. Fig. 6 shows the effect of varying the boundary angle θ for boundaries which are pinned at intervals of a constant spacing, d. The critical stress decreases when θ is increased. Fig. 7 shows the effect of varying the pinned spacing d for a boundary of a given angle, θ . The critical stress decreases with an increase in d. The critical stress is calculated below for a 1° tilt boundary with d/h=20, in alpha iron. The elastic constants are taken as follows:

$$G = 11.6 \times 10^6 \, \text{lb/in}^2$$
, $\nu = 0.3$,

then
$$(\tau^* - \tau_c)/G = 2 \times 10^{-4}$$
,

or $\tau^* - \tau_0 = 2320 \text{ lb/in}^2$. A quantitative estimate for the critical stress in a zinc crystal is not possible by the above analysis, because the approximation of isotropic elasticity is a poor approximation for zinc.

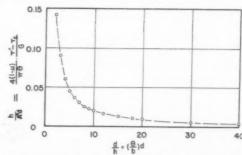


Fig. 7. Critical stress as a function of the spacing between pinned dislocations for a boundary of given angle, θ .

VOL. 7 1959



Fig. 8. Schematic drawing of a partially pinned dislocation under an applied stress.

The above analysis may be used to give an indication of the behavior of boundaries with non-equispaced pinned dislocations, since a dislocation in a boundary is influenced considerably more by the position of its nearest neighbors than by the position of dislocations further removed. The maximum stress concentration will occur at the pinned dislocation which has the largest number of free dislocations adjacent to it. The critical stress to move a group of free dislocations away from pinned dislocations will be approximately that given in Figs. 6 and 7. Large groups of free dislocations may move off while smaller groups of free dislocations with a higher critical stress remain behind. This may lead to the behavior observed in zinc where a single boundary splits into a pair of boundaries, one which is stationary and one which moves off under an applied stress.

The critical stresses calculated above may be compared to the stress required to pull a single dislocation out of an infinite wall. The maximum value of the critical stress calculated above occurs for the case n=2, in which every other dislocation is pinned. The critical stress ratio

$$(\tau^* - \tau_c)/G = 0.143 \ \pi b/4(1 - \nu)h$$

causes the free dislocations to move off. The original boundary then becomes two boundaries each with one half of the original boundary angle. The critical stress ratio required to pull a single dislocation out of a boundary has been calculated by Cottrell. (6) and in the notation of this paper is given by

$$(\tau^* - \tau_c)/G = 0.223\pi b/4(1 - \nu)h$$

It is evident from this calculation that a group of unpinned dislocations may be moved from a boundary at a lower stress level than that required to pull a single unpinned dislocation from a boundary.

BOUNDARIES CONTAINING PARTIALLY PINNED DISLOCATIONS

The individual dislocations in a boundary may be pinned at segments along their length, and be free to bow out on their slip plane between the pinned segments as shown schematically in Fig. 8.

Dislocations may pass obstacles which pin segments of the dislocation line by bowing around the obstacles and leaving unslipped regions around them as proposed by Orowan. (7) Stresses of the order of magnitude of Gb/L_i are required over the length L_i for such a process. Boundary motion in zinc occurs at stress levels of approximately 50 lb/in². With $G = 5.5 \times 10^6$ lb/in², a value of $L_i \cong 10^5 b$ is required. For a 1° tilt boundary, $h \simeq 57b$. Therefore dislocation lengths much greater than h must be unpinned before the bowing mechanism can take place. It is probable that the concentrated stress at the obstacle is sufficient to overcome the restraint on the dislocation before the unpinned length approaches 105b. Therefore we assume that pinned dislocations in zinc will move when the concentrated stress at the pinned segments becomes great enough to unpin the segments.

The stress concentration at the *i*th pinned segment along a dislocation may be found by a virtual work consideration. Let the entire dislocation be displaced a distance δ_y . The work done by the applied force and the Peierls force on the segment L_i is $(\tau_a - \tau_c)bL_i\delta_y$ where L_i is the total length of that portion of the dislocation that is restrained by the *i*th pinned segment. The average stress, τ_i , on the pinned segment opposing the motion of the dislocation does work $-\tau_i bl_i\delta_y$, where l_i is the length of the pinned segment. The net work done must be equal to zero for a system in equilibrium, so

or
$$(\tau_a - \tau_c)bl_i\delta_y - \tau_ibL_i\delta_y = 0$$

$$\tau_i/(\tau_a - \tau_c) = L_i/l_i$$
(9)

Equation 9 may be applied to partially pinned dislocations in boundaries where L_i must include that length of dislocations on adjacent slip planes which is restrained by the ith pinned segment. The quantity $\tau_i/(\tau_a-\tau_c)$ may therefore be different for pinned segments in boundaries as compared with similar segments on isolated dislocations.

A boundary with pinned segments distributed with a uniform spacing, L_0 , $(L_0 > h)$ is shown in Fig. 9. The length of dislocation line restrained by the ith

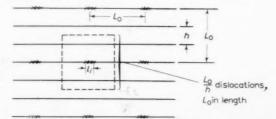


Fig. 9. Boundary with pinned segments distributed with a uniform spacing, L₀.

7 19 pinned segment is given by $L_i \cong L_0^2/h$. The concentrated stress at the *i*th pinned segment is then

$$\tau_i/(\tau_a - \tau_c) \cong L_0^2/l_i h \tag{10}$$

Combining equations (9) and (10) gives the ratio of the concentrated stress at a pinned segment in a boundary to that in a similarly pinned isolated dislocation, namely,

$$\frac{(\tau_i)_{\rm Boundary\ Dislocation}}{(\tau_i)_{\rm Isolated\ Dislocation}} = \frac{L_0}{h}\,,\quad (L_0>h). \eqno(11)$$

Boundaries may be moved before all of the dislocations are unpinned, as discussed above in the case of boundaries with free and completely pinned dislocations. The critical stress to move a partially pinned boundary, leaving some dislocations behind, is difficult to estimate. However, it is clear that lower critical stresses result when only segments of dislocations are pinned.

The relationships developed above are applied to three cases of pinned isolated dislocations and similarly pinned boundaries below:

Case 1. $L_0 \cong h$. The stress concentration at pinned segments is essentially the same for isolated dislocations and for boundary dislocations. Boundaries and isolated dislocations will therefore move at approximately the same stress.

VOL.

1959

Case 2. $L_0 > h$. Boundaries will move at a lower applied stress than isolated dislocations because of the higher concentrated stress at the pinned segments in the boundary.

Case 3. $L_0 < h$ (Dense pinning). A boundary dislocation which bows out is restrained by pinned segments above and below, so that isolated dislocations without such restraint should move at a lower applied stress.

Some of the isolated dislocations which are moved in such crystals will pile up against the boundary dislocations. The stress required to move a boundary then depends upon the number and distributions of dislocations which are piled up against the boundary, as well as the limiting strength of the pinning.

Experimental observation of the motion of boundaries in annealed zinc crystals have shown that boundaries move at stresses approximately equal to the stress required to cause general slip. (1,2) The actual force on the boundary dislocations is not known in these experiments, because the number and distribution of dislocations which pile up on the boundary before it moves is unknown. The actual

force on the dislocations in a boundary must be known before experimental observations can be compared with theory. Experiments on crystals which do not exhibit general slip at stress levels which produce boundary motion are therefore of considerable interest. The considerations discussed above indicate that such crystals may be grown from highly zone refined zinc in which the spacing of pinned segments is greater than the spacing of dislocations in the boundary.

CONCLUSIONS

The results of the theoretical analysis indicate that:

- (1) The behavior of a boundary when it is subjected to an applied stress is strongly influenced by the density and distribution of pinned segments along dislocations in the boundary.
- (2) A stress concentration exists at the pinned segments due to the fact that these segments obstruct the motion of the entire length of dislocation. Unpinned dislocations which are held in a boundary by their attraction to the pinned dislocations contribute to the stress concentration.
- (3) Significantly different stress concentrations at similarly pinned segments in isolated dislocations and in boundary dislocations may exist, depending upon the density of pinned segments. The critical stress required to move a small angle tilt boundary may be decreased by reducing the density of pinned segments along the dislocations. Boundary motion will occur at stress levels which do not produce general slip when the spacing of pinned segments is greater than the spacing of dislocations in the boundary.

ACKNOWLEDGMENTS

The author is indebted to Professors D. S. Clark and D. S. Wood of the California Institute of Technology for their help in the preparation of this manuscript, and for their encouragement during the course of the work.

REFERENCES

- C. H. Li, E. H. Edwards, J. Washburn and E. R. Parker, Acta Met. 1, 223 (1953).
- D. W. Bainbridge, C. H. Li and E. H. Edwards, Acta Met. 2, 322 (1954).
- A. T. Maroun, S. S. Sheinin and A. Rosenberg, Acta Met. 5, 117 (1957).
- 4. I. S. Servi, M. Stern and W. W. Webb. Private communication.
- J. M. Burgers, Proc. Kon. Ned. Akad. Wet. 42, 293 (1939).
 A. H. Cottrell, Symposium on Plastic Deformation of Crystalline Solids. Mellon Institute, Pittsburgh, 60 (1950).
- Crystalline Solids. Mellon Institute, Pittsburgh, 60 (1950).
 E. Orowan, Symposium on Internal Stresses p. 451.
 Institute of Metals, London (1947).

MECHANICAL PROPERTIES OF IRON AND SOME IRON ALLOYS WHILE UNDERGOING ALLOTROPIC TRANSFORMATION*

M. DE JONG and G. W. RATHENAU†

The plasticity during the allotropic transformation of pure iron, Fe + 0.008 wt % N and Fe + 0.2 wt % C has been investigated. This plasticity proves to be no kind of creep. The elongation is a linear function of the applied stress, when the crystals of the new phase grow in arbitrary directions. The external stress works upon a material with vanishing yield point. The elongation for zero external stress is $(1/3)(\Delta V/V)$ for iron $(\Delta V/V)$: relative difference of specific volumes).

When transforming pure coarse grained iron in a steep gradient of temperature along the axis of the specimen, the maximum change of length for zero external stress is $\Delta V/V$. For the $\gamma \to \alpha$ transformation no influence of stress on the maximum change of length is observed.

The results are discussed by assuming a tendency for the mean macroscopic dilatation to be zero along the phase boundary, as in the case of diffusionless transformations.

QUELQUES PROPRIETES MECANIQUES DU FER ET DE QUELQUES ALLIAGES DU FER PENDANT LA TRANSFORMATION ALLOTROPIQUE

Les auteurs étudient la plasticité pendant la transformation du fer pur, du Fe + 0,008% N et Fe + 0,2% C. Ils montrent qu'il ne s'agit pas d'une espèce de fluage. L'élongation est une fonction linéaire de la tension appliquée lorsque les cristaux de la nouvelle phase croissent dans une direction arbitraire. La tension extérieure agit sur un matériau avec un yield point voisin de zéro. L'élongation pour une tension extérieure nulle est 1/3 ($\Delta V/V$).

Au cours de la transformation du fer pur à gros grains dans un raide gradient de température le long de l'axe de l'échantillon, la variation maximum de la longueur pour une tension extérieure nulle est de $\Delta V/V$. Pour la transformation $\gamma \to \alpha$, les auteurs n'observent aucune influence de la tension sur la variation maximum de la longueur.

Ils interprétent les résultats en admettant une tendance à éviter le glissement sur des grandes distances le long de chaque plan du réseau, comme dans le cas des transformations dans diffusion.

MECHANISCHE EIGENSCHAFTEN VON EISEN UND EINIGEN EISENLEGIERUNGEN BEIM ABLAUF EINER ALLOTROPEN UMWANDLUNG

Das plastische Verhalten von reinem Eisen, Fe + 0,008 Gewichts-% N und Fe + 0,2 Gewichts-% C während des Ablaufs einer allotropen Umwandlung wurde untersucht. Dies Verhalten ist keine Art von Kriechen. Die Längenänderung ist eine lineare Funktion der angelegten Spannung, wenn die Kristalle der neuen Phase in beliebigen Richtungen wachsen. Die äussere Spannung greift an einem Material an, dessen Fliessgrenze verschwindet. Bei Verschwinden der äusseren Spannung beträgt die Längenänderung (1/3) ($\Delta V/V$).

Verläuft die Umwandlung bei reinem grobkörnigem Eisen in einem steilen Temperaturgradienten längs der Probenachse, dann ist bei Verschwinden der äusseren Spannung die maximale Längenänderung $\Delta V/V$. Für die $\gamma \to \alpha$ -Umwandlung liess sich kein Einfluss der Spannung auf die maximale Längenänderung beobachten.

Die Ergebnisse werden auf Grund der Annahme diskutiert, dass wie im Fall diffusionsloser Umwandlungen Gleiten über grosse Entfernungen entlang jeder Gitterebene nach Möglichkeit vermieden wied.

1. INTRODUCTION

It has been known for many years that some metallic materials are mechanically weak while undergoing allotropic transformations.^(1,2,3) We measured the changes of length of specimens of pure iron, of iron

containing traces of nitrogen and of an iron–carbon alloy (0.2 wt % C) while transforming under different external loads. Before describing this work it seems worth-while to survey some possible explanations of the mechanical weakness during transformation.

This weakness may be due to some kind of creep at the phase boundary. It will however be shown in the following account that the elongations measured for iron do not depend on the rate of transformation. The same has been found recently for the transformation of cobalt.⁽⁴⁾

Measurements by Brandsma and Lips⁽⁵⁾ indicate

^{*} This work is part of the research program of the "Stichting voor Fundamenteel Onderzoek der Materie (F.O.M.)" and was made possible by a financial support from the "Nederlandse Organisatie voor Zuiver Wetenschappelijk Onderzoek (Z.W.O.)" and the "Nederlandse Centrale Organisatie voor Toegepast Natuurwetenschappelijk Onderzoek (T.N.O.)".

Received June 17, 1958

[†] Natuurkundig Laboratorium, Universiteit van Amsterdam, Amsterdam.

mechanical weakness to occur also during recrystallization without phase transformations. This may be due to the formation of active Frank-Read sources during the rearrangement of the dislocation network. A similar explanation might hold for allotropic transformations.

A more specific explanation is based on the difference in density of the parent and of the new phase. Owing to this difference, internal stresses are thought to occur during transformation. The material yields to the superimposed external stress at a lower value because of the pre-existing internal stresses.

Another explanation is as follows. During transformation, especially in the martensitic case, out of the possible modes of transformation those are favoured which allow the largest elongation in the direction of the external stress. Examples of this have been given for the transformation of NiFe, (3) while the more clearly defined example of InTl has been dealt with by Burkart and Read. (6)

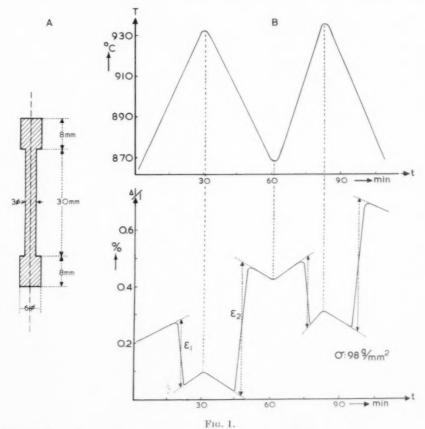
VOL.

1959

2. EXPERIMENTAL

The pure iron and an iron–carbon alloy (0.2 wt $^{\circ}$ / $_{\circ}$ of C) were obtained through the courtesy of Professor J. D. Fast, Eindhoven. (7)

The specimens were machined from drawn wires. After this the pure iron samples were recrystallized and decarburized 6 hr in an atmosphere of moist purified hydrogen at 870°C. The iron–carbon specimens were annealed 6 hr at 670°C in vacuum ($\leq 10^{-5}$ mm Hg). No indication of decarburization has been observed microscopically after all the experiments. The form of the specimens is shown in Fig. 1A. The change of length along the axis of the specimen was measured in an extensometer, functioning by the use of mechanical levers and an optical system. The total magnification was $\times 250$. The temperature at the middle and at the ends of the specimen was measured with chromel–alumel thermocouples, and at the middle was automatically recorded.



A: The shape of the specimen.

B: Change of length of a polycrystalline iron specimen containing 0.008 wt % N, while undergoing the $\alpha \rightarrow \gamma$ and the reverse transformation under a stress $\sigma = 98 \, \mathrm{g/mm^2}$. Vacuum: $< 10^{-5} \, \mathrm{mm} \, \mathrm{Hg}$; Temperature gradient along axis of specimen: $< 1^{\circ} \, \mathrm{C/cm}$; Grain size: about 100 grains per cross-section. To arrive at the elongations ε_1 and ε_2 the continuous change of length at both sides of the transformation temperature, due to thermal expansion and creep, has been extrapolated as shown by the dotted lines in the figure.

3. EXPERIMENTS ON IRON + 0.008 wt % N

The reproducibility of the measurements on pure iron was poor. Therefore at first we shall discuss experiments on some iron alloys which were reproducible. In contrast to the pure iron samples, these alloys were relatively fine grained in the α -phase and probably also in the γ -phase. The pure iron specimens had only a few crystals on the cross-sectional area of the specimen. (8) X-ray measurements in the α -phase gave no indication of a preferred orientation of the fine grained material.

In this section we shall deal with very lightly alloyed iron, while in the next section we shall describe measurements on an iron + 0.2 wt % C alloy. Small amounts of nitrogen were introduced by heating in a mixture of $\rm H_2$ and $\rm N_2$ in the γ -phase. The loaded specimens were only heat treated in vacuo to prevent loss of nitrogen. Reproducible results were obtained with amounts of 0.008 wt % N. The number of crystals in the α -phase per cross-sectional area then was about 100.

The elongation due to transformation under stress is represented in Fig. 1B. The effects due to the $\alpha \to \gamma$ transformation (ϵ_1) and the $\gamma \to \alpha$ transformation (ϵ_2) are different. These elongations are partly due to the difference in specific volume of the two phases, partly to the mechanical weakness under consideration. The values ϵ_1 , ϵ_2 were reproducible to ± 0.02 per cent.

An iron alloy containing small amounts both of nitrogen and aluminium (0.008 wt % N; 0.03–0.1 wt % Al) again had a relatively small grain size (\sim 35 grains per cross-section) in the α -phase and gave reproducible results. It was used to investigate the influence of the rate of heating and cooling and of a steep temperature gradient over the specimen (Table 1). No influence of a steep temperature gradient was found. Also the rate of heating and cooling did not affect the measurements. This is in accord with the

Table 1. Elongation during transformation of iron containing small amounts of N and Al for different rates of heating and cooling and for different values of the temperature gradient. Stress: $\sigma = 160 \, \mathrm{g/mm^2}$; Grain size: 35 grains per cross sectional area; Atmosphere: oxygen-free mixture of 75 % $\rm H_2 + 25$ % N_s, saturated with water at room temperature.

$\varepsilon_1(\alpha \to \gamma)$ (per cent)	$\begin{array}{c} \varepsilon_2(\gamma \to \alpha) \\ (\text{per cent})) \end{array}$	$\frac{\varepsilon_1 + \varepsilon_2}{(\text{per cent})}$	Rate of temp. change (°C/min)	Temp. gradient (°C/cm)
-0.20	0.53	0.33	7	< 1/3
-0.23	0.52	0.29	5	< 1/3
-0.23	0.55	0.32	3	< 1/3
-0.23	0.54	0.31	1	< 1/3
-0.22	0.53	0.31	3	5

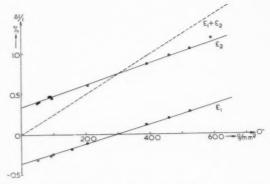


Fig. 2. Changes of length of polycrystalline iron specimens containing 0.008 wt % N as a function of stress while undergoing respectively the $\alpha \to \gamma$ and $\gamma \to \alpha$ transformations. Elongations: ε_1 and ε_2 respectively. The elongation $\varepsilon_1 + \varepsilon_2$ shown by the dotted line corresponds to a complete temperature cycle. Experimental conditions as in Fig. 1.

measurements on the iron–carbon alloy described in Section 4 and with measurements on cobalt by Bibring and Sebilleau. (4) Therefore the effect under consideration is not a time-dependent phenomenon, i.e. not a special kind of creep.

Measurements as shown in Fig. 1B result in the curves of Fig. 2 for the elongations ε_1 and ε_2 and the resultant elongation $\varepsilon_1 + \varepsilon_2$ as a function of stress. The values of ε_1 and ε_2 extrapolated to zero external stress are in good agreement with the value arrived at by X-ray measurement⁽⁹⁾ of the lattice constants near the transformation point $(\Delta l/l = 0.354~{\rm per~cent})$. It is interesting to note that $\varepsilon_1 + \varepsilon_2$ plotted vs. stress is a line through the origin.

19

4. EXPERIMENTS ON IRON + 0.2 wt % OF CARBON

Besides having the advantage over pure iron of giving reproducible results, these alloys have phase boundaries which are stationary even in the absence of a temperature gradient. The plastic deformation solely due to their motion can be separated off. Also the amount of transformed material can easily be controlled by changing the temperature. The two-phase region of the Fe + 0.2 wt % C alloy extends between 723°C and 825°C.

Fig. 3 shows the excess elongation due to a temperature cycle between T_1 and T_2 with $\Delta T = (T_2 - T_1) = 59^{\circ}\mathrm{C}$ and $T_m = (T_1 + T_2)/2 = 769^{\circ}\mathrm{C}$.

It can be seen that the variation of temperature leads to a large increase of the rate of elongation as compared to the rate at "constant temperature" (within $\pm 1^{\circ}$ C). The excess elongation per cycle increases quickly with ΔT ; however no excess elongation is measured at all if the temperature variation drops below a threshold value $(\Delta T)_0 \cong 9^{\circ}$ C.

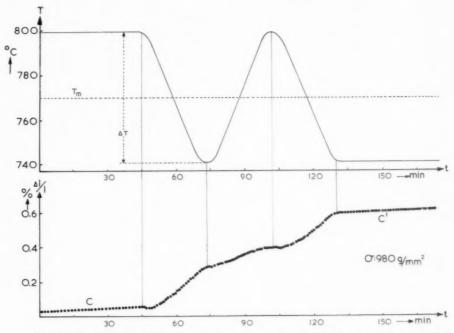


Fig. 3. Change of length of polycrystalline iron + 0.2 wt % C while undergoing periodical partial transformation in the $(\alpha + \gamma)$ -region under a stress $\sigma = 980$ g/mm². The measured points are indicated by filled circles. Shape of the specimens as in Fig. 1A. Vacuum: $<10^{-5}$ mm Hg; Temperature gradient along axis of specimen: $<1^{\circ}$ C/cm; Grain size: 75 μ .

It is therefore reasonable to consider the rate of deformation as measured for "constant temperature" (curve c and c' in Fig. 3) as creep, and to correct the excess elongation for this creep.

It is seen from Table 2 that the excess deformation per cycle after this correction is a constant, and does not depend on the rate of transformation in a given temperature interval. This proves again that our effect is no creep.

The elongation is a linear function of the amount of material transformed at constant stress, independent of the mean temperature T_m , as is shown in Fig. 4. The points in this graph have been arrived at in the

Table 2. Excess deformation per temperature cycle of the Fe + 0.2 wt % C alloy. Vacuum: $<10^{-5}$ mm Hg; Stress: $\sigma=980$ g/mm²; Temperature gradient along axis of specimen: $<1^{\circ}\text{C/cm}$; Grain size: 75 μ . Maximum temperature $T_2=783^{\circ}\text{C}$, minimum temperature $T_1=742^{\circ}\text{C}$.

	dl/l per cycle (per cent)
(a) Temperature variation sinusoidally with time. Time constant: $t = 45 \text{ min}$	0.175 ± 0.01
(b) as (a) but time constant: $t = 110 \text{ min}$	0.18 ± 0.01
(c) Temperature variation as a square sinus with time constant: $t = 90 \text{ min}$	0.17 ± 0.01

following way: Partial transformations in the two-phase region have been performed by varying the temperature periodically between different values of T_1 and T_2 at different mean temperatures T_m . The corresponding amount of transformed material after such a temperature cycle $T_1 \rightarrow T_2 \rightarrow T_1$ can be read from the equilibrium diagram of the iron-carbon system. The retardation in the establishment of the equilibrium state which in our case is about $(\Delta T)_0 \sim 9^{\circ} \mathrm{C}$ has been taken into account by

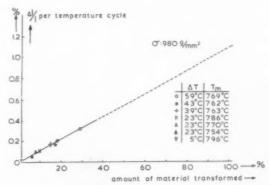


Fig. 4. Excess elongation at constant stress ($\sigma = 980 \ \mathrm{g/mm^2}$) as a function of the amount of material transformed after a complete temperature cycle within the two-phase region ($\alpha + \gamma$) at different mean temperatures T_m and different temperature intervals ΔT . Experimental conditions as in Fig. 3.

VOL.

1959

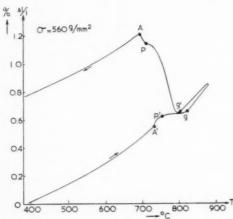


Fig. 5. Change of length of specimens of polycrystalline iron + 0.2 wt % C, while passing the whole $(\alpha+\gamma)$ -region both ways under a stress $\sigma=560~\mathrm{g/mm^2}.$ The rate of heating and cooling was constant except at the highest temperature. The parts of the curve correspond to the following processes; A': beginning of dissolution of pearlite and start of the ferrite–austenite transformation; P': pearlite dissolution completed; g: transformation into the γ -phase completed; g': start of the retransformation; P: start of the pearlite transformation; A: retransformation completed. Experimental conditions as in Fig. 3.

determining the amount of material transformed for the corrected temperatures:

$$[T_1 + \tfrac{1}{2}(\Delta T)_0] \!\to\! [T_2 - \tfrac{1}{2}(\Delta T)_0] \!\to\! [T_1 + \tfrac{1}{2}(\Delta T)_0]$$

In Figs. 5 and 6 the change with temperature of the length of a sample of the alloy is plotted for one passage both ways through the whole two-phase region. In these experiments the rates of heating and cooling have been kept constant except near the highest temperature. The different slopes in the

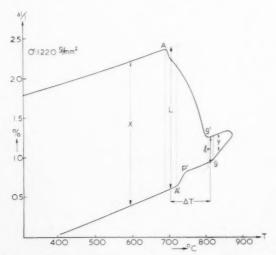


Fig. 6. Determination of the excess elongation Δl from curves such as in Fig. 5 by correcting for creep according to:

$$\begin{array}{c} \Delta l = L - l + \frac{1}{2}(dx/dT + dy/dT) \; \Delta T \\ (\sigma = 1220 \; \mathrm{g/mm^2}) \end{array}$$

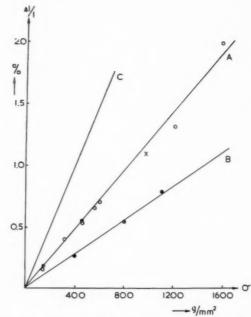


Fig. 7. Excess elongation of polycrystalline iron alloys due to a "both ways" passage through the ($\alpha + \gamma$)-field as a function of stress. Curve A: Fe + 0.2 wt % C. The pearlite reaction is included. The cross in the figure is arrived at by extrapolation of the curve of Fig. 4 to 100 per cent of material transformed.

Curve B: A commercial steel containing 0.23 wt % C. The pearlite reaction is included.

Curve C: Fe + 0.008 wt % N. The same curve as the dotted line in Fig. 2.

19

figures can be correlated with the two reactions taking place, namely at 723°C the pearlite–austenite transformation and in the interval 723°C–825°C the ferrite–austenite transformation.

The relevant parts of the curve are indicated in Fig. 5. The process of formation and dissolution of pearlite apparently corresponds to an excess elongation as does the pure $\alpha \rightarrow \gamma$ transformation.

In Fig. 7 curve A the total elongation that obtains for one complete $\alpha \to \gamma \to \alpha$ transformation is plotted as a function of stress. The points were obtained from analysis of measured curves such as that of Figs. 5 and 6. Some error is introduced by the following causes: first, the correction to be applied for creep is uncertain, while being large at larger stresses. Creep depends critically on stress.(11) This correction is described in the caption of Fig. 6. Secondly, because of retardations, the effect of the pearlite \(\alpha \) austenite reaction cannot be separated unambiguously. It is seen that the elongation as a function of stress for $\alpha \rightarrow \gamma \rightarrow \alpha$ (curve A, Fig. 7) is a straight line through the origin just as was found for the Fe + 0.008 wt % N alloy (Fig. 2). The cross in Fig. 7 corresponds to the extrapolation of the curve Fig. 4 to 100 per cent

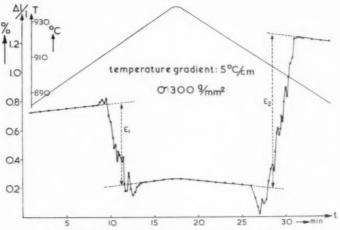
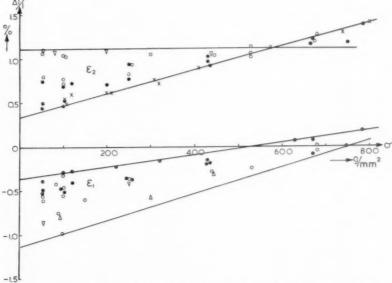


Fig. 8. Change of length of pure coarse-grained iron specimen while undergoing the $\alpha \to \gamma$ and $\gamma \to \alpha$ transformations under a stress $\sigma = 300 \text{ g/mm}^2$. Vacuum: $< 10^{-5} \text{ mm Hg}$; Temperature gradient along axis of specimen: 5°C/cm; Grain size: a few grains per cross section; ε_1 and ε_2 are arrived at as indicated in the figure.



VOL. 7 1959

Fig. 9. Excess elongation as a function of stress of pure coarse-grained iron

- undergoing respectively the α → γ and γ → α transformations.

 Temperature gradient along axis of specimen: 5°C/cm; Rate of heating and cooling: 3°C/min; Vacuum: ≤10⁻⁵ mm Hg.

 Temperature gradient along axis of specimen: ≤1°/cm; Rate of heating and cooling: 3°C/min; Vacuum: ≤10⁻⁵ mm Hg.
- ▼ Temperature gradient along axis of specimen: 5°/cm; Rate of heating and cooling: ½°C-1°C/min; Vacuum: ≤10⁻⁵ mm Hg.
- Conditions as in the case of the open circles, but the $\alpha \rightarrow \gamma$ transformation is
- preceded by a $\gamma \rightarrow \alpha$ transformation under a high stress (525 g/mm²). \times The specimens are cooled in a small current of wet H₂ to about 1 °C above the transformation point, then exposed to a large current emanating as a shower from small holes in a surrounding tube.

of material transformed. This point is in unexpectedly good agreement with the line drawn through the other points.

For comparison purposes some measurements have been included as line B in Fig. 7 of a commercial steel containing 0.23 wt % C (0.44 wt % Mn, 0.016 wt % P and 0.035 wt % S). The slope of curve A is steeper than that of curve B, probably due to the impurities in the steel.

It may be added that also for the pure iron-carbon alloy the excess elongation proved not to depend on the temperature gradient in which the specimen transformed ($<1^{\circ}/\text{cm} - 5^{\circ}/\text{cm}$).

5. EXPERIMENTS ON PURE COARSE GRAINED IRON

As has been mentioned the measurements on pure iron specimens were not reproducible. This is partly due to the fact that only a few(8) crystals occupy the cross-sectional area so that orientation effects come into play instead of averaging out. The elongation under stress vs. time for these specimens is never a smooth curve as Fig. 1B (except for the specimens in "group 3" below). An example is represented in Fig. 8. The specimens are sometimes slightly bent. It can be estimated that the retrogressing parts of the curve may be due to this bending. Fig. 8 shows how the elongations ε_1 and ε_2 are determined. The measurements of ε_1 and ε_2 as a function of stress fill fields in Fig. 9. The measuring points in this figure can be divided into three groups corresponding to the mode of growth of the crystals formed during transformation.

Group 1 (indicated by open markings) belongs to transformations in a steep gradient of temperature (5°/cm). The α-crystals in this case are elongated parallel to this gradient. The maximum value found for $|\varepsilon_1|$ and $|\varepsilon_2|$ at very small stresses is approximately equal to $|\Delta V/V|$, which is 1.062 per cent. (9) This is in agreement with observations of Lehr. (12) If we consider only the $\gamma \rightarrow \alpha$ transformation, for which both the external stress and the change of volume tend to give elongations, the maximum values of ε_2 are found to be independent of stress to a high degree: $\varepsilon_{2 \text{ max}} \sim \Delta V/V$.

Group 2 (indicated by filled circles) belongs to transformations in which the gradient has been avoided by a careful temperature control of both ends and the middle of the specimen. The crystals are large but not elongated in one particular direction. The measuring points of this group are in between those of group 1 and group 3.

Group 3 (indicated by crosses) belongs to crystals

grown in arbitrary directions during the $\gamma \rightarrow \alpha$ transformation. The specimens, after having been cooled in a small current of wet hydrogen to about 1°C above the transformation point, are suddenly exposed to a large current of H2 emanating as a shower from small holes in a surrounding tube. The measuring points fit the curve measured for the Fe-N (0.008 wt $\frac{9}{6}$ N) alloy in Fig. 2, giving $\frac{1}{3}\Delta V/V$ for very small

6. DISCUSSION

It is not yet possible to give a precise explanation of our experiments. This is partly due to the fact that in the case of iron we do not deal with single crystals of known orientation in the two transforming phases.

In a rough and qualitative way the experimental results can be explained if we assume(13) a tendency for the mean macroscopic dilatation to be zero along the phase boundary. This is a tendency to avoid slip over large distances along many lattice planes. It corresponds to a rigorous condition for diffusionless transformations. (14,15)

Consider first transformations in the absence of external stresses. If pure coarse-grained iron transforms in a steep temperature gradient along the axis of the specimen, the phase boundary can be approximated by a plane normal to the gradient, and the above assumption leads, as is observed, to $\Delta l/l \simeq$ $\Delta V/V$. If on the other hand the direction of the phase boundary is arbitrary as in group 3 for the transformation of coarse-grained iron (section 5) or in the case of the alloys (sections 3 and 4) the phase boundary can be approximated more or less by a closed surface. (8,16) If it is a sphere $\Delta l/l = \frac{1}{3}\Delta V/V$. This is in agreement with the measurements of Fig. 2 and the crosses in Fig. 9.

19

We now consider the elongations as a function of external stress. The experiments show that if the direction of the phase boundary is arbitrary, as in the case of group 3 of pure iron and of the alloys (sections 3, 4) the elongation is a linear function of the applied stress. This linearity is to be expected if the external stress removes the equivalence of the slip systems which, for a closed boundary, are activated by the change of volume. Slip systems which give elongation will be preferred in the case of tension. In the case of pressure, slip systems which give a decrease of length will prevail. The external stress may be considered to work on a specimen prestressed to above its yield point by the volume effect. For this external stress the material during transformation may be considered as having a small (in the case of iron a vanish-

ing) yield point.

If the phase boundary is plane, as was assumed for the transformation of pure coarse-grained iron in a steep gradient of temperature, the experiments show that we must differentiate between the $\gamma \rightarrow \alpha$ and the $\alpha \rightarrow \gamma$ transformations. In the first case the elongation in the interval of stresses investigated seems not to be enhanced by the external stress.

Several major problems remain:

(a) The mean macroscopic dilatation along a plane phase boundary $(\gamma \rightarrow \alpha)$ of pure coarse grained iron is small. Stress has a negligible influence upon the elongation in this case. We have not yet a model interpreting these observations. It is desirable to investigate whether $\Delta l/l = \Delta V/V$ is obtained by slip and diffusion or whether a special relationship exists between the orientations of the new and the disappearing phases.

(b) On the contrary in the reverse transformation $(\alpha \rightarrow \gamma)$ of the same material in a steep gradient of temperature, the influence of stress is considerable. The difference in behaviour of the $\gamma \rightarrow \alpha$ and $\alpha \rightarrow \gamma$ transformations may be connected with the fact that only in the first case does the stress favour the change of length due to the change of volume.

ACKNOWLEDGMENTS

Messrs M. E. Hermant, J. Q. Keyman and M. Th. van Ees have contributed to the work reported.

Professor Dr. W. G. Burgers, Dr. T. J. Tiedema and Ir. C. A. Verbraak of Delft have been kind enough to make X-ray diffraction photographs.

REFERENCES

- 1. A. SAUVEUR, Iron Age 113, 581 (1924).
- E. Scheil, Z. anorg. Chem. 207, 21 (1932).
- 3. G. Wassermann, Arch. Eisenhüttenw. 6, 347 (1933); 10, 321 (1937); 11, 89 (1937).
- 4. H. BIBRING and F. SEBILLEAU, C.R. Acad. Sci., Paris 244, 1496 (1957).
- 5. W. F. Brandsma and E. M. H. Lips, Z. Metallk. 28, 381 (1936).
- 6. M. W. Burkart and T. A. Read, Trans. Amer. Inst. Min. (Metall.) Engrs. 197, 1516 (1953).
- 7. J. D. Fast and A. I. Luteyn, Philips Tech. Rev. 15, 73 (1949)
- M. De Jong and G. W. Rathenau, Acta Met. 5, 679 (1957).
 Z. S. Basinski, W. Hume-Rothery and A. L. Sutton,
- Proc. Roy. Soc. B 229, 459 (1955).
 10. S. Darken and W. Gurry, Physical Chemistry of Metals p. 338. McGraw Hill, New York (1953).
- A. H. Sully, Metallic creep. Butterworths, London (1949).
 P. Lehr, C.R. Acad. Sci., Paris 242, 1172 (1956).
- 13. M. DE JONG and G. W. RATHENAU, Nature Lond. 181, 1396 (1958).
- 14. J. S. Bowles and C. S. Barrett, Progress in Metal
- Physics Vol. 3, p. 2. Pergamon Press, London (1952). 15. M. S. Wechsler, D. S. Liebermann and T. A. Read, Trans. Amer. Inst. Min. (Metall.) Engrs. 197, 1503 (1953).
- 16. G. W. RATHENAU and G. BAAS, Métaux, Corrosion, Indust. 29, 139 (1954).

ROOM TEMPERATURE DEFORMATION PROCESSES IN ZIRCONIUM*

E. J. RAPPERPORT†

A study has been made of the deformation processes in zirconium deformed in tension and compression at room temperature. The work was performed on single crystals and large grained samples of relatively high purity with a wide distribution of crystal orientation.

The only slip system observed was (1010) [1210] with a critical resolved shear stress of about 0.65 kg/mm² in compression. The active twin planes were $\{10\overline{12}\}$, $\{11\overline{21}\}$, $\{11\overline{22}\}$, and $\{11\overline{23}\}$. The shear magnitudes found for $(10\overline{12})$, $(11\overline{21})$, and $(11\overline{22})$ twins are about 0.17, 0.22, and 0.23 respectively, and the shear directions for these planes are $[\overline{10}11]$, $[11\overline{26}]$ and $[\overline{11}23]$, respectively.

LES PROCESSUS DE DEFORMATION DU ZIRCONIUM A TEMPERATURE AMBIANTE

L'auteur étudie le processus de déformation du zirconium déformé à température ambiante par tension et compression. Il effectue ses expériences sur des monocristaux et sur des échantillons à gros grains à pureté relativement élevée avec une large distribution de l'orientation cristalline.

Le seul système de glissement observé est (1010)[1210] avec une tension critique de cisaillement projetée d'environ 0,65 kg/mm² en compression. Les plans de maclage actifs sont {1012}, {1121}, {1122} et {1123}. Les grandeurs de cisaillement trouvées pour les macles (1012), (1121) et (1122) sont d'environ 0,17, 0,22 et 0,13, respectivement et les directions de cisaillement pour ces plans sont respectivement [1011], [1126] et [1123].

VERFORMUNGSVORGANGE BEI ZIRKON BEI RAUMTEMPERATUR

Die Verformungsvorgänge bei Zirkon wurden bei Raumtemperatur unter Zug- und Druckbeanspruchung studiert. Die Arbeit wurde an Einkristallen und an grobkörnigen Proben von verhältnismässig hoher Reinheit über eine weite Mannigfaltigkeit kristallographischer Orientierungen durchgeführt.

Das einzige beobachtete Gleitsystem war (1010) [1210] mit einer kritischen Schubspannung beim Druckversuch von etwa 0,65 kg/mm². Aktive Zwillingseben waren {1012}, {1121}, {1122} und {1123}. Die Scherungen für die (1012), (1121) und (1122) Zwillinge ergaben sich zu etwa, 0,17 bezw. 0,22 und 0,23 und die Scherungsrichtungen für diese Ebenen sind [1011] bezw. [1126] und [1123].

INTRODUCTION

Zirconium is a metal that has come under intensive investigation comparatively recently. It is of current interest because it combines some physical, nuclear, and corrosion properties that are highly desirable in nuclear reactor applications. However, very little work has been reported on the determination of the deformation processes of zirconium. The only information at the time of this writing was by F. D. Rosi (personal communication to A. R. Kaufmann, 1953), and the results of a preliminary investigation by Rapperport. (1) Rosi stated that at room temperature slip occurred predominantly on planes of the form {1010} and twinning on planes of the forms $\{10\overline{1}2\}$ and $\{11\overline{2}1\}$. In addition, Rosi suspected the presence of {1011} slip and {1122} twinning, although he had not found these planes experimentally.

Since zirconium is a close packed hexagonal metal with a c/a ratio⁽²⁾ similar to that of titanium, and since both are transition elements in Group IV-A, it is of

interest to see if the deformation processes are similar. The work of a number of investigators $^{(3,4,5,6)}$ has indicated a multiplicity of slip and twin systems in titanium. The slip planes reported are (0002), $\{10\overline{1}0\}$, and $\{10\overline{1}1\}$; and the twin planes are $\{10\overline{1}2, \{11\overline{2}1\}, \{11\overline{2}2\}, \{11\overline{2}3\}$, and $\{11\overline{2}4\}$. No experimental determinations of the twin elements other than the twin plane have been made.

19

PREPARATION OF SPECIMENS

Material

The zirconium used in this study was of two types: (1) as-deposited reactor grade crystal-bar zirconium; and (2) arc-melted and forged reactor grade crystal-bar. Table 1 shows typical chemical and spectrographic analyses of these materials, as received and after heat treatment.

Fabrication and heat treatment of crystal-bar specimens

The zirconium was machined into rectangular parallelepipeds about 0.2 in. square in cross-section and 2 in. long. After final machine grinding, the samples were hand polished through 4/0 abrasive paper, given a chemical etch in a nitric acid-hydrofluoric acid bath, then repolished on abrasive paper.

^{*} This work was done in part as a doctoral thesis in the Department of Metallurgy, Massachusetts Institute of Technology, under AEC Contract AT(30-1)-981, and in part at Nuclear Metals, Inc., under AEC Contract AT(30-1)-1565. Received February 26 1958; revised version June 26, 1958. † Nuclear Metals, Inc., Concord, Massachusetts, U.S.A.

Table 1. Typical chemical and spectrographic analyses of the zirconium used in this work. Analyses given for material as received and after heat treatment (Numbers indicate impurity content in parts per million by weight)

Element	Reactor grade crystal bar, as received	Crystal bar, after hydrogen removal anneal	Arc melted crystal bar, as received	Arc melted, after hydrogen removal and thermal cycling
Oxygen Carbon	235 110	200	190 30	185
Nitrogen	6		6	5
Hydrogen	40	2	46	1
Aluminum	40	_	20	
Calcium	30		30	
Chromium	30		30	
Copper	20		25	
Hafnium	320		320	
ron	220	230	75	
Iagnesium	6		8	
Ianganese	5		6	
Iolybdenum	< 10		10	
Vickel	40		30	
ead	10		9	
ilicon	20		30	< 20
in	8		15	
Titanium Tanadium	$ \begin{array}{r} $			

After paper polishing the second time, the samples were given an electropolish in an acetic acid-perchloric acid bath.

A hydrogen-removal heat treatment followed the polishing and etching steps. The samples were degreased, wrapped in tantalum, and inserted into a silica tube sealed at one end. The samples were annealed at 840°C for 10 days while a vacuum system continuously removed hydrogen at the other end. The reduction in the hydrogen content is shown in Table 1. Hydrogen forms a second phase in zirconium and must be removed to properly observe the deformation characteristics of the pure metal.

1959

The heat treatment at 840°C also served to yield large crystals covering the entire cross-section with

Fig. 1. Specimen of crystal-bar zirconium showing large grains formed by annealing at 840 °C for 10 days.

lengths of 1/4 in. or more (see Fig. 1). The specimen surfaces remained smooth, and the crystals were of good quality as judged from the sharpness of spots on Laue photographs and the uniform appearance of the grains under polarized light in a metallograph. The disadvantages of this technique are that the grains all are of similar orientation, and that there are macroscopic growth flaws present in the original crystal-bar.

Fabrication and heat treatment of arc-melted specimens

The initial steps in making large crystals of the arcmelted and forged zirconium were the same as those given above for the crystal-bar samples. In cases where large grains were not obtained, an additional heat treatment was necessary. This involved cycling above and below the alpha-beta transformation temperature in a manner similar to the method used by one group of investigators to make large crystals of titanium. (4)

The zirconium samples that were to be heat treated by cycling were re-wrapped in tantalum foil and sealed in silica containers at pressures less than 10^{-6} mm of mercury. They were then annealed at 1200° C for 4 hr, quickly transferred to a second furnace set at 840° C, and allowed to remain at the lower temperature for 5–10 days. The samples were then transferred back to the 1200° C furnace, and the whole cycle repeated several times. At the end of the last anneal at 840° C, the furnace temperature was dropped to room temperature at a rate of about 100° C/hr to avoid stressing the samples. After this

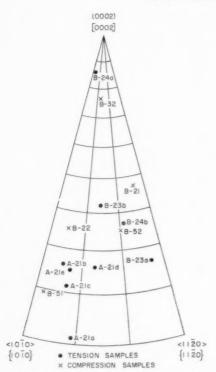


Fig. 2. Orientations of crystals of zirconium used. Points indicate stereographic projections of applied stress directions.

treatment, the surfaces of the samples were rough and rumpled, and it was necessary to repolish and etch to obtain essentially stress-free samples with rectangular cross-sections and plane faces.

Specimens containing large crystals covering the entire cross-section were retained as tensile samples or were cut into single crystals for compression work. The cutting was done very carefully to avoid mechanical twinning.

Angle measurement and orientation determination

The dihedral angles between adjacent faces of each of the specimens were measured by two different methods. One method was based on obtaining the normals to the faces by optical means,⁽⁷⁾ and the other method was direct measurement of the angles at the ends of the samples by the use of an optical comparator.

Back-reflection Laue photographs were made to determine the crystallographic orientation of the crystals to an estimated accuracy of 0.5°. Three faces of each crystal were indexed in this way.

Fig. 2 shows a stereographic triangle on which is plotted the tension and compression axes of the specimens tested. The five crystals in the A-21 series were produced from crystal-bar zirconium, and the others were from arc-melted material.

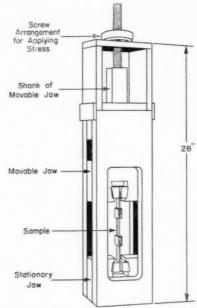


Fig. 3. Tensile device with calibrated screw to apply known axial strain to zirconium samples.

DEFORMATION OF SPECIMENS IN TENSION AND COMPRESSION

VOI

191

A single specimen containing five usable grains was deformed in tension with the apparatus shown in Fig. 3. The five crystals so tested were A-21a, A-21b, A-21c, A-21d, and A-21e. The total strain given the sample was 10.7 per cent, with intermediate metallographic examination at 0.55, 1.4, 2.2, 3.7, and 6.3 per cent strains. Four additional crystals were deformed in tension under conditions of known stress. These samples were held in grips and subjected to loads applied by adding water into a bucket attached to one of the grips. The crystals deformed in this manner were B-23a, B-23b, B-24a, and B-24b. These specimens were continuously observed through a microscope as the load was applied, and the loads corresponding to the appearance of the various deformation traces were recorded. Metallographic examination followed each appearance of new deformation traces.

Five single crystals, B-21, B-22, B-32, B-51, and B-52, were tested in compression in an apparatus designed to give uniaxial compression with minimal bending moments on the samples. (8) The samples were observed through a microscope during loading so that the first visible traces of slip or twinning might be noted, to enable computation of the resolved shear stress of the deformation. Loading and examination for new surface-traces was continued for each crystal to compressive loads about three times those required for the initial visible deformations.

ANALYSIS OF DEFORMATION PROCESSES Slip

The slip planes, as well as the twin planes, were determined by traces on two surfaces as described by Barrett(9) and Hall.(10) Single-trace methods described by Cahn⁽¹¹⁾ were also used on samples where it was not possible to pair traces on two surfaces. The angles that the traces made with the sample edges were measured with the aid of the rotating stage on the metallograph. These angles, suitably plotted on stereographic projections of the crystals, yielded the active planes.

The probable slip direction was inferred from metallographic examination of crystals having faint slip traces on some faces. The basis for such a determination is that the crystal surfaces making small angles with the slip direction have relatively little distortion normal to their surfaces. (12)

The critical resolved shear stress for slip is defined here as that stress, resolved in the plane and direction of slip, which is required to initiate optically perceptible slip. This stress was taken on six crystals four in compression, and two in tension.

Twinning

1959

The twin planes were also obtained from the angles that traces on two adjacent specimen surfaces make with the common edge. The twin planes (denoted as K₁) were all analyzed by two-trace methods, which represent rigorous solutions. The other twin elements were found with the aid of optical goniometer measurements. These elements are: η_1 , the direction of shear in the plane K₁: K₂, the second undistorted plane in the twin volume (the first is K_1); η_2 , a direction in K_2 defined by the intersection of K_2 and the plane of η_1 and the normal to K_1 ; and S, the twinning shear. The angle 2ϕ is the acute angle between K_1 and K_2 . The goniometer is used to measure the angle between

the exposed surface of the twin and the original surface of the specimen, by observing the change in angle as the specimen is rotated to reflect a light beam, first from the surface of the sample and then from the exposed surface of the twin, using the twin trace as the axis of rotation. Such measurements on the two-twin-traces on adjacent surfaces may be used to determine the twin elements analytically⁽⁷⁾ or by the application of stereographic projections. (7,13)

It was also possible to use the metallograph to measure the surface deformation produced in twinning. The shear associated with twinning displaces the sample edge; and, by obtaining angle measurements between the displaced edge segment and the original edge, one may determine the twin elements.(7)

A third technique used in this work to measure the surface change at a twin trace utilized an interference microscope. Measurements with this instrument gave the change in height across a twin trace. These data, combined with a knowledge of the twin plane and the projected breadth of the twin trace, were sufficient to fix the geometry of the shear and thence the twin elements.

The crystals used for the determination of twin elements were carefully chosen. Analyses were made on crystals when they were only slightly deformed, so that there were very few deformation traces to confuse the determinations. When possible, crystals were chosen which had only one twin family present.

RESULTS AND DISCUSSION

Slip

The experimental results are summarized in Tables 2 and 3. As may be seen in Table 2, every crystal that was tested deformed by slip on a {10I0} plane, and presumably in a (1120) direction. The slip direction was inferred from observations of slip traces on surfaces making small angles with the $(11\overline{2}0)$ direction in the

Table 2. Summary of deformation in crystals of zirconium tested in tension and compression at room temperature

Crystal	Crystal Crystal length	Raw	Direction	Maximum gross strain	Maximum axial stress	Slip	Slip direction	Critical shear stress (kg/mm ²)	Observed twin planes			
Ciyatai	(in.)	material	of stress	(per cent)	(kg/mm ²)	plane			(10T2)	{1121}	(1122)	(112)
A-21a	3/8	Crystal bar	Tension	10	(b)	(1010)	(a)	(b)	X	X		X
A-21b	3/16	Crystal bar	Tension	10	(b)	{10I0}	(a)	(b)	X	X	X	X
A-21e	1/4	Crystal bar	Tension	10	(b)	{10 T 0}	(a)	(b)	X	X	X	
A-21d	3/16	Crystal bar	Tension	10	(b)	{10 <u>T</u> 0}	(a)	(b)	X X X	X		X
A-21e	1/8	Crystal bar	Tension	10	(b)	{10 <u>T</u> 0}	(a)	(b)	X	X		
B-21	3/8	Arc-melted	Compression	(b)	4.8	$\{10\overline{1}0\}$	(1120)	0.69 ± 0.10		-7		
B-22	3/8	Arc-melted	Compression	(b)	4.3	{10 <u>1</u> 0}	(1120)	0.70 ± 0.10		X		
B-23a	1/2	Arc-melted	Tension	(b)	16.6	{10 <u>1</u> 0}	(a)	0.4	1			
B-23b	5/16	Arc-melted	Tension	(b)	16.6	{10 <u>T</u> 0}	(a)	0.4				
B-24a	1/2	Arc-melted	Tension	(b)	7.9	{10 <u>1</u> 0}	(a)	(b)	X	X		
B-24b	3/16	Arc-melted	Tension	(b)	7.9	(10 <u>T</u> 0)	(a)	(b)				
B-32	1/2	Arc-melted	Compression	(b)	6.6	{10 T 0}	(1120)	(b)		X	X	
B-51	3/4	Arc-melted	Compression	(b)	1.6	{10 T 0}	(1120)	0.61 ± 0.05				
B-52	5/8	Arc-melted	Compression	(b)	1.7	{10 T 0}	(1120)	0.62 ± 0.05			1	

probably $\langle 11\overline{2}0 \rangle$, but not determined not determined

plane observed

Table 3. Summary of twin elements of zirconium crystals deformed in tension and compression at room temperature

		Calculated shear		25 41 1 6	Experimental shear parameters						
Crystal designation	K ₁	Twin η_1	elements K_2	η_2		rs for given and K_2 $90^{\circ}-2\phi$	Method of obtaining primary shear data	metl	graphic nods 0°-2φ		$\begin{array}{c} { m etor} \\ { m hods} \\ 90^{\circ} - 2\phi \end{array}$
B-24a	(10Т2) [1	011]	(1012)	[1011]	0.167	4.8°	Optical goniometer Metallograph	$0.171 \\ 0.167$	4.9° 4.8°	$0.181 \\ 0.171$	5.2° 4.9°
B-32 First pair of traces	(1122) [1	[123]	$(11\overline{24})$	$[\overline{2243}]$	0.225	6.4°	Optical goniometer Metallograph	$0.242 \\ 0.228$	$\begin{array}{c} \textbf{6.9}^{\circ} \\ \textbf{6.5}^{\circ} \end{array}$	$0.239 \\ 0.235$	$\substack{6.8^{\circ} \\ 6.7^{\circ}}$
B-32 Second pair of traces	(a)	(a)	(a)	(a)			Optical goniometer	0.228	6.5°	0.228	6.5°
B-21 First pair of traces	(1121) [1	[126]	$(11\ \overline{2}\ \overline{16})$	[88 16 3]	0.216	6.16°	Optical goniometer Interference microscope	$0.217 \\ 0.210$	$\begin{array}{c} 6.2^{\circ} \\ 6.0^{\circ} \end{array}$	$0.199 \\ 0.203$	$\begin{array}{c} 5.7^{\circ} \\ 5.8^{\circ} \end{array}$
B-21 Second pair of traces	(a)	(a)	(a)	(a)			Interference microscope	0.210	6.0°	0.204	5.8°
B-22	(1121) [1	126]	$(11\ 2\ 16)$	[88 16 3]	0.216	6.16°	Optical goniometer	0.217	6.2°	0.213	6.1°

a = same elements as first pair of traces in sample.

active slip plane. Four of the crystals tested had surfaces with faint slip traces adjacent to surfaces containing distinct slip traces. In each of these crystals the $\langle 11\bar{2}0\rangle$ direction in the active slip plane made an angle of less than 15° with the specimen surface containing the faint traces. In two cases, B-32 and B-52, where the slip traces were extremely faint, the $\langle 11\bar{2}0\rangle$ direction made an angle of less than 2° with the surface having faint slip traces. The consistency of these observations points to $\langle 11\bar{2}0\rangle$ as the slip direction, which is in agreement with the criterion of slip occurring in directions of greatest atom density.

It was considered unusual that no basal slip was observed, since in five crystals the resolved shear stress on the basal plane, (0002), in a $\langle 11\bar{2}0\rangle$ direction exceeded the shear stresses resolved on the prism slip systems. These five crystals were B-21, B-32b, B-24a, B-24b, and B-32. In the case of B-24a, the resolved shear stress in a basal system was nine times that on the most favorable prism system. Moreover, some of these crystals were loaded to more than five times the load at which prism slip was first observed. Crystal B-21 was loaded to a shear stress of 2.4 kg/mm² on the basal system, then squeezed in a vise and still no basal slip was observed.

Since the zirconium used in this study had a relatively low oxygen and nitrogen content (see Table 1), the absence of basal slip is consistent with Churchman's⁽⁶⁾ data on titanium. He observed that

{1010} is the principal slip plane and is favoured by increasing purity.

The critical resolved shear stress for slip in the (1010) [1210] system was determined on six crystals—four in compression, and two in tension. The values determined in compression are considered more reliable because the possibility of extraneous stresses from bending moments was less than in the tensile loading. The values of critical resolved shear stress in compression range from $0.61\pm0.05~{\rm kg/mm^2}$ to $0.70\pm0.10~{\rm kg/mm^2}$, with the average at about $0.65~{\rm kg/mm^2}$. The consistency of the resolved shear stress in the four compression samples also tends to support the assumption that $\langle 11\bar{2}0\rangle$ is the slip direction.

Twinning

Twinning was found to occur on four different planes: {10I2}, {1121}, {1122}, and {1123}. The {1121} form was the most frequent, occurring in nine of the fourteen crystals tested; next was {10I2}, occurring in six; then {1122} and {1123}, each occurring in three crystals. The {1123} twins were observed only in samples which had undergone large plastic strains, and always seemed to occur in the highly stressed regions near grain boundaries. The surfaces of samples having {1123} twins were highly distorted, which made the determination of the elements of {1123} twins impractical by the techniques used.

The thickness of the members of each twin family

was relatively constant among the crystals tested. The $\{10\overline{1}2\}$ twins were thickest at about 30μ ; the $\{11\overline{2}2\}$ next at about 10μ ; and the $\{11\overline{2}1\}$ were the narrowest at about $1-2\mu$. Cahn has observed that the thicker the twin, the smaller the shear associated with that twin. (12) Comparison of the thicknesses just cited with the shears given in Table 3 shows an apparent deviation from this relationship as the {1121} twins, which are the narrowest, do not appear to have the largest shear.

The {1121} twin elements presented the greatest difficulty in analysis and the elements are the least certain. As stated above, twins of this family are only about 2μ thick, a size where Fraunhofer diffraction from the trace makes it difficult to ascertain the direction of the reflected light beam when making goniometric measurements. The magnitude of this effect is given in Table 4 for twin traces of typical breadths. This table gives the angle of divergence of the reflected light beam for each of the twins cited.

Table 4. Typical widths of twin-plane traces, and calculated values of the angles of divergence of reflected light A wavelength of 5000 Å is assumed.

Twin plane	Width of twin trace (μ)	Angle of divergence of reflected beam (degrees)
{10T2}	41	1.5
$\{11\overline{2}2\}$	12	5.0
{1121}	2	29.0

1959

Because of these diffraction effects, use was made of interference microscope techniques to get more reliable measurements of the surface deformations produced by $\{11\overline{2}1\}$ twins. The experimental shear values for $\{10\overline{1}2\}$ and $\{11\overline{2}2\}$ twins have an estimated error of less than 0.5° , plus or minus; that of $\{11\overline{2}1\}$ twins is estimated at less than 1°.

It is to be noted that, although the twinning shear and other elements for {1012} twins correspond to those expected for this system from simple crystal geometry conditions, the elements for $\{11\overline{2}1\}$ and {1122} are different from those inferred from such considerations (Hall⁽¹⁰⁾ or Rapperport⁽¹⁾). The {1012} twins may be viewed as forming by the homogeneous shearing of a subset of space lattice points with the required shuffling of atoms at other sites. For {1012} twins, it appears that half the space lattice points in the twinned volume (or one-quarter of the atoms) undergo homogeneous shear in the twin plane, in the direction of η_1 . This geometrical picture yields the observed twin elements for {10I2} twinning in zirconium, and also for other hexagonal close packed

metals such as zinc, magnesium, and cadmium.(14) However, when simple shear of the same subset of lattice points is used to generate a {1122} twin, a shear value of 0.965 is obtained.(1) A shear value of 0.623 is obtained for {1121} twins when the entire space lattice is homogeneously sheared in similar fashion. (1) These values of shear are much greater than the observed values of about 0.22.

In the cases of $\{11\overline{2}1\}$ and $\{11\overline{2}2\}$ twins, there are other subsets of lattice points which, when sheared by the observed macroscopic shear of about 6°, yield geometric twins of the lattice subsets. In the case of {1122} twins, it would seem that one-third of the atom positions participate in the homogeneous shear: in the case of $\{11\overline{2}1\}$ twins, the fraction is only 1/17. There is a large number of subsets which could conceivably shear to produce a twin, but currently it seems to be necessary to reply on experiments to determine which one is active in a given case. Cahn⁽¹⁵⁾ has recognized the difficulties in attempting to use simple geometric considerations alone to assign twin elements, and has pointed out the need for experimental verification of twin elements.

CONCLUSIONS

- 1. After removal of hydrogen, large zirconium crystals can be produced by either of two techniques: one is to heat the samples in vacuo for 8-10 days at 840°C; the other is to cycle the samples in vacuo several times between 4 hr at 1200°C and 5 days at 840°C.
- 2. Slip has been observed at room temperature only on the system (1010) [1210] in crystals having a wide range of orientation and relatively high purity. The critical resolved shear stress for slip on this system is about 0.65 kg/mm² in compression.
- 3. Deformation twins on $\{10\overline{1}2\}$, $\{11\overline{2}1\}$, $\{11\overline{2}2\}$, and {1123} planes were observed in zirconium crystals deformed at room temperature. Complete specifications of the twin elements are given for $\{10\overline{1}2\}$, $\{11\overline{2}1\}$, and {1122} twins, with some uncertainty in the values for the $\{11\overline{2}1\}$ type.

ACKNOWLEDGMENTS

The author is indebted to J. L. Klein and W. B. Nowak for their thoughtful criticism of the manuscript.

REFERENCES

- E. J. RAPPERPORT, Acta Met. 3 (2), 208 (1955).
 R. B. RUSSELL, J. Metals, N.Y. 6 (9), 1045 (1954).
 F. D. ROSI, C. A. DUBE and B. H. ALEXANDER, J. Metals, N.Y. 5 (2), 257 (1953).
- 4. E. A. Anderson, D. C. Jillson and S. R. Dunbar, J. Metals, N.Y. 5 (9), 1191 (1953).
- 5. T. S. Liu and M. A. Steinberg, J. Metals, N.Y. 4 (10), 1043 (1952).

- (1954).
- 7. E. J. RAPPERPORT and W. L. LEES, NMI-1189, TISE, Oak
- Ridge, Tennessee.
 8. E. J. Rapperport, Rev. Sci. Instrum. 27 (7), 446 (1956).
- 9. C. S. Barrett, Structure of Metals (2nd Ed.). McGraw-Hill, New York (1952).
- E. O. Hall, Twinning and Diffusionless Transformations in Metals. Butterworths, London (1954).
 R. W. Cahn, Acta Met. 1 (1), 49 (1953).
- 6. A. T. Churchman, Proc. Roy. Soc. A226 (1165), 216 12. R. W. Cahn, Plastic Deformation of Uranium, United States Atomic Energy Commission Technical Information Service, AERE-M/R-740, 1951 (Originally published at Atomic Energy Research Establishment, Harwell, Berkshire, England).
 - 13. A. B. Greninger and A. R. Troiano, Trans. Amer. Inst.
 - Min. (Metall.) Eng. 185, 590 (1949).
 14. E. Schmid and W. Boas, Plasticity of Crystals F. A. Hughes, London (1950). Translated from Kristallplastizitaet (1935).

19

R. W. Cahn, Advances in Physics 3 (12), 363 (1954).

VAPOR PRESSURE MEASUREMENTS OVER CALCIUM, MAGNESIUM, AND THEIR ALLOYS AND THE THERMODYNAMICS OF FORMATION OF CaMg,*

J. F. SMITH† and R. L. SMYTHE‡

Vapor pressures have been measured by the Knudsen effusion method over magnesium, calcium, and a series of calcium-magnesium alloys. Magnesium vapor pressures are in good agreement with previous work. Calcium vapor pressures are in reasonable agreement with previous measurements over liquid calcium but do not reproduce any of the past measurements over solid calcium. Vapor pressure measurements over the alloys were used to determine the free energy of formation of the compound, $CaMg_2$. The free energy of formation in kcal/mol can be expressed as

$$\Delta F^{\circ} = -8.3 + (1.1 \times 10^{-3}) T$$
.

The small values for the enthalpy and entropy of formation are consistent with the view that the compound forms because of atomic size considerations. An independent check on the enthalpy of formation was made by bomb calorimetry.

MESURES DE LA PRESSION DE VAPEUR AU-DESSUS DU CALCIUM, DU MAGNESIUM ET DE LEURS ALLIAGES THERMODYNAMIQUE DE LA FORMATION DE $Camg_2$

Les auteurs ont mesuré par la méthode de Knudsen, les pressions de vapeur au-dessus du magnésium, du calcium et d'un certain nombre de leurs alliages. Pour les pressions de vapeur du magnésium, les valeurs qu'ils obtiennent sont en bon accord avec les travaux antérieurs. Pour les pressions de vapeur du calcium au-dessus du calcium liquide, l'accord avec les valeurs actuellement admises n'est que relatif. Enfin, les valeurs déterminées par les auteurs pour la pression de vapeur au-dessus du calcium solide, ne correspondent nullement aux mesures antérieures. Les mesures de pression de vapeur au-dessus des alliages ont servi à déterminer l'énergie libre de formation du composé CaMg₂. L'énergie libre de formation en kcal/mol s'exprime par

$$\Delta F^{\circ} = -8.3 + (1.1 \times 10^{-3})T$$

Les valeurs faibles de l'enthalpie et de l'entropie de formation appuient l'hypothèse admettant que la formation de ce composé est liée à des considérations de taille atomique.

Une détermination séparée de l'enthalpie de formation a été réalisée à la bombe calorimétrique.

DAMPFDRUCKMESSUNGEN AN CALCIUM, MAGNESIUM UND IHREN LEGIERUNGEN UND DIE THERMODYNAMIK DER BILDUNG VON CaMg_2

Mit Hilfe der Ausströmungs-Methode nach Knudsen wurden die Dampfdrücke an Mangesium, Calcium und einer Reihe ihrer Legierungen gemessen. Die Dampfdrücke von Magnesium sind in guter Übereinstimmung mit früheren Arbeiten. Die Dampfdrücke über Calcium befinden sieh in vernünftiger Übereinstimmung mit früheren Messungen an flüssigem Calcium, geben jedoch keins der Ergebnisse früherer Messungen an festem Calcium wieder. Dampfdruckmessungen an den Legierungen wurden dazu benutzt, die freie Bildungsenergie der Verbindung CaMg₂ zu bestimmen; sie lässt sich (in kcal/mol) darstellen durch:

$$\Delta F^{\circ} = -8.3 + (1.1 \times 10^{-3})T.$$

Die geringen Werte für Bildungsenthalpie und -Entropie entsprechen der Anschauung, dass für die Bildung der Verbindung die Atomgrössen verantwortlich sind. Mit Hilfe von Bomben-Kalorimetrie wurde die Bildungsenthalpie unabhängig nachgeprüft.

1. INTRODUCTION

1959

Vapor pressures over the calcium–magnesium system were studied primarily to elucidate the thermodynamics associated with the formation of the compound ${\rm CaMg_2}$ and secondarily to attempt to resolve some of the conflicting data on the vapor pressure values of solid calcium. The compound ${\rm CaMg_2}$ crystallizes in the hexagonal C14 structure⁽¹⁾ and

belongs to the large group of compounds known as Laves phases. The Laves phases $^{(2)}$ all crystallize in three closely related structures, C14, C15, and C36, which differ only in layering arrangement. The important factor in the formation of the Laves structures seems to be the relative size of the constituent atoms. The geometry of the structures allows a 16-fold coordination around one atomic species and 12-fold coordination around the other atomic species. The average coordination is 13.33 which, in the case of calcium and magnesium, represents an increase of $1\frac{1}{3}$ bonds per atom over the elemental structures. A rough approximation for the

^{*} Contribution No. 625. Work was performed in the Ames Laboratory of the U. S. Atomic Energy Commission. Received April 18, 1958; in revised form July 11, 1958.

[†] Institute for Atomic Research and Department of Chemistry, Iowa State College, Ames, Iowa, U. S. A.
‡ Present address: Texas Instruments Inc., Dallas, Texas.

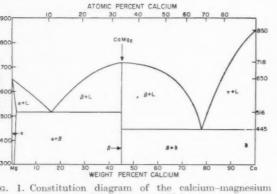


Fig. 1. Constitution diagram of the calcium-magnesium system (after Sager and Nelson).

heat of formation of CaMg2 may be made from the cohesive energies (3) of calcium and magnesium. If the bonding in the compound is not appreciably different from the bonding in the metallic elements, the increased number of bonds in the compound should cause a proportional increase in the cohesion. On this basis the heat of formation of the compound should be of the order of -12 to -15 kcal/mol.

The calcium-magnesium phase diagram⁽⁴⁾ is shown in Fig. 1. Features of the system that are desirable from the viewpoint of the present investigation are that the composition of the compound does not vary and the terminal solubilities are quite limited. On the magnesium rich side of the diagram the solubility of calcium^(5,6) is less than 1.5 at.% at all temperatures. On the calcium rich side, magnesium solubility is apparently negligible, (7) but the diagram is incomplete since the allotropy of calcium^(8,9) is quite sensitive to impurities.

On the basis of the phase diagram an analytical expression for the free energy of formation of the compound at a given temperature as a function of vapor pressures can be developed. The equilibrium between solid calcium and compound may be written,

$$\operatorname{Ca}(\alpha) + 2\operatorname{Mg}(g) \rightleftharpoons \operatorname{CaMg}_2(s), \Delta F^{\circ} = 2\operatorname{RT} \operatorname{ln} P', (1)$$

if it is assumed that the vapor pressure of magnesium over the system predominates to the extent that the vapor pressure of calcium may be neglected. Experimental verification of this assumption will be described in the results section. Magnesium sublimation may be written as

$$2 \text{ Mg (s)} \rightleftharpoons 2 \text{ Mg (g)}, \ \Delta F^{\circ} = -2 \ RT \ln P^{\circ}. \ (2)$$

Summation of equations (1) and (2) gives the expression for the formation of the compound from α -calcium and solid magnesium:

$$\mathrm{Ca}\left(\alpha\right)+2\,\mathrm{Mg}\left(\mathbf{s}\right)\rightleftharpoons\mathrm{CaMg}_{2}\left(\mathbf{s}\right),\Delta\boldsymbol{\mathit{F}}^{\circ}=2\,RT\ln\,P'/P^{\circ}.\tag{3}$$

2. METHOD AND APPARATUS

The Knudsen effusion method⁽¹⁰⁾ was employed for the vapor pressure determinations. In this method vapor at equilibrium pressure over a system in a closed container is allowed to escape through a small orifice into an evacuated region. The kinetic theory of gases may be used to calculate the vapor pressure if the amount of vapor escaping per unit time through the orifice is determined. In the present investigation the vapor was assumed to be monatomic and the amount of escaping vapor was determined by the weight loss as a function of time. The weighing was done with a quartz microbalance which was constructed by A. H. Daane and was based on a design published by Edwards and Baldwin. (11) Determination of the amount of escaping vapor by total weight loss is preferable to weighing or analyzing a condensed fraction of the escaped vapor, since errors arising from solid angle considerations, condensing efficiency, and analytical techniques are eliminated.

A diagram of the apparatus is shown in Fig. 2. The sample container was a tantalum bucket, 9 mm dia. and 11 mm high with 6 mil walls. The lid was fabricated from 3 mil tantalum sheet and was joined to the bucket by a gas-tight crimp seal. An orifice was drilled in the lid and subsequently reamed and burnished to a knife-edge. Orifice diameters were

19

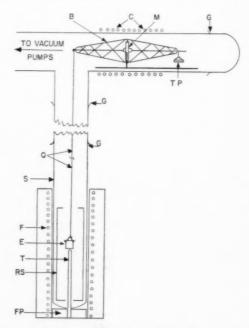


Fig. 2. Diagram of the experimental apparatus: B-Quartz fiber balance; C—Balance coil; M—Alnico magnet; G—Ground glass joints; TP—Tare pan; Q—Quartz fibers; S—Silica tube; F—Furnace windings; E—Effusion vessel; T—Thermocouple well; RS—Molybdenum radiation shield; FP-Firebrick plug.

measured under a microscope equipped with a Filar eyepiece which had been calibrated against a stage micrometer. Orifice diameters from 0.01 in. to 0.04 in. were used and measured vapor pressure values were found to be independent of orifice diameter. The tantalum bucket was suspended from the balance into a resistance furnace by means of a thin quartz fiber. The volume surrounding the balance and the tantalum bucket was evacuated. Temperatures were measured with a calibrated #22 B & S chromel—alumel thermocouple. A quartz finger protruding into the evacuated region within the furnace allowed the thermocouple tip to be in close proximity to the tantalum bucket.

Knudsen⁽¹⁰⁾ has shown that for the effusion method to be valid, the mean free path of the vapor particles within the container should be greater than ten times the orifice diameter. This condition places an upper limit on measurable vapor pressures which, with the orifice diameters used, was approximately 0.1 mm Hg. Pressures which were marginally above this limit were measured at high temperatures over pure magnesium and over magnesium plus compound. The data were retained, however, because of consistency with established trends. A lower limit of 10⁻⁵ mm Hg for measurable vapor pressures was due to the ultimate vacuum of the pumping system. The pumping system which consisted of a Welch Model 1400 roughing pump, a two-stage mercury diffusion pump, and a liquid nitrogen cold trap, produced an ultimate vacuum between 10⁻⁶ and 10⁻⁷ mm Hg when measured with a National Research type 507 ionization gauge. The lower limit for measurable vapor pressures is based on the empirical observation that reproducible data were not obtained when the system pressure was greater than ~0.01 times the vapor pressure being measured.

3. RESULTS

3.1. Magnesium

VOL.

1959

7

Measurements of the vapor pressure above triply distilled magnesium were made with the present apparatus over the temperature range 626–818°K and above a 21 at.% Ca–79 at.% Mg alloy over the temperature range 636–771°K. The data were treated in the manner described by Darken and Gurry (12) wherein a sigma function,

$$\Sigma = \Delta H_0 T^{-1} + I, \tag{4}$$

is defined in terms of the integration constants, ΔH_0 and I, which arise from the integrals, $\int \Delta C_p \, dT$ and $\int d(\Delta F^\circ/T)$, respectively. Values for the sigma function may be obtained from the measured vapor pressures at various temperatures using the relation

$$\begin{split} \Sigma_{\rm Mg} &= -4.575 \log P^0 - 2.694 \log T \\ &- (0.75 \times 10^{-3}) T + (0.39 \times 10^5) T^{-2} \end{split} \tag{5}$$

The numerical values in this equation are based upon a heat capacity for solid magnesium tabulated by Kelley,⁽¹³⁾

$$C_{p}$$
 (s) = 6.14 + $(1.50 \times 10^{-3})T - (0.78 \times 10^{5})T^{-2}$, (6)

and a value for magnesium vapor, $C_p=4.97$, which assumes the vapor behaves as an ideal monatomic gas. A plot of the sigma function vs. reciprocal temperature is shown in Fig. 3.

Values for ΔH_0 and I were obtained from equation (4) using the method of least squares and the numerical values of sigma at the temperatures of measurement. Values for the constants obtained from the vapor pressure measurements above pure magnesium and above the alloy were respectively: $\Delta H_0 = 35620$ and 35770 cal/mol, and I = -36.18 and -36.34 e.u./mol. These values agree within the experimental precision and verify that the calcium solubility in magnesium has a negligible effect on the vapor pressure measured over the alloy. The composite of the two sets of measurements gives the values, $\Delta H_0 = 35670 \pm 630$ cal/mol and I = -36.23 + 0.88 e.u./mol. These latter values were used to obtain the temperature dependence of the thermodynamic functions for the magnesium sublimation process:

$$\begin{split} \Delta F^\circ &= 35670 + 2.694 \ T \log \ T + (0.75 \times 10^{-3}) T^2 \\ &- (0.39 \times 10^5) T^{-1} - 36.23 \ T; \quad \text{(7a)} \\ \Delta H^\circ &= 35670 - 1.17 \ T - (0.75 \times 10^{-3}) T^2 \\ &- (0.78 \times 10^5) T^{-1}; \quad \text{(7b)} \\ \Delta S^\circ &= 35.06 - 2.694 \log \ T - (1.50 \times 10^{-3}) T \end{split}$$

 $-(0.39 \times 10^5) T^{-2}$. (7e)

A value for the entropy of sublimation, $\Delta S_{298}^{\circ}=27.51$ e.u./mol, calculated from equation (7c) is in good agreement with a value, $^{(14)}$ $\Delta S_{298}^{\circ}=27.74$ e.u./mol, which is based upon an entropy for the solid obtained from heat capacity measurements and a calculated entropy for the gas. An enthalpy of sublimation, $\Delta H_{298}^{\circ}=34.99\,\mathrm{kcal/mol}$, calculated from equation (7b) is within the quoted precision of the value, $\Delta H_{298}^{\circ}=35.6\pm0.8\,\mathrm{kcal/mol}$, tabulated by Kubaschewski and Evans. (15)

The temperature dependence of the vapor pressure of magnesium expressed on the basis of the present data is

$$\log\,P^\circ\,({\rm atm}) = 7.919 - 7796\,T^{-1} - 0.589\,\log\,T$$

$$- (0.16\times 10^{-3})T + (0.85\times 10^4)T^{-2} \quad (8)$$

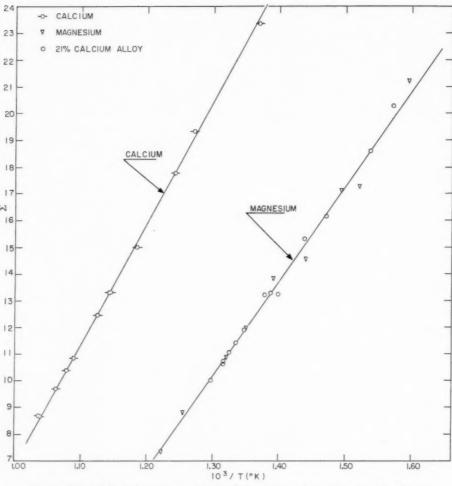


Fig. 3. Plot of sigma function vs. reciprocal temperature for magnesium and calcium.

The vapor pressures computed from this equation in the range 600–900°K are of the order of 10 per cent higher than vapor pressures computed from the relation tabulated by Kubaschewski and Evans.⁽¹⁵⁾

3.2. Calcium

Vapor pressures over solid calcium have previously been measured by Rudberg, (16) Pilling, (17) Douglas, (18) Tomlin, (19) and Priselkov and Nesmeyanov (20) and over liquid calcium by Hartmann and Schneider. (21) The results of these past measurements are plotted together with the present measurements in Fig. 4; the results of Pilling, Douglas, and Tomlin are plotted as a single line in the manner of Tomlin. Analysis of the calcium used in the present investigation showed the following impurity content: Mg, 0.01 wt.%; N, 0.01 wt.%; C, 0.02 wt.%; and Si, 0.005 wt.%. Ba, Be, B, Fe, and Al were spectroscopically estimated to be present in quantities less than 0.001 wt.% and Cd,

Cu, K, and Li were present to less than 0.0001 wt.%. No other common metallic impurities were detected. Vapor pressures were measured in the range, 730–965°K, and the data were treated in the same manner as the magnesium data. A plot of the sigma function vs. reciprocal temperature is shown in Fig. 3. A heat capacity for solid calcium, (13)

$$C_n(s) = 6.29 + (1.40 \times 10^{-3})T,$$
 (9)

19

and a value of 4.97 for gaseous calcium were used to evaluate the constants in the sigma function,

$$\Sigma_{\rm Ca} = -4.575 \log P - 3.04 \log T - (0.70 \times 10^{-3})T. \eqno(10)$$

Values for the constants, $\Delta H_0 = 45550 \pm 480$ cal/mol and $I = -38.76 \pm 0.56$ e.u./mol, were obtained. The temperature dependence of the thermodynamic functions for the sublimation process for β -calcium

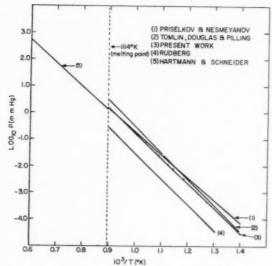


Fig. 4. Log vapor pressure vs. reciprocal temperature as determined by various investigators for calcium.

were found to be:

VOL.

1959

$$\Delta F^{\circ} = 45550 - 38.76 \ T + (0.70 \times 10^{-3}) T^2 + 3.04 \ T \log T;$$
 (11a)

$$\Delta H^{\circ} = 45550 - 1.32 \ T - (0.70 \times 10^{-3}) T^{2};$$
 (11b)

$$\Delta S^{\circ} = 37.44 - 3.04 \log T - (1.40 \times 10^{-3})T$$
. (11c)

An entropy of sublimation, $\Delta S_{738}^{\circ} = 27.69$ e.u., calculated from equation (11e) is somewhat greater than a value, $\Delta S_{738}^{\circ} = 24.95$ e.u., computed from entropy values and the heat capacity of α-calcium tabulated by Kelley (13,14) and the enthalpy of transition at 738°K listed by Kubaschewski. (22) An enthalpy, $\Delta H_{298}^{\circ} =$ 45.09 kcal/mol, calculated from equation (11b) is in poor agreement with a value of $\Delta H_{298}^{\circ} = 12.49 \text{ kcal/}$ mol tabulated by Kelley (23) which is not surprising since Kelley's value is based on the vapor pressure measurements of Pilling. The calcium used by Pilling was quite impure and was reported to contain 1.62% Mg and 1.25% CaCl₂. The presence of the magnesium would be expected to lead to abnormally high values for the measured vapor pressures. In addition the technique employed by Pilling is sus eptible to large experimental errors.

Comparison of the remaining vapor pressure data may be made with reference to Fig. 4. Rudberg's data are obviously low and may be discounted on the basis of the geometry of his effusion vessel and the placement of his heating element. Vapor pressures in mm Hg indicated at the melting point are: Hartmann and Schneider, 1.35; Douglas and Tomlin, 3.19; Priselkov and Nesmeyanov, 1.38; this investigation, 1.67. Approximate values for the heat of fusion may

be obtained by comparing the slopes of the curves in Fig. 4 above and below the melting point. The data of Priselkov and Nesmeyanov are inconsistent with those of Hartmann and Schneider since an exothermic fusion is indicated. Comparison of the curve of Tomlin and Douglas with that of Hartmann and Schneider indicates a heat of fusion of about 5 kcal/mol while comparison of the present data with that of Hartmann and Schneider indicates a heat of fusion of about 3 kcal/mol. Kubaschewski⁽²²⁾ lists a heat of fusion of 2.1 kcal/mol. On this basis it is felt that the present measurements are in better agreement with the work of Hartmann and Schneider than are the results of Tomlin and Douglas or of Priselkov and Nesmeyanov.

3.3. Calcium-magnesium alloys

In addition to the measurements on the 21 at.% alloy already discussed, vapor pressure measurements were made on alloys containing 40, 70, and 84 at. % calcium. These alloys were all on the calcium-rich side of the compound composition. The measured vapor pressures for samples of these alloys are in good agreement for the two phase region below the eutectic temperature. The results are shown in Fig. 5. Above the eutectic temperature the vapor pressure curves diverge, with the upper arm representing the equilibrium vapor pressures over the region of compound plus liquid and the lower arm representing the vapor pressures over the region of liquid plus solid calcium. Presumably all measurements for the alloys were taken above two phase regions since no indication of a liquidus temperature was observed in any of the vapor pressure curves. The close agreement between the measured vapor pressures above the eutectic temperature for the 40% and 70% alloys indicates that the 70% alloy is on the compound-rich side of the eutectic. This result supports the work of Klemm and Dinkelacker (24) who place the eutectic composition near 73 at.% rather than the 67 at.% indicated in Fig. 1. Further, the lack of an indication of a liquidus temperature in the vapor pressure curve for the 70% alloy implies a steeply rising liquidus line in the phase diagram.

To verify that the calcium contribution to the alloy vapor pressures was negligible, a chemical analysis was made. After several measurements on alloys, the metallic condensate on the walls above the effusion chamber was dissolved and analyzed by a volumetric method. (25) No calcium was detected. However, the small amount of sample and the sensitivity of the method allows only the statement that calcium was present to less than 1 at.%.

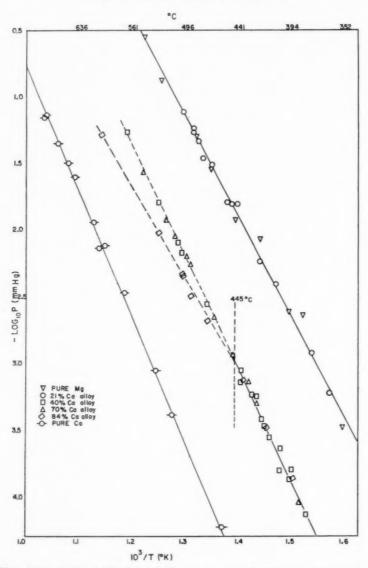


Fig. 5. Plot of the experimentally determined vapor pressure for the calcium-magnesium system.

Values for the free energy of the reaction described in equation (3) were computed from the measured vapor pressures over the 40, 70, and 84 at.% alloys in the temperature range, 655–718°K, below the eutectic temperature. Appropriate values for P° were obtained from equation (8). Since no heat capacity data for the compound, CaMg_2 , were available, it was assumed that ΔC_p was zero for the reaction. Values for the enthalpy and entropy of formation of the compound were then obtained by making a least squares fit to the temperature dependence of the computed free energies of formation. The resulting values were: $\Delta H^{\circ} = -8.3 \pm 2.9 \text{ kcal/mol}$ and $\Delta S^{\circ} = -1.1 \pm 4.3 \text{ e.u./mol}.$

4. DISCUSSION

The low values of the enthalpy and entropy of formation of the compound, CaMg_2 , are consistent with the view that the compound forms because of atomic size considerations. The entropy of formation is comparable in order of magnitude to the entropy of formation of the Laves phase, Na_2K , which was calculated to be 0.9 e.u./mol on the basis of heat capacity measurements. (13,26) The enthalpy of formation of CaMg_2 is only slightly less than the estimate based on an increase in the number of bonds in the compound compared to the elemental structures; the implication is that the bonding in the compound is comparable to the bonding in the elements. An

independent determination of the enthalpy of formation was made by bomb calorimetry. Heats of combustion were measured for two samples of CaMg₂ and for corresponding weights of unreacted calcium and magnesium. The difference between these heats of combustion was used to obtain the heat of formation, and, since the difference was small compared to the heats of combustion, the precision was poor. A value of -14 ± 10 kcal/mol was obtained. The agreement with the vapor pressure result is within the precision of measurement.

Values for the enthalpy of formation of CaMg₂ have been tabulated as -30 kcal/mol by Rossini et al. (27) and -21 kcal/mol by Kubaschewski and Evans. (15) Both of these values are based on measurements of heats of solution made by Biltz and Hohorst (28) on a 55% Ca-45% Mg alloy and on unreacted calcium and magnesium. Biltz and Hohorst reported a heat of formation of -43 kcal/mol for the compound which was believed to be Ca₃Mg₄. The difficulties and limitations of solution calorimetry have been adequately discussed by Kubaschewski and Evans. It is believed that the value obtained from vapor pressure measurements is a more reliable figure.

ACKNOWLEDGMENTS

VOL.

1959

The authors wish to thank Dr. A. H. Daane for the generous loan of his microbalance. Thanks are also due to Dr. Harvey Diehl for the use of his bomb calorimeter and to Mr. J. L. Christian for his assistance in making some of the experimental measurements.

REFERENCES

- 1. H. WITTE, Naturwiss. 25, 795 (1937).
- T. G. Massalski, Theory of Alloy Phases p. 107. American Society for Metals (1956); F. Laves, Ibid. p. 151.
- 3. H. Brooks, Theory of Alloy Phases p. 217, American Society for Metals (1956).
- 4. G. F. SAGER and B. J. NELSON, Metals Handbook p. 1185. American Society for Metals (1948).
 5. E. C. Burke, J. Metals, N.Y. 7, 285 (1955).
- 6. W. BULIAN and E. FAHRENHORST, Metallforschung 1, 70
- 7. H. Nowotny, quoted by F. Weibke and O. Kubaschewski, Thermochemie der Legierungen. Springer, Berlin (1943). 8. J. F. Smith, O. N. Carlson and R. W. Vest, J. Electro-
- chem. Soc. 103, 410 (1956).
 9. H. MELSERT, T. J. TIEDEMA and W. G. BURGERS, Acta
- Cryst. 9, 525 (1956).
- M. KNUDSEN, Ann. Physik 28, 999 (1909).
- 11. F. C. EDWARDS and R. R. BALDWIN, Anal. Chem. 23, 357 (1951)
- L. S. Darken and R. W. Gurry, Physical Chemistry of Metals, pp. 225-231. McGraw-Hill, New York (1953).
 K. K. Kelley, U. S. Bur. Mines Bull. No. 476 (1949).
 K. K. Kelley, U. S. Bur. Mines Bull. No. 477 (1950).
- 15. O. Kubaschewski and E. L. Evans, Metallurgical Thermo-
- chemistry Butterworth-Springer, London (1951).
 16. E. Rudberg, Phys. Rev. 46, 763 (1934).
 17. N. B. Pilling, Phys. Rev. 18, 362 (1921).
- P. E. DOUGLAS, Proc. Phys. Soc. B67, 783 (1954).
- 19. H. Tomlin, Ibid. 67B, 787 (1954).
- 20. Y. Priselkov and A. Nesmeyanov, Doklady Akad. Nauk SSSR 95, 1207 (1954).
- 21. H. HARTMANN and R. SCHNEIDER, Z. anorg. Chem. 180, 275 (1929).
- 22. O. Kubaschewski, Z. Elektrochem. 54, 275 (1950).
- 23. K. K. Kelley, U. S. Bur. Mines Bull. No. 383 (1935)
- 24. W. Klemm and F. Dinkelacker, Z. anorg. chem. 255, 2 (1947).
- 25. HARVEY DIEHL and J. L. ELLINGBOE, Anal. Chem. 28, 882 (1956).
- C. A. KRIER, R. S. CRAIG, and W. E. WALLACE, J. Phys.
- Chem. 61, 522 (1957).
- 27. F. Rossini et al., Selected Values of Chemical Thermodynamic Properties. National Bur. Standards Circular 500 (1952).
- 28. W. BILTZ and G. HOHORST, Z. anorg. Chem. 121, 1 (1922).

THE GROWTH OF TEMPER CARBON NODULES*

J. BURKE†

The equations relating the radius of a temper carbon nodule to the time of annealing during first stage graphitization are presented for each of the possible controlling mechanisms, and compared with experimental growth curves. The relation between these equations and that giving the fraction graphitization as a function of time is discussed. From these considerations it is concluded that, in the alloys considered, the rate of solution of cementite determines the rate of growth of graphite, except during the very early stages of the reaction.

LA CROISSANCE DES NODULES DE GRAPHITE

L'auteur donne les équations liant le rayon d'un nodule au temps de recuit, pendant le premier stade de la graphitisation, pour chacun des mécanismes possibles. Il les compare avec les courbes expérimentales de croissance. Il discute ensuite la relation entre ces équations et celle donnant le pourcentage de graphitisation en fonction du temps. De ces considérations, l'auteur conclut pour les alliages considérés, que la vitesse de dissolution de la cémentite détermine la vitesse de croissance du graphite, exception faite des tous premiers instants de la réaction.

DAS WACHSTUM VON TEMPERKOHLE-KNOTCHEN

Die Gleichungen, die den Radius eines Temperkohle-Knötchens mit der Wärmebehandlungszeit während des ersten Stadiums der Umwandlung von chemisch gebundenem Kohlenstoff in graphitischem verknüpfen, werden für jeden der möglichen Umwandlungsmechanismen dargelegt und mit experimentellen Wachstumskurven verglichen. Die Beziehung zwischen diesen Gleichungen und derjenigen, die den graphitisierten Bruchteil als Funktion der Zeit angibt, wirderörtert. Aus diesen Betrachtungen folgt, dass in den betrachteten Legierungen die Lösungsgeschwindigkeit des Zementits die Geschwindigkeit des Graphitwachstums bestimmt mit Ausnahme des Wachstums in den allerersten Stadien der Reaktion.

INTRODUCTION

Several mechanisms have been suggested as controlling the rate of first stage (gamma range) graphitization in white east irons and related alloys. These vary from relatively simple theories postulating control by one of the diffusion processes involved in the reaction (1,2) to the suggestion by Schwartz (3) that the rate of crystallization of graphite, the rate of diffusion of carbon in austenite and the rate of solution of cementite each exert control during successive stages. The graphitization reaction has two components, nucleation and growth, both of which have an important influence on the kinetics of the total reaction. To simplify the problem it is convenient to consider these two components separately. This discussion is limited to a consideration of the growth of temper carbon nodules. Several papers on this topic have appeared recently (4,5,6) but the operative controlling process is not yet established. This is partly because growth rates have not been measured in a sufficient number of alloys to test the theories rigorously, but also because the existing theories, with the exception

of the work of Birchenall and Mead, (6) are not based upon a satisfactory mathematical analysis.

19

In the present paper an attempt is made to develop equations of radial growth of graphite nodules for all the possible controlling mechanisms (except where these are available) and to assess the results in the light of the published growth data and other pertinent observations with a view to establishing the controlling mechanism. It will become clear from the following that only a limited number of high purity type alloys have been investigated in sufficient detail to permit even a tentative conclusion. The discussion, therefore, is limited to this class of alloy except where stated otherwise.

2. EXPERIMENTAL MEASUREMENTS OF THE RATE OF GROWTH OF GRAPHITE NODULES

The graphite nodules in annealed white irons take one of two forms, the flake-aggregate or the spherulitic. The factors which determine the morphology have been discussed elsewhere.^(7,8) Almost all the reported measurements of growth rates refer to the flake-aggregate variety, but in this paper no attempt will be made to discriminate between them and the general term 'nodule' will be used.

^{*} Received June 26, 1958.

[†] Department of Metallurgy, University of Liverpool.

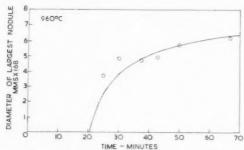


Fig. 1. Growth curve for high purity Fe-C-Si alloy (3.58% C, 1.12% Si), after Burke and Owen. (4).

The first measurements of growth rates were published by Brown and Hawkes⁽⁹⁾ who studied commercial blackheart irons using a technique developed by Mehl and his associates. This consists of measuring the diameter of the largest observable nodule in a series of samples annealed at successively longer times; plots of the maximum diameters as a function of time have a gradient which is twice the rate of radial growth. They found that the growth rate decreased continuously throughout the reaction, the growth curves fitting a parabolic equation,

$$r^2 = K_1 t \tag{1}$$

where r is the radius of the largest nodule after time t (measured from the end of the incubation period) and K_1 is a constant. They also observed that the carbide particles nearest to the nodules did not completely disappear before the more remote particles started to dissolve. Consequently, they suggested that the rate of solution of cementite was the slowest process, but no attempt was made to develop the idea quantitatively.

Independently, Burke and Owen, (4) using the same method as Brown and Hawkes, studied the rate of growth of nodules in high purity iron-earbon-silicon alloys. A curve typical of their results is shown in Fig. 1. They also concluded that the rate of growth decreased continuously. The results were discussed in terms of a model for first stage graphitization which gave good agreement with the measured rates of graphitization but which implied a constant rate of growth. Clearly, it is not possible to construct a straight line through all the points in Figure 1. Thus, at best the model can be only an approximation. Evidently, the good agreement with other experimental observations was fortuitous due to compensating errors in other assumptions. Diffusion of iron or silicon away from the nodule was thought to be the controlling process. Later, both the model and the interpretation were questioned by Birchenall and Mead. (6)

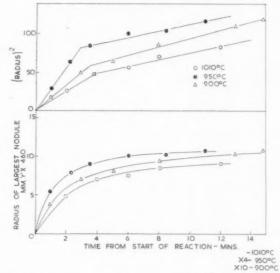


Fig. 2. Growth curves for high purity Fe–C–Si–S–Mn alloy (3.34% C, 0.91% Si, 0.17% Mn, 0.083% S), after Wilcock.

Additional growth curves for iron–carbon–silicon alloys were later published by Owen and Wilcock⁽⁵⁾ who also observed a decreasing rate of growth. These data were discussed in terms of a model which is essentially the same as that used by Burke and Owen. It was then suggested that the rate of crystallization of graphite controls during the initial stages and the rate of solution of cementite towards the end.

Recently, Wilcock⁽¹⁰⁾ has studied first stage graphitization in iron-carbon-silicon alloys containing manganese and sulphur. Some typical growth curves are shown in Fig. 2. He concluded that the data could be fitted by two interpenetrating parabolas as demonstrated in the upper graph. From activation energy considerations he concluded that carbon diffusion controlled the growth rate in the initial stages (corresponding to the first parabola) and diffusion of iron or silicon controlled in the second stage.

Birchenall and Mead⁽⁶⁾ developed an equation for the radius of a nodule as a function of time, on the assumption that growth was controlled by diffusion. By comparison with the results of Brown and Hawkes⁽⁹⁾ and Burke and Owen⁽⁴⁾ they concluded that the rate of carbon diffusion in austenite was the slowest step.

From this brief review it is clear that there is no general agreement about the process controlling the rate of growth.

3. THE POSSIBLE PROCESSES CONTROLLING THE RATE OF GROWTH

Metallographic evidence reveals that the graphite nodules grow within an austenite shell, outside of

VOL. 7 1959

which is a mixture of cementite and austenite. Thus, the basic steps involved are (1) the solution of cementite, (2) the transport of carbon atoms through the austenite. (3) the transfer of carbon atoms from the austenite on to the graphite lattice and (4) the diffusion of iron and silicon atoms away from the growing nodule. It is onceivable that any one of these may determine the growth rate. The problem is to determine which is the slowest process. The best method is to calculate rates of growth assuming that each is the governing process and compare with the experimental data. This has hitherto only been carried out for carbon diffusion and iron diffusion by Birchenall and Mead. (6) A second, and more usual method, is to derive the activation energies for the growth rate and compare it with that for the various processes determined in independent experiments. The first method is used here.

Growth controlled by a diffusion process

If the growth is controlled by diffusion the form of the rate curve is not dependent upon the species diffusing. The problem was considered by Birchenall and Mead⁽⁶⁾ who obtained the result

$$r^{2} = \left[\frac{2(C_{2} - C_{1})D}{(C_{0} - C_{1}) \left(1 - \left(\frac{C_{\infty} - C_{2}}{C_{0} - C_{1}} \right)^{1/3} \right)} \right] t \qquad (2)$$

in which C_0 , C_1 , C_2 and C_{∞} are respectively the concentration of the diffusing species considered in graphite, in austenite in equilibrium with graphite, in austenite in equilibrium with cementite and in the austenite-cementite mixture: r is the radius after time t and D the appropriate diffusion coefficient. Thus, the growth curve expected on the basis of diffusion control is parabolic. To distinguish between the various diffusing species it is necessary to evaluate the expression within the brackets—"the parabolic growth constant." This was done for iron and carbon diffusion. The growth data of Burke and Owen(4) were represented by parabolic curves and compared with the theoretical curves. It is claimed that the agreement is good when carbon diffusion is considered to be controlling. However, the method used to convert the experimental data into parabolic form was necessarily very approximate. In addition, some temperatures were mis-quoted by as much as 40°C. Thus, the agreement is of dubious significance.

Growth controlled by solution of cementite

As far as is known no growth equation has been derived previously on this basis. Consider the con-

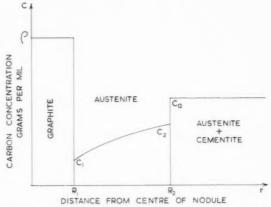


Fig. 3. Conditions existing during the growth of graphite nodule. Nodule, radius R_1 and density ρ , is surrounded by a shell of austenite, radius R_2 , the carbon concentration of which varies from C_1 to C_2 ; outside of this is a mixture of austenite and cementite of concentration C_a .

ditions shown in Fig. 3. A spherical graphite nodule, radius R_1 is growing in an austenite envelope, radius R_2 , which is surrounded by a mixture of cementite and austenite of composition C_a . Let the carbon concentration of the austenite adjacent to the graphite be C_1 and that next to the cementite–austenite mixture be C_2 , and the density of graphite be ρ .

The first step is to find the relationship between R_1 and R_2 . If R_1 increases by dR_1 whilst R_2 increases to $R_2 + dR_2$, the weight of carbon deposited onto the graphite during the increase of R_1 is $4\pi R_1^2 dR_1 \rho$. This must be equal to the weight of carbon swept up by the graphite interface moving through the austenite, $4\pi R_1^2 C_1 dR_1$, plus the carbon swept up by the moving austenite-mixture interface, $4\pi R_2^2 C_a dR_2$, less the amount left in the austenite at the periphery of the shell, $4\pi R_2^2 C_2 dR_2$. Thus,

$$R_1{}^2(\rho-C_1)dR_1=R_2{}^2(C_a-C_2)dR_2$$

which on integrating gives

$$\frac{R_2}{R_1} = \left(\frac{\rho - C_1}{C_a - C_2}\right)^{1/3} = \alpha. \tag{3}$$

19

This relationship is independent of the mechanism controlling growth.

The rate of growth, dR_1/dt is related to the flux of carbon atoms, J, to the interface by the equation

$$4\pi R_{1}^{2} \frac{dR_{1}}{dt} (\rho - C_{1}) = J. \tag{4}$$

The isothermal rate of solution of cementite can be defined as S grams of carbon per unit area of surface per unit time. The carbon flux is then S times the area of cementite. The difficulty is to evaluate the

surface area which is effectively contributing to the growth of any one nodule. The particles dissolving to supply carbon do not have to be contiguous with the austenite shell. The most reasonable approximation appears to be to take the effective surface area of cementite as equal to the outer surface of the austenite shell. Thus:

$$J = 4\pi R_2^2 S \tag{5}$$

and using equation (3)

$$J = 4\pi R_1^2 \alpha^2 S \tag{6}$$

Thus, equation (4) becomes

$$\frac{dR_1}{dt} = \frac{\alpha^2 S}{\rho - C_1} = \beta \tag{7}$$

and the radial rate of growth of an isolated nodule controlled by the rate of solution of cementite is a constant. Since the growth of neighbouring nodules is competitive an impingement term must be incorporated in the above expression. The usual method is to multiply the rate by the untransformed fraction (1-y) where y is the fraction graphitized at time t. Then

$$\frac{dR_1}{dt} = \beta(1-y). \tag{8}$$

It is known from dilatometric studies of isothermal graphitization in various high purity alloys that

$$y = 1 - \exp[-(t/K)^n]$$
 (9)

where n and k are constants. It has been found experimentally that, up to about 60 per cent transformation n=4.^(4,10) Equation (9) is discussed in more detail later.

Thus.

1959

$$\frac{dR_1}{dt} = \beta \, \exp_1 \left[-(t/k)^4 \right] \! . \tag{10}$$

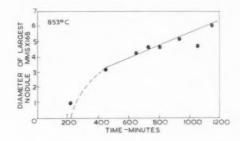
To integrate this expression the exponential is expanded in a series. Since k is equal to the time when y = 0.63, (4) up to this fraction of graphitization (t/k) is less than unity and the series is convergent.

$$\frac{dR_1}{dt} = \beta[1 - (t/k)^4 + (t/k)^8...]. \tag{11}$$

Integrating

$$R_1 = \beta \left[t - \frac{t^5}{5k^4} + \frac{t^9}{9k^8} \dots \right].$$
 (12)

Thus, the growth curves predicted should be approximately linear except when the impingement terms become important, i.e. at long times or small values of k:



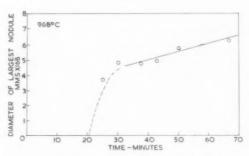


Fig. 4. Growth curves for high purity Fe-C-Si alloy (3.58% C, 1.12% Si), treated as two-stage curve.

The solution of cementite cannot be controlling in the initial stages of growth because at the start the austenite, in equilibrium with respect to cementite, is supersaturated relative to graphite and thus, for a short time at least, the nodule will obtain carbon by depletion of the austenite. During this stage the above analysis is not applicable and the rate of growth is governed by either diffusion or crystallization of graphite. As the available carbon is used up solution of cementite will start and, if it is the slowest process, will assume control. The growth curves should consist of two parts if cementite solution is the controlling factor: firstly, a transient stage during which the rate of growth decreases, and a second stage in which the curve should be approximately linear.

The available experimental data are consistent with this prediction. Fig. 4 shows two growth curves obtained in the earlier work on iron–carbon–silicon alloys⁽⁴⁾ from which it can be seen that the data can be well represented by a two stage curve. The transient stage is shown as a broken and the linear part as a full line. Some curves due to Wilcock⁽¹⁰⁾ are re-drawn in Fig. 5 and show a particularly good fit to this method of representation. Thus, it is concluded that the model is in good qualitative agreement with the experimental growth curves. A quantitative comparison is as yet not possible because no independent data relating to the rate of solution of cementite are available.

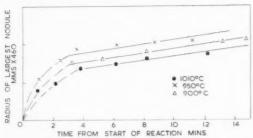


Fig. 5. The growth curves of Fig. 2 re-drawn as two-stage curves.

Growth controlled by the rate of crystallization of graphite

Let ϕ be the rate of crystallization defined as the weight of carbon transferred on to the graphite lattice from austenite in equilibrium with graphite, per unit area of surface, per unit time. Then the growth equation corresponding to (4) is

$$4\pi R_1^2 \frac{dR_1}{dt}(\rho) = 4\pi R_1^2 \phi. \tag{13}$$

In this case there are no impingement effects, since the rate at which carbon atoms are supplied is not important, and thus the rate of growth throughout the reaction is constant. The growth curves are linear and pass through the origin; zero time being taken as the start of the reaction.

It is clear that none of the experimental growthrate data (Figs. 1, 2) can be represented in this manner.

Discussion

At this point it is possible to eliminate the rate of crystallization of graphite. A certain amount of doubt still attaches to the other two processes. At least for high purity alloys the growth curves are in good qualitative accord with those predicted by a model in which the rate of solution of the carbide is the slowest step. But the same curves have been used to support suggestions of a parabolic growth law indicative of a diffusion controlled reaction. Thus, it seems that the experimental growth curves cannot be interpreted unequivocally. This unsatisfactory situation is due to the inherent experimental difficulties associated with these measurements. The nodules are seldom perfect spheres. Indeed flakeaggregate nodules often deviate quite markedly from this ideal. Thus there is some doubt as to what dimension is to be regarded as the 'radius' for the purpose of measurement. It is to be anticipated that this factor will give rise to considerable scatter in the experimental results, as a result of which the ambiguity referred to arises.

In view of this fact the experimental growth curves are not of themselves capable of deciding the issue. It is necessary to consider other features of the kinetics.

4. KINETICS OF FIRST STAGE GRAPHITIZATION

From a dilatometric study of first stage graphitization in iron–carbon–silicon alloys, Burke and Owen⁽⁴⁾ showed that the rate of reaction satisfied an equation, commonly used to describe nucleation and growth kinetics, of the form

$$y = 1 - \exp[-(t/k)^n].$$
 (9)

19

The value of n was found to be independent of temperature and composition within the range studied; the mean value was approximately 4.0. A similar equation was also used by Wilcock⁽¹⁰⁾ to describe graphitization in iron–carbon–silicon alloys containing manganese and sulphur; in this case n has the value of 4.0 (approximately) up to 60 per cent graphitization thereafter being in the range 2.5 to 3.0. Any model of the growth process must account satisfactorily for these values of the index n.

Particular forms of equation (9) have been derived by Zenor and Wert(11,12) and by Johnson and Mehl.(13) It is now clearly recognized that the variables determining the value of n are (1) the shape of the precipitate. (2) the form of the growth equation. (3) the form of the nucleation equation and (4) the geometry of any impingement effects. (14) If any three of these factors can be fixed or eliminated the fourth can be determined from the experimental value of n. The most common usage is to obtain information about the shape of submicroscopic precipitates. In the present case information is required about the form of the growth equation. Factors (1) and (4) can be accounted for by making the reasonable assumption that the graphite nodules are spherical in which case there can not be any impingement effects other than general soft impingement. Rates of nucleation, factor (3), have been measured by Brown and Hawkes⁽⁹⁾ (commercial alloys), Burke and Owen, (4) Owen and Wilcock⁽⁵⁾ and Wilcock⁽¹⁰⁾ The general features are well established. The number of nodules per unit volume increases continuously up to a maximum (Fig. 6) corresponding to 50-60 per cent graphitisation, and thereafter decreases due to the re-solution of small particles in favour of larger ones. Up to the maximum the volume nucleation frequency is always very nearly linear. After the re-solution commences nucleation effectively ceases and makes no further contribution to the rate of reaction. Thus, the

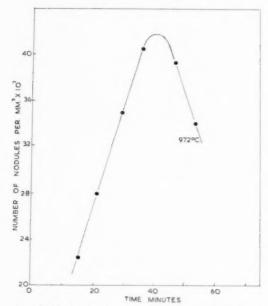


Fig. 6. Nucleation frequency curve for Fe-C-Si alloy (3.38%C, 1.13% Si), after Owen and Wilcock. (5)

nucleation equation can be written as

$$N = k_N t^a \tag{14}$$

where N is the number of nodules per unit volume at time t measured from the end of the incubation period, k_N a temperature dependent constant and a is a constant equal to unity up to 50–60 per cent reaction and zero thereafter.

Having defined factors (1), (3) and (4), it is now possible to deduce the nature of factor (2), the growth equation, from the experimental values of n by a mathematical technique similar to that used by Johnson and Mehl. (3) Writing the growth equation in the general form,

$$R_1 = k_R t^b \tag{15}$$

for the first part of the reaction corresponding to a = 1.

$$n = 3b + 1 \tag{16}$$

and for a=0

VOL.

1959

$$n = 3b. (17)$$

An interesting point which arises from equations (16) and (17) is that the value of n should be reduced by unity in the final stage of graphitization. Such a change has been detected by Wilcock.⁽¹⁰⁾

Equation (16) provides a basis for deciding between a diffusion process or cementite solution as the controlling step. Diffusion control requires a parabolic growth curve (equation 2) so that $b=\frac{1}{2}$. Thus up to 50–60 per cent graphitization, the value of n would

be 2.5. The difference between this theoretical value and the experimental value of 4.0 is greater than the possible experimental error. Thus, this is strong evidence, not considered by Birchenall and Mead, that the rate of growth is not controlled by diffusion of any species.

On the other hand the linear rate of growth predicted by equation (7) leads to b = 1 and n = 4 which is in complete accord with the value of n determined experimentally. Thus, it is concluded that the rate of solution of cementite is the rate controlling process.

However, the transient part of the growth curves should give rise to a different value of the index during the initial stages of the reaction; this has never been observed. There are several possible explanations.

(1) Ostberg⁽¹⁷⁾ has suggested that at a very early stage of the reaction the nucleation rate increases rapidly. The effect of this on n might compensate for any reduction due to the transient stage of growth.

(2) Some compensation may be provided by deviation from the assumed spherical geometry.

(3) The value of n is determined from the gradient of plots of log. log (1/(1-y)) against log t. It may be that the transient stage is of such a short duration that it cannot be detected on such plots.

(4) A decreased value of n in this first stage is to be anticipated only if the rate controlling process during this stage is diffusion. However, if, for example the rate of crystallization of graphite is the slowest initial step the value of n will remain unchanged.

5. DISCUSSION

There are a number of subsidiary arguments which can be used to support this conclusion. The nucleation frequency curve shown in Fig. (6) shows that a redistribution of nodule sizes occurs during graphitization. Small nodules redissolve and large ones grow. This starts before all the cementite has disappeared. Evidently, the small nodules are unstable relative to the larger ones; but even the smallest visible nodule must be stable relative to cementite otherwise graphitization would not be possible. Thus, it is to be expected that all sizes of graphite nodules would continue to grow until the cementite has disappeared. The fact that this is not so suggests that the cementite is not capable of dissolving sufficiently rapidly to provide the carbon necessary for the growth.

Moreover it is observed that carbide particles remote from a nodule start to dissolve before those adjacent to its austenite shell have completely vanished. (9,16,17) This also supports the view that cementite is the rate controlling process.

The decarburization of white cast iron has been

studied recently by Hughes and Moore(15) who concluded that the overall reaction rate is controlled by the rate of solution of cementite. Since decarburization involves the same steps as graphitization (solution of cementite and continuous removal of carbon by diffusion through austenite), this finding is in line with the present thesis.

It is concluded that the rate of growth of graphite nodules during first stage graphitization is controlled by the rate of solution of cementite. However, it must be emphasized that, since the value of the index n is an important part of the argument, this conclusion can be applied only to those alloys for which data relating to n are available. Investigation of a much wider range of composition is required before the generality of the conclusion can be assessed.

ACKNOWLEDGMENTS

The author is grateful to Professor W. S. Owen and to Dr. J. Wilcock for several critical discussions. Thanks are also extended to Dr. Wilcock for permission to use his data (Fig. 2) before publication and also to Mr. I. C. H. Hughes and Mr. C. T. Moore of the

British Cast Iron Research Association for information relating to work on decarburization.

REFERENCES

- 1. H. A. SCHWARTZ, Trans. Amer. Soc. Steel Treat. 9, 883 (1926).
- 2. K. P. Bunin and I. V. Salli, Dokl. Akad. Nauk SSSR 83, 841 (1952).
- 3. H. A. Schwartz, Trans. Amer. Soc. Metals 30, 1328 (1942). 4. J. BURKE and W. S. OWEN, J. Iron St. Inst. 176, 147 (1954).
- 5. W. S. OWEN and J. WILCOCK, J. Iron St. Inst. 182, 38 (1956).
- 6. C. E. BIRCHENALL and H. W. MEAD, J. Metals, N.Y. 8, No. 8 1004 (1956).
- 7. H. Morrogh, J. Iron St. Inst. 143, 207 (1941).
- 8. A. HULTGREN and G. OSTBERG, J. Iron St. Inst. 176, 351 (1954)
- 9. B. F. Brown and M. F. Hawkes, Trans. Amer. Foundrym. Ass. 59, 181 (1951)
- 10. J. WILCOCK, Ph.D. thesis, Liverpool University, to be published (1956).
- C. ZENER, J. Appl. Phys. 20, 950 (1949).
 C. A. WERT, J. Appl. Phys. 20, 943 (1949).
- 13. W. A. Johnson and R. F. Mehl, Trans Amer. Inst. Min. (Metall.) Engrs. 135, 416 (1939).
- 14. D. TURNBULL, Solid State Physics (Edited by F. Seitz and D. TURNBULL), Vol. 3, p. 226. Academic Press, New York
- 15. I. C. H. Hughes and C. T. Moore, private communication.
- J. Burke and W. S. Owen, J. Iron St. Inst. 177, 449 (1954)

19

17. G. OSBERG, J. Iron St. Inst. 186, 49 (1957).

AGING IN Au-Ni ALLOYS*

J. SIVERTSEN† and C. WERT‡

Measurements have been made of changes in some physical properties of quenched alloys of 70% Au-30% Ni when they were annealed at low temperatures. Changes in the electrical resistance, volume, and Young's modulus were observed to occur. They indicate that there is at least one metastable precipitate formed on low temperature annealing; it occurs about 104 times earlier than the main phase change which has been well studied previously. There is a critical temperature above which this low temperature phase is unstable; this is about 225°C. Exact description of the low temperature phase is not possible, but it does seem to be either (1) clusters of Au-rich or Ni-rich atoms or (2) regions of high geometrical order. Quenched-in vacancies are presumed to control the rate of the reaction but the precipitate is not thought to be simply clusters of vacancies.

VIEILLISSEMENT DES ALLIAGES Or-NICKEL

Les auteurs ont mesuré certaines modifications de propriétés physiques d'alliages à 70% Au-30% Ni trempés puis revenus à des températures basses. Ils ont observé des modifications de la résistance électrique, du volume et du module de Young. Celles-ci indiquent qu'il se forme au moins un précipité instable au cours du revenu; il apparaît 10^4 fois plus tôt que le principal changement de phase étudié précédemment. Il existe en outre une température critique, environ 225°C, au-dessus de laquelle cette phase est instable. Il n'est pas possible de décrire cette phase avec précision, mais il est vraisemblable que l'on se trouve en présence d'amas riches en atomes d'or ou de nickel ou encore de régions à ordre géométrique élevé. Les auteurs rapportent que les lacunes bloquées par la trempe contrôlent la vitesse de la réaction mais que, par contre, les précipités ne sont pas simplement des amas de lacunes.

ALTERUNGSVORGÄNGE IN Au-Ni LEGIERUNGEN

Die Änderungen einiger physikalischer Eigenschaften abgeschreckter Legierungen aus 70% Au-30% Ni wurden beim Auslagern bei tiefen Temperaturen gemessen. Es treten Änderungen des elektrischen Widerstandes, des Volumens und des Elastizitätsmoduls auf. Diese zeigen, dass sich beim Anlassen bei tiefer Temperatur mindestens eine metastabile Ausscheidung bildet, diese tritt etwa 104 mal früher auf, als die Haupt-Phasenumwandlung, die früher gut untersucht worden ist. Es gibt eine kritische Temperatur, oberhalb der die Tieftemperaturphase instabil ist, diese ist etwa 225°C. Eine genaue Beschreibung der Tieftemperaturphase ist nicht möglich, sie scheint indessen entweder (1) aus Ansammlungen von Gold- oder Nickelatomen, oder (2) aus Gebieten mit hoher geometrischer Ordnung zu bestehen. Abgeschreckte Leerstellen bestimmen vermutlich die Reaktionsgeschwindigkeit, aber die Ausscheidung wird nicht einfach für eine Ansammlung von Leerstellen gehalten.

1. INTRODUCTION

The study of precipitation phenomena in alloys has long been a major field of investigation. Many papers, both experimental and theoretical, have dealt with the extensive array of effects which commonly accompany precipitation in solids. At the present time investigations are being made in both of the two courses open; the one of extending the measurements to new systems, and the other of investigating in finer detail precipitations already known to occur in certain systems. The present study is of the latter type; it

is an experimental investigation of the precipitation of two phases in the binary system Au–Ni. Some of the aging effects occurring upon the annealing of alloys in this system have long been known; the present work shows, however, that there are effects in this system which had been completely missed in the earlier studies.

Examination of the history of the investigations on many alloy systems shows one common feature: as experimental methods are developed to look at the precipitates in more detail, the whole process from beginning to end is found to be more and more complex. So it is with the alloy system Au–Ni. The first investigations made in 1936 by Köster and Dannöhl showed a relatively simple behavior. (1) The solid solutions characteristic of high temperatures could readily be retained upon quenching to room temperature. As these solid solutions were aged at intermediate temperatures (between 400°C and 600°C

1959

^{*} This research was supported in part by the United States Air Force through the Air Force Office of Scientific Research of the Air Research and Development Command, under Contract No. AF 18 (603)—22. Reproduction in whole or in part is permitted for any purpose of the United States government. Received June 5, 1958.

[†] University of Illinois, Urbana, Illinois.

Now at the University of Minnesota. This paper is part of a Ph.D. Thesis submitted by J. Sivertsen to the Graduate College of the University of Illinois in February, 1958.

roughly) they decomposed by a discontinuous reaction into a mixture of a Au-rich and a Ni-rich solid solution. Many property changes were observed to occur during this reaction and they all followed the course of the reaction nicely; it appeared to be one of a few simple systems.

The first indication that these alloys had some peculiarities came as a result of some thesis studies by students of M. Cohen and B. Averbach. Two of these which have bearing on the present work were those of Flinn and of Seigle; short descriptions of these follow.

The investigation by Flinn et al. was an X-ray study of these alloys, mainly a study into the low angle scattering of the solid solutions. (2) They found that the high-temperature solid solutions had pronounced short-range-ordering. For a system which has a phase mixture as its stable structure at low temperatures to have short-range-ordering at high temperatures is unusual. One expects such a system to show clustering at high temperatures. They supposed that the alloy ordered partially to reduce lattice strain energy. A further feature of precipitation in this system concerns the way in which order persists during aging at an intermediate temperature (315°C). As long as any untransformed part of the solid solution exists, evidence of short-range-order is found. Apparently it does not disappear homogeneously during the aging.

To add weight to these results, one needs only to consider the thermodynamical studies of Seigle et al.⁽³⁾ They found enthalpies of mixing to be positive. Such a result taken together with the X-ray results cited above shows that the Au-Ni solid solutions do not fit the usual quasi-chemical theories in which the entire heat of mixing is an electrochemical bonding between nearest neighbors. They postulate that the strain energy of a lattice, occupied by atoms as dissimilar in size as these two are, must make a contribution to the enthalpy of mixing. Again this is compatible with short-range-ordering.

The present work adds still more complexity to aging in this system. It is found that there exists an additional stage of precipitation besides that which was observed by Köster and Dannöhl. This is a very early stage, being found at relatively low temperatures for this system ($<200^{\circ}$ C) and being completed in less than 1/10,000 of the time required for the main phase reaction. The first hint of this effect came from some internal friction work of Ang et al.⁽⁴⁾ This has been followed by measurements of changes upon aging in the electrical resistance, volume and elastic constants. These measurements are reported in this paper.

2. EXPERIMENTAL PROCEDURE AND RESULTS

The experiment to be described involved measurements of several types. To keep the form of the presentation simple we will therefore present the major results of each type of measurement as it is described.

(a) Preparation of specimens

A major part of the investigation was made with an alloy of nominal composition 70 at. % Au. The actual composition of the various melts varied slightly from this but not by more than ± 1.5 %. One alloy of 60% Au was prepared and a few measurements were made using it. This was done to determine that the effects seen were not peculiar to the exact composition of 70% Au. The gold and nickel used in making the alloys were of reasonably high purity, the gold being 99.98% pure, the nickel 99.9+% pure. See Fig. 1.

All alloys were made by melting together in alundum crucibles mixtures of the appropriate amounts of the pure constituents. The melts were made under various conditions to ensure that the experimental results were not peculiar to one type of specimen preparation. Some melts were made in a vacuum of about 10^{-3} – 10^{-4} mm of Hg; some were made under a helium atmosphere. Some melts were made in an electric furnace, others in a high-frequency induction furnace. In each case the molten alloy was held 150° C above the melting point for about 30 min, then was slowly cooled through its melting point to solidify the alloy. After this, all alloys were held at about 900° C (which is

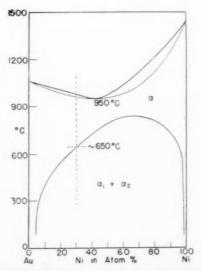


Fig. 1. Constitution diagram of Au-Ni system. The vertical dashed line shows the composition of most of the specimens used in this work.

about 50°C below the melting point for this composition) for 1 hr before being cooled to room temperature. All alloys were further annealed in vacuum for 4 days at 875°C to make them more homogeneous. These castings were rods about 1/4 in. diameter and 1 in. long. All showed a weight loss during their manufacture of less than 0.03 per cent and all are therefore presumed to have a composition close to 70% Au.

Specimens of the two types were made from these eastings by cold swaging and cold drawing them with appropriate intermediate anneals. A large number of specimens were made for resistance measurements; these were wires of about 0.03 in. diameter. A number of specimens were also made for elastic constant and length change measurements. These were short rods about 0.10 in. in diameter.

(b) The resistance measurements

VOL.

1959

The major part of this investigation was concerned with the changes in resistance occurring upon the annealing of the quenched alloys. Since the large change in resistance which accompanies the main phase reaction is well known, not much effort was spent examining it. Rather, the major effort was put into studying short-time changes occurring during the aging. This effect was found in a preliminary study to be of order 1 per cent of the resistance of a quenched specimen, so sensitive methods of measurement were developed to measure it accurately.

A standard potentiometer method was used to make the measurements. Two type K potentiometers were used to measure the potential across the sample and the current through it. From these measurements the resistance was calculated. The specimens themselves were 0.03 in. wires about 4 in. long. Potential and

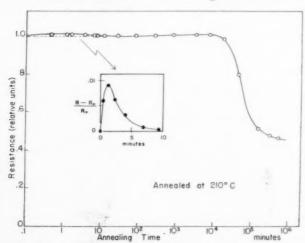


Fig. 2. Aging of a quenched alloy at 210°C. The inset shows an enlarged plot of the precipitation.

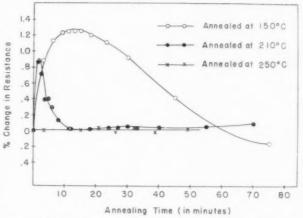


Fig. 3. The change in resistance vs. time at a number of aging temperatures. In each case the quench temperature was 700°C .

current leads were spot welded to the wires; these leads were finely drawn wires which could be folded along the specimens during heat treatments.

This method of measurement is an absolute method, so the temperature of measurement had to be controlled accurately. After some consideration of use of baths at other temperatures, an ice bath was selected as being simplest. It consisted of a large volume of crushed ice contained in a dewar. A copper container holding about 1 quart of acetone was placed in the ice bath; the specimen was immersed in the acetone during measurement. Temperature variations in the acetone were found to be less than 0.04°C. This corresponds to an inaccuracy in the total resistance of less than 0.01 per cent or to an inaccuracy in the effect being measured of less than 1 per cent.

The change in resistance which occurs when a quenched wire of this alloy is annealed at low temperature is shown in Fig. 2. For a temperature of 210°C the main phase change is found to occur in the time interval between 10⁴ and 10⁵ min; it is characterized by the large drop in resistance. This is the reaction studied by Köster and Dannöhl and others. At very short times, however, there is an additional effect shown magnified in the inset. It is characterized by a small increase in the resistance to a maximum, followed by a decrease to some new value (which for 210°C happens to be about the as-quenched value). It is this initial peak which has been studied in detail in the present work.

The problem of the quenching of these samples and their subsequent annealing was not difficult to solve. All heat treatments were carried out in a vacuum of order 10^{-5} to 5×10^{-6} mm of Hg. After appropriate time intervals at temperature, the samples were

quickly brought to room temperature by quenching them directly into a container of cold, out-gassed octoil-S which was inside the vacuum chamber. They

were then removed from the vacuum, mounted in the jig used for the resistance determination and measured.

The kinetics of this short-time annealing peak are strongly dependent on the annealing temperature. That this is so can be seen from Fig. 3. Here the data are shown for annealing at 150°C, 210°C and 250°C. Both the height of the peak and its position in time depend on temperature as is seen from observation of the curves for 150°C and 210°C. At 250°C and above no peak exists. Data were also obtained for other temperatures below 210°C. These curves are similar to the ones shown here; only the time scales and magnitudes of the peaks are different.

It is interesting to note that the data for the region below 210° C seem to indicate a thermally activated process. This is shown in Fig. 4 where a plot is made of the logarithm of time required for the maximum to be reached, as a function of 1/T. The data do lie on a straight line, the slope of which is about 15 k cal/mole.

The time required for the maximum in resistance to be reached is also a function of the quench temperature. The data of Fig. 5 show the results obtained in aging at 150°C a sample quenched from two different temperatures in the miscibility region. The rate of annealing is seen to increase as the quench temperature is raised.

Cold working after quenching does not affect this

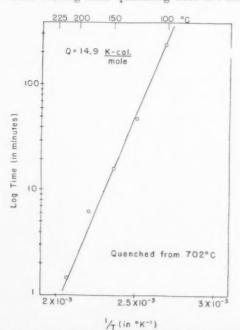


Fig. 4. A plot of the ln of the time for the resistance to reach a peak at the several aging temperatures.

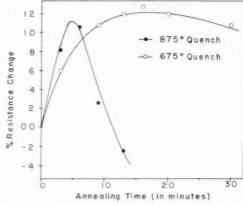


Fig. 5. The effect of quenching temperature on aging at 150°C.

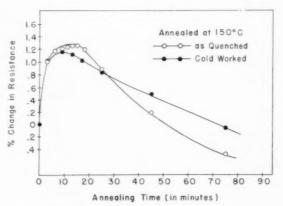


Fig. 6. Cold working following quenching has little effect on the aging.

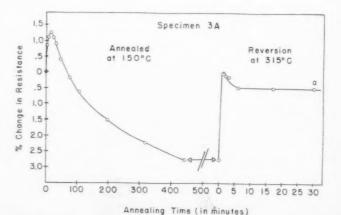


Fig. 7. Reversion of the precipitate following a step in aging temperature.

19

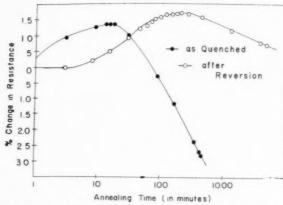


Fig. 8. After the reversion demonstrated in Fig. 7, aging occurs again at 150°C, but at a much slower rate.

low temperature annealing very drastically. A quenched specimen was twisted in a piece-wise fashion so that the net twist over the 4 in. length was about 450°. After this it was annealed in the normal fashion at 150°C. Data for the annealing after this treatment are shown in Fig. 6 along with data for an undeformed specimen. Although there is some change in the peak, it is certainly not a striking effect.

VOL.

1959

Alloy systems which show age-hardening frequently behave in the following particular manner if they are maintained at some aging temperature after partial or complete aging has been carried out at some lower temperature: the properties of the alloy oftentimes recover considerably the values approaching those of the as-quenched state before aging begins at the higher temperature. This process, called reversion, is thought to be caused by chemical or size instability at higher temperatures of structures formed at the lower temperature. Reversion has been seen in these alloys and it produces characteristic effects on the electrical resistance. A typical annealing cycle which shows this is given by the curves in Fig. 7, where annealing is carried out at 315°C after partial annealing at 150°C. The overshoot in the curve occurring in about 2 min at 315°C shows that the relatively large 2.7 per cent decrease at 150°C is completely wiped out before the specimen assumes its constant value characteristic of 315°C. This indicates that the structure formed at 150°C may have been completely redissolved at 315°C before the new state at 315°C was formed. This effect was also seen upon aging at 420°C following aging at 150°C. It was not seen upon aging at 205°C following aging at 150°C; the resistivity in this case rose smoothly from its value at 150°C to its new value characteristic of 205°C.

The annealing at 315°C referred to in the previous paragraph also produced an effect if the specimen is

subsequently reannealed at lower temperatures. The specimen was taken at point "a" in Fig. 7 and reannealed at 150° C. The resistance again went through the maximum characteristic of annealing at 150° C, but the rate was greatly reduced. That this is so is seen from the data of Fig. 8 for a "normal" sample $(-- \bullet --)$ and for the sample after reversion $(-- \circ --)$. The retardation of the effect by a factor of 10 in time is great enough to be of real significance.

(c) The length measurements

It was thought that the changes in structure upon annealing which cause the resistivity increase to occur might have a volume change associated with them. This is the case; it was observed by measuring the change in linear separation between two marks made on a polished specimen surface.

The instrument used for these measurements was a Gaertner traveling microscope with a length of travel of 3 cm. Markers on the polished surface were made either by scratching the surface with a razor blade or by making Vickers hardness indents. Distance could be read on a vernier scale to $\pm 5 \times 10^{-5}$ cm. Since the effect observed on annealing was about 0.05 per cent, the accuracy of the observations was only about 10 per cent.

In this instance also, the results depend on the temperature of annealing. The curves in Fig. 9 show that decreases in length are observed at 200°C and below, whereas an increase is observed at 250°C. Notice that the times involved for the effect to complete itself are of the same order as those observed for the electrical resistance to undergo its changes (see Fig. 3). This strongly suggests that the changes in length and change in resistivity are caused by the same phenomenon.

There is a somewhat larger volume change associated with the main phase reaction. The curve

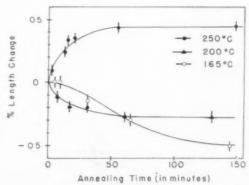


Fig. 9. Length changes accompanying aging at several temperatures after a quench from $700^{\circ}\mathrm{C}.$

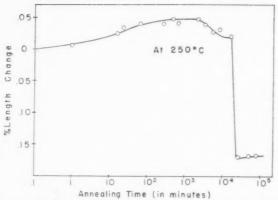


Fig. 10. The length change over the entire precipitation process at 250°C shows that two distinct processes are occurring. The large decrease in length at 2×10^4 min accompanies the massive formation of the phase mixture.

in Fig. 10 shows the change in length of a sample when it is annealed for long times at 250°C. Notice that the slight increase in length which occurs initially recovers somewhat as aging times are prolonged; then there follows a large decrease in length as the phase mixture forms. The sharpness of this decrease with time is somewhat surprising but it was reproduced in another sample so we believe it to be true.

Reversion is also seen in the length change measurements. A number of specimens were annealed at 160°C until a constant value for the length change was reached (this amounted to about 0·06 per cent). Some of these specimens were then annealed at 375°C and some at 200°C. The length changes observed at these two new temperatures are given in Fig. 11. Notice that reversion occurs at 375°C as indicated by the overshoot of the length before it approached a value characteristic of 375°C. At 200°C this does not occur; the new length at 200°C is attained in a monotonic manner.

(d) Young's modulus measurements

Variations in Young's modulus during the low temperature annealing treatments were also measured. It was hoped that these measurements would indicate either changes in fundamental force constants between atoms or of the role of the dislocation strain. These hopes were not realized, but the measurements do add some information about the low temperature annealing effect.

The measurements of changes in Young's modulus were made using a resonance method with a quartz piezoelectric rod as a driver. Observations were made at room temperature at about 40 kc/s. Annealing of the quenched rods was carried out at 165°C, 210°C and 250°C. The data for observations made during the

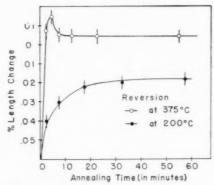


Fig. 11. Reversion following preliminary aging at 160 °C. At 375 °C, reversion is seen to occur. At 200 °C, it does not occur; the length goes smoothly to its correct value for aging at 200 °C.

short time annealing are presented in Fig. 12. In this temperature range at least, the modulus is seen to increase upon annealing. At 165°C the increase is quite considerable, over 1 per cent, while at 250°C it is about .75 per cent. The effect at temperatures intermediate to these extremes is seen to go through a minimum, being rather small at 210°C.

Reversion effects were studied also using the Young's modulus to measure the effect. Real effects were seen here also, but since these observations add nothing to those made for the resistance and length changes, these data will not be presented.

19

It is to be noted that the changes in Young's modulus are *real* effects: they are not *apparent* effects caused by the change in length of the resonant samples during aging. Not only is the change in length much too small to account for the size of the modulus change, but also it is of the wrong sign.

3. INTERPRETATION OF RESULTS

The measurements reported here show that the Au-Ni alloy system joins that large group of age

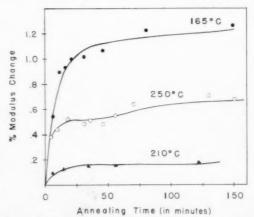


Fig. 12. The change in Young's modulus at three aging temperatures following quenching from 700°C.

hardening alloys for which the aging is multi-staged. It is also true in this instance, as is so in the others, that a detailed description of all the stages is not possible. Nevertheless, we would like to point out what seem to be the salient points that can be inferred from the data.

It is first of all clear that during the low temperature annealing, there is indeed an initial precipitate formed before the main phase separation occurs. Annealing at 150°C, for example, shows changes in all of the properties measured. Whether or not this initial stage is in any way related to the later stage does not seem clear. This initial effect is not peculiar to the alloy of 70–30 Au–Ni; it also produces similar resistivity changes in a 60–40 Au–Ni alloy at the same temperature.

There is some temperature above which this initial precipitate either is unstable or changes in character. That this is so can be seen by comparison of the resistivity vs. time plots for 150°C, 210°C and 250°C in Fig. 3. Since no change is evident in the latter case, it is reasonable to suppose that the precipitate does not form there. The critical temperature for stability of the precipitate surely lies between 210°C and 250°C; for convenience in discussion we will suppose it to be 225°C.

The low temperature precipitate produces well defined effects on the physical properties so far measured. These are shown schematically in Fig. 13 for annealing at 150°C; the changes are seen to occur at about the same time during the annealing. There exist at least two possibilities for the type of this precipitate; the one that it is a rearrangement of

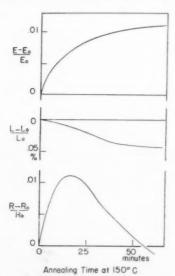


Fig. 13. Schematic of the change in properties accompanying aging at 150°C after a quench from 700°C.

vacancies retained upon quenching, the other that it is a true clustering of atoms.

The first of these, that it is a rearrangement of quenched vacancies can possibly explain the property changes sketched in Fig. 13. The increase in Young's modulus could simply be a result of the binding of dislocations by vacancy pinning. The decrease in length could be a shrinkage of the lattice as vacancies disappear. The total number of vacancies cannot be determined from this measurement alone. From Fig. 13 one would suppose that from 10^{-4} to 10^{-3} per cent disappeared completely; how many would cluster into voids and thus not contribute much to a volume decrease cannot be measured. The resistance change, an increase to a maximum followed by a larger decrease, is not so easy to explain since the annealingout of excess vacancies in pure metals has been observed to cause only a resistivity decrease. (6) It is possible, however, that in this alloy there is some critical size for the vacancy cluster for which the electron scattering is a maximum.

In spite of these arguments, we do not believe these effects to be only effects of vacancies. It seems unlikely that there would be this critical temperature, 225°C, above which the process would not go on. It is hard to see why the reversion effects would occur as they do, especially the effect of re-precipitation at 150°C after annealing and reversion at 315°C, Fig. 8. The vacancies retained after cooling from 315°C ought certainly to be fewer than these retained from an 875°C heat treatment. Yet the magnitude of the resistivity maximum is about the same, only the rate has changed.

The low temperature precipitate seems more likely to be some distinct clustering of atoms. These clusters might be clusters of Au-rich or Ni-rich atoms or they might be regions of higher geometrical order. In either case the property changes observed can be logically explained, largely perhaps because one doesn't know precisely the manner in which fine clusters should effect many of the physical properties. The changes in Young's modulus might be caused either by decrease in dislocation strain as the alloy is hardened by the clusters, or by a change in real atomic force constants as the environments of the atoms change somewhat. The length change on this model might then be caused by a true change in average lattice spacing as the alloy changed composition locally. (The length change here too might be caused by complete disappearance of vacancies. This model does not rule out quenched vacancies, it simply requires that the clusters be not clusters of vacancies). The resistivity change can also be explained as before;

after the clusters get to some large size they have lower resistivity than do the quenched alloys because they are regions either of purer metals or of higher geometrical order. Hence the resistivity of the quenched alloy annealed for 400 min at 150°C is nearly 3 per cent lower than the quenched alloy (see Fig. 7). The initial maximum of 1 per cent which occurs after about 10 min at 150°C (also Fig. 7) is again presumed to result from the clusters being at this time of some critical size for electron scattering.

On this model we do suppose that quenched-in vacancies play a role; this is the role of permitting to occur the atom movements necessary for the clusters to form. The vacancies then are the rate controlling factor. This position is certainly supported by the data plotted in Fig. 5; the rate of formation of the clusters is higher for an alloy quenched from a higher temperature (for which the number of quenched-in vacancies would be expected to be higher).

We have implicitly supposed that the property changes sketched in Fig. 13 are the result of a single process continuous in time. There is a chance that it is in fact a succession of two processes, one of which causes the resistivity to increase, the other to decrease. We believe that all the evidence does not support this view since the length change and modulus change do not show a two-stage effect.

The possibility that the clusters are regions of high short-range order or even regions of long-range order is an interesting one. The temperature at which the precipitate changes character, 225°C, might then be the critical temperature for ordering. It is interesting to observe that Flinn et al. looked with X-rays for possible structural changes upon annealing an alloy at 315°C, and failed to observe anything until the main phase reaction occurred. It is suggested that had they looked at lower temperature, they might at least have seen enhanced short range order.

Measurements of several types are certainly needed in this system now: (1) further X-ray measurements to look at the state of order or the cluster size of the low temperature precipitates, (2) magnetic measurements to see if they are ferromagnetic or (3) calorimetric measurements.

ACKNOWLEDGMENTS

Thanks are due to many members of our department for advice in the preparation of this manuscript. Special thanks are acknowledged to Mrs. R. Vook and Mrs. H. Birnbaum for assistance with many of the resistance measurements.

The authors acknowledge with thanks the grant of a fellowship by the Standard Oil Company of Indiana to support one of us (J. S.) during a large part of the period in which this work was carried out.

REFERENCES

- 1. W. KÖSTER and W. DANNÖHL, Z. Metallk. 38, 248 (1936).
- W. Kostek and W. Dannolli, Z. Medak. 36, 248 (1990).
 P. Flinn, B. L. Averbach and M. Cohen, Acta Met. 1, 673 (1951).

- L. Seigle, M. Cohen and B. L. Averbach, Trans. Amer. Inst. Min. (Metall.) Engrs. 194, 1320 (1952).
- Inst. Min. (Metall.) Engrs. 194, 1320 (1952).
 4. C. Ang, J. Sivertsen and C. Wert, Acta Met. 3, 558 (1955).
- H. K. Hardy and T. J. Heal, Progress in Metal Physics Vol. 5. Interscience Publishers, (1954).
- 6. J. BAUERLE and J. KOEHLER, Phys. Rev. 107, 1493 (1957).

THE ORIENTATION DEPENDENCE OF ETCHING EFFECTS ON GERMANIUM CRYSTALS*

P. J. HOLMES†

There is a marked variation with crystal orientation of the many well-known etchants for germanium. For example, some etchants (like CP-4) only form etch pits at dislocation sites when the surface is within a few degrees of (111) or (100). The detailed results of etching are dependent, in many cases, on the exact conditions of attack (temperature, impurity content of the semiconductor, etch composition, and illumination). A convenient way of studying these effects is by treating small polished hemispheres of single-crystal germanium, and examining the results as a function of their position on the crystal. By this means, real etch features may be distinguished, by their recurrence in positions determined by the crystal symmetry, from artefacts, and the time and expense of preparing many accurately oriented flat surfaces are avoided. Some etchants have been shown to attack all surface orientations similarly, while others (notably the $\mathrm{HF-H_2O_2}$ series of etchants) show certain effects only over angular ranges of a few degrees. There is some evidence that the variations are due not only to etch rate differences, but to changes in the actual mechanisms of etching with orientation.

INFLUENCE DE L'ORIENTATION DES CRISTAUX DE GERMANIUM SUR L'ACTION DES REACTIFS D'ATTAQUE

L'orientation cristalline exerce un effet important sur l'action des nombreux réactifs d'attaque du germanium. C'est ainsi que certains d'entre eux, tel le réactif CP-4, ne forment des piqures de corrosion sur les dislocations que si la surface est sensiblement orientée selon (111) ou (100). Les résultats obtenus par une telle attaque chimique dépendent très souvent des conditions exactes d'application (température, teneur en impuretés du semi-conducteur, composition du réactif.) Une méthode élégante pour étudier ces effets consiste à préparer des monocristaux hémisphériques polis de germanium; on interprétera alors les résultats de l'attaque en fonction de la position sur le cristal de la surface examinée.

De cette façon, on distinguera aisément les figures d'attaque réelles car la symétrie du cristal permet, par comparaison, d'identifier les artefacts. En outre, on épargne aussi du temps et de l'argent en évitant la préparation de nombreux monocristaux préorientés.

L'auteur montre que certains réactifs ont une action indépendante de l'orientation de la surface, alors que d'autres (notamment la série de réactifs HF-H₂O₂) ne manifestent leurs effets que dans le cas d'orientations précises à quelques degrés près.

L'auteur montre également que ces variations du pouvoir d'attaque résultent non seulement de vitesses d'attaque différentes mais aussi de modifications des mécanismes d'attaque en fonction de l'orientation.

DIE ORIENTIERUNGSABHÄNGIGKEIT DER ÄTZEFFEKTE BEI GERMANIUMKRISTALLEN

Die Wirkung vieler wohlbekannter Ätzmittel für Germanium ist ausgesprochen orientierungsabhängig. Einige Ätzmittel (wie CP-4) bilden beispielsweise Ätzgruben an Versetzungen nur, wenn die Oberfläche auf wenige Grad genau die Orientierung (111) oder (100) hat. In vielen Fällen hängen die Ätzergebnisse im einzelnen von den genauen Angriffsbedingungen ab (Temperatur, Gehalt des Halbeiters an Verunreinigungen, Zusammensetzung des Ätzmittels, Beleuchtung). Diese Effekte lassen sich bequem studieren, indem man kleine polierte Einkristall-Halbkugeln aus Germanium behandelt und die Abhängigkeit der Ergebnisse von der Lage auf dem Kristall betrachtet. Auf diese Weise kann man echte Ätzfiguren, die an Kristallagen gleicher Symmetrie wieder auftreten, von Artefakten unterscheiden; ausserdem spart man Zeit und Mühe, die mit der Herrichtung vieler genau orientierter ebener Flächen verbunden sind. Einige Ätzmittel greifen Oberflächen aller Orientierungen ähnlich an, während andere (besonders die Ätzmittel der Reihe HF-H₂O₂) gewisse Effekte nur innerhalb von Winkelbereichen weniger Grade zeigen. Es gibt Anzeichen dafür, dass diese Unterschiede nicht nur durch verschiedene Ätzgeschwindigkeiten bedingt sind, sondern dass sich der Ätzmechanismus selbst mit der Orientierung ändert.

INTRODUCTION

The simplest way of obtaining complete information on the orientation dependence of etching effects is to attack a hemisphere or sphere of single-crystal material. Ellis⁽¹⁾ has described the etching of small spheres of germanium in a variety of reagents until their shape was changed to polyhedra, indicating the relative etching rates of surfaces of different orientations.

In the present investigation, however, the object was to observe the appearance of differently oriented surfaces when treated for shorter periods. An advantage of studying a spherical surface, instead of a range of flat specimens, is that while true crystallographic effects are repeated in accordance with the cubic

VOL.

^{*} Received June 26, 1958.

[†] Research Laboratory, Associated Electrical Industries, Aldermaston Court, Aldermaston, Berkshire.

symmetry, artefacts are not so symmetrically distributed. Hemispheres were employed because they are much easier to produce to the requisite dimensions than spheres, while all the necessary information can still be obtained from them.

EXPERIMENTAL

A method of preparing hemispheres of germanium has been evolved by Gasson. (2) A slice of an ingot, just over \(\frac{1}{2} \) in. in diameter and \(\frac{1}{4} \) in. long, is ground hemispherical, with the aid of a radius gauge and progressively finer grade grinding papers. The specimen is then polished on Selvyt cloths impregnated with successively finer grades of Daidust, and carefully cleaned with distilled water and acetone. Some of the hemispheres were chemically polished in CP-4 (15 ml HF, 25 ml HNO3, 15 ml acetic acid with 0.3 ml bromine) before etching. This proved useful for revealing defective mechanical polishing, but was only used to a limited extent because, as is well known, this and similar acid etchants give rise to shallow conical dislocation etch pits on orientations near to {111} and sometimes near {100}. They are thus liable to initiate the formation of pits in regions of hemispheres where subsequent etchants would not, on their own, have any effect.

The hemispheres all had their bases cut parallel to the growth front of the ingots, which was either (111) or (100). The material was normally in the range $1{\text -}20~\Omega{\text -}\text{cm}$ resistivity, $p{\text -}\text{type}$ in the case of silicon and $n{\text -}\text{type}$ in the case of germanium. A few hemispheres of opposite conductivity types but similar resistivity were tried simultaneously in some of the etchants, but no measurable difference in the nature of the attack was observed, though the rates sometimes differed. A check was also made on similarly doped specimens of widely different resistivities and, except in the cases of some slow-acting etchants (which were also sensitive to illumination), no difference in the type of attack was found.

Etching times given are those recommended for the most easily interpreted results, measured from the onset of chemical reaction. 50–70 ml of etchant were used, after stirring, at room temperature under normal laboratory illumination, except where otherwise stated. The quicker acting etchants created enough agitation on their own, while the slower ones were stirred occasionally to ensure that there was no falling off in reaction rate due to local exhaustion of reagents.

Stereographic pole figures centred on (111) were plotted to describe the results, because photography of these small spheres is complicated by the

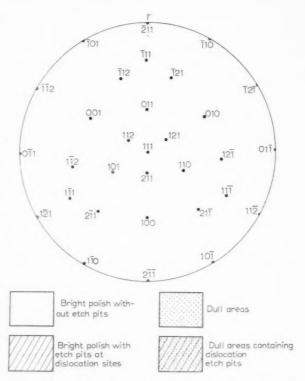


Fig. 1. Standard orientation and key to pole figures of etched germanium hemispheres.

19

difficulty of eliminating highlights. The methods of goniometric measurement employed should be capable of giving an accuracy of $\pm 1^{\circ}$ for the angular dimensions of a well-defined area on the hemisphere. In general, however, the exact boundaries of the regions are not so well defined, and a gradation from one type of surface to another may result in the positions of boundaries, especially of the larger regions, being only determinable to $\pm 2^{\circ}$ or 3° . For reasons of simplicity of these pole figures, the surfaces have been classified into four main types only (see key, Fig. 1) and further details, such as information on the shapes of etch pits and the fine structure of the background, are given in the text.

RESULTS*

1. Etchants with H2O2 as an oxidizing agent

 $100\text{-}volume~H_2O_2^{(3)}~(2\text{-}4~\text{hr})$ (Fig. 2). Small, dull, oval patches, slightly elongated towards {111}, are formed around {210}. These consist of minute undulations, less than 1 μ in size. The rest of the surface appears bright, with small dislocation etch pits appearing for some distance around {111} and

^{*} Other results obtained by these methods were presented at the Ninth Meeting of C.I.T.C.E., Paris, 1957.

{100} but none near {110}. Scratch marks and other surface blemishes are readily, though not deeply, attacked by this and most etchants containing an excess of H₂O₂.

The etch pattern on the hemisphere changes as HF is included in progressively larger proportions. $250~{\rm H}_2{\rm O}_2:1~{\rm HF}$ (3 hr) (Fig. 3) down to $100~{\rm H}_2{\rm O}_2:1~{\rm HF}(1\,{\rm hr})$ produces dull $\{210\}$ patches more elongated towards $\{100\}$, consisting of minute hillocks, elongated at right angles to this, completely covering the surface. In the region of $\{111\}$, extending as far out as $\{211\}$, rounded triangular dislocation etch pits, with facets appearing in plan like $\{100\}$ planes, are formed. Square etch pits also appear close to $\{100\}$, with $\langle110\rangle$ edges.

At proportions of $50~\rm{H_2O_2}:1~\rm{HF}$ (30 min) (Fig. 4), the dull patches take the form of single blobs centred on {110}. The variability in their shape from one experiment to the next suggests that this is a region of rapid change of etch pattern with concentration. Various shapes from roughly hexagonal to ovals, elongated towards {100}, have been observed. Elsewhere, the surface is bright, with slightly rounded triangular dislocation etch pits around {111} giving way to smaller canoe-shaped pits, elongated along $\langle 110 \rangle$, near $\langle 211 \rangle$. Square dislocation pits, with $\langle 110 \rangle$ edges, appear around {100}.

8 $\rm H_2O_2$: 1 HF (10 min) (Fig. 5). This gives dull {110} patches consisting of humps elongated in a perpendicular direction to this. The shapes of dislocation etch pits are as for the 50:1 case, and very small pits may be detected at most parts of the surface. Similar results are obtained from a mixture of $\rm 2~H_2O_2$: 1 HF (6 min), except for a further elongation of the dull {110} patches.

 $1~{\rm H_2O_2}:1~{\rm HF^{(3)}}$ (3 min) (Fig. 6). {111} regions are bright with very shallow rounded dislocation pits, and {100}'s are dull with similar pits over a small circular patch. Remainder of surface is bright, except for "cat's-eyes" joining {111} regions. These consist of a bright lenticular-shaped region containing oval dislocation etch pits near {110}, with a dull arc on either side, consisting of small humps with their length along the radii of the arcs. Larger diamond-shaped etch hillocks within these arcs, possibly due to dislocations, are elongated at right angles to the slight ridges along the centre of the bright regions (i.e. along the $\langle 110 \rangle$ zone circles).

 $1~\rm{H_2O_2}:2~\rm{HF}$ (20 min). Except for regions round $\{100\}$'s, all surfaces are slightly dulled by formation of a fine "mottled" structure. Small conical dislocation etch pits are formed over areas about 15° wide in the middle of each of these brighter $\{100\}$ regions.

Progressive dilution of HF-H2O2 with water

 $\rm H_2O_2: HF: \rm H_2O~(1:1:1)~(2~min)~(Fig.~7).~\{111\}$ areas show large shallow pits; about 5° away from the pole, these give way to oriented radial humps which are part of a modification of the $\{110\}$ "cat's-eye" pattern of the $\rm H_2O_2$ –HF etch. Along the clear centre of these patches, elongated pits are found, and a few small pits also appear in the $\{100\}$ regions.

No. 2 (Superoxol) etch (2 min) $^{4-7}$ (Fig. 8). Recipe: 1 HF, 1 H $_2$ O $_2$, 4H $_2$ O.

"Cat's-eyes" have now closed to form large dull areas (made up of small humps with their lengths along \$\langle 110 \rangle\$ zone circles) around \$\langle 110 \rangle\$, slightly elongated towards \$\langle 111 \rangle\$'s. The rest of the surface is bright, with near-triangular dislocation pits around \$\langle 111 \rangle\$ (pits occasionally appear right out to \$\langle 211 \rangle\$, where they are small and lenticular) and a smaller number of rounded ones in the \$\langle 100 \rangle\$ regions.

At a dilution of 1 part No. 2:3 parts water (30 min), the dull patches round {110} become roughly circular. Increasing the dilution to 1 part No. 2:6 parts water (2 hr) elongates the dull patches towards {100}'s (Fig. 9). The rounded etch pits in {111} regions give way to humps, elongated towards {111}'s, as the dull region is approached via {221}. About the stage of 1 part No. 2:8 parts water (3 hr) (Fig. 10), the dull patches are split by a brighter band joining {111}'s and showing roof-shaped {110} etch pits across the band. The dull patches now form a broad-armed Maltese cross pattern around {100}. radiating towards {110}.

1 part No. 2:50 parts water ("Dilute No. 2 etch")⁽⁵⁾ (48 hr) (Fig. 11). Arms of dull crosses are narrower and pits in {100} areas are not developed. Dislocation pits around {111} are shallow, detailed and well shaped, extending out to {211}, slowly changing shape with orientation.

No. 5 $etch^{(8)}$ (5 min). Recipe: 20 HF, 3 $\rm H_2O_2$, 12 $\rm H_2O$.

This etchant is one in which oxidation is insufficient to form products which are readily soluble, so that a yellow film of loosely-attached oxide forms on all surface orientations. The initial growth of this film on the hemisphere can be followed by watching the interference colours: {111} starts to react first, and the fringes spread out from these poles and converge on the {100} poles as new ones are generated by further growth at {111}. Owing to small local variations in the thickness of the film, the underlying germanium surface is etched unevenly to a shiny matt appearance, especially around {100} and {111} and the zone arcs joining these poles. In these regions the oxide may require brushing to

VOL. 7 1959

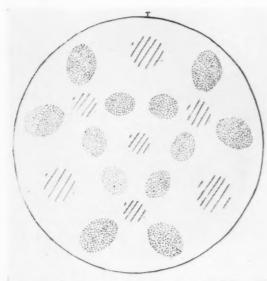


Fig. 2. Pole figures for HF–H $_2{\rm O}_3$ –H $_2{\rm O}$ mixtures: Hydrogen peroxide

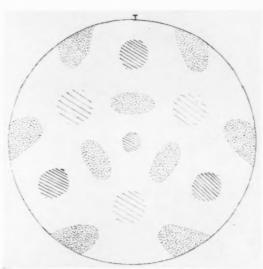


Fig. 4. Pole figures for HF–H $_2{\rm O}_2$ –H $_2{\rm O}$ mixtures: $50~{\rm H}_2{\rm O}_2$: $1~{\rm HF}$

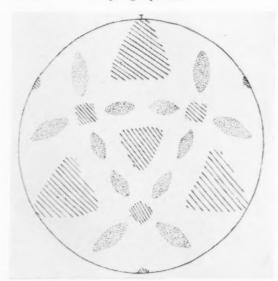


Fig. 3. Pole figures for HF–H $_2$ O $_2$ –H $_2$ O mixtures: 250 H $_2$ O $_2$: 1 HF

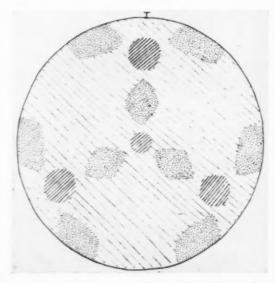


Fig. 5. Pole figures for HF-H₂O₂-H₂O mixtures: $8~\mathrm{H_2O_2}:1~\mathrm{HF}$

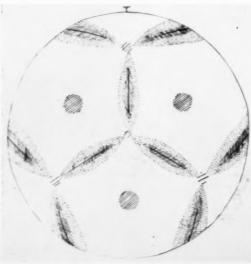


Fig. 6. Pole figures for HF-H₂O₂-H₂O mixtures: $1 \text{ H}_2\text{O}_2: 1 \text{ HF}$

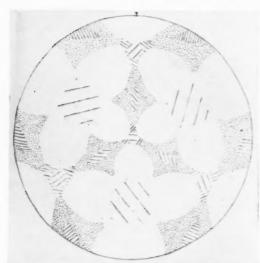


Fig. 7. Pole figures for HF–H $_2{\rm O}_2$ –H $_2{\rm O}$ mixtures; 1 H $_2{\rm O}_2$: 1 HF : 1 H $_2{\rm O}$

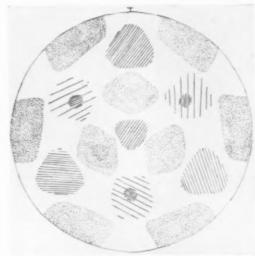


Fig. 9. Pole figures for HF–H₂O₂–H₂O mixtures: 1 H₂O₂ : 1 HF : 40 H₂O (No. 2 etch diluted 1 : 6)

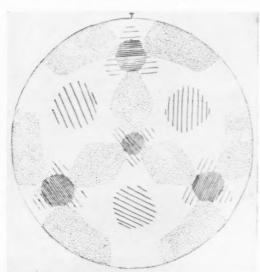


Fig. 8. Pole figures for $\mathrm{HF-H_2O_2-H_2O}$ mixtures: 1 $\mathrm{H_2O_2}$: 1 HF : 4 $\mathrm{H_2O}$ (No. 2 etch)

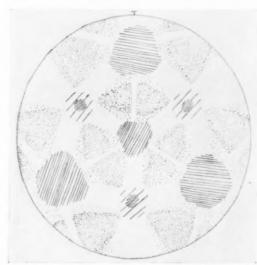


Fig. 10. Pole figures for $\mathrm{HF-H_2O_3-H_2O}$ mixtures: $1~\mathrm{H_2O_3}:1~\mathrm{HF}:52~\mathrm{H_2O}$ (No. 2 etch diluted 1:8)

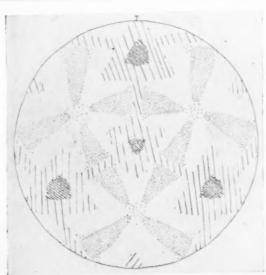


Fig. 11. Pole figures for $\mathrm{HF-H_2O_9-H_2O}$ mixtures: $1~\mathrm{H_2O_2}:1~\mathrm{HF}:304~\mathrm{H_2O}$ (No. 2 etch diluted 1:50)

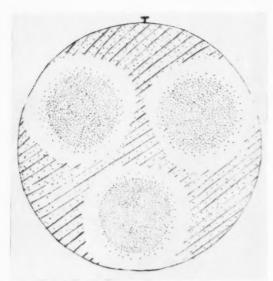


Fig. 12. Pole figure for WAg etch.

remove it from among the surface asperities, although elsewhere it floats off quite readily. No dislocation etch pits are formed.

2. Other etchants

WAg etch (1 min)⁽⁹⁾ (Fig. 12). Recipe: 2HF, 1 HNO₃, 2 of 5% AgNO₃ solution.

Large dull areas around {100}'s, fading into a narrow brighter region which outlines a continuous network made up of {111} areas linked up via {110}'s, the whole of which, though dull, contains crystallographic dislocation etch pits. Liability to uneven etching due to deposition of silver.

No. 1 etch (5 min) (Fig. 13). Recipe: 2 HF,

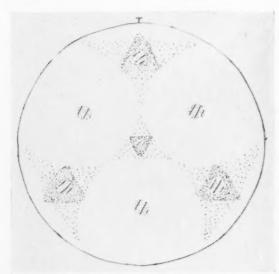


Fig. 13. Pole figure for No. 1 etch.

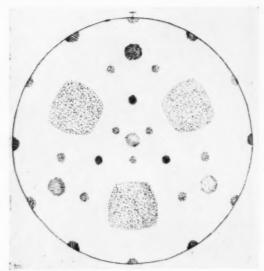


Fig. 14. Pole figure for No. 7 etch.

1 HNO₃, 1 of 10% Cu(NO₃)₂ solution.

Round pits over a small region around {111}, surrounded by rings of dull general pitting, with faint spikes pointing towards {110}. Small area of dislocation pits amid dull general pitting around {100}, with remainder of surface bright.

No. 7 etch⁽⁵⁾ (3 hr) (Fig. 14). Recipe: Pass $\rm Cl_2$ into ice-cold 0.8 N KOH until pH is 8–9. Add 15 ml of this solution to 60 ml of 0.5% KOH solution.

Large dull areas around {100}'s consisting of small rounded pyramidal pits; small dull areas about 6° wide around {211}. Remainder appears bright with a small area of dislocation etch pits (terraced cones) near {111}, and shallow round pitting over an area about 7° wide in {110} regions.

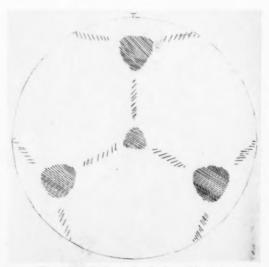


Fig. 15. Pole figure for ferricyanide etch.

Ferricyanide etch⁽¹⁰⁾ (2 min) (Fig. 15). Recipe: 6 g KOH, 4 g K_3 Fe(CN)₆, in 50 ml H_2 O.

All surfaces bright, with regions of well-marked crystallographic dislocation etch pits around {111} and smaller pits between these, near {110}.

The ferricyanide etch has been studied in some detail on $\{111\}$ planes, and surfaces close to that orientation. The angle of the facets of the best developed pits to the (111) surfaces has been measured, both by trigonometric and optical goniometric methods, to be in the range $16^{\circ}-20^{\circ}$, as compared with $70\frac{1}{2}^{\circ}$, which true $\{111\}$ facets would give. The way in which the pits change shape with surface orientation on a hemisphere is shown in Fig. 16. On the true (111) plane, the etch pits are equilateral triangular pyramids with $\langle 1\bar{1}0\rangle$ edges, and their shape changes as the angle of the surface to the (111) plane is increased until, at about 15° or so from (111)



1959

Fig. 16. Change of shape of ferricyanide etch pits with angle from (111) orientation.

(i.e. when one facet is almost parallel to the surface), they disappear. In fact, the change of shape is just what would be expected from the cutting of oblique sections of pyramids with sides at an angle of $16^{\circ}-20^{\circ}$ to the base; i.e. "spearheads" of acute angle as (211) is approached, and obtuse angle when the surface is tilted in the opposite direction towards (122). The figure shows that the shape of these etch pits could be used to estimate the orientations of surfaces near (111) to an accuracy of about 2° .

CONCLUSIONS

These results show a much wider variety of etching effects than could be explained by assuming all etchants to attack the germanium in the same manner but at different rates. The patterns of smooth, polished, pitted, and matt surfaces are, in many cases, characteristic of one type of etchant only, and cannot be reproduced by any other, even if the latter's concentration is adjusted to give the same pH or reaction rate. This suggests that the detailed mechanisms of removal of germanium atoms from the bulk, and of removal of etch products from the vicinity of the surface, are the features controlling the observed results.

The current theory of the chemistry of etching of semiconductors⁽¹¹⁾ is that oxidizing atoms, or ions, become attached to the surface atoms, probably by chemisorption, after which the bonds from these atoms to the bulk are broken by holes, generated near the surface by chemical action, or to a lesser extent by photoelectric means. This permits the oxidized germanium to be taken into solution by further complexing reactions.

The absorption properties of a given crystal surface for a given adsorbate depend on temperature, pressure or concentration, the nature of the absorption (physical or chemical), the distribution of sites, and the size of, and interaction between, the absorbed molecules or ions.(12) If chemisorption is the mechanism involved, the surface coverage required to satisfy all the available bonds is fixed. This will be attainable only if the adsorbed molecules are small enough to pack together with the requisite spacing, and do not interact strongly enough to prevent them being sited so close to one another. If the latter condition is not fulfilled, there may be a sharp increase in the difficulty of adsorbing further molecules, and therefore in the activation energy for adsorption. beyond a certain fraction of surface coverage. This critical value may vary considerably according to the nature of the adsorbate, and the surface orientation, so that fairly abrupt changes of etching behaviour

with orientation may be expected, as well as marked differences when small quantities of preferentially adsorbed material are added.

Adsorption, in addition to controlling the nature of the molecules or ions adjacent to the semiconductor surface, also brings about modifications of the energy levels, and therefore of the availability of the current carriers (within the solid) and ions (in the etchant) which are involved in the process of removing material. Individual adsorbed particles provide isolated energy levels which may accept or donate electrons, and when these become sufficiently dense they will interact to form a continuous band structure at the surface. The existence of charges on the surface will induce a space charge of opposite sign within the semiconductor, and if this is negative it will reduce the number of holes available to break the bonds to the surface atoms, and etching will be limited. Alternatively, an acceptor level at the surface will cause a positive space charge, excess holes, and enhanced etching. The limitation or enhancement of etch rate will thus be a function of the surface coverage of adsorbate, so that the latter factor may control not only the ability or otherwise of the solution to remove material, but also the ability of the semiconductor to release its own surface atoms.

The observations of the etching behaviour of hemispheres may thus be regarded as giving information comparable to that obtained by use of

the field emission microscope on certain metals with adsorbed layers. (12) In the field emission method the work function, or ease of extracting electrons, is measured as a function of nature and quantity of adsorbate, while in the studies described here we are observing the effectiveness of a variety of reacting ions at various concentrations for releasing holes at the surface. Another series of related experiments on the orientation dependence of reactivity are the observations of the rate of oxidation of copper and nickel spheres by Gwathmey and his co-workers. (13)

ACKNOWLEDGMENT

The author wishes to thank Dr. E. Billig for suggesting this work, Messrs. D. B. Gasson and F. D. Thornton for preparing the hemispheres, and Dr. T. E. Allibone, F.R.S. for permission to publish this paper.

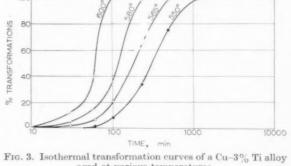
REFERENCES

- 1. R. C. Ellis, J. Appl. Phys. 25, 1497 (1954); Ibid. 28, 1068 (1957).
- D. B. Gasson, J. Sci. Instrum. 35, 33 (1958).
- 3. O. RÖSNER, Z. Metallk. 46, 225 (1955)
- 4. P. R. Camp, J. Electrochem. Soc. 102, 586 (1955).
- 5. S. G. Ellis, J. Appl. Phys. 26, 1140 (1955)
- B. W. BATTERMAN, J. Appl. Phys. 28, 1236 (1957).
 H. A. SCHELL, Z. Metallk. 47, 614 (1956).
- S. G. Ellis, J. Appl. Phys. 28, 1262 (1957).
 R. H. Wynne and C. Goldberg, J. Metals 5, 436 (1953).
- E. BILLIG, Proc. Roy. Soc. A 235, 37 (1956).
 D. R. TURNER, J. Electrochem. Soc. 103, 252 (1956).
- 12. B. M. W. TRAPNELL, Chemisorption. Butterworths Scientific Publications, London (1955).
- 13. A. T. GWATHMEY and A. F. BENTON, J. Chem. Phys. 8, 431 (1940) etc.

LETTERS TO THE EDITOR

On the structure changes produced by ageing of Cu-Ti alloy*

The structure changes were studied microscopically on Cu-3% Ti alloys, which were solution-treated and aged at the temperature from 550°C to 700°C. Observations on the cellular precipitation(1) were made for the specimens aged at the temperature between 550°C and 600°C (Fig. 1). It is disclosed that the precipitates started to grow at the grain boundaries, and spread gradually into the matrix. These regions have the lamellar pearlite type structure (Fig. 2), and the distance between the layers is over about 2μ . The rate of growth of the pearlite regions increases with the increasing ageing temperature, as shown in the isothermal transformation curves (Fig. 3). Together with the pearlite type structure, Widmanstätten type structure is observed for the specimens which were aged at the temperature between 620°C and 680°C (Fig. 4). However, when aged at 700°C, only Widmanstätten type structure can be found without any traces



aged at various temperatures.

of pearlite region (Fig. 5). And the size of the individual precipitates which can be found within Widmanstätten structure increases with the increasing ageing time. The shape of these precipitates is a striped plate, and the distance between them is about 3 u (Fig. 6).

For the specimens aged for 1 hr at 600°C and 700°C respectively, the crystal structure of the precipitates

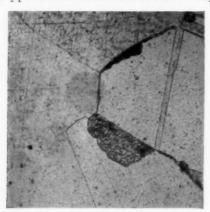


Fig. 1. Cu-3% Ti alloy aged 10 min at 600°C. ×500.

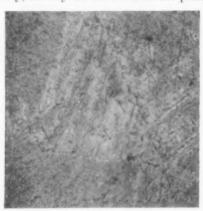


Fig. 4. Cu-3% Ti alloy aged 60 min at 640°C. ×312.

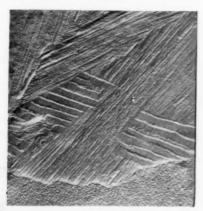


Fig. 2. Cu-3% Ti alloy aged 60 min at 600°C. ×1450. ACTA METALLURGICA, VOL. 7, APRIL 1959

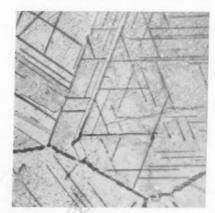


Fig. 5. Cu-3% Ti alloy aged 480 min at 700°C. ×500.

Fig. 6. Cu-3% Ti alloy aged 60 min at 700°C. × 500

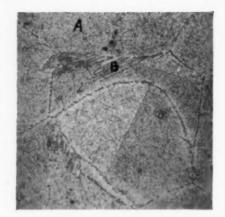


Fig. 8. Cu-3% Ti alloy aged 60 min at 600°C. × 312

which were extracted by 50% nitric acid is studied by means of X-ray (Fig. 7) as well as electron diffraction. It is shown, in both cases, that the precipitate is β' -Cu₃Ti, slightly deformed close packed hexagonal lattice. (2)

The orientation of the pearlite type precipitate within the matrix crystal is determined from, for instance, Fig. 8. As revealed by the traces of the precipitates, the orientation of the pearlite region B is the same as one of the directions of traces on the grain A. The plane within the matrix crystal upon which the precipitation of Widmanstätten type takes place, was determined by three methods, namely, (1) counting the maximum number of directions to which the precipitates are parallel within a given grain, (2) stereographic projection of the traces of the precipitates, and (3) relation between the directions of both precipitates and twin boundary. The results obtained by use of these methods (1), (2) and (3) are in good agreement, that is, β' -Cu₃Ti precipitates parallel to (111) plane of the matrix crystal.

The author believes that the pearlite regions which become visible when aged at relatively lower temperatures are the mechanical mixture of saturated solid solution and β' -Cu₃Ti, both of which are the decomposition products of the supersaturated solid solution. And the growth of the precipitates in these pearlite regions may proceed by means of diffusion of the

solute atoms along the boundary surface between the pearlite region and the supersaturated solid solution.

On the other hand, the growth of the Widmanstätten type precipitates which become visible when aged at relatively higher temperatures may be controlled by means of bulk diffusion of the solute. Since, in the course of the growth process, concentration of the solute in the matrix crystal decreases gradually, but being still maintained in supersaturated state, the precipitates grow by receiving the supply of the solute from all directions.

Taking into consideration of the generally acknow-leged fact that the grain boundary diffusion occurs at relatively lower temperatures than the bulk diffusion, it is understandable that discontinuous precipitation—precipitation of pearlite type—occurs at relatively lower temperatures, but continuous precipitation—precipitation of Widmanstätten type—occurs at relatively higher temperatures.

Тояню Дог

Central Research Laboratory Hitachi Ltd. Kokubunji, Tokyo, Japan

References

- D. TURNBULL and H. N. TREAFTIS, Acta. Met. 3, 43 (1955).
 N. KARLSSON, J. Inst. Met. 79, 391 (1951).
- * Received August 20, 1958



Fig. 7. X-ray diffraction patterns of pearlite type precipitate (up) and Widmanstätten type precipitate (down).

Sur l'oxydation du manganèse dans l'air aux température élevées*

L'oxydation du manganèse n'a fait l'objet, jusqu'à présent, que de deux travaux de Baldwin et de ses collaborateurs. (1,2) Etant donné que les derniers résultats de 1957, de ces auteurs, sont notablement différents de ceux qu'ils avaient présentés en 1954, nous avons estimé préférable de reprendre l'ensemble de la question dans un ample intervalle de température (400–1200°C).

Nous avons opéré sur des plaquettes de manganèse électrolytique de pureté supérieure à 99,9 pour cent. La préparation des échantillons dont la surface totale était de 1 à 3 cm² et l'épaisseur de 0,4 à 1,2 mm, comprenait les étapes suivantes: meulage, polissage aux papiers émeri jusqu' au 3/0, lavage dans plusieurs bains successifs de toluène, recuit dans le vide (10⁻⁴ mm Hg) à 650°C pendant 3 heures. Les échantillons étaient oxydés dans un four Chevenard vertical ouvert, à régulation dilatométrique. L'essai était caractérisé par l'augmentation de poids Δ m par cm² de surface initiale de l'échantillon et par l'épaisseur des diverses couches de la pellicule mesurée sur section polie et éventuellement attaquée.

Dans l'intervalle $400-850^{\circ}\mathrm{C}$, la pellicule est constituée de trois couches de MnO, de $\mathrm{Mn_3O_4}$ et de $\mathrm{MnO_2}$ (Fig. 1) dans celui de $900-1200^{\circ}\mathrm{C}$ de seulement 2 couches de MnO et de $\mathrm{Mn_3O_4}$ (Fig. 2a). Ce dernier résultat n'est pas surprenant étant donné que la tension de vapeur de l'oxyde $\mathrm{Mn_2O_3}$ atteint déjà 150 mm Hg à la température de $940^{\circ}\mathrm{C}$.

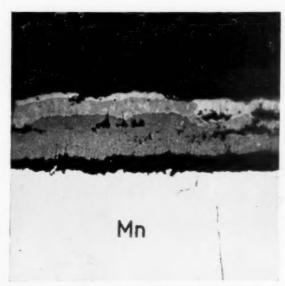
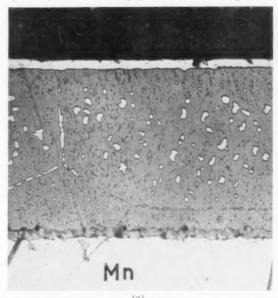


Fig. 1. Coupe d'une pellicule obtenue par oxydation superficielle du manganèse à 600° C, pendant 4 jours. $\times 703$.

Dans les pellicules formées aux températures supérieures à 800° C et refroidies dans l'air, on note de plus dans la partie externe de la couche de MnO une précipitation fine de $\mathrm{Mn_3O_4}$. Ce précipité se forme seulement au cours du refroidissement de l'échantillon par décomposition de la phase de protoxyde (décomposition qu'on a de bonnes raisons de croire proeutectoïde), car par trempe dans l'eau glacée, on obtient en général une couche de MnO homogène micrographiquement. Ce n'est que lorsque l'instabilité du protoxyde devient trop grande c'est-à-dire pour des



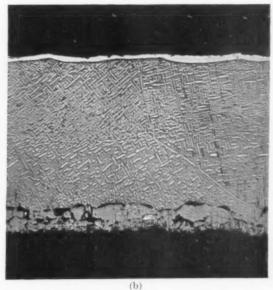


Fig. 2. Pellicule obtenue par oxydation à 1200°C, pendant 3mn 45 s. ×300. (a)—Echantillon retroid dans l'air, (b)—Echantillon trempé dans l'eau glacée.

VOL. 7 1959 pellicules formées aux températures supérieures à 1100°C que les trempes les plus énergiques sont impuissantes à empêcher la précipitation qui s'effectue suivant une structure de Widmanstätten (Fig. 2b). Ces particularités du précipité, sont très analogues à

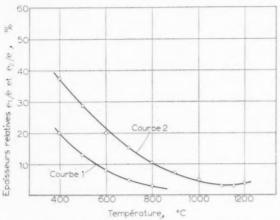


Fig. 3. Variation en fonction de la température des épaisseurs relatives (%) des couches de $\rm Mn_2O_3$ (courbe 1) et de $\rm Mn_3O_4$ (courbe 2) par rapport à l'épaisseur totale de la pellicule.

celles que nous avons observées dans l'étude de l'oxydation du fer. $^{(3)}$

Si l'on trace les diagrammes traduisant en coordonnées semi-logarithmiques respectivement la croissance aux différentes températures de l'épaisseur totale de la pellicule et des couches de MnO2 et de Mn3O4, on constate que les points expérimentaux relatifs aux essais isothermes se placent si on fait abstraction d'une courte période perturbée sur des droites passant très sensiblement par l'origine des coordonnées. Ceci équivaut à dire que la loi $e = k \sqrt{t}$ où e est l'épaisseur et k une constante, est vérifiée pour les trois couches de la pellicule dont les épaisseurs croissent ainsi paraboliquement en fonction du temps. On doit en conclure que le processus d'oxydation superficielle du Mn est régi dans l'intervalle étudié par la diffusion des divers ions qui y participent. En d'autres termes, les réactions qui se produisent aux interfaces des différentes couches de la pellicule n'ont aucune action limitative sur la vitesse de croissance de celles-ci.

Une conséquence directe de la croissance parabolique des couches est que leurs proportions dans la

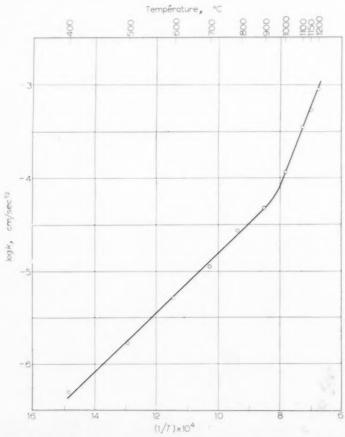


Fig. 4. Influence de la température sur la vitesse de croissance de la pellicule.

pellicule se maintiennent constantes au cours d'une oxydation isotherme. La Fig. 3 indique la variation en fonction de la température de ces proportions.

Enfin, la Fig. 4 donne la variation de la constante d'oxydation k relative à l'épaisseur totale de la pellicule en fonction de l'inverse de la température absolue 1/T. La courbe correspondante peut être assimilée comme on peut le constater à une succession de deux droites de pentes différentes. On en déduit que le processus d'oxydation peut être caractérisé dans l'intervalle 400-900°C par une chaleur d'activation égale à 29.200 cal/mole et dans l'intervalle 1000-1200°C par une chaleur d'activation égale à 79.800 cal/mole. La raison exacte du changement notable de la chaleur d'activation vers 950°C n'a pu être encore déterminée. Il ne semble pas en tout cas qu'il soit en liaison avec la transformation allotropique du manganèse qui se produit à température sensiblement plus élevée (1060°C-1100°C).

† Service de Chimie des Solides. Centre J. Païdassi† d'Etudes Nucleaires de Saclay, GIF-sur-YVETTE (S. et O.)

‡ Escuela de Inginiería Química Université de Concepción, Chili A. Echeverría‡

Bibliographie

- R. S. Gurnick et W. M. Baldwin, Jr., Trans. Amer. Soc. Metals 42, 308 (1950).
- E. B. Evans, C. A. Phanilkar et W. M. Baldwin Jr., J. Electrochem. Soc. 103, 367 (1956).
- 3. J. Païdassi, Acta Met. 3, 447 (1955).
 - * Received September 15, 1958.

* Cette recherche a fait l'objet du contrat nº 43, entre les auteurs et le "Consejo de Investigación Científica" de l'Université de Concepción (Chili).

Sur l'existence d'un processus de germination dans la sulfuration du cuivre aux températures élevées*

L'existence d'un processus de germination au cours de l'oxydation ménagée des surfaces métalliques aux températures élevées a été démontrée dans plusieurs cas particuliers depuis quelques années. (1,2,3) Nous nous sommes proposé de rechercher si un tel processus pouvait également se manifester au cours d'une réaction de sulfuration et nous avons choisi pour cette étude l'action d'un mélange d'hydrogène et d'hydrogène sulfuré sur le cuivre.

Les expériences ont été effectuées sur des échantillons de euivre de haute pureté (OFHC) dont la surface avait été préparée par un polissage électrolytique dans une solution aqueuse d'acide phosphorique, suivi d'un chauffage dans l'hydrogène. La sulfuration s'opère dans un appareil où circule en circuit fermé un mélange $\rm H_2\text{-}H_2S$ de composition déterminée; cette composition est fixée en faisant passer de l'hydrogène préalablement purifié sur un mélange de cuivre et de sulfure cuivreux, maintenu à température fixe. Les pressions partielles d'équilibre adoptées sont celles données par F. D. Richardson et J. E. Antill. (4) Aux températures comprises entre 800°C et 1000°C, pour des rapports $\rm H_2S/H_2$ variant de 1.10^{-3} à 5.10^{-3} et pour des pressions totales de 5-40 em de mercure, le phénomène de germination se manifeste.

La figure 1 représente deux surfaces sulfurées sous une pression totale de 10 cm Hg dans les conditions suivantes: l'une (a) à 850°C avec $\rm H_2S/H_2=1.8\cdot10^{-3}$ pendant 5 min l'autre (b) à 1000°C avec $\rm H_2S/H_2=3.10^{-3}$ pendant 30 min.

Une étude complète effectuée à 850°C en fonction des facteurs: pression totale, rapport H₂S/H₂, vitesse de circulation des gaz, durée d'exposition et orientation cristalline, nous a permis de mettre en évidence les particularités suivantes:

- (1°) L'apparition des germes est toujours précédée d'une période d'incubation dont la durée est d'autant plus grande que la pression partielle d'hydrogène sulfuré et la pression totale sont plus basses.
- (2°) le nombre des germes reste invariable en fonction du temps les autres variables étant fixées.
- (3°) Le nombre des germes croit avec la pression d'hydrogène sulfuré et en particulier avec la pression totale pour un même rapport $H_{\circ}S/H_{\circ}$.

Le domaine de germination peut être matérialisé sur un diagramme pression totale–temps représenté figure 2 pour un rapport $\rm H_2S/H_2=1.8\cdot10^{-3}$. On voit ainsi que sous une pression totale de 10 cm Hg ce n'est qu'au bout de 5 min que les germes apparaissent; ils se développent par croissance latérale pendant 45 min. période à l'issue de laquelle la surface entière se trouve recouverte de sulfure; la réaction se poursuit ultérieurement par croissance en épaisseur de la couche continue.

La morphologie et le nombre des germes sont fortement influencés par l'orientation cristalline du métal sur lequel ils ont pris naissance (Fig. 1). L'examen par diffraction électronique montre qu'il s'agit de cristaux de Cu₂S dont les orientations sont identiques sur un même cristal support.

L'ensemble de ces résultats permet de conclure que la réaction de sulfuration du cuivre donne lieu dans certaines conditions à un phénomène de germination, dont les caractéristiques générales présentent de

VOL. 7 1959

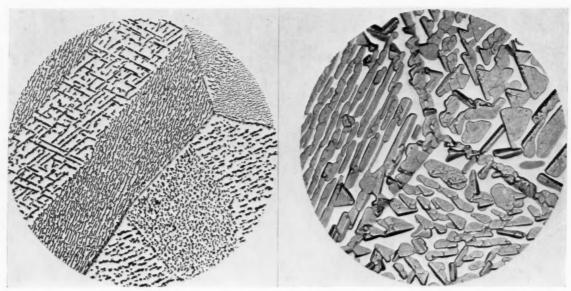
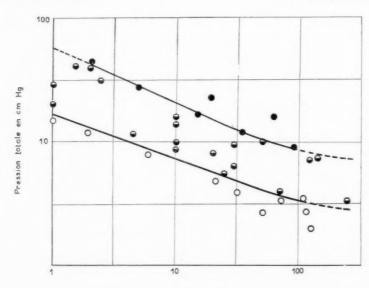


Fig. 1a. ×370.

Fig. 1b. $\times 370$.

19



Temps, minutes

Fig. 2. O surface spéculaire

germescouche continue

grandes analogies avec celles mises récemment en évidence par F. Grønlund(3) dans la réaction d'oxydation du cuivre.

J. OUDAR

Faculté des Sciences de Paris Laboratoire de Chimie Minérale B J. Bénard

References

- J. Bardolle et J. Benard, C. R. Acad. Sci., Paris 232, 231 (1951); Rev. Metall. 49, 613 (1951).
 E. Menzel et N. Stossel, Naturwiss. 41, 302 (1954).
 F. Grønlund, J. Chim. Phys. 53, 660 (1956). J. Bénard, F. Grønlund, J. Oudar, M. Duret, Z. für Electrochem.
- (sous presse)
 4. F. D. RICHARDSON et J. E. ANTILL, Trans. Faraday Soc. 51, 22 (1955).
 - * Received May 22, 1958.

THE DYNAMIC YIELDING OF A CARBON STEEL*

C. J. MAIDEN†

A criterion for dynamic yielding in steel is developed to give a theoretical relationship between the yield stress and time to yield for any given stress-time function and test temperature. This relationship is found to agree well with experimental results obtained from compressive impact tests on specimens of a medium-carbon steel at temperatures of $+15^{\circ}\text{C}$, -41°C , -84°C and -121°C .

The impact conditions under which twinning becomes a mechanism of deformation are found from metallographic examination of the tested specimens. It appears that twins form in the vicinity of a stress of 125,000 lb/in² and that this stress is little affected by the test temperature. This is thought to be due to the existence of a high activation energy for initiation of the twinning mechanism.

The results of tests in which specimens required two impacts to yield are also found to be in good agreement with the developed yield theory. These tests indicate that only a small number of dislocations relock immediately after the application of an impact stress of insufficient magnitude and duration to cause yielding. In addition several specimens were deformed a small amount dynamically prior to being reimpacted. It is found that an initial deformation of 0.2 per cent almost eliminates the upper yield point in a subsequent impact test.

LE CROCHET A LA LIMITE ELASTIQUE D'UN ACIER AU CARBONE AU COURS D'ESSAIS DYNAMIQUES

L'auteur établit, pour le crochet à la limite élastique dans l'acier au cours d'essais dynamiques, un critère fournissant une relation théorique entre la tension et le temps nécessaire pour produire ce crochet. Cette relation est valable pour n'importe quelle fonction tension-temps et pour une température d'essai quelconque. On constate en outre qu'elle est en bon accord avec les résultats expérimentaux obtenus au cours d'essais par choes sur des éprouvettes d'un acier demi-doux $(0.32~\%~\mathrm{C})$ aux températures de $+15~\mathrm{C}$, $-41~\mathrm{C}$, $-84~\mathrm{C}$, et $-121~\mathrm{C}$.

Les conditions d'impact pour lesquelles le maclage devient un mécanisme de déformation ont été obtenues par l'observation métallographique. Il apparaît que des macles se forment pour une tension d'environ 125.000 lb/cm² et que cette tension dépend très peu de la température de l'essai. Ce fait est sans doute lié à l'existence d'une énergie d'activation élevée pour le déclenchement du mécanisme de maclage.

Les résultats obtenus dans les essais au cours desquels les éprouvettes requièrent deux impacts pour donner lieu au crochet sont également en bon accord avec la théorie proposée. Ces expériences montrent qu'un petit nombre seulement de dislocations libres sont à nouveau bloquées lorsque la tension du choc est insuffisante en grandeur et en durée pour provoquer la formation du crochet. De plus, certains échantillons ont été légèrement déformés dynamiquement avant d'être soumis à un second impact. L'auteur trouve qu'une déformation initiale de 0.2% élimine presque complètement le crochet à la limite élastique dans un essai ultérieur par choc.

DAS DYNAMISCHE FLIESSEN VON KOHLENSTOFF-STAHL BEI TIEFEN TEMPERATUREN

Für das dynamische Fliessen von Stahl wird ein Kriterium entwickelt, das eine theoretische Beziehung zwischen der Fliesspannung und der Verzögerungszeit des Fliessens für jede gegebene Spannungs-Zeitfunktion und Versuchstemperatur gibt. Es wurde gefunden, dass diese Beziehung mit experimentellen Ergebnissen von Kompressions-Schlag Versuchen an Stahlproben mittleren Kohlenstoffgehalts bei $+15^{\circ}$ C, -41° C, -84° C und -121° C gut übereinstimmt.

Die Belastungsbedingungen, unter denen die Zwillingsbildung als Verformungsmechanismus in Erscheinung tritt, ergaben sich aus der metallographischen Prüfung der untersuchten Proben. Es scheint so, dass sich Zwillinge etwa bei einer Spannung von 125 000 lb/in² bilden und dass diese Spannung wenig von der Versuchstemperatur beeinflusst wird. Dies wird auf die Existenz einer hohen Aktivierungsenergie für den Beginn der Zwillingsbildung zurückgeführt.

Die Resultate von Untersuchungen, in denen die Proben zum Fliessen zwei Schläge benötigten, ergaben sich ebenfalls in guter Übereinstimmung mit der entwickelten Theorie. Diese Versuche zeigen, dass nur eine kleine Zahl von Versetzungen nach Einwirkung einer Schlagbeanspruchung, die zu klein und zeitlich zu kurz ist, um Fliessen auszulösen, wieder blockiert werden. Verschiedene Proben wurden vor dem zweiten Schlag zusätzlich um einen kleinen Betrag dynamisch verformt. Es wurde gefunden, dass eine Vorverformung von 0,2% beim nachfolgenden Schlagversuch die obere Streckgrenze beinahe beseitigt.

1. INTRODUCTION

Theories of dynamic yielding in steel have been proposed by Campbell⁽¹⁾ and by Hendrickson and Clark⁽²⁾. Hendrickson and Clark compared these theories with experimental results obtained from constant stress and constant strain-rate tests. At

the two test temperatures considered, the agreement between the experimental results and both theories was reasonably good. Campbell's theory, however, has an advantage in that it presents a comparatively simple relationship between the yield stress and time to yield, irrespective of the shape of the stress-time curve prior to yield.

In this paper Campbell's yield criterion is developed

VOL.

^{*} Received May 28, 1958.

[†] Engineering Laboratory, University of Oxford.

to give the relationship between the yield stress and time to yield at any test temperature. This relationship is then compared with experimental results obtained by impacting a medium-carbon steel at temperatures of $+15^{\circ}\text{C}$, -41°C , -84°C and -121°C . Also, to obtain information as to when twinning is initiated, all the specimens used in the investigation have been examined micrographically. The impact apparatus used and the experimental procedure have been described in earlier papers. $^{(3,4)}$

Finally the yield theory is compared with results obtained from room-temperature repeated impact tests. These tests were undertaken to investigate the effect of a previous impulsive stress on the dynamic yield strength of the steel. In some of these tests the first stress pulse was of insufficient magnitude and duration to cause yield, and in others yield did occur during the first impact.

2. A THEORY OF DYNAMIC YIELDING IN STEEL

For the purposes of this paper, yield is defined as that point where the strain rate increases suddenly as the stress rate falls to zero.

Campbell has proposed that yield will occur in mild steel when the density of released dislocations reaches a certain critical value. According to this criterion yield occurs at a time τ_y such that

$$\int_{0}^{\tau_{y}} \exp\left(-U/kT\right) dt = C \tag{1}$$

where U is the activation energy for the applied stress σ , k is Boltzmann's constant, T is the absolute temperature and C is a constant for the material. The constant C will evidently depend on the particular steel tested but should be independent of the stresstime variation corresponding to the test used, and also independent of the test temperature.

Theoretical activation energy curves have been derived by Cottrell and Bilby⁽⁵⁾ from a consideration of the mechanism of the release of a dislocation. Yokobori⁽⁶⁾ has shown that these activation energy curves may be approximately represented by equations of the form $U = -(1/n) \ln \sigma/\sigma_o$

where n is a constant and σ_a is the yield stress at 0° K. Substitution of this expression in equation (1) gives

$$\int_{a}^{\tau_{y}} \sigma^{z_{T}} dt = C \sigma_{a}^{z_{T}} = c_{T}$$

where α_T is a dimensionless quantity of magnitude 1/nkT and c_T is a constant at a constant temperature.

Thus, at a temperature T, yield is predicted to occur at a time τ_y such that

$$\int_{0}^{\tau_{y}} \sigma^{\alpha_{T}} dt = c_{T} \tag{2}$$

where c_T , α_T and T are related to the room temperature values of these quantities, c_R , α_R and R, by the expressions

$$\alpha_T = \alpha_R R / T \tag{3}$$

and

$$c_T = c_R \sigma_o^{\alpha_T - \alpha_R} \tag{4}$$

It is to be noted that this theory only applies for times to yield less than about 0.1 sec. It has been suggested⁽⁷⁾ that, in tests in which yield occurs after a greater duration than this, carbon atoms may have time to diffuse and relock some of the released dislocations. The theory does not take this into account.

3. SPECIMENS

The steel used was a medium-carbon steel (Park Gate M.2185) and had the following composition:

The method of machining the specimens from the original $2\frac{1}{2}$ in. diameter bar and the heat treatment to which the steel was subjected have been given in an earlier paper.⁽³⁾

4. EXPERIMENTAL RESULTS

VO!

19

Specimens were impacted at a number of velocities at $test temperatures of +15^{\circ}C, -41^{\circ}C, -84^{\circ}C and -121^{\circ}C$ respectively. The impact apparatus used to compress the specimens and the experimental procedure have been described elsewhere. (3) Stress-time oscillograms were obtained from resistance strain gauges mounted on a high-tensile steel weighbar and centred 3 in. from the upper face of the specimen. A typical oscillogram with calibration lines superimposed is shown in Fig. 2b. Each specimen record and an elastic record, obtained from impacting a high-tensile steel dummy specimen at the velocity concerned, were analysed by the method of Campbell and Duby(8) to obtain a stress-time curve for the specimen upper face. From such a stress-time curve the maximum point gave the yield stress and time to yield.

Tables 1, 2, 3 and 4 give results of the dynamic tests. In Table 4 only one result is presented. This is because at $-121^{\circ}\mathrm{C}$ it became extremely difficult to obtain good weighbar records. The weighbar record from which the results in Table 4 were derived was an exceptionally good one and hence the results tabulated can be expected to be as accurate as those obtained at the higher test temperatures.

Also tabulated in Table 1 are values of c_R calculated for each test. The value of α_R used in equation (2) in order to determine these values of c_R was 13.0. This figure for α_R had been suggested by Campbell

Table 1. Test temperature +15°C

Impact velocity (in./sec)	Time to yield (µsec)	$\begin{array}{c} {\rm Yield} \\ {\rm stress} \\ (10^3{\rm lb/in^2}) \end{array}$	$\int_{0}^{\tau_y} \left(\frac{\sigma}{10^5 \text{ lb/in}^2}\right)^{13} dt = c_h$ (μsec)
326	82 78	95 94	14.1 12.0
Average	80	94.5	13.0
340	73 69	96 97	15.1 16.1
Average	71	96.5	15.6
352	60 60	99 98	17.7 17.2
Average	60	98.5	17.5
365	52	102	17.3
430	32 34 34	109 109 108	14.3 20.5 17.1
Average	33	108.5	17.3
470	30 26 30	111 110 108	15.0 17.4 13.9
Average	29	109.5	15.4
503	28 28 26	115 111 112	19.9 15.0 18.3
Average	27	112.5	17.7

Average 16.4

and Duby⁽⁷⁾ from previous tests on steel of the same composition and heat treatment as that used in the present investigation. The values of c_R shown in Table 1 are approximately constant over the whole

1959

Table 2. Test temperature −41°C

Impact velocity (in./sec)	Time to yield (μsec)	Yield stress (10 ³ lb/in ²)
	45	119
430	45	114
	45	119
Average	45	117.5
	39	121
470	39	122
	39	121
Average	39	121.5
503	30	129
	32	126
Average	31	127.5

Table 3. Test temperature -84°C

Impact velocity (in./sec)	Time to yield (μsec)	Yield stress (10^3 lb/in^2)
	48	132
470	50	130
	50	130
Average	49	130.5
	38	133
503	40	136
	40	131
Average	39	133.5

range of impact velocities, thus indicating that the figure of 13.0 taken for α_R is a reasonable one. The value of c_R used in all subsequent calculations is the average value of 16.4 (in appropriate units).

It is possible to use this known figure for c_R to determine, from the theory, the yield stress and time to yield corresponding to any set of impact conditions used in the present investigation. To do this it is first necessary to obtain a value of α_T and hence c_T corresponding to each test temperature.

From equation (3), by using a value of 13.0 for α_R , it is found that the values of α_T at the other test temperatures are: 16.1 at -41° C, 19.8 at -84° C and 24.6 at -121° C. Thus, provided σ_o is known, equation (4) may be used to determine values of c_T .

Curve C in Fig. 1 shows the variation of static upper yield stress with test temperature for the steel under test. These results were obtained using the apparatus described elsewhere. (4) Also shown in Fig. 1 are results obtained by Baron (9) on steels of varying carbon content. In all cases the logarithm of the yield stress has been plotted against absolute temperature. A rough extrapolation of each curve to 0°K indicates that σ_o is fairly independent of the carbon content of the steel and may be taken in the range $200,000-260,000 \text{ lb/in}^2$. As the value of σ_{o} cannot be obtained any more accurately than this, it is proposed to consider values of σ_o of 200,000; 230,000 and 260,000 lb/in2 respectively. Hence for each set of impact conditions there will be three theoretical solutions, one corresponding to each assumed value

Table 4. Test temperature -121°C

Impact velocity (in./sec)	Time to yield (µsec)	Yield stress (10 ³ lb/in ²)
503	60	146

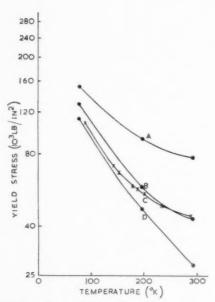


Fig. 1. The effect of test temperature on the static yield strength of a number of plain carbon steels. Curve A: 0.34% carbon steel (Baron). Curve B: 0.2% carbon steel (Baron). Curve C: 0.32% carbon steel (present investigation). Curve D: Armco iron (Baron).

of σ_o . The values of c_T obtained from equation (4) using these values of σ_o are tabulated in Table 5.

It has been found that until yield occurs the stress on a specimen upper face follows almost exactly the elastic stress-time curve for the impact velocity concerned. Now the theory predicts that, at a temperature T, yield will occur when the integral

$$\int_{o}^{t} \sigma^{\alpha_{T}} dt.$$

reaches a value c_T . Hence it is possible to determine the yield point, corresponding to certain impact conditions, by raising the relevant elastic stress–time curve to the required power α_T and finding the point on this curve at which the area under the curve has

TARLE !

Temperature (°C)	Value of σ_0 (10 ³ lb/in ²)	$c_T = c_R \Big(rac{\sigma_0}{10^5 \mathrm{lb/in^2}} \Big)^{lpha_T - lpha_R}$
(0)	(10-10/111-)	(µsec)
	200	139
-41	230	215
	260	318
	200	1,870
-84	230	4,730
	260	10,900
	200	51,000
-121	230	258,000
	260	1,067,000

Table 6. Test temperature -41°C

Impact velocity (in./sec)	Value of σ_0 (10° lb/in°)	Time to yield (μsec)	Yield stress (10 ³ lb/in ²)
	200	41	119.5
430	230	45	120
	260	49	120.5
	200	33	123
470	230	35.5	126
	260	37.5	128
	200	28	127
503	230	29.5	129
	260	31	132

reached the required value of c_T . This has been done for all impacts using the values of c_T presented in Table 5. The theoretical values of yield stress and time to yield at test temperatures of $-41^{\circ}\mathrm{C}$, $-84^{\circ}\mathrm{C}$ and $-121^{\circ}\mathrm{C}$ are tabulated in Tables 6, 7 and 8 respectively.

Table 7. Test temperature -84°C

Impact velocity (in./sec)	Value of σ_{θ} (10 ³ lb/in ²)	Time to yield (μsec)	Yield stress (10 ³ lb/in ²)
470	200 230 260	44 53 67	131.5 134 140
503	200 230 260	$34.5 \\ 39.5 \\ 46$	135 139.5 143

19

Table 8. Test temperature −121°C

Impact velocity (in./sec)	Value of σ_0 (10 ³ lb/in ²)	Time to yield (μsec)	Yield stress (10 ³ lb/in ²)
503	200 230	44.5 64	143 147
	260	during ap	ld not occur plication of pulse

A comparison of the results, shown in Tables 2, 3 and 4, with the theoretically derived yield values indicates that, for all three values of σ_o considered, the theory is in good agreement with the experimental results. Also it is to be noted that, owing to the formation of twins in impacts at -84°C and -121°C , it is expected that the theoretical values of yield stress and time to yield would be somewhat greater

than the experimental values at these temperatures. Taking this into account it would appear that a value for σ_0 of between 230,000 and 260,000 lb/in² gives the best agreement between the theory and the actual yield results.

5. TWINNING

All the specimens tested dynamically and also all those tested statically were examined for twin lamellae. It was found that twinning was not initiated in any of the static tests nor in any of the room-temperature dynamic tests. The predominant mechanism of deformation in all the dynamic tests was a very fine, almost indiscernible, slip in the ferrite. Twins were observed only in specimens impacted as follows:

- (a) at −41°C at an impact velocity of 503 in/sec.
- (b) at -84° C at impact velocities of 470 and 503 in/sec.
- (c) at -121°C at an impact velocity of 503 in/sec. Thus, as the highest stress sustained in any impact was the upper yield stress, the applied stresses at which twins were initiated at the four test tempera-
- tures are limited as follows: (See Tables 1, 2, 3 and 4)
 (a) at +15°C the stress at which twins formed must have been above 112,500 lb/in².
 - (b) at -41°C the stress at which twins formed must have been between 121,500 and 127,500 lb/in².
 - (c) at -84°C the stress at which twins formed must have been below 130,500 lb/in².
 - (d) at -121°C the stress at which twins formed must have been below 146,000 lb/in².

Hence, from the results presented so far, there is only sufficient information to determine the approximate stress range for the formation of twins at -41° C. It was decided to conduct further experiments to determine, as accurately as possible, the stresses at which twins were initiated at the other test temperatures.

The experimental procedure at -121°C was as follows. A specimen was impacted at this temperature at a velocity of 430 in./sec. The specimen showed no physical sign of having yielded and the weighbar record did not differ appreciably from the elastic record corresponding to the same impact velocity. However, examination of this specimen revealed the formation of fairly fine twins near the upper face of the specimen. As the maximum stress sustained was 132,000 lb/in2 it appears that the stress at which twins form at -121°C is less than this. The second and third tests were at impact velocities of 390 and 410 in./sec, the maximum stresses sustained by the specimens being 120,000 and 126,000 lb/in2 respectively. In neither of these tests were twins formed; hence it appears that at -121°C twins were initiated

at some stress between 126,000 and 132,000 lb/in². Thus the stress range for the initiation of twinning at -121° C differs little from the stress range found at -41° C.

Using a similar method to that used at -121° C it was found that twins were formed at -84° C at an applied stress in the vicinity of 130,000 lb/in². Unfortunately at room temperature the stress range of the impact apparatus was insufficient to initiate twinning; however, tension impact tests undertaken by Wood⁽¹⁰⁾, on steel of the same composition and heat treatment as that used in the present investigation, have indicated that twins occur at room temperature at an applied stress of approximately 125,000 lb/in².

The above results indicate that, for the steel tested, the stress required to initiate twinning does not vary a great deal with temperature. Cottrell and Bilby⁽¹⁾ have suggested a dislocation mechanism for twinning; hence it is reasonable to assume that thermal fluctuations will help in starting the mechanism. Thus one would expect the stress at which twinning is initiated to become higher as the test temperature becomes lower. The above experimental results have not disproved this possibility, but they indicate that the difference in stresses required to initiate twinning at various temperatures is small. It is thought that this is due to a high activation energy necessary to form twins.

6. REPEATED IMPACT TESTS

A series of room-temperature impacts were carried out on test specimens at impact velocities of 277, 293 305, 326 and 352 in./sec respectively. Within 15 min of the first impact each specimen was re-impacted at a velocity of 430 in./sec. It was found that only the specimens impacted at velocities of 326 and 352 in./sec were yielded during the first impact; the remainder yielded when re-impacted at 430 in./sec. This rather large velocity was chosen for the second impact as it gave well-defined dynamic upper yield points and hence enabled the effect of the previous impact to be easily observed.

Fig. 2 shows typical weighbar oscillograms with calibration lines superimposed. Fig. 2a refers to a test at an impact velocity of 305 in./sec in which no appreciable yielding of the specimen occurred. Figs. 2b, 2c and 2d refer to impacts at a velocity of 430 in./sec; Fig. 2b was obtained using a specimen that had suffered no prior dynamic compression; Fig. 2c corresponds to a specimen that had been pulsed, i.e. subjected to a rapidly applied stress of sufficient magnitude and duration to cause yielding, at a velocity of 293 in./sec; and Fig. 2d refers to a specimen

VOL. 7 1959

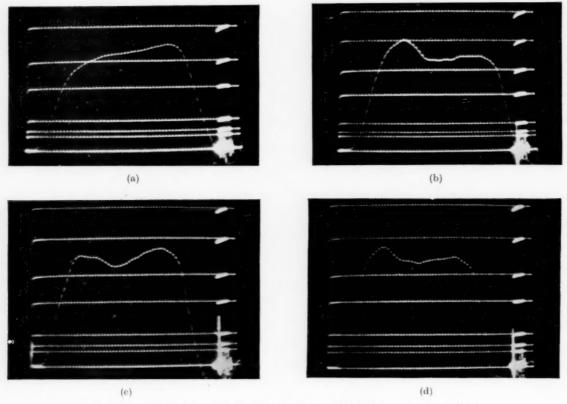


Fig. 2. Stress–time oscillograms. Test temperature: $+15^{\circ}$ C. Stresses corresponding to calibration lines: 0, 14, 19, 28, 56, 80, 112 and 140 \times 10³ lb/in².

that had been previously compressed 0.9 per cent at an impact velocity of 352 in./sec. All the traces are interrupted every 2 μ sec.

Stress-time curves for the top face of the specimens were derived by the usual method for all impacts. Fig. 3 shows the relevant portions of the derived

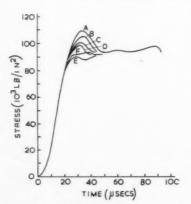


Fig. 3. Stress-time curves for the upper face of the specimens when impacted at 430 in./sec. Curve A: annealed specimen (not pulsed). Curves B, C, D: specimens pulsed at 277, 293 and 305 in./sec respectively. Curve E: specimen strained 0.2 per cent due to an impact at 326 in./sec. Curve F: specimen strained 0.9 per cent due to an impact at 352 in./sec.

stress-time curves for impacts at 430 in./sec. It is seen that the dynamic upper yield stress is reduced by pulsing without yielding; however, the lowest value of the yield stress does not occur until the steel has had 0.2 per cent prior dynamic strain. At this strain the upper yield point has almost been removed, as indeed it has after 0.9 per cent initial dynamic strain. A comparison of these results and those of an earlier investigation(3) indicate that, in a dynamic retest after 0.2 per cent deformation, the upper yield point has very nearly been eliminated, whereas in a static retest after 0.2 per cent permanent dynamic deformation there is still a very perceptible drop of stress at yield. This may possibly be explained by the fact that during a static retest carbon atoms can diffuse and relock the freed dislocations; however, in a dynamic retest there is insufficient time for any significant relocking to occur.

It is considered that the reduction in the dynamic upper stress yield after pulsing may be attributed to the freeing of a number of dislocations during this pulsing treatment. Earlier it was shown that results obtained from tests in which yield occurred in a single impact were in reasonable agreement with the

yield theory; hence the assumption that it is necessary to release a critical density of dislocations in order to cause yielding must be approximately correct. At room temperature this critical density may be taken as proportional to the average value of c_R (equation 2) which, for the steel under test, was found to be 16.4 (in appropriate units). It is of interest to see whether or not the value of the integral will be constant and of approximate value 16.4 for the above tests in which specimens required two impacts to yield.

Fig. 4 shows the curves of σ^{13} for those specimens requiring two impacts to yield. For each specimen the integral was evaluated graphically over the whole loading time. The values of c_R obtained were found to be 14.3, 16.6, 16.0 and 16.9, these values corresponding to a specimen not pulsed, and to specimens pulsed at impact velocities of 277, 293 and 305 in./sec respectively. Thus, considering the three latter specimens, the average value of the integral is 16.5. It was decided to check this value by impacting a specimen twice at the same impact velocity. The velocity chosen was 285 in./sec; this velocity being such that, although yield did not occur in the first impact, it was large enough to yield the specimen during the second impact. The value of c_R was found to be 17.2, 10.6 from the first impact and 6.6 before yield occurred in the second impact.

A comparison of the above values of c_R with the value of 16.4, obtained in tests in which yield occurred in a single impact, permits two main conclusions. The first is that the value of c_R is approximately constant, irrespective of the number of stress pulses required to cause yield; and the second is that the number of dislocations that relock after the first stress pulse must be small. These conclusions are consistent with the results of other investigators. Krafft⁽¹²⁾ has found that, provided the ageing period between pulses is small, a specimen yields when the cumulative time at a constant stress is approximately equal to the

1959

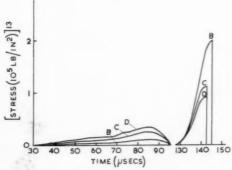


Fig. 4. Curves of (stress)¹³ v. time for those specimens requiring two impacts to yield. Curves B, C, D: specimens pulsed at 277, 293 and 305 in./sec respectively.

normal de lay-time at that stress. This result is in complete a ccordance with the above two conclusions. Also Vigness et al.(13) have found, from room-temperature repeated impact tests on a medium-carbon steel, that 'yield occurs when the summation of the proportiona te amount of damage reaches unity'; where the relative amount of damage that occurs during time spent at any stress level is taken as equivalent to the proportionate part that this time is to the delay-time for constant stress of the same level. Here again it may be shown that the above result is such that yield is expected to occur when the integral (equation 2) reaches a constant value c_R , irrespective of the number of stress pulses necessary to cause yield, and hence the number of dislocations that relock between pulses must be negligible.

7. CONCLUSIONS

1. The developed yield theory of dynamic yielding in steel is in good agreement with the experimental results. Twinning occurs in some of the low-temperature tests; this probably causes yielding to occur at lower stresses than would be required in the absence of twinning. Taking this into consideration, it appears that a value of σ_a between 230,000 and 260,000 lb/in² gives the best agreement between the theory and the experimental yield values. The results of the low-temperature static tests indicate that the actual value of σ_a is in the vicinity of this range of stresses.

2. At low temperatures and high strain rates the predominant mechanism of deformation is a fine slip in the ferrite; however, twin lamellae are also formed when the applied stress is great enough. The results obtained indicate that, for the steel tested, the stress at which twins form is approximately independent of test temperature and is about 125,000 lb/in².

3. The developed yield theory is also in good agreement with the results of tests in which specimens required two impacts to yield. Such a conclusion indicates that the number of released dislocations that relock after the application of a stress pulse, of insufficient magnitude and duration to cause yielding, is small.

4. An initial dynamic strain of 0.2 per cent is sufficient almost to eliminate the upper yield point in a subsequent dynamic test.

REFERENCES

- 1. J. D. CAMPBELL, Acta Met. 1, 706 (1953).
- J. A. HENDRICKSON and D. S. CLARK, Trans. Amer. Soc. Metals 50, Preprint No. 27 (1957).
 J. D. CAMPBELL and C. J. MAIDEN, J. Mech. Phys. Solids
- J. D. Campbell and C. J. Maiden, J. Mech. Phys. Solids 6, 53 (1957).
- C. J. Maiden and J. D. Campbell, Phil. Mag. 3, 872 (1958).
 A. H. Cottrell and B. A. Bilby, Proc. Phys. Soc. A62, 49 (1949).

- T. Yokobori, Phys. Rev. 88, 1423 (1952).
 J. D. Campbell and J. Duby, Proc. Inst. Mech. Engrs. Conf. (1957). In press.
 J. D. Campbell and J. Duby, Proc. Roy. Soc. A236, 24 (1956).
 H. G. Bringer, I. Leaving Conf. Leav. 152, 284, 1455.
- 9. H. G. BARON, J. Iron Steel Inst. 182, 354 (1956).

- E. O. Wood, Private Communication, Oxford Engng. Lab.
 A. H. COTTRELL and B. A. BILBY, Phil. Mag. 42, 573 (1951).
 J. M. KRAFFT, Trans. Amer. Soc. Metals 48, 249 (1956).
 I. VIGNESS, J. M. KRAFFT and R. C. SMITH, Proc. Inst. Mech. Engrs. Conf. (1957). In press.

ETUDE PAR ANALYSE THERMIQUE DES TRANSFORMATIONS ALLOTROPIQUES DU PLUTONIUM*

R. PASCARD†

Les transformations allotropiques du plutonium ont été mises en évidence par analyse thermique différentielle.

On donne une description des phénomènes observés tant au chauffage qu'au refroidissement. Un étalonnage préalable de l'appareil usuel permet en outre de mesurer avec une précision d'environ 20 pour cent les différentes chaleurs de transformation.

A STUDY BY THERMAL ANALYSIS OF THE ALLOTROPIC TRANSFORMATIONS OF PLUTONIUM

The successive transformations, including fusion, of metallic plutonium have been studied by differential thermal analysis. Heating and cooling curves are given.

Comparison with metallic standards of known heats of fusion give a first set of heats of transformation with a precision of about 20 per cent.

THERMISCHE ANALYSE DER ALLOTROPEN UMWANDLUNGEN VON PLUTONIUM

Mit Hilfe von thermischer Differentialanalyse wurden die allotropen Umwandlungen einschliesslich des Schmelzens von Plutonium untersucht.

Die beim Aufheizen wie beim Abkühlen beobachteten Kurven werden angegeben.

Nach Eichung mit Proben bekannter Schmelzwärme lassen sich die jeweiligen Umwandlungswarmen auf etwa 20% genau messen.

Il existe actuellement d'assez nombreuses publications consacrées à l'étude des changements de phase du plutonium. La plupart font état de méthodes descriptives (par exemple: dilatométrie, résistivité, analyse thermomagnétique) destinées avant tout à mettre en évidence l'existence des points de transformation du plutonium, mais ne fournissent pas une grandeur liée directement à des transformations. Par contre, la connaissance des chaleurs de transformation présente un intérêt fondamental du point de vue thermodynamique et peut apporter éventuellement des renseignements sur la nature des phases en équilibre.

On sait que ces chaleurs peuvent être déduites indirectement des courbes d'analyse thermique différentielle. Comme cette méthode était l'une de celles que nous nous étions fixées a priori pour caractériser les transformations allotropiques du plutonium, il nous a paru naturel de ne pas nous limiter à son aspect purement qualitatif et de l'adapter à la mesure des chaleurs de transformation.

Nous décrirons successivement le principe de la méthode, l'appareillage utilisé et enfin dans la deuxième partie l'essentiel des résultats obtenus avec le plutonium.

1. PRINCIPE

Nous avons admis que l'appareil classique pouvait, sans modifications essentielles, être étalonné directement en calories à l'aide d'échantillons de chaleur de transformation connue. Il devient alors possible, à condition d'observer une grande rigueur dans le montage, d'obtenir l'effet thermique cherché par simple comparaison.

L'analyse thermique différentielle consiste en principe à imposer à l'échantillon étudié (A) et à un échantillon de référence (B) un programme de chauffe à vitesse constante v, et à enregistrer directement en fonction de la température T de l'enceinte (ou, ce qui revient au même, du temps) la différence de température $\Theta_B - \Theta_A$ entre ces deux échantillons. En régime permanent, l'écart $\Theta_B - \Theta_A$ prend une valeur pratiquement constante a, qui, toutes choses égales par ailleurs, est proportionnelle à la vitesse de chauffe v.

Si t_1 est l'instant correspondant au début d'une transformation et t_2 l'instant final, l'analyse thermique différentielle quantitative postule que la quantité

$$\left[\int_{t_1}^{t_2}\!\! K[(\Theta_B-\Theta_A)-a]\,dt\right]$$

^{*} Received June 26, 1958.

[†] Laboratoire de Radiométallurgie, Centre d'Etudes Nucléaires de Fontenay-aux-Roses

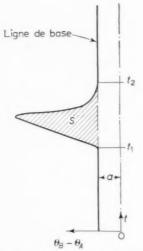


Fig. 1. Aspect général d'une transformation

représente exactement la quantité de chaleur mise en jeu au cours de la transformation. K est un coefficient global qui tient compte de tous les modes possibles de transmission calorifique et que l'on peut supposer constant dans le court intervalle t_2-t_1 . L'aire hachurée S, visible sur la Fig. 1, est donc directement proportionnelle à la chaleur dégagée (ou absorbée) Q:

$$Q=K\!\int_{t_1}^{t_2}\!\!\left[(\Theta_B-\Theta_A)-a\right]dt=K\!S$$

Si nous supposons maintenant que l'échantillon est d'asses petites dimensions pour qu'à tout instant on puisse le considérer à température uniforme, la chute de température entre l'enceinte et A a lieu uniquement dans la paroi du creuset (Fig. 2) et nous pouvons alors expliciter K:

$$K = K_c \lambda_c$$

où λ_e est la conductibilité thermique du creuset et K_c un facteur de dimension relatif au même creuset $K_c \sim s/e$ (s = surface du creuset en contact avec l'échantillon, e = épaisseur).

 $S=(1/K_c\lambda_c)Q$ ne dépend donc que des constantes thermiques relatives au système creuset-échantillon (A). Elle est indépendante de la vitesse de chauffe et de la nature de l'échantillon de référence B qui peut être choisi quelconque. Puisque d'autre part nous avons admis que la conductibilité calorifique de A n'intervenait pas, nous pourrons comparer directement les surfaces données par différents échantillons, pourvu que K_c et λ_c restent les mêmes.

On aperçoit immédiatement que cette méthode ne saurait prétendre à une grande précision. En effet, K_c et λ_c ne dépendront uniquement de la nature et de la surface de contact creuset-échantillon que si nous supposons par ailleurs que les contacts entre les

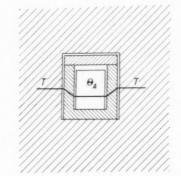


Fig. 2. Répartition de la température dans l'ensemble creuset-échantillon.

différentes surfaces d'échange thermique sont parfaits, cas idéal qu'on ne peut réaliser dans la pratique: en réalité K_c et λ_c sont des facteurs composites (analogues à une conductance, par exemple) qui ne peuvent être qu'estimés. Même en opérant toujours dans un creuset unique, on ne saurait garantir une reproductibilité parfaite.

En définitive, la méthode ne peut donc être justifiée que par une vérification expérimentale. Comme on le verra plus loin lorsque nous parlerons de l'étalonnage, les valeurs obtenues par comparaison des surfaces, pour des métaux de chaleur de fusion connue, sont en accord raisonnable avec les valeurs admises.

2. APPAREIL

19!

L'appareil utilisé ne diffère pas sensiblement de l'appareil habituel. On s'est attaché surtout à augmenter sa fidélité et sa sensibilité tout en réduisant les imperfections bien connues de certains montages qui sont:

- —une dérive continuelle et incontrôlable de la ligne de base.
- —de légères oscillations de cette ligne de base qui lui donnent un aspect tremblé.

Ces deux effets parasites peuvent, soit conduire à des résultats fantaisistes, soit au contraire masquer de faibles phénomènes réels.

1. Nous pensons qu'il est impossible de maîtriser complètement la dérive si l'on opère sous vide poussé, surtout dans le domaine des basses températures. A partir de 500°C, où le rayonnement devient prépondérant, la courbe enregistrée est plus stable mais elle reste sujette à des variations incontrôlables qui peuvent être dues, par exemple, à des sautes de vide. On obtient, au contraire, très facilement une parfaite régularité des échanges thermiques en opérant sous atmosphère contrôlée. La ligne de base devient rigoureusement rectiligne ce qui rend possible la détection de très faibles effets thermiques.

2. Les oscillations de la ligne de base sont en général attribuées à des effets d'induction. Nous pensons qu'elles sont, la plupart du temps, dues à des f.e.m. parasites variables qui existent réellement dans le circuit des thermocouples. Il convient donc de réduire au minimum les raccords par bornes à serrage, même entre fils identiques. En particulier, le raccordement des fils de couples à l'intérieur du tube laboratoire doit absoluement être protégé du rayonnement ou des mouvements de convection par un écran, sinon les oscillations peuvent atteindre $\pm 10~\mu V$.

En conclusion nous pouvons dire qu'un bon montage d'analyse thermique différentielle est celui qui fournit des courbes dont tous les détails sont interprétables.

(a) Échantillons et assemblage

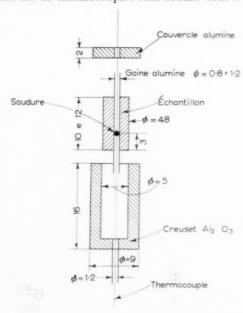
VOL.

1959

Les échantillons sont usinés en forme de cylindre s'adaptant au mieux aux dimensions intérieures du creuset, d'une volume d'environ 0,2 cm³.

Ils sont percés de part en part pour permettre le passage du couple et de sa gaine de protection en alumine. Les creusets, en alumine frittée, sont également percés pour la même raison. Il n'y a pas de variations importantes ni de dimensions, ni de propriétés thermiques, dans un lot de même fabrication mais on doit veiller particulièrement à la constance du diamètre extérieur (ici 9 mm) qui est extrêmement critique.

Les fils de thermocouples sont soudés bout à bout



Creuset et échantillon cotes en mm

Fig. 3. Détail de l'ensemble creuset échantillon.

de façon à former un fil unique. Cette disposition est préférable à la soudure en V car elle permet un encombrement réduit et surtout une mise en place stable de la soudure dans l'échantillon (Fig. 3).

Pour augmenter la sensibilité de l'appareil, on a choisi le couple chromel—constantan dont la f.e.m. est environ 1,6 fois plus forte que celle du couple chromel—alumel à la même température (1 mV représente environ 14°C). Nous estimons que ce couple permet facilement une reproductibilité des mesures à 0°3C près. Les fils, d'un diamètre de 3/10 mm, sont soudés à la soudeuse électrique par points.

Les deux creusets contenant les échantillons sont montés dans un porte-échantillons en cuivre, qui assure une bonne homogénéité de la température (Fig. 4). Grâce à la présence de deux bouchons en cuivre, on peut les considérer parfaitement enfermés dans une enceinte à température définie. Le point délicat du montage, surtout en boîte à gants, est évidemment la mise en place de la soudure que l'on s'est efforcé de placer au 1/3 de la hauteur de l'échantillon, à partir de la base.

L'assemblage du porte-échantillon terminé, l'ensemble est suspendu par une tige support (Fig. 4) à la tête métallique du tube à vide. A la partie supérieure les fils de couples sont raccordés par bornes à serrage. A la partie inférieure, le point triple est obtenu simplement en torsadant ensemble les trois fils. Un écran en acier inox, surmonté de bourre d'amiante, protège des mouvements de convection les raccords supérieurs. L'enceinte à vide ou à atmosphère contrôlée est un tube de silice de 35 mm de diamètre raccordé d'une façon étanche à la tête métallique par des joints caoutchouc.

(b) Montage

La figure 5 représente l'aspect général de l'appareil. Suivant une technique de plus en plus généralisée dans ce laboratoire, l'ensemble de pompage est entièrement à l'extérieur de la boîte à gants. La colonne de vide sert en même temps de support coulissant pour le four. Le four est du type Chevenard à programme de chauffe automatique par tige dilatable. Nous avons remplacé l'entraînement du tambour par mouvement d'horlogerie, qui ne donne que deux vitesses de chauffe, par un entraînement à friction et micromoteur qui permet toutes les vitesses de 0°5 à 10°C par minute environ (Fig. 6).

Après évacuation prolongée, l'atmosphère contrôlée, ici de l'argon pur, est introduite dans l'appareil après purification sur un fil de titane chauffé, jusqu'à une pression d'environ 900 g.

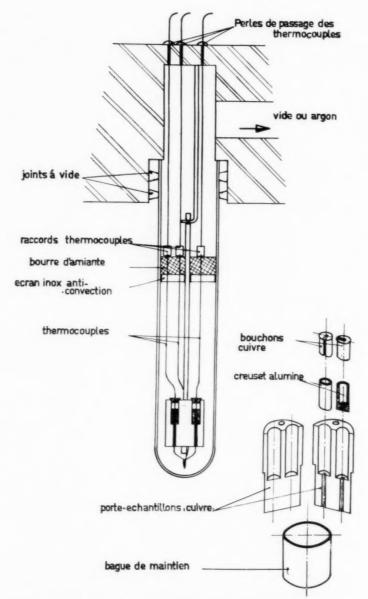


Fig. 4. Mise en place dans le tube laboratoire du porte échantillons—à droite détail du porte échantillon.

(c) Enregistrement

Les couples traversent directement la paroi de la boîte à gants et sont, après passage à la source froide constituée par de la glace fondante, reccordés aux enregistreurs qui sont

(1) un enregistreur Philips à plusieurs sensibilités qui donne la température de l'échantillon. Cet enregistreur n'est utilisé qu'à titre de contrôle pour vérifier la régularité de la vitesse de chauffe. Des mesures-précises sont effectuées régulièrement avec un potentimètre manuel A.O.I.P. dont la sensibilité est

d'environ $\pm 5~\mu\mathrm{V}$ dans toute l'étendue des f.e.m. à mesurer.

19

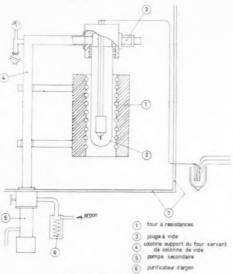
(2) la différence de température entre les deux échantillons est donnée par un enregistreur M.E.C.I. dont l'échelle totale de lecture de 250 mm correspond à une f.e.m. de 1 mV, soit dans notre cas particulier à environ 14°C. Un contacteur manuel permet de reporter sur la courbe les températures lues au potentiomètre manuel. La vitesse de découlement de cet enregistreur différentiel a été choisie à dessein

relativement grande (16 pouces à l'heure) de façon à augmenter la surface des pics.

3. ETALONNAGE

L'étalonnage a été effectué avec les métaux suivants, dont les températures et les chaleurs de fusion sont connues:

Il nous a permis tout d'abord de tracer la courbe f.e.m. = f(T). Même si des tables donnent les valeurs de cette f.e.m., il est absolument nécessaire d'étalonner les couples dans les conditions mêmes de l'expérience, car de nombreux effets secondaires et en particulier les pertes par conductibilité le long du fil peuvent empêcher la soudure d'être réellement en équilibre de température avec l'échantillon qui, rappelons-le, est de petites dimensions.



1959

Fig. 5. Montage général.

Nous avons ensuite vérifiié les points suivants:
—les surfaces enregistrées sont indépendantes des vitesses de chauffe.

—pour des réactions rapides isothermes, ce qui est le cas de la fusion, l'écart $\Theta_B - \Theta_A$ croît linéairement puisque Θ_A reste constant tandis que Θ_B continue à croître à vitesse constante. Les pics présentent donc une première partie rectiligne dont la pente est approximativement égale à la vitesse de chauffe du four comme on peut le voir sur la figure 7. On notera sur la courbe qui correspond à la cristallisation de l'aluminium une courte partie ab pratiquement horizontale qui traduit une légère surfusion (en ce point tout se passe comme si la vitesse de refroidissement était infinie). En b, la température

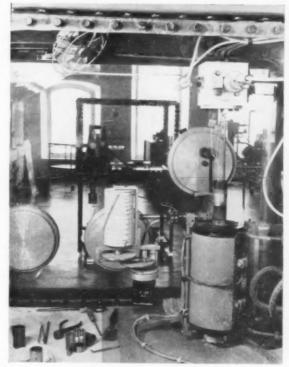


Fig. 6. Photographie du montage général en boîte à gants. On peut voir le four, la colonne de vide support, le tube laboratoire avec un échantillon prêt pour l'essai. Le dispositif de chauffe à vitesse variable ainsi qu'un porte échantillon sont visibles en détail.

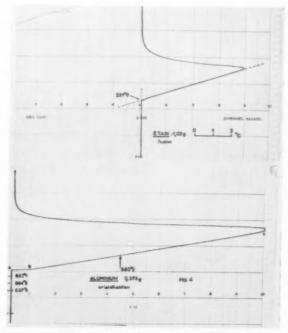


Fig. 7. Exemples de pics observés: fusion d'échantillons de Zn et d'Al.

du système a rejoint la température de fusion de l'aluminium et la cristallisation se poursuit ensuite à la même vitesse que le refroidissement du four (partie bc).

Nous avons vérifié également que les hauteurs des pies sont approximativement proportionnelles aux racines carrées des vitesses de chauffe. On a donc intérêt, en analyse qualitative, à adopter la vitesse de chauffe la plus grande possible.

Le tableau 1 donne les surfaces enregistrées pour les différents métaux et pour différentes vitesses de chauffe: de la température: la valeur obtenue pour Al, dont le point de fusion se situe dans une zone de température où le rayonnement doit déjà jouer un rôle important n'est pas affectée d'une erreur plus grande que celles relatives aux métaux de point de fusion voisins de celui du plomb. Il est probable que, à mesure que la température s'élève, l'augmentation de conductibilité due au rayonnement compense l'augmentation de résistivité du creuset (λ_c à 25°C $\simeq 3\lambda_c$ à 600°C pour $\mathrm{Al_2O_3}$).

Cette compensation se trouve réalisée tout à fait fortuitement avec le montage que nous avons choisi.

Tableau I. Comparaison des surfaces enregistrées S pour différents métaux, pour un même volume d'échantillon (environ: $0,2~{\rm cm^3.}$)

Nature de l'échantillon.	Sn	Bi	Cd	Pb	Zn	Al
Poids	1,02 g	1,66 g	1,47 g	2,04 g	1,35 g	0,375 g
S (unités arbitraires)	$\begin{array}{c} 25,7 \ (1,35) \\ 23,1 \ (1,25) \end{array}$	41,5 (1,6) 42,4 (1,2) 44,6 (1,15)	$\begin{array}{c} 33.5 \ (1.4) \\ 34.0 \ (1.4) \end{array}$	20,5 (2,5) 19,3 (1,6) 19,4 (1,3) 19,3 (1,1)	58,7 (2.2) 62,0 (1,5)	69,0 (1,0) 70,9 (1,5) 71,4 (2,7)
S (moyen)	24,4	42,8	33,7	19,6	60,3	70,1

-entre parenthèses, vitesses de chauffe exprimées en degrés/minute.

En choisissant comme étalon le plomb, dont la chaleur de fusion nous a paru la mieux établie, on obtient pour les chaleurs latentes les valeurs suivantes, que l'on peut comparer aux valeurs admises.

L'accord est donc raisonnable et justifie l'hypothèse faite au début à savoir que le terme $K_c\lambda_c$, qui a priori paraît dépendre de facteurs difficilement contrôlables, peut en fait être reproduit avec une bonne approximation. On notera qu'il est pratiquement indépendant

Tableau 2. Chaleurs de fusion mesurées (cal/g)

Echantillon	Observé	Référe des ta		Température de fusion
		(1)	(2)	(°C)
Sn	14,7	14,0	14,1	231°9
Bi	15,8	12,6	12,6	271°3
Cd	14,1	13,7	13,4	320°9
Pb	5,9	5,86	5,2	327°4
Zn	27,4	28,1	26,6	419°5
Al	81	76,8(?)	91,9	660°0

Référence (1): Handbook for Chemistry and Physics (1956). Référence (2): J. LUMSDEN, Thermodynamics of alloys. Monograph and Report Series n° 11, Institute of Metals, London (1952). Il parait cependant plus logique de choisir comme étalon, aux environs de 600° C, la chaleur de fusion de l'aluminium.

19

Remarque: Il convient de vérifier qu'il n'y a pas de variation trop importante de la ligne de base avant et après fusion. Dans le cas général une différence comparable à celle de la figure 8 ci-contre avec a' < a ne saurait s'expliquer par une variation de densité (dont dépend K_c comme on peut le montrer facilement) ou de chaleur spécifique (dont dépend a). Elle est due en réalité à un changement important dans la nature du contact creuset échantillon, ce qui se conçoit

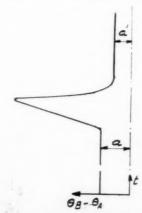


Fig. 8. Exemple de variation de la ligne de base.

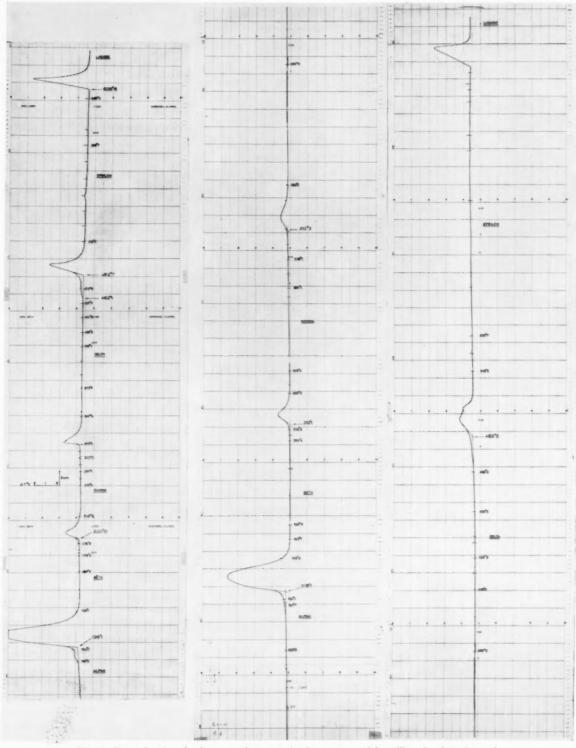


Fig. 9. Reproduction de deux courbes enregistrées avec un échantillon de plutonium—à gauche essai n° 2, à droite essai n° 14.

VOL. 7 1959 facilement si l'échantillon est au départ trop lâchement adjusté dans le creuset. Mais par contre, dans le cas du plutonium, nous verrons que de tels écarts sont effectivement dus à des changements importants de densité.

4. APPLICATION AU PLUTONIUM

On a utilisé un échantillon de haute pureté, provenant de l'Atomic Energy Commission des U.S.A., dont l'analyse spectrographique est la suivante (impuretés en parties par millions).

Il a été usiné aux dimensions indiquées précédemment, exception faite de la hauteur qui n'était que de 9 mm. Son poids initial était de 2,7 g. Une autre partie de ce même échantillon a été réservée à l'étude dilatométrique.⁽²⁾

(a) Caractérisation et températures des points de transformation

On a effectué environ vingt essais, dont sont extraites les deux courbes de la figure 9 (essais n° 2 et 14). Au 5ème essai une entrée d'air accidentelle a entrainé l'oxydation d'une partie de l'échantillon qui ne pesait plus que 1,7 g au cours des essais suivants. Cependant, les effets observés sont quantitativement aussi grands lors de l'essai n° 14, ce qui n'est pas surprenant puisqu'ils ne dépendent pratiquement que de la densité de remplissage (c'est-à-dire celle de l'échantillon), et non de la masse totale, tout au moins en première approximation.

D'autre part, l'essai n° 2 n'a pas été effectué avec le montage définitif, ce qui explique qu'on puisse y trouver encore deux anomalies évidentes, et dans certaines régions, de légères oscillations de la ligne de base.

On retrouve qualitativement toutes les transformations de phase du plutonium, exception faite de la transformation $\delta \rightarrow \delta'$, sur laquelle nous reviendrons plus loin.

Sur le tableau suivant sont portées les températures de transformation. Pour chaque transformation nous donnons deux températures:

L'une T est ce qu'on pourrait appeler température de transformation active. A cette température, définie par extrapolation comme l'indique la figure 10,

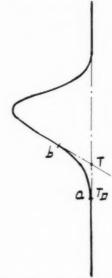


Fig. 10. Aspect général d'une transformation isotherme lente.

la réaction a atteint une vitesse notable, par opposition à la partie ab qui correspond à un démarrage progressif. L'autre température de début de transformation T_d , est relevée en a, point où la transformation a manifestement commencé. On doit noter que le repérage de T_D est affaire d'estimation.

VO

19

On voit donc que les pics observés s'écartent notablement, exception faite de la fusion, du schéma théorique donné à propos de l'étalonnage. Même pour de faibles vitesses de chauffe, la transformation ne peut suivre la vitesse imposée (qui serait celle du flux de chaleur par seconde), ce qui se traduit en définitive par un étalement plus ou moins accentué des pics; ceci est d'ailleurs un phénomène courant pour les transformations en phase solide, comme nous l'avons constaté pour les transitions du cobalt et du fer. Nous n'avons observé de changements de phase isothermes rapides que dans le cas de l'uranium $(U_{\alpha} \rightarrow U_{\beta})$ et $U_{\beta} \rightarrow U_{\gamma}$).

L'écart $T-T_D$ peut signifier, soit que la transformation est précédée d'une période d'induction, soit que la présence d'impuretés abaisse la température de transformation. En consultant le tableau, on constate que cet écart n'augmente pas d'une façon significative au fur et à mesure des essais ce qui autorise à conclure en faveur de la première hypothèse.

Enfin au cours des essais successifs, on a procédé à de fréquents démontages, pour changements de couple. Certains écarts sur les valeurs données peuvent donc être dus à de légères variations de position de la soudure des couples.

Nous examinerons tout d'abord les différentes transformations lors de la montée en température.

Tableau 3. Températures de transition observées au cours des essais successifs pour différentes vitesses de chauffe. Dans chaque case, valeurs de T(1) et de $T_D(2)$ et

No. de l'essai	de chauffe en deg/min	α-β	β-γ	γ-δ	δ–ε	Fusion	Crist.	εδ	δγ	γβ	β
1	2°5	126°6 119°0	217°5 217°5	320°1 320°1							
2	4°7	126°1	220°0 216°0	319°4 319°4	482°8 462°1	638°6					
3	2°0	125°9 120°4	216°3 214°0	?	485°2 480°8						
4	2°0	128°2 123°3	214°0 213°1								~8
5	1°7	126°9 120°4									
6	1°7	129°2 121°9									
7	2°0	128°2 116°1	213°4 212°1	313°0 310°8	487°6 480°8						
8	3°7	128°3 117°5	215°1 211°3	314°4 312°3	486°8 472°9						
9	5°3	128°3 117°5	216°2 213°1	314°4 312°3	486°1 467°0		-	493°4?	≃216°	≃{ Déb. 147 Fin 128	
10	3.0	130°4 117°5	219°5 214°5	319°4 316°5	491°3 475°4	641°3	641°6	499°0?	≥206°		
11	3°7	129°2 117°5	216°1 214°0	316°3 314°4	488°1 474°9	639°4	642°7	499° ?	≃177°		
13	2°5	130°1 123°3	217°1 215°1	317°3 315°1	488°1 476°6			501° ?			
14	2°2	128°1 116°9	213°1 210°2	312°3 309°2	483°3 473°3						
15	5°0	131°9 123°3	216°6 214°8	306°8 305°3	478°6 461°4						
17	4°7	131°2 120°4	217°1 214°5	305°3	478°9 469°6						
	$T \\ T_D$	128°1 119°3	216°3 213°9	316°3 313°8	486°6 472°2						

Transformation $\alpha \rightarrow \beta$. Initialement, à la température ordinaire, on observe que l'échantillon de plutonium est légèrement plus chaud que l'échantillon de référence qui est ici du cuivre. L'écart de température, faible mais significatif, est d'environ 0.3° C à la pression atmosphérique et de 3° C sous vide poussé.

Dès que l'on commence à chauffer, le plutonium s'échauffe moins vite que le cuivre et l'écart ne tarde pas à s'inverser. Comme d'autre part, la montée en température est imposée par le four lui-même et non par l'échantillon, le régime permanent est atteint à 100° C seulement environ, ce qui explique la forte

dérive constatée jusqu'à cette température qui nuit quelque peu au repérage de $T_{D}.\,$

On constate en général qu'après une assez longue période d'induction, la réaction procède rapidement à une vitesse qui peut être supérieure à la vitesse de chauffe, comme si on avait affaire à une réaction retardée.

Les températures moyennes observées sont les suivantes:

$$T = 128^{\circ}1$$
C $T_D = 119^{\circ}3$ C

L'écart observé qui atteint 10°C environ est nettement plus élevé que pour les autres transformations

V

mais peut paraître légitime, étant donné la température peu élevée.

Transformation $\beta \to \gamma$ et $\gamma \to \delta$. Ces deux transformations présentent les mêmes caractéristiques. Elles sont lentes, donnant lieu à des pics étalés surtout pour $\gamma \to \delta$ mais manifestent par contre un faible écart $T = T_D$.

Nous avons relevé:

$$\beta \rightarrow \gamma$$
 $T=216^{\circ}3$ C $T_D=213^{\circ}9$ C

$$\gamma \rightarrow \delta$$
 $T = 316^{\circ}3C$ $T_D = 313^{\circ}8C$

On doit accorder cependant une attention particulière à l'allure de la transformation $\gamma \to \delta$ sur la courbe n° 2 (Fig. 9). Elle a l'aspect caractéristique d'une réaction retardée avec un départ brutal pratiquement horizontal. Or, en consultant le tableau on voit qu'elle correspond précisément à une température élevée (319°4C) en comparaison de la moyenne générale des essais (316°3C). Ceci est à rapprocher de l'aspect également très particulier de la même transformation au retour qui peut suggérer une transformation martensitique.

Ce retard de la transformation au chauffage n'a été observé qu'une seule fois. Sur tous les autres essais, y compris le premier, l'allure générale est celle indiquée au début.

Transformation " $\delta \rightarrow \epsilon$." Bien que plus rapide que les deux transformations précédentes, elle manifeste toujours un écart $T-T_D$ important dont la valeur moyenne est de 14°C. Quoique T_D soit extrêmement difficile à repérer sur les derniers essais, le pic enregistré est toujours précédé d'un "pied" diffus; par contre, T_D paraît correspondre lors des premiers essais, à un décrochement net de la ligne de base, comme on peut le voir sur la figure 11 relative à l'essai n° 2. Dans ce cas particulier $T=482^\circ {\rm 8C}$ et $T_D\pm 462^\circ {\rm 1C}$, soit un écart de 20°7C. Ceci suggère que la température de début de transformation corresponde en fait à $\delta \rightarrow \delta'$, pour laquelle l'écart mesuré par d'autres méthodes est d'environ 21°C. $^{(2,3)}$

Il est également curieux de constater que la forme observée paraît être la traduction exacte en analyse thermique des phénomènes décrits par Ellinger⁽³⁾ à propos de l'observation aux rayons X des phases δ , δ' et ϵ .

La coexistence des trois phases δ , δ' et ϵ sur un large intervalle de température rendrait compte du début aplati du pie par suite d'une transformation faible mais continue de ces trois phases les unes dans les autres. Dans ce large domaine de coexistence, Ellinger distingue cependant deux transitions pratiquement totales $\delta \to \delta'$ à $465^{\circ}\mathrm{C}$ et $\delta' \to \epsilon$ de 485° à $490^{\circ}\mathrm{C}$ ce

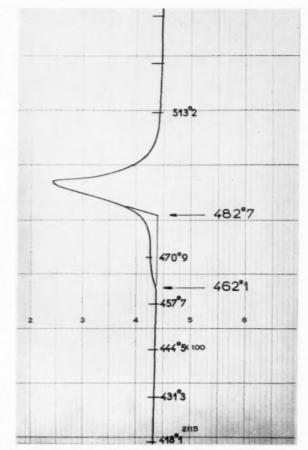


Fig. 11. Transformation " $\delta \to \varepsilon$ ". Détail extrait de la courbe n° 2 Fig. 9.

qui coincide parfaitement avec les températures que nous avons relevées.

Le phénomène n'étant pas suffisamment reproductible, nous donnons cette interprétation sous réserve de confirmation ultérieure.

Par la suite, nous avons admis que la transformation $\delta \to \delta'$ était soit passée inaperçue, soit insuffisamment dissociée de la transformation $\delta' \to \epsilon$, d'où le symbole " $\delta \to \epsilon$ " au lieu de $\delta' \to \epsilon$.

La transformation nous a paru extrêmement sensible à la présence d'impuretés. On notera à ce sujet que l'allure du pic s'est profondément modifiée de l'essai n° 2 à l'essai n° 14.

Fusion

Comme nous supposions qu'une contamination éventuelle du plutonium par le creuset aurait lieu principalement à la fusion, nous avons réduit au minimum les enregistrements complets de la courbe d'analyse thermique.

En éliminant la valeur de T_F fournie par l'essai

n° 14 pour lequel on a observé a postériori un glissement de l'assemblage du porte-échantillon à haute température, il reste seulement trois essais valables qui donnent les valeurs suivantes:

Tableau 4. Températures de fusion du plutonium

Essais	$T_{f fusion} \ (^{\circ}{ m C})$	Teristal.
n° 2	638°6	
n° 10	641°3	641°6
n° 11	639°4	642°7

Les valeurs fournies par l'essai n° 10 sont jugées les meilleures. En effet, au cours de l'essai n° 2 les températures ont été lues directement sur l'enregistreur dont la précision ne dépasse pas 3°C. Quant à l'essai n° 11, il est évident qu'une mauvaise mise en place de la soudure du thermocouple est responsable de l'écart observé entre les températures de fusion et de cristallisation.

En définitive, nous pouvons donner, pour la température de fusion du plutonium:

$$T_F=641^{\circ}\mathrm{C}$$

l'erreur probable peut être estimée à environ 1°5C, compte tenu du petit nombre d'essais effectués.

Rappelons que les thermocouples ont été étalonnés par rapport au point de fusion de l'aluminium supposé égal à 660°0C.

Transformations au refroidissement

VOL.

1959

Pour réduire la durée des essais, les refroidissements n'ont pas été effectués à vitesse contrôlée. Le four a été coupé immédiatement après la fusion du plutonium. Il suit donc sa propre loi de refroidissement d'abord rapide jusqu'à 450°C puis pratiquement constante jusqu'à 250°C pour devenir par la suite extrêmement lente jusqu'à la température ordinaire.

Nous avons fait les observations suivantes:

—cristallisation: elle a lieu sans surfusion décelable —transformation " $\epsilon \to \delta$ ": le début est constitué par un départ brusque caractéristique d'un certain retard. En dépit de ce retard manifeste, les températures relevées sont systématiquement supérieurs, et d'une façon significative, à la température de transformation au chauffage. On trouve que T est pratiquement égale à 500°C. Nous ne voyons pas, pour l'instant d'explication possible à cette anomalie. —transformation $\delta \to \gamma$: le phénomène est complétement différent de celui que l'on a observé lors de la chauffe. La transformation débute avec un retard important (environ 100°C) et se manifeste par une succession de petits pics très aigus (Fig. 12)

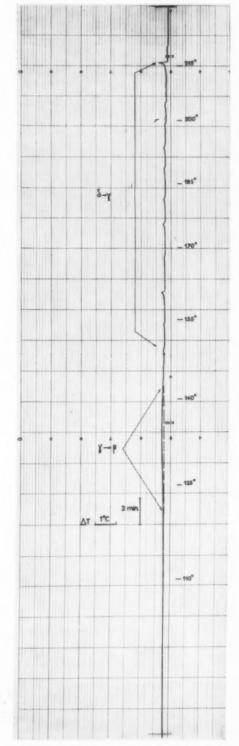


Fig. 12. Aspect des transformations $\delta \rightarrow \gamma$ et $\gamma \rightarrow \beta$ au refroidissement.

indiquant que la transformation procède par sautes successives. L'effet observé est donc le correspondant exact de celui qu'on observe en dilatométrie^(1,2) et permet de tirer les mêmes conclusions.

Les pics successifs observés sont assez comparables en nombre et en amplitude d'un essai à un autre (le premier est en général le plus important) et se poursuivent jusqu'à une température d'environ $150^{\circ}\mathrm{C}$ qui marque en même temps le début de la transformation $\gamma \to \beta$.

—transformation $\gamma \to \beta$: cette transformation est extrêmement diffuse (Fig. 12); elle peut même échapper complètement à l'examen. Il s'agit probablement d'une transformation dont la vitesse est entièrement dépendante de phénomènes de diffusion, puisque malgré l'importance du retard environ 70°), donc d'un excès d'énergie libre, sa vitesse reste faible.

Elle est pratiquement terminée à environ 130° C.—transformation $\beta \rightarrow \alpha$: comme les deux transformations précédentes, elle est caractérisée par un retard important malgré l'extrême lenteur du refroidissement du four dans la zone de température intéressante (environ 0.7° C/min). Elle a lieu vers 80° C. La fin de l'état métastable est marqué sur la courbe d'analyse thermique directe par un réchauffement brusque d'environ 3° C.

(b) Interprétation quantitative—chaleurs de transformations

La figure 9 permet immédiatement une appréciation relative de l'importance des différentes chaleurs de transformation. La courbe n° 14, qui rappelons-le, correspond au montage définitif, permet de contrôler qu'il n'y a pas de variation importante de l'écart moyen "a" tout au long de l'essai. Ceci indique qu'il en est de même du facteur $K_c\lambda_c$ et que l'on peut légitimement comparer les surfaces correspondant aux différentes chaleurs de transformation.

On remarquera que, spécialement après les transformations $\alpha \to \beta$ et $\gamma \to \delta$, la ligne de base ne reprend pas sa valeur primitive, mais une valeur inférieure. Or ces deux transformations sont précisément celles qui s'accompagnent de la plus forte expansion. Cette expansion est suffisante pour augmenter d'une façon significative les échanges thermiques et rendre compte de la diminution observée de l'écart "a".

Comme nous l'avons dit précédemment, les démontages successifs et les altérations subies par l'échantillon ont amené des modifications importantes du facteur $K_c\lambda_c$. Pour pouvoir comparer les différentes courbes entre elles nous avons procédé de la façon suivante:

La surface représentative de la transition " $\delta \to \epsilon$ " étant prise comme unité, on exprime en unités relatives les surfaces, ou, ce qui revient au même, les effets thermiques, correspondant aux autres transitions. Ceci permet de mettre tous les résultats à la même échelle que la courbe n° 2. Cette courbe est en effet celle pour laquelle la géométrie de l'échantillon est comparableaux étalons. Les surfaces moyennes ainsi obtenues sont converties directement en calories grâce à la correspondance obtenue au cours de l'étalonnage.

La chaleur de fusion du plomb, prise égale à 5,9 cal/g étant choisie comme étalon, on obtient finalement pour les différentes chaleurs de transformation, compte tenu des densités des diverses phases:

Tableau 5. Chalcurs obtenues pour les différentes transformations du Pu.

$\alpha \rightarrow \beta$	+1200 cal/mole	5,2 cal/g
$\beta \rightarrow \gamma$	+140	0,58
$\gamma \rightarrow \delta$	+130	0,54
$\delta \rightarrow \delta'$	< +40*	< 0.18*
"d $\rightarrow \varepsilon$ "	+380	1,6
T :	+480	1 2,0
$\varepsilon \to \text{Liq}$.	530†	2,2†

* En admettant raisonnablement que la chaleur de transformation $\delta \to \delta'$ est au plus égale au 1/3 de la plus petite chaleur de transformation mesurée.

19

 \dagger En prenant comme étalon, la chaleur de fusion de l'aluminium (90 cal/g), dont la température de fusion est voisine de celle du plutonium.

Seules sont publiées actuellement quelques mesures relatives à la transformation $\alpha \rightarrow \beta$.

Une première valeur de 925 cal, obtenue par Sandenaw et Gibney⁽⁴⁾ par une méthode calorimétrique est en bon accord avec celle que l'on peut déduire des courbes T=f(p) par application de la loi de Clapeyron–Clausius. Schonfeld⁽⁴⁾ obtient ainsi une chaleur de transformation de 985 cal.

Récemment, Dempsey et Kay, $^{(5)}$ en mesurant la vitesse d'échauffement sous l'effet de son rayonnement propre d'un échantillon de plutonium, et ceci dans des conditions adiabatiques, obtiennent pour $Q_{\alpha\beta}$ une valeur de 1,2 kcal. La méthode utilisée, qui réalise en fait un compromis entre la calorimétrie classique et l'analyse thermique différentielle est certainement plus directe que celle que nous avons employée. Cependant les auteurs n'accordent à leurs mesures qu'une précision de 20 pour cent environ, soit à peu près la même que celle que nous avons attribuée à nos propres mesures.

Les chaleurs de transformation ainsi trouvées, qui rappelons-le, ne prétendent pas à une grande précision,

permettent cependant de tirer quelques conclusions utiles:

—la transition $\alpha \rightarrow \beta$, fortement endothermique et accompagnée d'une grande expansion, correspond à un profond bouleversement structural, certainement plus important que celui que l'on observe dans le cas de la transition $\alpha \rightarrow \beta$ de l'uranium. Dans ce dernier cas Q n'est que de 674 cal, (6) et l'expansion est faible. Or Tucker (7) a montré que les structures U_{α} (8) et U_{β} quoiqu'apparemment très différentes peuvent se déduire l'une de l'autre par de faibles déplacements atomiques et que, surtout, on trouve dans les deux structures des distances interatomiques anormalement courtes, indices de liaisons covalentes.

Ceci nous conduit plutôt à rapprocher $Pu_{\alpha} \rightarrow Pu_{\beta}$ de $U_{\beta} \rightarrow U_{\gamma}$ pour laquelle Q=1134 cal⁽⁶⁾ et suggère que le fort effet thermique observé soit du à la rupture des liaisons à caractère covalent que l'on sait exister dans Pu_{α} .⁽⁹⁾

—les chaleurs de transformations $Q_{\beta \to \gamma}$, $Q_{\gamma \to \delta}$ et $Q_{a_{\delta \to \epsilon}n}$, sont de l'ordre de ce qu'on peut attendre pour des transitions de phases métalliques. $Q_{\beta \to \gamma}$ et $Q_{\gamma \to \delta}$, toutes deux spécialement faibles, suggèrent que les phases β et γ puissent être raccordées sans modifications profondes à la phase δ qui est la première phase réellement métallique que l'on rencontre au cours des transitions successives du plutonium. Ceci indique qu'il est peu probable que des liaisons covalentes puissent subsister dans Pu_{β} , quelle que puisse être par ailleurs la complexité de cette structure.

1959

- —Ellinger⁽³⁾ a montré que δ' (tétragonal centré) pouvait se déduire de δ (cubique à faces centrées) au prix d'une légère contraction suivant l'axe c. L'étroite parenté des deux structures explique la valeur très faible trouvée pour la chaleur de transition.
- —On peut constater qu'il existe en réalité entre δ' et ϵ , qui sont toutes deux des phases métalliques classiques, une différence d'énergie interne notablement plus grande qu'entre les phases β , γ et γ , δ .
- —On ne peut manquer d'être frappé par la valeur extrêmement faible de la chaleur de fusion. A la limite supérieure des erreurs possibles, nous croyons pouvoir affirmer qu'elle est en tout cas inférieure à 800 cal/mole, alors qu'on s'attendrait à trouver une valeur de l'ordre de RT_F , soit environ 2000 cal.

Nous avons cherché à confirmer cette valeur en examinant les quelques diagrammes d'alliages à base de plutonium déjà publiés.

On sait en effet que des considérations thermodynamiques permettent de relier les pentes du solidus et du liquidus au voisinage du corps pur:

$$Q_F/RT_F = T_F(C_L-C_{\it s})/(T_F-T)$$

- $-Q_F$ chaleur de fusion
- $-T_F$ temp. de fusion
- $-C_L$, C_s concentrations de l'impureté dans le liquidus et dans le solidus en équilibre à la température T.

Les diagrammes établis à Los Alamos donnent pour Q_E/RT les valeurs suivantes:

Mais c'est surtout le diagramme Pu–Fe récemment publié $^{(10)}$ établi avec un soin particulier dans la région riche en plutonium, qui peut fournir une confirmation valable. Dans ce cas pour $T=873^{\circ}~873^{\circ}{\rm K}~(T-T_F=40^{\circ}{\rm C})~C_L-C_s=1.3\times10^{-2}$ ce qui donne :

$$Q/RT = 0.30$$
 et $Q = 550$ cal

valeur en accord remarquable avec celle que nous avons déterminée.

Il parait donc bien confirmé que la chaleur de fusion du plutonium est anormalement faible.

On calculerait de même pour la transition $\delta' \to \epsilon$ une chaleur latente de 330 cal. Là encore, l'accord est excellent.

Cette faible chaleur latente trouverait son origine dans une étroite analogie entre les phases liquide et solide, analogie suggérée par la variation quasi nulle de densité à la fusion.

$$d = 16.51 \text{ g/cm}^3 \text{ à } 500^{\circ}\text{C}^{(11)}$$

$$d_T + 16.5 \text{ g/cm}^3 \text{ à } 665^{\circ}\text{C}^{(12)}$$

Si pour terminer, nous comparons les résultats obtenus par analyse thermique différentielle à ceux que fournissent l'analyse dilatométrique, nous constatons qu'à une forte expansion ne correspond pas nécessairement un fort effet thermique. Ceci est surtout flagrant pour la transformation $\gamma \to \delta$ qui pour une expansion totale comparable à celle de la transformation $\alpha \to \beta$ met en jeu une chaleur latente 10 fois moins élevée.

Sur le diagramme dilatométrique, l'écart ΔT relevé entre les témpératures finales et initiales d'une transformation, est en réalité l'écart de température du barreau de référence aux mêmes instants; il est donc comparable à l'écart $\Theta_B - \Theta_A$ que nous

enregistrons en analyse thermique (c'est-à-dire approximativement proportionnel à \sqrt{Q}). Ceci rend compte de l'allure pratiquement verticale de la transition $\gamma \rightarrow \delta$ sur les courbes dilatométriques. En contre, il faudrait également tenir compte des vitesses de transformations, mais cette réserve faite, on peut relier qualitativement les résultats obtenus par les deux méthodes.

REFERENCES

- 1. R. ABRAMSON, Etude Dilatométrique du Plutonium (communication présentée à la Conférence sur la Métallurgie du Plutonium, Chicago, 3-4 Nov. 1957).
- 2. R. Abramson, R. Boucher et al., Quelques Propriétés du Plutonium et de l'Alliage Aluminium-Plutonium (Seconde Conférence Internationale pour l'Utilisation Pacifique de l'Energie Nucléaire) A paraître.

 3. F. H. ELLINGER, J. Metals, 1256 (Octobre 1956).

 4. H. M. FINNISTON et J. P. HOWE, Metallurgy and Fuels

- 384.
 E. Dempsey et A. E. Kay, J. Inst. Met. 86, 379 (1957–58).
 D. C. Ginnings et R. J. Corruccini, J. Res. Nat. Bur. Stand. 39, 309 (1947).
- 7. Tucker et Senio, Acta Cryst. 6, 753 (1953).
- Jacob et Warren, J. Amer. Chem. Soc. 59, 2588 (1937). 9. W. H. Zachariasen et F. Ellinger, J. Chem. Phys. 811 (Sept. 1957).
- 10. P. G. MARDON, H. R. HAINES, J. H. PEARCE et M. B.
- Waldron, J. Inst. Met. 86, 166 (1957–58). 11. E. R. Jette, J. Chem. Phys. 23, (2), 365–368 (Fév. 1955).
- 12. A. Allen Comstock, Measurement of Plutonium Liquid Density, U.S.A.E.C. LA. 1348 (21 janvier 1952).

ABSOLUTE INTERFACIAL ENERGIES OF [001] TILT AND TWIST GRAIN BOUNDARIES IN COPPER*

N. A. GJOSTEIN† and F. N. RHINES;

The absolute interfacial energies of [001] tilt and twist boundaries in copper have been determined, by using a Zeiss Interference Microscope to measure the dihedral angles which form during the thermal grooving process. An analysis of the results obtained for small angle, lineage boundaries, in terms of the appropriate dislocation model, shows that the Read-Shockley equation predicts the energy up to misorientations of 5 to 6°, but that for larger misorientations, it gives much too small an energy. It is shown also that van der Merwe's treatment, which avoids some of the limitations present in the Read-Shockley derivation, is capable of predicting the energy up to misorientations of 8 to 9°. Moreover, from the analysis presented herein, it is possible to offer an explanation for the apparent agreement that was obtained, at large misorientations (25 to 30°), between the previous measurements of relative grain boundary energies and the Read-Shockley equation.

The large angle grain boundary is characterized by a broad maximum in energy that shows no energy cusps, for either tilt or twist boundaries. Both types of boundaries have nearly the same energy for misorientations less than 18°, but for the range of misorientations, over which there is a maximum in energy, twist boundaries have a lower energy by about 130 ergs/cm². An attempt to explain this difference from the results obtained from a calculation made on an atomic basis is discussed.

ENERGIES ABSOLUES d'INTERFACE DES JOINTS DE TORSION ET DE FLEXION [001] DU CUIVRE

Les énergies absolues d'interface des joints de torsion et de flexion [001] du cuivre sont déterminées au microscope interférentiel Zeiss, par la mesure des angles dièdres qui apparaissent au cours du mécanisme d'entaille thermique. L'analyse des résultats obtenus pour des joints à faible angle, compte tenu du modèle de dislocation approprié, montre que l'équation de Read-Shockley prévoit correctement l'énergie jusqu'à des divergences d'orientation de 5-6°, mais qu'au-delà elle conduit à une énergie trop faible. Cette analyse montre également que la méthode de Van der Merwe, qui évite certaines limitations de l'équation de Read-Shockley, permet de prévoir l'énergie jusqu'à des divergences d'orientation de 8-9°. En outre, la discussion des résultats obtenus ici, permet d'avancer une explication de l'accord apparent obtenu pour de grandes divergences (25-30°), entre les mesures obtenues précédemment et l'équation de Read-Shockley, dans le calcul des énergies relatives des joints.

Le joint à grand angle, qu'il soit de flexion ou de torsion, est caractérisé par un large maximum énergétique. Les deux types de joint ont pratiquement la même énergie pour des divergences d'orientation inférieures à 18°, mais pour les angles auxquels correspond un maximum énergétique, les joints de torsion ont une énergie moindre de 130 ergs/cm² environ. Les auteurs discutent alors, sur la base de leurs résultats, d'une tentative d'explication de cette différence, par un calcul qui s'appuie sur une base atomique.

ABSOLUTE GRENZFLACHENENERGIEN DER [100] NEIGUNGS. UND VERDREHUNGSKORNGRENZEN VON KUPFER

Die absoluten Grenzflächenenergien der [100] Neigungs- und Verdrehungskorngrenzen von Kupfer wurden bestimmt unter Verwendung eines Zeiss Interferenz-Mikroskops zur Messung der Diederwinkel, die sich beim thermischen Furchungsvorgang ausbilden. Eine Analyse der Ergebnisse an Kleinwinkel-Verzweigungsstrukturgrenzen auf Grund des angemessenen Versetzungmodells zeigt, dass die Read-Shockley-Gleichung die Energie bis zu Orientierungsunterschieden von 5 bis 6° voraussagt, sie gibt jedoch für grössere Oreintierungsunterschiede eine zu kleine Energie. Zudem wird gezeigt, dass die Behandlung van der Merwes, die einige Beschränkungen der Read-Shockleyschen Ableitung vermeidet, die Energie bis zu Orientierungsunterschieden von 8 bis 9° voraussagen kann. Weiterhin ist es durch die hier gegebene Analyse möglich eine Erklärung für die anscheinende Übereinstimmung zu bieten, die grossen Orientierungsunterschieden (25 bis 30°) zwischen früheren Messungen der relativen Korngrenzenergien und der Read-Shockley-Gleichung erhalten wurde.

Die Grosswinkelhorngrenze wird durch ein breites Energiemaximum charakterisiert, das weder für Neigungs- noch für Verdrehungskorngrenzen Energiespitzen aufweist. Beide Typen von Korngrenzen haben für Orientierungsunterschiede unterhalb 18° beinahe dieselbe Energie, doch im Bereich der Orientierungsunterschiede, in dem ein Maximum der Energie auftritt, haben die Verdrehungskorngrenzen eine um etwa 130 erg/cm² geringere Energie. Es wird ein Versuch erörtert diese Unterschiede aus den Ergebnissen einer atomistischen Berechnung zu erklären.

^{*} Abstracted from a thesis presented by the Aluminum Company of America Fellow, N. A. Gjostein, to the Faculty of the School of Engineering and Science, Carnegie Institute of Technology, in partial fulfillment of the requirements for the Degree of Doctor of Philosophy in Metallurgical Engineering, Received July 24, 1958.

Research and Development Laboratory, Thompson Ramo Wooldridge, Inc., Cleveland, Ohio. Department of Metallurgical Engineering, Carnegie Institute of Technology, Pittsburgh, Penna.

1. INTRODUCTION

From measurements of the absolute interfacial energies of small angle boundaries, it is possible to provide a rigorous test of the dislocation model of the grain boundary, for in this case the experimental energy-angle relationship may be compared quantitatively with the predicted relationships, which have been derived by Read and Shockley(1) and van der Merwe. (2) It is expected that the Read-Shockley treatment, which is based on linear elasticity theory, will be valid only when the spacing of the dislocations D is considerably larger than D_L , the diameter of a cylindrical surface, surrounding the dislocation line, which encloses material experiencing non-Hookean strains (D_L might be defined also as a dislocation width). Subject to this limitation Read and Shockley found that the interfacial energy E of an array of dislocations varies with the relative rotation θ between the crystals, according to the expression

$$E = E_0 \theta (A - \ln \theta) \tag{1}$$

where E_0 is a parameter which can be evaluated independently from known constants of the material and A is related directly to the core energy of the dislocation, i.e. the energy residing within the cylinder of diameter D_L .

When measurements of relative grain boundary energies $^{(3-7)}$ were compared with the Read–Shockley equation, it was found that equation (1) appeared to fit (qualitatively) the form of experimental E vs. θ curves up to large values of θ (25 to 30°), indicating that the dislocation widths in these materials were unusually small, i.e. $D_L \cong b$, where b is the magnitude of the Burger's vector \mathbf{b} . Concerning this anomaly, Lomer and Nye $^{(10)}$ have commented that it seems unreasonable for the dislocations to be so narrow, and Read $^{(8)}$ and Brooks $^{(9)}$ have indicated that the agreement at large angles is probably due to a fortuitous cancellation of errors in the derivation.

Further insight into this problem can be obtained from the following considerations. To compare the relative energy measurements with equation (1) it was necessary to fit the calculated curve to the large angle data; the result of this was that only the form of the energy–angle relationship was tested. It was not possible to determine whether the Read–Shockley equation gave the correct absolute magnitude of the grain boundary energy, for example, by obtaining an experimental value for E_0 at small angles, and comparing it with the proper theoretical value. It seems possible, therefore, that the values of the parameters used to fit the calculated curve to the large angle relative energy values may not have any theoretical

significance. An ambiguity of this sort can be avoided when absolute energies are measured, since in this case E_0 , which is obtained from a plot of E/θ vs. $\ln \theta$, can be compared with the value derived from the appropriate dislocation model. Absolute energies of tilt boundaries in silver⁽¹¹⁾ and zinc⁽¹²⁾ have been measured but in neither case was it possible to determine E_0 at small angles.

With the recent advances (13) in interference microscopy, it was felt that it would be feasible to determine the absolute energies of [001] tilt and twist boundaries in copper from measurements of dihedral angles formed by the thermal grooving process. (11,14) It was considered important to extend the measurements over as wide a range of θ as possible, with particular emphasis on small values of θ , and other discrete large values of θ , where energy cusps might be expected to occur. In addition, considerable attention was paid to the effect of boundary orientation on its energy. From these measurements, it was thought that it would be possible to draw conclusions, concerning the structures of both small and large angle boundaries, the latter type being particularly interesting in view of the possibility of calculating their energies on an atomic basis.(15,16)

2. EXPERIMENTAL PROCEDURE

19

2.1 Preparation of specimens

Cathode sheet copper, having a purity of 99.98 per cent Cu, was used to prepare from the melt(5) bierystals, containing [001] tilt and twist boundaries. Both types of bicrystals were prepared from seeds having a cube direction within 0.5° of their longitudinal axes. Thus, each pair of crystals had in common a cube direction, about which they were rotated with respect to each other by the angle θ . Tilt boundaries in the range $5^{\circ} < \theta < 78^{\circ}$ were symmetrical, i.e. the plane of the boundary made an angle $\theta/2$ with the [010] direction of either crystal. It was possible to extend the energy measurements to $\theta \simeq 0.6^{\circ}$ by making use of the lineage boundaries formed during the growth of most of the bicrystals. The lineage boundaries were asymmetric tilt boundaries, whose twist component rarely exceeded 0.2°. The asymmetry angle ϕ , i.e. the angle between the mean of [010] directions of the crystals and boundary plane varied from 0 to 28°.

In order to insure that the axis of relative rotation was within 1.0° of the [001] direction, and that the magnitude of the rotation θ could be predetermined with the same accuracy, the necessary seeding operations were done mechanically by means of a special type of goniometer.⁽¹⁷⁾ For the lineage

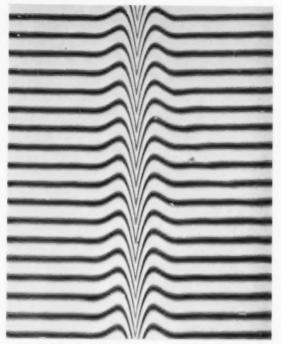


Fig. 1a. Interferogram showing the perpendicular-type fringe pattern of a thermal groove which formed at a 32° symmetrical [001] tilt boundary; the plane of the surface shown is parallel to the common [001] direction and normal to the grain boundary; contour interval, $0.27~\mu$; \times 762.

1959

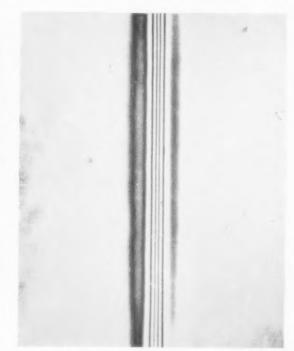


Fig. 1b. Interferogram showing the parallel-type fringe pattern of a thermal groove formed at a 37° symmetrical [001] tilt boundary; the plane of the surface shown is parallel to the common [001] direction and normal to the grain boundary; contour interval, $0.27\mu; \times 762$.

boundaries, θ was measured to $\pm 0.2^{\circ}$ by superimposing the Laue spots from each crystal on a single film. With some modification⁽¹⁷⁾ this method was used to measure θ for the large angle boundaries; the value obtained in this way was usually within 1.0° of the predetermined misorientation.

The bicrystals, which had a rectangular cross section $(\frac{3}{16} \text{ in.} \times 1 \text{ in.})$, were sectioned in a plane normal to the growth axis, and were deeply etched. Both the as-cast (top) surface and the cut surface were mechanically polished, and then electropolished (18) to prepare them for the thermal grooving treatment. In order to avoid the formation of facets on the surface, and to obtain reproducible dihedral angles, it was found necessary to anneal the specimens in a purified hydrogen atmosphere (passed through a Deoxo unit, and over copper turnings at 650°C). During this treatment, the specimens were supported in recrystallized alumina crucibles, surrounded by copper foil. The specimens were annealed for 37 hr at 1065°C; the shape of the thermal groove profile after annealing under these conditions is shown in Fig. 1a.

2.2 Measurement of dihedral angles

Dihedral angles were measured by the use of a Zeiss Interference Microscope. This instrument utilizes the Linnik interference system, (19) and is particularly well suited for large wedge angle interference. A discussion of the Linnik system, and its limitations with respect to measuring dihedral angles of thermal grooves has been given by Mykura. (13)

It is convenient to determine the dihedral angle from either perpendicular or parallel fringe patterns, Figs. 1a and 1b, respectively. Amelinckx⁽²⁰⁾ has shown that, for the perpendicular fringe pattern, the angle α , that one side of the groove makes with the vertical, is related to the corresponding fringe angle η by the relation

$$\tan \alpha = \frac{2L}{\lambda m} \tan \eta \tag{2}$$

where L is the fringe spacing, λ the wavelength of the light source, and m is the linear magnification. The errors involved in measuring η from enlarged photographs and the related errors in α have been discussed by Gjostein. This method is versatile, and can be used for either high or low energy boundaries. To give some idea of the magnitudes of α and η , it may be said that as α varied from 89°30′ to 80°0′, η varied from 50 to 10°.

Hilliard⁽²¹⁾ has suggested a method of determining α by plotting a profile from the parallel fringe pattern,

VO:

Fig. 1b. In this investigation it was found that this method could be applied only to grooves having a depth of greater than $0.5~\mu$, i.e. for high energy boundaries. Therefore, the majority of the measurements were made by using the first method, but, for some high energy boundaries, both techniques were used. Both methods give an over-estimate of α due to the obliquity effect, reported by Tolmon and Wood, for interference microscopes using convergent illumination. This results in an apparent decrease of about 10 per cent in the grain boundary energy. (17) Accordingly, all energy values reported herein have been increased by 10 per cent to compensate for this effect

3. RESULTS

During the course of this investigation, a variety of groove profiles was observed. It was found, however, that only the normal-type profile, having the characteristics shown in Fig. 1a, gave reproducible values of α . In Appendix I, evidence is presented which indicates that it is permissible to neglect the orientation dependent terms of Herring's general equation for interfacial equilibrium, (23,24) provided that the measurements of α are taken from normal profiles. Under these conditions, the grain boundary surface tension* γ_G may be calculated from the equation

$$\gamma_G = 2\gamma_S \cos \frac{\alpha + \beta}{2} \tag{3}$$

where α and β are the angles that each side of the groove makes with the vertical† and γ_S is the average surface tension of the free surface; the ratio γ_G/γ_S has been calculated from equation (2) and corrected by 10 per cent as indicated previously.

Tables 1 and 2 give the values of $\alpha + \beta$ obtained for [001] tilt and twist boundaries at $1065C_+^+$ from perpendicular fringe patterns, along with corrected ratios of γ_G/γ_S . Each value of $\alpha + \beta$ represents an average taken from 15 to 20 fringes. In many cases, the specimen was repolished and completely retreated to produce a new groove which was measured using 15 to 20 fringes. It was found that γ_G/γ_S was reproducible to within ± 10 per cent for most boundaries.

 \dagger The plane of the grain boundary was always within 2° of being normal to the free surface.

Table 1. Dihedral angles and ratio γ_g/γ_s for tilt boundaries at 1065°C .

9 (deg)	$\alpha + \beta$	Yg/Ys*
0.65	178°2′	0.038
0.7	177°42′	0.044
0.75	177°36′	0.047
0.85	177°32′	0.048
0.9	177°22′	0.051
1.3	176°40′	0.064
1.3	177°18′	0.052
1.5	176°36′	0.066
1.7	175°40′	0.084
3.0	174°54′	0.099
3.0	175°8′	0.094
5.5	173°4′	0.135
5.8	172°36′	0.144
9.0	169°36′	0.202
12.0	168°32′	0.222
16.0	164°54′	0.294
19.0	164°32′	0.300
22.0	163°8′	0.328
26.0	$162^{\circ}28'$	0.339
28.0	162°34′	0.338
32.0	161°38′	0.356
37.0	160°48′	0.350
40.0	160°42′	0.374
45.0	161°14′	0.362
53.0	161°56′	0.353
65.0	$163^{\circ}20'$	0.322
78.0	168°48′	0.217

^{*} Corrected for obliquity effect reported by Tolmon and Wood. $\ensuremath{^{(22)}}$

4. ANALYSIS OF RESULTS

Equation (1) can be used to represent the energy data by placing it in the form

$$R\gamma = R_0 \theta (A - \ln \theta) \tag{4}$$

where $R_{\gamma}=E/\gamma_S=\gamma_G/\gamma_S$, and $R_0=E_0/\gamma_S$. Plots of R_{γ}/θ vs. $\ln\theta$ for [001] tilt and twist boundaries are shown in Figs. 2 and 3, respectively. It can be seen

Table 2. Dihedral angles and ratio γ_g/γ_g for twist boundaries at 1065°C

θ (deg)	$\alpha + \beta$	$\gamma_{G}/\gamma_{S}^{-4}$
3.2	176°44′	0.063
3.8	175°28′	0.088
5.0	174°6′	0.115
6.0	173°2′	0.136
9.0	170°44′	0.180
10.0	170°12′	0.190
13.0	168°48′	0.218
15.0	168°0′	0.234
17.0	167°36′	0.240
23.0	166°36′	0.261
30.0	164°52′	0.293
35.0	164°8′	0.308
37.0	165°24′	0.282
40.0	164°4′	0.307
43.0	165°56′	0.295
45.0	164°52′	0.293

^{*} Corrected for the obliquity effect reported by Tolmon and

^{*} The definition of "surface tension" used here is that given by Herring⁽²⁴⁾ and should not be taken to mean "surface stress".

 $[\]mathring{+}$ There is a measurable temperature coefficient for γ_g in the case of large angle boundaries, but this effect does not influence the conclusions stated herein.

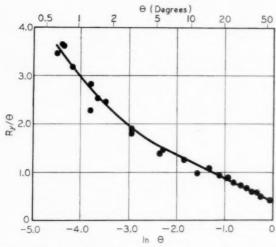


Fig. 2. Plot of R_2/θ vs. ln θ for [001] tilt boundaries at 1065°C.

that the data for tilt boundaries, Fig. 2, cannot be represented by one straight line, and that the slope $(-R_0)$ increases (negatively) as θ decreases. For purposes of analysis, the results were divided into two overlapping ranges, $0.6^{\circ} < \theta < 12^{\circ}$ and $3^{\circ} < \theta < 45^{\circ}$. Then, using the method of least squares, $^{(25)}$ linear regression lines were determined for each range of θ . From the slopes and the intercepts of the regression lines, it was possible to determine the small and large angle values for R_0 and A; these are given in Table 3.

VOL.

1959

In view of the results obtained for tilt boundaries, it was expected that a plot of R_{γ}/θ vs. $\ln \theta$ for twist boundaries also would show a change in slope at small

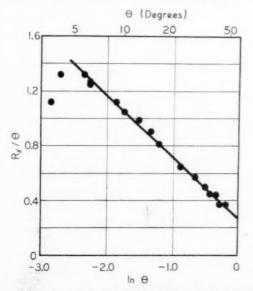


Fig. 3. Plot of R_{γ}/θ vs. $\ln \theta$ for [001] twist boundaries at 1065°C.

Table 3. Parameters R_0 and A as determined from $R\gamma/\theta$ vs. $\ln \theta$ plots

R_{0}	A	θ_{\max} * (deg)	Range of θ
[001] Tilt series- 0.91 + 0.05	-1065°C -0.72	10	$0.6 < \theta < 12$
	+0.71	43	$0.6 < \theta < 12$ $3 < \theta < 53$
[001] Twist serie			
0.46	0.54	36	$5 < \theta < 45$

^{*} Calculated from $A=1+\ln\,\theta_{
m max}$. (8)

values of θ . Unfortunately, it was not possible to obtain any energy data for $\theta < 3^{\circ}$ in this series and therefore it is not clear whether twist boundaries present the same effect, Fig. 3. The large angle values of R_0 and A for twist boundaries are given in Table 3.

Energy vs. θ curves, which were calculated from equation (4), using the large angle parameters, are shown in Figs. 4 and 5 with the experimental point superimposed. These curves have no theoretical significance, as will be seen in the next section, but they can be used as an empirical representation of the energy data over a wide range of θ . On these plots, in addition to the dimensionless ratio γ_G/γ_S , absolute values of γ_G are reported. For this purpose, γ_S was taken to be 1670 ergs/cm². According to Fisher and Dunn⁽²⁶⁾, the most reliable value of γ_S for copper is 1430 ergs/cm² in the range 950°C to 1050°C, as determined by Udin et al.(27) It has been pointed out, (28,29) however, that Udin et al. neglected the effect of transverse grain boundaries in computing γ_s . Taking the number of grains per unit length along the wire to be $80^{(29)}$ and $\gamma_G/\gamma_S = 0.37$, it can be shown that a more probable average value for γ_s is 1670 ergs/cm².

The calculated curve for the [001] tilt series has a maximum at $\theta=43^\circ$. Beyond $\theta=43^\circ$ the calculated curve would begin to decrease; therefore, in this region the curve has been drawn to fit the points, the dashed line indicating uncertainty in the data. The calculated curve which best fits the twist boundary series has a maximum at $\theta=36^\circ$, but the experimental points could as well fit a curve with a maximum at $\theta=45^\circ$. There is no need to extend the measurements beyond 45° because the energy-angle relationship for an [001] twist boundary series must be symmetrical about this value. The difference in the energy between tilt and twist boundaries is not very large until θ exceeds about 18° , where the tilt series has a higher energy, by some $130~\rm ergs/cm^2$.

It is important to mention here that no abnormal scatter, i.e. greater than ± 10 per cent, was observed

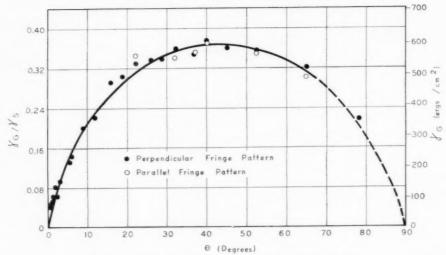


Fig. 4. Dependence of grain boundary energy on misorientation for [001] tilt boundaries at 1065°C. Solid line represents the curve calculated from equation (1), using the large angle parameters. Although the curve has no theoretical significance it can be used as an empirical representation of the energy data over the range $5^{\circ} < \theta < 43^{\circ}$. Beyond 43° , the curve has been drawn to fit the experimental points.

at $\theta=37^\circ$ (310) and $\theta=53^\circ$ (210), the presumed major energy cusp positions of the [001] tilt series. Since for each critical angle three different bicrystals were measured, the probability that the cusp has escaped detection is small. Moreover, no energy cusp was detected at 37° in the [001] twist series.

No effect of the orientation of the boundary upon its energy was found for large angle boundaries, including those near energy cusp positions.

5. DISCUSSION

5.1. Comparison of dislocation theory with absolute energies of small angle tilt boundaries

To provide a rigorous test for the Read-Shockley equation, it is necessary to compare the experimental values of the parameters E_0 and A with those derived from dislocation theory. Read and Shockley⁽³⁰⁾ have made use of Frank's formula⁽³¹⁾ to determine the dislocation content of an [001] tilt boundary in a face centered cubic lattice, and they find that there are two possible dislocation models. Model one consists of two sets of edge dislocations, having Burger's vectors

$$\mathbf{b}_1 = \frac{\sqrt{2}}{2} \, b \, [110] \quad \text{and} \quad \mathbf{b}_2 = \frac{\sqrt{2}}{2} \, b \, [1\overline{1}0].$$

For this model E_0 is given by

$$E_{0} = \frac{\cos \phi' + \sin \phi'}{4\pi} b \left(C_{11} + C_{12}\right) \times \sqrt{\frac{C_{44}(C_{11} - C_{12})}{C_{11}(C_{11} + C_{12} + 2C_{44})}}$$
 (5)

where $\phi'=\phi\pm45^\circ$ refers to the axes [110] and [110], the sign of 45° being chosen so that ϕ' and ϕ lie between 0 and 90°, and c_{11} , etc. are the elastic constants of the material. In the second model, four sets of of dislocations are needed; each set has equal edge and screw components. For copper, however, E_0 , calculated from this model, is higher than for the first one (31) and therefore, this model need not be considered further, since in a well-annealed specimen, the lowest energy configuration should obtain.

19

Table 4 gives the comparison between experimental and theoretical values of E_0 . The theoretical E_0 was computed from equation (5), using the room

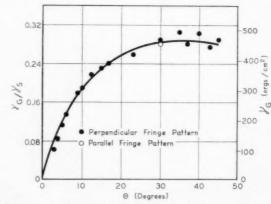


Fig. 5. Dependence of grain boundary energy on misorientation for [001] twist boundaries at 1065°C. The curve was calculated from equation (1), using the large angle parameters, and therefore it has no theoretical significance, but it can be used to represent the experimental points.

Table 4. Comparison of theoretical and experimental E_0 for [001] tilt boundaries

$E_0({ m ergs/cm^2})$	Method of determination
1550	Equation (5), with $\phi'=45^{\circ}$
$1480 \\ 1520 \pm 100$	Equation (6) Experimental value;* small angle boundaries
820 ± 15	Experimental value; * large angle boundaries

* Computed from appropriate R_0 in Table 3, using $\gamma_s = 1670 \text{ ergs/cm}^2$.

temperature elastic constants for copper, (32) reduced 15 per cent for temperature. (30) Two theoretical values of E_0 are given; one refers to $\phi'=45^\circ$ (θ was measured between the [100] directions) and the other is an average value \bar{E}_0 determined from the relation

$$\tilde{E}_0 = \frac{E_0(0)}{0.15 \,\pi} \int_{17^{\circ}}^{45^{\circ}} E_0(\phi') \, d\phi' = 1.35 \, E_0(0) \quad (6)$$

The averaging of E_0 was done because for $\theta < 5^{\circ}$ measurements were made on boundaries having a range of asymmetry from 45° to 17° .

Examination of the values listed in Table 4 reveals that the small angle E_0 agrees reasonably well with theory, considering the uncertainties involved in selecting the proper temperature coefficient for the elastic constants and in selecting the correct value for γ_S . It is an important point to note that the small angle value for E_0 agrees more closely with theory than does the large angle one, which differs by a factor of about 1.8.

1959

Experimental values for A also may be compared with dislocation theory. Read and Shockley⁽¹⁾ have shown that A can be expressed in terms of a non-Hookean energy $E_{\rm I}$ which resides inside a circle of radius $r_L = D_L/2$, and an elastic energy $E'_{\rm II}$, which depends on the unknown boundary conditions at r_L . They show that the unknowns r_L , $E_{\rm I}$ and $E'_{\rm II}$, can be represented by a single parameter $r_0 < r_L$, in which case

$$A_0 = 1 + \ln \frac{b}{2\pi \, r_0} \tag{7}$$

where A_0 refers to $\phi'=0$ or 90° . To evaluate r_0/b , it is necessary to make some assumption, concerning the stress–strain relationship for $r < r_L$. Nabarro⁽³³⁾, using the sinusoidal approximation of Peierls⁽³⁴⁾, has determined the energy associated with each edge dislocation of an interacting pair, and he shows that the same energy can be obtained from elasticity theory, if the integration is cut off at a radius

$$r_0 = \frac{b}{e(1-\sigma)} \tag{8}$$

where ϵ is the Naperian base and σ is Poisson's ratio.

Foreman, Jaswon and Wood⁽³⁵⁾ have considered more realistic force laws for the center of a dislocation from which Lomer⁽³³⁾ has obtained the energy per unit length of an edge dislocation in terms of a parameter a_0 which has the value of approximately four for copper. In this case, $\ln r_0/b$ can be expressed as

$$\ln r_0/b = \ln \frac{a_0}{1-\sigma} - 1 - \left[\frac{a_0 - 1}{2a_0}\right]^2. \tag{9}$$

Koehler (36), Brooks (9), and van der Merwe (2) also have given formulae for r_0 . Koehler's method, however, contains errors (33) and Brooks has assumed that the Read–Shockley equation is valid at large θ ; therefore, neither of these methods will be discussed. Van der Merwe's treatment will be considered below.

Table 5 lists the theoretical values of A_0 . These were derived from equation (7) using values of r_0/b obtained from equations (8) and (9). Experimental values of A_0 are listed in addition.

Although the theoretical treatment for A_0 is not as rigorous as that for E_0 , the fact that the small angle A_0 lies between the two best theoretical determinations is considered to be significant.

From the discussion that has preceded, it is clear that the energy of a dislocation boundary, according to the treatment of Read and Shockley, agrees with the measured energy only when θ is small. This fact can be demonstrated rather effectively by comparing the small angle experimental data with the theoretical E vs. θ curves, Fig. 6. Two Read–Shockley curves are shown. One was calculated from equation 1, using the small angle parameters (i.e. essentially the theoretical parameters), while the other one represents an empirical curve fitted to the large angle data. The theoretical curve fits the data very well up to about 5° to 6°. At larger angles it begins to deviate and shows much too small an energy at the theoretical maximum.

Nabarro⁽³³⁾ points out that the Read–Shockley formula was derived by integrating the elastic energy density from the core radius r_0 to a distance of the order $b/2\theta$, where the stress fields of the adjacent

Table 5. Comparison of theory with experiment for the parameter A.

A_0	Method of determination
-0.23	Theoretical; equations (7) and (8)
-1.50	Theoretical; equations (7) and (9)
-0.57 to -0.76	Experimental; * small angle value
0.86	Experimental; large angle value

^{*} Since A varies with ϕ' , (8) it was necessary to report a range of values for A_0 , corresponding to $\phi' = 45^{\circ}$ to 17°.

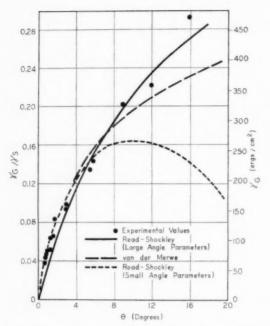


Fig. 6. Comparison of the energies of small angle, lineage boundaries with those predicted by the formulae of Read and Shockley⁽¹⁾ and van der Merwe.⁽²⁾

dislocations have equal importance. It is expected that this approximation will become invalid when $b/2\theta = r_L$ since at this point the greater part of the strain energy resides in regions near the dislocation cores, where the stress-strain relationship is non-linear. An estimate of r_L can be obtained from the treatment of dislocation widths given by Foreman $et~al.^{(35)}$ For $a_0=4$ (copper), Hooke's law becomes invalid at a distance (along the slip plane) of about 4.7b (see Figs. 2 and 3 in reference (35)). Assuming that this distance approximates r_L , it can be seen that it is comparable to the point at which the Read–Shockley curve begins to deviate appreciably from the experimental curve, i.e. at $\theta=5$ to 6° or equivalently D/2=5b.

As θ increases the higher order terms of the elastic stress field become important. Brooks has summed these terms, and he finds that they add an infinite series in powers of θ to A-ln θ , the first term being $b_1\theta^2$, where $b_1=1$. This factor would raise the theoretical E vs. θ curve slightly, but not enough to account for the discrepancy between the Read-Shockley formula and experiment, for $\theta > 5$ to 6° .

Van der Merwe⁽²⁾ avoids some of the difficulties inherent in the Read–Shockley method by assuming that the stress–strain relation at the interface is sinusoidal. Since van der Merwe accounts for the non-linear forces at the core of the dislocation, he is able to express A_0 as

$$A_0 = 1 + \ln \frac{(1 - \sigma)\mu_0}{(1 - 2\sigma)\pi\mu} \tag{10}$$

where μ is the elastic shear modulus and μ_0 is a constant of the same order of magnitude which determines the amplitude of the sinusoidal stressstrain relation. Taking $A_0 = -0.72$, Table 3, (neglecting the variation of A with ϕ') it was found that μ/μ_0 must be about 3.65, in order to make van der Merwe's E vs. θ formula⁽²⁾ agree with Read-Shockley's at small θ .* Based on these conditions, a theoretical curve was calculated from van der Merwe's(2) formula. It can be seen, Fig. 4, that it does not deviate appreciably from the experimental data until $\theta = 8$ to 9° . As θ increases beyond this point, the van der Merwe curve does not drop off rapidly, although it remains considerably below the actual energy curve. While this method seems to give better agreement for larger angles than Read-Shocklev's, it should be pointed out that the sine function, which has been used by van der Merwe, is probably not a good approximation to the force law for copper. This can be seen from the experimental finding that $\mu/\mu_0 > 1$. This inequality reflects the fact that the true stressstrain relation for copper has a much smaller maximum stress than that given by the sine function when its amplitude is fixed so as to agree with classical elasticity theory for small strains. Undoubtedly, the agreement between theory and experiment could be extended to larger values of θ , if, as Lomer and Nye⁽¹⁰⁾ suggest, van der Merwe's calculations were repeated, using the force law of Foreman et al. (35)

19

5.2. Comparison of results with previous energy data for tilt boundaries

In the past, measurements of the energies of tilt boundaries as a function of misorientation, with two exceptions, $^{(11,12)}$ have been made on a relative basis, and therefore it was not possible to obtain E_0 from a plot of E/θ vs. In θ . Instead the shape of relative energy-angle relationship was tested essentially by fitting the Read–Shockley equation to the large angle energy data; it was concluded $^{(1,7-9)}$ that the equation described the data very well over the entire range of θ . This investigation has demonstrated that such a

^{*} For small θ , van der Merwe's expression⁽²⁾ gives the same functional dependence of E on θ as the Read–Shockley formula. In order to make the magnitudes of each expression equivalent, however, the factor $\mu_0/2\pi(1-\sigma)$ of van der Merwe's equation must be replaced by the appropriate one from anisotropic elasticity theory, in addition to requiring that $\mu/\mu_0=3.65$.

procedure is not valid in the case of copper, since it results in values for E_0 and A_0 that are not in agreement with theory. The same situation may be true for the previous relative energy measurements. It will be recalled that Brooks' calculation of the experimental $E_0^{(9)}$ for Fe–Si boundaries from the relationship $E_0=E_{\rm max}/\theta_{\rm max}^{(8)}$ gave a value 50 per cent lower than the theoretical one. This might be expected, since large angle values for $E_{\rm max}$ and $\theta_{\rm max}$ were used.

Further support for this suggestion may be obtained from a consideration of the previous determinations of A. Unlike E_0 , the value of this constant can be determined from either absolute or relative energy measurements. This investigation has verified the idea put forth by Brooks⁽⁹⁾ and Parker et al.⁽¹²⁾ that A is a function of θ . The small angle A_0 for copper is comparable to the values, -0.82 to -1.62, obtained by Parker et al.(12) for small angle tilt boundaries in zinc. This fact, coupled with the knowledge that the theoretical A_0 value for copper probably lies in the range -0.23 to -1.50 (the larger negative value is probably more nearly correct), indicates that the positive values (0.20 to 0.55, with tin being an exception) obtained for other metals may be too large. It should be noted also that the large angle $A_0 = +0.86$, for copper* is similar to those obtained by previous investigators, indicating that they did not extend their measurements to small enough angles to detect a change in slope in the E/θ vs. In θ plot, and a consequent decrease toward negative values of A_0 .

5.3. Dislocation model and energies of [001] twist boundaries

1959

An exact evaluation of the energies of twist boundaries in terms of the appropriate dislocation model is difficult because of the lack of data at very small angles. Since the small angle E_0 could not be determined from an E/θ vs. ln θ plot, any analysis of the data must be carried out using the theoretical E_0 . Such an assumption is probably reasonable in view of the good agreement between experiment and theory for the case of tilt boundaries.

A twist boundary in the (001) plane consists of a crossed grid of screw dislocations, having Burger's vectors

$$\mathbf{b}_1 = \frac{\sqrt{2}}{2} b \, [110]$$
 and $\mathbf{b}_2 = \frac{\sqrt{2}}{2} b \, [1\overline{1}0.]$

 E_0 may be computed from the formula⁽⁸⁾.

$$E_0 = \frac{b}{2\pi} \sqrt{\frac{C_{44}(C_{11} - C_{12})}{2}} \tag{11}$$

From equation (11), E_0 was found to be 1450 ergs/cm², a value essentially the same as that calculated for tilt boundaries having variable asymmetry. For sufficiently small angles, such that $-\ln \theta \gg A$, it would be impossible with the present experimental techniques to measure the difference in their energies. There is some evidence, however, which indicates that A for small angle [001] twist boundaries is more negative than the corresponding value for tilt boundaries. This was shown in the following manner. The experimental energy for 3 to 9° was plotted on an expanded scale and the curve that fitted the points was extrapolated to the origin. Taking E_0 to be 1450 ergs/cm², E vs. θ curves were calculated for various values of A. The appropriate theoretical curve was taken to be the one which best fitted the extrapolated portion of the experimental curve over the largest range of θ . With this method, the best fit was obtained for A = -1.5in which case the two curves began to deviate near 2°. and the theoretical maximum occurred at approximately 5°.

Assuming A=-1.5, van der Merwe's treatment⁽²⁾ of the twist boundary gives $\mu/\mu_0=1.95$, confirming the suggestion put forth earlier to the effect that the sine function is not a good approximation to the force law for copper. Using $\mu/\mu_0=1.95$, an energy curve was calculated from van der Merwe's equation, which agreed well with the experimental curve up to 4° before falling below it. The analysis given above, suggests that screw dislocations begin to interact at larger spacings than edge dislocations, indicating that their widths are larger on the (001) plane. It is clear, however, that the lack of data for $\theta < 3^\circ$ makes it impossible to draw any conclusions concerning this latter point.

5.4. Structure and energy of the large angle grain boundary

It has been shown in the preceding sections that there appears to be no advantage in considering the large angle grain boundary in copper to be composed of dislocations, in order to compute theoretically its interfacial energy. It was decided, therefore, to attempt an explanation of such experimental facts as (1) the occurrence of a maximum in the energy-angle relationship beginning at 18 to 22° for [001] tilt and twist boundaries, and (2) the difference in maximum

^{*} It will be noted that $A_0=+0.86$ for copper is somewhat larger than the corresponding values for high energy boundaries in other materials. This results from the fact that in determining A_0 from an E/θ vs. In θ plot a more positive value will be obtained if more large angle data are included in the least squares analysis. In this investigation results up to $\theta=53^\circ$ were included, whereas previous investigators rarely included measurements beyond $\theta=30$ to 35° .

VO: 7

energies for tilt and twist boundaries by calculating the grain boundary energy on an atomic basis.

The complexity of this problem is considerably reduced when it is noted that for rational grain boundaries the geometry of the lattices requires that the atoms be arranged in repetitive patterns along the interface. The coincidence plots of Kronberg and $Wilson^{(37)}$ illustrate such patterns for [001] and [111] twist boundaries and similar patterns may be drawn for tilt boundaries. It is possible to find the energy of such a pattern, by assuming that the atoms interact according to central forces, provided that (1) the number and (2) the positions of the atoms within the unit are known. Friedel et al. (16) determined (1) and (2) by assuming that for the most part the atoms within the unit remained at their normal lattice sites; some atoms were removed from the pattern to avoid having interatomic bonds with large compressional strains. Vassamillet's(17) approach was to determine (1) and (2) from structure of boundaries found in soap bubble rafts.

In principle it should not be necessary to make some assumption concerning (1) and (2) but rather to determine them by requiring that the Helmholtz free energy of the pattern be stationary with respect to any virtual displacement of the pattern. When the atoms are assumed to interact according to central forces, this is equivalent to determining their positions from the condition that the resultant force on every atom in the pattern vanishes. If there are N atoms in the pattern, this condition results in a set of 3N simultaneous equations in 3N position co-ordinates. If multiple solutions for these equations arise, the correct ones are found by minimizing the total free energy of the pattern. Attempts were made to solve these equations for a very simple arrangement of atoms, but even in this case a prohibitive amount of work was involved.

An alternative procedure also was attempted. In this case, for a given boundary, several feasible numbers and arrangements of atoms were selected for the pattern, and for each pattern an energy (not a free energy) was calculated. This method led to considerable difficulty for primarily two reasons: (1) The interfacial energy was found to be very sensitive to the particular array of atoms used in the calculation, thus making it difficult to detect a trend toward a minimum energy configuration, and (2) this, in turn, made it impossible to compare the energies of two boundaries having different misorientations and consequently it was not possible to predict the point at which the energy maximum should begin.

Although, for the reasons mentioned in (1) and (2),

no quantitative comparison could be made between the calculated energies for twist and tilt boundaries, the calculation did give indications that the large angle twist boundary should have the lower energy. This is primarily due to the fact that on twisting two (001) planes about their common [001] direction the change in bond lengths across the interface appear to be less on the average than for a corresponding tilt rotation.

These calculations have demonstrated that it is not feasible to select the proper number and arrangement of atoms within the repetitive unit on the basis of a trial and error type calculation, and thus it seems that in order to predict the characteristics of large angle boundaries it will be necessary to determine these quantities from the conditions given earlier in this section.

As a final point, it is interesting to note that no energy cusps of appreciable depth, i.e. greater than ± 10 per cent, were found in either series. This may well mean that (1) the comparatively ordered arrangement of atoms needed to produce an energy cusp has been replaced by a more disordered one at the high temperature of measurement (1065°C), due to lowering of interfacial free energy that could occur from its higher entropy contribution, or (2) the crystals and/or the plane of the boundary were never sufficiently well-aligned to observe the effect.

6. CONCLUSIONS

(1) It has been possible to obtain reasonably accurate values for the absolute energies of small angle, lineage boundaries in copper. An analysis of these results in terms of the appropriate dislocation model shows that the Read-Shockley equation predicts the energy up to $\theta = 5$ to 6° , where the dislocations are about 10 atom planes apart. For angular misorientations larger than this value, linear elasticity theory no longer gives the correct energy, probably because most of the strain energy resides in regions where Hooke's law is not obeyed. For $\theta > 5$ to 6° van der Merwe's equation is a better approximation to the actual energy-angle relationship than that given by Read and Shockley. It was shown also that the Peierls' sinusoidal stress-strain relationship, used by van der Merwe, is not a very good representation to the actual force law for copper.

(2) The energy data for twist boundaries did not extend to small enough values of θ to provide a rigorous test of the dislocation model. An analysis of these results, however, suggests the deviations from the Read–Shockley equation occurs at smaller values of θ , i.e. 2 to 3°, than for the tilt boundaries.

(3) At large angles, both [001] tilt and twist boundaries, show a rather broad energy maximum beginning near 18 to 22°, with twist boundaries having a considerably lower maximum energy than tilt boundaries. It is shown that these effects cannot be predicted by assuming that the atoms interact according to central forces until the positions of atoms along the interface are known more accurately.

(4) For large angle boundaries (tilt or twist) no appreciable effect of boundary orientation on its energy was found, nor were any energy cusps observed.

APPENDIX I

Herring^(23,24) has demonstrated that pure metals at low temperatures should have a γ_s -plot composed of maxima and sharply-cusped minima (corresponding to low index planes). If this is the case, a smoothly curved surface should be replaced by a hill and valley structure, (23) i.e. faceting should occur. When faceting is present the local equilibrium condition at the root of a thermal groove can be represented by (23)

$$\gamma_G = 2\gamma_S \cos \alpha - 2 \frac{\partial \gamma_S}{\partial \alpha} \sin \alpha$$
 (1)

where α has been taken equal to β and γ_S is taken to be the same for both sides of the groove. If the γ_S plot exhibits sharply-cusped minima, the term $\frac{\partial \gamma_S}{\partial \alpha}$ may have an appreciable magnitude, and γ_G as calculated from equation 3 (text) will be subject to error.

Several factors indicate that $\frac{\partial \gamma_S}{\partial \alpha}$ is not large for copper at high temperatures (1065°C) under an oxygen-free atmosphere (purified hydrogen).

(1) The groove profile was smoothly curved down to the root; no large scale facets were observed with this type of profile.

(2) The ratios γ_G/γ_S were reasonably reproducible (±10%). If, as Brooks estimates,⁽⁹⁾ $\frac{2}{\gamma_S} \left| \frac{\partial \gamma_S}{\partial \alpha} \right|$ has the magnitude 0.01 for copper, it would be expected that γ_G/γ_S would fluctuate by ± 0.01 . For large angle boundaries this amount would be within the experimental error, but for lineage boundaries $\gamma_G \mid \gamma_S \simeq 0.04$, hence a variation of +0.01 should have been detected

(3) The shape of the normal profile agrees (21,17) reasonably well with that predicted by Mullins, (38) who in his treatment, neglected the variation of surface properties with orientation.

(4) If faceting is permitted to occur, the profile becomes badly distorted, and the dihedral angle fluctuates by large amounts.(17)

The effect discovered by Mykura, (39) i.e. for a given pair of twin boundaries in nickel, one dihedral angle is less than 180° and the other is greater 180° by nearly the same amount, shows that in this case may be as large as 0.05. Mykura gives the impression that all nickel twins exhibit this effect. but some recent observations (40) indicate that there are exceptions. Mykura also believes that the same is true for copper. During this investigation, twenty pairs of twin boundaries were examined, and the Mykura effect was found in only one case. Some pairs, however, showed decidedly unequal dihedral angles. both being less than 180°. This latter phenomenon was found to occur in some instances in grains which

Although much information has to be learned vet about the orientation dependence of γ_s , it is believed that the observations given above indicate that for copper surfaces at 1065 C in a hydrogen atmosphere the neglect of the term $\frac{2}{\gamma_S} \left| \frac{\partial \gamma_S}{\partial \alpha} \right|$ in computing $\gamma_G | \gamma_S |$ probably does not result in a large systematic error in the energy values reported herein.

have a slightly roughened surface.

ACKNOWLEDGMENTS

The authors wish to thank the Aluminum Company of America for supporting this research in the form of a fellowship grant to one of us (N. A. G.).

Thanks are due also to Dr. P. Shewmon for helpful discussions and for the preparation of many copper single crystals. The authors are indebted to the following laboratories for the generous use of their Interference Microscopes:

- (1) Westinghouse Research Laboratories, Westinghouse Electric Corp. (East Pittsburgh, Penna.)
- (2) Research Laboratories, Westinghouse Atomic Power Division (Bettis Plant).
- (3) Central Research Laboratories, Pittsburgh Plate Glass Company, (Creighton, Penna.).

REFERENCES

- W. T. READ and W. SHOCKLEY, Phys. Rev. 78, 275 (1950).
- J. H. VAN DER MERWE, Proc. Phys. Soc. A63, 616 (1950).
 C. G. DUNN and F. LIONETTI, Trans. Amer. Inst. Min. (Metall.) Engrs. 185, 125 (1949).
- 4. C. G. Dunn, F. W. Daniels and M. J. Bolton, Trans. Amer. Inst. Min. (Metall.) Engrs. 188, 1245 (1950)
- 5. K. T. Aust and B. Chalmers, Proc. Roy. Soc. A 201, 210
- 6. K. T. Aust and B. Chalmers, Proc. Roy. Soc. A 204, 359
- 7. K. T. Aust, Trans. Amer. Inst. Min. (Metall.) Engrs.
- 8. W. T. Read, Dislocations in Crystals. McGraw-Hill (1953). 9. H. Brooks, Metal Interfaces, p. 20. American Society for Metals Monograph (1951).
- 10. W. M. LOMER and J. F. NYE, Proc. Roy. Soc. A 212, 576 (1952).

VOL.

- 11. A. P. Greenough and R. King, J. Inst. Met. 79, 415 (1951).
- 12. R. B. Shaw, T. L. Johnston, R. J. Stokes, J. Washburn R. B. SHAW, T. L. JOHNSTON, R. J. STOKES, J. WASHBURN and E. R. Parker, Mineral Research Laboratory Report, Ser. 27, Issue 14. University of California (May, 1956).
 H. MYKURA, Proc. Phys. Soc. B 67, 281 (1954).
 B. CHALMERS, R. KING and R. SHUTTLEWORTH, Proc. Phys. Sept. A 104 (1977).
- Roy. Soc. A 193, 465 (1948).
- 15. J. FRIEDEL, B. D. CULLITY and C. CRUSSARD, Acta Met.
- 1, 79 (1953). 16. L. Vassamillet, Term Paper, Carnegie Institute of Technology (1954).
- N. A. GJOSTEIN, PhD Thesis, Carnegie Institute of Technology (February, 1958).
 18. P. Jacquet, Trans. Electrochem. Soc. **69**, 629 (1936).
- 19. W. Linnik, Dokl. Akad. Nauk SSSR 21 (1933).
- 20. S. Amelinckx, Physica 19, 1175 (1953).
- 21. J. E. HILLIARD, to be published.
- 22. J. R. Tolmon and J. G. Wood, J. Sci. Instrum. 33, 236 (1956).
- C. HERRING, The Physics of Powder Metallurgy, p. 143. McGraw-Hill (1951).
- 24. C. Herring, Structure and Properties of Solid Surfaces,
- p. 5. University of Chicago Press (1952). P. G. Hoel, Introduction to Mathematical Statistics, p. 76. Wiley, New York (1951).

- J. C. Fisher and C. G. Dunn, Imperfections in Nearly Perfect Crystals, p. 317. Wiley, New York (1950).
 H. Udin, A. J. Shaler and J. Wulff, J. Metals N.Y.
- 1, 186 (1949).
- 28. R. Shuttleworth, Discussion to reference 26.
- 29. H. Udin, Trans. Amer. Inst. Min. (Metall.) Engr. 189. 63 (1951).
- 30. W. T. READ and W. SHOCKLEY, Imperfections in Nearly
- Perfect Crystals, p. 352. Wiley, New York (1952).
 31. F. C. Frank, Carnegie Institute of Technology Symposium on the Plastic Deformation Solids. Office of Naval Research (1950).
- 32. E. SCHMID and W. Boas, Plasticity of Crystals. Hughes, London (1950).
- 33. F. R. N. NABARRO, Advanc. Phys. 1, 269 (1952).
- F. R. N. NABARRO, Advanc. Phys. 1, 269 (1952).
 R. E. PEIERLS, Proc. Phys. Soc. 52, 34 (1940).
 A. J. FOREMAN, M. A. JASWON and J. K. WOOD, Proc. Phys. Soc. A 64, 156 (1951).
 J. S. KOEHLER, Phys. Rev. 60, 397 (1941).
 M. L. KRONBERG and F. H. WILSON, Trans. Amer. Inst. Min. (Metall.) Engrs. 185, 501 (1949).
 W. W. MULLINS, J. App. Phys. 28, (3), 333 (1957).
 H. WYELDA, Acta Met. 5, 346 (1957).

- 39. H. MYKURA, Acta Met. 5, 346 (1957).
- 40. P. Shewmon, private communication.

OXIDATION KINETICS IN THE CASE OF AGEING OXIDE FILMS*

J. L. MEIJERING and M. L. VERHEIJKE†

The cubic relationship found by Hauffe and Kofstad for the oxidation of $\mathrm{Cu_2O}$ in the $800^\circ-1900^\circ\mathrm{C}$ range is confirmed, and also the abnormally low temperature coefficient of the rate constant. Special experiments show that ageing effects in the CuO layer must be responsible for this behaviour. Calculations of the oxidation kinetics are given for the case when the permeability (or its reciprocal) of the oxide formed changes exponentially with age.

CINETIQUE DE L'OXYDATION AU COURS DU VIEILLISSEMENT DE FILMS D'OXYDES

Les auteurs confirment la relation cubique découverte par Hauffe et Kofstad pour l'oxydation de ${\rm Cu_2O}$ entre ${\rm 800^{\circ}-1000^{\circ}C}$ ainsi que le coefficient anormal de la constante de vitesse à basse température. Des essais particuliers montrent que les effets de vieillissement dans la couche CuO seraient responsables de ce comportement. Les auteurs ont calculé la cinétique de l'oxydation dans le cas où la perméabilité (ou sa réciproque) de l'oxyde formé varie exponentiellement au cours du vieillissement.

OXYDATIONSKINETIK IM FALL VON ALTERNDEN OXYD-FILMEN

Die von Hauffe und Kofstad aufgefundene kubische Beziehung für die Oxydation von Cu₂O im 800–1000°C Bereich wird bestätigt, ebenso der abnormal niedere Temperaturkoeffizient der Geschwindigkeitskonstanten. Besondere Versuche zeigen, dass Alterungsvorgänge in der CuO-Schicht für dieses Verhalten verantwortlich sein müssen. Für den Fall, dass sich die Durchlässigkeit des gebildeten Oxyds (oder ihr Kehrwert) exponentiell mit dem Alter ändert, werden Berechnungen der Oxydationskinetik mitgeteilt.

1. INTRODUCTION

Hauffe and Kofstad⁽¹⁾ have examined the oxidation of $\mathrm{Cu_2O}$ to CuO by oxygen. Above 800°C they found a cubic relationship between the thickness ξ of the CuO film and the oxidation time t:

$$\xi^3 = K_3 t. \tag{1}$$

Even more remarkable, the coefficient K_3 was nearly independent of temperature, corresponding to an activation energy of 2 kcal only.

The cubic law (1) can be explained⁽²⁾ by electric field effects if the oxide thickness is of the order of, say, 1000Å. But in the case under consideration ξ becomes more than 100 times greater than this and it is difficult now to see that $d\xi/dt$ could be proportional to $1/\xi^2$.

In many cases of metal oxidation the parabolic law

$$\xi^2 = K_2 t \tag{2}$$

is valid. In some instances, however, a "modified parabolic law" has been introduced, K_2 not being constant but generally decreasing with t, resp. ξ . Sometimes then, (cf.⁽³⁾) a cubic plot appears to be quite satisfactory.

The cubic law generally holds for a limited

temperature range only and this is indeed found to be the case in the oxidation of $\mathrm{Cu}_2\mathrm{O}$ to $\mathrm{Cu}\mathrm{O}$. The validity of the cubic law, therefore, might be suspected as being fortuitous, ⁽⁴⁾ at least in some cases. In trying to explain more general deviations from the parabolic law proper, it does not appear attractive to take $d\xi/dt$ proportional to, say, $\xi^{-1.8}$ or some other function of the oxide thickness. We prefer to examine the assumption that the permeability of the oxide formed for the diffusing particles (Cu and/or O) is greatest when it is "fresh", and decreases with its age.

Such an ageing process will accelerate with increasing T, thus opposing the normal temperature dependence of the rate of oxidation. Such an effect is found with aluminium, where amorphous and crystalline oxide films play a role. From the experiments by Smeltzer⁽⁵⁾ it is seen that oxidation for 5 hr at 500° may yield a larger increase in weight than during the same time at 600° C.

The very small temperature coefficient of the oxidation of $\mathrm{Cu_2O}$ thus increases the probability that ageing plays a part.

2. NORMAL OXIDATION EXPERIMENTS $\label{eq:continuous} \mbox{WITH Cu_2O}$

The $\mathrm{Cu_2O}$ strips were made from electrolytic copper strip by oxidation at 1000°C in nitrogen with 4% $\mathrm{O_2}$.

^{*} Received July 8, 1958.

[†] Philips Research Laboratories, Eindhoven, Netherlands.

Apart from the first two experiments the copper strip was somewhat less than 0.2 mm thick, 70 mm long and 50 mm broad. As this oxidation was carried out in the same Chévenard apparatus as the later oxidation to CuO, each copper strip was bent into an approximately cylindrical shape, with 11 mm radius of curvature. The oxidation time was about 2.5 hr, several times more than is necessary for complete conversion of Cu into Cu₂O. The Cu₂O strips were then further oxidized in air at normal pressure. During that oxidation the weight increase was measured by recording the displacement of the arm of the Chévenard balance by an optical method. Microscopic examination showed the thickness of the CuO layer formed to be uniform, equal at the outer and inner curved surfaces, and in quantitative agreement with the weight increase.

Fig. 1 shows all results after 1 hr. The wide spread at 800°C becomes much less if the two experiments with thick strips are discarded. In any case the abnormally low temperature coefficient of the oxidation velocity in the 800°–1000°C range is borne out. It may even be negative, and this tendency is accentuated in the long-time experiments (see Fig. 2).

We did not investigate whether the higher oxidation rates of the thick $\mathrm{Cu_2O}$ strips are connected with the fact that 4 per cent of the surface was formed by the edges—against 1 per cent in all other strips—or with the longer time of oxidation to $\mathrm{Cu_2O}$ (4 hr). Hauffe and Kofstad found that the conditions of $\mathrm{Cu_2O}$ formation affect the subsequent rate of oxidation to CuO . They gave their $\mathrm{Cu_2O}$ strips a vacuum anneal at $1000^{\circ}\mathrm{C}$, which led to more reproducible results.

Fig. 2 shows that we too find the cubic law well

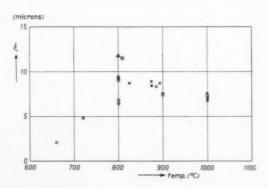


Fig. 1. Thickness of CuO layer after 1 hr oxidation of Cu₂O in air at different temperatures. Calculated from weight-increase, with 6.4 as density of CuO. \bigcirc Start experiment by pushing furnace around the Cu₂O strip. \times Id. by replacing nitrogen by air, strip being on temperature. \triangle As \bigcirc , but thicker strips. \square Evaluated from Hauffe and Kofstad. A cross coinciding with lowest circle but one at 800° is not shown. A triangle lies between the two upper circles.

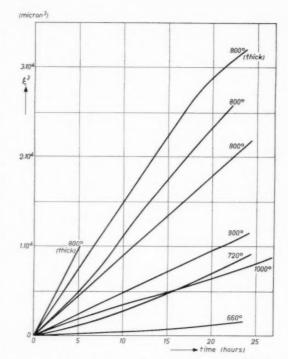


Fig. 2. $\xi^3=$ cube of CuO thickness as a function of oxidation time, long experiments. Start as indicated by \bigcirc in subscript Fig. 1.

fulfilled at 800° – 1000° C, although the deviations from a straight line are rather systematic.

The temperature dependence of K_3 in equation (1) as derived from Fig. 2 corresponds to an "activation energy" of roughly minus 15 keal. The difference between this and the +2 keal found by Hauffe and Kofstad may be due in some way to their preliminary vacuum anneal. It seems less probable that the discrepancy is due to the use of air by us and 1 atm. O_2 by the former authors. Only at 810°C do they appear to have used a range of O_2 pressures. Their mean K_3 value at 0.2 atm. O_2 is indicated in Fig. 1.

In the cubic plots shown by Hauffe and Kofstad the time does not exceed $1\frac{1}{2}$ hr. This suggests that their results should be compared to Fig. 1 rather than to Fig. 2; and Fig. 1 agrees roughly with activation energy zero.

Turning now to temperatures below 800°C, our 720° and 660° runs are seen to be far from being described by a cubic law. They are in fact roughly parabolic. It is also seen that the temperature dependence in this region is normal. Hauffe and Kofstad report that below 750°C, K_3 fell much more rapidly with T than above this temperature and that below 700°C an initial parabolic stage appeared, increasing in duration with decreasing temperature. The common results

VOI 7 19 of the two investigations may thus be stated as follows:

Between 800° and 1000°C , Cu_2O oxidizes according to a cubic law, the temperature dependence of the rate being abnormally low. Below 750°C this dependence becomes normal and the cubic law gives way more and more to the parabolic law.

Rather than try to clear up minor discrepancies and vary the oxygen pressure, etc., we proceeded with our object: to examine whether ageing effects play a role.

3. DIRECT AGEING EXPERIMENTS

These are quite simple in principle: stop the oxidation temporarily by replacing the air by a neutral atmosphere. After a certain time switch over to air again. The oxidation should then proceed slower than if no waiting period had been interposed. Dunn⁽⁶⁾, after finding that the rate of oxidation of activated copper to $\rm Cu_2O$ decreased with rising temperature around 225°C, carried out such experiments. At 209°C, by temporary evacuation of the $\rm O_2$ the subsequent oxidation could be slowed down about 50 per cent.

In our case matters are less simple, because at $800^{\circ}-1000^{\circ}$ C the reaction

1959

$$Cu_2O + \frac{1}{2}O_2 \rightleftharpoons 2CuO \tag{3}$$

proceeds appreciably to the right or left for quite small deviations from the equilibrium pressure or temperature. It proved virtually impossible to stop the oxidation during a long period. The course of the oxidation after an intermediate period resulting in partial reduction will be discussed in section 6, together with a deviation of the apparent equilibrium pressure for $\mathrm{Cu_2O/CuO}$ strips from that for powdered mixtures.

In four experiments the oxidation was not reversed but slowed down during the intermediate period. In

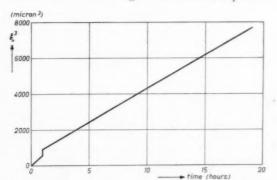


Fig. 3. ξ^3 as a function of oxidation time at 875°C. First hour in air, then 5 hr in $N_2 + 1.5\%$ O_2 , finally 18 hr in air again. The intermediate "waiting period" is not counted on the time axis.

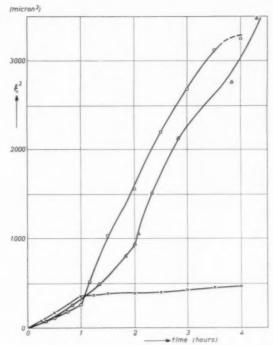


Fig. 4. ξ^3 as a function of oxidation time; Cu₂O in air. After 1 (resp. 2) hr temperature is changed (in about 10 min). \bigcirc 800° \rightarrow 1000°C; \times 1000° \rightarrow 810°C; \triangle 800° \rightarrow 900°C

three of them, nitrogen with 1.5% O₂ was used during this period, and subsequently $K_3 (= d\xi^3/dt)$ was on the average 2/3 of the value in the initial period in air, cf. Fig. 3. The fourth test, at 1000°C with 12% O₂, yielded a still smaller effect.

Results like Fig. 3 support but do not convincingly prove the ageing hypothesis, because the cubic law seems to be only approximately valid. In any case, this hypothesis itself practically excludes a precisely cubic course of normal uninterrupted oxidation, cf. section 5.

4. INDIRECT AGEING EXPERIMENTS

The abnormal temperature dependence of the oxidation between 800° and $1000^{\circ}\mathrm{C}$ enables us to make indirect ageing experiments by changing the temperature rather suddenly during the oxidation in air. If the temperature influence were inherently small, such a change would be expected to have no great effect. But if the quasi-independence on T is ascribed to compensation by ageing (see section 1), then a sudden rise from 800° to $1000^{\circ}\mathrm{C}$ should result—at least temporarily—in a markedly accelerated oxidation. Correspondingly, a decrease in T should slow down the oxidation rate. Fig. 4 shows that these expectations were fulfilled. The ratio of the rates just before and after the temperature change is a

factor 6 resp. 1/6 for 200° difference and about $2\frac{1}{2}$ for the $800^{\circ} \rightarrow 900^{\circ}$ experiment. These factors correspond to an activation energy of about 25 kcal.

We considered whether these effects might be due to trivial perturbations caused by the temperature changes. As far as we can see the only possibility would be offered by a much smaller thermal expansion of CuO than that of Cu₂O. This might cause rupture of the CuO layer on heating, and buckling on cooling. Inspection of Fig. 4 shows that one would have to assume a nearly complete tearing apart of the CuO/Cu₂O interface, exposing the Cu₂O to the air on heating or to closed lateral crevices (containing O₂ of lower pressure) on cooling. According to unpublished measurements of Mr. Steenbeeke in this laboratory the linear coefficient of expansion of Cu₂O at 900°C is about 4×10^{-6} degree⁻¹. Even taking that of CuO to be zero, this would amount to a

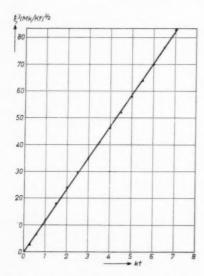


Fig. 5. Approximate linearity of ξ^3 vs. time according to equation (5), with f/(1-f)=0.4. The points lie firstly below, then above, below, and finally again above the straight line.

difference of 0.08 per cent only for 200° change in temperature. This could scarcely result in such gross effects, and indeed the three strips in question were as sound and smooth as those oxidized at constant temperature.*

We conclude that the experiments of Fig. 4 show that the peculiar temperature effects of Figs. 1 and 2 are indeed due to ageing.

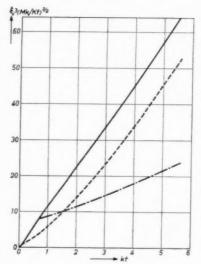


Fig. 6. Drawn curve shows approximate linearity of ξ^3 vs. time (same type as Fig. 5) according to the "refined reciprocal" approximation (equation (12), Appendix) with f=0.2. On this scale the deviations from linearity are difficult to judge; the curve really has two inflexion points, near kt=0.35 and 2, and the sequence of curvatures is like that shown by the points in Fig. 5. The two curves branching off represent calculated ageing experiments, see end of section 5. Oxidation is slowed down by an intermediate period (not counted on horizontal axis where oxidation is stopped isothermally: dashed curve. The dash-dot curve shows the slowing down by an abrupt decrease in temperature, although—with the parameters used—normal straightforward oxidation is virtually independent of T.

5. CALCULATIONS ON OXIDATION WITH AGE-DEPENDENT PERMEABILITY OF THE OXIDE LAYER FORMED

Let us take the differential equation

$$d\xi/dt = K\{f + (1 - f) \exp(-kt)\}/M\xi \tag{4}$$

19

which means that the permeability of the oxide formed changes exponentially with time from the

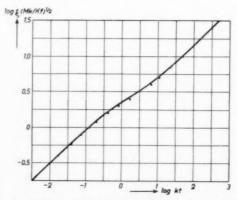


Fig. 7. Doubly logarithmic plot of ξ vs. t. Curve corresponds to drawn curve in Fig. 6, but extended to much longer times. The points are calculated with the simple equation (14), also with f=0.2.

Only the 720°-specimen showed a tendency of the CuO film to crack on cooling to room temperature after the experiment.

initial value K to a final value fK. M is a constant. Integration of (4) yields

$$\xi^2 = 2(1-f)\frac{K}{Mk} \left[1 - \exp{(-kt)} + \frac{f}{1-f}kt \right]. \eqno(5)$$

For values of the parameter f/(1-f) between 0.3 and 0.5 a *cubic plot* yields nearly a straight line, at least when kt is not too small or too large, cf. Fig. 5.

We also examined the supposition that the reciprocal of the permeability changes exponentially to the final value 1/fK. In this case the treatment can be refined (see Appendix and Fig. 6) by taking into account that the age of the oxide formed is not equal to t, but varies from 0 to t in the layer. Such a refinement for the non-reciprocal case corresponding to equation (4) would meet considerable mathematical difficulties. As is seen from Fig. 7, the refinement does not greatly alter the general trend of the oxidation. This is not surprising: if the cubic law is approximately fulfilled, only 1/8 of the oxide layer has an age of less than $\frac{1}{2}t$. Quantitative data further on in this section refer to the refined reciprocal approximation.

As is immediately clear from the nature of the ageing hypothesis, for very short and very long times oxidation is nearly parabolic ($n=d\log t/d\log \xi \cong 2$). In between, n goes through a maximum value which increases with decreasing f.* For f=0.2 (see Fig. 7) $n_{\rm max}=3.2$ and for f=0.05 it is 4.7.

VOL.

1959

The points on those curves where n=3 correspond to tangents to the ξ^3 , t curve (cf. Fig. 6) through the origin. For f>0.25, n does not attain 3, and the ξ^3 , t curve loses its doubly inflected character; the slope then increases monotonically.

In a certain ξ^3 , t diagram determined or calculated up to a total time t', we will draw a straight line through the origin in such a way that the absolute value of the maximum deviation Δt is a minimum. This "minimax" value of Δt , divided by t', may be called the m.m. deviation. For our five long-time experimental curves at $800^{\circ}-1000^{\circ}\mathrm{C}$ in Fig. 2 it was nearly 3 per cent on the average, and for the lines depicted in Hauffe and Kofstad's paper⁽¹⁾ about 4 per cent.

In Fig. 6, calculated for f = 0.2, it is 1 per cent. For small and large values of t' this is naturally more, but it remains 3 per cent or less over one order of magnitude in t'. For f = 0.3 this is the case in a t' range covering a factor three only, and for f = 0.5 the m.m. deviation attains about 7 per cent at best.

When f is smaller than 0.2 the inflection points are

further apart than in Fig. 6. The m.m. deviation is 3 per cent or less in a t' range covering a factor twenty for f=0.15. But if f=0.05 this is only the case in two rather narrow t' regions far apart. For intermediate times the m.m. deviation goes through a maximum of about 10 per cent. In this region the biquadratic law is better, the m.m. deviation for the ξ^4 , t diagrams coming down to 2 per cent.

According to the above the cubic law has no special clearly defined place in the case of ageing oxide films, but a more or less satisfactory pseudocubic law may be found rather often. With changing circumstances (e.g. the parameter f in our treatment) the cubic character may become better or worse. This does not mean however that, in the case of the oxidation of ${\rm Cu}_2{\rm O}, f$ must depend appreciably on T to account for the breakdown of the cubic law below 750°C. The parabolic character will be accentuated not only by very short or long times (see above), but also by low or high temperatures, even if f remains constant.

Both K and k will increase with temperature. Suppose K^3/k and f to be independent of T. The ratio of the co-ordinates in Fig. 6 for a given ξ^3 , t combination then remains constant, and thus also (approximately) the velocity of the oxidation if it is pseudocubic. But for decreasing temperatures the ξ^3 , t graphs become increasingly enlarged pictures of Fig. 6 near the origin, and at last the course becomes parabolic for not too long times. Simultaneously the temperature dependence of K is making itself felt in the oxidation velocity, in accordance with experiment (see section 2).

In Fig. 6 two calculated curves branching off from the normal f=0.2 curve are drawn. They simulate ageing experiments (cf. sections 3 and 4). One of them represents a run with abrupt decrease in temperature. It was assumed that f remains 0.2, that the permeability of each layer element (and thus K) falls to 1/5 and the ageing velocity constant k to 1/125 of their high-temperature values. Thus K^3/k remains constant, corresponding to the approximate independence of T of straightforward oxidation curves.

The other curve simulates an isothermal ageing experiment with a waiting period 20 times the first oxidation period, which is short: the curve branches off already at $[\xi(Mk/Kf)^{1/2}]^3 = 1$. Consequently the oxide layer is nowhere "old" at this moment, but ages considerably during the waiting period. The effect is less spectacular than that produced by lowering T. When during the "waiting period" oxidation is not stopped but only slowed down (cf. Fig. 3) it will be still less.

In view of the assumptions made, the curves in

^{*} When f > 1, so that ageing results in *increased* permeability, one gets deviations from the parabolic law towards the linear law.

Fig. 6 have only semi-quantitative value. Nevertheless they support the hypothesis that ageing plays a part in the oxidation of $\mathrm{Cu}_2\mathrm{O}$ to $\mathrm{Cu}\mathrm{O}$.

6. SOME CONSIDERATIONS ON THE NATURE OF THE AGEING PROCESS IN CuO

The preceding section shows that ageing effects may well lead to an approximately cubic law. Equation (4) and its reciprocal counterpart are of course only formal general examples, as the nature of the ageing process in CuO is not known. There are indications in the literature, however, that CuO formed by oxidation of copper is not always in the same state. Murison⁽⁷⁾ found an intermediate form of CuO, which according to Honjo⁽⁸⁾ (cf. also ref. ⁽⁹⁾) is better described as a fibrous pattern, and according to Matyáš⁽¹⁰⁾ as a defect structure. In our experiments the grain size of the CuO increased markedly with oxidation temperature, but it is improbable that this would be a decisive factor for the permeability. Sartell et al. (11) examined the oxidation of a 62/38 Cu-Ni alloy and found that the growth of the Cu₂O-NiO layer was accelerated by relaxation of stress brought about by recrystallization of the outer CuO layer, but the (parabolic) growth of the latter was unaffected.

The following observations may help in throwing light on the question of the ageing process. We observed the weight of crushed and ground Cu₂O/CuO strips heated e.g. in nitrogen with 1.5% O2 at oscillating temperatures. The equilibrium temperature of (3) for this O₂ pressure was found to be 900° + 5°C, in accord with accepted thermodynamic data. (12) But in our "direct ageing experiments" (section 3) we soon found that in this gas mixture the boundary temperature between increase and decrease of weight of the strips was about 875°C! This apparent shift of the equilibrium pressure would correspond to a 0.3 kcal/mole higher free energy of freshly formed CuO. But if in the crushed powder Cu₂O oxidizes, surely fresh CuO is formed too? This difficulty might be resolved by assuming that a less unstable CuO is formed in contact with "old" (stable)

In our first ageing experiments the "waiting period" resulted several times in a reduction. The subsequent oxidation after air had been admitted again was considerably accelerated, cf. Fig. 8. As Cu₂O has a smaller volume than 2CuO, the reduction may well lead to porous Cu₂O, which might possibly form micro-porous CuO on re-oxidation, resulting in an acceleration. But this lasts so long that apparently porous CuO is still forming after the porous Cu₂O has

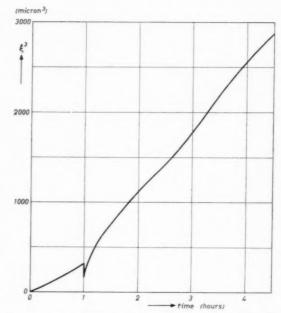


Fig. 8. ξ^3 as a function of oxidation time at 800°C. First hour in air, then 22 hr in N₂ with about 0.2% O₂, finally $3\frac{1}{2}$ hr in air again.

been consumed. This persistence by contact seems to be the counterpart of the anomaly described in the preceding paragraph, and suggests that the ageing process might consist in the removal of supernumerary lattice vacancies in CuO.

It is to be noted that the simple assumptions used for the calculations in the Appendix do not contain a direct coupling of permeabilities of adjacent CuO layers.

7. NON-PARABOLIC OXIDATION OF METALS

In our treatment of the oxidation of Cu₂O to CuO the fact that Cu₂O is an oxide plays no essential part. Ageing effects could just as well take place in the oxidation of a metal, and perhaps be responsible for the deviations from the parabolic law towards or beyond the cubic law as found in the cases of Ni^(13,14) Ti. (15,20) Zr(16,3) and Hf. (4) The occurrence of intermediate and continuously variable rate "laws" is presumably more easily explained by effects of time rather than of oxide thickness, when we exclude very thin films. Disagreement between results of different authors-which appears to be rather pronounced in the cases named—is probably due to impurities, cf. (18) In the ageing hypothesis not only the permeabilities themselves (before and/or after ageing) could be affected, but also the rate of ageing.

It is worth noting that Fig. 5 of ref. $^{(15)}$ closely resembles our Fig. 7: the oxidation of Ti at 600° C in

VOI 7 19 ${
m O_2}$ begins parabolic, then becomes cubic and later on parabolic again. But the formation of more than one oxide and the solubility of O in Ti are complications here. Anyhow, only special experiments can show whether in a particular case ageing effects are probable or not. We chose the oxidation of ${
m Cu_2O}$ because the slight temperature influence made these effects both likely a priori and easy to investigate.

APPENDIX

At a certain time t the film thickness is ξ . Let the effective concentration u of the diffusing species decrease with distance x from an equilibrium value u_o to zero at the other film boundary ($x=\xi$), where the film is growing. For our calculation it is immaterial whether e.g. O or Cu is diffusing through CuO. Even if the departure of a Cu atom (ion) from the Cu₂O/CuO interface would form one CuO there and one CuO at the CuO/gas interface, so that the film grows at both ends, the result would be unaffected, provided the diffusion coefficient D depends only on the age of the CuO.

If u_o —which we take independent of t—is small and the interface reactions are rapid, at a certain moment the diffusion stream $D\delta u/\delta x$ is the same for every x and equal to $Md\xi/dt$, where M is independent of t and of temperature. As

$$\int_0^{\xi} \frac{\delta u}{\delta x} dx = u_o$$
, we have the equation

$$\frac{u_0}{M} \cdot \frac{dt}{d\xi} = \int_0^{\xi} \frac{dx}{D} \,. \tag{6}$$

We now assume that

VOL.

1959

$$1/D = (1/fD_0)\{1 - (1 - f) \exp(-k\omega)\}$$
 (7)

where ω is the age of the oxide, varying with x. Equation (7) means that the diffusion coefficient falls with age towards the fraction f of the initial value, compare section 5.

If $t \equiv F(\xi)$, then the oxide situated at x has been formed at the time F(x), and thus

$$\omega = F(\xi) - F(x) = t - F(x).$$
 (8)

Substitution of (7) and (8) in (6) leads to

$$\frac{fu_0D_0}{M} \cdot \frac{dt}{d\xi} = \xi - (1 - f) \exp\left(-kt\right) \int_0^\xi \exp[kF(x)] dx. \tag{9}$$

If f = 1 this leads directly of course to the parabolic law.

We now call $\exp(kt) = z$. Multiplication of (9) by z and differentiation with respect to ξ yields

$$\frac{fu_0D_0}{Mk} \cdot \frac{d^2z}{d\xi^2} = \xi \frac{dz}{d\xi} + fz. \tag{10}$$

We call u_0D_0 the initial permeability K (cf. equation (4)) and introduce the dimensionless variable $w \equiv \xi(Mk/Kf)^{1/2}$. Thus (10) becomes

$$d^2z/dw^2 = w(dz/dw) + fz \tag{11}$$

a Weber differential equation. The general solution $^{(19)}$ is

$$z = C_1 \left\{ 1 + \frac{f}{2!} w^2 + \frac{f(2+f)}{4!} w^4 \dots \right\}$$

$$+ C_2 \left\{ w + \frac{1+f}{3!} w^3 + \frac{(1+f)(3+f)}{5!} w^5 \dots \right\}. \quad (12)$$

The initial conditions for w=0 are z=1 and dz/dw=0. Consequently $C_1=1$ and $C_2=0$, and we need only the former power series for normal uninterrupted isothermal oxidation. For w up to 5 or 6 it is conveniently computed on a desk machine. Only for f=0.05 and f=0.2 (Fig. 7) did we need large values of w, for which there is an asymptotic expansion. For our purpose the difference

$$\ln z - \frac{1}{2}w^2 + (1 - f) \ln w - \ln \left\{ 1 - \frac{(1 - f)(2 - f)}{2w^2} \right\}$$
 (13)

was already sufficiently constant at the highest values of w used in the first power series in (12).

The lower points in Fig. 7 are obtained by substituting simply t for ω in (7), yielding

$$z = 1 - f + f \exp\left(\frac{1}{2}w^2\right) \tag{14}$$

This approximation is the counterpart of (5).

The "ageing experiment" curves in Fig. 6 have been, however, calculated with (12) again, but here both power series are necessary. The constants C_1 and C_2 are determined by the values of z and dz/dw at the start of the second period (after the temperature drop or the "waiting period"), which can be evaluated without difficulty.

REFERENCES

- K. Hauffe and P. Kofstad, Z. Electrochem. 59, 399 (1955).
- N. Cabrera and N. F. Mott, Rep. Progr. Phys. 12, 163 (1949).
- E. A. Gulbransen and K. F. Andrew, Trans. Amer. Inst. Min. (Metall.) Engrs. 209, 394 (1957).
- W. W. SMELTZER and M. T. SIMNAD, Acta Met. 5, 328 (1957).
- W. W. SMELTZER, J. Electrochem. Soc. 103, 209 (1956).
- J. S. Dunn, Proc. Roy. Soc. A111, 210 (1926).
 C. A. Murison, Phil. Mag. 17, 96 (1934).
- 8. G. Honjo, J. Phys. Soc., Japan 4, 330 (1949).

- 9. K. R. DIXIT and V. V. AGASHE, Z. Naturf. 10A, 152 (1955).

- M. Matyáš, Czech. J. Phys. 5, 214 (1955).
 J. A. Sartell, S. Bendel, T. L. Johnston and C. H. Li, Trans. Amer. Soc. Metals. 50, 1047 (1958),
 O. Kubaschewski and J. A. Catterall, Thermochemical data of alloys. Pergamon Press, London and New York (1958)
- (1956).

 13. C. Wagner and K. Zimens, Acta Chem. Scand. 1, 574 (1947).

 14. E. A. Gulbransen and K. F. Andrew, J. Electrochem. Soc. 101, 128 (1954).
- 15. P. Kofstad and K. Hauffe, Werkstoffe u. Korr. 7, 642
- (1956). 16. J. Belle and M. W. Mallett, J. Electrochem. Soc. **101**, 339 (1954).
- 17. P. Kofstad, Nature, Lond. 179, 1362 (1957).
- O. Kubaschewski and O. von Goldbeck, Z. Metallk. 39, 158 (1948).
- E. KAMKE, Differentialgleichungen, Pt. I (4th Ed.). Akad. Verl. Ges., Leipzig (1951).
 P. KOFSTAD, K. HAUFFE and H. KJÖLLESDAL, Acta Chem.
- Scand. 12, 239 (1958).

A STUDY OF SLIP LINES IN $\alpha\textsc{-}\textsc{brass}$ as revealed by the electron microscope*

J. T. FOURIE† and H. G. F. WILSDORF!

The slip lines on α -brass single crystals are investigated with the electron microscope by means of repeated aimed replicas at various strains, and extensive measurements. The frequency of lines with given amounts of glide, the density of slip lines, and the average glide per line were determined for various values of stress and strain. Some measurements were also carried out on cross-slip lines. The major results are: (i) Many slip lines show a gradual growth in depth. (ii) This growth may take place even for lines which do not grow in length. (iii) The growth in depth is present already during easy glide, i.e. while the applied stress is constant. (iv) At low strains the slip line density in clusters is consistent with the idea that it is determined by the limiting distance at which dislocations on parallel slip planes can still pass each other under the influence of the applied stress. For higher stresses, however, the slip line density rises much slower than anticipated from this theory. (v) The slip line density is apparently directly connected with the shear stress since it does not seem to change during easy glide.

ETUDE AU MICROSCOPE ELECTRONIQUE DES LIGNES DE GLISSEMENT DU LAITON α

Les auteurs étudient au microscope électronique les lignes de glissement de monocristaux de laiton α au moyen de répliques successives de la même surface après différentes déformations. Pour différentes valeurs de la tension et de la déformation, ils déterminent ainsi la fréquence des lignes en fonction de l'importance du glissement, la densité des lignes, ainsi que le glissement moyen par ligne. Certaines mesures se rapportent également aux lignes de glissement croisé. Les résultats principaux sont: (i) De nombreuses lignes de glissement présentent une augmentation graduelle de leur profondeur. (ii) Celle-ci peut se marquer même pour des lignes dont la longueur demeure invariable (iii) et elle est déjà apparente au cours du glissement facile, c'est-à-dire lorsque la tension appliquée est constante. (iv) Aux faibles déformations, la densité des lignes de glissement dans les amas est en accord avec l'idée qu'elle est déterminée par la distance limite pour laquelle des dislocations sur des plans de glissement parallèles peuvent encore permuter l'une par rapport à l'autre sous l'influence de la tension appliquée. Toutefois, pour des tensions supérieures, la densité croît moins rapidement que ne le laisserait supposer la théorie. (v) La densité des lignes de glissement semble étroitement liée à la tension de cisaillement puisqu'elle ne paraît pas se modifier au cours du glissement facile.

EINE UNTERSUCHUNG DER GLEITLINIEN AUF α -MESSING MIT HILFE DES ELEKTRONENMIKROSKOPS

Die Gleitlinien auf α-Messing Einkristallen werden elektronenmikroskopisch mit Hilfe von wiederholten gezielten Abdrücken nach verschiedenen Dehnungen und durch umfassende Messungen untersucht. Die Häufigkeit der Linien mit gegebenen Gleitbeträgen, die Gleitliniendichte und die durchschnittliche Ableitung pro Linie wurden bei verschiedenen Spannungs- und Dehnungswerten bestimmt. An Quergleitlinien wurden ebenfalls einige Messungen ausgeführt. Die wichtigsten Ergebnisse sind: (I) Die Stufenhöhe von vielen Gleitlinien nimmt allmählich zu. (II) Sie kann sogar bei Gleitlinien wachsen, die nicht langer werden. (III) Die Zunahme der Stufenhöhe erfolgt schon im Easy-Glide-Bereich, d.h. während die angelegte Spannung konstant ist. (IV) Bei geringen Dehnungen ist die Gleitliniendichte in den Anhäufungen von Gleitlinien mit der Vorstellung verträglich, dass die Dichte durch den Mindestabstand bestimmt wird, unter welchem Versetzungen auf parallelen Gleitlinien unter dem Einfluss der angelegten Spannung einander eben noch passieren können. Bei höheren Spannungen steigt jedoch die Gleitliniendichte viel langsamer an, als diese Theorie erwarten lässt. (V) Die Gleitliniendichte ist offenbar direkt mit der Schubspannung verknüpft, da sie sich während des East-Glides nicht zu ändern scheint.

1. INTRODUCTION

During the past ten years much new information on the properties of slip lines has become available. (1-6) The present investigation was undertaken to obtain more detailed results, both qualitatively and quantitatively, for slip lines on α -brass. It is hoped that these will lead to a better understanding of the

^{*} This paper is published with permission of the South African Council for Scientific and Industrial Research.

Received July 14, 1958. † National Physical Research Laboratory, C.S.I.R., Pre-

[†] National Physical Research Laboratory, C.S.I.I. toria, South Africa.

[‡] Formerly at the National Physical Research Laboratory, C.S.I.R., Pretoria, South Africa; now at the Franklin Institute Laboratories for Research and Development, Philadelphia, Pa. U.S.A.

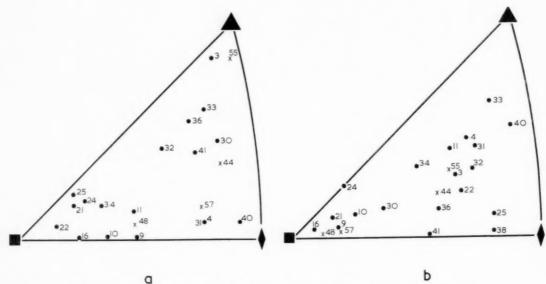


Fig. 1. Orientation of axes and surfaces of investigated crystals: (a) Axes, (b) Surfaces.

processes involved in the formation of slip lines. The reason why single crystals of $\alpha\text{-brass}$ were selected for this study is that the surface structures here are of a coarser type than those of pure metals, thus permitting relatively simple but at the same time accurate measurements to be carried out.

The aim of the present paper was to study three specific problems. Firstly, the behaviour of slip lines after their initial formation, i.e. whether, once formed, at least some of the lines grow in depth as deformation proceeds. Secondly, how the density of active slip planes, or in other words the number of slip lines normal to the slip planes, depends on stress and strain. Finally particular attention was given to the appearance, density and distribution of cross-slip lines.

Another important aspect of slip lines on α -brass, namely whether they represent "homogeneous" slip, i.e. sequences of atomic planes, each of which has slipped through just one interatomic distance, or whether they are of the "inhomogeneous" type, caused by many dislocations on a single atomic plane, has already been decided in favour of the latter possibility. (7.8) In the present investigation use was made of a replication technique which allows a series of replicas to be taken from approximately the same surface area of a sample after successive strain increments.

2. EXPERIMENTAL TECHNIQUE

(i) Preparation of samples

The single crystals used were prepared by a slightly modified Bridgman method described previously.⁽⁷⁾

Their chemical composition was about 20% zine, 80% copper with less than 0.05% impurities, and they were polished electrolytically in diluted phosphoric acid. Altogether twenty-two crystals have been examined with orientations as shown in Fig. 1 (determined from Laue back reflection photographs). Most of the crystals were deformed in a simple tensile testing machine at a strain rate of about $10^{-2}/\text{sec}$, usually in steps of roughly 0.1 shear, up to the strain at which the second system started to become active. The specimens were 120 mm long and had a cross-section of 1.3×3 mm². The work-hardening curves of four crystals are shown in Fig. 12.

19

Piercy et al. $^{(9)}$ have pointed out, in agreement with earlier observations, that the actual strain can show considerable variations along the length of an α -brass crystal, especially at small deformations. Therefore, by means of very fine markings, the centre portion of each crystal was divided into six equal parts of 3 mm length each. From these portions the replicas were taken and their actual deformations were evaluated so that a fairly accurate strain value could be ascribed to every replica.

For the investigations with the electron microscope, silicon monoxide replicas were used, except when it was desired to take replicas of the same surface area after successive deformations of the same specimen. In such cases the replicas were made following the bedaeryl–formvar–carbon replication technique of Bradley^(16,11). The investigations with the electron microscope were supplemented by light optical examinations throughout.

(ii) Techniques for the measurement of depths and density of slip lines

In the present paper the depths of many thousands of slip lines, and the slip line densities over lengths of many microns had to be determined from the electron micrographs, making it imperative somehow to simplify the procedures of measurement. This was done in two steps:

(a) The apparent width of a slip line, W, depends on the magnification, M, the shear along the slip plane, S, the angle between the slip plane and the surface, ϕ , and θ , the angle between slip line and slip direction, as $S = W/(M \cdot \cos \phi \cdot \sin \theta)$. In order to avoid unnecessary calculations, the magnifications for all samples were adjusted such that the factor $(M \cdot \cos \phi \cdot \sin \theta)$ equalled 1.11×10^4 , and thus a measured line width of 0.1 mm always corresponded to a true slip of 90 Å.

(b) In order to facilitate the actual measurements of line widths on the micrographs, a series of parallel lines were drawn on tracing cloth. It consisted of fifty-one straight, parallel lines, the widths of which increased in uniform steps from 0.06 mm to about 1 mm, in steps of about 0.03 mm, and then to 2.67 mm in steps of about 0.1 mm. The lines were numbered from 1 to 51, and their widths were accurately determined with a travelling microscope. The width of a slip line was then simply obtained by noting down the number of the line whose width was judged to be most closely similar to that of the slip line. The mean error was estimated to be approximately 5 per cent.

VOL.

1959

In the determination of slip line densities a complication arose through the strong tendency of the slip lines to form clusters. These clusters were separated by regions of varying widths which were virtually free of slip lines. In view of the fact that measurement and interpretation would have been rendered difficult by taking large completely unslipped regions into account, it was decided to measure slip line densities only within clusters. A "cluster" was taken to be any region in which the narrowest slip line bundle was at least as wide as the widest unslipped portion.

(iii) Some explanations to the curves representing the results of the measurements

For the series of repeated measurements after various elongations four crystals were chosen which combined large values of θ with low values of ϕ . This is advantageous because the slip lines are then best resolved, which leads to more reliable results. However, since the angles θ and ϕ do not primarily depend

on the crystal orientation, but on the surface orientation, it was, at the same time, possible to choose crystals with widely varying axis orientations.

For the purpose of obtaining distribution curves of the frequency of slip lines within given intervals of slip line depths, the reference lines on the measuring device were divided into the groups $0\text{--}0.09\,\mathrm{mm}$, $0.1\text{--}0.19\,\mathrm{mm}$ and so on. The percentage of lines in any one group was then plotted at the mean value, i.e. at $0.05\,\mathrm{mm} = 45\,\mathrm{\mathring{A}}$ for the first group, at $0.15\,\mathrm{mm} = 135\,\mathrm{\mathring{A}}$ for the second group etc. The same principle was employed for plotting mean shear values.

3. RESULTS

(i) Qualitative observations

A study of slip lines in \alpha-brass using a selected area replica technique(11) which enables the formation of slip lines in a specific area to be studied after various elongations, reveals a number of interesting points (Fig. 2): The earliest slip lines, at strains of up to a few per cent, appear in irregular groups. Within these groups the line depths vary from very small values to values of almost 1000 Å, apparently at random. This may simply be due to the fact that the centres of the slip processes which give rise to the slip lines may in some cases lie close to the surface of the specimen, while in others they lie at considerable distances from it. This possibility cannot be discounted in explaining the widely varying slip line depths in a-brass at all strains, although individual slip lines often appear to be of uniform strength over distances of many

As the strain is increased the gaps between the slip lines within the clusters gradually fill up and new clusters are also formed. A considerable percentage of lines appear to grow in depth, as can be seen from a close scrutiny of individual lines in Fig. 2. Unpredicted slip formed in the earliest stages of plastic deformation tends to remain unchanged throughout all subsequent strain increments. This does not hold true, however, for cross-slip lines.

At least two types of cross-slip lines can be distinguished. One type consists of lines, not markedly connected to any slip line of the main system; the other, for instance Figs. 3 and 4, is clearly linked to slip lines of the acting system. However, the two types of cross-slip might not be physically different, since the former type could be connected to the main system below the surface examined. Particularly deep slip lines (Fig. 13) mostly appear in conjunction with cross-slip lines linked to them, and where such deep lines grow in depth, the number of cross-slip lines linked to them usually increases.⁽⁷⁾

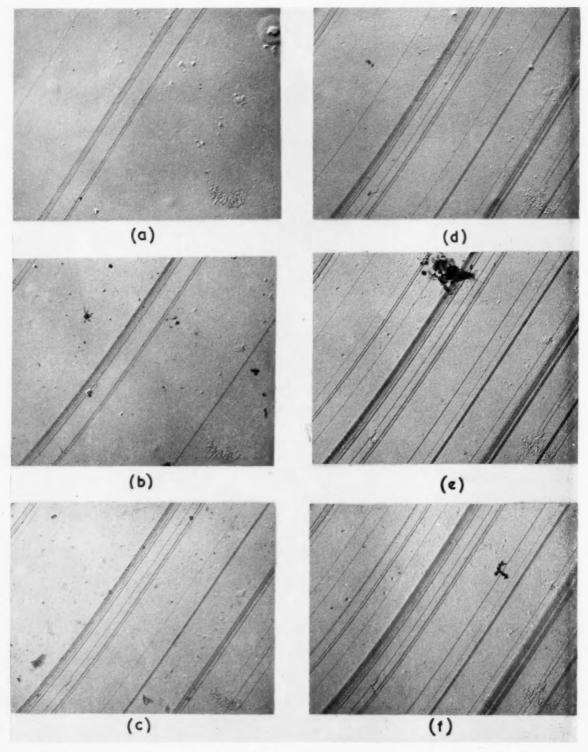


Fig. 2. Micrographs of a selected area showing the formation and growth of specific slip lines: (a) $\varepsilon=0.005$, $\gamma=0.01$; (b) $\varepsilon=0.015$, $\gamma=0.03$; (c) $\varepsilon=0.04$, $\gamma=0.08$; (d) $\varepsilon=0.06$, $\gamma=0.12$ (e) $\varepsilon=0.09$, $\gamma=0.18$; (f) $\varepsilon=0.10$, $\gamma=0.20$. $\times 10,000$.



Fig. 3. Cross-slip lines faintly linked with lines of the primary system. $\times 4200$.

(ii) Distribution of slip-line depths

VOL.

1959

The measurements of slip-line depths bear out the qualitative impressions gained from the micrographs. The curves of distribution for glide on slip lines are surprisingly similar for specimens with different strains as well as for crystals with different orientations. Fig. 5 gives the curves for crystals No. 44, 48, 55 and 57. The most frequent line depth always lies between 150 Å and 300 Å with about one third of the slip lines having depths between these limits.

The most frequent line depth always increases slightly with increasing strain. Simultaneously, the percentage of lines with the most frequent depth falls off a little, namely by roughly one quarter, from the lowest to the highest strains investigated. Taking together all lines for the four crystals which were closely examined, one finds that, at the lowest strains, at least 92 per cent have depths of up to and including 500 Å, but that this group constitutes only between 75 and 90 per cent of the total at the highest strains. At the same time the frequency of lines deeper than 1000 Å increases from 1.5 per cent to above 5 per cent. Thus on the average there is, with increasing strain, a definite but not very large shift towards greater slip line depths.

Considering the average glide per line, Figs. 6 and 10, instead of the distribution of line depths, one correspondingly finds that the former rises from about 275 Å to about 350 Å in the case of crystals 44 and 57, and from about 200 Å to 350 Å and 450 Å respectively in the cases of crystals 48 and 55.* These differences

(iii) Density of slip lines

For the determination of the number of slip lines per cm in the direction of the normal to the glide plane, (called in what follows the "density" of slip lines ρ) the number of lines, N, was determined for a length of L' perpendicular to the slip lines. The length, L, perpendicular to the slip planes to which L' corresponds is $L=L'\sin\phi$ where, as before, ϕ is the angle between slip plane and surface. The density of slip lines is then $\rho=MN/L=MN/(L'\sin\phi)$, with M the magnification. The results are given in Figs. 7 and 11 and their significance will be evaluated in the discussion.

(iv) The density of cross-slip lines

Although cross-slip appears to be very frequent in deformed polycrystalline α -brass it is much less prominent in single crystals. This makes it difficult to determine the average spacing of cross-slip lines with the electron microscope. For this reason the following method was employed:

On a series of micrographs from the same specimen having the magnification M, all cross-slip lines were counted, irrespective of their length or depth. Let N be the number of cross-slip lines which appear on the total area of a width W, measured parallel to the slip lines, and length L' perpendicular to them. The density of cross-slip lines on the plane containing the direction of these lines and being perpendicular to the cross-slip plane is then $\rho_c = NM^2/(WL'\sin\phi_c)$ where ϕ_c is the angle between the cross-slip plane and the

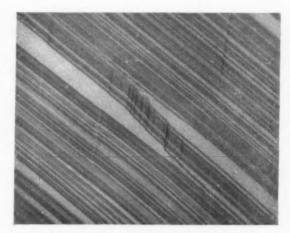
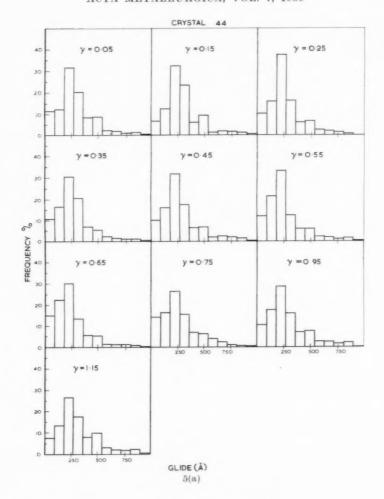


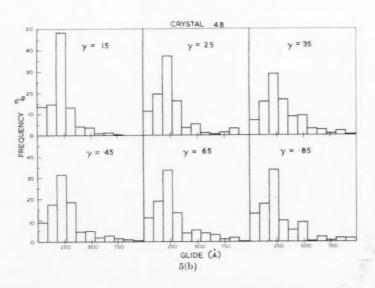
Fig. 4. Cross-slip lines clearly linked with lines of the primary system. ×20,000.

between the crystals indicate an orientation dependence which will be mentioned again later on.

^{*} Unfortunately the resolved shear stresses for the four crystals are not known at the highest strains, and for this reason the last measurements are always missing in figures involving the shear stress.



VOI 7 19



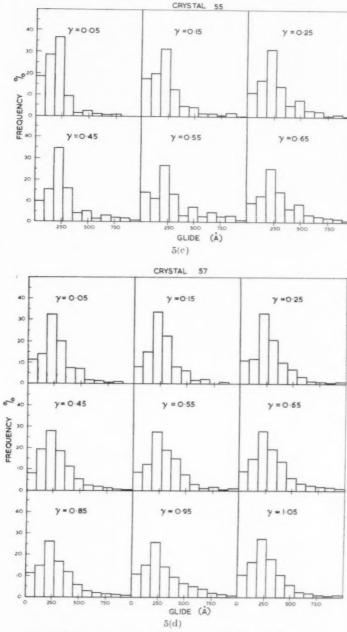


Fig. 5. Distribution of slip line depths for various strains.

surface. Areas scanned for any one specimen corresponded to between a few hundred to 2000 μ^2 perpendicular to the cross-slip plane. The dependence of the thus determined cross-slip density ρ_c on strain, γ , and stress, τ , is illustrated in Figs. 8 and 9.

VOL.

1959

4. DISCUSSION

The general way in which the slip line structure on α -brass develops is known and easy to summarize:

4

Starting with the lowest plastic strains, slip lines of greatly varying strengths suddenly appear, grouped together in clusters. As the strain increases, the clusters widen and more clusters are formed in the gaps between them, until the whole surface is covered with lines. The details in this process, however, are manifold and not easily understood.

In the first place one would like to answer the question whether most slip lines do grow in length or

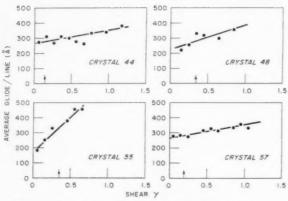


Fig. 6. Dependence of average glide/line on shear, Arrows indicate end of easy glide.

depth or both after they are formed, or if they remain stationary after their initial formation. Now, taking into account the results of measurements which are depicted in Figs. 5 and 7, and paying attention not so much to the curves drawn, which are rather uncertain, but more to the measured values, the following conclusions may be derived: The values for crystal 55 indicate a definite decrease in the frequency of lines at the peak of the distribution curves with increasing y. This decrease takes place although there is hardly any increase in the density of lines shown in Fig. 7. From this it can be deduced that in crystal 55, a substantial proportion of the slip lines do grow in depth as plastic deformation proceeds, providing one assumes that there is no inherent difference between the early clusters and those formed later. In crystal 55, then, it appears likely that clusters grow neither by filling up with slip lines nor by a lengthwise growth of the lines in them (since both these mechanisms would lead to an increase in slip line density) but by the lateral addition of lines, and by the gradual increase in the depth of many slip lines. This is also reflected by the values in Fig. 6.

The same conclusion can probably be drawn for crystal 48 but not for crystals 44 and 57. In them the

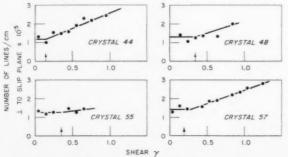


Fig. 7. Dependence of slip line density on shear. Arrows indicate end of easy glide.

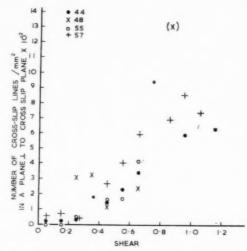


Fig. 8. The number of cross-slip lines/mm² in a plane perpendicular to the cross-slip plane as dependent on shear.

average depth of the slip steps also increases (Fig. 6) but this is coupled with a fairly large increase in slip line density (Fig. 7). This may mean (i) that the clusters are gradually filled up with lines which, on the average, are deeper than those formed earlier, or (ii) that many lines grow in length while they grow in depth, or (iii) that newly formed lines are in average shallower, but that this is more than counterbalanced by a strong depthgrowth of old slip lines. That individual lines do indeed grow in depth also in these crystals is clear from Fig. 2 which is a series of micrographs taken from the second portion of crystal 57. Evidently, then, a considerable percentage of slip lines do grow in the case of all crystals examined.

19!

If a freely acting dislocation source is situated on a free glide plane extending to a radius L from the

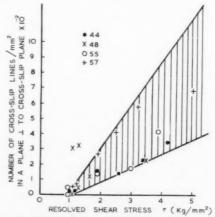


Fig. 9. The number of cross-slip lines/mm² in a plane perpendicular to the cross-slip plane as dependent on resolved shear stress.

source, such that the first dislocation is held up by an obstacle at that distance L and the following dislocations are piled up behind it, then the maximum slip in the vicinity of the source is expected to be

$$s = \pi L \tau / G, \tag{1}$$

where τ is the applied shear stress and G is the modulus of rigidity. Further, according to simple theory, the closest distance at which dislocations can pass each other under the stress τ is

$$y_0 = Gb/8\pi(1-\nu)\tau\tag{2}$$

with b the Burgers vector, and ν Poisson's ratio. (12) Then, in a slip line cluster the density of slip lines, ρ , should not be bigger than $\rho = 2/(3y_0)$, because the distance of separation, could, at best, vary between y_0 and $2y_0$.

Comparing these predictions with Figs. 10 and 11, which give the average glide of slip lines and the density of slip lines vs. τ , respectively, one finds that in neither case is there a proportionality with τ as predicted, but rather, one could approximate the curves as giving a proportionality with $\tau + \tau^*$ where the constant τ^* would be between 2 kg/mm² and a very large value. It is improbable that much significance is to be attached to this interpretation of the curves. If, however, the values found for the very lowest deformations are considered together with the assumption that the lines formed earliest arise under the least disturbed conditions, then one might expect to find the predicted behaviour. This yields the interesting result that all values for the density of slip lines, at the smallest strains, agree well i.e. better than

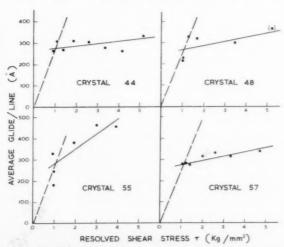


Fig. 10. Relationship between average glide/line and resolved shear stress. The broken lines are used to estimate the initial length of slip lines.

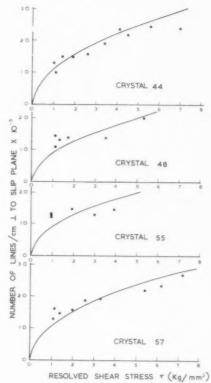


Fig. 11. Relationship between slip line density and resolved shear stress. Curves are calculated by formula of Leibfried and Haasen.

within 20 per cent error with the expression $\rho=2/(3y_0)=1.1\times 10^5\,\mathrm{cm^{-1}}$ for $\tau=1\,\mathrm{kg/mm^2}$ where the numerical value is obtained by simply inserting the appropriate values into the theoretical formula for y_0 . Furthermore, for the lowest strains all four crystals have an average slip line depth of 270 Å \pm 50 Å which, according to $s=\pi L\tau/G$, would correspond to $L=37~\mu$ or a total average slip line length of 75 μ .

Another possibility of interpreting the dependence of slip line density on shear stress is based on a theory by Leibfried and Haasen. (13) These authors consider the case of a number of active sources situated on or very close to a glide plane with their respective areas of action separated by uniformly spaced obstacles. Under these conditions they find for the smallest distance between slip lines

$$y_0 = 0.14 (Glb/\tau)^{\frac{1}{2}} \tag{3}$$

l being one half the distance between the sources contributing to the same slip line. (14) One would then expect a slip line density of

$$\rho = 2/3y_0 = 4.8(\tau/Glb)^{\frac{1}{2}} \tag{4}$$

VOL. 7 1959 0.7

0.6

0.5

CRYSTAL

0.8

07

0.6

0.5

0.4

0.3

0.2

0

0.8 SHEAR IN

0.7

0.6

0.5

0.4

0 3

0.2

0

0

0

RESOLVED SHEAR Y OR

CLUSTER

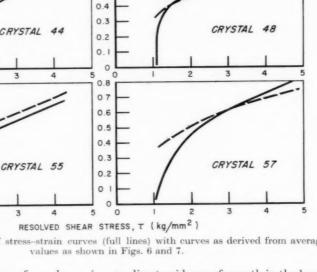


Fig. 12. Comparison of stress-strain curves (full lines) with curves as derived from average values as shown in Figs. 6 and 7.

4

which, with the appropriate values for a-brass is

$$ho = 4.8 imes 10^2 au^{rac{1}{2}} l^{-rac{1}{2}}$$

where τ is measured in kg/mm² and l in cm, giving ρ in lines/cm. In Fig. 11 the experimental values of $\rho(\tau)$ have been interpolated with this type of curve and a reasonably good fit was obtained with values of the proportionality constant

$$c = 4.8 \times 10^2 l^{-\frac{1}{2}}$$

between 0.9×10^5 and 1.1×10^5 . This would correspond to a value of $l = 0.21 \mu$ or a mutual distance between sources in the order of $\frac{1}{2} \mu$. This seems to be too low, and it should also be noted that for crystals 48 and 55 a straight line indicating constant slip line density would fit better than the parabolic law.

A strong argument in favour of the contention that the slip line density is determined by the shear stress, can be deduced from Fig. 7 which together with Fig. 6 forms the basis for the curves drawn as broken lines in Fig. 12. Although the interpolating curves are somewhat arbitrary, it is still highly probable that the slip line density in clusters does not change appreciably during easy glide. On the other hand, the average glide per line, Fig. 6, quite clearly rises as much during easy glide as later on when work hardening has set in. This somewhat surprising result is particularly clear from the values obtained from crystal 55.

Again focussing one's attention on crystal 55, there are two important observations which have already been discussed in the preceding paragraphs. There is no direct evidence of growth in the length of slip lines, but the slip line depth increases even during easy glide; i.e. while the stress remains constant. This can be explained in two ways: either the dislocations reach their equilibrium positions only after a considerable delay, or one must conclude that even during easy glide there acts a mechanism which eliminates dislocations from the slip planes. In the first case, the delay of dislocations attaining their equilibrium conditions could be due to some frictional force acting on them. The latter case could be realized through cross-slip, where it would be required that this does not lead to new slip lines but rather interconnects neighbouring slip lines, allowing the mutual annihilation of dislocations of opposite sign piled-up in them. Or if we adopted the idea of Haasen and Leibfried, we might follow their argument that the obstacles, separating adjacent sections of the slip plane and against which dislocations of opposite sign are piled-up from the two sides, are not ideally opaque, but allow some dislocations to escape to the other side and be annihilated by merging with the dislocations there. If one examines the physical meaning of these two possibilities in the case of α -brass, it is realized that they might very well be two aspects of the same process, inasmuch as Haasen and Leibfried stress that the piled-up groups of dislocations may not lie on exactly the same atomic plane.

VOI

19

With regard to cross-slip two aspects will be considered: The frequency of cross-slip lines and their dependence on crystal orientation for the four crystals investigated in detail, and the relationship between cross-slip lines and particularly deep slip lines.

The frequency of cross-slip lines (Fig. 9) shows a good proportionality with $\tau - \tau_{\rm crit}$ where τ is the applied shear stress and $\tau_{\rm crit}$ the critical shear stress. Although the scatter of the values for crystals 48 and 55 is rather large, it seems certain that the number of cross-slip lines per cm2, perpendicular to the crossslip planes, is higher for crystals 57 and 48 than for crystal 44 and this again higher than for crystal 55. This cannot be due to any differences in the resolved shear stress on the cross-slip plane since this is lowest for crystals 44 and 57. Rather it could be a consequence of a noncircular shape of dislocation loops emitted from an average dislocation source. The loops might be extended in the slip direction, as theoretical reasons as well as experimental evidence obtained in other materials suggest a slower progress of screw dislocations as compared to the edge components. Since only the number of cross-slip lines was determined, independent of their length, we would expect more but shorter lines, i.e. higher cross-slip line density, and larger θ_e , the angle between slip direction and cross-slip lines. In agreement with this idea the θ_c values at the beginning of slip, for the crystals 48, 57, 44 and 55 in this order, are 56°, 53°, 46° and 28° .

Lastly it seems probable that the visible cross-slip

VOL.

1959



Fig. 13. Deep slip lines often have numerous cross-slip lines joined to them. $\times 20,000$.

lines have little, if any, influence on the development of the slip line clusters, since crystals 48 and 55, for which the measurements for slip line depth and density are very closely similar throughout, are the most dissimilar with respect to visible cross-slip line density.

Very deep slip lines have nearly always numerous cross-slip lines joined to them. The most obvious interpretation of this result would be that a slip line can grow to considerable depth only if many of its dislocations are deflected into cross-slip lines. Another possible explanation would be that a slip line represents an obstacle against the propagation of cross-slip lines, being the more powerful the wider it is. Thus, a slip line accidentally deeper than its neighbours, could block several cross-slip lines. Once sufficiently big pile-ups had formed, the dislocations in slip line and in cross-slip line would begin to annihilate each other mutually, thereby joining the lines. Finally any particularly deep slip line might somehow activate or produce dislocation sources on the cross-slip planes which are situated in its vicinity.

ACKNOWLEDGMENTS

The authors wish to thank Dr. Doris Wilsdorf of the School of Metallurgical Engineering, University of Pennsylvania, for many valuable discussions. Mr. R. I. Slinger, now at the University of Pretoria, was partly responsible for the measurements on slip lines, and to him the authors would also like to express their appreciation.

REFERENCES

- R. D. HEIDENREICH and W. J. SHOCKLEY, J. Appl. Phys. 18, 1029 (1947).
- R. D. Heidenbeich and W. J. Shockley, The Strength of Solids p. 57. Physical Society, London (1948).
- 3. A. F. Brown, Advances in Phys. 1, 427 (1952).
- H. WILSDORF and D. KUHLMANN-WILSDORF, Z. Angew. Phys. 4, 361, 409, 418 (1952).
- 5. D. KUHLMANN-WILSDORF and H. WILSDORF, Acta Met. 1, 394 (1953).
- 6. S. MADER, Z. Phys. 149, 73 (1957).
- J. T. Fourie, Ph.D. Thesis, Pretoria University (1956).
 H. Wilsdorf and J. T. Fourie, Acta Met. 4, 271 (1956).
- H. WILSDORF and J. T. FOURIE, Acta Met. 4, 271 (1956).
 G. R. PIERCY, R. W. CAHN and A. H. COTTRELL, Acta Met. 3, 331 (1955).
- D. E. BRADLEY, J. Inst. Met. 83, 35 (1954).
- 11. J. T. Fourie, J. Appl. Phys. 29, 608 (1958).
- 12. D. KUHLMANN-WILSDORF, J. H. VAN DER MERWE and H. WILSDORF, Phil. Mag. 43, 632 (1952).
- 13. G. LEIBFRIED and P. HAASEN, Z. Phys. 137, 67 (1954).
- P. Haasen and H. Leibfried, Nachr. Akad. Wiss. Göttingen 31 (1954).

SELF-DIFFUSION IN INDIUM*

J. E. DICKEY+

Self-diffusion coefficients parallel (D_{\parallel}) and perpendicular (D_{\perp}) to the tetragonal axis were measured in paired samples of single-crystal indium in the range from 44° to 144°C. The ratio D_{\parallel}/D_{\perp} was found to be $\sim 0.75 \pm 0.05$ and was not noticeably temperature dependent. Thus the activation energies Q_{\parallel} and Q_{\perp} were about the same, 18.7 ± 0.3 kcal/mol. with $D_{0}(\perp) \sim 3.7$ and $D_{0}(\parallel) \sim 2.7$ cm²/sec. The smallest difference, $Q_{\parallel} - Q_{\perp}$, detectable in this experiment would have been about 0.6 kcal/mol. Mosaic boundaries observed in the single crystals may possibly have been responsible for a component of fast diffusion which contributed to the uncertainties in the measured D values. If the volume diffusion occurs by a vacancy mechanism, then it is reasonable to expect D_{\perp} to be greater than D_{\parallel} , as found, with Q_{\parallel} slightly higher than Q_{\perp} .

AUTODIFFUSION DE L'INDIUM

Les coefficients d'autodiffusion ont été mesurés parallèlement (D_{\parallel}) et perpendiculairement (D_{\perp}) à l'axe quadratique dans des couples de monocristaux d'indium pour un domaine de température allant de 44° à 144°C. Le rapport D_{\parallel}/D_{\perp} a été trouvé voisin de 0,75 \pm 0,05 et ne semble pas dépendre notablement de la température. Ainsi les énergies d'activation Q_{\parallel} et Q_{\perp} sont sensiblement les mêmes et égales à 18,7 \pm 0,3 kcal/mole avec $D_{0}(\perp) \sim$ 3,7 et $D_{0}(\parallel) \sim$ 2,7 cm²/sec. Ces expériences seraient cependant susceptibles de déceler une différence $Q_{\parallel}-Q_{\perp}$ allant jusqu'à 0,6 kcal/mole.

Les frontières mosaïques observées dans les monocristaux pourraient donner lieu à une composante de diffusion rapide qui contribuerait à rendre les mesures de D quelque peu incertaines. Si la diffusion en volume s'effectue par un mécanisme lacunaire, il est raisonnable de s'attendre à un D_{\perp} plus grand que D_{\parallel} ce qui a été trouvé, avec Q_{\parallel} légèrement plus élevé que Q_{\perp} .

DIE SELBSTDIFFUSION IM INDIUM

Die Selbstdiffusionskoeffizienten von Indium-Einkristallen parallel (D_{\parallel}) und senkrecht (D_{\perp}) zur tetragonalen Achse wurden im Bereich von 44° bis 144° C gemessen. Das Verhältnis D_{\parallel}/D_{\perp} ergab sich zu $\sim 0.75 \pm 0.05$, es hing nicht merklich von der Temperatur ab. So waren die Aktivierungsenergien Q_{\parallel} und Q_{\perp} etwa gleich gross, nämlich 18.7 ± 0.3 kcal/mol; mit $D_{0\perp} \sim 3.7$ und $D_{0\parallel} \sim 2.7$ cm²/sec. Die kleinste in dieser Untersuchung nachweisbare Differenz von $Q_{\parallel} - Q_{\perp}$ wäre etwa 0.6 kcal/mol gewesen. Mosaikgrenzen, die in den Einkristallen beobachtet worden waren, können möglicherweise für einen Anteil von rascher Diffusion verantwortlich gewesen sein, der zu der Unsicherheit der gemessenen D-Werte beitrug. Wenn die Volumdiffusion durch einen Leerstellenmechanismus vor sich geht, dann erwartet man vernünftigerweise, dass D_{\perp} grösser als D_{\parallel} ist, wie es gefunden wurde, wobei Q_{\parallel} etwas höher sein sollte als Q_{\perp} .

1. INTRODUCTION

As a continuation of a project in anisotropic selfdiffusion, (1,2,3) studies were made of tracer penetrations in indium which has a face-centered tetragonal structure with c/a ratio of about 1.07. Very few investigations of the physical properties of pure single crystals of this metal had been made before 1950. Vernon and Weintroub⁽⁴⁾ discovered that the thermal expansion coefficient along the c-axis (tetragonal axis) is negative. In later work Graham et al. (5) extended the temperature range of the expansion measurements to show that the lattice spacing c has a maximum at about room temperature, while a increases steadily from -183° to +135°C. Measurements by Winder and Smith (6) of the single-crystal elastic constants show the shear moduli to be anomalously low. Eckert and Drickamer⁽⁷⁾, in the process of experimenting with

diffusion in indium near the melting point, obtained enough low temperature data to determine a Q of 17,900 ($\pm 5\%$) cal/mol, and a D_0 of ~ 1.02 for polycrystalline samples.

EXPERIMENTAL DETAILS

Single crystals (cylindrical, 3/8 in. diameter) were grown in a vertical furnace by allowing the molten metal to cool very slowly through the freezing point. The ingots were contained in graphite-lined pyrex tubes which had been sealed off in rough vacuum. Two grades of material from the Indium Corporation of America were used: 99.97% pure pellets and a specially refined (99.995%) ingot. Orientations were determined by back-reflection Laue X-ray patterns. Samples were mounted on 3/8 in. diameter steel slugs with Sauereisen cement in order that they might be rigidly held during such operations as machining and sectioning. The indium itself is too soft to be handled very satisfactorily without this precaution. The crystals were sawed with a jeweler's thin (00) blade

^{*} This work was supported by U.S. Atomic Energy Commission contract. Received July 16, 1958.

[†] Department of Physics, Rensselaer Polytechnic Institute, Troy, New York.

and then microtomed. The thin polycrystalline layer which remained was removed by successive treatments in Tucker's reagent⁽⁸⁾ and two etches recommended for indium.⁽⁹⁾ The final single-crystal surfaces were plated in a sulfate bath⁽¹⁰⁾ containing the radioactive isotope In 114 (half-life 49 days⁽¹¹⁾). The thickness of the plated layers was calculated to be about 1000 Å.

The diffusion runs were made in thermistor-controlled furnaces in which the temperature remained constant to within $\pm \frac{1}{2}$ °C. Mercury thermometers used for quick readings were calibrated against a National Bureau of Standards Pt–PtRh thermocouple. The samples were not sealed off in glass since the risk of damage during this process and in the subsequent opening of the capsules seemed more objectionable than the slight oxidation that might occur. Indium is quite inert and there was practically no observable change in the appearance of the samples during the diffusion periods.

The diameters of the cylindrical specimens were reduced 30 to 60 mils to remove surface diffusion effects. The sectioning was done with the microtome, each slice being about 6μ in thickness. Slices were weighed individually to ± 0.01 mg. Thicknesses were calculated from the final diameter of the sample and the weight of each section. The thin slices were mounted flat on cellophane tape and counted directly with a thin-walled Geiger tube.

1959

Several experimental problems limited the accuracy attainable with the diffusion samples. First of all, it was not easy to obtain smooth evenly etched front surfaces because of the presence in all the crystals of faint network patterns, presumably mosaic boundaries made up of dislocations at which the observed etch pits could develop. (The subgrains were of order 1 mm² in cross-section. Evidence of misorientations of $\sim_{9}^{1^{\circ}}$ between adjacent subgrains was seen occasionally in the X-ray spots.) Secondly, the front surfaces had to be extremely flat to permit a successful alignment of the sample in the microtome before sectioning. (The microtome operated in such a way that the surface of the sample was held horizontal. Alignment could then be achieved by setting on this surface a small two-way bubble level mounted on a 1/4 in, diameter steel pedestal the base of which had been carefully machined flat.) Thirdly, most of the penetration plots gave some evidence of a fast component of diffusion which was tentatively attributed to the mosaic boundaries.

RESULTS

Because of the effects just enumerated, the largest errors in the D values could not be treated as random

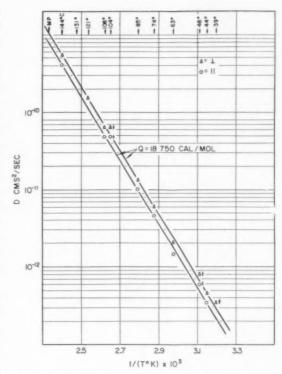


Fig. 1. Logarithm of diffusion coefficient D vs. the reciprocal of the absolute temperature ($10^3 \times 1/T^{\circ}$ K). Arrows beside data points indicate that these points should be lower, for reasons discussed in the text.

ones. Rather, the final curves in Fig. 1 were drawn by weighting heavily those results in which errors from misalignment and/or pitted front surfaces were known to be the least. Thus the arrows pointing downward (near the circles or triangles) indicate that lower diffusion coefficients would be expected for more satisfactory samples in each case. Most of the data points for diffusion in polycrystalline indium⁽⁷⁾ lie between the lines for D_{\parallel} and D_{\perp} in Fig. 1.

In Fig. 2 a set of penetration curves for the two orientations shows the effects of the fast diffusion. In general, penetration distances were from 3 to 6 mils, and the number of sections counted was from 15 to 30. For several of the plots, the initial activity was high enough that the fast-diffusion portion lay between 10 and 100 c.p.m./mg. In these cases the tails were approximately linear in x^2 . For this reason any corrections in the final D values were made on the assumption that the tails could be treated as straight lines, although this was not entirely obvious for plots in which the tails lay in the less accurate region of 1 to 10 c.p.m./mg.

The mosaic boundaries in the $D_{_{\parallel}}$ samples (in which the c-axis was necessarily perpendicular to the surface)

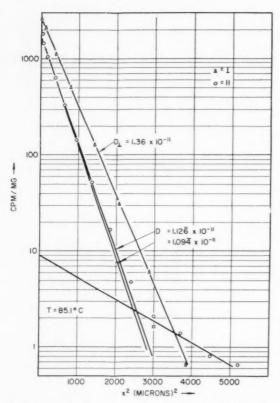


Fig. 2. Penetration curves for diffusion parallel and perpendicular to the c-axis at $T=85.1^{\circ}\mathrm{C}$. The coefficient D_{\parallel} has been corrected by about 3 per cent for the effects of fast diffusion, as shown.

nearly always showed some preferred orientation along [100] directions, while the mosaic patterns in D_1 samples were generally random networks. There seemed to be a tendency for the $D_{\scriptscriptstyle \parallel}$ samples to exhibit the larger fast-diffusion effects. It is not known whether this was significant or merely coincidental.

Consideration of the inaccuracies discussed above and the other usual sources of error inherent in the sectioning technique, as applied to tracer diffusion, leads to a final estimate that the D values are accurate to about ± 10 per cent, with misalignment errors <1 per cent. As mentioned previously, the errors in the points marked with the arrows in Fig. 1 fall outside these limits.

Since no consistent trend was found in the behavior of the ratio D_1/D_1 with temperature, it was concluded that the slopes of the two curves in Fig. 1 were roughly the same. Using the relation $D=D_0\exp{(-Q/RT)}$ one can obtain Q=18,750 cal/mol. Drawing other possible straight lines through the points, with due regard for the most reliable data, one obtains Q values between $\sim 18,300$ and $\sim 19,000$ cal/mol.

DISCUSSION

If the diffusion is assumed to take place by a vacancy mechanism then it is of interest to look at the saddle-point configurations for the two types of jump available to a diffusing atom. It could move to a neighboring vacant site in its own (001) plane (Mechanism 1). Or it could jump out of its (001) plane to a vacancy on one of eight possible equivalent sites (Mechanism 2). The distance of closest approach of the diffusing atom to the four members of the saddle configuration in Mechanism 1 is 0.643a (with no relaxation of the four atoms allowed). In comparison, the analogous distance for Mechanism 2 is 0.620a. (The average interatom distance for the equilibrium lattice is 0.725a at room temperature.) These mechanisms may be represented by the following relations:

$$D_1 = D_0(1) \exp(-Q_1/RT) \tag{1}$$

$$D_2 = D_0(2) \exp(-Q_2/RT) \tag{2}$$

The difference in saddle-point configurations will be taken to imply that the activation energy Q_2 is somewhat greater than Q_1 . Counting the number of ways a given atom can jump in a positive direction along the c-axis, or along a specified direction in a plane perpendicular to this axis, one can obtain an expression for the ratio of the diffusivities

$$\frac{D_1}{D_1} \! = \! \frac{2D_2(a/2)^2 + 2D_1(a/2)^2}{4D_2(c/2)^2} \tag{3}$$

195

where the squared quantities are weighting factors which account for the different distances involved in the jumps. Assuming, for purposes of discussion, that $D_0(1)=D_0(2),$ and using the measured value for $D_1/D_1\sim 1.33,$ one calculates that the difference Q_2-Q_1 may vary from $\sim\!440$ to 580 cal/mol in the temperature range employed in the diffusion experiment. A similar calculation for the difference Q_1-Q_1 gives values about half as large. Thus the difference between the actual values of Q_1 and Q_1 may well be within the experimental error.

One has the impression that the actual atomic motions must involve mainly shear strains since $Q_2 - Q_1$ is appreciably smaller than one would expect from a consideration of possible compressive strains for Mechanisms 1 and 2 with their different nearest-neighbor distances at the saddle-points.

A final note about the mosaic patterns may be of interest. These appeared to be about the same in crystals made from the two purities of metal purchased from the Indium Corporation of America. However, a

crystal grown by the same methods from a small ingot of 99.99+% pure indium obtained just recently from the American Smelting and Refining Company showed no sub-boundaries at all, even with intensified etching. Thus indium might be a suitable material for a critical study of the effects of impurities and substructure on diffusion in single crystals.

ACKNOWLEDGMENT

The author would like to thank Professor H. B. Huntington for suggesting the problem and for many helpful discussions on diffusion mechanisms.

VOL.

1959

REFERENCES

- 1. G. A. SHIRN, E. S. WAJDA and H. B. HUNTINGTON, Acta Met. 1, 513 (1953).
- 2. E. S. Wajda, G. A. Shirn and H. B. Huntington, Acta Met. 3, 39 (1955).
- 3. G. A. SHIRN, Acta Met. 3, 87 (1955).
- 4. E. V. VERNON and S. WEINTROUB, Proc. Phys. Soc. B 66, 887 (1953).
- 5. J. GRAHAM, A. MOORE and G. V. RAYNOR, J. Inst. Met. 84, 86 (1955).
 6. D. R. WINDER and C. S. SMITH, J. Phys. Chem. Solids 4,
- 128 (1958).
 R. E. ECKERT and H. G. DRICKAMER, J. Chem. Phys. 20,
- 13 (1952).
- 8. P. LACOMBE and L. BEAUJARD, J. Inst. Met. 74, 1 (1948). C. J. SMITHELLS, Metals Reference Book (2nd Ed.) Vol. 1. Interscience, New York (1955).
 H. B. LINFORD, Trans. Electrochem. Soc. 79, 443 (1941).
 L. GRODZINS and H. MOTZ, Phys. Rev. 102, 761 (1956).

A SIMPLIFIED DERIVATION OF THE QUASICHEMICAL APPROXIMATION IN ORDER-DISORDER THEORY*

J. M. HONIG†

A simplified procedure is presented, whereby the so-called quasichemical approximation in order-disorder theory is derived; the complexities attendant to other derivations are avoided. Following the procedure of Hijmans and de Boer, the lattice consisting of A and B units is decomposed into representative arrays of "bonds" and "points"; the energy, entropy, and free energy for this system of arrays is then found in terms of probabilities of encountering the possible configurations AA, AB, BB, B, or A. Upon proper minimization of the free energy, the quasichemical result (16) is found.

CALCUL SIMPLIFIE DE L'APPROXIMATION QUASI-CHIMIQUE DE LA THEORIE DE L'ORDRE-DESORDRE

Par une méthode simplifiée, l'auteur établit l'approximation quasi-chimique de la théorie de l'ordredésordre, évitant ainsi les aléa rencontrés dans d'autres méthodes. Suivant Hijmans et de Boer, le réseau formé d'unités A et B est décomposés en réseau de "liens" (interactions) et "points"; l'énergie, l'entropie et l'énergie libre de ce système sont alors déterminées par un calcul de probabilités de fréquence des configurations possibles AA, AB, BB, B ou A. En tenant compte du minimum d'énergie libre, l'approximation quasi-chimique est alors obtenue (16).

EINE VEREINFACHTE ABLEITUNG DER QUASICHEMISCHEN NAHERUNG DER THEORIE DER ORDNUNGSEINSTELLUNG

Ein vereinfachtes Verfahren wird vorgelegt, bei dem die sogenannte quasiehemische Näherung der Theorie der Ordnungseinstellung abgeleitet wird; dabei werden die bei anderen Ableitungen auftretenden Komplikationen vermieden. Nach dem Vorgang von Hijmans und de Boer wird das aus A und B Einheiten bestehende Gitter zerlegt in repräsentative Anordnungen von "Bindungsstrichen" und "Punkten"; die Energie, die Entropie und die freie Energie für dieses System von Anordnungen findet man dann ausgedrückt in den Wahrscheinlichkeiten, die möglichen Konfigurationen AA, AB, BB, B, oder A anzutreffen. Sucht man das Minimum der freien Energie in geeigneter Weise auf, so findet man das quasichemische Ergebnis (16).

The so-called quasichemical approximation is extensively used in mathematical analyses requiring the application of order-disorder theory for the interpretation of physical phenomena. The final result, given by equation (16) can readily be justified by heuristic arguments, but the more rigorous derivations provided to date^(1,2,3) are quite complex. The object of this publication is to present a simple method for obtaining the final expression. The procedure here is based on a series of publications by Hijmans and de Boer(3) who established a very powerful and generalized approach, from which the quasichemical result follows as a first approximation. The rather intricate procedure adopted by these writers can be avoided if one is interested only in the first order results.

THE LATTICE REPRESENTATION

As a concrete example, we shall consider a binary alloy consisting of components A and B: the methodology can be very readily extended to a collection

of spins aligned in parallel and antiparallel directions, and to other systems of a similar nature.

195

Each of the species A or B is assumed to be situated at one of the L lattice points of a perfect crystal. The approximation consists in decomposing the lattice into a set of simpler arrays, termed figure assemblies, whose statistical properties are representative of those for the solid under consideration. In introducing the quasichemical approximation, one neglects all interactions among the species save those between nearest neighbors. Consequently, the most complex representative array required for the lattice representation is the bond, which represents a pair of adjacent lattice sites, the latter often being termed points. If Z is the coordination number for the lattice, it is clear that the number of bonds obtainable by the decomposition process is (Z/2)L.

The above mentioned figure assembly also contains ZL points; since the correct number of sites in the lattice is L, it is clear that an overcount has occurred. This situation can be rectified by setting up a figure assembly consisting of (1-Z)L members. The fact that the number of constituents in the latter group

^{*} Received July 16, 1958.

[†] Department of Chemistry, Purdue University, Lafayette, Indiana.

is negative need cause no undue concern; it should be noted that the point figure assembly was set up for a corrective purpose and that the total number of sites, obtained from the two assemblies described above, is the positive quantity L.

Since each lattice site may be occupied by species A or B, it is clear that the bonds may be encountered in the configurations AA, AB or BA, and BB. Let us represent by β_0 , β_1 , β_2 the fraction of the (Z/2) L bonds in the above configurations. Similarly, let us designate by α_0 and α_1 the fraction of the (1-Z) L points in the configurations A and B.

The following interrelations are then immediately obtained:

$$\alpha_0 + \alpha_1 = 1 \tag{1}$$

$$\beta_0 + 2\beta_1 + \beta_2 = 1 \tag{2}$$

$$\alpha_1 = \beta_1 + \beta_2 \tag{3}$$

Equations (1) and (2) represent normalization conditions; these simply state that the fractional parts of the assembly, when added together, are equivalent to the entire assembly. The factor 2 in equation (2) results from the fact that the configurations AB and BA are equivalent. Equation (3) is known as consistency condition; it expresses the fact that the configuration B is encountered in the bond states BA or BB.

THE FREE ENERGY OF THE FIGURE ASSEMBLIES

The next step consists in obtaining an expression for the free energy of the bond and point figure assemblies. We define by ε_A and ε_B the energy of a point in configuration A and B respectively; likewise, ε_{AA} , ε_{AB} and ε_{BB} will represent the energies of the bond in the various indicated configurations. The total energy for the (Z/2) L bonds and (1-Z) L points is thus:

$$E = L\{(Z/2) (\beta_0 \varepsilon_{AA} + 2\beta_1 \varepsilon_{AB} + \beta_2 \varepsilon_{BB}) + (1 - Z) (\alpha_0 \varepsilon_A + \alpha_1 \varepsilon_B)\}$$
(4)

wherein each energy term is multiplied by the number of units in the corresponding configuration. The various contributions are then summed.

Next, the entropy of the system of figure assemblies will be considered. We introduce here the well known relation $S = k \ln W$, where W is the number of complexions consistent with the distribution of $(Z/2)L\beta_j$ (j=0, 1, 2) bond types among (Z/2)L bonds, and of $(1-Z)L\alpha_i$ (j=0, 1) point types among

(1-Z) L points. Thus,

$$\begin{split} S = k \ln \left\{ & \frac{(LZ/2)!}{(\beta_0 LZ/2)!(\beta_1 LZ/2)!^2 (\beta_2 LZ/2)!} \times \\ & \times \frac{(1-Z)L!}{(1-Z)\alpha_0 L!(1-Z)\alpha_1 L!} \right\} \end{split} \tag{5}$$

Since L is large, we introduce Stirling's approximation to find

$$\begin{split} S &= k \{ (ZL/2) \, \ln \, (ZL/2) - (\beta_0 ZL/2) \, \ln \, (\beta_0 ZL/2) \, - \\ &- (\beta_1 ZL) \, \ln \, (\beta_1 ZL/2) - (\beta_2 ZL/2) \, \ln \, (\beta_2 ZL/2) \, + \\ &+ (1-Z)L \, \ln \, (1-Z)L - (1-Z)\alpha_0 L \, \ln \, (1-Z)\alpha_0 L - \\ &- (1-Z)\alpha_1 L \, \ln \, (1-Z)\alpha_1 L \} \end{split} \tag{6}$$

If terms such as $\ln (\beta_j L/2)$ are now written out as $\ln L/2 + \ln \beta_j$, further cancellations occur and one is left with the simple expression

$$S = -k\{(LZ/2)(\beta_0 \ln \beta_0 + 2\beta_1 \ln \beta_1 + \beta_2 \ln \beta_2) + L(1 - Z)(\alpha_0 \ln \alpha_0 + \alpha_1 \ln \alpha_1)\}$$
(7)

The free energy expression may now readily be found by combining (4) and (7). It should be noted that the resulting equation is indicative of the properties of the figure assemblies. It is still necessary to determine the statistical properties for the lattice itself. To keep matters as simple as possible, a new assumption will now be introduced, to the effect that the free energy expression for the figure assemblies also applies to the lattice proper. This assumption shows very clearly the drastic simplification that is required to obtain the desired end result.

MINIMIZATION OF THE FREE ENERGY

To find the equilibrium value of the free energy it is necessary to minimize the appropriate expression. Before carrying out the differentiation, one must take account of the fact that the various α_j and β_j are not independent, since interrelations are provided by equations (1), (2), and (3). We shall arbitrarily select α_1 and β_2 as the independent variables and express the remaining quantities in terms of these. This leads to the relations

$$\alpha_0 = 1 - \alpha_1 \tag{8}$$

$$\beta_1 = \alpha_1 - \beta_2 \tag{9}$$

$$\beta_0 = 1 - \alpha_1 + \beta_2 \tag{10}$$

Thus, the free energy, F=E-TS will first be expressed in terms of $F(\alpha_1,\beta_2)$; subsequent minimization leads to the condition

$$\frac{\partial F}{\partial \alpha_1} \, \delta \alpha_1 + \frac{\partial F}{\partial \beta_2} \, \delta \beta_2 = 0 \eqno(11)$$

VOL. 7 1959 Since (11) is to apply for all conceivable independent variation in α_1 and β_2 , each coefficient must vanish identically. In view of (8)–(10) this leads to the two conditions.

$$\begin{split} \frac{\partial (E-TS)}{\partial \alpha_{1}} + \frac{\partial (E-TS)}{\partial \alpha_{0}} \frac{\partial \alpha_{0}}{\partial \alpha_{1}} + \frac{\partial (E-TS)}{\partial \beta_{0}} \frac{\partial \beta_{0}}{\partial \alpha_{1}} + \\ + \frac{\partial (E-TS)}{\partial \beta_{1}} \frac{\partial \beta_{1}}{\partial \alpha_{1}} = 0 \quad (12) \end{split}$$

$$\frac{\partial (E - TS)}{\partial \beta_2} + \frac{\partial (E - TS)}{\partial \beta_0} \frac{\partial \beta_0}{\partial \beta_2} + \frac{\partial (E - TS)}{\partial \beta_1} \frac{\partial \beta_1}{\partial \beta_2} = 0$$
(13)

Differentials such as $\partial \beta_0/\partial \alpha_1$ may be computed from relations (8)–(10); terms such as $\partial (E-TS)/\partial \beta_0$ are found from (4) and (7). Straightforward algebraic manipulations then lead to the following set of equilibrium conditions:

Equation (12) simplifies to

$$\begin{split} &(1-Z)[(\varepsilon_B-\varepsilon_A)+kT(\ln\,\alpha_1-\ln\,\alpha_0)] + \\ &+ Z[(\varepsilon_{AB}-\varepsilon_{AA})+kT(\ln\,\beta_1-\ln\,\beta_0)] = 0 \end{split} \label{eq:continuous} \tag{14}$$

and equation (13) results in

$$\begin{split} (Z/2)[(\varepsilon_{AA}+kT\ln\beta_0)-2(\varepsilon_{AB}+kT\ln\beta_1)+\\ +(\varepsilon_{BB}+kT\ln\beta_2)]=0 \quad (15) \end{split}$$

The last relation may be rewritten as

$$\beta_0\beta_2/\beta_1{}^2=K\quad K=\exp\left\{-(\varepsilon_{BB}+\varepsilon_{AA}-2\varepsilon_{AB})/kT\right\} \eqno(16)$$

which will immediately be recognized as one formulation of the quasichemical approximation.

CONCLUDING REMARKS

Equation (14) represents an equilibrium condition not normally encountered in elementary treatments of order–disorder phenomena. It arises from the fact that, throughout, α_1 was regarded as a variable. It is clear that this viewpoint is applicable, so long as one deals with a system such as a collection of spins, where the number of spins aligned with or against a predetermined axis is not known in advance. On the other hand, in the case of binary alloys, the composition of the material is controlled experimentally, and α_1 is therefore predetermined. In this particular case, only β_2 can be regarded as a variable. Equations (12) and (14) drop out and only equation (16) remains.

With the aid of equations (1), (2), (3) and (16) it is now possible to solve for β_1 , the result being

$$\beta_1 = \frac{-1 \pm (1 + 4(K - 1)\alpha_1 \alpha_0)^{1/2}}{2(K - 1)} \tag{17}$$

where the minus sign should be discarded in order that β_1 might remain within the limits (0, 1) as K assumes over all permissible values in the range $(0, \infty)$. The quantity β_2 may be found by using (17) in (3), and β_0 may be obtained from the normalization requirement (2).

The above indicates that the method of Hijmans and de Boer⁽³⁾ is very well suited for obtaining the well-known quasichemical results in an elementary fashion.

19!

REFERENCES

- 1. R. H. Fowler and E. A. Guggenheim, Statistical Thermo-
- dynamics. Cambridge University Press (1939).
 2. E. A. Guggenheim, Mixtures. Cambridge University
- 3. J. HIJMANS and J. DE BOER, Physica 21, 471, 485, 499 (1955)

LETTERS TO THE EDITOR

A size effect in plastic bending*

A common method that is used to test the strengths of filamentary specimens is to bend them until they deform plastically or break. It is the purpose of this note to point out that an intrinsic size effect becomes important in plastic bending when the diameter of a filament is about 1 µ or less. This size effect arises because the smallest possible plastic displacement that can be produced in a crystal is one unit lattice translation. In a uniform stress field a unit dislocation can always be moved into a crystal to such a position that the energy of the system is lowered (except for positions within a few lattice spacings from the surface). However, in the stress gradients of bent crystals this is only possible if the stress gradient exceeds a certain value which depends on the thickness of the crystal. The necessary stress gradient can be found as follows.

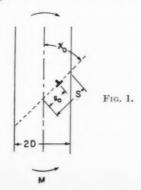
In Fig. 1, a dislocation is located at a distance s_o from the neutral plane. The shear stress on the dislocation is given by $(-s_o\tau_m/D)\sin\chi_o$ where $\tau_m=(MD/I)\sin\chi_o\cos\chi_o$; M is the applied bending moment and I is the moment of inertia of the cross-section. The shear stress along the glide plane due to the dislocation is $Kb/(s-s_o)$ where $K=G/2\pi(1-\nu)$ or $G/2\pi$ for edge and screw dislocations, respectively. G= shear modulus, b= Burgers vector, and $\nu=$ Poisson's ratio. The energy of the dislocation, E, is equal to the work done in forming it against its own stress field, minus the work done by moving the dislocation from S to $s=s_o$. That is:

VOL.

1959

$$E = \frac{Kb^2}{2} \int_{s_a+a}^S \frac{ds}{s-s_o} + \frac{-b\tau_m}{D} \sin \chi_o \int_{s_o}^S s \, ds$$

where a small region of radius a is not included in the



first integration. Thus:

$$egin{aligned} E &= rac{b au_m}{D}\sin\chi_o\left(s_o^{~2}-S^2
ight) + rac{Kb^2}{2}\lnrac{S-s_o}{a} \ &= rac{A}{D}(s_o^{~2}-S^2) + rac{Kb^2}{2}\lnrac{S-s_o}{a} \end{aligned}$$

where $A = b\tau_m \sin \chi_a$

The equilibrium position of the dislocation obtains when $dE/ds_a = 0$. That is, when:

$$(2A/D)\,s_o^{\,2} - (2AS/D)\,s_o + Kb^2/2 = 0$$

This equation for s_o has real roots only if:

$$A > (Kb^2 \sin^2 \chi_o)/D$$

So the condition for s_a to be greater than zero, that is, for plastic deformation to occur, is:

$$\tau_m > (Kb \sin \chi_o)/D$$

Since the yield stress of a crystal is usually about $G/10^4$, this condition does not become important until D is less than about 1 μ .

It is not proposed that this effect can account for the exceptional strengths that are observed for "whiskers". However, it can be an important contribution to strength for very small filaments or platelets which are tested in bending, and it should be considered in the interpretation of such tests.

J. J. GILMAN

General Electric Research Laboratory Schenectady, New York

* Received September 19, 1958.

The mechanism of dispersion hardening*

In recent years there has been a considerable interest in materials containing a finely dispersed second phase. Particularly, this interest has centered around materials in which the second phase consists of particles that are very stable at elevated temperatures, such as the refractory oxides. Some materials of this type have been found to exhibit rather remarkable high temperature mechanical properties, as well as an unusual reluctance to recrystallize.

There have been several attempts to explain the properties of these dispersion-hardened materials, but

none has been completely satisfactory to date. In general, these theories have been developed in terms of models of the interference to the movement of dislocations in the slip plane by particles of the second phase. (1–6)

Likewise, the more generally accepted theories of age hardening or precipitation hardening have been stated in terms of the strains introduced into the matrix by coherency between its lattice and that of a transition precipitate. These strains would then, presumably, interfere with dislocation motion in much the same manner as particles themselves, effectively producing a change in the parameters of the dispersion. (7) In these theories the particles are assumed to have sufficient strength that they are not deformed by the stresses in their local environment. High values of strength have been attributed to them due to their size and probable perfection. (6,8) Williams has shown that ordered precipitate particles can give rise to considerable strengthening in the absence of coherency strains or a high value of inherent strength. (9) In addition, he has shown that in cases where the strength of the precipitate is not necessarily greater than that of the matrix, some hardening can arise from the interaction of dislocations with hydrostatic stresses in the matrix. (10)

It is the purpose of this note to propose another way of looking at this problem. The essential feature of this approach is to consider the possibility that the observed effects in both age-hardened and dispersion-hardened systems are caused by the generation of dislocations, and the effective work hardening of the matrix. The change in properties is then primarily due to matrix work hardening, rather than to the interaction of dislocations with the particles or their strain fields directly.

There are several types of evidence that a considerable amount of plastic strain occurs in the matrix during age hardening, such as asterism in Laue patterns, blurring of matrix spots in Debye circles, and microscopic observation of "ripples" in the microstructure. (11–19) In addition, there is indirect evidence, such as subgrain formation, as detected by X-ray microscopy and by the breaking up of Laue spots, and the fact that many systems have been found to recrystallize as a result of precipitation. (7,11,13,20–27)

The problem then, is the identification of the mechanism by which the matrix can become strain-hardened during precipitation. It is proposed that this may be due to the generation of dislocations due to the large shear stresses that arise during the formation of a coherent transition precipitate. There is a considerable body of X-ray data on a number of

systems in which the transition precipitate has been found to exist in the form of a platelet coherent with the matrix in two dimensions, but not in three. The local strains in the matrix resulting from coherency along the planar interface can be quite large, and since the strain in the third direction is much less, the stress pattern in the vicinity of the particle will be one in which there will be a large difference between principal stresses, giving rise to a shear component, rather than being only hydrostatic in nature. Such shear stresses could then cause dislocation generation and work hardening during the process of particle formation.

The idea that slip in the matrix might be due to the stresses induced by coherency is not new, as it was presented some time ago by Geisler. (28) However, he felt that such slip would relieve some of the coherency strain and thus detract from the hardening, which he assumed to be due to the coherency strains themselves. Fisher and Hollomon (29) have also suggested that the observed hardening effects may be due to work hardening of the matrix as a result of precipitation-induced dislocation motion. According to their hypothesis, however, the driving force for dislocation glide is the free energy of precipitation, using Turnbull's model (39) of the diffusion of solute along a moving dislocation to a growing precipitate particle.

19

A different explanation must be found for the high strength of materials in which there is no coherency between the particles and the matrix, a condition that must certainly exist in many of those formed by the mixed powder processes. It is suggested that the strength of such materials may also be due to work hardening of the matrix by dislocation generation. The necessary shear stresses can arise from the fact that the thermal expansion behavior of the particles commonly employed, such as Al₂O₃ and BeO, is strongly anisotropic. If particles of such materials are embedded in a matrix of isotropic expansion characteristics, a change in temperature will cause the generation of a stress field in which there will also be a large difference between the principal stresses, and hence a large shear component.

If we assume that a particle of negligible dimensions interacts with an elastically isotropic matrix to produce principal stresses S_x , S_y , and S_z , the shear stress in any plane can be determined from the relation

$$\begin{split} S_s{}^2 &= (S_x - S_y)^2 \, \cos^2 \alpha \, \cos^2 \beta + (S_x - S_z)^2 \\ &\quad \cos^2 \alpha \, \cos^2 \gamma \, + (S_y - S_z)^2 \, \cos^2 \beta \, \cos^2 \gamma \end{split} \tag{1}$$

where S_s is the shear stress in a plane oriented at angles of α , β and γ with the x, y, and z axes, respectively.

If the stresses caused by the particle are such that S_y and S_z are equal, but different from S_x , the third term will drop out, and

$$S^2 = (S_x - S_y)^2 (\cos^2 \alpha) (\cos^2 \beta + \cos^2 \gamma).$$
 (2)

By use of the Pythagorean theorem it can be shown that

$$\cos^2 \alpha + \cos^2 \beta + \cos^2 \gamma = 1. \tag{3}$$

Equation (2) then becomes

$$S_s^2 = (S_x - S_y)^2 (\cos^2 \alpha) (1 - \cos^2 \alpha) \tag{4}$$

which will have a maximum when $\alpha = 45^{\circ}$. Under those conditions

$$S_{s,(\text{max})}^{2} = 0.25(S_{x} - S_{y})^{2}$$

or

VOL.

1959

$$S_{s(\text{max})} = 0.5(S_x - S_y).$$

In order to evaluate the quantity $(S_x - S_y)$ we may assume that we have a particle with expansion coefficients of K_x and K_y embedded in a matrix of expansion coefficient K_1 and elastic modulus E_1 .

Then S_x is approximately equal to $E_1(K_1 - K_x)\Delta T$, and $S_y \cong E_1(K_1 - K_y)\Delta T$. Therefore

$$(S_x - S_y) \cong E_1(K_y - K_x)\Delta T.$$

One might expect values of $(K_y - K_x)$ of the order of 1 to 13×10^6 per °C for various oxides. (31) If the matrix is copper, this would produce values of $S_{s(max)}$ of 9 to 117 lb/in2 per deg.

It is quite obvious that a very large temperature change is not necessary to produce stresses of the magnitude necessary to cause slip in the matrix.

It is suggested that the observed properties of dispersion-hardened materials are due to the combined effects of the dispersions in work-hardening the matrix and in affecting its annealing behavior.

Experimental work in this general area is currently being undertaken at Stanford under sponsorship of the National Science Foundation and the Office of Naval Research.

Stanford University Stanford, California R. A. Huggins

References

- 1. N. F. Mott and F. R. N. Nabarro, Proc. Phys. Soc. 52,
- N. F. MOTT, J. Inst. Met. 62, 367 (1946).
- 3. N. F. Mott and F. R. N. Nabarro, Report of a Conference on Strength of Solids, p. 1. Physical Society, London (1948).
- N. F. Mott, Imperfections in Nearly Perfect Crystals, p. 173. Wiley, New York (1952).
- 5. E. Orowan, Symposium on Internal Stresses in Metals and Alloys, p. 451. Institute of Metals (1948).
- 6. J. C. FISHER, E. W. HART and R. H. PRY, Acta Met. 1, 336 (1953).
- A. H. Geisler, Phase Transforma'ions in Solids, p. 387. Wiley, New York (1951).

- 8. W. W. Webb and W. D. Forgeng, Acta Met. 6, 462 (1958).
- 9. R. O. WILLIAMS, Acta Met. 5, 241 (1957). R. O. WILLIAMS, Acta Met. 5, 385 (1957)
- 11. C. S. BARRETT, H. F. KAISER and R. F. MEHL, Trans. Amer. Inst. Min. (Metall.) Engrs. 117, 39 (1935)
- A. GUINIER, Métaux, Corros-Usure 18, 209 (1943).
 A. GUINIER and P. JACQUET, Rev. Métall. 41, 1 (1944).
 A. G. Guy, C. S. Barrett and R. F. Mehl, Trans. Amer.
- Inst. Min. (Metall.) Engrs. 175, 216 (1948).

- A. GUINIER and P. JACQUET, Nature, Lond. 155, 695 (1945)
 M. L. V. GAYLER, Nature, Lond. 156, 333 (1945).
 M. L. V. GAYLER, J. Inst. Met. 73, 681 (1947).
 D. HARKER, Trans. ASM 32, 210 (1944).
- 19. D. HARKER and M. J. MURPHY, Trans. Amer. Inst. Min. (Metall.) Engrs. 161, 75 (1945)
- 20. C. S. Barrett, Trans. Amer. Inst. Min. (Metall.) Engrs. 161, 15 (1945).
- W. O. ALEXANDER, J. Inst. Met. 72, 681 (1946).
- 22. R. Becker and W. Doring, Ferromagnetismus. Springer, Berlin (1939).
- W. KÖSTER and A. SCHNEIDER, Z. Metallk. 29, 103 (1937) 24. A. GUINIER and P. JACQUET, C. R. Acad. Sci., Paris 217.
- 25. W. F. Cox and C. SYKES, J. Inst. Met. 66, 381 (1940).
- 26. N. AGEEW, M. HANSEN and G. SACHS, Z. Phys. 66, 350
- 27. F. W. Jones, P. Leech and C. Sykes, Proc. Roy. Soc. A181, 154, 181, 985 (1942).
- A. H. Geisler, Trans. Amer. Inst. Min. (Metall.) Engrs. 175, 238 (1948).
- J. C. FISHER and J. H. HOLLOMON, Acta Met. 3, 608 (1955).
 D. TURNBULL, Defects in Crystalline Solids. Physical
- Society, London (1955).
- R. L. Coble, Ceramic Fabrication Processes p. 213. Wiley, New York (1958).

*Received September 29, 1958.

Stacking faults in b.c.c. metals*

Stacking faults in b.e.c. metals are obtained where the dislocation $\frac{1}{2}a$ [11 $\overline{1}$] splits into partial dislocations

 $\frac{a}{6}[11\overline{1}]$ and $\frac{a}{3}[11\overline{1}]$. There are two types of stacking fault on {112} planes which may result. In Fig. 1a the atoms above the fault line have been moved by $\frac{a}{6}$ [11I] $\left(\frac{a}{3}$ [III] gives the same result. A movement

in the opposite direction $\frac{a}{6}[\overline{1}\overline{1}\overline{1}]$ or $\frac{a}{3}[\overline{1}\overline{1}\overline{1}]$ gives the type of fault discussed by Hirsch and Otte,(1) and Guentert and Warren. (2) In the type of stacking fault drawn in Figs. 1a and b the close distances produced are the same as in the type given by Hirsch and Otte. but instead of being perpendicular to the slip plane they lie at 30° to the slip plane as shown in Fig. 1b. They can therefore be relieved by shearing of neighbouring planes as well as expansion in or perpendicular to the slip plane. Fig. 2 shows the effect of spreading the fault over four planes and it can be seen that the resulting lattice outlined is approximately hexagonal. This is in fact analogous to the mechanism proposed

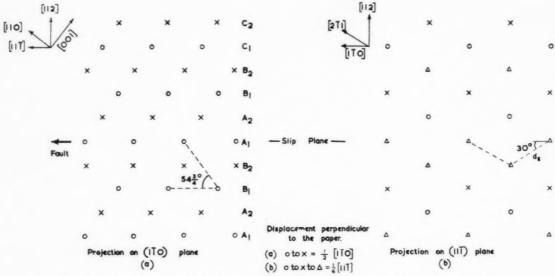


Fig. 1. Projection of atom positions on planes perpendicular to the plane of the deformation fault.

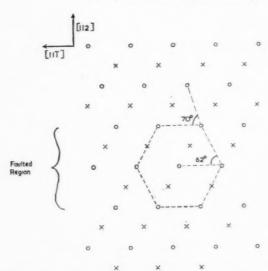


Fig. 2. Projection of atomic positions on a plane perpendicular to the plane of the deformation fault, when fault extends over four planes.

by Burgers⁽³⁾ for the transformation of β to α zirconium and titanium. It is known that cold work accelerates α formation on subsequent ageing and therefore it appears likely that this type of fault is more stable than the Hirsch and Otte type in titanium and zirconium, and aids the nucleation of α .

VO

19

The author gratefully acknowledges helpful discussion with Dr. P. B. Hirsch of the Cavendish Laboratory, and Dr. E. A. Calnan of Fulmer Research Institute.

J. M. SILCOCK

Fulmer Research Institute Stoke Poges, England Now at Liverpool University

References

- 1. P. B. Hirsch and H. M. Otte, Acta Cryst. 10, 447 (1957).
- O. J. GUENTERT and B. E. WARREN, J. Appl. Phys. 29, 40 (1958).
- W. G. Burgers, Physica's Grav 1, 561, 109 (1934).
 * Received October 1, 1958.

ERRATA

L. E. TANNER and R. MADDIN Acta Met. 7, 76-82 (1959)

In Fig. 6 on p.80, the symbols for specimens 42b and 42c should be transposed.

F. Blaha und B. Langenecker Acta Met. 7, 93-100 (1959)

Die Arbeit enthält zahlreiche Druckfehler, für welche die Autoren in keiner Weise verantwortlich sind. Die Verleger bedauern diesen Vorfall. Im besonderen sollte es auf Seite 97, 23–24 Zeile statt "...von etwa 2–3 g/mm² und als mittlere Schalldichte $\sim 10^{-8}~\rm Wsec/cm^3\ldots$ " heissen: "...von etwa 20–30 g/mm² und als mittlere Schalldichte $\sim 10^{-6}~\rm Wsec/cm^3\ldots$ "

THE MECHANICAL PROPERTIES OF IRRADIATED NIOBIUM*

M. J. MAKIN and F. J. MINTER†

The effect of heavy neutron irradiation ($\sim 10^{20}$ n cm⁻²) at 16°C on the mechanical properties of niobium has been investigated. Only a moderate increase in yield strength occurred immediately on irradiation (61,000 lb/in² to $\sim 77,000$ lb/in²) but on annealing in the temperature range $125^{\circ}-175^{\circ}$ C there was a further large increase with the formation of a yield drop at the start of the deformation. The activation energy has been measured, 1.30 ± 0.1 eV, and it is concluded that the process is due to vacancy migration, the yield drop being due to the condensation on dislocations of vacancies produced during irradiation. Recovery of irradiation hardening commences at 350°C and is complete after 1 hr at 600°C.

Technologically the most serious irradiation effect is the very large reduction in uniform elongation before fracture (17 per cent to <2.0 per cent) a consequence of a complete lack of capacity to work harden in irradiated material. Hence deformation, once started, continues in the same place until fracture occurs. The reduction in area at the fracture is quite large in the irradiated material (\sim 50 per cent c.f., 80 per cent in unirradiated niobium).

LES PROPRIETES MECANIQUES DU NIOBIUM IRRADIE

Les auteurs étudient l'influence d'une irradiation importante de neutrons $(10^{20} \text{ n cm}^{-2})$ à 16°C sur les propriétés mécaniques du niobium. Immédiatement après irradiation, seule une légère augmentation de la tension de déformation plastique est observée $(61\ 000\ \text{lb/in^2}\ \text{à}\ \sim\!77\ 000\ \text{lb/in^2})$. Après un traitement thermique entre 125° et 175°C , on constate une nouvelle augmentation importante avec la formation d'un crochet de traction au début de la déformation. L'énergie d'activation mesurée vaut $1.30\ \pm\ 0.1\ \text{eV}$; on en conclut que le processus repose sur la migration des lacunes, le crochet de traction étant provoqué par une condensation sur des dislocations de lacunes produites pendant l'irradiation. La restauration du durcissement causé par l'irradiation débute à 350°C et est totale après l'heure à 600°C .

Du point de vue technologique, l'effet le plus sérieux causé par l'irradiation est la très importante réduction de l'allongement uniforme avant rupture (17% à moins de 2,0%): conséquence d'une impossibilité totale de durcissement par écrouissage dans le métal irradié. Il en résulte que la déformation, une fois commencée, se continue au même endroit jusqu'à la rupture. La réduction de section à la rupture est très grande dans le matériau irradié (~50% de 80% dans le niobium non irradié).

DIE MECHANISCHEN EIGENSCHAFTEN VON BESTRAHLTEM NIOB

Der Einfluss starker Neutronenbestrahlung ($\sim 10^{20}$ n cm $^{-2}$) bei 16°C auf die mechanischen Eigenschaften von Niob wurde untersucht. Unmittelbar nach der Bestrahlung trat nur eine mässige Zunahme der Fliesspannung auf (von 61 000 lb/in² auf ~ 77 000 lb/in²), doch nach Wärmebehandlung im Temperaturbereich 125°–175°C ergab sieh eine weitere grosse Zunahme; dabei bildete sieh beim Verformungsbeginn eine obere Streckgrenze aus. Die Aktivierungsenergie wurde zu 1,30 \pm 0,1 eV gemessen, und man schliesst, dass der Vorgang von der Wanderung von Leerstellen herrührt; die obere Streckgrenze entsteht durch Kondensation der während der Bestrahlung erzeugten Leerstellen an Versetzungen. Die Erholung der Bestrahlungsverfestigung beginnt bei 350°C und ist nach einer Stunde bei 600°C vollständig abgelaufen.

Die technologisch schwerwiegendste Wirkung der Bestrahlung ist die sehr starke Herabsetzung der Bruchdehnung (von 17% auf <2,0%). Sie tritt auf, weil das bestrahlte Material seine Verfestigungsfähigkeit vollkommen verloren hat. Deshalb geht die Verformung, wenn sie einmal angefangen hat, an derselben Stelle weiter, bis der Bruch eintritt. Die Brucheinschnürung des bestrahlten Materials ist ziemlich gross ($\sim 50\%$ gegenüber 80% bei unbestrahltem Niob).

1. INTRODUCTION

The effect of neutron irradiation on the properties of niobium is of considerable technological interest in view of the projected use of this metal as a canning material in fast breeder reactors. The mechanical properties are of particular importance since the metal may be used structurally to restrain excessive

swelling of the fuel during irradiation. The ability of the can to do this has a vital effect on the useful life of the element and hence on the economy of the reactor.

The usual effect of neutron irradiation ($>10^{19}$ n cm²) on the mechanical properties of metals, (1-3) is to increase the yield stress and to a lesser extent the ultimate tensile strength, and to reduce the elongation to fracture. The present experiments were undertaken to determine the magnitude of these effects in

1959

^{*} Received August 26, 1958.

[†] Metallurgy Division, AERE, Harwell.

niobium and also to study the annealing characteristics of the damage; in fact, as will be described, further new and interesting effects were also observed which reveal a marked difference in behaviour between body centred and face centred cubic metals on irradiation.

2. EXPERIMENTAL METHOD

The niobium was supplied by Culcheth Laboratories in the form of annealed wire 0.040 in. diameter. The metal was prepared by a powder metallurgy process, the details of which have already been described, (4,5) and was then cold drawn to wire and annealed at 1200°C for 30 min. The greatest care was taken throughout to exclude contamination with oxygen, and the tensile results are in good agreement with previous work on material containing 0.16 wt. per cent oxygen. The grain size of the material was 0.013 mm.

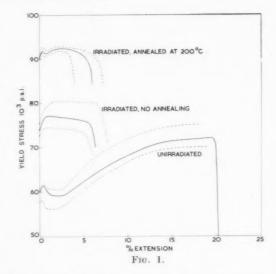
Wire specimens 3 in, long were used to minimize the induced radioactivity and also to enable a large number of specimens to be irradiated at one time under similar conditions. The irradiation was carried out at $16^{\circ}\mathrm{C}$ in the N.R.X. reactor at Chalk River to a total neutron dose of $2.3\times10^{20}\,\mathrm{n~cm^{-2}}$ with energy less than $0.6~\mathrm{eV}$ and approximately $1\times10^{20}~\mathrm{n~cm^{-2}}$ with energies greater than $0.6~\mathrm{eV}$. The proportion of fission flux (1 MeV $=10^6~\mathrm{eV}$) is high as the irradiation was carried out in a slug rod channel and was therefore close to the fuel.

Normal tensile tests were carried out in a modified Hounsfield tensometer with motor drive. The machine was mounted vertically and fitted with lead screens to protect the operators from radiation from the specimen. The stress was measured by an optical lever device with an accuracy of $\pm\,50$ lb/in² in 100,000. The strain was measured from the motion of the crosshead to within 0.01 per cent. A strain rate of 3×10^{-4} sec $^{-1}$ was used in all experiments.

EXPERIMENTAL RESULTS

3.1. Unirradiated niobium

The mechanical properties of unirradiated niobium are strongly dependent upon the oxygen content of the material as has been shown by Tottle⁽⁶⁾, and the present results, Table 1, Fig. 1, when compared with Tottle's, Table 2, suggest that the material used in this investigation contained slightly less than 0.16 wt. per cent oxygen. This conclusion is based upon the fact that the yield stress and ultimate tensile strength of the present material are slightly lower and the elongation to fracture slightly greater than



Tottle's results for niobium containing 0.16 per cent oxygen.

An appreciable yield point phenomenon is evident in unirradiated material at the start of deformation, followed by a relatively rapid rate of work hardening, and there is a considerable difference between the yield stress,* $\sim 60,000 \text{lb/in}^2$, and the ultimate strength, $\sim 73,000 \text{ lb/in}^2$. The reduction in area at the fracture is large, averaging 80 per cent.

19

3.2. Irradiated niobium

Considerable differences in behaviour are evident after irradiation, Table 1, Fig. 1. The yield strength is increased to between 74,000 lb/in2 and 77,000 lb/in2 and the yield drops observed in unirradiated material are no longer present. Instead there is rapid work hardening during the first 0.5 to 1 per cent deformation, when the maximum stress is achieved: thereafter the rate of work hardening is very small and there is a marked tendency for deformation to be localized to one region which thins rapidly until fracture. In this respect the over-all figures of the elongation to fracture in Fig. 3 and Table 1 are misleading in that measurements of the necked region in fractured specimens reveal that most of this deformation occurred locally around the fracture. In all cases the uniform elongation amounts to only 1-2 per cent but the reduction in area at the fracture is still very large, averaging 50 per cent.

3.3. Annealing behaviour

To determine the effect of heat treatment on the irradiation hardening a series of specimens were

^{*} The term "yield stress" is defined as the stress required to produce 0.2 per cent permanent deformation in the specimen.

Table 1. Tensile properties of niobium at 20°C

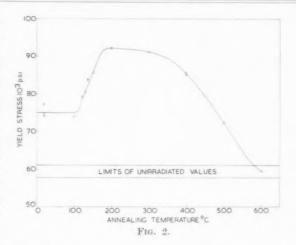
Treatment	Yield strength (0.2%) 10^3 (lb/in^2)	Ultimate tensile strength 10 ³ (lb/in ²)	% Elongation to fracture	% Reduction in area 87 79 83 48 55	
Unirradiated	57.8 57.6 60.3 61.1 60.3	68.6 70.0 75.2 72.2 73.8	21.5 19.8 19.0 21.4 21.5		
As irradiated	77.2 74.1 74.4	80.4 74.4 77.0	8.0 6.4 6.5		
Irradiated and annealed at 200°C for 60 min	92.2 92.2 91.2	92.8 92.7 91.7	6.8 7.7 4.2	47 68	

annealed at various temperatures before testing at 20°C. To prevent contamination from the atmosphere, and particularly oxygen pick-up, specimens were sealed in evacuated (10⁻⁵ mm Hg) silica tubes prior to annealing. The yield stress at 20°C as a function of annealing temperature for 60 min anneals is shown in Fig. 2 and reveals a marked increase (75,000 lb/in² to 92,000 lb/in2) which occurs in the range 100-200°C. The characteristics of the stress-strain curve are also changed, the rounded vield observed in irradiated specimens being replaced by a yield drop similar to that in unirradiated material, Fig. 1. The ultimate tensile strength is also increased on annealing but neither the over-all elongation to fracture nor the reduction in area are significantly affected, Fig. 3. It must be emphasized, however, that the great majority of the over-all elongation to fracture is accounted for by deformation near the fracture and measurements of the diameters of specimens indicate that the uniform elongation is very small indeed, (<2 per cent). In some specimens annealed at 200° or 300°C the whole of the deformation was localized to the region of the fracture, the rest of the specimen being completely undeformed to within the accuracy of the measurements (±0.2 per cent). That these

1959

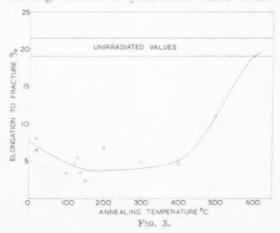
Table 2. Effect of oxygen on the tensile properties of niobium (Tottle⁽⁶⁾)

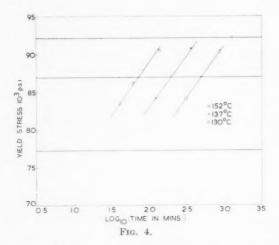
Oxygen content (wt. %)	Limit of proportionality 10 ³ (lb/in ²)	Ultimate tensile strength 10 ³ (lb/in ²)	% Elongation				
0.03	28.2	41.1	29.3				
0.161	61.2	76.4	16.9				
0.208	69.2	91.2	17.7				
0.279	77.5	99.2	20.7				
0.315	97.7	136.4	20.5				
0.371	106.2	136.6	10.4				
0.410	107.7	131.3	9.8				
0.565	Specimen crack	ed before testing					



changes on annealing were not due to oxygen contamination was proved by annealing unirradiated specimens under the same conditions, the results of which were identical with untreated unirradiated material.

The characteristics of the process responsible for the large increase in yield stress which occurs on



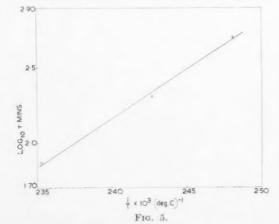


annealing between 100° and 200° C were determined by experiments in which specimens were annealed at 130° , 137° , and 152° C for various times, Fig. 4. Assuming that the process responsible for the increase obeys the usual relationship:

$$[te^{(-Q/KT)}] = \text{constant}$$

where t= time, Q= activation energy, T= absolute temperature. A value of the activation energy 1.30 ± 0.1 eV can be derived from a plot of $\ln t_{\mathrm{const}\;\sigma}$ against 1/T, Fig. 5.

Annealing for 60 min at temperatures higher than 350°C results in a decrease in the yield stress at 20°C, Fig. 3, and after 60 min at 600°C the yield stress was down to the unirradiated value. The temperature range over which recovery occurs appears to be somewhat greater in niobium (350°-600°C) than in other metals such as copper (300–400°C). Some recovery of the yield stress of irradiated niobium was evident on annealing at 400°C for 60 min but at this temperature there was no significant increase in elongation to fracture. Due to lack of specimens,



however, it was not possible to measure in detail the annealing characteristics.

The ability to completely anneal out the change in mechanical properties on irradiation demonstrates conclusively that the effects are directly due to irradiation and not to oxygen contamination in the reactor.

4. DISCUSSION

From a technological viewpoint one of the most serious effects of irradiation on niobium is the severe reduction in uniform elongation before the onset of necking and consequent fracture. In irradiated material annealed at 200°-300°C the uniform elongation was effectively zero and after fracture large regions of the specimen were completely undeformed. This behaviour is not in any way associated with brittleness of the material but is a consequence of the very low rate of work hardening after irradiation. Once deformation starts at a particular point the rate of work hardening is insufficient to compensate for the associated reduction in area so that deformation continues in this region until fracture occurs. The actual reduction in area at the fracture while not as large as in unirradiated niobium (~80 per cent) is still considerable (~50 per cent).

The behaviour of irradiated material at higher testing temperatures has not been measured and the room temperature behaviour will be modified by (1) a decrease in the yield stress and (2) a reduction in the rate of work hardening with increasing temperature. In other metals after irradiation, (2,3) however, there is in general a decrease in the uniform elongation before fracture with increasing temperature and it is therefore concluded that this behaviour of heavily irradiated niobium will persist up to temperatures where recovery of irradiation hardening occurs (>350°C).

The increase in yield stress immediately on irradiation is considerable $(60,000 \rightarrow 76,000 \text{ lb/in}^2)$ with the complete removal of the yield drop observed in unirradiated material (Fig. 1). Similar behaviour has been observed by Wilson and Billington⁽⁷⁾ in mild steel. If, as other experiments have suggested,⁽⁸⁻¹⁰⁾ irradiation hardening can be divided into two parts, (1) dislocation locking and (2) lattice hardening, then the removal of the yield drop indicates that in this case the lattice hardening (σi) predominates and exceeds the upper yield stress $(\sigma_{U.Y.S.})$. Under these conditions dislocations are generated at a lower stress than is required for their propagation through the metal

The marked increase in yield stress at 20° C after annealing between 100° and 200° C, Fig. 2, indicates

VOI 7 19

the existence of a thermally activated process in this temperature range. This process may be either an ageing process involving the redistribution of the damage responsible for the lattice hardening observed prior to annealing or it may be the migration of the irradiation produced vacancies. Of these possibilities three pieces of evidence support the hypothesis that vacancies are responsible. The limited temperature range over which the process occurs and the existence of an apparently unique activation energy strongly suggests that a single type of defect is responsible. The complex solution and precipitation phenomena in an age hardening process would not be expected to show these characteristics. In addition on annealing at 152°C the process proceeded to completion in 180 min and specimens annealed for times up to 1260 min retained the maximum yield stress. There was no sign of the softening on over-ageing normally encountered in an ageing process. Finally the occurrence of a yield drop after annealing but not before indicates that annealing has introduced dislocation locking. Again this is not in accordance with the usual behaviour of an age-hardening process. It is concluded therefore that the large increase in yield stress on annealing between 100° and 200°C is due to the migration of the vacancies produced during the irradiation and that the yield drop observed is due to the condensation of vacancies on to dislocation lines.

The observed activation energy for the process, $1.30 \, \mathrm{eV}$, and the temperature, $\sim \! 150^{\circ}\mathrm{C}$, at which it occurs are very close to the corresponding values for the recovery stage attributed to vacancies in molybdenum, namely $1.30 \, \mathrm{eV}$ at $\sim \! 150^{\circ}\mathrm{C}$. (11,12) Niobium and molybdenum have very similar melting points (2470 and 2650°C respectively) and it is possible therefore for their activation energies for vacancy migration to be almost equal.

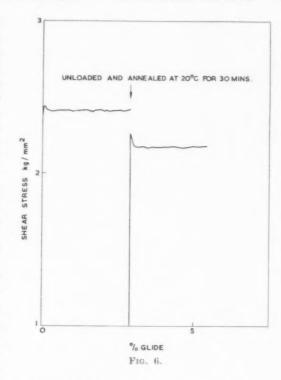
The average number of jumps made by a vacancy in niobium during this process can be calculated from the relation

$$n=v_0te^{-Q/KT}$$

where $v_0=10^{13}~{\rm sec^{-1}}$ and the other parameters have the definitions already given.

For the total increase in yield stress during the anneal the average number of jumps made by a vacancy is ~ 0.7 . This result is in agreement with Cottrell and Lomer's (13) analysis of the number of jumps in the equivalent stage in other metals after irradiation (1–100).

An increase in yield stress on annealing through the temperature range in which vacancies are thought to be mobile has also been observed in other irradiated



metals. Molybdenum⁽²⁾ after an irradiation of 5×10^{19} n cm⁻² developed a marked yield point and a small increase in flow stress after yield on annealing at 200°C which has been attributed to the condensation of vacancies onto dislocations. Similar phenomena have been observed in mild steel after irradiation.⁽¹⁴⁾ Copper single crystals⁽¹⁵⁾ irradiated at -195° C (8 \times 10¹⁷ n cm⁻²) also develop a yield point on annealing at 20°C but in this case annealing is accompanied by a 10 per cent reduction in flow stress, Fig. 6, whereas in niobium the yield stress increased by 23 per cent.

It would appear therefore that there is a distinct difference in behaviour between face centred and body centred cubic metals after irradiation, in that in face centred metals vacancies can annihilate interstitial damage whereas in body centred cubic metals this process does not occur. This conclusion is tentative, however, in view of the very great difference in irradiation doses under which the phenomena have been observed in copper on the one hand $(8 \times 10^{17} \text{ n cm}^{-2})$ and molybdenum, mild steel and niobium on the other $(1 \times 10^{19}\text{-}1 \times 10^{20} \text{ n cm}^{-2})$.

Recovery of irradiation hardening occurs in niobium in the temperature range 350–600°C during 60 min anneals (Fig. 2) with a full restoration of the elongation to fracture to the unirradiated value (Fig. 2). The activation energy for this process was not

VOL. 7 1959 measured. The wide temperature range over which it occurs, however, suggests that the process is not a simple one. This may be a consequence of the two types of hardening, dislocation locking and lattice hardening, which are believed to exist in irradiated metals.

ACKNOWLEDGMENTS

The authors wish to thank R. and D. Branch. Culcheth, for preparing the niobium wire, and Dr. A. H. Cottrell and Dr. H. M. Finniston for their advice and encouragement.

REFERENCES

1. C. R. Sutton, and D. O. Leeser, Nucleonics 12, 9 (1954).

- 2. M. J. Makin and E. Gillies, J. Inst. Met. 86, 108 (1957-8).
- M. J. Makin, J. Inst. Met. 86, 449 (1957–8).
 L. R. Williams, J. Inst. Met. 85, 385 (1956–7).
- 5. W. G. O'DRISCOLL and G. L. MILLER, J. Inst. Met. 85, 379 (1956-7).
- 6. C. R. TOTTLE, J. Inst. Met. 85, 375 (1956-7).
- 7. J. C. Wilson and D. S. Billington, Nuclear Engineering Congress, Cleveland, preprint No. 91 (1955); J. Metals 8, 665 (1956).
- M. J. Makin, Acta Met. 7, 233 (1959).
 A. T. Churchman, I. Mogford and A. H. Cottrell, Phil. Mag. 2, 1271 (1957).
- 10. A. D. WHAPHAM, Phil. Mag. 3, 103 (1958).
- 11. G. H. KINCHIN and M. W. THOMPSON, J. Nucl. Energy 6, 275 (1958).
- D. G. MARTIN, Acta Met. 5, 371 (1957).
- 13. W. M. LOMER and A. H. COTTRELL, Phil. Mag. 46, 711
- D. R. Harries, A.E.R.E. Report M/R 2536 (1958).
- 15. M. J. Makin, Acta Met. 6, 305 (1958).

FORME D'EQUILIBRE D'UN ARC DE DISLOCATION COIN EN PRESENCE D'UNE SURSATURATION DE LACUNES*

G. SAADA†

Nous étudions la forme d'un arc de dislocation en équilibre avec une sursaturation de lacunes. La méthode est voisine de celle utilisée par Burton, Cabrera et Frank pour l'étude des germes de croissance. Elle tient compte de ce que les dislocations montent hors de leur plan de glissement à l'aide de crans. Nous avons supposé les dislocations non dissociées. Avec des énergies de formation et d'interaction de crans raisonnables, nous trouvons que la forme des arcs de dislocation dépend fortement de la structure cristalline aux températures ordinaires. A très haute température $(kT\simeq 0.1~{\rm eV})$ l'arc a une forme plus circulaire. Dans tous les cas, le rayon de courbure moyen est du même ordre de grandeur que celui trouvé par Bardeen et Herring. En conclusion, nous étudions la possibilité, pour un arc de dislocation, d'engendrer des spirales.

EQUILIBRIUM SHAPE OF AN EDGE-DISLOCATION LOOP IN THE PRESENCE OF A SUPERSATURATION OF VACANCIES

The method used in this investigation is similar to that employed by Burton, Cabrera and Frank for the study of growth nuclei. It takes into account the fact that dislocations climb out of the slip plane with the aid of jogs. We have assumed undissociated dislocations. With reasonable energies of formation and interaction of these jogs, we find that the shape of the loops depends strongly on the crystalline structure at normal temperatures. At very high temperatures $(kT\simeq 0.1~{\rm eV})$ the shape of the loop approaches that of a circle. In all cases, the average radius of curvature is of the same order of magnitude as that found by Bardeen et Herring. In conclusion, we have studied the possibility for a dislocation loop to produce spirals.

GLEICHGEWICHTSFORM EINES STUFENVERSETZUNGSBOGENS BEI ÜBERSÄTTIGTER KONZENTRATION VON LEERSTELLEN

Es wird untersucht, welche Form ein Versetzungsbogen im Gleichgewicht mit einer übersättigten Konzentration von Leerstellen annimmt. Die Methode ist ähnlich der, wie sie von Burton, Cabrera und Frank beim Studium des Wachstums von Keimen benutzt wurde, Sie berücksichtigt, dass die Versetzungen mit Hilfe von Sprüngen aus ihrer Gleitebene klettern. Die Versetzungen werden dabei als nicht aufgespalten vorausgesetzt. Bei vernünftigen Annahmen über Bildungs— und Wechselwirkungsenergie der Sprünge ergibt sich, dass die Form der Bögen bei gewöhnlicher Temperatur stark von der Kristallstruktur abhängt. Bei sehr hoher Temperatur ($kT \approx 0.1 \, \mathrm{eV}$) nähert sich die Form mehr einem Kreisbogen. In allen Fällen ist der mittlere Krümmungsradius von gleicher Grössenordnung wie von Bardeen und Herring angegeben. Zum Schluss wird die Möglichkeit untersucht, dass ein Versetzungsbogen Spiralen bildet.

1. INTRODUCTION

La taille d'une boucle de dislocation coin en équilibre avec une sursaturation de lacunes a été étudiée par Bardeen et Herring. (1) Cette taille est obtenue en équilibrant l'effet de la tension de ligne qui tend à réduire la taille de la boucle par celui de la sursaturation de lacunes qui tend à l'augmenter. Herring néglige la structure atomique de la dislocation; il suppose que la ligne de dislocation peut prendre n'importe quelle orientation cristallographique, et sa tension de ligne ne dépend pas de cette orientation. La boucle de dislocation a, dans ces conditions, une forme circulaire. Weertman⁽²⁾ a montré récemment qu'une boucle de dislocation partiellement vis prend,

dans les mêmes conditions, une allure en hélice dont la projection parallèlement au vecteur de Burgers est le cercle calculé par Herring. Ces considérations ont été utilisées pour interpréter les familles de boucles et de spirales de dislocations, après certains traitements, dans les solides ioniques et le silicium.⁽³⁾

Cet article a pour but d'étudier dans quelles conditions la structure atomique du cristal peut influer sur la forme des boucles de dislocations.

Nous nous bornons à étudier l'équilibre d'un arc de dislocation coin dans un plan (001) d'un cristal cubique simple en présence d'une sursaturation de lacunes et en l'absence de tout autre défaut ou contrainte extérieure.

Nous supposerons que la ligne de dislocation est est spécialement stable dans les plans (100) et (010); elle ne peut alors monter que dans le plan (001) à l'aide de crans.

^{*} Reçule 8 Juillet, 1958.

[†] Centre de Recherches Métallurgiques, de l'Ecole des Mines de Paris.

VOI 7 195

2. METHODE DE CALCUL

Pour étudier la forme d'équilibre, nous employons une méthode analogue à celle qu'ont utilisé Burton et al. (4) dans l'étude des phénomènes de croissance.

2.1—Définition des crans d'ordre r

Soient dans un plan (001) deux axes Ox et Oy parallèles aux axes cristallographiques [100] et [010] et une ligne de dislocation coin parallèle à Ox (Fig. 1). On prendra comme unité la distance interatomique et on appelle cran positif d'ordre r sur cette dislocation un cran tel que y augmente de r unités au passage de la dislocation en ce point lorsqu'on se déplace vers les x positifs. On définit de même des crans négatifs d'ordre r.

On pose:

q(x) = probabilité pour qu'il n'y ait pas de crans au point d'abcisse x.

 $n_{+r}(x) =$ probabilité pour qu'il y ait un cran positif d'ordre r.

 $n_{-r}(x) =$ probabilité pour qu'il y ait un cran négatif d'ordre r.

$$g_{+r}(x) = n_{+r}(x)/q(x)$$
 $g_{-r}(x) = n_{-r}(x)/q(x)$

et, pour des raisons de commodité,

$$n_{+1}(x) = n_{+}(x), \quad n_{-1}(x) = n_{-}(x),$$

 $g_{+1}(x) = g_{+}(x), \quad g_{-1}(x) = g_{-}(x).$

2.2—Hypothèses simplificatrices

Les formules que nous allons développer ne sont qu'approximativement valables. Les hypothèses que nous allons faire ne modifient guère les conclusions générales, mais simplifient beaucoup les calculs. Ce sont les suivantes:

(a) Nous négligeons les interactions à distance (élastiques, électriques) entre les lacunes et les dislocations. Celles-ci ne font que modifier un peu la sursaturation en lacunes. Dans les cristaux ioniques,

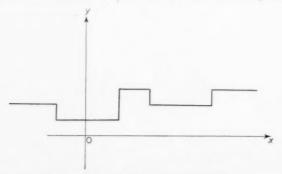


Fig. 1. Ligne de dislocation avec crans.

elles empêcheraient certaines configurations de la dislocation, dont la charge électrostatique serait trop forte.

(b) A cette remarque près, les calculs que nous allons développer s'appliqueraient dans leur principe aux solides ioniques, à la condition que les lacunes d'ions des deux signes soient mobiles et dans le même état de sursaturation, c'est-à-dire à des températures relativement élevées. Les constantes du problème seront cependant évaluées ici pour un métal.

(c) Nous négligeons l'interaction des crans à des distances grandes vis à vis de leur taille. Nous supposerons aussi constante et indépendante de la taille l de la boucle la partie de la tension de ligne qui est due aux distorsions à grande distances. On sait qu'en fait cette partie croit comme ln l. Les tailles l que nous calculerons seront, de ce fait, un peu trop grandes. La comparaison avec les résultats de Bardeen et Herring⁽¹⁾ montrera cependant que l'erreur faite ainsi est assez faible.

(d) Nous négligeons certaines configurations (Figs. 2 et 3) qui sont assez rares et se produisent essentiellement sur des arcs de dislocation parallèles aux directions [110] et [110] pour celles du type de la figure 3. La "rugosité" que nous calculerons sera, de ce fait, un peu trop faible. Les formules que nous donnerons ne donneront en particulier qu'une limite inférieure de la concentration des crans.

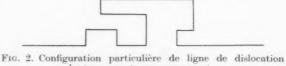
(e) Nous admettrons que la concentration en lacunes au voisinage de la boucle est constante. Les conditions dans lesquelles cette supposition est valable sont indiquées par Bardeen et Herring.⁽¹⁾

2.3—Etablissement de diverses formules reliant $g_{+r}(x)$, $g_{-r}(x)$, q(x) et la sursaturation en lacunes

Soient N la concentration atomique en lacunes, U_{fl} leur énergie de formation et leur sursaturation définie par

$$N = \alpha \exp\left(-U_{tl}/kT\right)$$

La température absolue T est supposée uniforme dans le cristal. Appliquons le principe du bilan détaillé aux configurations des figures (4a) et (4b).



dont nous ne tenons pas compte.

Fig. 3. Configuration particulière de ligne de dislocation dont nous ne tenons pas compte.

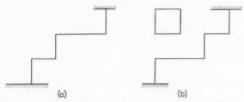


Fig. 4a, 4b. Application du principe du bilan détaillé.

Pour passer de (4a) à (4b), il faut fournir l'énergie $U_{fl},$ d'où

$$\alpha g_{+}(x+1) = g_{+}(x) \tag{1}$$

$$g_{-}(x+1) = \alpha g_{-}(x)$$
 (1')

Soit φ l'énergie à fournir pour passer de la configuration de la figure (5b) à celle de (5a). Posons $\eta=\exp{(-\varphi/2kT)}$. L'application du principe du bilan détaillé donne alors

$$\eta^2 g_+(x) = g_+(x-1) g_-(x) g_+(x+1)$$
 (2)



Fig. 5a, 5b. Application du principe du bilan détaillé.

Comme les configurations des figures (6a) et (6b) sont de même énergie, il vient de même

$$g_{+r}(x) g_{+}(x+2) = g_{+(r-1)}(x) g_{+2}(x+1)$$
 (3)

Enfin soit φ' l'énergie nécessaire pour passer de la configuration de la figure (7a) à celle de (7b). Il vient alors:

$$\eta'^2 g_+(x)g_+(x+2) = g_{+2}(x+1)$$
 (4)

avec

VOL.

1959

$$\eta' = \exp{(-\varphi'/2kT)}$$

De (3) et (4) nous tirons

$$g_{+r}(x) = \{g_{+}(x)\}^{r} \eta^{\prime 2(r-1)}$$
 (5)

et, par symétrie

$$g_{-r}(x) = \{g_{-}(x)\}^r \eta'^{2(r-1)} \tag{5'}$$

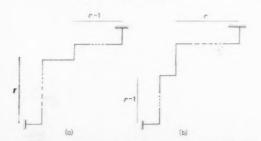


Fig. 6a, 6b. Application du principe du bilan détaillé.

Pour r=2, (4) et (5) nous donnent

$$\{g_+(x)\}^2 = g_+(x-1)g_+(x+1)$$
 (6)

De (6) et (2), nous tirons

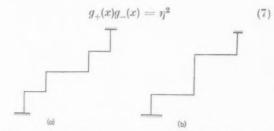


Fig. 7a, 7b. Application du principe du bilan détaillé.

De (6), nous tirons

$$g_{+}(x) = g_{+}(0) \exp(cx)$$
 (8)

où $g_+(0)$ est une constante et c une fonction de α . De (8) et (1), nous tirons

$$g_{+}(x) = g_{+}(0)\alpha^{-x}$$
 (9)

et son équivalent

$$g_{-}(x) = g_{-}(0)\alpha^x \tag{9'}$$

2.4—Calcul de q et q'

2.4.1—Considérons la ligne brisée de dislocation de la figure 8, formée de 2m segments de longueur b.



Fig. 8. Dislocation d'axe x'x à crans très rapprochés,

Appelons U_r l'énergie d'un segment rectiligne de dislocation de longueur rb. L'énergie W de la ligne de dislocation est alors:

$$W = 2mU_1 + (\mu b^3 m/4\pi K) \ln (R/\rho)$$

R et ρ sont les rayons de deux cylindres d'axe xx' tels que:

- (a) Pour tout point du cristal situé à une distance de x'x supérieure à R, la déformation élastique totale due à l'ensemble de la dislocation soit nulle.
- (b) La zone de cristal dans laquelle les segments de dislocations interagissent soit tout entière à une distance inférieure ou égale à ρ .

2.4.2—Calcul de φ . Nous supposons pour ce calcul que le vecteur de Burgers de la dislocation étudiée a pour grandeur une distance interatomique.

Considérons les configurations des figures (4a) et (4b). Nous pouvons prendre pour

(4a)
$$m \simeq 4.5$$
 et $\rho \simeq 2$

(4b)
$$m \simeq 4.5$$
 et $\rho \simeq 1$

VOI 7 195

Soient W_a et W_b les énergies respectives des configurations des figures (4a) et (4b). Nous avons

$$\begin{split} W_a &\simeq 3U_1 + 2U_2 + (\mu b^3/4\pi K) 4,5 \ln{(R/2)} \\ W_b &\simeq 9U_1 + (\mu b^3/4\pi K) 4,5 \ln{R} \\ \varphi &= W_b - W_a \simeq 6U_1 - 2U_2 + (4,5\mu b^3/4\pi K) \ln{l} \end{split}$$

Nous prendrons pour U_* la valeur

$$U_r = (\mu b^3 r/4\pi K) \ln 2r$$

qui est raisonnable pour des dislocations peu dissociées. (5) Pour les solides usuels, $\mu b^3/4\pi K \simeq 0.5$ eV. Nous avons donc

$$\varphi \simeq 1.1 \text{ eV}$$
 (10)

2.4.3—Calcul de φ' . On montre de même que φ' est donné par

$$\varphi' = 2U_2 - 4U_1 + (5\mu b^3/4\pi K) \ln 2 \simeq 1.6 \; \mathrm{eV} \; \; (11)$$

On utilisera parfois dans la suite du calcul pour des raisons de simplicité le facteur n défini par

$$\varphi' = n\varphi$$
 (12)

ou $\eta' = \eta^n$.

Les valeurs (10) et (11) donnent

$$n = 1.6/1.1 = 1.45$$
 (13)

2.4.4—Remarque. Les énergies φ et φ' sont calculées de façon très grossière. Nous montrerons plus loin que ceci n'a pas une grande importance.

3. FORMULES GENERALES DONNANT LA FORME D'EQUILIBRE D'UN ARC DE EN PRESENCE DE LACUNES

Nous pouvons écrire entre les q et les n une relation de normalisation:

$$q(x) + \sum_{r=1}^{r=\infty} \{n_{+r}(x) + n_{-r}(x)\} = 1$$
 (14)

Posons
$$\sum_{+} (x) = \sum_{r=1}^{r=\infty} g_{+r}(x), \quad \sum_{-} (x) = \sum_{r=1}^{r=\infty} g_{-r}(x)$$

(14) s'écrit alors:

$$q(x) = 1/\{1 + \sum_{x} (x) + \sum_{x} (x)\}$$
 (15)

Et d'après (5) et (5'):

$$\sum (x) = g_{-}(x)/\{1 - g_{+}(x)\eta'^{2}\}$$
 (16)

$$\sum (x) = g_{-}(x)/\{1 - g_{-}(x)\eta'^{2}\}$$
 (17)

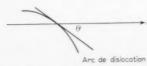


Fig. 9. Are de dislocation coupant Ox sous l'angle O.

Pour étudier la forme de la courbe d'équilibre, nous poserons (cf. Fig. 9)

$$dy/dx = h(x) = \operatorname{tg} \theta$$

Avec:

$$h(x) = \sum_{r=1}^{r=\infty} rq(x) \{g_{+r}(x) - g_{-r}(x)\}$$
 (18)

4. EQUILIBRE D'UNE BOUCLE DE DISLOCATION EN PRESENCE D'UNE SURATURATION DE LACUNES

4.1—Equations de la boucles

La boucle à l'équilibre, représentée figure 10, a

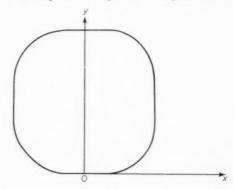


Fig. 10. Forme schématique d'équilibre de la boucle de dislocation.

les mêmes symétries que le réseau carré du plan (001). Nous prenons donc comme origine un point situé sur un axe de symétrie de la boucle.

Alors $g_+(0)=g_-(0)=\eta$ $g_+(x)=\eta \alpha^{-x} \qquad g_-(x)=\eta \alpha^{+x}$

$$q(x) = \frac{1 + \eta^2 \eta'^4 - \eta^2 \eta'^2 (\alpha^x + \alpha^{-x})}{1 - \eta^2 \eta'^2 (2 - \eta'^2) + (1 - \eta'^2) \eta (\alpha^x + \alpha^{-x})}$$
(19)

$$h(x) = \eta \, q(x) \left\{ \frac{\alpha^x}{(1 - \eta'^2 \eta \alpha^x)^2} - \frac{\alpha^{-x}}{(1 - \eta'^2 \eta \alpha^{-x})^2} \right\} \quad (20)$$

Pour $x=1=(2\varphi'+\varphi)/2kT\ln\alpha$, h(x) est infini. Le diamètre de la boucle est donc:

$$2l = \frac{1}{\ln \alpha} \frac{2\varphi' + \varphi}{2kT} = \frac{(2n+1)\varphi}{2kT \ln \alpha}$$
 (21)

4.2—Taille de la boucle

Nous pouvons faire quelques remarques sur la formule (21):

- (a) Le rayon l de la boucle est indépendant de l'énergie de formation des lacunes $U_{\mathcal{U}}$.
- (b) l est une fonction décroissante de la sursaturation α .

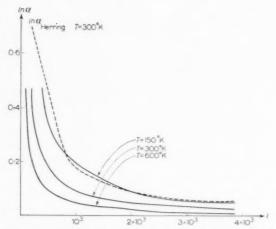


Fig. 11. Courbes indiquant la variation de la sursaturation α en fonction du rayon l de la boucle. En pointillés: résultats de Bardeen et Herring à 300°K. En traits pleins: application de la formule (21) à T=150°K, 300°K, 600°K.

(c) Si l'on remplace α dans (20), par sa valeur calculée dans (21), on voit que la forme de la courbe ne dépend pas de la sursaturation.

(d) Le calcul de Bardeen et Herring⁽¹⁾ donne:

$$l = \frac{\mu b^3}{4\pi K kT} \frac{\ln 4l}{\ln \alpha} \tag{22}$$

Les courbes de la figure 11 donnent la variation/de l en fonction de α

1959

—d'après la formule (22) à $T=300^{\circ}{\rm K}$ (courbe ponctuée)

—d'après la formule (21) à T = 600°K, 300°K, 150°K (courbes continues).

On voit que, pour une valeur de l donnée, la valeur de α prévue par Bardeen et Herring est un peu supérieure à la valeur calculée par la formule (21).

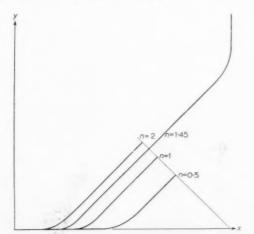


Fig. 12. Ares de boucle de dislocation à l'équilibre pour diverses valeurs de $n=\varphi'/\varphi$.

4.3—Forme de la boucle Γ

4.3.1—Formules approchées. Posons x/l = u et examinons ce que deviennent les formules (19) et (20) lorsque remplaçons α par sa valeur calculée dans (21).

A cause de la symétrie de la boucle, il sera suffisant de faire varier n de 0 à une valeur peu supérieure à $2^{-\frac{1}{2}}$ et en tous cas nettement inférieure à l'unité. Nous avons vu d'autre part que le rapport n est voisin de l'unité. Nous pouvons écrire dans ces conditions:*

$$q(u) \sim 1/\{1 + \eta^{1-(2n+1)u}\}\ h(u) \sim \{\eta^{1-(2n+1)u}\}/\{1 + \eta^{1-(2n+1)u}\}\ y(u) = \int_0^u h(\xi) d\xi \simeq \frac{2kT}{(2n+1)\varphi} \ln \frac{1 + \eta^{1-(2n+1)u}}{1 + \eta}$$

4.3.2—Etude à la température ambiante. On a alors

$$y \simeq \frac{1}{85.8} \ln \frac{1 + \exp(85.8u - 22)}{1 + \exp(-22)}$$

Nous avons représenté sur les courbes de la figure 12, un quart de la boucle Γ —le reste pouvant se déterminer aisément par symétrie—et les diverses courbes obtenues en faisant varier n, pour φ constant.

Précisons les résultats précédents.

Soit u_o l'abcisse du point d'intersection de Γ avec la parallèle à la bissectrice des axes [1 $\overline{10}$] passant par le centre de symétrie de Γ . On voit que u_o est toujours inférieur à 0,9 ce qui justifie l'approximation faite au paragraphe précédent. Nous avons représenté sur

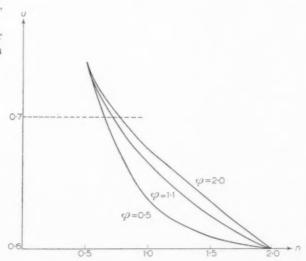


Fig. 13. Courbes donnant la variation de u_o défini au § 4.3.2. en fonction de n et φ . En pointillé, valeur de u_o correspondant à l'cercle.

^{*} De façon plus précise, ces approximations sont valables pour 0 < u < 0.9 et 0.6 < n < 3.

VOI 7 195

les courbes de la figure 13 la variation de u_o lorsque n et φ varient entre 0,5 et 2. En pointillé, nous avons représenté la valeur que prendrait u_o pour un cercle C de même centre et de même diamètre que Γ . Le courbe est assez voisine d'un cercle à hauta température. De plus u_o varie assez peu lorsque u et φ varient dans de larges intervalles. Ceci justifie la remarque (2.4.4).

4.3.3—Variation de la forme de la courbe avec la température. Nous avons traçé les courbes de la figure 14:

—en pointillé, un arc du cercle C

—en trait plein, les arcs des courbes Γ correspondant à $\varphi=1.1~{\rm eV}~n=1.45~kT=0.0025~{\rm eV},$ $0.025~{\rm eV}$ et $0.1~{\rm eV}.$

La courbe $kT=0.0025\,\mathrm{eV}$ est confondue avec la courbe $kT=0.025\,\mathrm{eV}$, ce qui implique que la courbe ne se modifie pas beaucoup lorsque la température descend au-dessous de l'ambiante.

Par contre pour kT=0.1 eV, c'est-à-dire à forte température le contour s'est adouci de façon très sensible et ressemble beaucoup plus au cercle de Bardeen et Herring.

Ces conclusions doivent être assez générales: les boucles formées à haute température et bloquées à ce moment par des impuretés doivent avoir une forme assez voisine du cercle. C'est bien le cas des expériences de Amelinckx et de Dash. Des boucles formées à plus basses températures, et en particulier a l'ambiante, ou audessous, doivent avoir des contours polygonaux. Ce semble parfois le cas des boucles observées au microscope électronique par Smallman sur l'aluminium trempé. (6)

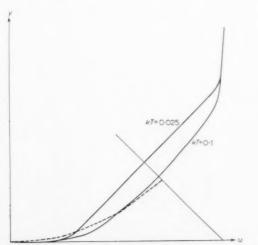


Fig. 14. Arc de dislocation à l'équilibre pour diverses températures. En pointillé, arc de cercle de même diamètre que la boucle.

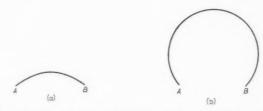


Fig. 15a et b. Forme d'équilibre d'arcs de dislocations passant par 2 points A et B tels que AB soit parallèle à un axe [010].

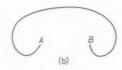
Fig. 15a. Equilibre stable.Fig. 15b. Equilibre instable.

5. ARCS DE DISLOCATION PASSANT PAR 2 POINTS A ET B

5.1—A et B sont un axe [010] ou [100]

5.1.1—AB < 2l. L'arc de dislocation peut prendre les deux positions de la figure 15. Pour passer de 15(a) stable à 15(b) instable, il faudrait fournir une certaine énergie d'activation.





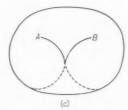


Fig. 16a, b, c. Boucles engendrées par l'arc de dislocation sous l'action de la sursaturation. AB est parallèle à [010].

5.1.2—AB>2l. L'arc va se développer suivant le processus de la figure 16, c'est-à-dire spiraler et engendrer des boucles. Remarquons que si AB>4l, on aura plutôt un phénomène analogue à celui de la figure 17, c'est-à-dire la que dislocation va contourner les points d'ancrage avant de produire des boucles. Dans les deux cas précédents, les boucles, une fois créées vont diffuser vers la surface.

5.2—Les points A et B ne sont pas sur un axe [010]

Si les points sont à une distance l'un de l'autre inférieure à une valeur d qui dépend de l'orientation de AB et qui est de l'ordre de $(2l/\cos\beta)$, β étant

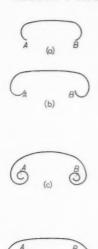


Fig. 17 a, b, c, d. Spirales engendrées par l'are de dislocation sous l'action de la sursaturation. AB est parallèle à [010].

l'angle de AB avec [010] (voir figure 18). On est ramené au cas 5.1.1, toutes choses égales d'ailleurs. (Fig. 8).

VOL.

1959

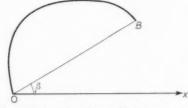


Fig. 18. Forme d'équilibre d'arcs de dislocation passant par 2 points A et B tels que AB fasse un angle φ avec [010].

Si les points sont à une distance supérieure à d, on assiste à un phénomène de spirale dans lequel la spirale s'enroule autour d'un seul des deux points. Voir figure 19.

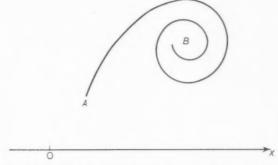


Fig. 19. Spirales engendrées par l'arc de dislocation sous l'action de la sursaturation. AB fait un angle avec [010].

6. REMARQUES

Sous les réserves faites précédemment, ce modèle permet moyennant des approximations simples de retrouver les résultats classiques de la montée des dislocations.

Les points d'ancrage sont vraisemblablement des sources de lacunes, ce qui augmente encore l'effet de spirale.

REMERCIEMENTS

Je tiens ici à exprimer mes remerciements à Monsieur Jacques Friedel qui m'a proposé cette étude pour les nombreux conseils qu'il a bien voulu me prodiguer tout au long de mon travail.

REFERENCES

- 1. J. Bardeen et C. Herring, Imperfections in Nearly Perfect
- J. Bardeen et C. Herring, Imperfections in Nearly Perfect Crystals. p. 275. New York (1952).
 Weertman, Helical Dislocations, Naval Research Labora-tory, Washington D.C., NRL Report 4979.
 S. Amelinckx, W. Bontinck, W. Dekeyser et F. Seitz, Phil. Mag. 2, 355 (1957); W. Bontinck et S. Amelinckx, Ibid 2, 94 (1957); W. C. Dash, Evidence of dislocation loss in deformed silicon. I. Appel Phys. 99 (4) (April 1967). jogs in deformed silicon, J. Appl. Phys. 29, (4) (April 1958)
- 4. W. K. Burton, N. Cabrera et F. C. Frank, The growth of crystals on the equilibrium structure of their surfaces *Phil. Trans.* **243,** A, (1950–51) 299 à 358.
- 5. J. FRIEDEL, Les Dislocations. Gauthiers-Villars, Paris
- 6. R. SMALLMAN, à paraître.

CREEP PROCESSES IN POLYCRYSTALLINE ALUMINIUM*

W. A. RACHINGER†

Plastic deformation of a polycrystalline aggregate is due to one or both of two processes, namely, grain deformation and grain sliding. It is shown that in aluminium slowly extended at 300°C the surface of the specimen deforms by grain elongation whilst the interior deforms by grain sliding. This difference in behaviour underlines the danger of assuming surface observations typical of the interior.

MECANISMES DE FLUAGE DANS L'ALUMINIUM POLYCRISTALLIN

La déformation plastique d'un agrégat polycristallin est dû à l'un ou l'autre des deux mécanismes suivants: déformation du grain ou glissement du grain.

L'auteur montre que dans l'aluminium étiré lentement à 300°C, la surface de l'échantillon se déforme par allongement des grains tandis que l'intérieur se déforme par glissement.

Cette différence de comportement montre le danger qu'il y a à interpréter les observations superficielles pour en déduire le comportement interne de l'agrégat.

KRIECHPROZESSE IN POLYKRISTALLINEM ALUMINIUM

Bei der plastischen Verformung von polykristallinem Material sind zwei Prozesse—einzeln oder zusammen—beteiligt, nämlich Kornverformung und Korngleitung. Es wird gezeigt, dass bei langsamer Dehnung von Aluminium bei 300°C die Probenoberfläche sich durch plastische Verlängerung der Körner verformt, das Innere dagegen durch Gleiten der Körner. Dieser Unterschied im Verhalten unterstreicht, wie gefährlich es ist, Oberflächenbeobachtungen als typisch für das Innere anzusehen.

1. INTRODUCTION

Some years ago it was shown that, during the slow deformation of polycrystalline aluminium at high temperatures, the grains in the centre of the specimen remained essentially equiaxed even though the specimen had been elongated by as much as 50 per cent. (1) Under these same conditions the surface grains elongated considerably. The grain elongation decreased with increasing distance below the surface and at a distance of two grain diameters it reached the small value characteristic of the interior of the specimen.

The equiaxed nature of the interior grains has two possible interpretations:

(a) The predominant mechanism of deformation in the interior is grain boundary sliding. The change in specimen shape is produced by the grains sliding over each other with attendant grain boundary migration, the grains, on the average, remaining unchanged in shape.

(b) The interior grains elongate by slip movements but, under the action of tension forces in the boundaries, grain boundary migration causes a return to equiaxed shape.

Certain indirect evidence cited in the paper⁽¹⁾ supported the first of these possibilities. If this is correct, the results indicate quite clearly that the surface grains deform by a mechanism which is not representative of the specimen as a whole. This is a most important point since observations on the nature

of creep processes are generally made at the specimen surface.

On the other hand McLean⁽²⁾ has suggested that the second interpretation (b) may be correct and that the deformation mechanism is the same at the surface as in the interior. The difference in final grain shape is attributed to the ability of the boundary tension forces to cause "rounding-off" of the grains in the interior.

195

One may distinguish between these two hypotheses by slowly deforming an elongated grain structure at elevated temperature. If (a) is correct the grain elongation would remain unchanged, whilst if (b) is correct the grains should revert to equiaxed shape. It is of course necessary that no recrystallization or large scale grain growth should take place during the test. For this reason the elongated grain structure must be produced either by rapid deformation at elevated temperature prior to slow straining or by incremental rapid straining during the slow straining test.

EXPERIMENTAL METHODS AND RESULTS

The material used was aluminium of 99.99% purity subjected to severe forging to achieve fineness and uniformity of grain size on recrystallization after the final rolling. Tensile specimens of 2 in. gauge length and cross-section 0.3×0.2 in. were tested in a Polanyi type machine. All tests were carried out at 300°C at either the slow rate of 0.16 per cent elongation/hr or the rapid rate of 10 per cent/min. The grain elongations were measured by the grain counting technique used previously. (1) After straining, the specimen was sectioned, electropolished and the numbers of grains per unit length in both the

^{*} Received July 28, 1958.

[†] Australian Defence Scientific Service (Aeronautical Research Laboratories, Dept. of Supply, Melbourne, Australia).

longitudinal and transverse directions were measured. From these the grain elongation was calculated, its accuracy being determined by statistical methods.

Three types of experiment were carried out:

1. Slow straining at 300°C of a specimen initially in the equiaxed and recrystallized condition

Since the material used was of a slightly different purity to that used in the earlier work it was necessary to check the earlier observations. A specimen of grain size 14.8 grains/mm was slowly extended by 50 per cent at 300°C, and grain counts were then made just below the surface and also on a central section. The 95 per cent confidence ranges of the grain elongation at 0.003 in, below the surface and at the centre were respectively 23 + 6 and 6 + 6 per cent. This was in good agreement with the earlier observations.

2. Slow straining and intermediate rapid strainings of an equiaxed specimen at 300°C

The purpose of this experiment was to see whether it was possible to maintain an elongated grain structure under conditions of slow deformation at 300°C. and thus test the validity of hypotheses (a) and (b).

An annealed tensile specimen having equiaxed grains of size 16.2 grains/mm was slow strained at 300°C with 12 rapid strainings, each of approximately 4 per cent, being given during the test. On completion of the test the total elongation was 62 per cent, 15 per cent of this being due to slow straining and 47 per cent to rapid straining. Rapid straining at 300°C is known to produce grain elongation. (1) The measured grain elongation on a central section was 51 + 8 per cent, which is in good agreement with the 47 per cent which would be expected on the basis of hypothesis (a).

1959

This experiment with intermediate rapid straining was considered a fairer test of the hypotheses than one in which a specimen, initially heavily deformed, was slow strained. Here it could be objected that grain boundary migration may be inhibited by internal derangements produced by the heavy deformation. This would not be expected in the present case since Wood and Suiter(3) have shown that for moderate pre-strains (of the order of 10 per cent), a polycrystal would revert, during slow deformation, to an equilibrium sub-structure dependent only on the rate and temperature of deformation. This may also be true of larger deformations, but it is not proven. Thus, in the present experiment the specimen was allowed to recover, between successive rapid strainings, to the state characteristic of slow deformation at 300°C. It was in fact found that the sub-structure

in this specimen was identical with that observed in the annealed specimen which had been slow strained at 300°C. Thus there is no reason to suspect that boundary migration processes should be inhibited in one case and not in the other.

3. Slow straining at 300°C of an elongated grain structure produced by rolling

This experiment, although open to the objections cited in the previous section, was carried out to show how a heavily elongated grain structure can be maintained under slow straining at 300°C.

It was found that hot rolling at 500°C produced greatly elongated grains which did not recrystallize on testing at 300°C. A tensile specimen cut longitudinally from this hot-rolled strip was slow strained 16 per cent at 300°C. It was then sectioned on a plane parallel to the rolling direction and perpendicular to the rolling plane. Grains viewed in this section present the greatest length-width ratio. The measured value of this ratio after slow straining was 2.5-3.0, the range of values being the 95 per cent confidence range. The corresponding ratio for the as-rolled strip was 2.8-3.4. Thus, in accord with hypothesis (a) the elongated grains have been little affected by the slow straining. If hypothesis (b) were true the length-width ratio for the slowly deformed specimen would be unity.

The sub-structure, as observed microscopically, in the hot-rolled specimen after slow straining was identical with that produced in the other experiments. It seems, therefore, that even an initial heavy deformation would have no inhibiting effect on subsequent boundary migration.

DISCUSSION

The results indicate quite clearly that, under the experimental conditions used, grain sliding is the predominant deformation process in the specimen interior. However, grain deformation is of considerable importance at the specimen surface. The assumption that measurements made at the specimen surface are typical of the specimen as a whole is, for these experimental conditions, fallacious and, in general, open to doubt.

ACKNOWLEDGMENTS

The author wishes to thank the Chief Scientist. Australian Defence Scientific Service, Department of Supply, Melbourne, Australia, for permission to publish.

REFERENCES

- W. A. RACHINGER, J. Inst. Met. 81, 33 (1952).
- D. McLean, Grain Boundaries in Metals. Oxford (1957).
 W. A. Wood and J. W. Suiter, J. Inst. Met. 80, 501 (1952).

THEORY OF ORDER IN TERNARY ALLOYS-II*

K. F. WOJCIECHOWSKI†

A statistical theory of the order–disorder transformations for ternary alloys of arbitrary composition and crystal structure is given. Long-range and short-range order parameters are defined, and equations connecting these parameters are given. The general formula for configurational free energy is deduced and the method of calculation of the order–disorder transition temperature is shown. As examples the Heusler alloys Cu₂MnAl and Cu₂(MnAl) and the alloys Ag–Mg–Sn are considered.

UNE THÉORIE DE L'ORDE LES ALLIAGES TERNAIRES—II

On a donné une théorie statistique des passages ordre-désordre des alliages ternaires à composition et structure cristallique quelconque. On a défini des paramètres petit et grad distance d'ordre et on a donné des équations liant ces paramètres. On a obtenu la formule générale pour énergie libre et indiqué un moyen de calculer la température du passage ordre-désordre. Comme exemples on a examiné les alliages du type Heusler $\operatorname{Cu_2MnAl}$ et $\operatorname{Cu_2(MnAl)}$ et les alliages du system $\operatorname{Ag-Mg-Sn}$.

ORDNUNGSTHEORIE DREIFACHER LEGIERUNGEN-II

In der Arbeit wird eine statistische Theorie der Ordnung-Unordnungsübergänge in den dreifachen Legierungen von beliebiger Zusammensetzung und Kristallstruktur gegeben. Es werden die Fern- und Nahordnungsparameter definiert und die Gleichungen zwischen ihnen aufgestellt. Eine allgemeine Formel für die freie Energie wird ausgerechnet und eine Rechnungsmethode für die Ordnung-Unordnungsübergangstemperatur angegeben. Als Beispiele werden die Heuslerlegierungen $\mathrm{Cu}_2\mathrm{MnAl}$ und $\mathrm{Cu}_2\mathrm{(MnAl)}$ betrachtet sowie Legierungen vom $\mathrm{Ag-Mg-Sn}$ System.

INTRODUCTION

In the previous paper⁽¹⁾ some general considerations concerning the order–disorder transformations in ternary alloys have been presented. As an example the Heusler alloy Cu₂(MnAl)⁺ has been considered and in this case an expression of configurational free energy given. In addition the order–disorder transition temperature was calculated. All the considerations in paper I regarded the simple types of ternary alloys. In the present paper we shall give general principles of the statistical theory of order–disorder transformations in ternary alloys. The theory is a particular case of the general theory⁽²⁾ that allows us to describe the order in arbitrary (with respect to composition and crystal structure) n-component alloys.

Although a large number of various ternary alloys have been examined^(3,4) no general theory has been obtained. Therefore it seems useful to give a uniform theory, that makes it possible to consider any ternary alloy.

DEFINITION OF THE LONG-RANGE ORDER PARAMETERS

In paper I a general definition of the long-range order parameters has been formulated, in such a way that some additional conditions have been imposed on $a_{i\mu}$ § being in a state of complete order or complete disorder. In general, when s_k may be an arbitrary function of $a_{i\mu}$ and c_i , nothing more can be said about this definition. But when we present the form of this function we can write the *explicit* definition of long-range order parameters for any ternary alloy.

VOI

195

As all the fundamental equations which connect $a_{i\mu}$ with N_i and M_{μ} are linear, we shall require that s_k must be linearly expressed by $a_{i\mu}$ and c_i . When such an assumption is made we can synonymously define the long-range order parameters for arbitrary n-component alloy as follows⁽²⁾

$$s_k = s_{i\mu} = \frac{p_{i\mu} - c_i}{p_{i\mu}^{\ 0} - c_i}, \quad k = 1, 2, \dots, m.$$
 (1)

where m can be found from equation (4) in paper I. $p_{i\mu}^{0}$ in equation (1) denotes the value of $p_{i\mu}$ for the state of complete order. This value is determined by the superlattice of the alloy.

The linear definition (1) presents the conception of disorder, defining this state as such for which $p_{i\mu}=c_{i\cdot}$

The number m of independent long-range order parameters was expressed in paper I by the rank of the matrix of coefficients of the linear forms (1)

^{*} Received July 31, 1958

[†] Department of Experimental Physics, Wrocław University, Poland.

[‡] Here we shall denote by Cu₂(MnAl) the Heusler alloy which in paper I we have denoted simply by Cu₂MnAl; but now we shall consider its superlattice as consisting of two sublattices. The symbol Cu₂MnAl in the present paper refers to the Heusler alloy with three sublattices.

ACTA METALLURGICA, VOL. 7, JUNE 1959

[§] All the notations in this paper are the same as in paper I.

The only difference is that sublattice-sites will be always denoted by greek indices and instead of r which represented.

denoted by greek indices and instead of r which represented, in paper I, successive shells of some atom, we shall write ρ .

and (2) in that paper. This rank can be expressed by n and $l^{(5)}$ and it is easy to show that

$$m = nl - l - n + 1. \tag{2}$$

In our case as n=3 the above expression can be simplified as follows

$$m = 2(l-1).$$
 (2a)

Now we shall give some concrete examples of the application of the definition (1).

(a) The alloys of the system Ag-Mg-Sn. It is experimentally established (6) that alloys of the system Ag-Mg-Sn have an ordered structure as is shown in Fig. 1. The sublattice-sites 1 and 2 are always occupied by Ag atoms and sublattice-sites 3 by Mg atoms for any composition of the alloy. The sublattice-sites 4 are randomly occupied by Ag, Mg and Sn atoms.

In the case given equations (1, I) and (2, I) become

As l=4, we introduce six long-range order parameters. We shall treat a_{11} , a_{13} , a_{34} , a_{33} , a_{24} , a_{22} as independent. From equation (1) and Fig. 1 we obtain

$$\begin{split} s_1 &= s_{11} = \frac{p_{11} - c_1}{1 - c_1} = \frac{4a_{11} - N_1}{N - N_1} \,, \\ s_2 &= s_{13} = \frac{p_{13} - c_1}{0 - c_1} = 1 - \frac{4a_{13}}{N_1} \,, \\ s_3 &= s_{34} = \frac{p_{34} - c_3}{\frac{4N_3}{N} - c_3} = \frac{4a_{34} - N_3}{3N_3} \,, \\ s_4 &= s_{33} = \frac{p_{33} - c_3}{0 - c_3} = 1 - \frac{4a_{33}}{N_3} \,, \\ s_5 &= s_{24} = \frac{p_{24} - c_2}{\frac{4N_2 - N}{N} - c_2} = \frac{4a_{24} - N_2}{3N_2 - N} \end{split}$$

$$s_{6} = s_{22} = \frac{p_{22} - c_{2}}{0 - c_{2}} = 1 - \frac{4a_{22}}{N_{2}}.$$

(b) Heusler alloy $\operatorname{Cu_2MnAl}$. The Hausler alloy $\operatorname{Cu_2MnAl}$ was considered by Matsuda, (3) who also gave definitions of the long-rage order parameters. He chose $a_{11}, a_{22}, a_{33}, a_{21}$ as independent. From graphs of $s_k = f_k(a_{i\mu})$ it is easy to deduce that two of

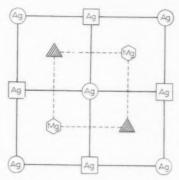


Fig. 1. Unit cell of the ordered ternary Ag-Mg-Sn alloy.(6)

- \bigcirc —lattice-sites of sublattice 1 \square —lattice-sites of sublattice 2 height 0,
- \bigcirc —lattice-sites of sublattice $\stackrel{3}{4}$ height $\stackrel{1}{4}$.

Matsuda's parameters are identical (see Fig. 2). The segments a, b, c of Fig. 2 represent the graphs of four Matsuda parameters. Two of them are identical and are therefore represented by the same segment b. It is seen from Fig. 2 that instead of one Matsuda definition we take another one represented for example by segment d. This definition is as follows

$$s_4 = s_{23} = \frac{p_{23} - c_2}{0 - c_2} = 1 - \frac{16a_{23}}{N}. \tag{5}$$

AVERAGE CONFIGURATIONAL ENERGY

In paper I an expression for average configurational energy E was given based on formula (15, I). There the average number $q_{kj}(\rho)$ of the pairs of atoms k–j with the distance ρ between them was not precisely calculated. The formula (15, I) is not general and may be applied only to alloys whose superlattice consists of equivalent sublattices. Below we give a general formula for $q_{kj}(\rho)$ for an arbitrary ternary alloy, as far as composition and crystal structure is concerned:

$$q_{kj}(\rho) = \frac{1}{2} \sum_{\mu,\nu}^{l} z_{\mu\nu}(\rho) a_{k\mu} p_{j\nu}, \qquad k, j = 1, 2, 3.$$
 (6)

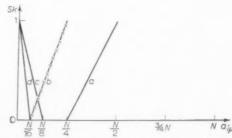


Fig. 2. The graphical representation of the dependence $s_k = \hat{f}_k (a_{i\mu})$ for the Cu₂MnAl alloy.

VOL.

1959

$$E(s_1, \dots, s_m) = -\frac{1}{2} \sum_{\rho} \sum_{k,j}^{3} \sum_{\mu,\nu}^{l} \{z_{\mu\nu}(\rho) a_{k\mu}(s_1, \dots, s_m) \times p_{j\nu}(s_1, \dots, s_m) V_{kj}(\rho) \}.$$
(7)

From equation (7) and the expression for W, which is formulated in paper I and describes the number of ways of arranging of N atoms on the lattice-sites, we can write a general formula of configurational free energy for an arbitrary ternary alloy with zero order approximation when neglecting the correlation between the atoms in the lattice-sites of the alloy

$$\begin{split} F(s_1,\ldots,s_m) &= E(s_1,\ldots,s_m) \\ &+ kT\sum\limits_{\mu=1}^l\sum\limits_{i=1}^3 \{a_{i\mu}(\ln a_{i\mu}-1)\} + \text{const.} \end{split}$$

SHORT-RANGE ORDER

To date no-one has examined short-range order in ternary alloys. We shall now therefore discuss the problem of defining the short-range order parameters for arbitrary ternary alloys and determine their connection with the long-range order parameters. For this purpose we shall denote by $Q_{kj}^{\mu\nu}(\rho)$ the number of pairs of atoms $k\!-\!j$ with the distance ρ between them and such that an atom of type k is in the μ th sublattice and an atom j in the ν th sublattice.

It is the consequence of the definition that

$$Q_{ki}^{\quad \nu\nu}(\rho) = Q_{ik}^{\quad \nu\mu}(\rho). \tag{8}$$

The sum of all the $Q_{kj}^{\mu\nu}(\rho)$ terms gives the total number of pairs $Q(\rho)$ of atoms with the distance ρ . The total number of pairs $Q(\rho)$ can also be obtained when summing all the $q_{kj}(\rho)$ terms, hence

$$\begin{split} &\sum\limits_{\nu\,=\,1}^{l}\;\sum\limits_{\,k\,=\,1}^{\,3}\;Q_{kk}^{\;\;\nu ,}(\rho)\,+\,\tfrac{1}{2}\!\!\left\{\sum\limits_{\,\mu\,\neq\,\nu}^{\,l}\;\sum\limits_{\,k\,=\,1}^{\,3}Q_{kk}^{\;\;\mu \nu}(\rho)\,+\right.\\ &\left.\qquad +\;\sum\limits_{\,\mu,\nu}^{\,l}\;\sum\limits_{\,k\,\neq\,i}^{\,3}Q_{kj}^{\;\;\mu \nu}(\rho)\!\right\}=\sum\limits_{\,k\,=\,1}^{\,3}\;\sum\limits_{\,j\,=\,1}^{\,3}q_{kj}(\rho)=Q(\rho). \end{split}$$

When summing over j on the right, the last equation can be written according to (6) as follows

$$\sum_{\nu=1}^{l} \sum_{k=1}^{3} Q_{kk}^{\nu\nu}(\rho) + \frac{1}{2} \left\{ \sum_{\mu\neq\nu}^{l} \sum_{k=1}^{3} Q_{kk}^{\mu\nu}(\rho) + \sum_{\mu,\nu}^{l} \sum_{k\neq j}^{3} Q_{kj}^{\mu\nu}(\rho) \right\} = \frac{1}{2} \sum_{\mu,\nu}^{l} \sum_{k=1}^{3} z_{\mu\nu}(\rho) a_{k\mu}. \tag{9}$$

When omitting the summing over k and μ in (9) we obtain the equations which connect $Q_{kj}^{\mu\nu}(\rho)$ with $a_{k\mu}$. For example we shall write these equations explicitly,

when $\rho = 1$ and $Q_{kk}^{rr}(1) = 0$. From (9) we obtain

$$\sum_{r=1}^{l} \left\{ Q_{kk}^{\mu r}(1) + \sum_{j \neq k}^{3} Q_{kj}^{\mu r}(1) \right\} = a_{k\mu} \sum_{r=1}^{l} z_{\mu r}(1), k=1,2,3 \atop \mu=1,\ldots,l. \tag{10}$$

Some of the equations (10) are a linear combination of the other so that only a certain number i of all $Q_{kj}^{\mu\nu}(1)$ from equation (10) is linearly independent. These linearly independent $Q_{kj}^{\mu\nu}(1)$ we shall denote shortly by $Q_j(1)$, $j=1,2,\ldots,i$. When $Q_j{}^0(\rho)$ and $Q_j{}^d(\rho)$ are $Q_j(\rho)$ for the states of complete order and complete disorder respectively we can determine the short-range order parameters $\sigma_i(\rho)$ as follows

$$\sigma_{j}(
ho) = rac{Q_{j}(
ho) - Q_{j}{}^{d}(
ho)}{Q_{j}{}^{0}(
ho) - Q_{j}{}^{d}(
ho)} \;\;, \quad j = 1, 2, \dots, i. \quad (11)$$

SHORT-RANGE ORDER IN HEUSLER ALLOY Cu₂(MnAl)

The introduction of short-range order parameters allows us to apply to ternary alloys a generalized quasi-chemical method. This method is a first approximation because it gives information about the correlation of the atom pairs. It turns out however that practical calculations lead to some very complicated mathematical problems, which can not be solved exactly. We shall show this for the case of the simplest ternary alloy, that is $\mathrm{Cu_2(MnAl)}$. To simplify the problem let us take into account only the nearest neighbourhood $\rho=1$.

Now we need not write upper indices $\mu\nu$ in $Q_{kj}^{\mu\nu}(1)$ because l=2, so instead of $Q_{kj}^{-12}(1)$ we shall write simply Q_{kj} . This will mean that atom k being placed in sublattice 1, has as its nearest neighbour atom j which is located in sublattice 2.

In the present case the equations (10) will have the form

$$\begin{aligned} Q_{11} + Q_{12} + Q_{13} &= 8a_{11}, \\ Q_{22} + Q_{21} + Q_{23} &= 8a_{31}, \\ Q_{33} + Q_{31} + Q_{32} &= 8a_{31}, \\ Q_{11} + Q_{21} + Q_{31} &= 8a_{12}, \\ Q_{22} + Q_{12} + Q_{32} &= 8a_{22}, \\ Q_{33} + Q_{13} + Q_{33} &= 8a_{32}. \end{aligned}$$

$$(12)$$

It can be easily verified that in the above equations we have four independent Q_{kj} . As such let us choose: $Q_{11}, Q_{12}, Q_{21}, Q_{23}$.

Now as:
$$Q_{11}^d = N$$
, $Q_{11}^\sigma = 0$; $Q_{12}^d = \frac{N}{2}$, $Q_{12}^\sigma = 2N$;

$$Q^d_{21}=rac{N}{2}\,,\;Q^\sigma_{21}=0;\;\;Q^d_{33}=rac{N}{4}\,,\;\;Q^\sigma_{33}=0,\;\;{
m from\;\;the}$$

VOI 7 19 definition (11) we shall find

$$\begin{split} Q_{11} &= N(1-\sigma_1), \\ Q_{12} &= \frac{N}{2} (1+3\sigma_2), \\ Q_{21} &= \frac{N}{2} (1-\sigma_3), \\ Q_{33} &= \frac{N}{4} (1-\sigma_4). \end{split} \tag{13}$$

From equations (12) and (13) we can calculate all other Q_{ki} terms.

We shall now find the mutual connection of the long-range and short-range order parameters from the relation below

$$\frac{\partial}{\partial \sigma_i} \left\{ -\sum_{k,j}^3 Q_{kj} V_{kj} - kT \ln W(s_1, s_2, \sigma_1, \sigma_2, \sigma_3, \sigma_4) \right\} = 0, \tag{14}$$

where $W(s_1, \ldots, s_m, \sigma_1, \ldots, \sigma_i)$ is given⁽²⁾ as

$$W(s_1, \ldots, s_m, \sigma_1, \ldots, \sigma_i) = W(s_1, \ldots, s_m) \frac{\prod\limits_{k,j}^{3} Q_{kj}^d!}{\prod\limits_{l} Q_{kj}!}, \quad (15)$$

and $W(s_1, \ldots, s_m)$ by formula (18, I). Equations (14) can be written

VOL.

1959

7

$$\begin{split} \frac{Q_{22}Q_{13}Q_{31}}{Q_{11}Q_{23}Q_{32}} &= \exp{(-V_1/kT)}, \\ \frac{Q_{12}Q_{23}}{Q_{13}Q_{22}} &= \exp{(-V_2/kT)}, \\ \frac{Q_{31}Q_{22}}{Q_{21}Q_{32}} &= \exp{(-V_3/kT)}, \\ \frac{Q_{23}Q_{32}}{Q_{23}Q_{32}} &= \exp{(-V_4/kT)}. \end{split} \tag{16}$$

where V_j , j=1,2,3,4, are linear combinations of $V_{kj}(1)$.

The system (16) is a system of four square equations in relation to σ_1 , σ_2 , σ_3 , σ_4 . The exact solution of this system is impossible. Application of the mathematical approximations even in the simplest case may lessen the exactness of the first approximation. Therefore in paper I we have drawn attention to the fact, that, in the case of ternary alloys, only the zero order approximation gives the results for which only some physical simplifications have been made.

THE ORDER-DISORDER TRANSITION TEMPERATURE

In paper I we have drawn attention to the difficulty of defining the order–disorder transition temperature T_p . Now as has been shown, $^{(7)}$ T_p synonymously defined by the system of equations below

$$\frac{\partial F(s_1, \dots, s_m, T, V)}{\partial s_k} = 0, \quad k = 1, 2, \dots, m.$$

$$F(s_1, \dots, s_m, T, V) = F(0, \dots, 0, T, V),$$

$$(17)$$

where V is a linear combination of $V_{ki}(\rho)$.

Having solved m+1 equations of the system (17) we obtain T_p and m values $s_k^{(Tp)}$ $(k=1,2,\ldots,m)$ corresponding to T_p .

CONCLUSIONS

The above considerations set out in both papers (I and II) give the possibility of examining the order—disorder transformations in ternary alloys with arbitrary composition and crystal structure. The only parameters of the theory are energies of interaction $V_{kj}(\rho)$ which are to be determined by experiment.

The actual defined short-range order parameters of ternary alloys can be determined, e.g. by X-ray diffraction methods. It is, however, to be emphasized that for ternary alloys each short-range order parameter is represented by several long-range order parameters; while in the case of binary alloys there is synonymous dependence of long- and short-range order parameters. This is comprehensible because of the existence of some additional configurations of the three kinds of the atoms in l sublattices of the alloy.

In general it is the case that ternary alloys represent a much more complicated problem than binary alloys. To solve this problem it is impossible to apply any over simplified generalizations of well-known and developed methods applicable to binary alloys. Therefore only after the acquisition of a greater quantity of experimental data (that to date is insufficient) will it be possible to apply this theory to particular cases and compare its results with experiment.

REFERENCES

- K. F. Wojciechowski, Acta Met. 6, 369 (1958).
- 2. K. F. Wojciechowski, Acta Phys. Polon. (in press).
- S. Matsuda, J. Phys. Soc. Japan 8, 20 (1953).
- S. Hosoya, J. Phys. Soc. Japan 9, 489 (1954).
- A. N. Mień, Fizika mietallow i mietallowiedienije (in press).
 W. G. Henry and G. V. Raynor, Canad. J. Phys. 30,
- S. Świerczkowski and K. F. Wojciechowski, Bull. Pol. Acad. Sci., math. phys. ser. 6, No. 9, 585 (1958).

THE HARDENING AND EMBRITTLEMENT OF MILD STEEL BY CYCLIC STRESSING AT THE FATIGUE LIMIT*†

J. HOLDEN:

The dependence of yield stress at 20° C and fracture stress at -196° C upon grain size has been investigated for a mild steel before and after prolonged cyclic stressing at the fatigue limit. After cyclic stressing the initial slip is coarse, and restricted to planes which have been active in cycling; consequently the hardening revealed by yield and fracture observations is characteristic of the regions of fatigue damage. The cyclic hardening and embrittlement, also investigated by notched impact tests, are not adequately accounted for by processes of ageing and precipitation on the planes active in fatigue.

LE DURCISSEMENT ET LA FRAGILITE DE L'ACIER DOUX SOUMIS A UN CYCLE DE TENSIONS A LA LIMITE DE FATIGUE

L'auteur a étudié, pour l'acier doux, la relation existant entre la limite élastique à 20° C, ainsi que la charge de rupture à -196° C, et le grain size avant et après un cycle de tensions prolongé à la limite de fatigue.

Après un tel cycle, le glissement initial est diffus et limité aux plans actifs. En conséquence, le durcissement révélé par des observations de déformation et de rupture est caractéristique des régions dégradées par la fatigue.

Le durcissement critique et la fragilité, étudiés également par des essais de résilience, ne sont pas correctement expliqués par les mécanismes de vieillissement et de précipitation sur les plans sensibles au phénomène de fatigue.

DIE VERFESTIGUNG UND VERSPRÖDUNG VON FLUSSEISEN DURCH ZYKLISCHE BEANSPRUCHUNG AN DER ERMÜDUNGSGRENZE

Die Abhängigkeit der Fliesspannung bei 20°C und der Bruchspannung bei -196°C von der Korngrösse wurde bei Flusseisen vor und nach einer ausgedehnten zyklischen Beanspruchung an der Ermüdungsgrenze untersucht. Nach der zyklischen Beanspruchung ist die anfängliche Gleitung grob und auf die Ebenen beschränkt, die bei der Wechselbeanspruchung aktiv gewesen waren; folglich ist die bei Fliesspannungs— und Bruchbeobachtungen feststellbare Verfestigung charakterisisch für die Gebiete mit Ermüdungsschädigung. Die zyklische Verfestigung und Versprödung, die auch mit Kerbschlagversuchen untersucht wurde, wird durch Alterungs— und Ausscheidungsvorgänge auf den bei der Ermüdung aktiven Ebenen nicht ausreichend erklärt.

INTRODUCTION

The stress–strain relationship of a metal hardened by many cycles of stress at the usual testing frequencies ($\sim 10^2$ c/s) has recently been used to contrast cyclic hardening with that produced in unidirectional deformation and by irradiation. Broom and ${\rm Ham^{(1)}}$ have found that cyclically-hardened copper shows a temperature dependence of flow stress comparable with that of irradiation hardened copper and quite different from that produced by unidirectional deformation. The same authors have also investigated the softening that cyclic stressing can effect in metals hardened by other working processes⁽²⁾ and have put forward evidence that point defects are involved in the softening.

These observations have suggested that an important contribution to cyclic hardening arises from the

production of point defects. In the present experiments cyclic hardening was investigated by determining the grain-size dependence of the tensile yield stress, σ_y , and the fracture stress σ_f , for a steel before and after a cyclic treatment. It has been shown^(3,4) that these quantities vary with the grain size, l, of the metal as:

$$\sigma_y = \sigma_o + k_y l^{-\frac{1}{2}}$$

$$\sigma_t = \sigma_o + k_t l^{-\frac{1}{2}}$$
(1)

The theoretical interpretation of these formulae^(5,6) is based on the idea that the passage of a free dislocation across a slip plane will be opposed by a frictional force, σ_o , due to the presence of, for example, precipitates and other dislocations, in addition to the effect of the lattice itself. When a stress σ is used to activate a slip plane a resultant stress $(\sigma - \sigma_o)$ will pile-up the dislocations against a grain boundary. The stress concentration produced may be sufficient to open a crack at the end of the slip band; k_f is therefore a measure of the stress needed to crack the metal. It is found to depend essentially upon the surface energy/unit area of the newly formed crack surfaces. Alternatively, if the stresses at a piled-up group cause further plastic yielding, k_g measures the

^{*} Received July 28, 1958.

[†] This work has been carried out as part of the research programme of the Mechanical Engineering Research Board of the Department of Scientific and Industrial Research and is published by permission of the Director of Mechanical Engineering Research, Department of Scientific and Industrial Research

^{*} Mechanical Engineering Research Laboratory, East Kilbride, Glasgow.

stress needed to start the yielding in grains around the pile-up; k_y is thus sensitive to the way the dislocations are locked in position. The measurement of σ_o , k_y and k_f before and after cyclic stressing would be expected to reflect the characteristics of the fatigue-hardened material.

The objection has sometimes been raised that bulk measurements upon fatigued material cannot be sensitive to the changes produced by the cyclic stressing, since such stresses localize their effect in regions of stress concentration. On a microscopic scale it is also known that the slip zones active in fatigue occupy only a small proportion of the plastic grains, (7) consequently the contribution of these parts of the grain in a subsequent deformation might be masked by the contribution of the rest of the grain. During the present experiments evidence was found that the initial tensile deformation which took place after cyclic hardening did so by slip which was restricted to the zones which had been active during the cycling. The bulk measurements of yield stress and fracture stress were therefore considered to reflect sensitively the structural changes brought about by fatigue.

EXPERIMENTAL METHOD

Direct stress fatigue specimens of 1 in. diameter at the gauge length were made from a mild steel, composition 0.09% C; 0.13% Si; 0.04% S; 0.015% P 0.42% Mn, heat treated in the form of 3 in. diameter bars to a range of grain sizes. Four grain sizes ranging from 110 to 630 grains/mm² were obtained by heating at temperatures up to 1050°C for times of up to 24 hr. Maximum rates of cooling arose in air cooling the bars. A small grain size of 960 grains/mm² was obtained by water quenching from 880°C followed by heat treatment at 650°C for 2 hr and air cooling.

After cyclic stressing the gauge length of the fatigue specimens was used to make tensile specimens, diameter 0.156 in., and impact specimens, $10~\mathrm{mm} \times 5~\mathrm{mm}$, having a Charpy vee-notch. The axis of each tensile specimen was parallel to that of the original direct stress fatigue specimen. In each impact specimen the notch axis was at right angles to the fatigue specimen axis. Specimens to determine the initial properties of the materials of various grain sizes were cut from the grips of the fatigue specimens at similar axial positions to those from the gauge length.

The tensile tests were carried out in a hard beam machine at a strain rate of $1.1 \times 10^{-4} \, \mathrm{sec^{-1}}$, test temperatures being obtained by liquid baths. Experimental points reported refer to the average of two specimens.

The cyclic history appropriate to the present investigation was considered to be that involving the maximum number of cycles before failure. The limited number of cycles characteristic of mild-steel fatigue fracture was extended by resorting to a coaxing procedure. The initial stress range applied, +9 tons/ in², was well below the estimated fatigue limit of all the materials and successive increments of approximately ± 1 ton/in² were made to this stress range after the specimen had endured several million cycles at each level. At the ultimate stress level applied, the tendency of the specimens to heat was opposed by the effect of an air blower and the specimen was maintained at about room temperature. In two particular cases referred to in detail below, the temperature of the fatigue specimen was allowed to rise at the ultimate stress level, a procedure which curtailed the life of the specimen in comparison with the cooled state.

The elapsed time between fatigue treatment and the testing of the tensile specimens from the fatigue specimen was sufficient to enable the tensile and impact specimens to be described as fully aged. The coaxing procedure may be regarded as a limiting case of fatigue fracture under low stress conditions.

RESULTS OF TENSILE TESTS

The cyclic histories of the specimens of various grain sizes are shown in Fig. 1; also indicated are the observed lower yield points at 20°C for each material as heat treated. It is clear that the stress at which fatigue failure occurs does not show the sensitivity to grain size which characterizes the yield point. Conventional fatigue tests on ingot iron⁽⁸⁾ have also indicated that the fatigue limit for the range of grain sizes used in the present work is independent of grain size.

The tensile data obtained at 20°C and -196°C are summarized in Table 1. The uniform ductility is measured as $\ln A_o/A_m$, the necking ductility as $\ln A_m/$ A_f where A_o ; A_m ; A_f refer to the original crosssectional area of the tensile specimen, the area at maximum load and the area at fracture respectively. The characteristic changes in the tensile test curves at 20°C and -196°C as a result of the cyclic treatment are shown in Fig. 2. For each grain size the cyclic stressing caused a hardening with elimination of the yield point phenomenon at 20°C. The absence of yielding is also followed by a considerably reduced uniform ductility: the necking ductility is however unchanged. This last observation is not unexpected since, at necking, all the grains in the neck undergo considerable deformation and mask the contribution

VOL. 7 1959

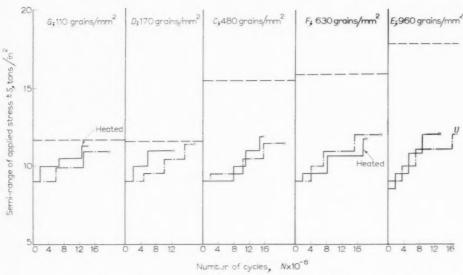


Fig. 1. Cyclic history of direct stress fatigue specimens of various grain sizes. Frequency $2000\,c/\mathrm{min}$. Original yield points indicated by broken lines.

Table 1. Changes in tensile properties at 20°C and -196°C of mild-steel specimens of various grain sizes as a result of cyclic treatment

	20°C				−196°C					
	G	D	С	F	E	G	D	C	F	E
Grain size (grains/mm²)	110	170	480	630	960	110	170	480	630	960
Uniform ductility	0.29	0.27	0.28	0.29	0.27	0.02	0.06	0.13	0.16	0.17
Necking ductility	0.77	0.76	0.76	0.80	1.08	0	0	0	0	0.26
Yield point (tons/in ²)	11.7	11.6	15.5	15.9	17.8	43.0	45.6	49.0	50.4	52.9
Fracture stress (tons/in ²)					-	45.0	46.8	52.2	54.0	57.0
	After cyclic stressing				After cyclic stressing					
Uniform ductility	0.13	0.12	0.13	0.10	0.15	0	0	0	0	0.09
Necking ductility	0.63	0.80	0.75	0.78	0.96	0	0	0	0	0
Limit of proportionality (tons/in²)	16.5	17.4	20.8	21.9	22.0	-	-	-	-	-
Fracture stress (tons/in ²)	-	-				59.5	60.6	63.0	62.9	63.2

of the particular grains hardened by the cyclic stressing at a relatively low stress level. Comparison of fracture stresses at $20^{\circ}\mathrm{C}$ before and after cyclic stressing is not therefore useful owing to this masking effect which attends necking. At $-196^{\circ}\mathrm{C}$ all the materials of different grain sizes, with the exception of the smallest, failed without necking but with reduction of area before fatigue. After fatigue they failed in a completely brittle manner with no detectable reduction of area. The smallest grain-size material failed without necking and with greatly reduced uniform ductility after the cyclic treatment.

In order to compare directly the effect of the cyclic stressing on the fracture stress, it was necessary to allow for the change in fracture stress produced in the original materials by the strain that took place prior to fracture. Following Petch, $^{(4)}$ this was done by measuring the fracture stress at $-196^{\circ}\mathrm{C}$ for a number of specimens of a given grain size pre-strained at $20^{\circ}\mathrm{C}$ by various small amounts. The resulting relation between fracture stress and total plastic extension to fracture was used to reduce the observed fracture stresses for the materials of various grain sizes to the zero elongation value given in Table 1.

195

The strain-hardening exponent n defined up to the point of maximum load by the relation $\sigma = A\delta^n$, where σ refers to the true stress and δ the true strain, was measured for tensile deformation at 20°C. It was found to decrease between 38 per cent and 47 per cent for the various grain sizes as a result of the cyclic treatment.

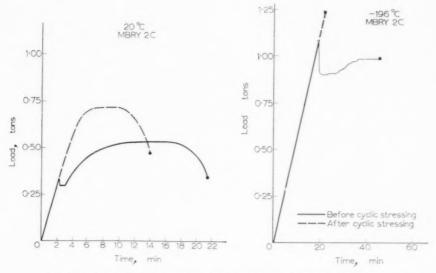


Fig. 2. Load/time curves to fracture for mild steel before and after cyclic stressing. Strain rate $1.1 \times 10^{-4} \, \mathrm{sec^{-1}}$.

GRAIN-SIZE EFFECTS

The tensile test data plotted as a function of grain size for comparison with equations (1) are shown in Fig. 3.

After fatigue the yield points at 20°C have the same slope, k_y , as that given by the original materials; they are displaced to higher values, i.e. higher σ_o , by a small amount ~ 3 tons/in². The absence of yielding in the fatigued material at -196°C precludes comparison of k_y at this temperature. The observed value of $(k_y)_{-196}$ °C/ $(k_y)_{20}$ °C $\equiv 1.7$ for the original material

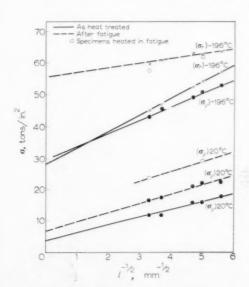


Fig. 3. Grain size dependence of tensile properties at $20^{\circ}\mathrm{C}$ and $-196^{\circ}\mathrm{C}$.

compares reasonably with the theoretical estimate by Stroh. (6)

Comparison of the fracture stresses at $-196^{\circ}\mathrm{C}$ indicates a large increase of σ_{o} of about 26 tons/in² due to the cyclic treatment. This is accompanied by a decrease in the value of k_{f} , the slope of the fracture stress curve.

In addition to the observations on fatigue specimens kept cool throughout the cyclic stressing, tensile data were obtained from two fatigue specimens of extreme grain sizes which were allowed to heat up during the time the final stress level was applied. Temperatures in the region of 250°C, estimated from the tint of the oxide film formed on the gauge length, were attained for times of several hours before fracture terminated the test. The data, although limited, indicated a rise \sim 7 tons/in² in the value of $(\sigma_a)_{20^{\circ}C}$ over the value attained in a specimen subject to a similar cyclic history but kept cool. Measured at -196° C the value of σ_{o} from the specimens allowed to heat did not appear to exceed that characterizing the cool specimens. The specimens from both cooled and self-heated materials were completely brittle when tested at -196° C; therefore surface flaws and defects in axiality of loading would have tended to give low values of fracture stress. The large increases in fracture stress observed after fatigue are not thought to be enhanced by the testing conditions. One premature fracture was met in the tensile tests and this took place well within the grip radius where scratches had not been removed in the specimen preparation. To ensure that thermal effects alone were not responsible for the

VOL. 7 1959

Fig. 4. Coarse slip bands in fatigue hardened material, G. (White light fringes).

increase in $(\sigma_o)_{20^{\circ}\mathrm{C}}$ for the self-heated fatigue specimens, control specimens of the original material E were heated at 250°C–300°C for several hours. The yield point at 20°C was not affected by this treatment.

The value of $(k_f)_{-196^{\circ}\text{C}}$ for the original material was found to be 2.3×10^8 e.g.s. units in good agreement with the theoretical value of 2.1×10^8 e.g.s. units calculated by Stroh.⁽⁶⁾

METALLOGRAPHIC OBSERVATIONS

Lüders bands developed during the extension of the original materials; no bands were observed in the fatigue-hardened state as would be expected following the suppression of the yield phenomenon. The slip bands formed in the plastic grains during tensile tests on the fatigued material were coarse and frequently ran straight across the grain, in contrast to the usual vein-like slip markings within a Lüders band. This extremely coarse slip was suited to interferometric measurement of slip-band height. At 1 per cent plastic extension, coarse slip bands were marked by surface steps from 1500 to 2500 Å in height. Fig. 4 shows such steps and also indicates the characteristic way they intrude for a short distance into an adjacent grain. The slip band structure at 1 per cent plastic deformation in the original materials was characterized by finely spaced bands making height measurement difficult; an estimate of 500 Å was made for the surface steps.

The materials allowed to heat during the fatigue test showed a structure within the grains which was sensitively attacked during etching processes, cf. Fig. 5, and which was not a surface effect since the material was cut from within the interior of the fatigue test piece. Similar patterns of individual etch pits were observed to persist in a grain as surface layers were

removed up to depths of the order of 20 per cent of the grain diameter. This structure could not be produced by repeated strain and ageing treatments of the original materials. It is of interest to note that the observed structure results from a test procedure, namely, allowing the fatigue specimen to heat up to 250°C for a few hours, which curtails the life of the specimen. In contrast to this it is known that the temperature dependence of fatigue life of mild steel shows a maximum at about 200-250°C, (9) and that this maximum appears to be a strain-ageing effect. Precipitation effects within grains during fatigue might therefore be expected to be associated with enhanced life rather than with curtailment as is the case with the structure observed in the self-heated specimens. The structure is not therefore thought to be a simple carbide precipitation effect as observed by Hempel and Houdremont(10) during fatigue of prestrained iron.

195

During tensile tests of material containing the dotted structure within the grains, slip was observed to take place by coarse rectilinear bands and in addition the bands were confined to planes containing the dotted structure. If it is assumed that this structure identifies the planes active in the cyclic treatment, and as this treatment considerably hardens the material, it is remarkable that the slip is confined to these hardened planes. This effect is illustrated in Fig. 6. It may also be noted that the coarse slip takes place in material in which the yield phenomenon has been suppressed. The dotted structure interacts with slip on other planes in a characteristic manner. The slip on intersecting planes was produced by compressing the specimens by about 5 per cent along an axis other than the one used in tension. The intersecting slip lines are frequently observed to stop on

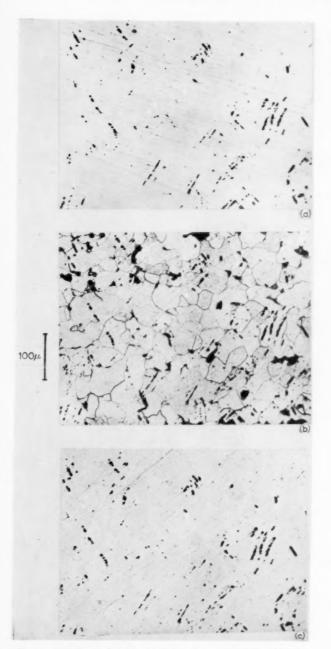


Fig. 5. Localized fatigue structure in specimens allowed to heat.

- (a) Specimen etched and repolished to remove grain structure.
- (b) Same field, re-etched.
- (c) Same field, repolished.

the dotted structure or to suffer large displacements. Although tensile specimens of fatigued-hardened

material failed in a completely brittle manner at —196°C they did not show such good {100} cleavage when plated and sectioned as the original materials which failed with considerable reduction of area.

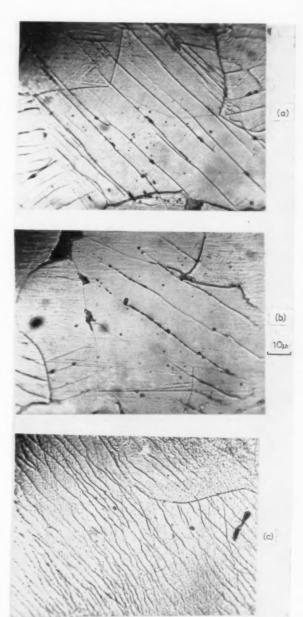


Fig. 6. (a) and (b) Coarse slip taking place only on planes characterized by fatigue structure, 1 per cent extension. (c) Fine slip in same material before fatigue, 1 per cent extension. The surface preparation was identical in each case.

Examination of specimens containing the dotted structure revealed that this was due to the brittle fracture passing through some grains by a path partly parallel to the slip planes containing the structure. The fatigue hardening had therefore produced a structure on some slip planes which competed with

VOL. 7 1959 cleavage as a brittle fracture path at $-196^{\circ}\mathrm{C}$. In the course of sectioning plated specimens it was invariably found that fatigued material, fractured at $-196^{\circ}\mathrm{C}$ in tension and left for some weeks in dry air, was characterized by a layer between the plating and the steel. No such prominent corrosion layer was observed on sections of the original materials when fractured under similar conditions and left in air for some 6 months.

IMPACT TESTS

The notched impact specimens cut from the fatigued materials showed a large increase in the brittle-toductile transition temperature. This was not accompanied by any decrease in the energy absorbed in impact fracture in the ductile range, as in the case of irradiation embrittlement.(11) This difference can be ascribed to the localized nature of the fatigue hardening in contrast to the uniform changes due to irradiation. Thus the deformation in the notch region in the ductile range involves most of the grains, many of which have not suffered cyclic plastic deformation at the low stress range used in the cyclic treatment. The resultant bulk behaviour as measured by energy absorption is insensitive to the presence of regions of evelic hardening. Within the brittle fracture range however these limited regions can be effective in influencing the energy absorbed, since they can initiate a crack in a few adjacent grains at the notch root. The dependence of transition temperature, T° , K, upon grain size is indicated in Fig. 7, the grain size being expressed by a logarithmic scale of A.S.T.M. grain-size numbers.

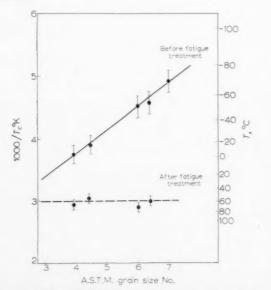


Fig. 7. Variation of transition temperature T, with grain size.

A theory of the transition temperature for brittleness has been given by Stroh⁽⁶⁾ from consideration of the temperature dependence of the delay time for yield. The transition temperature was found to vary with grain size as

$$rac{1}{T_c} = -rac{7}{2} \cdot rac{k}{U} \cdot \log l + {
m const.}$$

where U is the activation energy needed to free a dislocation and k is Boltzmann's constant. Using this relation the embrittlement of mild steel was found to be characterized by a value of $U \sim 0.3$ eV which was consistent with the estimate⁽¹²⁾ of the activation energy to release a dislocation from a carbon-atom atmosphere. For the steel used in the present work a value of $U \sim 0.45$ eV is found for the materials as heat treated. After cyclic stressing a very flat relation between $1/T_c$ and log l is found and this would indicate that at the high strain rates occurring in the impact tests the dislocations are locked by a mechanism involving a considerably higher activation energy than that of Cottrell locking.

DISCUSSION

The observations on the hardening produced by cyclic stressing at the fatigue limit raise two main questions. Is the hardening due to strain ageing and precipitate formation on the active slip planes during fatigue, that is, to an increase in the frictional term σ_0 ? Why is slip in tensile tests after low stress fatigue limited to planes which have been hardened during the cyclic stressing?

195

Cracknell and Petch(13) have investigated the hardening due to precipitate formation in a 0.12% C steel. They have shown that the yield stress over a range of grain sizes can be raised by a few tons/in2 by small precipitates, and that the increase is independent of temperature. The increase reached a maximum and then fell off as the precipitates were overaged. The observed fatigue hardening however shows a large increase in the frictional resistance to the moving dislocations, measured at -196°C, over the value at 20°C. In addition, the value of $(\sigma_o)_{20^{\circ}C}$ for the fatigue-hardened material was increased from 7 tons/in2 to 14 tons/in2 by allowing the material to heat during the last few hours of the fatigue test. This increase was not reflected in the value of $(\sigma_o)_{-196^{\circ}C}$. This characteristic, and also the fact that the value of $(\sigma_o)_{-196^{\circ}\mathrm{C}}$ arises from the completely brittle fracture of the tensile specimens, suggest that at -196°C, and for the strain rate used, the fatigue-hardened structure can exert a powerful locking action on the dislocations.

This view is also supported by the impact observations, which suggest a much larger activation energy to release dislocations in the hardened material than the value associated with Cottrell locking in mild steel.

Hardening with these characteristics might arise if. after cyclic stressing, small cavities had been produced on the active slip planes. Fujita(14) has suggested that parallel rows of unlike-edge dislocations in slip planes, ~10 Å apart from each other, might be forced together during fatigue to produce long cavities. In this situation the dislocations would be attracted to the cavities by image forces and Friedel⁽¹⁵⁾ has suggested that in the absence of thermal fluctuations the locking would be severe. The image force locking at higher temperatures and low rates of strain, as used in the present experiments, might not cause a significant change in the value of $(k_y)_{20^{\circ}\text{C}}$ in view of the locking due to carbon and nitrogen atoms already present in the materials. The contribution of the cavities to the hardening would then be by offering a resistance to the movement of dislocations and tending to increase the value of σ_0 in the manner of precipitates.(16) At the high strain rates used in the impact tests, the locking due to the cavities would again be expected to be effective.

The postulation of cavities on the slip planes active during fatigue would account for the observed structure within the grains and its etching characteristics. It would also allow an interpretation of the observed reduction of k_f since the effective value of γ , the surface energy/unit area of a newly formed crack, would be reduced if the crack was formed along a slip plane already containing small voids.

1959

On the basis of the theory that plastic deformation releases dislocations from a random dislocation network⁽¹⁷⁾ it is difficult to account for the observation that, with cyclically-hardened material, coarse slip, initially limited to hardened planes, occurs in subsequent tensile deformation. Coarse slip has been observed in irradiated metals and in alloys with short range order. This has been interpreted (18,19) as a consequence not of the limited number and distribution of sources but as due to the changes caused on a slip plane by the passage of a dislocation, which then enable further dislocations to pass along the same plane more easily. Such mechanisms appear, however, to involve a yield elongation as a consequence of coarse slip, whereas coarse slip in fatigue-hardened material is associated with a suppression of the yield phenomenon. Orowan⁽²⁰⁾ has suggested that the usual prolific appearance of slip bands at a yield point may not be entirely due to inherent sources but may depend upon some preparatory slip from them, leading to the

production of new dislocations of adequate length and suitable orientation to act as further sources under the applied stress. If the preparatory slip is produced by low cyclic stress, the new lengths of dislocations created might be expected to be shorter in length than those created by unidirectional slip, and incapable of acting as further sources except at much higher stresses than the original yield point. Preparatory eyclic stressing might, therefore, cause slip to be initially limited to planes containing inherent sources in a subsequent tensile deformation. The limitation of initial slip would be expected to reduce the work of deformation involved in the spreading of a brittle fracture in the fatigued material. Since the brittle fracture path in such material involves slip planes as well as {100} cleavages, there would be less grain boundary tearing during brittle fracture and therefore a decrease in the work of deformation. The contribution of this work to the effective surface energy of the crack would therefore be decreased in the fatigued material and result in a reduction in the value of $(k_f)_{-196^{\circ}\text{C}}$

The suppression of the yield phenomenon in the fatigue hardened materials can be ascribed to the development of conditions which decrease the effectiveness with which the dislocations arriving at the boundar; of a plastic grain can activate sources in surrounding grains. The limitation of initial slip in the plastic grains to a few planes, and the added frictional forces which have to be overcome on these planes by the moving dislocations, would be such conditions.

CONCLUSIONS

The hardening produced by the cyclic conditions used in the present work does not have temperature characteristics which can be accounted for by the presence of precipitates on the slip planes which were active during cyclic stressing. The localized slip which is observed in tensile tests after preparatory cyclic stressing is thought to be due to a limitation of dislocation source distribution, rather than to any softening of the structure by changes caused during the movement of the initial mobile dislocations.

REFERENCES

- 1. T. Broom and R. K. Ham, Proc. Roy. Soc. A242, 166 (1957).
- N. H. Polakowski and A. Palchoudhuri, Proc. Amer. Soc. Test. Mat. 54, 701 (1954).
- 3. E. O. Hall, Proc. Phys. Soc. B64, 747 (1951).
- 4. N. J. Petch, J. Iron St. Inst. 174, 25 (1953).
- 5. N. F. MOTT, J. Iron St. Inst. 183, 233 (1956).
- 6. A. N. Stroh, Advanc. Phys. 6, (24), (1957).
- N. THOMPSON, N. J. WADSWORTH and N. LOUAT, Phil. Mag. 1, 113 (1956).
- P. Laurent, Colloquium on Fatigue, International Union of Theoretical and Applied Mechanics, Stockholm (1955).

- 9. J. C. LEVY and G. M. SINCLAIR, Proc. Amer. Soc. Test. Mat.
- 55, 866 (1955).10. M. HEMPEL and HOUDREMONT, Stahl. u. Eisen, Düsseldorf 73, 1503 (1953).
- 11. C. R. SUTTON and D. O. LESSER, Nucleonics 12, 8 (1954).
- 12. A. H. COTTRELL and B. A. BILBY, Proc. Phys. Soc. A62,
- 13. A. CRACKNELL and N. J. PETCH, Acta Met. 3, 186 (1955).
- 14. F. E. FUJITA, Science Rep. Res. Inst. for Steel 6. (6) 565 (1954).
- 15. J. FRIEDEL, Les Dislocations. Gauthier-Villars, Paris
- S. FRIEDEL, Les Disocutions. Gauthier-Vihars, Paris (1956).
 N. F. Mott and F. R. N. Nabarro, Rep. of Bristol Conf. on Strength of Solids. Physical Society, London (1948).
 N. F. Mott, Phil. Mag. 43, 1151 (1952).
 A. H. Cottrell, Monograph No. 23. Institute of Metals, London (1957).
- London (1957).

 19. D. Kuhlmann-Wilsdorf, Phil. Mag. 3, (26) 125 (1958).

 20. E. Orowan, Dislocations in Metals. American Institute
- of Mining and Metallurgical Engineers, New York (1954).

DECORATION AND ETCHING OF SILVER-DOPED ROCKSALT CRYSTALS BY SURFACE GAS REACTIONS*

W. BONTINCK and W. DEKEYSER†

Silver-doped rocksalt crystals were treated with different hydrocarbons and with a mixture of $\mathrm{CH_4}$ and $\mathrm{O_2}$ at higher temperatures. Besides decoration of dislocations and in some cases cavity formation, spiral etch-pits were formed after a treatment with $\mathrm{CH_4}$ and $\mathrm{O_2}$. The decoration is due to electrons from hydrogen or free radicals. The spiral etch-pits are presumably formed by an inhomogeneous concentration of reaction products in the gaseous vapour phase round an active site.

LA DECORATION ET L'ATTAQUE DE CRISTAUX DE SEL GEMME DOPES A L'ARGENT AU COURS DE REACTIONS SUPERFICIELLES GAZEUSES

Les auteurs ont traité des cristaux de sel gemme dopés à l'argent par différent hydrocarbures et par un mélange de CH_4 et d' O_2 à des températures plus élevées.

A côté de la décoration des dislocations et dans certains cas de la formation de cavités, des piqûres de corrosion en spirale ont été obtenues après un traitement au CH_4 et à ΓO_2 .

La décoration est due aux électrons de l'hydrogène ou des radicaux libres. Les piqures de corrosion en spirale sont vraisemblablement formées par une concentration non homogène de produits de la réaction dans la phase gazeuse et à proximité d'un site actif.

DEKORIERUNG UND ÄTZUNG VON SILBERDOTIERTEN STEINSALZKRISTALLEN DURCH GASREAKTIONEN AN DER OBERFLÄCHE

Silberdotierte Steinsalzkristalle wurde mit verschiedenen Kohlenwasserstoffen und mit einer Mischung von $\mathrm{CH_4}$ und $\mathrm{O_2}$ bei höheren Temperaturen behandelt. Ausser der Dekorierung von Versetzungen und gelegentlicher Bildung von Hohlräumen entstanden nach einer Behandlung mit $\mathrm{CH_4}$ und $\mathrm{O_2}$ spiralartige Ätzgrübchen. Die Dekorierung rührt von Elektronen von Wasserstoff oder freien Radikalen her. Die spiralförmigen Ätzgrübchen bilden sich vermutlich infolge einer inhomogenen Konzentration der Reaktionsprodukte in der gasförmigen Dampfphase in unmittelbarer Umgebung einer aktiven Stelle.

1. INTRODUCTION

In this laboratory the decoration of dislocations in alkali halides has been extensively studied. Most commonly, the crystals are doped with silver chloride or silver nitrate and heated afterwards in hydrogen at a relatively high temperature. By this procedure silver specks or cavities filled with the decomposition products of the nitrate are formed along the dislocation lines. (1,2,3) In both cases it could be shown that electrons given off by the hydrogen are responsible for the reduction of the Ag+ and NO₃- ions. (3) In this paper we report similar experiments in which other gases, such as CH4, C2H4, C2H2 and a mixture of $\mathrm{CH_4}$ and $\mathrm{O_2}$ were used for the reduction. In the latter case spirally terraced etch-pits, of the type found on etched germanium and silicon surfaces, were formed.

In all experiments, crystals of NaCl, doped with AgCl or $AgNO_3$ were heated at $700^{\circ}C$ under a continuous flow of the purified hydrocarbons or of the mixture of CH_4 and O_2 . The end products could be collected for examination with a mass spectrometer.

2. EXPERIMENTAL RESULTS AND DISCUSSION

A treatment with pure CH4 gave no results at all. When C₂H₄ and C₂H₂ were used, the well known polymerization and carbonization was observed. The crystals were coated with a carbon film and when this was removed they exhibited the same characteristics as those treated in hydrogen: decoration of the dislocations with silver specks or cavities and an identical absorption spectrum. For the same reaction time the decoration was however less deep than when pure hydrogen was used. The most probable reason is that fewer electrons are given off during the dissociation and subsequent molecular rearrangement of the gases. The electrons must originate from hydrogen or from free radicals. Attempts to establish this more precisely failed. Mass spectroscopic analysis of the end products revealed no difference with or without crystals in the reaction tube. The observed decoration is therefore only an indication that secondary stages exist between the dissociation and subsequent molecular rearrangement of the products. When a mixture of CH₄ and O₂ was used no carbon formation or polymerization was observed. The decoration must result here, as it is highly improbable that hydrogen would be present in an oxygen atmosphere, from free radicals formed during the oxidation. Here too

† Laboratorium voor Kristalkunde, Rozier, 6, Gent/Belgium.

^{*} This work is part of a research scheme (C.E.S.) sponsored by I.R.S.I.A. (Brussels). Received August 7, 1958.

Fig. 1. (a,b,c) Spiral etch-pits on rocksalt crystals, doped with Ag salts, after thermal treatment in a CH₄ + O₂ atmosphere. $\times 120$

no evidence could be obtained on the nature of these free radicals. However, spiral etch-pits were formed on the surface. In most cases the pits have only a helical character in the centre; some are solely formed by concentric terraces (Fig. 1 a, b, c). Fig. 2 reproduces an interferogram of one of the spiral etch-pits. The general characteristic is that the step-height is large and ranges from 12 to 6μ . Similar etch-pits with step-heights of the order of 1μ or more have been found by a number of authors, especially on germanium and silicon single crystals. $^{(4-10)}$

In our case it must be noted that the etching is due to the presence of dry water vapour, so that the

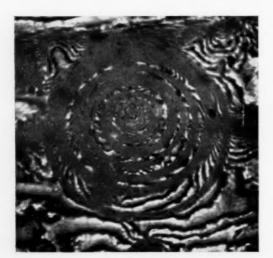
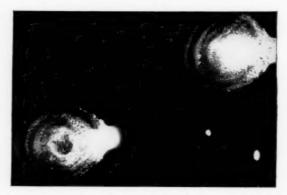


Fig. 2. Interferogram of a spiral etch-pit. ×120

experimental conditions are different from the other experiments where spiral etch-pits are formed. We may however accept that in both cases the formation of these etch-pits is the result of the same mechanism.

Amelinckx and the present authors suggested that these pits resulted from the etching of helical dislocations, and that the step-height was equal to the pitch of the helix. (11-13) This was proved by these authors on calcium fluoride and in a more direct way by Dash on silicon. (14) Dash however, pointed out that the correspondence was not one to one i.e. every time a helical dislocation is etched in the proper way a spiral etch-pit results, but a spirally terraced etch pit with a large step-height is not necessarily connected with a helical dislocation. Our experiments with halides support this view, because (a) helical dislocations are rare in halides⁽¹⁵⁾ (b) a hydrogen treatment of crystals which were poorly decorated and well etched after a CH4-O2 treatment did not reveal any trace of dislocations ending at the bottom of the pits (c) no etch-pits of the usual type were found. It thus seems



195

Fig. 3. The borders of the spiral etch-pits are more decorated than the rest of the crystal surface. $\times 120$

clear that the spirally terraced pits can originate at other spots than emergence points of dislocations. Impurity atoms, giving rise to surface electronic levels can probably also act as active centres for the surface reaction. The methane or oxygen molecules chemisorbed at those sites will react with the other partner to form carbon oxides and water, which in turn reacts with the rocksalt. A probable reaction is given by the equation

and this is not impossible at this higher temperature as both reaction products are more volatile than rocksalt

The formation of the etch-pits depends now entirely upon the nature and the concentration of the reaction

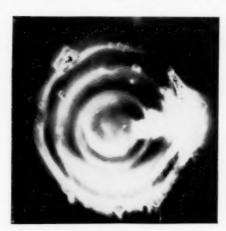


Fig. 4. Cavities which are formed at the borders of the spiral etch-pits. $\times 120$

products in the vapour phase in the vicinity of the active site. An inhomogeneous etching results, in the sense described by Lang, and the inhomogeneity is produced here by the reaction products and their evacuation.

When the radius of the etch-pit becomes larger, the concentration will become more and more homogeneous, which will result in the formation of the circular steps which are observed. In our case, the reaction rate normal to the surface is of the same order as the etching rate parallel to the surface. This promotes the formation of very deep etch-pits.

VOL.

1959

The borders of the etch-pits are always heavily decorated, which proves that these parts of the crystal surface are more active for gas reactions (Fig. 3). This is supported by the fact that with rocksalt erystals doped with AgNO3, cavities are formed at the borders of the steps (Fig. 4).

We presume that in the case of Ge and Si, it must be the concentration gradient of the reaction products in the etching solution near the active site which in some cases must be responsible for the formation of the spiral etch-pits.

REFERENCES

- I. W. Maenhout-van der Vorst and W. Dekeyser, Phil. Mag. 1, 882 (1956).
- 2. S. Amelinckx, Lake Placid Conference on Dislocations (1957).
- 3. S. AMELINCKX, W. MAENHOUT-VAN DER VORST and W. Dekeyser, Acta Met. (in press
- 4. T. L. Johnson, C. H. Li and C. I. Knudson, J. Appl. Phys. 28, 746 (1957
- 5. W. BARDSLEY and B. W. STRAUGHAN, J. Electronics 1, 561 (1956).
- 6. F. L. Vogel and L. C. Lovell, J. Appl. Phys. 27, 1413 (1956)

- A. R. Lang, J. Appl. Phys. 28, 497 (1957).
 N. Dash, J. Appl. Phys. 27, 1193 (1956).
 S. C. Ellis, J. Appl. Phys. 26, 1140 (1955)
 S. Amelinckx, W. Bontinck and W. Dekeyser, Phil.
- Mag. 2, 1264 (1957). 11. W. Bontinck and S. Amelinckx, Phil. Mag. 2, 94 (1957).
- 12. S. AMELINCKX, W. BONTINCK, W. DEKEYSER and F.
- SEITZ, Phil. Mag. 2, 355 (1957). 13. W. BONTINCK, Phil. Mag. 2, 561 (1957).
- 14. S. AMELINCKX, W. BONTINCK and W. MAENHOUT-VAN DER VORST, Physica 23, 270 (1957).
- 15. N. Dash, private communication.

APPEARANCE OF DISLOCATIONS IN METAL CRYSTALS ON EVAPORATION: TWINNING DISLOCATIONS AND THEIR RELATION TO ANNEALING TWINS IN COPPER*

E. VOTAVA and A. BERGHEZAN†

Evaporation of copper surfaces produces a step-structure which is related to the orientation of the crystals. On non-coherent twin boundaries this step-structure takes up a characteristic aspect in which two cases can be distinguished, namely: (a) simple or multiple evaporation spirals, or (b) evaporation channels. An interpretation in terms of twinning dislocations is given.

Furthermore, the sense of the spirals is determined by the direction of the displacement of the non-coherent twin boundary. This is due to the twin dislocation loops which are confined in the {111} planes and have opposite signs at the two emergence points.

FORMATION DE DISLOCATIONS DANS LES CRISTAUX METALLIQUES OBTENUS PAR EVAPORATION: DISLOCATIONS DE MACLAGE ET LEUR RELATION AVEC LES MACLES DE RECUIT DU CUIVRE

L'évaporation de surfaces de cuivre produit une structure à gradins qui est en relation avec l'orientation des cristaux. Sur des frontières de macles non cohérentes, cette structure revêt un aspect caractéristique où deux cas peuvent être distingués;

(a) des spirales d'évaporation simples ou multiples;

(b) des canaux d'évaporation.

Les auteurs proposent une interprétation basée sur les dislocations de maclage. En outre, le sens des spirales est déterminé par la direction de déplacement de la frontière de macle non cohérente. Ceci est dû aux boucles de dislocation de macle qui sont confinées dans les plans {111} et qui ont des signes opposés à leurs deux points d'émergence.

ERSCHEINEN DER VERSETZUNGEN VON METALLKRISTALLEN BEIM VERDAMPFEN: ZWILLINGSVERSETZUNGEN UND IHRE BEZIEHUNG ZU REKRISTALLISATIONSZWILLINGEN BEI KUPFER

Bei der Verdampfung von Kupferoberflächen entsteht eine Stufenstruktur, die von der Orientierung der Kristalle abhängt. An nichtkohärenten Zwillingsgrenzen nimmt diese Stufenstruktur charakteristische Formen an, von denen zwei Fälle unterschieden werden können, nämlich: (a) einfache oder mehrfache Verdampfungsspiralen oder (b) Verdampfungskanäle. Es wird eine Deutung anhand von Zwillingsversetzungen gegeben.

Weiterhin wird der Sinn der Spiralen durch die Verschiebungsrichtung der nichtkohärenten Zwillingsgrenze bestimmt. Dies rührt davon her, dass die Ringe der Zwillingsversetzungen auf die {111}-Ebenen beschränkt sind und an den beiden Austrittspunkten entgegengesetzte Vorzeichen haben.

INTRODUCTION

Copper, like most f.c.c. metals and unlike hexagonal and b.c.c. metals, forms annealing twins. These twins can easily be recognized under the microscope by their lath shaped form and their rectilinear boundaries. These rectilinear boundaries represent on the surface the trace of the twinning plane, the mirror plane of the two twinned crystals. The atoms of the twinning plane are shared by the two neighbouring crystals, and matching across this interface is perfect. For this reason these boundaries are called "coherent twin boundaries".(1) Along the coherent twin boundaries there are very often cross-discontinuities in the twinning plane which are called "non-coherent twin boundaries" and exact matching of neighbouring atoms across them is no longer possible. It is also important to stress the very frequent association of

the coherent twin boundaries with the non-coherent boundaries. The latter can naturally join the "normal" grain boundaries where they produce a small deviation.

In contrast to the frequency of recrystallization twins, mechanical twins in f.c.c. metals are produced only under special conditions. Thus Blewitt et al.⁽²⁾ have found mechanical twins in copper, gold and silver deformed at 4.2°K and 77.3°K, Haasen⁽³⁾ in nickel at 4.2°K and 20°K and Suzuki and Barrett⁽⁴⁾ in silver–gold alloys at temperatures under 0°C. These authors explain the deformation of these f.c.c. metals by twinning in terms of the movement of partial dislocations (twinning dislocations) which are bounded on the {111} planes. Their stress induced movement leaves behind stacking faults, which form elementary twins.

In the following sections, some experimental results on recrystallization twins in copper are reported and it will be shown that here too, the twinning dislocations play an important rôle.

^{*}This work is part of a project sponsored by Union Carbide Corporation, New York. Received August 7, 1958. † European Research Associates, s.a. 95, rue Gatti de Gamond, Brussels, Belgium.

THE EVIDENCE OF DISLOCATIONS IN COPPER CRYSTALS

It is now generally accepted that the growth of crystals at small supersaturations is made possible, as predicted by Frank⁽⁵⁾, by the presence of screw-dislocations and proceeds by the well-known spiral mechanism.^(6,7) The resulting surface configuration has a spiral form. In turn, the spirals represent a valuable proof of the presence of screw-dislocations.

For the evaporation of crystals it seems therefore reasonable to accept the reverse spiral mechanism, (8) which has already been confirmed for ionic crystals by one of us. (9) In this case the screw-dislocations become visible by evaporation spirals. This technique has now been extended to metals, (10) especially to copper as an example of a f.c.c. metal.

Cold rolled bars of electrolytic copper have been used, which were heated under vacuum $(1-4\times10^{-4}$ mm Hg) in a quartz tube, either by high frequency or in a resistance furnace at between 900° and 1000° C. The heating by high frequency gave as good results in 2-5 hr of annealing as did 2-4 days heating with a resistance furnace.

During heating a considerable amount of copper is deposited on the inner wall of the quartz tube. By this process the different crystals formed during recrystallization become visible in the same way as on etching. Microscopic observation shows that a characteristic evaporation structure is formed, and using multiple beam interferometry this has been shown to be a step-structure.

The evaporation of crystal surfaces is naturally the result of several processes: (a) The release of the atoms from the lattice and partly direct evaporation (b) Surface diffusion of the atoms and then again (c) some evaporation. Menzel^(II) showed the very important rôle of surface diffusion which produces a transformation of the surface configuration. For the development of the step-structure a small amount of oxygen, either in the remaining atmosphere or as dissolved in the metal, seems to be necessary as Elam^(I2), Menzel^(II), Chalmers et al.^(I3) and Moreau and Bénard^(I4) have shown. It is certain that in our experiments the oxygen fixation on the steps helps to show up this structure.

The following aspects of this step-structure are important:

(a) The morphology of the evaporation figures is related to the orientation of the crystals as the figures change every time a grain boundary is crossed.

(b) Evaporation line figures of the two twinned crystals meet at coherent twin boundaries, revealing in a striking way the exact matching of the atoms



Fig. 1. ×1096

across the twin plane. At the normal grain boundaries the lines meet only by chance.

(c) Non-coherent twin boundaries are associated either with one or more well developed spirals or with a deep channel. In Fig. 1 some of these aspects are clearly visible. In the centre there is an especially well developed evaporation spiral which has its origin on a non-coherent twin boundary. In the upper left corner a second twin boundary traverses the photograph; on both sides, the symmetry of the evaporation lines shows that this boundary is the trace of a twin plane which is almost perpendicular to the crystal surface. Removal of successive layers by evaporation and surface diffusion has brought into the surface the low index planes such as {111} and {100} giving rise to a roof-like configuration.

Fig. 2 shows another well developed single spiral at the non-coherent boundary of a micro-twin (left hand side of the micrograph).

Whenever several successive non-coherent twin boundaries displaced in the same direction are present, each one of them is associated with a spiral having the same serew sense (Fig. 3).



Fig. 2. ×1247

VOL.

1959

Fig. 3. ×1061



Fig. 5. ×1008

Figs. 4, 5 and 6 show other examples of the various aspects of single or multiple spirals starting at non-coherent twin boundaries.

As the evaporation velocity is related to the step height, the different spirals will have different evaporation velocities, which will be greater for smaller step heights. For this reason, separated multiple spirals can meet together during their development by evaporation (Fig. 4). It is interesting to note that the step-height of the spirals seems to be related to the width of the non-coherent twin boundaries. Even without exact measurements, this is clearly visible on the micrographs (Fig. 4). We must mention here, that the exact measurement of the step-height of the different spirals was not possible because of the roof-like surface configuration on these twin boundaries and the high magnification used.

Another feature, extremely important for the present study, is the correlation between the direction of displacement of the twin boundary and the sense of the spiral developed. This is shown in Fig. 7 where left and right handed evaporation spirals are present



Fig. 6. ×787



Fig. 4. ×1352



Fig. 7. ×956

along the same twin boundary because the two non-coherent twin boundaries have opposite displacements. The same feature can be seen in Fig. 8, but as the distance between the two non-coherent twin boundaries is much smaller here the two spirals meet and develop together. On this micrograph, the non-coherent twin boundaries are no longer visible; they become perceptible only by a slight bending of the twin boundary and accordingly the step height is very small. Finally, Fig. 9 shows the same for a micro-twin and so proves in a general way this relationship.

Apart from the spiral figures, non-coherent twin boundaries in some other orientations are marked by deep channels. Fig. 10 shows this clearly in the crystal at the centre of the photograph. In another crystal above a spiral structure is visible. This micrograph represents also a good general example of the surface structure after evaporation.

(d) Inside the crystals spirals have only rarely been found and are not related to the non-coherent twin boundaries, as can be seen on the right hand side of Fig. 2. However, on single crystals a greater frequency of spirals has been found as can be seen in Fig. 11. Here, the evaporation spirals mark the emergence points of total dislocations.

1959

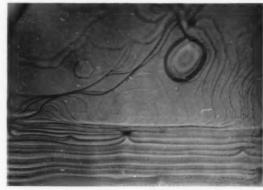


Fig. 8. ×1029



Fig. 9. ×693

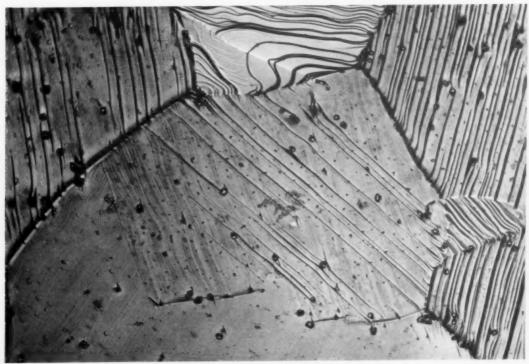


Fig. 10. ×1305

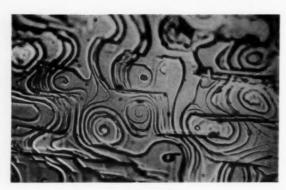
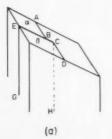


Fig. 11. ×722

DISCUSSION

The interesting fact of this study is the association of the non-coherent twin boundaries either with spiral figures or with deep channels, both of which represent the emergence points of dislocation lines on the surface. Whereas inside the crystals the emergence of total dislocations gives a full explanation of the observed figures, at the non-coherent twin boundaries the total dislocations cannot produce the necessary twin relation. Frank⁽¹⁵⁾, Frank and Van der Merve⁽¹⁶⁾, Thompson and Millard⁽¹⁷⁾ in studying the formation and growth of mechanical twins have suggested that some kind of partial dislocations of the Shockley type, called "twin dislocations," can satisfactorily explain the twinning. We think that this explanation also applies to annealing twins.

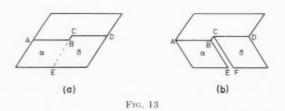


(b)

Fig. 12

When a recrystallization twin terminates inside the crystal or has a non-coherent twin boundary, these discontinuities are the emergence points of Shockley partial dislocations surrounding the stacking faults. The width of the non-coherent twin boundary is therefore directly related to the number of Shockley partial or twin dislocations.

Alternatively one may approach this matter by cutting a solid block so as to give a twin having a non-coherent boundary in the surface. The block of the Fig. 12a is cut in the plane ECHG and then the parts α and β are pushed in a direction EG parallel to this plane until the two angles γ and γ' are equal. A twin is formed with the configuration of Fig. 12b. AB and CD are then the traces of {111} twin planes and BC the non-coherent twin boundary, created by the twin dislocation with screw character. So the step BCFE will wind up in a spiral during evaporation, because it is fixed in C by the twin dislocation. This model explains not only the spiral formation at the non-coherent twin boundary, but also the relation between step-height and width of the non-coherent twin boundary, which are both related to the number of twin dislocations. A similar approach can be used for twin-dislocations with edge character. Here, however, it is evident that only a channel can be expected after evaporation (Fig. 13a, b).



195

The twin dislocations or Shockley partials are confined to the twinning planes {111} and form dislocation loops inside the crystal. As the character of the dislocation changes along the dislocation line when the loop arrives at the surface, its emergence points can have a screw, an edge or mixed character depending upon the orientation.

A dislocation loop coming to the surface has two emergence points which are usually in the same position but of opposite sign. Figs. 7, 8 and 9 show such loops coming to the surface in two emergence points, both of which are screw but of opposite sign as the spirals have opposite senses. Fig. 14 shows schematically these loops confined to the twinning plane.

The relation of the recrystallization twins to the twinning-dislocations is well demonstrated. This

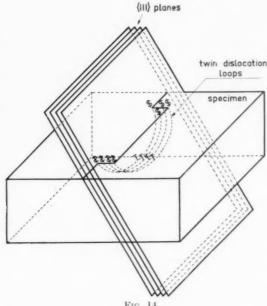


Fig. 14 relation leads to some consequences imposed by the properties of the twin dislocations. The most important is due to the confinement of the Shockley partial dislocations in the {111} planes so that they can move only in directions parallel to these planes.

VOL.

1959

Thus, the formation of recrystallization twins must be related to the octahedral planes and their growth or disappearance must be parallel to the same planes.

In the literature, there are several indications, (19.20.21) that the growth of recrystallization twins is parallel to the {111} plane. We have tried to verify these observations in a systematic way. For this purpose a double colouring technique previously used by one of us, (22) to follow the displacement of the grain boundaries, was applied to follow the growth and the disappearance of annealing twins. For colouring we used Jacquet's method, (23) which consists of the formation of thin sulphide layers on the copper surface exhibiting interference colours. The colouring is made, the layer is dissolved, the sample annealed and after annealing coloured again. By this method it is possible to see the initial and final positions of the boundaries and to follow their movement. Fig. 15 shows a micrograph in which the initial and final positions of the twin boundaries are clearly visible. The final position is represented by the zig-zag boundary between the light and dark regions of the photograph. The zig-zag boundary indicates clearly that the movement of the twin boundaries is parallel to the twin plane {111} and that the initial straight non-coherent boundaries move in sections, possibly

with different velocities. The zig-zag boundary shows that when an initial straight non-coherent twin boundary is large enough to contain a large number of twin dislocations, these dislocations can move independently in smaller numbers. As a consequence, it seems impossible to determine a definite crystallographic plane of the non-coherent boundary because of the chance stopping of twin dislocations. This movement can occur by the expansion or the contraction of the dislocation loops as can be seen in Fig. 14. In a recrystallized matrix, the driving force seems to lie in the tendency of dislocation loops to reduce the enclosed surface. However, this cannot explain the large expansion of these loops in a deformed matrix. (24) While this movement is very similar to the movement of the grain boundaries, (25) in a deformed matrix the loops move away from the centre of curvature, that is to say in a recrystallized matrix the loops usually contract and in the deformed matrix expand.



Fig. 15. $\times 473$

The main conclusion of this work is that noncoherent twin boundaries are the emergence points of twin dislocations. This easts a new light on the preferential etching of these boundaries in contrast to coherent boundaries, (26.27.28) and the preferential precipitation at their sites. (29,22,30)

ACKNOWLEDGMENT

We are indebted to Dr. R. H. Gillette for continued interest in this work.

REFERENCES

- R. L. Fullmann, J. Appl. Phys. 22, 456 (1951).
 T. H. Blewitt, R. R. Coltmann and J. K. Redman, J. Appl. Phys. 28, 651 (1957).
 P. Haasen, Phil. Mag. 3, 384 (1958).
 H. Suzuki and C. S. Barrett, Acta Met. 6, 156 (1958).

- 5. F. C. Frank, Disc. Faraday Soc. 186, 48 (1949).
- 6. W. Dekeyser and S. Amelinckx, Les Dislocations et la Croissance des Cristaux, Masson, Paris (1955).

- worths, London (1953).
- 8. N. Cabrera, J. Chim. Phys. 53, 675 (1956).
- 9. S. AMELINCKX and E. VOTAVA, Naturwissenschaften 41,
- E. Votava, Z. Metallk. 47, 309 (1956). 10. E. Votava, A. Berghezan and R. H. Gillette, Naturwissenschaften **44**, 372 (1957). 11. E. Menzel, Z. Phys. **132**, 508 (1952). 12. C. F. Elam, Trans. Faraday Soc. **32**, 1604 (1936).

- 13. B. Chalmers, R. King and R. Shuttleworth, Proc.

- B. CHALMERS, I. KING and R. SHETTERWORTH, 1796.
 Roy. Soc. A 193, 465 (1948).
 J. MOREAU and J. BÉNARD, J. Inst. Met. 83, 87 (1955).
 F. C. FRANK, Phil. Mag. 42, 809 (1951).
 F. C. FRANK and H. J. VAN DER MERVE, Proc. Roy. Soc. A 198, 205 (1949).
- 17. N. THOMPSON and D. J. MILLARD, Phil. Mag. 43, 422 (1952).
- R. B. Heidenreich and W. Shockley, Report of a conference on the strength of solids, University of Bristol; England. Physical Society London (1948).
- 19. J. E. Burke, Trans. Amer. Inst. Min. (Metall.) Engrs. 188, 1324 (1950).
- 20. W. G. Burgers and J. J. A. Ploos van Amstel, Physica 5, 305 (1938).
- 21. G. W. RATHENAU and G. BAAS, Physica 17, (1951).

- 7. A. R. Verma, Crystal Growth and Dislocations. Butter- 22. A. Berghezan, Thesis—Paris 1952—Public. Sc. et Techn. Min. Air, Nr. 283, p. 29 (1953).
 - M. P. A. JACQUET, Rev. Min. 42, 133 (1945).
 - 24. E. Votava, unpublished results.
 - 25. R. H. Beck, Metal Interfaces. p. 208 American Society for Metals, Cleveland (1952).
 - 26. P. LACOMBE and N. YAMAQUIS, C. R. Acad. Sci. Paris
 - 921, 921 (1947).
 N. Yamaquis and P. Lacombe, C. R. Acad. Sci. Paris
 - 226, 498 (1948).
 G. Chaudron, P. Lacombe, N. Yamaquis, C. R. Acad. Sci. Paris 226, 1372 (1948).
 - 29. P. J. E. FORSYTH, G. J. METCALFE, R. KING and B. Chalmers, Nature, Lond. 158, 875 (1946).
 - 30. H. HATWELL and A. BERGHEZAN, Conference on precipitation in steel. Sheffield, July 1958 (in the press).
 - 31. R. MADDIN, C. H. MATHEWSON and W. R. HILBOARD,
 - Trans. Amer. Inst. Min. (Metall.) Engrs. 185, 655 (1949). 32. R. L. FULLMANN and J. C. FISHER, J. Appl. Phys. 22, 1350 (1951).
 - 33. W. G. Burgers, Proc. Kon. Ned. Akad. Wet. 50, 588 (1947).

 - W. G. Burgers, *Physica* **15**, 95 (1949).
 W. G. Burgers, J. C. Meijs and T. J. Tiedema, *Acta Met.* 1, 75 (1953).

THE DIFFUSION OF CARBON DURING PRECIPITATION IN α-IRON*

R. H. DOREMUS+

The activation energy for precipitation of carbon from α -iron was measured to be 17.1 \pm 0.5 kcal/mole by starting the precipitation at one temperature and finishing it at another. The activation energy was the same within experimental error for aging temperatures from 0° to 170°C, for samples strained up to 4 per cent, and for samples of different concentration. This energy is appreciably smaller than that of 20.1 kcal/mole for carbon diffusion in α -iron measured from elastic relaxation methods. Possible reasons for this difference are discussed, but no satisfactory explanation for it is found.

LA DIFFUSION DU CARBONE AU COURS DE LA PRECIPITATION DANS LE FER ALPHA

L'énergie d'activation pour la précipitation du carbone dans le fer alpha a été mesurée en débutant la précipitation à une température et en la terminant à une autre. La valeur ainsi obtenue est de 17.1 ± 0.5 kcal/mole. L'énergie d'activation demeure inchangée pour des températures de vieillissement entre 0° et 170° C pour des échantillons déformés de 4% max. et pour des échantillons de concentration différente en carbone. Cette énergie est relativement plus petite que celle (20.1 kcal/mole) obtenu pour la diffusion du carbone dans le fer alpha par des méthodes de relaxation élastique.

Les raisons possibles de cette différence sont discutées par l'auteur mais une explication satisfaisante n'a pas été trouvée.

DIFFUSION VON KOHLENSTOFF WAHREND DER AUSSCHEIDUNG IN α-EISEN

Die Aktivierungsenergie für die Ausscheidung von Kohlenstoff aus α -Eisen wurde zu 17.1 ± 0.5 keal/Mol bestimmt, indem man Beginn und Ende der Ausscheidung bei verschiedenen Temperaturen verlaufen liess. Innerhalb des experimentellen Fehlers ergab sich derselbe Wert für Anlasstemperaturen von 0° bis 170° C, für Verformungsgrade bis 4% und für verschiedene Konzentrationen. Diese Energie ist erheblich geringer als der Wert von 20.1 kcal/Mol, den man mit Hilfe der elastischen Relaxation für die Diffusion von Kohlenstoff in α -Eisen misst. Mögliche Ursachen für diesen Unterschied werden diskutiert, doch fand sich keine befriedigende Erklärung.

INTRODUCTION

1959

Carbon atoms diffuse through the iron matrix to growing carbide particles when these particles precipitate from a supersaturated solution in α -iron. This diffusion is generally assumed to control the rate of growth of the carbide phase, and the diffusion coefficient of carbon is calculated from the results of Wert. Wert measured this diffusion coefficient with a variety of experimental methods over a wide temperature range, and he found the results were best fitted by the equation

$$D = 0.02 \exp(-20,100/RT). \tag{1}$$

Below 125°C Wert measured the diffusion coefficient by means of the elastic after effect and internal friction of carburized iron. Both these methods measure the relaxation time for the return of the interstitial carbon atoms to their equilibrium configuration after this configuration is disturbed by a small stress. Thus the rate of jumping of the carbon atoms from one interstitial site to a neighboring one is directly measured. Wert also measured the

diffusion coefficient of carbon in iron at 150°C and 200°C from the rate of carbide precipitation. In this method the precipitation is started at one temperature T_1 and completed at a higher temperature T_2 . The ratio of the rates of precipitation at the two temperatures is taken to be proportional to the ratio of the carbon diffusion coefficients, since the number of carbide particles should remain constant throughout a run under these experimental conditions. Here the long-range diffusion of the carbon through the iron to the particles is measured, rather than the jumping rate from one interstitial site to another. However, if no "short circuits" for diffusion of carbon to the particles exist, and if the precipitation rate is entirely controlled by solute diffusion through the matrix, this method should give the same activation energy for diffusion as the relaxation methods. Wert found that his measurements at 150°C and 200°C by the precipitation method compared fairly well with those from the relaxation methods.

To determine if the diffusion coefficient calculated from equation (I) is indeed the one involved in the precipitation of carbon from α -iron, the activation energy of the precipitation process was measured by the method of Wert. This activation energy was found

^{*} Received August 15, 1958.

[†] General Electric Research Laboratory, Schenectady, N.Y.

to be appreciably less than 20.1 kcal, and experiments to examine this discrepancy are described and discussed in this report.

EXPERIMENTAL

The rate of carbide precipitation from a-iron was calculated from internal friction measurements on carburized iron wires. The materials and methods have been described. (2) Wires of vacuum-melted iron were cleaned of residual nitrogen and carbon by treatment with wet hydrogen, recrystallized from the y-region to give a large grain size, carburized at about 700°C, and water-quenched to room temperature. The wires were then aged at a certain temperature T_1 until from 30% to 50% of the carbon had precipitated; then they were aged at a higher or lower temperature T_2 for the remainder of the precipitation. At intervals throughout the process the concentration of carbon still in solution was measured from the internal friction peak. The fraction of total precipitation W is then given by

$$W = (Q_o^{-1} - Q_t^{-1})/(Q_o^{-1} - Q_t^{-1})$$

where Q^{-1} is the height of the internal friction peak and the subscripts o, t, and f refer to the start, the time t, and the end of the precipitation process, respectively. A value of 1.1×10^{-3} was used for Q_f^{-1} in all the runs.

RESULTS

The experimental results are summarized in Table 1. All wires except number six were quenched from 700°C, so their initial carbon concentrations (2,3)

TABLE 1

Run no.	T_1	T_2	ρ	Q	Remarks
1	0	37	41	16.8	
2 3	37	120	360	17.1	
3	120	37	330	16.9	1% strain
4	120	37	300	16.6	4% strain
5	62	120	50	17.6	
6	62	120	50	17.6	Lower conc.
7	120	62	50	17.6	
8	80	120	11.5	16.8	
9	120	170	11	16.6	

were about 0.025 wt. %. Sample 6 was carburized at 700°C and then quenched from 610°C, so its carbon concentration was about 0.012 wt. %. Wire number one only was quenched directly into an ice bath. To insure uniform deformation the grain size of sample four was kept small by not recrystallizing it from the γ -region. The activation energy Q was calculated from the ratio ρ between the precipitation rates at T_1 and T_2 (in degrees K) with the following equation:

$$Q = R \ln \rho / [(1/T_1) - (1/T_2)] \tag{2}$$

195

In Table 1, ρ is always greater than one, so if $T_1>T_2$ the sign of Q calculated from equation (2) must be changed.

Three representative runs are plotted in Fig. 1. In these runs the wires were cycled between the same temperatures, as shown in Table 1; T_1 was 62°C for runs 5 and 6 but 120°C for run 7. Thus for runs 5 and 6 the time at $T_2=120$ °C was multiplied by

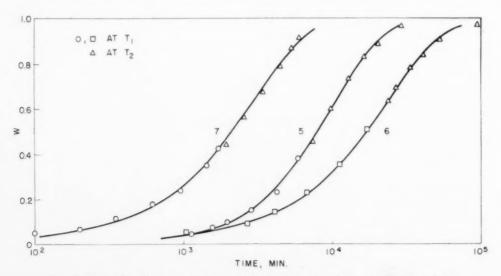


Fig. 1. Thermal cycling runs for the precipitation of carbon from α -iron. Lines drawn from equation (3) with a=300 for runs 6 and 7, and $a=50{,}000$ for run 5. Divide the time scale by ten for run 7.

fifty $(=\rho)$ to give the points in Fig. 1, whereas for run 7 the time at T_2 was divided by fifty for the points plotted. The lines in Fig. 1 were drawn from a numerical integration of the equation

$$\int_{\sigma}^{z} \frac{z \, dz}{a(1 - W)} = Kt \tag{3}$$

in which a is a dimensionless parameter, t is the time, and K is a constant for any particular run that depends upon the temperature and the number density and shape of the precipitate particles. The relation between W and z is:

$$aW = 2z + z^2 + (4z^3/3\pi^2).$$

Equation (3) was derived for the diffusion-controlled growth of asymmetric particles, (4) but it will be used here strictly as an empirical relation. The equation

$$-\ln\left(1 - W\right) = Kt^n \tag{4}$$

with n a constant, is frequently compared to precipitation data, but equation (3) fitted the present results better than this equation.

DISCUSSION

There are several assumptions involved in using this method to find the activation energy for precipitation. One assumption is that the number of precipitate particles is constant throughout the precipitation process and at both temperatures. In all of the runs reported here the curves plotted with the ratios p given in Table 1, such as those shown in Fig. 1, could be superimposed on the curves that resulted when a sample was aged at a temperature of T_1 throughout the entire precipitation process. For example, the curve for run 7 in Fig. 1 superimposes exactly on the curve in Fig. 1, ref. 2 for a unstrained wire aged at 120°C. These correspondences are good evidence that the number of particles is indeed constant, because a change in the number of particles by dissolution or formation at T_2 would result in different kinetic behavior at T_2 . Furthermore these results argue against any nucleation during the measured precipitation period, because the rate of such nucleation would almost certainly have a different temperature dependence than the growth rate of the particles. Thus the model proposed by Wepner⁽⁵⁾ cannot apply to this system, because this model requires continued nucleation throughout the precipitation process.

The average value of Q from Table 1 is 17.1 kcal/mole with a variation of ± 0.5 kcal/mole. In an earlier study Wert⁽⁶⁾ reported a value of 17.5 \pm 1.7 kcal/mole from similar experiments on precipitation rates of

carbon in α-iron in the range 100°-150°C. The points in Fig. 4 of ref. 1 that were determined by the precipitation method seem to fall slightly below the curve for equation (1) although the graph is too small to make an accurate estimate. In any event the activation energy for precipitation seems to be appreciably lower than the activation energy for diffusion that is calculated from the relaxation experiments. The temperature of maximum internal friction at a given frequency did not vary with degree of precipitation for the runs reported in Table 1: this same result has been found by other workers. (7,8) Thus the relaxation process is not affected by the presence of precipitate particles, and the rate at which carbon atoms jump from one interstitial site to another is constant throughout the precipitation process.

The activation energy for precipitation will equal that for diffusion only if the precipitation process is entirely controlled by solute diffusion through the matrix. If a reaction at the particle surface is slow enough it may also influence the kinetics of precipitation. When a surface reaction entirely controls precipitation. W is proportional to t^3 for spherical particles in the early stages of precipitation: for mixed reaction and diffusion controlled processes the proportionality is between $t^{3/2}$ and t^3 for spherical particles. (9) For aging temperatures above about 60°C the exponent of initial time-dependence of W is always less than 3/2 for the precipitation of carbon in a-iron, so a reaction at the particle interface is probably not influential in this process, although one cannot eliminate it completely from the experimental evidence available. In the remainder of this discussion we will assume that interface reactions are unimportant in the precipitation of carbon from α -iron.

The results in Table 1 show that the activation energy for precipitation of carbon in α -iron is constant within experimental error from 0° to 170° C at least. Neither changes in carbon concentration nor coldworking seem to affect this activation energy. The kinetics of carbide precipitation below about 60° C are different from those at higher temperatures. This phenomenon will be discussed more completely in a separate report, but it is interesting to note here that the activation energy for particle growth is not affected by this change. Presumably the different kinetics are caused by different nucleation mechanisms and consequent variations in the number density of particles, rather than any change in growth mechanism.

The lower activation energy for long-range diffusion of carbon atoms to precipitate particles may be caused

VOL. 7 1959

by diffusion short circuits in the iron matrix. Grain boundaries can act as short circuits for diffusion in precipitation. (10) but the large grain size in the present samples eliminates this possibility. Isolated disloeation lines may also provide routes for rapid diffusion.(11) thus giving a lower activation energy for long-range diffusion than for site exchange. To test this possibility two wires were strained after quenching, and then the activation energy for precipitation was determined in the same way as for the unstrained wires. As shown in Table 1 the activation energies for wires strained 1 per cent and 4 per cent were the same, within experimental error, as for the unstrained wires. Therefore a large change in the dislocation density does not appreciably affect the activation energy for diffusion in precipitation, and dislocation lines are probably not acting as diffusion short circuits. The strain field around a precipitate particle may enhance solute diffusion in its vicinity, but in this case one would expect that the activation energy would depend upon the particle size. As will be discussed in another report, the number density of carbide particles was much greater at lower aging temperatures for the same carbon concentration, so the particle size was smaller, particularly for sample number one. This sample gave the same activation energy as the others, however, so the diffusion was apparently not strongly affected by the size of the precipitate particles. Quenched-in defects might cause a lower activation energy for diffusion, but a wire that was air-quenched showed about the same rate of precipitation as the waterquenched wires, although some carbon precipitated at higher temperatures in the air-quench. Thus none of the more obvious possibilities for short circuiting diffusion seems to be operative here, although a more subtle mechanism may be responsible for the lower activation energy of precipitation.

One can estimate the pre-exponential factor appropriate to an activation energy of 17.1 kcal/mole for diffusion during precipitation if the carbide

particle size is known. Coercive force measurements(12) indicate that the carbide particle diameter at aging temperatures from 200° to 250°C is in the range 500-1000 Å at about 95 per cent precipitation, although this estimate is rather uncertain. From an electron micrograph, Tsou et al. (13) concluded that the carbide particles in α-iron aged 1 hr at 100°C were about 300–500 Å in diameter. If a value of 400 Å is used with comparable data on precipitation, the carbon diffusion coefficient at 100°C can be estimated to be roughly 10⁻¹³ cm²/sec. Then the diffusion coefficient of carbon during precipitation in a-iron is approximately

$$(10^{-3}) \exp(-17,100/RT)$$
.

The absolute values of number densities of carbide particles that have been calculated using equation (1) must be questioned as a result of this study. In particular the calculations of the author in two previous reports(2,4) should be modified somewhat, although the qualitative conclusions of these studies are not altered by this change in the diffusion coefficient of carbon.

ACKNOWLEDGMENTS

The author would like to thank R. W. Powers, D. Turnbull, and D. A. Vermilyea for helpful suggestions on this work.

195

REFERENCES

- 1. C. WERT, Phys. Rev. 79, 601 (1950).
- 2. R. H. DOREMUS, Acta Met. 6, 674 (1958).
- 3. G. Lagerberg and A. Josefsson, Acta Met. 3, 236 (1955).
- 4. R. H. DOREMUS, Acta Met. 5, 393 (1957).
- W. WEPNER, Arch. Eisenhüttenw. 24, 275 (1953).
- C. Wert, J. Appl. Phys. 20, 943 (1949).
- 7. J. D. Fast und L. J. DIJKSTRA, Philips Techn. Rev. 13, 172 (1951).
- 8. W. KÖSTER, L. BANGERT, and R. HAHN, Arch. Eisen-
- hüttenw. **25**, 569 (1954). 9. D. Turnbull, Acta Met. **1**, 764 (1953).
- 10. D. Turnbull, Defects in Crystalline Solids, p. 203. Physical Society, London (1954).
- E. W. Hart, Acta Met. 5, 507 (1957).
- L. J. DIJSTRA and C. WERT, Phys. Rev. 79, 979 (1959).
 A. L. TSOU, J. NUTTING and J. W. MENTER, J. Iron St. Inst. 172, 163 (1952).

OBSERVATIONS ON REGULAR ARRAYS OF ETCH PITS IN A TITANIUM–10% MOLYBDENUM ALLOY*

T. H. SCHOFIELD and A. E. BACON†

Regular arrays of etch pits observed in rapidly cooled titanium-10% molybdenum alloys are considered to indicate the sites of unstable groups of dislocations which collapse, at slower rates of cooling, into a more stable network of sub-grain boundaries.

OBSERVATIONS DE RESEAUX REGULIERS DE PIQURES DE CORROSION DANS UN ALLIAGE TITANE-10% DE MOLYBDENE

Les auteurs ont observé des réseaux réguliers de piqures de corrosion dans un alliage de titane-10%0 molybdène refroidi rapidement. Ils pensent que ces réseaux indiquent les sites de groupes instables de dislocations qui pour des vitesses de refroidissement plus faibles donneront lieu à la formation d'un réseau plus stable de sous-frontières.

BEOBACHTUNGEN VON REGELMÄSSIGEN ANORDNUNGEN VON ATZGRÜBCHEN BEI EINER TITAN-10% MOLYBDÄN-LEGIERUNG

Es wird angenommen, dass regelmässige Anordnungen von Ätzgrübchen, die auf rasch gekühlten Titan-10% Molybdän-Legierungen beobachtet werden, die Lagen von instabilen Versetzungsgruppen anzeigen, welche bei langsameren Abkühlgeschwindigkeiten in ein stabileres Netzwerk von Subgrenzen übergehen.

INTRODUCTION

Regular arrays of dislocations have been revealed in transparent crystals of inorganic salts by a technique known as "decoration". For example, Hedges and Mitchell⁽¹⁾ have observed dislocation sites in the form of small arrays and nets in crystals of silver bromide, which have been revealed by precipitation of metallic silver after exposure to light. Similarly, Amelinckx⁽²⁾ has shown regular and extensive networks in strained single crystals of alkaline chlorides containing small amounts of silver halides which were reduced by treatment in hydrogen at low temperatures.

1959

Sub-grain boundaries have been observed in metals and alloys for many years and it is now generally accepted that they consist of dislocations decorated by precipitates or solute atoms.

Large and regular arrays of dislocations do not however appear to have been seen in metals and alloys, although McQuillan⁽³⁾ has shown a regular pattern of "precipitate" in a titanium– 10° /₀ chromium alloy which may indicate precipitation at regularly spaced dislocations. Recently, Feltham⁽⁴⁾ has revealed semi-regular arrays of etch pits in slightly deformed nickel. Extensive and regular arrays of etch pits have been studied by the authors in some titanium alloys, in particular titanium–molybdenum and titanium–iron. The present work is concerned with such arrays in a titanium– 10° /₀ molybdenum alloy after cooling from the β -phase field at a rate which is rather critical.

EXPERIMENTAL

The regular arrays of etch pits are found in small scale Jominy test specimens. This test consists of heating a small cylinder of the alloy 1 (15.9 mm long, 3.2 mm dia.) in the β -phase field (925°C) and rapidly quenching one end in a jet of water. The specimen thus cools at progressively different rates along its length. A mid-longitudinal section is polished and, after suitable etching, the section towards the less rapidly cooled end shows regular arrays of etch pits, incomplete sub-grain boundaries and small areas free from etch pits (Fig. 1). The quenched end of the specimen does not show either etch pits or sub-grain boundaries. The hardness shows a progressive increase of about 200 points (D.P.H) from the quenched to the more slowly cooled end of the specimen. The etching reagent used consists of either an aqueous solution containing 0.5% hydrofluoric acid and 1% nitric acid or Keller's reagent. § Hot 20% sulphuric acid, although less convenient to use, gives similar results. The occurrence of the etch pits is thus not specific to a particular reagent.

The occurrence of large and regular arrays is comparatively rare but small and often irregular arrays consisting of about 10–20 pits are common. Figs. 3–6 are typical examples of the larger and regular arrays observed. The average density of pits in these arrays

^{*} The work described in this paper has been carried out as part of the General Research Programme of the National Physical Laboratory. Received August 1, 1958.

[†] National Physical Laboratory, Teddington, England.

^{*} Several specimens of the alloy were prepared by melting together titanium sponge (D.P.H. 130) and high-purity molybdenum in an arc furnace. The melted buttons were generally heated at 1100°C for 4 hr and water quenched before preparation of the Jominy test specimens. Similar results were obtained on alloys prepared from van Arkel titanium.

[§] Sodium fluoride 0.5 g, hydrochloric acid 2 ml, nitric acid 1 ml water 97 ml.

Fig. 1. Relatively slowly cooled end of Jominy test specimen. Opposite end quenched with water jet from 925 $^{\circ}$ C.

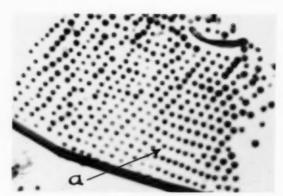
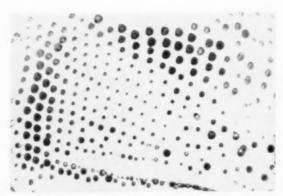


Fig. 4. Array near grain boundary showing "dislocation".



Fig. 2. Relatively slowly cooled end of Jominy test specimen. Opposite end quenched on metal plate from $850^{\circ}\mathrm{C}$



195

Fig. 5. Array showing segregation of pits at sub-grain boundary, and adjacent zone free from pits.

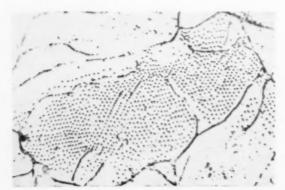


Fig. 3. Large array in sub-grain showing regular groups.

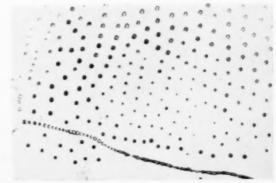


Fig. 6. As Fig. 5 after removal of about 30 μ and re-etching.

varies between 0.2 and 2.0×10^8 cm², i.e. the average spacing between pits is $0.7\text{--}2.2 \times 10^{-4}$ cm $(0.7\text{--}2.2~\mu)$. The pits tend to be rounded but rarely seem to be completely circular in contour; occasionally pits with three curved sides are observed. After normal periods of etching the pits are funnel-shaped and the depth is about twice the diameter.

If a Jominy test specimen is heated to a lower temperature in the β -phase field (850°C) and the end which is normally quenched by a water jet is allowed instead to fall on a metal plate, the rate of cooling along the specimen is reduced and the microstructure at a corresponding position to the normally quenched specimen now consists of a complete network of subgrain boundaries with no regular arrays of etch pits, although traces of a finer sub-grain network of precipitate are visible in some of the larger sub-grains (Fig. 2).

Repeated polishing and re-etching, removing approximately 1 μ of surface at each stage, shows that the pits in regular arrays reappear although their relative positions are displaced with depth. This demonstrates that each pit represents either a line or a very closely spaced series of points, running approximately, but not exactly, parallel, and at right angles to the etched surface. The length of these lines is in some cases at least 30 u. At greater depths below the original surface the pattern of the group is either lost completely, or becomes unrecognisable. Fig. 6 shows the array in Fig. 5 after removing approximately 30 μ and re-etching. The thickness of material removed is in this case about equal to the width of the array. When a section is taken through a group of pits and at right angles to the original surface, no group of roughly parallel lines can be revealed by etching. The etching patterns thus appear only when the etched surface is at a suitable inclination which appears to be approximately normal to the lines. Consequently the loss of the patterns at depths greater than 30 μ may mean only that the lines have altered in direction to such a degree that etch pits are no longer produced. The microstructures of specimens showing regular arrays is similar in sections taken in different directions. This suggests that the proportion of lines approximately normal to the etched surface is independent of the orientation of the surface.

1959

Fig. 5 also shows what appears to be a grouping of pits at a sub-grain boundary with an adjacent region free from pits, while Fig. 6 illustrates the same sub-boundary which now consists of a single row of pits.

Zones free from etch pits are frequently observed adjacent to sub-boundaries (Figs. 3, 5 and 6). Similar zones have been observed by Wyon and Marchin⁽⁵⁾ in

aluminium, and by Feltham (loc. cit.) in nickel. Assuming that the etch pits indicate dislocation sites, the former authors suggest that precipitation along the boundaries has denuded the surrounding region of impurity atoms, and that etch pits form only at those boundaries which contain impurities; while Feltham assumes that the strong interaction between pile-ups near the boundaries has virtually depleted the zone of dislocations.

Fig. 3 shows a large array within a sub-grain, and it is difficult to decide whether some rows of pits may be regarded as sub-boundaries or part of the array; it is probable that there is no definite distinction. It will be seen that the whole array may be sub-divided into small groups each of which has a fairly regular pattern. Although the spacing along a particular line of etch pits is generally uniform it varies in different lines and in different groups. These differences in spacing between adjacent lines or groups give rise to configurations, as at 'a' in Fig. 4, which bear a geometrical resemblance to dislocations in a lattice of atoms.

The etch pits in some arrays are fairly uniform in size (Fig. 3) while in others the sizes vary (Fig. 5). Pits of one size also tend to congregate together and the arrangement repeats on repolishing and re-etching. The reasons for these differences is not apparent but it may be associated with the different inclination of the lines with respect to the surface or, possibly, to varying degrees of decoration.

Figs. 7 and 8 show respectively a small array before and after making a microhardness indentation. Fig. 9 shows the same array after removing approximately

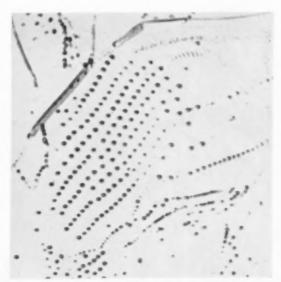


Fig. 7. Typical array. ×2500.

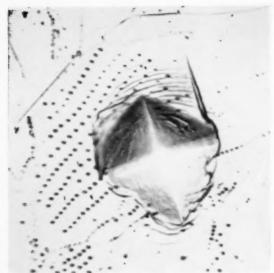


Fig. 8. As Fig. 7 after micro-hardness indentation. ×2500.

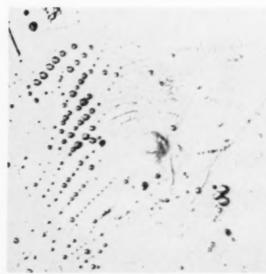


Fig. 9. As Fig. 8 after removal of approximately 2 μ by repolishing. Subsequently deeply etched. $\times 2500$.

 $2~\mu$ from the surface by light polishing and re-etching. The regular rows of etch pits no longer reappear in the highly strained region adjacent to the indentation.

CONCLUSIONS

It is concluded that the regular arrays of etch pits observed in titanium–10% molybdenum alloy after critical rates of cooling from the β -phase field indicate the sites of dislocations decorated by solute atoms.

Some evidence for this conclusion is provided by the general lack of distinction between the etch pits which delineate sub-grain boundaries, and which would be agreed represent dislocation sites, and those in regular arrays. That etch pits do not reform, in the highly strained region adjacent to a hardness indentation, suggests that the strain is sufficient to remove the dislocations from their atmospheres of solute atoms which do not then act as sources of etch pits.

The configuration of the arrays resembles those suggested in the classical work of Taylor⁽⁶⁾ except that the dislocation lines are curved and therefore are not pure edge.

It is probable that the strains set up during rapid cooling, and by the partial β - α transformation, result in the movement of the dislocations which temporarily segregate into regular but unstable groups and which collapse into a more stable network of sub-grain boundaries when the rate of cooling is somewhat lower.

This paper is published by permission of the Director of the National Physical Laboratory.

REFERENCES

- J. M. Hedges and J. W. Mitchell, Phil. Mag. 7 (44) 223-(1953).
- S. AMELINCKX, Acta Met. 6 (1) 34 (1958).
- M. K. McQuillan, The Mechanism of Phase Transformations in Metals, p. 290. Monograph and Report Series No. 18, Institute of Metals, London (1957).
- 4. P. Feltham, J. Inst. Met. 86, 237 (1957-58)
- 5. WYON and MARCHIN, Comptes Rendus 238, 2420 (1954).
- 6. G. I. Taylor, Proc. Roy. Soc. 145 A, 262 (1934).

A CORRELATION OF DATA ON DIFFUSION OF SOLUTES IN FACE-CENTERED CUBIC METALS*

D. TURNBULL and R. E. HOFFMAN†

It is shown that the available data on the diffusion coefficients of substitutional solutes B in dilute face-centered cubic solutions in A can be described approximately by the equation:

$$\Delta F'_{\rm B} - \Delta F'_{\rm A} = \frac{Q_{\rm A}}{4} \frac{U_{\rm A} - U_{\rm B} - \overline{\Delta U}_{\rm AB}}{U_{\rm A}} \, \cdot \label{eq:delta-F}$$

 $\Delta F'_{\rm B}$ and $\Delta F'_{\rm A}$ are the free energies of activation for solute and solvent diffusion at the melting point of the pure solvent; $Q_{\rm A}$ is the activation energy for self-diffusion in pure A; $U_{\rm A}$ and $U_{\rm B}$ are the cohesive energies of pure A and pure B respectively and $\overline{\Delta U_{\rm AB}}$ is the heat of solution of B in A.

This correlation, though not in strict accord with the nearest neighbor model for solutions, was suggested by it.

UNE CORRELATION DES RESULTATS DE DIFFUSION D'ELEMENTS SOLUTES DANS LES METAUX CUBIQUES A FACES CENTREES

Les auteurs montrent que les données sur les coéfficients de diffusion de solutés de substitution B dans des solutions diluées A cubiques à faces centrées peuvent être décrites approximativement par l'équation :

$$\Delta F'_{\mathrm{B}} - \Delta F'_{\mathrm{A}} = \frac{Q_{\mathrm{A}}}{4} \frac{U_{\mathrm{A}} - U_{\mathrm{B}} - \overline{\Delta U}_{\mathrm{AB}}}{U_{\mathrm{A}}}.$$

Dans celle-ci, $\Delta F'_{\rm B}$ et $\Delta F'_{\rm A}$ sont les énergies libres d'activation du soluté et de diffusion du solvant au point de fusion du solvant pur; $Q_{\rm A}$ est l'énergie d'activation d'auto-diffusion dans A pur; $U_{\rm A}$ et $U_{\rm B}$ sont les énergies de cohésion de A et B purs et $\overline{\Delta U}_{\rm AB}$ est la chaleur de solution de B dans A.

Cette relation bien qu'elle ne soit pas en accord strict avec le modèle du plus proche voisin a cependant été déduite de celui-ci.

EINE BEZIEHUNG ZWISCHEN DEN KENNGROSSEN DER DIFFUSION GELÖSTER ATOME IN KUBISCH-FLÄCHENZENTRIERTEN METALLEN

Die vorhandenen Angaben über die Diffusionskoeffizienten von B-Atomen, die sich auf Gitterplätzen einer kubisch-flächenzentrierten Matrix A in verdünnter Lösung befinden, können genähert durch folgende Gleichung wiedergegeben werden:

$$\Delta F'_{\mathrm{B}} - \Delta F'_{\mathrm{A}} = rac{Q_{\mathrm{A}}}{4} \, rac{U_{\mathrm{A}} - U_{\mathrm{B}} - \overline{\Delta U}_{\mathrm{AB}}}{U_{\mathrm{A}}} \, .$$

 $\Delta F'_{\rm B}$ und $\Delta F'_{\rm A}$ sind die freien Aktivierungsenergien für die Diffusion der gelösten bzw. der Matrixatome beim Schmelzpunkt des reinen Lösungsmittels; $Q_{\rm A}$ ist die Aktivierungsenergie für die Selbstdiffusion von reinem A; $U_{\rm A}$ und $U_{\rm B}$ sind die Kohäsionsenergien von reinem A bzw. B und $\overline{\Delta U}_{\rm AB}$ ist die Lösungswärme von B in A.

Diese Beziehung folgt zwar nicht streng aus einem Modell nächster Nachbarn für die Lösung, wird aber durch ein solches Modell nahegelegt.

1. INTRODUCTION

1959

Lazarus and his associates⁽¹⁾ found that the rate of diffusion of solute atoms in silver and copper solutions often increases with increasing excess of the valence of the solute over the solvent. Lazarus⁽²⁾ attributed this result to a repulsion between solute and solvent atoms brought about by imperfect screening of the excess solute nuclear charge. It was supposed that this repulsion would decrease the energy necessary to

create and move a lattice vacancy. These energy decrements were calculated by application of the Thomas–Fermi model and their sum was found to be in fair agreement with the observed difference in activation energy for solute and solvent self-diffusion in many cases. Lazarus obtains in general

$$(V_{\rm A} - V_{\rm B}) = K(Q_{\rm A} - Q_{\rm B})$$
 (1)

where V, Q, A and B denote respectively valence, activation energy for diffusion, solvent and solute. This equation should hold irrespective of the sign of $V_{\rm A}-V_{\rm B}$.

In the calculation it was assumed tacitly that the

^{*} This work was supported by the United States Atomic Energy Commission under contract No. N-31-109-Eng-2. Received August 25, 1958.

[†] General Electric Research Laboratory, Schenectady, New York.

exchange of vacancies with atoms in the first coordination shell of the solute imposes no limitation on the rate of diffusion (see Wyllie⁽³⁾ and Hoffman, Turnbull and Hart^(4,5) for discussion of this point). The agreement between the results of the calculation and experiment seemed to show that this assumption is justified and that the effects on solute diffusion of factors other than valence are unimportant.

However it was found later that the diffusion rate of some solutes is not adequately described by the valence theory. In particular, the rates of solute and solvent diffusion are substantially different in some noble metal systems (Cu, Ag, Au) where there is no valence difference. Also Lazarus et al. (6) found that the activation energy for the diffusion of the solutes Ni, Co and Fe into Cu decreased after Ni with decreasing atomic number contrary to what seemed to be required by the theory.

We have noted that in these exceptional cases the activation free energy for solute diffusion seems to correlate with the binding energy of the solute in solution inferred from the heat of solution. Actually Lazarus calculates the displacement of the binding energy due to imperfect screening and relates this directly to the difference in activation energy between solute and solvent diffusion. Therefore it is of interest to see if there is a relation between $Q_{\rm B}$ and the actual binding energy of the solute.

In this note we propose a correlation suggested by the nearest neighbor (quasichemical) theory between the free energy of activation for the diffusion of solute atoms in face centered cubic metals and the solute binding energies.

2. DEVELOPMENT OF CORRELATION

We assume the vacancy mechanism for diffusion; then the activation energy for diffusion of component i may be expressed

$$Q_i = E_i{}^f + E_i{}^m \tag{2}$$

where E_i^f and E_i^m are, respectively, the energies necessary to form and move the vacancy. Using the nearest neighbor theory as a guide, the binding energy $U_{\rm AB}$ of the solute atom B in solution in A, relative to the dilute vapor, may be written:

$$U_{\rm AB} = \frac{\overline{\Delta U}_{\rm AB} + U_{\rm B} + U_{\rm A}}{2} \tag{3}$$

where $U_{\rm B}$ is the binding energy of pure B in the face centered cubic modification, $U_{\rm A}$ is the binding energy in pure A and $\overline{\Delta U}_{\rm AB}$ is the partial molar energy of solution of B in A.

We now suppose that the activation energies for

exchange of the solvent or the solute with a vacancy are in the ratios of the corresponding binding energies; thus:

$$E_{\rm B}{}^m = E_{\Lambda}{}^m \frac{U_{\rm AB}}{U_{\Lambda}} \,. \tag{4}$$

Similarly and with the use of the nearest neighbor model we estimate for the energy of formation of a lattice vacancy in the first coordination shell of the solute:

$$E_{\rm B}{}^{f} = E_{\rm A}{}^{f} \left(\frac{11}{12} + \frac{1}{12} \frac{U_{\rm AB}}{U_{\rm A}} \right).$$
 (5)

From equations (2), (3), (4) and (5) we find:

$$Q_{\rm A} - Q_{\rm B} = \Delta Q = \left(\frac{U_{\rm A} - U_{\rm B} - \overline{\Delta U}_{\rm AB}}{2 \ U}\right) \times \left(\frac{E_{\rm A}^f}{12} + E_{\rm A}^m\right) \quad (6)$$

This value for ΔQ is, in the case of metal systems, much smaller than that, $\Delta Q \geqslant U_{\rm A} - U_{\rm AB}$, which would have been obtained by strict application of the nearest neighbor theory.

3. COMPARISON OF CORRELATION WITH EXPERIMENT

The displacement of activation energy given by (6) is markedly dependent on $E_{\rm A}{}^m$ which has been measured only in a few instances. For all our comparisons we shall accept, arbitrarily, the ratio 0.45 between $E_{\rm A}{}^m$ and $Q_{\rm A}$ found for gold by Baurle and Koehler.⁽⁷⁾ With this equation (6) becomes:

$$\Delta Q \approx \frac{Q_{\rm A}}{4} \left[\frac{U_{\rm A} - U_{\rm B} - \overline{\Delta U}_{\rm AB}}{U_{\rm A}} \right] \tag{7}$$

19

 ΔQ values for various face-centered cubic metal systems are tabulated in Table 1. The binding energies, columns 7 and 8, used in these calculations are taken from the compilation of Wigner and Seitz. (8) It was assumed that the energy of solution is equal to the heat of solution. The heats of solution of gold in copper, silver, and nickel and for nickel in gold are taken from the literature. (9,10) Those for nickel in copper and iron in cobalt are probably small because of the absence of intermediate phases, and are arbitrarily set equal to zero; all others were estimated from the change in solid solubility with temperature. An aggregate uncertainty of 5 kcal/g atom in the quantity $U_{\rm A} - U_{\rm B} - \overline{\Delta U}_{\rm AB}$ would correspond to about 0.8 kcal/g atom uncertainty in the calculated value of ΔQ .

Considering the reproducibility of activation energies by different laboratories it seems that the

TABLE 1

Solvent	Solute	$\begin{array}{c} D_{\theta} \\ (\mathrm{cm^2~sec^{-1}}) \end{array}$	$\frac{Q~(\text{keal/}}{\text{gm atom}})$	${\rm Log}\ D_{\rm M.P.}$	Diffusion references	$\begin{array}{c} (-U_{\partial \mathbf{A}}) \\ \text{kcal/g} \\ \text{atom} \end{array}$	$\begin{array}{c} (-U_{\rm B}) \\ {\rm keal/g} \\ {\rm atom} \end{array}$	$\overline{\Delta U}_{ ext{AB}}$ keal/g atom	ΔQ cale.	$\Delta(\Delta F')$ observed
copper	copper	$0.20 \\ 0.621$	47.12 49.56	$-8.293 \\ -8.194$	12 13	81.2	_	_	_	
copper	silver	$0.846 \\ 0.23$	47.29 44.0	$-7.694 \\ -7.729$	13 14	_	69.0	+11	+3.4	+3.4
copper	gold	$0.69 \\ 0.10$	$\frac{49.7}{44.9}$	$-8.171 \\ -8.236$	14 15	-	82.3*	-4	-0.8	+0.2
copper	iron	1.4	51.8	-8.202	6		96.7	+15	-0.1	+0.2
copper	cobalt	$0.885 \\ 1.93$	51.59 54.1	$-8.467 \\ -8.433$	13 6		105	+11	-1.9	-1.3
copper	nickel	2.7	56.5	-8.674	6	-	101.1	0	-2.9	-2.7
silver	silver	0.725	45.5	-8.204	16	69.0	-		-	-
silver	copper	1.23	46.1	-8.081	17		81.2	+9	-0.5	+0.7
silver	gold	$0.26 \\ 0.41$	$45.5 \\ 46.4$	$-8.649 \\ -8.611$	18 19		82.3*	-5	-3.0	-2.4
silver	thallium	0.15	37.9	-7.541	20		43.3	+2	+4.6	+3.7
silver	lead	0.22	38.1	-7.410	4	-	46.5	+9	-5.2	+4.5
gold	gold	0.14	42.9	-7.781	19	82.3*				_
0	0.265	45.3	-7.987	21						
		0.031	39.36	-7.947	22					
gold	nickel	0.30	46.0	-8.047	23	-	101.1	+13	-0.7	-0.7
nickel	nickel	1.27	66.8	-8.359	24	101.1	_	_		_
nickel	gold	2.0	65.0	-7.934	25		82.3*	+13	+4.9	+3.4
cobalt	cobalt	0.83	67.7	-8.521	26	105	_	_		_
cobalt	iron	0.21	62.7	-8.494	26		96.7	0	+1.3	+0.2

^{*} This value is smaller by 10 kcal/g atom than some which have appeared in the literature. Our choice is that also recommended in reference 10.

uncertainties in activation energies for solute diffusion, due to systematic errors, are of the order of 5 per cent. However there is much closer agreement on the comparative free energies of activation at the temperatures of measurement. Therefore we have chosen to compare ΔQ with $\Delta(\Delta F')$ at the melting temperature of the solvent. $\Delta(\Delta F')$ is given by:

$$\Delta(\Delta F') = \Delta F'_{\rm A} - \Delta F'_{\rm B} = RT \, \ln \left(\frac{D_{\rm B}}{D_{\rm A}}\right) \quad (8)$$

where $D_{\rm B}$ and $D_{\rm A}$ are, respectively, the diffusion coefficients of solute and solvent at temperature T and infinite dilution. This comparison of ΔQ with $\Delta(\Delta F')$ can be valid strictly only if the entropies of activation are proportional to the energies of activation. However such a proportionality is implied by the current theories for diffusion. (11)

4. DISCUSSION

The comparisons of ΔQ and $\Delta(\Delta F')$ are shown in the table and the correspondence is quite good. In 9 cases out of 12 the sign of $\Delta(\Delta F')$ is predicted correctly and in the other 3 cases both $\Delta(\Delta F')$ and ΔQ are less than 1 kcal/g atom. In no case is the deviation of $\Delta(\Delta F')$ from the calculated ΔQ greater than 1.4 kcal/g atom.

In general the correlation appears to be quite successful. In particular it holds quite well in the cases where the Lazarus valence theory fails. Thus the correlation places $\Delta(\Delta F')$ for the diffusion of Ni, Co, or Fe into Cu in the right order and gives, in agreement with experiment, a substantial $\Delta(\Delta F')$ for the diffusion of Ag into Cu. The experimental ΔQ 's do not agree at all well with the calculated. However, as noted above, there is considerable uncertainty in the experimental ΔQ 's.

In arriving at our correlation we assumed tacitly, as did Lazarus, that solute diffusion is not limited by the exchange of vacancies with atoms in the first coordination shell of the solute. By a further application of the nearest neighbor model it is possible to estimate the frequency of this exchange as well as the vacancy concentration in the shell. From this the effect of solute concentration on the self-diffusion of the solvent can be calculated. The effect so calculated for systems in which ΔQ is large and positive (e.g. dilute solutions of lead in silver) is much smaller than observed. However as noted earlier the ΔQ used in our correlation is much less than the actual deficiency in solute binding $(U_{\rm A} - U_{\rm AB})$ given by the nearest neighbor model. Probably this deficiency is not localized in the "bonds" between the solute atom and its immediate neighbors. It is perhaps more accurate to suppose that it is spread over a small region around the solute atom and among AA as well as AB bonds. Hence the solvent atoms neighboring the solute would

VOL. 7 1959 exchange more frequently with vacancies than calculated by the nearest neighbor theory.

It is of interest that Van Itterbeek and Thomaes⁽²⁷⁾ had established a correlation between the viscosity of certain liquid organic solutions and heat of solution which is somewhat analogous to our correlation of solute diffusion in metals.

ACKNOWLEDGMENTS

The authors are pleased to acknowledge valuable discussions on this subject with Dr. E. W. Hart and Professor I. Prigogine.

REFERENCES

- D. Lazarus, Impurities and Imperfections pp. 107-120. American Society for Metals, Cleveland (1955).
- D. LAZARUS, Phys. Rev. 93, 973 (1954).
 G. WYLLIE, Proc. Phys. Soc. 59, 694 (1947).
- 4. R. E. Hoffman, D. Turnbull and E. W. Hart, Acta Met. 3, 417 (1955).
- 5. E. W. Hart, R. E. Hoffman and D. Turnbull, Acta Met. 5, 592 (1957)
- 6. F. Seitz and D. Lazarus, Diffusion in Metals Progress Report. University of Illinois (June 15, 1956).
- 7. J. E. BAUERLE and J. S. KOEHLER, Phys. Rev. 107, 1493
- 8. E. P. WIGNER and F. SEITZ, Solid State Physics, Vol. 1, p. 97, Academic Press, New York (1955).

- 9. R. A. ORIANI, Acta Met. 2, 608 (1954).
- 10. Selected Values, Thermodynamic Properties of Metals and Alloys, Minerals Research Laboratory, University of California (1956).
- 11. A. LECLAIRE, Progress in Metal Physics, Vol. 4, p. 265.
- Pergamon Press, London (1953). 12. A. Kuper, H. Letaw, Jr., L. Slifkin, E. Sonder and
- C. T. TOMIZUKA, Phys. Rev. 96, 1224 (1954).

 13. W. L. MERCER and R. SHUTTLEWORTH, to be published. 14. C. T. Tomizuka, Bull. Amer. Phys. Soc. Ser. II, 3, 123
- (1957).15. A. B. Martin, R. D. Johnson and Frank Asaro, J. Appl. Phys. 25, 364 (1954).
- 16. L. SLIFKIN, D. LAZARUS and C. T. TOMIZUKA, J. Appl.
- Phys. 23, 1032 (1952). 17. A. SAWATZKY and F. E. JAUMOT, Jr., J. Metals, N.Y.
- to be published.

 18. F. E. Jaumot, Jr. and A. Sawatzky, J. Appl. Phys.
- 1186 (1956).
 H. W. Mead and C. E. BIRCHENALL, J. Metals, N.Y. 9, 874 (1957).
- 20. R. E. HOFFMAN, Acta Met. 6, 95 (1958).
- 21. A. C. Gatos and A. D. Kurtz, J. Metals, N. Y. 6, 16 (1954).
- B. Okkerse, *Phys. Rev.* **103**, 1246 (1956).
 J. E. Reynolds, B. L. Averbach and Morris Cohen, *Acta Met.* **5**, 29 (1957).
- 24. R. E. Hoffman, F. W. Pikus and R. A. Ward, J. Metals, N.Y. 8, 483 (1956).
- 25. A. D. Kurtz, B. L. Averbach and M. L. Cohen, Acta Met. 3, 442 (1955).
- 26. H. W. MEAD and C. E. BIRCHENALL, J. Metals, N.Y. 7, 994 (1955).
- 27. J. VAN ITTERBEEK, Thesis, Free University of Brussels

GRAIN GROWTH IN ZONE-REFINED TIN*

E. L. HOLMES and W. C. WINEGARD†

Grain growth experiments have been performed with zone-refined tin of very high purity. A single growth law obeying the simple $t^{1/2}$ relation was obtained over the range of temperatures $167^{\circ}\text{C}-220^{\circ}\text{C}$. The activation energy for grain growth was calculated to be 6.0 ± 0.6 kcal/g atom, which is comparable to the previous result of 6.7 ± 0.7 kcal/g atom on zone-refined lead. Application of the equation for grain growth, as developed by Burke and Turnbull, yielded free energies of activation comparable in magnitude to those obtained in liquid self-diffusion.

LA CROISSANCE GRANULAIRE DANS L'ETAIN DE ZONE FONDUE

Des expériences de croissance granulaire ont été réalisées sur de l'étain de zone fondue de très haute pureté.

Une loi de croissance obéissant à la relation simple $t^{1/2}$ a été obtenue pour une gamme de températures de 167° à 220°C. Par ailleurs, on calcule la valeur de l'énergie d'activation pour la croissance granulaire; elle est de 6.0 ± 0.6 kcal/atome g et est du même ordre de grandeur que le résultat précédent de 6.7 ± 0.7 kcal/atome g pour le plomb de zone fondue.

Ainsi que l'ont démontré Burke et Turnbull l'application de cette équation pour une croissance granulaire, produit des énergies libres d'activation du même ordre de grandeur que celles obtenues pour l'auto-diffusion en phase liquide.

KORNWACHSTUM IN ZONENGEREINIGTEM ZINN

Mit zonengereinigtem Zinn sehr hoher Reinheit wurden Kornwachstumsversuche angestellt. Im Temperaturbereich von 167°C bis 220°C ergab sieh ein einheitliches Wachstumsgesetz, das der einfachen $t^{1/2}$ -Beziehung folgt. Die Aktivierungsenergie für das Kornwachstum wurde zu 6.0 \pm 0.6 keal/g atom berechnet, sie ist vergleichbar mit dem früheren Erggebnis von 6,7 \pm 0,7 keal/g Atom an zonengereinigtem Blei. Die Anwendung der von Burke und Turnbull entwickelten Gleichungen für das Kornwachstum lieferte freie Aktivierungsenergien, die grössenordnungsmässig vergleichbar sind mit denjenigen, die sich aus der Selbstdiffusion im flüssigen Zustand ergeben.

1. INTRODUCTION

VOL.

1959

On the basis of the many investigations of grain growth, as summarized in the review articles of Burke and Turnbull, (1) Beck, (2) and Fullman, (3) the activation energy for grain growth in zone-refined lead, viz. $6.7 \pm 0.7 \, \text{kcal/g}$ atom, as obtained by Bolling and Winegard, (4) would appear much lower than might have been anticipated.

The present investigation of grain growth in zonerefined tin was undertaken in the hope that these additional results would yield sufficient information to suggest a possible mechanism of grain boundary migration in zone-refined materials.

2. EXPERIMENTAL PROCEDURE

Preliminary experiments on Johnson and Matthey spectrographically pure tin indicated that the cast structure had an effect on grain growth after deformation and subsequent recrystallization. This was not found to be the case with zone-refined tin, which suggests that it was the result of non-uniform distribution of impurity in the as-cast Johnson and Matthey tin. Nevertheless, to eliminate any possible effects of the as-cast structure, and also to provide flat surfaces, the cast buttons of zone-refined tin

weighing approximately 14.5 g were first deformed under a drop-hammer with polished surfaces, and allowed to recrystallize at room temperature. For the grain growth experiments, these coin-shaped, fine-grained specimens which were 4.5 mm thick and 25 mm in diameter, were deformed for a second time under the drop-hammer to specimens 3.0 mm thick and about 30 mm in diameter.

The basic material used in the investigation was Extra Pure Tin (99.998+ per cent) obtained from the Vulcan Detinning Company. This tin was zone-refined *in vacuo* to an estimated purity of 99.999 per cent or greater, as indicated by its solidification characteristics. (5)

Grain growth occurred very rapidly at the temperatures used in this investigation, and so it was necessary to elevate the temperature of the specimen very quickly. A controlled temperature hot bath of Dow Corning Silicone Fluid 550 was chosen as the annealing system. After a selected annealing time had elapsed, the sample was quenched in a cold water bath.

As previously observed with zone-refined lead, (4) the tin recrystallized to a grain size visible to the eye as fast as a quick-acting etchant could reveal the structure, and so no doubts were held about the achievement of full recrystallization. An equal short time was allowed to elapse between the deformation and annealing for all specimens. After annealing

Received June 23, 1958; revised version August 20, 1958.
 Department of Metallurgical Engineering, University of Toronto, Toronto, Ontario, Canada.

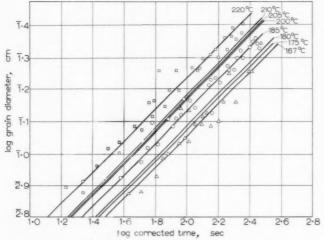


Fig. 1. Log-log plot of grain diameter vs. corrected time. ⊡—220°C, ⊙—185°C, △—167°C.

and etching in a suitable acidic ferric chloride solution, the average grain diameter was determined by counting grains intersected by several random traverses on the surface of the specimen.

To eliminate the possibility that the results were influenced primarily by the surface, the grain counting was carried out on the same specimen after various amounts of the surface had been removed by electropolishing. No change in the average grain diameter was observed.

3. TREATMENT OF RESULTS

The results were obtained in the form of average grain diameters at particular experimental times at different temperatures. For the reasons previously discussed⁽⁴⁾ the experimental time is not the true time necessary for a specimen to reach its measured grain size. A time-correction was obtained by fitting the experimental points to sets of curves obeying equation (1) using different time exponents. In each case the experimental points fitted closely a curve using n =0.5 and the shift along the time axis necessary to make the curves coincide gave the time correction. The time-corrections obtained varied from -8 sec at the lowest temperature to −12 sec at 220°C. Since by using the corrections obtained in this way, the shorttime points on Fig. 1 give a straight line with the long-time points which are relatively time-correction insensitive, it may be assumed that the corrections used are reasonably accurate.

Fig. 1 is a graph of log grain diameter vs. log corrected time. Each line on Fig. 1 was obtained by drawing the best straight line through the experimental points at the given temperature, after the time-correction had been made. The individual lines

were then plotted together on the same scale to give the composite plot shown on Fig. 1. To indicate the number of specimens used and the scatter obtained experimental points are shown for the temperatures 167°C, 185°C and 220°C. The scatter of experimental points was similar to that found in the previous work⁽⁴⁾ and was reduced when impurity was added to the tin.

4. THE TIME EXPONENT

When the time correction was applied, the equation for grain growth as proposed by Beck *et al.*⁽⁶⁾ was found to hold—viz.

$$D = At^n = (Kt)^n. (1)$$

VO:

19

From a logarithmic plot, as shown in Fig. 1, an average time exponent of 0.50 was determined which had only small random variations over the temperature range investigated. The range of temperature used was between 167°C and 220°C; below 167°C there was obvious evidence of discontinuous grain growth.

5. ACTIVATION ENERGY

Writing the constant K of equation (1) as

$$K = K_0 e^{-Q/RT} \tag{2}$$

an activation energy, Q, in the Arrhenius sense may be determined. The activation energy, obtained by plotting the logarithm of the rate of grain growth against the reciprocal absolute temperature, as in Fig. 2, was found to be $6.0\,\mathrm{kcal/g}$ atom with an estimated error of 10 per cent. The points on Fig. 2 were obtained by taking the logarithm of the rate of grain growth at 100 sec for various temperatures from Fig. 1. The same procedure using the rate at

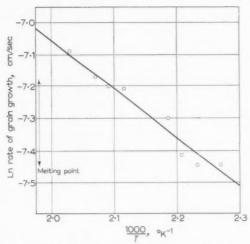


Fig. 2. A graph of the logarithm of the rate of grain growth at 100 sec vs. 1000/T°K.

longer times where the time correction becomes less significant gave the same figure for the activation energy. The rate constant was determined as $0.12 \, \mathrm{cm}^2/\mathrm{sec}$.

6. DISCUSSION

By applying the equation of Turnbull⁽⁷⁾ in the same way as attempted by Bolling and Winegard⁽⁴⁾, the free energy of activation for grain growth was obtained. The constants used were the same as those chosen by Bolling and Winegard⁽⁴⁾ except that the gram atomic volume of the metal, V, was 14.9 cm³/g atom, and the value for the specific grain boundary free energy was 100 ergs/cm² as estimated by Aust and Chalmers⁽⁸⁾. For the mean temperature used, the free energy of activation for grain growth or grain boundary

migration was calculated to be 3.4 kcal/g atom.

6.1. Comparison to liquid self-diffusion

The values for the measured energies of activation and the calculated values of the free energies of activation, both for grain growth and liquid selfdiffusion in tin and lead, are listed in Table 1.

It is immediately apparent that the calculated values of the free energies of activation for grain growth are comparable in magnitude to the values derived for liquid self-diffusion.

If a high angle boundary may be regarded as a supercooled layer two atoms thick, then the grain boundary free energy may be expressed as the sum of the excess free energy of the supercooled layer over the solid plus twice the liquid-solid interfacial free energy. (11) The values of the free energies of activation for grain growth calculated on this basis are also expressed in Table 1.

The experimental activation energies together with the derived free energies of activation suggest that a close similarity may exist between the mechanism for self-diffusion in the liquid state and the mechanism for grain boundary migration. This might then be regarded as adding support to the concept of a high angle grain boundary as having a random misfit structure resembling more closely that of a liquid than any other known configuration. This concept also receives support from the work of $Ke^{(12)}$ on grain boundary viscosities.

It should be noted that the values of the free energy of activation for liquid self-diffusion were obtained by assuming self-diffusion to be a nearequilibrium process to which transition state theory

TABLE I

Metal	Grain	n growth in zone-refined	Liquid self-diffusion				
	Experimental	Free energy of activation at mean temperature investigated	Free energy of activation calculated by regarding the boundary as a supercooled layer two atoms thick		Experimental	Free energy of activation close to	
	activation energy keal/g atom	kcal/g atom This value being calculated using constants chosen by Bolling and Winegard ⁽⁴⁾	(a) At mean temperature investigated kcal/g atom	(b) Close to melting tempera- ture kcal/g atom	activation energy kcal/g atom	freezing temperature keal/g atom	
Tin Lead	$\begin{array}{c} 6.0 \pm 0.6 \\ 6.7 \pm 0.7^{(4)} \end{array}$	$3.4 \\ 6.3^{(4)}$	3.7 5.5	3.4 4.9	4.0 ⁽⁹⁾ 4.5 ⁽¹⁰⁾	3.3 4.4	

VOL. 7 1959 may properly be applied and, following le Claire(13) using an expression of the form

$$D = \frac{a^2 kT}{6 h} \exp \frac{\Delta F_A}{RT}$$
 (3)

where kT/h is the frequency factor and a is the jump distance taken as 2×10^{-8} cm. The same assumptions are made in the derivation of the free energy of activation for grain boundary self-diffusion in lead, as discussed below.

6.2. Comparison to grain boundary self-diffusion

It has been suggested (14,15) that the elementary process in grain boundary migration is closely related to the elementary process in grain boundary selfdiffusion so that the free energy of activation for grain boundary migration should be of the same order of magnitude as for grain boundary self-diffusion.

Following Hoffman and Turnbull(16) and Wadja et al.(17), in assuming a boundary width of 5 Å, the results obtained by Okkerse(18) for grain boundary diffusion in lead may be expressed as

$$D = 1.62 \exp(15,700/RT)$$

from which a free energy of activation of 6.6 kcal/g atom for grain boundary diffusion near the melting temperature may be obtained. This value is different from the value quoted by Bolling and Winegard⁽⁴⁾ for the following reasons: (1) The previous figure was calculated for the mean of the temperature range investigated, while the present figure was determined at the melting point. (2) A jump distance of 2 Å has been used in this calculation instead of 5 Å, to be consistent with the values used for grain growth.(1) (3) A boundary width of 5 Å has been used here whereas Okkerse⁽¹⁸⁾ used a value of 10 Å. (4) The general formula for transition state theory, as given in equation (3), is used rather than the formula of Eyring⁽¹⁹⁾. It should be remembered that the lead used in the investigation by Okkerse was relatively impure, and that the data obtained for grain boundary diffusion depends upon a relation with considerable mathematical simplifications, as derived by Fisher⁽²⁰⁾. Nevertheless, the value obtained for the free energy of activation for grain boundary self-diffusion in lead near the melting temperature is clearly of the same order of magnitude as that obtained in the grain growth experiments.

It might be expected that grain boundary selfdiffusion studies in zone-refined materials, perhaps combined with a more detailed and rigorous study of the diffusion problem, would substantiate the supposition that diffusion in the boundary is an important factor in grain boundary migration.

7. CONCLUSION

The similarity between the values obtained for activation energies and free energies of activation for grain growth in zone-refined lead and tin and those published for liquid self-diffusion suggests that the elemental process may be the same in both cases and may be regarded as adding support to the theory that the structure of high angle boundaries is liquid-like in nature.

The similarity in order of magnitude between the free energy of activation for liquid self-diffusion, grain growth and grain boundary self-diffusion near the melting temperature may be significant and is worthy of experimental investigation on high purity zonerefined materials.

ACKNOWLEDGMENTS

The authors are grateful to the Defence Research Board of Canada (Grant No. 9535-01) for financial support. One of the authors, E. L. H., received an International Nickel Co. Fellowship during the course of this work. The staff and graduate students of the Department of Metallurgical Engineering of the University of Toronto are to be thanked for their interest and stimulating discussions. The continued support and encouragement of Dr. L. M. Pidgeon is also gratefully acknowledged.

REFERENCES

19

- 1. J. E. BURKE and D. TURNBULL, Progress in Metal Physics, Vol. 3, p. 220. Pergamon Press, London (1952).
- 2. P. A. Beck, Advanc. Phys. 3, 245 (1954).
- 3. R. L. Fullman, Metal Interfaces. American Society for Metals (1952).
- 4. G. F. Bolling and W. C. Winegard, Acta Met. 6, 283 (1958).
- 5. W. A. TILLER and J. W. RUTTER, Canad. J. Phys. 34. 96 (1956).
- P. A. Beck, J. C. Kremer, L. J. Demer and M. L. Holzworth, Trans. Amer. Inst. Min. (Metall.) Engrs. 175, 372 (1948).
- D. Turnbull, Trans. Amer. Inst. Min. (Metall.) Engrs. 191, 661 (1951)
- K. T. Aust and B. Chalmers, Proc. Roy. Soc. A 201, 210 (1950).
- G. CARERI and A. PAOLETTI, Nuovo Cim. Ser. 10, 2, 574 (1955)
- S. J. ROTHMAN and L. D. HALL, Trans. Amer. Inst. Min. (Metall.) Engrs. 206, 199 (1956).
- 11. D. McLean, Grain Boundaries in Metals, p. 73. Oxford
- University Press (1957). 12. T. S. KE, *Phys. Rev.* **71**, 533 (1947)
- 13. A. D. LE CLAIRE, Progress in Metal Physics, Vol. 1, p. 334. Pergamon Press, London (1949). P. A. Beck, P. R. Sperry and H. Hu, J. Appl. Phys. 21,
- 420 (1950).
- D. TURNBULL, Atom Movements. American Society for Metals (1951).
- 16. R. E. HOFFMAN and D. TURNBULL, J. Appl. Phys. 22, 634 (1951).
- 17. E. S. WADJA, G. A. SHIRN and H. B. HUNTINGTON, Acta Met. 3, 39 (1955).
- 18. B. OKKERSE, Acta Met. 2, 551 (1954).
- 19. S. GLASSTONE, K. J. LAIDLER and H. EYRING, Theory of Rate Processes, p. 524. McGraw-Hill, New York (1941) 20. J. C. Fisher, J. Appl. Phys. 22, 74 (1951).

TERNARY CARBIDES OF THE TRANSITION METALS NICKEL, COBALT, IRON, MANGANESE WITH ZINC AND TIN*

H. H. STADELMAIER† and L. J. HUETTER

In the ternary systems Co–Sn–C, Fe–Sn–C, Ni–Zn–C, Co–Zn–C, and Fe–Zn–C double carbides were found that correspond to the formula T_3BC_s , where T is the transition metal. These compounds have an ordered face-centered cubic structure and together with the known compounds Mn_3SnC and Mn_3ZnC belong to the group of carbides reported previously by the authors.

LES CARBURES TERNAIRES DES METAUX DE TRANSITION NICKEL, COBALT, FER, MANGANESE AVEC LE ZINC ET L'ETAIN

Dans les systèmes ternaires Co–Sn–C, Fe–Sn–C, Ni–Zn–C, Co–Zn–C et Fe–Zn–C, on a identifié des carbures triples correspondant à la formule T_aBC_x où T est le métal de transition.

Ces composés ont une structure c.f.c. ordonnée et, de même que les composés connus $\rm Mn_3SnC$ et $\rm Mn_3ZnC$, appartiennent au groupe de carbutes précédemment identifié par les auteurs.

TERNÄRE KARBIDE DER ÜBERGANGSMETALLE NICKEL, KOBALT, EISEN, MANGAN MIT ZINK UND ZINN

In den ternären Systemen Co–Sn–C, Fe–Sn–C, Ni–Zn–C, Co–Zn–C und Fe–Zn–C wurden Doppelkarbide gefunden, die der Formel $\mathrm{T_3EC_z}$ entsprechen, wobei T das Übergangsmetall bedeutet. Diese Verbindungen haben ein geordnetes flächenzentriertkubisches Gitter und gehören zusammen mit den bereits bekannten Verbindungen $\mathrm{Mn_3SnC}$ und $\mathrm{Mn_3ZnC}$ einer Gruppe von Karbiden an, über die von den Verfassern kürzlich berichtet wurde.

1. INTRODUCTION

The existence of a class of ternary carbides of aluminum or magnesium with the iron group of the first long period was reported recently.(1) Therein the metal atoms occupy the points of a face-centered cubic lattice of the ordered type T₂B, where T is the transition metal and B is aluminum or magnesium. Similar compounds, containing manganese together with an element of the B sub-group of the periodic system and carbon, were reported by Morgan⁽²⁾ and Butters and Myers^(3,4) in connection with their magnetic properties. Morgan views these phases as stabilization (by adding the B-metal) of Mn₄C which apparently does not exist in the equilibrium system but is obtained by quenching from 1050°C. In alloys ranging from Mn₇₉In₁C₂₀ to Mn₇₄In₆C₂₀ and $\mathrm{Mn_{78}Sn_{2}C_{20}}$ to $\mathrm{Mn_{70}Sn_{10}C_{20}}$ he found increasing amounts of face-centered cubic material in equilibrium with other phases. He also found in a wide range around Mn₃AlC a single-phase alloy with an ordered face-centered cubic structure, so that he should be credited with first reporting this phase. Butters and Myers⁽³⁾ obtained single-phase Mn₃ZnC with an ordered face-centered cubic structure by sintering compacted powder. They also reported on

the structure and magnetic properties of Mn₃AlC.⁽⁴⁾ Both compounds are shown to have the perovskite structure so that the carbon atoms do not occupy the available octahedral interstices at random but are also on a superlattice. The electrical conductivity of the two compounds is metallic, and the magnetic saturation moment is close to one Bohr magneton per manganese atom.

The work mentioned above has prompted a series of systematic investigations by the authors to determine which face-centered cubic ternary carbides are formed with transition metals and B-metals. A description of those with tin and zinc follows.

2. TIN COMPOUNDS

Ternary alloys of nickel, cobalt, iron with tin and carbon were obtained by induction melting in a crucible of machined Acheson graphite. They were sand-cast to avoid chilling. In no case was the ternary compound obtained as a single phase; solidification does not appear to be congruent. A face-centered cubic compound is identified by demonstrating its co-existence with the first binary compound in the system T–B (range 1, Fig. 1) and with the transition metal or its terminal solid solution (range 2, Fig. 1). The proportions between equilibrium phases, which were used to establish the carbon content of the carbides, were found microscopically

1959

^{*} Received August 29, 1958.

[†] Department of Engineering Research, North Carolina State College, Raleigh, North Carolina.

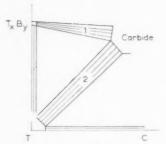


Fig. 1. Location of ternary alloys.

and supported by densitometer measurements of X-ray powder patterns. (In comparing lines of face-centered cubic and body-centered cubic structures corrections were made for multiplicity and packing density of lattice planes.) In the compounds with tin the superstructure lines with $h^2 + k^2 + l^2 = 1, 2, 5, 6$, and 9 are readily observed.

2.1. Nickel-tin-carbon

A series of alloys of nickel and tin, progressing in steps of 5 wt. % Sn up to 40 wt. % Sn, were melted and allowed to pick up carbon. This produced no evidence of a face-centered cubic ternary compound. Binary Ni₃Sn, which is hexagonal, (5) dissolves little or no carbon. Thus the total carbon content of an alloy of 72.6 at. % Ni, 24.1 at % Sn, and 3.3 at. % C is accounted for by the nodular graphite. In this respect the ordered close-packed hexagonal compound Ni₃Sn differs from the ordered face-centered cubic binary compound Ni₃Al, which is capable of dissolving 5.8 at. % C. (1) The terminal solid solution of tin and carbon in nickel has an observed maximum lattice constant of 3.56 kX, as against that of the binary solid solution of tin in nickel, which is 3.54 kX.

2.2. Cobalt-tin-carbon

In the binary side diagram Co-Sn the phase adjacent to cobalt is an orthorhombic compound solidifying congruently at the composition Co₂Sn but existing at about 41 at. % Sn at lower temperatures. Ternary alloys, ranging in their weight ratios of Co: Sn from 95:5 to 55:45 were investigated. They all show a face-centered cubic phase in equilibrium with either cobalt, the binary cobalt-tin compound, or both. This ternary compound has a superlattice and a lattice constant of 3.77 kX. Above a Co: Sn weight ratio of 70:30 the ternary phase appears as the primary microconstituent. An alloy of 77.3 at. % Co, 16.5 at. % Sn and 6.2 at. % C contained no graphite. Its ratio of CooSn: carbide: Co was 20:40:40. Neglecting the carbon content of the other two phases, that of the carbide is about

15 at. %. Basing the formula on the ideal composition of an ordered face-centered cubic alloy and the estimated carbon, this compound is $\rm Co_3SnC_{0.7}$. A single Curie point is observed in the alloys. That it must be associated with the cobalt solid solution follows from the Curie temperature, which is above $1000^{\circ}\rm C$, and the decreasing magnetization with increasing tin content. Therefore the cobalt—tin carbide is non-magnetic down to room temperature.

2.3. Iron-tin-carbon

The iron-tin system has a closed gamma loop so that the iron-rich terminal solid solution is bodycentered cubic. (6) The binary alloy corresponding to the composition Fe₃Sn is a two-phase mixture of alpha iron and hexagonal FeSn. Ternary alloys of iron, tin, and carbon, ranging in the weight ratio of Fe: Sn from 95: 5 to 50: 50, contained a prominent face-centered cubic phase accompanied by the terminal solid solution of iron, binary FeSn, or both. At lower tin contents Fe₂C is also present. The facecentered cubic phase is ordered and has a maximum lattice constant of 3.85 kX. An alloy of 72.9 at. % Fe, 13.0 at. % Sn, and 14.1 at. % C, containing no graphite and Fe₃C, had a ratio of alpha iron: ternary compound of 1:3. Since the carbon content of the iron will be negligible, an approximate formula Fe₃SnC is obtained for the carbide. As before, the iron: tin ratio is based on the ideal value of the ordered structure, whereas in reality the tin content of the compound must be a little under the ideal 20 atomic per cent in this particular alloy as seen from the analysis.

VOI

191

This carbide is ferromagnetic. A sample of 79.3 at. % Fe, 5.4 at. % Sn, and 15.3 at. % C has a Curie point of 260°C. In an alloy of 62.5 at. % Fe, 21.4 at. % Sn and 16.1 at. % C containing carbide with some FeSn and Fe, the Curie point is 220°C.

2.4. Manganese-tin-carbon

The binary system Mn–Sn does not contain a face-centered cubic compound. (6) Morgan (2) reports a face-centered cubic ferromagnetic phase at varying tin contents and a fixed atomic ratio Mn : C=4:1. Lattice constants begin close to that of a face-centered cubic binary phase listed by Morgan as Mn₄C and increase with increasing tin content. Mn₄C is not a stable compound, nor is it a high-temperature phase of the system Mn–C; (6) it is obtained by water quenching from 1050° C, together with some Mn₂₃C₆. Since the ordered face-centered cubic ternary phase is not found in the equilibrium diagram of either binary side system, it must be a

true ternary compound. After homogenizing at 1050° C, Morgan's alloy of the composition corresponding to $\mathrm{Mn_{63}Sn_{21}C_{16}}$ showed an ordered face-centered cubic structure with a lattice constant of $3.98~\mathrm{kX}$. This carbide is ferromagnetic.

3. ZINC COMPOUNDS

With exception of the system Ni-Zn-C, zinc compounds could not be obtained by melting because of the violent evaporation of zinc. Therefore alloys with cobalt and iron were obtained by reacting binary alloys of the transition metals and carbon with molten zinc. With this technique the ternary carbide was found in a diffusion layer on the surface of the T-C alloy. The layer grew to a thickness of one to two millimeters in one hour at 700°C and 750°C, respectively. Binary compounds coexisting with the carbide were readily identified by X-ray diffraction. For the compound with manganese, information from the work of Butters and Myers⁽³⁾ is included. Because of the small difference in the scattering factors of the iron metals and zinc, the superstructure lines are weak. None were observed in the compounds with nickel and cobalt, but this does not necessarily preclude their existence.

3.1. Nickel-zinc-carbon

In the binary system Ni–Zn the terminal solid solution exists up to about 26 at. % Zn. This high solubility is confirmed by Lihl who finds a solubility limit of 24.5 at. % at 250 °C with alloys prepared by amalgamation. The maximum lattice constant of this face-centered cubic solid solution is 3.58 kX as against 3.52 kX of pure nickel.

An alloy with 72.4 at. % Ni, 21.6 at. % Zn and 6.0 at. % C showed two metallic phases and no graphite in the microscope. X-ray diffraction analysis yielded two face-centered cubic phases with lattice constants of 3.55 and 3.65 kX in proportions of 3:2 as determined by densitometer measurements. Neglecting the solubility of carbon in the terminal solid solution, the carbon content of the other phase is about 15 atomic per cent. When the zinc content of the alloys is lowered, the amount of the phase with the higher lattice constant decreases. Thus a sample with 77.3 at. % Ni, 12.3 at. % Zn, and 10.4 at. % C showed a ratio of 7:2 between the nickel solid solution (lattice constant 3.53 kX in this alloy) and the other phase (3.65 kX). Besides, it contained nodular graphite in appreciable quantity. Since the system Ni-C contains no face-centered cubic phase, it is obvious that the phase with the higher lattice constant is a ternary compound which can be represented by the formula $\rm Ni_3ZnC_{0.7}$ if the Ni : Zn ratio is fixed by analogy with other compounds of this type. The alloy with 21.6 at. % Zn has a single Curie point at 70°C which must be attributed to the nickel solid solution. Therefore there is no indication that this ternary earbide is ferromagnetic.

3.2. Cobalt-zinc-carbon

From the work of Schramm⁽⁹⁾ it follows that cobalt has high solubility for zinc at high temperatures but that the solubility limit is at 3.7 at $^{\circ}$ /₀ Zn at 400°C. The maximum lattice constant of the undercooled solid solution is 3.64 kX.

Treatment of a eutectic alloy of cobalt and carbon for one hour in molten zinc at 700°C produces three zones between the frozen melt and the cobalt-carbon alloy. The first zone, which is adjacent to the cobaltcarbon, is graphite-free cobalt. This is followed by a sharply delineated zone with a face-centered cubic structure and a lattice constant of 3.72 kX. Finally there is a zone of particles of the face-centered cubic phase embedded in a zinc-rich binary phase. Since there is no face-centered cubic binary phase in the Co-Zn or Co-C system, the phase with the lattice constant of 3.72 kX is a ternary compound. The graphite-free zone of cobalt clearly indicates that carbon has diffused to the compound. This is further evidenced by the lattice constant of the compound which is higher than the maximum value of the quenched binary solid solution of 37.5 at. % Zn. This ternary carbide shall be designated as Co₃SnC_x, where x is of the order of unity. Magnetic measurements were not fully conclusive because of the interference by the transformation effects of residual cobalt, but there is no indication that the carbide is ferromagnetic.

3.3. Iron-zinc-carbon

In the binary system Fe–Zn face-centered cubic gamma iron has, above the eutectoid temperature of 623°C, an extended range of existence with a maximum solubility of 42 at. % Zn. (10) This phase cannot be retained to lower temperatures even by quenching. Therefore neither of the binary side diagrams of the ternary system Fe–Zn–C contains a stable face-centered cubic phase.

When an iron–carbon alloy of 4.5 wt. per cent combined carbon (white cast iron) is reacted with molten zinc at 750°C, two zones are found between the iron–carbon and the melt. The one adjacent to the iron–carbon is a face-centered cubic phase with a lattice constant of 3.80 kX. The structure is ordered, as evidenced by the (110) superstructure line. The

VOL. 7 1959 outer layer contains a mixture of the same cubic phase with the binary iron–zinc phase of the gamma-brass type found at 70 at. % Zn. A control specimen of pure iron treated together with the iron–carbon alloy showed no face-centered cubic phase. This is evidently a ternary carbide of the type Fe₃ZnC_x. It is ferromagnetic and shows a Curie point of 95°C.

3.4. Manganese-zinc-carbon

The binary system Mn-C has the mentioned unstable face-centered cubic phase Mn₄C reported by Morgan. (2) Binary Mn-Zn contains face-centered cubic gamma manganese above 554°C and up to about 35 at. % Zn(II) or 28 at. % according to Schramm⁽¹²⁾. Butters and Myers⁽³⁾ report on the structure and properties of single-phase ternary alloys in the composition range from Mn₇₀Zn₁₀C₂₀ to $\mathrm{Mn_{60}Zn_{20}C_{20}}$. They are face-centered cubic; all superstructure lines are present. The lattice constants range from 3.899 to 3.925 kX, the Curie points from 488 to 80°C. Since the binary solution of zinc in manganese is not magnetic, the ferromagnetic ternary alloy cannot be a mere extension of gamma manganese to lower temperatures by addition of zinc and carbon.

4. SUMMARY OF DATA ON TERNARY CARBIDES

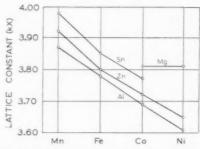
The ternary carbides with tin and zinc are compiled in Table 1, together with those reported earlier. They have the following characteristics:

- The same trend towards increasing lattice constants from Ni to Mn as observed in the compounds with aluminum⁽¹⁾ is seen in Fig. 2.
- (2) The lattice constants with tin are higher than those with zinc, in agreement with the larger size of the tin atom. When the aluminum compounds are also considered, it is seen that

Table 1. Face-centered cubic carbides of type T₃BC_x

Compound	æ	Max. observed lattice constant	Magnetic	Source
Mn ₃ AlC _x	1	3.87	yes	(2), (4), (1
Fe ₃ AlC	0.66	3.78	ves	(16)
Co.AlC.	0.59	3.69	yes	(1)
Ni ₃ AlC,	0.29	3.61	no	(1)
Co ₂ MgC,		3.81		(1)
Ni ₃ MgC,	0.5 - 1.25	3.81	no	(17)
Mn ₃ SnC,	0.8	3.98	yes	(2)
Fe ₃ SnC _r	1	3.85	yes	*
Co ₃ SnC _x	0.7	3.77	no	16
Mn ₃ ZnC,	1	3.92	yes	(3)
Fe ₃ ZnC _x		3.80	ves	*
Co ₃ ZnC,		3.72	no (?)	
Ni ₂ ZnC,	0.7	3.65	no	*

^{*} This paper.



Ni 2.49

the correlation between atomic size (Gold-schmidt diameter) of the B-metal and the lattice constant of the carbide is no longer unique. Thus the positions of aluminum and zinc in Fig. 2 are the reverse of what might be expected.

Zn 2.75

- (3) Binary side systems T–Zn and T–Al form electron compounds.
- (4) The manganese compounds exist over a wide range of B-metal content. There is a much smaller range of existence in the compounds with iron, cobalt, and nickel. This is also reflected in the spread in the lattice constants which is small for the latter three.
- (5) The earbides with manganese and iron are all ferromagnetic.

5. DISCUSSION

The stability of these carbides might be discussed on the following basis:

If the carbides are thought of as face-centered cubic $\mathrm{M_4C}$, where M is a metal atom, the function of the B-metal might be to expand the lattice beyond the size provided by the T-metal alone, thus better accommodating the carbon atom, in agreement with Hägg's rule. (13) It has been shown for the carbides with aluminum, however, that this effect can be quite small because ordering between T and B contracts the lattice, leaving a net expansion which might not be significant. (1)

The mounting evidence that these carbides form with metals involved in electron compounds points to their electronic nature. A crude description might be attempted by invoking Ekman's rule⁽¹⁴⁾ whereby the iron metals have a valence approximately equal to zero. Hypothetical carbon-free T₃B would have electron: atom ratios of 1/2, 3/4, and 1 for divalent, trivalent, and tetravalent B-metals, respectively. If,

as in terminal solid solutions with copper, a ratio greater than one is most favourable for the facecentered cubic structure, it could exist only by borrowing additional electrons from the carbon atom.

Apart from size, there is another geometrical aspect to consider. In the ideal perovskite type structure each carbon atom is surrounded only by transition metal neighbors and is not in contact with the B-metal atoms. This reminds of the suggestion by Rundle⁽¹⁵⁾ that the face-centered cubic carbides owe their structure to the possibility of providing the carbon atom with six T-metal neighbors on three mutually perpendicular axes, leading to a bond formed by the combination of one hybrid (sp) with two (p) orbitals. In the majority of the T_3BC_r type of earbides, where $x \leq 1$, it is plausible to assume that the carbon atom will occupy this preferred site, though it has actually been demonstrated only for Mn₃ZnC and Mn_3AlC . Where x > 1, contact with the B atoms is still avoided if the B-metal content is below the ideal 20 atomic per cent. In those carbides which exist over a wide range of composition there appears to be such a balance between B-metal and carbon content. In this connection it is also interest-

VOL.

1959

ing to note that no close-packed hexagonal carbides of this type have been observed.

ACKNOWLEDGMENTS

The assistance of Miss A. C. Fraker in performing the X-ray diffraction work is gratefully acknowledged.

This work was supported by the Office of Ordnance Research, U.S. Army.

REFERENCES

- 1. L. J. HUETTER and H. H. STADELMAIER, Acta Met. 6, 367 (1958).
- E. R. Morgan, J. Metals, N.Y. 6, 983 (1954).
- 3. R. G. BUTTERS and H. P. MYERS, Phil. Mag. 46, 132 (1955).
- 4. R. G. BUTTERS and H. P. MYERS, Phil. Mag. 46, 895 (1955).
- 5. P. Rahlfs, Metallwirtschaft 16, 343 (1937); O. Nial, Z. anorg. Chem. 238, 287 (1938), cited by reference 6.
- M. Hansen and K. Anderko, Constitution of Binary Alloys. McGraw-Hill, New York (1958).
- J. SCHRAMM, Z. Metallk. 30, 131 (1938).
- 8. F. Lihl, Z. Metallk. 46, 438 (1955).
- 9. J. SCHRAMM, Z. Metallk. 33, 46 (1941). 10. J. SCHRAMM, Z. Metallk. 30, 122 (1938).
- 11. E. V. POTTER and R. W. HUBER, Trans. Amer. Soc.
- Metals 41, 1001 (1949). 12. J. Schramm, unpublished work, listed by reference 6.
- G. HÄGG, Z. phys. Chem. B12, 33 (1931).
 W. EKMAN, Z. phys. Chem. B12, 57 (1931).
- R. E. RUNDLE, Acta Cryst. 1, 180 (1948).
 R. F. MORRAL, J. Iron St. Inst. 130, 419 (1934).
- 17. E. SCHEIL and L. HÜTTER, Z. Metallk. 44, 387 (1953).

Lattice parameters of solid solutions of phosphorus in iron*

In the course of some investigations of the physical properties of iron containing small quantities of phosphorus it was found necessary to know whether the solid solutions are substitutional or interstitial. Since the smallest distance between phosphorus atoms in the orthorhombic and cubic forms is about 2.2 Å, while the diameter of the largest interstitial hole in α -iron is only about 0.7 Å, it is highly likely that the solution will be substitutional. The phosphorus interatomic distance is also smaller than that for iron in the two cubic forms, which is about 2.5 Å. Thus the lattice parameter will probably decrease with increasing phosphorus content. However the phosphorus could conceivably increase the parameter slightly but the rate of increase would be much less than that for an interstitial solution. In either case the rate of change of parameter with composition will give an unambiguous test of the solid solution type.

Lattice parameter measurements were made on a diffractometer, using the normal geometry, with a focusing circle of radius 13 cm. Cobalt Ka, radiation was used, the wavelength being taken as 1.78890 Å.(1) This was produced using a sealed off X-ray tube and a quartz crystal monochromator with a slit accurately set at its focus to remove the α_2 component. The diffracted X-ray intensity was measured using a Geiger counter mounted behind a slit subtending a horizontal angle of 3.8' with respect to the diffractometer axis and having a height of 2.5 mm. The incident X-ray beam was monitored by another Geiger counter recording the diffracted intensity from an interposed aluminium foil. Diffraction line profiles were obtained by measuring the intensity for increments of 0.5' of the Bragg angle θ . The position of the line can be defined in a number of ways; for example, as the centroid or the intersection of the line and the locus of the midpoints of the chords parallel to the abscissa. For symmetrical lines both definitions coincide and as this was practically the case for all except the lowest order (110) line the latter simple graphical method was used. The position of the zero, $\theta = 0$, on the diffractometer scale was determined in two ways. Firstly intensity profiles of the incident beam were measured for two values δ and $\pi + \delta$ of the phase of the detector slit relative to the specimen surface. The profiles were very nearly 'Dirichlet' functions with ACTA METALLURGICA, VOL. 7, JUNE 1959

corners at the diffractometer angles ϕ_1 , ϕ_2 , ϕ_3 , and ϕ_4 . Using the adjustments on the apparatus it was possible to make $\phi_1 - \phi_2$ equal to $\phi_3 - \phi_4$ and ϕ_2 equal to ϕ_3 . The diffractometer axis then lies in the specimen surface, the error being about $+5 \times 10^{-4}$ em; it bisects the incident beam, the error being about $\pm 1'$ and $\phi_2 = \phi_3$ is the position of the zero, the error being about $\pm 10''$. Secondly the positions ϕ and ϕ' of the (110) line for the two phases were determined and the zero is then given by $\frac{1}{2}(\phi + \phi')$. The difference between the zeros, as determined by these two methods, was not greater than about 20". Values of ϕ corresponding to each diffraction line were then determined and the effective values of the lattice spacing d calculated. These spacings will not be the true ones but will be subject to a systematic error

 $\frac{\Delta d}{d}$ due to the instrumental aberrations which is given by a relation of the form:

$$\frac{\Delta d}{d} = -A + B \cot^2 \theta + \frac{\cos^2 \theta}{2 u R} + \frac{S}{R} \cos \theta \cot \theta^{(2,3)}$$

VOI

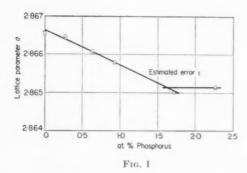
19

where A and B are positive functions of the beam apertures, μ is the absorption coefficient, R is the radius of the focusing circle and S is the displacement of the specimen surface behind the diffractometer axis. For the experimental arrangement used here the last three terms were of comparable magnitude so that only for θ greater than about 50° , when $\cos\theta \simeq \cot\theta$, can the above relation be written in the simple form:

$$\frac{\Delta a}{a} = \frac{\Delta d}{d} \simeq -A + C \cot^2 \theta$$

where a is the length of the cube cell edge. By plotting the value of a, corrected to give a value corresponding to a temperature of 25°C, corresponding to each line as a function of $\cot^2\theta$, a good straight line was obtained for the (211) (220) and (310) lines. Extrapolating to $\theta=\pi/2$ gives the correct value of a apart from the additive constants Aa, which is approximately 10^{-5} Å and $\Delta a \simeq 9 \times 10^{-5}$ Å representing the correction for the refractive index.

Alloys were prepared by adding phosphorus to molten iron containing the following impurities: C 0.0025%, Si 0.003%, Mn 0.005%, S 0.0046%, P 0.001%, Ni 0.007%, Cr 0.001%, Cu 0.005%, Al 0.004%, O₂ 0.001%, N₂ 0.001% and H₂ 0.000005%. They were homogenized by heating $in\ vacuo$ for 48 hr



at 1200°C. It was not found possible to produce grain sizes smaller than about 0.5 mm in the higher phosphorus alloys and the diffraction line profiles were not sufficiently smooth. Specimens were consequently prepared by filing and sieving to give particles of the order 0.04 mm in size, compacting these into disks 1.6 cm in diameter and about 2 mm thick, using a pressure of about 40 tons p.s.i. and then annealing in vacuo for 1 hr at 950°C. This treatment gave a line width for the (310) line of only $\Delta\theta \simeq 12'$ which compares well with the value of 10′ calculated from the beam apertures and the radiation width of the X-ray source.

The values obtained are shown plotted in Fig. 1 and it is evident that the phosphorus forms a substitutional solid solution. From the relative positions of the points corresponding to the same chemical composition the experimental error for the measurement of a is of the order $1:10^5$ and it is likely that the deviations from the line are due to small errors in the chemical analysis, which were estimated to be about ± 0.04 atomic per cent. The value of a determined for pure iron using three different specimens was 2.86654 + 0.00003 Å and agrees well with the values given in the literature. (4) The solubility limit appears to be about 1.6 at. per cent for $T=950^{\circ}\mathrm{C}$ and is probably lower than Haughton's (5) value of 3.6 per cent due to the comparatively slow rate of cooling. Further work on this is in progress.

Acknowledgments

The work described above has been carried out as part of the General Research Programme of the National Physical Laboratory, and this note is published by permission of the Director of the Laboratory.

B. GALE

National Physical Laboratory Teddington England

VOL.

1959

References

- 1. W. L. Bragg, J. Sci. Instrum. 24, 27 (1947).
- E. R. Pike, J. Sci. Instrum. 34, 355 (1957).
 A. J. C. Wilson, J. Sci. Instrum. 27, 321 (1950).
- 4. H. E. SWANSON, R. K. FUYAT and G. M. UGRIMIC, N.B.S. Circular 539, 4, 3.
- 5. J. L. HAUGHTON, J. Iron St. Inst. 115, 417 (1927).
 - * Received August 22, 1958.

High temperature intercrystalline cracking*

In a recent Letter to the Editor, (1) Kramer and Machlin have presented evidence that the amount of grain boundary cracking in nickel strained at 920°C is proportional to the per cent elongation, and argue that these data support a mechanism of growth of cracks suggested earlier by Chen and Machlin⁽²⁾, and also by Gifkins⁽³⁾. Furthermore, the authors state that this result is believed to be a strong argument against the vacancy condensation mechanisms of grain boundary void growth.

Although the relationship observed by Kramer and Machlin can be logically explained by the suggested mechanism, it is our opinion that the micro-structural appearance of specimens strained at elevated temperatures frequently does not support the idea that cracks grow mainly by grain boundary sliding. For example in Fig. 1, representing a deoxidized copper specimen strained to fracture at the rate of 1 per cent per hour at 800°C, extended cracks are observed which tend to lie in horizontal planes. The top and bottom surfaces of the slender cracks match closely, and the mating surfaces are appreciably displaced only in the vertical direction. Very few small voids or strings of small voids can be observed at the grain boundaries at higher magnification, suggesting that the cracks did not grow by the linking of several small voids. Configurations of this type are often observed in metals, and it is difficult to visualize how they could have arisen purely by grain boundary sliding. In addition, recent experiments by Shepard and Giedt⁽⁴⁾ prove that intergranular fracture in ingot iron can occur with practically no grain boundary shearing. Chen and Machlin(5) have themselves shown that intergranular cracks in copper will extend under the action of a transverse tensile stress, in the apparent absence of grain boundary sliding (Fig. 7 of reference 5).

Extended cracks such as those shown in Fig. 1 appear to have grown outward along the grain boundary in a roughly horizontal plane, as if the boundary were being opened by a zipper. This might represent a process of ductile fracture along the grain boundary, as suggested by others; i.e., the crack may

Fig. 1. Grain boundary cracking in deoxidized copper strained 1 per cent per hour at 800°C to fracture. ×13.

propagate by "tearing" of the grain boundary at the crack edge, under action of the operative tensile stresses. It is also possible to imagine that the crack propagates because of the flow of vacancies from the grain boundary to the crack edge. (6) The concentration of tensile stress acting across the grain boundary at the crack edge would tend to raise the vacancy concentration at the boundary. A gradient of vacancy concentration between the crack edge and contiguous grain boundary is thus established. Since grain boundaries are effective sources and sinks for lattice vacancies, and the diffusion path is short, it is conceivable that the resulting vacancy flux could be large enough to produce observable crack growth. It will be noted that this vacancy mechanism of crack growth differs from that suggested by Greenwood et al., (7) Machlin (8), Crussard and Friedel (9), and others, by its emphasis on the role of the grain boundary as a vacancy source.

Neither of the crack growth mechanisms discussed above has yet been developed quantitatively to a sufficient extent to say whether a linear relationship between cracked area and total elongation would exist, such as that observed by Kramer and Machlin. In considering this possibility, one is led to ask over what range of stress and other conditions the linear relationship is observed. For example, it is commonly believed that grain boundary cracking does not become important until the end of the second stage of creep. This suggests different rates of crack formation in the second and third stages of creep. It would be interesting to know the relationship of the Kramer and Machlin data to the creep curve. Another

point in question is the degree to which the submitted data reflect the rate of initiation as opposed to the rate of growth of cracks. The occurrence of isolated extended cracks such as those shown in Fig. 1 implies a high crack growth rate, relative to the rate of crack initiation. Crack initiation and crack growth may therefore be governed by quite different physical processes. Chen and Machlin⁽⁵⁾ have previously offered convincing evidence that cracks are initiated by grain boundary sliding. It is difficult for us to accept at present the data of reference I as convincing evidence that grain boundary cracks generally grow by the same mechanism.

L. L. SEIGLE

Sylvania Electric Products Inc. Bayside, New York

References

- 1. D. Kramer and E. S. Machlin, Acta Met. 6, 454 (1958).
- 2. C. W. Chen and E. S. Machlin, Acta Met. 4, 655 (1956).
- R. D. GIFKINS, Acta Met. 4, 98 (1956).
- L. A. SHEPARD and W. H. GIEDT, NACA Technical Note 4285, (August 1958).
- C. W. CHEN and E. S. Machlin, Trans. Amer. Inst. Min. (Metall.) Engrs. 209, 829 (1957).
- R. W. Balluffi and L. L. Seigle, Acta Met. 5, 449 (1957).
 J. N. Greenwood, D. R. Miller and J. W. Suiter,
- J. N. GREENWOOD, D. R. MILLER and J. W. SUITER, Acta Met. 2, 250 (1954).
- E. S. Machlin, Trans. Amer. Inst. Min. (Metall.) Engrs. 8, 106 (1956).
- C. CRUSSARD and J. FRIEDEL, N.P.L. Symposium on the Creep and Fracture of Metals, p. 243. H.M.S.O., London (1956).
 - * Received October 27, 1958.

Anomalous increase of resistivity during ageing of aluminium-silver alloys*

It is well known that during the room temperature ageing of quenched Al-Cu alloys (Cu ~2-5%) (namely during the pre-precipitation process(1) in which the formation of copper rich "zones", called Guinier-Preston zones, takes place) one observes an increase of resistivity followed after some time by a decrease; (2) this "anomalous" initial increase of resistivity might be due, a priori, to coherency strains of the smaller zones⁽²⁾ or to an abnormal scattering of zones when they reach a critical dimension comparable with the wave length of the free electrons (~10 Å) as proposed by Mott⁽³⁾. A very similar phenomenon is observable also in Al-Zn alloys as it was reported incidentally, as far as 1932, by Fink and Van Horn⁽⁴⁾ for an Al-Zn 12.7% alloy in a research on the equilibrium diagram of the zinc-aluminium system.

The object of this preliminary note is to point out that selecting suitable experimental conditions, a similar initial anomalous increase of resistivity can be VOI 7 19 observed also during ageing of Al–Ag alloys. In the meantime some new observations for an Al–Zn alloy will be also reported.

To detect the phenomenon we have employed wire samples of ϕ 1 mm with four soldered contacts, carrying out measurements by the usual potentiometric system at liquid nitrogen temperature. After quenching in brine at 2°C, samples have been dipped immediately in liquid nitrogen; annealings have been carried out at various temperatures employing proper liquid stirred baths.

Examples of isothermal ageing results, referring to some very dilute Al-Ag alloys, are reported in Fig. 1 (for the key of the curves see Table 1): in ordinate the absolute variation of resistivity, with reference to the initial value after quenching, is indicated. The initial anomalous increase of resistivity shown in Fig. 1 is similar to that observable in Al-Cu and Al-Zn alloys and cannot be confused obviously with the increase reported⁽⁵⁾ in later stage of precipitation in more concentrated Al-Ag alloys. We attribute this observed maximum to a very quick clustering of the silver atoms, although the distance for clustering seems to be large in consequence of the dilution of the alloys; the subsequent decrease of resistivity should be related not only to an increasing in size of clusters (as in Al-Cu alloys) but also (at least in these dilute alloys) to a loss of quenched-in vacancies (6) as apparent for pure aluminium (curve A in Fig. 1). The presence of a maximum of resistivity in function of size of clusters in Al-Ag alloys was independently assumed to exist also by Köster and Schüle⁽⁷⁾ to explain some other properties of Al-Ag alloys.

From Fig. 1 and other not shown results, the following principal features of the phenomenon seems to be well established: (1) the increase of the annealing temperature reduces the time to reach the maximum (it would be difficult to observe it at room temperature) and (2) decreases the amplitude of the maximum; (3) the increase of the quenching temperature decreases

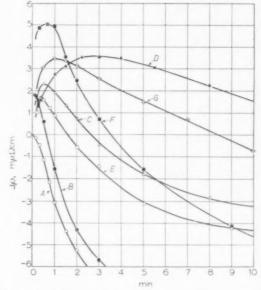


Fig. 1. Isothermal ageing curves for some dilute Al–Ag alloys (for the key of the curves see Table 1). The variation of resistivity $\Delta \rho$ is computed from the initial value of resistivity after quenching of each sample.

the time to reach the maximum; (4) the increase of the Ag content increases the amplitude of the maximum. It is to note that the preceding points (1) and (3) are in agreement, at least in a qualitative way, with the hypothesis of a role of quenched-in vacancies in increasing the rate of diffusion in pre-precipitation; (8) point (1) should be obviously related to the increased mobility of vacancies increasing the annealing temperature and point (3) to an increase of the concentration of quenched-in vacancies increasing the quenching temperature. (9)

This initial anomalous increase of resistivity is also observable with higher Ag content as shown in Fig. 2 (see again Table 1) for an Al-Ag 8.1% alloy, the necessary precautions being the lowering of the annealing temperature (following the preceding point (1) and the quenching temperature (following point 3).

Table 1. Key for the isothermal annealing curves of Figs. 1 and 2. Q is the quenching temperature and R the annealing temperature

Symbol	Fig. 1			Fig. 2				
	Ag (%)	Q (°C)	R (°C)	Ag (%)	Zn (%)	$Q^{-}({}^{\circ}\mathbf{C})$	R (°C)	
A	(Al 99.995%)	550	-40	8.1	_	400	0	
В	0.35	550	0	8.1	_	400	-20	
C	0.35	550	-20	8.1	_	400	-40	
D	0.35	550	-40	8.1		400	-54	
E	0.19	550	-20	8.1	400000	450	-50	
E F	0.72	550	-20	8.1	_	550	-65	
G	0.35	535	-20	Married Street	10 25	330	+20	
H	-			_	10.25	222	20	

VOL. 7 1959

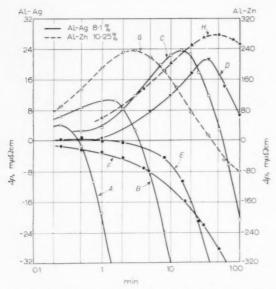


Fig. 2. Isothermal ageing curves for Al-Ag and Al-Zn alloys (for the key of the curves see Table 1). The variation of resistivity $\Delta \rho$ is computed from the initial value of resistivity after quenching of each sample.

These conditions can explain why Turnbull and Treaftis⁽¹⁰⁾ did not observe the presence of a maximum of resistivity in a recent study on the rate of clustering in Al-Ag alloys as they have been quenching from 550°C. Really by quenching from a high temperature clustering can take place during the quenching action itself, and zones can grow up more than the critical size so that only a decrease of resistivity is observed in ageing; this view is confirmed by the fact that the initial value (after quenching) of the resistivity of a sample is much lower after quenching from 550°C (curve F, Fig. 2) than from 400°C (for instance curve B, Fig. 2) the difference being about 200 m $\mu\Omega$ cm.

In the same Fig. 2 isothermal ageing curves obtained with the same experimental procedure are shown also for an Al-Zn 10.25% alloy confirming the presence of the maximum (note the high value of the increase of resistivity in this alloy); other additional results not reported here have shown that the preceeding points (1) and (3) are quite valuable also for this alloy.

As the anomalous increase of resistivity is observable in three alloys in which surely the pre-precipitation phenomenon takes place⁽¹⁾ the question arises if it is a general property of the pre-precipitation phenomenon. For this purpose it would be interesting to examine the features of other binary or more complex aluminium alloys. At present we have only examined in preliminary experiments some Al-Si alloys (Si 1.3%); till now however it has not been possible to

detect no anomalous increase of resistivity before the decrease due to precipitation. This result can be considered, perhaps, a proof that in these alloys no pre-precipitation phenomenon takes place.

About the cause of the increase of resistivity in Al-Cu, Al-Zn and Al-Ag alloys, if the phenomenon has a common origin, the explanation in terms of Mott's proposal seems to be preferred; really in consequence of equality of atomic radius of Al and Ag atoms, silver clusters should have no appreciable coherency strains.

Now a more complete study of the phenomenon in Al-Ag and Al-Zn alloys is in course, the intention being to utilize it to gain a better understanding of the role of vacancies in pre-precipitation; results will appear in due time on appropriate papers.

The authors are grateful to Prof. C. Panseri, Director of I.S.M.L., for encouragement and criticism.

T. FEDERIGHI

19

L. Passari

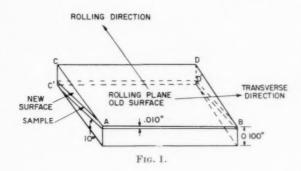
Istituto Sperimentale Metalli Leggeri C.P.129, Novara, Italy

References

- 1. A. GUINIER, Trans. Amer. Inst. Min. (Metall.) Engrs. 206, 673 (1956).
- 2. A. H. Geisler, Symposium on Phase Transformations in
- Solids, p. 387. Wiley, New York (1951). 3. N. F. Mott, J. Inst. Met. **60**, 267 (1937)
- W.L. FINK and K. R. VAN HORN, Trans. Amer. Inst. Min. (Metall.) Engrs. 99, 132 (1932).
- 5. A. H. GEISLER, C. S. BARRETT and R. F. MEHL, Trans. Amer. Inst. Min. (Metall.) Engrs. 152, 182 (1943). 6. C. Panseri and T. Federighi, Phil. Mag. 3, 1223 (1958).
- W. KÖSTER and W. SCHÜLE, Z. Metallk. 48, 628 (1957).
 T. FEDERIGHI, Acta Met. 6, 379 (1958).
 R. GRAF, C.R. Acad. Sci. Paris 245, 1544 (1958).
- 10. D. TURNBULL and H. N. TREAFTIS, Acta Met. 5, 534 (1957).
 - * Received October 2, 1958.

A mechanism for secondary recrystallization in high-purity silicon iron*

A successful experiment has been performed that identifies the orientation dependent selectivity mechanism for secondary recrystallization in high purity silicon iron. The alloy containing 3.25 per cent silicon and a total impurity content of approximately 0.005 per cent will form a strong cube texture by secondary recrystallization when annealed at temperatures of 1000 to 1300°C. A suitable mechanism to explain the discontinuous growth of the cube grains should account for all experimental observations. Experimental identification of the mechanism requires that no other possible mechanism is consistent with all of the experimental observations.

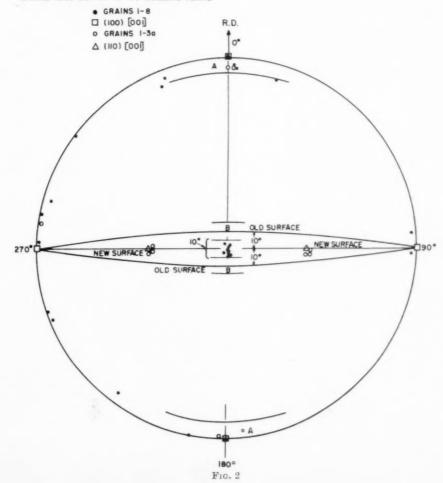


Some of the possible mechanisms for texture selection are listed as follows: (1) A larger grain boundary driving force for cube oriented grains caused entirely by a favorable size advantage (the observations of Assmus *et al.* cast doubt on this mechanism⁽¹⁾); (2) A larger driving force due to differences in grain perfection favoring the cube

grains, which are assumed in this mechanism to be the most perfect; (3) A greater growth rate of cube oriented grains not because of a larger driving force, but because of greater boundary mobility. The mobility would derive from the orientation relationship of the cube grains and the preferred orientations of the matrix grains; (4) A larger additional driving force for the cube oriented grains derived from a surface energy dependence on orientation. This additional driving force would have to favor the (100) plane in overcoming restraining forces such as those caused by thermal grooving at the boundary between grains, and particle inhibition of the boundaries.

Mechanisms (1), (2) and (3) relate to a rolling plane-rolling direction set of coordinates, but mechanism (4) is not restricted in this manner. For example, a section may be taken from a sufficiently thick sample to provide an entirely new reference





VOL.

7

surface. Thus if one or more of the first three mechanisms select the cube grains for discontinuous growth, changing the surface reference would also change the texture with respect to the new surface. This possibility is the basis of the present experiment.

In all of the materials studied it was seen that the (100) planes of the cube secondary grains were within 5° of the plane of the sheet. These samples were usually of 0.012 or 0.006 in. thickness. The experiment was designed to isolate mechanism (4) from the others. A sample was removed from 0.100 in. thick material (taken at an earlier stage of the processing) by grinding the thick sample at an angle of 10 degrees to the surface and to the rolling direction. The sample was ground to 0.010 in. and electropolished to 0.006 in. to remove cold work resulting from the grinding operation. The relationship of the new surface of the sample with the old surface is shown in Fig. 1. The sample was then annealed at 1200°C for 15 min in vacuum. A second identical sample was annealed for 30 min. The secondary grains of both samples were examined by X-ray techniques to determine their orientation. It was found that the cube secondary grains in both samples were all within 5° of the plane of the sample i.e., parallel to the new surface. There were three (110) grains formed in the second sample by tertiary recrystallization. (2) These grains had (110) planes within 5° of the plane of the surface. A plot of the cube poles of both types of grains is shown in Fig. 2. Both the old surface and the new surface are plotted on the stereographic projection. Check samples taken parallel to the surface of the 0.100 in. sample produced the same result.

The results clearly indicate that mechanism (4) is the one that accounts for the sharp alignment of the cube planes with respect to the plane of the surface of the sample. An additional feature is required—a rapid increase in surface energy with angular deviations beyond 5°—but this behavior near a low index plane is not unexpected. The theory of surface energy variations near low index planes more or less predicts this behavior. Thus the lower surface energy of the (100) planes provides the additional driving force for early discontinuous growth of the cube grains.

J. L. WALTER

General Electric Research Laboratory Schenectady, New York

References

- F. Assmus, K. Detert and G. Ibe, Z. Metallk. 48, 344 (1957).
- J. L. Walter and C. G. Dunn, Tertiary Recrystallization in Silicon Iron, to be published.
 - * Received November 12, 1958.

Expansion coefficient of plastically deformed steel*

Changes in the expansion coefficient were measured in annealed and in hardened and tempered steel samples after plastic deformation in tension. These measurements were made in order to investigate the effect of a sharp yield point on the expansivity. In the case of aluminum, which has a smooth stress-strain curve, the expansivity increased approximately 2–4 per cent after plastic tensile deformation. (1) However, previous investigators (2,3) have reported abrupt changes in the expansion coefficient, generally negative, associated with the discontinuous yielding in mild steel.

Tensile test specimens of standard dimensions $(0.252 \, \mathrm{in.})$ diameter $\times 2.5 \, \mathrm{in.}$ gage length) were prepared from polycrystalline steel rod containing 0.27 per cent C and 0.50 per cent Mn. Specimen A was annealed at $1675^{\circ}\mathrm{F}$ for 1 hr and furnace cooled. Specimens B and C were water quenched from $1675^{\circ}\mathrm{F}$, and then tempered at $1100^{\circ}\mathrm{F}$ and $600^{\circ}\mathrm{F}$, respectively, for 1 hr. Specimen A (annealed) had a marked yield point, specimen B $(1100^{\circ}\mathrm{F})$ exhibited a less well-defined yield point, and specimen C $(600^{\circ}\mathrm{F})$ showed a continuous strain hardening curve.

After straining in tension to a selected stress, the load was removed and the expansion coefficient was measured with a quartz rod dilatometer. The specimen and dilatometer were totally immersed in silicone oil which was heated slowly through the temperature range $22-50^{\circ}\mathrm{C}$. The specimen elongation was detected by a sensitive microformer relay and read directly from a calibrated electro-limit gage. The strain sensitivity of the dilatometer was about 2×10^{-6} . Tensile strains were measured by SR-4 electrical resistance strain gages mounted on the specimen as described elsewhere. Stress levels were increased in steps until necking occurred. Elastic limit at 10^{-6} strain and yield stress values were then measured.

19

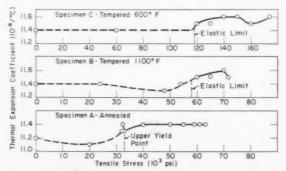


Fig. 1. Effect of previously applied stress on the thermal expansion coefficient of 0.27 per cent carbon steel.

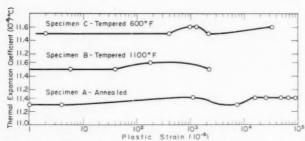


Fig. 2. Effect of plastic strain on the thermal expansion coefficient of 0.27 per cent carbon steel.

The elastic limit values for specimens A, B and C were $32,200 \, \mathrm{lb/in^2}$, $58,000 \, \mathrm{lb/in^2}$ and $118,000 \, \mathrm{lb/in^2}$, respectively. For specimen A, the upper yield point was $33,000 \, \mathrm{lb/in^2}$; the lower yield point was $31,800 \, \mathrm{lb/in^2}$. In specimen B, rapid yielding occurred at a stress of about $71,000 \, \mathrm{lb/in^2}$.

Values of the expansion coefficient, a, as functions of the applied stress and the residual strain are shown in Figs. 1 and 2, respectively. After elastic straining, a slight decrease in a was detected in specimens A and B, similar to the results of Muir(2), who associated this effect with the elastic negative strains often found after tensile loading in the elastic range. However, significant increases in expansion coefficient did not appear until the beginning of plastic flow. Upon further cold working, Figs. 1 and 2 show: (1) Increases in expansion coefficient were detected in the microstrain range at the very beginning of plastic deformation. (2) An increase in expansivity of the order of 1-2 per cent was found and this increased expansion persisted throughout the plastic strain region until necking occurred. (3) There appears to be a partial return to the unstressed value of a at about 0.2 per cent residual strain for the tempered steels which do not possess a discontinuous yield point. (4) In the annealed steel, an increase in a of about 1 per cent was detected after the initial Luder's strain in the region of the lower yield point (32,400 lb/in2). After a subsequent decrease with slightly higher strain, a increased again in the strain hardening region and remained stable with further extensions until necking occurred. The sharp changes in a reported by previous investigators (2,3) in the region of the yield point were not found.

It has been suggested in previous work⁽¹⁾ that the expansivity increase observed with small plastic strains may result from the expansion of mobile dislocation loops causing localized increases in strain. Pinning of the loops by interaction with other dislocations or solute atoms would be expected to reduce this additional expansion component. The increase in α found in the case of annealed steel in the neigh-

borhood of the lower yield point may then be explained as the result of the sudden increase in dislocation mobility associated with the sharp yield point as dislocations break away from their pinning points. The subsequent decrease in α at 0.8 per cent strain, as well as the decrease in the tempered steels at about 0.2 per cent strain, can be attributed to the pinning of mobile loops by dislocation interactions. Increases in expansion coefficient with greater strains may be due to the presence of other types of lattice defects such as vacancies.

The authors are grateful to the M.I.T. Instrumentation Laboratory and the U.S. Air Force for their sponsorship of this work.

> M. J. HORDON B. L. AVERBACH

Department of Metallurgy Massachusetts Institute of Technology Cambridge, Massachusetts

References

- M. J. HORDON, B. S. LEMENT and B. L. AVERBACH, Acta Met. 6, 446 (1958).
- H. Muir, Sc.D. Thesis, Department of Metallurgy, M.I.T. (1953).
- J. L. ROSENHOLTZ and D. T. SMITH, J. Appl. Phys. 21, 396 (1950).
 - * Received November 17, 1958.

Remarques sur l'emploi des repères inertes (markers) pour les études de diffusion dans les phases plastiques*

L'utilisation de repères inertes pour marquer l'interface originale dans les études de diffusion apparaît fort séduisante à première vue et elle a permis des observations très intéressantes. De nombreux auteurs ont utilisé des repères inertes dans l'étude des phénomènes d'oxydation des métaux, aboutissant parfois à des conclusions opposées. Nous pensons que ceci tient aux difficultés de leur mise en oeuvre et qu'il convient de mettre en garde contre les erreurs d'interprétation que peut causer leur comportement dans le cas d'un déplacement rapide de l'interface lorsque la phase dans laquelle ils se trouvent est plastique.

Dans le cas de l'oxydation du fer, par exemple, un article récent⁽³⁾ concluait en faveur de la diffusion de l'oxygène dans FeO à haute température parce que des fils de Pt posés sur une plaquette de fer avant oxydation à 1000°C ont été retrouvés au milieu du protoxyde sur la coupe polie. Or, la micrographie montrait un oxyde détaché du fer, très poreux avec, en particulier, une "cheminée de cavités" entre le repère et le métal.

Nous avions nous-mêmes fait de nombreuses expériences dans ce domaine de températures en employant divers types de repères inertes, ce qui nous avait permis d'en étudier le comportement et de mettre au point une technique qui semble donner des résultats valables. (4) En effet, la première difficulté consiste à fixer le repère de façon à ce qu'il soit absolument en contact avec le métal au début de la réaction. Ensuite, il ne faut pas que le repère soit sollicité par une action mécanique au cours de la réaction. Il semble qu'à haute température le protoxyde de fer soit plastique; si un fil de platine est tendu de telle façon qu'il exerce une pression sur le protoxyde, celui-ci fluera autour du fil en se ressoudant éventuellement après passage du fil. Or, dans l'expérience que nous critiquons, les fils de Pt étaient tendus par un poids à chaque bout au début de l'oxydation. A mesure que celle-ci progresse, l'action des poids est annihilée parce que les fils sont enrobés par l'oxyde qui pousse sur les côtés de la plaquette.



Fig. 1.

Par ailleurs, on sait que les arêtes s'oxydent moins vite que le centre des plaquettes. Donc, de toute façon, les fils deviennent fixés en deux points audessus de l'interface qui se déplace rapidement à 1000° . Il est donc normal de les retrouver au milieu de l'oxyde sans que la diffusion de l'oxygène y soit pour quelque chose.

Pour obvier à cet inconvénient dans la mesure du possible, nous utilisons la technique suivante: sur une plaquette de fer pur chromée puis abrasée de façon à mettre le fer à nu sur une des grandes faces, nous soudons à l'are aux deux bouts des fils de platine de 50 μ de diamètre. Après oxydation à 1000° dans l'air, la coupe polie nous montre que les trois fils se retrouvent à des distances différentes de l'interface (Fig. 1). Si on effectue la coupe plus près des soudures, l'un des fils apparaît relié au métal par un



Fig. 2.

pédoncule (Fig. 2). On remarque que l'oxyde est parfaitement adhérent au métal. L'utilisation de faces chromées permet de mesurer le déplacement de l'interface fer-oxyde et des repères (ici 730 u) par rapport à un plan qui reste pratiquement fixe au cours de l'oxydation. L'éloignement de l'interface des autre fils s'expliquerait difficilement par une différence de vitesse de diffusion de l'oxygène. Il est bien plus vraisemblable qu'ils n'aient pas été parfaitement en contact avec le métal au debut de l'oxydation. Il faudrait donc fixer les fils en plusieurs endroits. Mais ceci conduit à une autre cause d'erreur. En effet, la fusion du platine recouvre le fer sur une surface relativement grande. Or, on constate que la présence d'un fil même mince, ralentit le déplacement de l'interface (Fig. 3). La multiplication des points de soudure aboutirait donc à une modification importante des conditions d'oxydation. C'est pourquoi l'utilisation, soit de dépôts électrolytiques, soit de poudres telles que Cr.O. comme repères inertes n'est pas à conseiller.

191

Enfin, il est difficile de trouver une matière absolument inerte vis-à-vis du métal et de son oxyde. Dans



Fig. 3.

le cas du fer, par exemple, la silice est proscrite puisqu'elle réagit avec FeO pour former de la fayalite et même le platine est d'emploi criticable puisque le fer y diffuse, ce qui conduit parfois à une oxydation interne du fil.

En conclusion, nous pensons qu'il convient de n'employer les repères inertes dans les études d'oxydation qu'en prenant des précautions pour qu'ils soient parfaitement adhérents au métal avant oxydation, qu'ils ne soient pas soumis à des actions mécaniques au cours de la réaction et de n'interpréter les résultats obtenus qu'avec la plus grande prudence et que lorsque plusieurs expériences ont prouvé leur reproductibilité.

Enfin, accessoirement, notons que nos propres expériences de fils repères tendent à indiquer que seuls les ions fer diffusent dans FeO même à 1000°C, mais qu'il conviendrait de confirmer ces résultats par une méthode plus sûre.

M. CAGNET

Institut de Recherches J. Moreau

de la Sidérurgie St. Germain-en-laye (S & O)

Bibliographie

- A. D. SMIGELSKAS et E. O. KIRKENDALL, Trans. Amer. Inst. Min. (Metall.) Engrs., Techn. Publ. n° 2071 (1946).
 L. B. PFEIL, J. Iron St. Inst. 123, 251 (1931); B. W.
- L. B. PFEIL, J. Iron St. Inst. 123, 251 (1931); B. W. DUNNINGTON, F. H. BECK et M. G. FONTANA, Corrosion 8, 2 (1952); B. ILSCHNER et H. PFEIFFER, Naturwissenschaften 40, 603 (1953); K. Sachs, Metallurgia, Manchr. 54, 11 (1956).
- H. J. Engell et F. Wever, Acta Met. 5, 695 (1957).
 J. Moreau et M. Cagnet, Rev. Métall., 55, 1091 (1958) Publ. IRSID, Serre A, n° 193.
 - *Received November 18, 1958.

Erwiderung auf den Brief an den Herausgeber der Herren Cagnet und Moreau*

Wir möchten den Herren Cagnet und Moreau herzlich für ihr Interesse an unseren Versuchen mit inerten Marken⁽¹⁾ danken. Ihre Bedenken hinsichtlich der Auswertung von derartigen Versuchen sind zweifellos berechtigt. Die von den Herren gegebene Deutung unserer Versuche dürfte jedoch nicht zutreffen. Cagnet und Moreau nehmen an, dass das Oxyd ausschliesslich durch Wanderung des Eisens und Anbau von Gitterbausteinen an der äusseren Phasengrenze weiterwächst. In diesem Falle bleibt eine Marke auch dann an der Phasengrenze Eisen/Oxyd, wenn sie vom Oxyd umhüllt wird und nicht auf dem Metall aufgeschweisst ist. Voraussetzung hierfür ist nur, dass sie zu Beginn der Oxydation auf dem Metall aufgelegen hat, und das war bei unserer Versuchführung sichergestellt. Trotzdem lagen die Marken nach dem Versuch in der Oxydschicht. Als Möglichkeit

einer Deutung hierfür erwähnten wir in der angegebenen Arbeit eine Sauerstoffdiffusion im Wüstit bei Temperaturen oberhalb 850°C. Weitere Untersuchungen zeigten, dass die Marken auch in diesem Temperaturgebiet nur dann im Inneren des Oxyds vorgefunden werden, wenn der innere Teil der Wüstitschicht in Form von Säulen mit kanalartigen Hohlräumen ausgebildet ist. Es ist anzunehmen, dass eine solche Struktur des Oxyds entsteht, wenn sich die Oxydschicht bei ihrer Bildung vom Metall ablöst. Durch Zersetzung des nunmehr vom Eisen abgetrennten Wüstits gelangt Sauerstoff an die Eisenoberfläche, so dass hier die Wüstit-Säulen entstehen können, die den Spalt überbrücken. Wie Herr L. Himmel in einem Briefwechsel mit uns ausführte, ist es möglich, dass die Zunderschicht beim Ablatzen vom Metall die Platinmarken mit sich nimmt, so dass die Marken nach Versuchsende zwischen diesen Säulen und dem kompakten Teil der Zunderschicht vorgefunden werden. Ob diese Deutung zutrifft, lässt sich noch nicht mit Sicherheit entscheiden.

Max-Planek-Institut fur Eisenforschung Düsseldorf, Germany

F. WEVER H. J. ENGELL

References

- 1. H. J. ENGELL and F. WEVER, Acta Met. 5, 695 (1957).
 - * Received December 29, 1958.

Experimental evidence of boundary migration*

Several authors have investigated the phenomenon of boundary migration, connected with gradual grain growth. $^{(1-4)}$

The migration proceeds by the movement of the boundaries in the direction of their centres of curvature and hence large grains grow at the expense of the surrounding smaller grains which disappear progressively.

All the methods suggested to give evidence to this process are based upon a discontinuous observation of the successive positions taken by the grain boundaries.

In particular, Sperry⁽⁵⁾ has suggested a technique for aluminum and Bardolle one for iron, ⁽⁶⁾

After each thermal treatment, Sperry makes an electrolytic oxidation of the specimen, followed by an observation at the microscope in polarized light.

Bardolle makes use of the different colours, obtained by treating the specimen at 290°C in oxygen, which indicate the grain boundary perfectly. By a successive treatment at 850°C in vacuum these colours disappear (FeO reduces to Fe). Hence it is possible to follow

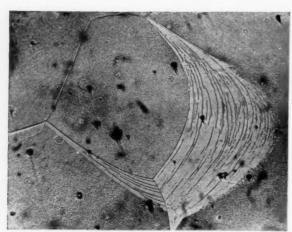


Fig. 1. Fe-Si 3.5 per cent annealed at 1100°C for 5 min with a ratio $pH_2O/pH_2 = 4.3 \times 10^{-5}$. ×15.

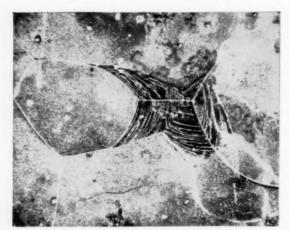


Fig. 2. Fe-Si 3.5 per cent annealed at 1100°C for 5 min with a ratio $pH_2O/pH_2 = 4.3 \times 10^{-5}$. ×8 (dark field).

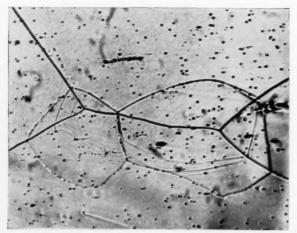


Fig. 3. Fe-Si 6.4 per cent annealed at 1000°C for 24 hr with a ratio pH₂O/pH₂ = 1.3×10^{-5} . $\times 32$

the whole process of grain growth by a series of heat treatments at high temperature in vacuum followed by oxidations at lower temperature.

In investigating the phenomena of oxidation of pure iron and Fe-Si alloys at temperatures from 1000 to 1300°C⁽⁷⁾ we have noticed that atmospheres, slightly oxidizing towards silicon (pH2O/pH2 in the ratios $1.3 \times 10^{-5} \div 4.3 \times 10^{-5}$), were suitable for the observation of grain boundary migration. By using this technique on specimens, electrolytically polished, the displacements of the boundaries, up to their equilibrium positions, appear in direct evidence at the end of the heat treatment. In fact for reasons which are not yet clear, the recrystallized regions are less susceptible to oxidation than both grain boundary and unrecrystallized regions. The consequence is that each step of the boundary displacement, due to small variations of temperature or to other causes, is marked by an oxide trace. Hence each trace indicates the positions occupied by the boundary at a given time.

Two examples are given in Figs. 1 and 2. Fig. 1 gives a typical case of shortening of the boundary, Fig. 2 reports the growth of two crystals with the formation of a new boundary at about 90° with regard to the former.

On the other hand, when the temperature of hydrogen annealing is very high, the grain boundaries positions are also revealed in absence of oxidation by the deformation of the metal surface close to the boundary itself. This is due to the equilibrium between the interfacial tension of the boundary and the surface tension of the metal. The presence of traces of oxygen, adsorbed on the surface, lowers the surface tension while the grain boundary tension remains the same and strengthens the effect. As the boundary migrates from a certain position to another the trace of the former position disappears very slowly and can still be observed after a long time. An example relative to Fe-Si 6.4 per cent annealed at 1000°C for 24 hr is given in Fig. 3. In this example it is particularly interesting to observe the anchoring effect of the impurities present in the metal.

Istituto Elettrotechnico Nazionale

A. FERRO

"Galileo Ferraris"

C. SARI

Centro Studi Elettrofisica—Torino G. VENTURELLO

References

- 1. D. DARKEN and E. R. PARKER, Trans. Amer. Inst. Min. (Metall.) Engrs. 34, 156 (1945).
- C. S. SMITH, Trans. Amer. Inst. (Metall.) Engrs. 175, 15
- J. E. Burke, Trans. Amer. Inst. (Metall.) Engrs. 180, 103 (1949).

- P. A. Beck and Ph. R. Sperry, J. Appl. Phys. 21, 150 (1950).
- Ph. R. Sperry, Trans. Amer. Inst. (Metall.) Engrs. 188, 103 (1949).
- J. BARDOLLE, C.R. Acad. Sci. Paris 234, 2200 (1952);
 Rev. Métall. 613 (1952).
- A. Ferro, C. Sari and G. Venturello, Metall. Ital. 50, 484 (1958).
 - * Received 26 November, 1958.

Recovery of lattice expansion of irradiated molybdenum*

Thermal annealing of the extra lattice parameter expansion in irradiated commercial molybdenum containing some residual cold work was investigated in order to obtain new information concerning the nature of point defect recovery in a solid.

The original stock for the specimens was wrought commercial molybdenum which had the following composition in wt. per cent: Fe, 0.03; Mn, 0.01; Al, 0.01; Ni, 0.01; Si, 0.01; Mg, 0.01; Cu, 0.01. Samples $0.5 \times 0.5 \times 0.1$ in. were treated prior to

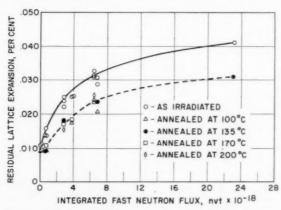


Fig. 1. Lattice expansion as a function of neutron flux; as irradiated (solid line), after completion of initial recovery (dashed line).

irradiation for 1 hr in vacuum at 900°C. The molybdenum was irradiated at the Materials Testing Reactor, exposed to the cooling water at a temperature of 30 to $40^{\circ}\mathrm{C}$ in an estimated fast neutron flux of 1.8×10^{13} neutrons per cm²-sec. Various exposures from 6.5×10^{16} to 2.3×10^{19} nvt were obtained. After irradiation, the material was stored at room temperature for times of approximately one to two years and the lattice parameter determined by X-ray measurements.

The effect of irradiating molybdenum at an average temperature of 35°C is to increase the dimensions of

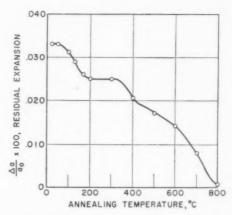


Fig. 2. Isochronal recovery of lattice expansion (time at temperature was 1 hr).

the body-centered crystal lattice. The shape of the exposure curve is shown in Fig. 1. Although there is an initial rise, the effect of additional exposure becomes less marked at the higher irradiation levels. The largest increase in lattice dimensions was 0.041 per cent at 2.3×10^{19} nvt. A preliminary set of heat treatments indicated that radiation induced lattice expansion could be decreased at temperatures above 50°C. Furthermore, (see Fig. 2) the recovery could be separated into three temperature regions characteristic of different mechanisms of defect removal. These processes occurred at 100-200°C, 400°C, and at 500-800°C. The recovery mechanism accounting for the first drop in lattice parameter was investigated using nine samples representing various initial values of lattice expansion. The annealing treatments of two samples at 100°C, four at 135°C, and three at 170°C were continued until no further change in lattice dimensions could be detected. The isothermal lattice parameter recovery curves are presented in Fig. 3. The marked time dependence which characterizes this

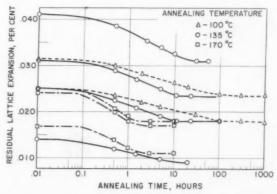


Fig. 3. Isothermal annealing curves for nine irradiated molybdenum specimens.

recovery should be noted. For example, for three samples with an initial expansion of 0.025 per cent, the recovery is complete after approximately 1.5 hr at 170°C, 11 hr at 135°C, and 100 hr at 100°C. In this temperature region, the amount of recovery was independent of temperature for sets of samples with the same initial lattice expansion. The residual lattice expansion present after annealing these and other samples at 100–200°C is included in Fig. 2. It can be seen that, over the entire range of neutron exposures, 20–30 per cent of the total radiation induced lattice expansion has been recovered. None of these samples showed any further decrease in lattice parameter until temperatures greater than 300°C were reached.

It is evident from the exposure curve that a substantial number of interstitials were present after neutron irradiation at 30 to 40° C. It is also apparent that a large number persist after annealing at $100-170^{\circ}$ C.

The fact that three temperature ranges for lattice parameter recovery were noted suggests that the initial migrating defect reacts in a complex manner with the surroundings. If an interstitial is migrating from 100 to 170°C, it may be reacting with impurities, dislocations, or with other interstitials. There were a number of impurity atoms present in the commercial molybdenum and the total per cent far exceeded the estimated number of interstitials and vacancies. The dislocation density of the molybdenum was higher than that of recrystallized material. Examination of the recovery data obtained at 100 to 170°C indicated that a conventional plot of log time vs. 1/T for any given amount of lattice recovery would not yield a unique value of the activation energy. In fact, the magnitude of an activation energy calculated from such a plot would increase as recovery progressed. This type of behavior may be observed in cases where the contribution of the recovering defect to the observed property change is not constant. Strict obedience to first or second order kinetics was not observed over the entire range of data, but it appears that first order kinetics provide the best description of the recovery, especially at 135 and 170°C. In view of these facts, it seems likely that the mechanism of lattice parameter recovery between 100 and 170°C is the trapping of migrating interstitials at small impurity atoms.

Acknowledgments

I wish to thank M. L. Sorick for assisting with the lattice parameter measurements, and W. V. Cummings for guidance in the early stages of the X-ray work. I also wish to acknowledge helpful and stimulating

discussions with J. C. Tobin, J. M. Tobin, and H. H. Yoshikawa.

D. L. GRAY

VO

19

Hanford Atomic Products Operation Richland, Washington

* Work done under Contract, W-31-109-Eng-52 between the Atomic Energy Commission and the General Electric Company. Received 10 November, 1958; in revised form 15 December, 1958.

Direct observation of sub-structures in martensite*

In 1954, it was reported by the present writers $^{(1)}$ that fine straight parallel bands were found in the electron-micrograph of the surface relief of a martensite plate of Fe-30% Ni alloy. They had a spacing of about 200 Å, and were interpreted as surface traces of the transformation shears.

To examine whether the traces are also present in the interior of the martensite plate, direct observation has been made using a thin foil which was obtained by electrolytic polishing of a subzero-cooled plate of 0.2 mm thick. Fig. 1 is an example of electronmicrographs taken. As seen in this figure, there were found fine parallel fringes in martensite plates. Fig. 2 is another example. Detailed inspection of these fringes enables us to find a unit of group consisting of a few lines. The spacing between the two unit fringes is 100-400 Å, which is of the same order as that of the fine bands found in the surface relief. The unit fringe has such behaviours as may be interpreted as the effect of a wedge shape. According to the selected area diffraction, the fringes are parallel to the (112) plane of the martensite plate. On the other hand the diffuseness of the X-ray diffraction line {200} predicts the presence of stacking faults at {112} planes whose spacing is also of the same order. And therefore it is probable that the unit fringe is due to a stacking fault which occurred during the transformation. Thus it is concluded that the traces of the transformation slips are also present in the form of stacking faults in the interior of the martensite plate.

The details will be described in some journal published in Japan.

Institute of Scientific and Industrial Research Osaka University Sakai, Osaka, Japan Z. NISHIYAMA K. SHIMIZU

Fig. 1. Martensite in Fe-30.64% Ni alloy, showing straight parallel fringes.

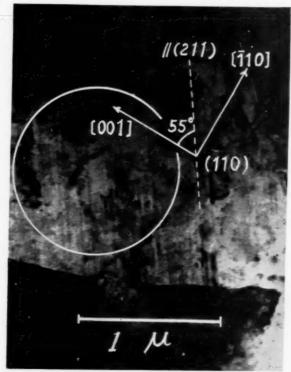


Fig. 2. Martensite in Fe-30.64% Ni alloy, showing straight parallel fringes.

Reference

- Z. Nishiyama, Symposium at the 3rd Congress of the International Union of Crystallography (1954);
 Z. Nishiyama, K. Shimizu and S. Sato, Mem. Inst. Sci. Ind. Res., Osaka Univ., 13, 1 (1956).
 - * Received 13 December, 1958.

Kinetics of vacancy precipitation in a silver-zinc solid solution*

The primary solid solution of Zn in Ag lends itself particularly well to the study of atomic mobility by virtue of the large Zener anelastic relaxation (or "pair reorientation effect") that it shows under an applied static or alternating stress. Such an alloy has therefore been used to study the effects of quenched-in vacancies on the rate of atom movements, and in this way to observe the manner in which excess vacancies anneal out. The previous studies have shown that vacancies anneal out in the range between 50° and 80°C in two stages, the first being much more rapid than the second. It was also demonstrated that cold working increases the rate at which vacancies anneal out of the alloy after quenching.

The purpose of this note is to describe a more quantitative study of the annealing kinetics of vacancies than had been carried out previously, both for

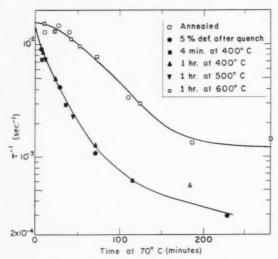


Fig. 1. Effect of 5 per cent deformation and subsequent annealing on the early stage of the vacancy decay curve. In all cases, regardless of annealing temperature, the specimen was quenched from 400°C. The equilibrium value of τ^{-1} at $70^{\circ}\mathrm{C}$ is 2×10^{-6} sec⁻¹.

undeformed and for deformed samples. As a result of this work it will be shown that the kinetics for the deformed alloy are quite different from those of the undeformed samples.

The anelastic relaxation time, τ , was measured after quenching by means of static measurements (elastic after-effect) using the techniques described in the earlier papers. The alloy used was Ag-33 at. % Zn. If c is the vacancy concentration (expressed as a mole fraction), the rate of relaxation, τ^{-1} , which is a measure of the rate of atom movement, must be proportional to c so long as atom movements take place through a vacancy mechanism, i.e.

$$\tau^{-1}(t) = Ac(t) \tag{1}$$

where the proportionality constant, A, depends on the temperature of measurement through a Boltzmann factor involving the activation energy for motion of a vacancy. Thus, the quantity τ^{-1} at a given temperature is a relative measure of the vacancy concentration and decreases with annealing as c approaches its equilibrium value. The earlier work showed that a plot of $\log \tau^{-1}$ against time, obtained by successively twisting and untwisting a quenched wire of the alloy at a given anneal temperature, gives two distinct stages with a sharp break in slope between them. The present study concentrates on the early part of this vacancy decay curve. Fig. 1 shows this early stage of vacancy annealing for a series of successive runs on a single sample at an anneal temperature of 70°C. Before each run, the sample was quenched from 400°C. The initial value $(\tau^{-1} = 0.014 \text{ sec}^{-1})$ is

estimated to correspond to a quenched-in vacancy concentration of about 3×10^{-5} , by the method described in reference 2. The condition of the alloy for each run is described next to the appropriate point in the inset of the figure. The open circles represent the case of the sample that was annealed at 650°C prior to its quench from 400°C. In the next run, the same sample was first requenched from 400°C and then extended by 5 per cent. The rate of decrease of the vacancy concentration with time is now considerably higher; however the starting value is unchanged, which implies that the initial vacancy concentration was not affected by the deformation. In the third run, the sample was heated 4 min at 400°C, then quenched and annealed at 70°C without additional deformation. The results show that in spite of the 400°C anneal, the vacancy decay curve is the same as in the previous run. For run No. 4 the sample was reheated to 400°C for 1 hr before quenching and annealing. Again the points lie on the lower curve of Fig. 1. The sample was next held for 1 hr at 500°C then requenched from 400°C and annealed (run No. 5), with no change in the vacancy decay curve. Finally, it was held for 1 hr at 600°C then again quenched from 400°C and run at 70°C. The results show most strikingly that the change in the vacancy decay curve due to the 5 per cent cold work persisted until the last run, before which the sample had been given the 600°C anneal. Correspondingly, back reflection X-ray Laue photographs showed that there was no detectable recovery of the asterism produced by the deformation until after the 600°C anneal, at which point the spots again became sharp.

The data of Fig. 1, as well as other runs of similar types, were analysed in terms of the well-known precipitation law:

$$dW/dt \approx (1 - W)t^{m-1} \tag{2}$$

19

where W is the fraction of the vacancies which have annealed out at any time, t. Integration gives: $1 - W = \exp{(-\alpha t^m)}$. The constant m is called the growth exponent. Zener⁽³⁾ has shown that, for diffusion-limited precipitation where the nuclei are present at t = 0, the value of m may be related to the shape of the precipitate particles. To obtain the growth exponent experimentally, it is convenient to make use of the solution of equation (2) in the form

$$\ln \ln (1 - W)^{-1} = \ln \alpha + m \ln t \tag{3}$$

which predicts a straight line plot of log log $(1 - W)^{-1}$ vs. log t with slope equal to the growth exponent, m. In order to obtain the growth exponent for the precipitation of vacancies in an undeformed sample, the

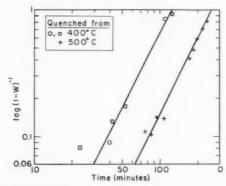


Fig. 2. Plot of log log $(1 - W)^{-1}$ vs. log time for undeformed Ag-Zn specimens quenched from 400°C and 500°C and run at 70°C. The slope of the lines drawn is m = 2.0.

fraction of vacancies precipitated (relative to the end of the first stage as the completion of the process) is plotted in the manner suggested by equation (3). Fig. 2 shows this type of plot for the data of the upper curve of Fig. 1, as well as for another undeformed sample quenched from 500°C and annealed at 70°C. From Fig. 2, the value m=2 appears to give the best fit to the experimental results.

In a similar way, for the deformed sample, the lower curve of Fig. 1 is used to obtain 1 - W, the fraction of vacancies remaining at time t which, when plotted according to equation (3), gives Fig. 3. This plot shows that the early part of the vacancy decay curve for the deformed alloy can be fitted quite well to a growth exponent of 2/3.

1959

The results reported here show a striking similarity to those for the precipitation of C in α-Fe of Wert⁽⁴⁾ and Harper⁽⁵⁾. In both cases there is a change of growth exponent produced by deformation. Such a change implies that the mode of precipitation changes after deformation. The value m = 3/2 for the precipitation of carbon in undeformed iron has been interpreted (3,4) in terms of the formation of spherical precipitate particles under diffusion-controlled conditions. After deformation, Harper found that the value of m has become equal to 2/3, consistent with the Cottrell-Bilby⁽⁶⁾ equation for strain ageing. In the present case of vacancy precipitation the value m=2 for the undeformed case may be interpreted collapsed vacancy disks or dislocation loops.* Such

loops have actually been observed by Hirsch and coworkers⁽⁷⁾ in quenched Al by means of transmission electron microscopy. On the other hand, the 2/3-law after cold working again agrees with the Cottrell-Bilby theory. The latter theory not only predicts the m-value but also gives an expression for the constant a in equation (3), namely:

$$\alpha = K(\gamma D/kT)^{2/3} \cdot L \tag{4}$$

where K includes known elastic and crystallographic constants of the matrix material, γ is the fractional size difference between the precipitating atom and the solvent atom, D is the diffusion coefficient of the precipitating atom, L is the dislocation density (total dislocation length per cm³), and kT has its usual meaning. In the present case, where the "precipitating atom" is the vacancy, a reasonable value for γ is about 0.2, D at 70°C is estimated to be 2×10^{-13} cm²/ sec (from the known activation energy for vacancy migration in Ag- $Zn^{(2)}$), while K is calculated to be 5×10^{-13} . Putting these numbers, and the value $\alpha = 8.7 \times 10^{-3} \ {
m sec^{-2/3}}$ obtained from the intercept of Fig. 3, into equation (4) gives $L=2\times 10^{10}~{\rm cm^{-2}}$ for the 5 per cent deformed alloy. The reasonableness of this number serves to support the application of the Cottrell-Bilby theory to the precipitation of vacancies in the cold-worked Ag-Zn alloy.

The success of the Cottrell-Bilby theory in the case of vacancy precipitation is somewhat surprising in view of the fact that the theory fails to take into account the diffusion flow due to the concentration gradient near the dislocation. This effect complicates the problem⁽⁸⁾ to produce a deviation from the m=2/3law which should appear both in the case of solute precipitation observed by Harper, and in the present case of vacancy precipitation. A second complication arises from the fact that there is a change in the

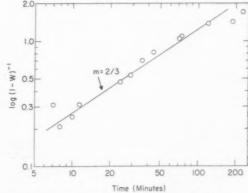


Fig. 3. Same plot as Fig. 2 for the case of the 5 per cent deformed sample. Quenching temperature: 400°C ; run temperature: 70°C . The slope of the line drawn is 2/3.

as due to the precipitation of vacancies in the form of

^{*} For precipitation of a second phase in the form of a disk, Zener has proposed an m = 5/2 law. In the case of vacancies, however, there is no growth of the disk in thickness, which means that one must deduct from m = 5/2, a value of 1/2 for the growth of the thickness by diffusion. In both these cases it should be emphasized that the precipitation process is assumed to involve growth only and all nuclei are assumed to be present at t=0.

dilatation about a vacancy (i.e. in γ) as it moves into the stress field of the dislocation.⁽⁹⁾ This effect is expected to lower the apparent m-value to 1/2, as observed in Wintenberger's experiments⁽¹⁰⁾ on quenched and deformed aluminum. (The difference between the present results and those in aluminum may be related to the fact that in Ag–Zn the dislocations are extended while in Al they are not.)

It should be emphasized that the mere fact that vacancies anneal out faster after deformation does not mean that they were going to dislocations in the undeformed sample, as some authors have supposed. The present work shows that deformation produces a change in the kinetics of vacancy annealing, indicating that vacancies go to dislocations only in the deformed samples.

Acknowledgments

This work was carried out at Yale University where it was supported by the Office of Ordance Research. The authors are indebted to Dr. B. S. Berry for helpful discussions of this problem.

A. S. Nowick

I.B.M. Research Centre Yorktown Heights, N.Y.

A. E. Roswell

R.C.A. Semiconductor and Materials Division Summerville, N.J.

References

- A. S. Nowick and R. J. Sladek, Acta Met. 1, 131 (1953).
 A. E. Roswell and A. S. Nowick, J. Metals, N.Y. 5, 1259 (1953).
- 3. C. ZENER, J. Appl. Phys. 20, 950 (1949).
- C. Wert, J. Appl. Phys. 20, 943 (1949).
 S. Harper, Phys. Rev. 83, 709 (1951).
 A. H. Cottrell and B. A. Bilby, Proc. Phys. Soc. A62,
- 49 (1949).
 P. B. Hirsch, J. Silcox, R. E. Smallman and W. H. Westmacott, *Phil. Mag.* 3, 897 (1958).
- F. S. Ham, Bull. Amer. Phys. Soc. Ser. II 3, 254 (1958).
 J. D. ESHELBY, Phil. Trans. Roy. Soc. A244, 87 (1951).
 M. WINTENBERGER, C.R. Acad. Sci. Paris 244, 2800 (1957).
 - * Received 19 December, 1958.

Fractional nucleation in the ageing of an aluminium-4.25 wt.% copper alloy*

The isothermal ageing of quenched aluminium—copper alloys generally involves an incubation period whose duration depends on the composition of the supersaturated solid solution and the temperature of ageing. Hardy⁽¹⁾ showed that for a given alloy within the compositional range 2 to 4.5 wt.% copper the relationship between incubation values (as determined by hardness measurements) and temperature may be represented by a group of interpenetrating *C*-curves.

These curves correspond to the initial formation of various transformation products e.g. G.P. [1] zones, θ' .

In the present investigation, step-quenching experiments were made to determine the effects of fractional nucleation, during incubation, on the ageing of an aluminium-copper alloy. The concept of fractional nucleation is that proposed by Scheil⁽²⁾ in relation to the transformation of austenite under non-isothermal conditions. It involves the expressing of the time for which a specimen is treated within the incubation period at a given temperature, as a fraction of the incubation period at that temperature, and also the correlation of the sum of the fractions at various temperatures with the time at which transformation begins during continuous cooling.

An alloy containing 4.25 wt.% copper was used: this alloy had previously been prepared and studied by Chitty⁽³⁾ in an investigation of ageing characteristics. Specimens quenched from 525°C were aged at temperatures of 100, 130 and 160°C for times of up to about 8 hr, and hardness/ageing-time curves were determined. (The experimental details were essentially the same as those described by Chitty). Within this temperature range the decomposition of the supersaturated solution commences with the formation of G.P. [1] zones, this giving rise to an increase in hardness. (1) A typical ageing curve is given in Fig. 1. The incubation periods at the three ageing temperatures were taken as the times when a definite and continuous tendency towards higher hardness was shown. The investigation of fractional nucleation effects involved the following two series of stepquenching experiments:

VOI

191

(1) Normal quenching

Specimens, which had been solution-treated and quenched were aged for approximately 50 per cent of the incubation period in an oil bath maintained at either 160 or 130°C, and were transferred to another oil bath held at either 130 or 100°C respectively, where ageing was allowed to proceed beyond the completion of incubation. The time required to complete incubation at the lower treatment–temperature was expressed as a fraction of the normal incubation period for full isothermal ageing at this temperature.

(2) Inverse quenching

After treatment for 50 per cent of the incubation period at either 100 or 130°C, ageing was continued at either 130 or 160°C respectively, and the fractional time for the completion of incubation at the upper temperature was determined.

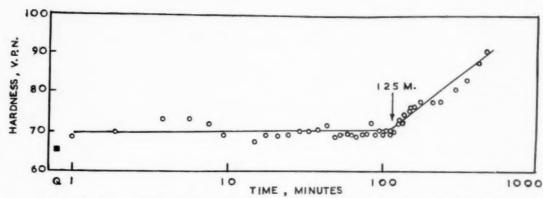


Fig. 1. Aluminium-4.25 wt% copper alloy. Hardness/ageing-time curve for full isothermal ageing at 160°C.

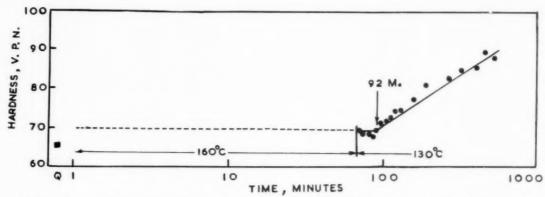


Fig.~2.~Aluminium-4.25~wt%~copper~alloy.~Hardness/ageing-time~curve~for~normal~step-quenching~from~160-130°C.

In both series of experiments the times of transfer from one ageing bath to another were of the order of 5 sec. A typical ageing curve for a step-quenching experiment is shown in Fig. 2.

In Tables 1 and 2, the incubation times for all the experiments are stated with an estimated maximum error of ± 10 min. The sums of the fractions for the various pairs of step-quenching experiments are shown in Table 2, the maximum error being estimated as ± 25 per cent of the stated values.

Despite the large range of error it is considered that there is a significant trend in the results, in that the sums of the fractions are lower for the normal step-quenching than for the inverse treatments. It is of interest to consider this in relation to the Scheil theory of fractional nucleation, and to the experimental results obtained by Moore⁽⁴⁾ for the transformation of austenite in an alloy steel. The Scheil theory proposes that if the continuous cooling of austenite is considered in terms of a series of small temperature ranges, and the time taken to cool through each of these ranges is expressed as a fraction of the incubation period at the mean temperature of the range, then transformation

should begin when the sum of the fractions for successive temperature ranges becomes unity. Moore found that for continuous cooling conditions there was a good correlation between the experimentally observed times for the beginning of transformation and those predicted by the theory. However, in step-quenching experiments the correlation was not

Table 1. Full isothermal ageing

Temperature (°C)	100	130	160
Incubation time (min)	145	70	125

Table 2. Step-quenching

Treatment	Normal		Inverse	
temperatures (°C)	130-100	160-130	100-130	130-160
Total incubation time (min)	85	92	125	127
Sum of fractions	0.85	0.95	1.3	1.25

good. In normal step-quenching experiments, where the nucleating phase was the same at both temperatures the sums of the fractions were less than unity. The results of the present work (see Table 2) indicate the same trend, although in view of the possible range of error this is not established satisfactorily. Thus it appeared that a given fraction of the incubation period spent at the upper treatment temperature was equivalent to a greater fraction of the incubation period at a lower temperature. Moore suggested that since the critical nucleus size decreases with temperature, embryos formed during fractional nucleation at the upper temperature would correspond more nearly to the critical size characteristic of the lower temperature. The same explanation may be applicable to the results of the ageing experiments. In the inverse step-quenching experiments made in the present work the sums of the fractions show a definite tendency to be greater than unity. This may be tentatively explained on the assumption that embryos formed at the lower treatment temperature would be smaller than those formed in the same fractional time at the upper temperature.

> V. B. GHATE D. R. F. WEST

Metallurgy Department Imperial College of Science and Technology London, S.W.7

References

- H. K. Hardy, J. Inst. Met. 79, 321 (1951); Ibid. 82, 236 (1953-54).
- 2. E. Scheil, Arch. Eisenhüttenw. 8, 565 (1934-35).
- A. CHITTY, J. Inst. Met. 86, 65 (1957-58).
 P. T. MOORE, J. Iron St. Inst. 177, 305 (1954).
 - * Received December 29, 1958.

Dislocation-free precipitates*

Lath-like precipitates of Mo₂C have been seen in the electron microscope which are transparent and appear to be free from dislocations. Examples are shown in Fig. 1 of precipitates extracted from a Cr–Mo steel by the extraction-replica technique. The dark markings in these precipitates move when the specimen is tilted and so are interference fringes. No fixed markings which could be dislocations have been seen.

In addition smoothly curved precipitates are also seen, as in Fig. 2, which resemble bent whiskers in appearance though not in size. If they are bent elastically the stresses in them are very large. At the centre of Fig. 2 can be seen the most sharply bent precipitate so far observed; the surface stress in this particle would be one-twentieth of the Young's



Fig. 1. Precipitates extracted from a Cr–Mo steel. Extraction replica. $\times 100,000$.

modulus. We believe these precipitates were bent elastically during the extraction process and are trapped in position by other precipitates and the replica. This seems more likely than that they have

19



Fig. 2. Sharply bent precipitate indicating a surface stress one-twentieth of the Young's modulus. Extraction replica. $\times 25.000$.

been bent plastically or grew bent, since it seems improbable that this amount of plastic bending would occur in Mo₂C or that it would always result in such uniform curvatures as in Fig. 2; moreover experience with optical metallography indicates that when rods or platelets occur none is bent in situ. An expected corollary was that apparently cracked precipitates were seen; they were bent sharply through large angles, presumably because the fracture limit had been exceeded.

The two observations together make it seem a fair conclusion that these small precipitates are dislocation-free, and therefore strong and good barriers to slip in the matrix.

These observations were made incidentally during a study of the connection between precipitation in an

1959

alloy steel and its creep strength. Details of composition, technique etc. are given in the report of that ${\rm work.}^{(1)}$

Acknowledgment

This work was carried out as part of the General Research Programme of the National Physical Laboratory and is published by permission of the Director of the Laboratory.

D. McLean

National Physical Laboratory

K. F. HALE

Teddington

Middlesex, England

Reference

- K. F. Hale, Proc. Fourth Int. Conf. on Electron Microscopy, Berlin. To be published.
 - * Received January 9, 1959.

ERRATUM

J. W. Cahn: The kinetics of cellular segregation reactions. Acta Met. 7, 18 (1959).

Equation 10 on p. 22 should read:

$$\beta = -\frac{kM\sigma^2V^2}{D_B\,\delta\Delta F_0} = \frac{\alpha^3(P')^2}{P+2\alpha P'}$$

The formula on the second line of the second column of p. 22 should read:

$$R = -2\alpha P'$$

Fig. 2 caption should read:

$$\beta = -kMV^2\sigma^2/D_B\,\delta\Delta F_0$$

19!

$$\alpha = kGS^2/D_R\delta$$

ZUM MAGNETISCHEN VERHALTEN VON ALUMINIUM UND ALUMINIUM-MISCHKRISTALLEN*

VON R. LINGELBACH† und E. VOGT‡

Suszeptibilitätsmessungen an Aluminium zwischen 67° und 293°K ergaben das für den Spinparamagnetismus von Bandelektronen zu erwartende Verhalten. Aus dem für T=0 extrapolierten χ folgt ein Wert für die Zustandsdichte $N(E_0)$ an der Fermi-Grenze, der überraschend gut mit einer theoretischen Berechnung von Matyas und mit dem aus der gemessenen Elektronenwärme abzuleitenden Wert übereinstimmt. Dagegen nimmt χ mit steigender Temperatur wesentlich steiler ab, als nach der N(E)-Funktion von Matyas zu erwarten ist. Die von Auer gemessenen durch Fremdmetallzusatz bewirkten Änderungen von χ werden zur Diskussion herangezogen. Verdünnt im Al-Gitter gelöstes Mangan bewirkt einen starken Zusatzparamagnetismus, der auffälligerweise nicht die sonst bei kleinen Mn-Konzentrationen meist beobachtete Temperaturabhängigkeit zeigt.

ON THE MAGNETIC BEHAVIOUR OF ALUMINIUM AND ALUMINIUM SOLID SOLUTIONS

Measurements of susceptibility of aluminium between 67°K and 293°K showed a behaviour which is to be expected for the paramagnetism due to the spins of the conduction electrons. Extrapolation of χ to T=0 yields a value for the density of states $N(E_0)$ at the Fermi surface which agrees surprisingly well with the theoretical calculations of Matyas and with the value that can be derived from the measured specific heat of the electrons. On the other hand χ decreases with increasing temperature more rapidly than one would expect according to the N(E) function of Matyas. The changes of χ by addition of other metals as measured by Auer are employed in the discussion. Manganese in dilute solid solution in Al gives rise to a strong additional paramagnetism which does not show the temperature dependence that is generally observed at low Mn concentrations.

SUR LE COMPORTEMENT MAGNETIQUE DE L'ALUMINIUM

Des mesures de susceptibilité de l'aluminium entre 67° et 293° K donnent valeurs prévues pour le paramagnétisme du spin des électrons des bandes. L'extrapolation de la fonction χ pour T=0 donne une valeur pour la fonction $N(E_0)$ qui concorde d'une façon étonnante avec les calculs théoriques de Matyas et avec la valeur à déduire de l'énergie mesurée des électrons.

Par contre, quand la température croît, χ décroît plus fortement que ne le prévoit la fonction N(E) de Matyas. Pour la discussion, l'auteur se base sur les changements de la fonction χ mesurée par Auer grâce à l'addition de métaux étrangers.

La solution diluée de Manganèse dans le réseau de l'aluminium produit un fort paramagnétisme additionnel, qui ne montre pas la dependance de la température observée généralement pour de faibles concentrations en manganèse.

EINLEITUNG

In einer früheren Arbeit⁽¹⁾ war das magnetische Verhalten der Al-reichen Seite des Systems Al–Mn behandelt worden, wobei das Hauptgewicht auf den Al-reichsten intermediären Phasen ${\rm Al}_6{\rm Mn}$ und ${\rm Al}_4{\rm Mn}$ lag. In Ergänzung zu dieser Arbeit werden im folgenden die damals an Al und den Al-Mischkristallen mit Mn gefundenen Ergebnisse ausführlicher mitgeteilt und zusammen mit Messungen von Auer^(2,3) im Rahmen der Metallelektronentheorie diskutiert.

Für die magnetischen Messungen wurde die Gouysche Zylinderwägungsmethode verwandt. Durch Messung der Feldstärkenabhängigkeit wurde der verhältnismässig geringe Einfluss ferromagnetischer Verunreinigungen ausgeschaltet. Die Temperaturabhängigkeit der Suszeptibilität von Al (Fig. 1) sowie

von den Legierungen mit 0,306 und 0.405 At% Mn (Fig. 4a) wurde genauer verfolgt, indem während langsamer Erwärmung fortlaufend Messungen (insgesamt etwa 30) abwechselnd bei zwei Feldstärken durchgeführt wurden; aus den interpolierten $\chi(T)$ -Kurven für die beiden Feldstärken konnten dann die korrigierten Kurven der genannten Figuren ermittelt werden. Die Legierungen mit 0,674 und 1,64 At% Mn wurden bei 67°, 82° und 293°K mit fünf verschiedenen Feldstärken gemessen.

ALUMINIUM

In Fig. 1 ist die gemessene Temperaturabhängigkeit der Atomsuszeptibilität des reinen Aluminium wiedergegeben, zusammen mit sechs Messpunkten von Auer⁽³⁾, von denen die beiden in den von uns untersuchten Temperaturbereich fallenden recht gut mit unseren Messungen übereinstimmen. Aus der genaueren Verfolgung der Temperaturabhängigkeit geht aber hervor, dass die $\chi(T)$ -Kurve unterhalb von ca.

1959

^{*} Received August 18, 1958.

[†] Jetzt Buderus'sche Eisenwerke Wetzlar.

[‡] Physikalisches Institut der Universität Marburg.

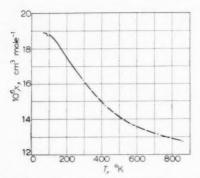


Fig. 1. Temperaturabhängigkeit der Suszeptibilität von Aluminium. × Auer⁽³⁾; —diese Arbeit.

 200°K zur T-Achse konkav gekrümmt ist und offenbar horizontal einem Grenzwert $\chi(0)$ zustrebt. Das ist das für Metallelektronen nach Pauli zu erwartende Verhalten. Für den Spinparamagnetismus ergibt nämlich die Theorie den folgenden Ausdruck:⁽⁴⁾

$$\chi_p = 2\mu_0^2 N(E_0) \left\{ 1 - \frac{\pi^2}{6} (kT)^2 \left[\left(\frac{N'(E_0)}{N(E_0)} \right)^2 - \frac{N''(E_0)}{N(E_0)} \right] + \cdots \right\} = \chi_p(0) \left\{ 1 - \alpha T^2 + \cdots \right\} \quad (1)$$

 μ_0 : Bohrsches Magneton; k: Boltzmann-Konstante; N(E): Zustandsdichte pro Mol; E_0 : Fermigrenzenergie.

Unter Berücksichtigung des Wertes $-2.3\cdot 10^{-6}$ cm³ Mol⁻¹ für den Diamagnetismus der abgeschlossenen Schalen ergibt sich aus dem aus unseren Messungen extrapolierten $\chi(0)$ für die Valenzelektronen des Al: $\chi_p(0) = 21.3\cdot 10^{-6}$ cm³ Mol⁻¹. Dabei ist freilich der Diamagnetismus der Metallelektronen vernachlässigt.

Überraschenderweise stimmt, wie Tab. 1 zeigt, der

TABELLE 1.

Werte berechnet	$(\mathrm{eV}^{-1}\mathrm{mol}^{-1})$	$(\mathrm{eV}^{-2}\mathrm{mol}^{-1})$
aus der Suszeptibilität aus der Theorie von Matyas	$2.0 \cdot 10^{23}$ $2.4 \cdot -$	ca. 25 · 10 ²³
aus der spez. Wärme	1.9 -	***

aus diesem Wert für $\chi_{\scriptscriptstyle D}(0)$ nach (1) berechnete Wert der Zustandsdichte an der Fermi-Grenze $N(E_0)$ recht befriedigend überein sowohl mit dem aus Messungen der spezifischen Wärme⁽⁵⁾ erhaltenen Wert, als auch mit dem Wert für $N(E_0)$, der aus einer theoretischen Berechnung der Eigenwertdichteverteilung nach Matyas^(6,7) folgt. Fig. 2 zeigt die von Matyas berechnete Zustandsdichte N(E) für Aluminium.

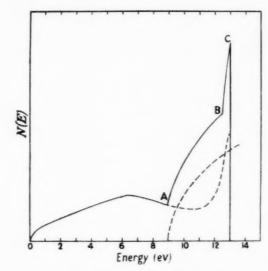


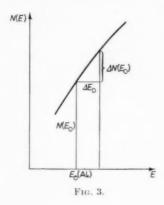
Fig. 2. Zustandsdichte im Valenzelektronenband von Al (nach Matyas).

Diese Übereinstimmung legt den Versuch nahe, auch über die Grösse $N'(E_0) = (dN/dE)_{E_0}$ voneinander unabhängige Aussagen zu machen und diese miteinander zu vergleichen. Die folgenden Möglichkeiten stehen hierfür zur Verfügung:

 Aus der in Fig. 2 wiedergegebenen Zustandsdichtefunktion von Matyas folgt der in der letzten Spalte von Tab. 1 angegebene Wert. 19

(2) Aus der Temperaturabhängigkeit der Suszeptibilität von Al bei tiefen Temperaturen lässt sich der Koeffizient a in (1) bestimmen, und zwar ergibt sich, wenn man von den bei 100° und 200°K erhaltenen y-Werten ausgeht und den Diamagnetismus der abgeschlossenen Schalen wie oben berücksichtigt: $\alpha = 1.94 \cdot 10^{-6} \text{ grad}^{-2}$. Aus α lässt sich $N'(E_0)$ nach (1) berechnen, wenn man das 2. Glied der Klammer $N''(E_0)/N(E_0)$ vernachlässigen kann. Der so berechnete Wert für $N'(E_0)$ ist gleichfalls in Tab. 1 angegeben. Er ist ein Höchstwert, wenn die Krümmung der Funktion N(E) an der Stelle E_0 negativ ist. Für die Funktion von Matyas (2) trifft das zu. Da andererseits die Kurve von Matyas an der Fermi-Grenze nur schwach gekrümmt ist, würde die Berücksichtigung von $N''(E_0)$ in (1) den in Tab. 1 angegebenen ersten Wert für $N'(E_0)$ nicht wesentlich erniedrigen. Für die Neigung der Zustandsdichtefunktion $N'(E_0)$ würde man also aus der Temperaturabhängigkeit von Xn einen um eine Zehnerpotenz grösseren Wert folgern als die Matyas-Funktion besitzt.

Bei höheren Temperaturen ändert nach Auers Messungen (Fig. 1) die Krümmung der $\chi(T)$ -Kurve ihr Vorzeichen. Das wäre in Sommerfelds Ausdruck



(1) nur durch Einführung von Gliedern höherer Potenzen von T zu erfassen.

(3) Ein dritter Weg zur Berechnung von $N'(E_0)$ ergibt sich aus der Suszeptibilität von Mischkristallen des Al mit Metallen anderer Wertigkeit.

EINFLUSS GELÖSTER FREMDMETALLE MIT ABGESCHLOSSENEM ATOMRUMPF

Werden in das Al-Gitter Fremdatome anderer Wertigkeit eingebaut, die mit dem Grundmetall gemeinsame Energiebänder der Valenzelektronen bilden, so ist möglicherweise für die Änderung des Metallelektronenparamagnetismus $\Delta\chi_p$ neben einem nur schwer abschätzbaren Einfluss der Gitterkonstantenänderung in erster Linie die Verschiebung ΔE_0 der Fermi-Grenzenergie infolge der geänderten mittleren Valenzelektronenzahl als verantwortlich anzusehen. Legt man dieses Modell zugrunde, so erhält man für die Änderung der Valenzelektronenzahl pro Mol (vgl. Fig. 3):

$$(z-3)N_L c/100 = 2N(E_0)\Delta E_0 + N'(E_0)(\Delta E_0)^2$$
 (2)

Vernachlässigt man für kleine Konzentrationen (e) des Zusatzmetalls das in ΔE_0 quadratische Glied, so wird die durch den Zusatz bedingte Änderung des Elektronenparamagnetismus in tiefer Temperatur nach (1):

$$\Delta \chi_p = 2\mu_0^2 N'(E_0) \Delta E_0 = \frac{c}{100} \frac{(z-3)N_L \mu_0^2}{N(E_0)} N'(E_0) \ (3)$$

Aus dieser Gleichung lässt sich $N'(E_0)$ berechnen, wenn man aus der gemessenen Suszeptibilitätsänderung unter Berücksichtigung der Differenz des Ionendiamagnetismus zwischen Zusatzelement und Aluminium Δ_{Z_n} berechnet.

Die Änderung der Suszeptibilität des Aluminiums durch verschiedene Zusatzmetalle hat Auer⁽²⁾ untersucht. Wendet man auf diese allerdings nur bei Zimmertemperatur durchgeführten Messungen unter Vernachlässigung der Suszeptibilitätsdifferenz zwischen 0°K und 300°K die geschilderte sicherlich grob vereinfachte Überlegung an, so erhält man die in Tab. 2 zusammengestellten Ergebnisse. (Für das

TABELLE 2.

Zusatz- element	$(At_{>0}^{0/})$	$\chi \cdot 10^{-6}$	$-\frac{\Delta\chi_p \cdot 10^{6*}}{c/100}$	$N'(E_0) \cdot 10^{-23}$
Li	0.97	14,46	304	9,4
Cu	1.0	15,94	136	4,2
Ag	0,51	16,43	169	5,2
Mg	1,0	15,79	159	9,8
Mg	2,0	14,40	147	9,4
Zn	1,0	15,84	148	9,2
Ga	1.0	16,71	63	_
In	0,5	17.17	38	-
Ge	0,25	17,25	56	

* Bezogen auf $\chi_{Al}=17{,}40\cdot10^{-6}~\rm{cm^3~mol^{-1}}.$

in dieser Untersuchung verwandte Aluminium fand Auer etwas stärkeren Paramagnetismus als in seiner späteren Arbeit.⁽³⁾)

Wenn der Einfluss der gelösten Fremdatome auf die Suszeptibilität des Al allein in einer Verschiebung der Fermi-Grenze bestände, dann müssten die dreiwertigen Metalle Ga und In ohne Wirkung sein, und das vierwertige Ge müsste durch Verschiebung der Fermi-Grenze nach rechts (Fig. 2) ein positives $\Delta \chi_p$ bewirken. Auers Befunde zeigen also, dass noch andere Wirkungen an der Erzeugung der Suszeptibilitätsänderung durch Fremdmetalle beteiligt sind.

Immerhin ist die atomare Suszeptibilitätserniedrigung (Spalte 4 in Tab. 2) für die ein- und zweiwertigen Elemente viel grösser als für die drei- und vierwertigen. Die nach dem vereinfachten Modell berechneten Werte für $N'(E_0)$ liegen nun zwischen den nach Methode 1 und 2 im vorigen Abschnitt berechneten Werten (Tab. 1). Auch ergibt sich für Li bemerkenswerte Übereinstimmung mit Mg und Zn, während allerdings Cu und Ag zu einem erheblich kleineren $N'(E_0)$ führen. Diese Ergebnisse der Auswertung scheinen uns doch der Mitteilung wert und können vielleicht einen Ansatzpunkt für verfeinerte elektronentheoretische Betrachtungen bilden.

ALUMINIUM-MISCHKRISTALLE MIT MANGAN

Wie schon Auer $^{(2)}$ fand, wird durch Aufnahme von Mn in das Gitter der Paramagnetismus des Al stark erhöht. Auer untersuchte drei Legierungen bis 0,5 At $^{\circ}_{0}$ bei Raumtemperatur. Unsere Messungen reichten bis 1,64 At $^{\circ}_{0}$ und erstreckten sich auf den Temperaturbereich 67° bis 293°K.

Die Herstellung und die Analyse der Proben

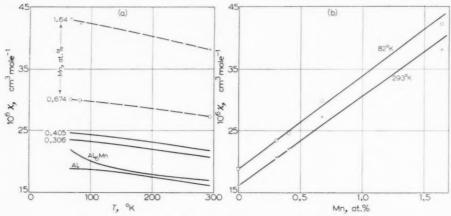


Fig. 4. Suszeptibilität der Aluminium-Mischkristalle mit Mangan.

verdanken wir der Isabellen-Hütte, Heusler K. G Dillenburg.* Nach Hofmann(8) kann durch grosse Abkühlungsgeschwindigkeit die Löslichkeitsgrenze, die nach Butchers u. Hume-Rothery(9) z.B. bei 658°C 0.672 At% Mn beträgt, erheblich überschritten werden. Die von uns untersuchte stark übersättigte Mischkristallprobe mit 1,64 At% Mn wurde durch Ausgiessen der Schmelze in eine Kupferkokille erhalten. Der Mischkristallcharakter auch dieser Probe ergab sich aus Messungen des spezifischen Widerstandes unserer Probenreihe, die in befriedigender Übereinstimmung mit den Befunden von Dix et al.(10) und von Fahrenhorst u. Hofmann(11) standen. Die Proben mit geringerem Mn-Gehalt wurden vor der Messung fünf Stunden im Vakuum bei 650°C geglüht und anschliessend abgeschreckt.

Die Atomsuszeptibilität der Legierungen wächst etwa proportional zum Mn-Gehalt und erreicht schon bei 1 At% den doppelten Betrag des reinen Al (Fig. 4b). Dagegen wird die Temperaturabhängigkeit von χ durch den Mn-Zusatz nicht geändert (Fig. 4a). Mangan verhält sich also magnetisch im Al-Gitter völlig anders als im Gitter der einwertigen Metalle Cu, Ag und Au, in die es unter Befolgung des Curie-Weiss-Gesetzes mit einem effektiven Moment von 5 bis 6 Magnetonen eintritt. (12) Die Al-Mn-Mischkristalle ähneln vielmehr in ihrem magnetischen Verhalten den Cu-Ni-Legierungen, in denen das Ni einen temperaturunabhängigen Paramagnetismus bewirkt. (12)

Es ist also formal möglich, auch auf die Al-Mn-Legierungen die Betrachtungsweise des vorigen Abschnitts anzuwenden. Nimmt man an, dass die Mn-Atome sämtliche d- und s-Elektronen an das gemeinsame Valenzelektronenband abgeben, so kann man nach (3) auch aus dem $\Delta\chi_p$ der Mn-Legierungen auf die Neigung der Zustandsdichtefunktion des Aluminiums an der Fermi-Grenze $N'(E_0)$ schliessen. Man erhält so etwa den Wert $25\cdot 10^{-23}\,\mathrm{eV^{-2}}\,\mathrm{mol^{-1}},$ der mit dem aus der Temperaturabhängigkeit der Suszeptibilität des reinen Al abgeleiteten Wert (Methode 2) übereinstimmt. Jedoch soll dieser Übereinstimmung keine besondere Bedeutung zugemessen werden, denn im Fall des Mn ist das der Berechnung zugrunde gelegte Modell besonders unbefriedigend.

19

Zur Deutung des sehr schwachen Paramagnetismus der Al-reichsten intermediären Phase Al₆Mn wurde in Verfolgung der Vorstellungen von Raynor⁽¹³⁾ sogar die entgegengesetzte Annahme gemacht, dass die d-Schalen der Mn-Atome in dieser Phase durch Valenzelektronen der Al-Atome weitgehend aufgefüllt werden. (1) In Ergänzung zu der erwähnten Mitteilung⁽¹⁾ sei hier noch auf die Temperaturabhängigkeit der Suszeptibilität der Phase AleMn hingewiesen. Wie Fig. 4a zeigt, ist sie durchaus anders als die des reinen Al und die der Al-Mn-Mischkristalle. Sie verläuft mit entgegengesetzter Krümmung. Das bedeutet möglicherweise, dass in der Phase AleMn ein kleiner Bruchteil der Mn-Atome lokalisierte d-Lücken-Momente mit Curie-Weiss-schem Paramagnetismus besitzt.

Für den temperaturunabhängigen Paramagnetismus des im Al-Gitter gelösten Mn im Gegensatz zu dem Verhalten des Mn in Cu, Ag und Au hat Friedel⁽¹⁴⁾ eine Deutung gegeben, die sich auch auf das elektrische Verhalten der Legierungen mit Übergangselementen erstreckt. Hingewiesen sei auch noch auf einen Deutungsvorschlag für ähnliche Befunde an

 $[\]mbox{*}$ Hierfür sei Herrn Dr. O. Heusler herzlicher Dank ausegsprochen.

Mischkristallen des Chrom mit Co und Ni, auf Grund lokaler Magnetisierungen der Metallelektronen in der Umgebung gelöster Fremdatome mit magnetischem Moment. (15)

LITERATUR

- E. Vogt, Appl. Sci. Res. B 4, 34 (1954).
 H. Auer, Z. Phys. 92, 283 (1934).
 H. Auer, Z. Metallk. 28, 164 (1936).
 Vgl. etwa Sommerfeld-Bethe, Handb. d. Physik Bd. 24, 2 S. 476. Springer, Berlin (1933).
 J. Kok u. W. H. Keesom, Physica 4, 835 (1937).
 Z. Matyas, Phil. Mag. 39, 429 (1948).

- Vgl. G. V. RAYNOR, Rep. Progr. Phys. 15, 173 (1952).
 W. HOFMANN, Aluminium, Berl. 20, 865 (1938).
 E. BUTCHERS u. W. HUME-ROTHERY, J. Inst. Met. 71, 87 (1945).
- 10. E. H. DIX, W. L. FINK u. L. A. WILLEY, Trans. Amer. Inst. Min. (Metall.) Engrs. 104, 335 (1933).
- 11. E. Fahrenhorst u. W. Hofmann, Metallwirtschaft 19, 891 (1940).
- 12. Vgl. etwa E. Vogt, Z. Elektrochem. 45, 597 (1939); u. Physikalische Eigenschaften der Metalle I. Akad.
- Verl. Ges., Leipzig (1958).

 13. G. V. RAYNOR, Progress in Metal Physics Vol. 1, p. 1.
- Butterworths, London (1949). 14. J. FRIEDEL, Canad. J. Phys. **34**, 1190 (1956).
- 15. R. LINGELBACH, Z. Phys. Chem. NF 14, 1 (1958).

EFFECTS OF TORSION ON THE TENSILE STRESS-STRAIN CURVE OF ALUMINIUM*

D. B. HOLT+

The work hardening of aluminium single crystals was investigated by alternate tensile and torsional deformation. The relative increase of tensile flow stress due to twisting was systematically investigated in relation to prior extension, crystal orientation and amount of twist. Crystallographic analysis of slip lines was carried out. This showed that several modes of torsional deformation occurred in different orientation regions. Some of these modes correspond to proposed dislocation mechanisms. Analysis of the azimuthal distributions of tensile slip lines on crystals which have been twisted and extended showed that dislocation barriers were formed in agreement with the Lomer-Cottrell theory of sessile dislocations. The relative increase of tensile flow stress and the change of hardening rate due to twisting are discussed in terms of dislocation theory.

EFFETS DE LA TORSION SUR LA COURBE TENSION-DEFORMATION DE L'ALUMINIUM

Le durcissement par déformation de monocristaux d'aluminium a été étudié pour des tractions et des torsions alternées. L'augmentation relative de la tension de glissement due à la torsion a été systématiquement suivie en relation avec l'extension préalable, l'orientation du cristal et le degré de torsion. Une analyse cristallographique des lignes de glissement a également été réalisée. Cette étude a montré que plusieurs modes de torsion apparaissent dans des régions d'orientations différentes. Certains de ces modes correspondent à des mécanismes connus basés sue les dislocations. L'examen des distributions azimuthales des lignes de glissement sur des cristaux déformés par torsion et par traction a montré que les barrières de dislocations sont formées en accord avec la théorie des dislocations sessiles de Lomer-Cottrell. L'augmentation relative de la tension de glissement et la variation de la vitesse de durcissement dues à la torsion sont discutées dans le cadre de la théorie des dislocations.

DIE WIRKUNG VON TORSION AUF DIE VERFESTIGUNGSKURVE IM ZUGVERSUCH BEI ALUMINIUM

Die Verfestigung von Aluminium-Einkristallen wurde durch abwechselnde Zug- und Torsionsverformung untersucht. Die relative Zunahme der Fließspannung im Zugversuch infolge einer Torsion wurde systematisch in Abhängigkeit von der Vorverformung, der Kristallorientierung und dem Torsionsbetrag untersucht. Die Gleitlinien wurden kristallographisch analysiert. Dies zeigte, dass in verschiedenen Orientierungsbereichen verschiedene Torsionsverformungsarten auftreten. Einige dieser Arten entsprechen vorgeschlagenen Versetzungsmechanismen. Eine Analyse der azimutalen Verteilung von Gleitlinien des Zugversuchs auf Kristallen, die tordiert und gezogen worden waren, zeigte, dass sich Versetzungshindernisse in Übereinstimmung mit der Lomer-Cottrellschen Theorie der unbeweglichen Versetzungen gebildet hatten. Die relative Zunahme der Fließspannung im Zugversuch und die Änderung des Verfestigungsanstiegs infolge von Torsion werden mit Hilfe der Versetzungstheorie diskutiert.

1. INTRODUCTION

Four dislocation mechanisms have been proposed which can contribute to work hardening. (1) Lomer⁽¹⁾ and Cottrell⁽²⁾ suggested that parallel dislocations on intersecting slip planes attracted and formed sessile dislocation configurations which acted as barriers to further dislocation movement. The condition that this should happen is that the Burgers vectors of the dislocations should add together in the form

$$\begin{array}{l} \frac{1}{2}\mathbf{a}[10\overline{1}] + \frac{1}{2}\mathbf{a}[011] \rightarrow \frac{1}{2}\mathbf{a}[110] \rightarrow \frac{1}{6}\mathbf{a}[11\overline{2}] \\ + \frac{1}{6}\mathbf{a}[112] + \frac{1}{6}\mathbf{a}[110] \end{array}$$

to lower the total energy. The Burgers vectors of the interacting dislocations are at 60° to the line of

intersection of the two slip planes and thus at 60° to the lines of the dislocations. The resulting Burgers vector does not lie in either slip plane and the resulting dislocation splits up into 3 dislocations bounding 2 noncoplanar stacking faults. (2) Dislocations accumulating in the lattice(3) or dislocation pile-ups at barriers (4) set up internal stresses opposing the motion of subsequent dislocations. (3) A geometrical consequence of the cutting of one dislocation through another on an intersecting plane is the creation of jogs in both. (5) This requires a certain amount of energy. The effect is a resistance to the motion of a dislocation through a lattice containing intersecting dislocations. This "forest" mechanism of hardening was first discussed by Cottrell⁽⁶⁾. (4) By a number of dislocation processes, especially the motion of jogged screw dislocations, vacancies and interstitialcies are created.(7) Again energy is required

^{*} Received August 27, 1958.

[†] Department of Physics, Witwatersrand University, Johannesburg, South Africa; formerly of Department of Physical Metallurgy, University of Birmingham, England.

ACTA METALLURGICA, VOL. 7, JULY 1959

and, at least below a certain temperature, (8) a resistance results. At temperatures at which the rate of self-diffusion is low these point defects constitute debris which impedes dislocation motion. (4,7)* At higher temperatures point defects accelerate diffusion and consequently recovery. (4) Under quenching conditions vacancies may migrate to dislocations and lock them. (9)

All the above phenomena will occur under the appropriate conditions. However, the relative importance of the different processes will vary widely with prestrain, crystal structure, temperature and purity. Considerable progress has been made in studying these problems by two experimental approaches.

The first approach is to study the effect of temperature on the flow stress. Since the dislocation hardening mechanisms have different temperature dependences, this allows the hardening due to particular mechanisms to be determined. Adams and Cottrell(10) measured the reversible changes of flow stress with temperature in copper single crystals. They found the flow stress to be unaffected by rises of temperature from 90°K to 180°K, to fall rapidly from 180°K to 250°K and to be virtually unaffected from 250°K to 473°K. This is interpreted as evidence that between 180°K and 250°K vacancy generation ceases to contribute to the hardness. However, Makin⁽¹¹⁾ found the drop in flow stress to be considerably smaller than reported by Adams and Cottrell. Large yield drops accompanied by Luders bands have been reported in aluminium crystals strained at higher temperatures after large extensions at lower temperatures. (12,13) This work softening was thought to be due to the unlocking of sessiles at the heads of pile-ups by the combination of stress and higher temperature. Later slip line studies indicated that work softening occurred through cross slip at higher temperatures caused by mutual annihilation of piled-up screw dislocations of opposite sign. (14)

1959

The second approach is to study the hardening effects of dislocation distributions introduced by bending or twisting. Washburn⁽¹⁵⁾ employed both techniques using zinc crystals. He found twisting to increase the yield stress for subsequent deformation. The increase of flow stress rose with increasing angle of twist. Bending was found to produce little effect. When bending was followed by annealing at 400°C to produce a sharp tilt boundary, however, an increase of yield stress for subsequent deformation was produced which increased with the boundary angle.

Paxton and Cottrell⁽¹⁶⁾ found twisting to have a number of effects on the tensile stress-strain curves of aluminium single crystals. Twists of a few tenths of a degree were given after about one tenth of a per cent elongation. It was found that sharp increases of flow stress were produced. The slopes of the curves were either unchanged or, in a few cases, increased.

Seeger and his co-workers (17,18) made a systematic study of work hardening in copper by combined tensile and torsional experiments on tubular single crystals. This work was combined with studies of the orientation and temperature dependence of flow stress and observation of slip line lengths as a function of strain. Their conclusion was that the hardening in copper was mainly due to the Mott pile-up mechanism. Basinski(19) studied the temperature and strain rate dependence of flow stress in copper, aluminium, silver and iron and concluded that in the face-centred cubic metals the main obstacle to flow is provided by the forest of intersecting dislocations and that in iron the results were consistent with the assumption that the long range forces are provided by the dislocation forest but that the short range forces primarily result from the Peierls-Nabarro force. The present paper reports the results of a systematic extension of the work of Paxton and Cottrell to considerably greater twists and prior deformations.

2. EXPERIMENTAL METHOD

Single crystals of 99,996 per cent aluminium supplied by the Aluminum Company of America were grown by both the strain anneal and soft mould(20) methods. No difference in mechanical properties was found between specimens prepared by the two techniques. Strain-anneal crystals were designated by a number, soft mould crystals by a number plus the letter "m". When more than one specimen was cut from a single crystal, individual specimens were indicated by superscripts, e.g. 19m^I and 19m^{II}. Orientations were determined by the back-reflection Laue method. (21) Two methods of mounting in duralumin end-pieces were used: welding and grub-screws. Each resulted in a few spoilages. Gauge lengths of specimens ranged from 4.5 to 6 cm. Diameters of specimens after electropolishing were 3 to 3.5 mm.

The machine used for combined tensile and torsional testing was a modified Polanyi hard-beam machine. A steel strip was used to suspend the crystal from the stress-measuring beam. This had considerable torsional stiffness and made it unnecessary to clamp the top of the crystal before

^{*} Note added in proof: Studies of the annealing out of electrical resistivity and of hardness, however, indicate that point defects do not contribute significantly to work hardening. (45)

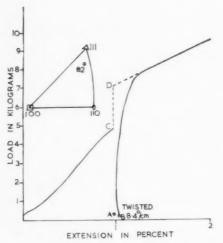


Fig. 1. Load-extension curve of specimen 82.

twisting. The use of gearing in the cross-head to rotate the lower end of the crystal enabled smooth and controlled twisting to be applied.

It was found that certain anomalous features of the experimental curves could only be eliminated by making certain that there was no torque in the strip suspension on reloading after twisting. Mirrors were attached to each end-piece of the specimen and one to the lower end of the suspension. Light beams from these mirrors were focused on a large curved screen. It was also found that twisting under load caused considerable elongation of the specimen. Therefore, the prodecure adopted was to extend the specimen by the desired amount and to unload to a few hundred grams to maintain alignment. The lower grip was then rotated to give the required plastic twist and rotated back to the initial position of the suspension.

3. RESULTS AND DISCUSSION

3.1. Preliminaries

Plastic length changes of a few hundredths of a millimetre were found to result in some crystals from twisting under even very small tensile loads. It was found that if twisting a crystal produced no length change, twisting in the opposite sense produced no change either. But if twisting produced a contraction, reverse twisting produced an extension and conversely. It seems therefore that these length changes are due to a genuine, orientation-dependent coupling of tensile and torsional deformation.

In general the reloading curve did not join uninterruptedly on to the prestrain curve and was nonlinear. Such behaviour is also observed on unloading and reloading during pure tensile or compression tests^(22,23,24) and is attributable to the anelasticity of the specimen and machine members.

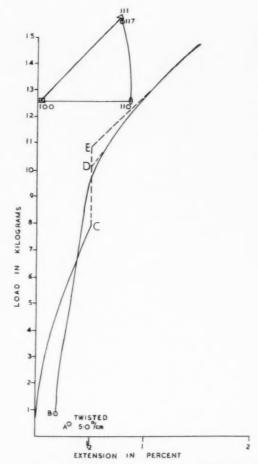


Fig. 2. Load-extension curve of specimen 117.

VOI

19

The construction adopted in order to obtain a measure of the hardening produced by a twist is shown in Fig. 1. By extrapolating the post-twist curve back a value of the post-twist flow stress at the extension reached before unloading is obtained. Note that this specimen extended on twisting from point A reached on unloading to point B reached after twisting. Fig. 2 shows a case where the post-twist curve is paraboloidal (and where the specimen experienced a contraction on twisting). In such cases tangents to the curve were extrapolated back so as to give approximate upper and lower limits to the post-twist flow stress. Experience showed that this somewhat arbitrary procedure did permit the tracing of rather clear-cut patterns in the effects of twisting.

3.2. Modes of torsional deformation

To discuss twist hardening in terms of dislocations a knowledge of the slip systems operative is necessary. Four modes of torsional deformation were found to occur.

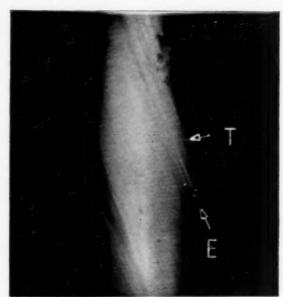


Fig. 3. Slip lines on specimen 19m^{II} at the end of the test. (Taken at one of the positions marked B in Fig. 4.) $\times 50$. E is a tensile slip line and T is a transverse torsional slip line.

The first mode occurred in specimens like 19m¹¹ (see Fig. 11) with axes near [111]. This mode produced transverse torsional slip lines, approximately perpendicular to the specimen axis as shown in Fig. 3. At six azimuths the transverse torsional slip lines faded out as in Figs. 3 and 4. These points of interruption were found to be the positions at which one of the three [110] directions in the torsional slip plane is tangential to the surface of the specimen. The word "interruption" will be used systematically to indicate an absence of slip lines of this type. The slip lines produced on extending this specimen were traces of

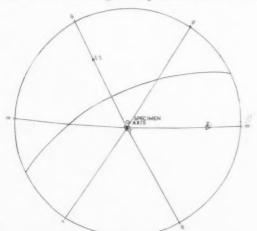


Fig. 4. Stereogram of specimen 19m^{II} after deformation. The pole marked T is that of the plane of transverse torsional slip. The positions marked B are the azimuths at which the torsional slip lines were found to be interrupted.

the plane with pole marked E_1 . A second specimen from the same crystal showed extension slip lines corresponding to double glide on the planes E_1 and E_2 of Fig. 4.

The second mode of torsional deformation occurs in specimens with axes further from [111] towards [110] like $24\mathrm{m^{IV}}$ shown in Fig. 11. In this mode slip takes place in four quadrants of the cross-section as shown in Fig. 5. Two opposite quadrants showed transverse torsional slip lines, the other two showed longitudinal torsional slip lines parallel to the axis. Figs. 6, 7 and 8 are photomicrographs taken in a quadrant of longitudinal torsional slip, at a quadrant boundary and in a quadrant of transverse torsional slip, respectively. Analysis showed the transverse torsional slip

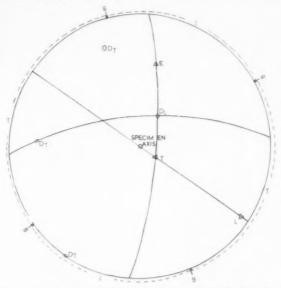


Fig. 5. Stereogram of specimen 24mW after deformation. The poles marked E, T and L are those of the planes of tensile, transverse torsional and longitudinal torsional slip, respectively. The positions marked B are the boundaries of the quadrants of torsional slip. Around the circumference of each quadrant is shown the type of torsional slip, transverse or longitudinal, appearing at those azimuths.

lines to be traces of the same plane as in specimen $19\mathrm{m}^{11}$. This plane of transverse torsional slip contains the three slip directions marked D_{T} in Fig. 5. The longitudinal slip lines were too nearly parallel to the axis to be accurately analysed but were probably the traces of the (111) plane marked L in Fig. 5. Extension slip lines were traces of the plane E of Fig. 5.

The third mode of torsional deformation occurs in specimens with axes near [110] like 9m¹¹ as shown in Fig. 11. This mode produced longitudinal torsional slip lines at all azimuths around the specimen surface. While other forms of torsional slip lines were as clear and readily seen as tensile slip lines, these longitudinal

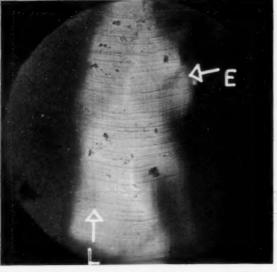
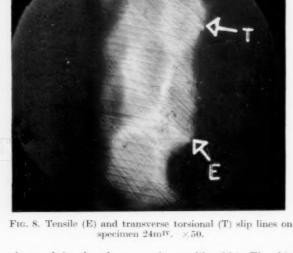


Fig. 6. Tensile (E) and longitudinal torsional (L) slip lines on specimen 24mIV. \times 50.



torsional slip lines were very faint and could best be seen by oblique illumination. They became less and less visible as the axes of the specimens approached [110]. Again accurate stereographic analysis was impossible but the longitudinal slip lines were probably the traces of the two (111) planes marked L in Fig. 9 which have as common slip direction the [110] direction near the specimen axis. Extension slip lines were traces of the plane E of Fig. 9.

The fourth mode of torsional deformation was

observed in the three specimens like 134, Fig. 10, which were grown with axes near [100] as shown in Fig. 11. Again slip lines of two planes occurred in quadrants of the surface. In this case stereographic analysis showed torsional slip in the two pairs of quadrants to have occurred on planes with poles in the circles marked N_1 and N_2 . That is, torsional slip for these orientations occurred on non-octahedral planes. The regions of the surface covered by slip lines of the systems N_1 and N_2 are such as to be

195

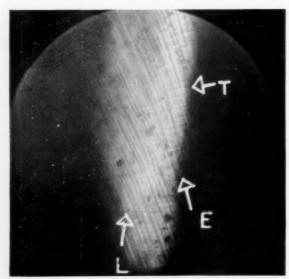


Fig. 7. Tensile (E), longitudinal torsional (L) and transverse torsional (T) slip lines at a quadrant boundary on specimen 24mIv. ×50.

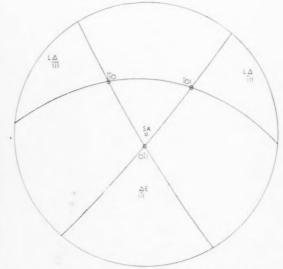


Fig. 9. Stereogram of specimen $9\mathrm{m}^{11}$ after deformation. The poles marked E and L are those of the plane of tensile slip and the probable planes of longitudinal torsional slip. respectively.

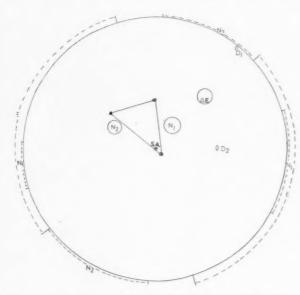


Fig. 10. Stereogram of specimen 134 after deformation. The specimen axis is perpendicular to the plane of the paper at the point marked S.A. Tensile slip lines appearing at the azimuths marked E around the circumference correspond to a plane with its pole in the circle marked E. Torsional slip lines indicated by N_1 and N_2 correspond to non-octahedral planes with poles in the circles marked.

consistent with slip in the [110] directions D_1 and D_2 of Fig. 10, respectively. Extension of specimen 134 produced slip line traces of the (111) plane with pole marked E.

In Fig. 11 is summarized the observed distribution of the modes of torsional deformation. Dotted lines have been drawn to give a rough indication of the shapes of the region around [111] in which transverse torsional slip lines only are seen and the region around [100] in which only non-octahedral torsional slip lines are seen. Note that there is also a region around [110] in which only longitudinal torsional slip lines are seen. The mode of torsional slip in the region between the [100] and [110] areas is not clear. Of the 5 specimens studied in this region two showed only longitudinal slip lines, two showed transverse and longitudinal lines and one showed two quadrants of longitudinal slip and two quadrants of non-octahedral slip (a fifth mode of deformation).

3.2.1. Discussion. Dislocation mechanisms which correspond to two of the three types of torsional slip lines observed have been discussed in the literature.

Transverse torsional slip lines indicate rotational slip.⁽²⁵⁾ Thus rotational slip is one of the modes of torsional slip in aluminium. The hexagonal dislocation networks treated by Frank⁽²⁶⁾ and shown in Fig. 12(c) include one lying in a (111) plane and giving rotation about the [111] axis. Creation of such

a network would therefore yield the observed torsion and transverse torsional slip lines. The creation of the network would require complex dislocation interactions however, and such networks have to date only been observed in annealed crystals. (27-29) Whelan et al. (39) have observed hexagonal networks formed by dislocation interactions without annealing in stainless steel foils. These are not the strain-free twist boundaries treated by Frank, however.

Another mechanism is the creation of the crossed grids of screw dislocations^(31,32) shown in Fig. 12(d). Brown⁽³³⁾ has given a stress analysis of this mechanism of rotational slip. From the experiments of Edwards and Washburn (34) it seems that dislocations with one Burgers vector will obstruct the motion over the slip plane of dislocations of a different Burgers vector. Moreover it seems improbable that six Frank-Read sources-all the same, correct length and positioned at points around the circumference of the crystal as required for either mechanism as shown in Fig. 12(a)would be found in a single slip plane frequently enough to allow anything like uniform torsional deformation. Thus there are difficulties with the coplanar crossed grids mechanism and with the hexagonal net mechanism. An alternative would be for the Frank-Read sources for the dislocations of the required six Burgers vectors of Fig. 12(a) to lie in a number of neighbouring slip planes. This would give the required dislocation grids of Fig. 12(b) on separate planes. Such a dislocation distribution would have a higher energy than the coplanar crossed grid or hexagonal net. However, the long

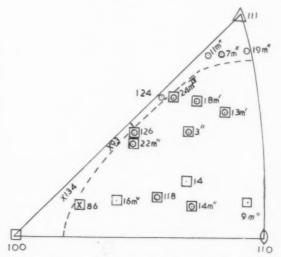


Fig. 11. Orientations of crystals showing the three types of torsional slip lines: ○ transverse torsional slip lines, ⊡ longitudinal torsional slip lines, × non-octahedral torsional slip lines.

range stresses of an interleaved set of grids on closely spaced planes would nearly cancel and thus such an arrangement would be fairly stable. The dislocations of the different grids, being screws, could finally move perpendicularly to the torsional slip planes onto a single common plane. But in any case stable small plastic twists can be produced in which the flow stress has been exceeded only in a thin surface shell. In such cases the grids of screw dislocations cannot have moved in far enough for mutual cancellation of long range stresses. Therefore, somehow, grids of screws

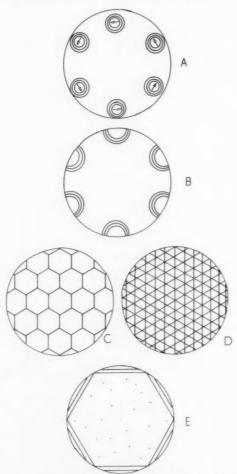


Fig. 12. (a) The six Frank–Read sources required for rotational slip. Each is represented by the first few dislocation loops generated (schematically drawn as circles) and their Burgers vector. (b) A certain number of loops have been generated from each source and piled up under the oxide skin. The skin has ruptured and the unwanted outer portion of each loop has escaped. This is the situation immediately beyond the peak of Fig. 15. (c) Idealized hexagonal dislocation network resulting from rotational slip. (d) Idealized crossed grid of screw dislocations resulting from rotational slip. (e) In general, but especially for small twists and in work hardened crystals, the torsional dislocations will only move inward a certain distance, leaving an elastically stressed core as shown. The dots represent barriers such as a forest of dislocations in a work-hardened crystal.

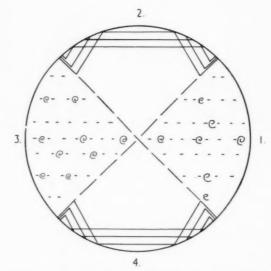


Fig. 13. Presumed torsional dislocation arrangement for twisted crystals of orientations like that of specimen 24miv. The spirals represent screw dislocations parallel to the specimen axis and normal to the cross-section shown. These dislocations move inward on the dashed planes during twisting. Longitudinal torsional slip lines are seen in quadrants 1 and 3 and transverse torsional slip lines in quadrants 2 and 4.

can be stabilized even without stress field cancellation. Thus the dislocation distribution in twisted crystals with axes near [111] is probably more like that shown in Fig. 12(e) with the grids on neighbouring (111) planes than like those of Figs. 12(e) or (d) in general. Dash⁽³⁵⁾ has observed the dislocation pattern of Fig. 12(b) at the surface of twisted crystals of this orientation.

195

Paxton and Cottrell⁽¹⁶⁾ described a second type of torsional deformation as "analogous to that which occurs when a bundle of parallel wires is twisted, allowing free sliding between contracting wires". Eshelby⁽³⁶⁾ has treated the ease of a screw dislocation parallel to the axis of a cylindrical crystal. He showed that the twist produced depended on the distance of the dislocation from the axis. The twist is a maximum when the screw is at the axis and zero when it is at the surface. The movement radially inward of screw dislocations parallel to the axis, therefore, is a mechanism corresponding to the longitudinal torsional slip lines. Note that specimen 24m^{IV} showed longitudinal torsional slip lines only in two quadrants of the cross-section. These quadrants are precisely those in which the planes of longitudinal torsional slip are approximately radial as can be seen in Fig. 5 (compare Fig. 13 in which the dislocations introduced in the different quadrants are shown schematically). In crystals with axes near [110] torsional deformation occurred with the appearance of longitudinal slip lines

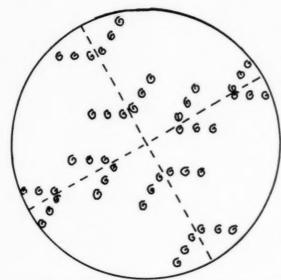


Fig. 14. Presumed dislocation distribution in a crystal with axis near [110] after a large twist with no prior work-hardening. The spirals represent screw dislocations perpendicular to the plane of the paper.

VOL.

1959

at all azimuths. This probably indicates slip by screws parallel to the axis moving approximately radially inward on the two (111) planes having a common [110] direction near the specimen axis. The final dislocation distribution if the dislocations move right in to the centre and pile up against each other is shown in Fig. 14. Gough, Wright and Hanson (37) fatigued a single crystal of this orientation in torsion. On sectioning and polishing they observed a "herringbone pattern" of this type (presumably visible due to precipitation hardening at the pile-ups). For smaller twists and in the presence of work hardening the dislocations will not move right in but will produce a deformed outer shell and an elastically stressed inner core similarly to the case shown in Fig. 12(e). As the crystal axis approaches [110] the Burgers vector becomes more nearly parallel to the surface. Therefore less and less of a step is produced on the specimen surface where the rejected portions of the Frank-Read loops escape. This is the explanation of the poor visibility of the longitudinal torsional slip lines.

No mechanism which would correspond to the nonoctahedral torsional slip lines seen on specimens with axes near [100] has been suggested.

3.3. The twist dependence of hardening by twisting

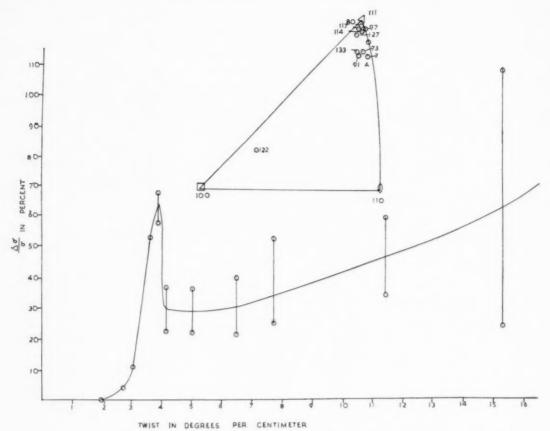
A group of specimens with axes very near the [111] pole were tested. Each was extended $\frac{1}{2}$ per cent and given a different twist. No simple pattern appeared from the load–extension curves. $\Delta \sigma$, the increase of resolved shear stress for flow, was calculated from the

increase of load (from C to D in Fig. 1, for example). In cases like Fig. 2 the upper and lower limits of $\Delta\sigma$ were calculated from CE and CD, respectively. $\Delta\sigma$ was plotted against the twist but no order appeared. It was then found that $\Delta\sigma/\sigma$, the increase of flow stress divided by the flow stress (at C) before twisting, did give a smooth curve when plotted against twist as shown in Fig. 15. The data for the specimens plotted in this Figure are listed in Table 1. It was found that

TABLE 1,			
Specimen	$(\Delta\sigma/\sigma) \times 100$ (%)	Twist (deg/em)	Prior extension (%)
97	0	1.98	0.52
7	3.7	2.71	0.44
114	10.7	3.02	0.49
125	52.2	3.60	0.50
78	68	3.89	0.49
	57		
81	36.5	4.12	0.49
	22.4		
117	35.8	4.99	0.50
	21.9		
122	39.4	6.47	0.52
	21.5		
80	51.8	7.68	0.51
	24.8		
91A	58.6	11.4	0.52
	34.2		
133	107	15.3	0.51
	23.5		

 $\Delta\sigma/\sigma$ values fell on the same curve for crystals from within regions corresponding approximately with those of Fig. 11. Thus, as Fig. 15 shows, crystals from the regions around [111] and [100] gave results fitting a single curve. Note that: (1) no hardening occurs for twists of less than $2^{\circ}/\text{cm}$. (2) the hardening increases rapidly with twist from $2^{\circ}/\text{cm}$ to about 60 per cent at $4^{\circ}/\text{cm}$ then falls to about 30 per cent at $5^{\circ}_{2}/\text{cm}$ and rises again from $5^{\circ}_{2}/\text{cm}$ onwards. (3) for twists of $2^{\circ}/\text{cm}$ to $4^{\circ}/\text{cm}$ the post-twist load–extension curves of the individual crystals were linear. For twists beyond the peak of Fig. 15, the post-twist curves of the individual crystals became paraboloidal as indicated by the upper and lower limits obtained for $\Delta\sigma/\sigma$.

Six crystals were tested from the region between [111] and [110] in which both transverse and longitudinal torsional slip lines had been observed. These gave much larger values of $\Delta\sigma/\sigma$. Three specimens, numbers 14, 118 and 14m^I, from nearer [110] gave values of $\Delta\sigma/\sigma$ lying on a still higher curve. Data from these specimens are listed in Table 2 and plotted in Fig. 16. Note that the form of the curve is very similar to that of Fig. 15. Dr. J. D. Eshelby suggested⁽³⁸⁾ that the fall in the curves of $\Delta\sigma/\sigma$ against



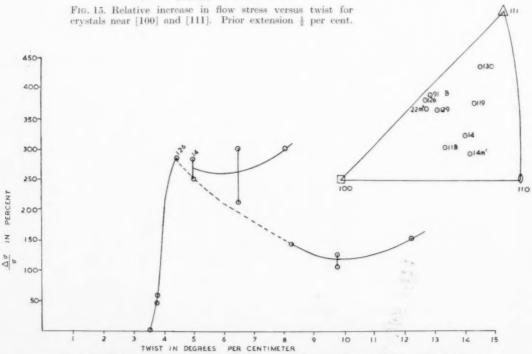


Fig. 16. Relative increase in flow stress vs. twist for crystals further from [100] and 1111] than those plotted in Fig. 15. Prior extension $\frac{1}{2}$ per cent.

TABLE 2.

Specimen	$(\Delta\sigma/\sigma) \times 100 (\%)$	Twist (deg/cm)	Prior extension (%)
91B	0	3.45	0.57
129	58.0 46.9	3.78	0.52
126	285	4.43	0.53
14	284 250	4.99	0.52
$14 \mathrm{m}^{\mathrm{I}}$	300 211	6.46	0.49
118	300	8.02	0.52
130	140	8.24	0.49
119	148 109	9.75	0.55
$22\mathrm{mm}$	151	12.2	0.48

twist might be due to the sudden escape of dislocation pile-ups through the surface oxide skin after a certain twist. Observation showed in fact that for crystals of this orientation and prestrain torsional slip lines appeared suddenly after a plastic twist of $4\frac{1}{2}$ °/cm.

To study the effect of prior extension on this

1959

behaviour a group of specimens were each extended 2 per cent and given a different twist. Data are given in Table 3 and Fig. 17. Specimens from crystals 11m,

TABLE 3.

TABLE O.				
Specimen	$(\Delta\sigma/\sigma) \times 100 ~(\%)$	Twist (deg/cm)	Prior extension (%)	
$19 \mathrm{m}^{\mathrm{IV}}$	0	1.55	1.98	
$11\mathrm{m}^{\mathrm{I}}$	0	2.57	1.93	
$11 \mathrm{m}^{\mathrm{m}}$	0	3.01	2.01	
$11 \mathrm{m}^{\mathrm{H}}$	1.5	3.27	2.04	
$19 \mathrm{m}^{\mathrm{II}}$	4.8	3.48	1.99	
	1.7			
11miv	1.4	3.64	2.08	
$13 \mathrm{m}^{\mathrm{I}}$	49.6	3.94	2.03	
	31.1			
19mH	7.2	4.98	2.00	
	2.8			
$24 \mathrm{m}^{\mathrm{IV}}$	19.1	5.88	2.04	
19mI	12.7	6.30	1.97	
	3.2			
3mIII	10.5	7.03	2.02	
24mIII	24.4	7.39	2.04	
3mII	10.0	8.11	1.97	
$24 \mathrm{m}^{\mathrm{I}}$	26.4	9.38	2.02	
311	59.7	10.3	2.01	

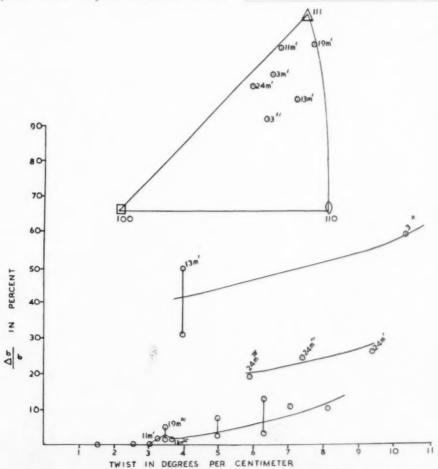


Fig. 17. Relative increase in flow stress vs. twist. Prior extension 2 per cent.

14-

Fig. 18. Load-extension curve of specimen 11mm.

EXTENSION IN PERCENT

BOO 3.017cm

195

from $\xi = \frac{3}{4}R$ to $\xi = \frac{1}{4}R$. Then α will increase by

$$\begin{split} \alpha(\frac{1}{4}R) &- \alpha(\frac{3}{4}R) = \frac{\mathbf{b}}{\pi R^2} \left(\frac{(\frac{3}{4}R)^2}{R^2} - \frac{(\frac{1}{4}R)^2}{R^2} \right) \\ &= \frac{\mathbf{b}}{\pi R^2} \left(\frac{9}{16} - \frac{1}{16} \right) = \frac{\mathbf{b}}{2\pi R^2} \end{split}$$

for each such dislocation. For aluminium $\mathbf{b} \cong 3 \times 10^{-8} \, \mathrm{cm}$ and the specimens of these experiments had radii $R \cong 10^{-1} \, \mathrm{cm}$. Figs. 15, 16 and 17 show that twists of 2 or 3°/cm (say $\beta = 5 \times 10^{-2} \, \mathrm{radian}$) can be accommodated by rearrangement. The total number of dislocations required to move in order to accommodate this twist by rearrangement is

$$N = rac{2\pi R^2}{\mathbf{b}} eta = rac{2\pi 10^{-2}}{3 imes 10^{-8}} \, 5 imes 10^{-2} {\,\cong\,} 10^5.$$

Thus the number of these dislocations per cm2 is

$$=\frac{N}{\pi R^2} = \frac{10^5}{\pi 10^{-2}} \cong 3 \times 10^6.$$

Figs. 15 and 17 show that, beyond the peak, $\Delta \sigma/\sigma$ increases approximately linearly with twist. If for

19m and 3m, with axes near [111] gave values falling on a single (bottom) curve. Specimens from crystal 24m gave higher values of $\Delta\sigma/\sigma$ and specimens 13m^I and 3 oriented nearest [110] gave still higher values of $\Delta\sigma/\sigma$. Thus orientation dependence for 2 per cent is the same as that for $\frac{1}{2}$ per cent prior extension. The shape of the curve is similar to those of Figs. 15 and 16: no hardening for twists of less than 3°/cm, a rise to a twist of about $3\frac{1}{2}$ °/cm, then a fall and subsequent rise. Twist slip lines did not appear on specimen 11m^{I} but did appear on specimens 19m^{III} and 11m^{IV} . That is, once again twist slip lines appeared at or after the peak in the curve. For any orientation and twist the hardening is much less after 2 per cent than after $\frac{1}{2}$ per cent prior deformation.

3.3.1. Discussion. Figs. 15, 16 and 17 show that there is a certain plastic twist below which no hardening is produced. This is because in any crystal there will be some dislocations with Burgers vectors having components parallel to the axis. By moving these dislocations radially inward a certain twist can be accommodated without introducing new dislocations, and thus without producing any increase of flow stress. Such re-arrangement can affect the rates of work hardening and/or recovery during subsequent tensile deformation. This is shown by cases such as Fig. 18 when a change of slope though no increase of flow stress was produced by twisting. The amount of twist which can be accommodated will depend upon the number of dislocations involved and the distance each can move radially. These in turn will depend upon the amount of prior deformation and the orientation. Fig. 15 shows that crystals near [111] extended } per cent prior to twisting can accommodate 2°/cm without increase of flow stress. Crystals of similar orientations extended 2 per cent prior to twisting as Fig. 17 shows can accommodate 3°/cm without increase of flow stress. In other words, with increasing prior extension in this range more and more of the twist is being accommodated by rearrangement.

A brief calculation will show the order of magnitude involved to be reasonable. According to Eshelby⁽³⁶⁾ the twist due to a screw dislocation parallel to the axis of a cylindrical specimen is

$$\alpha(\xi) = \frac{\mathbf{b}}{\pi R^2} \left(1 - \frac{\xi^2}{R^2} \right) \tag{1}$$

where α is the relative rotation of two cross-sections of the cylinder unit distance apart, \mathbf{b} is the Burgers vector, R the radius of the cylinder and ξ the distance of the dislocation from the axis. Suppose that on the average each dislocation parallel to the axis moves in



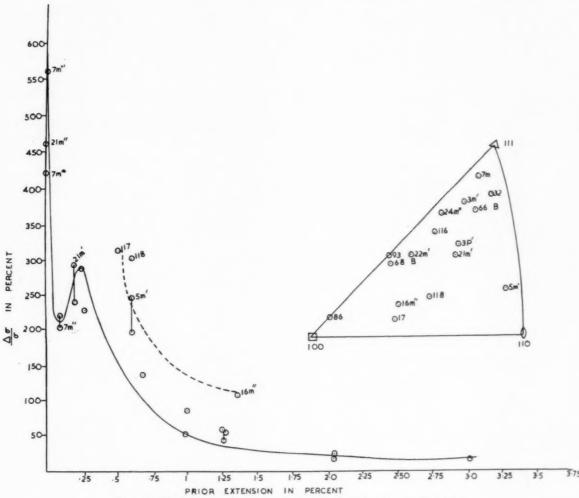


Fig. 19. Relative increase in flow stress vs. prior extension. Twist 84°/cm.

TABLE 4.

TABLE 4.			
Specimen	$(\Delta\sigma/\sigma) \times 100$ (%)	Prior extension (%)	Twist
7mm	560	0	8.29
	416		
21mH	457	0	8.26
7mH	218	0.09	8.19
	203		
$21 \mathrm{m}^{\mathrm{I}}$	290	0.19	8.29
	239		
92	287	0.25	8.25
66B	228	0.27	8.80
17	312	0.50	7.63
118	300	0.52	8.02
$5m^{1}$	244	0.52	8.25
86	136	0.69	8.35
82	51	0.98	8.40
3	84	1.00	8.13
$22 \mathrm{m}^{\mathrm{H}}$	56	1.25	8.12
	43		
16mII	107	1.37	8.10
3mH	10	1.97	8.11
116	19	2.04	8.18
68B	21	2.05	8.21
$24\mathrm{m}^{\mathrm{H}}$	15	3.01	8.48

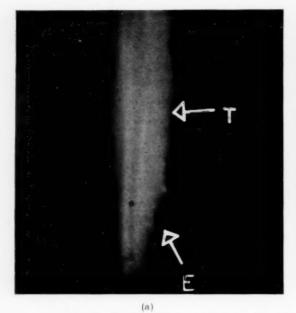
torsional deformation by any mode⁽¹⁶⁾ the density of dislocations introduced is proportional to twist, then $\Delta \sigma/\sigma$ is proportional to the density of torsional dislocations introduced.

3.4. The dependence of hardening by twisting on the prior extension

The specimens used for this study had widely varying orientations as shown in Fig. 19. Each was twisted $84^{\circ}/\text{cm}$ after a different prior extension as given in Table 4. Again it was found that $\Delta\sigma/\sigma$ was the significant quantity. Data for this series of experiments is plotted in Fig. 19. The broken curve is for values obtained with crystals 17, 118, 5m^{I} and 1m^{II} which are those nearer [110]. The solid curve fits, with more scatter, the remaining specimens. Note that for this twist and these orientations $\Delta\sigma/\sigma$ (1) falls steeply from zero to 0.125 per cent prior

VOL.

1959



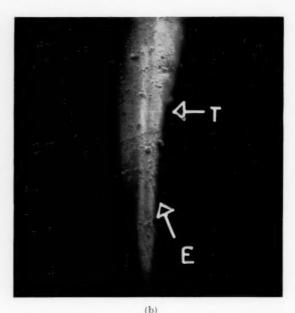


Fig. 20. Slip lines on specimen 7m^{II}. E: tensile slip lines, T: transverse torsional slip lines. (a) Top, (b) bottom of specimen. ×50.

extension, (2) rises from 0.125 to 0.25 per cent prior extension and (3) steadily falls thereafter, becoming approximately constant for prior extensions of more than about 2 per cent.

The initial sharp fall and subsequent rise in $\Delta \sigma / \sigma$ with increasing prior extension is a consequence of the fact that hardening by twisting does not result unless the tensile and torsional slip lines intersect. This had been discovered in the case of a specimen with axis near [111] extended 1 per cent and twisted 8.4°/ cm. From Fig. 19 this would be expected to give an increase of flow stress of about 90 per cent. In fact no increase at all was produced. The specimen had a taper and the tensile slip lines all appeared in the thinner half of the gauge length and the torsional slip lines in the thicker half with intersection only in a small region at the centre. The explanation of the form of the initial portion of Fig. 19 then is as follows. For zero prior extension torsional slip fills the whole gauge length. All (subsequent) tensile slip must then intersect torsional slip and great hardening results. For approximately 1/8 per cent extension the gauge length is non-uniformly filled with tensile slip. Torsional slip occurs preferentially in the undeformed or less deformed regions and a marked decrease in hardening is observed. Fig. 20 shows the slip lines on specimen 7m^{II} after twisting. The photomicrographs were taken at points a centimetre above and below the centre. Note that at the bottom there is a concentration of tensile slip and little or no torsional

slip. At the top there is a little tensile slip and a concentration of torsional slip. After about \(\frac{1}{4} \) per cent extension for these orientations, the gauge length is filled with tensile slip. Thus again tensile and torsional slip must intersect and the hardening is a maximum.

It is well known that easy glide in α-brass occurs during the propagation of an initial Luders band along the gauge length. This suggested an experiment to check the above idea. Two α-brass specimens were cut from a single crystal. The first was extended and gave 17 per cent easy glide. The second specimen was extended and twisted, extended and twisted. Easy glide continued. Only after twisting sufficiently the third time to fill all the gauge length not containing tensile slip with torsional slip lines was easy glide stopped. Thus only after sufficient torsional dislocations have been introduced to fill all the undeformed regions of the crystal is the propagation of the Luders band impeded and easy glide brought to an end. A large yield point was observed at the onset of plastic extension and a large torsional yield point was observed the first time the specimen was twisted.

To study the effect of variation of the twist on this behaviour a second group of specimens were tested. Each was twisted $9\frac{1}{2}$ °/cm after a different prior extension as given in Table 5. The results are plotted in Fig. 21. Too few specimens were tested to enable any conclusions to be drawn concerning orientation differences. A single approximate curve is drawn for

VOI 7 195

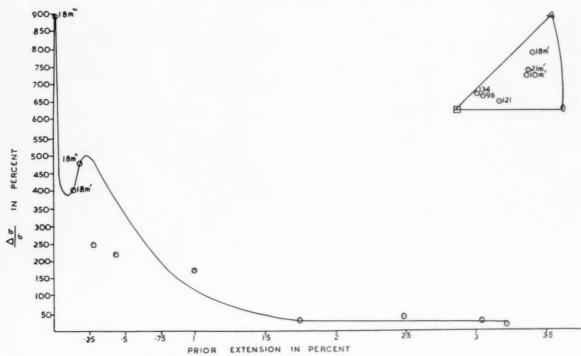


Fig. 21. Relative increase of flow stress versus prior extension. Twist 94°/cm.

all points therefore. The shape of the curve is the same as that for a twist of $8\frac{1}{4}$ °/cm.

1959

The reality of the initial fall and subsequent rise in $\Delta\sigma/\sigma$ with increasing prior extension is well shown by specimens 18m^{III} , 18m^{I} and 18m^{II} cut from the same crystal. The curves drawn in the range of prior extensions from 0 to 0.25 per cent in Figs. 19 and 21 merely indicate the trend. Since the initial fall and subsequent rise of $\Delta\sigma/\sigma$ with increasing prior deformation is a consequence of the changing distributions of slip it must be extraordinarily affected by variations in cross-section, crystal perfection, mishandling, etc. Thus values obtained in this initial range will probably show large scatter. However, the diminution of the hardening effect by the avoidance

of tensile slip lines by torsional slip in this range is clearly established.

3.4.1. Discussion. The α -brass experiments and the curves of Figs. 19 and 21 for prior deformations between 0 and $\frac{1}{4}$ per cent showed that hardening occurred when and only when tensile and torsional slip intersected. This fact is consistent with sessile-formation or jog-production as the dislocation mechanism responsible for hardening on twisting.

For prior deformations of 1 per cent to 2 per cent $\Delta \sigma / \sigma$ falls with increasing deformation but beyond 2 per cent it becomes approximately constant. It has been shown that the twist accommodated by rearrangement increases with prior deformation from per cent to 2 per cent at least for crystals near [111]. In this range the portion of the constant total twist of Figs. 19 or 21 which introduces new dislocations therefore decreases. $\Delta \sigma$ is proportional to the number of dislocations introduced by twisting. Therefore, $\Delta \sigma$ for a constant total twist must fall with prior deformation from 1 per cent to 2 per cent. For prior deformations greater than 2 per cent, $\Delta \sigma / \sigma$ becomes roughly constant, but σ continues to increase, though at a decreasing rate, with prior extensions greater than 2 per cent. $\Delta \sigma$ must, therefore, also begin to rise in this range. Hence more of the constant twist is being accommodated by introducing new dislocations and less by re-arranging dislocations already present.

TABLE 5.

Specimen	$(\Delta\sigma/\sigma) \times 100~(\%)$	Prior extension (%)	Twist (deg./cm
18mm	892	0	9.50
18mI	400	0.14	9.44
18mH	478	0.18	9.46
$21 \mathrm{m}^{\mathrm{IV}}$	247	0.28	9.55
$21\mathrm{m}^{\mathrm{III}}$	219	0.45	9.56
96	171	1.00	9.53
10mn	26	1.75	9.50
10mtv	40	2.50	9.46
121	29	3.05	9.16
134	17 10	3.22	9.40

This must mean that the decrease in the distance that each dislocation with a Burgers vector having a component parallel to the axis can move becomes more important than the increase with increasing prior deformation in the numbers of such dislocations.

3.5. Orientation dependence

The orientation dependence of hardening by twisting followed the same pattern as the orientation distribution of the different modes of torsional deformation. The orientation dependence of $\Delta \sigma / \sigma$ for any twist and prior deformation from Figs. 15, 16, 17, 19 and 21 may be summed up as follows. Crystals with axes in the regions about [100] and [111] of Figs. 11 were least hardened. Crystals oriented near the boundary in Fig. 11 experienced greater hardening. Crystals nearest [110] gave the largest values of $\Delta \sigma / \sigma$ for any given prior deformation and twist. This orientation dependence is partly due to the dependence of $\Delta \sigma$ on the mode of torsional deformation of the crystal. Partly it is due to the dependence of σ on the orientation. Thus σ at the end of the prior extension was least for crystals nearest [110] and $\Delta \sigma / \sigma$ for any given twist, therefore, largest.

3.6. Changes of hardening rate after twisting

Paxton and Cottrell⁽¹⁶⁾ reported that their stress-strain curves after twisting were either parallel to the prestrain curve or more steeply rising. This behaviour was confirmed in a few preliminary tests. Twisting of copper single crystals has been reported as having no effect on work-hardening rate in tension in tubular single crystals, but as decreasing the hardening rate in reverse testing of solid crystals. In the present series of experiments much larger twists were applied after much larger prior extensions than those of Paxton and Cottrell. Under these conditions the great majority of specimens experienced a decrease of slope after twisting as for example in Fig. 1.

Certain striking regularities in the effect of twisting on the slope and shape of the load–extension curves of individual crystals were found in the course of the work reported in the preceding sections of this paper. It has already been remarked that of the crystals of Fig. 15 and Table 1, those given twists up to 3.60°/cm had linear post-twist curves as for example in Fig. 22, while those given twists of 3.89°/cm or more (at or past the peak of Fig. 15) had paraboloidal post-twist curves as for example in Fig. 2. That is, the shape of the post-twist load-extension curves changed at the peak of the hardening versus twist curve when dislocation pile-ups escaped and twist slip lines appeared.

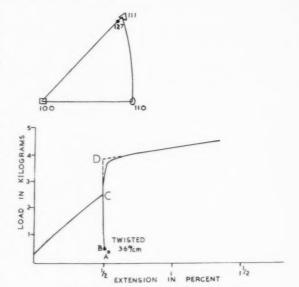


Fig. 22. Load-extension curve of specimen 127.

The specimens of Table 3 and Fig. 17 were given various twists after 2 per cent prior extension. Those specimens having an increase of flow stress ($\Delta\sigma/\sigma>0$) due to twisting all had a decrease in slope after twisting.

VOI

19

The specimens of Table 4 oriented near [100] and [111] gave points lying on or near the solid curve of Fig. 19. Of these specimens 7m^{III}, 21m^{II} and 7m^{II} showed no change of slope after twisting. Specimens given prior deformations of 0.19 per cent or more before the standard twist of 8½ /cm showed decreases of slope after twisting. That is, specimens given prior extensions equal to or less than that at the minimum of the $\Delta \sigma / \sigma$ vs. prior extension curve experienced no change of slope. Specimens given prior extensions larger than that at the minimum of the curve experienced decreases in the slope of their individual loadextension curves. The specimens of Table 5 and Fig. 21 were given various extensions prior to a twist of 9½°/cm. All these specimens had a decreased loadextension slope after twisting.

A noteworthy fact is that in some cases a decrease of slope occurred even when there was no increase of flow stress on twisting as in Fig. 18. In fact all the specimens of Table 3 and Fig. 17 which did not harden on twisting (19m^{IV}, 11m^I and 11m^{III}) nevertheless experienced decreases of slope. A further significant phenomenon is illustrated by Fig. 18. That is that a decrease in slope on twisting was sometimes accompanied by a change from paraboloidal to linear in the shape of the curve.

3.6.1. Discussion. Small twists after small prior extensions (as in the experiments of Paxton and

Cottrell and a few of the preliminary experiments in the present work) produced either an increased or unchanged slope of the tensile load-extension curve. The increases of slope were produced on twisting specimens during easy glide. The effect of the twist in this case is to disrupt laminar flow and precipitate turbulence. Larger twists after larger prior deformations generally produced a decrease of slope. The slope of any load-extension curve can be simply regarded as the resultant effect of two opposed processes: work-hardening and recovery. The first process operates to continually increase the flow stress as deformation proceeds and the second undoes the first and tends to reduce the flow stress. On this simple view it may be said that the effect of the dislocations introduced by twists after large prior deformation is to increase the rate of recovery more than the rate of work-hardening. This is not surprising since at large strains, stress-strain curves are generally parabolic. That is the slope of the curve is steadily decreasing and the effect of twisting in this range is merely to further an already operating trend.

Much of the theorizing about work hardening has been directed to predicting either parabolic or linear stress–strain curves. It has been shown above that the curve can be changed from linear to parabolic and vice versa by twisting. Thus in the case of crystals near [111] like those of Fig. 15 when the pile-ups escape through the oxide skin (i.e. from Fig. 12(a) to to (b)) the post-twist load–extension curve changed from linear to parabolic and at the same point $\Delta\sigma/\sigma$ dropped to half its former value. Specimen 11m^{III}, Fig. 18, experienced no increase of flow stress on twisting. Thus the twist was accommodated by moving inward dislocations having Burgers vectors

with components parallel to the axis. This sufficed to change the shape of the load-extension curve which had been parabolic to linear. These phenomena appear to be of great theoretical importance.

3.7. Transient hardening

It was found that after considerable deformation, the first part of the post-twist load-extension curve passed well above the backward extrapolation of the final curve. This is clearly shown in Fig. 23. In this case the phenomenon did not appear after the first or second twist. After the third twist it appeared for the first time while the fourth twist produced only transient hardening. That is the final curve after the fourth twist was a continuation of that before the twist. When a specimen was repeatedly extended and twisted transient hardening always appeared. Eventually $\Delta \sigma$ became zero and only transient hardening resulted from twisting.

A small yield point (30–60 g fall in load) usually occurred during the zero hardening rate extension of transient hardening. It was not possible to observe whether this zero hardening rate extension was accompanied by the propagation of a Luders band along the specimen. Electropolishing (or etching) the specimen before twisting suppressed the transient hardening even if it had already appeared after previous twists.

When the torsional deformation is confined to the surface the interior is elastically stressed. Etching off a layer of aluminium would then permit the specimen to untwist. Experiments were done on a few specimens after testing using a glass tube scaled to the lower end of the specimen with scaling wax. The specimens were clamped at the bottom, the top being left free with a

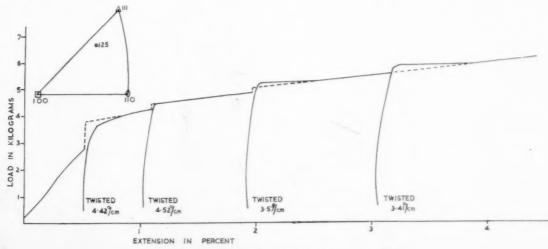


Fig. 23. Load-extension curve of specimen 125.

VOL. 7 1959

small mirror attached. The specimens were twisted and an etchant was poured into the tube around the specimen. 3 per cent phosphoric acid which removes the oxide film(39) but does not attack the metal produced no effect under any circumstances. Tucker's etch⁽⁴⁰⁾ which macroscopically etches aluminium was also used. With this reagent it was found that specimens which had had small prior deformations did not untwist. For larger prior deformations untwisting did occur as the surface layers of the metal were removed. The crudity of the method and the unevenness of the chemical attack precluded any quantitative conclusions. However, untwisting on etching did appear at about the same prior deformations as transient hardening. The proportion of the twist recovered on etching grew with increasing prior deformation.

3.7. Discussion. Transient hardening and the confinement of torsional deformation to the surface layers appeared to be closely connected. This can be understood from a comparison of the dislocation models of Fig. 12. Fig 12(d) (or possibly 12(e)) shows the result of a large twist on virgin or slightly extended crystals. Torsional dislocations are evenly distributed across the crystal. In these cases subsequent tensile dislocations interact with the torsional dislocations either through sessile-formation or jog-production and work hardening begins immediately at the flow stress as increased by torsion as shown in Fig. 24(a). After larger prior extensions the crystal is full of dislocation barriers. Torsional dislocations produced by Frank-Read sources near the surface do not penetrate into the interior, but remain in the surface layer, as shown in Fig. 21(e). In the limit, twisting merely produces a hard shell. Then, etching off surface layers allows the crystal to untwist. On reloading after twisting in this range deformation does not begin until the stress is great enough to force dislocations out through the shell as at point B in Fig. 24(b). No new dislocations have been introduced into the interior by twisting. Therefore, work hardening continues there at the old rate along the dotted line. At point C the interior has become hardened to the same flow stress as the shell. The load-extension curve then continues as if no twist

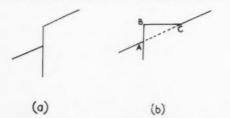


Fig. 24. Schematic load-extension curves on twisting (a) after small prior extensions and (b) after large prior extensions (transient hardening).

had been given. These arguments apply whatever the mode of torsional deformation. Thus work hardening occurs only when the tensile and torsional dislocations intersect.

3.8. Tensile slip line distribution

Dr. Cahn⁽⁴¹⁾ suggested that the azimuthal distribution of tensile slip lines after twisting would be affected if sessile formation occurred. This is because torsional deformation, as shown in Figs. 12, 13 and 14, introduces different sorts of dislocations into different regions of the specimen. Subsequent tensile dislocations may interact with some of the torsional dislocations and not others. This should prevent the formation of tensile slip in certain sectors more than in others.

A number of crystals were tested by giving large twists followed by substantial extensions. It was found that for crystals oriented near [110] (e.g. 9m^{II} in Fig. 9), tensile slip lines appeared at all azimuths (except, of course, that for 1° or 2° where the operative slip direction is tangential to the specimen surface the slip lines are interrupted). Specimens like 2^I in which quadrants of transverse and longitudinal torsional slip occurred as shown in Fig. 25, also showed tensile slip lines at all azimuths. Crystals like 1^{II} near [111], which experienced pure rotational slip, showed tensile slip lines only in certain sectors of the surface as shown in Fig. 26.

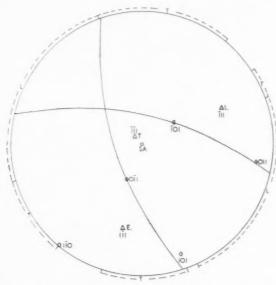
VOI

191

3.8.1. Discussion: Sessile formation. Specimen 1¹¹ was twisted so that the portion of the crystal above the stereogram of Fig. 26 was rotated in a clockwise sense relative to the portion below. It is clear that torsional dislocations were generated at the surface and moved inwards. In the following analysis it will be assumed that the torsional dislocations move in only a fraction of the radius so that the dislocations in any sector of the surface all have one Burgers vector. The tensile dislocations in all regions are assumed to have both Burgers vectors of the operative slip direction. Positive directions of the dislocations were arbitrarily chosen in the clockwise sense in Fig. 27. Using Bilby's right hand rule⁽⁴²⁾ the Burgers vectors shown in Fig. 27 as occurring in different sectors were derived. In this crystal the tensile slip direction [110] was that for maximum resolved shear stress. The direction [101] was slightly less highly stressed. Moreover, no narrow region of interruption, such as appears at positions at which the Burgers vector is tangential to the crystal surface, was found at the positions corresponding to [101] which lie in the regions in which tensile slip lines appeared. (The interruption of tensile slip lines at the position marked

E.I. in Figure 26 does not correspond to either of the possible tensile slip directions and is probably spurious.) Had the operative slip direction been [$\overline{1}01$] such regions would have appeared. This fact also indicates [$\overline{1}\overline{1}0$] to have been the operative slip direction. The tensile dislocations are therefore assumed to have Burgers vectors $\pm \frac{1}{2}\mathbf{a}[\overline{1}10]$.

The criteria given by Lomer and modified by Cottrell for the formation of their sessile dislocations involve restrictions on both the Burgers vectors and the line orientations of the interacting dislocations. The line orientations of both tensile and torsional dislocations in the present case are unknown. They probably vary from point to point along the disloca-



VOL.

1959

Fig. 25. Stereogram of specimen 2¹ after deformation. The poles marked E, L and T are those of the planes of tensile and longitudinal torsional slip and of transverse torsional slip, respectively. The position of the specimen axis is denoted S.A. Longitudinal and transverse torsional slip lines are visible at the azimuths marked L and T around the circumference.

tions. It is possible that if portions of two dislocations locally suitably oriented react the forces involved will lead to a progressive drawing together of the entire lengths of the dislocations (in a manner reminiscent of a zip fastener) to form a sessile. In the following analysis line orientations are not discussed. It is found that the observations are consistent with the hypothesis that Lomer-Cottrell sessiles are formed wherever the Burgers vectors are suitable.

Taking the possible dislocation reactions, sector by sector, in this specimen we have:

Sector 1:
$$\frac{1}{2}\mathbf{a}[101] + \frac{1}{2}\mathbf{a}[110] \rightarrow \frac{1}{2}\mathbf{a}[211]$$

 $\frac{1}{2}\mathbf{a}[101] + \frac{1}{2}\mathbf{a}[110] \rightarrow \frac{1}{2}\mathbf{a}[011]$



Fig. 26. Stereogram of specimen 1^{II} after deformation. The positions denoted S.A., T and E are the specimen axis and the poles of the transverse torsional and tensile slip planes, respectively. The azimuths denoted I are those at which the torsional slip lines were interrupted. Tensile slip lines appeared only at the azimuths denoted E around the circumference. At the azimuth denoted E.I. the tensile slip lines were interrupted.

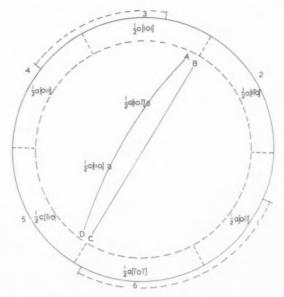


Fig. 27. Stereogram of the Burgers vectors of the torsional and tensile dislocations in specimen 1^{II}. This figure is derived from Fig. 26. In each sector of the surface shell the Burgers vector of the torsional dislocations present is shown. On the tensile slip plane ABCD the Burgers vectors are $\frac{1}{2} \pm a[110]$. Tensile slip lines appear at all azimuths except those indicated by the broken line outside the circumference of the stereogram. That is, within the experimental error, tensile slip lines are absent from sectors 1 and 3.

VC

19

The latter reaction leads to the formation of sessiles.

Sector 2:
$$\frac{1}{2}\mathbf{a}[\overline{1}10] + \frac{1}{2}\mathbf{a}[\overline{1}\overline{1}0] \rightarrow \frac{1}{2}\mathbf{a}[\overline{2}00]$$

 $\frac{1}{2}\mathbf{a}[\overline{1}10] + \frac{1}{2}\mathbf{a}[\overline{1}10] \rightarrow \frac{1}{2}\mathbf{a}[\overline{2}020]$

No sessiles are formed.

Sector 3:
$$\frac{1}{2}\mathbf{a}[101] + \frac{1}{2}\mathbf{a}[\overline{110}] \rightarrow \frac{1}{2}\mathbf{a}[0\overline{11}]$$

 $\frac{1}{2}\mathbf{a}[101] + \frac{1}{2}\mathbf{a}[110] \rightarrow \frac{1}{2}\mathbf{a}[2\overline{11}]$

The first of these reactions leads to sessile formation.

Sector 4:
$$\frac{1}{2}\mathbf{a}[1\overline{1}0] + \frac{1}{2}\mathbf{a}[\overline{11}0] \rightarrow \frac{1}{2}\mathbf{a}[0\overline{2}0]$$

 $\frac{1}{2}\mathbf{a}[1\overline{1}0] + \frac{1}{2}\mathbf{a}[110] \rightarrow \frac{1}{2}\mathbf{a}[200]$

No sessiles are formed.

In the remaining sectors the torsional Burgers vectors lie in the tensile slip plane and can therefore not form sessiles with the tensile dislocations.

Certain portions of the crystal surface were found to be free of tensile slip lines, and, within the considerable experimental error in comparing azimuths in the X-ray orientation determination and slip line observations, these coincided with sectors 1 and 3. These are the sectors in which the above analysis showed the Burgers vectors to be suitable for Lomer–Cottrell sessile formation. In sectors 2, 4, 5 and 6 where obstacles were not formed, slip lines appeared. If the less highly stressed tensile slip direction [101] had operated, sessiles would

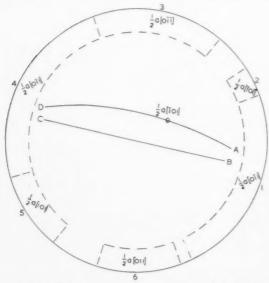


Fig. 28. Stereogram of the Burgers vectors of the torsional and tensile dislocations in specimen 21. This figure is derived from Fig. 25. In each sector of the surface shell the Burgers vector of the torsional dislocations present is shown. The tensile slip plane is ABCD and the tensile Burgers vectors are $\pm \frac{1}{2}a[101]$. Tensile slip lines appear in all regions of the

have been formed in sectors 2 and 4 and absent in sectors 1 and 3.

The portion of specimen $2^{\rm I}$ above the plane of the stereogram of Fig. 25 was twisted counterclockwise relative to that below. Up out of the figure and clockwise in the figure were chosen as the positive directions of torsional dislocations. Analysis yielded the torsional Burgers vectors shown in the six sectors of the cylindrical surface shell of Fig. 28. The tensile Burgers vectors are $\pm \frac{1}{2}\mathbf{a}[\overline{1}01]$. The possible dislocation reactions in this specimen are:

Sector 1:
$$\frac{1}{2}\mathbf{a}[\overline{1}01] + \frac{1}{2}\mathbf{a}[\overline{1}01] \rightarrow \frac{1}{2}\mathbf{a}[\overline{2}02]$$

 $\frac{1}{2}\mathbf{a}[\overline{1}01] + \frac{1}{2}\mathbf{a}[\overline{1}0\overline{1}] \rightarrow \frac{1}{2}\mathbf{a}[\overline{0}00]$
Sector 2: $\frac{1}{2}\mathbf{a}[\overline{1}01] + \frac{1}{2}\mathbf{a}[\overline{1}01] \rightarrow \frac{1}{2}\mathbf{a}[\overline{2}00]$
 $\frac{1}{2}\mathbf{a}[\overline{1}01] + \frac{1}{2}\mathbf{a}[\overline{1}0\overline{1}] \rightarrow \frac{1}{2}\mathbf{a}[\overline{2}00]$
Sector 3: $\frac{1}{2}\mathbf{a}[\overline{0}11] + \frac{1}{2}\mathbf{a}[\overline{1}01] \rightarrow \frac{1}{2}\mathbf{a}[\overline{1}12]$

Sector 3:
$$\frac{1}{2}\mathbf{a}[011] + \frac{1}{2}\mathbf{a}[101] \rightarrow \frac{1}{2}\mathbf{a}[112]$$

 $\frac{1}{2}\mathbf{a}[011] + \frac{1}{2}\mathbf{a}[101] \rightarrow \frac{1}{2}\mathbf{a}[110]$

The latter reaction yields a dislocation with Burgers vector in the tensile slip plane, and therefore no sessiles form.

$$\begin{array}{ll} Sector \ 4\colon & \frac{1}{2}\mathbf{a}[\overline{1}01] + \frac{1}{2}\mathbf{a}[\overline{1}01] \to \frac{1}{2}\mathbf{a}[\overline{2}02] \\ & \frac{1}{2}\mathbf{a}[\overline{1}01] + \frac{1}{2}\mathbf{a}[\overline{1}01] \to \frac{1}{2}\mathbf{a}[\overline{0}00] \\ Sector \ 5\colon & \frac{1}{2}\mathbf{a}[\overline{1}01] + \frac{1}{2}\mathbf{a}[\overline{1}01] \to \frac{1}{2}\mathbf{a}[\overline{2}00] \\ & \frac{1}{2}\mathbf{a}[\overline{1}01] + \frac{1}{2}\mathbf{a}[\overline{1}01] \to \frac{1}{2}\mathbf{a}[\overline{1}10] \\ Sector \ 6\colon & \frac{1}{2}\mathbf{a}[\overline{0}\overline{1}1] + \frac{1}{2}\mathbf{a}[\overline{1}01] \to \frac{1}{2}\mathbf{a}[\overline{1}\overline{1}2] \\ & \frac{1}{2}\mathbf{a}[\overline{0}\overline{1}1] + \frac{1}{2}\mathbf{a}[\overline{1}01] \to \frac{1}{2}\mathbf{a}[\overline{1}\overline{1}2] \end{array}$$

The first of the reactions in sector 6 yields a dislocation with its Burgers vector in the tensile slip plane. Hence, according to this analysis, sessiles are nowhere formed in the specimen. This is consistent with the observation of tensile slip lines in all regions around the cylindrical surface.

The fact that the top of specimen $9m^{11}$ was twisted counterclockwise relative to the bottom, together with the choice of the direction up out of the plane of the stereogram of Fig. 9 as the positive direction along the torsional dislocation lines leads to $\frac{1}{2}\mathbf{a}[011]$ as the torsional Burgers vector in all sectors of Fig. 29. However the torsional dislocations in the 4 sectors do differ in slip plane. The torsional dislocations of sectors 1 and 3 moved inwards on (111) planes while those in sectors 2 and 4 moved on (111) planes. From this it follows that torsional dislocations in sectors 1 and 3 cannot react with tensile dislocations of Burgers vectors $\pm \frac{1}{2}\mathbf{a}[110]$ to form sessiles for the interacting Burgers vectors both lie in the torsional slip plane.

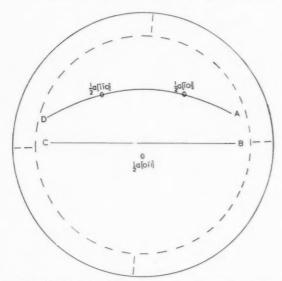


Fig. 29. Stereogram of the Burgers vector of the torsional and tensile dislocations in specimen $9m^{\Pi}$. This figure is derived from Fig. 9. In all sectors of the cylindrical surface shell the torsional dislocations have the Burgers vector $\frac{1}{2}\mathbf{a}[011]$. On the tensile slip plane ABCD both $\pm\frac{1}{2}\mathbf{a}[110]$ and $\pm\frac{1}{2}\mathbf{a}[101]$ occur. Tensile slip lines appear in all regions of the surface.

Similarly torsional dislocations in sectors 2 and 4 cannot form sessiles with tensile dislocations of Burgers vectors $\pm \frac{1}{2} \mathbf{a} [\bar{1}01]$. The possible dislocation reactions, therefore, are:

Sectors 1 and 3:
$$\frac{1}{2}\mathbf{a}[\overline{101}] + \frac{1}{2}\mathbf{a}[0\overline{11}] \rightarrow \frac{1}{2}\mathbf{a}[\overline{112}]$$

 $\frac{1}{2}\mathbf{a}[10\overline{1}] + \frac{1}{2}\mathbf{a}[0\overline{11}] \rightarrow \frac{1}{2}\mathbf{a}[1\overline{10}]$

VOL.

1959

The latter reaction leads to sessile formation.

Sectors 2 and 4:
$$\frac{1}{2}\mathbf{a}[\overline{110}] + \frac{1}{2}\mathbf{a}[0\overline{11}] \rightarrow \frac{1}{2}\mathbf{a}[\overline{121}]$$

 $\frac{1}{2}\mathbf{a}[110] + \frac{1}{2}\mathbf{a}[0\overline{11}] \rightarrow \frac{1}{2}\mathbf{a}[101]$

The latter reaction leads to sessile formation.

In these specimens tensile slip lines appeared at all azimuths. Three explanations suggest themselves. (1) Sessiles do not in fact form because the torsional dislocations are of exact screw orientation parallel to [011] and nowhere parallel to either [110] or [101] as they would have to be for the long range attractions leading to the dislocation reactions⁽¹⁾ to operate. However, it is most improbable that except perhaps at very low temperatures the torsional dislocations would have such line orientations. As previously mentioned, zippering may occur and render the initial positions of the dislocations relatively unimportant. Even if zippering does not occur, short lengths of sessile formed where line orientations are favourable

may produce effective blocking of slip line development. (2) The sessile forming reactions do occur but the effect is immediately to stop the operation of the Frank-Read sources yielding tensile dislocations of Burgers vectors $\pm \frac{1}{2}\mathbf{a}[\overline{1}01]$ in sectors 1 and 3 but leaving Frank-Read sources yielding tensile dislocations of Burgers vectors + \(\frac{1}{2}\alpha[110]\) free to operate and conversely in sectors 2 and 4. This explanation appears unsatisfactory since the formation of sessiles to block the operation of certain Frank-Read sources is at the same time the creation of obstacles to slip by dislocations of any sort. If we are to retain the argument already applied to specimens 1^{II} and 2^I, we must rule out both these explanations. (3) Sessiles form in all 4 sectors and inhibit tensile slip equally in all sectors. The non-uniform distribution of tensile slip in specimen 111 was a reflection of the nonuniform distribution of sessile-forming reactions round the specimen surface. The uniform distribution of tensile slip lines round specimen 31 reflected the uniform absence of sessile-forming reactions from all sectors of that specimen. The uniform presence of tensile slip lines round specimen 9m^{II} is then a reflection of the uniform occurrence of sessile formation in all sectors. The formation of sessiles in all sectors of specimens of this orientation would lead to great torsional hardening. It has been pointed out that for a given tensile prior deformation and a given twist specimens of this orientation gave the largest values of $\Delta \sigma / \sigma$. This explanation, therefore, seems the simplest and most satisfactory.

Thus it appears that obstacles to the propagation of tensile slip are formed in accordance with the Lomer–Cottrell reaction, wherever the Burgers vectors of the reacting dislocations are suitable.

4. GENERAL DISCUSSION

There are two sorts of effects to be explained: immediate and continuing. It has been shown that twisting can produce an immediate increment of tensile flow stress and that it can change the rate or form of subsequent tensile work hardening. The dislocations introduced by twisting may do one of several things: (1) add to the density of the Cottrell forest, (2) form sessiles or (3) form new piled-up groups. In this section the two sorts of effects will be discussed in terms of these three possible actions.

An immediate increment of tensile flow stress can be due⁽¹⁶⁾ to an addition to the Cottrell forest of

$$\rho = \theta/\mathbf{b}$$
 (2)

dislocations where ρ is the density of dislocations introduced, θ is the plastic twist and **b** is the Burgers

VOI 7

vector, or the increment may be due to these torsional dislocations going into piled up groups producing internal stresses. Vacancies, interstitials and their generation may contribute to the flow stress but quantitative theories of these effects have not been developed. An increment of flow stress is not likely to be due to the formation of sessiles, for the stress field of a sessile is not sufficiently greater than that of a single dislocation to explain the marked effects observed. On the other hand it is difficult to see how the addition of torsional dislocations to pile-ups or to the Cottrell forest could permanently alter the rate or form of work hardening. However, sessile formation by creating new obstacles and hence altering slip distances(17) and giving rise to new pile-ups could exert a continuing influence. A decrease in the slip distance means an increase in the work hardening rate if the law of work hardening is linear. (18) The opposite effect was in fact observed in most cases.

For reasons discussed above a quantitative comparison of the increment of flow stress results will only be made with the pile-up and the forest theories. This will be followed by a brief consideration in terms of dislocation theory of the changes of slope and of shape of the stress-strain curve due to twisting.

We shall proceed on the simplifying assumption that *both* Cottrell forest hardening⁽⁶⁾ and Mott pile-up hardening⁽⁴⁾ lead to the relationship

$$\sigma = A \rho^{\frac{1}{2}} \tag{3}$$

where σ is the flow stress, A is a constant $= \mathbf{b}\mu$ where \mathbf{b} is the Burgers vector ($\simeq 3$ Å) and μ is the modulus of rigidity ($= 2.65 \times 10^{11}$ dynes/cm²), and ρ is the density of dislocations. The actual forms of the constants are (1) for the pile-up theory $\mu \mathbf{b} \sqrt{n}/2\pi$ where n is the (constant) number of dislocations in any pile-up, thus if n=1000 the Mott constant is ~ 5 times greater than that assumed and (2) for the forest theory the constant is $\alpha \mu \mathbf{b}$ where α is a constant $\simeq 1.^{(43)}$ Professor Nabarro⁽⁴⁴⁾ suggested that if the torsional dislocations produce hardening by a different mechanism from that previously operative in tensile slip the two effects can be added in the form

$$\sigma + \Delta \sigma = A(\rho)^{\frac{1}{2}} + A(\Delta \rho)^{\frac{1}{2}} \tag{4}$$

whereas, if the mechanisms operative are the same the addition takes the form

$$\sigma + \Delta \sigma = A(\rho + \Delta \rho)^{\frac{1}{2}} \tag{5}$$

An order of magnitude check will now be made of the above relationships against the results obtained on 3 of the specimens of Table 1 and Fig. 15. Throughout this section θ has been corrected to θ_c by sub-

Table 6. Density of dislocations introduced by twisting derived from equation (2)

Specimen	$\Delta ho= heta_c/{f b}$				
117	1.7 × 10 ⁶ /cm.				
80	$1.7 \times 10^{6} / \mathrm{cm}^{3}$ 3.3×10^{6}				
91A	5.5×10^{6}				

tracting $2^{\circ}/\text{cm}$, the twist accommodated by rearrangement for these crystals and, for simplicity, the mean of the upper and lower limits of $\Delta \sigma$ has been used.

Geometrically, torsional hardening appears likely to be by the forest mechanism. However, if hardening be by the pile-up mechanism these latter dislocation densities would only be divided by ~5. The discrepancy between the dislocation densities of Tables 6 and 7 is probably due to the density of dislocations introduced by twisting being greater than the geometrically necessary minimum density given by equation (2) and Table 6. The density of dislocations introduced by twisting can become greater than the density calculated from equation (2) for either of two reasons. (1) Equation (2) gives only the excess density of dislocations with Burgers vectors of one sign which are introduced. It is known that in the analogous case of bending, a large density of dislocations is introduced above the number geometrically required to accommodate the plastic bending. It is particularly to be expected that in conditions of turbulent deformation the total number of dislocations introduced will be greater than the excess of dislocations with Burgers vectors of the required sign which is given in Table 6. (2) Equation (2) gives the density of dislocations required to accommodate the plastic twist if the dislocations be uniformly distributed over the cross-section of the crystal. Equation (1) shows that if the dislocations introduced move inwards lesser distances than those required to give a uniform distribution the total number introduced will have to be greater than that given by equation (2). It is, therefore, to be expected that in a work hardened crystal the density of dislocations introduced by twisting will exceed the minimum value given in Table 6.

Table 7. Density of dislocations introduced by twisting derived from equation (3)

Specimen	$\Delta \sigma$	$\Delta ho = (\Delta \sigma/A)^2$
117	$5.7 imes 10^7 \mathrm{dynes/cm^2}$	$2.2 imes 10^8 m /cm^2$
80	2.4×10^{7}	3.8×10^{7}
91A	4.3×10^{7}	1.3×10^8

Table 8. Density of dislocations present before twisting derived from equation (3)

Specimen	σ	$\rho = (\sigma/A)^2$
117	$1.9 \times 10^8 \; m dynes/cm^2$ 7.5×10^7	$2.3 imes 10^9 m /cm^3$
80	7.5×10^{7}	3.8×10^8
91A	9.2×10^{7}	5.6×10^{8}

Geometrically, tensile hardening appears likely to be mainly by the pile-up mechanism so that these dislocation densities should probably be divided by \sim 5.

Equation (5) may be rewritten as

$$\sigma + \Delta \sigma = A(\rho + \Delta \rho)^{\frac{1}{2}} = A \rho^{\frac{1}{2}} (1 + \frac{1}{2} \theta / \mathbf{b} \rho)$$
 for
$$\Delta \rho = \theta / \mathbf{b} \ll \rho$$
 i.e.
$$\Delta \sigma = \frac{A \theta}{2 \mathbf{b} \rho^{\frac{1}{2}}}$$

$$\therefore \Delta \sigma / \sigma = \frac{A \theta}{2 \mathbf{b} \rho^{\frac{1}{2}}} \times \frac{1}{A \rho^{\frac{1}{2}}} = \frac{\theta}{2 \mathbf{b} \rho}$$
 (6)

If $\Delta \sigma$ is due to forest hardening and σ to pile-up hardening, equation (6) would become

$$\frac{\Delta\sigma}{\sigma}\!\cong\!\frac{\theta}{10\mathbf{b}\rho}$$

i.e. if the dislocation densities of Tables 8 and 9 are reduced owing to the fact that the pile-up constant, A, is greater than the assumed value for A, they are reduced by the same factor. Assuming equation (3) to govern tensile hardening, the discrepancy between the results of Tables 8 and 9 must mean that tensile and torsional hardening cannot be added in accordance with equation (5). This in turn implies that the two hardening mechanisms are different, i.e. presumably tensile hardening occurs by means of the pile-up mechanism while torsional hardening of the tensile slip plane is by the forest mechanism.

It is apparent from Tables 7 and 8 that $\Delta \sigma$ cannot be simply proportional to $\theta^{\frac{1}{2}}$ as equations 2 and 4 together indicate. The plastic history of the specimen has to be taken into account. The experimental relationship beyond the peak of Fig. 15 is in fact

$$\Delta \sigma / \sigma \propto \theta$$
 (7)

Table 9. Densities of dislocations present before twisting derived from equation (6)

Specimen 117	$\Delta\sigma/\sigma$	θ_c	$\rho = \frac{\theta}{2\mathbf{b}} \frac{\sigma}{\Delta \sigma}$		
117	~0.29	3.0°	$3.0 \times 10^6 \mathrm{/cm^3}$		
80	~ 0.38	5.7°	$4.3 imes 10^6$		
91A	~ 0.46	9.4°	$5.9 imes 10^6$		

 $\Delta \sigma \propto \theta^{\frac{1}{2}}$ is not obeyed because equation (2) does not hold for work hardened specimens as discussed in connection with Tables 6 and 7. Equation (7) can be qualitatively explained on either of the ideas discussed in relation to the discrepancy between the results of Tables 6 and 7. In particular work hardening (increasing σ) makes deformation more 'turbulent' and this may markedly increase the number of dislocations introduced by a given twist above the number given by equation (2). Alternatively, since with increasing work hardening the distance which the dislocations can move inward from the surface decreases, the number of dislocations required for a given twist may increase rapidly with prestrain and hence with σ . This idea has experimental support from the results on transient hardening. Both viewpoints indicate that $\Delta \sigma$ should increase with σ as required by equation (7).

In section 3.6 a number of qualitative ideas were put forward in discussing the work hardening rate changes following twisting. These can now be interpreted in terms of dislocation theory.

Small twists during easy glide lead to increases of the slope of the stress-strain curve. Twisting results in either the formation of sessiles or the formation of a Cottrell forest, or both. This changes the mechanism and rate of hardening from those of easy glide to those of rapid linear hardening, i.e. it changes Stage I to Stage II hardening.(18) In other cases these latter mechanisms are already operative and no change of work hardening rate is produced by twisting. Larger twists after larger prestrains generally result in decreases of the work hardening rate. The steady fall in the slope of the stress-strain curve in Stage III, or parabolic hardening, is due to cross-slip resulting in annihilation of dislocations in pile-ups. (14,18) decrease in slope could, therefore, be due to twisting facilitating subsequent cross slip. It is not obvious, however, why this should be so.

Two observations appear difficult to fit into Seeger's picture⁽¹⁸⁾ of work hardening. Firstly, Fig. 18 shows a case in which accommodation of plastic twisting by moving inwards dislocations with Burgers vectors having components parallel to the specimen axis resulted in a decrease of slope and a change of shape from parabolic to linear. On Seeger's present picture a change from parabolic to linear or Stage III to Stage II hardening implies the stopping of cross-slip, which seems very difficult to understand. If this did occur, however, it should lead to an increase of slope, contrary to observation. Secondly, the shape of the load–extension curves of the specimens of Fig. 15 changed from linear to parabolic when the torsional

dislocation pile-ups escaped through the oxide skin. This seems to imply that on tensile reloading after a twist which does not rupture the oxide skin no tensile cross-slip occurs and linear (Stage II) hardening results. But on tensile reloading after a larger twist when half the 'trees' of the forest introduced have escaped through the skin, tensile cross-slip occurs and parabolic hardening results. There appears to be no reason why this should be so.

5. CONCLUSIONS

Geometrically, it appears probable that tensile hardening occurs largely by the pile-up mechanism and torsional hardening by the forest mechanism. The results of Tables 8 and 9 indicate that the hardening in the two cases is due to different mechanisms. The quantitative discrepancies between theory and experiment have been shown to be resolvable. Theoretical and experimental work(18) indicate that hardening due to pile-up and forest mechanisms should be of comparable importance in aluminium at room temperature. This is in agreement with the fact that torsion leads to increases in tensile flow stress comparable with the pre-existing flow stress. The present results are, therefore, all consistent with the idea that tensile hardening occurs mainly by the pile-up mechanism and torsional hardening occurs mainly by the forest mechanism. The sessile formation which occurs is probably mainly responsible for the continuing effects due to torsion. However, certain of the effects of twisting on the tensile work hardening rate do not fit in with Seeger's account(18) of work hardening.

ACKNOWLEDGMENTS

The present work was started and the initial lines of attack were suggested by Dr. A. H. Cottrell. The experimental work was done in the Metallurgy Department of the University of Birmingham. For the hospitality of the Department thanks are due to Professors A. J. Murphy and G. V. Raynor. During this period financial support was provided first by a D.S.I.R. Research Contract and later by a University of Birmingham Research Fellowship. For helpful discussions thanks are due especially to Drs. R. W. Cahn, J. D. Eshelby, A. Seeger and to Professor F. R. N. Nabarro.

REFERENCES

- 1. W. M. LOMER, Phil. Mag. 42, 1327 (1951).
- A. H. COTTRELL, Phil. Mag. 43, 645 (1952).
 G. I. TAYLOR, Proc. Roy. Soc. A145, 362 (1934).
- N. F. Mott, Phil. Mag. 43, 1131 (1952).
 R. D. Heidenreich and W. Shockley, Report of a Conference on the Strength of Solids. Physical Society, London (1948).
- A. H. COTTRELL, J. Mech. Phys. Solids 1, 53 (1952).
 F. SEITZ, Advanc. Phys. 1, 43 (1952).
 A. SEEGER, Phil. Mag. 46, 1194 (1955).
- R. MADDIN and A. H. COTTRELL, Proc. Roy. Soc. A233,
- 17 (1955). 10. M. A. ADAMS and A. H. COTTRELL, Phil. Mag. 46, 1187 (1955).
- 11. M. J. MAKIN, Phil. Mag. 3, 309 (1958).
- 12. R. J. STOKES and A. H. COTTRELL, Acta Met. 2, 341 (1954). 13. A. H. COTTRELL and R. J. STOKES, Proc. Roy. Soc. A233, 17 (1955).
- 14. A. Kelly, Phil. Mag. 1, 835 (1956).
- 15. J. Washburn, J. Metals, N.Y. 7, 675 (1955).
- 16. H. W. PAXTON and A. H. COTTRELL, Acta Met. 2, 3 (1954). 17. A. SEEGER, J. DIEHL, S. MADER and H. REBSTOCK,
- Phil. Mag. 2, 1 (1957).
 18. A. Seeger, Dislocations and Mechanical Properties of Crystals, p. 243. Wiley, New York (1957).
- Z. S. Basinski, Report of Second Symposium on Melting, Diffusion, and Related Topics, N.R.C. Res. News, p. 68 (Feb. 1958).
- 20. T. S. NOGGLE, Rev. Sci. Instrum. 24, 184 (1953).
- 21. C. S. BARRETT, The Structure of Metals, Second Edn. pp. 185–190. McGraw-Hill, London (1953). F. D. Rosi and C. H. Mathewson, Trans. Amer. Inst.
- Min. (Metall.) Engrs. 188, 1159 (1950). 23. A. H. COTTRELL and V. AYETKIN, J. Inst. Met. 77, 389
- (1950).
- 24. J. D. Lubahn, J. Metals, N.Y. 7, 1031 (1955).
- H. WILMAN, Nature, Lond. 165, 321 (1950).
- 26. F. C. Frank, Report of a Conference on Defects in Crystalline Solids. Physical Society, London (1955)

VOI

- 27. J. M. HEDGES and J. W. MITCHELL, Phil. Mag. 44, 223 (1953).
- S. AMELINCKX, Phil. Mag. 1, 269 (1956)
- 29. T. Suzuki and R. Imura, Report of a Conference on Defects
- in Crystalline Solids. Physical Society, London (1955). 30. M. J. Whelan, P. B. Hirsch, R. W. Horne and W. Bollman, Proc. Roy. Soc. A240, 524 (1957).
- 31. F. C. Frank, Report of a Conference on the Strength of Solids. Physical Society, London (1948).
 32. J. H. VAN DER MERWE, Proc. Phys. Soc. A63, 616 (1950).
- 33. N. Brown, Trans. Amer. Inst. Min. (Metall.) Engrs. 203, 134 (1955).
- 34 E. H. EDWARDS and J. WASHBURN, J. Metals, N.Y. 6, 1239 (1954).
- W. C. Dash, J. Appl. Phys. 27, 1193 (1956).
 J. D. Eshelby, J. Appl. Phys. 24, 176 (1953).
 H. J. Gough, S. J. Wright and D. Hanson, J. Inst.
- Met. 36, 173 (1926).
- J. D. ESHELBY, private communication.
 C. S. BARRETT, P. M. AZIZ and I. MARKSON, J. Metals, N.Y. 5, 1655 (1953).
- 40. G. L. Kehl, The Principles of Metallographic Practice, Second Edn., McGraw-Hill, New York, p. 380 (1943).
- 41. R. W. CAHN, private communication.
- 42. B. A. Bilby, Research, Lond. 387 (1952). A. H. COTTRELL, Dislocations and Plastic Flow in Crystals. Oxford University Press (1953).
- 44. F. R. N. Nabarro, private communication.
- 45. W. Boas, Dislocations and Mechanical Properties of Crystals, Wiley, New York (1958).

THE FLOW STRESS OF IRON AND ITS DEPENDENCE ON IMPURITIES*

G. SCHOECK† and A. SEEGER‡

In the stress field of a dislocation an ordering of solute interstitials takes place. By this Snoek-effect dislocations are locked in times which are too short to allow the formation of Cottrell atmospheres. The locking energy and the stress to free the dislocation is calculated for a screw dislocation in α -iron. If the dislocation moves, a frictional force is caused by the Snoek-effect and its magnitude is calculated. It is suggested that this mechanism determines the flow stress of α -iron above room temperature and experimental results are discussed which support this point of view.

LA TENSION DE CISAILLEMENT DU FER EN RELATION AVEC LA TENEUR EN IMPURETES

Dans le champ de tension d'une dislocation, les atomes interstitiels dissous sont ordonnés. Par cet effet (effet de Snoek), les dislocations sont bloquées en des temps trop courts pour permettre la formation d'atmosphères de Cottrell. Les auteurs déterminent l'énergie de blocage et la tension nécessaire pour libérer une dislocation-vis dans le fer α . Ils calculent également la force de friction due à l'effet Snoeck, lorsque la dislocation se meut. Ils pensent que ce mécanisme gouverne la tension de glissement du fer α au-dessus de la temperature ambiante, et ils discutent de résultats expérimentaux qui sont en accord avec ce point de vue.

DIE FLIESSPANNUNG VON EISEN UND IHRE ABHAENGIGKEIT VOM VERUNREINIGUNGSGEHALT

Im Spannungsfeld einer Versetzung werden Einlagerungsatome in bestimmter Weise geordnet. Durch diesen "Snoek-Effekt" werden die Versetzungen verankert in Zeiträumen, die zu kurz sind um die Bildung von "Cottrell-Wolken" zu erlauben. Die Verankerungsenergie und die notwendige Spannung für das Losreissen der Versetzungen werden berechnet am Beispiel einer Schraubenve setzung in α -Eisen. Wenn sich die Versetzung bewegt, resultiert eine Reibungskraft infolge des Snoek-Effekts, deren Grösse berechnet wird. Es wird vorgeschlagen, dass die Fliesspannung in α -Eisen oberhalb Raumtemperatur durch diesen Mechanismus bestimmt wird, und Experimente werden diskutiert, die diese Auffassung unterstützen.

1. INTRODUCTION

1959

It has been recognized for a long time that the yield phenomenon in iron and other b.c.c. metals is closely connected with the presence of impurity atoms such as carbon or nitrogen in interstitial positions. Cottrell and his co-workers (1,2) were first to point out that the existence of a yield-point might be related to the locking of dislocations by solute atoms. The yield phenomenon was attributed to the tearing-off of dislocations from impurity atmospheres by the applied stress. This locking should be especially pronounced if the solute atoms cause large lattice distortions, which is the case for interstitial atoms. Although the locking of dislocations by an impurity atmosphere certainly plays an important role in the yield phenomenon the total process of yielding is much more complex and not yet completely understood. In order to indicate some of the present difficulties we mention that the lower yield stress of iron is nearly temperature

independent between room temperature and 200°C , (3) whereas the concept of the "tearing-off" of dislocations from impurity atmospheres inevitably leads to a strongly temperature dependent yield stress. Difficulties also arise in the interpretation of delay time experiments as shown by the discussions at the Lake Placid Conference. (4)

The locking of dislocations can take place if solute atoms diffuse in the energy gradient of the dislocation stress field towards the dislocation. In his original treatment of the formation of an atmosphere around dislocations. Cottrell took the lattice distortion around a solute atom to be that due to a center of dilatation. (5) This gave rise to an interaction with edge dislocations only, since the lattice distortion around screw dislocations is free of dilatation if nonlinear elastic effects are neglected. It was however pointed out by Nabarro (6) that due to the tetragonal distortion around an interstitial carbon (or nitrogen) atom in b.c.c. metals there will also be an interaction with the shear stresses around a screw dislocation. As was shown by Cochardt et al. (7) this will lead to the formation of an atmosphere around screw

^{*} Received September 18, 1958.

[†] Westinghouse Research Laboratories, Pittsburgh 35, Pennsylvania.

[†] Max-Plank-Institut für Metallforschung, Stuttgart, Germany.

dislocations too. On account of this the original Cottrell treatment has to be modified considerably.

Let us consider a b.c.c. lattice in which the concentration of interstitial atoms is low enough to keep the interaction between interstitials small. Then there exist three types of interstitial sites corresponding to the three directions of tetragonality and if no applied stress is acting the three kinds of interstitial sites will be occupied by the same fraction of interstitial atoms. If, however, an applied (non-hydrostatic) stress is acting the energy of interaction between the stress and the interstitials will in general depend on the type of site occupied. Hence at temperatures where the interstitials can diffuse, an applied stress will cause a redistribution in the population of the different lattice sites and the population of the sites with lower energy will increase, whereas that of the sites with higher energy will decrease. This process is known as the Snoek effect(8) and it gives rise to a well established internal friction peak.

A similar redistribution of interstitials on different lattice sites will take place in the stress field of a dislocation. By such a process the energy of the system is lowered and therefore the dislocation locked. But whereas locking due to atmosphere formation needs diffusion of interstitials over long distances, the locking due to the Snoek effect is accomplished merely by atomic rearrangement between neighboring lattice sites and therefore takes place in times which are orders of magnitude smaller.

The locking due to this local atomic rearrangement and its consequences in regard to microcreep and internal friction have already been considered by one of us. (9) It is the purpose of this paper to give a more detailed calculation of the effect and to compare the results with recent experiments. In the following section the energy will be calculated which is released by the Snoek effect in the stress field of a dislocation and the stress to unlock the dislocation will be determined. In the third section the modifications are considered which will arise if the dislocation line is moving. In the last section we will discuss some general features of the flow stress of iron and their interpretation will be given in terms of the dislocation mechanism discussed in Sections 2 and 3.

2. LOCKING BY AN ORDERED ATMOSPHERE

Let us consider a screw dislocation in α -iron containing a small homogeneous concentration of carbon atoms in interstitial solid solution. The carbon atoms are located in the center of the [100], [010] or [001] edge of the unit cell or in equivalent positions.

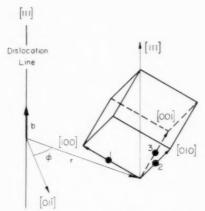


Fig. 1. Orientational relationships of interstitial carbon atoms in the neighborhood of a screw dislocation in a b.c.c. lattice.

These positions may be denoted by site number 1, 2 or 3, respectively (Fig. 1). The dislocation line is in the [111] direction. Due to the lattice distortion around the interstitials there is an elastic interaction with the dislocation line and the interaction energy of an atom in site i is given by $^{(7)}$

$$u_i = \frac{A}{r} \cos{[\varphi - (i-1)2\pi/3]} \qquad i = 1, 2, 3 \quad (1)$$

195

where r is the radius vector from the dislocation line to the solute atom, φ the angle between the radius vector and the [01I] direction. The interaction constant A for carbon in α -iron has a value of $A=1.84\times 10^{-20}$ dyn cm².* The interaction potential for different sites is shown in Fig. A1, and is discussed more fully in Appendix A.† According to this interaction potential there are 3 angular sectors around a screw dislocation where the interstitials stay preferentially in position 1, 2 or 3, respectively. If we introduce a screw dislocation into the crystal, and

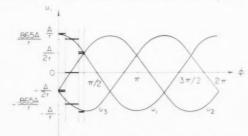


Fig. A1. The interaction potential u_i of a single carbon atom with a screw dislocation and the average values taken to evaluate the total interaction energy U_0 .

† Appendices A and B will be supplied by the Authors on application.

^{*} We are indebted to Dr. E. Kröner for pointing out that the value of A given in reference (7) is too large by about 50 per cent, since the shear modulus of a polycrystalline sample has been used instead of the anisotropic modulus $\frac{1}{2}(c_{11} - c_{12})$.

have it rest for a time interval which is too short for long range diffusion to occur, the total concentration c_0 of interstitials will remain constant and homogeneous throughout the crystal. The population of the different sites will change, however. When thermal equilibrium with respect to the population of different sites is reached the equilibrium concentration \bar{c}_i in site i as given by statistical thermodynamics will be

$$\hat{c}_i = c_0 \frac{e^{-u_i/kT}}{\sum e^{-u_i/kT}} \qquad i = 1, 2, 3$$
 (2)

Due to this local ordering of interstitials the line energy of the dislocation is decreased by an amount U_0 compared with a dislocation surrounded by randomly arranged interstitials. The decrease in energy U_0 is the sum of all interaction energies between individual interstitial atoms and dislocation and hence given by

$$U_0 = \int_0^{2\pi} \int_0^L \Sigma_i \, \tilde{c}_i u_i r \, dr \, d\varphi \tag{3}$$

where L is the usual cut-off radius of the order of 10^{-4} cm which takes care of the cancellation of the stress field by neighboring dislocations. The integration is carried out in the Appendix A by dividing in different angular sectors and taking the average values of u_i and \hat{c}_i , the error involved being less than a few per cent. The result is

$$U_0 = 2\pi \frac{p}{a^3} \frac{A^2}{kT} \left[1.1 + \log \frac{LkT}{A} \right] \tag{4}$$

provided $L\gg A/kT$. Here a denotes the lattice constant and $p=\frac{1}{2}c_0a^3$ the atomic fraction of interstitials.

The temperature dependence of the elastic constants in A^2 is to a large extent balanced by the temperature dependence in the logarithmic term. We may therefore take both A and log T at room temperature; with $L=10^{-4}\,\mathrm{cm}$ we obtain to a good approximation for all temperatures

$$U_0 = K \frac{p}{a^3} \frac{A^2}{kT} \tag{5}$$

with K = 41 for carbon in α -iron.

1959

 U_0 as obtained in equation (5) represents a lowering of the line energy of a screw dislocation surrounded by an ordered interstitial distribution compared with a dislocation surrounded by a random distribution of interstitials. In order to move the dislocation we have now to apply a certain force since we must supply energy to bring the dislocation into a region where the interstitials, are randomly distributed. A detailed calculation of this force will be made in the next

section. Here we may use a simple physical argument: Due to the thermal energy the region where the ordering of interstitials takes place has a certain radius R. It is given by the distance where the interaction energy u_i between dislocation and interstitials has the same value as the thermal energy kT. Outside this region the thermal energy will effectually randomize the distribution whereas inside of R the atmosphere will be strongly ordered. If we take the maximum value of the interaction energy u_i from equation (1) we arrive at a "radius" of the atmosphere given by

$$R = \frac{A}{kT} \tag{6}$$

Now the force per unit length on a dislocation due to a shear stress τ is τb , where $b=\frac{1}{2}\sqrt{3}a$ is the Burger's vector of the dislocation. If we therefore keep the distribution of interstitials fixed and move the dislocation out of its potential valley of depth U_0 and half-width R the stress necessary is given by the equation

$$\tau b = \frac{1}{2} \frac{U_0}{R} \tag{7}$$

In combining equation (5) to (7) we obtain then finally

$$\tau = 20.5 \frac{A}{ha^3} p \tag{8}$$

An important result in equation (8) is that the stress is proportional to the atomic concentration and independent of the temperature. That is due to the fact that U^0 and R in equation (7) are both inversely proportional to the temperature.

3. DISTRIBUTION AROUND MOVING DISLOCATION

The calculations of the previous section apply only if the dislocation is accelerated from rest. If the dislocation is moving with a constant velocity a a dynamic equilibrium will be reached where the dislocations lowers its line energy by an amount $U(\alpha)$ which is smaller than U_0 because the equilibrium concentration of equation (2) will not be reached. A dragging force on the moving dislocation will result because energy is dissipated during the ordering which takes place when a dislocation passes through a certain lattice region. This dragging force vanishes only at infinitely low velocities where the ordering always reaches thermodynamic equilibrium or at infinitely high velocities where no redistribution takes place. In order to calculate this dragging force we have first to obtain the rate of atomic redistribution

VOL

7

195

around a stationary dislocation and from this we then will get the distribution during steady state movement.

Let us consider a volume element near a dislocation. As previously, we denote the total concentration of interstitials by c_0 and the instantaneous concentration on site i by c_i . Let ω_{ik} be the rate of transition of an interstitial from site i to site k. Then the rate of change of c_i is given by

$$\frac{\partial c_i}{\partial t} = \sum_{k} \left(-\omega_{ik} c_i + \omega_{ki} c_k \right) \qquad \begin{array}{c} i, k = 1, 2, 3 \\ i \neq k \end{array} \tag{9}$$

If the interaction energy u_i of the interstitial with the dislocation is small compared with its activation energy of diffusion, ω_{ik} can be expressed by

$$\omega_{ik} = \beta v_0 \exp\left(-\frac{\Delta G - u_i}{kT}\right) = \beta v \exp\left(\frac{u_i}{kT}\right) = \beta \omega_i. \tag{10}$$

Here r_0 is the vibrational frequency of the interstitial, ΔG is the free energy of activation for diffusion of the interstitial and r the jump frequency of the interstitial in an unstressed lattice. β is a geometrical factor which depends on the geometry of vacant interstitial sites around an interstitial atom. If we allow only jumps to the nearest or next nearest neighbored sites as we will assume further on, then $\beta=\frac{1}{2}$. Equation (10) implies that the rate with which the interstitials leave a certain site depends only on the site occupied before the jump, and therefore in the final equation occurs only ω_i which is the rate interstitials jump out of site i.

The system given by equation (9) of three linear differential equations could be solved generally and would give the local concentration c_i of interstitials in position i as a function of time. For the problem under consideration we have, however, to know the local interaction energy density ρ and how ρ changes with time. These quantities are given by

$$\rho = \sum_{i} u_i c_i \tag{11a}$$

$$\frac{\partial \rho}{\partial t} = \sum_{i} u_{i} \frac{\partial c_{i}}{\partial t}$$
 (11b)

where $\partial c_i/\partial t$ is given by equation (9).

In order to obtain an equation for ρ we make some simplifying assumptions with respect to the interaction energy u_i given by equation (1). Since the distribution has a threefold symmetry around the screw dislocation we consider only the sector $\frac{2\pi}{3} \leq \varphi \leq \frac{4\pi}{3}$ in which the interstitial in position 1 has the lowest energy. We use here the correct

potential for u_1 but replace u_2 and u_3 by their mean value. Due to the special form of equation (1) this means

$$u_2 = u_3 = -\frac{u_1}{2} \tag{12}$$

As shown in Appendix B we obtain then in sector 1 (and therefore with cyclic permutation of the indices in each sector)

$$\frac{\partial \rho}{\partial t} = -\left(\omega_1 + \frac{1}{2}\omega_2\right)(\rho - \rho_0) \tag{13}$$

Here ρ is the actual energy density and ρ_0 the energy density if the population in the different sites has reached thermal equilibrium. In order to obtain equation (13) we actually have transformed equation (11b) to normal coordinates by use of equation (12).

After obtaining ρ we get the total interaction energy of the dislocation with its atmosphere U merely by integrating over the volume around the dislocation, since by definition

$$U = \int_0^{2\pi} \int_0^L \rho r \, dr \, d\varphi \tag{14}$$

Actually we can perform this integration on both sides of the differential equation (13). Now we note that the frequency factor

$$\omega_1 + \frac{1}{2}\omega_2 = (e^{-R/r} + \frac{1}{2} e^{R/2r})v$$

is only a weak function of the distance r from the dislocation line for large values of r and varies strongly only in a region very close to the dislocation which makes a small contribution to the integral. We may therefore replace it by its mean value $\tilde{v} = 3/2r$ in order to perform the integration. Then we arrive at

$$\frac{\partial U}{\partial t} = -\tilde{\mathbf{r}}(U - U_0) \tag{15}$$

where U is the instantaneous energy of the dislocation and $U_{\mathbf{0}}$ the energy in thermal equilibrium given by equation (4).

Equation (15) applies for a dislocation at a fixed position with an arbitrary concentration of interstitials in different sites (however with homogeneous total concentration) around the dislocation line. It states that the rate of change of the line energy is proportional to the deviation from the equilibrium line energy U_0 .

We consider now a dislocation moving along a straight line which may be chosen as x-coordinate. Due to the movement the atmosphere of ordered interstitials will become asymmetric. The center of the

ordered atmosphere will lag behind the dislocation and therefore it has to move against an energy gradient. The line energy U of the dislocation will depend on its position x as well as on time t. If however the dislocation is moving with constant velocity α and if a steady state is reached then the energy U will be constant or

$$\frac{dU}{dt} = \alpha \frac{\partial U}{\partial x} + \frac{\partial U}{\partial t} = 0 \tag{16}$$

Here $\partial U/\partial x$ is the change in dislocation energy due to change in position and $\partial U/\partial t$ the change due to the thermodynamic ordering which is going on constantly.

The force F required to move the dislocation is defined as

$$F = -\frac{\partial U}{\partial x} \tag{17}$$

However, in steady state we obtain according to equation (16) also

$$F = \frac{1}{\alpha} \frac{\partial U}{\partial t} \tag{18}$$

and since we are able to obtain an equation for $\partial U/\partial t$ we will use equation (18) to calculate F.

For the further considerations we have now to investigate how the carbon distribution within a certain region in the crystal is affected by a dislocation at a large distance from this region. For this purpose we chose a linear coordinate x with origin x=0 in the center of this region and describe the region by a radius vector r with origin at x=0. The dislocation may move towards the origin with constant velocity α starting at $x=-\infty$ and may be for the moment at a distance x. For our purpose we can characterize the carbon distribution around the origin by the energy a fictitious dislocation at the origin would acquire. Therefore we define an energy density α corresponding to equation (11a) by

$$\sigma = \sum_{i} u_i(r)c_i(r-x) \tag{19}$$

where $c_i(r-x)$ represents the concentration of interstitials at point r modified by a dislocation at the point x, and u_i the interaction energy of an interstitial at point r with a fictitious dislocation at x=0. If x is fixed the change in σ is given corresponding to equation (13) by

$$\frac{\partial \sigma(r,t)}{\partial t} = -\hat{r}[\sigma(r,t) - \sigma_0(r,x)] \tag{20}$$

We define further a line energy V(t) corresponding to equation (14)

$$V(t) = \int_0^{2\pi} \int_0^L \sigma(r, t) r \, dr \, d\varphi \tag{21}$$

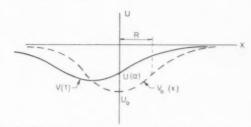


Fig. 2. Dislocation energy in a Snoek-atmosphere. $V_0(x)$ represents the energy a dislocation at x would have in the atmosphere which got ordered by a dislocation resting at the origin. V(t) represents the situation for a dislocation moving in steady state with velocity α .

by integrating σ around the origin in a cylindric volume with axis parallel to the dislocation line. Physically V(t) is the energy a fictitious dislocation at the origin would acquire in the field of impurity atoms ordered by a dislocation line at x. Schematically the situation is shown in Fig. 2. If we perform this integration on equation (20) we obtain

$$\frac{\partial V(t)}{\partial t} = -\tilde{v}[V(t) - V_0(x)] \tag{22}$$

If x=0, equation (22) is identical with equation (15) and the energy V becomes the line energy U of the dislocation. According to the definition of V the term $V_0(x)$ can therefore be expressed quite generally as

$$V_0(x) = U_0 g(x) \tag{23}$$

with
$$g(0) = 1$$
 (23a)

and
$$g(\pm \infty) = 0$$
 (23b)

 U_0 is the equilibrium energy given by equation (3). The boundary condition (23b) for g(x) states that the interaction energy in the region around the origin vanishes if the dislocation is at infinite distance. In other words this means that at infinite distance from the dislocation line the atmosphere is completely random.

For a dislocation moving with constant velocity α we set $x = \alpha t$ thereby assuming that at t = 0 the dislocation passes through the origin x = 0. We obtain then as the differential equation for V

$$\frac{\partial V}{\partial t} = -\hat{\mathbf{r}}[V - U_0 g(\alpha t)] \tag{24}$$

The solution of this equation with the appropriate boundary condition V=0 at $t=-\infty$ is

$$V(t) = \tilde{v} U_0 e^{-\tilde{v}t} \int_{-\infty}^{t} g(\alpha t) e^{\tilde{v}t} dt \qquad (25)$$

Taking the value V(0) at t=0 when the dislocation passes through the origin gives the energy $U(\alpha)$ of the

VOL.

moving dislocation line (see Fig. 2). To obtain the driving force we take $\partial V/\partial t$ which at t=0 is equivalent to $\partial U/\partial t$. From equation (18b) we then obtain finally for the force

$$F(\alpha) = \frac{1}{\alpha} \frac{\partial V}{\partial t} \Big|_{t=0} = \frac{U_0 \tilde{r}}{\alpha} \left[1 - \tilde{r} \int_0^\infty g(\alpha t) e^{-\tilde{r}t} dt \right]$$
 (26)

By using the theorems of Laplace transformations (10) it can be generally shown that with the boundary conditions equation (23a, b) the force $F(\alpha)$ vanishes at the velocities $\alpha = 0$ and $\alpha = \infty$, a result which has been anticipated by physical reasoning.

If we want now the explicit expression for $F(\alpha)$ and especially its maximum value we have to know the analytical form for g(x) defined by equation (23). This function cannot be exactly expressed in closed form. However, from the physical meaning of $V_0(x) = U_0 g(x)$ we can conclude that g(x) has a form similar to

$$g(x) = e^{-(x^2/R^2)}$$
 (27a)

or $g(x) = \frac{R^2}{R^2 + x^2}$ (27b)

where R is the radius of the ordered atmosphere defined in equation (6). For the further considerations we use equation (27a). The final result does not sensitively depend on the exact form of g(x) and would only differ by a numerical factor close to one if we use equation (27b) instead. Integration of equation (26) gives then

$$F(\alpha) = \frac{\bar{r}U_0}{\alpha} \left[1 - \frac{\bar{r}\sqrt{\pi}R}{2\alpha} \left(1 - \phi \left(\frac{\bar{r}R}{2\alpha} \right) \right) \exp \left(\frac{\bar{r}R}{2\alpha} \right)^2 \right]$$
 (28)

where $\phi(x)$ is the error integral. The function $F(\alpha)$ is

plotted in Fig. 3. The force has a maximum at a velocity

$$\alpha_0 = \frac{2}{3}\bar{\nu}R = \nu R \tag{29}$$

or, in other words, the maximum friction occurs when the dislocation moves over the half-width R of the distribution in the relaxation time $1/\nu$ of the atmosphere. The maximum value of the force is

$$F_0 = \frac{1}{2} \frac{U_0}{R} \tag{30}$$

VOI

195

which is the same as estimated earlier in equation (7). This means that if the applied stress τ is smaller than $\tau_0 = F_0/b$ serew dislocations can move only with velocity α smaller than α_0 . For iron at room temperature α_0 is of the order of 20 atomic distances per second. This would correspond to a strain rate of the order $10^{-6}~{\rm sec}^{-1}$, which is a slow creep deformation if we assume a reasonable dislocation density of 10^8 . Only if the applied stress τ exceeds τ_0 can the dislocations move with a speed larger than α_0 and then their velocity will be limited by other factors.

The calculation of the critical flow stress in the present and in the preceding section has been made for a screw dislocation but the results should apply also in a similar way to edge dislocations, since in the stress field of an edge dislocation an interstitial atom in different lattice positions has a different interaction energy, too.⁽⁷⁾ The difference in interaction energy between different sites is however smaller around edge dislocations. Hence the Snoek-effect should be less pronounced and therefore the critical flow stress due to this effect should be smaller.

THE FLOW STRESS OF IRON AND ITS INTERPRETATION

We shall now discuss how the flow stress of iron is influenced by the Snoek-effect occurring in the stress

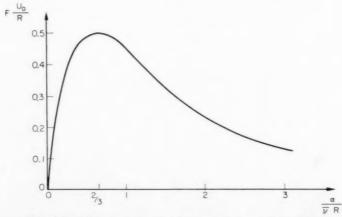


Fig. 3. The force F to move a dislocation in steady state as a function of the dislocation velocity α .

field around dislocations as calculated in the previous sections. The treatment here follows in part a discussion given elsewhere by one of the authors. (11)

The typical features of the temperature dependence of the yield stress τ_0 of iron are shown in Fig. 4. At low temperatures (region A) the critical shear stress is strongly temperature dependent. After suitable heat-treatment a yield-phenomenon can be observed. Region B, in which the yield stress is almost temperature independent, extends from room temperature up to at least 200°C. $^{(3,12)}$ In this region the yield phenomenon is observed in much the same way as in stage I. At higher temperatures, around 200°C, serrated yielding and jerky flow occur. In region C the yield-stress drops considerably below the level of stage B. $^{(13)}$ Very little quantitative data on this region are available, however.

In region A the temperature dependence and variation with carbon content of the yield stress are qualitatively what one would expect on the basis of the theory of locking by impurity clouds as given by Cottrell and Bilby⁽²⁾ and by Fisher⁽¹⁴⁾. There is striking disagreement, however, between these theories and experiments in stage B, in particular with regard to the temperature dependence of the critical shear stress.

1959

The fact that the critical shear stress τ_0 is temperature independent in region B cannot be explained by assuming that in this region the long range elastic interaction between dislocations determines τ_0 . This is the case in pure metals and generally also in relatively impure f.c.c. metals where the interaction between (substitutional) impurity atoms and dislocations is small. However in b.c.c. iron there is strong evidence that even in region B carbon atoms contribute in an essential way to the yield stress: (1) τ_0 depends on the carbon content (for details see below); (2) it is too large to be explained by dislocation interaction; (3) the yield phenomenon or serrated yielding, both of which are ascribed to the

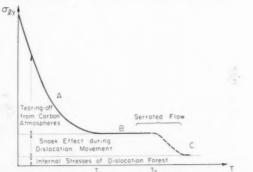


Fig. 4. Schematic temperature dependence of the flow stress in iron containing carbon or nitrogen.

presence of impurity atoms, can be observed in region B or in the transition region between B and C. We are of the opinion that the flow stress in region B is essentially determined by the mechanisms discussed in Sections 2 and 3.

The discussions of Sections 2 and 3 refer to the behavior of isolated dislocations. The effects described there should influence the micro-strain observed before the upper yield stress is reached. However, the experimental evidence on the micro-strain region is rather limited. Although the details of the yield phenomenon and of the nucleation of Luders bands are not yet completely understood, it seems plausible that the physical processes controlling the lower yield stress are much the same as those contributing to the micro-strain before yielding. We shall therefore base our discussion on the lower yield stress, on which considerably more experimental data are available.

First a comparison with experiments shows that the flow stress in iron single crystals above room temperature is of the magnitude we would expect from the theory. Between room temperature and 100°C Allen et al.(12) obtained a resolved shear stress at the lower yield point of $\tau_{ly} = 3.2 \times 10^8 \text{ dyn/cm}^2$ at a concentration of carbon and nitrogen of $p \approx 2 \times 10^{-4}$, Vogel and Brick (3) obtained between room temperature and 200°C a value of $\tau_{ly} = 2.8 \times 10^8 \, \mathrm{dyn/cm^2}$ and from the heat treatment of their samples one can conclude that their carbon concentration was also of the order of $p \approx 2 \times 10^{-4}$. With this value of p the value from equation (9) becomes $\tau_0 = 1.3 \times 10^8$. dyn/ cm2 Now we have to keep in mind that the friction stress due to the Snoek effect is additive to each other stress opposing the dislocation movement. Since considerable plastic flow can only occur if moving dislocations overcome the internal stresses τ_G of other dislocations in the crystal we expect

$$\tau_{ly} = \tau_0 + \tau_G \tag{31}$$

as schematically shown in Fig. 4.

Since $\tau_G \approx \frac{1}{5}b\sqrt{N}^{(15)}$, where G is the shear modulus, b the Burgers vector and N the dislocation density, we obtain with a reasonable value of $N \approx 10^8 \text{ cm}^{-2}$, for the internal stress $\tau_G \approx 1 \times 10^8 \text{ dyn/cm}^2$. Adding up τ_0 and τ_G gives a value which is of the magnitude of the observed yield stress τ_{ly} and except for the temperature dependence of the elastic constants it is temperature independent.

Another strong indication that the flow stress in iron is determined by the Snoek effect is given by the experiments of Heslop and Petch⁽¹⁶⁾. Fig. 5 taken from their work shows the lower yield point σ_{ly} of iron (extrapolated to infinite grain size) as a function

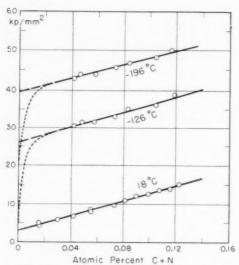


Fig. 5. The lower yield stress of α -iron as a function of the concentration of carbon and nitrogen in solid solution. After Heslop and Petch. (16)

of carbon and nitrogen content p in solid solution (also checked by internal friction measurements) for three different temperatures. The characteristic feature of Fig. 5 is that for sufficiently large carbon concentration there is a linear and temperature independent increase of σ_{ly} with p. We attribute this increase to the presence of a Snoek-effect and there is actually very good agreement between the experiments and the theoretical results from Sections 2 and 3. From equation (8) or equation (30) we obtain a theoretical value

$$\frac{\partial \tau_0}{\partial p} = 0.205 \frac{A}{ba^3} = 65 \frac{kp/\text{mm}^2}{\text{at.}^0/_0}$$

for the concentration dependence of τ_0 .

The experimental value after conversion from tension stress σ_{ly} into resolved shear stress gives

$$rac{\partial au_0}{\partial p} = rac{1}{2} rac{\partial \sigma_{ly}}{\partial p} = 45 rac{kp/\mathrm{mm}^2}{\mathrm{at.\%}}$$

If we take account of the fact that the theoretical value was obtained for screw dislocations and therefore is higher than the value for edge or intermediate type dislocations, the agreement is very good.

We interpret Fig. 5 as follows: If we could start from carbon free iron, small additions of carbon would tend to condense on dislocation lines until saturation is reached. From there on further additions of carbon go exclusively into the matrix (to the extent that the solubility limit at the homogenizing temperature allows.)

The temperature dependent part of σ_{ly} may be due

to an intrinsic frictional force on dislocations, then the measured values will extrapolate linearly down to zero percent carbon (dotted line). The temperature dependence could also be caused by the locking of dislocations by Cottrell clouds, then it would decrease rapidly at very small carbon concentrations (dashed line). However the carbon atoms dissolved in the matrix increase the yield stress by the Snoek-effect in a practically temperature independent way. As we have seen above this accounts quantitatively for this linear part of σ_{ty} vs p in Fig. 5.

Finally we want to discuss qualitatively the phenomena which occur at higher temperatures such as blue brittleness and serrated yielding, which are thought to be due to the interaction of solute atoms with moving dislocations. In addition to the effects discussed by Nabarro⁽⁶⁾ and Cottrell⁽¹⁷⁾ we have to take into account the additional action of the Snoekeffect.

At the temperature T_1 (Fig. 4) which is about room temperature in iron thermal fluctuations are large enough to free dislocations from their relatively narrow potential troughs⁽²⁾ of their Cottrell atmospheres even at negligible small stresses, so that the Cottrell mechanism becomes uneffective. This explains why for $T>T_1$ the yield stress is practically temperature independent. However in order that dislocations can move they still have to escape from their Snoekatmosphere which has a radius of about 20 b at room temperature.

199

These freed dislocations move through the lattice and are slowed down at places where the randomly varying internal stress field τ_G opposes their movement or are even stopped momentarily at local obstacles such as intersecting dislocation lines. As soon as they are slowed down or stopped, ordering of carbon atoms will take place and the dislocation will be locked again by the Snoek effect. In order to obtain a macroscopic deformation the applied stress has to exceed the stress τ_0 necessary to free dislocations from "Snoek-atmospheres". At somewhat larger temperatures two other effects occur. If the dislocation is slowed down long range diffusion of carbon atoms will take place towards the dislocation to form a Cottrell cloud which exerts a dragging force. At the same time this will also lead to an increased locking force by the Snoek-effect since the concentration of carbon atoms is increased in the neighborhood of the dislocation. Hence a dislocation once slowed down will be slowed down even more and a higher force will be necessary to free it again. At even higher temperatures the carbon atoms may become so mobile that they can be dragged along with a dislocation. But at the same

time their ordering also can take place so fast that the Snoek-effect now losses its influence.

Undoubtedly these effects are responsible for blue brittleness and jerky flow observed at higher temperatures, but it is rather difficult to calculate their relative importance to obtain a quantitative picture. We can, however, make an estimate of the temperature T_{o} (Fig. 4) at which the influence of the Snoek effect disappears due to the fact that the ordering takes place too fast. This will happen at strain rate $\dot{\varepsilon}$ where $\dot{\varepsilon} < N\alpha_0 b$. Here N is the density of moving dislocations and α_0 their critical velocity. From equation (29) we obtain then

$$\frac{\dot{\varepsilon}}{Nb} \le \nu_0 \frac{A}{kT} e^{-AG/kT} \tag{32}$$

with the meaning of the symbols defined earlier. With reasonable values of $\dot{\varepsilon} \approx 10^{-3} \, \mathrm{sec^{-1}}$ to $10^{-4} \, \mathrm{sec^{-1}}$ and $N\approx 10^6~\rm cm^{-2}$ to $10^8~\rm cm^{-2}$ we obtain T_2 between 230°C and 480°C. Although the estimate is rather crude, it is encouraging to notice that the observed drop in flow stresses actually occurs in this temperature range.

REFERENCES

- 1. A. H. Cottrell, Report of a Conference on the Strength of
- Solids, p. 30. The Physical Society, London (1948).

 2. A. H. COTTRELL and B. A. BILBY, Proc. Phys. Soc. A62, 49 (1949).
- 3. F. L. VOGEL and R. M. BRICK, Trans. Amer. Inst. Min. (Metall.) Engrs. 197, 700 (1953).
- 4. D. S. Wood, Dislocations and Mechanical Properties of Crystals (J. Fisher, Editor) p. 417. Wiley, New York (1957).
- 5. A. E. Love, Mathematical Theory of Elasticity. Uni-
- versity Press, Cambridge (1927).
 6. F. R. N. Nabarbo, Report of a Conference on the Strength of Solids, p. 38. The Physical Society, London (1948).
- 7. A. COCHARDT, G. SCHOECK and H. WIEDERSICH, Acta Met. 3, 533 (1955).
- 8. J. Snoek, Physica 8, 711 (1941)
- 9. G. Schoeck, Phys. Rev. 102, 1458 (1956).
- 10. G. Doetsch, Tabellen zur Laplacetransformation. Springer, Berlin (1947)
- 11. A. Seeger, Handbuch der Physik VII, 2, p. 183. Springer, Berlin (1958).
- 12. N. P. Allen, B. E. Hopkins and J. E. McKenan, Proc. Roy. Soc. A234, 221 (1956).
- 13. W. Knorr, Diplomarbeit, Stuttgart (1951).
- J. C. Fisher, Trans. Amer. Soc. Metals 47, 451 (1955).
 A. Seeger, Dislocations and Mechanical Properties of
- Crystals (J. Fisher, Editor) p. 243. Wiley, New York
- 16. J. HESLOP and N. J. PETCH, Phil. Mag. 1, 866 (1956).
- 17. A. H. COTTRELL, Properties and Microstructure, p. 131. American Society for Metals, Cleveland, (1954).

ELECTRICAL RESISTIVITY RECOVERY IN COLD-WORKED AND ELECTRON-IRRADIATED NICKEL*

A. SOSIN and J. A. BRINKMAN†

Pure nickel wires have been subjected to electron irradiation and cold work. Electrical resistivity recovery, starting at room temperature and extending to the recrystallization range, was studied. Recovery stages near 100°C (Stage III) and 270°C (Stage IV) were found to occur by a diffusion process following cold work; dislocations are believed to be the defect sinks. Stage III was found to obey a second-order chemical rate equation following irradiation; Stage IV is essentially absent. An activation energy for defect migration of about 1.05 eV was found in Stage III following both irradiation and cold work; the energy associated with defect migration in Stage IV is not as well determined.

These measurements plus other available data on nickel indicate that the defect migrating in Stage III is an interstitial atom in Stage IV a vacancy. The close similarity between the recovery in nickel and that in copper suggests a similar assignment in copper.

RESTAURATION DE LA RESISTIVITE ELECTRIQUE DANS LE NICKEL IRRADIE PAR ELECTRONS ET DEFORME

Des fils de nickel purs ont été soumis à un bombardement d'électrons et déformés à froid. Les auteurs ont étudié la restauration de la résistivité électrique depuis la température ambiante jusqu'à celle de la recristallisation. Ils ont trouvé que les stades de restauration aux environs de 100° C (3° stade) et 270° C (4° stade) résultent d'un mécanisme de diffusion provenant de la déformation; les auteurs pense que les dislocations servent de puits pour les autres défauts. Après irradiation, le 3° stade de la restauration obéit à une équation du 2° ordre de la vitesse de la réaction chimique; le 4° stade n'existe pas. Les auteurs ont trouvé que l'énergie d'activation pour le déplacement des défauts était de 1,05 électrons volts au cours du 3° stade consécutif à l'irradiation et à la déformation; l'énergie associée avec cette migration au cours du 4° stade n'est pas bien définie. Ces résultats, ainsi que d'autres, indiquent que le défaut se déplaçant au cours du 3° stade est un atome interstitiel, tandis qu'au cours du 4° stade, il s'agit d'une lacune. La similitude entre la restauration du nickel et celle du cuivre suggère, pour ce dernier, une interprétation identique.

ERHOLUNG DES ELEKTRISCHEN WIDERSTANDES VON KALTVERFORMTEM UND ELEKTRONENBESTRAHLTEM NICKEL

Drähte aus reinem Nickel wurden der Elektronenbestrahlung und Kaltverformung unterworfen. Die Erholung des elektrischen Widerstandes wurde von Raumtemperatur bis zum Rekristallisationsbereich untersucht. Es ergab sich, dass den Erholungsstufen bei $100^{\circ}\mathrm{C}$ (Stufe III) und bei $270^{\circ}\mathrm{C}$ (Stufe IV) nach Kaltverformung ein Diffusionsprozess zugrunde liegt; vermutlich wirken Versetzungen als Senken für die Fehlstellen. Nach Bestrahlung ergab sich für Stufe III eine Reaktionsgleichung 2. Ordnung; Stufe IV fehlt im wesentlichen. Für die Wanderung der Fehlstelle in Stufe III wurde nach Bestrahlung wie nach Kaltverformung eine Aktivierungsenergie von etwa 1,05 eV gefunden; die der Fehlstellenwanderung in Stufe IV entsprechende Energie liess sich nicht so gut bestimmen.

Diese Messungen deuten in Verbindung mit anderen verfügbaren Angaben über Nickel darauf hin, dass es sich bei der wandernden Fehlstelle in Stufe III um Zwischengitteratome handelt, in Stufe IV um Leerstellen. Die grosse Ähnlichkeit zwischen der Erholung von Nickel und der von Kupfer legt für Kupfer eine ähnliche Zuordnung nahe.

1. INTRODUCTION

In the study of the production and motion of lattice defects in metals it is desirable, if not necessary, to examine the behavior of these defects in more than one metal. The similarities and differences in the behavior in different metals offer a guide in the interpretation of the defect phenomena. Among the metals, copper has received the greatest amount of attention. Nickel has been chosen for the present

investigation. A comparison of the results in these two metals is given at the end of this paper.

19

The immediate impetus for choosing nickel is to be found in the work of Clarebrough, Hargreaves, Michell and West. (1-3) They measured the release of energy stored in pure copper, arsenic-doped copper and moderately pure nickel by cold work. Their results are shown in Figs. 1-3. The points to be noted here are the following:

 In pure copper (Fig. 1), the majority of the energy released in the recovery stage centered at about 290°C is associated with recrystallization.

^{*} Received July 21, 1958; in revised form October 1, 1958. † Atomics International, A Division of North American Aviation, Inc., Canoga Park, California.

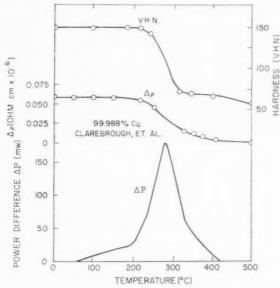


Fig. 1. Stored energy release, resistivity recovery, and Vickers hardness recovery of pure copper cold-worked at room temperature by Clarebrough $et\ al.^{(1-3)}$

There is, however, a definite skewness in the peak indicating that more than one recovery process is operating.

(2) In arsenical copper (Fig. 2), the recrystallization peak is quite clearly defined and centered at about 330°C. The evidence for a second process is less clear.

1959

(3) In nickel, two distinct stages exist. Clarebrough

et al. have concluded on the basis of these measurements and associated measurements of electrical resistivity, density and lattice parameter, that the lower recovery stage is most probably associated with the migration and subsequent annihilation of vacancies; the upper stage is due to recrystallization. The purity of the nickel was 99.6 per cent.

(4) Later work⁽⁴⁾ on purer (99.85 per cent) nickel reveals some evidence for still a third process. From the available data, one can merely say that the "center temperature" for this stage is probably somewhere below 100°C. This later work was not known by us until the present work work was nearly complete.

The measurements of the recovery of stored energy, hardness, resistivity, lattice parameter and density changes following cold work, presented by Clarebrough et al., are extremely valuable. It was felt that an understanding of the recovery processes would be substantially aided by a detailed study of the kinetics of recovery. We have made such a study of the recovery of electrical resistivity in nickel following cold work and, to further aid the interpretation, we have also studied the recovery in nickel irradiated with 1.25 MeV electrons.

The interpretation of the processes occurring during the various recovery stages is of utmost importance to imperfection studies in metals. Perhaps the most central point of disagreement has been the assignment

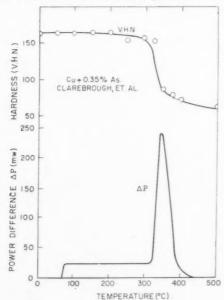


Fig. 2. Stored energy release and Vickers hardness recovery of arsenical-copper coldworked at room temperature by Clarebrough $et\ al.^{(1-3)}$

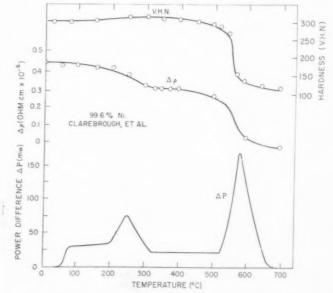


Fig. 3. Stored energy release, resistivity recovery and Vickers hardness recovery of moderately pure nickel cold-worked at room temperature by Clarebrough $et\ al.^{1-3}$

i de la companya de l

19

of temperature regions and activation energies to vacancy and interstitial migration in copper. Since the evidence for vacancy migration in nickel presented by Clarebrough et al. seems quite conclusive, we have accepted this interpretation as our basic hypothesis. From the results of our recovery studies, we are then able to make a definitive identification of the temperature range in which interstitials migrate. These studies also allow us to make a comparison between the recovery observed in nickel and copper. It is found that these recoveries parallel each other sufficiently well to allow us to draw conclusions regarding the temperature regions in which interstitials and vacancies migrate in copper.

It is obvious that a more straightforward approach toward studying defect migration in copper would be to work with copper itself. Studies⁽⁵⁾ of the present nature have been made in copper for this purpose but have not been entirely satisfactory since defect migration is found to overlap recrystallization, as shown in Fig. 1. We have chosen the more diverse route for three reasons:

- The results of Clarebrough et al. form a working basis for interpretation,
- (2) point defect recovery was shown to be more distinctly separated from recrystallization in nickel than copper, and

(3) the results in nickel are important in themselves. Unless specifically stated otherwise, all the data presented were obtained using 99.98 per cent pure nickel. All samples were in wire form made by drawing through dies at or slightly below room temperature. Any pre-test annealing was done in vacuo at or above 700°C. It is found during the course of the experiments that annealing conditions were quite critical; the wires were extremely susceptible to contamination.

The electron-irradiated samples were mounted on lavite holders and subsequently annealed prior to irradiation. The experimental arrangement was similar to that used by Meechan and Brinkman⁽⁶⁾. Irradiations were carried out at about 90°K. Recovery studies were started at room temperature. The cold-worked wires were also mounted on lavite holders of various forms.

Recovery studies were made in a water bath for temperatures up to 100°C and in a Fisher wax bath for temperatures between 100° and 350°C. Higher temperature studies were performed in a furnace where the samples were protected by an argon atmosphere. Electrical resistance measurements were made in a liquid helium bath using the conventional four-probe potentiometric method. The residual resis-

tivity of annealed samples used in these experiments varied between 4×10^{-8} and $6\times 10^{-8}\,\Omega\text{-cm}.$ Substantially higher values were found on a number of occasions. The cause was traced to faulty annealing procedure, as suggested above. Such samples were rejected.

2. DISCUSSION OF KINETICS ANALYSIS

The method of analysis used in the kinetics study follows that of Meechan and Brinkman⁽⁶⁾. In this method, two specimens with identical histories are used. In the case of electron irradiation, two distinct wires were pre-annealed together and irradiated to approximately the same resistivity increase. In the case of cold work, wire was prepared by drawing; this wire was then cut into two parts, yielding the two required specimens.

The first specimen was annealed at a series of successively higher temperatures for equal time intervals. In the case of electron irradiation, this specimen was heated in fifteen degree intervals; the time at each temperature was five minutes. In the case of cold work, the specimen reported here was heated in ten degree intervals; the time at each temperature was five minutes.

The second specimen was annealed isothermally at a temperature near the "center" of each of the main recovery stages revealed by the first specimen. For the cold-worked specimen, the temperatures used were 82° and $260^{\circ}\mathrm{C}$; in the case of electron irradiation, one isothermal was made at $100^{\circ}\mathrm{C}$.

As discussed by Meechan and Brinkman, the resulting data may be analyzed for several factors. If the recovery obeys a chemical rate equation, the part, p, of the property being monitored which is associated with the annihilating defects, should follow an equation:

$$dp = -Kp^{\gamma} dt, \tag{1}$$

during an isothermal recovery. Here γ is the order of the reaction. Integration of equation (1) gives:

$$p^{1-\gamma} = C(t+M). \tag{2}$$

Here C is a temperature dependent constant and M is an integration constant representing the time which would be required for the defect concentration to be reduced, as a result of isothermal annealing, from an infinite value to that value corresponding to p_0 , the initial value of p. It is assumed that the property being measured (resistivity) is proportional to the concentration of the migrating defect.

A test of the validity of the chemical rate equation can therefore be made by plotting $\ln p$ vs. $\ln (t + M)$. If the chemical rate equation is valid, a value of M

should exist so that this plot is a straight line. The slope of the line is then a measure of γ .

Contrary to the implicit assumption often made, it is not necessary for a chemical rate equation to be obeyed in a solid-state recovery reaction. Indeed, as discussed below, it was found that the cold-work recovery stages failed to yield straight lines in the $\ln p$ vs. $\ln (t+M)$ plot for any value of M. In these cases, the isothermal data were re-analyzed to see whether the rate equation governing the process was one describing random migration of defects to sinks of infinite capacity or one in which the sink capacity is finite and reduced during the recovery. The behavior of p as a function of time over the entire length of the recovery stage for such a process depends on the details of the model chosen. We have investigated three such models:

- (1) The volume diffusion of point defects to the boundaries (i.e. grain boundaries or mosaic boundaries) of spheres,
- (2) the volume diffusion of point defects to internal cylinders (i.e. isolated dislocations), and
- (3) the volume diffusion of point defects to internal spheres (i.e. jogs, clusters, etc.).

A dependence of p on time can be found for each of these models, although not necessarily in closed form. Since the models are obviously oversimplified, and since the time dependence is sensitive to the particular model, there is usually little hope of fitting the entire recovery process by such an analysis. However, it can be shown that, in any model involving random migration of an initially uniform distribution of point defects to a fixed array of infinite sinks, the dependence of p on time is the familiar $t^{1/2}$ associated with diffusion phenomena for sufficiently small values of time.

A simple test of this model can be made by plotting $\Delta p \equiv (p_0-p) \text{ vs } t^{1/2}$. We have done this for the recovery stages observed following cold work, for small values of t. The slopes of the straight lines one expects are equal to $1/\tau^{1/2}$, where τ is a "lifetime" associated with the diffusion process. The values of τ for the three models are:(7)

$$\tau = \frac{a^2}{\pi^2 D},\tag{3a}$$

$$\tau = (16a^2n^2\pi D)^{-1},\tag{3b}$$

$$\tau = (64a^4n^2\pi D)^{-1},\tag{3c}$$

respectively. Here a is the radius of the sink and n is the appropriate sink concentration. Note that in equation (3a), the radius, a, is intimately related to the distance which a defect must migrate before reaching

the surface of the sink, being the maximum distance from the surface. In equations (3b) and (3c), the radius, a, is a measure of the size of the sink but is not intimately related to the migration distance for the defects. D is the diffusion coefficient, presumed to have the familiar temperature dependence,

$$D = D_0 e^{-E_m/kT}, \tag{4}$$

where E_m is the activation energy for migration of the defects. One might expect, therefore, to be able to determine E_m as well by studying the temperature dependence of τ .

The data have been analyzed more directly for E_m . By comparing the isothermal curves with the tempering curves for identical specimens, one can determine the time τ_i at which a value p_i in the isothermal curve is reached equal to the value of p measured at the end of the ith pulse on the tempering curve, carried out at a temperature T_i . According to this procedure, the important quantity to consider is not τ_i but $\Delta \tau_i \equiv \tau_i - \tau_{i-1}$. Any straight line section obtained on a plot of $\ln \Delta \tau_i$ vs. $1/T_i$ is characterized by a unique activation energy given by the expression: $^{(6)}$

$$\ln \Delta \tau_i = C' - \frac{E}{kT_i}, \qquad (5)$$

where C' is a constant.

3. PRESENTATION OF RESULTS AND INTERPRETATION

3.1. Electron irradiation

The resistivity, ρ , vs. exposure curve for nickel irradiated near 90°K with 1.25 MeV electrons is given in Fig. 4. The damage rate is linear with a slope of $8.5 \times 10^{-28} \,\Omega$ -cm per electron/cm². The tempering curve for the same sample is given in Fig. 5. The tempering was begun at room temperature. An annealing stage centered at about 370°K is observed. Fig. 6 gives the isothermal recovery at 100°C for this sample. The isothermal and tempering curves are then compared to give a $\ln \Delta \tau_i$ vs. 1/T plot shown in Fig. 7. The straight line criterion for a singly activated process is seen to hold. From a least squares fit of the data, the activation energy for this stage was found to be $1.03\,\mathrm{eV}\pm0.04\,\mathrm{eV}$. Returning to the data for the isothermal recovery, a plot of $\ln \Delta \rho$ vs. $\ln t$ (where $\Delta \rho$ is the resistivity change associated with a given recovery stage) is given in Fig. 8. The circled points are the original data. It was then necessary to choose a time, M, to add to all of the observed times, as explained above. M=25 min was found to provide a best fit so that the readjusted data would fit a

VOL. 7 1959

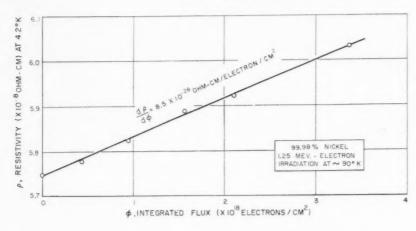


Fig. 4. Electrical resistivity as a function of integrated electron flux for 99.98 per cent pure nickel. Irradiation was carried out at about $90^{\circ}\mathrm{K}$ using $1.25~\mathrm{MeV}$ electrons.

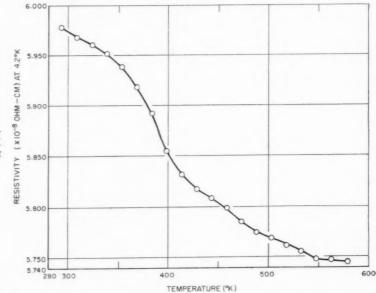


Fig. 5. Isochronal recovery of resistivity in pure nickel irradiated at about $90^{\circ} \rm K$ with 1.25 MeV electrons. The tempering rate is $3^{\circ} \rm K/min$.

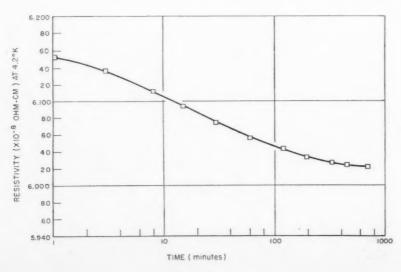


Fig. 6. Isothermal recovery at 100° C in 99.98 per cent pure nickel irradiated at about 90° K with 1.25~MeV electrons.

straight line. The readjusted data points are enclosed by triangles. The slope of this line is $m=-1.01\pm0.01$, showing that the recovery kinetics obey the chemical rate equation with an order for the kinetics

of
$$\gamma = 1 - \frac{1}{m} = 1.99 \pm 0.01$$
.

The data concerning this recovery stage, to be called Stage III, are convincing evidence that the recovery obeys a second order chemical rate process. The bases for this confidence are the excellent straight line fits obtained on the activation energy plot and on the order of kinetics plot and, perhaps most important, the fact that the order deduced is sensibly integral and small. The interpretation of a fractional order or one which is greater than three, say, is difficult.

Taking into account the simple nature of the damage produced by electron irradiation, the above data should, presumably, be interpreted in terms of (1) annihilation of interstitial atoms at vacancies, (2) annihilation of vacancies at interstitial atoms, (3) divacancy production and rapid annihilation, or

(4) di-interstitial production and rapid annihilation. These interpretations will be further discussed below.

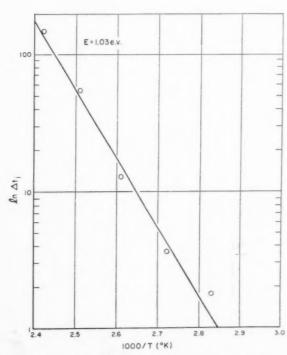


Fig. 7. An analysis of the data of Figs. 5 and 6 to determine the energy of migration for the defect migrating in Stage III in 99.98 per cent pure nickel after electron irradiation.

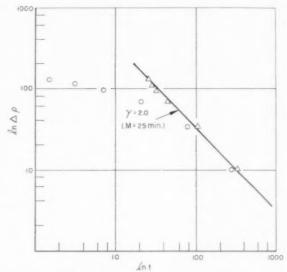


Fig. 8. An analysis of the isothermal recovery data of Fig. 6 to determine the order of chemical kinetics governing the process in Stage III in 99.98 per cent pure nickel after electron irradiation.

3.2. Cold work

Guided by the work of Clarebrough et al., an initial study was made of cold work recovery via a tempering procedure. The first results are shown in Fig. 9 and are represented by the circled points. The unexpectedly large drop found between the first reading at room temperature and the one at 125°C prompted us to make another study; these results are given in the same figure by the points enclosed with triangles. These samples received a nominal 40 per cent area reduction. It may be significant that the recovery observed near 100°C is larger in the second sample than in the first. It is believed that this difference is due to the additional care which was exercised in maintaining the second sample at a lower temperature during cold work. For comparison, Fig. 10 gives the recovery of a sample which was elongated 10 per cent.

In all cases, the existence of three recovery stages is found. These are Stage V, centered about 500°C; Stage IV, centered about 270°C; and Stage III, centered about 90°C. Guided by these data, a detailed study was made of Stages 111 and IV.

Before discussing the results of the detailed study, two points should be mentioned. The Stage III recovery in cold work found here was somewhat unexpected in view of the fact that the work of Clarebrough et al. fails to show it. The reasons for this discrepancy are not known. A number of possibilities exist. Their resistivity measurements were made on a sample whose geometry is far from

VOL. 7 1959

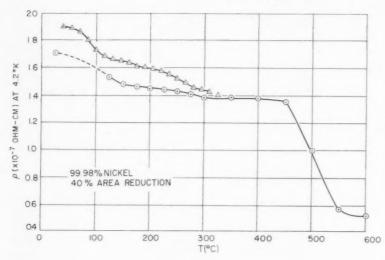


Fig. 9. Resistivity recovery of 99.98 per cent pure nickel following a nominal 40 per cent reduction in area by cold-drawing near room temperature.

ideal for these measurements, although excellent for the other measurements they made. Furthermore, the measurements were made at 20°C. Our measurements, as stated previously, were made in a liquid helium bath where the thermal resistivity is greatly reduced. It seems fair to claim greater sensitivity in this work.

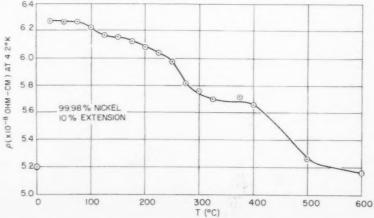
There is, perhaps, a better way of explaining this discrepancy by referring to the purity of the samples used here and by Clarebrough⁽²⁾. We have found that Stage III is completely masked by impurities. In fact, the residual resistivity has been found to increase upon annealing in this temperature range for a sample of 99.4 per cent purity. This is the range of purity used by Clarebrough *et al.* in their earlier work. It should be noted further that a rise in resistivity was also found in the corresponding temperature range for the arsenical copper with a similar amount of impurity. The reason for this rise remains to be determined: Boas⁽⁴⁾ suggests that it is due to

the movement of dislocations away from their atmospheres under thermal activation.

Another observation to be made concerning Figs. 9 and 10 is the relative sizes of recovery Stages III and IV. Stage III is enhanced in size for the 40 per cent cold-drawn sample compared with the 10 per cent tensile-tested sample. This has been investigated in further detail and will be discussed shortly.

The detailed process study is presented in Figs. 11–13 for a new sample, cold-drawn to 56 per cent area reduction. Fig. 11 is the tempering curve, starting at room temperature. Fig. 12 is the isothermal recovery curve for Stage III taken at 82°C. Fig. 13 is the isothermal recovery curve for Stage IV taken at 260°C. In each case, the temperature of recovery was chosen to be somewhat below the "center temperature" to make the time scale convenient. The ln $\Delta \tau_i$ vs. $1/T_i$ plots deduced from these figures are given in Figs. 14 and 15. A well defined activation energy is found in Stage III; $E=1.08\pm0.09\,\mathrm{eV}$





VOI 7 19

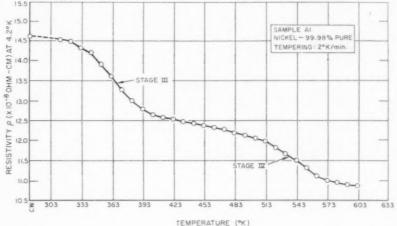


Fig. 11. Isochronal recovery of resistivity in 99.98 per cent pure nickel following a nominal 40 per cent area reduction by wire-drawing near room temperature.

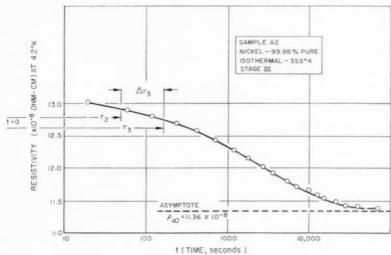


Fig. 12. Isothermal recovery at 82°C in Stage III for a 99.98 per cent pure nickel wire with the identical history of the wire shown in Fig. 11. The quantities τ_2 , τ_3 and $\Delta \tau_3$, are related to the method of analysis used and explained in the text.

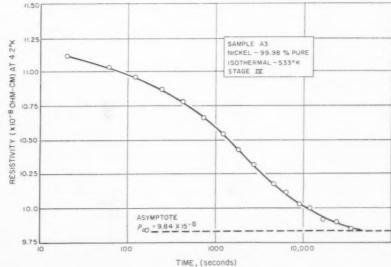


Fig. 13. Isothermal recovery in Stage IV at 533°K for the same nickel wire used in Fig. 12.



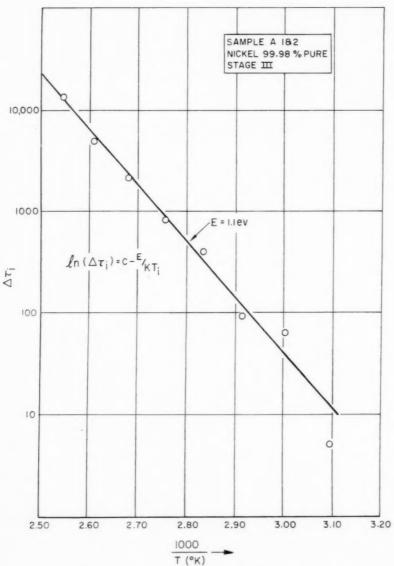


Fig. 14. An analysis of Figs. 11 and 12 to determine the energy of migration for the defect migrating in Stage III following cold-drawing of 99.98 per cent pure nickel.

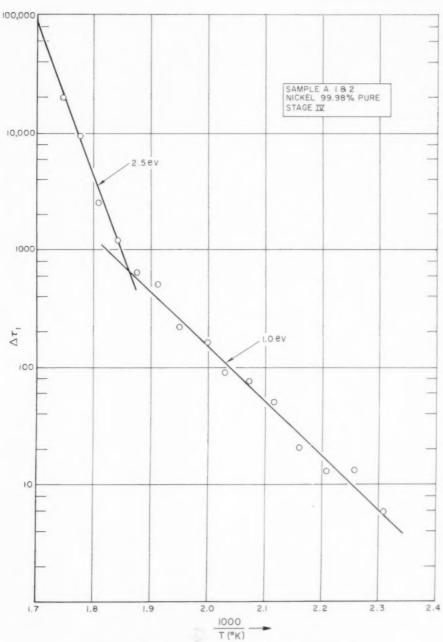


Fig. 15. An analysis of Figs. 11 and 13 to determine the activation energies ascribed to the recovery in Stage IV following cold-drawing of 99.98 per cent pure nickel.

VOL. 7 1959

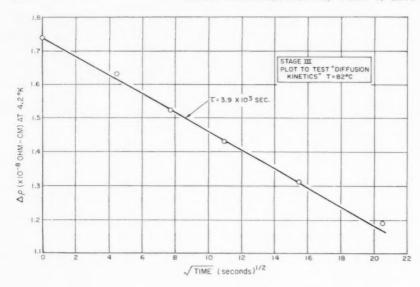


Fig. 16. Replot of the data of Fig. 12 for short times to determine whether the process is one described by volume diffusion of defects to a random array of infinite capacity sinks.

VOI

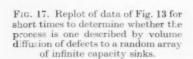
195

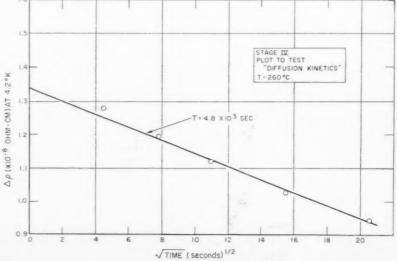
(as determined by a least squares fit of the data). Two processes appear to be distinguishable in Stage IV with activation energies of approximately $1~\rm eV$ and $2.5~\rm eV$.

A plot of $\ln \Delta \rho$ vs. $\ln t$ has also been made for each of these stages. In neither case was it possible to obtain a straight line with adjustment of M, the time parameter appearing in equation (2). This is evidence that the processes operating are not governed by a chemical rate equation. We have, therefore, plotted $\Delta \rho$ vs. $t^{1/2}$ for reasonably short times as a test of diffusion-type kinetics (i.e. volume diffusion to infinite sinks). These plots are given in Figs. 16 and 17. In both cases straight lines were obtained. The characteristic relaxation times for these stages and this amount of cold work are 3.9×10^3 sec in Stage

III (at 82°C) and 4.8×10^3 sec in Stage IV (at 260°C).

The conclusions to be drawn from these data for Stage III are quite clear. Evidently some point defect is migrating to infinite sinks, presumably related to dislocations. Unfortunately, the situation in Stage IV is not as simple to interpret. The evidence suggests, once again, the migration of point defects to infinite sinks but the presence of two activation energies complicates the picture. Furthermore, the values of activation energies for these two processes are anomalous. A value of 1 eV in Stage IV seems difficult to understand, 1.08 eV having been found to characterize the single process in Stage III. The value of 2.5 eV is unreasonably high, assuming that it is reasonable to expect the activation energies for different processes to follow a pattern proportional to





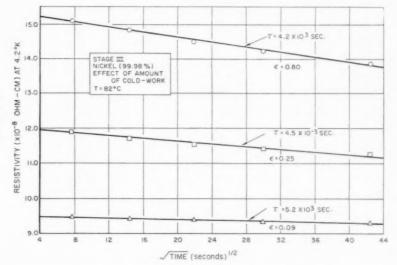


Fig. 18. A resistivity vs. time $^{1/2}$ plot for 99.98 per cent pure nickel wires to determine the effect of various amounts of cold work on the defect lifetime at 82°C. ε is the amount of strain and τ is a measure of the defect lifetime.

VOL.

1959

the melting temperature. The experiment was repeated to resolve this difficulty. The presence of two activation energies persisted, however, with no additional information being obtained.

If the interpretation of the migration of point defects to infinite sinks is correct, one would expect that the "lifetime" for these defects would be a function of the amount of cold work, which determines the sink concentration. This expectation is shown in equations (3b) and (3c); in both cases the lifetime is inversely proportional to the square of the defect concentration. Equation (3a) does not explicitly state such a dependence.

To test these ideas, three more wires were colddrawn. The area reductions were approximately 9, 25 and 80 per cent. These wires were isothermally annealed, first at 82°C, later at 260°C. These results are shown in Figs. 18 and 19. A dependence of lifetime on amount of cold work is observed in the correct direction in Stage III but the dependence of lifetime on the amount of cold work, as expressed by the amount of area reduction, for instance, is less than was anticipated. The lifetime for the defects in Stage IV is remarkable, being independent of the amount of cold work for the samples tested.

It is also interesting to note the amount of resistivity recovery found in each stage for these wires. The magnitude of the recovery in Stage III is found to depend almost linearly on the amount of area reduction. A fit of the present data gives $\Delta \rho = \varepsilon^{0.8}$, where ε is the amount of strain (i.e. area reduction). The uncertainty in the amount of strain and in the

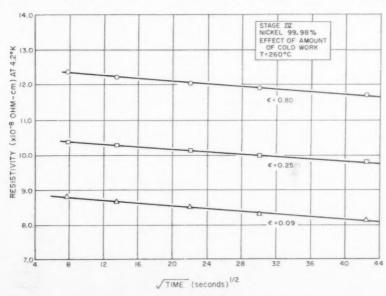


Fig. 19. A resistivity vs. time $^{1/2}$ plot for 99.98 per cent pure nickel wires to determine the effect of various amounts of cold work on the defect lifetime at 260°C. ε is the amount of strain. The lifetime is found to be independent of ε .

magnitudes of the recovery to be attributed to the stage make this dependence subject to sizeable uncertainty. The magnitude of recovery in Stage IV is found to be independent of the amount of strain for the range of strains investigated.

The behavior of these lifetimes and the constancy of the magnitude of the recovery in Stage IV are not entirely clear. The magnitude of the recovery in Stage III seems to be reasonable. The small variation of lifetime can be understood by referring to equation (3a); one need only to assume that the spacing between boundaries serving as traps for the point defects is only slightly affected by the amount of cold work.

4. DISCUSSION

The present experiments and those pertinent to these can be understood, in most part at least, by the following model. The defect migrating in Stage III is an interstitial atom; the defect migrating in Stage IV is a vacancy. In the case of electron irradiation, the defects produced are predominantly isolated interstitials and vacancies. These recombine, in most part, by a bi-molecular process in Stage III. The remaining portion which does not anneal in Stage III is to be associated with point defects trapped during irradiation and Stage III annealing. In nominally pure materials, impurities in low concentration provide adequate trapping sites for such a process. In the case of cold work, the migrating defects remain the same but the effective trapping sites or sinks for these defects are dislocation arrangements.

These interpretations agree with the deductions of Clarebrough et al. (2) and the subsequent analysis of Nicholas (8). Nicholas has analyzed the shape of the stored energy release in Stage IV, as well as the shift in the peak due to different heating rates. From this analysis, Nicholas deduced an activation energy of 0.98 eV. He has concluded that the Stage IV recovery is due to vacancy migration, di-vacancy migration or interstitial migration. Referring to the calculations of Huntington on interstitial migration and to the calculations of Bartlett and Dienes on di-vacancy migration in copper, and extending these calculations to nickel in a qualitative manner, he has shown a definite preference for the vacancy migration interpretation. He further points out that the density changes observed are not of the correct magnitude for interstitial annihilation. The interpretation of Stage IV in terms of interstitial migration is completely eliminated here by the bimolecular recovery found in Stage III, assuming that interstitials move at a lower temperature than vacancies. This assumption is generally

accepted in the noble metals and is expected to hold for nickel as well. It might be argued that the di-vacancy migration mechanism for Stage IV could apply if Stage III is interpreted as di-vacancy formation in the case of electron irradiation. The difficulty with this interpretation is that no Stage IV recovery is found following electron irradiation although divacancies would have been produced in Stage III in view of the observed second order kinetics.

The model presented thus far has not revealed the identity of the dislocation arrangements serving as infinite sinks for the migrating defects. These sinks are believed to be mosaic boundaries or boundaries of the "particles" found by Gay, Hirsch and Kelly (9) in cold-worked nickel from X-ray diffraction data. It is pertinent to point out that the proposed model for the recovery in Stages III and IV following cold work explicitly assumes infinite capacity sinks. The physical soundness of this assumption is demonstrated by the recent work of Thomson⁽¹⁰⁾, who has shown that the migration of a given concentration of defects to dislocations has almost no effect on the migration of further defects to dislocations; therefore, dislocations are potentially infinite sinks. Nicholas (8) is also led to this conclusion. He is able to deduce, from the data, a value of $D_0/a^2 = 5.5 \times 10^5 \, {\rm sec^{-1}}$ for Stage IV. Our analysis gives $D/a^2 = 1/\pi^2\tau = 2 \times$ 10^{-4} sec^{-1} . D_0 and D are related as shown in equation (4). Taking an activation energy of 1 eV, we find $D_0/a^2 = 6 \times 10^4 \text{ sec}^{-1}$. With the large amount of uncertainty involved in such calculations, agreement to an order of magnitude seems reasonable. Nicholas'(8) value, using the analysis of LeClaire(11), leads to a "particle" size of about 7 μ ; our value leads to one of about 2 \mu. The observed values of Gay Hirsch and Kelly⁽⁹⁾ were in the range of 1.9 μ to 0.04μ for 33 per cent rolling.

VOI

195

Despite the apparent consistency of the proposed model, it is necessary to point out again that not all of the data are suitably accounted for by the model. It is particularly difficult to understand the pair of activation energies found in Stage IV. Although some of the initial interest in nickel was due to the evident separation of Stages IV and V, the present work and other associated work in this laboratory have demonstrated that Stage V recovery in nickel does overlap Stage IV recovery to some extent. It is believed that the larger activation energy, about 2.5 eV, is more properly associated with Stage V recovery. Further evidence for this interpretation is the activation energy determined by Burgess and Smoluchowski⁽¹²⁾ for self diffusion in nickel: 2.8 eV.

Assuming that the 2.5 eV energy can be accounted

for by a self diffusion process (presumably the formation and motion of vacancies, initiating dislocation elimb), it remains difficult to understand the lower activation energy, 1 eV, in light of the 1.08 eV found in Stage III. One way to account for this apparent anomaly is to assume that the ratio of the values of the diffusion coefficient, D_0 , for the defects in Stage III and Stage IV is approximately 10^4 . While this is possible, it does not seem likely. Whatever the explanation of this anomaly is, it must account for the agreement between the present results and the analysis of Nicholas⁽⁸⁾.

Recently, Berghout $^{(13)}$ has calculated the effect of the strain field around a dislocation upon the diffusion coefficient, D, for vacancies. His results indicate that D is very sensitive to the polar position of the vacancy with respect to the dislocation for an appreciable distance from the dislocation. He also finds that the apparent activation energy may be shifted by as much as $0.5 \, {\rm eV}$. It is possible that the difficulties discussed above are due to this effect. Such a calculation for interstitials should show similar results; the magnitude of the effect might be appreciably altered, however, due to the large elastic strain associated with the interstitial. If this is correct, Stage III should also exhibit the anomaly, contrary to what is observed.

Still another difficulty requiring clarification is the constancy of the magnitude and lifetime for recovery in Stage IV mentioned earlier. One might speculate that these data are related to the nature of plastic flow. At small deformations where a relatively small amount of cross slip occurs the production of point defects is controlled by energy considerations favoring the formation of vacancies as compared to the formation of interstitials. In a later stage of flow cross slip predominates, point defect production is primarily geometrical in nature, and interstitial production becomes more important. Obviously a complete understanding of the recovery is lacking at this time. Further work in progress on nickel should help in arriving at this understanding.

5. A COMPARISON OF THE RECOVERY CHARACTERISTICS OF COPPER AND NICKEL

The theories of imperfections in metals have leaned very heavily on the data on copper. There are excellent reasons for this, both theoretical and experimental. It is, however, necessary to consider data on other metals. The most conspicuous example of this point is the work on the quenching of gold; (14) to date, no comprehensive work on the quenching of copper has been published. It has been the belief

that by quenching one would achieve the simplest concentration of defects, an excess of astable vacancies.

In pursuing copper as a "standard material," it has been the hope that other metals would behave more or less similarly depending on how closely their other properties resemble those of copper. In particular, it was expected that silver and gold would be very close to copper in their behaviors. To some extent the expectation is realized, but the deviations are important. Most conspicuous of the deviations is the relative magnitude of the recovery stages near 40°K(15) and 240°K(16) for these three materials, following deuteron bombardment at 12°K. These recovery stages are hereafter referred to as Stages I and III. respectively. In Stage I, copper recovers the most. silver is intermediate and gold the least. The situation is just reversed in Stage III, suggesting an interrelationship between the two stages.

The behavior of copper has served as a guide in a large part of our work in nickel. Some degree of similarity should be expected. The two atoms are of nearly equal mass; both structures are face-centered cubic. Particularly interesting to this comparison is the data concerning the neutron bombardment of copper doped with as much as 1 per cent nickel. (17) This doped sample shows essentially the same behavior in Stages I and II (temperature region between I and III) as pure copper.

There are also reasons to expect possible differences between nickel and copper. The electronic structure is, at first glance, significantly different. Copper has a $3d^{10} \ 4s^1$ structure, accounting for its simple electronic properties. Metallic nickel has a $3d^{10-0.6} \ 4s^{0.6}$ structure. The hole in the d-band accounts for nickel's ferromagnetic behavior. The fact that nickel is ferromagnetic should be borne in mind but not overemphasized. In fact, it is the opinion of the authors, on the basis of the available data, that this has little, if any importance in the discussion of the radiation damage or cold-work effects with which this paper is concerned.

A comparison of the recoveries of copper and nickel is presented below. The recovery data following electron irradiation and cold work are summarized in Table 1.

5.1. Stages I and II

Neutron bombardments of copper and nickel have been performed by the Oak Ridge group at 22.4°K.⁽¹⁹⁾ The damage rates $(d\rho/d\phi)$, where ρ is the resistivity of the samples and ϕ is the integrated neutron flux) are 1.1×10^{-26} and $3.3 \times 10^{-26} \, \Omega$ -cm per neutron/cm², respectively. The recoveries up to 90°K are quite

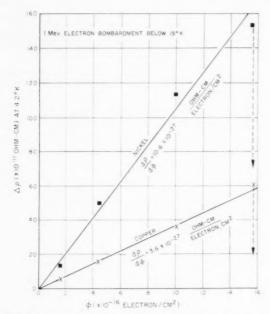


Fig. 20. A comparison of electrical resistivity changes due to irradiation with 1 MeV electrons below 15°K as a function of integrated flux. The dashed vertical lines indicate the extent of recovery following irradiation due to warming to about 60°K for a short period of time.

similar; about 40 to 50 per cent of the resistivity recovers. In both materials, a dominant recovery region is found: Stage I is present after irradiation, centered at about $40^{\circ} \rm K$.

We have also irradiated copper and nickel (99.99 per cent pure Cu, 99.98 per cent pure Ni) at temperatures below 15°K. The samples were irradiated simultaneously with 1 MeV electrons. The damage rates were found to be 3.6×10^{-27} and 10.6×10^{-27} Ω -cm per electron/cm². Note that the damage rates in both types of bombardment differ by a factor of three. Upon warming to 60° K, 60 to 70 per cent of the resistivity recovers in each. These results are given in Fig. 20.

Similar data for wires elongated while in a liquid-

helium bath have also been reported. (20) An 18 per cent extension produced a change in resistivity in copper of $2.9 \times 10^{-8} \,\Omega$ -cm; a 14 per cent extension produced a change in resistivity in nickel of $6.2 \times 10^{-8} \,\Delta$ -cm. The ratio of the resistivity changes, adjusted for the slightly different amounts of cold work, is about 2.5. Upon warming to 90° K, about 2 per cent of the resistivity change recovered in each wire. In neither case was a sharp recovery stage found in this temperature region: Stage I is absent in cold work.

5.2. Stages III, IV and V

The most important data for the present discussion is given in Table 1. In addition, recovery curves for the two metals are compared in Fig. 21 on a temperature scale reduced by the respective melting temperatures. The details of the recovery in Stage IV following cold work for copper are complicated by overlap with Stage V; recrystallization is found to commence even in Stage IV.²¹

Stage IV has not been clearly discerned following irradiation for copper. The only evidences for such recovery are the "tail" of the recovery shown in Fig. 21 and the phenomenon of radiation annealing reported by Meechan. (22) The interpretation of the latter is that the vacancies and interstitials created by the electron bombardment are quickly annihilated at dislocations during the irradiation rather than by direct interstitial-vacancy annihilation, since the concentration of point defects is never allowed to build up to any appreciable extent. The irradiation is carried out at a temperature where Stage IV recovery occurs, e.g. 150°C. Since the point defects do not remain, they do not contribute to resistivity; they do allow dislocation climb and rearrangement, and a net resistivity decrease is observed. Observation of this effect in nickel would be helpful in confirming this model, and might shed some light on the Stage IV activation energy anomaly as well.

19

Table 1. A comparison of recovery following electron irradiation and cold-working of copper and nickel

	Stage III					Stage IV						
	T_{c}	T_m	E_m	(eV)	Ki	netics	$T_c/$	T_m	E_m (e	V)	Kine	ties
Copper Nickel	e.w. 0.18 ² 0.20 ^c	$e^- \ 0.23^b \ 0.22^c$	$\begin{array}{c} { m c.w.} \\ 0.7 \\ 1.08^c \end{array}$	$e^- \ 0.60^b \ 1.03^c$	e.w. Dife	$egin{array}{l} \mathrm{e}^- \ \gamma &= 2^b \ \gamma &= 2^c \end{array}$	$^{ m e.w.}_{0.30^d}_{0.31^c}$	e- 0.30°	c.w. * - 1.19 ^d • 1.0 ^e	e ⁻ 1.28 ^e	$\begin{array}{c} \mathrm{c.w.} \\ \mathrm{Dif}^d \\ \mathrm{Dif}^c \end{array}$	e-

a. see reference 21, b. see reference 6, c. present work, d. see reference 5, e. see reference 22.

 T_c/T_m = ratio of the temperature at the "center" of the recovery stage to the melting temperature. E_m = the activation energy for migration of the defect moving during the recovery. c.w. = results for coldwork. γ = the order of the chemical-rate equation obeyed by the moving defect. e^- = results for electron irradiation. Dif = indicates that the process occurs by a diffusion mechanism.

The situation regarding Stage V in both copper and nickel, i.e. recrystallization with a self-diffusion activation energy, is relatively well understood for the purpose of this paper.

5.3. Conclusions

1959

In comparing the behaviors of copper and nickel, it is of interest to propose, following a suggestion by migration given previously for nickel is correct and applies as well to copper.

ACKNOWLEDGMENTS

The authors express their thanks to H. Neely for performing the experiments on radiation effects and to L. H. Rachal for performing the experiments on cold-working effects. Helpful discussions with C. J. Meechan are also gratefully acknowledged.

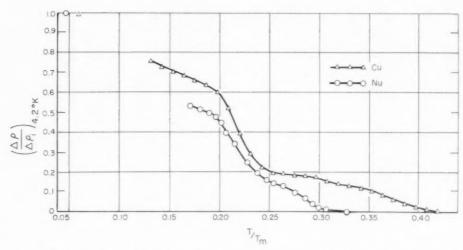


Fig. 21. A comparison of electrical resistivity recovery in 99.99 per cent pure copper and 99.8 per cent pure nickel following 1.25 MeV electron irradiation near 90°K. ρ_i is the total residual resistivity change due to bombardment. T_m is the melting temperature.

A. Seeger⁽²³⁾, that the residual electrical resistivity of the two metals should behave quite similarly. This is true since the residual portion of the electrical resistivity of nickel is determined primarily by the s-electrons with spin parallel to the d-band holes. S-electrons with parallel spin suffer appreciable d-band scattering. If the differences between nickel and copper can be accounted for by such a simple model, one would expect the conductivity of nickel at very low temperatures to be lower than the conductivity of copper in the ratio of 0.3:1 since the carrier concentration is reduced by essentially this ratio. Allowing for some contribution from the other 0.3 electrons, one might expect the resistivities to vary by about one-third. This confirms the findings as shown above and suggests that the defect configurations in the two metals following cold work and radiation damage may be quite similar.

On the basis of the large amount of similarity, it seems fair to conclude that the data on copper and nickel reaffirm and supplement each other. If this is accepted, one can conclude that the model for defect This work was performed for the United States Atomic Energy Commission under Contract AT-11-1-GEN-8.

REFERENCES

- L. M. CLAREBROUGH, M. E. HARGREAVES, D. MICHELL and G. W. West, Proc. Roy. Soc., Lond. A215, 507 (1952).
- L. M. CLAREBROUGH, M. E. HARGREAVES and G. W. WEST, Proc. Roy. Soc., Lond. A232, 252 (1955); Phil. Mag. 1, 528 (1956).
- 3. D. MICHELL, Phil. Mag. 1, 584 (1956).
- W. Boas, Dislocations and Mechanical Properties of Crystals p. 333. Wiley, New York (1957).
- J. A. BRINKMAN, C. E. DIXON and C. J. MEECHAN, Acta Met. 2, 38 (1954); D. B. BOWEN, R. R. EGGLESTON and R. H. KRODSCOT, J. April Phys. 93, 630 (1952)
- R. H. KROPSCOT, J. Appl. Phys. 23, 630 (1952).
 C. J. MEECHAN and J. A. BRINKMAN, Phys. Rev. 103, 1193 (1956).
- R. M. Barrer, Diffusion in and through Solids. Macmillan, New York (1941).
- 8. J. F. NICHOLAS, Phil. Mag. 46, 87 (1955).
- P. GAY, P. B. HIRSCH and A. KELLY, Acta Met. 1, 315 (1953).
- R. THOMSON, Acta Met. 6, 23 (1958).
- 11. A. D. LECLAIRE, Acta Met. 1, 438 (1953).
- H. Burgess and R. Smoluchowski, J. Appl. Phys. 26, 491 (1955).
- C. W. BERGHOUT, Thesis, de Technische Hogeschool te Delft; Acta Met. 6, 613 (1958)
- J. E. BAUERLE and J. S. KOEHLER, Phys. Rev. 107, 1493 (1957).

- 94, 496 (1954). 16. J. W. Marx, H. G. Cooper and J. W. Henderson,
- J. W. MARX, H. G. COOPER and J. W. HENDERSON, Phys. Rev. 88, 106 (1952).
 T. H. BLEWITT, R. R. COLTMAN, D. E. KLABUNDE and T. S. NOGGLE, J. Appl. Phys. 28, 639 (1957).
 N. F. MOTT and H. JONES, The Theory of the Properties of Metals and Alloys p. 222. Oxford University Press. (1936); R. J. WEISS and J. J. DEMARCO, Rev. Mod. Phys. 30, 59 (1958).
- 15. H. G. Cooper, J. S. Koehler and J. W. Marx, Phys. Rev. 19. T. H. Blewitt, R. R. Coltman, D. K. Holmes and
 - T. S. Noggle ORNL-2188, (1956).
 20. C. J. Meechan and A. Sosin, J. Appl. Phys. 29, 738 C. J. MEECHAN and A. SOSIN, J. Appl. Phys. (1958).
 R. R. EGGLESTON, Acta Met. 1, 679 (1953).
 C. J. MEECHAN, J. Appl. Phys. 28, 197 (1957).
 A. SEEGER, Z. Phys. 144, 637 (1956).

DIE ENERGIE UND DER ELEKTRISCHE WIDERSTAND VON GROSSWINKELKORNGRENZEN IN METALLEN*†

A. SEEGER und G. SCHOTTKY!

Mit Hilfe der Elektronentheorie der Metalle wird für ein einfaches Modell die Energie und der elektrische Widerstand von Grosswinkelkorngrenzen berechnet. Der Grundgedanke ist, dass an der Korngrenze die Atome einen etwas grösseren mittleren Abstand haben als im idealen Kristall. Der durch die Verschiebung der Ionenrümpfe entstehende Mangel an positiver Ladung muss durch Umlagerungen im Elektronengas des Metalls abgeschirmt werden. Die mit dieser Umlagerung verbundene Energieerhöhung wird für ein Gas quasi-freier Elektronen berechnet und bei Silber und Kupfer in überraschend guter Übereinstimmung mit den Messwerten der Korngrenzenenergie gefunden. Daraus wird geschlossen, dass das Modell tatsächlich den wichtigsten Beitrag zur Energie von Grosswinkelkorngrenzen in Metallen erfasst. Mit demselben Modell wird auch der elektrische Widerstand einer Korngrenze berechnet und zur Abschätzung des Verhältnisses von Widerstandsänderung zu Dichteänderung benützt. Es zeigt sich, dass dieses etwas kleiner als bei Leerstellen und Zwischengitteratomen ist.

ENERGY AND ELECTRICAL RESISTIVITY OF HIGH-ANGLE GRAIN BOUNDARIES IN METALS

Electron theory of metals is employed to calculate the energy and the electrical resistivity for a simple model of high-angle grain boundaries. The basic idea is this: At the grain boundary the average distance between atoms is somewhat larger than in the ideal crystal. The displaced positive charge of the atom cores has to be screened by a redistribution of the conduction electrons. The increase in energy due to this redistribution is calculated for a gas of quasi-free electrons. For silver and copper surprisingly good agreement with measurements of grain boundary energies is found. From this it is concluded that the model accounts for the main contribution to the energy of high-angle grain boundaries in metals. The same model is used to calculate the electrical resistivity of a grain boundary and to estimate the ratio between increase in resistivity and relative charge in crystal density. This ratio turns out to be somewhat smaller than that for vacancies and interstitials.

L'ENERGIE ET LA RESISTIVITE ELECTRIQUE DES JOINTS DE GRAINS A GRAND ANGLE DANS LES METAUX

Les auteurs utilisent la théorie électronique des métaux pour calculer l'énergie et la résistivité électrique pour un modèle simple de joints à grand angle. L'idée fondamentale est la suivante: à la frontière, la distance moyenne entre atomes est un peu plus grande que dans le cristal idéal. Le déplacement de la charge positive des noyaux doit être compensé par une redistribution des électrons de conduction. L'augmentation d'énergie provoquée par cet effet est calculée pour un gaz d'électrons quasi libres. Dans le cas de l'argent et du cuivre, le résultat est en excellent accord avec les valeurs mesurées pour les énergies de frontière. On en conclut que le modèle adopté explique la partie essentielle de cette énergie.

Le même modèle a servi au calcul de la résistivité electrique du joint et l'estimation du rapport entre l'augmentation de résistivité et la variation relative de la densité. Ce rapport s'avère légèrement plus petit que celui prévu pour des lacunes et interstitiels.

1. EINLEITUNG UND ÜBERBLICK

Das Hauptthema der vorliegenden Arbeit ist die Berechnung der spezifischen Flächenenergie (im folgenden kurz Energie genannt) von Grosswinkelkorngrenzen. Die Unterscheidung zwischen Kleinwinkelkorngrenzen und Grosswinkelkorngrenzen treffen wir folgendermassen: Wir sprechen von einer Kleinwinkelkorngrenze, wenn die Struktur der Korngrenze durch das Burgers-Braggsche Versetzungs-

modell der Korngrenzen gut dargestellt werden kann. $^{(1,2)}$ Ist dies nicht der Fall, so bezeichnen wir die Korngrenze als *Grosswinkelkorngrenze*. Unterhalb von welchem Orientierungsunterschied ϑ zwischen den Körnern auf beiden Seiten der Korngrenze das Versetzungsmodell eine zufriedenstellende Beschreibung der Verhältnisse gibt, hängt von mancherlei Nebenumständen ab: Von der zu beschreibenden Eigenschaft (z.B. Korngrenzenenergie, Einfluss der Korngrenze auf die Kristalldichte, die Diffusion, oder auf den elektrischen Widerstand etc.), von der Orientierung der Korngrenze gegenüber den kristallographischen Richtungen der Kristalle, von der Versetzungsweite und damit den Eigenschaften

VOL.

^{*} Received September 8, 1958.

[†] Elektronentheoretische Untersuchungen über Fehlstellen in Metallen VII.

[‡] Max-Planck-Institut für Metallforschung, Stuttgart, und Institut für theoretische und angewandte Physik der Technischen Hochschule Stuttgart.

der Atome und Ionen und anderem mehr.* Als ersten Anhaltspunkt kann man benützen, dass das Versetzungsmodell im allgemeinen zu versagen beginnt, wenn der Abstand der parallelen Versetzungslinien in der Korngrenze nurmehr einige Atomabstände beträgt, der Orientierungsunterschied ϑ also etwa 15° bis 20° ist. Hierbei spielen Einzelheiten des verwendeten Modells eine Rolle, z.B. ob man bei Berechnung der Korngrenzenenergie nach dem Versetzungsmodell wie Read und Shockley(3) noch einen experimentell zu bestimmenden Parameter mitführt, ob man wie Seeger und Hörnig⁽⁴⁾ das Peierlssche Modell verwendet und dadurch den bei Read und Shockley noch verfügbaren Parameter im Rahmen der Theorie festlegt, oder ob man die nichtlineare Elastizitätstheorie zugrunde legt, was für eine quantitative Behandlung des Einflusses der Korngrenzen auf die Kristalldichte und die Fremd- und Selbstdiffusion unerlässlich ist.

Für Grosswinkelkorngrenzen gibt es zwar verschiedene geometrische Beschreibungen der Korngrenzenstruktur (z.B. diejenigen von Mott, T'ing Sui Kê, Smoluchowski-siehe die zusammenfassende Darstellung⁽⁵⁾—sowie von Teissier du Cros⁽⁶⁾), aber ausser einer einfachen Abschätzung von Friedel, Cullity und Crussard⁽⁷⁾, die sich mit der Variation der Korngrenzenenergie mit der Orientierung befasst, gibt es unseres Wissens keine theoretische Berechnung der Energie von Grosswinkelkorngrenzen. Experimentell ist bekannt (siehe z.B. die Messungen von Aust und Chalmers an Zinn und Blei(8), dass die Energie von Grosswinkelkorngrenzen vielfach vom Korngrenzenwinkel ϑ unabhängig ist. Dies gilt, wenn man von kohärenten Zwillingsgrenzen absieht, was wir in dieser Arbeit tun wollen.

Wir berichten in der vorliegenden Mitteilung über eine elektronentheoretische Berechnung der Korngrenzenenergie einwertiger Metalle, die von denselben Grundideen ausgeht wie die Berechnungen der Bildungsenergie von Leerstellen durch Fumi⁽⁹⁾ und der Assoziationsenergie von Doppelleerstellen durch Seeger und Bross.⁽¹⁰⁾ In unserem Modell hängt die Korngrenzenenergie eng zusammen mit

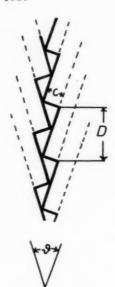


Fig. 1. Readsches Modell für eine Grosswinkelkorngrenze mit Korngrenzenwinkel ϑ . Die Spuren der auf der Korngrenze endigenden Netzebenen sind gestrichelt gezeichnet.

der Vergrösserung des Kristallvolumens durch die Korngrenze. Da man nach einem Gedanken von Read zeigen kann, dass diese Volumvergrösserung bei Grosswinkelkorngrenzen in guter Näherung vom Korngrenzenwinkel θ unabhängig ist, lässt sich mit unserem Modell der oben erwähnte experimentelle Befund verstehen. Wir werden ferner sehen, dass sich auch der absolute Betrag der Korngrenzenenergie in der richtigen Grössenordnung ergibt. In Abschnitt 4 werden wir das erwähnte Modell benützen, um eine theoretische Abschätzung des Beitrags von Grosswinkelkorngrenzen zum elektrischen Widerstand von Metallen zu geben, für den experimentelle Werte nicht vorzuliegen scheinen.

191

2. DAS MODELL

Es ist anschaulich klar und auf zahlreichen Abbildungen des Braggschen Seifenblasenmodells deutlich zu erkennen, dass eine Grosswinkelkorngrenze in dicht gepackten Kristallstrukturen ein Gebiet weniger dichter Packung und damit geringerer Dichte als der ungestörte Kristall darstellt. Ein schematisches Bild der Verhältnisse gibt die auf Read (11) zurückgehende Fig. 1. Die Volumvergrösserung pro Flächeneinheit der Korngrenze ΔV ist gegeben durch

$$\Delta V = \frac{c \cdot D}{2} \cdot \frac{1}{D} = \frac{c}{2}. \tag{1}$$

Für die Stufenhöhe \tilde{c} der einzelnen auf der Korngrenze endigenden Netzebenen setzen wir den Abstand

^{*} Es handelt sich bei dem Unterschied zwischen Grosswinkelkorngrenzen und Kleinwinkelkorngrenzen um eine theoretische Fragestellung. Vom experimentellen Standpunkt aus erscheint es zweckmässig, die Trennlinie zwischen Korngrenzen mit grossen Orientierungsunterschieden zwischen benachbarten Körnern und solchen mit kleinen Orientierungsunterschieden anders (nämlich bei wesentlich kleineren Werten von ϑ) zu ziehen. Wir unterscheiden zwischen Grobkorngrenzen, die mit den klassischen metallographischen Methoden des Ätzens und Polierens sichtbar gemacht werden können, und Feinkorngrenzen (wie sie z.B. bei der Polygonisierung oder bei der Zellbildung entstehen), deren Nachweis verfeinerter Verfahren bedarf.

der dichtgepackten Ebenen ein, der beim kubischflächenzentrierten Gitter mit der Kantenlänge a_0 des Elementarwürfels gemäss der Gleichung

$$c = a_0 / \sqrt{3} \tag{2}$$

zusammenhängt. Da das Atomvolumen $\Omega=a_0^3/4$ beträgt, ist die Zahl Z der pro Flächeneinheit einer Korngrenze fehlenden Atome

$$Z = 4c/2a_0^3 = 2\sqrt{3}/3a_0^2 = 1{,}15/a_0^2.$$
 (3)

Die Volumvergrösserung durch eine Korngrenze beträgt in diesem Modell grössenordnungsmässig ein Atomvolumen pro Elementarwürfelfläche. Bemerkenswert ist, worauf Read^{(11)} hinweist, dass in Gl. (1) der Abstand D der auf der Korngrenze endigenden Netzebenen herausfällt, so dass die berechnete Volumänderung unabhängig vom Korngrenzenwinkel θ ist. Dies gilt natürlich nicht mehr für kleine Winkel θ , bei denen das Modell Fig. 1 durch das Versetzungsmodell zu ersetzen ist.

Ähnliche Volumänderungen wie nach Fig. 1 erhält man durch Auszählen der Atome auf beiden Seiten einer Korngrenze im Seifenblasenmodell. Wir haben die bekannte Aufnahme von C. S. Smith⁽¹²⁾ benützt und daraus die Zahl der in einer {111}-Ebene in Grosswinkelkorngrenzen fehlenden Atome ermittelt. Dividiert man diese Zahl mit dem Abstand c der {111}-Ebenen, so bekommt man für die Volumänderung pro Flächeneinheit

$$\Delta V = Z\Omega = 0.9\Omega/a_0^2. \tag{4}$$

also einen ähnlichen Wert wie in Gl. (3).

1959

Sowohl in Gl. (3) wie in Gl. (4) ist die Volumänderung durch eine Korngrenze überschätzt worden. Im Modell Fig. 1 sind weder die Kompressibilität der einzelnen Atome und Netzebenen noch die Anziehungskräfte zwischen den Atomen berücksichtigt. Die "Atome" des Seifenblasenmodells sind zwar kompressibel, doch sind die Anziehungskräfte in diesem Modell wesentlich schwächer als bei einem Metall. Die Annahme, dass Z bei einem Metall gegenüber Gl. (4) im selben Mass verringert wird wie beim Übergang vom Modell Fig. 1 zum Seifenblasenmodell dürfte etwa den wirklichen Verhältnissen entsprechen. Wir nehmen deshalb an, dass bei einem kubisch-flächenzentrierten Metall Z zwischen $0.6a_0^{-2}$ und $0.7a_0^{-2}$ liegt.

Zur Berechnung der Korngrenzenenergie einwertiger Metalle verwenden wir folgendes, für verschiedene Zwecke gut bewährtes Modell: Das Metall ist aufgebaut aus einwertigen positiv geladenen Ionen, die in eine gleichförmige Verteilung "freier"

Elektronen mit entgegengesetzt gleicher Gesamtladung eingebettet sind. Die oben berechneten Volumänderungen geben die Zahl der aus der Korngrenze "herausgedrängten" positiven Ladungen an. Würden die Elektronen nicht teilweise den Ionenrümpfen folgen, so wäre eine negative Aufladung der Korngrenze mit weitreichendem elektrischen Feld die Folge. Dies ist natürlich in einem Metall wegen der Beweglichkeit der Ladungsträger nicht möglich. Infolgedessen ordnen sich die Elektronen so um, dass die effektive negative Ladung der Korngrenze abgeschirmt wird. Diese Umordnung im Elektronengas ist mit einem Energieaufwand verbunden, den wir als Hauptbeitrag zur Korngrenzenenergie ansehen und im nächsten Paragraphen mit Hilfe eines einfachen, der Rechnung zugänglichen Modells ermitteln werden.

3. BERECHNUNG DER KORNGRENZENENERGIE

Die Ermittlung des genauen Potentialverlaufs in der Nähe einer Korngrenze und die Berechnung der damit zusammenhängenden Erhöhung der Energie des Elektronengases wäre eine sehr schwierige Aufgabe. Wir verwenden ein vereinfachtes Verfahren, das zuerst von Friedel $^{(13)}$ in der Theorie der Legierungen benützt worden ist. Es besteht darin, einen plausiblen und mathematisch gut zu behandelnden Verlauf der potentiellen Energie U der Elektronen zugrunde zu legen und einen zur freien Verfügung gehaltenen Parameter (z.B. die Stärke des Potentials) so zu wählen, dass die in Abschnitt 2 erwähnte Ladungsbedingung (Gleichheit der in der Korngrenze "fehlenden" positiven Ladung und der abschirmenden Ladung) erfüllt ist.

Den von uns benützten Verlauf U(x) der potentiellen Energie zeigt Fig. 2, in der 2B eine effektive Breite der in der y,z-Ebene liegenden Korngrenze ist. Ist $U(x) \equiv 0$, so kann man die Eigenfunktionen der Elektronen in der Form (von einem Normierungsfaktor abgesehen)

$$\psi = \frac{\sin}{\cos} k_x x \cdot \frac{\sin}{\cos} k_y y \cdot \frac{\sin}{\cos} k_z z \tag{5}$$

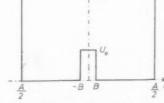


Fig. 2. Potentialverlauf U(x) für die Berechnung der Korngrenzenenergie. Die Höhe der Potentialschwelle ist U_0 , die Breite 2B.

VOI 7

schreiben. Die zugehörige Energie eines Elektrons in einem Zustand mit den Wellenzahlen $(k_x,\,k_y,\,k_z)$ ist

$$\epsilon = \frac{\hbar^2}{2m^*} (k_x^2 + k_y^2 + k_z^2) \equiv \frac{\hbar^2}{2m^*} k^2,$$
 (6)

wo \hbar die durch 2π geteilte Plancksche Konstante und m^* die effektive Masse der Elektronen ist. Im Bereich $-B \leq x \leq +B$ ist aus Stetigkeitsgründen die y- und z-Abhängigkeit der ψ -Funktion dieselbe wie in Gl. (5), so dass wir nur den x-abhängigen Faktor der ψ -Funktion, den wir mit $f_i(x)$ (i=0: symmetrische Lösung; i=1: antisymmetrische Lösung) abkürzen wollen, zu betrachten brauchen.

Ist $U_0 > \epsilon$, so gilt im Intervall $-B \leq x \leq +B$

$$f_0(x) = \cos \kappa_x x f_1(x) = \sin \kappa_x x$$
(7)

mit

$$\kappa_x^{\ 2} = \frac{2m^*}{\hbar^2}\,U_0 - k_x^{\ 2}. \eqno(8)$$

Ist $U_0 < \epsilon$, so treten an die Stelle der Gl. (7) und (8) die Ausdrücke

$$f_0(x) = \cos k_x' x f_1(x) = \sin k_x' x$$

$$(9)$$

und

$$k_{x}{'^{2}}=k_{x}{}^{2}-\frac{2m^{*}}{\hbar^{2}}\,U_{0}. \tag{10}$$

Die Eigenfunktionen für x>B schreiben wir in der Form

$$f_0(x) = \cos(k_x x + \eta_0) f_1(x) = \sin(k_x x + \eta_1).$$
 (11)

Die Anschlussbedingungen besagen bekanntlich, dass für die Funktionen Gl. (11) und Gl. (9) bzw. Gl. (7) $\frac{df(x)/dx}{f(x)}$ an den Stellen $x=\pm$ B übereinstimmen müssen. Dies führt auf

$$\begin{split} &\eta_0 = - \mathrm{arc} \operatorname{tg} \left(\frac{\kappa_x}{k_x} \operatorname{tg} \, B \kappa_x \right) - B k_x \\ &\eta_1 = \mathrm{arc} \operatorname{tg} \left(\frac{k_x}{\kappa_x} \operatorname{tg} \, B \kappa_x \right) - B k_x, \\ &\eta_0 = - B k_x \\ &\eta_1 = \mathrm{arc} \operatorname{tg} \, B k_x - B k_x, \\ &\eta_0 = \mathrm{arc} \operatorname{tg} \left(\frac{k_x'}{k_x} \operatorname{tg} \, B k_x' \right) - B k_x \\ &\eta_1 = \mathrm{arc} \operatorname{tg} \left(\frac{k_x'}{k_x'} \operatorname{tg} \, B k_x' \right) - B k_x. \\ &\eta_1 = \mathrm{arc} \operatorname{tg} \left(\frac{k_x}{k_x'} \operatorname{tg} \, B k_x' \right) - B k_x. \end{split}$$

Wie man sieht, ergibt sich für $B \to 0$ (für festes U_0), und für $U_0 \to 0$, also beim Fehlen des von der Korngrenze herrührenden "Störpotentials", $\eta_0 = 0$ und $\eta_1 = 0$. η_0 und η_1 bedeuten somit die Phasenverschiebungen, die in den Elektronenwellenfunktionen durch die Einführung der Korngrenze entstehen. Die Phasenverschiebungen hängen eng mit der von den Korngrenzen abgestossenen Ladung und mit der Energieänderung im Elektronengas zusammen.

Um dies im Einzelnen zu zeigen, betrachten wir die Zustandsdichte im k-Raum. Die Wellenfunktionen Gl. (5) müssen für $x, y, z = \pm \frac{A}{2}$ verschwinden. (Wir denken uns der Einfachheit halber den Kristall in y- und z-Richtung in gleicher Weise wie in x-Richtung begrenzt.) Man erhält

$$\cos k_i \, \frac{A}{2} = 0; \ k_i = \frac{2\pi}{A} \left(n + \frac{1}{2} \right), \ n \ge 0 \text{ ganz}$$

$$\sin k_i \, \frac{A}{2} = 0; \ k_i = \frac{2\pi}{A} \, n, \qquad n > 0 \text{ ganz}$$

Die Zustandsdichte im Oktanten $k_i \geq 0$ des k-Raums ist somit für jede der 8 in Gl. (5) enthaltenen Lösungstypen $A^3/(2\pi)^3$. Der Einfachheit halber kann man sich die zugehörigen Zustandspunkte über den gesamten k-Raum verteilt denken und erhält dann als Gesamtzustandsdichte im ganzen k-Raum ebenfalls $A^3/(2\pi)^3$.

Im "gestörten" Fall treten an Stelle von Gl. (15) die Gleichungen

$$k_x \frac{A}{2} + \eta_0 = \left(n + \frac{1}{2}\right)\pi$$

$$k_x \frac{A}{2} + \eta_1 = n\pi. \tag{16}$$

Die Wellenzahlvektoren werden bei der Einführung der Störung also um

$$\Delta k_x = -\eta_i(k_x) \cdot \frac{2}{A} \qquad i = 0, 1 \tag{17}$$

geändert. Nach Friedel^{(13)} ist die Zahl der durch das Störpotential abgestossenen Elementarladungen gleich der beim Einführen der Störung über die Fermioberfläche verschobenen Zustände (unter Berücksichtigung des Elektronenspins). Wir kennzeichnen hier die Fermioberfläche durch die Wellenzahl $k_{\rm F}$ an der Fermioberfläche und die Fermienergie

$$\zeta = \frac{\hbar^2}{2m^*} k_{\rm F}^2.$$
 (18)

Pro Flächeneinheit der Korngrenze ist die Zahl der aus dem Fermikörper hinausgeschobenen Zustände (einschliesslich Spin)

$$Z = -\frac{1}{\pi^2} \sum_{i=0,1} \int_0^{k_{\rm F}} \eta_i(k_x) k_x \, dk_x. \tag{19}$$

Die so errechnete Zahl Z muss bei einwertigen Metallen gleich der in Ziff. 2 besprochenen Zahl Z sein.

Die Änderung der Energieeigenwerte Gl. (6) durch das Störpotential beträgt

$$\Delta \epsilon = \frac{\hbar^2}{m^*} k_x \Delta k_x = -\frac{2}{A} \frac{\hbar^2}{m^*} k_x \eta_i \quad (i = 0, 1). \quad (20)$$

Die Änderung ΔE_1 der Summe der Elektronenenergien (pro Flächeneinheit gerechnet) erhält man durch Summation über den Fermikörper in guter Näherung zu

$$\begin{split} \Delta E_1 &= -\frac{2\hbar^2}{m^*} \frac{1}{(2\pi)^3} \int \int \int k_x (\eta_0 + \eta_1) \, dk_x \, dk_y \, dk_z \\ &= -\xi \cdot \frac{1}{\pi^2} \sum_{i=0,1} \int_0^{k_{\rm F}} k_x \Big(1 - \frac{k_x^{-2}}{k_{\rm F}^{-2}} \Big) \eta_i(k_x) \, dk_x. \end{split}$$
 (21)

Die Vergrösserung des Kristalls um Z Atomvolumina führt zu einer Erniedrigung der kinetischen Energie des Elektronengases um

$$\Delta E_2 = \frac{2}{5} Z \zeta, \tag{22}$$

so dass sich schliesslich als Korngrenzenenergie unseres Modells

$$\Delta E = \Delta E_1 - \Delta E_2 \tag{23}$$

ergibt.

VOL.

1959

Zur numerischen Ermittlung von ΔE als Funktion von Z hat man so vorzugehen, dass man die effektive Breite 2B der Schwelle durch Wahl des Parameters $k_{\rm F}B$ festlegt. (Bei kubisch-flächenzentrierten einwertigen Metallen ist $k_{\rm F}a_0={}^3\sqrt{12\pi^2}=4{,}91;$ speziell bei Kupfer $k_{\rm F}=1{,}37$ Å $^{-1}$.) Für verschiedene Werte von U_0 erhält man zusammengehörige Wertepaare ΔE und Z. Für $Bk_{\rm F}\ll 1$ (und gegen unendlich gehendes U_0) ergibt sich

$$\begin{split} Z = & \frac{k_{\rm F}^2}{\pi^2} \left\{ \frac{\pi}{4} - \frac{1}{2} \left(1 + \beta^2 \right) \text{ are } \cot \beta + \frac{\beta}{2} + \right. \\ & \left. + \frac{2}{3} B k_{\rm F} \cdot \beta^2 (1 - \beta \text{ are } \cot \beta) \right\} \ \, (24) \end{split}$$

und

$$\Delta E_1 = \zeta \cdot \frac{k_{\text{F}}^2}{\pi^2} \Big\{\! \frac{\pi}{8} - \frac{1}{4} \, (1+\beta^2)^2 \operatorname{arc} \cot \beta + \frac{5}{12} \, \beta + \frac{\beta^3}{4}$$

$$+\left.rac{4}{9}\,Bk_{\mathrm{F}}\cdoteta^{2}\Big(1+rac{3}{2}\,eta^{2}-rac{3}{2}\,eta(1+eta^{2})rc\coteta\Big)
ight|,$$
(25)

wobei zur Abkürzung die beim Grenzübergang endlich bleibende Grösse

$$\beta = \frac{U_0}{\zeta} \cdot Bk_{\rm F} \tag{26}$$

eingeführt wurde.

Für grössere $Bk_{\rm F}$ muss man die Integrale Gl. (19) und Gl. (21) numerisch auswerten. Das Ergebnis der zahlenmässigen Auswertung ist in Fig. 3 dargestellt. Ein interessantes und wichtiges Resultat ist, dass für $Za_0^2 < 1$ die Korngrenzenenergie nur wenig von der Breite B des Potentials abhängt.

4. ABSCHÄTZUNG DES ELEKTRISCHEN WIDER-STANDS EINER KORNGRENZE

Das in Abschnitt 3 zur Berechnung der Korngrenzenenergie verwendete Modell kann auch zur Abschätzung des elektrischen Widerstands von Grosswinkelkorngrenzen benützt werden. In diesem Modell werden Elektronen, deren Wellenzahlvektor k parallel

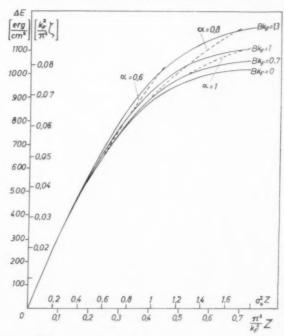


Fig. 3. Elektronischer Anteil ΔE der Korngrenzenenergie als Funktion von $a_0{}^2Z$ (spezifische Volumvergrösserung der Korngrenze) bzw. $\pi^2Z/k_F{}^2$ mit Bk_F als Parameter (ausgezogene Kurven). Die Zahlenangaben für ΔE sind in Einheiten von $(k_F/\pi)^2\zeta$ bzw. (für Silber, $a_0=4.078\cdot 10^{-8}$ cm, $k_F=1,204\cdot 10^{8}$ cm $^{-1}$, $m^*=m$) in erg/cm 2 gemacht. Die gestrichelten Kurven sind für verschiedene Werte des Parameters α (Gl. 30a) berechnet.

zu einer ebenen, unendlich ausgedehnt gedachten Korngrenze ist, nicht gestreut. Man kann also einen Reflexionskoeffizienten R definieren, der das Verhältnis der reflektierten zur auffallenden Intensität einer auf die Korngrenze auftreffenden ebenen Welle ergibt und der nur von der Wellenvektorkomponente k_x parallel zur Korngrenzennormalen abhängt.

Eine kurze Rechnung zeigt, dass R mit den in Abschnitt 3 berechneten Phasenkonstanten η_0 und η_1 nach der Beziehung

$$R = \sin^2\left(\eta_0 - \eta_1\right) \tag{27}$$

zusammenhängt. Den Zusammenhang zwischen dem Reflexionskoeffizienten R und dem zusätzlichen elektrischen Widerstand $\Delta \zeta$ haben für die hier vorliegende Geometrie und für das benutzte Modell sphärischer Energieflächen Stehle⁽¹⁴⁾ und Seeger⁽¹⁵⁾ angegeben. Bezeichnet θ den Winkel zwischen dem k-Vektor der einfallenden Welle und der Korngrenzennormalen, ist also an der Fermioberfläche

$$\cos \theta = k_x/k_F, \tag{28}$$

so gilt unter der Annahme, dass $\Delta \rho$ klein ist gegen den gesamten elektrischen Widerstand des Metalls, für den Korngrenzenwiderstand

$$\Delta \rho = \frac{m^*}{e^2 n_0} \overline{\tau^{-1}},\tag{29a}$$

$$\overline{\tau^{-1}} = 2 \frac{F}{V} \frac{\hbar k_F}{m^*} \int_0^{\pi/2} R(\theta) \cos^3 \theta \sin \theta \ d\theta. \quad (29b)$$

Hier bedeuten n_0 die Zahl der Leitungselektronen pro Volumeneinheit, e die elektrische Elementarladung und F/V die Korngrenzenfläche pro Volumeneinheit. In Gl. (29b) ist eine Verteilung der Richtungen der Korngrenzen angenommen, die mindestens kubische Symmetrie hat, und somit berücksichtigt, dass nur ein Drittel der gesamten Korngrenzenfläche F für die Streuung der Leitungselektronen wirksam ist.

Aus Gl. (12) findet man nach einigen Umformungen

$$R = \alpha^4 \sin^2 \left(2Bk_{\rm F}\sqrt{\alpha^2-\cos^2\theta}\right)/[4\cos^2\theta(\alpha^2-\cos^2\theta)]$$

+
$$[\alpha^4 \sin^2(2Bk_F\sqrt{\alpha^2 - \cos^2\theta})]$$
 (30)

mit der Abkürzung

$$\alpha^2 = \frac{2m^*U_0}{\hbar^2 k_{_{\rm F}}{}^2} = U_0/\zeta \; . \tag{30a} \label{eq:alpha}$$

Damit geht Gl. (29b) über in

$$\overline{\tau^{-1}} = 2 \, \frac{F}{V} \frac{\hbar k_{\rm F}}{m^*} \, \alpha^4 \int_{\sqrt{1-1/\alpha^2}}^1 \frac{x(1-x^2)\, \sin^2\gamma x}{4x^2(1-x^2) \, + \, \sin^2\gamma x} \, dx \tag{31a}$$

mit

$$\gamma = 2\alpha B k_{\rm F}. \tag{31b}$$

Gl. (31a) eignet sich für die numerische Auswertung, wenn $\alpha^2 \geqslant 1$ ist. Für $\alpha^2 \leqslant 1$ ist es zweckmässig, den mittleren Reflexionskoeffizienten

$$\bar{R} = \int_0^{\frac{\pi}{2}} R(\theta) \cos^3 \theta \sin \theta \, d\theta \tag{32}$$

in der Form

$$\overline{R} = \alpha^4 \int_0^1 \frac{\sin^2 \gamma x \cdot x (1 - x^2)}{4x^2 (1 - x^2) + \sin^2 \gamma x} dx +
+ \alpha^4 \int_0^{\sqrt{\frac{1}{\alpha^2} - 1}} \frac{x (1 + x^2) \sin^2 \gamma x}{4x^2 (1 + x^2) + \sin^2 \gamma x} dx$$
(33)

zu schreiben. Man sieht leicht ein, dass für $\gamma \to \infty$, also sehr "breite" Korngrenzen $(Bk_{\rm F} \to \infty)$, sich $\overline{R}=1/4$ gibt. Mit der in Abschnitt 3 benützten Abkürzung β gilt für $Bk_{\rm F} \ll 1$

$$\begin{split} \overline{R} &= \frac{\beta^2}{2} \left(1 - \beta^2 \ln \frac{\beta^2 + 1}{\beta^2} \right) + \\ &+ \frac{2}{3} B k_{\rm F} \beta^3 \left(1 + \frac{\beta^2}{\beta^2 + 1} - 2\beta^2 \ln \frac{\beta^2 + 1}{\beta^2} \right). \end{split} \tag{34}$$

In Fig. 4 ist \overline{R} als Funktion von $a_0^2 Z\left(\text{bzw.}\frac{\pi^2}{k_F^2}Z\right)$ mit Bk_F als Kurvenparameter aufgetragen. Ferner sind in Fig. 4 diejenigen Kurven gestrichelt angegeben, die man erhält, wenn man $\alpha=(U_0/\zeta)^{1/2}$, also die Höhe der Potentialschwelle, als Parameter

195

Für einen Vergleich mit experimentellen Daten und mit Ergebnissen über den elektrischen Widerstand von anderen Fehlstellen ist es bequem, das Verhältnis der Änderung $\Delta \rho$ des spezifischen elektrischen Widerstands zur relativen Volumänderung zu betrachten. Dies ist in Fig. 5 geschehen. Wir werden in Ziff. 5 darauf zurückkommen.

5. DISKUSSION DER ERGEBNISSE

In Abschnitt 3 und 4 haben wir mit einem vereinfachten elektronentheoretischen Modell die spezifische Korngrenzenenergie einer Grosswinkelkorngrenze in einem einwertigen Metall berechnet. In den Fig. 3 bis 5 sind die Resultate als Funktion des spezifischen Zusatzvolumens der Korngrenze aufgetragen ($Z={\rm Zahl}$ der pro Flächeneinheit der Korngrenze "fehlenden" Atome). Die Potentialschwelle, durch die die Korngrenze beschrieben wurde, wurde (mit Hilfe geeigneter dimensionsloser Grössen) entweder durch ihre Breite B oder ihre Höhe U_0 als Parameter charakterisiert.

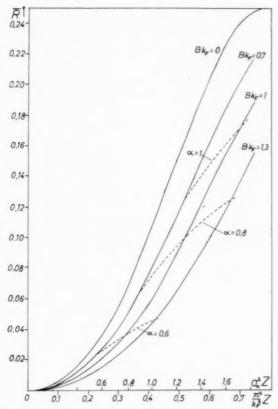


Fig. 4. Der mittlere Reflexionskoeffizient R einer Grosswinkelkorngrenze als Funktion von $a_0^2 Z$. Parameter sind $Bk_{\rm F}$ (ausgezogene Kurven) und α (gestrichelte Kurven).

1959

Die für Z zugrunde zu legende Grössenordnung wurde in Abschnitt 2 besprochen; wir haben dort gefunden, dass für die kubischflächenzentrierten Edelmetalle die Kantenlänge a_0 des Elementarwürfels Za_0^2 wohl zwischen 0,6 und 0,7 liegen dürfte. In diesem Bereich hängt die Korngrenzenenergie

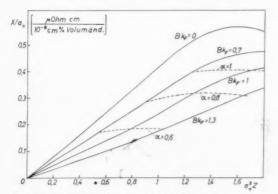


Fig. 5. X/a_0 (vergl. Gl. 35) als Funktion von $a_0{}^2Z$. X bedeutet die Änderung des spezifischen Widerstands geteilt durch die relative Volumänderung und wird in μ Ohm cm/ 0 0 Volumänderung erhalten, wenn man die Ordinaten von Fig. 5 mit der in Ängström–Einheiten ausgedrückten Gitterkonstanten a_0 multipliziert.

kaum von B und U_0 ab; es ergibt sich $\Delta E \approx 0,055 \, \frac{k_{\rm F}^2}{\pi^2} \, \zeta.$

Die experimentelle Bestimmung von Korngrenzenenergien von Metallen wird von McLean (5) ausführlich besprochen; die bis Anfang 1955 bekanntgewordenen experimentellen Daten sind in der dortigen Tabelle 3.1 aufgeführt. Dabei handelt es sich durchweg um freie Energien, die bei den oft nicht sehr weit vom Schmelzpunkt entfernt liegenden Messtemperaturen kleiner als die (von uns berechneten) inneren Energien sind. Aus neuester Zeit liegen jedoch an Ag, Al und Zn auch kalorimetrische Messungen der inneren Energie vor(16); diejenigen an Silber liefern Korngrenzenenergien zwischen 720 erg/cm² und 845 erg/cm². Als theoretischer Wert ergibt sich für Silber, wenn man die effektive Masse m* der Leitungselektronen gleich der Elektronenmasse m setzt, $E = 700 \text{ erg/cm}^2$, also die experimentell bestimmte Grössenordnung. Ähnliche Werte ergeben sich, wenn man nach den Vorschlägen von Åström(16) und McLean(5) die von Greenough und King(10) gemessenen freien Energien hinsichtlich der Temperaturabhängigkeit der freien Korngrenzenenergie korrigiert.

An Kupfer liegen bis jetzt nur Messungen der freien Energie vor: die Messungen vier verschiedener Autoren liefern freie Korngrenzenenergien zwischen 490 erg/cm² und 860 erg/cm² (siehe⁽⁵⁾). Berücksichtigt man wiederum die Temperaturabhängigkeit der freien Energie, so kommt man auf innere Energien zwischen 800 erg/cm² und 1200 erg/cm². Der theoretische Wert für Kupfer ist etwas unsicher, da die effektive Masse der Leitungselektronen nicht genau bekannt ist. Benützt man den aus optischen und thermischen Daten abgeleiteten und in der Literatur vielfach verwendeten Wert $m^* = 1,45m$, so erhält man eine Korngrenzenenergie von 800 erg/cm2; benützt man näher bei m liegende Werte für m*, so ergibt sich die Korngrenzenenergie entsprechend grösser.

Der Vergleich zwischen Experiment und Theorie zeigt, dass unser einfaches Modell einer Korngrenze die Beobachtungen recht gut wiedergibt. Dies gilt zunächst für den in Abschnitt I und 2 besprochenen Befund, dass bei Grosswinkelkorngrenzen die Korngrenzenenergie praktisch unabhängig vom Korngrenzenwinkel ist, bei Edelmetallen aber auch für die absolute Grösse der Korngrenzenenergie. Hinsichtlich der Absolutgrösse könnte man fast vollkommene Übereinstimmung mit den experimentellen Ergebnissen bekommen, wenn man das spezifische Korngrenzenvolumen etwas grösser wählte als wir es

getan haben. Dies zeigt nach unserer Auffassung, dass der in der vorliegenden Arbeit behandelte "elektronische" Beitrag wohl den Hauptanteil zur Korngrenzenenergie der einwertigen Metalle gibt. Alle andern Beiträge, z.B. die von der Wechselwirkung der Ionenrümpfe herrührenden, sind offensichtlich wesentlich kleiner oder kompensieren sich gegenseitig.

Die in Abb. 3 wiedergegebenen Zahlenwerte sind unter der Annahme "quasi-freier" Leitungselektronen ausgerechnet. Dies dürfte für die Edelmetalle eine zulässige Annahme darstellen, da bei diesen etwaige stärkere Abweichungen der Energieflächen von der Kugelgestalt auf die unmittelbare Umgebung der Fermioberfläche beschränkt sind, in die Berechnung der Energieänderung jedoch vor allem die Elektronenzustände im Innern des Fermikörpers eingehen. Hingegen muss man für quantitative Rechnungen bei mehrwertigen Metallen sicherlich die von der Kugelgestalt abweichende Form der Energieflächen berücksichtigen. Darüber hinaus hängt die Korngrenzenenergie in unserem Modell davon ab, ob der Ionenrumpf bei dem betreffenden Metall klein gegen den Atomabstand ist oder nicht. Im ersten Fall dürfte die Volumvergrösserung an der Korngrenze erheblich kleiner als oben abgeschätzt sein und damit auch die Korngrenzenenergie zu kleineren Werten hin tendieren. Dies scheint bei Aluminium zuzutreffen, wo trotz verhältnismässig grosser Fermienergie die Korngrenzenenergie nach Åström⁽¹⁶⁾ nur 600 erg/cm² bis 650 erg/cm² beträgt.

Anomal hoch wurde dagegen von Åström⁽¹⁶⁾ die Korngrenzenenergie in Zink gefunden, nämlich in der Grössenordnung 1600 erg/cm² bis 1900 erg/cm². Ohne detaillierte Rechnungen kann man zweifellos nicht sagen, ob ein derart grosser Wert sich mit unserem Modell verstehen lässt oder nicht. Verständlich dagegen ist, dass die Volumvergrösserung und damit die Energie einer Korngrenze ceteris paribus in einem hexagonalen Metall wesentlich grösser als in einem kubisch-flächenzentrierten Metall ist. Dies ist dadurch bedingt, dass man wegen der niedrigeren Symmetrie des hexagonalen Gitters zwei verschieden orientierte hexagonale Kristallite im Durchschnitt weniger gut zusammenpassen kann als zwei Kristallite kubisch-flächenzentrierter Struktur. Es wäre sicherlich interessant, diese Überlegungen bei Kobalt, wo man in einem für die Messungen geeigneten Temperaturbereich sowohl die kubischflächenzentrierte als auch die hexagonale Struktur findet, experimentell weiter zu verfolgen.

Die Diskussion über die Korngrenzenenergie abschliessend, wollen wir nochmals darauf hinweisen,

dass für kleine Orientierungsunterschiede zwischen benachbarten Körnern das von uns behandelte Modell durch das eingangs erwähnte Versetzungsmodell zu ergänzen ist. Eine selbstverständliche Forderung ist, dass für mittlere Orientierungsunterschiede, d.h. 20° bis 30°, die beiden Modelle etwa dieselbe Grössenordnung für die Korngrenzenenergie liefern. Dies ist bei Kupfer und Silber in der Tat der Fall.

Wir diskutieren nun noch kurz die in Ziff. 4 gegebene Abschätzung des elektrischen Widerstands einer Grosswinkelkorngrenze. Diese ist ziemlich grob, da sie der Gitterstruktur in den beiden Körnern und dem tatsächlichen Verlauf der Wellenfunktionen in den ungestörten Kristallbereichen nicht Rechnung trägt und da bekannt^(14,15) ist, dass in die Berechnung des elektrischen Widerstands eines Stapelfehlers der genaue Verlauf der Wellenfunktionen wesentlich eingeht. Im vorliegenden Fall liegen die Verhältnisse allerdings insofern etwas günstiger, als die ziemlich hohe Potentialschwelle an der Korngrenze die Wellenfunktionen sehr stark modifiziert und die Elektronen auf der einen Seite der Korngrenze doch nicht so sehr viel vom Detailcharakter der Wellenfunktionen auf der andern Seite "merken".

Vom praktischen Standpunkt aus interessiert vor allem das Verhältnis der Änderung des spezifischen elektrischen Widerstands zur relativen Änderung des Kristallvolumens, da dieses Verhältnis für die quantitative Diskussion der Wirkungen anderer Gitterfehler (Leerstellen, Zwischengitteratome, Versetzungen) eine Rolle spielt und man wissen möchte, ob man bei feinkörnigem Material den Einfluss der Korngrösse berücksichtigen muss. In Fig. 5 ist dementsprechend die Grösse

$$X/a_0 = k_{\rm F} a_0 \frac{2\hbar}{e^2 n_0 \Omega} \frac{\bar{R}}{Z{a_0}^2} \tag{35}$$

190

für ein einwertiges kubisch flächenzentriertes Metall gegen $a_0{}^2Z$ aufgetragen, und zwar in Einheiten

$$\left[\frac{\mu \text{Ohm cm}}{10^{-8} \text{ cm} \cdot \% \text{ Volumänderung}}\right].$$

X bedeutet bei statistischer oder kubisch-symmetrischer Verteilung der Korngrenzenanordnung gerade das oben erwähnte Verhältnis der Änderung des spezifischen Widerstands zu relativer Volumänderung. Für ein bestimmtes Wertepaar von a_0^2Z und $Bk_{\rm F}$ (bzw. α) liest man an der Ordinate von Fig. 5 einen bestimmten Zahlenwert ab. Multipliziert man diesen mit dem in Å gemessenen Zahlenwert von a_0 , so bekommt man X in der üblichen Einheit uOhm-cm/ $^{\circ}$ 0 Volumänderung. In dieser Einheit liegen

für die Edelmetalle die theoretischen Werte zwischen 0.5 und 1.2, also um einen Faktor der Grössenordnung 2 bis 3 kleiner als die zum Teil experimentell, zum Teil theoretisch gefundenen Werte für Leerstellen, Zwischengitteratome und aufgespaltene Versetzungen. Hat man einen Korndurchmesser $d = 10^4 a_0$, so beträgt die relative Volumänderung nach unseren Abschätzungen bei den Edelmetallen 5×10^{-5} . Dies bedeutet, dass man bei Messungen, während deren sich die Korngrösse sehr stark ändert, unter Umständen den Einfluss der Korngrenzen auf die Dichteänderung, den elektrischen Widerstand (und auch die freiwerdende innere Energie) berücksichtigen muss.

LITERATUR

1. J. M. Burgers, Akad. Wet. Verh. Amst. 42, 293 (1939); Proc. Phys. Soc. 52, 23 (1940).

VOL.

1959

- 2. W. L. Bragg, Proc. Phys. Soc. 52, 54 (1940).
- 3. W. T. READ und W. SHOCKLEY, Phys. Rev. 78, 275 (1950); Imperfections in Nearly Perfect Crystals, p. 352. Wiley, New York (1952).
- 4. A. Seeger, Handbuch der Physik, Bd. VII/1, S. 654. Springer-Verlag, Berlin-Göttingen-Heidelberg (1955).
- 5. D. McLean, Grain Boundaries in Metals. Clarendon Press, Oxford (1957).
- F. Teissier du Cros, Verformung und Fliessen des Festkörpers, Kolloquium, Madrid, September 1955, S. 137.
- Springer-Verlag, Berlin-Göttingen-Heidelberg (1956).
 7. J. FRIEDEL, B. D. CULLITY and C. CRUSSARD, Acta Met. 1, 79 (1953).
- 8. K. T. Aust und B. Chalmers, Proc. Roy. Soc. A 201, 210 (1950); *Ibid.* **204**, 359 (1951). 9. F. G. Fumi, *Phil. Mag.* **46**, 1007 (1955).
- 10. A. SEEGER und H. Bross, Z. Phys. 145, 161 (1956).
- 11. W. T. READ, Dislocations in Crystals, p. 172. McGraw-Hill, New York (1953).
- 12. C. S. SMITH, Metal Progr. 58, 479 (1950).
- 13. J. FRIEDEL, Phil. Mag. 43, 153 (1952); Advanc. Phys. 3, 446 (1954).
- H. Stehle, Dissertation, Stuttgart (1957).
 A. Seeger, Canad. J. Phys. 34, 1219 (1956).
 H. U. Äström, Ark. Fys. 13, 69 (1957).

EFFECT OF APPLIED TENSILE STRESS ON PHASE TRANSFORMATIONS IN STEEL*

L. F. PORTER† and P. C. ROSENTHAL‡

Using a specially designed apparatus capable of making simultaneous measurements of the electrical resistance and the extension of a wire specimen during rapid quenching or isothermal transformation, the transformation characteristics of a eutectoid steel have been studied under dead-weight tensile loading. Data obtained on transformation to pearlite, bainite, and martensite indicate that there is a threshold stress above which transformation is accelerated. When transforming under load, extensive plastic deformation is noted coincident with transformation. There also appears to be a threshold stress associated with the plastic deformation. In the case of transformation to pearlite and bainite, increased rates of transformation occur at the same threshold stress as the plastic deformation. On transformation to martensite gross plastic deformation occurs at very low stress, while the M_g temperature is not raised until stresses on the order of 28,500 lb/in² are reached.

To account for the coincidence of transformation and plastic extension it is proposed that dislocations piled up at grain boundaries and other barriers produce stress fields which result in increased rates of nucleation. Moreover, when the nucleus loses coherency with the parent austenite, the advancing interface acts as a sink for the piled-up dislocations and thus plastic deformation is observed. According to this picture, the threshold stress is the stress necessary to move free dislocations out from their sources to produce the piled-up arrays. The difference in the behavior of the martensite transformation under load can be explained on the basis of the differences between the mechanism of formation of martensite and that of pearlite and bainite.

EFFET D'UNE DEFORMATION PAR TRACTION SUR LES TRANSFORMATIONS DE PHASE DE L'ACIER

Les auteurs étudient les charactéristiques de la transformation d'un acier eutectoïde soumis à une déformation par traction. A cette fin, ils utilisent un montage spécial permettant de mesurer simultanément la résistance électrique et l'allongement d'un fil au cours d'une trempe énergique ou d'une transformation isotherme. Les résultats obtenus pour les transformations perlitiques, bainitiques et martensitiques indiquent qu'il existe un seuil de tension au-dessus duquel la transformation est accélérée. Lorsque la transformation a lieu sous charge, une déformation plastique importante se marque simultanément à la transformation. Il semble exister également un seuil de tension associé à la déformation plastique. Dans le cas des transformations perlitiques et bainitiques, l'accélération de la vitesse de la transformation se produit pour le même seuil de tension que pour la déformation plastique. Pour le transformation martensitique, une déformation plastique importante apparaît pour une tension très faible tandis que la température M_s n'est accrue que pour des tensions de l'ordre de $28\,5001\,\mathrm{lb/in^2}$

195

Les auteurs proposent d'interpréter cette coıncidence de la transformation et de la déformation plastique par un empilement de dislocations aux frontières granulaires. Ces empilements et autres barrières similaires produisent des champs de tensions d'où résulteront des vitesses de germination accrues. En outre, lorsque le germe n'est plus cohérent vis-à-vis de la matrice austénitique, l'interface en mouvement agit comme un puits pour l'empilement des dislocations et la déformation plastique en résulte. D'après ce modèle, le seuil de tensions correspond à la tension nécessaire pour déplacer les dislocations libres de leurs sources afin de provoquer des réseaux d'empilement. La différence de comportement de la transformation martensitique sous charge peut être expliquée sur la base des différences entre le mécanisme de la déformation de la martensite et celui de la ferrite et de la bainite.

BEEINFLUSSUNG VON PHASENUMWANDLUNGEN VON STAHL DURCH ZUGSPANNUNG

Mit Hilfe eines besonders konstruierten Apparates, der es gestattet, während schnellen Abschreckens oder isothermer Umwandlung einer Drahtprobe gleichzeitig deren elektrischen Widerstand und Verlängerung zu messen, wurde der Verlauf der Umwandlung von eutektoidem Stahl unter konstanter Zuglast untersucht. Bei der Umwandlung zu Perlit, Bainit und Martensit lassen die Messungen auf eine Schwellenspannung schliessen, oberhalb deren die Umwandlung beschleunigt ist. Verläuft die Umwandlung unter Last, so ist sie von grossen plastischen Verformungen begleitet. Auch für die plastische Verformung scheint es eine Schwellenspannung zu geben. Im Fall von Perlit und Bainit ist die Schwellenspannung für die Umwandlung und die plastische Verformung dieselbe. Bei der Martensitumwandlung tritt bei sehr niedriger Spannung bereits grosse plastische Verformung auf, die M_s -Temperatur steigt jedoch erst von Spannungen der Grössenordnung 28.500 lb/in² (=20 kg/mm²) ab an.

^{*} Based on a thesis submitted in partial fulfillment of the requirements for a Ph.D. at the University of Wisconsin. Received June 4, 1958; revised version December 29, 1958.

[†] Now with the Applied Research Laboratory, U.S. Steel Corp., Monroeville, Penn.

Zur Erklärung des gleichzeitigen Auftretens von Umwandlung und plastischer Dehnung wird vorgeschlagen, dass die Spannungsfelder von Versetzungen, die sich an Korngrenzen und anderen Hindernissen aufstauen, verstärkte Keimbildung zur Folge haben. Wenn der Keim dann die Kohärenz mit der Austenitmatrix verliert, bilden die entstehenden Phasengrenzflächen Senken für die aufgestauten Versetzungen, und man beobachtet plastische Verformung. Nach dieser Vorstellung ist also die Schwellenspannung diejenige Spannung, die notwendig ist, um freie Versetzungen von ihren Quellen zu lösen und so die aufgestauten Gruppen zu bilden. Das unterschiedliche Verhalten der Martensitumwandlung unter Last lässt sich auf Grund der Unterschiede zwischen den Bildungsmechanismen von Martensit einerseits und Perlit und Bainit andererseits verstehen.

1. INTRODUCTION

Until recently it was assumed by most metallurgists that stress would have little influence on phase transformations in solids. This view is indeed justified if one considers only the possible effects of stress on phase equilibria. For instance applying the Le Chatelier principle to the A_3 equilibrium in a eutectoid carbon steel, it can be shown that it takes a triaxial stress of $12{,}750\ \rm{lb/in^2}$ to change this equilibrium temperature $1^{\circ}\rm{C}$.

When one looks at the kinetics of phase transformation, however, the picture is quite different. The experimental evidence of Jepson and Thomson⁽¹⁾ and Bhattacharyya and Kehl⁽²⁾ indicate that the bainite and pearlite transformation in steel is accelerated by applied uniaxial stress. Since the work of Scheil⁽³⁾ a number of investigators^(4–9) have found a marked influence of stress on the martensite transformation in iron–nickel alloys as well as in the non-ferrous systems of gold–cadmium, indium–thallium and lithium–magnesium.

The present investigation was conducted in an attempt to obtain a unified picture of the effect of applied tensile stress on the bainite, pearlite and martensite transformations in a eutectoid carbon steel. The results have been analyzed and an explanation has been proposed based on dislocation theory.

2. EXPERIMENTAL METHOD

The material used throughout the investigation consisted of 0.040 in. diameter music wire having the following composition:

The wire was judged metallographically homogeneous as received and was used without further homogenizing heat treatment.

The progress of the transformation was obtained by recording the electrical resistivity of the specimen. The resistivity measurements, corrected for any plastic deformation occurring during the test, were converted to percent transformation using the first approximation that the percentage of the total resistance difference between austenite and the completely transformed structure at a given temperature was equal to the volume per cent of the transformed phases present. The validity of this approximation was checked using metallographic methods and was found to be within the accuracy of the metallographic estimation throughout most of the transformation range.

In order to obtain the required data, apparatus had to be developed capable of simultaneously recording temperature, resistance and the other variables of interest which were changing during isothermal transformation or during continuous cooling. The system which was finally evolved is an adaptation of an apparatus described by Colner and Zmeskal⁽¹⁰⁾. The primary advantage of the system is that no movement of the specimen from an austenitizing furnace to a quenchant is necessary. Instead, the wire specimen is heated in a purified helium atmosphere to austenitizing temperature and held for the required austenitizing time by passing a high amperage alternating electric current through it. After proper austenitizing. the high amperage current is replaced with a direct current resistance measuring circuit, and the specimen is quenched with a high velocity stream of helium gas to a predetermined isothermal temperature or to room temperature. In isothermal tests, the isothermal temperature is maintained by surrounding the specimen with a wire-wound tube furnace having a controlled central zone of uniform temperature. In order to transform under stress, arrangements are made for applying a dead-weight tensile load to the specimen. A schematic diagram of the apparatus with the specimen assembled and in place is shown in Fig. 1.

When making isothermal tests, the IR drop through the specimen is recorded on a photoelectric potentiometer. In order to study the martensite transformation, it is necessary to record five variables on a sixchannel recording oscillograph operating at a chart speed of 1 in./sec. Reproductions of the changes in resistance recorded during an isothermal test and of the change in the five variables recorded during a continuous cooling test are shown in Fig. 2. Careful

1959

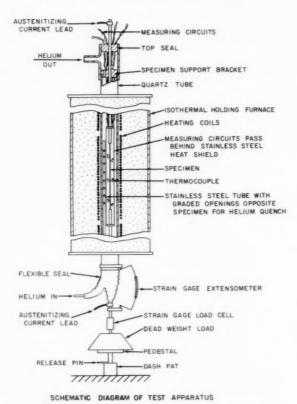


Fig. 1. Schematic diagram of apparatus for observing transformation under applied dead-weight tensile loads.

195

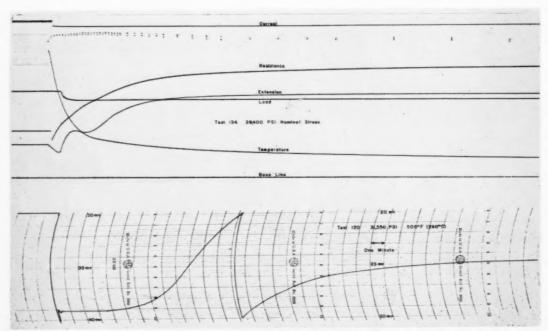


Fig. 2. Reproductions of records showing changes in variables during continuous cooling test (top) and the change in resistance during isothermal test (bottom).

EFFECT OF STRESS ON THE BAINITE TRANSFORMATION 260° C-500° F ISOTHERM AUTOCATALYTIC PLOT

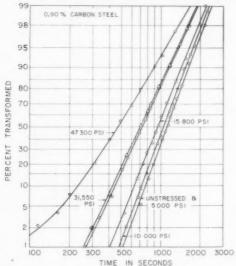


Fig. 3. Typical autocatalytic plot showing effect of applied tensile stress on bainite transformation at 260°C.

calibration and checking of the apparatus indicated that, during test, temperatures remained uniform along the specimen and that the accuracy of the recorded information was limited primarily by the ability to read the charts.

3. RESULTS

The results are most conveniently divided into three groups: results obtained on isothermal tests in the bainite region, less complete results obtained isothermally and by continuous cooling in the pearlite region, and results obtained for the martensite transformation on quenching.

Transformation to bainite

VOL.

1959

In the bainite region the transformation characteristics were determined for a series of increasing applied uniaxial tensile stresses at isothermal temperatures of 260°C (500°F), 316°C (600°F) and 371°C (700°F). The results indicate that above a certain threshold stress applied tensile stress markedly accelerates the transformation. It appears that the degree of acceleration, as measured by the decrease in time to achieve a given amount of transformation, is a linear function of the applied stress, especially at the lower stress levels.

Instead of plotting per cent transformation vs. log time to produce the typical sigmoid curve, the resistance measurements were converted to percent transformation and plotted on an autocatalytic plot. The type of plot obeys the following equation:

$$\log (P/100 - P) = K \log t + C$$



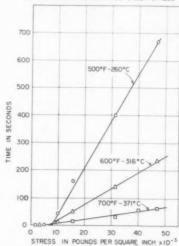


Fig. 4. The manner in which the applied stress decreases the transformation time. Note the threshold at 6000–8000 lb/in²

where P is the amount transformed and t is time, K and C being constants. Its use for representing the bainite transformation was first suggested by Austin and Rickett⁽¹¹⁾ who showed that the original data of Davenport and Bain⁽¹²⁾ for the bainite transformation lay on a straight line when plotted in this way. While the fact that a straight line results is probably without real significance, such a plot does aid in establishing start and completion times for the reaction (on the basis of 1 per cent and 99 per cent transformation) and promotes confidence in the experimental results when they plot on a straight line.

Fig. 3 is an autocatalytic plot showing the effect of applied stress on the kinetics of the bainite transformation at 260°C. One notes that the experimental results plot as straight lines at all but the highest stress level. It is apparent that applied tensile stress, while markedly increasing transformation rates, has a greater effect on the early stages of the transformation than on the later stages. Results at 316°C and 371°C show the same characteristics as those at 260°C but of course transformation occurs in shorter times. Furthermore, if one examines the decrease in transformation time as a function of applied stress, another important effect is noted. In Fig. 4 the decrease in time to achieve 50 per cent transformation has been plotted against applied stress. The decrease is found to be proportional to applied stress and, on the basis of the extrapolated plots, the minimum stress needed to produce accelerated transformation is found to be 8000 lb/in² at 260°C, approximately 7000 lb/in² at 316°C, and 6000 lb/in2 at 371°C.



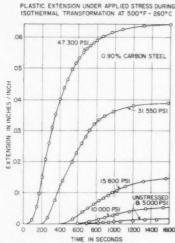


Fig. 5. The progress of the deformation which occurs coincident with isothermal transformation to bainite at $^{260^{\circ}\mathrm{C}}$

Shortly before evidence of transformation was noted by a change in electrical resistance, the specimen began to extend plastically at a rather rapid rate. The extension continued throughout the major portion of the transformation, ceasing somewhat before resistivity measurements indicated that the transformation was complete. The progress of the rapid extension occurring during transformation at 260°C is shown in Fig. 5. Again these results are typical of the form of the extension curves obtained at the higher temperatures. The total extension suffered by the specimen is found to be proportional to the applied stress and, at the maximum stresses investigated, is approxi-

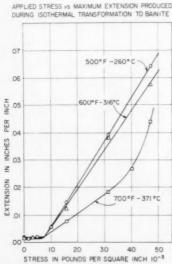


Fig. 6. The relationship obtained between applied stress and extension. Note that the same thresholds are observed as in Fig. 4.

EFFECT OF APPLIED STRESS ON PLASTIC EXTENSION
DURING ISOTHERMAL TRANSFORMATION

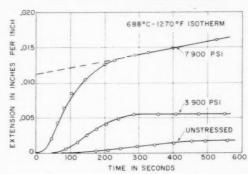


Fig. 7. Extension measurements made during isothermal transformation to pearlite at 688°C.

mately 35 times higher than that resulting from transformation without applied stress.

If one plots maximum extension as a function of stress (Fig. 6) one finds that at lower stresses a straight line relationship exists and the extrapolated straight lines have threshold values which are approximately the same as the thresholds obtained on extrapolation of the transformation time vs. stress curves. There appears to be an intimate relationship between the rapid extension noted and the increased transformation rates. Indeed, the onset of the rapid extension under load is found to be a more sensitive indication of the start of transformation than are the resistivity measurements, since it is observed before a change in resistance is detected.

Transformation to pearlite

Only a few isothermal tests were carried out in the pearlite range at 688°C (1270°F). Results of resistance measurements made to determine the isothermal transformation characteristics under load were generally unsatisfactory, owing to difficulties in attaining the isothermal temperature and to the rapid change in transformation kinetics with temperature in this region. The results did indicate that transformation was accelerated by stresses below 4000 lb/in² and again rapid extension was observed to occur slightly before the resistance measurements indicated that transformation was in progress.

The results shown in Fig. 7 are typical of the extension measurements made during isothermal transformation in the pearlite region. At a stress of 7900 lb/in² it is seen that rapid extension occurs and is completed in about 300 sec, after which a steady rate of creep continues. It is interesting to note that under the conditions of this test the pearlite transformation is completed in somewhat under an hour and that in

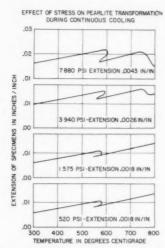


Fig. 8. Reproductions of records of extension obtained during continuous cooling through the pearlite region.

300 sec the specimen is somewhat less than 50 per cent transformed. At the lower stress of 3950 lb/in² rapid extension and its subsequent early completion is noted again. In this case no creep is observed after the rapid extension has ceased.

Additional data obtained by continuous cooling through the pearlite region substantiate the isothermal results. Here again data obtained from extension measurements prove to be most reliable. Fig. 8 shows the effect of increasing the applied tensile stress on the extension occurring during transformation. Examination of Fig. 8 shows that applied stresses of 1575 lb/in² and below do not alter the temperature range of recalescence and therefore do not accelerate the pearlite transformation. Likewise, these low stresses do not result in extension in excess of the normal transformation dilatation. At higher stresses, evidence of acceleration of the transformation as well as plastic

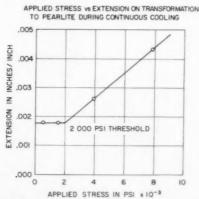


Fig. 9. The relationship between applied stress and the extension obtained during continuous cooling through the pearlite region.

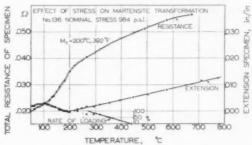


Fig. 10. Results of resistance and extension measurements made during quenching to form martensite at low applied stresses. The lower plot gives the percentage of the total load applied in the temperature range indicated.

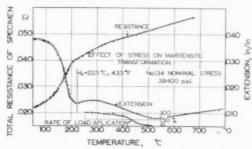


Fig. 11. Results of resistance and extension measurements made at high applied tensile stresses. The lower plot gives the percentage of the total load applied in the temperature range indicated.

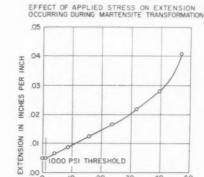


Fig. 12. Applied stresses in excess of 1000 lb/in² cause extension during the martensite transformation.

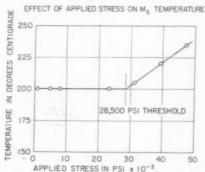


Fig. 13. The M_z temperature is not affected until stresses over 28,500 lb/in² are applied.

7 1959 extension during transformation is observed. As with the bainite data, extrapolated linear plots of the extension data (Fig. 9) indicate a threshold for plastic extension coincident with accelerated transformation. In the case of pearlite, the threshold occurs at a stress of 2000 lb/in² as compared with the 8000 lb/in² deduced for the bainite transformation at $260^{\circ}\mathrm{C}$.

Martensite transformation

Representative examples of the data obtained on quenching to form martensite under various applied loads are given in Figs. 10 and 11. Here again it is noted that rapid extension occurs during transformation. The effect of stress on the extension and transformation are presented in Figs. 12 and 13.

The results are quite different from those obtained previously for bainite and pearlite. It is observed that the threshold for increased extension is very low. about 1000 lb/in², while no effect on the M_{\circ} temperature is observed until a stress of approximately 28,500 lb/in2 is reached. It is also evident from Figs. 10 and 11 that the beginning of rapid extension is coincident with the M, temperature, as measured by resistance, instead of preceding it as in the case of bainite and pearlite transformations. Measurements of hardness and of retained austenite content by integrated X-ray intensity methods indicate that the applied stress has little influence on the total amount of martensite formed. While the progress of transformation was not calculated from the resistivity measurements, the shapes of the resistivity curves obtained under stresses of over 28,500 lb/in2 indicate that the stress-induced transformation occurring at temperatures in excess of 200° C, the normal M, temperature, progresses at a much slower rate with decreasing temperature than does the normal transformation occurring below 200°C. In other words, stress-induced transformation occurs and progresses slowly at temperatures above 200°C, but when the normal M, temperature is reached the normal transformation begins and progresses just as it would if no stress were present.

4. DISCUSSION OF RESULTS

The results indicate that there is a threshold stress associated with plastic extension during transformation, and in the pearlite and bainite regions this is also the threshold stress for increased rates of transformation. Thus when the applied stress exceeds a certain value, transformation rates are accelerated, and when transformation occurs, the yield strength of the steel is suddenly markedly reduced. Conditions are somewhat different in the case of martensite formation.

0.2% OFFSET YIELD STRENGTH OF METASTABLE AUSTENITE VS SQUARE ROOT OF TEMPERATURE

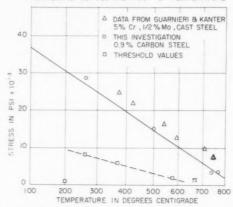


Fig. 14. An estimation of the yield strength of metastable austenite in the material used in this study. Note the low values of the thresholds compared with the yield strength.

Here plastic extension during transformation occurs at very low stress while an increase in M_s temperature does not occur until a very high stress is reached.

The threshold stress is very low compared to the stress being sustained by the specimen up to the time transformation begins. Indeed, it is much lower than the probable 0.2 per cent offset yield stress. A rather good estimate of the yield strength of the metastable austenite may be obtained from the loads which it was able to sustain during isothermal studies. Two additional pieces of information on this point are also available. First, it is known that the yield stress should vary as the square root of the absolute temperature (13) and secondly, Guarnieri and Kanter⁽¹⁴⁾ have made 0.2 per cent offset yield stress measurements on metastable austenite in 5% chromium-1% molybdenum steel which can be compared with the present data. In Fig. 14, a stress vs. \sqrt{T} plot of data derived from isothermal and continuous cooling data is compared with the data of Guarnieri and Kanter, and the estimated temperature vs. 0.2 per cent offset yield stress relationship for the material used in this study is indicated. Also shown are the threshold stresses in the pearlite, bainite and martensite regions.

195

The question one naturally asks is: "What is the mechanism by which the resistance to flow is lowered during transformation, and what determines the threshold stress?" Plastic flow during transformation under load has been reported previously (2,14,15) but a detailed explanation is usually lacking. Boas (16) states that it may be possible that the high mobility of the atoms at the interface between old and new phase during transformation gives rise to weakness and plasticity of the metal in the same way as does the

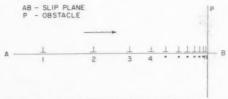
VOL.

1959

high mobility at grain boundaries at elevated temperatures. However, Boas' suggestion can not tell the whole story. It is difficult to see how isolated transforming nuclei, such as must be present when the effect is first noted, could, by the mobility of their boundary atoms alone, account for gross plastic deformation of the remaining matrix. Moreover, on the basis of the results presented here, any complete explanation would have to account for the observed threshold for plastic deformation during transformation and for the fact that the same threshold is observed for increased rates of transformation.

If one rejects the explanation that the increased mobility of the atoms at the transforming interface, in itself, can account for the plastic deformation accompanying transformation under load, one must examine the other possible sources of resistance to deformation which might be altered by the initiation of transfor-These sources are alloying elements in solution, precipitates, interacting dislocations, and the difficulty of transmitting slip from one grain to another. In austenite, the high solubility of the alloying elements present and the elevated temperatures involved would lead one to believe that their contribution to the yield strength must be small. Cottrell anchoring of dislocations is not strong because, for the temperatures involved, atmospheres of solute atoms, especially carbon and nitrogen, are probably not condensed at the dislocations in the face-centered cubic lattice. Precipitates, as such, are not present. Taking everything into account, it would appear that it must be the release of the resistance to deformation offered primarily by the grain boundaries, and to some extent by the interacting dislocations, which is responsible for the plastic flow associated with transformation.

Grain boundaries offer resistance to slip because the direction of the plane of slip changes at the boundary. Moreover, in order to take into account the effect of grain size, Nabarro $^{(17)}$ suggests that there be a region $10^{-4}\,$ cm thick at the grain boundaries where the coherence of the grains causes severe elastic distortion and slip on unfavorable planes, in which case, extra



THE PILING OF DISLOCATIONS AGAINST AN OBSTACLE FROM COTTRELL

Fig. 15. A schematic representation of a pile-up array of dislocations after Cottrell.

work must be done in order to drive dislocations against these stresses.

Transformation could alter the influence of grain boundaries in the following way. Dislocations move out from dislocation sources at relatively low stresses, but extensive yielding is not observed because the dislocations are held up at the grain boundaries. This results in a piling-up of dislocations into an equilibrium distribution against the boundaries as shown schematically in Fig. 15. The nucleation of the transformation causes a collapse of the resistance offered by the grain boundaries, allowing the dislocation arrays to move forward, and thus the rapid extension coincident with transformation is noted.

If the picture is to be complete it remains to be shown that, under stress, an array of dislocations blocked at a grain boundary will promote increased transformation rates. It is generally conceded that the stresses involved can not greatly influence diffusion rates and that the increased rate of transformation must be mostly associated with increased rates of nucleation. Using the results of Cottrell(18) and Eshelby et al. (19), Koehler (20) has shown that, in an array of edge dislocations blocked by an obstacle as shown in Fig. 15, there can be a high concentration of tensile stress over a considerable region in the vicinity of the dislocation nearest the obstacle, and extensive dilatation of the lattice can occur in the region below this dislocation. The extraordinary dilatation of the lattice promotes the formation of the stable phases through the action of the LeChatelier principle. Moreover, because of the number of piled-up arrays produced, more nuclei will be activated, resulting in a reduction in the distance an atom must diffuse before reaching the nearest nuclei. Finally, the internal stress gradient near the first dislocation will tend to accelerate diffusion. (21) For these reasons, the normal rate of nucleation of the stable phases will be materially increased when dislocation arrays pile up at grain boundaries under the action of applied stress.

The mechanism whereby applied tensile stress influences transformation in the bainite and pearlite regions may thus be described as follows: The threshold stress represents the effective stress necessary to cause dislocations to move out from dislocation sources and begin piling up at grain boundaries. The dislocation arrays thus formed produce a large concentration of tensile stress in the vicinity of the leading dislocation. This stress and its accompanying dilatation of the crystal lattice result in increased rates of nucleation and therefore in increased rates of transformation. When the nuclei lose coherency with the parent lattice, the dislocation arrays are freed from

their barriers. The growing interface acts as a sink as well as a source for dislocations. Thus dislocation movement is again possible and rapid deformation occurs coincident with transformation. Deformation can continue until the phases being formed are continuous. This accounts for the completion of plastic deformation after only about 50% of the pearlite has been formed and not until about 95% of the bainite has been formed, since pearlite becomes continuous much earlier than bainite.

Petch's work⁽²²⁾, on the relationship between the lower yield point, the tensile stress necessary to move a dislocation freed from its atmosphere, and the grain size in ferrite, although not directly comparable, lends support to the idea that the threshold stress observed in the present investigation is indeed the effective tensile stress necessary to move dislocations out from their sources to form dislocation arrays.

It is also interesting to note that, according to the proposed mechanism, either uniaxial tension or compression should show increased rates of transformation, since the active component of the stress is the shear stress along the slip direction and the sign of the shear stress is not involved. Results obtained by Jepson and Thomson⁽¹⁾ indicate that this is indeed the case.

If nucleation rates were accelerated uniformly throughout the transformation, the resulting autocatalytic plot would be displaced to shorter times but would still be parallel to the original unstressed plot. In the present case the slopes change as stress is increased so that the plots have a larger separation at the start of transformation than at the completion of transformation. This indicates that in the early stages of transformation nucleation is accelerated much more than during the later stages. The early stages of transformation are believed to be accelerated by the formation of more and larger pile-ups and the increased stress concentration below pile-ups. Once transformation is under way, however, the pile-ups begin to be released and their influence is soon lost.

At high applied stresses the early portions of the autocatalytic plots depart from linearity (see curve for 47,300 lb/in² applied stress, Fig. 3). This is believed to be associated with plastic deformation resulting from stresses in excess of the yield stress. The slip bands resulting from such deformation probably produce atomic configurations which act as additional nucleation sites within the grains. This type of mechanism has been reviewed by Averbach⁽²³⁾ and is well known in age hardening systems.

In all cases it has been assumed that dislocation movement must occur to produce the stress concentrations and atomic configurations which lead to increased transformation. However, the dislocations do not appear greatly to influence transformation merely by the act of moving through the lattice, since the rate of plastic deformation is greatest during the middle stages of transformation while the amount by which the transformation is accelerated is greatest at the start of transformation.

It will be remembered that in examining the effect of applied stress on the martensite transformation, loads were applied at elevated temperatures during rapid cooling, and some plastic deformation occurred before the material became cool enough to support the load. Thus the austenite was strained when the M_{\star} temperature was reached, and for loads which raised the M_{\circ} temperature, some plastic deformation was probably still in progress when transformation started. From Fig. 15 the 0.2 per cent offset yield strength of austenite in the vicinity of the normal M_{\circ} (200°C) is estimated as 31,000 lb/in2 and on the basis of a square root dependence between threshold stress and temperature one would expect a threshold of about 10,000 lb/in2 whereas the actual threshold occurs at 1,000 lb/in². No change in the M_s is noted coincident with the threshold stress, and none occurs until stresses over 30,000 are applied.

The most obvious explanation for the increased extension observed at low stress when austenite is transformed to martensite is that low applied stress causes the martensite plates to form with a preferred orientation, resulting in the concomitant change in length even though the transformation kinetics have not been changed a detectable amount. Enhanced deformation under load as a result of preferred orientation during the martensite transformation has been reported by Chang and Read(7) in the case of the gold-cadmium system. However, in the present case, a careful search using metallographic techniques failed to reveal any preferred orientation during the early stages of transformation to martensite under stress, and X-ray diffraction techniques failed to reveal any preferred orientation in the completely transformed martensite structure.

19!

The experimental results might better be explained in a second way. It is well known that some of the free energy which must be available to form a martensite plate is released as kinetic energy during the formation of the plate. This kinetic energy manifests itself as observable slip in the austenite adjacent to the newly formed plate and in a shock wave which passes through the austenite, often resulting in an audible click. Perhaps the "triggering off" of pre-existing martensite embryos supplies the energy necessary to drive dislocations through the austenite.

forming pile-ups which are forced hard against the grain boundaries. Thus, in the case of the martensite transformation, the energy to move the dislocations out from their sources and to force arrays against the grain boundaries is supplied by the transformation, and only a small additional applied stress is required to activate slip in preferred directions in the adjacent grains and thus cause the observed extension.

An accurate description of the cause of the deformation which is observed to accompany transformation under stress probably involves both the effects of preferred orientation of the transformation products and the plastic deformation mechanism described in this paper, the relative importance of the two mechanisms being dependent on the system involved and the experimental conditions. In this case it would appear that the latter mechanism is predominant.

Why applied stresses begin to influence M_s only in excess of 28,500 lb/in² is not easily understood. This influence cannot result solely from plastic deformation. For example, it has been demonstrated frequently that martensite can be isothermally formed by plastic deformation at temperatures between M_s and a higher critical temperature known as M_d . But if this mechanism were active in the present case, one would expect that as soon as plastic deformation occurred below M_d martensite would be produced and there would be a sudden jump in the temperature of transformation from the normal M_s at 200°C to some higher temperature (M_d) instead of the actual experience of the gradually rising transformation temperature as the stress is raised above 28,500 lb/in².

It is apparent that the experimental results have brought to light several features of the effect of stress on the martensite transformation which are not readily explained by our present understanding of the transformation. Further study of the effect of stress on martensite formation under varying conditions of plastic deformation and grain size should prove to be a fruitful field of investigation.

From the practical point of view, consideration of the thresholds for plastic deformation, especially the low threshold on transformation to martensite, should prove of importance in the prediction and interpretation of residual stress patterns resulting from heat treatment, just as an awareness of the effect of stress on transformation kinetics is helpful in explaining anomalous internal structures often observed in heat treated steels.

5. CONCLUSIONS

Using special high speed recording techniques, transformation under applied tensile loads has been studied in a eutectoid carbon steel. It has been shown that stress in excess of a threshold value is capable of accelerating transformation to pearlite and bainite, and of raising the M_s temperature. Plastic extension of the specimen occurs coincident with transformation when the applied load exceeds a given threshold. In the case of pearlite and bainite transformation, the threshold for plastic extension is found to have the same value as the threshold for accelerated transformation. On transformation to martensite, the threshold stress for plastic extension has a surprisingly low value while the applied loads have no effect on the M_s temperature until very high stresses are reached.

It is proposed that on transformation to pearlite and bainite the threshold stress is the effective stress required to move dislocations out from their sources. The dislocations move to the grain boundaries or other barriers where they form piled-up arrays. It is further suggested that the stress concentration existing on the leading dislocation of such an array is responsible for the increased rates of transformation observed.

To account for the low threshold for plastic extension observed on transformation to martensite, the explanation offered is that the kinetic energy released when a plate of martensite forms is capable of moving dislocations out from their sources and forcing pile-ups arrays against the grain boundaries, so that only a small additional applied stress is necessary to activate slip in adjacent grains and produce gross plastic deformation. The high threshold needed to raise the M_s temperature is difficult to explain on the basis of our present knowledge of the mechanism of martensite formation. It appears that more information is needed on the way grain size and prior plastic deformation influence stress-induced transformation to martensite.

It is believed that consideration of the thresholds for plastic deformation and accelerated transformation should be of importance in studying residual stress patterns and structural anomalies which occur in heat treated steels.

ACKNOWLEDGMENTS

The authors are especially grateful to the Chain Belt Company of Milwaukee, Wisconsin, for sponsoring this investigation and to J. J. Scales and the members of the metallurgical staff at Chain Belt Company for their helpful discussion, interest and encouragement.

REFERENCES

 M. D. Jerson and F. C. Thomson, Acceleration of the Rate of Isothermal Transformation of Austenite, J. Iron St. Inst. 162, 49 (1949).

VOL. 7 1959

- S. BHATTACHARYYA and G. L. KEHL, Isothermal Transformation of Austenite under Externally Applied Tensile Stress, Trans. Amer. Soc. Metals 47, 351 (1955).
- E. SCHEIL, Über die Umwandlung des Austenits in Martensit in Eisen-Nickel-Legierungen unter Belastung, Z. Anorg. Allgem. Chem. 207, 21 (1932).
- A. W. McReynolds, Effect of Stress and Deformation on the Martensite Transformation, J. Appl. Phys. 20, 896 (1949)
- S. A. KULIN, M. COHEN and B. L. AVERBACH, Effect of Applied Stress on the Martensite Transformation, Trans. Amer. Inst. Min. (Metall.) Engrs. 194, 661 (1952).
- J. R. Patel and M. Cohen, Criterion for the Action of Applied Stress in the Martensite Transformation, Acta Met. 1, 531 (1953).
- L. C. CHANG and T. A. READ, Plastic Deformation and Diffusionless Phase Changes in Metals—The Gold-Cadmium Beta Phase, Trans. Amer. Inst. Min. (Metall.) Engrs. 191, 47 (1951).
- M. W. Burkart and T. A. Read, Diffusionless Phase Changes in the Indium-Thallium System, Trans. Amer. Inst. Min. (Metall.) Engrs. 197, 1516 (1953).
- C. S. Barrett and O. R. Trautz, Low Temperature Transformation in Lithium and Lithium-Magnesium Alloys, Metals Tech. 15, T.P. No. 2346 (1948).
- W. H. Colner and O. Zmeskal, An Electrical Resistance Apparatus for Studying Transformation in Stainless Steel, Trans. Amer. Soc. Metals 44, 1158 (1952).
- J. B. Austin and R. L. Rickett, Kinetics of the Decomposition of Austenite at Constant Temperature, Metals Tech., 5, T.P. No. 964 (1938).
- 12. E. S. DAVENPORT and E. C. BAIN, Transformation of

- Austenite at Constant Subcritical Temperatures, Trans. Amer. Inst. Min. (Metall.) Engrs. 90, 117 (1930).
- A. Kochendörfer, Plastische Eigenschaften von Kristallen und Metallischen Werkstoffen. Springer-Verlag, Berlin (1941).
- G. J. GUARNIERI and J. J. KANTER, Some characteristics of the Metastable Austenite of 4-6% Chromium plus ½% Molybdenum Cast Steel, Trans. Amer. Soc. Metals 40, 1147 (1948).
- A. Sauveur, The Metallography and Heat Treatment of Iron and Steel. The University Press, Cambridge, Massachusetts (1926).
- W. Boas, Physics of Metals and Alloys, p. 121. Wiley, New York (1949).
- F. R. N. NABARRO, Some Recent Developments in Rheology. British Rheologists' Club, London (1950).
- A. H. COTTRELL, Theory of Dislocations, Progress in Metal Physics, Vol. 1, Chapter 2. Interscience, New York (1950).
- J. D. ESHELBY, F. C. FRANK, and F. R. N. NABARRO, The Equilibrium of Linear Arrays of Dislocations, *Phil. Mag.* 42, 351 (1951).
- J. S. Koehler, The Production of Large Tensile Stresses by Dislocations, Phys. Rev. 85, 480 (1952).
- F. R. N. Nabarro, Symposium on Internal Stress in Metals and Alloys, p. 237. Institute of Metals, London (1948).
- J. HESLOP and N. J. PETCH, The Stress to Move a Free Dislocation in Alpha Iron, Phil. Mag. 1, 866 (1956).
- B. L. AVERBACH, The Effect of Plastic Deformation on Solid Reactions, Cold Working of Metals, p. 262. American Society for Metals, Cleveland (1949).

VOI

195

LETTERS TO THE EDITOR

Precipitation on dislocations in aluminium– 4% copper alloys*

Recent observations on aluminium–4% copper alloys quenched from the solid solution temperature have shown that many dislocations are present in the form of helices (1). These have been revealed by transmission electron microscopy of thin foils prepared from the quenched specimens. The axes of the helices (and their Burgers vectors) have been shown to be parallel to $\langle 110 \rangle$, i.e. the helices are formed by the winding up of screw dislocations about their axes as a result of the condensation of excess vacancies retained by quenching. From these observations it became apparent that many of the published reports of precipitation at dislocations in aluminium–copper alloys (2–5) can now be effectively explained in terms of helical dislocations.

A pure screw dislocation is not a favourable site for solute segregation because this would not give rise to any strain relief. However, an edge dislocation can attract solute atoms and in the case of copper in aluminium, the segregation of copper atoms will relieve the compressive strains. During quenching, when a pure screw dislocation winds up into a helix as a result of climb it will aquire edge characteristics around the cylinder containing the dislocation line and the Burgers vector. It is probable that the vacancies producing this climb also bring solute atoms to the dislocation. The edge parts of the helices will then be favourable places for the copper atoms to segregate. Thus during ageing of the alloy



Fig. 1. Thin foil of specimen quenched from 540° C. $\times 40.000$.

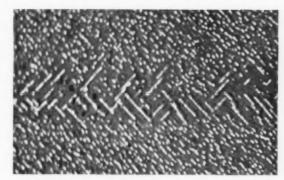


Fig. 2. Oxide replica from specimen quenched from 540° C and aged 84 hr at 165° C. $\times 40{,}000$.

it would be expected that precipitates should form at these sites along the helices. This is confirmed by the following.

Fig. 1 shows helical dislocations viewed along their length in a thin foil of [110] orientation. In this position, the helices appear as a sine curve and are long because their axes are parallel to the foil surface along [I10]. Fig. 2 shows an oxide replica taken from the alloy after ageing at 165°C in which the surface is (100) and the axis of the preferential array of precipitates is also [T10]. It can be seen by comparing these micrographs that the separation of the θ' plates is of the order of the pitch of the helices i.e. the edge components of the helices are the sites for preferential precipitation. The length of the arrays will depend on the orientation of section. In Fig. 3 rows of helices are observed on inclined slip planes in the thin foil, and thus appear more like loops than the sine form of Fig. 1. Such an arrangement can account for the arrays of

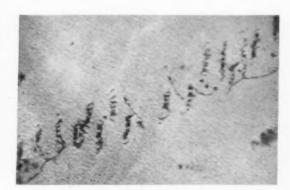


Fig. 3. Thin foil of specimen quenched from 540 °C. $\times 30,000$.

Fig. 4. Oxide replica from specimen quenched from 540°C and aged 100~hr at 210°C . $\times 12,000$.

precipitates shown in Fig. 4 which is an oxide replica taken from the alloy after ageing at 200°C. Again, the edge parts of helices must be the nucleating centres for preferential precipitation of θ' plates.

G. Thomas

Metallurgy Department Cambridge University J. NUTTING

References

- G. THOMAS and M. J. WHELAN, Phil. Mag., 4, 511, (1959).
 G. THOMAS and J. NUTTING, Inst. Metals Monogr. and Rep. Ser. No. 18, p. 57, (1955).
- H. WILSDORF and D. KUHLMANN-WILSDORF, Defects in Crystalline Solids, p. 175. Physical Society, London (1955).
- R. Castaing and A. Guinier, C. R. Acad. Sci. Paris 228, 2033. (1949).
- P. Lacombe and A. Berghezan, C. R. Acad. Sci. Paris 229, 365, (1949).
- 6. G. THOMAS, Phil. Mag., in press (1959).

* Received January 17, 1959.

On the conditions governing the brittle fracture of iron single crystals*

Several recent investigations⁽¹⁻³⁾ have shown that iron single crystals stressed in tension may show either a ductile or brittle behavior depending on orientation, purity and temperature. At -253°C Allen et al.⁽¹⁾ observed cleavage fracture for all orientations. At -196°C the crystals within about 30°C from [001] failed by cleavage while other orientations exhibited appreciable ductility. These results were qualitatively substantiated by Cox et al.⁽²⁾ and Biggs and Pratt⁽³⁾. Biggs and Pratt⁽³⁾ observed that the range of orientations exhibiting a brittle behavior was decreased by decreasing the

carbon content of the crystals, a result which they ascribed to a decrease in the critical shear stress for slip. Biggs and Pratt also observed that mechanical twinning preceded cleavage failure and proposed that the formation of a mechanical twin boundary provided the barrier to dislocation motion which is necessary for the explanation of cleavage failure on the basis of a dislocation model.⁽⁴⁾

The hypothesis that mechanical twin boundaries provide the barriers which lead to dislocation pile up and cleavage may be shown to be consistent with an orientation dependence for the type of failure observed. Allen et al.(1) have examined the various twinning systems which are operative in iron under the conditions that the twinning shear be compatible with the applied tensile stress and that the operative twin system be that which has the maximum resolved shear stress on the twin plane and in the twinning shear direction. Their results are shown in Fig. 1 which also contains the ductile-brittle boundaries observed by various authors at -196°C. The numbering of the various $\{112\}\langle 111\rangle$ twin systems refers to the convention introduced by Schmid and Boas⁽⁵⁾ and which is reproduced in Fig. 2. Of the possible twin systems only 3, 7 and 12 contain the [111] slip direction in the twin plane.

The effectiveness of a mechanical twin boundary for causing cleavage fracture as a result of dislocation pile up is expected to depend on the ability of the boundary to prevent the passage of dislocations through the boundary into the twinned lattice. Examination of the orientation relationships for twin systems 3, 7, and 12 shows that the twin planes contain the [111] slip direction and that one of the

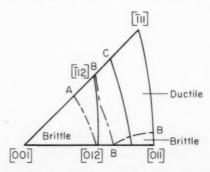


Fig. 1. Predicted twin systems and observed ductile brittle boundaries. Predicted systems: Point [001]: 1, 2, 7, 8; Point [011]: 7, 8, 11, 12; Point [111]: 2, 6, 7, 9, 10, 12; Line [001]–[012]: 7, 8; Line [012]–[011]: 7, 8; Line [011]–[111]; 7, 12; Line [112]–[111]: 2, 7; Line [001]–[112]: 8; Area [001]–[012]–[111]–[112]: 7, Ductile Brittle Boundaries: A–Biggs and Pratt (decarburized crystals); B–Allen et al.; C–Cox et al., Biggs and Pratt (carburized crystals) The slip direction is the [111]

direction.

VOI 7 195

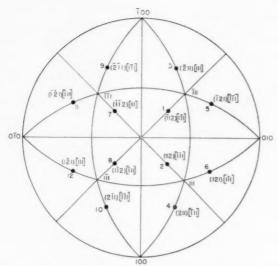


Fig. 2. Twinning systems in iron. Numbered 1-12 after Schmid and Boas.

{110} planes of the twin is favorably oriented for slip in each case. Therefore, passage of dislocations through the mechanical twin planes associated with these twin systems should occur quite readily and consequently they should not lead to dislocation pile up. Twinning on the other systems does not meet the above requirements. The twin planes associated with them can therefore act as barriers to dislocation motion and may cause pile ups with subsequent cleavage in the manner postulated by Biggs and Pratt⁽³⁾. The inability of certain twin boundaries to cause cleavage is indicated by the stress-strain curve of Biggs and Pratt for crystal MS11 which failed in a ductile manner despite of the formation of twins. This crystal was expected to twin on system 7.

VOL.

1959

Examination of Fig. 1 indicates that, at -196°C, the range of orientations for which brittle behavior is observed corresponds approximately to the region in which twin system 8 is expected to be dominant while the orientation range for which ductile behavior is observed corresponds to the region in which twin system 7 is expected to operate. For the [011] orientation, twinning on systems 7, 8, 11 and 12 is equally favored and should lead to cleavage failure. This has been reported by Allen et al.(1) for orientations close to the [011]. Crystals of the [111] orientation should similarly fail by cleavage.

While the assignment of twin systems to the various regions of the stereographic triangle, as shown in Fig. 1, takes into account the magnitude of the shear stress resolved on the twin plane and in the twinning shear direction, the differences in

resolved shear stresses for twin systems 7 and 8 are quite small for most orientations. The observation of Allen et al.(1) of cleavage failure for all orientations examined at -253°C may be the result of the formation of twins of system 8 for all orientations as a consequence of the increased stress required for twinning at this temperature. At room temperature slip apparently precedes and inhibits twinning. resulting in a ductile behavior for all orientations. (2,3)

H. K. BIRNBAUM

The Institute for the Study of Metals The University of Chicago Chicago 37, Illinois

References

- 1. N. P. Allen, B. E. Hopkins and J. E. McLennan, Proc. Roy. Soc. A234, 221 (1956).
- J. J. Cox, G. T. Horne and R. F. Mehl, Trans. Amer. Soc. Metals 49, 118 (1957)
- 3. W. D. Biggs and P. L. Pratt, Acta Met. 6, 694 (1958).
- A. N. Stroh, Phil. Mag. Suppl. 6, 418 (1957).
 E. Schmid and W. Boas, Plasticity of Crystals (1950).

*Received January 19, 1959

Au sujet de la fragilite du fer de zone fondue a basse temperature*

Un article récent de Biggs et Pratt⁽¹⁾ sur la déformation et la rupture du fer aux basses températures nous incite à rappeler quelques résultats obtenus au cours de nos recherches.

Ces auteurs ont effectué leur étude sur des monocristaux de fer Armco ou d'acier doux. Ils ont mis en évidence la fragilité à basse température dans un certain domaine d'orientation. De plus, ils ont montré que, en soumettant leurs éprouvettes susceptibles de se rompre de manière fragile, à un prétractionnement correspondant à la limite élastique inférieure, elles présentaient alors une déformation ductile. Dans ce cas. on n'observe plus de macles sur les échantillons.

Dans nos expériences, nous avons utilisé des éprouvettes polycristallines de fer purifié par zone fondue. (2) Les courbes de traction ont été tracées à la température de l'azote liquide. Nous avons montré que, pour un métal donné, il est possible d'observer différents modes de déformation. (3) Quand le recuit préliminaire de l'éprouvette a été fait au-dessus d'une certaine température appelée température critique de recuit, la rupture se produit dans le domaine de déformation élastique (Fig. 1a). Quand le recuit a été fait à une température inférieure, les courbes de traction peuvent présenter le type b ou c, le premier correspondant, au-delà de la limite élastique, à une

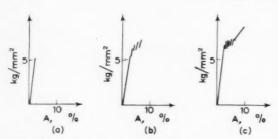


Fig. 1. Courbes de traction dans l'azote liquide d'éprouvettes de fer de zone fondue présentant: (a) la fragilité,
(b) une déformation par macles, (c) une déformation par macles suivie de déformation plastique.

déformation par macles, le second présentant un domaine de déformation plastique après le domaine de déformation par macles.

Dans le cas du fer de zone fondue, soumis à l'essai de traction à -196° C la température critique de recuit est voisine de 650° C.

Nous avons montré que la pureté du métal a une influence sur la température critique de recuit. L'addition de quelques millièmes pour cent de carbone au fer de zone fondue l'élève de 50°C au moins. Le fer électrolytique de pureté très inférieure à celle du fer de zone fondue⁽⁴⁾ présente une température critique voisine de 850°C.

Dans le cas du fer Armco, on ne peut obtenir la fragilité du metal que si les éprouvettes sont, au préalable, recuites pendant 6 jours à 950°C dans l'hydrogène.

Quel que soit le métal utilisé la cassure des échantillons qui se déforment selon les types a et b présenteau

microscope électronique un aspect de rivières caractéristique de la déformation par clivage. (5) Dans le cas d'une déformation du type c on peut observer à la fois des rivières et des cupules, celles-ci étant caractéristiques d'une déformation ductile pure (Fig. 2).

Quel que soit le mode de déformation, l'examen microscopique des éprouvettes après rupture montre la présence de macles mécaniques. Elles prennent naissance aux têtes des éprouvettes comme le montre un échantillon dont la traction a été arrêtée avant d'atteindre la rupture.

Un prétractionnement fait à la temperature ambiante, et correspondant à la limite élastique inférieure, donne de la ductilité au métal qui, sans ce traitement, se déformerait selon le type b, et il n'est plus possible d'observer de macles à la surface du métal. Le prétractionnement est sans effet sur le fer qui se déforme selon les types a ou c.

Nos expériences mettent donc en évidence l'influence de la pureté du fer sur sa fragilité à basse température et montrent que, pour un métal de haute pureté, la fragilité dépend de la température du recuit préalable.

Laboratoire de Vitry du C.N.R.S.

SIMONE BESNARD
J. Talbot
Vitry sur Seine
France

Bibliographie

19

 W. D. Biggs and P. L. Pratt, Acta Met. 6, 694 (1958).
 J. Talbot, Ph., Albert et G. Chaudron, C.R. Acad. Sci., Paris 244, 1577 (1957).



Fig. 2. Microfractographie électronique d'un échantillon se déformant selon le type c. On remarque l'existence simultanée de rivières et de cupules. $\times 5000$

 S. Besnard et J. Talbot, C.R. Acad. Sci., Paris 247, 1612 (1958).

 J. Talbot, Ph., Albert M. Caron et G. Chaudron, Rev. Métall. 12, 817 (1953).

 C. CRUSSARD, R. BORIONE, J. PLATEAU, Y. MORILLON et F. MARATRAY, Rev. Métall. 53, 426 (1956).

* Received January 22, 1959.

VOL.

1959

Some further observations on the growth of copper whiskers from cuprous iodide*

In a previous paper⁽¹⁾ the author described the conditions for the growth of a variety of metal whiskers from their halides. The growth of copper whiskers by the hydrogen reduction of CuI was investigated in greater detail. It was demonstrated that at 570°C (melting point of CuI is 588°C) the whiskers lengthen by the addition of material at their tips and hence it was concluded that the whiskers grow by a vapor phase transport mechanism. It was also shown that if the whiskers grow by the condensation of copper vapor according to the reaction

$$\begin{array}{ccc} 2~\mathrm{CuI}~\mathrm{(vapor)} + \mathrm{H_2} \! \to \! 2\mathrm{HI} + 2\mathrm{Cu}~\mathrm{(vapor)} \\ & \downarrow & \mathrm{Cu}~\mathrm{(whisker)} \end{array} \tag{1}$$

the supersaturation of the copper vapor has to be 10^4 to 10^6 to account for the observed axial growth rates. Since two-dimensional nucleation of copper on copper can occur readily at much lower supersaturations (producing equiaxed crystals) Coleman and Sears⁽²⁾ and the author⁽³⁾ proposed that the whiskers grow by the condensation of CuI vapor on the whisker surfaces and the preferential reduction of the adsorbed CuI molecules at the tips of the growing whiskers. If this hypothesis is correct the axial growth rate of the whiskers should be proportional to the rate of arrival of CuI molecules at the tip of the whisker. If we neglect surface diffusion of CuI on the sides of the whiskers the maximum possible axial growth rate, $L_{\rm max}$ of the whiskers is given by

$$L_{
m max} = rac{p^0_{
m (CuI)} M_{
m Cu}}{
ho_{
m Cu} \sqrt{2\pi} M_{
m CuI} R T}$$
 (2)

where $p^0_{\text{CuI}} = \text{equilibrium pressure of CuI}$ at temperature T,

 $M_{\mathrm{Cu}},\ M_{\mathrm{CuI}} = \mathrm{molecular}$ weights of Cu and CuI,

 $\rho_{\text{Cu}} = \text{density of Cu},$

R = gas constant.

To confirm the above relation the axial growth rates, L_{exp} , of copper whiskers as a function of

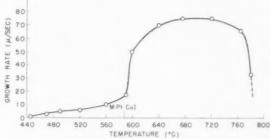


Fig. 1. Axial growth rate of copper whiskers as function of temperature.

temperature were measured. Since it was found too difficult to follow the growth of individual whiskers directly, the following procedure was adopted. A boat filled with CuI was brought to temperature in an atmosphere of nitrogen. Hydrogen was then introduced for a short time interval after which the boat was pulled into a cooling chamber. The length of the longest whisker divided by the growth time was then taken as the growth rate. A number of tests with varying time intervals were made to give the resulting data a fair degree of reliability.

In Fig. 1 the axial growth rates determined by the above method are plotted as a function of temperature. Below the melting point of CuI the rate increases steadily with temperature. At the melting point there is an abrupt increase in $L_{\rm exp}$ with a levelling off and a final decrease at higher temperatures. The logarithm of the growth rate below 590°C is plotted as a function of 1/T in Fig. 2 together with the theoretical growth rate given by equation (2). It is seen that the temperature dependence of $L_{\rm max}$ and

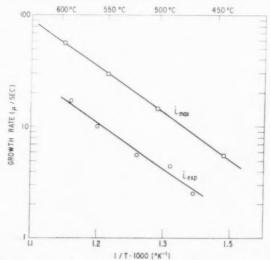


Fig. 2. Comparison between observed growth rates and those given by equation (2) below the melting point of CuI.

 $L_{\rm exp}$ is approximately the same giving support to the hypothesis that the growth rate, at least below the melting point of CuI, is primarily controlled by the vapor pressure of CuI. The reason that $L_{\rm exp}$ is only about $1/3 L_{\text{max}}$ is probably due to (1) the vapor pressure of CuI surrounding the whiskers never quite reaches p^0_{CuI} and (2) the CuI molecules have to diffuse through the H2 and HI gas.

The hypothesis that whisker growth occurs by the adsorption of CuI and its catalytic reduction at the whisker tip presumes that (1) the reduction of CuI in the vapor phase is negligible and (2) the whisker tip has different properties than the sides of the whisker. Sears(2) has proposed that whiskers contain only axial dislocations and hence the whisker tip would contain permanent surface steps whereas the whisker sides would not. If halide molecules are reduced rapidly only at surface steps the catalytic activity of the tip can be understood. Further support(3) for the catalytic reduction mechanism is that copper deposits from a mixture of CuI vapor and hydrogen much more readily on a crystalline surface than on a polished

The abrupt increase of L at the melting point of the CuI and its temperature dependence above 590° is at present not understood. Gorsuch(4) proposed that in the case of iron where such an increase is also observed the surfaces of the whiskers become covered with liquid halide which flows to the tip of the whiskers. It is of interest however that at no temperature does the growth rate of the copper whiskers exceed the value predicted by equation (2).

S. S. BRENNER

General Electric Research Laboratory Schenactady, N.Y.

References

S. S. Brenner, Acta Met. 4, 62 (1956).
 R. V. Coleman and G. W. Sears, Acta Met. 5, 131 (1957).
 S. S. Brenner, Thesis, R.P.I. May 1957.

4. P. Gorsuch, To be published.

* Received February 9, 1959.

Low temperature creep of rock salt single crystals*

The behaviour of rocksalt under constant load was examined at 35°C. The specimens were cylindric, the diameter 5 mm and the effective length 20 mm. They were machined as shown on Fig. 1 from parallelipipeda cleaved from pure crystals grown from the melt in this laboratory. The specimens were fixed in a frame F with analdite, copper cylinders were attached in

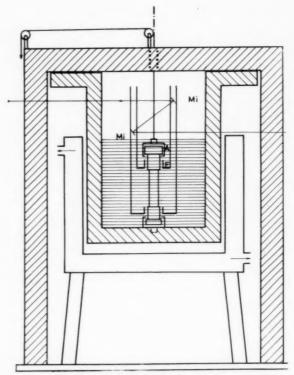


Fig. 1. Experimental set up.

195

the same way to the terminal parts (Fig. 1). The extension was measured optically with the aid of mirrors Mi. After a final etch to remove the outer layers of the central part, the specimen was immersed in a bath of degassed paraffin to prevent further contact with the air.(1) The oil was kept at a constant temperature by means of a Höppler thermostat and the whole set up was in a room where temperature fluctuations were negligeable.

Low loads gave no appreciable effect, relatively high loads: 250, 300, 350 and 450 g/mm² were therefore used. When the load was applied, a jerky motion was observed. The time interval between two successive elongations was too small to be recorded with the set up at our disposal. Such a behaviour has been described by M. Klassen-Nekludowa⁽²⁾. After this initial period continuous flow started, the results are summarized in Fig. 2. Each curve is a mean between several runs. These curves obviously indicate that the process is complex, the different stages are more clearly separated as the load is higher. Similar complex creep curves have recently been reported by Van Bueren⁽³⁾ in the case of germanium single crystals. In the curves presented here, the initial deformation has been disregarded. One can conclude that the process always starts with creep of the α -type followed by some β -creep after

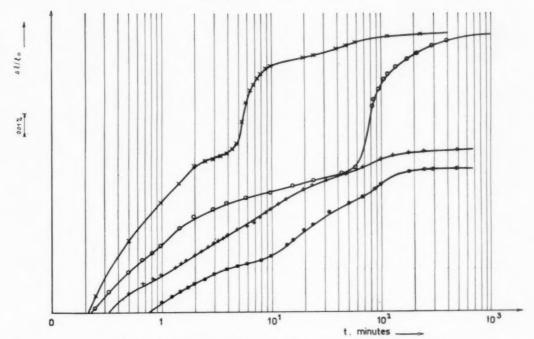


Fig. 2. Results: • 250 g/mm²; + 300 g/mm²; ○ 350 g/mm²; × 450 g/mm².

which a new sequence of α - and β -creep takes place.

We believe that the interpretation of the process could be given along following lines: the different α-stages may consist of a kind of non-persistent work-hardening, i.e. a formation of piled up groups blocked against barriers until they are released by the effect of another process, occurring in the next stage. This may be connected with rapid climb such as described by Friedel⁽⁴⁾. The initially blocked sources are freed and can give a new piling up, which results in a further creep of the first type. This process can go on as long as the applied load produces enough stresses to overcome the energy necessary for it.

This work is part of a research program (C.E.S.) sponsored by I.R.S.I.A. (Institut pour l'encouragement de la Recherche Scientifique dans l'Industrie et l'Agriculture) (Brussels, Belgium) to which the authors are greatly indebted.

C.S.K., Mol, Belgium R. Strumane Laboratorium voor Kristalkunde W. Dekeyser Rozier 6, Gent, Belgium

References

- 1. E. Aerts and W. Dekeyser, Acta Met. 4, 557 (1956).
- 2. M. Klassen-Nakludowa, Z. Phys. 55, 555 (1929).
- 3. H. G. VAN BUEREN, Physica, 24, 831 (1958).
- J. FRIEDEL, Les Dislocations, p. 63. Gauthier Villard, Paris, (1955).
 - * Received January 18, 1959

Thermal etching of silver surfaces parallel to {110} planes*

It has been shown recently that thermal etching of single crystals of silver will not occur if their surface is nearly parallel to a {110} plane, whereas for other orientations {111} and {100} facets may be revealed on etching⁽¹⁾ (Fig. 1). The range around {110} in which etching does not take place is small, and therefore thermal etching provides a sensitive indicator for the flatness of the surface. The purpose of this note is to illustrate this and to show that the waviness of a surface polished electrolytically is sufficient to change its etching behaviour.

A polycrystalline specimen of silver of about 2 mm grain size was electropolished and thermally etched in air for 15 min at 900°C. Several crystals had a {110} plane nearly parallel to the surface and these showed etch patterns with ridges lying in two directions. Fig. 2 gives a typical example of such a surface. Within each region of the surface only one direction of the ridges appears. The average orientation of the crystal is shown at P in Fig. 1.

The angle between the two sets of ridges shown by the lines A and B is 30° and the angle between traces of the (I11) and (111) planes calculated from the stereographic projection for point P is also 30° . For crystal oriented at Q in Fig. 1 the angle between the sets of ridges was 16° and the angle between the {111} planes was calculated to be $15\frac{1}{2}^{\circ}$. This correspondence

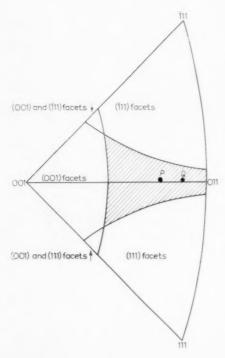


Fig. 1.

which was confirmed in other crystals strongly suggests that both the (I11) and (111) planes are revealed by etching.

Micro-examination of the same field under oblique illumination (Fig. 3) showed light and dark patches which corresponded to the random hill and valley relief structure left by the electropolishing prior to thermal etching. The light and dark patches also corresponded to the two groups of thermally etched ridges. The type of etching is thus very sensitive to surface slope. A multiple beam interferometric pattern of the same field (Fig. 4) enables the angle of slope of those parts of the hills which correspond to each type of etching to be measured relative to the general surface. It was found invariably that the two types of etching were confined to areas of the surface where the surface contours were parallel to the direction of the lines A and B in Fig. 2. Changes of slope of less than 1° brought the surface orientation in many cases into a region suitable for etching. With the surface orientations represented by the shaded region of Fig. 1 and within about 10° of the {110} plane a surface tilt of less than 3° is sufficient to bring the surface into a region capable of etching to reveal {111} planes.

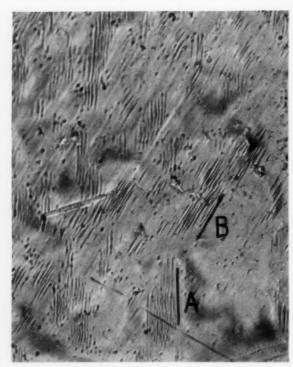


Fig. 2. Thermally etched ridges on previously electropolished silver. The ridges run in two directions as shown by the lines A and B (crystal P of Fig. 1). $\times 260$



195

Fig. 3. Oblique illumination of the same field as Fig. 2 showing that local surface slopes determine the position of the two types of ridges. $\times 260$

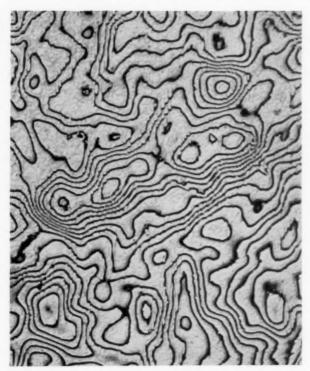


Fig. 4. Multiple beam interferometry pattern of same field as Fig. 2. Measurements show that variations of slope of less than 1° can determine the etching behaviour. $\times 260$

Thus the thermal etching characteristics of crystals in this region provide a sensitive indication of the general flatness of the surface. In this case where the specimen was electropolished, tilts of about 2° were present which have caused localized differences in the type of etching. The experiments illustrate the care which must be taken in comparing etching patterns when only the average surface orientation is known.

E. D. HONDROS A. J. W. MOORE

Division of Tribophysics Commonwealth Scientific and Industrial Research Organization University of Melbourne

1959

Reference

A. J. W. Moore, Acta Met. 6, 293 (1958).

* Received October 14, 1958.

Der Einfluss feindisperser Ausscheidungen auf die Koerzitivkraft von Transformatorenblech*

Bei der Glühbehandlung von handelsüblichen Transformatorenblechen mit 4.1% Si (ca. 0.05% C; 0.09% Mn; 0.013% P; 0.032% S und 0.29% Cu nach Angaben des Herstellers) stellten wir im Temperaturbereich um 500°C einen Anstieg der Koerzitivkraft

fest. Diese Anomalie hatte sehon Köster anlässlich seiner Untersuchungen über den Einfluss von Si auf die mechanische und magnetische Aushärtung von kohlenstoffhaltigem Eisen gefunden. (1) Da die Ursache für dieses Verhalten noch unbekannt ist, führten wir die nachstehenden Untersuchungen durch.

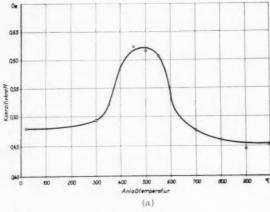
Die Proben bestanden aus 0,35 mm dickem, warmgewalztem Transformatorenblech, das wir in 8 mm breite und 20 cm lange Streifen geschnitten haben. Diese homogenisierten wir ½ bis 1 h bei 1000°C und schreckten sie anschliessend in Wasser auf Zimmertemperatur ab. Die Koerzitivkraft betrug nach der Glühung 0,4 bis 0,5 Oe. So vorbehandelt, wurden die Proben zunächst ½ h bei 300°C angelassen und anschliessend in Wasser abgeschreckt, darauf bei 350°C angelassen und wieder abgeschreckt usw. bis 1000°C. Die abgeschreckten Proben wurden zwischen den Teilglühungen magnetisch bzw. mikroskopisch bei Zimmertemperatur untersucht. Sämtliche Glühungen einschliesslich des Abschreckens wurden bei einem Vakuum von 10-2 Torr und darunter durchgeführt.

Die Koerzitivkraft wurde statisch gemessen; sie ist in Abb. Ia in Abhängigkeit von der Anlasstemperatur aufgetragen. Bei etwa 500°C durchläuft die Koerzitivkraft ein Maximum. Die Höhe des Maximums war bei den verschiedenen Proben – vermutlich wegen des örtlich schwankenden Kohlenstoffgehaltes — unterschiedlich; neben Proben, deren Maximum Koerzitivkraftwerte bis zu 1,5 Oe erreichte, gab es solche, bei denen nur ein schwacher Anstieg der Koerzitivkraft festzustellen war.

Die Lage und Höhe des Maximums ist auch von der Dauer der einzelnen Teilglühungen abhängig, im Bereich der verwendeten Glühzeiten jedoch nicht sehr stark; z.B. blieb das Maximum beim Übergang von ½- zu ¼-stündigen Glühungen bis auf die Steilheit der rechten Flanke nahezu unverändert. Das ist darauf zurückzuführen, dass der zeitliche Anstieg der Koerzitivkraft bei Glühtemperaturen unter 500°C verhältnismässig schwach ist und erst bei höheren Temperaturen merklichen Einfluss gewinnt.

Um die Zeitabhängigkeit der Koerzitivkraft zu verfolgen, wurden Anlassglühungen bei konstanter Temperatur vorgenommen. Der Anlassprozess wurde in zeitlichen Abständen unterbrochen und die Proben aus dem Ofen genommen, abgeschreckt und untersucht. Die Glühtemperatur geht dabei als Parameter ein; bei beispielsweise 500°C erhielten wir die in Abb. I b gezeigte Abhängigkeit der Koerzitivkraft von der Anlassdauer.

Sowohl der zeitliche als auch der temperaturabhängige Verlauf der Koerzitivkraft zeigte bei allen Versuchen die charakteristischen Merkmale eines



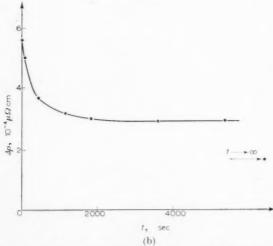


Abb. I. Einfluss der Anlasstemperatur und der Anlasszeit auf die Koerzitivkraft von warmgewalztem Transformatorenblech nach vorheriger $\frac{1}{2}$ -stündiger Homogenisierung bei 1000°C und Abschrecken in Wasser. Die Anlassglühungen erfolgten:

Ia, bei stufenweise steigenden Temperaturen jeweils $\frac{1}{2}$ h lang. 1b, bei einer Temperatur von 500°C.

Die Koerzitivkraftmessungen wurden bei Zimmertemperatur durchgeführt; die Proben wurden zu diesem Zweck aus dem Ofen genommen und in Wasser abgeschreckt.

Ausscheidungsprozesses, wie sie Köster auch an kohlenstoffhaltigem aber siliziumfreiem α -Eisen erhalten hatte. Dort wird die Anomalie durch eine Fe₃C-Ausscheidung verursacht, deren maximaler Einfluss auf die Koerzitivkraft bei etwa 250°C liegt. Auch bei der vorliegenden Untersuchung stellte sich heraus, dass der Anstieg der Koerzitivkraft von feindispersen Ausscheidungen hervorgerufen wird. Die ausgeschiedenen Teilchen (Abb. 2) haben plattenförmige Gestalt mit unregelmässiger Umrandung, ähnlich denen, die Pitsch in aufgekohltem Carbonyleisen gefunden hat. Die Teilchendurchmesser liegen zwischen 1 und 6 μ , die Dicke unter 0.4 μ , so dass eine lichtmikroskopische Beobachtung möglich war. Abbildung 3 zeigt die elektronenmikroskopische Aufnahme



ABB. 2. Ausscheidungen in 0,35 mm dickem, warmgewalztem Transformatorenblech mit 4,1% Si. Glühbehandlung: $\frac{1}{2}$ h bei 1000°C homogenisiert und abgeschreckt, $H_c=0,52$ Oe. Anschliessend 1 h bei 500°C angelassen, $H_c=0,98$ Oe. Ätzmittel: 3%jige alkoholische HNO3.



Abb. 3. Ausscheidungen wie in Abb. 2. Elektronenoptische Aufnahme. Präparierung: Der geätzte Schliff wurde mit Kohle bedampft. Das Kohlehautchen wurde anschliessend mit WO $_3$ schräg bedampft. 1 μ

VO 7 19

einiger Teilchen bei 12000-facher Vergrösserung. Die Ausscheidung erfolgte stets orientiert; durch Strukturätzung haben wir festgestellt, dass die Teilchenebenen parallel zur (100)-Ebene des Grundgitters ausgerichtet sind. In der Abbildung 2 ist das beobachtete Korn ungefähr in der (111)-Ebene angeschnitten worden. Neben einzelnen Ausscheidungen fanden wir auch grössere kettenförmig angeordnete Ansammlungen von Ausscheidungen mit Längen bis 80 µ (Abb. 4).

Bei Anlasstemperaturen unterhalb 400°C und oberhalb 600°C konnten lichtmikroskopisch keine Ausscheidungen festgestellt werden. Das ist auf das Wachstum bei niedrigen Temperaturen und auf die Wiederauflösung der Teilchen im Grundgitter bei höheren Temperaturen zurückzuführen. (4)

Der beobachtete Zusammenhang zwischen der Teilchenausscheidung und dem Anstieg der Koerzitivkraft lässt sich mit ausreichender Näherung durch eine Theorie von Néel über den Einfluss von Poren und Einschlüssen auf die Koerzitivkraft ferromagnetischer Stoffe beschreiben. (5) Danach ist die Koerzitivkraft von der Menge, der Form und vom Dispersionsgrad der Einschlüsse abhängig; von besonders grosser Wirkung sind platten-bzw. nadelförmige Teilchen, deren Grösse mit der Blochwanddicke vergleichbar ist. In Übereinstimmung damit ist die beobachtete mittlere Teilchendicke im Maximum der Koerzitivkraft grössenordnungsmässig gleich der theoretisch errechneten Blochwanddicke ($\approx 0.06 \,\mu$ bei 4% igem Si-Eisen).

Ausscheidungen fanden wir sowohl bei schlussgeglühten als auch bei noch nicht schlussgeglühten Blechen von verschiedenen Herstellern. Die chemische Zusammensetzung der Ausscheidungen konnte wegen zu geringer Menge nicht bestimmt werden. Es ist nicht ausgeschlossen, dass die Ausscheidungen und der

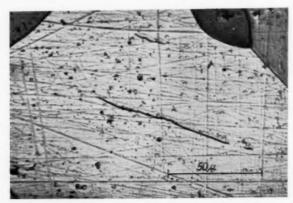


Abb. 4. Kettenförmige Ansammlung von Ausscheidungen. Glühbehandlung wie in Abb. 2.

damit verbundene Anstieg der Wattverluste auch in der Praxis eine Rolle spielt, wenn bei der Schlussglühung nicht dafür gesorgt wird, dass das Absinken der Ofentemperatur zwischen 900 und 500°C ausreichend langsam erfolgt.

Ein ähnlicher Ausscheidungsprozess im gleichen Temperaturgebiet wurde von Gengnagel in einer Al-Fe-Legierung mit 10% Al beobachtet. (6) Die ausgeschiedenen Teilchen waren ebenfalls plattenförmig und bestanden vermutlich aus einer Kohlenstoffverbindung. Kein Zusammenhang scheint jedoch mit den Untersuchungen von Lihl und Zemsch zu bestehen, die bei Glühuntersuchungen an Transformatorenstahl mit 4,3% Si nadelförmige Ausscheidungen fanden.⁽⁷⁾ Diese Ausscheidungen wurden bei Temperaturen von 900°C und nach einer Glühdauer von rund 10 h erhalten.

Frau I. Bauer danke ich für die sorgfältige Anfertigung der Metallschliffe. Für die Herstellung der elektronenmikroskopischen Aufnahmen und die damit verbundenen präparativen Arbeiten bin ich Herrn Dipl.-Phys. H. Schröder zu ausserordentlichem Dank verpflichtet.

R. WAGNER

Institut für Magnetische Werkstoffe der Deutschen Akademie der Wissenschaften zu Berlin.

Jena, Helmholtzweg 4

Literatur

- 1. Erörterungsbeitrag von W. Köster, Stahl u. Eisen, 54, W. KÖSTER, Arch. Eisenhüttenw. 21, 680-681 (1934); 305-314 (1950).
- W. Köster, Z. Anorg. Chem. 179, 297–308 (1929); Arch. Eisenhüttenw. 2, 503–522 (1929).
- 3. W. Pitsch, Acta Met. 5, 175-176 (1957)
- G. Masing, Arch. Eisenhüttenw. 2, 185 (1928–29).
 L. Néel, Ann. Univ. Grenoble 22, 299 (1946).
- H. GENGNAGEL, Vortrag a.d. Tagung d. Arbeitsgemein-schaft "Ferromagnetismus" am 26, und 27. Sept. 1958 in Dortmund.
- F. Lihl und P. Zemsch, Arch. Eisenhüttenw. 26, 535-540 (1955); F. Lihl, Radex Rdsch. 460-472 (1955); F. Lihl, Acta Phys. Austr. 11, 232-240 (1957).
 - * Received December 11, 1958.

On the pressure of hydrogen in cavities of steel*

In steel, hydrogen forms two phases, a solution of hydrogen in ferrite and a gas phase at internal voids and cavities. At low pressures Sievert's law is valid

$$\frac{a}{p^{1/2}} = K$$

where a is the activity of dissolved hydrogen, which at high temperatures is proportional to its concentration C, and p is the pressure of hydrogen in the gas phase. At low temperatures with usual hydrogen contents this equilibrium leads to very high pressures, at which considerable deviations from Sievert's law can be expected. A complete thermodynamic treatment was presented by Phragmén⁽¹⁾ but small modifications of his results seem to be justified.

Let us consider how the equilibrium is affected by temperature and pressure

$$\begin{split} d\ln K &= \left(\frac{\partial \ln K}{\partial T}\right)_p dT - \frac{1}{RT} \left(\frac{\partial F}{\partial p}\right)_T dp \\ \\ d\ln K &= \frac{\Delta H^\circ}{RT^2} dT - \frac{\Delta v}{RT} dp \end{split}$$

further

$$\left(\frac{\partial \Delta H^{\circ}}{\partial T}\right)_{p} = \Delta c_{p} = \tilde{c}_{p} - \left[\frac{1}{2}c_{p}\right]$$

and

$$\Delta v = \bar{v} - \frac{1}{2}v.$$

The specific heat of hydrogen gas $c_p \simeq 7.0$ cal/mole. The specific heat of dissolved hydrogen $\tilde{c}_p \simeq \tilde{c}_v$ has a value between 1.5R and 3R, the former representing a monatomic gas at constant volume, where atoms have complete freedom of movement, and the latter a compound with atoms at restricted positions. Let us write $\tilde{c} = (1.75 + n)R$, where -0.25 < n < 1.25. \tilde{v} is the partial specific volume of dissolved hydrogen and v the specific volume of hydrogen gas, which with an approximate equation of state can be expressed as:

$$v = \frac{RT}{p} + \alpha$$
.

Inserting these values one obtains

$$d\ln K = \left(\frac{\Delta H_0}{RT^2} + \frac{n}{T}\right)dT + \left(\frac{\alpha/2 - \tilde{v}}{RT} + \frac{1}{2n}\right)dp$$

where ΔH_0 is an integration constant, and finally

$$C = K_1 f^{-1} p^{1/2} T^n \exp \left(- \, \frac{\Delta H_0 - (\alpha/2 - \bar{v}) p}{RT} \right) \, (1)$$

where K_1 is an integration constant and f the activity coefficient of dissolved hydrogen. Usually only the total hydrogen content C_0 is known, which is the sum of hydrogen dissolved, included in cavities and adsorbed; with the above equation of state

$$C_{0} = (1 - V)C + V \frac{pT_{0}}{p_{0}T} \left(1 + \frac{\alpha p}{RT}\right)^{-1} + S(p, t) (2)$$

where V is the volume fraction of the gas phase, S(p,t) the amount of adsorbed hydrogen, while p_0 and T_0 refer to the standard state.

The estimation of the constants involves some

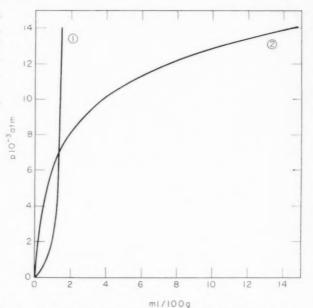


Fig. 1. Equilibrium pressure of included (1) and dissolved (2) hydrogen at room temperature.

uncertainties. At high temperatures and low pressures f = 1 and the exponential term of equation (1) involving p becomes negligible. According to Kawai⁽²⁾ $n \simeq 1$; assuming this value K_1 and ΔH_0 can be evaluated from solubility measurements at temperatures above 400°C.(3) This renders for unalloyed steel $K_1=1.4 imes10^{-3}~(\mathrm{deg^{-1}~atm^{-1/2}})$ and $\Delta H_0/R=2300$ (deg). The extrapolated solubility at room temperature is three times higher than would be obtained with n=0 and the corresponding constants. \bar{v} is 2.0 ml/g.(1) a can be evaluated from Bridgman's(4) measurements, according to which a decreases at 30°C with pressure from 18 ml/mole to 14 ml/mole at 13000 atm. These values appear somewhat low, as other measurements at moderate pressures (up to 2000 atm) render values above 20 ml/mole. An average of 18 ml/mole in the pressure range of interest appears reasonable.

195

The activity coefficient f is expected to be lowered by the interaction between hydrogen and dislocations or other solute atoms. The number of dislocation sites in annealed steel is $\simeq 0.5 \times 10^{16}$ cm⁻³, whereas 1 ml/100 g hydrogen represents 35×10^{16} atoms/cm³. Thus, even if several atoms are affected at each dislocation site, the total volume involved is only a fraction of 1 ml/100g. At large hydrogen concentrations f will not be affected appreciably, but it will be lowered to some extent at low temperatures and small pressures (for example at room temperature at p < 2000-3000 atm). V is about $10^{-4(5,2)}$. S can be regarded as independent of pressure, as practically

complete surface saturation is achieved already at low pressures, and would be expected to be small compared with the amount of hydrogen in the gas phase, unless the pressure is very low or the surface to volume ratio of cavities high. The latter might be the case for adsorption on vacancies. (6) For adsorption of 1 ml/ 100 g a vacancy concentration of about 10⁻⁶ would be required, which is much larger than expected for annealed steel. Thus even vacancy adsorption can be neglected.

Fig. 1 shows the equilibrium pressure at room temperature for included and dissolved hydrogen separately, calculated according to the above assumptions and with f = 1. The total content is the sum of partial contents at a certain pressure. The curves represent a reasonable approximation for annealed steel; after cold-working, of course, f becomes largely reduced and S might become important, and the pressure at a certain concentration will decrease markedly.

F. DE KAZINCZY

Dept. of Metallurgy Massachusetts Institute of Technology Cambridge, Massachusetts

References

- 1. G. Phragmén, Jernkontor. Ann. 128, 537 (1944).
- 2. M. Kawai, private communication.
- 3. W. GELLER and TAK-Ho Sun, Arch. Eisenhüttenw., 21, 423 (1950).4. P. V. BRIDGMAN, Proc. Amer. Acad. Arts. Sci. 59, 173
- (1924).
- 5. F. DE KAZINCZY, J. Iron St. Inst., 177, 85 (1954).
- 6. W. R. Heller, 'Stress Corrosion Cracking and Embrittlement', p. 163. Wiley, New York (1956).
 - * Received October 16, 1958.

BOOK REVIEW

W. B. Pearson: A Handbook of Lattice Spacings and Structures of Metals and Alloys, Pergamon Press, London. 1958. 1044 pp., 12½ gns.

This is a very timely book. In the research and development work embracing many branches of physics, chemistry and metallurgy, it is often necessary to know the structure or the lattice spacings of various metals and alloys. During the last few decades numerous publications on this subject have appeared in a great variety of journals and clearly there was need for a comprehensive handbook containing assembled and suitably digested information of this kind.

The size and contents of the present book reveal the surprisingly large amount of material already existing in the literature. They also show that preparing the book has been a formidable task.

In the first 75 pages (part I) the application of various X-ray methods to determination of structure and measurement of lattice spacings is described in some detail, including the question of units and errors. This is followed by a digested review of the importance and the role played by the structure and lattice spacings in the theory of metals and alloys.

In the first 43 pages of part II the author provides a review of various crystallographic "Strukturbericht" types followed by 130 pages with tabulated structure data for the elements and various intermediate phases and compounds. The actual review of data collected from literature is presented alphabetically in the remaining 796 pages.

There is a certain parallel between this kind of book and a telephone directory: both are extremely useful and contain an enormous amount of information. Almost from habit one is tempted on first encounter to flick through the pages to check one's own 'number', or those of one's friends, and it is disappointing to find that a few are missing. However, considering the unusual difficulties in producing such a reference work there are only very few errors or typographic mistakes present, and a very high standard is clearly shown in both preparatory and publishing stages.

When practical knowledge and theoretical background in relation to the alloy theory are needed Dr. Pearson shows himself well qualified to be the author of this work. Indeed the introductory part, although of necessity rather concentrated, reads like a little book of its own and can be recommended to a research student in the field.

In the subsequent sections one's appetite for making use of already available data for interpretation of alloying behaviour is whetted by the useful diagrams in which lattice spacings based on a common solvent are plotted together. One could visualize countless future papers springing from this book as a source were it not for the fact that, unfortunately, much of the data on intermediate phases are often contradictory or insufficiently precise to be of immediate use in a more advanced theory. Looking through the pages one can see the enormity of the task lying ahead, depressing in the quantity and exciting in its possibilities.

On the whole this is an invaluable reference book to all workers in the field of metals and alloys. Despite the forbidding cost it should find its way to almost everyone's bookshelf.

T. B. Massalski

VOI

19

THE CUBIC-HEXAGONAL TRANSFORMATION IN SINGLE CRYSTALS OF COBALT AND COBALT-NICKEL ALLOYS*

P. GAUNT† and J. W. CHRISTIAN‡

Kinetic and crystallographic observations on the natural and stress-induced transformations in single crystals of cobalt and cobalt-nickel alloys have confirmed the martensitic nature of the change. The shape deformation has been measured for the stress-induced transformation in alloys; the habit plane is not determined by a maximum resolved shear stress condition. The accommodation stresses produced by transformation have very marked effects, and thermal cycling eventually leads to stability of the cubic form down to liquid-air temperatures.

LA TRANSFORMATION CUBIQUE—HEXAGONALE DANS LES MONOCRISTAUX DE COBALT ET D'ALLIAGES COBALT—NICKEL

Le caractère martensitique de cette modification a été confirmé sur des monocristaux de cobalt et d'alliages de cobalt—nickel par des observations cinétiques et cristallographiques des transformations naturelles et sous tension.

La déformation a été mesurée pour la transformation sous tension dans les alliages; le plan d'habitat n'est pas déterminé par une tension critique de cisaillement. Les tensions d'accommodation produites par la transformation ont des effets très marqués et un cycle thermique permet éventuellement une stabilité de la forme cubique jusqu'à la température de l'air liquide.

DIE KUBISCH-HEXAGONALE UMWANDLUNG VON EINKRISTALLEN AUS KOBALT UND KOBALT-NICKEL-LEGIERUNGEN.

Kinetische und kristallographische Beobachtungen der natürlichen und der spannungsinduzierten Umwandlung von Einkristallen aus Kobalt und Kobalt—Nickel-Legierungen bestätigten die martensitische Natur dieser Umwandlung. Bei der spannungsinduzierten Umwandlung von Legierungen wurde die Gestaltsänderung gemessen, die Habitusebene ist nicht durch eine Bedingung maximaler Schubspannung bestimmt. Die durch die Umwandlung hervorgerufenen Anpassungsspannungen haben sehr ausgeprägte Wirkungen und wiederholtes Glühen und Abkühlen führt schliesslich zur Stabilität der kubischen Modifikation bis hinunter zur Temperatur der flüssigen Luft.

1. INTRODUCTION

This work was undertaken to provide further information on the crystallography and kinetics of the f.c.c.-h.c.p. transformation, and to examine some consequences of the Bilby-Seeger theory for cobalt. Many of the results duplicate those recently reported by Takeuchi and Honma(1) and Bibring. Sebilleau and Bückle(2), and these will not be described in detail. The present observations were made on single crystals and coarse poly-crystals of cobalt and cobalt-nickel alloys, and relate to both natural and stress-induced transformations. Specimens were prepared by diamond dust polishing, followed by electropolishing in an orthophosphoric acid solution (sp. gr. ~ 1.35). When both phases were present in alloy specimens, this electropolish etched the h.c.p. plates, and a hydrochloric acid-ethyl alcohol bath

was used instead. The transformation was followed visually and by cinéphotography, using a hot stage microscope with a high current heater of tantalum foil. Laue photographs were taken with a semi-microbeam camera of the type described by Cahn⁽³⁾, and with a high temperature camera developed for this work.

2. THE TRANSFORMATION IN PURE COBALT

Most of the experiments were made with a large single crystal, kindly presented to us by Dr. J. Crangle, which was cut into three specimens. When heated through the transformation range in a small temperature gradient, fine parallel markings appeared on the surface, and spread from one end of the crystal to the other. The markings did not disappear on cooling, and there was no obvious change in appearance on subsequent thermal cycling through the transformation. After polishing away the markings, they reappeared at the transformation temperature on the next half cycle. One specimen developed

^{*} Received September 2, 1958.

[†] Department of Physics, The University, Sheffield; formerly Department of Metallurgy, University Museum, Oxford.

[‡] Department of Metallurgy, University Museum, Oxford.
ACTA METALLURGICA, VOL. 7, AUGUST 1959

small islands of different orientation after many cycles in which the maximum temperature (1000° C) was well above the transformation range; another specimen annealed at 1000° C for 24 hr after cycling became polycrystalline.

Kinetic observations on the formation of the bands and nucleation of new bands ahead of the advancing set duplicate those made by Bibring et al. on polycrystalline specimens. Resolvable detail within the main bands (i.e. finer bands) was found to persist up to the limit of optical magnification, and careful examination also showed that fine markings of very low contrast covered the apparently clear regions of surface between main markings. This conflicts with the results of the French workers, who found the surface between optically visible markings to be structureless, even under the electron microscope, except for an occasional band of ~500 Å width. Although the conditions in the two sets of experiments were not identical, it is possible that fine bands of very low contrast are present in all specimens, and lack of contrast may also explain why Takeuchi and Honma were unable to see any markings in pure cobalt.

The secondary markings described by Bibring et al. never appeared in single crystal transformations, and all markings were very straight and extended across the crystal. The markings were always parallel to the trace of the habit plane in the surface. Cubic spots were never detected in oscillation photographs at room temperature, although this is probably the most sensitive way of detecting small amounts of retained cubic material. Stacking fault streaks were visible on these photographs, and became more pronounced after several cycles.

The orientation relation was confirmed more accurately than in previous work by taking Laue photographs of the cubic and hexagonal single crystals which transformed into each other in the high temperature Laue camera. Superposition of the photographs confirmed the parallelism of close-packed planes and of close-packed directions within these planes to $\pm \frac{1}{2}^{\circ}$.

A polycrystalline specimen (grain diameter ~ 0.5 cm) was used for thermal analysis of the transformation. The main cooling arrest was at 419°C, with a supercooling of $\pm \frac{1}{2}$ °C, and there were a number of subsidiary arrests at lower temperatures, possibly representing bursts of martensite formation. Only one heating arrest was observed, at 435°C. The hysteresis of ~ 16 °C is considerably smaller than that of ~ 40 °C found by Troiano and Tokich⁽⁴⁾ and Bibring and Sebilleau⁽⁵⁾, but the grain size in the earlier experiments was probably much smaller.

3. SPONTANEOUS TRANSFORMATION IN COBALT-NICKEL ALLOYS

Four alloys containing 29.6, 30.0, 30.3 and 30.5 per cent nickel were prepared by melting in vacuo in alumina crucibles, and subsequently annealing for 18 hr at 1350°C. The three lower alloys were h.c.p. at room temperature, and strong markings were produced on heating into the cubic region. Repolishing and reheating produced markings again on several subsequent cycles, but the markings became fainter and eventually did not appear. The specimens were then found to be cubic at room temperature. Cooling by quenching into liquid oxygen produced markings again, and the specimens were found to have transformed partially to hexagonal. Reheating and cooling gave entirely cubic phase at room temperature, and it was possible to repeat these cycles several times. Eventually the material was almost entirely cubic, even after cooling to liquid-oxygen temperature.

The 30.5 per cent alloy was cubic at room temperature after high temperature annealing. Markings were produced by quenching into liquid oxygen, but after one or two cycles the hysteresis gap became too wide, and the specimens remained cubic at all temperatures.

VOI

195

Part of the 30 per cent nickel ingot was given a high temperature anneal, and then very slowly cooled through the transformation range. Strong markings in four different areas, each with different trace directions, were produced, and Laue photographs showed there were four corresponding hexagonal orientations. The orientations were consistent with the assumption that they had all formed from a single cubic crystal, and the markings were parallel to the four sets of basal planes, corresponding to the four sets of cubic {111} planes. The specimen was then cycled through the transformation range without disturbing the surface; after two cycles, the orientations had not changed, but after a dozen cycles, the specimen was entirely cubic. The cubic orientation in regions 1, 2 and 4 was that expected from the hexagonal orientations, but region 3 was a cubic twin on the {111} habit plane of that region. Following this treatment, the ingot was annealed at 550°C for 24 hr. At room temperature, it remained entirely cubic, but areas 2, 3 and 4 then had the expected orientation, whilst region 1 was a cubic twin of this orientation on the {111} plane of its own markings. These effects were found only in one specimen; repeated attempts to produce twinned cubic regions by cycling of other specimens were unsuccessful.

An attempt to grow a single crystal of the 30.3 per cent nickel alloy from the melt gave a hexagonal

bicrystal, the two orientations having been derived from a single cubic crystal. Oscillation photographs of this specimen showed faint cubic spots, corresponding to the predicted parent orientation of the two hexagonal crystals, and there were strong stacking fault streaks. After only three heating cycles, the

transformation to a depth of ~0.1 mm, and both phases were present if electropolishing did not remove a sufficient surface layer.

A cubic single crystal of the 30.3 per cent alloy was obtained as described above. A small compression produced a very narrow band of marking in the

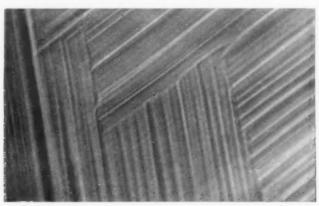


Fig. 1. Surface markings at the boundary of two hexagonal orientations in a 30.3 per cent nickel alloy. ×1600.

specimen was a cubic single crystal. Two surface analysis was used to confirm that the observed markings were indeed traces of $(0001)_h//\{111\}_c$ planes. The meeting line of the two hexagonal orientations is shown in Fig. 1; the crystals are separated by boundary surfaces parallel alternately to the habit planes (basal planes) of each orientation. This type of interface was always observed when hexagonal crystals had been derived from a common cubic parent.

Ciné-films of the transformation show features such as lengthwise growth, sharpening and thickening of the visible bands, all of which have been observed in other martensitic transformations. The markings were much stronger than those in pure cobalt, but also showed resolvable detail, and strong bands appeared to result from many finer bands in which the tilts partially co-operate. Electron-microscope photographs, and investigation by an optical method (6) showed that the surface profile was irregular and rounded, rather than composed of sharp tilts.

4. STRESS-INDUCED TRANSFORMATION IN COBALT-NICKEL ALLOYS

Specimens of 30 per cent and 30.3 per cent nickel alloys were retained in cubic form at room temperature after several transformation cycles. Compression of these specimens then caused partial transformation to the hexagonal form. The cold-work caused by grinding and mechanical polishing also produced

centre of this specimen, and microbeam Laue photographs from this region included extra hexagonal spots, thus proving directly that the markings were associated with the transformation. The orientation relation was confirmed to within $\pm 15'$. After reheating the specimen to produce entirely cubic phase, and repolishing, it was gently squeezed to produce markings all over the surface; their formation was accompanied by cracking noises. In this and other experiments, the 'transformation cry' was used to determine when maximum transformation had been achieved; further compression produced only mechanical deformation. The markings were in two sets, corresponding to the original orientations of the hexagonal bicrystal, and on the original sites.

The stress-induced transformations produced macroscopic tilts which in favourable cases could be measured on two adjacent surfaces. Several specimens of the two alloys were prepared and converted to cubic form by cycling, and then electropolished on at least two adjacent surfaces. Most specimens were single crystals, but some contained two cubic orientations. Each specimen was compressed along a chosen direction until all transformation ceased, and the surface tilts in the banded regions were measured optically. In regions with a large amount of transformation and closely spaced bands, the tilts were ill-defined, and the image of the illumination source in the auxiliary microscope was a continuous streak, like that observed after spontaneous transformation.

VOL. 7 1959 When isolated or well separated parallel plates were formed, however, two spots could be observed, one from the matrix and one from the tilted bands.

Assuming the shape deformation to be a simple shear, the direction and magnitude of the shear may be deduced from tilt measurements in two surfaces. The results are summarised in Fig. 2, where the plane of projection represents the habit plane, dots are compression axes, and the arrows represent the shear directions. The experimentally determined directions cluster around $\langle 112 \rangle$, the largest deviation being for compression 3. The observed shear magnitudes were generally less than the theoretical 0.353, the mean value from the seven determinations being 0.30 with a standard deviation of 0.06.

The choice of the {111}(112) shear system is clearly not governed by a maximum resolved shear stress criterion; the axis 6/7, for example, gives a very small resolved shear stress in the observed shear directions. Detailed calculation shows that many of the other compression axes give larger resolved shear stresses in a (112) direction of a {111} plane not chosen as the habit plane. System 5 was derived from the same cubic crystal as system 3, the cubic orientation having been restored by heating, using a different compression axis. The habit plane and hexagonal orientation remained unchanged, but a new shear direction was chosen. Similarly systems 6 and 4 were derived from the same parent grain by different compressions. The near coincidence of axes 6 and 7 is accidental.

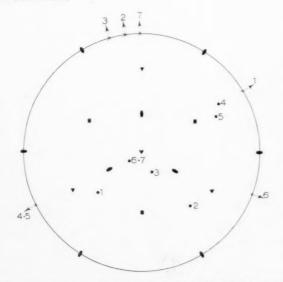


Fig. 2. The shape deformation associated with stress-induced transformation in cobalt—nickel alloys. The habit plane is in the plane of projection. • compression axes. $\leftarrow \times$ shear directions. Observed shears were:—(1) 0.24, (2) 0.29, (3) 0.28, (4) 0.35, (5) 0.31, (6) 0.25, (7) 0.41.

Although the habit plane is chosen independently of the stress axis, the shear direction is the (112) direction of greatest resolved shear stress within the habit plane, at least for systems 2, 3, 4 and 5. For the axis 6/7, the resolved shear stress is almost identical in two of the (112) directions, and each was chosen in separate specimens. The compression along axis 1 is noteworthy in that the observed shear direction is an anti-transformation (112) direction, i.e. the shear would produce A-A stacking of adjacent {111} layers. The reverse of this direction, which would effect the transformation, would presumably operate under a tensile stress. The only reasonable explanation of the observation seems to be that very fine shears are alternating on the two (112) directions at 60° to the observed direction, the results adding to give the observed macroscopic effect. It can be seen that axis 1 is situated nearly symmetrically to these two directions, although the difference is greater than for axis 6/7. Calculation shows, however, that for axis 1, the resolved shear stress in one of these directions is about twice that in the other, and it is not at all clear why both should be operative.

5. DISCUSSION

195

The observations on the stress-induced transformation show conclusively that this change may properly be described as martensitic, not only in the sense that growth of the phase is not thermally activated, but also in terms of a formal definition requiring a shape change. (7) The spontaneous transformation also apparently involves regions of homogeneous shear, but these are much narrower since there is no preferred shear direction. The recent electron microscope work of Takeuchi and Honma⁽¹⁾ has demonstrated very effectively that in spontaneously transformed alloy specimens, bands representing all three possible shear directions are present. In pure cobalt, the bands are much narrower, and visible optical effects are apparently caused by some form of bunching, the mean tilt being not quite zero over regions much wider than the regions of homogeneous shear. Bands are not always visible in pure cobalt: it is possible that they are observed more readily in single crystals, where the stresses opposing further growth of a region of homogeneous shear are much smaller than in polycrystals, once the band has spread across the crystal.

The dislocation node theory of the transformation^(8,9) has been placed in quantitative form by Seeger^(10,11). He envisages the reaction beginning from individual stacking faults (extended dislocations) of the cubic lattice, and the critical condition is

that the half-dislocations have sufficient energy to overcome their mutual repulsion when they pass two planes apart, after the first revolution. This is only possible if the half-dislocations acquire kinetic energy, and with this assumption, Seeger is able to explain the magnitude of the supercooling needed to effect transformation. The agreement is not so good with the smaller supercooling found in the present work. and this description is not entirely convincing in other respects.

The present experiments on thermal cycling show that the hysteresis increases markedly with the number of transformation cycles. The evidence strongly suggests that this is a result of plastic deformation caused by the shape change of the transformation, as concluded by Edmondson and Ko⁽¹²⁾ for steels, and this is supported by the recrystallization of some specimens when heated to high temperatures. After cycling, the critical condition for transformation thus seems to be that the effective stress on the half-dislocations should be able to drive them through the matrix hardened by deformation. Although the critical condition in annealed material may be different, there is other evidence suggesting that the nuclei may not be single stacking faults.

The crystallographic results for stress-induced transformations imply the operation of preferred nucleation sites, since the habit plane is not necessarily the {111} plane of greatest resolved shear stress. This is also shown by the reversible crystallography of single crystal transformations, the reversibility being destroyed only by high temperature annealing. In one set of experiments, cubic twin crystals were produced by the heating transformation, but the twinning plane was the {111} plane formed from the hexagonal basal plane. Finally, in the spontaneous transformation in cobalt, the bands are so fine that an unreasonably large dislocation density would be required if each of them originated from a separate dislocation source.

VOL.

1959

The above reasoning suggests that the Bilby-Seeger

dislocation theory of the transformation may be correct for visible bands, but it is less probable that the critical condition for transformation is the first passing of the half-dislocations: the operative nuclei may be thicker than single stacking faults, and not entirely destroyed by the reverse transformation. It seems probable that the half-dislocations bounding a single stacking fault will begin to move as soon as the free energy difference has the right sign, (13) and will complete nearly a revolution at very low values of the driving force, before being stopped by each other's stress field. If this be true, there will be no opportunity to acquire the kinetic energy postulated by Seeger.

One of the initial objects of this work was to attempt to produce a single interface transformation in a cobalt or cobalt-nickel single crystal. This has not been achieved, but the regions of homogeneous shear have been widened sufficiently by stress to show that the very large theoretical shear is actually produced by the atomic mechanism of transformation.

ACKNOWLEDGMENTS

We should like to express our thanks to Professor Hume-Rothery for his interest in this work.

REFERENCES

- 1. S. TAKEUCHI and T. HONMA, Sci. Rep. Res. Inst. Tokohu Univ. 9, 492, 508 (1957)
- 2. H. BIBRING, F. SEBILLEAU and C. BÜCKLE, J. Inst. Met. to be published.
- R. W. CAHN, J. Sci. Instrum. 30, 201 (1953).
- 4. A. R. TROIANO and J. L. TOKICH, Trans. Amer. Inst. Min. (Metall.) Engs. 175, 728 (1948).
- 5. H. BIBRING and F. SEBILLEAU, Rev. Métall. 52, 569 (1955). 6. Z. S. Basinski and J. W. Christian, J. Inst. Met. 80,
- 659 (1951-52). 7. B. A. BILBY and J. W. CHRISTIAN, The Mechanism of
- Phase Transformations in Metals, p. 121. Institute of Metals, London (1955).
- 8. B. A. Bilby, Phil. Mag. 44, 782 (1953).
- 9. Z. S. Basinski and J. W. Christian, Phil. Mag. 44, 791 (1953).
- 10. A. SEEGER, Z. Metallk. 44, 247 (1953).
- 11. A. SEEGER, Z. Metallk. 47, 653 (1956).
- 12. B. EDMONDSON and T. Ko, Acta Met. 2, 535 (1954).
- 13. J. W. CHRISTIAN, Proc. Roy. Soc. A 206, 51 (1951).

THE CRYSTALLOGRAPHY OF THE $\beta\text{--}\alpha$ TRANSFORMATION IN ZIRCONIUM AND IN TWO TITANIUM-MOLYBDENUM ALLOYS*

P. GAUNT† and J. W. CHRISTIAN‡

The habit planes and orientation relationships associated with the transformation have been studied in two specimens of crystal bar zirconium. The results are very similar to those of earlier workers for titanium, but the habit planes lie a little nearer to the $\{001\}$ – $\{111\}$ boundary and the $\{1120\}_{\alpha}$ pole is displaced a little further from $\{111\}$ towards $\{110\}$ than in titanium. The results are compared with the predictions of the Bowles–Mackenzie theory; as with titanium, best agreement is obtained with a type A (α^+, ω^+) solution, but in the present work it is not possible to obtain exact agreement for both orientations and habit planes. X-ray and kinetic observations both show that deformation accompanying transformation is much more severe in zirconium than in titanium, possibly as a result of a larger volume change, and the discrepancies may be due to the accommodation stresses.

The habit planes and shape deformations have been determined for stress-induced martensite in quenched titanium alloys containing 11 per cent and 12.5 per cent molybdenum. In the 12.5 per cent alloy, only $\{344\}$ type martensite was produced by stress, but both $\{334\}$ and $\{344\}$ types were produced in the other alloy, with the $\{334\}$ predominating. The observed shear directions for the $\{334\}$ martensite agreed with the predictions of the type A (α^+, ω^+) solution. A tentative orientation relation was obtained for one plate of $\{344\}$ martensite; the present theory of this type of transformation is briefly discussed.

LA CRISTALLOGRAPHIE DE LA TRANSFORMATION β - α DANS LE ZIRCONIUM ET DANS DEUX ALLIAGES TITANE-MOLYBDENE

Sur deux cristaux de zirconium, les auteurs étudient les plans d'habitat et les relations d'orientation associées avec la transformation $\beta-\alpha$. Les résultats qu'ils obtiennent sont très semblables à ceux déjà connus pour le titane, mais les plans d'habitat sont un peu plus proches de la frontière $\{001\}$ – $\{111\}$ et le pôle $\{1120\}_{\alpha}$ est déplacé de $\{111\}$ jusqu'à $\{110\}$. Les résultats sont comparés avec les prévisions de la théorie de Bowles–Mackenzie; comme dans le cas du titane, un meilleur accord s'obtient avec une solution du type A (α^+, ω^+) , mais dans le présent travail il n'est pas possible d'obtenir un accord complet, à la fois pour les orientations et pour les plans d'habitat. Des observations de cinétique et aux rayons X montrent que la déformation qui accompagne cette transformation est plus sévère dans le zirconium que dans le titane. Ceci peut résulter d'une plus grande modification de volume et les écarts peuvent être dus aux tensions d'accomodation.

195

Les plans d'habitat et les déformations volumétriques ont ét édéterminés pour une martensite produite dans des alliages trempés de titane contenant 11 et 12,5% de molybdène. Dans l'alliage à 12,5%, seule la martensite type $\{344\}$ a été obtenue par l'application d'une tension de compression tandis que les deux types de martensite $\{334\}$ et $\{344\}$ apparaissent dans l'autre alliage avec prédominance de la martensite $\{334\}$. Les directions de cisaillement observées pour la martensite $\{334\}$ sont en accord avec les prédictions de la solution du type A (α^+, ω^+) . Les auteurs ont obtenu une relation d'orientation provisoire pour une plaquette de martensite $\{344\}$. Enfin, ils discutent brièvement de la théorie qu'ils proposent pour ce type de transformation.

DIE KRISTALLOGRAPHIE DER $\beta\!\!-\!\!\alpha\!\!-\!\!\text{UMWANDLUNG}$ VON ZIRKON UND VON ZWEI TITAN-MOLYBDÄN-LEGIERUNGEN

Die zu der Umwandlung gehörigen Habitusebenen und Orientierungsbeziehungen wurden an zwei stabförmigen Zirkonkristallen untersucht. Die Ergebnisse sind denen früherer Arbeiten über Titan sehr ähnlich, aber Habitusebenen liegen etwas näher zur $\{001\}$ – $\{111\}$ -Grenze hin und der $\{1120\}_{\alpha}$ -Pol ist etwas stärker von $\{111\}$ in Richtung auf $\{110\}$ verschoben als bei Titan. Die Ergebnisse werden mit den Voraussagen der Theorie von Bowles–Mackenzie verglichen; wie bei Titan wird die beste Übereinstimmung mit einer Lösung von Typ $A(\mathbf{x}^+, \omega^+)$ erzielt, aber in der vorliegenden Arbeit war es nicht möglich, exakte Übereinstimmung sowohl für Orientierungen wie Habitusebenen zu erzielen. Beobachtungen der Kinetik wie solche mit Röntgenstrahlen zeigen, dass die Umwandlung viel stärkere Verformungen hervorruft als bei Titan, möglicherweise infolge einer grösseren Volumänderung; die Unstimmigkeiten können durch die hierbei auftretenden Eigenspannungen verursacht sein.

Bei durch äussere Spannung hervorgerufener Martensit-Umwandlung abgeschreckter Titanlegierungen mit 11% bzw. 12,5% Molybdän wurden die Habitusebenen und Gestaltänderungen bestimmt. Bei der Legierung mit 12,5% entstand infolge der Spannung nur Martensit vom Typ {344}, bei der anderen neben {344} hauptsächlich {334}. Die beobachteten Scherungsrichtungen beim {334}-Martensit stimmten mit den Vorhersagen auf Grund einer Lösung des Typs A (α^+, ω^+) überein. Versuchsweise wurde eine Orientierungsbeziehung für eine Platte von {344}-Martensit aufgestellt; die heutige Theorie dieser Art von Umwandlung wird kurz diskutiert.

^{*} Received September 2, 1958.

[†] Department of Physics, The University, Sheffield; formerly at Department of Metallurgy, University Museum, Oxford.

[‡] Department of Metallurgy, University Museum, Oxford.

1. INTRODUCTION

This paper describes experimental work on the crystallography and kinetics of the β (b.c.c.) \rightarrow α (h.e.p.) transformation in zirconium and in two titanium-molybdenum alloys. Specimens for the crystallographic work on zirconium were taken from iodide crystal bar, and very many crystals were examined in attempts to find specimens with 'good' habit plane markings. Two six-sided specimens were used for the detailed investigations, one (Specimen A) being obtained direct from Metropolitan-Vickers, Manchester, and the other (Specimen B) from A.E.R.E., Harwell. For the kinetic observations, some coarsegrained zirconium specimens were obtained by annealing zirconium wire at 820°C for seven days. Alloy specimens for crystallography were prepared by argon are melting and were then annealed at 1150°C for 36 hr before quenching into brine.

Zirconium was chemically polished, as recommended by Cain⁽¹⁾, and titanium alloys were also chemically polished in a nitric acid–hydrofluoric acid bath. Conventional techniques were used for X-ray examination, microscopy, etc., but the heat treatment of zirconium presented some difficulties, and a very high vacuum was needed for successful hot stage microscopy. Tilt measurements were made by an optical method.⁽²⁾ The specimen was mounted on a small goniometer head, and an auxiliary microscope substituted for one half of a binocular eyepiece was used to focus the images of the illumination source.

2. RIDGE MARKINGS ON SPECIMEN A

Specimen A, as received, showed two distinct types of marking on three of its six faces. In addition to imperfectly developed habit plane markings similar to those found in titanium, these faces contained regions of very prominent and very straight ridge markings (see Fig. 1). In one face, the ridges had five independent directions, but in the two adjacent faces only three such directions were found. Assuming the ridges to be the traces of planes, they were related to each other like the {110} planes of a cubic crystal. The b.c.c. orientation thus implied was approximately consistent with the shape of the crystal, but the rod axis was inclined at 13° to a (111) direction. Fig. 3 shows a stereographic projection in Face 1 of the crystal, the cubic orientation having been obtained by rotating a standard projection until the {110} poles coincide with the trace normals of the ridge markings in this face. X-ray results showed that the numbered {110} poles were parallel to basal planes of the various hexagonal orientations present, so that the



Fig. 1. "Ridge" markings on crystal bar zirconium. Oblique illumination. $\times 200$.



Fig. 2. Isolated ridge: sharp demarcation of α orientations shown by polarized light. $\times 70$.

interpretation is consistent with the Burgers orientation relation.

Very few of the ridge markings followed round from one face into the adjacent surface. Under polarized light, some ridges were seen to form sharp demarcations between areas of different α orientation (see Fig. 2). Some of the ridges had measurable tilts; the main ridges in the face with five sets were composed of oppositely tilted parts (angle of tilt $10^{\circ}20' \pm 30'$) meeting in a midrib. Traces of the same {110} plane had tilts of approximately $\pm 9^{\circ}30'$ in an adjacent surface. The tilts were remarkably constant, but their significance is not clear; since the surface profile in all faces was of the type shown in Figure 1 the ridges cannot be the surface manifestation of a simple shear.

3. X-RAY WORK ON SPECIMEN A

Semi-microbeam Laue photographs were taken from many areas of the specimen, each of which appeared under polarized light to be a large a grain. The photographs were, in general, uninterpretable; several intense but broad reflections together with weak diffuse reflections were produced after about 120 mA hr (using a tungsten target), but there were few, if any, zones. The orientations of the α grains were therefore found by a glancing angle oscillation technique, the specimen being adjusted by trial and error until a $\langle 11\overline{2}0 \rangle$ or a [0001] axis was vertical. Recognizable layer lines were then produced, although the spots were very large, and the setting of the specimen was not critical to within ~1°. Extra spots not attributable to the α -zirconium pattern were also found, and these were provisionally identified as arising from zirconium hydride (ZrH). The {111} hydride spot always occurred on the {1011} Laue streak, thus implying a definite orientation relation between the two lattices. Polished and etched surfaces of the crystal bar showed a black precipitate in needle-like form, and this is believed to be hydride, which may precipitate at the β - α transformation; the precipitate is not present in a specimen of zirconium containing less than 20 p.p.m. of hydrogen, kindly given us by Dr. P. C. L. Pfeil.

The orientations found from the oscillation photographs are plotted in Fig. 3, and are consistent with the ridge marking orientation. The results also confirm the Burgers orientation relation within the accuracy attainable ($\pm 2^{\circ}$). The ambiguity in the β orientation discussed by Ginnekin and Burgers⁽³⁾ does not arise, since basal planes not parallel to the external faces were located by the X-ray method. The orientations having been determined, it was

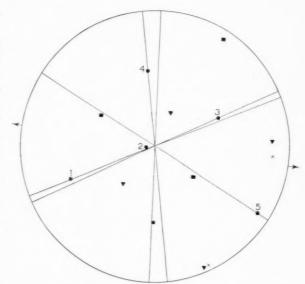


Fig. 3. Trace normals of ridges on specimen A, and orientation of original β crystal.

- {100} poles.
- ▲ {111} poles.

• $\{110\}$ poles, the numbered poles being parallel to $(0001)\alpha$ poles.

× {1120}_α poles •• rod axis.

found that interpretable Laue photographs could be obtained when the X-ray beam was parallel to the six-fold axis, but the spots were very distorted.

4. HABIT PLANE FOR SPECIMEN A

In ridge free regions, habit plane markings similar to those found in titanium were observed. There were three classes of these markings:—

- (1) Straight parallel markings which were rather faint, and occurred together with similar markings at approximately 90°. Polarized light and X-ray examination showed that these were areas in which the α basal planes were nearly parallel to the surface.
- (2) Very rough, strong markings which were only approximately parallel to each other; under high magnification, there was found a 5° scatter in the directions of the traces.
- (3) Faint but clear and straight markings interspersed with class 2 markings in a characteristic manner

Ten independent trace directions from one face were plotted in a single stereographic triangle, and nine of them passed through a small circle of 3° diameter. The remaining trace was straight and parallel (class 3). The centre of the circle of intersection was at $\{0.461,\ 0.512,\ 0.725\}_{\beta}$ which is near $\{334\}_{\beta}$. This analysis gave the habit plane in general

VOI 7 195 indices. By correlating individual traces with the corresponding orientations, the variant of the habit plane for a particular orientation relation was found to be:

$$(011)_{\beta} \, / \, / \, (0001)_{\alpha} \qquad [1\overline{1}1]_{\beta} \; nearly \, / \, / \; to \; [1\overline{2}10]_{\alpha}$$

Habit plane
$$(\overline{0.72}, \overline{0.51}, 0.46)_{\beta} \pm 2^{\circ}$$

or $(\overline{0.72}, \overline{0.46}, 0.51)_{\beta} \pm 2^{\circ}$

This habit plane and variant was confirmed by two surface analysis in two areas.

The strengths of the three classes of markings may be correlated with the relation of the macroscopic shear direction to the surface. It was not possible to measure the shape deformation for zirconium, but an approximate analysis suggests that the shear direction is nearly in the basal plane, and for the variant above, it is close to [322]. The more accurate analysis of Mackenzie and Bowles⁽⁶⁾ gives a shear direction which is approximately between $[3\overline{2}2]$ and $[2\overline{1}1]$ but rather closer to the former (see Section 9). Class 1 markings are weak because the two possible shear directions producing a basal plane almost parallel to the surface both lie nearly in the surface. Class 2 markings occur when the basal plane is at 90° or 60° to the surface; in the former case, both possible shear directions are at a large angle to the surface, and produce the strong markings. When the basal plane is at 60° to the surface one shear direction is at a large angle to the surface, and the other is at a small angle. The surface then contains strong (class 2) markings interspersed with weak (class 3) markings. The class 3 markings, however, are not parallel to habit plane traces, but to basal plane traces. It is believed that these represent accommodation slip, and that they mask the weak habit plane markings. The accommodation slip is believed to be basal plane α slip, rather than $\langle 110 \rangle_{\beta}$ slip, since no slip markings were observed in class 1 regions, even although the habit plane markings were very weak there also. Similar slip markings in weak habit areas with the basal plane at 60° to the surface were observed by Williams, Cahn and Barrett(4) in titanium.

1959

5. ORIENTATION RELATIONS AND HABIT PLANE OF SPECIMEN B

Preliminary examination of this specimen was made by Z. S. Basinski. It had 'good' habit plane markings in one face, most of them being much straighter than those in specimen A, but no ridge markings. The same three classes of habit markings were found, and Laue photographs taken from class 1 regions were readily interpretable. Only four independent trace

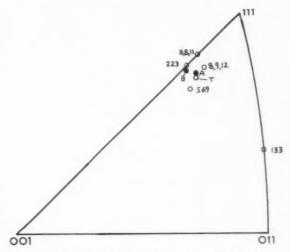


Fig. 4. Habit planes in zirconium crystal bar. Filled circles are experimental poles for specimens A and B. {569}: Approximate habit plane for zirconium, according to Ginneken and Burgers⁽³⁾. {8, 9, 12}: Habit plane for titanium, according to Williams et al. (4) {8,8,11}: Habit plane for titanium according to Newkirk and Geisler (5). T: Habit plane for titanium according to theory of Mackenzie and Bowles. (6)

directions were available for single surface analysis on this specimen; the habit plane obtained was $\{0.468, 0.488, 0.737\}_{\beta}$. This pole, together with that from specimen A is plotted in Fig. 4. Despite the small number of traces, the result from specimen B may be more accurate than that from Specimen A because of the straighter markings.

With this specimen, a Laue photograph showing superimposed reflections from two areas with parallel basal planes enabled the angle between the two orientations to be measured as $7^{\circ}30' \pm 36'$. This gives the orientation relation

$$(011)_{\beta} \mathbin{/} \mathbin{/} (0001)_{\alpha}$$

$$[1\overline{1}1]_{\beta}$$
: $[1\overline{2}10]_{\alpha} = 1^{\circ}30'$ toward $[0\overline{1}1]_{\beta}$.

6. KINETIC OBSERVATIONS ON THE ZIRCONIUM TRANSFORMATION

Polished coarse-grain zirconium samples were heated and cooled through the transformation range under a hot stage microscope. With slow heating and cooling rates (\sim 2°/min), no change was observed on the surface, apart from grain boundary movements made visible by thermal etching of the boundaries. Rapid cooling of the specimen produced surface distortion, and the room temperature structure (Fig. 5) was very confused. In some experiments, the temperature gradient was so arranged that the colder end of the specimen was not heated into the α phase, and after rapid cooling, the martensitic structure in the transformed part of the specimen was much better

Fig. 5. Surface relief effects produced by rapidly cooling a coarse-grained zirconium wire specimen from above the transformation temperature. $\times 200$.

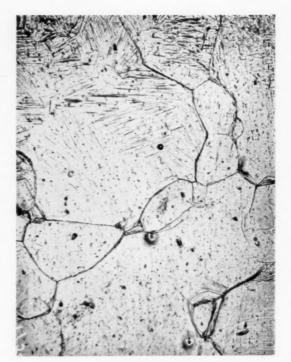


Fig. 6. Surface relief effects produced in similar manner, but unmarked portion was below the transformation temperature throughout the experiment. $\times 200$.

defined in the regions adjacent to the untransformed part (Fig. 6). Ciné-films also showed that the transformation markings were relatively straight and parallel immediately below the transformation range, and the transition to the confused rumpled structure took place gradually on further cooling.

After cooling to room temperature, the markings were irreversible on reheating into the β range. Cycling through a more limited temperature range (about 500°C) gave reversible markings which appeared on cooling and disappeared again on heating. Laue photographs from the large α grains of the annealed wire specimens were extremely sharp, but after a single cycle through the transformation range the unsatisfactory diffuse photographs characteristic of the crystal bar specimens were obtained. A further anneal below the transformation temperature restored the specimen to its initial state, giving sharp patterns.

During attempts to produce better transformation markings in a crystal bar specimen, an unusual thermal etching effect was observed. The specimen had been heated for 24 hr at 1300°C and then allowed to cool to room temperature. Three grains were thermally etched on the specimen, and the surface within these grains contained fine striations which

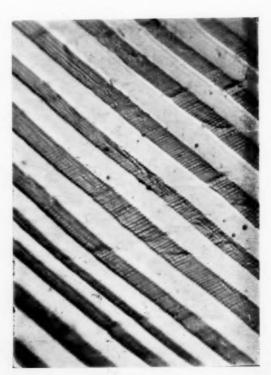


Fig. 7. Thermally etched zirconium crystal bar. ×1300.

VOI 7 195



Fig. 8. Relief effects due to stress-induced martensite in titanium-12.5 per cent molybdenum alloy. ×150.

were always parallel but not necessarily straight (Fig. 7). The markings changed direction in different grains, and could only be seen at high magnification. When the surface was polished and etched, a fragmented α structure was revealed, bearing no relation to the thermally etched markings.

7. HABIT PLANE AND SHAPE DEFORMATION IN A TITANIUM-12.5% MOLYBDENUM ALLOY

The alloy work was undertaken because the current theory does not seem to explain the results adequately, despite its success in pure titanium. Attempts to produce stress-induced martensitic transformation in β -phase zirconium alloys, retained by quenching, were all unsuccessful. As reported by previous workers, it was quite easy to transform titanium–molybdenum alloys by application of compressive stresses.

After quenching from 1150° C, the specimens had a coarse-grained β structure (grain diameter ~ 2 mm), with sub-boundaries in some of the larger grains. Four rectangular faces were polished, so that the grain boundaries could be followed from face to face, and the orientations of the larger grains were found from Laue photographs. Martensitic plates were then produced by compression along the length of the specimen; considerable stress had to be applied, and the transformation was accompanied by cracking

noises. The appearance of the plates is shown in Fig. 8, which also illustrates propagation or sympathetic nucleation across a grain boundary.

The habit plane and direction and magnitude of the macroscopic shear (assuming the shape deformation to be a simple shear) were found for six different habit systems, five of them from one specimen, by two surface analysis of the trace directions and tilts. Each reading was repeated about six times at various points on an individual plate, and on different parallel plates of the same system. The standard deviation of trace direction measurements was about 8' of arc and of tilt measurements between 7' and 20' of are, depending on the thickness of plate. The main error in habit determination was thus in the correlation of the trace directions with the Laue photographs ($\sim +2^{\circ}$); the corresponding error in the shear direction is estimated at $\pm 4^{\circ}$ and in shear magnitude +4 per cent.

The results are plotted in Fig. 9. All the habit plane determinations lay within a circle of about 6° radius near $(0.373,\ 0.611,\ 0.698)_{\beta}$ and five of the shear directions in a circle of 9° radius near $[\overline{0.917},\ 0.282,\ 0.282]_{\beta}$. The mean value of the shear was 0.277, the standard deviation from the mean among the results being 0.009. The scatter is thus rather larger than the expected experimental error, as also concluded by $\mathrm{Liu}^{(7)}$. The scatter may be due to the constraints imposed by the matrix on the growing plate, especially near grain boundaries. In one large grain, a small change in the tilt (from $10^{\circ}30'$ to 10°) was found on penetrating inwards from a free edge towards a grain boundary.

One of the shear directions (system 5) was a long way from the scatter circle of the other five traces, and was close to the (147) direction observed by Weinig and Machlin⁽⁸⁾. Part of this grain, however, was rather severely deformed during formation of the plates: and redetermination of the orientation of the deformed region moved the shear direction near to the other five and the habit plane to the other side of the (011)-(111) boundary. The shear direction from this grain is thus not very reliable, but the shear magnitude has been included in the mean result. Attempts to calculate the shear from the deviation of scratches gave inconsistent results, possibly because of 'feathering' of the plates⁽⁹⁾ on a fine scale. Fig. 10 shows some plates where the feathering is visible under the microscope.

Many attempts were made to determine the orientation of the α lattice using the plate exposure method of Weinig and Machlin. Laue patterns differing from those of the matrix were obtained, but showed

VOL. 7 1959



Fig. 10. "Feathering" of martensite plates in a titanium-12.5 per cent molybdenum alloy. ×150.

streaking of spots towards a {112} pole, making interpretation difficult. From only one plate was it possible to derive a tentative orientation relationship; this was equivalent to relation B of Liu,⁽⁷⁾ and corresponds approximately to the Burgers relation with the basal plane normal to the habit plane. For the variant of the habit plane plotted in Fig. 9, this relation is:

 $\begin{array}{l} (0001)_{\alpha} \, / \, / \, (011)_{\beta} \\ \\ [11\overline{2}0]_{\alpha} : [111]_{\beta} \sim 1^{\circ} \quad \text{towards} \, [100]_{\beta} \\ \\ \text{Habit plane} \, \sim (344)_{\beta} \end{array}$

Oscillation photographs about $\langle 110 \rangle_{\beta}$ axes did not show any reflections from the h.c.p. phase, but some extra reflections were found, most of which lay along the b.c.c. layer lines. It is believed that these represent a fine precipitate formed during the quench, but the pattern did not agree with that of the ω phase in titanium–vanadium and titanium–manganese alloys. The measured lattice parameter of the solid specimen, using a back reflection camera, was $3.255 \pm 0.001 \, kX$.

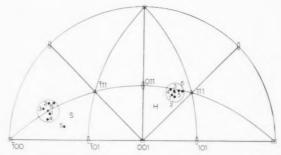


Fig. 9. Habit plane (H) and macroscopic shear direction (S) for stress-induced martensite in a titanium-12.5 per cent molybdenum alloy. The shear magnitudes were (1) 0.268, (2) 0.272, (3) 0.283, (4) 0.272, (5) 0.246, (6) 0.290.

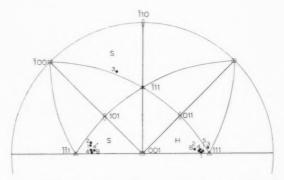


Fig. 11. Habit plane (H) and macroscopic shear direction (S) for stress-induced martensite in a titanium—11 per cent molybdenum alloy. System 3, which is of {344} type, has been plotted in the adjacent unit triangle for greater clarity. 4 and 4' represent alternative shears found from two different tilts measured in one set of plates. B gives the habit plane and shear direction for pure titanium according to the Mackenzie and Bowles theory.

8. HABIT PLANE AND SHAPE DEFORMATION IN A TITANIUM-11% MOLYBDENUM ALLOY

The results of habit plane determinations from five systems in one specimen, and of shear determinations from four of these systems, are shown in Fig. 11. One habit system was of the {344} type; the other four clustered closely around {0.500, 0.515, 0.668} and were of the {334} type (see discussion). The shear results, however, had a very wide scatter, and parallel plates ostensibly belonging to the same habit system showed differences of up to 4° in the measured angles of tilt. On occasion, two tilts were found in one plate.

The parameters of the {344} system were similar to those found for the 12.5 per cent alloy.

9. COMPARISON WITH THEORETICAL PREDICTIONS FOR ZIRCONIUM

For all known transformations for b.c.c. to h.c.p. the correspondence used by Mackenzie and Bowles⁽⁶⁾ and Christian ⁽¹⁰⁾ seems to be correct. For the variant

of the orientation relation given in Sections 4 and 5, this correspondence is specified by:

$$(\alpha' \mathbf{C}\beta) = \begin{pmatrix} 1 & \frac{1}{2} & -\frac{1}{2} \\ 0 & 1 & -1 \\ 0 & \frac{1}{2} & \frac{1}{2} \end{pmatrix} \quad (\beta \mathbf{C}\alpha') = \begin{pmatrix} 1 & -\frac{1}{2} & 0 \\ 0 & \frac{1}{2} & 1 \\ 0 & -\frac{1}{2} & 1 \end{pmatrix}$$

where the three axis system \mathbf{a}_1 , \mathbf{a}_2 , \mathbf{c} has been used for the hexagonal (α') basis. This is identical with the Mackenzie–Bowles variant if their orthorhombic cell is defined by \mathbf{a}_1 , $2\mathbf{a}_1 + \mathbf{a}_2$, \mathbf{c} ; it is an equivalent variant of the correspondence used by Christian.

The lattice parameters of the two forms of zirconium are given by Lustmann and Kerze⁽¹¹⁾ as:

$$\begin{array}{ll} \mathbf{\alpha}: a = 3.248kX, \, c = 5.198kX, \quad \text{and} \quad \beta: a_0 \\ = 3.609kX \end{array}$$

The corresponding principal strains are 2 per cent expansion along [011]₈, which becomes [0001]_a, 10 per cent expansion along $[01\overline{1}]_{\beta}$, which becomes $[01\overline{1}0]_{\alpha}$ $(\equiv [120]_{\alpha})$, and 10 per cent contraction along $[100]_{\beta}$, which becomes $[2\overline{110}]_{\alpha}$ ($\equiv [100]_{\alpha}$). The Burgers mechanism of transformation(12) implicitly assumed this correspondence, and accomplished most of the length changes normal to [011] by means of a shear on $(\overline{211})$, $[1\overline{11}]_{\beta}$; the remaining adjustments were not considered in detail. Since the principal strain in the [011] direction is so small, it is tempting to retain Burgers assumption that this direction is exactly parallel to the hexagonal c axis, and that the requisite strain is taken elastically at the interface and subsequently relaxed plastically. If the restriction to a rational habit plane is removed, the theory is then analogous to that of Frank for steels, (13) except that the structures can be matched at the interface without a set of dislocations. With the above parameters, the invariant line in the (011) plane (the shear direction) is readily found to be $\sim [3\overline{2}2]$, and the habit plane, defined by this line and by [011] is $(\overline{433})$. Alternatively, the assumption of a uniform dilatation rather than a uniaxial expansion to equalize the repeat distances along [011], and [0001], gives a habit plane (127.57.5). Both of these planes are near to the experimental habit planes of the present work, and to the generally accepted results of previous workers on titanium(4,5) and zirconium.(3)

Although the approximate theory does not describe the transformation crystallography adequately, it is useful in showing the physical significance of the experimental results, which tends to be obscured by the mathematics of the Bowles–Mackenzie theory. Thus the observations that the orientation relation is close to the Burgers relation, that the habit plane is nearly normal to the basal plane, and that the shape deformation $^{(14)}$ is nearly a simple shear, are all a consequence of the small principal strain parallel to the c axis. If this were less than 1 per cent, the simple theory might be directly applicable (the Bowles–Mackenzie theory requires a dilatation of $\sim 3/4$ per cent for titanium), and the lattice and shape deformations would coincide.

The crystallographic results for zirconium imply that the transformation is similar in type to that in titanium. All the features of the titanium transformation found by Williams et al. (4) seem to be duplicated in zirconium, except that the small angle between different basal planes derived from a common $\{110\}_{\beta}$ plane was not observed. In particular, the small displacement of a $\langle 1120\rangle_{\alpha}$ pole from a $\langle 111\rangle_{\beta}$ towards a $\langle 110\rangle_{\beta}$ indicates that the transformation is neither type A $(\alpha^+ \omega^+)$ nor type B of the classification given by Mackenzie and Bowles (6). In Fig. 4, the experimental habit planes were plotted together with the type A $(\alpha^+ \omega^+)$ prediction for titanium. The agreement is good, but the zirconium habit planes lie nearer to the $\{001\}$ – $\{111\}$ boundary.

Fig. 12 shows part of the Mackenzie and Bowles curves for $(\alpha^+ \omega^+)$ transformations plotted on an enlarged scale, with two variants of the habit planes found for Specimens A and B marked. With the above parameters for zirconium $(\gamma^2 = (c/a)^2 = 2.57, (a/a_0)^2 = 0.809)$, a rather large dilatation of about 1.5 per cent is needed to bring the habit plane to a position near the experimental results. This best position is at 14° to the {111} pole, instead of the experimental 12°. It is clear that agreement is better with $\gamma^2 = 2.55$, and this is not unreasonable since the results quoted by Lustmann and Kerze had to be extrapolated from

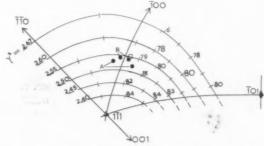


Fig. 12. Part of the Mackenzie and Bowles net, showing the variation of the habit plane for a type A $(\alpha^+ \ \omega^+)$ solution. Some values of $100 \ \theta^z$ are marked along the curves. Two variants of the experimental habit planes for specimens A and B are plotted as filled circles; the open square is the theoretical habit plane for $\gamma^z = 2.55, \ \theta^z = 0.786$.

7 1959 $600^{\circ}\mathrm{C}.$ In titanium, and presumably in zirconium, the effect of impurities introduced during high temperature lattice spacing work is to increase γ much more than $a.^{(15)}$

With $\theta^2 = 0.786$, $\delta = 0.986$ so that $|\delta - 1|$ is still rather large compared with other martensitic transformations. Numerical calculation of the invariant line strain gives (in Bowles–Mackenzie notation):

$$(\mathbf{B}\mathbf{S}\mathbf{B}) = \begin{pmatrix} 0.882711 & -0.068523 & 0.074835 \\ 0.055674 & 1.041239 & -0.038796 \\ -0.061008 & -0.041244 & 1.040931 \end{pmatrix}$$

and the habit plane is (783110, 463227, 482916). As shown in Fig. 12, this is in good agreement with the experimental results.

The above results represent one of four possible variants in which the basal plane is nearly parallel to (011). All orientations are close to the Burgers relation; as shown by Mackenzie and Bowles⁽⁶⁾, the most convenient way of examining the orientation results is to calculate the angles between equivalent planes in different variants. Using their notation, the angles between possible basal plane variants were calculated as:

$$1 \rightarrow 3 = 0.50^{\circ}$$
$$1 \rightarrow 2 = 0.48^{\circ}$$

In view of the difficulty in obtaining sharp diffraction spots, these angles are consistent with the experimental failure to detect this difference.

For the angles between $\{11\overline{2}0\}$ planes (or directions) from variants with nearly parallel basal planes:

$$1 \times \rightarrow 4 \bullet = 10.68^{\circ}$$

 $1 \times \rightarrow 2 \bullet = 10.68^{\circ}$

which is appreciably larger than the experimental 7.5°; indeed the $\{11\overline{2}0\}_{\pi}$ plane which is nearly parallel to a $\{111\}_{\beta}$ is very slightly displaced towards the $\{100\}_{\beta}$ rather than the $\{110\}_{\beta}$. A numerical solution of the $(\alpha^- \omega^+)$ type has also been calculated, in case the smaller value of θ^2 gives better agreement here. For this solution, the angles between nearly parallel basal plane variants are less than 0.25°, but the angles between corresponding $\{11\overline{2}0\}$ planes of variants with nearly parallel basal planes are $\sim 11.40^\circ$. The $\{11\overline{2}0\}_{\pi}$ plane is thus further displaced towards $\{100\}_{\delta}$.

The reason for the discrepancy between theory and experiment for the $(\alpha^+ \omega^+)$ solution is not clear. The orientation relation of the Mackenzie-Bowles theory

will be in better agreement with experiment if a larger value of θ^2 is taken, and if the lattice parameters are correct this seems likely, as $|\delta - 1|$ will also be reduced. The habit plane, however, will then move inwards from the (111)-(100) boundary quite rapidly. The present experimental results thus cannot be explained exactly in terms of the theory, but this is, perhaps, not surprising in view of mounting experimental evidence that there is a real scatter in individual habit planes. (16) The kinetic observations on the irreversibility of the transformation, and the effects of transformation on the quality of the X-ray photographs, all show that accommodation stresses produce exceptionally severe effects in zirconium. It has recently been suggested(17) that accommodation strain energy is important in determining δ and hence θ .

It is possible that another assumption about the plane of the lattice invariant shear will produce better results, although this does not seem probable in view of the success of the Mackenzie–Bowles theory for titanium. The interpretation of the ridge markings on specimen A is very uncertain at present, and will not be discussed here.

10. CRYSTALLOGRAPHY OF THE TITANIUM ALLOY TRANSFORMATIONS

VOL

195

In agreement with earlier workers, two distinct types of habit plane were found in the titaniummolybdenum alloys. It is convenient to refer to these as {334} and {344}, although the experimental points for both habits scatter across the stereographic triangle. Because of this scatter, the experimental determination of the habit plane normal does not necessarily fix the type of habit; plane 2 in Fig. 9, for example, could be equally well described as near (344) or (334). Figs. 9 and 11 show, however, that the two classes are quite distinct when the shear directions are determined. For {334} habits, the shear direction lies close to a great circle passing through the {111} and {001} poles of the unit triangle containing the habit plane normal, and for {344} habits, the shear direction is close to a great circle through the {111} and {011} poles.

In the present work, {344} type martensite only was produced in the 12.5 per cent molybdenum alloy, in agreement with Liu's results. (7) Liu, however, states that only {344} martensite was produced by stress, or by quenching in liquid oxygen, in alloys of lower molybdenum content, whereas both types were formed by stress in the present work in the 11 per cent alloy, and the {334} type was predominant. The difference may be a consequence of the formation of

{334} martensite during quenching to room temperature in Liu's experiments; this was not observed in the present work. These results do not support Liu's hypothesis that the type of martensite depends only on the temperature of formation.

The centres of the scatter circles for the habit plane and shear directions in Fig. 9 are 86° apart, instead of the expected 90° (only the shear component of the shape deformation is measured). The scatter of these measurements is much greater than the experimental errors, probably because of stresses in the matrix when a plate is formed. For the {334} systems in Fig. 11, the habit plane scatter is within the experimental error although the shear direction scatter is very large. Liu also observed less scatter in {334} than in {344} systems, but attributed this to the formation of his {334} plates during quenching rather than by applied stress.

The choice of habit plane variant in the 12.5 per cent alloy was governed by a maximum resolved shear stress condition. It thus appears that potential nuclei on several different habit plane variants can be made to grow by application of stress, the choice depending on the stress axis. This contrasts with the behaviour of cobalt-nickel alloys. (18) However, the resolved shear stress in the shear direction of the {344} system of the 11 per cent alloy was greater than that in any of the {334} systems, but only one out of five sets of habit planes was {344}. Thus for this alloy {334} nuclei are either more numerous, or more readily capable of growing under stress.

VOL.

1959

The positions of the habit plane and shear direction predicted by the Bowles-Mackenzie theory for pure titanium are also plotted in Fig. 11, and provide further confirmation of the success of this theory for {334} type martensite. The agreement between observed and calculated shear directions is particularly satisfactory, since it was not possible to find this direction experimentally in either pure titanium or zirconium.

The orientation relation found for the {344} martensite of the 12.5 per cent alloy in the present work is very provisional. Changing to the standard variant used by Mackenzie and Bowles, the habit plane is near to $(3\overline{44})$ and the shear direction is near to $[8\overline{33}]$. This habit plane could represent a type A $(\alpha^- \omega^-)$ solution, or a type B solution, but it is difficult to make further comparisons in the absence of information on the hexagonal parameters. Using Weinig and Machlin's parameters for the 11 per cent alloy, $\gamma^2 =$ 2.2 and both solutions then require $\theta^2 \sim 0.90$ which differs considerably from the experimental $(a/a_0)^2 =$ 0.82. For the class B solution, the predicted direction of displacement for $\theta^2 = 0.90$ is on the correct great circle, but is near [III], over 30° from the observed direction of the shear component of the displacement. This implies there is a considerable non-shear component of the shape deformation, since the chosen parameters require an appreciable volume change in the invariant line strain. This has to be balanced by a large $|\delta - 1|$ if there is only a small overall volume change. The magnitude of the shear component may be calculated from an equation given by Christian⁽¹⁰⁾, and is 0.22 as compared with the experimental 0.28. The agreement is improved by changing the parameters γ^2 and θ^2 , but the habit plane solution then approaches the {334} type.

Similar difficulties are encountered if the solution is assumed to be of the A $(\alpha^- \omega^-)$ type. Again there is a large dilatation (assuming Weinig and Machlin's parameters), and a correspondingly large non-shear component of the invariant plane shape deformation. It is clear that further work is needed to explain the {344} habits.

ACKNOWLEDGMENTS

We should like to thank Dr. T. Raine and Dr. P. C. L. Pfeil for assistance in obtaining suitable zirconium specimens. Part of the experimental work was assisted by a general research grant made to the laboratory by the British Non-Ferrous Metals Research Association. We are grateful to Professor Hume-Rothery for his interest and support.

REFERENCES

- 1. F. M. Cain, Zirconium and Zirconium Alloys, p. 176. American Society for Metals, Cleveland (1953).
- 2. Z. S. Basinski and J. W. Christian, J. Inst. Met. 80, 659 (1951-2).
- 3. A. J. J. VAN GINNEKEN and W. G. BURGERS, Acta Cryst. 5, 548 (1952).
- 4. A. J. WILLIAMS, R. W. CAHN and C. S. BARRETT, Acta Met. 2, 117 (1954). 5. J. B. NEWKIRK and A. H. GEISLER, Acta Met. 1, 370
- (1953).6. J. K. Mackenzie and J. S. Bowles, Acta Met. 5, 137
- (1957).Y. C. Liu, Trans. Amer. Inst. Min. (Metall.) Engrs. 206.
- 1036 (1956). S. Weinig and E. S. Machlin, Trans. Amer. Inst. Min.
- (Metall.) Engrs. 200, 1280 (1954).
- B. R. BUTCHER and A. H. ROWE, The Mechanism of Phase Transformations in Metals, p. 229. The Institute of Metals, London (1955).
- J. W. Christian, J. Inst. Met. 84, 386 (1955–56).
 B. Lustmann and F. Kerze. The Metallurgy of Zirconium.
- McGraw-Hill, New York (1955). 12. W. G. Burgers, *Physica* **1**, 561 (1934).
- 13. F. C. Frank, Acta Met. 12, 15 (1953). 14. B. A. BILBY and J. W. CHRISTIAN, The Mechanism of Phase Transformations in Metals, p. 121. The Institute
- of Metals, London (1955). 15. J. SPREADBOROUGH, unpublished work.
- 16. H. M. Otte and T. A. Read, Trans. Amer. Inst. Min. (Metall.) Engrs. 209, 412 (1957)
- J. W. Christian, Acta Met. 6, 377 (1958).
 P. Gaunt and J. W. Christian, Acta Met. 7, 529 (1959).

THE DISSIPATION OF ENERGY DURING PLASTIC DEFORMATION*

J. F. NICHOLAS†

Various mechanisms are considered for the dissipation as heat of the mechanical energy of deformation in a cold-worked metal. Since dislocations seem to account for at most 10 per cent of this dissipation, the creation and annihilation of point defects is considered in some detail. It is concluded that the dissipation may be accounted for satisfactorily in this way.

LA DISSIPATION DE L'ENERGIE AU COURS DE LA DEFORMATION PLASTIQUE

Divers mécanismes sont envisagés pour expliquer la dissipation sous forme calorifique de l'énergie mécanique de déformation dans un métal écroui. Comme les dislocations ne semblent justifier qu'environ 10% de cette dissipation, la création et la suppression de défauts ponctuels sont considérées en détail. L'auteur conclut que cette façon de voir rend bien compte de la dissipation étudiée.

DIE ENERGIEDISSIPATION WÄHREND PLASTISCHER VERFORMUNG.

Für die Überführung der mechanischen Verformungsenergie eines kaltverformten Metalls in Wärme werden verschiedene Mechanismen betrachtet. Da Versetzungen für höchstens 10% dieser Überführung aufzukommen scheinen, wird die Erzeugung und Vernichtung von Punktfehlstellen ausführlich betrachtet. Es folgt, dass die Dissipation auf diese Weise befriedigend erklärt werden kann.

1. INTRODUCTION

Most of the energy expended in deforming a metal is dissipated as heat and only a small proportion is stored in the metal. Considerable research has been carried out on the mammer in which this latter energy is stored⁽¹⁾ but no satisfactory picture has yet been given for the mechanism by which most of the mechanical energy is converted to heat. Various possibilities are considered in this paper. It appears that, at high strains, the only process capable of dissipating sufficient energy is the creation and annihilation of point defects, although the creation and annihilation of dislocations may make a significant contribution.

2. STATEMENT OF PROBLEM

We can express the incremental work, dW, done on unit volume of a crystal as

$$dW = dE + dS + \gamma \, dA,\tag{1}$$

where E is the energy dissipated as heat, S is the stored energy that can be liberated on annealing, γ is the specific surface energy, and A is the surface area per unit volume. In general, at high strains,

$$\gamma dA \ll dS \ll dW$$
.

so that we can write, as a good approximation,

$$dW = dE. (2)$$

Then, since $dW = \tau d\varepsilon$ where τ is the stress and ε the strain, we have

$$dE/d\varepsilon = \tau. \tag{3}$$

In order to treat $dE/d\varepsilon$ in terms of dislocations, we will consider a crystal consisting of a set of parallel slip planes of equal area, deforming by the movement of dislocations of Burgers vector \boldsymbol{b} . If these dislocations move an average distance dx, the strain

$$d\varepsilon = Nb \, dx,\tag{4}$$

where N is the length of these dislocation lines per unit volume and certain geometrical factors have been neglected. Then, from (3) and (4), we can calculate the dissipation of energy when unit length of dislocation moves through unit distance as

$$dE/N dx = b\tau. (5)$$

Since the energy of formation E_F of unit length of dislocation line is given by

$$E_F = K\mu b^2, \tag{6}$$

where μ is the shear modulus and K is a factor rather less than 1 for a reasonable density of dislocations, the distance L through which the dislocation moves in dissipating an energy equal to its energy of formation is given by

$$L = NE_F \, dx/dE = K\mu b/\tau. \tag{7}$$

Some values of L are given in Table 1 where the stresses are typical of those operating in a

^{*} Received September 23, 1958.

[†] Division of Tribophysics, Commonwealth Scientific and Industrial Research Organization, University of Melbourne, Australia.

heavily-worked specimen and K has been taken as one. These values are, in effect, upper estimates for L, since K will usually be less than one for the density of dislocations in such a specimen. It can be seen that each dislocation dissipates an energy equal to its energy of formation in about 1000 Å or less.

3. CONSIDERATION OF POSSIBLE MECHANISMS

Four possible mechanisms for dissipating the energy will be considered, viz.

- the moving dislocations acquire a large kinetic energy that is released when the dislocation is stopped;
- (2) the dislocations dissipate energy continuously through thermoelastic damping, radiation damping, and scattering of sound waves;
- (3) large lengths of dislocation line are created and annihilated during the deformation; and
- (4) large numbers of point defects are created and annihilated during the deformation.

The first two possibilities have been considered in detail by various authors and found to provide inadequate dissipation of energy unless the dislocations are moving at speeds comparable to that of sound.⁽³⁾ The evidence available at present suggests that dislocations do not move at such high speeds, so that we will henceforth ignore possibilities (1) and (2).

The third possibility implies that, in a heavily deformed metal, the average displacement of a dislocation between creation and annihilation, here called the slip distance, is of the order of L ($\simeq 10^3 \, \text{Å}$). The best measurements of slip distances under these conditions are those of Seeger, Diehl, Mader and Rebstock. (4) These workers strained copper heavily $(\varepsilon = 0.6)$, polished it, strained it further ($\Delta \varepsilon = 0.05$), and then took electron micrographs. These showed main slip-lines, $2-4 \times 10^4 \,\text{Å}$ in length, together with shorter cross-slip lines. Since the cross slip of a dislocation out of a pile-up is simply a continuation of its movement, the mean slip distance of a dislocation here appears to be of the order of a few microns, i.e. $\simeq 10L$. Thus, this mechanism accounts for rather less than 10 per cent of the dissipated energy.

TABLE 1.

Metal	Magnitude of Burgers vector,	Shear modulus,	Operative stress,	L
	(Å)	(kg/mm^2)	(kg/mm^2)	(Å)
Al	2.8	$2.8 imes 10^3$	15	510
Cu	2.5	$7.5 imes 10^3$	20	950
Ni	2.5	12×10^3	30	1000

This last conclusion would be modified if individual slip-lines actually consisted of short lengths of line, each length arising from a different dislocation. In this case, the slip distance of an individual dislocation might be of the order of L. However, for slip lines to form in this way, the operating sources would have to be grouped together in neighbouring planes and we might then expect, if the surface is typical of the interior, to see slip lines at certain stages composed of short discrete lengths of line. This last effect has not been observed.

The fourth possibility, creation and annihilation of point defects, has not been considered previously from the present point of view but is treated in some detail below. The results suggest that this mechanism could dissipate sufficient energy.

4. CREATION AND ANNIHILATION OF POINT DEFECTS

The mechanism envisaged here is that the moving dislocations, on cutting through the Cottrell forest, become jogged and then create trails of point defects behind them during their further movement. Nearly all of these defects then disappear rapidly either by absorption at sinks or by recombination with other defects. Such recombination may take the form of annihilation or the creation of clusters or stacking faults.

4.1 Creation of defects

In the general case, the dislocation lines will be of complex shape and not amenable to exact treatment. However, two extreme cases, which are mathematically tractable, will be treated in detail here and a more realistic case then considered in the light of these results. In this section, consideration is restricted to copper since this is the only metal where reasonable estimates have been given for the energies of point defects. The cases to be considered are:

- the dislocation lines remain straight and point defects are formed individually;
- (2) the moving dislocations loop around the intersecting dislocations and produce rows of defects when the loop reunites, after which the jogs glide conservatively out of the crystal; and
- (3) a more realistic case.

Case (1)—Straight dislocations: defects produced individually

We suppose that, at a given stage, the jogs which are capable of producing defects are spaced an average distance l_j apart along the moving dislocations and that interstitials are being produced with twice the

1959

frequency of vacancies (cf. Cottrell⁽⁵⁾). Then the energy necessary to form defects during a dislocation movement dx is given by

$$dE = U_d N \, dx/l_i \, b, \tag{8}$$

where $U_d = \frac{1}{3}U_v + \frac{2}{3}U_i$ and U_v , U_i are the energies of formation of vacancies and interstitials.

In order to explain the whole of the dissipation given by equation (5), we need

$$l_i = U_d/\tau b^2. (9)$$

For copper, taking $U_d=4\,\mathrm{eV}$, we find $l_j=500\,\mathrm{\AA}$. In the appendix, l_j is estimated on the assumption that the dislocation moves forward with a mean speed v and that jogs when formed oscillate along the dislocation with a mean speed v_j , in the absence of an applied stress. It is shown there that a dislocation acquires effectively its equilibrium number of jogs after moving forward a distance of less than $100\,\mathrm{\AA}$, and that the equilibrium value of l_i is given by

$$l_i = (v_i/v\rho)^{1/2}, (10)$$

where ρ is the number of dislocations that cut unit area of the glide plane and create, on the gliding dislocations, jogs capable of producing defects.

On substituting $l_j = 500$ Å into equation (10), we find

$$v_i/v = 3 \times 10^{-11} \rho.$$
 (11)

No reliable estimate of v_j/v is available but we would certainly expect it to exceed one and this is consistent with equation (11) if ρ is of the order of $10^{11} \, \mathrm{cm}^{-2}$. For the purposes of the present discussion we will assume that $\rho = 2 \times 10^{11} \, \mathrm{cm}^{-2}$ for the value $\tau = 20 \, \mathrm{kg/mm}^2$ used above. This gives $v_j/v = 6$.

It should be noted that, if $v_j/v > 3 \times 10^{-11} \rho$, then insufficient energy is dissipated whereas, if $v_j/v < 3 \times 10^{-11} \rho$, this theory would predict more energy dissipation than is found experimentally.

Case (2)—Defects produced in rows: jog subsequently glides out of crystal

In this case, each time a moving dislocation intersects a stationary dislocation of the correct type, a row of defects is produced and this process is independent of any other intersections. Then, if n_g is the average number of defects produced per intersection, the energy dissipated is given by

$$dE = \rho N \, dx \, n_a U_d \,. \tag{12}$$

Thence, by elimination between equations (5) and (12), we find

$$n_g = \tau b/\rho U_d \,. \tag{13}$$

For copper, taking $ho=2 imes10^{11}\,\mathrm{cm}^{-2}$, we find

 $n_g = 40$. In this estimate, we have retained the value of 4 eV for U_d , since, although a row of vacancies will have less energy than the same number of isolated vacancies, the reverse may well be true for a short row of interstitials.

Case (3)—A more realistic case

Neither of the above simple cases provides quite enough energy dissipation since, under the assumptions of case (1), a true value of v_j/v would probably exceed 6, while in case (2) n_g is more likely to be of the order of 10, rather than 40. However, both these cases are unrealistic in that the first assumes instantaneous break-through at intersections, while the second assumes indefinitely continued conservative motion of a jog along the whole length of a dislocation.

A more realistic case would be one where the defects are formed in rows (as in case (2)) but where the jog, after it has been formed, glides only a short distance and is then arrested. Such arrests will arise as soon as the direction of the dislocation line deviates from the direction of conservative motion of the jog, i.e. when the dislocation line no longer lies in the plane defined by the Burgers vectors of the two dislocations which intersected to form the jog. It is clear that any given jog can then give rise to several rows of defects before it either glides out of the crystal or is annihilated by a jog of opposite type. We can again express the energy dissipation in the form of equation (12) if we now interpret n_a as the total number of defects produced by an "average" jog. On this basis, a value of 40 for n_a becomes reasonable.

19!

4.2 Annihilation of defects

The above discussion has been concerned with the creation of the defects but, in order to dissipate energy as heat, these defects must subsequently disappear or aggregate into clusters of low energy. No detailed theoretical consideration has been given to this part of the process since there is such uncertainty about the distribution of the defects as formed.

On the experimental side, however, the available evidence (see discussion by Clarebrough, Hargreaves, and West⁽⁶⁾) show that, in copper, some point defects are present after deformation at sub-zero temperatures but none after deformation at room temperature. Furthermore, those that are present after the deformation at low temperatures disappear on annealing at, or below, room temperature. Thus, in deformation at room temperature any point defects formed should be sufficiently mobile to annihilate themselves and hence to dissipate their energy as heat during the formation.

On the other hand, in nickel after deformation at room temperature, some vacancies are still present. The theory given here implies that these must be simply a residual concentration (of the order of 1 per cent) of the total number formed during the deformation. It does not help to solve the problem of why this concentration is effectively independent of the amount of deformation. (6) It suggests, however, that the amount of energy stored should be a sensitive function of the temperature of deformation. In particular, if the deformation is carried out at a low enough temperature, almost all the energy should be stored. Experimental work on this line would be very interesting.

It may be noted here that recent work by Dash⁽⁷⁾ on silicon provides direct experimental evidence for the creation of point defects as envisaged above. His work also points to a subsequent clustering of the defects and hence a dissipation of energy. A quantitative comparison of his data with the present theory will not be attempted here because of the difference between the materials used.

5. CONCLUSIONS

VOL.

1959

7

The above arguments have shown that, within the limits of the mechanisms listed in Section 3. dislocations alone cannot account for the dissipation of energy during cold work at room temperature. However, on theoretical grounds, sufficient point defects should be created to account for the dissipation provided they can subsequently cluster or annihilate each other. Experimental evidence suggests that, in copper at least, the defects are sufficiently mobile to do so.

The calculations could be extended by considering the dissociation of dislocations and the glide of jogs at an oblique angle to the average direction of the dislocation line; however, in view of the present uncertainty about dislocation speeds, such refinements do not seem worthwhile.

ACKNOWLEDGMENTS

I would like to thank Dr. W. Boas for suggesting the problem and for his encouragement throughout. Thanks are also due to Drs. L. M. Clarebrough, M. E. Hargreaves, and A. K. Head for much helpful discussion and criticism.

REFERENCES

- 1. A. L. TITCHENER and M. B. BEVER, Progr. Met. Phys. 7,
- 2. A. H. COTTRELL, Dislocations and Plastic Flow in Crystals, p. 17. Clarendon Press, Oxford (1953).
- 3. A. H. COTTRELL, Dislocations and Plastic Flow in Crystals,
- р. 66. Clarendon Press, Oxford (1953). 4. A. Seeger, J. Diehl, S. Mader and H. Rebstock, Phil. Mag. 2, 323 (1957).

- A. H. COTTRELL, Dislocations and Mechanical Properties of Crystals, Conference at Lake Placid, p. 509. John Wiley, New York (1957).
- 6. L. M. Clarebrough, M. E. Hargreaves and G. W. West, Proc. Roy. Soc. A232, 252 (1955).
 W. C. DASH, J. Appl. Phys. 29, 705 (1958).

APPENDIX-ESTIMATION OF I,

In order to estimate l_i we can write down a differential equation for $n_i = 1/l_i =$ the number of jogs per unit length of dislocation. We have

$$\frac{dn_{\scriptscriptstyle j}}{dt} = \rho\,\frac{dx}{dt} - k_1 n_{\scriptscriptstyle j} \rho\,\frac{dx}{dt} - k_2 n_{\scriptscriptstyle j}^{\,\,2}, \eqno({\rm A.1})$$

where t is the time and k_1 , k_2 are constants. The first term on the right of equation (A.1) gives the number of extra jogs formed at new intersections, while the second term is the correction to this to allow for the possibility of annihilation of an existing jog by a incipient jog of opposite type. The third term gives the loss of jogs due to annihilation of opposite pairs by movement along the dislocation. Losses due to movement of the jogs to the ends of the dislocation are neglected. Strictly, equation (A.1) should be replaced by two equations, one for the number of vacancy-producing jogs and one for the number of interstitial-producing jogs. However, for the present purpose, such a refinement is unnecessary and we assume that half the jogs are of each type.

Estimation of k,

We consider the equilibrium value of n_i in the case of $k_2 = 0$. Then equation (A.1) gives $k_1 = (1/n_j)_{eq} = (l_j)_{eq}$. However, the equilibrium value of l_i should be equal, in this case, to the interaction cross-section for jogs, i.e. the length over which an existing jog will interact with a new one as soon as it is formed. A reasonable estimate for k_1 is therefore 3b.

Estimation of k2

We consider unit length of dislocation as being divided by the jogs into n_i intervals of random length. Then the number of intervals of length b is given approximately by $n_i\{1 - \exp(-n_i b)\} \simeq n_i^2 b$, if $n_i b \ll 1$. However, if each jog is jumping ν times per second the length of such an interval should change by b, 2ν times per second and one half of these changes should reduce the length to zero, i.e. the number of intervals going to zero each second is vbn,2. Since an interval going to zero causes a loss of either two jogs (if they are of opposite type) or of none (if they are of the same type), the rate of loss of jogs from this cause is $\nu b n_i^2$. Thus, $k_2 = \nu b = v_i$, say, where v_i is the mean speed of movement of a jog along the dislocation.

Equation (A.1) can now be solved if we put dx/dt = v = constant and take the initial condition as $n_i = 0$ at x = 0.

On the reasonable assumptions that $v_j > v$ and $\rho < 10^{12} \, {\rm cm}^{-2}$, the solution becomes

$$n_i \simeq (v \rho/v_i)^{1/2} \tanh [(v_i \rho/v)^{1/2} x].$$

Therefore,

$$(n_j)_{\rm eq} = 1/(l_j)_{\rm eq} = (v\rho/v_j)^{1/2}.$$

Further, n_j reaches $0.9(n_j)_{\rm eq}$ in a distance of about $1.5~(v/\rho v_j)^{1/2}$. Thus, even if the dislocation has no jogs initially, it has virtually its equilibrium number after a distance of the order of 10^{-6} cm.

ÉLIMINATION DES LACUNES DANS LES ALUMINIUMS TRÈS PURS*†

M. WINTENBERGER!

Dans les aluminiums purs, après une trempe à l'air, l'excès de résistivité dû aux lacunes s'élimine complètement à la température ordinaire. La vitesse d'élimination des lacunes augmente avec la densité de dislocations. Nous avons supposé que les dislocations éliminent toutes les lacunes par interaction élastique. Nous avons pu, alors, ayant déterminé l'énergie de diffusion des lacunes évaluer la densité de dislocations introduites par écrouissage.

Nous avons cherché l'influence des dislocations et des lacunes créées par déformation plastique sur la résistivité.

Si la vitesse de trempe est grande les lacunes s'éliminent en formant des défauts qui ont une forte résistivité.

THE ELIMINATION OF VACANCIES IN HIGH-PURITY ALUMINIUM

In high-purity aluminium, air-cooled from elevated temperatures, the resistivity increment due to vacancies is completely eliminated at room temperature. The rate of this recovery increases with the dislocation density. The author supposes that dislocations remove all the vacancies by a process of elastic interaction. It is thus possible, after having determined the energy of diffusion of vacancies, to evaluate the dislocation density produced by cold-working.

The influence on the electrical resistivity of dislocations and vacancies created by plastic deformation is also studied.

On high quenching rates the vacancies are eliminated by the formation of other crystal defects possessing a high resistivity.

VERSCHWINDEN VON LEERSTELLEN IN SEHR REINEM ALUMINIUM

Bei sehr reinem Aluminium verschwindet der Zusatzwiderstand, der durch Abschrecken an Luft eingefroren wird, bei Raumtemperatur völlig. Die Schnelligkeit des Verschwindens steigt mit der Versetzungsdichte. Nach Bestimmung der Wanderungsenergie der Leerstellen liess sich auf Grund der Annahme, dass die Leerstellen infolge elastischer Wechselwirkung mit den Versetzungen an diesen verschwinden, die Versetzungsdichte nach Kaltverformung bestimmen.

Der Einfluss der bei plastischer Verformung entstandenen Versetzungen und Leerstellen auf den elektrischen Widerstand wurde untersucht. Bei grosser Abschreckgeschwindigkeit bilden die Leerstellen bei ihrem Verschwinden Defekte, deren Widerstand gross ist.

1. INTRODUCTION

Par des mesures de résistivité électrique, nous avons étudié sur l'aluminium l'élimination des lacunes en sursaturation au voisinage de la température ordinaire.

Pour obtenir des lacunes, nous avons utilisé deux procédés. La trempe qui permet de conserver une partie des défauts ponctuels en équilibre thermique aux températures élevées et la déformation plastique qui crée à la fois des défauts ponctuels et des dislocations.

Les défauts ponctuels en sursaturation ont tendance à s'éliminer par diffusion vers les imperfections cristallines jusqu'à ce que la concentration d'équilibre soit atteinte. Les atomes interstitiels qui déforment beaucoup le réseau s'éliminent à des températures très basses, de quelques dizaines de degrés absolus. Nous n'obtiendrons donc en général que des lacunes. Nous avons choisi l'aluminium comme matériau d'étude car nous disposions d'aluminiums très purs en particulier ceux préparés au laboratoire du C.N.R.S. de Vitry par zone fondue. (1,2) Ces aluminiums contiennent environ 5 atomes par million d'impuretés, ce qui limite les interactions entre les défauts cristallins et les impuretés.

De nombreux auteurs ont étudié les lacunes dans différents métaux, (3-5) mais des travaux récents sur le rôle des lacunes dans la formation des zones des alliages durcissables viennent souligner l'intérêt de l'aluminium. (6,7)

2. PROCÈDE DE MESURE

D'après la loi de Matthiessen, la résistivité électrique d'un métal bon conducteur à une température T est la somme de la résistivité idéale $\rho_{\theta}\left(T'\right)$ qui ne dépend que de la température et diminue avec elle, et de la résistivité résiduelle ρ_{r} qui varie linéairement avec la concentration des imperfections cristallines; ρ_{r} est indépendant de la température:

$$\rho_T = \rho_\theta(T) + \rho_r$$

La variation relative de ρ_T , pour une concentration

1959

^{*} Reçu le 23 septembre, 1958

[†] Cette recherche a été réalisée sous la direction de Monsieur le Professeur Chaudron au Laboratoire de Vitry du C.N.R.S.

[†] Régie Nationale des Usines Renault, Service 872, Billancourt, Seine.

y a peu d'autres défauts et que la température est plus basse. Aussi avons-nous suivi la résistivité électrique d'aluminiums en général très purs à la température de l'hydrogène liquide (20°K). Par exemple, pour un aluminium de zone fondue trempé à l'air depuis 550°C, l'augmentation de résistivité résiduelle

due aux lacunes est trois fois plus grande que la résistivité due à l'agitation thermique et aux impuretés.

déterminée d'un défaut est d'autant plus grande qu'il

puretés. Nous mesurons le rapport $\frac{R_{\rm H_2}}{R_{\rm N_2}}$ des résistances de fils aux températures de l'hydrogène et de l'azote liquide (20°K et 77°K). Les fils de mesure ont 150 mm de longueur et 0,4 mm de diamètre. Après recuit à haute température, les fils sont constitués d'un empilement de cristaux, chaque grain occupant toute la section du fil.

En négligeant la dilatation thermique, le rapport des résistances électriques vaut le rapport $\frac{\rho_{\rm H_2}}{\rho_{\rm N_2}}$ des résistivités.

Dans nos expériences ρ_{τ} est petit devant $\rho_{\theta}(N_2)$. ρ_{N_2} est donc à peu près constant et nous déterminons ainsi ρ_{H_*} en valeur relative.

On obtient $\frac{R_{\rm H_2}}{R_{\rm N_2}}$ en mesurant à difference de potentiel constante les intensités qui traversent les fils de mesures à 20°K et 77°K. Les intensités sont grandes (environ 0,3 A à 20°K); elles sont lues sur un milliampèremètre. Les différences de potentiel sont très faibles (quelques μ V); elles sont déterminées avec un amplificateur galvanométrique à contre-réaction du type de celui utilisé par MacDonald(8–10).

Ce procédé de mesure évite la connaissance des dimensions géométriques de l'échantillon, que des traitements peuvent modifier pendant une experience.

Pour avoir la valeur absolue des résistivités, nous avons déterminé indépendamment ρ_{N_2} en mesurant

par la même méthode $\frac{\rho_{\rm N_0}}{\rho_{20^{\circ}{\rm C}}}$. $\rho_{20^{\circ}{\rm C}}$ est donné dans les tables.

La précision de la méthode diminue quand la concentration des impuretés et des autres défauts cristallins augmente. En moyenne l'erreur absolue est de $5\times 10^{-6} \rho_{20^{\circ}\mathrm{C}}$.

3. ÊLIMINATION DES LACUNES APRÈS UNE TREMPE À L'AIR

Après une trempe à l'air, l'excès de résistivité électrique diminue rapidement en quelques heures à la température ordinaire (Fig. 1a) et s'élimine complètement, (ce qui n'est pas le cas, nous le verrons plus loin, après des trempes plus rapides).

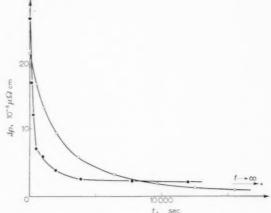


Fig. 1. (a) ° Restauration de la résistivité après une trempe à l'air. (b) ° Restauration de la résistivité après une trempe à l'air et un allongement de 8%. L'excès initial de résistivité est alors plus grand que pour (a) car la déformation plastique introduit des lacunes et des dislocations. La résistivité ne se restaure pas complètement car les dislocations ne s'éliminent pas complètement à 20°C.

Dans ces conditions, les lacunes s'éliminent donc complètement ou bien forment des défauts qui ont très peu d'action sur la résistivité électrique. Dans nos expériences, la dimension des cristaux est suffisante pour que la surface et les joints de grains interviennent peu dans l'élimination des lacunes.

Il est facile, par contre, de montrer que les dislocations peuvent éliminer efficacement les lacunes.^(11,12) Si, aussitôt après une trempe à l'air, on allonge le fil de mesure, la densité de dislocations est augmentée et la résistivité se restaure beaucoup plus rapidement que sans écrouissage (Fig. 1b).

Pour étudier la cinétique de l'élimination, il est nécessaire de connaître le début du phénomène. Ceci ne nous a pas semblé possible après une trempe à l'air, car une partie des lacunes a pu s'éliminer pendant le refroidissement. Aussi, immédiatement après la trempe à l'air, nous avons allongé légèrement le fil par traction. Nous supposons alors que le début de l'élimination des lacunes avec les dislocations introduites coı̈ncide avec la fin de la déformation.

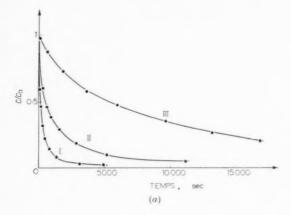
Dans ces conditions, la concentration c des lacunes en fonction du temps t est bien représentée par une équation de la forme (Fig. 2):

$$c = \mathrm{c_0} \exp{[-A(t)^m]} \qquad c_0 = \text{ concentration initiale}$$

Pour neuf expériences dans les quelles la déformation et la concentration initiale ${\bf c_0}$ variaient, nous avons eu:

Nous avons interprêté ce résultat en supposant que

VOI 7 19



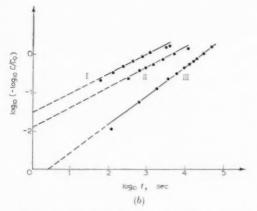


FIG. 2. (a) Variation de c/c_0 en fonction du temps à 17°C. I: après trempe à l'air et 9% d'allongement. II: après trempe à l'air et 3,5% d'allongement. III: après trempe à l'air sans allongement. (b) Représentation logarithmique des courbes de la Fig. 2 (a)

1959

$$\log_{10}\left(-\log_{10}\frac{c}{c_0}\right) = \log_{10}\log_{10}e + \log_{10}A + m\log_{10}t$$

les lacunes sont éliminées uniquement par les dislocations et que la vitesse d'élimination est déterminée par la vitesse d'arrivée des lacunes aux dislocations. (13) Les dislocations peuvent attirer les lacunes par interaction élastique suivant un mécanisme comparable à celui développé par Cottrell et Bilby pour les atomes de carbone dans le fer α . (14) Un calcul simple de Coulomb et Friedel (15), modifié comme l'avait déjà fait Harper (16) pour tenir compte de la diffusion, conduit à

$$c = c_{\mathrm{0}} \exp \left[-\pi \rho_{\mathrm{D}} \! \left(\! \frac{D_{\mathrm{L}} \; \mu \; b^5 \! t}{5 kT} \! \right)^{\! \mathrm{0,5}} \right] \label{eq:constraint}$$

 $ho_{
m D}=$ densité des dislocations

 $D_{\rm L}=$ coefficient de diffusion des lacunes

 $\mu = \text{module de cisaillement.}$

b =plus petite distance interatomique

Nous pouvons donc ainsi expliquer nos résultats.

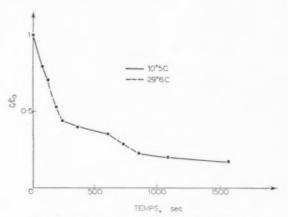


Fig. 3. Influence d'un changement de température sur l'élimination des lacunes.

Dans la formule précédente, deux quantités $D_{\rm L}$ et $\rho_{\rm D}$ ne sont pas connues. $D_{\rm L}$ est de la forme:

$$D_{\rm L} = D_0 \exp\left(-U_{D_{\rm L}}/kT\right)$$

 $U_{D_{\rm L}} =$ énergie de diffusion des lacunes avec $D_0 \simeq 1.^{(17)}$ Nous avons déterminé $U_{D_{\rm L}}$ en suivant alternativement à deux températures l'élimination des lacunes (Fig. 3). Du rapport des pentes aux discontinuités, nous avons obtenu:

$$U_{D_L} = 0.58 \pm 0.05 \text{ eV}$$

ce qui donne:

$$D_{\rm L} \simeq 10^{-10} \ {\rm cm^2 \, sec^{-1}}$$

Nous pouvons alors évaluer les densités de dislocations $\rho_{\rm D}$ introduites par allongement (Fig. 4)

$$ho_{
m D} = 16 \cdot 10^{10}
m arepsilon \qquad \qquad arepsilon = {
m d\'eformation}$$

La valeur de la densité de dislocations est vraisemblable. Elle augmente à peu près linéairement avec la déformation.

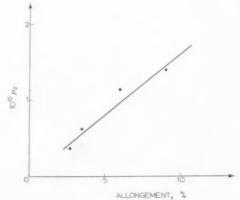


Fig. 4. Densité de dislocations introduites par allongement (Al à 30 p.p.m. d'impuretés).

VOI 7 195

Les courbes III de la Fig. 2 montrent qu'après une trempe à l'air seule la loi d'élimination ne semble plus être la même qu'après trempe à l'air et déformation plastique. On peut expliquer cette différence en supposant que le mécanisme est toujours le même mais que l'élimination a commencé pendant le refroidissement. Selon cette hypothèse, pour expliquer la forme des courbes 50% environ des lacunes devraient s'éliminer pendant le refroidissement.

Nous avons, d'autre part, étudié l'influence des impuretés courantes de l'aluminium pour des concentrations de 10 à 200 p.p.m. Dans ce domaine, la loi d'élimination garde la même forme mais, pour un même allongement après trempe à l'air, la vitesse d'élimination augmente avec la concentration en impuretés. Dans ces limites, les impuretés n'auraient pas d'action directe sur le mécanisme d'élimination, mais leur présence augmenterait plutôt la densité de dislocations d'un facteur 2 entre 10 et 200 p.p.m. (18) (voir paragraphe suivant).

4. LACUNES ET DISLOCATIONS CRÉÉES PAR ALLONGEMENT PLASTIQUE

Par déformation plastique, on introduit dans le réseau cristallin des dislocations et des défauts ponctuels. (19) Comme nous avons opéré à la température ordinaire, les atomes interstitiels qui auraient pu se former doivent s'éliminer très rapidement et on ne peut sans doute pas les observer dans nos expériences.

L'augmentation de résistivité électrique due à la déformation plastique diminue d'abord très rapidement puis ensuite beaucoup plus lentement, mais ne s'élimine pas complètement après plusieurs mois à 20°C même pour les aluminiums de zone fondue (Fig. 5). Les lacunes disparaîtraient d'abord; la restaura-

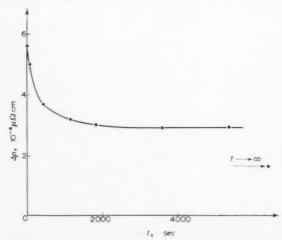
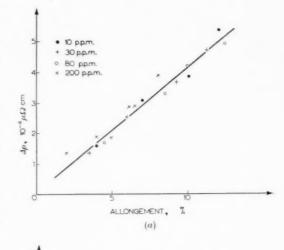


Fig. 5. Evolution de la résistivité électrique après un allongement de $7\frac{9}{9}$.



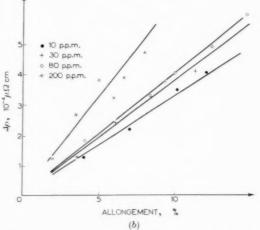


Fig. 6. (a) Influence des impuretés sur la résistivité électrique des lacunes introduites par allongement.
(b) Influence des impuretés sur la résistivité électrique des dislocations introduites par allongement.

tion lente viendrait d'une annihilation ou d'un réarrangement des dislocations. Nous avons vérifié que la première restauration, attribuée aux lacunes, se fait suivant la même loi que l'élimination des lacunes après trempe à l'air et déformation (paragraphe précédent).

Pour séparer l'action des lacunes et des dislocations sur la résistivité, nous avons supposé d'une manière un peu arbitraire que la diminution de résistivité pendant les 4 heures qui suivent la déformation vient de la disparition des lacunes; l'excès de résistivité qui reste alors est dû aux dislocations.

Nous avons des aluminiums de différentes puretés entre 10 et 200 p.p.m. Toutes les impuretés sont alors en solution solide.

Les résultats sont donnés sur les Fig. 6a et 6b. Les augmentations de résistivité et par suite la concentration des lacunes et la densité de dislocations augmentent linéairement avec la déformation.

Pour les métaux les plus purs, l'augmentation de résistivité due aux lacunes est à peu près la même que celle due aux dislocations.

La déformation plastique introduit assez peu de lacunes; une trempe à l'air depuis 600°C en donne 10 fois plus qu'un allongement de 10%. Les lacunes augmentent la résistivité d'une manière indépendante de la pureté (Fig. 6a):

$$\Delta \rho(\mu\Omega \text{ cm}) = 4 \cdot 10^{-3} \varepsilon$$

Nous n'avons pas d'explication de ce résultat.

Par contre, à déformation égale, la densité de dislocations augmente avec la concentration en impuretés (Fig. 6b). Ce résultat peut s'interprêter si la présence d'impuretés limite la dimension des boucles de dislocations. Si L est le diamètre moyen de ces boucles: $^{(20)}$

$$arepsilon = rac{
ho_{
m D}}{4}\,bL \qquad b = {
m longueur~du~vecteur~de~Burgers}$$

Ainsi les boucles de dislocations seraient deux fois plus courtes dans un aluminium à 200 p.p.m. d'impuretés que dans un aluminium de zone fondue (10 p.p.m.).

Pour un aluminium à 30 p.p.m., nous avons:

VOL.

$$\Delta \rho(\mu\Omega \text{ cm}) = 3.7 \cdot 10^{-3} \varepsilon$$

Au paragraphe précédent, nous avions obtenu pour ce même aluminium:

$$ho_{\mathrm{D}} = 16 \cdot 10^{10} \varepsilon$$

En supposant que toutes les dislocations agissent de la même manière sur la résistivité, les deux formules précédentes donnent par division l'influence des dislocations sur la résistivité^(*)

$$\Delta \rho \left(\mu \Omega \text{ cm} \right) = 2.3 \cdot 10^{-14} \rho_{\text{D}}$$

La résistivité due aux dislocations diminue très lentement avec le temps à 20°C. La restauration augmente avec la pureté. Elle est sensible même pour un aluminium à 200 p.p.m. d'impuretés.

Concentration en impuretés (p.p.m.)	10	30	200
Proportion de résistivité, due aux dislocations, restaurée après 100 jours à 20°C	0,65	0,55	≥ 0,30

^(*) Le Dr. A. Seeger nous a fait remarquer que l'influence des dislocations sur la résistivité doit dépendre de leur orientation par rapport au champ électrique. Le résultat précédent n'est donc qu'une moyenne si on suppose que la distribution des dislocations est à peu près isotrope.

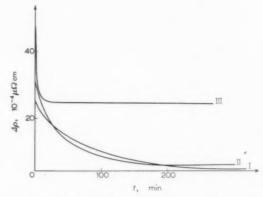


Fig. 7. Influence de la vitesse de trempe sur l'élimination des lacunes. I—Trempe à l'air depuis 580°C. III—Trempe à l'air depuis 580°C. III—Trempe à l'eau depuis 580°C.

Par ailleurs, nous avons fait quelques déformations à la température de l'azote liquide. Nous n'avons pas remarqué d'évolution de la résistivité en maintenant dans l'azote liquide l'échantillon pendant 2 heures après la déformation. Comme les atomes interstitiels doivent s'éliminer à des températures inférieures, il est vraisemblable qu'après des allongements de 10% il n'y a pas d'atomes interstitiels en concentration appréciable. A déformation égale, l'allongement produit alors 1,7 fois plus de dislocations et 3 fois plus de lacunes qu'à la température ordinaire.

5. INFLUENCE DE LA VITESSE DE REFROIDISSEMENT

La Fig. 7 montre la variation de la résistivité électrique pendant l'élimination des lacunes à 20°C après une trempe à l'air (I), après une trempe particulièrement rapide à l'air (II) et après une trempe à l'eau (III). Nous remarquerons trois faits principaux:

- (1°) L'excès initial de résistivité augmente avec la rapidité de la trempe, une partie des lacunes doit s'éliminer pendant le refroidissement.
- (2°) La vitesse de restauration de la résistivité augmente aussi avec la vitesse de trempe: si les lacunes s'éliminent aux dislocations, on peut attribuer ceci aux déformations de trempe.
- (3°) Plus la trempe est rapide, plus grand est l'excès de résistivité permanent observé après un temps très long.

Les déformations de trempe peuvent difficilement expliquer cet excès de résistivité après une trempe à l'eau car il faudrait une densité de dislocations comparable à celle introduite par 60% d'allongement.

Il faut donc penser qu'après des refroidissements rapides les lacunes s'éliminent en formant des défauts qui influent encore fortement sur la résistivité. Il



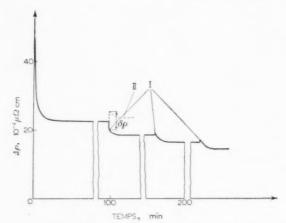


Fig. 8. Influence d'allongements plastiques successifs de 3% sur l'excès rémanent de résistivité électrique après une trempe à l'eau. I—Résistivité électrique mesurée immédiatement après la déformation. II—Courbe montrant l'évolution de la résistivité électrique après un allongement de 3% d'un fil recuit et refroidi lentement.

est d'ailleurs possible de diminuer cet excès de résistivité par des allongements successifs (Fig. 8). Après une première déformation de 3%, nous avons observé une diminution immédiate de la résistivité suivie d'une évolution plus lente. La déformation plastique a introduit des lacunes et des dislocations. La diminution lente de la résistivité correspond sensiblement à celle que donneraient les lacunes formées par l'allongement. Il faut donc supposer que les dislocations pendant leur mouvement ont éliminé des défauts, ce qui a réduit la résistivité de $\delta\rho$ (Fig. 8). Les allongements suivants ne donnent plus une diminution immédiate de la résistivité mais après l'élimination des lacunes la résistivité est néanmoins abaissée.

Nous avons rapproché ces résultats des propriétés mécaniques, après différents refroidissements, de fils monocristallins d'aluminium (Fig. 9). Ces fils avaient le même diamètre que ceux utilisés pour les mesures de résistivité. Nos résultats sont comparables à ceux que Maddin et Cottrell⁽²¹⁾ avaient déjà obtenus. Après

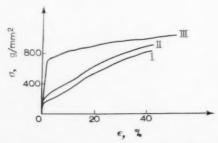


Fig. 9. Courbes de traction de fils monocristallins d'aluminium. I: après un refroidissement lent. II: après une trempe à l'air. III: après une trempe à l'eau.

une trempe à l'air, la courbe de traction est légèrement au-dessus de celle d'un fil refroidi lentement. Après une trempe à l'eau, la limite élastique est considérablement augmentée et le durcissement est faible.

Il y a deux hypothèses pour expliquer ces effets sur les propriétés mécaniques. Maddin et Cottrell⁽²¹⁾ supposent que les lacunes sont absorbées par les dislocations en formant des crans qui s'opposent au mouvement des dislocations. Friedel^(15,20) pense que les lacunes précipitent le long des dislocations en petites cavités qui les bloquent. Cette dernière hypothèse semble mieux s'accorder avec nos expériences sur la trempe à l'eau. Les petites cavités peuvent en effet présenter une résistivité assez grande.⁽²²⁾ Les dislocations dans leur mouvement peuvent en faciliter l'évaporation, soit par la chaleur dégagée soit en les déformant en passant au travers.

Après une trempe à l'air, les lacunes en plus faible concentration à la température ordinaire s'élimine-raient par déplacement des crans de dislocations, ce qui ne modifierait que très peu la résistivité électrique. La formation des cavités serait donc favorisée par une concentration élevée de lacunes et par une température d'élimination suffisamment basse.

6. CONCLUSION

Cette étude a été faite sur des aluminiums contenant entre 10 et 200 p.p.m. d'impuretés. Les plus purs, préparés par zone fondue nous ont donné une grande précision expérimentale; leur pureté limite, de plus, les interactions entre les lacunes et les impuretés.

Après une trempe à l'air, l'excès de résistivité dû aux lacunes s'élimine complètement. Comme la vitesse de restauration de la résistivité augmente avec la densité de dislocations, nous avons supposé que les lacunes s'éliminent alors par diffusion des crans de dislocations. On peut interprêter la cinétique de l'élimination en supposant que les dislocations attirent les lacunes par interaction élastique. Ayant déterminé l'énergie de diffusion des lacunes:

$$U_{D_{
m L}} = 0.58 \pm 0.05 \, {
m eV}$$

nous avons alors pu évaluer la densité de dislocations introduite par allongement. Pour un aluminium à 30 p.p.m. d'impuretés, nous avons:

$$\rho_{\mathrm{D}} = 16 \cdot 10^{10} \varepsilon$$

Entre 10 et 200 p.p.m. les impuretés courantes de l'aluminium ne modifient pas le mécanisme de l'élimination.

Nous avons, d'autre part, étudié les augmentations de résistivité dues aux lacunes et aux dislocations introduites par allongement plastique. Pour les lacunes:

$$\Delta \rho \left(\mu \Omega \text{ cm} \right) = 4 \cdot 10^{-3} \varepsilon$$

et ceci indépendamment de la pureté.

La densité de dislocations, par contre, semble augmenter, à déformation égale, quand la pureté diminue. Pour un aluminium à 30 p.p.m. d'impuretés:

$$\Delta \rho \, (\mu \Omega \, \mathrm{cm}) = 3.7 \cdot 10^{-3} \varepsilon$$

L'influence des dislocations sur la résistivité est donc, en movenne:

$$\Delta \rho \; (\mu \Omega \; \mathrm{cm}) = 2.3 \cdot 10^{-14} \rho_{\mathrm{D}}$$

Finalement, la vitesse de trempe paraît modifier le mécanisme de disparition des lacunes. Après une trempe à l'air, les lacunes s'élimineraient par diffusion des crans de dislocations. Après une trempe à l'eau, les lacunes formeraient des défauts ayant une forte résistivité électrique. Des dislocations en mouvement éliminent partiellement ces défauts qui pourraient être des petites cavités formées par précipitation de lacunes.

BIBLIOGRAPHIE

1. F. Montariol, R. Reich, Ph. Albert et G. Chaudron, C.R. Acad. Sci. Paris 238, 815 (1954).

- 2. G. CHAUDRON, Ph. ALBERT, M. CARON, F. MONTARIOL et M. Wintenberger Inst. Int. Froid Louvain, 2 (1956). Annexe.
- 3. J. W. Kauffman et J. S. Koehler, Phys. Rev. 88, 149 (1952)
- 4. F. J. Bradshaw et S. Pearson, Phil. Mag. 1, 812 (1956).
- 5. G. Panseri, F. Gatto et T. Federighi, Acta Met. 5, 50 (1957).
- 6. R. Graf, C.R. Acad. Sci. Paris 246, 1544 (1958)
- 7. G. Panseri, F. Gatto et T. Federighi, Acta Met. 6, 198 (1958).
- 8. D. K. C. MacDonald et K. Mendelsohn, Proc. Roy. Soc. A 202, 103 (1950).
- 9. M. CARON, Thèses, Publ. Sci. et Techn. Minist. Air France n° 328 (1957).
- 10. M. WINTENBERGER, Thèses à paraître.
- 11. M. WINTENBERGER, C.R. Acad. Sci. Paris 242, 128 (1956).
- 12. S. Pearson et F. J. Bradshaw, Phil. Mag. 1, 880 (1956).
- 13. M. WINTENBERGER, C.R. Acad. Sci. Paris 244, 2800 (1957).
- 14. A. H. COTTRELL et B. A. BILBY, Proc. Phys. Soc. A 62, 49 (1949).
- 15. P. COULOMB et J. FRIEDEL, Dislocations and Mechanical Properties of Crystals, p. 555 Wiley, New York (1957). 16. S. Harper, Phys. Rev. 83, 709 (1951).
- 17. A. D. LECLAIRE, Acta Met. 1, 438 (1953).
- M. WINTENBERGER, Rev. Met. 12, 942 (1957).
 J. MOLENAAR et W. M. AARTS, Nature, Lond. 166, 690 (1950).
- 20. J. FRIEDEL, Les Dislocations. Gauthier-Villars, Paris (1956).
- 21. R. MADDIN et A. H. COTTRELL, Phil. Mag. 46, 735 (1955).
- 22. D. L. DEXTER, Phys. Rev. 103, 107 (1956).

SUR LE BLOCAGE DES DISLOCATIONS PAR DES CAVITES OU DE PETITS PRECIPITES*

P. COULOMB†

Nous considérons un cristal dont les dislocations seraient bloquées par un chapelet de petites cavités. Nous analysons en détail comment l'agitation thermique et les contraintes appliquées permettent aux dislocations de quitter les cavités. Nous montrons que la chaleur d'activation du phénomène varie de façon linéaire avec la contrainte appliquée, suivant une formule dont nous avions déjà donné une forme approchée. Il en résulte que la limite élastique σ est donnée à 0° K par la formule de Frank et Read σ $\mu b/l$, où μ est une constante élastique, b le vecteur de Burgers et l l'équidistance des cavités le long d'une dislocation; σ/μ doit décroître linéairement à température croissante, mais avec une pente négligeable dès que le diamètre des cavités dépasse quelques b. La même analyse s'applique au blocage des dislocations par des chapelets de petits précipités.

ON THE BLOCKING OF DISLOCATIONS BY CAVITIES AND SMALL PRECIPITATE PARTICLES

The author considers a crystal in which the dislocations are blocked by a ring of small cavities. The influence of thermal agitation and applied stresses on the liberation of the blocked dislocations from the cavities is studied in detail. It is shown that the heat of activation of the phenomenon varies linearly with the applied stress in a manner similar to that which has already been proposed by the author.

The yield stress, σ , is given, at 0° K, by the Frank-Read relationship $\sigma = \mu b/l$. Here μ is elastic constant, b is the Burger's vector, and l the distance between voids along a dislocation. The ratio σ/μ has to decrease linearly with increasing temperature. The slope of this curve is negligible when the diameter of the cavity is larger than several Burger's vectors. The same analysis is applied to the blocking of dislocations by rings of small precipitate particles.

ÜBER DIE BLOCKIERUNG VON VERSETZUNGEN DURCH HOHLRÄUME ODER KLEINE AUSSCHEIDUNGEN

Ein Kristall wird betrachet, dessen Versetzungen durch eine Reihe von kleinen Hohlräumen festgehalten werden. Es wird genau untersucht, wie die thermische Bewegung und die angelegten Spannungen den Versetzungen erlauben, die Hohlräume zu verlassen. Die Aktivierungsenergie des Vorgangs variiert in linearer Weise mit der angelegten Spannung gemäss einer Formel, die schon in angenäherter Form mitgeteilt worden ist. Es folgt daraus, dass bei 0°K die elastische Grenze durch die Formel von Frank und Read $\sigma = \mu b/l$ gegeben ist, dabei ist μ eine elastische Konstante, b der Burgersvektor und l der (gleichmässige) Abstand von Hohlräumen entlang einer Versetzungslinie. σ/μ nimmt mit wachsender Temperatur linear ab. Sobald aber der Druchmesser der Holhräume einige b überschreitet, ist die Neigung vernachlässigbar. Dieselbe Behandlung kann auf die Blockierung von Versetzungen durch Reihen von kleinen Ausscheidungen angewendet werden.

Nous étudions dans cet article la variation en fonction de la température de recuit, de la résistance mécanique d'un métal dont les dislocations sont bloquées par un chapelet de cavités sphériques ou de précipités. L'énergie d'échappement d'une dislocation, calculée en tenant compte de l'attraction de la dislocation par les cavités est donnée par une formule très proche de la formule approchée obtenue par nous antérieurement.(1) Il résulte de cette formule que la résistance mécanique doit décroître de façon linéaire à température croissante, alors qu'un blocage par nuage de Cottrell fournirait une loi à peu près hyperbolique à haute température. (2) On a ainsi un critère pour distinguer ces deux types de blocage.

195

1.1. Les deux possibilités d'échappement

Nous montrons en annexe que la forme d'équilibre d'une dislocation fixée par deux cavités de rayon $P^{(3)}$ et soumise à une contrainte appliquée $\sigma = \mu \xi$. s'éloigne peu de segments de rayons vecteurs de longueur P/4 au voisinage de chaque sphère, reliés par un arc de cercle tangent de rayon $R \sim T/\sigma b \sim b/2\xi$. La forme d'équilibre est ainsi définie par l'angle θ (courbe I de la Fig. 2). On voit facilement que

$$\sin \theta = (2l - \frac{5}{2}P\cos \theta)\frac{\xi}{h}$$

Nous avons calculé l'énergie à fournir à un arc pour qu'il quitte la ligne des sphères (Fig. 1); nous avons d'autre part calculé l'énergie à fournir à deux arcs

^{1.} ENERGIE D'ECHAPPEMENT D'UNE BOUCLE DE DISLOCATION

^{*} Reçu le 23 septembre, 1958

Centre de Recherches Métallurgiques de l'Ecole des Mines

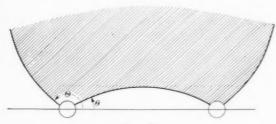


Fig. 1.

consécutifs pour qu'ils se rejoignent et échappent à la sphère intermédiaire (position II de la Fig. 2).

1.2. Echappement entre deux sphères

Nous n'avons fait qu'un calcul approché (en négligeant le rayon des sphères), car les chiffres obtenus dépassent largement ceux que nous trouverons au paragraphe 1.3. Nous supposons que la ligne de dislocation est un arc de cercle dont le rayon varie sous l'effet de l'agitation thermique.

Dans ce cas (Fig. 1):

VOL.

1959

$$\begin{split} \frac{\Delta E_1}{\mu b^3} &= \frac{1}{2} \, \frac{\Delta l_1}{b} - \xi \, \frac{\Delta S_1}{b^2} = \frac{l}{b} \, \frac{\Theta}{\sin \Theta} - \frac{\theta}{2\xi} - \\ &\quad - \frac{\xi l^2}{2 \, \sin^2 \Theta} \left(2\Theta - \sin 2\Theta \right) - \frac{1}{8\xi} \left(2\theta - \sin 2\theta \right) \end{split}$$

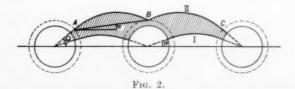
 Θ et θ étant les angles de départ de la dislocation à l'équilibre et au maximum d'énergie (position d'échappement). En écrivant $d\Delta E_1/d\Theta=0$, nous obtenons $2\xi l/b=\sin\Theta$. La valeur de Θ inférieure à $\pi/2$ ainsi définie est la position d'équilibre $\Theta_1=\theta$, l'autre $\Theta_2=\pi-\Theta_1=\Theta$ correspond à l'échappement. En reportant ces valeurs nous obtenons:

$$\frac{\Delta E_1}{\mu b^3} = \frac{1}{4\xi} (\pi - 2\theta - \sin 2\theta)$$

1.3. Echappement entre trois sphères

Nous supposons que l'agitation thermique fait passer un arc de dislocation de sa position d'équilibre à la position excitée ABC (Fig. 2) où les arcs AB et BC ont leurs courbures d'équilibre. Nous négligeons l'énergie du point anguleux B (Fig. 2), mais nous tenons compte de l'action des sphères. Nous obtenons les relations géométriques implicites:

$$\mathit{tg}\varepsilon = \frac{\frac{5}{4}P(1-\sin\,\Omega)}{2l-\frac{5}{4}P\cos\,\Omega}\,\mathrm{et}\,\sin\,(\Omega-\varepsilon) = \frac{2l-\frac{5}{4}P\cos\,\Omega}{2R\cos\,\varepsilon}$$



entre les angles ε et Ω ; l'énergie d'échappement est donnée alors par:

$$\begin{split} \frac{\Delta E_2}{\mu b^3} &= \frac{1}{2} \frac{\Delta l_2}{b} - \xi \frac{\Delta S_2}{b^2} \\ \Delta l_2 &= \frac{2b}{\xi} \left(\Omega - \varepsilon - \theta\right) - \frac{P}{2} \\ \Delta S_2 &= \frac{5}{4} P (2l - \frac{5}{4} P \cos \Omega) \left(1 + \sin \Omega\right) + \\ &+ \frac{b^2}{2 \xi^2} (\Omega - \varepsilon - \sin(\Omega - \varepsilon) \cos(\Omega - \varepsilon) - \theta + \sin \theta \cos \theta) \\ &= \pi \frac{P^2}{2} - \frac{25}{16} P^2 (\Omega - \sin \Omega \cos \Omega) + \frac{9}{16} P^2 (\Omega - 2\theta) \end{split}$$

 $-5 P \sin \theta (l - \frac{5}{4} P \cos \theta) + \frac{25}{9} P^2(\theta - \sin \theta \cos \theta)$

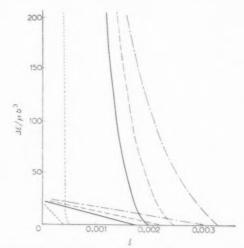


Fig. 3. Energie d'échappement d'une dislocation bloquée par des sphères de rayon $40\ b$ distantes de $2000\ b$, $500\ b$, $400\ b$ ou $300\ b$. On a calculé les courbes en supposant que l'échappement avait lieu entre deux ou trois sphères.

1.4. Comparaison des deux modes d'échappement

La Fig. 3 montre que dans les quatre cas que nous avons calculés numériquement, allant de sphères très éloignées (l/P=25) à des sphères proches (l/P=3,75), le mode d'échappement entre trois sphères correspond à une énergie bien plus faible, surtout pour des contraintes faibles et des sphères éloignées. Pour des sphères plus proches $(l/P \ll 3,75)$, nos approximations concernant la forme d'équilibre de la dislocation ne seraient plus valables.

Dans les limites explorées, l'échappement entre trois sphères est donc le mécanisme qui agit effectivement. On voit (Fig. 4) que les points calculés se placent très sensiblement sur des droites (avec peut-être une

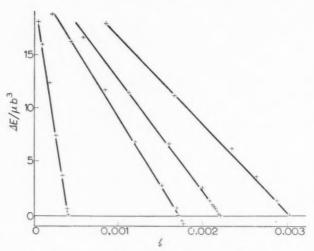


Fig. 4. Energie d'échappement d'une dislocation bloquée par des sphères. De gauche á droite $l/P=25;\ 6,25;\ 5;\ {\rm et}\ 3,75,$

très légère concavité vers le bas). L'équation $\Delta E(\xi)$ prend donc la forme approchée

$$\frac{\Delta E}{\mu b^3} = \frac{P}{b} \propto \left(1 - 2\beta \, \frac{l}{b} \, \xi \right)$$

avec:

1/P		α	β
3.75		1.24	1,10
3,75 5	,	1,16	1,13
6,25	,	1,10	1,16
25		0.99	1.23

Les coefficients α et β diffèrent peu de la valeur 1 qui correspond à la formule simple de notre premier article (réf. 1, page 567).

2. VARIATION DE LA RESISTANCE MECANIQUE AVEC LA TEMPERATURE

2.1. Nous pouvons maintenant estimer la loi de variation en fonction de la température, de la limite élastique d'un métal possédant de telles cavités le long de ses dislocations, et la comparer aux résultats expérimentaux. La vitesse de déformation par traction $d\varepsilon/dt$ d'un métal ayant par em³ N dislocations de longueur L sur lesquelles se sont formées des cavités de rayon P à des distances 2l l'une de l'autre sera:

$$\frac{d\varepsilon}{dt} = \frac{vb}{2l} e^{-AE/kT} \cdot \frac{L}{2l} ND^2nb$$

où ν est la fréquence de vibration atomique, D le diamètre du grain métallique, et n le nombre d'échap-

pements entraînés par un arc qui a quitté sa ligne de cavités:

$$\Delta E = \mu b^2 P \alpha \bigg[1 - \frac{2\beta l \xi}{b} \bigg] = kT \log \frac{n \nu N L D^2 b^2}{(2l)^2 (d\varepsilon/dt)}$$

On en tire:

$$\sigma = \mu \xi = \frac{\mu b}{2\beta l} \left[1 - \frac{kT}{\mu b^2 P \alpha} \log \frac{n \nu b^2 N L D^2}{(2l)^2 (d \varepsilon / d t)} \right]$$

Nous voyons que $\frac{\sigma}{\mu}$ (T) est linéaire, alors qu'un mécanisme de blocage par les nuages de Cottrell donnerait une loi en 1/T. Nous avons également $\sigma = \frac{\mu b}{2\beta l} \simeq \frac{\mu b}{2l}$ pour T=0.

2.2. On peut comparer ces résultats aux propriétés mécaniques

—des métaux contenant des précipités: Jaoul publiera prochainement ses expériences sur un acier inoxydable où le blocage est fourni par des précipités de carbure. (4)

—des métaux irradiés et recuits, mais l'interprétation est rendue délicate par la formation simultanée d'interstitiels et de lacunes.

-des métaux trempés et recuits.

2.3. Kauffman et Meshii⁽⁵⁾ ont récemment étudié la trempe et le recuit des fils d'or. Ils trouvent une valeur à peu près constante de l'augmentation finale de la limite élastique pour des recuits entre 25 et $100^{\circ}\mathrm{C}$. Leur valeur de $450~\mathrm{g/mm^2}$ environ doit correspondre à $\mu b/2\beta l$, contrainte d'échappement au zéro absolu pour des sphères de rayon P espacées de 2l. On trouve ainsi $\beta l \sim 3100b$.

La variation relative de la limite élastique entre $25 \text{ et } 100^{\circ} \text{ est}$

$$\frac{\Delta\sigma}{\sigma} \sim \frac{k\Delta T}{\mu b^2 P} \log \frac{nvb^2 N L D^2}{(2l)^2 \ d\varepsilon/dt}$$

Dans ces expériences $\frac{d\varepsilon}{dt} = 0,00042 \ s^{-1}, D^2 \sim 10^{-7} \mathrm{cm}^2,$ $v \sim 10^{13}, b \sim 2.5 \cdot 10^{-8} \text{ cm}, NL \sim 10^{8} \text{ cm}^{-2}, \Delta T = 75^{\circ}$

d'où
$$\frac{\Delta\sigma}{\sigma} \sim \frac{1.37\cdot 10^{-4}}{\alpha} \left(\frac{40b}{P}\right) \log_{10} \frac{n10^{11}}{4} \sim 0.12 \frac{b}{P}$$

Si nous prenons $\Delta \sigma / \sigma < 5\%$, nous trouvons P >2,5b. Notre modèle est donc tout a fait compatible avec ces expériences: Il suffit que le métal ait ses dislocations fixées par des cavités de rayon supérieur à quelques b et espacées d'environ 6000b.

CONCLUSION

La fixation de dislocations dans un métal par des défauts localisés entraîne une variation linéaire de la limite élastique en fonction de la température. Cette variation s'oppose à la décroissance hyperbolique que l'on constate lorsque les dislocations sont fixées dans toute leur longueur par des nuages d'impuretés.

Je tiens à remercier Monsieur J. Friedel qui m'a suggéré cette étude, et qui en a suivi le développement.

BIBLIOGAPHIE

- P. COULOMB et J. FRIEDEL, Dislocations and Mechanical Properties of Crystals, p. 555. Wiley, New York (1957).
 F. C. FISHER, Trans. Amer. Soc. Metals 47, 451 (1955).
 P. COULOMB, Acta Met. 5, 538 (1957).

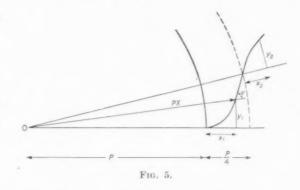
- 4. B. JAOUL, à paraître.
- 5. J. W. Kaufmann et M. Meshii, à paraître.

ANNEXE: FORME D'UNE DISLOCATION ENTRE CAVITES SPHERIQUES

Un arc de dislocation est soumis à sa tension de ligne que nous supposons constante, et à l'interaction avec la cavité sphérique de rayon P. Nous admettons que l'interaction d'un arc élémentaire et de la cavité est la même que celle de la cavité et de la composante de l'are normale au rayon vecteur, l'origine étant placée au centre d'une cavité (Fig. 5). L'équation d'équilibre est:

$$\sigma b \sqrt{1 + y'^2} = \frac{Ty''}{1 + y'^2} + \varphi \sin^2 V$$
 (1)

Nous remplacerons φ par les deux valeurs approchées précédemment calculées (dont l'une présente une



erreur d'impression dans la référence 3)

$$\begin{split} P &< \sqrt{x^2 + y^2} < 1.25P \\ \varphi &\sim \frac{0.3}{\pi} \frac{\mu b^2}{P} \Big(\frac{1}{X - 1} - 0.355 \ln(X - 1) + \ldots \Big) \\ 1.25P &< \sqrt{x^2 + y^2} \qquad \varphi \sim \frac{0.4 \, \mu b^2}{P} \, X^{-4} \end{split}$$

Dans l'enveloppe sphérique entre P et 1.25P, l'équation (1) a alors pour solution

$$y_1 = \frac{Cx_1^2}{2\lambda} - \frac{C^2x_1^3}{6\lambda^2} + \left(1 + \frac{\lambda^2}{CP} + \frac{3}{2}\lambda^2\right)\frac{C^3x_1^4}{12\lambda^5} + \dots$$

$$\text{avec} \quad C = \frac{\sigma\pi}{0.3\,ub} \quad \text{et} \quad \lambda = \frac{\pi T}{0.3\,ub^2}$$

Avec $\sigma = \mu \xi$, $T \sim \mu b^2/2$, nous trouvons que y_1 , au point où nous quittons cette approximation, vaut environ $0.06P^2\xi/b$, et que $y_1' \sim 0.5\xi P/b$ (pour $\xi <$ 1/400 et $P \sim 40b \rightarrow y_1 < 0.25b$ et $y_1' < 0.005$). La courbe reste donc ici très proche du rayon vecteur.

A l'extérieur (Fig. 5) nous partons avec une pente

$${y_2}' = {y_1}' - \frac{y_1}{1.25P} \sim 0.45 \frac{P\xi}{b}$$

L'équation d'équilibre approchée est alors

$$\sigma b \sqrt{1 + {y_2}^{'2}} = T {y_2}^{''} + \frac{0.4 \ \mu b^2}{P} \left(\frac{16}{25}\right) \frac{{y_2}^{'2}}{1 + {y_2}^{'2}}$$

Le rapport du dernier terme au premier vaut au départ $0.032\xi P/b$ et reste toujours inférieur à 0.07 $\xi P/b$; nous pouvons donc négliger le dernier terme et admettre que la courbe cherchée est composée des deux rayons vecteurs de longueur P/4 reliés par l'arc de cercle tangent de rayon $T/\sigma b \sim b/2\xi$.

1959

THERMODYNAMICS OF LIQUID Mg-Bi ALLOYS*

J. J. EGAN†

Thermodynamic studies on liquid Mg-Bi alloys have been carried out using the e.m.f. method. A cell is described, suitable for measuring Mg activities in this system. Values of the excess partial molar free energy, the relative partial molar free energy, entropy, and enthalpy are listed along with the corresponding integral quantities. The results are compared with previous vapor pressure and calorimetric measurements as well as investigations of the phase diagram. Wagner's interpretation in terms of electronic constitution is consistent with the present data.

THERMODYNAMIQUE DES ALLIAGES LIQUIDES Mg-Bi

L'auteur a poursuivi des études thermodynamiques des alliages liquides Mg-Bi en utilisant la méthode de la f.e.m. Il décrit une cellule convenant pour la mesure des activités de Mg dans ce système. Les valeurs de l'énergie libre molaire partielle en excès, de l'énergie libre molaire partielle relative, de l'entropie et de l'enthalpie sont fournies avec les intégrales associées. Ces résultats sont comparés aux mesures calorimétriques et de tensions de vapeur aussi bien qu'aux recherches sur le diagramme d'état. L'interprétation de Wagner sur la base de la constitution électronique est compatible avec les données présentes.

ZUR THERMODYNAMIK FLÜSSIGER Mg-Bi-LEGIERUNGEN

Messungen der EMK wurden zu thermodynamischen Studien über flüssige Mg-Bi-Legierungen benutzt. Es wird eine Zelle beschrieben, mit der man die Aktivität des Mg in diesem System messen kann. Werte für den Überschuss der partiellen molaren freien Energie (gegenüber idealer Mischung), für die relative partielle molare freie Energie, Entropie und Enthalpie sind zusammen mit den entsprechenden integralen Grössen aufgeführt. Die Ergebnisse werden mit früheren Dampfdruckmessungen, kalorimetrischen Messungen und Analysen des Phasendiagramms verglichen. Wagners elektronentheoretische Deutung stimmt mit den hier vorgetragenen Messungen überein.

1. INTRODUCTION

Previous thermodynamic studies of the Mg–Bi system have recently been listed and evaluated by Kubaschewski and Catterall⁽¹⁾. Vapor pressure measurements⁽²⁾ together with calorimetric investigations^(3,4) of the alloys have been carried out by Kubaschewski and co-workers. The system is characterized by large deviations from Raoult's law in Bi-rich alloys with a large change in the chemical potential of Mg near the composition Mg₃Bi₂ as was expected from an examination of the phase diagram⁽⁵⁾ by Hauffe and Wagner⁽⁶⁾.

In this study the e.m.f. method^(7,8) was used to study these alloys. Electrode concentration cells of the following types were operated:

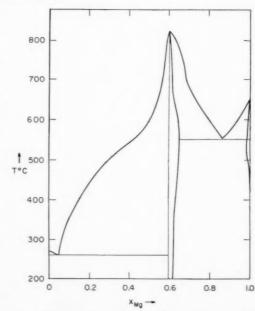
$$Mg(s \text{ or } l) \mid NaCl\text{-}KCl\text{-}MgCl_2 \text{ (Eut.)} \mid Mg\text{-}Bi(l)$$
 (I)

$$\label{eq:mg-Bi(l)_1 Mg-Bi(l)_2} \operatorname{Mg-Bi(l)_1} \big| \operatorname{NaCl-KCl-MgCl_2} \left(\operatorname{Eut.} \right) \big| \operatorname{Mg-Bi(l)_2} \tag{II}$$

$$m Mg(s~or~l)~|~LiCl ext{-}KCl~(Eut.) + 5\% MgCl_2~|~Mg ext{-}Bi(l)$$

where the eutectic mixture of the electrolyte in cells I and II contained 50 mol % MgCl₂; (9) s and l refer to the solid and liquid state, respectively.

Cells of type II were generally employed to measure alloys with high melting points, eliminating the



195

Fig. 1. Phase diagram of the Mg-Bi system according to Grube.

necessity of using highly volatile Mg. Here one of the alloy electrodes would previously be measured in a cell of type I.

Results with alloys of composition $x_{\rm Mg} > 0.70$ were not reproducible when the ternary electrolyte was used. Apparently Mg from Mg-rich alloys dissolved in the salt with a corresponding change in composition.

^{*} This work done under the auspices of the United States Atomic Energy Commission. Received August 15, 1958; in revised form October 3, 1958.

[†] Brookhaven National Laboratory.

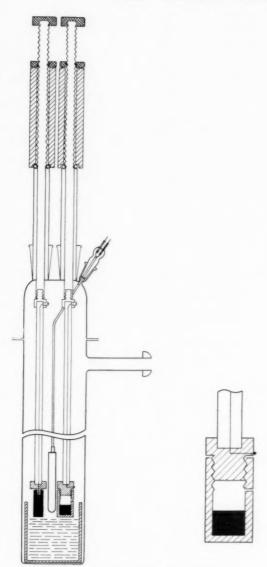


Fig. 2. The cell used to study Mg-Bi alloys

The binary eutectic was therefore employed in this region and found satisfactory.

2. EXPERIMENTAL DETAILS

The cell design used is shown in Fig. 2. The entire assembly fits into a furnace whose temperature is controlled by a recording potentiometer. The fused chloride electrolyte is held in a molybdenum crucible which in turn is protected by a larger Vycor tube. The liquid alloy electrode, shown on the right, is contained in a small molybdenum cup with a hole allowing contact with the fused salt. On the left is shown the pure Mg electrode, in this case a solid. When a liquid Mg electrode is used, an arrangement

similar to the alloy electrode holder is employed, although the hole is on the bottom of the cup since molten Mg floats on the salt. In the center is a chromel-alumel thermocouple protected by a 1-mil tantalum foil cover. Tantalum wires, protected by alundum tubes and welded to the electrode holders are led out of the cell through movable shaft seals at the top of the apparatus. The seals allow the electrodes to be raised and lowered without admitting air into the cell. They are constructed of "tru-bore" tubing and tightly fitting Kovar rods. A wax seal joins the cover of the cell to the Vycor protecting tube for easy assembly. The cell is attached to a vacuum line and a source of purified argon⁽¹⁰⁾ by the side arm.

The molybdenum cups used to contain the alloys were cleaned by inductively heating them inside a fast pumping, high vacuum system at 2000°C. This procedure would clean all surface contamination and degas the crucibles. (11) The alloys were prepared separately before each cell run by heating the elements together under argon in the molybdenum cups. The temperature was kept above the liquidus as shown in Fig. 1 and the heating time ranged from three hours to fifteen minutes depending upon the composition. The more volatile Mg-rich alloys could not be heated as long as the Bi-rich alloys.

Molybdenum proved to be very inert to Mg, the alloys and the molten salts. Since chemical analyses were obtained on many of the alloys, the molybdenum would be machined away after a run and the entire alloy analysed. Data from the measurement were not used if an alloy changed composition by more than 2 mol %.

The dryness and purity conditions of fused salts used as electrolytes in e.m.f. measurements have been emphasized previously.^(7,8,12) Care was therefore exercised in preparing the salts. Briefly, mixtures of the proper composition were dehydrated in a high vacuum over two Pyrex glass frits for a day or longer. They were then gradually (four hours) heated to the melting point and filtered through the frits by applying argon pressure.

The NaCl, KCl and LiCl were reagent grade materials and the MgCl_2 , an anhydrous by-product of Ti production from the Carborundum Company. The purity of the Mg and Bi metals used was 99.98% and 99.99%, respectively.

3. RESULTS

The e.m.f. of cells I, II and III at $700\mathrm{C}^\circ$ are reported in Table 1 for various concentrations of Mg. Here $x_{\mathrm{Mg(1)}}$ and $x_{\mathrm{Mg(2)}}$ represent the mole fraction of Mg in each electrode and the last column gives the

1959

VOI 7

Table 1. Results of e.m.f. measurements on cells of type I II and III. $x_{\text{Mg(1)}}$ and $x_{\text{Mg(2)}}$ represent the composition of each electrode.

XMg(1)	$x_{\mathrm{Mg}(2)}$	$_{ m (Vs)}^{ m e.m.f.}$	Temperatur range (°C)
1	0.10	0.314	490-620
1	0.10	0.308	490-620
	0.10	0.316	490-620
1	0.15	0.291	420-620
	0.23	0.275	490-600
1	0.29	0.261	550-640
1	0.41	0.241	550-630
0.10	0.45	-0.094	600-640
1	0.47	0.220	590-635
0.10	0.49	-0.102	620-660
1	0.50	0.220	650-760
0.30	0.53	-0.066	730-815
0.10	0.55	-0.117	720-780
1	0.55	0.190	720-780
1	0.565	0.170	750-800
1	0.58	0.142	780-810
1	0.58	0.155	800-830
0.33	0.63	-0.191	800-845
0.10	0.65	-0.254	800-850
0.25	0.65	-0.220	790-830
0.85	0.70	0.021	720-780
1	0.75	0.028	680-760
1	0.85	0.013	560-640

temperature range over which the cell was operated. All measurements were made on liquid alloys.

For any one temperature, in the composition range $0.70 < x_{\rm Mg} < 0.55$, the e.m.f. readings would not vary by more than 2 mV throughout the course of a day. This held true with or without temperature cycling. For the other concentrations which were necessarily measured at higher temperatures (see Fig. 1), the reproducibility was not this good, the potentials varying sometimes by as much as 5 mV in the course of several hours. This is presumably due to the high volatility of Mg at these temperatures. In all experiments a period of 1 or 2 hr was allowed for a cell to come to equilibrium after start-up.

Precision between separate runs was better than 3% in the region $0.70 \leqslant x_{\rm Mg} \leqslant 0.55$ and better than 10% with $0.70 > x_{\rm Mg} > 0.55$.

Since the cells were found to be more stable and reproducible under 650°C, measurements were taken below this temperature for the lower melting alloys. The e.m.f's. were then extrapolated to 700°C using the measured temperature coefficients. When solid Mg was used as a reference electrode a small correction was also added for the entropy of fusion of Mg.^(8,12) This procedure, although indirect, was thought to be more accurate than the straightforward one of taking all cell measurements at 700°C.

In the concentration range where the alloys were solid at 700°C, potentials were observed at a higher temperature and the results extrapolated down to

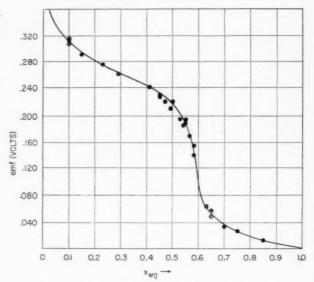


Fig. 3. Experimentally determined e.m.f. values vs. composition of alloys at 700°C.

 700°C ; consequently, values in this range are for hypothetical undercooled alloys.

In no case did extrapolation exceed 100°C. Fig. 3 shows the e.m.f. values referred to liquid Mg as the standard state. The points between $x_{\rm Mg}=0.55$ and $x_{\rm Mg}=0.60$ were obtained by liquid state coulometric titrations using cells of type I in a manner similar to Wagner and Wagner^(13,14). After starting with a liquid alloy whose Mg mole fraction was 0.55, the cell was shorted through a variable resistor, with the current regulated to approximately 20 mA and monitored with an accurate milliammeter. After each electrolysis the e.m.f. did not come to a steady value for several hours due presumably to slow equalization of concentration differences in the alloy. These equilibrium values of e.m.f. are reported in Table 1.

Relative partial molar quantities derived from the cell measurements are listed in Table 2. The relative partial molar free energy of Mg, F_{Mg}^{M} , is obtained by equation (1):

$$F_{M\sigma}^{M} = -n\mathcal{F}E, \tag{1}$$

where \mathscr{F} is the Faraday constant, n the valence of Mg in the salt, and E the e.m.f. Activity and activity coefficients of Mg $(a_{\rm Mg}$ and $f_{\rm Mg})$ follow from (2):

$$F_{\text{Mg}}^{\text{M}} = \text{RT ln } a_{\text{Mg}} = \text{RT ln } f_{\text{Mg}} x_{\text{Mg}}.$$
 (2)

The excess partial molar free energy of Mg was derived from the definition given by equation (3).

$$F_{\mathrm{Mg}}^{\mathrm{E}} \equiv F_{\mathrm{Mg}}^{\mathrm{M}} - RT \ln x_{\mathrm{Mg}}.$$
 (3)

Smoothed values of the excess partial molar free

Table 2. Smoothed values of thermodynamic quantities at 700°C for liquid Mg-Bi alloys.

$x_{\rm Mg}$	$F_{ m Mg}^{ m M}({ m cal})$	$F_{ m Mg}^{ m E}({ m cal})$	$a_{ m Mg}$	$f_{ m Mg}$	$S_{ m Mg}^{ m M}({ m e.u.})$	$H_{ m Mg}^{ m M}({ m cal})$
0.10	-14,400	-9,950	5.6×10^{-4}	5.6×10^{-3}	3.7	-10,950
0.20	-12,930	-9,820	1.2×10^{-3}	6.2×10^{-3}	2.5	-10,600
0.30	-12,050	-9,700	2.0×10^{-3}	6.6×10^{-3}	1.5	-10,630
0.40	-11.160	-9,400	3.1×10^{-3}	7.8×10^{-3}	0.2	-10,970
0.50	-10,000	-8,650	5.6×10^{-3}	1.1×10^{-2}	-6.1	-15,700
0.55	-8,760	-7.610	1.1×10^{-2}	1.9×10^{-3}	-9.0	-17.160
0.65	-2.445	-1.610	2.8×10^{-1}	4.3×10^{-1}	11.0	+6,850
0.70	-1,750	-1.020	4.1×10^{-1}	5.8×10^{-1}	8.0	+4,750
0.80	-920	-490	6.2×10^{-1}	7.7×10^{-1}	3.6	+1,900
0.90	-370	-165	8.3×10^{-1}	9.3×10^{-1}	0.8	+700
1.00	0	0	1	1	0	0

energy and activity of Mg are shown graphically in Figs. 4 and 5.

Fig. 6 shows smoothed values of the relative partial molar entropy of Mg calculated from the temperature coefficients of the cells using equation (4):

$$S_{\mathrm{Mg}}^{\mathrm{M}} = n \mathscr{F} \left(\frac{\partial E}{\partial T} \right)_{P,x_{\mathrm{Mg}}}$$
 (4)

Precision in the region $0.70 \leqslant x_{\rm Mg} \leqslant 0.55$ for $S_{\rm Mg}$ was better than 10 per cent, whereas in the region $0.70 > x_{\rm Mg} > 0.55$ values sometimes varied up to 25 per cent.

The uncertainties introduced into the extrapolated values of e.m.f. and $F_{\rm Mg}^{\rm M}$ by this lack of precision however were relatively small, generally not more than 1 mV (46 cal) except in the concentration range close to ${\rm Mg_3Bi_2}$ where they could reach 5 mV (230 cal). On the other hand the $H_{\rm Mg}^{\rm M}$ values could be effected by as much as 1 kcal in the vicinity of $x_{\rm Mg}=0.60$.

1959

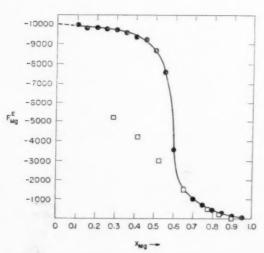


Fig. 4. The excess partial molar free energy of Mg vs. composition at 700°C. The squares represent the data of Vetter and Kubaschewski.

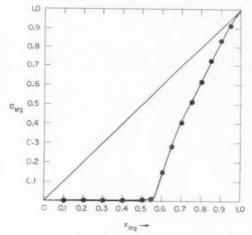


Fig. 5. Activity of Mg vs. composition at 700°C.

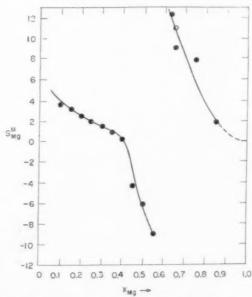
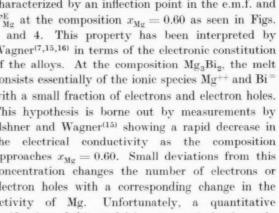


Fig. 6. Relative partial molar entropy of Mg vs. composition.



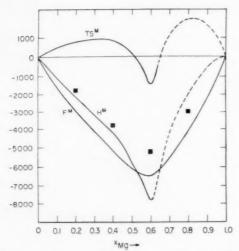


Fig. 7. Relative integral molar quantities of Mg-Bi vs. composition at 700°C. The squares represent the data of Seith and Kubaschewski.

The relative partial molar enthalpy, $H_{\mathrm{M}g}^{\mathrm{M}}$, was calculated by means of equation (5):

$$H_{M\sigma}^{M} = F_{M\sigma}^{M} + TS_{M\sigma}^{M}$$
 (5)

Fig. 7 shows the relative integral molar quantities, $F^{\rm M}$, $H^{\rm M}$, and $TS^{\rm M}$. They were obtained by graphical integrations using equations (6), (7) and (8). Again, the accuracy of the quantities H^{M} and TS^{M} is not expected to be high, especially in the region of high Mg concentration, where all errors are compounded by graphical integration. For this reason the results with $x_{\text{Mg}} > 0.60$ are designated by a dashed line.

$$F^{\text{M}} = (1 - x_{\text{Mg}}) \int_{0}^{x_{\text{Mg}}} \frac{F_{\text{Mg}}^{\text{M}}}{(1 - x_{\text{Mg}})^{2}} dx_{\text{Mg}} + + RT(x_{\text{Mg}} \ln x_{\text{Mg}} + x_{\text{Bi}} \ln x_{\text{Bi}}) \quad (6)$$

$$H^{M} = (1 - x_{Mg}) \int_{0}^{x_{Mg}} \frac{H_{Mg}^{M}}{(1 - x_{Mg})^{2}} dx_{Mg}$$
(7)
$$S^{M} = \frac{H^{M} - F^{M}}{T}.$$
(8)

$$S^{\mathrm{M}} = \frac{H^{\mathrm{M}} - F^{\mathrm{M}}}{T} \,. \tag{8}$$

4. DISCUSSION

Results of vapor pressure measurements by Vetter and Kubaschewski⁽²⁾ using the transportation method are represented by the squares in Fig. 4. The discrepancy between the two sets of data is rather pronounced in Bi-rich alloys which may be an indication that species containing both Mg and Bi atoms exist in the vapor phase over these alloys. The squares in Fig. 7 show values of $H^{\rm M}$ measured calorimetrically by Seith and Kubaschewski. (3) In this case there is a disagreement between data in Mg-rich alloys. However, it may be noticed that the agreement would be quite good if $S^{\mathbf{M}}$ in this work was assumed to be nearly ideal. Further experiments are probably needed on the entropy values of this system.

Calculating F_{Mg}^{M} from the phase diagram using equations given by Hauffe and Wagner (6), one obtains values considerably more negative than those measured. This would indicate that the shape of the liquidus in the vicinity of the maximum is not quite as sharp as shown in Fig. 1.

The thermodynamic behavior of Mg-Bi alloys is characterized by an inflection point in the e.m.f. and $F_{\rm Mg}^{\rm E}$ at the composition $x_{\rm Mg}=0.60$ as seen in Figs. 3 and 4. This property has been interpreted by Wagner^(7,15,16) in terms of the electronic constitution of the alloys. At the composition Mg3Bi2, the melt consists essentially of the ionic species Mg++ and Bi with a small fraction of electrons and electron holes. This hypothesis is borne out by measurements by Ilshner and Wagner⁽¹⁵⁾ showing a rapid decrease in the electrical conductivity as the composition approaches $x_{Mg} = 0.60$. Small deviations from this concentration changes the number of electrons or electron holes with a corresponding change in the activity of Mg. Unfortunately, a quantitative verification of this model is not practical using only three values of the e.m.f. between $0.55 < x_{\rm Mg} < 0.65$.

ACKNOWLEDGMENTS

19

I would like to thank Dr. Richard Wiswall for his support and illuminating discussions during the course of this work. I am also indebted to Dr. Carl Wagner for many helpful suggestions. Mr. John Bracker was invaluable, since he operated a majority of the cells and contributed very much in the way of experimental design.

REFERENCES

- 1. O. Kubaschewski and J. A. Catterall, Thermochemical Data of Alloys. Pergamon Press, London (1956).
- 2. F. VETTER and O. KUBASCHEWSKI, Z. Electrochem. 57, 243 (1953).
- W. SEITH and O. KUBASCHEWSKI, Z. Electrochem. 43, 743 (1937).
- 4. O. Kubaschewski and A. Walter, Z. Electrochem. 45, 630, 732 (1939).
- 5. G. GRUBE, L. MOHR and R. BORNHAK, Z. Electrochem. 40, 143 (1934).
- 6. K. HAUFFE and C. WAGNER, Z. Electrochem. 46, 160 (1940). 7. C. Wagner, Thermodynamics of Alloys. Addison-Wesley,
- Cambridge, Mass. (1952) 8. O. Kubaschewski and E. Evans, Metallurgical Thermo-
- chemistry. Pergamon Press, London (1956). 9. International Critical Tables, Vol. IV, p 81. McGraw-Hill,
- New York (1928). 10. A. SEYBOLT and J. BURKE, Procedures in Experimental
- Metallurgy, Wiley, New York (1953). 11. F. NORTON and A. MARSHALL, Trans. Amer. Inst. Min. (Metall.) Engrs. 156, 351 (1944).
- 12. R. A. ORIANI, J. Electrochem. Soc., 103, 194 (1956).
- 13. C. WAGNER, J. Chem. Phys. 21, 1819 (1953) 14. J. B. WAGNER and C. WAGNER, J. Chem. Phys. 26, 1602
- 15. B. ILSCHNER and C. WAGNER, Acta Met. 6, 712 (1958).
- 16. C. Wagner, private communication.

THE EFFECT OF COLD WORK ON THE ELECTRICAL RESISTIVITY OF COPPER SOLID SOLUTION ALLOYS*

W. R. HIBBARD, Jr.+

Measurements of stress and strain during tensile deformation at 78°K and after subsequent recovery treatments suggest that in solid solution alloys the higher strength is primarily associated with the higher yield stress and the presence of additional or more effective dislocation barriers in the initial structure rather than the more rapid or effective generation of dislocation barriers for a given strain during strain hardening. The characteristics of these dislocation barriers can not be determined from the experiments, but the alloys may contain:

- (1) more dislocations or slower moving dislocations;
- (2) more vacancy-solute atom combinations;
- (3) smaller substructure;
- (4) localized structure effects such as clustering, short range order, etc.

Measurements of resistivity and strain during tensile deformation at 78°K and after subsequent recovery treatments can be interpreted as follows:

- (a) More stable point defects occur in the alloys, i.e. the same number are produced in both copper and the alloys but more remain in the alloys;
- (b) The interaction of the point defects with solute atoms enhances the scattering power of the solute atoms.

L'INFLUENCE DE L'ECROUISSAGE SUR LA RESISTIVITE ELECTRIQUE DES SOLUTIONS SOLIDES A BASE DE CUIVRE

Les mesures de la tension et de la déformation à 78°K et après des restaurations ultérieures suggèrent que la résistance la plus élevée atteinte par des solutions solids est associée essentiellement à la plus haute limite élastique et à la présence de barrières de dislocations additionnelles ou plus efficaces dans la structure initiale plutôt qu'à la génération plus rapide ou plus effective de telles barrières pour une déformation déterminée.

Les caractères de ces barrières ne peuvent pas être déduits de ces expériences mais les alliages peuvent contenir:

- 1) plus de dislocations ou des dislocations plus lentes
- 2) plus de couples lacune-solution
- 3) une sous-structure plus fine

VOL.

1959

4) des effets de structure locale tels que ségrégats, ordre à petite distance, etc.

Les mesures indiquées plus haut peuvent être interprétées comme suit:

 a) des défauts ponctuels plus stables existent dans les alliages, c'est-à-dire bien que le même nombre de ces défauts soient formés dans le cuivre et dans les alliages, un nombre plus grand subsiste dans les alliages
 b) les interactions des défauts ponctuels et des atomes dissous augmentent le facteur de diffusion de ces derniers.

DER EINFLUSS VON KALTVERFORMUNG AUF DEN ELEKTRISCHEN WIDERSTAND VON KUPFERMISCHKRISTALLEN

Messungen von Spannung und Dehnung während einer Zugverformung bei 78°K und nach anschliessenden Erholungsbehandlungen führen zu der Annahme, dass die höhere Festigkeit von Mischkristallen hauptsächlich mit der höheren Fliessspannung und der Anwesenheit von zusätzlichen oder wirkungsvolleren Versetzungshindernissen in der Grundstruktur verknüpft ist und nicht mit der rascheren oder wirkungsvolleren Bildung von Versetzungshindernissen während der Verfestigung. Die Eigenschaften dieser Versetzungshindernisse können nicht aus den Experimenten bestimmt werden; die Legierungen können jedoch enthalten:

- 1) mehr Versetzungen oder solche die sich langsamer bewegen;
- 2) mehr Kombinationen von Leerstellen mit gelösten Atomen;
- 3) kleinere Substruktur;
- 4) lokalisierte Struktureffekte, wie Nahentmischung, Nahordnung usw.

Messungen von Widerstand und Dehnung während einer Zugverformung bei 78°K und nach anschliesenden Erholungsbehandlungen können folgendermassen gedeutet werden:

a) In den Legierungen sind stabilere punktförmige Fehlstellen vorhanden, d.h. sowohl in Kupfer als auch in Legierungen wird dieselbe Anzahl erzeugt, aber in den Legierungen bleiben mehr zurück;
b) die Wechselwirkung von punktförmigen Fehlstellen mit gelösten Atomen erhöht das Streuvermögen der gelösten Atome.

77

1. INTRODUCTION

A considerable volume of literature relating the electrical properties of cold worked metals to the presence of lattice defects has been recently summarized by van Buren. (1) From the recovery kinetics of resistivity induced by cold work at low temperatures, it is possible (within limits of controversy) to identify interstitials, vacancies and dislocations induced in pure metals by cold working. Particularly inviting is the simplified interpretation of Pry and Hennig(2) who associate resistivity increments remaining after recovery at room temperature only with excess dislocations. This interpretation offers a possible approach to the knotty problem of solid solution hardening, recently discussed by the author. (4) Linde⁽⁵⁾ has already applied resistivity measurements to this problem but under conditions of complex deformation (heavy rolling) and uncertain temperature (room temperature and temperature rise induced by rolling).

The solid solution strengthening results from solute atom interactions such as:

- (1) Geometric interactions involving lattice distortion, (6) elastic interaction between solute atoms and dislocations, (7) short range order, (8) long range order (7,9) and substructure size. (10)
- (2) Electrical interactions such as dipoles around dislocations which interact with solute ions causing valency effects. (11)
- (3) Chemical interactions due to structure changes between extended partial dislocations.⁽¹²⁾

All of these structural mechanisms are reactions between solute atoms and dislocations and are related to numbers of dislocations generated by strain and remaining in the structure. The Pry–Hennig⁽²⁾ interpretation of resistivity increments offered a technique for measuring these quantities and thus this investigation was undertaken.

2. EXPERIMENTAL PROCEDURE

Specimens of 0.050 in. diam. wires described in Table 1 (from a previous study⁽¹⁴⁾) were deformed in tension in the Pry–Hennig⁽²⁾ apparatus modified by Pugh⁽¹³⁾ to reduce drift. Electrical resistivity, stress and strain were simultaneously measured at 78°K during straining up to about 0.30 true strain. Then the external stress was removed and specimens were recovered at temperatures of 195°K, 273°K, 298°K, 323°K, 373°K or 423°K for times of 5, 15 and/or 60 min. After each recovery treatment, the resistivity at 78°K was remeasured. Straining was resumed after each series of recovery treatments on a given specimen. Some measurements were made during straining at

 $20^{\circ}\mathrm{K}$. Some recovery treatments were carried out at $473^{\circ}\mathrm{K}$ and $523^{\circ}\mathrm{K}$. Stress, strain and resistivity measurements were also made on specimens strained up to a total of 0.30 true strain in increments of 0.03–0.05 at $78^{\circ}\mathrm{K}$ with each increment followed by five minutes recovery at $298^{\circ}\mathrm{K}$. This latter treatment will be called the Pry–Hennig cycle.

3. RESULTS

The results at 78° K are plotted in Figs. 1–8 and at 20° K in Figs. 9–11. In general, the data from specimen to specimen are reproducible within about 500 lb/in² and $0.006~\mu\Omega$ cm. It should be noted that the alloys have about the same stress–strain curves at each

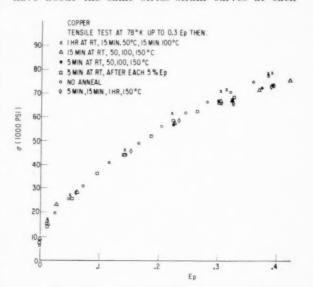


Fig. 1. Stress-strain curves for copper at 78°K.

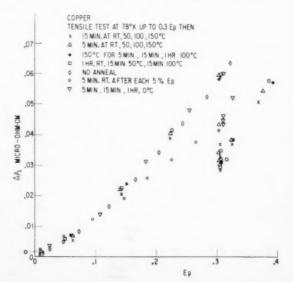


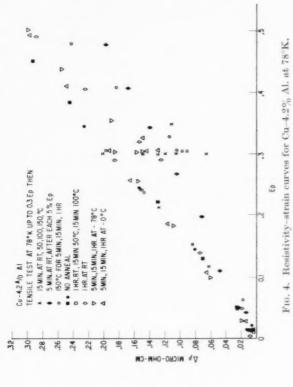
Fig. 2. Resistivity-strain curves for copper at 78°K.

78°K.

Si at

Resistivity-strain curves for Cu-2.7%

9 Fig.

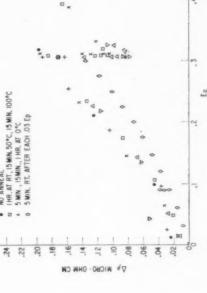


VOL. 7 1959

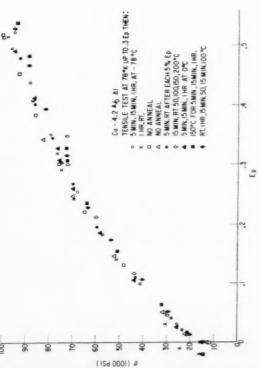
Cu-2.7 A₀Si Tensile Test at 78°K up to 0.3 E_p Then: 15min. at Rt, 50, 100, 150°C 5 min. Rt, 50°C, 100°C, 150°C 1 HR. AT RT, 15 MIN. 50°C, 15 MIN. 100°C 5 MIN., ISMIN., I HR. 150°C NO ANNEAL

28

.26



Stress-strain curves for Cu-2.7% Si at 78°K.





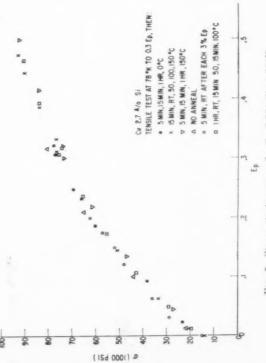


FIG. 5.

COPPER - 8.4 % Zn TENSILE TEST 78°K UP TO .3 Ep THEN: 15 MIN. AT RT, 50, 100, 150, 200, 250°C

.26

5 MIN.AT RT, 50, 100, 150, "C 150°C FOR 5 MIN., 15 MIN., 1 HR. NO ANNEAL I HR RT, 15 MIN., 50°C, 15 MIN., 100°C 1 HR. RT 5 MIN.AT RM. TEMP. AFTER EACH 5% E.p.

5, 15,60 MIN. AT - 78°C

12

8 9

8

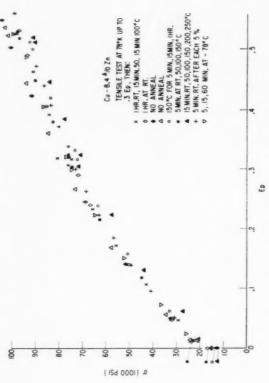


Fig. 8. Stress-strain curves for Cu-8.4% Zn at 78°K.

Fig. 7. Resistivity-strain curves for Cu-8.4% Zn at 78°K.

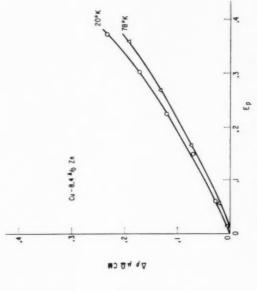


Fig. 10. Resistivity–strain curves for Cu–8.4% Zn at 20°K and $78^{\circ}\mathrm{K}_{\odot}$

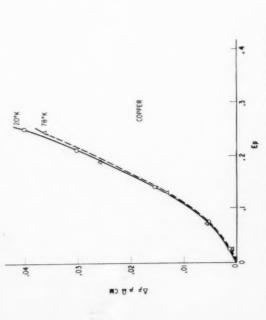


Fig. 9. Resistivity-strain curves for Cu at 20°K and 78°K.

VOI 7 19

Specimen	Heat treatment	Av. diam. Yield strength grain size $(1000 \text{ lb/in}^2 \text{ at } \epsilon = 0.01)$		(Ω en 20°K	$ \begin{array}{c} \rho_0 \\ \times 10^{-7}) \\ 78^{\circ} K \end{array} $	299°K		
		(mm)	20°K	78°K	299°K			
Cu-99.999%	2 hr at 380°C	0.0132	18.1	13.6	11.3	0.0494	1.41	16.4
Cu-8.39 at. % Zn	2 hr at 445°C	0.0125	23.0	18.2	15.8	6.88	8.64	38.5
Cu-2.68 at. % Si	2 hr at 480°C	0.0109	21.0	17.8	14.5	33.1	35.9	101.8
Cu-4.15 at. % Al	2 hr at 470°C	0.0117	22.8	18.0	15.8	15.01	16.41	66.1

temperature. (14) The annealing treatments resulted in the stress recovery up to about 5 per cent and the resistivity recovery up to about 60 per cent. These results are summarized in Table 2. The Pry–Hennig cycle technique resulted in essentially the same resistivity and stress as a comparable single strain and single recovery treatment (e.g. in copper $\Delta \rho = 0.0425$ vs. 0.0432, in Cu–Zn $\Delta \rho = 0.0971$ vs. 0.0962). The resistivity increment was larger for straining at 20°K than at 78°K.

4. DISCUSSION OF RESULTS

4.1. Deformation

1959

Van Buren⁽¹⁾ has shown that resistivity-strain relations can be represented by the general empirical formula

$$\Delta \rho = a \varepsilon^p$$

where a is a constant about 0.1 and p is a constant about 3/2. This type of plot is shown in Fig. 12, where the constants are p = about 5/4 and a is 0.3 for copper and about 0.7 for the alloys. These constants differ slightly from those of van Buren. These graphs are similar in form to $\log \sigma$ vs. $\log \varepsilon$ plots for copper

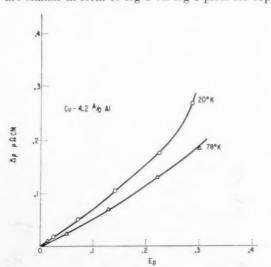


Fig. 11. Resistivity–strain curves for Cu–4.2% Al at 20°K and 78°K.

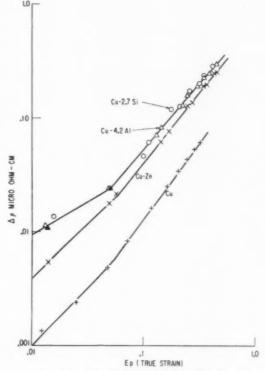


Fig. 12. Log resistivity vs. log strain curves.

alloys including a segment of lower slope (\sim 1) (a=0.07) associated with early strain.*

Fig. 13 indicates that at a given strain the resistivity increment at 78°K in the alloys is about twice that of the pure copper. This difference suggests that if a constant strain results in the generation of a given number of dislocations: (1) more point defects are generated per dislocation in the alloys than in pure copper; (2) about twice as many point defects or dislocations remain in the alloys; or (3) due to

^{*} This segment of lower slope suggests that fewer defects remain or are formed per increment of strain during the early stages of deformation. According to van Buren⁽¹⁾, simple glide should result in p=3/2 for point defects and p=3/4 for line dislocations. For multiple glide, p=2 for point defects. The lower slope in Fig. 12 is about 1, i.e. simple glide with a mixture of both point and line defects and the large slope is 5/4, i.e. multiple glide with a mixture of both point and line defects.

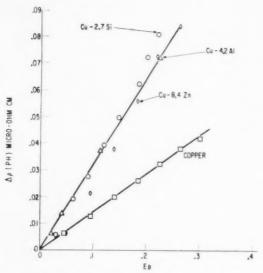


Fig. 13. Pry-Hennig resistivity-strain curves.

segregation or to overlap, the effects of a defect on the electron scattering power⁽⁵⁾ is twice as large in the alloys as compared to pure copper. It should be noted that although the alloys have very different resistivities (3–10 $\mu\Omega$ cm) the resistivity increment is similar at a given strain within about the same limits as the similarity of the stress–strain curve. This suggests that it is $\Delta\rho$ not $\Delta\rho/\rho$ which is related to strain and that it should be similar for a similar stress level in a given type of solid solution alloy.

This latter point is qualitatively confirmed in Fig. 14. In addition, if a given stress level is a measure of the number of sources operating, it also suggests, that in the alloys there are twice as many generated defects

or twice as many stuck, or they are twice as effective in raising the resistivity as compared to pure copper.*

Both sets of data, however, indicate that there is a unique combination of resistivity, stress and strain independent of composition in which any combination of two (e.g. stress and strain) determines the third (e.g. resistivity). The next step is to try to deduce the types of defects from recovery behaviour.

4.2. Recovery

The resistivity recovery data in Table 2 are plotted isothermally in Figs. 15–18 and isochronally in Fig. 19. The various stages of recovery are indicated in Figs. 15–18 in accordance with van Buren's summary⁽¹⁾ and the assumption that the alloys behave similarly to pure copper.

It was thought by using the techniques of Meechan and Brinkman⁽¹⁶⁾ involving temperature—time equivalencies, characteristic activation energies could be calculated and identified. Unfortunately the data are not sufficiently overlapping to avoid the uncertainty of interpolation and extrapolation. The resulting activation energies over the temperature range were much too small, (varying from 0.1 to 0.5 eV) for vacancy mobility (~I eV). The results certainly indicate that the activation energies are higher for the alloys and that there is no simple, single recovery process in this temperature range (195–423°K).

19

^{*} R. H. Pry pointed out that the order of the resistivity increments in Fig. 14 is zinc, silicon and aluminum, which is different from the order of the initial resistivities, i.e. zinc, aluminum and silicon. This difference suggests that the increment is not the result of a simple dislocation solute atom interaction. A plot of $(\Delta\sigma)^2$ as a function of $\Delta\rho$ results in a series of straight lines with increasing slopes in the same order as those in Fig. 14.

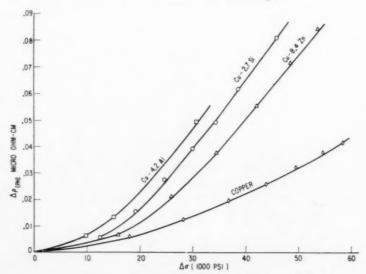


Fig. 14. Pry-Hennig resistivity-stress curves.

Table 2. Per cent recovery $\Delta \rho$ —tensile test at 78°K to 0.3 $\varepsilon \rho$,

Temp. (°K)	Tir	ne (Minutes)	
remp. (K)	5	15	60
	Cu: Δ_{o}	$=0.0591~\mu\Omega$ er	m.
195	26.0	30.5	31.5
273	40.5	42.1	43.1
323	42.3	43.9 ± 0.3	_
373	46.3	50.0 ± 2.1	
423	48.8 ± 0.1	51.2 ± 0.4	51.2
	Cu-8.4 at. % Z	$\Delta n; \ \Delta \rho = 0.171$	3 μΩ er
195	13.2	16.5	17.3
273	25.8	30.9	35.0
323	34.1	37.9 ± 0.7	_
373	41.3	44.4 ± 0.7	_
423	53.9	57.4 ± 0.1	59.2
473	_	59.0	_
523	_	63.5	_
	Cu-4.2 at. %	Al; $\Delta \rho = 0.194$	8 μΩ e
195	16.5	17.5	
273		31.5	32.9
323		40.7 ± 4	-
373	36.2	45.9	-
423	45.4 ± 1.6	47.9	53.5
	Cu-2.7 at. %	Si; $\Delta = 0.193$	l μΩ er
195	17.9	19.7	20.7
273	25.9		30.0
323	37.6	37.1	
373	44.3	42.7	-
423	50.5	50.1	54.0

Room temp. data-% recovery $\Delta \rho$. Time indicates time out of liquid nitrogen. Time at room temp. uncertain, but comparable

VOL.

1959

	(Time Minutes)		
	5	15	60
Cu	30.0	37.0	41.8
Cu-8.4 at. % Zn	31.7	_	34.1
Cu-8.4 at. % Zn Cu-4.2 at. % Al	24.2	26.1	41.9
Cu-2.7 at. % Si	18.4	28.2	33.4

Recovery of stress level estimated from σ - ε curve

	195°K	273°K	298°K	373°K	423°K
Cu	No	No	Some	Yes	Yes
Cu-8.4 at. % Zn	No	No	No	Yes	Yes
Cu-4.2 at. % Al Cu-2.7 at. % Si	No No	No No	No No	Yes Yes	Yes Yes

The data in Table 2 show that the resistivity recovery treatments up to room temperature remove excess defects which have little or no effect on strength, i.e. no dislocation barriers. Since it is estimated (1–3) that the resistivity increment recovered up to room temperature is due to interstitials, excess vacancies and combinations of defects and since annihilation by

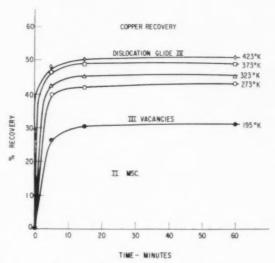


Fig. 15. Isothermal recovery of copper.

climb is unlikely at these temperatures, the residual resistivity not recovered at room temperature is associated with excess dislocations or dislocation barriers.

Using the Pry–Hennig technique⁽²⁾ i.e. a 5 min room temperature anneal after each 0.03– $0.05\varepsilon\rho$ increments, the anneal reduces the resistivity increment but causes little or no stress recovery.* Thus, it can be assumed that the residual resistivity increment is a measure of stuck dislocations or such dislocation barriers which affect strength and that portion which

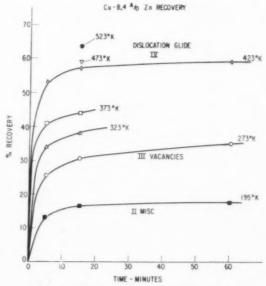


Fig. 16. Isothermal recovery of Cu-8.4% Zn.

^{*} There is a small effect (about 5%) in the case of copper but not in the case of the alloys.

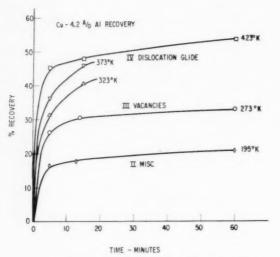


Fig. 17. Isothermal recovery of Cu-4.2% Al.

was removed by the anneal is of little significance to the strength anyway. Analysis on this basis leads to the conclusions that the resistivity increment per increment of strain is a little less than half as large in pure copper (0.125–0.154 $\mu\Omega$ cm) as compared to the alloys (0.270-0.458 $\mu\Omega$ cm). The strain hardening $(\Delta\sigma/\Delta\varepsilon\rho)$ however, is about the same for both the pure copper $(0.98-3.27 \times 10^5 \text{ lb/in}^2)$ and the alloys $(1.12-4.75 \times 10^5 \, \text{lb/in}^2)$ as is shown in Fig. 20, i.e. the stress-strain curves are approximately the same in shape, but displaced by the difference in yield strength and initial strain hardening up to about $0.03 \ \varepsilon$. This suggests that the larger resistivity increment in the alloys shown in Fig. 21 is associated with either differences in electron scattering power and the same number of dislocations stuck during straining* or a larger number of dislocations is generated in the alloys but is no more effective as dislocation barriers than the smaller number generated in pure copper.†

For copper, the cumulative resistivity increment which anneals out during the Pry-Hennig technique is larger than the difference between the resistivity measured on a test run wholly at 78°K and that measured on a Pry–Hennig test. These data are plotted in Fig. 22. This result has been interpreted as indicating that copper saturated with respect to defects removed by the Pry–Hennig treatment. (2) For the alloys, this is not the case. The cumulative resistivity increment which anneals out is less than the difference between the resistivity values for the two methods. This suggests that the alloys do not saturate and have a larger capacity for the type of defects removed by the Pry–Hennig treatment. Alternatively, it can be interpreted from Fig. 22 that room temperature is too low a temperature to remove the point defects from the alloys, in which case the stress and resistivity are not uniquely related.

Apparently those dislocation barriers which are responsible for solid solution strengthening are present either in the initial material, e.g. the sub-structure, or form during the early stages of deformation. Apparently those dislocation barriers which are responsible for strain hardening occur in equal numbers in both pure copper and the alloys since the strain hardening increment is similar in both materials. Intuitively, it is believed that the most important effect is the interaction between dislocations and solute atoms. This interaction can be due to either smaller substructure size (for a given grain size) of the alloys and the strengthening effect of solute atoms interacting at this larger area of substructure boundary, or local structure effects such as short range order or clustering, etc. Either of these effects can be rationalized with the larger $\Delta \rho / \Delta \varepsilon$ but similar $\Delta \sigma / \Delta \varepsilon$ found in the alloys as compared to copper. The extension of the Pry-Hennig technique(2) to alloys did not result in any simple unique interpretation as it did with pure copper using polycrystalline wire.

195

If Mathiesen's rule is valid for the effects involved, then the alloys are weaker than the resistivity would suggest on the basis of either the van Buren⁽¹⁵⁾ or Pry–Hennig⁽²⁾ interpretation. If Mathiesen's rule is not valid, then the influence of the alloy additions is to increase the scattering power of all the defects (solute atoms, vacancies, dislocations, etc.) as a result of cold work.

The resistivity strain measurements during tensile deformation at 78°K and after subsequent recovery treatments can be interpreted⁽³⁾ based on the following information:

- (1) Interstitials move at temperatures below 80°K.
- (2) Solute atoms can trap interstitials.
- (3) Interstitials are produced by moving dislocations.

^{*} J. C. Fisher suggested that if this enhanced scattering power is due to solute atom-dislocation pinning, yielding effects should appear as the Pry-Hennig type of strain cycle progresses. Yielding effects do appear. Alternatively, more point defects may be generated per doslocation in the alloys and remain behind in association with solute atoms to cause a large effect on resistivity but not on strength.

[†] For example, if the important difference is substructure size, the larger numbers of dislocations in the alloys might collect on the sub-boundaries changing their angle from 1° to 5° . This change would effect the resistivity but not the strength. Another possibility suggested by R. W. Guard is that the dislocations in the alloy have a lower average velocity and thus $\Delta\sigma/\Delta\varepsilon$ at a given strain is not a true measure of the relative strain hardening for a given number of dislocations generated since ε is a measure of both the number and velocity of the dislocations.

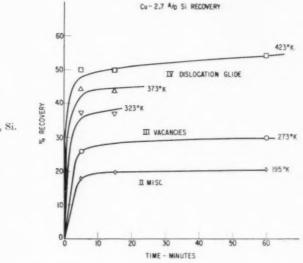


Fig. 18. Isothermal recovery of Cu-2.7% Si.

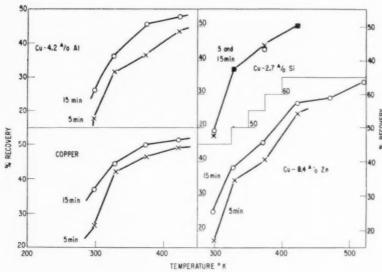
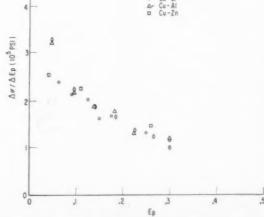


Fig. 19. Isochronal recovery curves,



Fig. 20. Strain hardening-strain curves.



VOL. 7 1959

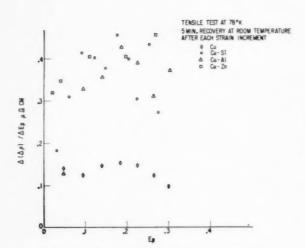


Fig. 21. Resistivity increment-strain curves.

The difference between the resistivity-strain measurements produced by straining at 20°K and 78°K suggest that there are more interstitials formed in the alloys than in pure copper. In addition, vacancies can be trapped by solute atoms. The resulting interpretation is as follows:

- (a) More stable point defects occur in the alloys, i.e. the same numbers are produced in both copper and the alloys but more remain in the alloys.
- (b) The interaction of the point defects with solute atoms enhances the scattering power of the solute atoms.

5. SUMMARY

Measurements of stress and strain during tensile deformation at 78°K and after subsequent recovery treatments suggest that in solid solution alloys the higher strength is primarily associated with the higher yield stress and the presence of additional or more effective dislocation barriers in the initial structure rather than the more rapid or effective generation of dislocation barriers for a given strain during strain hardening. The characteristics of these dislocation barriers can not be determined from the experiments, but the alloys may contain:

- (1) more dislocations or slower moving dislocations;
- (2) more vacancy-solute atom combinations;
- (3) smaller substructure;
- (4) localized structure effects such as clustering. short range order, etc.

Measurements of resistivity and strain during tensile deformation at 78°K and after subsequent recovery treatments can be interpreted as follows:

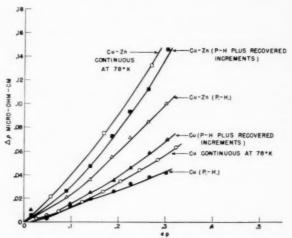


Fig. 22. Accumulative resistivity-strain curves.

- (a) More stable point defects occur in the alloys, i.e. the same number are produced in both copper and the alloys but more remain in the alloys;
- (b) The interaction of the point defects with solute atoms enhances the scattering power of the solute atoms

ACKNOWLEDGMENTS

VOI

195

The experiments were carried out by Helmut Brandhorst with assistance from Robert Berning and John Steadwell and advice from J. W. Pugh and R. H. Pry. The metallography was done by William Roman. Discussions with Drs. R. H. Pry, R. M. Walker, J. W. Corbett, J. C. Fisher, R. W. Schmitt, W. G. Johnston, J. J. Becker, J. R. Low, Jr. and R. W. Guard were most helpful.

REFERENCES

- 1. H. G. VAN BUREN, Philips Res. Rep. 12, 1-45, 190-239,
- R. H. PRY and R. W. HENNIG, Acta Met. 2, 318 (1954).
- R. M. Walker, private communication.
- W. R. Hibbard, Jr., Trans. Amer. Inst. Min. (Metall) Engrs. 1 (1958).
- 5. J. O. LINDE, Appl. Sci. Res. B 4, 73 (1954).
- W. B. Pearson, Canad. J. Phys. 35, 358 (1957).
 A. H. Cottrell, Trans. Amer. Soc. Metals A 46, 131 (1954).
- J. C. FISHER, Acta Met. 2, 9 (1954).
 G. W. Ardley, Acta Met. 3, 525 (1955).
- 10. E. R. Parker and T. H. Hazlett, Trans. Amer. Soc. Metals A 46, 30 (1954).
- A. H. COTTRELL, S. G. HUNTER and F. R. N. NABARRO, Phil. Mag. 44, 1064 (1953).
- 12. H. SUZUKI Sci. Rep. Res. Met., Tohoku Univ., A 4, 455 (1952)
- 13. J. W. Pugh, private communication.
- N. G. AINSLIE, R. W. GUARD and W. R. HIBBARD, Jr., to be published, Trans. Amer. Inst. Min. (Metall.) Engrs. (1959).
- 15. H. G. VAN BUREN, Acta Met. 1, 464 (1953).
- 16. C. J. MEECHAN and J. A. BRINKMAN, Phys. Rev. 103, 1193 (1956).

THE LATTICE STABILITY OF METALS-I. TITANIUM AND ZIRCONIUM*†

LARRY KAUFMANT

The difference in free energy between the b.c.c. and h.c.p. modifications of titanium and zirconium have been calculated between 0° K and 2000° K by using existing thermodynamic data. These results have been employed to investigate the energetics of the b.c.c. \Rightarrow h.c.p. reactions in the Ti–Zr system and in a series of titanium-base alloy systems. It is found that the chemical driving force for martensitic b.c.c. \Rightarrow h.c.p. reactions in these systems is about 50 cal/mol. This value, compared to 300 cal/mol for iron-base alloys, can be explained by the difference in physical characteristics of martensitic transformations in iron-base and in titanium-base alloys. A method is suggested for estimating M_s vs. composition curves for titanium and zirconium-base systems where such data are presently unavailable.

LA STABILITE RETICULAIRE DES METAUX—I. TITANE ET ZIRCONIUM

La différence d'énergie libre entre les variétés cubique centrée et hexagonale compacte du titane et du zirconium a été calculée entre $0^{\circ} K$ et $2000^{\circ} K$ sur la base des données thermodynamiques existantes, Ces résultats ont été utilisés pour étudier les caractères énergétiques des transformations c.c. \Rightarrow hex. dans le système Ti–Zn et dans une série d'alliages à base de titane. L'auteur a trouvé que l'énergie nécessaire pour les transformations martensitiques e.c. \rightarrow hex. est d'environ 50 cal/mole dans ces systèmes. Comparée à 300 cal/mole pour les alliages à base de fer, cette valeur peut être expliquée par la différence des caractéristiques physiques des transformations martensitiques dans les alliages à base de fer et à base de titane. L'auteur suggère une méthode pour prévoir M_8 en jet des courbes de composition pour les systèmes à base de titane et de zirconium, pour lesquels ces données étaient inconnues.

DIE STABILITÄT VON METALLGITTERN—I. TITAN UND ZIRKON

Mit Hilfe von vorhandenen thermodynamischen Daten wurden die Unterschiede der freien Energie zwischen den kubisch raumzentrierten und den hexagonal dichtest gepackten Modifikationen von Titan und Zirkon im Temperaturbereich von $0^\circ \mathrm{K}$ bis $2000^\circ \mathrm{K}$ berechnet. Diese Ergebnisse wurden verwendet zur Untersuchung der Energieverhältnisse bei der Umwandlung kubisch raumzentriert \rightleftharpoons hexagonal dichtest gepackt im Ti–Zr-System und in einer Reihe von Legierungssystemen auf Titanbasis. Es ergab sich, dass die chemische treibende Kraft für die martensitischen Umwandlungen kubisch raumzentriert \rightarrow hexagonal dichtest gepackt in diesem System etwa 50 cal/Mol beträgt. Dieser Wert, dem in den Systemen auf Eisenbasis 300 cal/mol entsprechen, kann durch den Unterschied im physikalischen Charakter der Martensitumwandlungen bei Eisen- und bei Titanlegierungen erklärt werden. Es wird eine Methode vorgeschlagen, um die Abhängigkeit des M_{S} -Punktes von der Zusammensetzung von Titan- und Zirkonlegierungen in solchen Fällen abzuschätzen, bei denen diese Daten zur Zeit nicht vorliegen.

1. INTRODUCTION

The relative stability of atomic configurations (such as f.c.e., b.c.c. and h.c.p. structures) in metals and alloys is a fundamental aspect of metal physics and technology. A satisfactory understanding of this problem could have widespread applicability in both theoretical and practical areas of solid state science. Unfortunately, many inherent difficulties arise in the first-principle calculations of cohesive energies of metals. (1) Such calculations, based on quantum mechanics, do not have sufficient accuracy to distinguish between various polymorphic forms of a metal; in fact, differences in atomic configuration are usually neglected, (2) and at present, there is little hope of predicting the relative stability of different lattices in this way.

On the other hand, a realistic approach to the problem can be made through the interplay of

thermodynamics and physical phenomena. In certain cases the difference in free energy, $\Delta F_A^{\alpha \to \beta}(T)$ between two polymorphs α and β of a pure metal A can be deduced as a function of temperature, from the observable physical properties of the metal. The value of this function at 0°K is the difference in cohesive energy between the two lattices being compared. In addition, as it will be shown, $\Delta F_A^{\alpha \to \beta}(T)$ is of importance in predicting the temperature and composition ranges where the α or β structures are stable in alloy systems containing element A. Furthermore, data concerning $\Delta F_{\Lambda}^{\alpha \to \beta}(T)$ are necessary for interpreting certain types of activity measurements. To demonstrate the importance of this kind of data in solid state thermodynamics it is instructive to review the thermodynamics of alloy phases in a purely formal way.

Consider an alloy system A–B in which x represents the atomic fraction of element B. Suppose that there are two phases, α and β , which exist in this system. The free energy of the α phase, F^{α} , and the free energy

^{*} Received October 17, 1958.

 $[\]dagger$ This work has been sponsored by the Office of Naval Research, Washington, D.C.

^{*} Manufacturing Laboratories, Inc., Cambridge, Mass.

of the β phase, F^{β} , may be described at a temperature T by equations (1) and (2)

$$\begin{split} F^{\mathrm{x}} &= (1-x) F_{\mathrm{A}}{}^{\mathrm{x}} + x F_{\mathrm{B}}{}^{\mathrm{x}} + F_{\mathrm{E}}{}^{\mathrm{x}} \\ &\quad + R T (x \ln x + (1-x) \ln (1-x)) \quad (1) \\ F^{\beta} &= (1-x) F_{\mathrm{A}}{}^{\beta} + x F_{\mathrm{B}}{}^{\beta} + F_{\mathrm{E}}{}^{\beta} \\ &\quad + R T (x \ln x + (1-x) \ln (1-x)) \quad (2) \end{split}$$

In equations (1) and (2) $F_A{}^{\alpha}$ and $F_A{}^{\beta}$ are the free energies of the α and β modifications of element A, while $F_B{}^{\alpha}$ and $F_B{}^{\beta}$ are the free energies of the α and β modifications of element B. The excess free energies of mixing of the α and β phases in the alloy system A–B are represented by $F_E{}^{\alpha}$ and $F_E{}^{\beta}$. In equations (1) and (2) $F_A{}^{\alpha}$, $F_A{}^{\beta}$, $F_B{}^{\alpha}$ and $F_B{}^{\beta}$ are functions of temperature, while $F_E{}^{\alpha}$ and $F_E{}^{\beta}$ are functions of temperature and composition.

The partial molar free energies of A and B in an alloy containing x atomic fractions of B are \overline{F}_A and \overline{F}_B , respectively. These quantities are defined as follows:

$$\bar{F}_{\rm A} = F - x \frac{\partial F}{\partial r}$$
 (3)

$$\bar{F}_{\mathrm{B}} = F + (1 - x) \frac{\partial F}{\partial x}$$
 (4)

If, at a temperature T, there exists a two phase $\alpha + \beta$ field bounded by compositions x_{α} and x_{β} , then equilibrium requirements dictate that for the particular values of T, x_{α} and x_{β}

$$\left. \bar{F}_{\mathbf{A}}^{\alpha} \right|_{x_{\alpha}} = \left. \bar{F}_{\mathbf{A}}^{\beta} \right|_{x_{\beta}} \tag{5}$$

$$\left. F_{\mathrm{B}}^{\alpha} \right|_{x_{\alpha}} = \left. F_{\mathrm{B}}^{\beta} \right|_{x_{\beta}}$$
 (6)

Equations (5) and (6) are the equivalent of the rule of common tangents and describe mathematically the condition of equilibration of the partial molar free energies (or chemical potentials) in a system at equilibrium. Equations (1–6) yield:

$$\Delta F_{\rm A}^{\alpha \to \beta} + RT \ln \frac{1 - x_{\beta}}{1 - x_{\alpha}} = \left(F_{\rm E}{}^{\alpha} - x \frac{\partial F_{\rm E}{}^{\alpha}}{\partial x} \right)_{x_{\beta}} - \left(F_{\rm E}{}^{\beta} - x \frac{\partial F_{\rm E}{}^{\beta}}{\partial x} \right)_{x_{\beta}}$$
(7)

$$\Delta F_{\rm B}^{\alpha \to \beta} + RT \ln \frac{x_{\beta}}{x_{\alpha}} = \left(F_{\rm E}^{\alpha} + (1-x) \frac{\partial F_{\rm E}^{\alpha}}{\partial x} \right)_{x_{\alpha}} - \left(F_{\rm E}^{\beta} + (1-x) \frac{\partial F_{\rm E}^{\beta}}{\partial x} \right)_{x_{\beta}}$$
(8)

as the condition for equilibrium. Equations (7) and (8) show directly how the difference in free energies

between the α and β modifications of elements A and B contribute to the final values of x_{α} and x_{β} at a temperature T and thereby lead to the establishment of the equilibrium diagram.

The chemical activity, $a_{\rm A}$, of component A can be defined in terms of the partial molar free energy of element A if a standard state or reference state for the activity measurement is chosen. By definition, the activity of element in the α phase, relative to pure ${\bf A}^{\alpha}$, is given by equation (9)

$$RT \ln a_{\Lambda}{}^{\alpha}_{ \alpha} = \bar{F}_{\Lambda}{}^{\alpha} - F_{\Lambda}{}^{\alpha} \tag{9}$$

If the reference state for the measurement is pure \mathbf{A}^{β} then

$$RT \ln a_{\text{A}}^{\alpha} \Big|_{\text{A}^{\beta}} = \overline{F}_{\text{A}}^{\alpha} - F_{\text{A}}^{\beta} \tag{10}$$

VOI

195

Similar expressions can be deduced for the activity of element A in the β phase relative to pure A^{α} and pure A^{β} . Now consider a temperature T in the A–B system where α and β phase fields exist, and where the stable modification of A is the α phase. Activity measurements of A in the α phase (relative to pure A^{α}) as a function of composition will yield direct information concerning the solution properties of α A–B alloys since

$$RT \ln a_{\text{A}}^{\alpha} \Big|_{\text{A}^{\alpha}} = F_{\text{A}}^{\alpha} - F_{\text{A}}^{\alpha} = RT \ln (1 - x) + \left(F_{\text{E}}^{\alpha} - x \frac{\partial F_{\text{E}}^{\alpha}}{\partial x} \right)$$
 (11)

It is evident that measurements of $a_{\rm A}{}^{\alpha}|_{{\rm A}^{\alpha}}$ as a function of composition will yield information concerning the compositional dependence of $\left(F_{\rm E}{}^{\alpha}-x\frac{\partial F_{\rm E}{}^{\alpha}}{\partial x}\right)$ from which it may be possible to deduce $F_{\rm E}{}^{\alpha}$ by integration. However, suppose that the activity of element A in the β phase is also measured as a function of composition. In this case, the reference state is pure ${\rm A}^{\alpha}$. Hence, the measurements yield data concerning

$$\begin{split} RT \ln a_{\Lambda}{}^{\beta}\Big|_{\Lambda^{\alpha}} &= \left. F_{\Lambda}{}^{\beta} - F_{\Lambda}{}^{\alpha} = RT \ln \left(1 - x \right) \right. \\ &+ \left. \left(F_{E}{}^{\beta} - x \frac{\partial F_{E}{}^{\beta}}{\partial x} \right) + \Delta F_{\Lambda}^{\alpha \to \beta} \right. \end{aligned} \tag{12}$$

In this case, the measurement of $a_{\Lambda}{}^{\beta}_{\Lambda}{}^{\alpha}$ as a function of composition does not yield unambiguous information concerning $F_{\rm E}{}^{\beta}$, unless $\Delta F_{\Lambda}^{\alpha \to \beta}$ is known at the temperature in question. There are many examples of the measurements described by equation (12) in the literature. For example, $a_{\rm Zn}{}^{\alpha}_{\rm Zn}{}^{\gamma}$, the activity of zinc in the α (f.c.c.) phase of the CuZn and AgZn

systems relative to η (h.c.p.) Zn has been measured; $a_{\text{Cu}}^{\beta}|_{\text{Cu}^{\alpha}}$, the activity of copper in the β (b.c.c.) phase of the CuZn system relative to α (f.c.c.) Cu has been determined; $a_{\text{Al}^{\alpha}}|_{\text{Al}^{\gamma}}$, the activity of aluminum in the α (b.c.c.) phase of the FeAl system relative to pure γ (f.c.c.) Al has been measured α and so on. These are a few examples of cases where the activity measurements cannot yield direct information concerning the solution free energies of the phases in question because the differences in free energy between h.c.p. and f.c.c. Zn, b.c.c. and f.c.c. Cu and b.c.c. and f.c.c. Al are not known. There are other instances where knowledge of the relative stability of various atomic configurations of the elements would be invaluable in interpreting activity data.

In addition to the equilibrium situations described above, there is another class of solid-state transformations which can be understood only if $\Delta F_{\Lambda}^{\alpha\to\beta}(T)$ data are available. Martensitic or diffusionless transformations are the alloy analogues of polymorphism in pure metals, and occur when the atomic configuration changes abruptly on cooling and heating. However, these reactions sometimes exhibit large degrees of supercooling and superheating, and hence, do not normally occur at the temperature where the free energy difference is zero. From equations (1) and (2) the chemical driving force for a martensitic $\beta\to\alpha'$ reaction which occurs during cooling in the A–B system is given by⁽⁵⁾

$$\Delta F^{\alpha'\to\beta} = (1-x)\Delta F_{\rm A}^{\alpha\to\beta} + x\Delta F_{\rm B}^{\alpha\to\beta} + \Delta F_{\rm E}^{\alpha\to\beta} \quad (13)$$

For a given alloy of composition x there exists a temperature T_0 at which $\Delta F^{\alpha' \to \beta} = 0$. The M_s temperature at which the $\beta \rightarrow \alpha'$ reaction begins on cooling lies below T_0 . The value of $\Delta F^{\alpha' \to \beta}$ at M_8 represents the chemical driving force for the initiation of the reaction. Although the exact value of $\Delta F^{lpha'
ightarrow eta}_{M_8}$ depends upon strain and surface energy factors characteristic of the martensitic reaction in question, the temperature range of transformation depends largely on the temperature and composition dependence of $\Delta F^{\alpha' \to \beta}$. In turn, $\Delta F^{\alpha' \to \beta}$ is directly related (equation 13) to the relative stability of elements A and B in the α and β modifications. The f.c.c. \rightarrow b.c.c. reactions in Fe-Ni and Fe-Mn alloys, as well as the b.e.c. → h.c.p. reactions in titanium-base alloys are prime examples of these structural transformations.

Another application of martensitic thermodynamics is the calculation of the enthalpy change attending martensitic transformations. (5) If $\Delta F^{\alpha' \to \beta}$ is known as a function of temperature and composition then the

enthalpy difference $\Delta H^{\alpha' \to \beta}$ can be calculated directly.

$$\Delta H^{\alpha' \to \beta} = \Delta F^{\alpha' \to \beta} - T \frac{\partial \Delta F^{\alpha' \to \beta}}{\partial T}$$
 (14)

The calculated enthalpy changes can be compared directly with measured heats of reaction. Such a comparison has been carried out for reactions which take place in Fe–Ni alloys with satisfactory results.⁽⁶⁾

These considerations clearly indicate the value of information concerning the relative stability of various atomic configurations of pure elements to the interpretation and prediction of phase transformations in metallic systems. It is a well known fact that the difference in free energy between b.c.c. and f.c.c. iron and f.c.c. and h.c.p. cobalt are important in determining the properties of iron-base and cobalt-base alloys. Similarly, metallurgists are accustomed to view the determination of the heat of fusion of element A^{α} , $\Delta H_{\Lambda}^{A \to L}$, and the melting temperature of A^{α} , $T_{\rm M}(A^{\alpha})$, as sources of information concerning the relative stability of the α and liquid phases of element A in the temperature range near $T_{\rm M}(A^{\alpha})$ i.e.

$$\Delta F_{\rm A}^{\alpha \to L} \approx \frac{\Delta H_{\rm A}^{\alpha \to L}}{T_{\rm M}} \left(T_{\rm M} - T \right) \eqno(15)$$

It is also important to have information concerning the relative stability of atomic configurations even if they do not exist. The mere fact that b.c.c. Ni or f.c.c. V have not been found in nature simply indicates that in nickel the f.c.c. configuration has a lower free energy than the b.c.c. structure between 0°K and its melting point and that the reverse is true for vanadium between 0°K and its melting point. The thermodynamic considerations presented here clearly demonstrate the desirability of having data relating to the relative stability of b.c.c. and f.c.c. structures in nickel, vanadium and other elements over a wide range of temperatures.

Apart from the obvious value of such data in the field of phase transformations, there is another important application of stability information. The current development of the dislocation theory has shown that stacking faults in h.c.p. and f.c.c. metals can account for many of the observed mechanical and physical properties.⁽⁷⁾ The propensity toward fault formation during deformation is dependent upon the stacking-fault energy, and a good deal of effort has been devoted towards deriving stacking-fault energies for various metals and alloys. For the case of Co a very good estimate of the stacking-fault energy can be made because the difference in free energy between the h.c.p. and f.c.c. configurations is known. Similar information for other metals would provide an

VOL.

1959

7

excellent basis for predicting the probability of producing stacking faults during deformation.

In view of the difficulties in making accurate firstprinciple calculations the cohesive energy of various atomic configurations of elements, the problem of obtaining values of $\Delta F_{\rm A}^{\alpha \to \beta}(T)$ seems overwhelming. Recently however Weiss and Tauer (8-10) have suggested an attractive scheme for systematizing the presently known factors which play a role in determining lattice stability. This approach merits consideration since it attempts to formulate $\Delta F_{\rm A}^{\alpha \to \beta}(T)$ in terms of a small number of physically meaningful parameters. In spite of the fact that several approximations are made in this procedure, these approximations are certainly as reliable as the available data for $\Delta F_A^{\alpha \to \beta}(T)$. The chief advantage of this approach is that it permits a formulation of the temperature dependence of $\Delta F_A^{\alpha \to \beta}(T)$ in terms of a number of parameters which may be directly measured or indirectly deduced under certain conditions.

Under these circumstances it seems appropriate to explore the applicability of the Weiss-Tauer formulation to the data available for various elements and alloy systems in an attempt to deduce the relevant values of the stability determining parameters.

2. DEPENDENCE OF THE FREE ENERGY DIFFERENCE $\Delta F_{\rm A}^{\alpha \to \beta}(T)$ ON PHYSICAL PARAMETERS (8–10)

The free energy of the α modification of pure A may be expressed as the sum of a magnetic term $F_A{}^\alpha(\mu)$ and a non-magnetic term $F_A{}^\alpha(\tau)$. For the case of metals which do not exhibit ferromagnetic or antiferromagnetic behavior $F_A{}^\alpha(\mu) \sim 0$ and

$$\begin{split} F_{\text{A}}{}^{\text{a}} &\simeq F_{\text{A}}{}^{\text{a}}(\tau) \simeq H_{\text{A}}{}^{\text{a}}(\tau_0) + F\!\left(\!\frac{\theta_{\text{A}}{}^{\text{a}}}{T}\!\right) \\ &- \frac{10^{-4}R}{2}\!\left\lceil \left(\!\frac{3}{2}\,T - \theta_{\text{A}}{}^{\text{a}}\right)^2 + \frac{3}{4}\,T^2\right\rceil - \frac{\gamma_{\text{A}}{}^{\text{a}}T^2}{2} \end{split} \tag{16}$$

Equation (16) assumes that the non-magnetic specific heat can be represented by a single valued average Debye θ , a constant electronic specific heat coefficient, γ , and an approximate C_p-C_v correction.* On this basis (dropping the sub- and superscripts for convenience)

$$C_p \simeq C_v(\theta/T)[1 + 10^{-4}T] + \gamma T$$
 (17)

 $where^{(11)}$

$$C_v(\theta/T) = 3R \left[\frac{12T^3}{\theta^3} \int_0^{\theta/T} \frac{y^3 dy}{e^y - 1} - \frac{3\theta}{T(e^{\theta/T} - 1)} \right] \ (18)$$

Accurate tables for $C_v(\theta/T)$ and $U(\theta/T)$, the temperature-dependent Debye energy, have been published by Beattie⁽¹²⁾. Recently Marcus⁽¹³⁾ has carried out an accurate calculation of the Debye entropy. These values have been used, together with the $U(\theta/T)$ values previously published⁽¹²⁾ to construct Table 1 which gives the temperature dependent Debye free energy $F(\theta/T)$ as a function of (θ/T) .

The total Debye free energy is equal to $F(\theta/T)$ plus a Debye zero point energy which is equal to $9R\theta/8$. The zero point non-magnetic energy $H_{\Lambda}^{\alpha}(\tau_0)$ is defined as the sum of $9R\theta/8$ plus an additional term, $\varepsilon_{\Lambda}^{\alpha}$, which is a constant, and which arises from electronic and lattice contributions.⁽¹⁴⁾ Hence,

$$H_{\Lambda}{}^{\alpha}(\tau_0) = \varepsilon_{\Lambda}{}^{\alpha} + \frac{9}{8} R \theta_{\Lambda}{}^{\alpha} \tag{19}$$

195

Consequently for elements which do not exhibit ferro or antiferromagnetic properties

$$\Delta F_{\mathbf{A}}^{\mathbf{a} \to \beta}(T) \simeq \Delta H_{\mathbf{A}}^{\mathbf{a} \to \beta}(\tau_{0}) + F(\theta_{\mathbf{A}}^{\beta}/T) - F(\theta_{\mathbf{A}}^{\mathbf{a}}/T)$$
$$-\frac{10^{-4}R}{2} \left[\left(\frac{3}{2} T - \theta_{\mathbf{A}}^{\beta} \right)^{2} - \left(\frac{3}{2} T - \theta_{\mathbf{A}}^{\mathbf{a}} \right)^{2} \right]$$
$$-\frac{T^{2}}{2} \left(\gamma_{\mathbf{A}}^{\beta} - \gamma_{\mathbf{A}}^{\mathbf{a}} \right) \quad (20)$$

* See Appendix

Table 1. Debye free energy function -F/RT = 1/R(S - U/T)

θ/T	0.00	0.01	0.02	0.03	0.04	0.05	0.06	0.07	0.08	0.09
0.00	_	_	_	11.5534	10.7015	10.0433	9.5075	9.0562	8.6667	8.3245
0.10	8.0195	7.7447	7.4947	7.2656	7.0544	6.8584	6.6758	6.5050	6.3445	6.1932
0.20	6.0503	5.9149	5.7863	5.6638	5.5470	5.4354	5.3287	5.2263	5.1280	5.0336
0.30	4.9427	4.8551	4.7706	4.6891	4.6103	4.5340	4.4602	4.3887	4.3194	4.2522
0.40	4.1869	4.1234	4.0618	4.0018	3.9434	3.8866	3.8312	3.7773	3.7247	3.6733
0.50	3.6232	3.5743	3.5265	3.4799	3.4342	3.3896	3.3460	3.3033	3.2615	3.2206
0.60	3.1805	3.1413	3.1028	3.0652	3.0282	2.9920	2.9565	2.9216	2.8874	2.8538
0.70	2.8209	2.7885	2.7568	2.7255	2.6949	2.6647	2.6351	2.6060	2.5774	2.5493
0.80	2.5216	2.4944	2.4676	2.4413	2.4153	2.3898	2.3647	2.3400	2.3157	2.2917
0.90	2.2681	2.2449	2.2220	2.1994	2.1772	2.1553	2.1337	2.1125	2.0915	2.0708
1.00	2.0505	-		-			_			

Equation (20) should provide a suitable description of the temperature dependence of the difference in free energy between the α (h.c.p.) and β (b.c.c.) modifications of titanium and zirconium.

3. THE DIFFERENCE IN FREE ENERGY BETWEEN THE H.C.P. AND B.C.C. PHASES OF TITANIUM AND ZIRCONIUM

In order to express $\Delta F_{\Lambda}^{\alpha \to \beta}(T)$ as an explicit function of T for titanium and zirconium it is necessary to evaluate the following parameters for both elements:

$$\Delta H^{\alpha \to \beta}(\tau_0)$$
, θ^{α} , θ^{β} , γ^{α} and γ^{β} .

The values of γ_{Ti}^{α} and γ_{Zr}^{α} are available from low temperature (i.e. 1°K to 4°K) specific heat measurements. Average values(15) for these quantities are 8.25×10^{-4} and 7.1×10^{-4} cal ${}^{\circ}{
m K}^{-2}$ mol⁻¹, respectively. By using these values together with the available data for C_p^{α} vs. T (15°K to 300°K) for titanium(16) and zirconium(17) it is possible to deduce average values for θ_{Ti}^{α} and θ_{Zr}^{α} . These turn out to be 365°K and 260°K, respectively. In addition specific heat data on C_p^{β} for titanium⁽¹⁸⁾ indicate a value of about 7.5 cal/mol °K (1150°K to 1500°) and a value of C_n^{β} for zirconium⁽¹⁹⁾ of about 7.3 cal/mol °K (1140 to 1400°K). By approximating $C_v \sim 3R$ in this temperature range $\gamma_{Ti}^{\ \beta}$ and $\gamma_{Zr}^{\ \beta}$ can be estimated as 5.7×10^{-4} and 4.4×10^{-4} cal/mol⁻¹ $^{\circ}\text{K}^{-2}$. These considerations leave only $\Delta H^{\alpha \to \beta}(\tau_0)$ and θ^{β} to be evaluated for both elements. These parameters can be deduced since (20,21)

VOL.

1959

$$\begin{split} \Delta F_{\mathrm{Ti}}^{\alpha \to \beta}(T=1155^{\circ}\mathrm{K}) &= 0; \\ \Delta H_{\mathrm{Ti}}^{\alpha \to \beta}(T=1155^{\circ}\mathrm{K}) &= +1050 \; \mathrm{cal/mol} \\ \Delta F_{\mathrm{Zr}}^{\alpha \to \beta}(T=1143^{\circ}\mathrm{K}) &= 0; \\ \Delta H_{\mathrm{Zr}}^{\alpha \to \beta}(T=1143^{\circ}\mathrm{K}) &= +1040 \; \mathrm{cal/mol} \end{split}$$

The resulting values of θ^{β} and $\Delta H^{\alpha \to \beta}(\tau_0)$ are given in Table 2.

The total zero point energy difference $\Delta H^{z \to \beta}(\tau_0)$ is related to the difference in zero point cohesive energy $\Delta \varepsilon^{\alpha \to \beta}$ as follows:

$$\Delta H^{\alpha \to \beta}(\tau_0) = \Delta \varepsilon^{\alpha \to \beta} + \frac{9}{8} R(\theta^{\beta} - \theta^{\alpha}) \qquad (22)$$

Table 2. The thermodynamic parameters of the h.c.p. and b.c.c. phases of titanium and zirconium

6)°K	γ cal mol ⁻¹ $^{\circ}$ K ⁻²	$\Delta H^{\alpha \to \beta} (\tau_0)$ cal/mol	$\Delta arepsilon^{lpha ightarrow eta}$ cal/mol
Tiα Tiβ	365 299	$8.25 imes 10^{-4} \ 5.7 imes 10^{-4}$	+1080	+1227
$Z_{\Gamma^{\beta}}$	260 212	$7.1 \times 10^{-4} \ 4.4 \times 10^{-4}$	+1125	+1233

It is interesting to note that the values of $\Delta \varepsilon^{z \to \beta}$ are almost identical for both titanium and zirconium. This finding is not at all surprising in view of the similarity in electronic structures of these elements. $\Delta F_{\rm Tl}^{\alpha \to \beta}$ and $\Delta F_{\rm Zr}^{\alpha \to \beta}$ can now be calculated as a function of temperature by using the data in Table 2. Table 3 gives the results of these calculations.

Fig. 1 shows $\Delta F_{\mathrm{Tl}}^{\alpha \to \beta}$ between 0°K and 2000°K along with the recent experimental values determined by A. D. McQuillan by means of vapor pressure measurements on the Ti–H system. (20) McQuillan's values of $\Delta F_{\mathrm{Tl}}^{\alpha \to \beta}$ were determined by using equation (7) (where subscript A stands for Ti) and experimentally determining $F_{\mathrm{E}}{}^{\alpha}$ and $F_{\mathrm{E}}{}^{\beta}$ as well as x_{α} and x_{β} for the Ti–H system as a function of temperature. These measurements permit direct calculation of $\Delta F_{\mathrm{Tl}}^{\alpha \to \beta}$. The agreement with the calculated curve is quite satisfactory over the range of temperature where the measurements are available.

It is now possible to estimate the melting temperature of h.c.p. Ti and Zr. The entropy of melting of the b.c.c. phase of Ti and Zr (i.e. $\Delta S_{\mathrm{Ti}}^{\alpha\to L}$ and $\Delta S_{\mathrm{Zr}}^{\alpha\to L}$) may be estimated as $2.3\pm0.4~\mathrm{cal/mol^{-1}}$. The melting temperature $^{(22)}$ of Ti $^{\beta}$ is 1941°K while the melting temperature $^{(23)}$ for Zr $^{\beta}$ is 2125°K. Reference to Table 3 shows that

$$\Delta F_{\text{Ti}}^{\alpha \to \beta} \sim +900 - 0.8T \text{ cal/mol (1500°K to 2000°K)}$$
(23)

and

$$\Delta F_{\rm Zr}^{\alpha \to \beta} \sim +720 - 0.7 T \text{ eal/mol } (1700^{\circ} \text{K to } 2000^{\circ} \text{K})$$
(24)

Table 3. The difference in free energy between the h.c.p. and b.e.e. modifications of titanium and zirconium

$T({}^{\circ}\mathrm{K})$	$\Delta F_{\mathrm{Ti}}^{lpha ightarrow eta}$ cal/mol	$\Delta F_{ m Zr}^{lpha ightarroweta}$ cal/mol
0	+1080	+1125
100	+1015	+1055
200	+940	+965
300	+845	+865
400	+750	+755
500	+650	+645
600	+550	+540
700	+450	+435
800	+350	+330
900	+250	+230
1000	+150	+135
1100	+50	+37
1200	-41	-54
1300	-130	-145
1400	-215	-230
1500	-300	-315
1600	-380	-395
1700	-460	-470
1800	-540	-540
1900	-620	-610
2000	-700	-680

Table 4. The melting temperatures and heats of fusion of h.c.p. and b.c.c. titanium and zirconium

	$T_{\mathrm{M}}(^{\circ}\mathrm{K})$	$\Delta H^{^{2\rightarrow L}}$ cal/mol	$\Delta H^{\beta \to L}$ eal/mol
Tiα Tiβ	$\frac{1730 \pm 30}{1941}$	$+5400 \pm 800$	$+4470 \pm 700$
$Z_{r\beta}$	$\frac{1860 \pm 40}{2125}$	$+5600\pm900$	$+4900\pm850$

furthermore

$$\Delta F_A^{\beta \to L} \simeq \Delta S_A^{\beta \to L} (T_M(A^\beta) - T)$$
 (25)

$$\Delta F_{\Lambda}^{\alpha \to L} = \Delta F_{\Lambda}^{\alpha \to \beta} + \Delta F_{\Lambda}^{\beta \to L} \tag{26}$$

From equations (23–26), estimates can be made of $T_{\rm M}({\rm Zr^z})$, $T_{\rm M}({\rm Ti^z})$, $\Delta H_{\rm Ti}^{z \to L}$ and $\Delta H_{\rm Zr}^{z \to L}$. These values are shown in Table 4. A graphical construction of this procedure is shown for titanium in Fig. 1.

It is instructive to compare the calculated and observed Debye θ and melting points for titanium and zirconium with neighboring elements on the basis of the Lindemann formula⁽²⁴⁾

$$C_{\rm L} = \theta v_{\rm a}^{\frac{1}{3}} \left(\frac{M}{T_{\rm M}}\right)^{\frac{1}{2}} \tag{27}$$

where v_a is the atomic volume and M is the atomic weight. According to the Lindemann formula C_L should be a constant for chemically similar elements having the same structure. Table 5 shows the results of the calculation of C_L for several b.c.c. and closepacked transition elements as well as for Ti and Zr. (In these calculations v_a is in units of Å³ per atom.)

Table 5. Calculation of the Lindemann constant

Element	Structure	θ °K	$C_{\mathbf{L}}$
Ti	b.e.e.	299	122
	h.c.p.	365	159
Zr	b.e.e.	212	126
	h.c.p.	260	164
Co*	f.e.e.	390	161
Ni	f.c.c.	390	159
Cu	f.e.e.	315	154
V	b.e.e.	340	135
Cb	b.c.c.	250	119
Ta	b.e.e.	230	142

* θ (f.e.e.) Co is taken approximately equal to θ (h.e.p.) Co.

Reference to Table 5 shows that the value of $C_{\rm L}$ for the b.c.c. structures of Ti and Zr agree very well with those of neighboring b.c.c. elements, while the values of $C_{\rm L}$ for the h.c.p. structures agree with the values of close-packed transition elements.

4. ENERGETICS OF H.C.P. \rightleftharpoons B.C.C. REACTIONS IN Ti–Zr ALLOYS

Having evaluated $\Delta F_{\mathrm{Ti}}^{z \to \beta}$ and $\Delta F_{\mathrm{Zr}}^{z \to \beta}$ it is now possible to consider the energetics of the h.e.p. \rightleftharpoons b.e.c. reactions in the Ti–Zr system. Fig. 2 shows the Ti–Zr phase diagram⁽²⁵⁾ as well as the position of the M_{s} temperature of Ti–Zr alloys.⁽²⁶⁾

The free energy of the α and β phases of this alloy system can be expressed by substituting Ti for subscript A and Zr for subscript B in equations (1) and (2). In turn, equations (7) and (8) for equilibrium at the phase boundaries can be directly formulated with the same substitutions. Finally, an equation

191

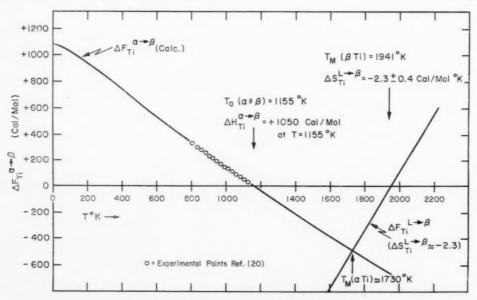


Fig. 1. The difference in free energy between b.c.c. and h.e.p. titanium, $\Delta F_{\mathrm{Tl}}^{z\to\beta}$, as a function of temperature.

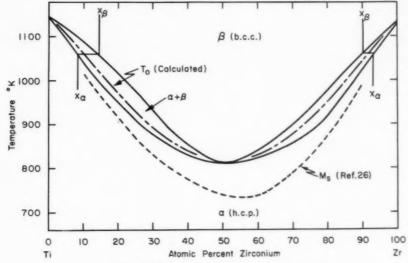


Fig. 2. Titanium-zirconium phase diagram. (25)

giving the difference in free energy, $\Delta F^{\alpha' \to \beta}$, as a function of temperature for an alloy of fixed composition can be derived by using equation (13). At present there is no information available regarding the solution thermodynamics of b.c.c. or h.c.p. Ti–Zr alloys (i.e. F_E^{α} and F_E^{β} are not known for this system). In order to obtain any quantitative information on the energetics of the $\alpha \rightleftharpoons \beta$ reactions in this system certain approximations must be made concerning F_E^{α} and F_E^{β} . Nevertheless it is possible to reach a qualitative conclusion concerning the relative values of F_E^{α} and F_E^{β} between 800°K and 1150°K from general considerations.

Consider equation (13) for x (atomic-fraction of zirconium) = 0.5 at $T=810^{\circ} \mathrm{K}$, which is the minimum point of the $\alpha+\beta$ field. Since $\Delta F^{\alpha'\to\beta}=0$ under these conditions,

$$0 = 0.5(+340) + 0.5(+320) + \Delta F_{\rm E}^{\alpha \to \beta} \text{ cal/mol} \quad (28)$$

or

VOL.

1959

7

$$\Delta F_{\rm E}^{\alpha \to \beta} = F_{\rm E}^{\ \beta} - F_{\rm E}^{\ \alpha} = -330 \ {\rm cal/mol} \eqno(29)$$

Equation (29) implies that the deviations from ideality (for ideal solutions the excess free energy of mixing is zero) in the β solid solution are more negative than the deviations in the α phase within this temperature range. If the reverse were true the phase diagram would exhibit a maximum rather than a minimum for the $\alpha+\beta$ field. If $F_{\rm E}{}^{\alpha}$ were equal to $F_{\rm E}{}^{\beta}$ (for example, suppose that both solutions were ideal) then the $T_0{}^{-}x$ curve, along which $\Delta F^{\alpha'\to\beta}=0$, would be a straight line connecting $T=1155{}^{\circ}{\rm K}, x=0$ and $T=1143{}^{\circ}{\rm K}, x=1$. The fact that the real $T_0{}^{-}x$ curve, which must lie within the two-phase field, is below the

above mentioned straight line indicates that $\Delta F_{\rm E}^{z\to\beta}$ is negative between 800°K and 1150°K.

As mentioned previously, a quantitative approach to the $\alpha \rightleftharpoons \beta$ energetics can be made if approximations for $F_E{}^\alpha$ and $F_E{}^\beta$ are considered. In general the excess free energy of mixing may be approximated by

$$F_E^{\alpha} = x(1-x)(A_0 + A_1x + A_2x^2 + A_3x^3 + \dots)$$
 (30)

Equation (30) represents a power series expansion for $F_{\rm E}^{\ \ z}$ in which all of the A's are temperature dependent. The regular solution model drops all but A_0 , the first term (and sometimes requires that the first term be constant). The subregular model⁽²⁷⁾ drops all but the first and second terms, A_0 and A_1 , and allows both to vary with temperature. The quasi-chemical model⁽²⁸⁾ retains all of the A's but specifies additional equations relating each of the individual A's. If, in the present case, an approximation is made by setting

$$F_{\mathbf{E}}{}^{\alpha} = x(1-x)A \tag{31}$$

$$F_{\mathbf{E}}{}^{\beta} = x(1-x)B \tag{32}$$

where A and B are temperature dependent, then equations (7) and (8) reduce to

$$\Delta F_{\mathrm{Ti}}^{\alpha \to \beta} + RT \ln \frac{1 - x_{\beta}}{1 - x_{\alpha}} = x_{\alpha}^{2}A - x_{\beta}^{2}B \quad (33)$$

and

$$\Delta F_{\rm Zr}^{\alpha \to \beta} + RT \ln \frac{x_{\beta}}{x_{\alpha}} = (1 - x_{\alpha})^2 A - (1 - x_{\beta})^2 B$$
 (34)

or

ToK

1100

1000

900

810

(B-A) cal/mol

191

 x_0

Zr-rich

 x_{β}

Table 6. Application of symmetrical excess free energy of mixing approximations to the $\alpha \rightleftharpoons \beta$ equilibrium in the Ti–Zr system

(B-A) cal/mol

-911

-1003

-1164

-1320

 $(B-A) = \{x_{\alpha}^{2}(1-2x_{\beta}) - x_{\beta}^{2}(1-2x_{\alpha})\}^{-1}$

0.04

0.14

0.26

 $egin{align} & imes \Big[(x_eta^2 - x_lpha^2) \Big(\Delta F_{
m Zr}^{lpha
ightarrow eta} + \, RT \, \ln rac{x_eta}{x_lpha} \Big) \ &+ ((1-x_lpha)^2 - (1-x_eta)^2) \Big(\Delta F_{
m Ti}^{lpha
ightarrow eta} \end{aligned}$

 x_0

Ti-rich

(0.055)

(0.163)

(0.282)

(0.508)

 x_{β}

0.08

0.22

0.33

 $+ RT \ln \frac{1-x_{\beta}}{1-x_{\alpha}}$ (35)

Fortunately, the Ti–Zr diagram offers the possibility of checking the assumptions made in equations (31) and (32). At each temperature between 810°K and 1140°K there are two sets of x_{α} and x_{β} values which are in equilibrium. Fig. 2 shows both sets of x_{α} and x_{β} values at 1060°K. If both sets are substituted into equation (35) for a given T, identical values of (B-A) should result. If greatly differing values result then equations (31) and (32) are not valid, and higher order compositional terms in equation (30) must be retained. Table 6, shows the values of x_{α} and x_{β} substituted into equation (35) together with the results for (B-A). The value for 810°K can be calculated directly from equations (29) (31) and (32) and is equal to $-4 \times 330 = -1320$ cal/mol.

Reference to Table 6 shows that the (B-A) values calculated from Ti-rich and Zr-rich sets are in good agreement, hence the symmetrical assumption of equations (31) and (32) can be considered a good approximation for the Ti–Zr system. Furthermore, the calculated results for (B-A) between $1100^{\circ}\mathrm{K}$ and $810^{\circ}\mathrm{K}$ may be expressed by the following equation

$$(B-A) = -2340 + 1.26T \text{ cal/mol}$$
 (36)

Equation (36) yields -954, -1080, -1206 and -1319 cal/mol, respectively, for T=1100,1000,900 and 810° K in good agreement with the values in Table 6. Consequently equation (13) can be written explicitly for the Ti–Zr system as follows:

$$\begin{split} \Delta F^{\alpha'\to\beta} &= (1-x)\Delta F^{\alpha\to\beta}_{\mathrm{Ti}} + x\Delta F^{\alpha\to\beta}_{\mathrm{Zr}} - x(1-x) \\ &\quad \times (2340-1.26T) \text{ col/mol} \quad (37) \end{split}$$

Equation (37) can be used to compute x_0 , at which

 $\Delta F^{x'\to\beta}=0$ for temperatures between 1100°K and 810°K. The calculated x_0 values which define the $x_0\!\!-\!T$ or $T_0\!\!-\!\!x$ curve are given in Table 6 and are shown in Fig. 2. Equation (37) can also be used to compute $\Delta F^{x'\to\beta}$ as a function of T for various Ti–Zr alloys. The results of such a calculation for a series of alloys are shown in Fig. 3. In Fig. 3 the M_s temperature for each alloy is indicated by a point on the $\Delta F^{x'\to\beta}$ vs. T curve. The chemical driving force, $\Delta F^{x'\to\beta}|_{M_s}$, for the $\beta\to\alpha'$ reaction in Ti–Zr alloys is seen to be about 50 cal/mol.

It is instructive to compare this result with the corresponding value of $\Delta F^{\alpha' \to \gamma}|_{M_8}$ in iron-base alloys. The chemical driving force for diffusionless martensite transformations in iron–nickel and iron–carbon alloys at moderately low temperatures (300°K–600°K) is about 300 cal/mol. (5) The strain and surface energies

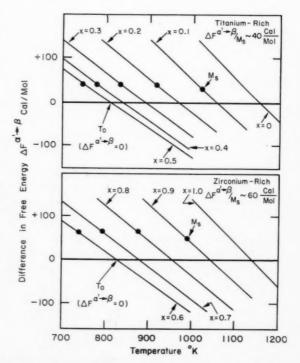


Fig. 3. The chemical driving force for martensitic transformations in titanium-zirconium alloys as a function of composition and temperature.

associated with the transformation are dependent upon the following quantities:⁽⁵⁾

- (1) The shear modulus of the alloy;
- (2) The homogeneous shear strain associated with the transformation:
- (3) The heterogeneous strain or dislocation spacing in the austenite-martensite interface.

The transformation strain energy depends upon (1) and (2), while the surface energy depends upon (1) and (3). Both the strain and surface energy tend to oppose the transformation and the sum of strain and surface energy must be supplied by the chemical driving force in order for the reaction to proceed. The modulus of iron-base alloys in the range 300-600°K, where the (225) habit predominates, is about four times larger than the modulus of titanium between 700-1000°K. The homogeneous strain, (2), for the reaction is (29) 0.22 to 0.28 in titanium alloys and (30) 0.18 to 0.20 in iron-base alloys. Frank's analysis of the (225) austenite-martensite interface in iron-base alloys(31) indicates that the heterogeneous strain can be described by having the interface composed of screw dislocations spaced about 18 Å apart, giving rise to a heterogeneous strain of 1/14. This array of dislocations results in an interfacial energy of about 200 ergs/cm^{2,(5)} In the case of titanium base alloys there has not been a detailed description of the α'/β interface. However, Mac-Kenzie and Bowles(32) have analyzed the crystallography of the transformation. Their analysis suggests that the transformation can be accomplished by a total strain which is close to an invariant plane strain (i.e. a homogeneous strain) which would imply a small heterogeneous strain (or a large dislocation spacing) and hence a small interfacial energy for the α'/β interface in titanium alloys.

1959

The combination of these factors indicate that the "back stress" (i.e. the sum of surface and strain energies⁽⁵⁾) opposing the martensitic reaction in titanium base alloys between 700 and 1000°K is considerably smaller than the back stress opposing the reaction in iron-base alloys in the range 300°K–600°K. This conclusion is in line with the result that the chemical driving force for the martensitic reaction in titanium alloys is smaller than the corresponding driving force for the reaction in iron base alloys (i.e. 50 vs. 300 cal/mol.).

In order to obtain a complete and explicit formulation of the thermodynamics of the Ti–Zr system it is necessary to decompose the sum of (B-A) into individual expressions for B and A. While this decomposition is possible in principle, it does not seem feasible in practice. The present phase diagram does not have

sufficient accuracy to yield four parameters, which would be required to specify A and B explicitly. The present statement of equation (36) for (B-A) requires the evaluation of only two parameters from the phase diagram.

5. EXTENSION TO TITANIUM-RICH ALLOYS

The calculations of $\Delta F_{\mathrm{Ti}}^{x\to\beta}$ carried out in Section 3, and the subsequent calculation of the driving force for martensitic transformations in Ti–Zr alloys in Section 4 makes it feasible to investigate the energetics of the diffusionless reactions which have been observed in titanium base alloys. If it were possible to formulate $\Delta F^{x'\to\beta}$ as an explicit function of x and T for the system Ti–B then T_0 vs. x could be calculated and compared with the M_s vs. x curve. On the basis of the Ti–Zr calculations T_0 should lie about $50^{\circ}\mathrm{C}$ above M_s (since the entropy change attending the h.c.p. \to b.c.c. reactions is about 1 cal/mol $^{\circ}\mathrm{K}$) in moderately dilute titanium base alloys.

The initial problem in making such a calculation lies in the formulation of $\Delta F^{\alpha' \to \beta}(x, T)$ for the Ti-B system in explicit terms. This formulation can be carried out for moderately dilute alloys (i.e. $x \leq 0.15$) for systems containing an expanded β field where the solubility limit of the α phase, x_{α} , is less than 0.07 in the temperature range of interest. The only approximations required in such a calculation is that the compositional dependence of $F_{\rm E}{}^{\alpha}$ and $F_{\rm E}{}^{\beta}$ is given by x(1-x) or that the form of the excess free energies are similar to those assumed in the Ti-Zr analysis of Section 4 (i.e. equations (31) and (32)). Unfortunately this assumption cannot be checked as in the Ti-Zr system. However, if the α and β solutions are moderately dilute $(x_x < 0.07, x < 0.15, x_\beta < 0.20)$ then this assumption may be rationalized by noting that the power series expansion for $F_E^{\ z}$ in terms of the A's in equation (30) may be approximated by the leading term. The resulting approximate formulation of $\Delta F^{\alpha' \to \beta}(x, T)$ is identical to equation (15) of reference 6 which was derived under similar conditions, and is given by equation (38)

$$\Delta F^{\alpha' \to \beta} \sim (1 - x) \Delta F_{\text{Ti}}^{\alpha \to \beta} - x \left\{ RT \ln \frac{x_{\beta}}{x_{\alpha}} - \frac{(x - 2x_{\beta} + x_{\beta}^{2})}{x_{\beta}^{2}} \left(\Delta F_{\text{Ti}}^{\alpha \to \beta} + RT \ln \frac{1 - x_{\beta}}{1 - x_{\alpha}} \right) \right\}$$
(38)

In equation (38) $\Delta F^{\alpha' \to \beta}$ is given approximately for a Ti-B alloy containing x atomic fractions of B at a temperature T where the equilibrium boundary compositions are x_{α} and x_{β} , respectively, subject to the above mentioned limitations. If x_{α} and x_{β} are known

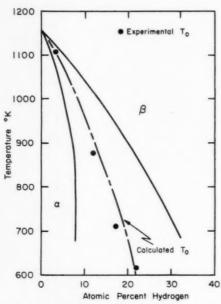


Fig. 4. The titanium-hydrogen system. (23)

as a function of T (i.e. if the equilibrium diagram is available) then $\Delta F^{\alpha' \to \beta}$ can be calculated over a range of x and T and the T_0 –x curve for the Ti–B system can be deduced.

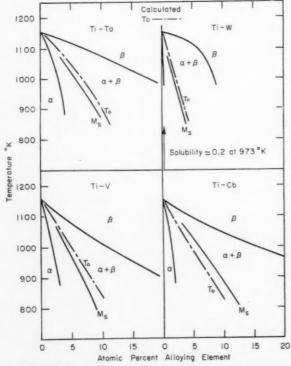


Fig. 5. B.C.C. and h.c.p. phase relations in titanium-base alloys.

In order to check the reliability of the approximate formulation given by equation (38) it is instructive to calculate T_0 vs. x for the Ti–H system in which T_0 has been experimentally determined for several alloys. (33) Fig. 4 shows the results of such a calculation and the agreement between the calculated T_0 –x curve (dash-dotted line) and the experimental points is obviously quite satisfactory. This is true in spite of the fact that the calculations have been carried out slightly outside of the limits of moderately dilute solutions.

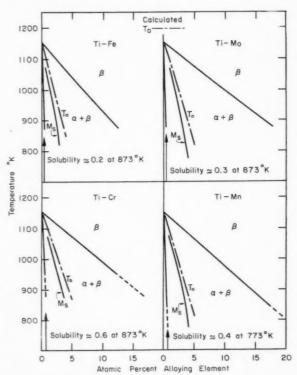


Fig. 6. B.C.C. and h.c.p. phase relations in titanium-base

Figs. 5 and 6 extend equation (38) to eight additional titanium-base alloy systems. In each case, the phase diagram is taken from the recent compilation due to Hansen (34) and the calculated T_0 -x curve (dash-dotted line) is compared with the $M_{\rm S}$ observed by Duwez (26). In seven of the eight cases, T_0 lies slightly above $M_{\rm S}$ with the difference (T_0 - $M_{\rm S}$) being of the order of 50°K. The Ti-Cb system is an interesting example in which the obviously incorrect result that T_0 is below $M_{\rm S}$ is obtained. It is instructive to inquire into the implications of the agreement (or disagreement in the case of Ti-Cb) between the calculated T_0 and the observed $M_{\rm S}$.

In the present calculations the following data or factors are involved:

- (1) the approximation introduced for $F_{\rm E}{}^{\alpha}$ and $F_{\rm E}{}^{\beta}$
- (2) the measured M_8 vs. x curve
- (3) the phase diagram

VOL.

1959

(4) the values for $\Delta F_{\text{Ti}}^{\alpha \to \beta}$.

The assumptions introduced under (1) are approximations at best, however this circumstance is somewhat mitigated by the fact that $\Delta F^{\alpha' \to \beta}$ is being calculated for moderately dilute alloys. Moreover there is no reason to suspect a priori that (1) should be a poorer approximation for Ti–Cb alloys than it is for the other systems shown in Figs. 4, 5 and 6. The M_s -x curves shown in Figs. 5 and 6 were all determined at about the same time by Duwez and should be of comparable accuracy. On the other hand, phase diagrams used in these calculations were determined by various workers, and in this sense are subject to "systematic errors." This leaves the $\Delta F_{\mathrm{Ti}}^{x \to \beta}$ values calculated in Section 3 as a possible source of error.

The values of $\Delta F_{\mathrm{Ti}}^{\alpha \to \beta}$ at temperatures between 700°K and 1155°K depend primarily upon two quantities, T_0 for pure titanium and $\Delta H_{\mathrm{Ti}}^{\alpha \to \beta}(T=1155)$ which was taken equal to +1050 cal/mol. The value of $T_0 = 1155$ °K for pure titanium is fairly well established, however, it must be pointed out that there is some disagreement over the value for $\Delta H_{\text{Ti}}^{\alpha \to \beta}$ (T=1155). This value was communicated to the author by A. D. McQuillan and was derived from recent (1957) measurements on the activity of a and β Ti-H alloys. It has been independently substantiated by Staskiewicz(37) who utilized a calorimetric technique. Recently, however, Backhurst (35) suggested a value of about 850 cal/mol based upon calorimetric measurements. It is natural to inquire how a substitution of 850 cal/mol would effect the results of Sections 3 and 5. This may be seen qualitatively as follows: A twenty per cent reduction in $\Delta H_{\text{Ti}}^{\alpha \to \beta}(1155)$ (i.e. 1050 to 850) would result in a twenty per cent reduction in $\Delta S_{\mathrm{Ti}}^{\alpha \to \beta}$ and a corresponding decrease in the values of $\Delta F_{\mathrm{Ti}}^{\alpha o \beta}$ given in Table 3 for temperatures below 1155°K. In turn, the first term in equation (38) which is positive would be reduced for a fixed value of x. The second term in equation (38) which is negative would change slightly. Consequently the substitution of 850 for 1050 would result in lower values of T_0 for each x than are shown in Figs. 5 and 6. The "degree of lowering" would be sufficient to bring the T_0 -x curve into coincidence with the M_s -x curve for most of the Ti-B systems, and aggravate the present unsatisfactory situation in the Ti-Cb system.

In view of these circumstances, it appears that the present value of $\Delta H_{\rm Tl}^{\alpha \to \beta}(T=1155)=+1050$ cal/mol

is the most satisfactory and that the discrepancy in the Ti-Cb system may be due to inaccuracies in the published phase diagram.

It should be noted that the present approach can be utilized to calculate the latent heat of the martensitic transformations in Ti–B alloys. Unfortunately there are no experimentally determined values of $\Delta H^{\alpha' \to \beta}|_{M_8}$ available for titanium-base alloys. Finally, these calculations may be carried out for Zr-base alloys or additional Ti-base alloys in order to estimate M_8 where such data are not experimentally available.

6. SUMMARY

(1) The necessity for having reliable numerical information concerning the relative stability of the b.c.c., f.c.c. and h.c.p. modifications of metals has been demonstrated. It is shown that stability data are indispensable to a real understanding of two-phase equilibria, martensitic transformations, solution thermodynamics, and stacking fault energies in metallic alloy phases. Although it is now impossible to obtain such information from first principle quantum mechanical calculations, it does seem feasible to approach this problem from a thermodynamic point of view.

(2) The Weiss-Tauer formulation of the free energy difference between two allotropes of a metal in terms of a few physical parameters has been applied to the energetics of the b.c.c. \rightleftharpoons h.c.p. reactions in titanium and zirconium. By using available thermodynamic data, it is possible to estimate the Debye θ of b.c.c. Ti and Zr. In addition, the melting temperatures of the h.c.p. modifications of Ti and Zr have been estimated, as well as the cohesive energy difference between the h.c.p. and b.c.c. modifications of both elements.

It is found that the cohesive energy difference is about 1230 cal/mol for both metals. Furthermore, the Lindemann constant for the b.c.c. phases of Ti and Zr are found to be similar to the Lindemann constant for the neighboring b.c.c. elements V, Cb and Ta. On the other hand, the constants for the h.c.p. forms of Ti and Zr are about 30 per cent larger than the b.c.c. constants and agree with the values obtained for the close-packed metals Cu, Ni and Co.

(3) The differences in free energy between b.c.c. and h.c.p. Ti and Zr have been calculated between 0°K and 2000°K. These values have been used to derive the energetics of the b.c.c. ⇒ h.c.p. reactions in the Ti–Zr system. It is found that the excess free energies of mixing of the b.c.c. and h.c.p. phases of this system can be approximated by symmetrical temperature-dependent functions. The chemical driving force for

19

the initiation of martensitic $\beta \rightarrow \alpha'$ reactions in this system is about 50 cal/mol. The difference between the required chemical driving force for martensitic transformations in titanium-base and iron-base alloys can be explained by considering the relevant physical and crystallographic parameters (relating to the strain and surface energies) associated with each alloy system.

(4) An approximate method has been evolved for computing the difference in free energy between the b.c.e. and h.e.p. phases (in a specific type of titaniumbase system) as a function of temperature, for moderately dilute alloys. This formulation has been used to calculate the T_0 -x curve for a series of alloy systems. In most cases a good correspondence is found between the calculated T_0 -x curve and the experimental M_s -x curve, the latter lying about 50°C below the former. It is suggested that this method be applied to estimate the M_s -x curve for appropriate Ti and Zr base systems where such data are presently unavailable.

ACKNOWLEDGMENTS

The author is indebted to Dr. R. J. Weiss of OMRO. Watertown Arsenal for several stimulating discussions during the course of this work. The continuing interest and encouragement of Dr. S. A. Kulin of the Physical Metallurgy Division of Manufacturing Laboratories, Cambridge, Mass., and of Professor M. Cohen of M.I.T. is gratefully acknowledged.

The author is especially indebted to Professor A. D. McQuillan of the University of Birmingham for making his experimental results on titanium available prior to publication.

APPENDIX

The C_p - C_r correction term in equation (16) can be derived from equation (17) to a first approximation by assuming that $C_v \sim 3RT/\theta$ between 0°K and θ °K and $C_r \sim 3R$ for $T > \theta$. In this case

$$egin{align} 10^{-4} igg[\int_0^T C_v T \, dT - T \! \int_0^T C_v \, dT igg] = \ & - rac{10^{-4} R}{2} igg[\left(rac{3}{2} \, T - heta
ight)^2 + rac{3}{4} \, T^2 igg] \; ext{(A-1)} \end{split}$$

A more accurate approximation can be made by setting(36)

$$C_v \left(\frac{\theta}{T}\right) \sim 3R/1 + \frac{\theta^2}{20T^2}$$
 (A-2)

Table A-1. Approximate C_v - C_v correction to the free energy

T/θ	Correction (A-1) $(\times \frac{1}{2}R10^{-4}\theta^2)$	Correction (A-3 $(\times \frac{1}{2}R10^{-4}\theta^2)$
2	-7	-8.5
3	-19	-21.4
4	-37	-40.2
5	-61	-65.0
6	-91	-96.0

which is a better fit to $C_{\nu}(\theta/T)$. In this case,

$$\begin{split} 10^{-4} \bigg[\int_0^T \!\! C_v T \, dT - T \! \int_0^T \!\! C_v \, dT \bigg] = \\ 10^{-4} \bigg[3R\theta^2 P - T U \bigg(\frac{\theta}{T} \bigg) \bigg] \ \ \text{(A-3)} \end{split}$$

where

$$U\left(\frac{\theta}{T}\right) = \int_{0}^{T} C_{v} dT \tag{A-4}$$

and

$$P = \left\{ \frac{T^2}{2\theta^2} - \frac{1}{40} \ln \left[\frac{20T^2}{\theta^2} + 1 \right] \right\}$$
 (A-5)

Table A-1 contains the results of calculating the C_{p} - C_{p} correction to the free energy by using equations A-1 and A-3.

For $T \approx 6\theta$ the difference between the A-1 and A-3 corrections is about $5R10^{-4}\theta^2/2$ cal/mol. In the present calculation however we are interested in free energy differences so that for the case of titanium for example, the difference between the A-1 and A-3 approximations at $T \approx 6\theta$ (1500 to 1800°K) would be about $5R \times 10^{-4} ((365)^2 - (299)^2)/2 \approx 20$ cal/mol. This is not a very serious difference in view of the crudeness of the approximation introduced in equation (17). Furthermore this difference is probably reduced by evaluating θ_{Ti}^{β} at 1155°K. Under these circumstances A-1 is sufficient for the present purposes.

REFERENCES

- 1. J. C. Slater, Band Theory of Bonding in Metals: Theory of Alloy Phases. A.S.M. Cleveland, Ohio (1955).
- E. P. WIGNER, Solid State Physics, Vol. 1, p. 97. Academic Press, New York (1955).
- 3. O. KUBACHEWSKI and J. CATTERALL, Thermochemical Data of Alloys. Pergamon Press, London (1956).
- S. V. RADCLIFFE, private communication.
 L. KAUFMAN and M. COHEN, Progress in Metal Physics, Vol. 7, p. 165. Pergamon Press, London (1958).
 L. KAUFMAN and M. COHEN, Trans. Amer. Inst. Min.
- (Metall.) Engrs. 206, 1391 (1956).
- 7. A. Seeger, Dislocations and Mechanical Properties of Crystals, p. 243. Wiley, New York (1956).
 8. K. J. Tauer and R. J. Weiss, J. Phys. Chem. Solids 2,
- 237 (1957).

- 9. R. J. Weiss and K. J. Tauer, Phys. Rev. 102, 1490 (1956). 10. K. J. TAUER and R. J. WEISS, J. Phys. Chem. Solids 4, 135
- (1958)
- D. H. Menzel, Fundamental Formulas of Physics, p. 604. 11. Prentice Hall, New York (1955).
- J. BEATTIE, J. Math. Phys. 6, 1, M.I.T. Cambridge (1926).
- 13. P. Marcus, Computational Laboratory, Carnegie Institute of Technology (private communication to R. J. Weiss).
- 14. K. Fuchs, Proc. Roy. Soc. A151, 585 (1935). American Institute of Physics Handbook. McGraw-Hill, New York (1957).
- C. W. Kothen and H. L. Johnston, J. Amer. Chem. Soc. 75, 3101 (1953).
- G. B. SKINNER and H. L. JOHNSTON, J. Amer. Chem. Soc.
- 73, 4549 (1951).18. F. M. Jaeger, E. Rosenbohm and R. Fonteyne, Rec.
- Trav. Chim. Pays-Bas 55, 615 (1936).
 19. J. P. COUGHLIN and E. C. KING, J. Amer. Chem. Soc. 72, 2262 (1950).
- A. D. McQuillan, private communication.
 G. B. Skinner, Ph.D. Thesis, Ohio State University (1951);
 R. Hultgren, Selected Values for the Thermodynamic Properties of Metals and Alloys: University of California, Berkley (1957).
- A. D. McQuillan and M. K. McQuillan, Titanium Butterworths Scientific Publications, London (1956).

- 23. G. L. MILLER, Zirconium. Butterworths Scientific Publications, London (1957).
- N. F. MOTT and H. JONES, The Theory of the Properties of
- Metals and Alloys. Oxford (1936).

 25. E. T. Hayes, A. H. Roberson and O. G. Paasche, Rep. Invest. U.S. Bur. Min. No. 4826 (1951).

 26. P. Duwez, Trans. Amer. Soc. Metals 45, 934 (1953); P.
- Duwez, J. Inst. Met. 80, 525 (1951).
- 27. H. K. HARDY, Acta Met. 1, 203 (1953).
- J. HILLIARD, B. L. AVERBACH and M. COHEN, Acta Met. 2, 621 (1954).
- A. J. WILLIAMS, R. W. CAHN and C. S. BARRETT, Acta Met. 2, 117 (1954).
- A. B. Greninger and A. R. Troiano, *Trans. Amer. Inst. Min. (Metall.) Engrs.* **185**, 590 (1949); E. S. Machlin and M. Cohen, *Ibid.* **191**, 1019 (1951); J. S. Bowles, *Acta Chem. Acta Chem. Acta Chem. Communication of the communicatio* Cryst. 4, 162 (1951).
- 31. F. C. Frank, Acta Met. 1, 15 (1953).
- J. K. MACKENZIE and J. S. BOWLES, Acta Met. 5, 137 (1957)
- 33. A. D. McQuillan, Proc. Roy. Soc. A204, 309 (1950).
- 34. M. Hansen, Constitution of Binary Alloys. McGraw-Hill, New York (1958).
- I. BACKHURST, J. Iron St. Inst. 189, 124 (1958).
- 36. R. J. Weiss, private communication.
- 37. B. Staskiewicz, Ph.D. Thesis, Carnegie Institute of Technology (1953).

UNTERSUCHUNGEN ÜBER EINE NEUE ART DER SEKUNDÄRREKRISTALLISATION IN Fe-3%SI-LEGIERUNGEN*

K. DETERT+

Es wird über die Untersuchungsergebnisse berichtet, die darauf schliessen lassen, dass der bisher nicht beobachtete Fall einer Sekundärrekristallisation aufgetreten ist, bei der das normale Kornwachstum durch die Probendicke abgebremst wird, ehe ein zweidimensionales selektives Kornwachstum einsetzt. Theoretische Überlegungen zeigen, dass die experimentellen Beobachtungen in Einklang gebracht werden können mit der Hypothese, dass die Unterschiede der Oberflächenenergie der verschiedenen Kristallflächen die Ursache für die Wachstumsselektion sind.

INVESTIGATIONS ON A NEW KIND OF SECONDARY RECRYSTALLIZATION IN IRON-3 % SILICON ALLOYS

A case of secondary recrystallization not observed until now is reported, where the sample thickness stops the normal grain growth before two-dimensional selective growth begins. As is concluded from theoretical considerations, the experimental results are consistent with the hypothesis, that the selective growth is due to differences in surface energy of the different crystallographic surfaces.

ÉTUDE D'UN NOUVEAU PHÉNOMÈNE DE RECRISTALLISATION SECONDAIRE D'ALLIAGES FER-3% SILICIUM

L'auteur décrit des essais dans lesquels il apparaît un phénomène de recristallisation secondaire qui n'a pas été mis en évidence jusqu'ici. Cette recristallisation prend naissance où la croissance normale des grains est freinée par l'épaisseur de l'éprouvette.

Des considérations théoriques permettent de conclure que les observations expérimentales concordent avec l'hypothèse que des différences d'énergie superficielle des différents plans cristallins sont la cause de la croissance sélective.

A. EINFÜHRUNG

Schon in einer früheren Arbeit⁽¹⁾ konnte mitgeteilt werden, dass in Eisen–3%Silizium unter gewissen Voraussetzungen eine Würfellage als Folge einer Sekundärrekristallisation entsteht. Die hier berichteten Untersuchungen beschäftigten sich vor allem mit dem Studium der metallphysikalischen Ursachen dieser Sekundärrekristallisation.

Man hat erkannt, dass eine solche sekundäre Rekristallisation dann auftreten kann, wenn das normale Kornwachstum, dass lediglich zu einer Kornvergröberung bei Verlängerung der Glühbehandlung führt, durch irgend einen Mechanismus behindert wird, und eine kleine Minderheit von Körnern davon eine Ausnahme macht. (2) Da diese Minderheit dann unbeschränkt wachsen kann, bildet sie die Keime für die sekundäre Rekristallisation. Auf diese Weise wird das Gefüge wesentlich grobkörniger. Was den hier behandelten Fall so interessant macht, ist die Tatsache, dass dabei die Texturbeziehungen wesentlich verwandelt werden können. (1)

Beck und Mitarbeiter(3) haben schon 1938 gezeigt,

dass infolge der Behinderung des normalen Kornwachstums durch Legierungselemente, die zu Einschlüssen oder Ausscheidungen führen, eine Sekundärrekristallisation hervorgerufen werden kann.

Auch bei Fe-Si lässt sich bei Vorliegen gewisser Verunreinigungen das gleiche Verhalten beobachten. (4,5,6)

Beek und Sperry haben darauf aufmerksam gemacht, dass auch eine starke Vorzugsorientierung das normale Kornwachstum behindert, und dass eine Sekundärrekristallisation unter gewissen Umständen durch diesen Effekt hervorgerufen werden kann. (7) Dunn hat diesen Effekt gerade an Eisen–Silizium näher studiert. (8,9)

Beck und Mitarbeiter haben festgestellt, dass die Probendimension selbst eine Behinderung des normalen Kornwachstums bewirkt. (10) Man hat in Bändern und Drähten beobachtet, dass das normale Kornwachstum abgestoppt wird, wenn der Korndurchmesser die Bandstärke bzw. Drahtdicke erreicht hat. Diese Erscheinung kann auch sehr deutlich bei Blechen aus Eisen-Silizium beobachtet werden. Das Abbrechen des normalen Kornwachstums bei einer bestimmten Korngrösse, die von der Banddicke abhängt, ist deutlich nachzuweisen. Allerdings kann dabei der durchschnittliche Korndurchmesser auch um den

1959

^{*} Received October 6, 1958; revised version December 30,

[†] Vacuumschmelze, Hanau, now at Institut für Metallkunde der Technischen Universität, Berlin-Charlottenburg, Germany.

ACTA METALLURGICA, VOL. 7, SEPTEMBER 1959 589

6 E E

195

Faktor 2–3 grösser werden.⁽¹¹⁾ Der Gedanke liegt nahe, dass auch diese Behinderung des normalen Kornwachstums eine Sekundärrekristallisation auslöst.⁽¹¹⁾ Das ist bisher jedoch nicht beobachtet worden, was vermutlich daran liegt, dass die geometrische Behinderung für alle Körner ohne Ausnahme gilt und so keine Minderheit bleibt, die zu ungehindertem Wachstum fähig ist.

Im folgenden sollen die Untersuchungen zusammengestellt werden, die den Nachweis bringen, dass die Sekundärrekristallisation in Würfellage, über die schon berichtet wurde, diesen bisher nicht beobachteten Fall der Sekundärrekristallisation darstellt.

B. VERSUCHSDURCHFÜHRUNG

Die Untersuchungen der Orientierungszusammenhänge bei dem selektiven Kornwachstum erfolgten in erster Linie mit der optischen Methode, über die an anderer Stelle berichtet wird⁽¹⁾ und die auf Tamman⁽¹²⁾ zurückgeht. Die röntgenographischen Texturuntersuchungen wurden am Texturgoniometer von Siemens & Halske⁽¹³⁾ durchgeführt. Verwendet wurde MoStrahlung mit Zirkonfilter.

Die Schichtliniendiagramme der Polfiguren sind auf die Intensität einer regellosen Probe als Einheit bezogen. (14) In den Fällen, in denen Polfiguren aus optischen Orientierungsbestimmungen entstanden sind, wurde dieselbe Methode verwandt, die schon Dunn (15) bei Untersuchungen an Fe-Si-Legierungen eingeführt hat. Die Genauigkeit der Schichtliniendiagramme liegt bei 10 Prozent für die Intensitätsangaben. (16)

Um Untersuchungen des Kornwachstums durchführen zu können, wurden Probenstreifen verschieden lange Zeiten bei konstanter Glühtemperatur geglüht.

Über die Herstellung der Proben kann ebenfalls an anderer Stelle nachgelesen werden. (1) Um den Einfluss der verschiedenen Verformungsgrade zu bestimmen, wurde nur der letzte Abwalzgrad bei den verschiedenen Bändern der gleichen Charge variiert.

C. EXPERIMENTELLE UNTERSUCHUNGEN

Die Versuche, über die hier berichtet wird, wurden an sehr reinem vacuumgeschmolzenem Material durchgeführt, das keinerlei Anzeichen aufwies, dass eine zweite Phase ausgeschieden wird oder sich sehr dispers verteilte Fremdpartikel im Gefüge befinden (vgl. dazu Abb. 1).

Deshalb darf man wohl von vornherein ausschliessen dass eine Behinderung des normalen Kornwachstums durch fein verteilte Partikel einer zweiten Phase die Ursache für das Zustandekommen der Sekundärrekristallisation abgeben kann.



Abb. 1. Elektronenmikriskopische Aufnahme einer Korngrenze in Fe-3%Si rekristallisiert. $\times 13000$

1. Texturuntersuchungen

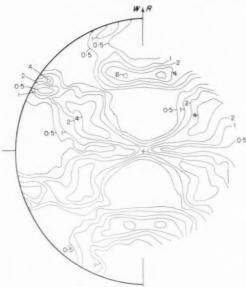
In kaltgewalzten und rekristallisierend geglühten Blechen aus Eisen-Silizium ist das Auftreten von bestimmten Texturen kaum zu vermeiden. Man kann daher, wie sehon an anderer Stelle gezeigt, (1) die hier untersuchte Art der Sekundärrekristallisation zunächst als eine besondere Form des von Dunn studierten selektiven Kornwachstums deuten, das seine Ursache in der Behinderung des normalen Kornwachstums durch Vorzugsorientierung des Gefüges besitzt. Die eingehenden Untersuchungen der Texturverhältnisse konnten jedoch diese Hypothese entkräften.

Um das Verhalten bei verschiedenen Texturen untersuchen zu können, wurde der Endverformungsgrad variiert. Als besonders charakteristisch werden die Verhältnisse bei sehr starker Verformung, mittlerer Verformung und schwacher Verformung dargestellt. In den Abbildungen 2 bis 7 werden die Rekristallisationstexturen sowie diejenigen Texturen, die anschliessend durch Sekundärrekristallisation entstanden sind, als Polfiguren der (200)-Reflexe dargestellt. Bei schwacher Verformung (vgl. Abb. 6) ist im primärrekristallisierten Blech eine Textur gerade angedeutet.

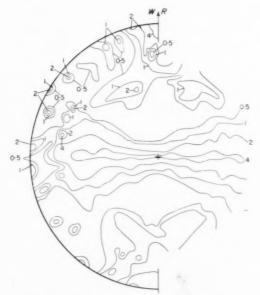
Die ausserordentliche Schärfe der Intensitätsmaxima im Zentrum der Polfiguren von den sekundärrekristallisierten Bändern fällt auf. Sie hat darin ihre Ursache, dass keine Körner mehr im Gefüge vorhanden sind, bei denen eine Würfelfläche stärker als 7° gegen die Bandoberfläche geneigt ist (siehe dazu Abb. 8). Man kann daraus auf eine Wachstumsselektion bei der Sekundärrekristallisation schliessen, die sich auf die Flächenorientierung bezüglich der Bandoberfläche bezieht und dabei nur einen ungewöhnlich engen Winkelbereich zulässt. Weiterhin scheint diese Selektion ganz unabhängig von der Textur zu sein.

Bezüglich der Kantenorientierung deuten sich

Abb. 2–7: (200)-Polfiguren F_3 –3%Si, 0,04 mm.



Авв. 2. 95% verformt, 1100°C geglüht, primär rekristallisiert.



Aвв. 4. 50% verformt, 1100% geglüht, primär rekristallisiert.

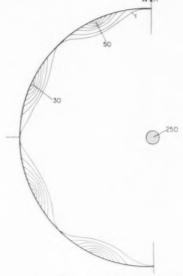
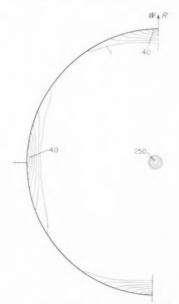


Abb. 3. 95% verformt, 1100°C geglüht, sekundär rekristallisiert.



Aвв. 5. 50% verformt, 1100°C geglüht, sekundär rekristallisiert.

VOL. 7 1959

Aвв. 6. 13% verformt, 1100°C geglüht, primär rekristallisiert (vgl. S. 591).

charakteristische Zusammenhänge zwischen Rekristallisationstextur und anschliessender sekundärer Rekristallisationstextur an. Ob man daraus schon auf eine durch die Gefügeorientierung bedingte Wachstumsselektion schliessen darf, sollten die im folgenden beschriebenen Untersuchungen klären.

Die Untersuchungen hatten, wie schon beschrieben, gezeigt, dass sich die Sekundärrekristallisationstextur dadurch kennzeichnet, dass alle Körner mit einer



Aвв. 7. 13% verformt, 1100°C geglüht, sekundär rekristallisiert. (vgl. 8. 591).

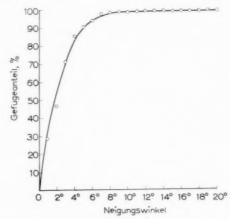


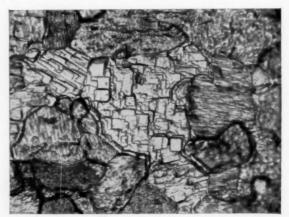
Abb. 8. Neigung der Würfelflächen gegen die Bandoberfläche im sekundär rekristallisierten FeSi. Bandstärke 0,06 mm.

Würfelfläche ihres Gitters parallel zur Oberfläche stehen. Daher ist es relativ einfach, die jenigen Körner im Primärgefüge aufzusuchen, die als Keime in Frage kommen können. Abb. 9 zeigt das Bild des Primärgefüges nach geeigneter Ätzung, in dem sich ein solches Korn, das als Keim in Frage kommt, befindet. Die jenigen Körner, bei denen eine Würfelfläche des Kristallgitters so orientiert ist, dass sie weniger als 5°-7° gegen die Bandoberfläche geneigt ist, zeichnen sich durch quadratische Ätzgruben aus und sind leicht von den übrigen Körnern zu unterscheiden. In der Regel sind es nur sehr wenige Körner, etwa 1-2 prozent der Gesamtzahl, jedoch reicht die Anzahl aus, um die notwendige Zahl der Keime abzugeben, wie aus Tabelle 1 zu ersehen.

VOI

19

Aus der Tabelle geht hervor, dass eine besondere Keimauswahl kaum noch stattfinden kann, da die Zahl der Keime die Zahl der im Sekundärgefüge ausgewachsenen Körner nur wenig übertrifft.



Aвв. 9. Ätzgruben in einem Korn mit Würfellage im primär rekristallisierten Gefüge. $\times 200$.

Tabelle 1. Keimzahl n im Primärgefüge; Kornzahl N im Sekundärgefüge (bezogen auf 1 cm² Oberfläche)

	n	N
sehr starke Verformung	90	25
nittlere Verformung	200	100
schwache Verformung	100	17

Um die Frage der Selektion noch weiter zu klären, wurde die Orientierung der Würfelkanten in diesen Körnern bestimmt. Es ergab sich dabei nun, dass die Würfelkantenorientierung der Keime und Sekundärkörner übereinstimmt. Man erkennt das aus Abb. 10 a-c. Über dem Azimut als Abszisse wurde die relative Häufigkeit aufgetragen, mit der man Gefügekörner bzw. Keime antrifft, deren Würfelkantenrichtungen gerade in einen 1° breiten Winkelbereich fallen.*

Daraus darf man dann schliessen, dass eine Selektion bezüglich der Würfelkantenrichtung bei der Sekundärrekristallisation nicht vorliegt. Die Würfelkantenrorientierung ist schon durch die Orientierung der Keime festgelegt.

Es kann wohl ausgeschlossen werden, dass der von Dunn beschriebene Fall der Sekundärrekristallisation durch Texturbehinderung des normalen Kornwachstums die entscheidende Rolle spielt. Es wäre schwer zu erklären, wie die bei den verschiedenen Verformungsgraden so unterschiedlichen Texturverhältnisse immer die gleiche Selektion bezüglich der Parallelstellung der Würfelfläche des Gitters zur Bandoberfläche hervorrufen können. Geradezu unverständlich wird der Fall für das schwach verformte Material, wo

VOL.

1959

man kaum von einer Rekristallisationstextur sprechen kann. Man kann auch durch geeignete Verformungsbehandlung dafür sorgen, dass schon in der Primärrekristallisationstextur Würfeltextur oder andere Texturen überwiegen, die dafür sorgen, dass eine recht beträchtliche Anzahl von Körnern (mehr als 30 Prozent des Gesamtgefüges) in der Orientierung vorliegen, die zu Keimen prädestiniert sind, weil eine Würfelfläche des Gitters parallel zur Bandoberfläche liegt. Die Tatsache, dass man auch in diesem Falle Sekundärrekristallisation erhalten kann, widerspricht dem von Dunn näher studierten Mechanismus, bei dem die Zahl der Keime 5 Prozent nicht übersteigen darf.

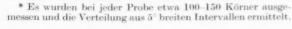
Man kann daraus schliessen, dass eine Selektion stattfindet, die offenbar unabhängig von der Rekristallisationstextur ist und dadurch zustande kommt, dass Kristalle wachstumsbegünstigt sind, bei denen eine Würfelfläche des Kristallgitters parallel zur Bandoberfläche liegt. Schon eine Abweichung von mehr als 5° – 7° genügt, um die Wachstumsbegünstigung auszuschalten.

2. Kristallwachstum

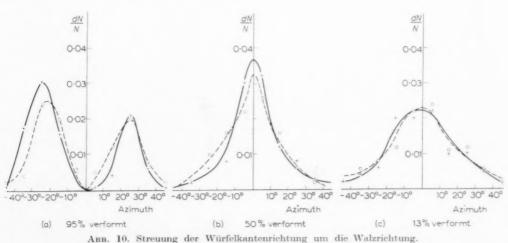
Eingehende Untersuchungen des Kristallwachstums vor dem Einsetzen der Sekundärrekristallisation ergaben, dass man ein ausgeprägtes normales Kornwachstum beobachten kann. Es wurden bei verschiedenen Temperaturen Glühbehandlungen durchgeführt und dabei die mittlere Korngrösse sowie die Häufigkeit der einzelnen Korngrössen bestimmt.

Die Verteilung der Korngrösse entspricht dabei dem Verhalten, wie es bei Aluminium nachgewiesen werden konnte. (11,17,18) Man kann diese Verteilung etwa mit einer Gaussverteilung über dem logarithmisch aufgetragenen Korndurchmesser annähern (vgl.

-Körner im Sekundärgefüge



-Keime im Primärgefüge



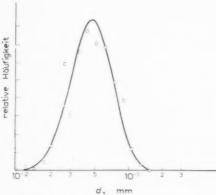


Abb. 11. Verteilung des Korndurchmessers bei 1000°C.

Abb. 11). Auch die Körner, die später als Keime für die Sekundärrekristallisation dienen, gehorchen genau der gleichen Verteilung ihrer Korngrösse.

In Abb. 12 wurde das Wachstum des mittleren Korndurchmessers D in Abhängigkeit von der Glühzeit bei 800°C aufgetragen. Der Korndurchmesser D strebt einem Endwert zu, der nicht überschritten wird. Ein solches Verhalten führt man auf das Vorhandensien einer feinverteilten zweiten Phase zurück, die das Kornwachstum bei einer bestimmten Korngrösse abstoppt. Der Endwert der Korngrösse ist für die einzelnen Glühtemperaturen verschieden. Ein ähnliches Ergebnis hat Wiener⁽¹⁹⁾ aus seinen Untersuchungen am reinen Eisen mitgeteilt. Er hat diese Temperaturabhängigkeit auf die temperaturabhängige Löslichkeit des Kohlenstoffes zurückgeführt. Eine ähnliche Erklärung mag auch für unsere Untersuchungen zutreffen. Der Sprung der Korngrösse zwischen 800° und 950°C kann dann wohl besser durch die Reinigung des Materials vom Kohlenstoff in der Wasserstoffatmosphäre erklärt werden.

Bei Temperaturen oberhalb 950°C findet man in den 0,04 mm starken Proben keine Temperaturabhängigkeit der durch normales Kornwachstum erreichbaren Endkorngrössen. Jetzt wird das Kornwachstum offenbar durch den Einfluss der Banddicke gehemmt. $^{(10)}$ Bei dickeren Bändern liegt diese

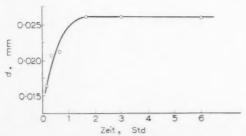


ABB. 12. Kornwachstum bei 800°C.

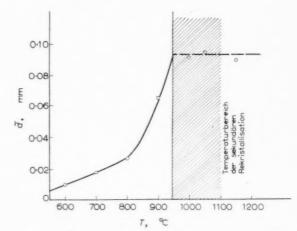


Abb. 13. Endwert der Korngrösse nach normalen Kornwachstum bei 0,04 mm starkem Band.

Temperaturgrenze höher; was verständlich ist, da sich jetzt der Einfluss der Probendimension erst bei grösserem Korndurchmesser auswirken kann. Wichtig ist die Beobachtung, dass eine Sekundärrekristallisation nur in dem Temperaturbereich zu erzielen ist, wo die Endkorngrösse durch die Probendimension bestimmt wird. Die vor dem Einsetzen der Sekundärrekristallisation erreichte Korngrösse ist in Tabelle 2 angegeben. Art der Schlussglühbehandlung und Rekristallisationstextur üben nur geringen Einfluss auf die Endkorngrösse nach dem normalen Kornwachstum aus. Die Art der Schlussglühatmosphäre ist jedoch von ganz besonderer Wichtigkeit für das Auftreten der Sekundärrekristallisation. Sie tritt nämlich nur dann auf, wenn eine äusserst saubere Glühatmosphäre dafür sorgt, dass bei der Glühung eine spiegelblanke Metalloberfläche entsteht.

191

Nach Tabelle 2 müssen die Körner vor dem Einsetzen der Sekundärrekristallisation sehon so gross sein, dass alle Körner mit wenigen Ausnahmen durch die Banddicke hindurch gewachsen sind und zwei freie Oberflächen besitzen. Das lässt erkennen, dass wir es mit einer Wachstumsauslese beim zweidimensionalen Kornwachstum zu tun haben.

Tabelle 2 (vergl. Abb. 13). Vor dem Beginn der Sekundärrekristallisation erreichte mittlere Korngrösse

Bandstärke	Korndurchmesser
0.04	0.09
0,06	0,13
0.08	0.18
0,13	0,28
0.18	0,40
0,30	0,70

In der Regel wird jeboch das dreidimensionale Kornwachstum nicht durch ein zweidimensionales Wachstum fortgesetzt, wenn die Körner die Bandstärke erreicht haben. (10,11,20) Es wurde vermutet, dass die Triebkraft dafür zu gering wird. (21)

D. DEUTUNG

Man kann daher die Ursache der beobachteten Wachstumsauslese nicht auf bekannte Vorgänge beim Kristallwachstum zurückführen. Sie hängt offenbar davon ab, dass eine Würfelfläche des Kristallgitters der Bandoberfläche parallel liegt. Abweichungen von mehr als 5°-7° heben diese Selektion auf.

Die Vorstellungen über das Kornwachstum, das sich an die Rekristallisation anschliesst, stimmen heute darin überein, dass die treibende Kraft des Kornwachstums in der Korngrenzenenergie sitzt. Wenn aber die Körner die Grösse der Probendimension besitzen, bilden freie Oberflächen einen wesentlichen Anteil ihrer Begrenzung, und man sollte deshalb einen Einfluss der Oberflächenenergie auf zweidimensionales Kornwachstum erwarten dürfen. Schon 1949 haben Kronberg und Wilson⁽²²⁾ einen Hinweis gegeben, dass bei der Sekundärrekristallisation von Kupfer die Unterschiede der Oberflächenenergie eine Rolle spielen könnten. Für verschiedene Netzebenen des Gitters ergeben sich auch verschiedene Werte für die Oberflächenenergie. Bekanntlich sinkt für die niedrig indizierten Netzebenen der Wert der Oberflächenenergie beträchtlich unter den Durchschnittswert der Oberfiächenenergie, (23) so dass eine Sekundärrekristallisation infolge Wachstumsselektion von Körnern mit einer niedrig indizierten Netzebene ohne weiteres verständlich würde.

VOL.

1959

Wenn man bisher eine solche Selektion nicht beobachtet hat, so liegt es wohl daran, dass nur selten beim Glühen freie Metalloberflächen ausgebildet werden. Die Adsorption von Fremdstoffen und die Bildung von Oxydhäuten verändern jedoch die Verhältnisse der Oberflächenenergie ganz wesentlich. Ausserdem setzt beim Glühen das thermische Anätzen der Korngrenzen auf der Probenoberfläche ein, worin die Ursache für das Abbremsen des Kornwachstums zu suchen ist, wenn die Körner die Dimension der Banddicke erreicht haben. Dass ein thermisches Anätzen das weitere Kornwachstum nicht vollständig zum Stillstand bringen sollte, hat Mullins in ausführlichen Überlegungen dargelegt. (24)* Ein wirkliches Abstoppen des Kornwachstums, wie es zumeist berichtet wird, ist danach nur dadurch zu verstehen,

Es lässt sich somit auch verstehen, warum die hier beobachtete Sekundärrekristallisation eine ganz besonders saubere Glühatmosphäre zur Voraussetzung hat, die dafür sorgt, dass die Metalloberfläche weitgehend frei von jeder Art adsorbierter Fremdstoffe oder Oxydhäute gehalten wird. Denn erst dann werden die hier dargestellten Überlegungen über die Oberflächenenergien gültig.

Im folgenden sollen diese qualitativen Überlegungen durch theoretische Modellvorstellungen etwas eingehender gestützt werden.

Theoretische Überlegungen

(a) Oberflächenenergie. Zwar ist theoretisch einzusehen, dass die Oberflächenenergie einer niedrig indizierten Ebene, wie die Würfelfläche (100) und die Dodekaederfläche (110) im kubisch raumzentrierten Gitter, niedriger liegt als der Durchschnittswert der Oberflächenenergie. (Die Arbeiten von Moore⁽²³⁾ zeigen, dass in kubisch flächenzentrierten Metallen die (111) und (120) Ebenen als niedrig indizierte Ebenen eine um 10-20 Frozent geringere Oberflächenenergie besitzen müssen, als dem Durchschnitt entspricht.) Schwierigkeiten macht nur die Bevorzugung der (100) Ebene vor der (110) Ebene, denn man hätte zunächst für die dichtest belegte Netzebene auch die niedrigste Oberflächenenergie erwartet. Man weiss jedoch, dass als Spaltfläche in α-Eisen ebenso wie in Eisen-3%Si die Würfelfläche bevorzugt wird, was darauf hindeutet, dass vielleicht die Würfelfläche die niedrigste Oberflächenenergie besitzt.

Bei unseren Untersuchungen fiel auf, dass beim thermischen Flächenätzen fast nur (100) Ebenen als freigelegte Kristallflächen auftreten, so dass man daraus nach Moore entnehmen kann, dass diese Ebenen die geringste Oberflächenenergie besitzen sollten. Wenn auch eine eindeutige Entscheidung nur durch direkte Messungen zu erwarten ist, so lassen sich gegen die theoretischen Überlegungen von Fricke(25) oder von McLachlan,(26) nach denen die (110) Ebene eine geringere Oberflächenenergie als die (100) Ebene besitzen müsste, einige begründete Einwände aufstellen, die ein umgekehrtes Ergebnis zur Folge haben würden. Eine genaue Berechnung der Oberflächenenergie nach der Methode von Huang und Wyllie⁽²⁷⁾ für bestimmte Kristallflächen dürfte auf unüberwindliche Schwierigkeiten stossen, weil über die elektronischen Bindungsverhältnisse der Oberflächenatome in Legierungen wenig Aussagen gemacht

wenn infolge von Verunreinigungen im Metall oder nicht ganz sauberer Glühatmosphäre die Korngrenzen durch Ausscheidungen oder Fremdpartikel fixiert werden.

^{*} Mullins hat dabei auch die Idee diskutiert, dass Unterschiede der Oberflächenenergien das zweidimensionale Kornwachstum fördern.

werden können. Gerade diese Arbeit zeigt, wie verwickelt die Verhältnisse an der Oberfläche sind, so dass die einfachen Modelle von Fricke oder von McLachlan den wahren Verhältnissen kaum gerecht zu werden vermögen. Jedoch darf man wohl aus diesen Modellen entnehmen, warum die genannten Ebenen eine wesentlich geringere Oberflächenenergie besitzen als andere Kristallflächen und dass diese Eigenschaft verloren gehen muss, wenn die Ebenen nur wenig von der Parallellage zur Bandoberfläche abweichen. Weiterhin lassen diese Überlegungen vermuten, dass bei kubisch raumzentrierten Metallen relative Unterschiede der Oberflächenenergie von 20-30 Prozent sicher nicht zu hoch gegriffen sein werden. Damit kommt man in die Nähe der Korngrenzenenergie. Denn man geht wohl nicht sehr fehl in der Annahme, dass die Korngrenzenenergie etwa ein Drittel der Oberflächenenergie beträgt. (28) Man sollte daraus schliessen können, dass bei der Bildung von wirklich freien Metalloberflächen und der weitgehenden Vermeidung eines thermischen Anätzens ein selektives zweidimensionales Kornwachstum auftreten müsste, was die folgenden Überlegungen eingehender zeigen sollen.

(b) Kornwachstum. Man geht von der bekannten Beziehung für die lineare Kornwachstumsgeschwindigkeit G aus:

$$G = k \cdot \Delta F \tag{b. 1}$$

 $k={
m von\, der\, Zeit}$ unabhängiger Faktor, der die Beweglichkeit der Korngrenzen charakterisiert.

 $\Delta F = \text{der beim Kornwachstum freiwerdende Energie-betrag, bezogen auf die Volumeneinheit.}$

Beim zweidimensionalen Wachsen eines einzelnen Kornes gegen die Matrix (vergl. dazu die Figur in Abb. 14) muss man die Vergrösserung Δu des Kornumfanges u, das Aufzehren der Korngrenzenstücke Δs der n angrenzenden Körner mit dem mittleren Korndurchmesser d_0 und die Umwandlung der Oberflächenenergie im Stück Δf auf beiden Seiten der Oberfläche des Bandes bei der Energiebilanz berücksichtigen.



Abb. 14. Ein selektiv wachsendes Korn im Primärgefüge (schematisch).

$$\Delta F = [-\gamma \cdot \Delta u \cdot b + n\gamma \Delta s \cdot b + 2\Delta f(\bar{\sigma} - \sigma_0)]/\Delta f \cdot b \quad (b. 2)$$

b = Banddicke.

 $\gamma = \text{Korngrenzenenergie (erg/cm}^2).$

\(\bar{\sigma}\) = Durchschnittswert der Oberflächenenergie der anstossenden K\(\bar{\sigma}\)rner.

 σ_0 = Oberflächenenergie des auswachsenden Kornes.

Betrachten wir nur den Fall, dass das auswachsende Korn beträchtlich grösser als die Körner der Restmatrix mit dem Durchmesser d_0 geworden ist, dann kann $n \approx u/d$ gesetzt werden und der Beitrag von Δu gegenüber den anderen Grössen vernachlässigt werden. Es gilt dann

$$\Delta F = \gamma (1/d_0) + 2\Delta \sigma/b \tag{b. 3}$$

Diese Beziehung sagt folgendes aus:

Nimmt man an, dass $\Delta\sigma$ ebenso wie γ von der Zeit und Glühtemperatur nicht abhängen, so sollte für die kinetischen Beziehungen dieser Art der Sekundärrekristallisation die gleiche Charakteristik zu finden sein, wie sie von den anderen Arten der Sekundärrekristallisation her bekannt ist. Das ist auch der Fall, wie in einer späteren Arbeit gezeigt wird. Die Kornwachstumsgeschwindigkeit wird lediglich um einen konstanten Faktor $2\Delta\sigma/b$ erweitert.

Dieses Zusatzglied ist jedoch bandstärkenabhängig, so dass man daraus schliessen kann, dass die Kornwachstumsgeschwindigkeit mit abnehmender Banddicke zunimmt, was ebenfalls experimentell nachgewiesen wurde.

Eine Wachstumsselektion unter dem Einfluss der Oberflächenenergie darf erst dann erwartet werden, wenn das Zusatzglied den Anteil der Korngrenzenenergie überwiegt oder wenigstens in etwa gleichkommt. Das erklärt die Tabelle 2, die angibt, dass eine feste Relation d_0 zu b existiert.

In einem späteren Abschnitt wird dann durch eine Abschätzung gezeigt, dass d_0 tatsächlich so gross ist, dass ein Überwiegen des Oberflächenterms angenommen werden muss.

Mit der Beziehung (b. 3) kann man deshalb erklären, warum gerade bei dünnen Bandstärken diese Selektion bevorzugt auftritt und technisch leichter zu erzielen ist.

Für den Beginn der Sekundärrekristallisation sind die Verhältnisse zu unübersichtlich, als dass sich eine eindeutige Beziehung aufstellen liesse. Beziehung (b. 2) macht deutlich, dass auch die Konfiguration der Körner für die Selektion massgeblich wird.

Eine weitere Komplikation ist dadurch gegeben,



Abb. 15. Gekrümmte Korngrenzen in einem Querschliff durch ein rekristallisiertes Blech aus Fe-3%Si, 0,35 mm

dass man immer noch vorhandene Fremdpartikel berücksichtigen muss, die das Kornwachstum stören. Man müsste in die Ausdrücke für die freie Energie noch ein Zusatzglied einfügen. Eine rohe Abschätzung des Einflusses von Fremdpartikeln erhält man jedoch, wenn man sich überlegt, dass das normale Kornwachstum nicht eher durch Verunreinigungen abgestoppt werden darf, bevor der Korndurchmesser d_0 erreicht ist, wie er in der Tabelle 2 enthalten ist.

(c) Es soll hier noch ein verfeinertes Modell für das Kornwachstum angegeben werden. Bisher sind wir bei unseren Überlegungen von gestreckten Korngrenzen ausgegangen. Jedoch spielt sich das Kornwachstum so ab, dass die Korngrenzen gekrümmt sind und in Richtung des Krümmungsmittelpunktes wandern. Eine solche Krümmung der Korngrenzen wird durch die Unterschiede in der Oberflächenspannung hervorgerufen. (Vgl. Abb. 15.)

In der Figur der Abb. 16 ist angenommen, dass sich die wandernde Korngrenze kreisförmig quer durch das Blech der Dicke b ausgebildet hat. Der Anteil der freien Energie, der durch diese Krümmung für das Kornwachstum gewonnen wird, ist dann

$$\Delta F = \gamma(1/r_1) \tag{e. 1}$$

 $\gamma = Korngrenzenspannung$

 $r_1 = \text{Krümmungsradius}$

Der Krümmungsradius kann abgeschätzt werden, weil der Grenzwinkel α der Korngrenze mit der Oberfläche dadurch vorgegeben ist, dass die Vektorsumme der Grenzflächenspannungen verschwinden muss. Es ist

$$1/r_1 = 2(\cos \alpha)/b \tag{e. 2}$$

damit wird

1959

$$\Delta F = 2A/b \tag{e. 3}$$

$$A = (\bar{\sigma}^2 - \sigma_0^2 + \gamma^2)/2\sigma_0 \tag{c. 4}$$

womit wir einen ähnlichen Ausdruck wie in (b. 3) erhalten; es ist lediglich anstelle der Differenz der Oberflächenspannungen der etwas kompliziertere Ausdruck A getreten.

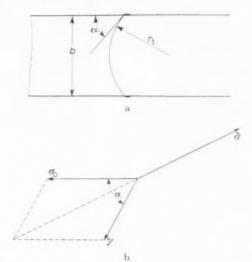


ABB. 16. Korngrenze quer durch das Band (schematisch).

Man kann daher die Gleichungen in Abschnitt bdadurch modifizieren, dass man A anstelle $\Delta \sigma$ setzt.

(d) Abschätzung. Die angedeuteten Modelle können natürlich die wahren Verhältnisse mit ihrer verwickelten geometrischen Struktur des Gefüges nicht wiedergeben. Sie stellen lediglich den Versuch dar, durch stark vereinfachende Annahmen die wesentlichen Züge des zweidimensionalen Kornwachstums unter Berücksichtigung der Oberflächenenergie zu überblicken. Immerhin ist trotz der starken Vereinfachung ein Bild entstanden, das die experimentellen Beobachtungen verstehen lässt. Aus den Modellen sind Beziehungen entwickelt, die sich auch quantitativ abschätzen und mit den experimentellen Ergebnissen vergleichen lassen. Messungen der Korngrenzen- und Oberflächenenergien für Eisen-Silizium-Legierungen sind uns nicht bekannt. Aus den Untersuchungen von Udin und Mitarbeitern (29) über Oberflächenenergien von Metallen unterhalb des Schmelzpunktes darf man wohl vermuten, dass die Oberflächenenergie der von uns verwendeten Eisensiliziumproben zwischen 1000 und 2000 erg/cm² liegen wird. Wir setzen daher für die mittlere Oberflächenenergie $\bar{\sigma} = 1500 \text{ erg/cm}^2$; wie weiter oben begründet, nehmen wir an, dass die Würfelfläche eine um 20 Prozent niedrigere Oberflächenenergie besitzt, d.h. also $\sigma_0 = 1200 \text{ erg/cm}^2$. Für die mittlere Korngrenzenenergie setzen wir 1/3 des Wertes für die Oberflächenenergie, $-\gamma = 500 \text{ erg/m}^2$, -und sind damit in der Nähe des von van Vlack(30) bestimmten Wertes, der für die Korngrenzenenergie von α Eisen 770 erg/cm2 angibt. Zwar sind die so angenommenen Werte nicht korrekt, jedoch dürfte das daraus resultierende Ergebnis für die Abschätzung genügend verlässlich sein, da das Modell nur einen

ganz rohen Vergleich mit den experimentellen Ergebnissen zulässt. Wir erhalten

 $f\ddot{u}r A = 230 \text{ erg/cm}^2$

für den Grenzwinkel $\alpha=62^{\circ}$

für den Krümmungsradius $r_1 = 1,1 b$

Man erkennt daraus, dass man zu ganz brauchbaren Übereinstimmungen mit dem Experiment kommt. Aus Gleichung (b. 3) liesst man ab, dass der Anteil der Oberflächenenergie ebenso gross ist wie der Anteil der Korngrenzenenergie, wenn $d_0 = 1.1 b$ geworden ist. In den hier beschriebenen Untersuchungen ist d_0 , der Korndurchmesser des primär rekristallisierten Gefüges, etwa doppelt so gross wie die Bandstärke wenn das selektive Kornwachstum stattfindet. Nach dieser Abschätzung muss dann die Oberflächenenergie den überwiegenden Anteil der Energie ausmachen, die das selektive Kornwachstum treibt.

Herrn Dr. Deisinger und Herrn Dr. Assmus gebührt mein voller Dank, dass mir diese wissenschaftlich so ausserordentlich ergiebige Aufgabe zur Bearbeitung übertragen wurde.

Ich danke Frau Dr. I. Pfeiffer für die Durchführung elektronenmikroskopischen Untersuchungen, Herrn Dr. H. Thomas, Herrn Dr. G. Baer und Herrn Dipl. Phys. G. Ibe für ihre Ratschläge und Anregungen bei den Texturuntersuchungen. Fräulein B. Hess wird für die Hilfe bei den Kornwachstumsuntersuchungen gedankt. Den Herren Dr. G. Wiener. Dr. Bailer und Dr. Albert aus den Westinghouse Laboratories wird für Diskussionen und Anregungen sowie für die Mitteilungen ihrer Untersuchungen ähnlicher Art gedankt, die sich auf den Fortgang unserer Arbeiten förderlich ausgewirkt haben.

ANMERKUNG

Inzwischen sind Arbeiten mit ähnlichen Ergebnissen bekannt geworden, wonach bei Eisen-Silizium-Legierungen Oberflächeneffekte eine besondere Selektion des

zweidimensionalen Kornwachstums hervorrufen.* Die Arbeiten zeigen, dass dabei recht verwickelte Verhältnisse vorliegen und ausser einer Sekundär-Rekristallisation in Würfellage auch eine Tertiär-Rekristallisation in Gosslage auftreten kann.

LITERATUR

- 1. F. Assmus, K. Detert und G. Ibe, Z. Metallk. 48, 344
- 2. J. E. Burke und D. Turnbull, Recristallization and Grain Growth, Progress in Metal Physics Vol. 3. Pergamon Press, London (1952).
- P. A. BECK, M. L. HOLZWORTH und P. R. SPERRY, Met. Techn. 15 (1948), Techn. Publ. 2475.
 W. MORILL, Metal Progress 54, 625 (1948).
- J. Fast, Philips Res. Rep. 11, 490-91 (1956).
- K. DETERT, Metall, 12, 817 (1958).
 P. A. BECK und P. R. SPERRY, Trans. Amer. Inst. Min.
- (Metall.) Engrs. 185, 240 (1949).
- C. G. Dunn, Acta Met. 1, 163 (1953). 9. C. G. Dunn, Acta Met. 2, 173 (1954).
- 10. P. A. BECK, J. C. KREMER, L. J. DEMER und M. L. Holzworth, Trans. Amer. Inst. Min. (Metall.) Engrs. 175, 372-400 (1948).
- 11. P. A. Beck, in Annealing of Cold Worked Metals, Phil. Mag. Suppl. **3**, 245 (1954). 12. G. Tamman, Z. anorg. allgem. Chem. **148**, 293 (1925). 13. H. Neff, Z. Metallk. **47**, 646 (1956).

- 14. J. GREWEN, A. SEGMÜLLER und G. WASSERMANN, Arch. Eisenhüttenw. 29, 115 (1958).
- EISERBRUIGHERW. 23, 113 (1850). 15. C. G. Dunn, J. Appl. Phys. 25, 233 (1954). 16. A. Merlini und P. A. Beck, Acta Met. 1, 230 (1953). 17. W. Dickenscheid und H. J. Seemann, Z. Metallk. 44,
- 211 (1953). 18. P. FELTHAM, Acta Met. 5, 97-105 (1957).
- G. Wiener, Trans. Amer. Met. Soc. No. 17 (1951).
 J. E. Burke und J. G. Schiau, Trans. Amer. Inst. Min. (Metall.) Engrs. 175, 141 (1948).

19!

- 21. C. S. SMITH, Trans. Amer. Inst. Min. (Metall.) Engrs. 175, 15 (1948).
- 22. M. L. KRONBERG und F. H. WILSON, Trans. Amer. Inst. Min. (Metall.) Engrs. 185, 501 (1949).
- A. J. M. MOORE, Acta Met. 6, 293 (1958).
 W. W. MULLINS, Acta Met. 6, 414 (1958).
- R. FRICKE, Z. phys. Chem. Abt. B 52, 284 (1942).
- 26. D. McLachlan, Acta Met. 5, 111 (1957).
- 27. K. HUANG und G. WYLLIE, Proc. Phys. Soc. Lond. A62, 180 (1949).
- 28. H. Udin, Trans. Amer. Inst. Min. (Metall.) Engrs. 189, 63 (1951).
- 29. H. Udin, A. J. Shaler und J. Wulff, Trans. Amer. Inst. Min. (Metall.) Engrs. 185, 196 (1949).
 F. H. BUTTNER, H. UDIN und J. WULFF, Ibid. 191, 1209
 - (1951)E. R. Funk, H. Udin und J. Wulff, Ibid. 191, 1206 (1951)
- 30. L. H. VAN VLACK J. Metals 251 (1951).

^{*} J. L. Walter, C. G. Dunn, Gen. Electr. Lab. Report No.

LATTICE DEFECTS IN A COPPER-ALUMINUM ALLOY*

M. S. WECHSLER and R. H. KERNOHAN†

Static (at-temperature) resistivity measurements and measurements after air-cooling and water-quenching indicate an excess resistivity contribution at temperatures above 200° C in Cu–Al (15 at.% Al) single crystals. From the static measurements, the energy of formation of the configuration responsible for the excess resistivity is determined to be about $0.2~{\rm eV}$. Annealing experiments after quenching from 450° C were conducted, from which the activation energy for motion was evaluated. These experiments are correlated with a previous investigation of the effect of neutron irradiation on Cu–Al alloys, and a discussion is given in terms of short-range ordering and the annealing of lattice vacancies.

SUR LES DÉFAUTS DE RÉSEAU DANS UN ALLIAGE CUIVRE-ALUMINIUM

Des mesures de résistivité à la même température (statique) et des mesures après refroidissement à l'air et après trempe fournissent des valeurs en excès à des températures au-dessus de 200° C, pour des monocristaux de cuivre-aluminium (15 at.% Al). A partir de mesures statiques, l'énergie de formation de la configuration responsable de ces valeurs a été trouvée de l'ordre de 0,2 eV. Des recuits après trempe à 450° C ont permis d'évaluer l'énergie d'activation du mouvement. Ces expériences sont en relation avec une étude précédente sur l'influence de l'irradiation des neutrons dans les alliages Cu–Al et la discussion se base sur l'ordre à petite distance et la restauration des lacunes du réseau.

GITTERFEHLSTELLEN IN EINER KUPFER-ALUMINIUM-LEGIERUNG

Statische Widerstandsmessungen (bei der betreffenden Temperatur) und Messungen nach Luftabkühlung und Abschrecken in Wasser ergeben an Cu–Al(15 At. % Al)-Einkristallen bei Temperaturen oberhalb 200°C einen zusätzlichen Widerstandbeitrag. Durch die statischen Messungen wurde die Bildungsenergie der für den Zusatzwiderstand verantwortlichen Konfiguration zu etwa 0,2 eV bestimmt. Nach Abschrecken von 450°C wurden Erholungsversuche durchgeführt, aus denen die Aktivierungsenergie für die Wanderung bsetimmt wurde. Disse Experimente hängen mit einer früheren Untersuchung über die Wirkung von Neutronenbestrahlung auf Cu–Al-Legierungen zusammen. Sie werden mit Hilfe von Vorstellungen über eine Nahordnungseinstellung und die Erholung von Gitterleerstellen diskutiert.

1. INTRODUCTION

1959

In a previous paper, $^{(1)}$ the effect of neutron irradiation on α -solid-solution Cu–Al alloys was described. When the alloys are irradiated near room temperature, a decrease in resistivity is observed. The magnitude of the decrease is larger for alloys of higher Al content (0.18 $\mu\Omega$ em for the 15 at.% Al alloy) and no decrease in resistivity is observed for pure Cu. The process that brings about the decrease in resistivity for the alloys is very likely diffusion-controlled, since no decrease takes place upon irradiation at $-120^{\circ}\mathrm{C}$. However, if the sample is warmed above $-50^{\circ}\mathrm{C}$ following irradiation at $-120^{\circ}\mathrm{C}$, the decrease in resistivity will set in.

In a general way, the alloy may be considered to be in a metastable state in its original condition. Then, the irradiation triggers or accelerates a diffusioncontrolled process by which the material proceeds toward thermodynamic equilibrium, with an attendant

decrease in resistivity. The nature of this metastability is difficult to ascertain on the basis of resistivity measurements alone, but several suggestions may be made. (1) One possibility is that the alloy initially has less than the equilibrium amount of order. In this case, we must specify that the order is local, since no superlattice is present in these alloys. The irradiation may then be thought to introduce lattice vacancies which enhance atomic movements so that shortrange ordering takes place at a lower temperature than for the unirradiated alloy. This short-range ordering is assumed to result in the observed decrease in resistivity. An explanation in terms of short-range ordering has been given(2,3) for similar irradiation effects on Cu-Zn. An alternative explanation is that the metastability arises from the retention of a nonequilibrium concentration of lattice vacancies in the original preparation of the alloy. In this event, the neutron bombardment may introduce special sites at which the annihilation of the excess vacancies takes place more readily than in the absence of the irradiation. The annealing out of the excess vacancies is accompanied by the observed decrease in resistivity,

^{*} Solid State Division, Oak Ridge National Laboratory, Oak Ridge, Tennessee. Received October 22, 1958.

[†] Oak Ridge National Laboratory is operated by Union Carbide Corporation for the U.S. Atomic Energy Commission.

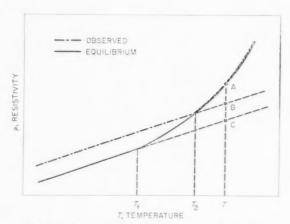


Fig. 1. Resistivity vs. temperature (schematic).

The above discussion suggests that a non-equilibrium defect structure* is inadvertently retained in the original preparation of the alloy, despite the slow cooling that is employed. The circumstances that give rise to this situation are illustrated schematically in Fig. 1. If it were possible to maintain equilibrium during cooling, the ρ vs. T dependence would follow the solid curve. At temperatures above T_1 , the defects are in equilibrium in sufficient quantity to make a significant contribution to the resistivity. At temperature T, this contribution is given by AC. However, under actual conditions, the atomic mobilities may be so low at a temperature T_2 that, upon cooling below T_2 , the defects characteristic of this temperature are frozen into the lattice. The contribution to the resistivity of this non-equilibrium configuration is indicated by BC. The decrease in resistivity that takes place upon neutron irradiation(1) near room temperature is 0.18 $\mu\Omega$ cm for Cu-Al (15 at. % Al). Regarding this decrease as that necessary to bring the sample to thermal equilibrium, we may take BC = 0.18 $\mu\Omega$ cm for this alloy. Upon cooling below T_2 , the resistivity follows the curve labelled "observed". Thus, in order for the retention of a non-equilibrium configuration to take place upon slow cooling, a temperature T_{o} must exist at which the equilibrium concentration of defects is significant and yet the atomic mobilities are low. This implies that the energy of formation, ε_F , of the defect must be low and the activation energy for motion, ε_M , must be high. The experiments described in this paper indicate that these conditions are met in the 15 at. % Al Cu-Al alloy. The temperature T_2 is as low as 200°C. This is found to be the case from two types of experiments. In the first instance, static (at-temperature) measurements were made,

which show the effect of an additional contribution to the resistivity above 200°C. From these measurements, a value of ε_F was deduced. Secondly, experiments were performed in which excess resistivities were retained upon air-cooling and water-quenching from temperatures above 200°C. In addition, annealing experiments after quenching are described from which ε_M was determined.

2. EXPERIMENTAL DETAILS

The alloy was prepared by the Metallurgy Division at ORNL by vacuum melting and casting. The base constituents were electrolytic Cu of 99.92% purity and Al of 99.99% purity. All samples contained 15.0 \pm 0.5 at.% Al and received an initial annealing treatment, consisting of holding several hours at 750°C followed by cooling at a rate of about 15°C/hr to room temperature. With the exception of a few quenching experiments on 56 mil Cu-Al wire (Fig. 6), all of the measurements were made on rod-shaped single erystals, \frac{1}{2} in. diam., containing short nibs that served as voltage contacts. The single crystals were prepared by re-melting the alloy material in a split graphite mold and lowering through a temperature gradient in a vacuum furnace. The 56 mil wire was prepared by swaging and drawing a portion of the same alloy stock as was used for the single crystals. Voltage contacts were applied by spot-welding short sections of the alloy wire transversely on the sample wire.

19

The resistivity measurements were made by the double-potentiometer method, using a Rubicon sixdial thermo-free potentiometer. For the at-temperature measurements, the sample was kept in an inert atmosphere inside a wire-wound tube furnace. The temperature was measured using thermocouples adjacent to but not in contact with the samples. For the experiments on the effect of air-cooling or quenching, the samples were held in a salt-bath controlled at the appropriate temperatures. The air-cooling was done in still air at room temperature and the quenching was done by quickly removing the sample from the salt bath and immersing it in water at room temperature. For the annealing measurements after quenching, the samples were placed in a constant-temperature silicone oil bath and the resistivity measurements were made

A high-speed oscillograph was used to measure the cooling rates during the air-cooling and during quenching of the single crystals. A constant current was passed through the sample during the cooling and the voltage across the nibs of the sample was fed to the oscillograph. The current was too low to cause a measurable increase in the sample temperature Cu–Al

^{*} In this paper, the term ''defect'' is used loosely to include departure from equilibrium order.

wire of the same composition as the sample was used to make the voltage contacts in order to reduce thermal e.m.f.'s. The procedure for the air-cooling and the quenching closely approximated that used during the actual measurements. In this way, a trace of the resistance of the sample versus time during the cooling was obtained from which the temperature-time curve could be deduced. Upon cooling from 450°C, the cooling rates were as follows. For the air-cooling, the temperature-time curve was linear during the first ten seconds corresponding to a rate of 8°C/sec and 50 sec were required to reach 200°C. For the quenching, the maximum cooling rate was 4500°C/sec and the temperature reached 200°C in about 0.09 sec. The temperature of the sample decreased about 10°C during the time necessary to transfer it from the salt bath to the quenching water. No correction was made for this decrease in temperature. To insure that the response characteristics of the oscillograph were not being exceeded, a bare thermocouple was quenched. In this case, the observed cooling rate was 104°C/sec. The quenching characteristics reported here are approximately the same as those measured by a different technique on another material4 using samples of the same size and shape and the same quenching procedure.

3. RESULTS

3.1. Static measurements

1959

For the static (at-temperature) measurements, two runs were made, the first extending to 404°C and the second to 664°C. The heating and cooling rates were less than 6°C/hr. The results are shown in Fig. 2. The temperature dependence appears linear between room temperature and 200°C. The dashed line in Fig. 2 represents the extrapolation of the least squares straight line through the points of Run No. 1 measured between room temperature and 200°C. A quadratic extrapolation of these points differs only slightly from the linear extrapolation and the results described below do not change significantly if the

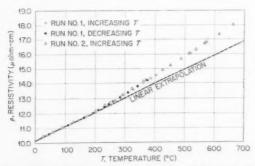


Fig. 2. Resistivity vs. temperature, Cu-Al (15 at. % Al).

quadratic extrapolation is used. The positive deviation of the observed resistivity values above 200°C from the extrapolated line suggests that lattice defects come into equilibrium above 200°C and cause an increase in resistivity. If the formation of the defect is a single, thermally-activated process, this excess resistivity is expected to be of the form

$$\Delta \rho = A \exp\left(-\varepsilon_F/kT\right) \tag{1}$$

where A is independent of the temperature T and ε_{F} is the energy of formation of the defect. Accordingly, the excess resistivity is plotted on a log scale vs. 1/T in Fig. 3 (open circles). The points between 320 and 660°C satisfy equation (1) with the value $\varepsilon_F =$ 0.19 eV, but at lower temperatures the open circles fall lower than is predicted by equation (1) using this energy of formation. However, as was discussed in the Introduction, it may be deduced from the effect of neutron irradiation on this alloy(1) that, at temperatures above $T_2 = 200^{\circ}$ C (Fig. 1), the equilibrium excess resistivity is not given by the observed excess resistivity (AB, Fig. 1) but by AB + BC where BC = 0.18 $\mu\Omega$ cm. When the $\Delta\rho$ values determined from Fig. 2 are increased by 0.18 $\mu\Omega$ cm (filled circles, Fig. 3), it is found that equation (1) is satisfied over the entire range of temperatures. The energy of formation in this case is $\varepsilon_F = 0.15 \text{ eV}$.

3.2. Measurements upon air-cooling

It was mentioned earlier that the decrease in resistivity upon neutron bombardment may indicate that a non-equilibrium concentration of defects is retained in the alloy, even after slow cooling (~15°C/ hr). If this is the case, we would expect larger amounts of excess resistivity to be retained upon air-cooling, where the cooling-rate is greater by a factor of more than 103.

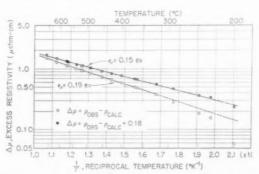


Fig. 3. Excess resistivity vs. reciprocal absolute temperature, Cu–Al (15 at.% Al). $\rho_{\rm calc}$ refers to the extrapolated values in Fig. 2. The value 0.18 $\mu\Omega$ cm is the decrease in resistivity observed upon neutron irradiation near room temperature (ref. 1).

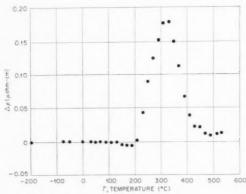


Fig. 4. Air-cooling experiment. Excess resistivity as a function of holding temperature, Cu–Al (15 at. % Al). All measurements were made at -196°C. The sample was held 30 min at each temperature. For temperatures above room temperature, the sample was air-cooled to room temperature and then placed in liquid nitrogen for measurement.

The effect of air-cooling is illustrated in Fig. 4. where the results of an isochronal annealing experiment are seen. The sample was held for 30 min at higher and higher temperatures and returned to -196°C for measurement between each anneal. Above room temperature, the samples were cooled in air before placing them in the liquid nitrogen. Fig. 4 shows a slight tendency for the resistivity to decrease upon holding between 150 and 200°C. But when the samples are cooled in air from above 200°C, the resistivity increases. However, the increase in resistivity retained upon air-cooling continues only to about 310°C. When the air-cooling is carried out from a temperature above 310°C, the retained resistivity decreases again. Upon air-cooling from 500°C, the resistivity at -196°C is only slightly higher than the original value.

The data shown in Fig. 5 illustrate some additional aspects of this type of experiment. This sample had been previously bombarded by neutrons at -120°C and then annealed at 0°C. This treatment caused the resistivity to lie about 0.065 $\mu\Omega$ cm below its preirradiation value, as has been described earlier.(1) Two isochronal annealing runs, similar to the one illustrated in Fig. 4, were carried out on the irradiated sample. In this case, however, the measurements were made at 0°C. Furthermore, for the first run, the time of hold at each temperature was two hours and, for the second run, it was five minutes. An increase in resistivity was observed upon air-cooling from temperatures up to about 310°C, and, upon aircooling from above 310°C, the resistivity at 0°C decreased again (points A to B). Thus, the behavior above 200°C is quite similar to that shown in Fig. 4 and indicates that the same results are obtained

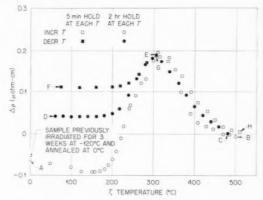


Fig. 5. Air-cooling experiment on a Cu–Al (15 at.% Al) sample previously irradiated for three weeks at -120°C and annealed at 0°C. All measurements at 0°C.

whether the measurements are made at 0°C or at $-196^{\circ}\mathrm{C}$. Also, the similarity between Figs. 4 and 5 suggests that the effect of the irradiation is dissipated when the temperature is raised above about $200^{\circ}\mathrm{C}$. This is further indicated by the sequence of measurements from C to D, where the annealing temperature is decreased. The resistivity levels off when the cooling is done from temperatures below $200^{\circ}\mathrm{C}$ at a value above the original resistivity. Thus, the lower resistivities induced by the irradiation are not recovered upon decreasing the temperature once again below $200^{\circ}\mathrm{C}$.

19

The effect of reducing the time of hold at each temperature is shown by the sequence of points from E to F in Fig. 5. The resistivity at 0°C upon air-cooling from 310°C was the same for the five-minute hold as for the two-hour hold. But, upon decreasing the annealing temperature, we find that the resistivity levels off at a higher value for the five-minute holds than for the two-hour holds (point F as compared with point D, Fig. 5). This is apparently the result of the slowness of the approach to equilibrium at temperatures below about 250°C. When the air-cooling is done from temperatures above 310°C, essentially the same curve is traced for the points obtained with five-minute holds at each temperature (points G to H) as for those with two-hour holds.

3.3. Quenching measurements

It is to be expected that larger amounts of excess resistivity are retained in the crystal as a result of the greater cooling rates used in the quenching experiments. This is shown to be the case in Fig. 6 where the quenched-in resistivity is compared with the resistivity retained upon air-cooling and with the excess resistivity deduced from the static measurements. It is seen that a maximum of about 0.5 $\mu\Omega$ cm

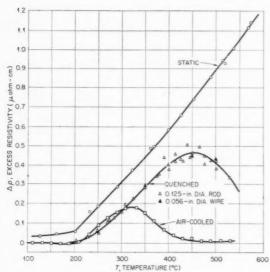


Fig. 6. Excess resistivity vs. temperature measured by the static method, by air-cooling and by water-quenching. Cu-Al (15 at.% Al).

is retained upon quenching from 450°C as compared with a maximum of about 0.2 $\mu\Omega$ cm upon air-cooling from 310°C. There appears to be no difference in the quenching results for the 56 mil wire as compared with those for the one-eighth inch rods. The excess resistivity begins to be apparent upon heat-treating at 200°C for both air-cooling and quenching. This is also the temperature at which the static measurements begin to indicate an additional contribution to the resistivity. The static measurements for Run No. 2 (Fig. 2) are those plotted in Fig. 6.

VOL.

1959

The kinetics of the annealing of the resistivity retained upon quenching from 450°C were also studied. Before quenching, the resistivity of the sample was measured in the annealed condition at a number of temperatures between -196°C and 200°C. The total amount of quenched-in resistivity was determined by measuring the resistivity at -196°C immediately after quenching. Then the sample was placed in the annealing bath at temperatures between 45 and 100°C and the resistivity was measured in situ as a function of time at the annealing temperature. The resistivity had begun to decrease by the time the first measurement was made, but the measurements at −196°C could be used to deduce the initial quenched value, ρ_i , at the annealing temperature. The annealing process appeared to be close to completion when the measurements were discontinued for the runs at 62 to 100°C. In each case, it was found that the final value was slightly (about 0.04 $\mu\Omega$ cm) lower than the resistivity determined prior to the quenching. The decrease at 45°C was exceedingly slow and the run at

this temperature was stopped before the final resistivity was reached. For purposes of calculation, the final value for the anneal at $45^{\circ}\mathrm{C}$ was taken to be the value measured at this temperature before quenching. For all the annealing runs, a parameter f was calculated corresponding to the fractional departure from completion of the annealing process, where

$$f = (\rho - \rho_f)/(\rho_i - \rho_f)$$

and ρ , ρ_i , and ρ_f are the resistivity at time t, the initial resistivity immediately after quenching, and the final resistivity, respectively. In Fig. 7, f is plotted as a function of the annealing time. The times for specified fractional amounts of annealing are plotted to a log scale in Fig. 8 vs. the reciprocal

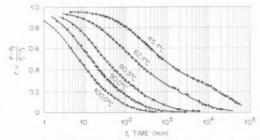


Fig. 7. Normalized isothermal annealing curves after quenching from 450°C. The magnitude of the quenched-in resistivity was about 0.45 $\mu\Omega$ cm. Cu–Al (15 at.% Al).

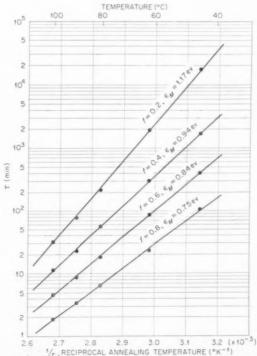


Fig. 8. Activation energy curves for annealing after quenching from 450°C, Cu-Al (15 at.% Al).

$$\tau = \tau_0 \exp\left(\varepsilon_M/kT\right) \tag{2}$$

is well satisfied, and the activation energy, ε_M , increases as the process goes on. The activation energy is plotted vs. f in Fig. 9. The activation energy increases linearly with the fractional amount of completion of the annealing process until the process is about 0.4 from completion. At this point, ε_{11} appears to increase somewhat more sharply. The final value at f = 0 is about 1.2 eV. The ε_M vs. fcurve obtained upon annealing after irradiation at -120°C (ref. 1) is also shown in Fig. 9. The irradiation lowers ε_{M} considerably in the early stages of the annealing. In fact, the curve appears to extrapolate to $\varepsilon_M = 0$ at the start of the process. The curve for the irradiation case in Fig. 9 shows no sudden increase in ε_M at the low f values and $\varepsilon_M = 1.0 \, \mathrm{eV}$ at the completion of the process.

4. DISCUSSION

In the static method of deducing the presence of lattice defects that come into equilibrium at higher temperatures, the resistivity observed at the higher temperatures is considered to consist of the superposition of the normal resistivity and the contribution made by the defects. In order to carry out the separation of these two contributions to the observed resistivity, it is necessary to assume values for the

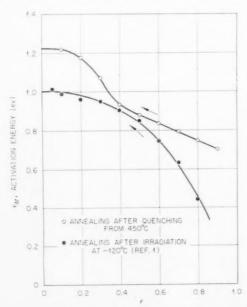


Fig. 9. ϵ_n vs. f for annealing after quenching from 450°C and after irradiation for three weeks at -120°C. f represents fractional departure from completion of the process. Cu–Al (15 at.% Al).

normal resistivity. It is here that the chief difficulty exists. In the work of Meechan and Eggleston (5) on pure Cu and Au, a quadratic extrapolation of the resistivity observed at lower temperatures was used. The excess resistivity determined in this way was found to obey quite closely the Arrhenius dependence of equation (1). However, it was pointed out by Nicholas⁽⁶⁾ that there is little theoretical justification for the use of such an extrapolation and other possibilities were suggested to explain the apparent anomalous resistivity at the higher temperatures that did not involve the assumption of defect concentrations. Nevertheless, in a later paper, Jongenburger (7) showed that an analysis of previous data on the thermal expansion of Cu and Zu agrees closely with the results of Meechan and Eggleston. In Jongenburger's analysis, the data was fitted at the lower temperatures to both a straight line and a Grüneisen curve and the extrapolation of these in the higher temperature region was used to determine the normal resistivity. Little difference in the results for the two types of extrapolations was found. It was also pointed out by Jongenburger that higher excess resistivities and lower ε_F values are obtained from static measurements on pure gold than are obtained by quenching.(8-11)

In the present investigation, an attempt was made to determine whether the data obtained for the static measurements (Fig. 2) is better fitted by assuming an excess resistivity contribution given by equation (1) or by assuming the existence of higher order terms in the temperature dependence of the normal resistivity. Calculations were made* to determine the least squares fit of the data of Run No. 2, Fig. 2, to the following two expressions

$$\rho = A + BT + C \exp(-\theta/T) \tag{3}$$

19

and

$$\rho = a + bT + cT^2 + dT^3 \tag{4}$$

each of which contains four adjustable constants. The results were inconclusive, in that the standard error associated with equation (3) was only slightly less than that for equation (4). The energy of formation corresponding to θ in equation (3) was $0.16 \, \mathrm{eV}$. However, the uncertainty as to whether equation (3) or equation (4) is applicable is largely dispelled by the results of the quenching and air-cooling experiments (Fig. 6). Since all measurements for these experiments are made at the same temperature, the additional

^{*} We are indebted to N. M. Dismuke and A. H. Culkowski for carrying out the calculations on the ORNL ORACLE computer.

resistivity at temperatures above 200°C must be due to the presence of defects (equation 3) rather than the temperature dependence of the normal resistivity (equation 4).

The energy of formation of about 0.2 eV that we observe for Cu-Al (15 at. % Al) is quite low compared with the values of about 0.70 eV reported by Jongenburger⁽⁷⁾ and 0.90 eV reported by Meechan and Eggleston⁽⁵⁾ for pure Cu. It has been observed previously that the energy of formation in alloys is lower than for pure metals. Quenching experiments on 70/30 α-brass have been reported⁽¹²⁾ that indicate an energy of formation of 0.34 eV. Also, in the case of the quenching of an Au-Cd alloy near the 50 at. % composition, values of 0.38 eV and 0.28 eV were obtained as a result of resistivity(4) and density(13) measurements, respectively. Stress relaxation measurements(14,15) have been performed on quenched Ag-Zn alloys (near 30 at. % Zn). The relaxation time immediately after quenching was found to be proportional to exp (ε_E/kT) corresponding to the value $\varepsilon_F = 0.19 \, \mathrm{eV}$ (see Fig. 1, reference 14). However, equilibrium measurements of the composite activation energy for relaxation, ε_{R} , and quench-annealing measurements for the activation energy for motion, ε_M , were not consistent with such a low value for ε_F , since ε_R - ε_M was found to be significantly greater than $0.19 \; \mathrm{eV}$. Therefore, it was concluded $^{(14)}$ that the true value of ε_F was more reliably given by $\varepsilon_R - \varepsilon_M =$

The above-mentioned quenching results on alloys have been interpreted chiefly in terms of the quenching and annealing of lattice vacancies, although in the case of the quenching of a-brass(12) an explanation in terms of short-range order was also considered. We shall first discuss our results in terms of lattice vacancies. The theoretical basis for the smaller formation energy of a vacancy in an alloy as compared with that in the pure metal is discussed by Lomer. (16) It is pointed out that an interaction may exist between vacancies and solute atoms that causes the energy to form a vacancy in the alloy to be reduced from that in the pure metal by an amount that corresponds to the energy of this interaction. This "binding energy" is expected to be relatively large in the case of a large solute atom such as Al. Nevertheless, as in the case of a-brass, (16) certain difficulties must be reconciled. One such difficulty is the magnitude of the binding energy. The energy of formation of vacancies in pure Cu has been reported to be 0.70 eV(7) and 0.90 eV.(5) If we use the value 0.8 eV for pure Cu and 0.2 eV for Cu-Al, we must predict 0.6 eV for the binding energy. This is larger than is

expected. For example, the calculation by Alfred and March⁽¹⁷⁾ of the interaction between a vacancy in Cu and a divalent impurity atom gives a value of less than 0.1 eV. Furthermore, as is pointed out by Lomer(16) in connection with the similar situation in α-brass, a large vacancy-solute interaction is inconsistent with the approximate equality of the activation energies for Cu and Zn in the alloy as determined by tracer diffusion measurements. (18)

On the assumption that the excess resistivity is due to vacancy concentrations, we may calculate approximate values for the entropy of formation of a vacancy in the alloy and the concentration of vacancies at the melting point. The concentration, c_V , is considered to be given by the usual expression

$$c_V = \exp\left(S_F/k - \varepsilon_F/kT\right) \tag{5}$$

where S_F is the entropy of formation. On the basis of the data shown in Fig. 3 and Jongenburger's (19) calculation of 1.3 $\mu\Omega$ cm per at.% vacancies for pure Cu, we find that $S_F/k = -2.1$. This result should be regarded with caution, since theoretical considerations⁽²⁰⁻²³⁾ predict a positive entropy of formation of a vacancy in pure metals. This arises because the atoms neighboring a vacancy acquire an additional freedom of motion, which lowers the frequency of vibration and raises the entropy. If this is the case in the alloy, it is unlikely that the negative entropy that we calculate is related to an error in the factor 1.3 $\mu\Omega$ cm per at.% vacancies, since this quantity would have to be reduced by a factor of about ten to make our calculations yield $S_F/k = 0$. However, the calculated value for S_F/k is fairly sensitive to the measured value of ε_F and, corresponding to the same $\Delta \rho$ values at 450°C as are shown in Fig. 3, ε_F must be raised to about 0.31 eV to give $S_F/k = 0$. On the other hand, it may be that atomic oscillations are more restricted in the neighborhood of a vacancy in alloys, leading to a negative entropy of formation. This might be expected to be the case if there were a strong solute-vacancy interaction. From equation (5) we find also that the vacancy concentration at the melting point (1040°C) is 2.1%. This is a factor of approximately five greater than that estimated by Li and Nowick(24) from stress-relaxation measurements on a Cu-Al alloy of similar composition.

An interesting aspect of the results of our quenching experiments is that, when the quenching temperature exceeds 450°C, the amount of retained resistivity begins once again to decrease. Similarly, for air-cooling experiments the maximum retained resistivity is obtained at 310°C. These observations indicate that the annealing-out of the excess resistivity occurs more

VOL.

1959

rapidly for higher quenching temperatures (T_{Ω}) . For $T_{O} > 450$ °C, the annealing rate becomes so high relative to the cooling rate that the excess resistivity characteristic of 450°C cannot be retained. The cooling rate for the air-cooling is a factor of about 500 smaller than for the quenching, so that for the air-cooling this effect takes place at a lower temperature. A similar effect was observed in the quenching of pure gold. Bauerle and Koehler(8) found that the annealing was much more rapid for higher quenching temperatures, although in this case no departure from equation (1) was noted for the highest T_Q used. The quenching experiments on pure gold were interpreted⁽²⁵⁾ in terms of the quenching-in of lattice vacancies. It was suggested that the reduction in annealing time for higher T_O was due to the larger number of divacancies or other vacancy aggregates at higher temperatures. Divacancies (26) and certain larger vacancy groups (27)* are expected to have lower activation energies for motion than single vacancies. Furthermore, clustering of the multiple vacancies may take place in the early stages of the annealing. These clusters may serve as sinks at which single vacancies are annihilated. Thus, the multiple vacancies formed at higher temperatures may cause the entire annealing process to be accelerated. This effect should be particularly important for the quenching and air-cooling experiments on Cu-Al, because of the high initial concentration of vacancies. In fact, the multiple vacancies at the higher temperatures may cause the annealing to be sufficiently rapid during the cooling to prevent the retention of vacancies characteristic of these temperatures. This would give rise to the maximum in the $\Delta \rho$ vs. T curves in Fig. 6 for quenching and air-cooling.

The annealing measurements after quenching from $450^{\circ}\mathrm{C}$ show that ε_{M} increases as the annealing proceeds. This behavior also suggests that there is more than one annealing entity and that the predominant motion shifts during the course of the annealing from the defects having lower activation energies for motion to those having higher energies. The average number of vacancy jumps, n_{J} , that a vacancy makes before it is annihilated may be estimated from the annealing data. For annealing at a constant temperature, the number of jumps is given by

$$n_J = \tau \Gamma \tag{6}$$

where τ is the time for the annealing and Γ is the jump rate. Γ may be written

$$\Gamma = Z\nu \exp(S_M/k) \exp(-\varepsilon_M/kT) \tag{7}$$

where Z=12, $\nu \simeq 10^{13} \text{ sec}^{-1}$, and $\exp (S_M/k) \simeq 1$. For the vacancies that are being annihilated when the process is half over, we find that $n_J = 5 \times 10^4$ jumps, using $\varepsilon_M=0.88~{\rm eV}$ for f=0.5 (Fig. 9). This number of vacancy jumps is significantly less than that obtained as a result of quench-annealing measurements on pure metals. For example, Pearson and Bradshaw estimate that n_J is of the order of 10^9 or 10^{10} jumps for Au, (9) Pt, (28) and Al. (29) On the other hand, from 5×10^4 to 10^6 jumps are estimated for Ag-Zn (approximately 30 at.% Zn) as a result of stress relaxation measurements. (14,15) It may be that n_I is characteristically smaller for solid solution alloys than for pure metals, although further work needs to be done to test this point. If n_J in equation (6) is calculated for values of τ and ε_M corresponding to other values of f, it is found that $n_J=2\times 10^6\,\mathrm{jumps}$ for f = 0.9 and decreases with decreasing values of f. A decrease in the number of jumps as the annealing proceeds is to be expected, if the clusters formed by the vacancies that anneal early in the process act as sinks for those that anneal later. The argument remains the same if the clusters are considered to collapse and form dislocation loops, since these loops may then serve as vacancy sinks. Such dislocation loops have been seen in the electron microscope for quenched aluminum. (30) At the outset of the annealing, only pre-existing dislocations would serve as sinks. The necessary dislocation density, d, may be calculated from n_J on the assumption that each site on a dislocation line constitutes a point where vacancies may be annihilated. Then, the number of annihilation sites per cm³ is d/a_0 where a_0 is the lattice parameter. Since the total number of lattice sites per cm³ is of the order of a_0^{-3} , on the average only one jump in every da_0^2 jumps is to an annihilation site, whereby $n_J =$ $1/da_0^2$. Early in the annealing process (f = 0.9), we find $n_{J} = 2 \times 10^{6}$ from which we deduce a dislocation density of about 5×10^8 dislocations per cm². This appears to be a reasonable value for an upper limit (since d(f = 0.9) > d(f = 1.0)) to the concentration of pre-existing dislocations. But, if the subsequent annealing were to continue to be at dislocations, the concentration of dislocations would have to increase rapidly. For example, at f = 0.5, $n_J = 5 \times 10^4$ jumps, which corresponds to a dislocation density of about 2×10^{10} dislocations per cm². It should be mentioned that the use of the observed activation energies (Fig. 9) in equations (6) and (7) to calculate n_J is based on the assumption that the observed ε_M 's are indeed the energies with which defects annealing at a given stage of the process move. Whether this

19

^{*} The authors are indebted to A. K. Seeger for the opportunity to see reference 27 in advance of publication.

assumption is correct depends upon the details of the activation energy spectrum and the distribution of sinks.

In an alloy containing a solute concentration of 15 at.%, it is unlikely that the equilibrium atomic arrangement is a completely random one. Indeed, recent measurements in this Laboratory (31) of the X-ray diffuse scattering from an annealed and a neutron-irradiated single crystal of Cu-Al have indicated that the alloy contains a significant amount of short-range order. It is important, therefore, to consider the possibility that the extra resistivity at temperatures above 200°C is due to a decrease in the equilibrium short-range order. Unfortunately, little theoretical information (12,32) is available concerning the relation between short-range order and electrical resistivity. Also, resistivity measurements have led to the conclusion that an increase in short-range order increases the resistivity of $\mathrm{Cu_3Au^{(33)}}$ and decreases the resistivity of Cu-Zn. (34) Nevertheless, since the atomic rearrangements during the ordering process occur by a vacancy mechanism, the kinetics of ordering are governed by the concentrations and mobilities of vacancies. Therefore, much of the above discussion concerning the quench-annealing measurements applies also to the case of ordering. On this basis, an interesting possibility presents itself for an explanation of the maxima in the quenching and air-cooling curves in Fig. 6. It may be that, although the major effect of the quenching is to retain lesser amounts of shortrange order, vacancies are also quenched in at the higher temperatures. The additional vacancies may accelerate the ordering reaction, so that there is a tendency to maintain equilibrium short-range order during the cooling from higher temperatures.

VOL.

1959

ACKNOWLEDGMENTS

The advice and co-operation of D. S. Billington and other members of the Solid State Division are greatly appreciated. We wish also to thank H. B. Huntington.

J. H. Crawford, Jr., and D. K. Holmes for helpful discussions. Kind assistance was furnished by J. E. Thomas in the making of measurements and by F. A. Sherrill, J. A. Milko and J. B. Flynn in the preparation of the samples.

REFERENCES

- 1. M. S. Wechsler and R. H. Kernohan, J. Phys. Chem. Solids. 7, 307 (1958).
- 2. D. B. ROSENBLATT, R. SMOLUCHOWSKI and G. J. DIENES, J. Appl. Phys. 26, 1044 (1955).
- 3. A. C. Damask, J. Phys. Chem. Solids 4, 177 (1958).
- 4. M. S. WECHSLER, Acta Met. 5, 150 (1957).
- 5. C. J. MEECHAN and R. R. EGGLESTON, Acta Met. 2, 680 (1954).
- 6. J. F. NICHOLAS, Acta Met. 3, 411 (1955).
- P. Jongenburger, Phys. Rev. 106, 66 (1957).
 J. E. Bauerle and J. S. Koehler, Phys. Rev. 107, 1493 (1957)
- 9. F. J. Bradshaw and S. Pearson, Phil. Mag. 2, 379 (1957).
- 10. J. W. Kauffman and J. S. Koehler, Phys. Rev. 97, 555 (1955)
- 11. B. G. Lazarev and O. N. Ovcharenko, Dokl. Akad. Nauk. S.S.S.R. 100, 875 (1955).
- See T. Broom, Advance Phys. 3, 26 (1954).
- 13. W. J. STURM and M. S. WECHSLER, J. Appl. Phys. 28, 1509 (1957).
- 14. A. S. Nowick and R. J. Sladek, Acta Met. 1, 131 (1953).
- 15. A. E. ROSWELL and A. S. NOWICK, Trans. Amer. Inst. Min. (Metall) Engrs. 197, 1259 (1953).
- 16. W. M. LOMER, Institute of Metals Monograph No. 23, p. 79. London (1957).
- 17. L. C. R. ALFRED and N. H. MARCH, Phil. Mag. 2, 985 (1957).
- 18. J. HINO, C. TOMIZUKA and C. WERT, Acta Met. 5, 41 (1957).
- 19. P. Jongenburger, Appl. Sci. Res. B 3, 237 (1953).
- 20. C. ZENER, J. Appl. Phys. 22, 372 (1951).
- 21. A. D. LECLAIRE, Acta Met. 1, 438 (1953).
- 22. H. Brooks, Impurities and Imperfections, p. 1. American Society for Metals, Cleveland (1955).
- 23. H. B. Huntington, G. A. Shirn and E. S. Wajda, Phys. Rev. 99, 1085 (1955). 24. C. Y. Li and A. S. Nowick, Phys. Rev. 103, 294 (1956).
- 25. J. S. Koehler, F. Seitz and J. E. Bauerle, Phys. Rev. 107, 1499 (1957).
- 26. J. H. BARTLETT and G. J. DIENES, Phys. Rev. 89, 848 (1953).
- 27. A. K. Seeger, Ser. V, Proceedings of the Second International Conference on the Peaceful Uses of Atomic Energy, 1958. Pergamon Press, New York.
- 28. F. J. Bradshaw and S. Pearson, Phil. Mag. 1, 812 (1956).
- 29. F. J. Bradshaw and S. Pearson, Phil. Mag. 2, 570 (1957).
- P. B. Hirsch, J. Silcox, R. E. Smallman and K. H. Westmacott, *Phil. Mag.* 3, 897 (1958).
- 31. B. S. Borie, private communication.
- 32. J. B. Gibson, J. Phys. Chem. Solids 1, 27 (1956).
- A. C. Damask, J. Phys. Chem. Solids 1, 23 (1956).
 A. C. Damask, J. Appl. Phys. 27, 610 (1956).

PLASTIC ANISOTROPY OF LIF AND OTHER ROCKSALT-TYPE CRYSTALS*

J. J. GILMAN†

The stresses needed to cause (110) dislocations to move on (100) as compared with (110) planes have been measured in torsion tests in LiF and in potassium halide crystals. Glide is much more difficult on (100) planes than on (110) planes in LiF, except for temperatures above about 400°C.

It is shown that the ease of $\{100\}$ glide increases relative to $\{110\}$ glide through the series KCl \rightarrow KBr \rightarrow KI and that PbTe prefers to glide on $\{100\}$ planes. Thus $\{100\}$ glide seems to be favored by high ionic polarizability as Buerger first suggested.

These results show that the atomic structures at the cores of dislocations play an important role in the behaviors of alkali halide crystals.

ANISOTROPIE DE PLASTICITÉ DES CRISTAUX DE FLUORURE DE LITHIUM ET D'AUTRES CRISTAUX DU TYPE CHLORURE DE SODIUM

Les tensions nécessaires pour provoquer le mouvement des dislocations $\langle 110 \rangle$ sur les plans $\{100\}$ comparées à celles nécessaires pour les déplacements sur les plans $\{110\}$ ont été mesurées par des essais de torsion sur des cristaux de fluorure de lithium et d'halogénure de potassium. Le glissement est beaucoup plus difficile sur les plans $\{100\}$ que sur les plans $\{110\}$ dans le fluorure de lithium, excepté pour les températures supérieures à 400° C environ. On peut montrer que la facilité de glissement sur les plans $\{100\}$ vis-à-vis du glissement sur les plans $\{110\}$ s'accroit suivant la série de cristaux KCl \rightarrow KBr \rightarrow KI et que dans les cristaux de PbTe, le glissement se fait de préférence sur les plans $\{100\}$. Ainsi le glissement sur les plans $\{100\}$ semble être favorisé par l'aptitude à l'ionisation élevée, comme Buerger l'a le premier suggéré. Ces résultats montrent que la structure atomique au coeur des dislocations joue un rôle important pour le comportement des cristaux d'halogénures alcalins.

PLASTISCHE ANISOTROPIE VON LIF UND ANDEREN KRISTALLEN MIT STEINSALZSTRUKTUR

An Hand von Torsiionsversuchen mit LiF und Kalium-Halogenidkristallen wurden die zur Bewegung einer (110)-Versetzung auf $\{100\}$ - und $\{110\}$ - Ebenen notwendigen Spannungen gemessen und miteinander verglichen. Die Gleitung ist bei LiF auf $\{100\}$ - Ebenen viel schwieriger als auf $\{110\}$ - Ebenen, ausgenommen bei Temperaturen oberhalb von etwa 400° C.

Es wird gezeigt, dass die Bevorzugung der $\{100\}$ -Gleitung vor der $\{110\}$ -Gleitung in der Reihe $KCl \to KBr \to KJ$ zunimmt und dass bei PbTe die Gleitung auf $\{100\}$ -Ebenen bevorzugt wird. Demnach scheint eine hohe Polarisierbarkeit der Ionen die $\{100\}$ -Gleitung zu begünstigen, wie zuerst Buerger vermutete.

Die Ergebnisse zeigen, dass die atomaren Strukturen in den Versetzungskernen für das Verhalten der Alkali-Halogenide eine wichtige Rolle spielen.

1. INTRODUCTION

Although they much prefer to glide on {110} planes, LiF crystals can be forced to glide on {100} planes by means of a suitable stress distribution. At the same time their glide direction remains fixed at \$\langle\$110\$. This plastic anisotropy is of interest for several reasons. First, because elementery criteria such as that of Chalmers and Martius (10) predict that {100} should be the preferred glide plane in LiF. Second, because this is a clear cut instance in which the detailed structure at the core of a glide dislocation plays an important role in the plastic behavior of crystals. Third, because some rocksalt-type crystals prefer to glide on {110} planes and others on {100} planes. Why? Finally, knowledge of plastic anisotropy as a function of

temperature gives some insight to the temperature dependence of plastic flow in general.

A series of excellent papers by M. J. Buerger⁽¹⁾ first spotlighted the "anomalous" behavior of rock-salt-type crystals with respect to their glide planes. Buerger studied and compiled the glide elements for many crystals. (His results plus later results for LiF and the silver halides are given in Table 1.) He found that while the primary glide direction in NaCl-type crystals is always \$\langle 110 \rangle, \dagger^+\$ some compounds prefer \$\langle 100 \rangle\$ glide planes (PbS, PbTe), some prefer \$\langle 110 \rangle\$ glide planes (LiF, MgO, NaCl), and some are in between (KBr, KI and especially the silver halides). The most fundamental property which Buerger could find that showed good correlation with this behavior

^{*} Received October 22, 1958.

[†] General Electric Research Laboratory, Schenectady, New

 $[\]mbox{\ \ \ }^+_+$ Rachinger $^{(2)}$ disputes this, but see the experimental results in this paper on PbTe.

Table 1. Comparison of the primary glide planes of rocksalt-type crystals with other properties

Crystal	Primary glide plane	e point		C_{11} (10 ¹¹ dyn/em ⁻²)	Cauchy ratio (C_{44}/C_{11})	Elastic anis. $2C_{44}/(C_{11} - C_{12})$	Polarizabilities			
							$^{\alpha^+}_{(10^{-24}~{\rm cm}^3)}$	α^{-} $(10^{-24} \text{ cm}^{3})$	Σ_{α}	- Lattice constant (A)
LiF	110	840	244	11.3	1.4	1.82	0.03	1.0	1.0	4.01
NaF	110	985	215		******		0.18	1.0	1.2	4.62
MgO	110	2500	950	28.6	1.7	1.49	0.09	3.1	3.2	4.20
NaCl	110	801	184	4.9	1.1	0.70	0.18	3.7	3.9	5.63
KCl	110	776	165	4.1	0.89	0.37	0.84	3.7	4.5	6.28
NaBr	110	775	176	3.9	1.0	0.68	0.18	4.8	5.0	5.94
RbCI	110	715	161	_			1.4	3.7	5.1	6.57
KBr	110	730	159	3.5	0.88	0.35	0.84	4.8	5.6	6.58
NaI	110	651	164				0.18	7.1	7.3	6,46
KI	110	723	151	2.7	1.10	0.37	0.84	7.1	7.9	7.05
AgCl	110	455	206	6.0	0.17	0.53	1.70	3:7	5.4	5.55
AgBr	110	434	202	5.6	0.22	0.63	1.70	4.8	6.5	5,76
PbS	100	1114	650	10.2	0.66	0.78	3.1	10.2	13.0	5.97
PbTe	100	904	620	-		_	3.1	14.0	17.0	6.34

is ionic polarizability.* Crystals with high polarizabilities tend to glide on {100} planes, and Mueller⁽³⁾ gave a semi-quantitative rationalization of this fact. Later, Stepanov obtained data for AgCl and AgBr,⁽⁴⁾ and he also concluded that polarizability is an important factor, because AgCl and NaCl have similar lattice energies (Table 1), but very different plastic behaviors.

The first quantitative measurements of plastic anisotropy were made by Dommerich⁽⁵⁾. She stressed variously orientated NaCl crystals and found that the critical shear stress for $\{100\}$ glide was 240 g mm⁻² in comparison with 76 g mm⁻² for $\{110\}$ glide.

1959

Recent theoretical work has been done by Huntington, Dickey and Thomson⁽⁶⁾. It will be discussed after the present experiments have been described.

2. EXPERIMENTAL RESULTS

The present experiments make use of a fact that has been established through etch-pit studies of dislocations in LiF crystals.⁽⁷⁾ This is that the yield stress of a crystal is proportional to the stress that is required to move dislocations at moderate velocities through the crystal. Therefore, the yield stress values that are reported here indicate relative dislocation mobilities.

In a tension, compression, or bend test of a cleaved rod of a NaCl-type crystal, four of the primary glide planes {110} lie at angles of 45° to the direction of the principal stress. Thus they experience the maximum applied shear stress, and all of the deformation occurs on them. However, in a torsion test, the plane of maximum shear stress is perpendicular to the

Square mono-crystalline rods ($\frac{1}{8} \times \frac{1}{8} \times 1\frac{1}{2}$ in.) were cleaved from larger blocks that were purchased from the Harshaw Chemical Company. About $\frac{1}{2}$ in. at the end of each rod was coated with electroplater's stop-off lacquer, and the central section was reduced in size by means of chemical polishing. (8) This procedure was used for LiF, KCl, KBr and KI.

2.1. Lithium fluoride

The LiF specimens were then mounted in a torsion jig that was loaded by means of an Instron testing machine and torque-deflection curves were recorded. The rate of twisting was 2.2×10^{-9} rad sec⁻¹, giving a strain rate of about 2.2×10^{-6} sec⁻¹. It was found that the specimens broke brittlely at room temperature, so a small furnace was constructed to heat the center of the gage length to a few hundred degrees centigrade. Then it was found that the crystals suddenly yielded at critical torques that depended strongly on the test temperature. Yielding was usually accompanied by a small drop in the torque followed by rapid hardening.

When a torque, T, is applied to a square bar of thickness, b, the maximum shear stresses occur at the middles of the sides and have the values:⁽⁹⁾

torsion axis. Hence, it is parallel to a {100} plane if the torsion axis is parallel to an edge of a cleaved rod. Furthermore, there is a zero shear stress on {110} planes because they lie parallel to the directions of the principal stresses. As a result, NaCl-type crystals can be forced to glide on {100} planes if they are stressed in pure torsion, and this was the method used in this work.

^{*} It may be seen in Table 1 that things like the lattice energy and the melting points do not show good correlation, because the lead and silver compounds break the trends.

Shear stresses that were calculated in this way from the critical yielding torques are given in Fig. 1. For comparison, the results of some previous bend tests (8) in which $\{110\}\ \langle 110\rangle$ was the operative glide system are also plotted. The strain rate in the bend tests was somewhat higher ($\sim\!\!3=10^{-5}~{\rm sec}^{-1}$) than in the torsion tests, but this has only a small effect on yield stresses.

Macroscopic and microscopic examinations made it clear that glide did indeed occur on \$\{100\}\$ planes of the twisted crystals. Some of the evidence is given in Fig. 2 which shows crystals etched so as to develop dislocation etchpits. Fig. 2a shows a band of pits that lies parallel to a (100) plane, and Fig. 2b shows similar bands at high magnification. Because of the catastrophic yielding of the crystals there was usually a substantial amount of glide in them before a test could be stopped. Thus the glide bands were quite broad. Also, the bands tended to have quite irregular shapes as compared with the straight bands after \$\{110\}\$ glide. The bands were parallel to either the transverse \$\{100\}\$ plane or one of the \$\{100\}\$ planes that was parallel to the twist axis.

It was not clear from the torsion tests what the operative glide direction was. It could be any direction lying in the $\{100\}$ planes with the most likely candidates being $\langle 110 \rangle$ or $\langle 100 \rangle$. In order to settle the question, shear tests were made.

The shear test specimens were in the form of square rods about $\frac{1}{8}$ in. square and $1\frac{1}{2}$ in. long. These rods were gripped at each end and over about $\frac{1}{2}$ in. of their center section. On each side of the center section was a short section that was not in the grips. These ungripped sections were the portions of the crystals that were subjected to shearing forces. In order to minimize the bending moments, and maximize the shearing stresses, the shear sections were made quite short: 0.020 in. Two shearing jigs were used. One held crystals so that the shearing force was parallel to $\langle 100 \rangle$; and the other $\langle 110 \rangle$. In both cases the plane of shear was $\{100\}$. The jigs were attached to long pull rods so that they could be enclosed by a furnace on the Instron machine.

At low temperatures the LiF crystals could not be sheared plastically; they always fractured first. However, at temperatures above about 500°C plastic shearing occurred. It occurred most easily in the $\{110\}$ directions. For example, at 600°C the shear stress to cause $\{100\}\langle110\rangle$ shear was $\sim\!380~\text{g mm}^{-2}$, whereas for $\{100\}\langle100\rangle$ shear it was $\sim\!530~\text{g mm}^{-2}$ (values are averages of three tests each).

It may be seen in Fig. 1 that the yield stress in torsion at 600°C was 400–600 g mm⁻², and this is

consistent with the shear tests. Also, the fact that the stress for $\langle 100 \rangle$ shear was about $\sqrt{2}$ times the stress for $\langle 110 \rangle$ shear suggests that dislocations with $\langle 100 \rangle$ Burgers vectors were not involved in the shear tests at all. Rather, two sets of $\langle 110 \rangle$ dislocations gave net shears in $\langle 100 \rangle$ directions.

On the basis of the shear test results, it is concluded that $\langle 110 \rangle$ was the operative glide direction in the LiF torsion tests.

2.2. Potassium halides

The results of tests on KCl, KBr and KI are given in Table 2. These tests were all performed at room temperature which means an almost constant homologous temperature since these crystals have melting points that are nearly equal (Table 1). The surfaces of the twisted crystals exhibited $\{100\}$ glide bands when they were examined after the tests and the compressed crystals exhibited (100) birefringence bands; thus the expected glide planes were operative. It may be seen that the stress for $\{100\}$ glide increases progressively through the series KI \rightarrow KBr \rightarrow KCl, while the stress for $\{110\}$ glide remains roughly constant.

Table 2. Comparison of yield stresses for {100} and {110} glide in potassium halides

VOI

19

G I	Yield stre	sses (g mm ⁻²)	Ratio	
Crystal	Torsion	Compression	$\left(\frac{\text{corp.}}{\text{comp.}}\right)$	
KI	187	39	4.8	
KBr	290	42	6.9	
KCl	380	36	10.5	

2.3. Lead telluride

Since Rachinger⁽²⁾ states that $\langle 100 \rangle$ is the *primary* glide direction in PbTe, whereas Buerger states that $\langle 110 \rangle$ is the *primary* direction, some check experiments were made. These experiments were more direct than those of either Buerger or Rachinger.

Crystals of PbTe about 5 mm dia. and 12 mm long were compressed (yielding at about 700 g mm⁻²). The direction of compression was roughly parallel to a (111) direction so that all possible glide planes and directions were subjected to roughly equal shear stresses. From the orientations and intensities of the glide lines along the glide ellipses, the glide plane {100} and glide direction [110] were determined. Thus Buerger's result is confirmed, and Rachinger's is in doubt.

3. DISCUSSION

The plastic anisotropy of LiF is very large. Fig. 1 shows that the temperature must be raised $400-600^{\circ}\text{K}$ to cause $\{100\}$ glide at the same stress as $\{110\}$

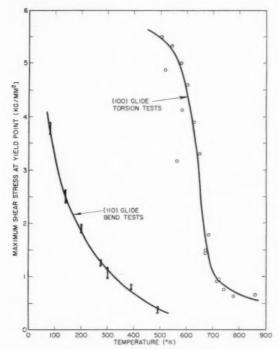
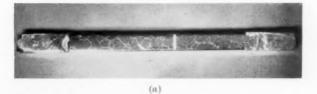
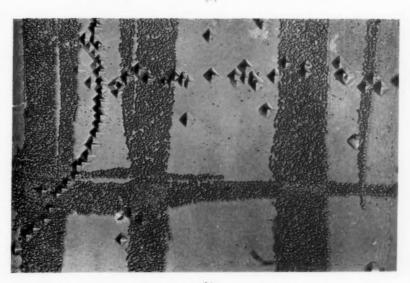


Fig. 1. Comparison of stress for (100) glide with stress for (110) glide in LiF crystals.





(b) Fig. 2. Crystals etched before and after torsion tests. (a) Single broad glide band on $\{100\}$ plane in crystal that was twisted at $300^{\circ}\mathrm{C}$. $\times 2$. (b) Dislocation etch pits in $\{100\}$ glide bands. Torsion axis was horizontal. $\times 250$.

VOL. 7 1959 glide. In terms of stress, there is a factor of about 15 between the stress for {100} and {110} glide at 500°K. Let us consider what explanations are possible for this behavior in terms of dislocation theory. We must keep in mind that PbS and PbTe are also anisotropic, but in the opposite sense to LiF.

Fig. 3 illustrates gliding on the two different planes. The Burgers vector, **b**, is the same in both cases, but the planes have a spacing of $a=d_0$ for $\{100\}$ glide and $d_0\sqrt{2}$ for $\{110\}$ glide. Thus the criterion of Chalmers and Martius⁽¹⁰⁾, that $\beta=b/a$ should be a minimum for the primary glide plane, fails.

Since the simple geometric model fails we next consider the anisotropy of the elastic constants of rocksalt-type crystals. In Table 1 it may be seen that neither the magnitude of the elastic constant, C_{11} , nor the anisotropy constant, A,* correlates with the observed primary glide plane. However, the refined anisotropic theory of Eshelby(11) does give some correlation with experiment. For convenience in calculating the constants of Eshelby's theory, the formulas worked out by Foreman(12) for cubic crystals were used. Calculations were made for LiF and PbS because these are the most extreme cases for which elastic constant data are available. Average elastic constants for LiF, including the most recent work by Briscoe and Squire⁽¹³⁾, were used; and for PbS, the values found by Ramachandran and Wooster⁽¹⁴⁾. The values are:

	LiF	PbS
$c_{11} \\ c_{12} \\ c_{44}$	$11.3 \times 10^{11} \mathrm{dyn/cm^{-2}} \ 4.4 \times 10^{11} \mathrm{dyn/cm^{-2}} \ 6.3 \times 10^{11} \mathrm{dyn/cm^{-2}}$	$10.2 \times 10^{11} \mathrm{dyn/cm^{-2}} \ 3.8 \times 10^{11} \mathrm{dyn/cm^{-2}} \ 2.5 \times 10^{11} \mathrm{dyn/cm^{-2}} \ $

From these constants and the lattice constants, the elastic energy factors, K; the dislocation widths, w; and the Peierls stresses, τ_p ; were calculated (Table 3).

The values of K and τ_p given in Table 3 show that the anisotropic elastic theory predicts the correct glide planes in LiF and PbS crystals. However, this can be considered to be little more than a trend because the differences in the predicted energies and stresses are small, and the Peierls stresses are much larger than can be expected. Furthermore, if one does not use the extreme case of LiF but passes to NaCl, then the elastic theory makes the wrong prediction. (6) Therefore, it seems clear that one must look beyond the elastic theory for an explanation of the behavior.

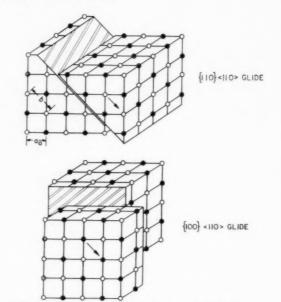


Fig. 3. Translation gliding in the same direction, but on two different planes in crystals with the rocksalt structure.

Huntington, Dickey and Thomson(6) have calculated the energies of dislocations in NaCl by considering the interionic forces explicitly. For the energy of a {110} (110) edge dislocation they give the value $(1.81 \ln R/a + 1.37) \times 10^7 \, \text{eV cm}^{-1}$, and for a $\{100\}\langle110\rangle$ edge dislocation (1.62 ln $R/a+3.8) imes 10^7$ eV cm⁻¹. Here the first terms are the elastic energies and the second terms are "core" energies. Although the $3.8 \times 10^7 \, \mathrm{eV} \, \mathrm{cm}^{-1}$ core energy for the {100} dislocation is only an estimate, it is considerably greater than the core energy for the {110} dislocation. Also, Huntington et al. suggest that one might expect a large Peierls stress ($\sim 2.2 \times 10^9 \, \mathrm{dyn/cm^{-2}}$) for {100} dislocations because of repulsions between the cores of the chlorine ions. This Peierls stress is of the right order of magnitude to explain the present results for LiF, although it is a very approximate value.

19

The point of this discussion thus far has been that the glide plane in NaCl-type crystals seems to be determined by the structure of the cores of the glide dislocations so that detailed calculations of the type that Huntington *et al.* have carried out are required to adequately explain the observations. However, a

Table 3. Parameters for edge dislocations using anisotropic elastic theory

	$K (10^{11} \mathrm{dyn/em^2})$		w		$\tau_p (10^{10} \mathrm{dyn/cm^2})$	
	(100)	(110)	(100)	(110)	(100)	(110)
LiF PbS	7.8 3.9	5.8 4.1	$0.62a_0 \\ 0.78$	$0.60a_{9} \\ 0.45$	4.3 1.4	$\frac{3.4}{3.5}$

^{*} $A=2C_{44}/(C_{11}-C_{12})=$ ratio of shear constant on $\{100\}$ planes to shear constant on $\{110\}$ planes.

simple qualitative picture of the situation can be gained by applying the results of Buerger and Mueller to dislocations.

Buerger⁽¹⁾ pointed out that when the two halves of a NaCl-type crystal are in the mid-glide position (displacement = b/2) on a {100} plane, the electrostatic binding is completely destroyed. This is because only repulsive forces exist between nearest neighbors across the glide plane. This same thing happens at the core of a {100} (110) dislocation. Since the binding is destroyed, the surfaces on either side of the glide plane are free surfaces. If the energy that is needed to create these surfaces is dissipated as a dislocation moves, then a stress will resist the dislocation motion. This stress will be simply $2\gamma/\mathbf{b}$, where γ is the specific surface energy. Gamma is about 190 ergs cm⁻² for LiF so the resistive stress would be $\sim 1.3 \times 10^{10} \, \mathrm{dyn}/$ cm⁻². This is more than enough to account for the resistance of LiF to {100} glide.

Buerger showed that the relative sizes of the ions in rocksalt-type crystals do not determine their plastic behavior. He suggested, and Mueller(3) made a detailed analysis to show, that the polarizability of the ions can be expected to have an important effect. Mueller's analysis indicates that {100} glide is favored by high polarizabilities whereas {110} glide is relatively unaffected. The same would be true for calculations like those of Huntington, Dickey and Thomson. The ionic polarizabilities, a, and their sums are listed in Table 1, and it may be seen that the tendency for {100} glide to occur increases with increasing polarizability (or ion size). The same trend is seen in Table 2 at constant homologous temperature.

VOL.

1959

The trend in Table 1 appears to be broken by the silver halides. However, if one considers the fraction of the binding energy that is contributed by Van der Waals forces rather than simply the polarizability, then the trend is restored. This agrees with the monotonic increase in electrical conductivity that occurs from top to bottom in Table 1.

The temperature dependence of {100} glide in LiF has special significance. The line tensions of {100} and {110} dislocations are approximately the same and are not sensitive to temperature because they consist mostly of elastic energy. Therefore, it is not feasible to explain the large temperature differences in Figure 1 on the basis of a temperature activated process which involves the elastic energy of a dislocation (like the unpinning of loops of dislocations, for example). It seems clear in this case that {100} glide becomes active when it does because of changes that occur in the crystal lattice as its temperature

is increased. Thus the process may not be "temperature activated" but may become active when the "Peierls force" decreases sufficiently to allow flow to occur at the applied stress level.

4. SUMMARY

Measurements are reported of the stresses required to cause LiF crystals to glide on {100} planes, and evidence is given to show that the glide occurs in (110) directions. The measured stresses for {100} (110) glide are much higher at given temperatures than the stresses for {110}(110) glide, and they are strongly temperature dependent.

Measurements in the series of potassium halides (KCl, KBr, KI) have been made, and they indicate that {100} glide is favored by increasing polarizability of the ions.

The primary glide elements of PbTe have been checked and found to be {100}(110), in agreement with the previous result of Buerger.

Elementary elastic dislocation models cannot explain the above results. The behavior of LiF and its relation to the behavior of other rocksalt-type crystals can only be explained in terms of the core structures of dislocations.

ACKNOWLEDGMENTS

The mechanical tests that are described here were performed by Mr. V. J. DeCarlo. The author is indebted to Dr. M. L. Kronberg for bringing his attention to the papers of Buerger, and to Dr. W. G. Johnston who contributed constructive criticism of the manuscript. Dr. R. Newman provided a PbTe crystal.

REFERENCES

- 1. M. J. Buerger, Amer. Min. 15, 21, 35 (1930).
- W. A. Rachinger, Acta Met. 4, 647 (1956).
- H. MUELLER, Amer. Min. 16, 237 (1931).
 A. W. STEPANOV, Phys. Z. Sowjet. 6, 312 (1934); Ibid. 8, 25 (1935).
- S. Dommerich, Z. Phys. 90, 189 (1934).
- 6. H. B. Huntington, J. E. Dickey and R. Thomson, Phys. Rev. 100, 1117 (1955)
- 7. W. G. JOHNSTON and J. J. GILMAN, Jour. Appl. Phys. 30, 129 (1959).
- 8. J. J. GILMAN and W. G. JOHNSTON, Dislocations and Mechanical Properties of Crystals, p. 116. Wiley, New York (1957).
- 9. S. TIMOSHENKO and G. MACCULLOUGH, Elements of the Strength of Materials, p. 82. Van Nostrand, New York (1940).
- B. CHALMERS and U. MARTIUS, Proc. Phys. Soc. A 213, 175 (1952); Nature, Lond. 167, 681 (1951).

- J. D. ESHELBY, Phil. Mag. 40, 903 (1949).
 A. J. E. FOREMAN, Acta Met. 3, 322 (1955).
 C. V. BRISCOE and C. F. SQUIRE, Phys. Rev. 106, 1175 (1957)
- 14. G. N. RAMACHANDRAN and W. A. WOOSTER, Acta Cryst., Camb. 4, 431 (1951).
- 15. C. KITTEL, Introduction to Solid State Physics. Wiley, New York (1953).
- R. F. S. Hearmon, Advanc. Phys. 5, 323 (1956).
- 17. L. Pauling, Proc. Roy. Soc. A, 114, 181 (1927).

CREEP IN FACE-CENTRED CUBIC METALS WITH SPECIAL REFERENCE TO COPPER*

P. FELTHAM† and J. D. MEAKIN†

The equilibrium creep rate of oxygen-free high-conductivity copper (99.99%) of constant grain size, subject to constant stress (σ) in vacuo in the range 400–700°C, was found to satisfy the relation $\dot{\epsilon} = A_0(T) \exp{[-(H-q\sigma)/kT]}$. Two sets of the parameters A_0 , H and q were however required at any given temperature, one below and one above a critical tensile stress $\sigma_c(T)$, above which Cottrell–Lomer locking appeared to become a less effective impediment to slip than at lower stresses. Vacancies travelling along dislocations from grain boundaries to jogs are thought to assist the climb of edge dislocations, which process seems to be rate determining. The activation energies H and H' (below σ_c') are therefore reduced below the value expected for self-diffusion to 32 and 28 keal/g atom, respectively, which are close to the activation energy for vacancy migration. Cross-slip and polygonization appear to take place in the transient stage of creep. In single crystals H was found to be equal to the activation energy for self-diffusion (49 kcal/g atom) over the same temperature range.

LE FLUAGE DANS LES MÉTAUX CUBIQUES A FACES CENTRÉES ET SPECIALEMENT DANS LE CUIVRE

La vitesse de fluage dans la zone de fluage à vitesse constante pour un cuivre de haute conductibilité exempt d'oxygène et à grains de grosseur constante, satisfait à la relation $\dot{e}=A_0(T)$ exp $[-(H-q\sigma)/kT]$, lorsque l'essai est réalisé sous vide à une tension constante σ et pour des températures de 400 à 700°C. Deux groupes de paramètres A_0 , H et q sont cependant nécessaires à chaque température, l'un pour les tensions supérieures à la tension critique de traction σ_c ' (T) et l'autre pour les tensions inférieures à cette valeur. Au-dessus de celle-ci, le blocage de Cottrell-Lomer deviendrait un obstacle au glissement moins actif que pour les tensions faibles. On pense que les lacunes se déplaçant le long des dislocations en partant des joints de grains vers les crans des dislocations aident à la montée des dislocations-coins. Les énergies d'activation H et H' (en-dessous de σ_c ') sont réduites à une valeur inférieure à celle que l'on pouvait s'attendre à partir de l'auto-diffusion; elles sont respectivement de 32 et de 28 kg cal/atome gr., cette dernière valeur étant proche de l'énergie d'activation pour la migration des lacunes. La déviation de glissement et la polygonisation sont des phénomènes qui apparaissent au cours du fluage transitoire. Dans les monocristaux, la valeur H a été trouvée égale à l'énergie d'activation pour l'auto-diffusion (49 kg cal par atome gr.) pour la gamme de températures envisagée ci-dessus.

DAS KRIECHEN VON KUBISCH-FLÄCHENZENTRIERTEN METALLEN UNTER BESONDERER BERÜCKSICHTIGUNG VON KUPFER

OFHC-Kupfer (99,99%) mit gleichmässiger Korngrösse wurde im Vakuum im Temperaturbereich von 400–700°C mit einer konstanten Spannung (σ) belastet; dabei ergab sich eine stationäre Kriechgeschwindigkeit, die der Beziehung $\dot{\varepsilon}=A_0(T)\exp{[-(H-q\sigma)/kT]}$ genügt. Es sind jedoch bei jeder Temperatur zwei Sätze von Parametern A_0 , H und q notwendig, einer unterhalb und einer oberhalb von einer kritischen Zugspannung $\sigma_c'(T)$, oberhalb welcher offenbar Lomer–Cottrell-Versetzungen die Gleitung weniger wirkungsvoll behindern können, als bei tieferen Spannungen. Es wird angenommen, dass Leerstellen, die von Korngrenzen entlang Versetzungen zu Versetzungssprüngen wandern, das Klettern von Stufenversetzungen unterstützen; dieser Prozess scheint die Geschwindigkeit zu bestimmen. Die Aktivierungsenergien H und H' (unterhalb σ_c') werden deshalb unter den Wert, den man für Selbstdiffusion erwartet, herabgesetzt auf 32 beziehungsweise 28 keal/g Atom; diese Werte kommen der Aktivierungsenergie für Leerstellenwanderung nahe. Quergleitung und Polygonisation scheinen im Übergangsstadium des Kriechens stattzufinden. Bei Einkristallen ergab sich H in demselben Temperaturbereich zu 49 keal/g Atom, dies ist gleich der Aktivierungsenergie für Selbstdiffusion.

1. INTRODUCTION

The main object of the present work was to study the mechanism of high-temperature creep in facecentred cubic metals in the light of recent theories of the processes of work-hardening⁽¹⁻³⁾ and recovery,^(4,5) both of which are of fundamental importance in creep. Copper was chosen for the experimental work because of all face-centred metals it has been investigated in

most detail, and the available material was thought to be of likely value in the analysis of the results. Also, as copper has a low stacking-fault energy, (6) and therefore forms strong Cottrell–Lomer barriers, its work-hardening characteristics, and hence also its high-temperature creep properties, were anticipated to be different, in some respects at least, from those of metals in which the barriers are weaker and slip is less impeded than in copper at corresponding temperatures, e.g. aluminium and lead. Effects arising from the blocking of slip by barriers were expected to yield

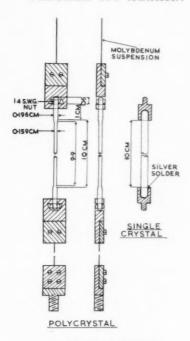
VOI

7

19

^{*} Received January 15, 1958; in revised form October 27, 1958.

[†] The University, Leeds, Yorkshire, England.



SPECIMEN MOUNTING
Fig. 1. Method of mounting specimens.

significant evidence as to the nature of the creep mechanism.

2. MATERIALS AND METHOD

1959

Oxygen-free high-conductivity copper was used in the preparation of all specimens. Analysis showed the "as received" copper to be of purity somewhat better than 99.99 per cent; separate analysis of the content of sulphur and the more common metallic impurities yielded in parts per million: Fe 40, S 8, Ag 6, Ni 5, Pb 4, As 0, Sn 0, and Bi 0.

Specimens with a gauge length of 10 cm were made from cold-drawn rods of 0.2 cm diameter by first etching a length of 9.9 cm of each rod down to 0.17 cm diameter and then finishing the shoulders and polishing to ''0000' on a watch-maker's lathe. The dimensions of a typical specimen are shown in Fig. 1. The length indicated, namely 9.9 cm, is that measured at room temperature; at the temperatures at which creep takes place the length approaches closely to the 10 cm necessary for the proper working of the constant-stress device. The tolerance on the diameter over the gauge length was less than ± 0.005 cm. Specimens intented for micrographic work were electropolished in Jacquet's⁽⁷⁾ reagent prior to insertion into the furnace.

A few single crystals were also required. These were made by Bridgman's method by lowering copper rods sealed into evacuated silica tubes of 0.27 cm bore through a vertical furnace having a hot zone at 1350°C

at a rate of 2 cm/hr. From crystals grown in this manner some with orientations well within the stereographic triangle were selected, and lengths measuring 12 cm were carefully cut from each by means of a small saw. After silver-soldering such a piece into stainless-steel grips a 10 cm gauge length remained exposed (Fig. 1). The constant-stress beam, which was designed for polycrystals, will not maintain the shear stress on the active slip plane of the crystal exactly constant but, as the crystals were used mainly for determinations of activation energies by the method of abrupt temperature changes and for microscopy, the gradual variation of stress during creep was unimportant.

All polycrystalline specimens were vacuum annealed in situ at 650°C for 30 min at a pressure of less than 1μ Hg of air prior to the application of the constant stress. The risk of bending the annealed rods by handling was thus eliminated. This heat-treatment resulted in a stable grain size of $3\times 10^{-3}\,\mathrm{cm}$; the grain size being taken to be the square root of the mean grain area as measured by using a field of vision containing between 200 and 300 grains. Twin boundaries were ignored.

The stress on the polycrystalline specimens was maintained constant by means of an Andrade–Chalmers beam which, together with a differentially wound furnace, was mounted in a steel vacuum chamber. Temperature was measured by means of two chromel–alumel thermocouples, with their junctions almost in contact with the specimen. The furnace temperature was thermostatically controlled; fluctuations around the nominal value were generally less than 1.5°C. Details of the design of the equipment and of the method of measuring strain have been given previously.⁽⁹⁾

The method of abrupt temperature changes, sometimes referred to as "temperature-cycling" (8.10) was utilized to determine the activation energy of the creep process in polycrystals and single crystals. In such a test the temperature is rapidly lowered (or raised) above (or below) the established value by a small amount, e.g. 20–25°C in our case, and the activation energy is obtained from the ratio of the logarithms of the creep rates corresponding to the two temperatures, as will be discussed later. It was found possible to effect such a change in temperature within 1–2 min.

The grain size dependence of the steady creep rate was measured only at 500°C; for that purpose specimens with various grain sizes were obtained by the choice of suitable combinations of annealing times and temperatures from within the ranges 0.3–0.6 hour and 550–700°C, respectively.

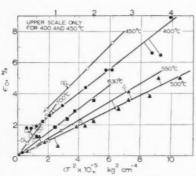


Fig. 2. Dependence of the instantaneous strain ε_0 on the applied tensile stress σ .

3. EXPERIMENTAL RESULTS

3.1. The initial extension

The tensile strain ε_0 , as measured within 1–2 sec after the application of the tensile stress σ at the beginning of a creep test, was expected to obey the work-hardening law⁽¹¹⁾

$$\sigma^2 = \chi_p(\varepsilon_0 - \varepsilon_c), \tag{1}$$

where χ_p , the coefficient of 'parabolic' work-hardening, and the (generally negligible) intercept ε_c of the parabola on the strain axis depend upon the temperature. The measurement of ε_0 is difficult and, although attempts were made to minimize experimental error, the scatter was appreciable. Nevertheless, the results show that the law given by equation 1 was obeyed.* (Fig. 2).

Fig. 3 shows $\log \chi_p$ plotted against T. On extrapolation the line passes through the melting point T_m . The three points at 77, 195 and 293°K were obtained in tensile tests⁽²⁾ with copper from the same stock.

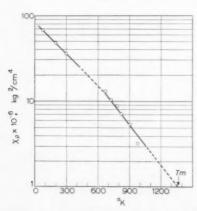


Fig. 3. Temperature-dependence of the coefficient of 'parabolic' work-hardening χ_p .

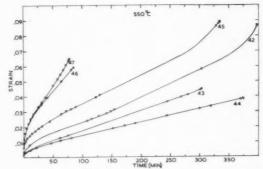


Fig. 4. Creep at 550°C. For curves 42, 43 and 48 multiply the calibration of the time scale by 10, 4 and 2, respectively.

The choice of the semi-log representation was prompted by considerations to be discussed in 4.1.

3.2. Steady state creep and transient creep

A set of typical creep curves is shown in Figs. 4 and 5; curves obtained at other temperatures have been given in full elsewhere. (12) The transition from the transient to the steady stage was generally smooth although in a few cases, particularly at high strain rates, an irregular behaviour such as is well known to indicate recrystallization(9.11.13) was observed, e.g. curve "50" in Fig. 5. In such cases the strain rate eventually attained a steady value close to that observed just prior to the onset of recrystallization. The stress-dependence of the steady creep rate measured in these experiments is shown in Fig. 6. Each isotherm, with the exception of that for 700°C, consists of two linear portions intersecting at a temperature-dependent value of the stress, which we shall refer to as the critical stress σ_c . At 700°C the break in the isotherm may of course exist at a stress below 100 kg/cm².

The transient creep was found to obey the well-known Andrade Law

$$\varepsilon_{\rm tr} = \beta t^{1/3} \tag{2}$$

exemplified by the curves for the runs at 550°C (Fig. 7), which are typical of all such curves obtained in the

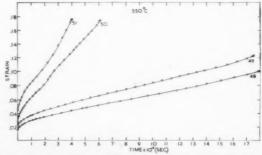


Fig. 5. Creep at 550°C. For curves 42, 43 and 48 multiply the calibration of the time scale by 10, 4 and 2 respectively.

^{*} That the lines for 400 and 450°C do not pass through the origin is thought to be due to the fact that at these comparatively low temperatures the linear part of the work-hardening curve, which precedes the parabolic part, (2) is not yet negligible.

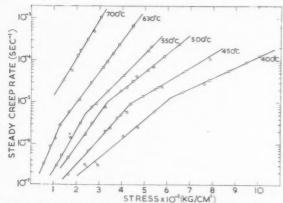


Fig. 6. Creep isotherms of polycrystalline copper of mean grain diameter 3 × 10⁻³ cm.

range 400–700°C. Beyond the arrows significant deviations from this law were however found although the stage of decelerating creep had by no means terminated. We shall revert to the consideration of this anomaly later. A relation between β and the steady creep rate $\dot{\varepsilon}_{\rm st}$ of the form

$$\beta \propto \dot{\varepsilon}_{\rm st}^{1/2}$$
 (3)

is indicated by the data in Fig. 8.

3.3. Tertiary creep and fracture

1959

Tertiary creep was not studied in detail, mainly because some necking generally occurred in the fracture zone of the specimen, and this interfered with the constancy of the stress. Except with the highest creep rates fractures were predominantly intergranular. Not all specimens were extended to the point of fracture. Times to fracture t_f are correlated with the steady strain rate in Fig. 9. A straight line in this representation indicates a power law

$$t_{f} = (K/\hat{\varepsilon}_{st})^{m}, \tag{4}$$

SEC $^{\prime 3}$ Fig. 7. The $t^{1/3}$ -part of the transient creep.

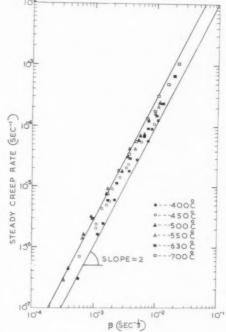


Fig. 8. The relation between the steady creep rate and β . (Equation 3),

where K is a constant having the dimensions of strain. The magnitude of m, corresponding to the line drawn through the points is 1.0.

3.4. Measurement of activation energies

The activation energy H of the steady creep was obtained by the method described by Dorn, ^(8,10) by means of the relation

$$\dot{\varepsilon}_1\!/\dot{\varepsilon}_2 = \exp{[(-H/k)(T_1^{\;-1} - \;T_2^{\;-1})]}. \eqno(5)$$

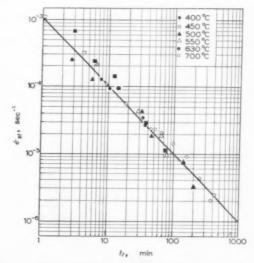


Fig. 9. The relation between the steady creep rate and the time to fracture.

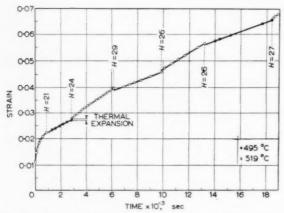


Fig. 10. A typical creep curve obtained on temperaturecycling.

In such a determination the temperature was raised (or dropped) rapidly by 20-25°C, and the steady strain rates corresponding to the two temperatures were recorded. Fig. 10 shows a creep curve obtained in this manner; the last four readings, which lie in the steady stage, give an average activation energy of 27 kcal/g atom. No transients were observed after T_2 had been reached, either on raising or dropping the temperature in this "cycling"; the activation energies were also equal in either case. This was found also to be the case in the $t^{1/3}$ -stage (not studied in the experiment represented by Fig. 10), in which however an activation energy of about 49 kcal/g was obtained. The probable significance of the high activation energy in this stage will be considered in 4.4. The values of H for the steady stage of creep are shown in Fig. 11.

4. DISCUSSION OF EXPERIMENTAL RESULTS

4.1. The initial extension

During the short period in which the actual application of the load to the specimen takes place the latter is in fact subjected to a tensile test at a strain rate of about 10⁻² sec⁻¹, in which however only the last point (σ, ε_0) is recorded. Now, the work-hardening of polycrystalline copper from the same stock as used in the present work had been studied by Feltham and Meakin, (2) and it was desirable to examine the hightemperature stress-strain curves (Fig. 2) in the light of their work. They show that in the range 77-293°K investigated by them χ_{ν} (equation 1) is proportional to the tensile stress σ_e at which Cottrell-Lomer barriers cease to be effective obstacles to the propagation to slip. The temperature-dependence of χ_{ν} should therefore be the same as that of σ_e , and for our purposes it is therefore sufficient to consider the temperature-dependence of the latter parameter.

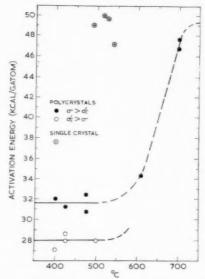


Fig. 11. Temperature dependence of the activation energy H.

If the Cottrell-Lomer barriers fail by a "break-through" mechanism of the type considered by Stroh⁽¹⁴⁾, then it is easily verified from the relation between σ_c^2 and T for copper (his Fig. 4) that

$$\log \left(\sigma_c / G \right) \simeq c_1 - c_2 T, \tag{6}$$

19

where G is the shear modulus and c_1 and c_2 are constants. The linear relation between χ_p and T in semi-log coordinates is already implied by equation 6. However, Seeger and coworkers⁽¹⁾ believe that the mode of failure discussed by Stroh is unlikely to occur in practice, and that the barriers would cease to be effective when dislocations could escape over them by cross-slip. The graphical representation of the activation energy for cross-slip⁽¹⁵⁾ shows that

$$E_{\rm es} \simeq k_1 - k_2 \log \left(\sigma_{\rm c} / G \right), \tag{7}$$

and if the criterion for the occurrence of cross-slip is taken to be $E_{\rm es}=m'kT$, where m' is a constant, then equation 7 gives the same functional form for the temperature-dependence of σ_e as equation (6).

The linearity of the $\log \chi_p$ vs. T relation (Fig. 3) suggests that the mode of hardening during the initial extension is in fact of the same kind as that occurring in tensile tests at lower temperatures. As can be seen (Fig. 3), the line representing the low-temperature data does not extrapolate well to χ_p -values obtained from the initial extension in creep experiments. It would not, in fact, be expected to do so, first because the strain rates in the tensile tests were about an order of magnitude smaller than those prevailing during the initial extension, and second, because of the temperature-dependence of G, and the basically approximate nature of equation (6).

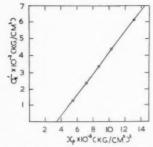


Fig. 12. Relation between the critical tensile stress σ'_c and the coefficient of work-hardening χ_p . The temperatures corresponding to the measured points are given in Table 1.

4.2. Steady state creep

A number of workers $^{(9.16-18)}$ have found the rate equation

$$\dot{\varepsilon}_{\rm st} = A_0 \exp\left(-H/kT\right) \sinh\left(q\sigma/kT\right)$$
 (8)

suitable for the representation of the steady strain rate of creep isotherms of annealed metals in terms of the applied tensile stress σ and the temperature T. The parameters A_0, H and q are independent of σ and, except for $q,^{(19)}$ are generally assumed not to depend upon the temperature. A small variation of A_0 with tepmerature could of course easily escape notice in view of the preponderance of the highly temperature-sensitive exponential term. If $q\sigma/kT$ is greater than about 2, a condition which was fulfilled in all runs in the present work, equation (8) can be written in the form

$$\dot{\varepsilon}_{\rm st} = \frac{1}{2} A_0 \exp\left[-(H - q\sigma)/kT\right],\tag{9}$$

which implies a linear relation between $\log \dot{\varepsilon}_{\rm st}$ and σ at any given temperature. Fig. 6 shows that such a relation exists, but that a fairly abrupt change of slope takes place in each isotherm at a characteristic tensile stress $\sigma_c'(T)$, i.e. q takes a different value below σ_c' than above σ_c' .

The breaks in the curves in Fig. 6 are not artefacts due to the use of an inappropriate representation, as may be seen from the following considerations.

(1) While it is possible to represent the data in Fig. 6 reasonably well by power laws, the exponent of the stress is then neither temperature-independent nor rational, varying from about 3 to about 6 over the temperature range here considered. It is difficult to ascribe any physical significance to such a representation.

(2) The use of a complex law of the form $\sigma^n \exp{(q\sigma/kT)}$, with n a small positive or negative integer, does not result in the disappearance of the inflexion in the isotherms. The case with n=2 was worked out in detail. The curves were not straight, and the systematic temperature-dependence of σ_c shown by the original representation was lost.

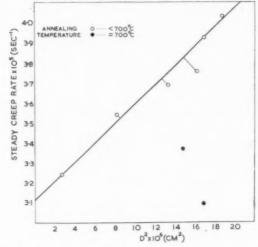


Fig. 13. Grain size dependence of the steady creep rate. $(500^{\circ}\text{C}, 500 \text{ kg/cm}^{2})$.

(3) The temperature-dependence of σ_c appears to be of the same kind as that of χ_p (Fig. 12), which suggests that there may be a definite change in the mode of hardening at σ_c from one characteristic at lower stresses to one in which Cottrell–Lomer barriers are less effective obstacles to the propagation of slip in the work-hardened structure characteristic of the equilibrium. Such a loss of effectiveness would be consistent with the observation that

(4) below σ_{c}' a grain-size dependence of the equilibrium creep rate was not observed, while above σ_{c}' , when the grain boundaries might be expected to become important as barriers to slip, the creep rate was found to be proportional to D^{2} , where D is the mean grain diameter (Fig. 13).

(5) There appears to be a significant difference in the mode of slip apparent in micrographs of specimen surfaces, depending on whether creep had taken place above or below σ_c . In the former case only do slip lines appear to traverse the grains (Figs. 14 and 15).

(6) The activation energy H, as determined by the temperature cycling method, appears to be about 10 per cent larger for creep at stresses above σ_c than for creep below σ_c (Fig. 11).

(7) Finally, the measured points in Fig. 6 show no systematic deviation from linearity either below or above σ_c .

Thus two sets of parameters are required in equation 8, one if $\sigma > \sigma_c'$, which will be denoted by A_0 , H and q, and another one if $\sigma < \sigma_c'$, which will be denoted by A_0' , H' and q'. The values of q and q' are shown in Fig. 16.

It is clear from the graphs that

$$q = q_0 \exp(-E/kT)$$

VOL. 7 1959 and

Fig. 14. Surface of specimen showing etch pit distribution characteristic below σ'_{e} . (500°C, 270 kg/cm²). The etch pits, like those shown in Fig. 15, developed during storage of the specimens in a vacuum dessicator for several months, and are probably due to slow attack by vapours of grease or plasticine.

$$q' = q_0' \exp(-E/kT),$$
 (10)

the activation energy E (=7.0 kcal/g atom) being the same in both cases. The probable significance of equation (10), which has its equivalents for other metals, has been discussed by Feltham⁽¹⁹⁾; we shall return to the consideration of q and q' in Section 5.

As may easily be verified, the isotherms of each set in Fig. 6 converge very nearly to a point on extrapolating, a behaviour of such curves previously noted by Fastov⁽¹⁷⁾. It follows, on writing equation (9) in the form

$$\dot{\varepsilon}_{\rm st} = \frac{1}{2} A \exp{(q\sigma/kT)},\tag{11}$$

that the term

$$A \equiv A_0 \exp\left(-H/kT\right) \tag{12}$$

is virtually temperature independent (Fig. 17), and that consequently the "structure term" A_0 must diminish rapidly with increasing temperature over the major part of the temperature interval here considered. It is important to bear in mind that A_0 is characteristic

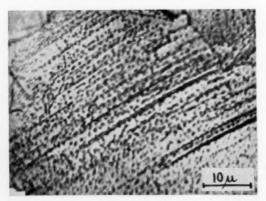


Fig. 15. Etch pits on the surface of a specimen which had crept at 500°C at a stress of 550 kg/cm². The transgranular slip lines are characteristic above σ'_e .

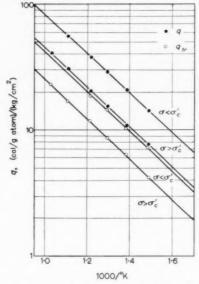


Fig. 16. Temperature-dependence of q and q'. (Equation 10).

of the structure developed in the metal in the course of reaching the steady stage in isothermal creep, the metal being initially annealed and un-loaded. Equations (11) and (12) are therefore equations of the isotherms (Fig. 6), not equations of state of the metal. (20) In fact, the absence of transients and the observation that the same value of H is obtained in a temperature eycling test irrespective of whether $T_2 > T_1$ or $T_2 < T_1$ (equation 5) suggests that if the stress is maintained on the specimen during the transition from one temperature to another one close to it, and if the transition takes place rapidly enough, then virtually no structural changes take place in the metal, and A_0 may be taken to remain constant. This constancy of A_0 will be assumed in dealing with the measurement of activation energies below.

19

While A (equation 11) can be determined from the isotherms of Fig. 6, A_0 and $\exp(-H/kT)$ cannot be separated except by the use of the temperature cycling method, which allows H to be determined.

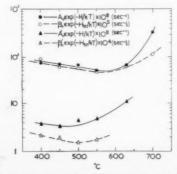


Fig. 17. Temperature dependence of A, A', β and β' .

4.3. Measurement of activation energies

Basinskii⁽²¹⁾ has recently shown that if no recovery occurs in a temperature cycling test in the transition from T_1 to T_2 either, as he assumes, because the temperature is so low that dislocation climb cannot take place or, in our case, because the transition is sufficiently rapid, then equation (5) does not yield H but $H = \eta q_1 \sigma$, where

$$\eta = (T/G)(dG/dT),$$

and G is the shear modulus. On substituting for G and dG/dT values given by Koester $et~al.^{(22)}$, one finds that over the temperature range considered $\eta \simeq 0.1$, so that the value of $\eta q_1 \sigma$ never exceeds about 0.02H in our case. This lies within the limits of experimental error for H; equation (5) can be and was in fact therefore used without correction in evaluating H.

4.4. Transient creep

1959

Referring to equation (2), if the basic modes of recovery in the $t^{1/3}$ -stage and in the stage of steady creep were identical, one should have $^{(23-25)}$

$$\beta = {\rm const.} \ (\dot{\varepsilon}_{\rm st})^{1/3} = {\textstyle \frac{1}{2}} \beta_0 \, \{ \exp{[-Q(\sigma)/kT]} \}^{1/3} \ (13)$$
 i.e. $Q(\sigma) = H - q\sigma$. As was already noted, the experimentally determined exponent of $\dot{\varepsilon}_{\rm st}$ obtained from the data in Figs. 8 and 18 is not $1/3$ but $1/2$ (equation 3). Since, however, $Q(\sigma)$ and t must have the same exponent which, in view of the $t^{1/3}$ -form of the time-dependence of the early part of the transient stage of creep, must be equal to $1/3$ (equation 2), it is only possible to conclude that in the present case the recovery process operative in this stage is different from that occurring in the steady stage. This conclusion was experimentally verified: an activation energy

$$H_s = 49 \text{ keal/g atom},$$

and not one of about 32 kcal/g atom (Fig. 11), was obtained by the temperature cycling method in the $t^{1/3}$ -stage.

If we write

$$\beta = \frac{1}{2}\beta_0 \exp\left[-(H_{\rm tr} - q_{\rm tr}\sigma)/kT\right],$$
 (14)

then, from equation (9) and the experimentally established relation given by equation (3), we must have

$$H_{\rm tr}/H = q_{\rm tr}/q = \frac{1}{2},$$
 (15)

and also (equations 2 and 14)

$$H_{\rm tr}/H_s = q_{\rm tr}/q_s = 1/3,$$
 (16)

where we have written $Q(\sigma) = H_s - q_s \sigma$. Also $H_s/H = 3/2$; this relation, which follows from equations (15) and (16), was well satisfied by the measured values of H and H_s of 32 and 49 kcal/g atom, respectively. With these values of H and H_s the value of $H_{\rm tr}$

must be close to 16 kcal/g atom (a slightly smaller value would be expected for $H_{\rm tr}'$, i.e. with $\sigma < \sigma_{\rm c}'$). The relation $q_{\rm tr}/q = 1/2$ was also confirmed in all cases, as is easily verified from the mutual displacement of the lines representing q and $q_{\rm tr}$ in Fig. 16, for stress above as well as below $\sigma_{\rm c}'$.

Values of q_s were not measured, and the relations

$$q_s=3q_{
m tr}=3q/2$$

implied by equations (15) and (16) were not therefore checked.

The foregoing considerations also account for the observed more rapid deceleration of the transient creep after the $t^{1/3}$ -stage has terminated, for towards the end of this part of the transient stage the recovery mechanism changes from the one having an activation energy of about 49 kcal/g atom, characteristic of the $t^{1/3}$ -creep, to one with an activation energy of 28-32 keal/g atom, which is also characteristic of the subsequent steady stage. The second recovery process, although having a lower activation energy then that responsible for the $t^{1/3}$ -creep, is the slower of the two; we shall return to this point in Section 5. The differences in the recovery mechanisms in these two parts of the transient stage do not appear to be paralleled by essential differences in the respective hardening mechanisms. Thus, there is a striking similarity in the isotherms representing the $t^{1/3}$ and steady creep rates (Figs. 6 and 18), as well as in the temperature dependence of the structure term A (equation 12) and the corresponding term $\beta_0 \exp(-H_{tr}/kT)$ (equation 14); the breaks in the isotherms in Fig. 18 occur at the same stresses as the corresponding breaks in the curves in Fig. 6.

4.5. Time to fracture

The power law given by equation (4), and its application to the creep life of several metals have recently been discussed by Oding and Burdukski⁽²⁶⁾ and the

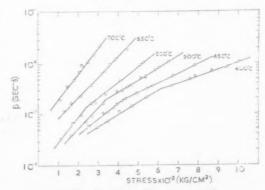


Fig. 18. Stress-dependence of β .

present authors.⁽²⁷⁾ If it is assumed that fracture is induced by the growth of pores heterogeneously nucleated at grain boundaries to a critical size at which they join up to form cracks, and that (1) a constant fraction of the vacancies generated in creep are absorbed by the pores, (2) the density of vacancies is proportional to the creep rate, and (3) the steady strain rate may be taken as a measure of the average

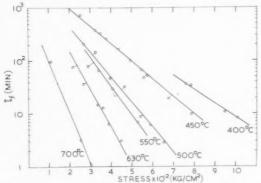


Fig. 19. Stress-dependence of the time to fracture.

creep rate covering all stages of creep, equation (4), with m=1, is immediately obtained. It then implies

$$t_{\scriptscriptstyle f} = (K/A_0) \exp\left[(H_{\scriptscriptstyle f} - q_{\scriptscriptstyle f} \sigma)/kT\right] \tag{17}$$

where

$$H_f = H$$
 and $q_f = q$,

with A_0 having the same significance as in equation 9. The applicability of equation (17) is apparent from the correlations in Figs. 9 and 19. K was found to be equal to 0.33 and, within experimental error, independent of the temperature (Table 1). The identity of q and q_d

	TA	BLE 1				
Temperature (°C)	400	450	500	550	630	700
$\sigma' e \text{ kg/cm}^2$ $Z_B \times 10^{-6} \text{ kg}^2/\text{cm}^4$ $A_0 \text{ sec}^{-1}$ $A'_0 \text{ sec}^{-1}$ K(equation 4) $\beta_0 \text{ sec}^{-1/3}$ $\beta'_0 \text{ sec}^{-1/3}$	$\begin{array}{c} 614\\ 13.1\\ 1.6\times10^4\\ 41\\ 0.35\\ 130\\ 32\\ \end{array}$	436 10.3 2900 8.9 0.36 40 13	335 8.7 660 3.3 0.32 18 5.9	238 7.1 140 1.2 0.31 8.0 3.0	128 5.5 33 0.59 0.33 4.4	$2.9 \times 10^{5} \\ 0.34 \\ - \\ 0.34$

was also confirmed by means of the isotherms shown in Figs. 6 and 19; in view of the already established validity of equation (17) the identity of H_f and H follows.

Although the validity of equation (4) (with m=1) does not establish the correctness of the assumptions from which it is shown to be derivable, recent experimental evidence^(28,29) that grain boundaries can be very efficient sources and sinks of vacancies, as well as Lozinskii's⁽³⁰⁾ observation that temperature cycling

can aid the formation of intergranular holes in creep (presumably by the precipitation of vacancies on lowering the temperature in each cycle), suggest that the assumptions made are probably not far from the truth.

5. THEORY

5.1. Activation energies

In a recent discussion of several models of the mechanism of creep Mott(31) concludes that in order to account for the observed creep behaviour of metals it seems necessary to assume that the stress does lower the activation energy. Basinski(21) has also established, mainly on the basis of an analysis of the creep data of Sherby et al. (32), obtained for high purity aluminium over a wide range of temperatures, that, contrary to the views of Sherby and co-workers, the data presented seemed to support rather than contradict the theories requiring a stress-dependent activation energy. Theories of creep embodying the assumption of a stress-independent activation energy, e.g. that of Dorn, (8) Weertman and Shahinian (33) and others are therefore seriously questioned. That of Weertman and Shahinian in particular has been criticized by Meakin⁽³⁴⁾. Their treatment leads to a linear relation between the steady strain rate and $\sigma^{4.6}$; it is not born out by the present work (see for example 4.2.). We shall therefore assume in our considerations that equation (9), used for the correlation of our creep data, indicates a linear dependence of the activation energy on the applied stress, and we shall show that such a stress-dependence is not incompatible with a recovery mechanism involving the climb of edge dislocations.

19!

A linear stress-dependence of the activation energy, and the fact that q is not a material constant, but appears to depend upon the dimensions of comparatively stable dislocation configurations, (11.19) are clear indications that the activation energy cannot be identified with either that for cross-slip by pure screw dislocations or with that for the break-through of Cottrell-Lomer barriers, both of which are of the form given by equation (7). Now, the existence of steady creep suggests that in this stage at least dislocations are lost at approximately the same rate as at which they are generated. Some may of course accumulate at sub-boundaries (35,36) without significantly reducing the creep rate, particularly if the slight hardening resulting from this should at the same time be compensated for by the formation of intergranular voids or other weaknesses. A complete compensation of hardening resulting from one process, by softening due to the other unrelated one, would however be rather fortuitous, and could hardly be held responsible

for the considerable extend of the stage of equilibrium creep and its occurrence at all temperatures in the range studied. We shall therefore assume that the most important effect of recovery is the loss of dislocations from the grains. Of the possible processes, namely mutual annihilation of screw dislocation, and mutual annihilation of edge dislocations the slower one will necessarily control the equilibrium creep rate, but this need not be so in the stage of transient creep, when the easier, more rapid, process may "exhaust" itself first.

The linear dependence of the activation energy on the stress indicates that some of the processes listed in Table 2 may be operative; these would be expected to have activation energies close or equal to either that of self-diffusion, vacancy migration or vacancy formation. Values of these, given in the literature, are as follows: $H_s=49~{\rm kcal/gatom},^{(37)}H_m=27-31~{\rm kcal/g}$ atom, $^{(5,38,39)}$ and $H_f=18-21~{\rm kcal/g}$ atom. $^{(5,38,39)}$

TABLE 2

	Process	Activation energy expected
(i)	Screw dislocation, containing jogs, moving slowly	H_s
(ii)	Screw dislocation, containing jogs,	
(iii)	moving fast Serew dislocation, containing jogs, moving slowly in a vacancy	H_f
	supersaturation	H_m
(iv)	Edge dislocation, containing jogs, climbing	H_{s}
(v)	Edge dislocation, containing jogs, climbing in a vacancy super- saturation	H_m

An activation energy corresponding to (ii) was not observed. The process⁽⁴⁰⁾ is in fact unlikely in creep, as serew dislocations would not move fast enough to escape from the point defects formed by jogs, a mechanism which would otherwise enable them to free themselves of the point defects without the need for the latter to migrate away from the jogs after formation. We believe however that of the remaining processes listed in Table 2 (i), (iv) and (v) are rate determining under certain specific conditions which we shall consider.

5.2. Recovery processes

VOL.

1959

In their study of slip-propagation in aluminium crystals deformed at room temperature Chen and Pond⁽⁴¹⁾ found that the screw components of the dislocation loops tended to be held up in the crystal,

and propagated slowly; the edge components, by contrast, appeared on the crystal surface instantaneously and fully formed. This difference in behaviour is due to the strong impediment of the movement of screw dislocations by jogs. Non-conservatively moving jogs cannot run off the screw dislocation by movement along the dislocation, for the latter is bulged out into a cusp by the stress, and the jog, sitting at the node, is therefore flanked by the arms of the cusp which are partly "edge". The jog must therefore move with the dislocation, requiring an activation energy depending linearly upon the stress. with H equal to H_s . This process could be rate controlling in the steady stage only if the edge components of the dislocation loops could escape more readily than the screws, otherwise an accumulation of edge dislocations in pile-ups or polygon walls would lead to a progressive deceleration of creep. It could determine the creep rate, for example, in single crystals of aluminium if, as in Chen's and Pond's experiments, the edge dislocations can escape through the crystal surface, or in polycrystals if grain boundaries are ready sinks for edge dislocations, and intragranular obstacles do not prevent the dislocations from reaching these. (11) Harper et al. (42) have proposed an interpretation of the high-temperature creep of polycrystalline aluminium at very low stresses, as observed by them, on the basis of this mechanism. but it is not clear from their paper whether a steady stage was in fact attained.

We believe however that the recovery process in the $t^{1/3}$ -stage in copper, for which H was found to be equal to H_* (equation 13), is in fact controlled by (i). If it were (iv) then, as climb is the slowest of all processes under consideration (Mott(31)), it would be difficult to account for the enhanced deceleration observed after the $t^{1/3}$ -stage, for an even slower process is thereby indicated. This consideration holds a fortiori in view of the decline of H from about 49 to about 30 keal/g atom during the transition from the $i^{1/3}$ -part to the late part of the transient stage. The screw dislocations lost in the $t^{1/3}$ -stage would be those piled up against Cottrell-Lomer barriers during the work-hardening(2) induced by the initial loading. The edge parts of the loops would remain confined to their original slip planes by Cottrell-Lomer locking, and would thus block the sources from which they had originated. At this stage each grain would contain predominantly edge dislocations; some joined to similar dislocations on parallel slip planes by segments of edge dislocations lying in the cross-slip system. (43.11) These links in the cross-slip system replace the screw dislocations from which they

originated as the result of cross-slip. The enhanced stresses at the leading dislocations of pile-ups would there induce climb. The ensuing polygonization would then lead to a more uniform distribution of dislocations and to a levelling of local stress peaks. The sources would also again become operative due to unblocking by the relaxation of the back shear stress associated with the loss of dislocations from the pile-ups.

We believe that the second, slower, part of the transient creep occurs during this period of polygonization. The structure at the end of this stage, i.e. many small sources, each enclosed by only a few dislocations which had originated from it, together with dislocations in polygon walls, we consider to be characteristic of the steady stage. Climb continues to be rate controlling in the steady stage in which, in view of the low activation energy (Fig. 11), process (v) appears to take place.

That the activation energy is lower than H_s seems to us to be a consequence of the ability (a) of grain boundaries to act as reservoirs of vacancies, (28,29) and (b) of dislocations to drain vacancies from these. For in this way 'equilibrium' or quenched-in vacancies (including those formed in the $t^{1/3}$ -stage), collected from the lattice by the entire grain boundary surface, are channelled back into the grains along the dislocations, which provide easy paths for them; and where such vacancies lie next to jogs the latter may move non-conservatively without the need to form vacancies. An activation energy close to that for vacancy migration would be expected. In a recent theoretical study of the kinetics of interaction between vacancies and dislocations in copper and gold Kimura et al.(44) suggest that vacancies will condense on dislocations to form small clusters of up to 10 vacancies. Further growth of the clusters, by absorption of vacancies channelled along them by dislocations, results in their collapse to give small stacking faults bounded by sessile dislocations. Evidence for the existence of sessile rings which seem to have originated in this way has recently been obtained by Hirsch et al. (45) in quenched aluminium. Jogs would probably be preferred sites for the condensation of such clusters.

The presence of vacancies next to jogs can account for the observed reduction of the activation energy from H_s to a value close to H_m . At a sufficiently high temperature, determined by the interaction energy between vacancies and dislocations, localization of vacancies on dislocations would cease, and the activation energy should rise to H_s over a small temperature interval. A sharp transition from 30 to 49 kcal/g atom between 600 and 700°C was in fact observed (Fig. 11).

Above about 700°C we should then expect (iv) to be rate determining. This view is favoured by the monotone rise of q with temperature right up to 700°C (Fig. 13), which suggests that except for the evaporation of vacancies from dislocations no essential qualitative change occurs in the intragranular structure between 600 and 700°C. The rapid increase of A_0 on approaching 700°C (Table 2) may be a consequence of the absence of a frictional drag on dislocations by vacancies; on the other hand the low value of σ_c which is possibly zero at 700°C (Fig. 12 and Table 1), suggests very weak Cottrell–Lomer locking, and the possibility that (i) may be rate controlling cannot be dismissed. The high value of A_0 could also be reconciled with such a change of mechanism. (11)

5.3. Creep of copper single crystals

A few observations made on single crystals in the range $490\text{-}600^{\circ}\text{C}$ with an applied tensile stress of $200~\text{kg/cm^2}$, which gave a resolved shear stress of about $100~\text{kg/cm^2}$, indicated (iv) as the most likely process in the steady stage. In a typical experiment (560°C) the tensile strain rate fell rapidly to about $5\times10^{-5}~\text{sec}^{-1}$, but a truly constant value was not reached even after many hours, when the test was discontinued. By then creep had virtually ceased; this could not however be ascribed to the inadequacies of the constant-stress beam. The activation energy was in all stages found to be equal to that of self-diffusion (Fig. 12).

It seems that the rapid deceleration of the creep early in the test is due to the loss of screw dislocations, as in polycrystals in the $t^{1/3}$ -stage. Prominent cross-slip is in evidence on the surface of crystals examined after creep (Figs. 20–23). Band-formation, generally associated with intimate cross-slip, is clearly visible. The steady stage, if attained, is most probably controlled by (iv); the virtual cessation of creep, referred to above, could then find a ready explanation in terms of the extreme slowness of climb.

The fact that activation energies close to H_m were not observed may be a consequence of the absence of sufficient vacancy reservoirs such as condensed clusters and grain boundaries, or (and) of a lower density of vacancy channels, particularly as only one slip system appeared to be prominent in single crystals.

5.4. The climb mechanism

As creep controlled by the movement of screw dislocations has been discussed previously, (II) we shall here deal only with the climb mechanism. In particular we wish to show that the stress can reduce the activation energy of climb.

VOI 7 19



Fig. 20. Segmented slip-bands in a single crystal in the zone of emergence of edge dislocations. (500°C, tensile strain 50%).



Fig. 21. As Fig. 20, but zone of exit of screw dislocations.

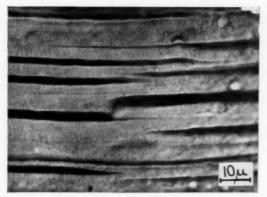


Fig. 22. As Fig. 20, showing details of bands and cross-slip.

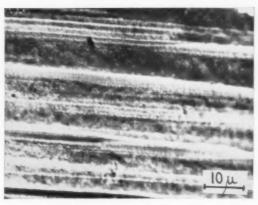


Fig. 23. As Fig. 20, showing structure within bands.

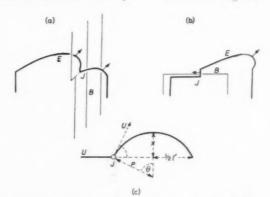


Fig. 24. Jog-assisted climb of edge dislocations over barriers.

VOL. 7 1959

VOI 7 19!

We shall therefore consider two cases, by way of example, in which an edge dislocation is held up by a barrier, B, (Fig. 24) which in (a) is a screw or edge dislocation of a wall or pile-up which, owing to a jog, the oncoming edge dislocation cannot cut, and in (b) a short length of another edge dislocation stablized by nodal points of the Frank–Read net or by some other obstacle such as a Cottrell–Lomer barrier (not shown). For our present purposes it is sufficient to regard the dislocation as undissociated.

In both cases shown in Fig. 24 there is a resultant force on the jog; in (a) the jog is forced to the right, in (b) to the left. The dislocation climbs as a result of the migration of the jog and, having surmounted the obstacle, is in a position to slip further. The resultant force on the jog along the dislocation line depends on the difference in the curvatures of the segments on its right and left, respectively.

Referring to the simple special case shown in Fig. 24c, we see that the force on the jog due to the line tension U is

$$F = U(1 - \cos \theta) = Ux/\rho, \tag{18}$$

or, since

$$U \simeq b \rho \tau$$
.

where τ is the shear stress acting on the dislocation,

$$F \simeq bx\tau.$$
 (19)

Since also

$$0 < x < l'/2 < l'_{PR}/2,$$
 (20)

where l'_{FR} is the length at which the loop becomes unstable, one may write for the average value of F:

$$\bar{F} = \alpha' b l'_{FR} (\sigma - \sigma_{V}),$$
 (21)

where we have put

$$\tau = (\sigma - \sigma_{\rm Y})/2,\tag{22}$$

and where $\alpha' < 1/4$. The stress $\sigma_{\rm Y}$ is the yield stress of the crystal, i.e. the stress below which plastic deformation does not take place. We should expect it to be proportional to, but somewhat less than, the intercepts of the isotherms on the stress axis in Fig. 6. The parameter q' (equation 11) associated with σ is then given by

$$q' = \alpha' b^2 l'_{FR} \tag{23}$$

which, on taking $l'_{\rm FR}=2\mu$ and $\alpha'=0.1$, gives values of q which are of the right order of magnitude.

5.5. The creep rate due to climb

A detailed theoretical treatment of creep must await further studies of the role of intragranular substructures in the recovery and work-hardening processes involved. We shall here attempt only to outline a model which seems to account for the most important features observed.

In the model of climb we shall consider an edge dislocation which, having cut through a simple subboundary, is pinned at a jog such as J (Fig. 24a), or lies behind a rigid barrier, e.g. a Cottrell–Lomer sessile dislocation (Fig. 24b). In the first case, before the jogged dislocation can proceed along the slip plane, the jog must climb (as shown by the arrow) a certain distance l' away from the wall, the distance being of the order of the mesh size of the dislocation grid of the sub-boundary. In the second case climb must take place over a distance of the order of either the length of the barrier or the length $l'_{\rm FR}$, whichever is shorter.

If, in general, we denote the climb distance by $fl'_{\rm FR}$, where f is a fraction of order unity, depending upon the details of the configuration, e.g. as shown in Fig. 24a or 24b, then a jog can traverse this distance in the time

$$t_i = v^{-1}(fl'_{FR}/b) \exp[Q'(\sigma)/kT],$$
 (24)

where $v \sim 10^{12} \, \mathrm{sec^{-1}}$, and

$$Q'(\sigma) = H' - q'(\sigma - \sigma_{\rm Y}). \tag{25}$$

The average time of climb of such a segment over the barrier would then take place in time t, which would be rather longer than t_j , for climb-sustaining jogs may not be present at all times in every such segment. We shall therefore write

$$t = t_i/p, \tag{26}$$

p being a dimensionless real fraction. As the jogs in copper are not of thermal origin, $^{(46)}$ but arise from the intersection of dislocations, p will depend upon the density and mode of distribution of dislocations in the grains. In single crystals, in which slip during creep takes place predominantly on one slip system, intersection of the dislocation in this slip system by dislocations in the conjugate system—and hence the formation of jogs—may be a comparatively rare occurrence, and p would then be small.

In accordance with our discussion in 5.2, we shall take as our model of the intragranular structure during steady creep a distribution of small slip zones confined by Cottrell–Lomer barriers or terminating in polygon walls, or both. Above σ_c we shall assume grain boundaries to be important obstacles.

Now, the strain $\dot{\varepsilon}$ in a crystal containing N sources (zones) per unit volume is $^{(43)}$

$$\dot{\varepsilon} = NLL'bn,\tag{27}$$

where L and L' are the slip distances of edge and screw dislocations, respectively, and n the (small)

number of dislocations per source. If we assume that all the n loops can climb, then

$$dn/dt = n/st, (28)$$

where t is as given by equation (26), and s is the number of times a dislocation has to climb between source and sink. We shall write equation (28) in the form

$$\dot{n} = z/t, \tag{29}$$

assuming z to be of order unity. From equations (27) and (29) we obtain

$$\dot{\varepsilon} = A'_0 \exp\left[-(H' - q'\sigma)/kT\right],\tag{30}$$

with

VOL.

1959

$$A'_{0} = \frac{NLL'b^{2}vzp}{fl'_{\text{FR}}\exp\left(q'\sigma_{\text{Y}}/kT\right)}. \tag{31}$$

Equation (30) is of the same form as the equation of the creep isotherms (equation 9) used to represent the experimental results. On taking $N=10^8~{\rm cm}^{-3}$, $L=L'=10^{-3}~{\rm cm}$, $b^2=5\times 10^{-16}~{\rm cm}^2$, $\nu=10^{12}~{\rm sec}^{-1}$, z=1, p/f=1, $\exp{(q'\sigma_{\rm Y}/kT)}=2$ and $l'_{\rm FR}=2\times 10^{-4}~{\rm cm}$, one obtains

$$A'_{0} \simeq 100 \text{ sec}^{-1}$$
. (32)

If, for $\sigma > \sigma'_c$, we use the same approximations but, as discussed, take the slip distance equal to the grain size D, i.e. replace LL' by $D^2 (= 10^{-5} \, \mathrm{cm}^2)$ in equation 31, we obtain the grain size dependence of the creep rate indicated by Fig. 13. Also then

$$A_0 \simeq 1000 \text{ sec}^{-1}$$
. (33)

In view of the approximations and simplifications made the values of A_0 and A'_0 (equations 32 and 33) can be regarded as being in quite satisfactory agreement with the values found experimentally (Table 1). The effect of polygonization and of the dissociation of dislocations has not been allowed for explicitly, and also too little is known about the temperature-dependence of most of the parameters defining A_0 and A'_0 (equation 31) to warrant a more detailed study of the model at present.

ACKNOWLEDGMENT

One of us (J. D. M.) is indebted to the Department of Scientific and Industrial Research for a maintenance grant.

REFERENCES

- A. Seeger, J. Diehl, S. Mader and H. Rebstock, *Phil. Mag.* 2, 323 (1957).
- 2. P. FELTHAM and J. D. MEAKIN, Phil. Mag. 2, 1237 (1957).
- G. Bassi, Z. Metallk. 48, 190 (1957).
 W. Boas, Bristol Conference on Defects in Crystalline Solids,
- p. 212. Physical Society, London (1955).
 J. A. BRINKMAN, C. E. DIXON and C. J. MEECHAN, Acta Met. 2, 38 (1954).
- 6. A. SEEGER, Z. Naturf. 9a, 856 (1954). 7. P. A. Jacquet, Acta Met. 2, 752 (1954).
- 8. J. E. Dorn, Conference on Creep and Fracture of Metals at High Temperatures, p. 89. H.M. Stationery Office, London,
- High Temperatures, p. 89. H.M. Stationery Office, London (1956).
 9. P. Feltham, Proc. Phys. Soc. B66, 865 (1953).
- 10. H. Huang, O. D. Sherby and J. E. Dorn, Trans. Amer.
- Inst. Min. (Metall.) Engrs. 206, 1385 (1956).
 P. Feltham, Proc. Phys. Soc. B69, 1173 (1956).
- 12. J. D. Meakin, Ph.D. Thesis. The University, Leeds (1957).
- 13. E. N. DA C. ANDRADE, Nature, Lond. 162, 410 (1948).
- A. N. STROH, Phil. Mag. 1, 489 (1956).
 G. SCHOECK and A. SEEGER, Bristol Conference on Defects
- G. SCHOECK and A. SEEGER, Bristol Conference on Defects in Crystalline Solids, p. 340. Physical Society, London (1955).
- A. H. COTTRELL and V. AYTEKIN, J. Inst. Met. 77, 389 (1950).
- N. S. Fastov, Zh. tekh. eksp. fiz. 20, 543 (1950).
 A. S. Novick and E. S. Machlin, J. Appl. Phys. 18, 79
- 18. A. S. NOVICK and E. S. MACHLIN, J. Appl. Phys. 18, 7 (1947).
- 19. P. FELTHAM, Phil. Mag. 2, 584 (1957).
- P. Feltham, Nature, Lond. 169, 976 (1952).
- Z. S. Basinski, Acta Met. 5, 684 (1957).
- W. Koester, L. Bangert and W. Lang, Z. Metallk. 46, 84 (1955).
- 23. N. F. MOTT, Phil. Mag. 44, 742 (1953).
- 24. P. Feltham, Brit. J. Appl. Phys. 6, 26 (1955).
- 25. P. FELTHAM, Phil. Mag. 45, 9 (1954).
- I. A. ODING and W. W. BURDUKSKI, Deformation and Flow of Solids, p. 298. Springer, Berlin (1956).
- P. FELTHAM and J. D. MEAKIN, Rheologica Acta 1, 176 (1958).
- R. S. Barnes, G. B. Redding and A. H. Cottrell, Phil. Mag. 3, 97 (1958).
- D. Turnbull, Bristol Conference on Defects in Crystalline Solids, p. 202. Physical Society, London (1955).
- M. G. Lozinskii, Metalloved. i Obrabotka Metallov (11), 18 (1957).
- N. F. MOTT, Conference on Creep and Fracture of Metals at High Temperatures, p. 21. H.M. Stationery Office, London (1956).
- O. D. SHERBY, J. L. LYTTON and J. E. DORN, Acta Met. 5, 219 (1957).
- J. WEERTMAN and P. SHAHINIAN, J. Metals, N.Y. 8, 1223 (1956).
- 34. J. D. MEAKIN, J. Metals, N.Y. 9, 1297 (1957).
- 35. D. McLean, J. Inst. Met. 81, 287 (1953).
- B. Ancker, T. H. Hazlett and E. R. Parker, J. Appl. Phys. 27, 333 (1956).
- 37. L. Mercer, Ph.D. Thesis, The University, Leeds (1955).
- 38. S. D. Gertsriken, *Dokl. Akad. Nauk. SSSR* **98**, 211 (1954).
 39. C. J. Meechan and R. R. Eggleston, *Acta Met.* **2**, 680
- (1954).40. A. SEEGER, Phil. Mag. 46, 1194 (1955).
- N. K. Chen and R. B. Pond, Trans. Amer. Inst. Min. (Metall.) Engrs. 194, 1085 (1952).
- J. G. Harper, L. A. Shepard and J. E. Dorn, Acta Met. 6, 509 (1958).
- 43. N. F. MOTT, Phil. Mag. 43, 1151 (1952).
- 44. H. Kimura, R. Maddin and D. Kuhlmann-Wilsdorf, Private communication.
- P. B. HIRSCH, J. SILCOX, R. E. SMALLMAN and K. H. WESTMACOTT, Phil. Mag. 3, 897 (1958).
- WESTMACOTT, Phil. Mag. 3, 897 (1958). 46. D. McLean and A. Franks, Phil. Mag. 1, 101 (1956).

STRESS INDUCED ORDERING AND STRAIN-AGEING IN LOW CARBON STEELS*

D. V. WILSON† and B. RUSSELL† with an Appendix by J. D. ESHELBY ..

Part of the increase in yield stress during the strain-ageing of a low-carbon steel develops too rapidly to be explained by long-range diffusion. The rate at which the initial rapid rise in yield stress develops and the dependence of its magnitude on the dissolved solute content are shown to be those expected from a contribution due to stress-induced ordering of the interstitial solute atoms in the stress fields of dislocations. A simple theoretical treatment gives values in reasonable agreement with experiment.

LA RÉORGANISATION ATOMIQUE DUE AUX TENSIONS ET LE VIEILLISSEMENT DE DÉFORMATION DANS LES ACIERS A FAIBLE TENEUR EN CARBONE

L'augmentation de la limite élastique pendant le vieillissement de déformation d'un acier à faible teneur en carbone se fait trop rapidement pour être expliquée par une diffusion à grande distance. Les auteurs montrent que la vitesse avec laquelle s'accroit, au début, la limite élastique et la dépendance de son amplitude avec la teneur en éléments dissous sont celles qu'on s'attendrait à trouver en tenant compte de la réorganisation atomique provoquée par des tensions des atomes interstitiels situés dans le champ de tension des dislocations. Un raisonnement théorique simple donne des valeurs en bon accord avec l'expérience.

SPANNUNGSINDUZIERTE ORDNUNG UND RECKALTERUNG BEI KOHLENSTOFFARMEN STÄHLEN

Ein Teil der Fliessspannungserhöhung bei der Reckalterung eines kohlenstoffarmen Stahls entwickelt sich zu rasch, um durch Diffusion über grössere Entfernung hinweg erklärbar zu sein. Die Geschwindigkeit, mit der sich die anfänglich rasche Erhöhung der Fliessspannung entwickelt und die Abhängigkeit ihrer Grösse vom Gehalt an gelöstem Legierungszusatz entsprechen den Erwartungen in Bezug auf einen Beitrag aufgrund spannungsinduzierter Ordnungseinstellung der auf Zwischengitterplätzen gelösten Atome in den Spannungsfeldern von Versetzungen. Eine einfache theoretische Behandlung ergibt Werte, die ausreichend mit dem Experiment übereinstimmen.

1. INTRODUCTION

Nabarro⁽¹⁾, in 1948, pointed out that the diffusion of carbon in iron can affect mechanical properties by three mechanisms. These are the stress-induced ordering of carbon atoms among the possible sets of interstitial sites (Snoek(2)), the segregation of carbon to form dislocation atmospheres (Cottrell(3)) and the precipitation of iron carbide particles.

Each of these kinds of solute redistribution can occur during the strain-ageing of steel. The Cottrell mechanism is of first importance in causing the return of the sharp yield point, while an increase in the steel's ability to work-harden and reduction in its ductility in the later stages of ageing are probably associated with precipitation of carbides or nitrides. (4)

The possible contribution to the rise in yield stress made by ordering of solute atoms in the stress fields of dislocations has generally been ignored. Recently, however, Schoeck⁽⁵⁾ has discussed the dragging force on moving dislocations due to this effect. Since only atomic jumps between neighbouring lattice sites are involved, ordering will be more rapid by orders of magnitude than is segregation to form atmospheres. In the case of carbon and nitrogen in iron any contribution to strain-ageing made by this effect should be completed within a few seconds at room temperatures.

19

It is expected that the magnitude of the effects due to such ordering will be proportional to the amount of dissolved interstitial solute. The size of the yield point which develops as a result of atmosphere locking, on the other hand, can be shown to be essentially independent of the solute content provided this exceeds the small quantity, (generally a few thousandths of an atom per cent), required to complete atmosphere formation. (6)

A treatment due to Eshelby which is given in the appendix to this paper, provides a method for calculating the force required to move a dislocation when ordering has taken place. This suggests that the effect on yield stress should be appreciable in quenched steels.

In the experiments described here evidence of the effects of stress-induced ordering of the interstitial solutes, in prestrained low-carbon steel, has been sought by measuring the changes in yield stress during the early stages of strain-ageing.

^{*} Received October 9, 1958.

[†] Department of Industrial Metallurgy, The University, Birmingham 15, England.

^{*} Department of Physical Metallurgy, The University, Birmingham 15, England.

2. EXPERIMENTAL METHOD

A steel of the following composition in weight per cent was used in the majority of the experiments: C 0.039; N 0.0044; Mn 0.40; S 0.017; Si and P 0.008; Ni and Cu 0.05.

Specimens of 0.050×0.60 in, cross-section were prestrained through the initial yield, aged and then tested in a hard beam machine. The observation of small yield points was simplified because ageing could be carried out without removing the specimen from the machine for all the shorter times.

The amount of solute in solid solution was varied by heating specimens in vacuo at suitable temperatures in the range 200° to 700°C, for times sufficient to reach equilibrium, and then quenching in water. An extremely low solute content was obtained by heating in wet hydrogen at 800°C for 48 h.

3. RESULTS

Fig. 1 summarizes results given by a series of specimens all quenched from 600°C, prestrained 4 per cent, unloaded and then aged at 20°C for times up to 15 h before testing. Initially these specimens would have, in weight per cent, about 0.01 carbon and 0.0044 nitrogen in solution.

The increase in yield stress, ΔY , is taken as the difference between the upper yield stress, after strain-ageing for time t, and the flow stress observed at the end of prestraining (Fig. 1). The maximum rise in yield stress due to strain ageing, $\Delta Y_{\rm max}$, was obtained only after very prolonged ageing (>10⁴ min at 60°C). If we assume, for atmosphere formation, that ΔY is proportional to the amount of solute

1959

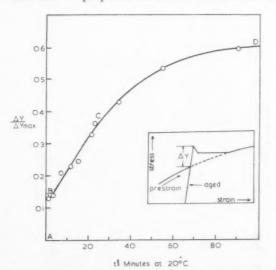


Fig. 1. The fractional return of the yield point as a function of $t^{2/3}$ for specimens quenched from 600° C and prestrained 4 per cent.

collected by the dislocations then, according to the Cottrell–Bilby equation, $^{(7)}$ ΔY should increase proportionately to $t^{2/3}$ during the early stages of ageing. In Fig. 1 the portion of the curve BCD shows this now familiar feature of strain ageing due to atmosphere formation. If ΔY were proportional to the amount of solute segregating throughout the ageing process the dislocation density required to give the rate of ageing indicated by the linear portion BC would be about 2×10^{11} lines per cm². This is reasonable (but probably high because the solute becomes less effective in raising the yield stress in the later stages of ageing). Fig. 1 shows there was an initial rise in ΔY which occurred much too rapidly to be accounted for by atmosphere formation.

In low-carbon steel specimens the extent of this initial rapid ageing was found to be strongly dependent on the quenching temperature but the effect was absent in specimens from which the carbon and nitrogen had been removed by annealing in wet hydrogen. The effect was insensitive to grain size in the range 50 to 1800 grains per mm² and appeared to be only weakly dependent on the amount of prestrain.

Fig. 2 shows the extent of the rapid ageing effect observed in specimens of differing dissolved solute contents, all prestrained 4 per cent and aged for 2 min at 20°C. The increase in yield stress was evidently close to being proportional to the amount of dissolved solute, but the increase was greater if ageing was carried out without removing the prestraining load. The total interstitial solute content of the hydrogentreated specimens was probably less than 0.0001 weight per cent. These were quenched from 700°C but gave no evidence of an increase in yield stress if

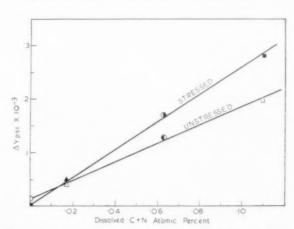
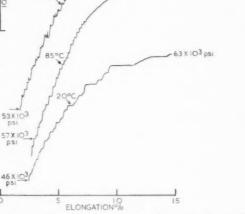


Fig. 2. Increase in yield stress in low-carbon steel prestrained 4 per cent and aged for two minutes at 20°C after quenching from the following temperatures: △ ▲ 200°C; ● ④ 600°C; □ ■ 700°C. □ ■ Wet-hydrogen-treated steel quenched from 700°C.

psi X 10-3



130

STRESS

the load were maintained during ageing. Unloaded specimens showed a small effect which is probably not due to strain-ageing but may be related to dislocation

Fig. 3. Strain-ageing at −12 °C in specimens quenched from 700°C and prestrained 4 per cent.

rearrangement on unloading, as discussed by Haasen and Kelly.(8) When ageing was carried out without removing the prestraining load it is likely that the apparent

ageing rate was influenced by creep (amounting to about 0.08 per cent extension in 2 min). At 20°C the testing machine could not be unloaded sufficiently rapidly to obtain any estimate of the rate of rapid ageing in the unloaded condition, but experiments in which the specimen were unloaded rapidly to about 90 per cent of the prestrain load and then reloaded immediately, suggested that about two-thirds of the full rapid ageing effect developed within the first 2 to 4 sec at room temperature. Tests at reduced temperatures showed that about two-thirds of the effect developed in 2 min at -10°C but that there was negligible ageing in 2 min at -60°C. Fig. 3 shows results obtained with a series of specimens all quenched from 700°C and then tested and aged at -12°C. Ageing was in this case carried out with a reduced applied load which was generally between 80 and 90 per cent of the load at the end of prestrain. The results show that the initial rapid rise in yield stress was about 63 per cent complete in 100 sec at -12°C. This is in reasonable agreement with relaxation times observed in the case of the elastic after-effect due to

Test pieces freshly quenched from temperatures above about 550°C showed irregular flow at room temperature during continuous straining at low strain rates. Fig. 4 illustrates stress-strain curves recorded at 20°C, 85°C and 130°C using specimens quenched from 700°C and strained at a rate of 10⁻⁴ sec⁻¹. The irregularities observed at room temperature may be described as repeated yielding rather than jerky flow, which is observed at high temperatures. At 85°C and higher temperatures precipitation of an appreciable

the ordering of carbon in iron. (9)

Fig. 4. Effect of temperature on the flow behaviour of low-carbon steel quenched from 700°C and strained at $10^{-4}~{\rm sec^{-1}}$.

proportion of the dissolved carbon would occur once the specimen was deformed. This may account for the unusual character of the behaviour at 85°C.

4. CONCLUSIONS

Part of the increase in yield stress during the strain-ageing of a low-carbon steel develops too rapidly to be explained by long range diffusion of carbon and nitrogen to dislocations.

This initial rapid ageing shows characteristics to be expected from a contribution due to local ordering of the interstitial atoms in the stress fields of dislocations. Unlike the effects due to segregation, its magnitude is evidently proportional to the amount of dissolved solute. Thus the effect is small in slowly cooled steels (and, presumably, its contribution will always be small in the later stages of strain ageing, when the solute content of the matrix has been sufficiently reduced).

Experiments at -12° C, made with a reduced applied load, have shown that the rate is consistent with a process involving jumps of a single atomic spacing by the carbon atoms. Observed values of the upper yield points are in reasonable agreement with predictions based on Eshelby's treatment, particularly for specimens aged with only a small relaxation of the prestraining load.

Low-carbon steel quenched from temperatures above about 550°C shows repeated yielding at room temperature during continuous straining at low strain rates. This may also be due to stress-induced ordering VOI 191

of carbon. The room temperature effect differs from high temperature jerky flow (associated with the migration of solute atoms with dislocations(1,10) in that the former is only appreciable when the dissolved solute content exceeds several hundredths of an atom per cent.

APPENDIX

Suppose (Fig. 5) that a dislocation is introduced into a crystal of ferrite. Initially the carbon and nitrogen atoms are distributed randomly among the midpoints of 100, 010 and 001 cube edges. However, it may be energetically advantageous for them all to move into a particular one of these positions if the resulting tetragonality tends to annul the stress due to the dislocation. At large distances from the dislocation thermal agitation will over-ride this tendency. According to an estimate of Zener(11) a tensile strain of 0.005 induces substantial ordering at room temperature, and such a strain is to be found within about 20 atomic spacings of a dislocation.

With the configuration of Fig. 5 (an edge dislocation* with 110 slip plane) the interstitial atoms to the right of the dislocation will enter 010 positions. On the left the dislocation stress is reversed and they will enter 100 positions. We may say that the dislocation has trapped itself between two regions of martensite M and M'. In these regions there will be a shear stress $\pm \sigma$ superimposed on the stress field of the dislocation, and of such a sign as to oppose its motion. Any applied shear stress must exceed σ before the dislocation can move, provided there is no time for the interstitials to re-arrange themselves.

1959

We tentatively identify σ with the resolved shear stress corresponding to ΔY . In doing so we assume that σ is additive to the other hardening mechanisms operating. The stress σ is proportional to the maximum tetragonality which the interstitials can produce, that is, to their concentration. Hence ΔY is

To estimate σ we note that, if the region M were not embedded in the ferrite matrix, ordering to form martensite would cause a fractional extension 0.86c in the 010 direction and a contraction -0.08c in the 100 direction, where c is the atomic fraction of either carbon or nitrogen atoms(12) or, we shall assume, a mixture of them. This is equivalent to a shear strain

$$e = \frac{1}{2}(0.86 + 0.08)c \simeq \frac{1}{2}c$$

in the slip-plane. Complete inhibition of this free strain by a rigid matrix would evidently set up a stress $2 \mu e$, where μ is the shear modulus. In fact, the matrix only partly inhibits the strain, giving rise to a stress $\sigma = 2 \gamma \mu e$, where γ is an "accommodation factor". (13) In general, y is a function of position, but it is constant if M is some form of ellipsoid. We shall assume that M is a long circular cylinder parallel to the dislocation axis. Then $\gamma = \frac{1}{2}$, taking Poisson's ratio to be $\frac{1}{4}$. (In the notation of (13) p. 391, $\gamma = 1-2S_{1212}$ where S_{1212} is to be found from (3.7) and (3.17) with a=b). In the most favourable case the applied shear stress on the slip-plane is half the applied tensile stress, and so

$$\begin{array}{l} \Delta \, Y = \frac{2}{3} \mu c \\ = 6.6 \, \times \, 10^6 c \; \mathrm{lb/in^2} \end{array}$$

if we take $\mu = 1.1 \times 10^7$ lb/in².

This is about twice the observed value. The geometrical arrangement of Fig. 5 was chosen to make the situation as clear as possible. As it happens, any other arrangement gives a somewhat lower value for ΔY .

REFERENCES

- 1. F. R. N. Nabarro, Report on Strength of Solids, p. 38. Physical Society, London (1948).
- 2. J. L. SNOEK, Physica 8, 711, 734 (1941).
- 3. A. H. Cottrell, Report on Strength of Solids, p. 30. Physical Society, London (1948).
- 4. B. B. Hundy, Metallurgia 53, 203 (1956). G. Schoeck, Phys. Rev. 102, 1458 (1956).
- 6. D. V. Wilson and B. Russell, Acta. Mta. To be
- published.
 A. H. COTTRELL and B. A. BILBY, Proc. Phys. Soc. A 62, 49 (1949).
- 8. P. Haasen and A. Kelly, Acta Met. 5, 192 (1957).
- G. RICHTER, Ann. Phys. 32, 683 (1938).
 A. H. COTTRELL, Phil. Mag. 44, 829 (1953).
- 11. C. Zener, Elasticity and Anelasticity of Metals, p. 122. University of Chicago Press (1948)
- 12. K. H. JACK, Proc. Roy. Soc. A 208, 200 (1951).
- 13. J. D. ESHELBY, Proc. Roy. Soc. A 241, 376 (1957).

proportional to the concentration, as observed. On this model ΔY should be substantially independent of temperature.

^{*} Since slip takes place in the 111 direction the dislocation must have a screw component perpendicular to the plane of the figure. It may be neglected provided (as we shall assume) the applied shear stress is in the plane of the figure.

MORPHOLOGY AND CRYSTAL STRUCTURE OF CARBIDES PRECIPITATED FROM SOLID SOLUTION IN ALPHA IRON*

W. C. LESLIE,† R. M. FISHER† and N. SEN†

The carbides precipitated from solid solution in high-purity iron–carbon alloys, in two low-carbon steels and in an iron–carbon–3.25% silicon alloy were studied by electron microscopy and diffraction. In the iron–carbon alloy and in the two low-carbon steels the carbide precipitates in a dendritic form during aging following quenching. In specimens quenched directly to the aging temperature oblong plates appeared, along with dendrites. Both of these forms are cementite (Fe₃C) and no diffraction evidence of precipitation of epsilon carbide was found.

The time required for formation of identifiable particles at 250°C corresponds to the time reported by others for 70 per cent completion of the precipitation reaction, as measured by internal friction. At 150°C the time required for formation of such particles was much longer than the time for completion of precipitation, as measured by internal friction.

The dendritic carbides in Fe–C alloys appear to precipitate on {110} planes of ferrite, with branches along (111) directions.

In the iron-3.25% silicon alloy the carbides take the form of lenticular disks precipitated on $\{100\}$ planes of the ferrite matrix; the crystal structure of this carbide was not determined but it is neither epsilon nor cementite. The disks are displaced by grain boundary films of cementite during prolonged aging.

MORPHOLOGIE ET STRUCTURE CRISTALLINE DES CARBURES PRECIPITÉS À PARTIR D'UNE SOLUTION SOLIDE DE FER α

À l'aide de la microscopie et de la diffraction électroniques, les auteurs ont étudié les carbures précipités à partir de la solution solide dans des alliages fer-carbone de très haute pureté, dans deux aciers à bas carbone et dans un alliage fer-carbone-3,25% silicium.

Dans l'alliage Fe–C et dans les deux aciers à bas carbone, les carbures précipitent sous une forme dendritique pendant le vieillissement après trempe. Dans les échantillons trempés directement à la température de vieillissement, apparaissent des plaquettes oblongues en même temps que des dendrites. Ces deux formes sont constituées par la cémentite (Fe $_3$ C) et la diffraction ne révèle aucune trace de carbure ε .

Le temps nécessaire à la formation de particules identifiables à 250°C correspond au temps mesuré par frottement interne et requis pour que la précipitation soit réalisée à 70 per cent. Au contraire à 150°C, le temps relatif à la formation de ces particules est beaucoup plus long que celui indiqué par le frottement interne pour le déroulement complet de la précipitation.

Les carbures dendritiques dans les alliages Fe–C précipitent sur les plans {110} de la ferrite, avec des ramifications le long des directions (111).

Dans l'alliage Fe-C-3,25% Si, les carbures prennent la forme de disques lenticulaires précipitant sur les plans $\{100\}$ de la matrice ferritique. La structure cristalline bien que non déterminée, ne peut être celle du carbure ε ni de la cémentite. Au cours d'un vieillissement prolongé, ces disques sont déplacés par des films de cémentite le long des joints de grains.

MORPHOLOGIE UND KRISTALLSTRUKTUR VON KARBIDAUSSCHEIDUNGEN AUS ALPHA-EISEN-MISCHKRISTALLEN

Die Karbidausscheidungen aus Mischkristallen von hochreinen Eisen-Kohlenstofflegierungen, zwei kohlenstoffarmen Stählen und einer Eisen-Kohlenstoff-3,25% Silizium-Legierung wurden mit dem Elektronenmikroskop und mit Elektronenbeugung untersucht. Aus der Eisen-Kohlenstoff-Legierung und aus den zwei kohlenstoffarmen Stählen scheidet sich das Karbid während des Auslagerns nach dem Abschrecken in dendritischer Form aus. In Proben, die direkt auf die Auslagerungstemperatur abgeschreckt worden waren, erschienen längliche Plättehen zusammen mit Dendriten. Beide Formen sind Zementit (Fe $_3$ C) und die Beugungsaufnahmen gaben keinen Hinweis auf die Ausscheidung von Epsilon-Karbid.

Die Zeit, die bei 250°C notwendig ist, damit sich identifizierbare Teilchen bilden, entspricht der von anderen mitgeteilten Zeit, in der die Ausscheidungsreaktion nach Ausweis von Dämpfungsmessungen zu 70% abgelaufen ist. Bei 150°C war die zur Bildung solcher Teilchen notwendige Zeit viel länger als die Zeit, in der die Ausscheidung nach Ausweis von Dämpfungsmessungen vollständig abgelaufen ist.

Die dendritischen Karbide der Fe-C-Legierungen scheinen sich auf den {110}-Ebenen des Ferrits auszuscheiden mit Ästen längs (111)-Richtungen.

In der Eisen-3,25% Silizium-Legierung scheiden sich die Karbide in der Form von linsenförmigen Scheiben auf den {100}-Ebenen der Ferritmatrix aus. Die Kristallstruktur dieser Karbide wurde nicht bestimmt, sie ist aber weder Epsilon noch Zementit. Nach längerem Auslagern werden diese Scheiben durch Korngrenzenzementit ersetzt.

^{*} Received November 13, 1958.

[†] Edgar C. Bain Laboratory for Fundamental Research, United States Steel Corporation Research Center, Monroeville, Pennsylvania.

INTRODUCTION

The precipitation of carbon from super-saturated ferrite during quench-aging has been a subject of considerable interest for a number of years. A

micrograph* of Fig. 1. Electron micrographs made several years ago of an extraction replica of a quenchaged low-carbon steel showed that what appeared as plates or needles in optical micrographs were

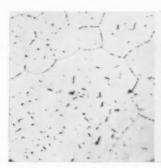


Fig. 1. Carbides precipitated in 0.02% C rimmed steel held 10 min at 705°C, quenched to 425°C, aged 10 min, brinequenched. Picral etch. ×1000.

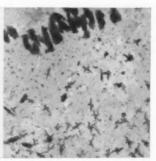


Fig. 2. Grain boundary and dispersed carbides in 0.04% C rimmed steel held 20 min at 720°C, quenched to 315°C, aged 20 min, brine-quenched. Extraction replica. × 20,000.

review of the numerous papers on this topic shows that a number of discrepancies have arisen which need to be resolved. For example, the carbides have been calculated to be spherical from analysis of the time dependence of the change of internal friction during aging(1,2) and electron micrographs purporting to show this shape have been published. (3) Similar calculations have been made to show that the particles must be plate-like(4,6) and electron micrographs which appear to support this view have been presented. (5,9) It has been claimed that two forms of carbide are precipitated from super-saturated solid solution in alpha iron. (7,8,9,23) According to these reports cementite (Fe₃C) forms during aging at about 200°C or above whereas at lower temperatures epsilon (Fe2.4C) occurs. However, internal friction measurements indicate that the precipitation of carbon from solid solution in ferrite is a single-stage process. (1,10,11) Also, a recent analysis by Ham(10) has shown that in general the time rate law of a precipitation reaction does not depend upon particle shape providing the precipitated particle remains geometrically similar, in contradiction to the earlier suggestion by Zener(19) which was used in the calculations previously mentioned.

1959

Many observations, made at this laboratory, of the carbides precipitated in low-carbon steel during quench-aging indicated that these carbides were certainly not spherical⁽¹²⁾ but rather, seemed to take the form of plates or needles, as shown in the optical

actually more complex shapes, as shown in Fig. 2. In addition, the electron diffraction patterns from particles extracted from a number of specimens were not compatible with the crystal structure of epsilon carbide. These observations, and the conflicting claims in the literature, provided the impetus for a more thorough investigation of the precipitation of carbon from super-saturated alpha iron.

As will be described later, improvements in techniques of electron microscopy and diffraction now make it possible to determine the shape and crystal structure of the precipitated carbides with more certainty.

In a paper published after this work was completed, Pitsch and Schrader⁽²⁰⁾ have reported results similar to part of the work reported here.

2. MATERIALS AND PROCEDURES

The compositions of the materials used are listed in Table 1. The high-purity iron was obtained in the form of a 25 lb ingot from National Research Corporation. The major impurity was 0.033% silicon. Steel I was an enameling iron in the form of hot-rolled sheet, 0.140 in. thick. Steel P was hot-rolled low-carbon sheet 0.127 in. thick. Steel A was a hot-rolled silicon steel in the form of sheet 0.110 in. thick.

A $\frac{1}{2}$ in. thick slice was cut, perpendicular to the long axis of the high-purity iron ingot, then cold

^{*} All micrographs reduced approximately $50\,\%$ in reproductions.

Table 1. % Composition of materials used

	C	Mn	P	S	Si	Cu	Ni	Cr
High- purity iron* Steel I		< 0.01		0.006 0.034		0,006 0.01	0.006 0.01	0.002
Steel P Steel A	0.05	0.52		0.01 0.014	3.29	0.01	0.01	

^{*} Al, 0.001; N, 0.0013; O, 0.0057; Mo, 0.003.

rolled to a thickness of 0.035 in. Strips 1 in. wide were annealed in dry, purified hydrogen at 740° C for 6 h, then cooled in hydrogen in the cold zone of the furnace. They were then carburized in H_{\circ} –C H_{4}

Electron diffraction patterns were obtained from particles on these replicas.

3. RESULTS AND DISCUSSIONS

A. Precipitate morphology

The extraction replica technique of electron microscopy is very well suited to the determination of the shape and crystal structure of very small particles precipitated from solid solution. Details of the particles are not obscured by shadowing and electron diffraction patterns can be obtained without interference from the matrix or from thin surface films. There are a few inherent limitations, however, that should be recognized. During the second etch,

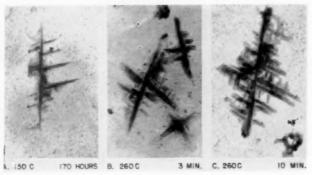


Fig. 3. Dendritic carbides precipitated during aging of Fe-0.014C alloy, brine quenched from 740°C, aged as noted. Extraction replicas. ×40.000.

mixtures at 740°C to carbon contents in the range 0.009 to 0.014%, and cooled in the cold zone of the furnace. The nitrogen content after this treatment was 0.0003%. After cutting into smaller sections, the specimens were sealed into evacuated silica tubes, solution treated at 740°C for 1/2 hr, then brine quenched. The subsequent aging treatments were done in lead–bismuth baths and were terminated by brine quenching.

The two commercial low-carbon steels were solution-treated for 20 min at 720°C, then either brine quenched to room temperature and reheated to the aging temperature, or quenched directly to the aging temperature. The specimens were brine quenched at the end of the aging period. Observations of the microstructure were made as soon as possible after aging.

Metallographic specimens were polished and etched in the usual manner. Most of the electron microscope observations were made on extraction replicas. (13) The etchant used with these replicas was picral, with an addition of 2 ml Zephiran chloride per 100 ml.

through the replica, particles below the original surface may be exposed sufficiently to be pulled off with the replica. More particles appear than can be seen on an equal area of polished and etched surface, so that attempts to determine the density of precipitate from extraction replicas are not justified. During the separation, the angular relationships between the particles may be changed slightly so it is not advisable to use extraction replicas in habit plane determinations. The angles within a given particle, however, remain unchanged by the extraction.

The dendritic shape of the carbide precipitate, as suggested in Fig. 2 can be seen clearly in the micrographs of Fig. 3 at higher magnification. These micrographs show the particles in extraction replicas taken of specimens aged at 150° and at 260°C following a brine-quench from 740°C. There are two principal directions in the dendrite subtending an angle in the range 68°-73°. A third direction is faintly visible in Fig. 3A, 3B and 3C, subtending angles of about 50° and 60° with the two principal directions. The branches of the dendrite appear to be made up of

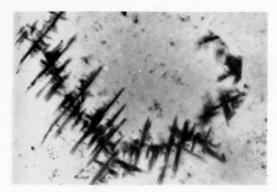


Fig. 4. String of dendritic carbides in Fe-0.014C alloy, quenched from 740°C, aged 3 min at 250°C. Extraction replica. $\times 40.000$.

bundles of narrow rods. The morphology of this carbide will be discussed further in a later section dealing with electron diffraction analysis of the particles.

The distribution of the precipitate particles is frequently nonuniform. Typical denuded grain boundary regions are shown in Figs. 1 and 2. Occasionally stringers of the dendritic carbides were observed, as shown in Fig. 4. These probably result from nucleation of carbides along dislocation lines. Similar stringers were observed at earlier stages of precipitation, as shown in Fig. 5, taken from a specimen of the 0.014% carbon iron aged 30 min at 200°C following a quench. The contrast of the material deposited on the replica is very low. It is probably carbon from "atmospheres" condensed along the dislocation line. This material did not give a crystalline electron diffraction pattern.

1959

The difficulty of resolving the complex shape of the dendritic particles by conventional surface replica methods is illustrated by the comparison of Figs. 6A and 6B. Both micrographs were taken of a specimen of 0.009% C iron aged for 1 min at 315°C



Fig. 5. An early stage in the precipitation of dendritic carbides showing darkened unresolvable areas. Fe-0.014C alloy, brine-quenched from 740°C, aged 30 min at 200°C. Extraction replica. $\times 50.000$.

following a quench. The shadowing process obscures the detail of the dendrites. Depending upon the angle between the specimen surface and the plane of the particle, shadowed replicas can give the appearance of either plate-like or spherical particles.

The dendritic carbides were observed both in the high-purity iron-carbon alloys and in the two steels employed. The particles formed in the steels were smaller for corresponding aging times and temperatures and exhibited less extensive branching than those in the iron-carbon alloys. This can be seen by comparing Fig. 7B with Fig 3C. There was no discernible difference between the carbides in the two low-carbon steels; i.e. the difference in manganese content, 0.05% and 0.52%, did not seem to influence the size or shape of the carbide particles.

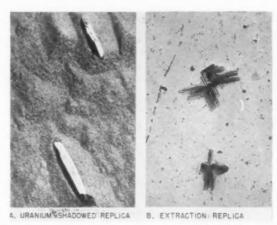


Fig. 6. Comparison between appearance of carbides on a shadowed replica and on an extraction replica. Fe–0.009C alloy, brine-quenched from $740\,^{\circ}\mathrm{C},$ aged 1 min at $315\,^{\circ}\mathrm{C}.$ $\times 50,000.$

In all the alloys examined the dendritic form persisted over a wide range of aging temperatures, as can be seen in the micrographs of Fig. 7, covering aging temperatures from 150° to 524°C. At the higher aging temperatures the dendrites become shorter and thicker. The characteristic 70° angle persists even when coalescence is well advanced, (Fig. 7E).

Some of the specimens contained a small number of aggregates such as are shown in Figs. 3B and 8. These take the form of sets of L-shaped lines. The lines are approximately 30 Å wide and 100 Å apart. No electron diffraction patterns could be obtained from this precipitate. Pitsch(21) has found particles with the same morphology and with the epsilon carbide structure in quench-aged iron-carbon-nitrogen alloys. The presence of such particles in our specimens containing only 0.0003% nitrogen, however,

Fig. 7. Dendritic carbides precipitated in steel I (except A) in the aging temperature range $150^{\circ}-425^{\circ}\mathrm{C}$. Extraction replicas.

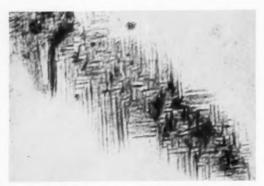
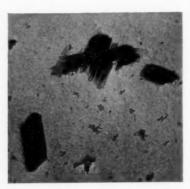


Fig. 8. Carbide aggregate in Fe=0.096C alloy, aged 1 hr at 260 °C. Extraction replica. $\times 200,000.$



19

Fig. 9. Dendrite and oblong plates of cementite in 0.014% C ferrite, solution treated 740°C, quenched to 372°C, aged 30 min. Extraction replica. $\times 55,000.$

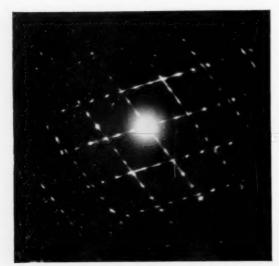


Fig. 10. Electron diffraction pattern of dendritie cementite particle in Fig. 9.

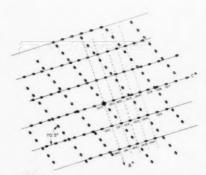


Fig. 11. Indexing of spot pattern on basis of cementite structure.



Fig. 12. Large dendritic carbide in Fe-0.096C alloy, held 1 hr at 260 °C. Extraction replica. $\times 200,000$.

makes it doubtful that nitrogen is required for their formation.

1959

When specimens were quenched directly to the aging temperature after solution treatment, two forms of carbide were observed. These take the form of dendrites and oblong plates, as shown in Fig. 9. The frequency of occurrence of the two forms depends upon the aging temperature. Relatively few of the plates were formed at 315°C, but this form predominates when the aging temperature is 455°C. Dendrites grown in this manner become quite large. The largest dendrites observed were those separated from the ferritic areas of a high-purity iron specimen carburized to 0.096% carbon, cooled in the carburizing gas in the cold zone of the furnace, then aged at various temperatures. The dendrites grown in this manner reached a maximum length of about 10⁻³ cm. One such is shown in Fig. 12.

B. Identification of crystal structure of carbides precipitated from ferrite

The carbide particles which precipitate during aging from ferrite are too small and too few in number in the samples to be identified by X-ray diffraction techniques. However, it was possible to obtain electron diffraction powder patterns from groups of particles and cross-grating patterns from single particles on extraction replicas. Most of the patterns were taken with a Siemens Elmiskop I operating at

80 kV. As a check on the calibration some diffraction patterns were taken of particles which had been shadowed with gold so that both patterns were superimposed. Using this method the accuracy of the data is about 1/2 per cent. However, caution is required in comparing electron diffraction data from such small and very thin crystals with X-ray diffraction data from bulk samples. The relative intensities of diffraction lines may be quite different and if the particle has only a few unit cells along one or even two dimensions a great many diffraction lines will be missing entirely. This effect is also observed for X-ray diffraction and is particularly troublesome in identification of cementite because of the complex structure. The large change in the X-ray diffraction pattern of cementite during the progress of tempering has been discussed by Jack (16).

Table 2 lists transmission electron diffraction data for a group of dendritic carbides of a sample of the 0.014% carbon iron aged for 100 hr at 100°C. A sufficient number of particles had formed to give a powder pattern. Similar patterns were obtained from a number of other specimens. The data are compared with the standard pattern for cementite and epsilon carbide. These measurements, as well as visual comparison of the actual plates with similar patterns from known cementite and epsilon carbide, leave no doubt that the dendrites are cementite rather than epsilon.

Identification of the powder patterns as cementite

Table 2. Interplanar spacings (Å) for dendritic carbides (Fe-0.014C, aged 100 hr at 200°C)

Observed spacing	Intensity*	Epsilon carbide† $(Fe_{2.4}C)$	$\begin{array}{c} {\rm Cementite} \dagger \\ {\rm (Fe_3C)} \end{array}$	Miller indices of crystal planes
3.33	W		3.358	002
2.54	M		2.536	020
2.40	M	2.40	2.371	021
2.21	W		12.248	200
			2.207	120
2.11	W	2.15	2.098	121
2.02	S		2.018	022
1.85	W.		1.862	113
1.66	W	1.60	1.679	023
1.40	W		1.403	024
1.33	VW	1.36	1.326	312
1.18	W	1.23	1.189	025

^{*} Intensities: S—strong, M—medium, W—weak, VW—very weak.

† Data from Jack (16).

is confirmed by analysis of electron diffraction patterns of single particles. Fig. 10 shows the electron diffraction pattern of the carbide particle in Fig. 9. Similar electron diffraction patterns were obtained from dendritic particles over the full range of aging temperatures and times. This pattern is actually the superposition of two patterns at an angle of 70° and is a result of the fact that the dendrite has two principal directions and so diffracts as two crystals. During the early stages of growth of the dendrites a third direction is faintly visible, as mentioned previously, but it does not appear to contribute to the diffraction pattern and vanishes as aging progresses. When the particle has relatively few side branches, one of the line patterns is very much weaker than the other.

With the selected area electron diffraction technique it is possible to relate the crystallographic direction with the dimensions of the crystal. The electron diffraction pattern obtained is equivalent to a plane section through the reciprocal lattice of the diffracting crystal. The coordinates of the diffracting spots may be equal to the Miller indices of the crystal or else related to them in a simple manner. The pattern shown in Fig. 10 cannot be obtained from epsilon carbide, but as shown in the sketch of Fig. 11, it can be obtained from cementite.

The crystal grows with the b axis of the orthorhombic cementite unit cell aligned along the length of branches of the dendrite, the c axis perpendicular to the branches and in the plane of the particle and the a axis aligned through the particle. The streaking of the diffraction spots along the C^* direction is a result of the fact that the branches of the dendrites are actually a parallel array of very narrow rods, as is

apparent in Figs. 3, 6 and 12. These rods are 35 to 50 Å wide, which is only 5 to 7 unit cell distances, so the diffraction spots are stretched out along the directions of the branches of the dendrites. Even the large dendrites formed by quenching directly to the aging temperature or by gas cooling from the solution temperature exhibit this diffraction streaking. The micrograph of Fig. 12 shows the make-up of such a dendrite. Each rod in the branches diffracts as a separate crystal although they are all oriented in the same way.

The oblong plates which occur during aging following a quench directly to an elevated aging temperature give an electron diffraction spot pattern which can also be interpreted as cementite. In this instance the diffraction pattern is the same as that obtained from lamellae of cementite formed during the growth of pearlite.⁽¹³⁾ The direction through the thin plate is along the c axis of the orthorhombic cell.

The small size and complex shape of the dendritic carbide increase the difficulty of determining the habit plane of this precipitate. The observation that at least five directions of the precipitate can be seen in one grain (Fig 1) eliminates the possibility of $\{100\}$ or $\{111\}$ habit planes, unless more than one carbide is present or more than one habit plane is adopted. The constant 70° angle observed between the branches of the dendrites corresponds to the 70° 32' angle between $\langle 111 \rangle$ directions on $\{110\}$ planes. In his most recent paper on this subject, Pitsch⁽²⁰⁾ suggests this habit plane and growth direction. The choice seems reasonable. Fig. 13 is a sketch showing the structure and

19

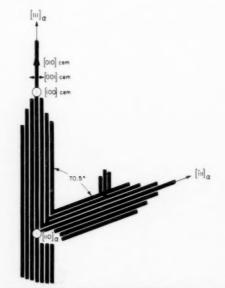


Fig. 13. Orientation of growth of dendritic cementite in ferrite.

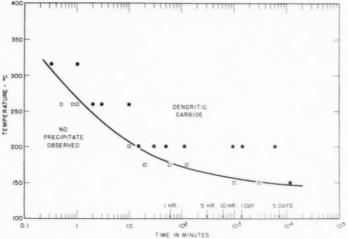


Fig. 14. Time required for precipitation of dendritic carbide from supersaturated alpha iron (0.014% C, brine-quenched from 740°C, reheated to temperates indicated).

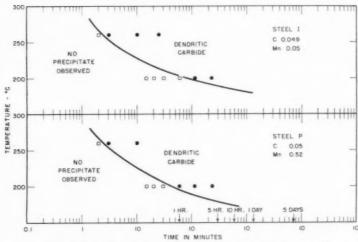


Fig. 15. Time required for precipitation of dendritic carbide from two low-carbon steels (brine-quenched from 720°C, reheated to temperatures indicated).

growth orientation of the dendrites. The carbides grow along the b axis of the orthorhombic cell which is the close-packed direction of iron atoms in the cementite structure. This same growth direction is observed for the carbides precipitated during growth of pearlite and bainite.⁽²²⁾ The third direction of growth, faintly visible in several of the figures, and making angles of about 50° and 60° with the two principal directions, cannot be a $\langle 111 \rangle$ direction.

C. Kinetics of precipitation

The time required for precipitation of carbides from solution-treated and brine-quenched alpha iron, containing 0.014% carbon, in the temperature range 150° to $315^{\circ}\mathrm{C}$, is indicated in Fig. 14. The times

required for precipitation of carbides in the two commercial low-carbon steels, at 200° and 260°C, are shown in Fig. 15. The curves are based on the first observation of a clearly defined precipitate on an extraction replica in the electron microscope. These observations were supplemented by the usual techniques of optical microscopy. Results obtained by both procedures agreed well. When clearly defined precipitates were obtained on the replicas, precipitation could be observed on polished and etched surfaces by light microscopy, although the precipitate could not be resolved.

When the time required for formation of the first recognizable precipitate is plotted vs. the reciprocal of the absolute temperature, the slope of the line

VOL. 7 1959

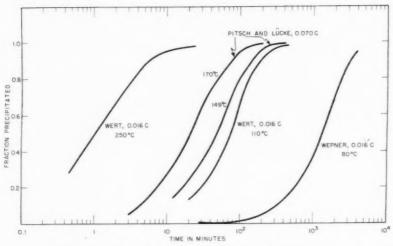


Fig. 16. Kinetics of precipitation of carbon from supersaturated solution in alpha iron, as measured by internal friction.

corresponds to an activation energy of 20,100 cal, the commonly accepted value for the activation energy for diffusion of carbon in alpha iron. The time required for observation of the first precipitate at 150° C, however, is much longer than predicted by this relationship. A possible explanation of this discrepancy is discussed later.

Very little difference was noted between the rates of precipitation in the two commercial steels despite the considerable difference in manganese content. Precipitation was slightly more rapid in the high-purity iron than in either of the two steels, but the difference in solution temperatures makes the comparison uncertain. At 200°C, a precipitate was observed after 15 min in the high purity iron as compared with 1–2 hr for the steels.

It is interesting to compare the curves of Figs. 14 and 15 with the data for the rate of precipitation of carbon, as measured by internal friction, shown in Fig. 16. At 260°C, a precipitate was observed in the high-purity iron-carbon alloy after 2 min. Wert's internal friction data(11) at 250°C indicate that the precipitation is about 70 per cent completed after 2 min. At 170°C, the internal friction measurements of Pitsch and Lücke⁽¹⁴⁾ indicate that the precipitation of carbon is completed in about 200 min, which was found in this investigation to be about the time required to form the first recognizable precipitate. At 150°C, complete precipitation occurred in about 400 min, according to Pitsch and Lücke(14), but no precipitate was observed on extraction replicas until after 10,000 min. Thus, as the aging temperature decreases, the formation of the first recognizable precipitate lags behind the completion of precipitation

of carbon as measured by internal friction. This may be due to the fact that very small particles on the replica, even though they are above the limit of resolution of the microscope, are not recognized as carbides.

Another possibility is that rate of precipitation in the specimens used may differ from those used in the internal friction work. It would be desirable to perform both internal friction measurements and electron microscopy on the same specimen.

19

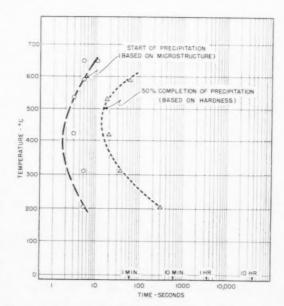


Fig. 17. Approximate length of time required for start and for 50 per cent completion of isothermal precipitation of cementite in 0.02% C rimmed steel. Prior solution treatment 10 min at 705°C, quenched directly to the aging temperature.

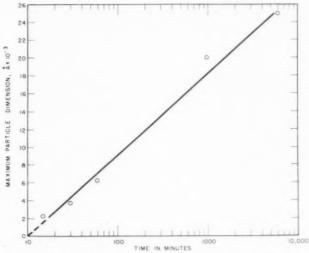


Fig. 18. Rate of growth of dendritic carbides at 200°C after quenching from 740°C and reheating (C=0.014%).

In discussing rate of isothermal precipitation of carbon from supersaturated solid solution in alpha iron, a distinction must be made between (1) the rate measured after quenching from the solution temperature to room temperature and reheating to the aging temperature, and (2) the rate measured after quenching directly to the aging temperature from the solution temperature. The latter is the more rapid of the two. This is shown by a comparison of Fig. 14 with Fig. 17 taken from Rickett and Kristufek. (12) After quenching directly from 705° to 200°C, a precipitate is observed after about 5 sec; if the specimen is quenched from 740°C to room temperature, then placed in a lead–bismuth bath at 200°C, about 30 min is required to form a recognizable precipitate.

A sufficient number of observations were made of samples of high-purity iron aged at 200°C to allow a reasonably accurate determination of the rate of growth of the carbide particles. The length of the largest particle observed after each aging period was measured. Because of the shape of the particles, this is a measurement of one-dimensional growth. The rate can be represented as a logarithmic function of time, as shown in Fig. 18. An extrapolation of the curve indicates that the length of the particle would be zero at 10 min which is a good check on the direct observation (Fig. 14).

D. Carbides precipitated from silicon ferrite

The presence of up to 0.5% manganese appears to have little effect on the kinetics of precipitation or the form of the carbide in iron–carbon alloys. The presence of silicon, however, produces pronounced

effects. Fig. 19 shows typical grain boundary carbides in a 3.20% Si, 0.01%C alloy, cooled slowly from 870%C. These grain boundary carbides could not be removed on an extraction replica, but deep etching left the carbide in relief so that electron diffraction patterns could be obtained by reflection from the surface of the sample. Table 3 lists the interplanar spacings of the grain boundary film. Comparison of these spacings with those of cementite ${\rm Fe_3C},^{(16)}$ also listed in the table, identifies the carbide film as cementite. This result agrees with that recently reported by Leak and Leak⁽¹⁵⁾.

The occurrence in silicon steel of a precipitate which has a needle-like appearance in a polished and etched cross section has been observed for many years. This precipitate can be formed by various treatments, including air cooling from high temperatures, heating to high temperatures followed by an isothermal treatment in the temperature range from about 250° to 600°C, and brine quenching from an elevated temperature followed by an isothermal treatment.

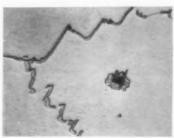


Fig. 19. Grain boundary cementite in 3.20% Si, 0.01% C alloy, slowly cooled from 870°C. Picral—nital etch. ×2000.

VOL. 7 1959

Table 3. Interplanar spacings (Å) for grain boundary carbide in silicon steel

Observed spacing	${\rm Fe}_3{\rm C}^{(16)}$	Miller indices of crystal planes
_	5.072	010
2.54	2.536	020
1.70	1.691	030
1.268	1.268	040
1.016	1.015	050
3.74	3.75	101
3.02	3.018	111
2.10	2.098	121
1.54	1.539	131
1.21	1.202	141
1.87	1.862	202
1.75	1.756	212
1.51	1.506	222
1.25	1.255	232
1.05	1.052	242
1.245	1.250	303
1.23	1.212	313
1.12	1.123	323
1.00	1.005	333

Fig. 20 is a micrograph showing a typical occurrence of this precipitate in Steel A, heated in an evacuated silica capsule to 1315°C (at which temperature the steel was completely ferritic) then air cooled to room temperature. The relatively large particles shown in Fig. 21 were obtained by heating the same steel to 1315°C, quenching to 315°C, then holding for 2 hr. Although their composition is unknown, these

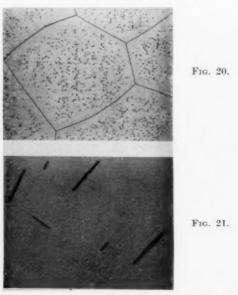


Fig. 20. Lenticular carbides in steel A, air cooled from 1315 °C. Picral-nital etch. $\times 100$.

Fig. 21. Lenticular carbides in steel A, quenched from 1315°C to 315°C, held 2 hr. Picral-nital etch. $\times 2000$.

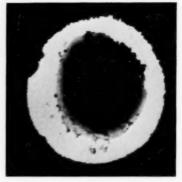


Fig. 22. Lenticular carbide from steel A, quenched from 1315° C to 315° C, held 2 hr. Extraction replica. $\times 20,000$.

particles are believed to be carbides. They are found only in iron-silicon alloys containing carbon, and they are displaced by grain boundary cementite films after prolonged heating. The particles have the shape of round, lenticular disks, as shown in the electron micrograph of Fig. 22. The diameter-to-thickness ratio is about 25 to 1.

Since not more than three directions of the precipitate are observed within one grain, it can be inferred that the lenticular carbides precipitate on $\{100\}$ planes of the ferrite. This was checked by determining the orientation of a large grain showing clearly defined precipitate directions. The poles of the $\{100\}$ planes of the grain fell on the normals to the traces of the precipitate. This same observation was recently reported by Suits and Low⁽¹⁷⁾.

A typical electron diffraction pattern of a single particle is shown in Fig. 23. The diffraction spots



Fig. 23. Electron diffraction spot pattern obtained from lenticular carbide shadowed with palladium.

VOI 7 195



Fig. 24. Indexing of spot pattern of Fig. 23.

form a square network although many points are missing and others are very weak. Except for intensity, all points in such a pattern are equivalent and so the innermost spots must be indexed as (030), etc, in order to avoid fractional indices. This is shown in Fig. 24. The interplanar distances were determined accurately by shadowing an extraction replica with palladium so that the electron diffraction pattern of the palladium and a precipitated particle were superimposed. The data are listed in Table 4. It can be concluded that the lenticular precipitate in low-carbon silicon steel is neither cementite nor epsilon carbide but another carbide of unknown composition and structure.

VOL.

1959

The spacing of the most intense diffraction spots is the same as the (110) and the (200) spacings in alpha iron. This observation, coupled with the observation that the habit plane is $\{100\}_{\alpha}$ indicates that the iron atoms have the same arrangement in the particles as in the ferrite matrix (in directions parallel to the surface of the particle). That is, the iron atoms are probably coherent on the surface of the particle; this could account for the lenticular shape of even the largest particles.

The relatively low intensity of the diffraction spots other than those already mentioned suggests that they may be due to superlattice reflections. This might indicate that the precipitate contains silicon atoms in an ordered arrangement, inasmuch as the scattering from carbon atoms is too weak to be observed. The other possibility is that the crystal structure of the precipitate is actually complex with a large unit cell so that it contains a number of planes with a very low density of atoms. Although the square array of diffraction spots suggests a cubic or tetragonal structure, these are unlikely because of the large number of omissions in the pattern.

Attempts to determine the silicon content of the particles by use of the electron probe microanalyzer

Table 4. Observed and calculated interplanar spacings for lenticular carbides

Observed spacing	Intensity	Calculated spacing	Co-ordinates of diffraction spots
		6.06	100
		3.03	200
2.02	S	2.02	300
1.515	W	1.515	400
1.212	M	1.212	500
1.01	M.	1.01	600
		4.28	110
		2.14	220
1.43	S	1.427	330
		1.07	440
		2.67	120
1.34	WM	1.335	240
1.94	WM	1.938	130
		0.969	260
1.47	W	1.468	140
		1.19	150
1.56	WM	1.563	230
1.04	W	1.038	350
1.21		1.212	340

Intensities: S—strong, M—medium, WM—medio-weak W—weak.

were unsuccessful, but the presence of silicon in the carbide was indicated.

4. SUMMARY AND CONCLUSIONS

The development of improved techniques of electron microscopy and electron diffraction has led to the clarification of existing discrepancies concerning the precipitation of carbon from supersaturated solid solution in alpha iron. Some of the previous interpretations (3,5,9) were erroneous because of the limitations of the experimental techniques used. Calculation of particle shape from rate of precipitation has recently been shown to be fallacious, (18) and this is confirmed by the observations reported herein.

The carbides precipitated during the quench aging of supersaturated alpha iron take several forms; dendrites, oblong plates and L-shaped arrays of parallel lines have been observed. The dendrites precipitate in the temperature range 150°–480°C, and they are the predominant form at the lower temperatures. The oblong plates predominate at temperatures above about 400°C. Both forms appear to be cementite, Fe₃C. The branches of the dendrites seem to be made up of bundles of thin cementite rods. These branches have two principal directions of growth, with an angle of 70° between them, and a third minor direction.

No indication was found of the presence of epsilon carbide. However, no diffraction patterns could be obtained from the L-shaped arrays, and their structure is unknown.

At low aging temperatures, the rate of precipitation, measured by electron and optical metallography, is much slower than the rate of precipitation measured by internal friction. This disagreement may be due to an inability to recognize very fine precipitate particles on extraction replicas or to differences in specimen composition and history, solution temperature, and aging procedure.

The habit planes of Fe₃C precipitated from unalloyed alpha iron are probably {110}_a. The principal directions of growth in this plane are $\langle 111 \rangle_{\alpha}$. A third minor direction of growth remains unknown.

The presence of up to 0.5% manganese has little effect upon the morphology, rate of precipitation, or habit of the carbides precipitated from ferrite, but the presence of 3.25% silicon has a pronounced effect. The carbides precipitated during aging of the iron-carbon-silicon alloy take the form of lenticular disks on {100} planes of the ferrite. The crystal structure of these carbides is unknown, but they are neither cementite (Fe₃C) nor epsilon carbide (Fe₃₄C).

ACKNOWLEDGMENT

The thanks of the authors are due to Albert Szirmae for the preparation of many excellent electron micrographs, to C. P. Stroble, K. G. Carroll, R. P.

Smith and J. C. Swartz for their help in other phases of the work, and to R. L. Rickett for suggestions which led to the investigation.

REFERENCES

- C. Wert, J. Appl. Phys. 20, 943 (1949).
- C. Wert and C. Zener, *Ibid.* 21, 5 (1950).
 J. Radavich and C. Wert, *Ibid.* 22, 367 (1951).
- 4. W. Pitsch, Acta Met. 3, 542 (1955).
- 5. W. Pitsch, Ibid. 5, 175 (1957)
- R. H. DOREMUS, *Ibid.* 5, 393 (1957).
 A. L. TSOU, J. NUTTING and J. W. MENTER, *J. Iron* St. Inst. 172, 163 (1952).
- 8. O. Krisement, Arkiv Fys. 7, 353 (1955).
- 9. G. LAGERBERG and B. S. LEMENT, Trans. Amer. Soc. Metals 50, 141 (1958).
- 10. L. J. Dijkstra, Trans. Amer. Inst. Min. (Metall.) Engrs. 185, 252 (1949).
- C. Wert, Thermodynamics in Physical Metallurgy, p. 178. American Society for Metals, Cleveland, Ohio (1950).
- 12. R. L. RICKETT and F. C. KRISTUFEK, Trans. Amer. Soc.
- Metals 41, 1113 (1949).
 R. M. Fisher, Symposium on Techniques for Electron Microscopy. ASTM (1953).
- 14. W. PITSCH and K. LÜCKE, Arch. Eisenhüttenw. 27, 45 (1956).
- 15. D. A. LEAK and G. M. LEAK, J. Iron St. Inst. 189, 256 (1958).
- K. H. Jack, J. Iron St. Inst. 169, 26 (1951).
- 17. J. C. Suits and J. R. Low, Jr., Acta Met. 5, 285 (1957).
- F. S. Ham, J. Phys. Chem. Solids 6, 335 (1958).
- C. ZENER, J. Appl. Phys. 20, 950 (1949).
- 20. W. PITSCH and A. SCHRADER, Arch. Eisenhüttenw. 29, 485 (1958).
- 21. W. Pitsch. Private Communication.
- 22. R. M. FISHER, 4th International Congress on Electron Microscopy, Berlin (September 1958)

19

23. F. W. C. Boswell, Acta Cryst., Camb. 11, 51 (1958).

LETTERS TO THE EDITOR

Twinning in tantalum*

Recently, Barrett and Bakish were able to cause deformation twinning in tantalum by impact working at liquid nitrogen temperature, but not at dry ice or room temperatures. (1) Bechtold had previously reported

Bechtold reported 0.01% nitrogen and 0.010% carbon.

At this laboratory, during the course of an investigation of tantalum as a reactor material, twinning of high purity tantalum has been observed after impact

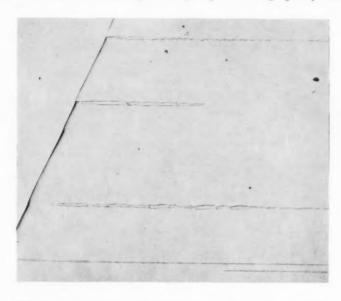


Fig. 1. Mechanical twins in tantalum. Specimen mechanically polished and etched in 2 parts lactic acid, 1 part HF, and 1 part HNO $_3$ for 40 min. and then in equal parts in HF and HNO $_3$ for 5 min. $\times 100$.



Fig. 2. Mechanical twins in tantalum. Specimen polished and etched as in Fig. 1. \times 500.

that tantalum did not twin when strained in tension at temperatures as low as that of liquid nitrogen. The metal used in both investigations was of nominal 99.9% purity. Barrett and Bakish reported impurities of 0.03% carbon and 0.03% iron, while ACTA METALLURGICA, VOL. 7, SEPTEMBER 1959 645

deformation by hammering at room temperature. The material used was cut from an ingot which had been electron beam melted. The average grain size was 4 mm by the intercept method. Results of a chemical analysis of the tantalum are listed in Table 1.

Table 1. Chemical analysis of electron beam melted tantalum

Element	p.p.m.	Element	p.p.m.	Element	p.p.m.
C	20	Al	<10*	Co	< 20*
H ₂	10	Ti	< 5*	Ni	< 10*
N ₂ O ₂ Si	15	L	< 20*	Zr	< 30*
Og	8	Cr	<10*	Cb	<2004
Si	3	Mn	< 3*	Mo	< 504
Cu	<2*	Fe	<10*	W	$<100^{\circ}$

^{*} Represents limit of detection.

Photomicrographs of the twins are shown in Figs. 1 and 2. In general, the twins had serrated boundaries quite similar to those of Neumann bands in iron.

The results of the present experiment, together with those reported by Barrett and Bakish, indicate that increasing the purity of tantalum increases the ease with which twins may be formed. This is opposite to the effect reported for alpha iron, at least with respect to carbon, nitrogen and silicon. (3,4)

Further studies of the effects of impurities on twinning in tantalum are planned as a part of the over-all tantalum investigation.

The authors wish to acknowledge their indebtedness to Mrs. Katherine Imlah for the metallography.

Work performed under the auspices of the U.S. Atomic Energy Commission.

R. W. Anderson

Los Alamos Scientific Laboratory S. University of California Los Alamos, New Mexico

S. E. Bronisz

References

 C. S. Barrett and R. Bakish Trans. Amer. Inst. Min. (Metall.) Engrs. 212, 122 (1958).

2. J. H. BECHTOLD, Acta Met. 3, 249 (1955).

C. F. TIPPER and E. O. Hall, J. Iron St. Inst. 175, 9 (1953).
 J. R. Low and R. G. FEUSTEL, Acta Met. 1, 185 (1953).

Some observations on mechanisms of growth of metal whiskers*

Fydrogen reduction of metal halides is now a standard method for growing metal whiskers of copper, silver, iron, cobalt, nickel and manganese. (1-4) Detailed mechanisms based on the action of screw dislocations to provide appropriate growth steps have been proposed to account for the formation of these whiskers. (5.6) An analysis of the thermodynamics, (7) and observations of the growth process (1.8) and the dislocation structure of the resulting crystals (9.10.11) have been reported. However, there is not yet satisfactory understanding of the mechanisms. We

report here some preliminary observations of the growth of copper whiskers by hydrogen reduction of cuprous chloride that yield some insight into these mechanisms.

Experimental

The whiskers were grown in a 1 in. diameter quartz combustion tube, heated to about 540°C . Purified hydrogen was passed through it at ~ 60 ml/min (S.T.P.). The resistance heated furnace was constructed with a 3/4 in. wide slot along the top so that the top of the reaction tube was a few degrees cooler than the bottom. Light from an arc lamp was admitted through the slot. When the furnace reached 540°C , a boat filled with cuprous chloride was pushed (without opening the reaction tube) into the hot zone. It was viewed from the end of the tube with an American Optical High-Temperature Microscope at a magnification of $\times 25$.

The salt melted after a few seconds, darkened, and then became coated with a film of copper. In 1-2 min, whiskers of about 2-10 u diameter started to grow from this surface and from adjacent surfaces of the boat on which cuprous chloride and copper had appeared. Growth by addition of material to the base or to the tip of the whisker can be distinguished by observing changes in distance between a fixed irregularity on the lateral surfaces and the ends of the whisker. Initial growth occurred by addition of metal at the whisker base, at rates on the order of 10 μ /sec. Most of the initial growth took place while the copper film on the salt was repeatedly ruptured by gas bubbling out of the melt. The whiskers were usually less than 2 mm long and many broke off at or near their bases shortly after formation, to drift upward through the surrounding gas or to fall back into the melt. After a few minutes, the rate of detachment of whiskers decreased, but continued slowly throughout the experiment. Many more whiskers were formed than appeared on the boat after a run since most of them broke loose. Many of the thicker whiskers, particularly those growing near the outer edges of the CuCl, reached 5 to 10 mm in length without detachment. Some of the drifting whiskers quite frequently stuck to the latter, resulting in a telegraph pole-like structure.

Besides the basal growth described above, some of the longer whiskers were observed to lengthen by addition of metal at their tips. The rate of this process was about an order of magnitude slower than basal growth. Often fragments that stuck to other whiskers grew further in their new sites.

Formation of helical whiskers was also observed in detail. This occurred when one of the drifting VOI 7 195

^{*} Received March 2, 1959.

whiskers happened to stick to the tip of another whisker that was growing at its tip. The fragment did not stick tightly but gyrated around its point of attachment, while growth of the original whiskers in a helical form took place at this junction. Fig. 1 shows a copper helix, which was observed to form in this way. Sometimes the rotation ceased and the original whisker continued to grow in a straight line. Brenner has observed particles on the tips of copper filaments during growth.⁽⁸⁾

These whiskers showed the characteristic high strength as evidenced by elastic recovery from bending strains on the order of 0.5 per cent. Some of the larger crystals (filaments) had normal strength properties. The X-ray examination of a few whiskers using the method of Dragsdorf and Webb⁽¹¹⁾ revealed no evidence for axial screw dislocations in agreement with previous results on copper whiskers.

Discussion

The observation of simultaneous tip and basal growth during formation of copper whiskers from liquid cuprous chloride indicates that there is not necessarily a unique mechanism by which metal whiskers are formed in a particular system. Tip growth of copper from liquid CuI, iron from liquid FeCl₂ and FeBr₂, and silver from liquid AgI has been observed, while basal growth of iron from solid FeBr₂ and FeCl₂, silver from liquid AgCl has also been observed, (1.9) but we know of no other system in which both have been observed simultaneously.

Our observations suggest that basal growth occurred in our system by direct addition of copper from supersaturated liquid CuCl to growth steps

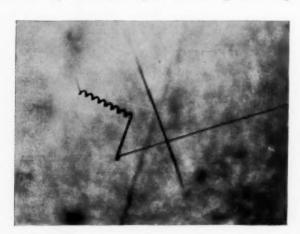


Fig. 1. Copper whisker with a helical section that was observed to form when a short fragment stuck to the whisker tip during growth. The short straight section at the top of the helix is the fragment responsible for the helix formation. ×70.

on the bottom face of a crystal, the top of which is pushed up out of the solution by addition of material at the bottom. Amelinekx⁽¹²⁾ proposed an analogous mechanism for basal growth of NaCl whiskers from saturated aqueous solution on a porous substrate. Some basal growth may occur in systems in which it has not yet been observed and this may be a common mode of whisker nucleation.

Although it is possible that mass transport to the whisker tip during tip growth occurred only by condensation of liquid CuCl on the whisker tip or liquid film migration along the whisker, the alternative of tip growth by vapor phase transport of metal halide without condensation to a liquid is also plausible [see references (7), (13) and page 101 in (8)].

The attachment of a whisker segment at the tip of a growing whisker is clearly responsible for formation of helical whiskers in this system, but the details of the mechanism by which the attached segment systematically alters the growth direction are not at all clear. Although this phenomenon does not necessarily apply to formation of all helical metal whiskers, it indicates that the problem is sometimes rather different than is assumed in previously proposed mechanisms. (14.15)

Detachment of whisker segments is either a consequence of insecure initial attachment because of initial growth from a liquid, or of re-solution in the atmosphere during composition fluctuations. Both may occur and the existence of fluctuations is indicated by observation of outbursts of gas from the liquid and blowing of whisker fragments to the top of the reaction tube. Re-solution or detachment of whiskers after formation may account for the notorious unpredictability of whisker formation in other systems. Collision of detached fragments with other whiskers yields some rather grotesque whisker forms that have previously been unexplained.

Although there is no X-ray diffraction evidence for the presence of axial screw dislocations in these whiskers after completion of growth, it is difficult to explain the occurrence of this one-dimensional growth without invoking a screw dislocation mechanism. It is possible for dislocations present during growth to climb or possibly to glide out of these whiskers during growth or to be present in a paired configuration and thus escape detection in X-ray studies. However, the fact that each complete whisker seems to grow for roughly the same length of time and then stops growing, while other immediately adjacent whiskers start or continue to grow, suggests that the time of retention of a dislocation may govern whisker length.

Apparently, the details of the mechanisms of

growth of metal whiskers by reduction of salts are yet to be established.

It is a pleasure to acknowledge the substantial assistance of Mr. A. F. Silvaggi in carrying out the experiments.

W. J. ALLAN

Metals Research Laboratories W. W. WEBB Union Carbide Metals Company Division of Union Carbide Corporation Niagara Falls, New York

References

1. S. S. Brenner, Acta Met. 4, 62 (1956).

2. G. W. SEARS, A. GATTI and R. L. FULLMAN, Acta Met. 2.

3. A. W. COCHARDT and H. WIEDERSICH, Naturwiss. 11, 342 (1955).

4. E. F. RIEBLING and W. W. WEBB, Science 126, 309 (1957).

S. S. BRENNER and G. W. SEARS, Acta Met. 4, 268 (1956).

G. W. Sears, Acta Met. 3, 361 (1955).

7. W. W. Webb and E. F. Riebling, J. Chem. Phys. 28, 1242 (1958).

8. F. R. Nabarro, Growth and Perfection of Crystals, pp. 13-101. John Wiley, New York (1958).

9. W. W. Webb, Growth and Perfection of Crystals, pp.

230-238. John Wiley, New York (1958) 10. W. W. Webb, R. D. Dragsdorf and W. D. Forgeng,

Phys. Rev. 108, 408 (1957). 11. R. D. Dragsdorf and W. W. Webb, J. Appl. Phys. 29,

12. S. AMELINCKX, Physica 24, 390 (1958). 13. R. V. COLEMAN and G. W. SEARS, Acta Met. 5, 131 (1957).

14. W. W. Webb, R. D. Dragsdorf and W. D. Forgeng, Phys. Rev. **108**, 498 (1957). 15. S. AMELINCKX, Phil. Mag. **3**, 425 (1958).

* Received March 2, 1959.

Discussion of "Shear along grain boundaries of an aluminum-10% zinc alloy deformed at room temperature"(1)*

The observation that grain boundary sliding can occur at room temperature in an aluminum-10% zinc alloy was made some years ago. (2.3) Summarizing this work, it was found that delayed intercrystalline fracture occurred when specimens were stressed in non-corroding environments and that behind the fracture, short intercrystalline cracks at right angles to the stress were present; these cracks are typical of what is observed in other metals when stressed at elevated temperatures, such that grain boundary sliding occurs. Later work(3) confirmed this and also showed typical localized strain markings running from the point of intersection of grain boundaries into the neighbouring grain. The authors(1) consider that the aluminum-10% zinc alloy is anomalous because grain boundary shear is taking place at 0.33 of the absolute solidus temperature. This is not necessarily so, because their experiments were probably done on material which was not single phase. Earlier work(2)

has shown that this alloy age hardens at room temperature very rapidly after quenching from the a phase; for the 10% zinc alloy the hardness increased from 46 VHN 25 sec after quenching to 87 VHN after 2 min. After ageing for 1 day at room temperature, Gayler's "light phenomenon" was observed at the grain boundaries and in subsequent work(3) this was shown to be softer than the matrix.

This grain boundary phase is an equilibrium structure and thus, by increasing the zinc content of the alloy the difference in plastic properties between the grain boundary and matrix is increased. This should lead to greater sensitivity to intergranular fracture, which was found to be so(4) for a 13% zinc alloy. In addition it is possible to remove this sensitivity to intergranular fracture by ageing at an elevated temperature for sufficient time to give an equilibrium structure i.e. a zinc rich precipitate in a depleted solid solution matrix.

Similar work(2) on an aluminum-4% copper alloy showed that if the alloy was heat treated to produce the "light phenomenon" delayed intercrystalline cracking occurred when stressed at room temperature, but if the alloy was aged at room temperature intercrystalline cracking did not take place. These results suggest that the authors are not dealing with a single solid solution but with a two phase structure, and it is this which is responsible for the observed grain boundary shear at room temperature.

E. C. W. PERRYMAN

195

Atomic Energy of Canada Ltd. Chalk River, Ontario Canada

References

- 1. A. R. CHAUDHURI, J. E. MAHAFFY and N. J. GRANT, Acta Met. 7, 60 (1959).
- 2. E. C. W. PERRYMAN and J. C. BLADE, J. Inst. Met. 77, 263 (1950)
- 3. E. C. W. Perryman, Stress Corrosion Cracking and Em-
- brittlement. John Wiley, New York (1956).
 E. C. W. PERRYMAN, C. R. Acad. Sci., Paris 235 (16), 884
 - * Received March 2, 1959.

On the thermal etching of silicon iron*

The formation of striations or steps and of boundary grooves at metal surfaces are two effects of thermal etching that occur when metals are heated to relatively high temperatures. This letter presents some observations on the thermal etching of silicon iron.

Polycrystalline sheet specimens, 0.012 in, thick of high purity silicon iron, containing about 3% silicon,

were used. Striations formed on certain grains when the samples were heated in atmospheres of argon. If the conditions of material and anneal time were correct, steps would also form when specimens were annealed in vacuum. Fig. 1 shows the orientations of grains that thermally etch and of some that do not etch when the material is annealed in argon at 1200°C. Striations occurred only in grains having orientations near (100) and (111). Small facet-like steps formed on grains having orientations near (110). These steps were so small that the net effect of the anneal was to leave the surface of the (110) grains almost specular. The thermally etched surface of a grain near the (100) orientation is shown in Fig. 2. In the regions of flat surface the striations are straight, but where the surface is rough the striations are curved. The large smooth step shown in the figure formed in such a rough region. The normal to the step was measured by reflected light and, within experimental error, was found to coincide with the pole of the (100)

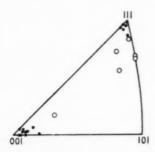


Fig. 1. Relation between orientation and thermal etching behavior. Orientations that etch: solid circles. Orientations that do not etch: open circles.

plane of the crystal. Similar measurements on other crystals indicated that the flat steps were either (100) or (111) surfaces.

Fig. 3, taken from earlier work,⁽¹⁾ shows thermal etching of a grain near (100) annealed in vacuum at 1050°C. Longer anneals at the same or higher temperatures in vacuum remove the striations. Thus the thermal etching is only temporary and indicates changing conditions. This will be discussed later. When the material is heated in argon the etching effects are not transitory; specimens previously annealed in vacuum and free of striations will again thermally etch if reannealed in argon.

The above effects noted for silicon iron have two things in common with other metals. First, the thermally exposed faces are low index planes. (2-7) The second effect involves the atmosphere and the composition of the material. (2.8)

The present observations on the effect of atmo-

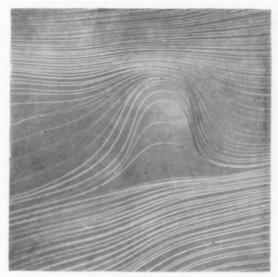


Fig. 2, (100) faces revealed by an 8 hr argon anneal at 1250° C. $\times 750$.

spheres and composition of the material on the etching behavior of silicon iron may be understood on the basis of the oxygen contained either in the atmosphere or in the material as has been noted also for other metals. $^{(4,6,8)}$ It is known that the argon used during the anneals of the silicon iron contained some oxygen. It is also known that oxygen is removed from the silicon iron during the vacuum anneal at high temperatures if the pressure is less than 5×10^{-3} mm mercury. The initial formation of an etched surface in vacuum and the subsequent removal of the etching

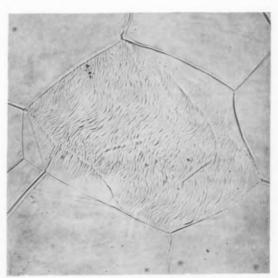


Fig. 3. Thermally etched surface of a cube oriented grain after a vacuum anneal of 80 min at $1050\,^{\circ}\mathrm{C.}$ $\times 250$.

effects may be explained in terms of the oxygen contained in the material passing through a critical range. Thus when the amount of oxygen in the material and at the surface drops below about 10 parts per million, etching ceases. The argon used during the anneals supplies the correct amount of oxygen for thermal etching of surfaces near (100) and (111).

It is clear that thermal etching produces a larger area of gas—metal interface than is present in the unetched surface. This increase in area may be explained in terms of the orientation dependent surface energy, the specific values being lower for low index planes. (4-9) The atoms at the surface are rearranged in a manner such as to expose low index planes and thereby reduce the total surface energy. This change of the surface free energy is thought to depend on the manner in which oxygen is adsorbed on different crystal planes. (4,7) Thus, the adsorption of oxygen on different crystallographic planes alters the relative surface energies of these planes. (4)

The authors are grateful for the assistance given by H. Brandhorst and Miss E. Freeman and for the valuable discussions with Dr. G. Ehrlich.

General Electric Research Laboratory Schenectady, N.Y. C. G. Dunn

J. L. WALTER

References

 C. G. Dunn and J. L. Walter, Initial Growth Behavior of a Secondary Recrystallization Cube-Oriented Nucleus, Cleveland AIME Meeting (1958). Also J. Metals 10, 573 (1958).

C. F. Elam, Trans. Faraday Soc. 32, 1604 (1936).
 F. W. Young, J. Appl. Phys. 27, 554 (1956).

 B. CHALMERS, R. KING and R. SHUTTLEWORTH, Proc. Roy. Soc. A 193, 465 (1948).

5. A. J. W. Moore, Acta Met. 6, 293 (1958).

- J. Benard and J. Moreau, C.R. Acad. Sci., Paris 238, 1659 (1954).
- J. Moreau and J. Benard, J. Chim. Phys. 53, 787 (1956).
 J. Benard, J. Moreau, and F. Gronlund, C.R. Acad. Sci., Paris 246, 756 (1958).
- 9. C. Herring, Phys. Rev. 82, 87 (1951).

* Received February 16, 1959; revised version March 5, 1959.

Radiation-induced precipitation sites in potassium chloride*

Recently⁽¹⁾ a suggestion has been made concerning the nature of the possible nucleation sites, other than existing dislocations or grain boundaries, in a quenched supersaturated solid solution. It appears that there is some evidence that small prismatic dislocation loops, resulting from vacancy condensation, might act as such. Hirsch and Silcox⁽²⁾ have presented direct evidence that quenching actually results in the formation of either prismatic loops (in aluminium) or more complicated tetrahedral defects (in gold), so this suggestion is quite reasonable.

The purpose of this note is to present evidence that not only quenching but also X-irradiation may create nucleation centers for precipitation in the alkali halides.

It was shown previously⁽³⁾ that the dislocations in potassium chloride single crystals doped with silver nitrate (0.4 wt.% addition to the melt) can be decorated by X-irradiating for 4 hr, followed by annealing in air for 1 hr at 600°C. The crystals as grown are perfectly clear when viewed in the ultramicroscope; after X-irradiation they are still optically clear although of course coloured. The decoration after heating is due to the formation of small cubic cavities centered on the dislocations: they are filled with gas under pressure. The walls of the cavities are covered with silver. The gases result from the decomposition of the NO₃ group; they precipitate during the anneal in air. Apart from the heterogeneous precipitation at individual dislocations, homogeneous precipitation is also observed, after long irradiation times, in a layer which extends inward from a few microns under the irradiated surface.

To separate the effect due to X-irradiation, decoration was also achieved by hydrogen treatment at the same temperature. The decoration is then of the same type, although the cavities are somewhat larger. It is found however that in the latter case the random precipitation is almost completely absent. It is therefore suggested that the apparently randomly distributed precipitates in the irradiated specimens are formed at the clusters of vacancies (or complex colour centres) generated near the surface during irradiation and the subsequent anneal. The clusters considered here are very probably the same as those that cause radiation hardening in the alkali halides. (4)

VOI

19

Sufficiently near to the surface the vacancies would get a chance, during the anneal, to escape at the surface before they form a cluster capable of nucleating a precipitate. No random precipitates would therefore form in this region. Further behind the surface however, they could form either small loops or larger clusters which could then act as nucleation centres for precipitates.

The majority of precipitates form what are apparently plate like cavities in the cube plane (Fig. 1). The vicinity of grain boundaries and isolated dislocations is always depleted of precipitates.

The way in which a cluster of vacancies could act as a site for the formation of gas filled cavities is as

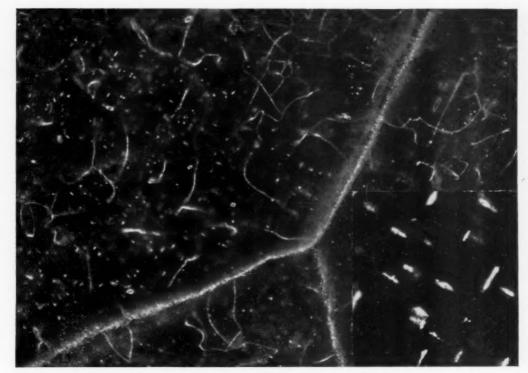


Fig. 1. Specimen of KCl doped with ${\rm AgNO_3}$ after X-irradiation (6 hr) and anneal in air. Note the decoration of dislocations and the random precipitation ($\times 250$). Inset: enlarged view of random precipitates ($\times 900$).

follows. Suppose that a vacancy cluster captures a few gas molecules; the gas will then exert a pressure on the walls of the small cavity. This pressure will cause an elastic interaction with other vacancies in the neighbourhood, which will migrate towards it, and enlarge it, and so relieve the pressure.

I wish to thank Prof. W. Dekeyser for his continuous interest and for helpful discussions. This work is part of a research programme supported by I.R.S.I.A. (Institut pour l'encouragement de la Recherche Scientifique dans l'Industrie et l'Agriculture; Comité d'étude de l'Etat Solide).

S. AMELINCKX

Laboratorium voor Kristalkunde Rozier 6, Gent, Belgium

References

- 1. A. Boltax, Acta Met. 6, 721 (1958).
- P. B. Hirsch and J. Silcox, in Growth and Perfection of Crystals edited by Doremus, Roberts and Turnbull, p. 262.
 Wiley, New York (1958).
- 3. S. AMELINCKX, Phil. Mag. 3, 653 (1958).
- E. Aerts, S. Amelinckx and W. Dekeyser, Acta Met. 7, 29 (1959).
 - * Received February 28, 1959.

Temperature gradient grain boundary migration*

Grain boundaries have been observed to migrate in a temperature gradient towards higher temperatures. (1.2) This phenomenon can be explained by a mechanism similar to temperature gradient zone melting, (3) if one assumes that the grain boundary has a finite thickness and behaves as a distinct phase. This assumption seems to be supported by the recent work of Cahn and Hilliard (4), and Inman and Tipler (5).

In order that temperature gradient zone melting may take place in a given system, certain conditions have to be fulfilled. The same conditions can be applied to the temperature gradient migration of a solid phase in a two phase system of appropriate geometry. These conditions are as follows:

- (a) the equilibrium concentration of solute must be different in the two phases, at a given temperature,
- (b) the equilibrium concentration of solute in one or both phases should vary with temperature,
- (c) the rate of diffusion of solute in one of the phases must be substantially higher than in the other.

If we accept that for a given concentration in the bulk material the grain boundary concentration is a function of temperature, ⁽⁶⁾ a grain boundary becomes essentially a thin slab of "second phase" in the bulk material. The temperature dependence of the grain boundary concentration can be approximately described by an equation of the form:

$$C_{gb} \cong AC \exp(Q/RT)$$
 (1)

where C_{gb} = concentration in the grain boundary

C =concentration in the bulk

Q= difference between elastic distortion energy due to the presence of a solute atom in the lattice and in the grain boundary.

R = gas constant

T = absolute temperature

A = constant

Although Q varies from one system to another, it is always a positive quantity, and the grain boundary concentration is always a decreasing function of temperature.

Grain boundary migration, regardless of the nature of the driving force, must be accompanied by mass transfer across the grain boundary. Under appropriate driving forces, the rate of grain boundary migration can be substantially higher than the rate of self-diffusion or the rate of diffusion of most solutes in the bulk material. It is, therefore, reasonable to assume that the diffusion rate across grain boundaries is substantially higher than in the bulk material. Thus, a grain boundary fulfills all the necessary conditions for temperature gradient migration with respect to the adjacent crystals.

Let us consider a system consisting of two crystals separated by a large angle grain boundary. In this system, let A designate the solvent or main constituent, and B all the solutes or impurities.

Let us assume that for a given concentration of B in the bulk material, the grain boundary has reached a concentration in B corresponding to a

temperature T_1 . This concentration exceeds the concentration in the bulk, as shown by equation (1). Let us now impose on the system a temperature gradient in a direction normal to the plane of the grain boundary; which gives a temperature difference across the grain boundary $T_3 - T_2$ with $T_3 > T_2$ $> T_1$. Under these conditions the concentration of the grain boundary in B will tend to decrease and adjust to the value corresponding to equilibrium between bulk and grain boundary at T_2 for one side, and T_3 for the other side. When steady state is reached, a concentration gradient will be established across the grain boundary, the lower concentration corresponding to the hotter side. B will, therefore, diffuse toward the hotter side, where it will "dissolve" A from the bulk. Simultaneously A will flow toward the colder side, where it will be "rejected" into the bulk. Mass transfer can thus be obtained across the grain boundary, which will migrate as a result of this process.

The above considerations, of course, implicitly assume that the only driving force for migration to which the grain boundary is subject is due to the temperature gradient. In other words, under isothermal conditions the grain boundary would remain stationary.

C. ELBAUM

195

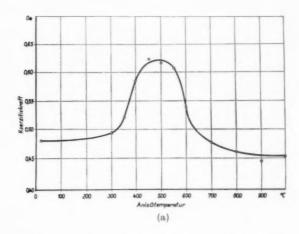
Division of Engineering and Applied Physics Harvard University, Cambridge, Mass.

References

- H. Suzuki, J. Phys. Soc. Japan 6, 522 (1951).
- M. Robert, A. Robilliard, and P. Lacombe; C. R. Acad. Sci., Paris 240, 1089 (1955).
- W. G. PFANN, Trans. Amer. Inst. Min. (Metall.) Engrs. 203, 961 (1955).
- J. W. Cahn, and J. E. Hilliard, J. Chem. Phys. 28, 258 (1958).
- M. C. Inman and H. R. Tipler, Acta Met. 6, 73 (1958).
 D. McLean, Grain Boundaries in Metals, p. 116-120. Clarendon Press, Oxford (1957).
 - * Received March 5, 1959.

R. WAGNER: Der Einfluss feindisperser Ausscheidungen auf die Koerzitivkraft von Transformatorenblech. Acta Met. 7, 523 (1959).

According to an error an incorrect block was used for Fig. 1b on p. 524 of the above paper. The complete figure is reproduced below.



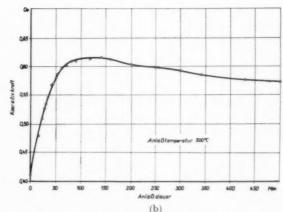


ABB. I. Einfluss der Anlasstemperatur und der Anlasszeit auf die Koerzitivkraft von warmgewalztem Transformatorenblech nach vorheriger ½-stündiger Homogenisierung bei 1000°C und Abschrecken in Wasser. Die Anlassglühungen erfolgten:

1a, bei stufenweise steigenden Temperaturen jeweils ½h lang.

1b, bei einer Temperatur von 500°C.

VOL.

1959

Die Koerzitivkraftmessungen wurden bei Zimmertemperatur durchgeführt; die Proben wurden zu diesem Zweck aus dem Ofen genommen und in Wasser abgeschreckt.

VOI

THE KINETICS OF THE FIRST STAGE OF TEMPERING*

M. HILLERT †

The methods are discussed of evaluating from experimental data the activation energy of a process and the exponent in the kinetic equations. The value of the exponent is subject to considerable uncertainty, being very sensitive to the choice of impingement factor and to a variation of the activation energy.

The kinetics of the first stage of tempering of martensite is accounted for in terms of ordinary diffusion without using the dislocation-attraction model. The diffusion coefficient of carbon in martensite is derived theoretically and an exponential variation with carbon content is found, explaining the discontinuous character of the first stage of tempering.

LA CINÉTIQUE DU PREMIER STADE DU REVENU

L'auteur discute les méthodes de calcul de l'énergie d'activation d'une réaction et de l'exposant des équations cinétiques à partir de données expérimentales. La détermination de la valeur de l'exposant est susceptible d'une grande imprécision, en fonction du choix du facteur de correction et de la variation de l'énergie d'activation.

La cinétique du premier stade du revenu de la martensite est interprétée comme une diffusion ordinaire sans utiliser le modèle d'attraction des dislocations. Le coefficient de diffusion du carbone dans la martensite est déduit théoriquement et l'on trouve également une variation expérimentale en fonction de la teneur en carbone, qui explique le caractère discontinu de ce premier stade du revenu.

ZUR KINETIK DES ERSTEN ANLASSSTADIUMS

Es werden die Methoden diskutiert, mit deren Hilfe man aus experimentellen Ergebnissen die Aktivierungsenergie eines Prozesses und den in den kinetischen Gleichungen auftretenden Exponenten bestimmt. Der Wert des Exponenten unterliegt beträchtlicher Unsicherheit, da er von der Wahl des Korrekturfaktors für die Treff-Wahrscheinlichkeit (impingement factor) und von Veränderungen der Aktivierungsenergie empfindlich abhängt.

Die Kinetik des ersten Anlassstadiums lässt sich auf Grund normaler Diffusion verstehen ohne Zuhilfenahme der Anziehung durch Versetzungen. Der Diffusionskoeffizient von Kohlenstoff in Martensit wird theoretisch berechnet; es ergibt sich eine exponentielle Abhängigkeit von der Kohlenstoffkonzentration, die den unstetigen Charakter des ersten Stadiums beim Anlassen erklärt.

INTRODUCTION

The kinetics of the first stage of tempering of martensite, i.e. the precipitation of ε -carbide from martensite, has recently been the subject of a number of investigations. (1–5) Averbach and Cohen (1) suggested that the rate of reaction was controlled by diffusion of carbon, and they applied the generalized Johnson–Mehl equation

$$\partial f/\partial t = (1-f)nKt^{n-1}$$
 (1a)

$$-\ln\left(1 - f\right) = Kt^n \tag{1b}$$

in order to account for the experimental data. However, the values of the exponent obtained were surprisingly low (n=0.3) considering that Zener's theoretical treatment⁽⁶⁾ of the diffusion-controlled growth of a precipitate yields n=0.5 as the lowest possible value. Later Krisement⁽⁴⁾ obtained even lower values of the exponent (n=0.1) from experimental data. Another difficulty has been that the activation energy values obtained for the reaction

have not been comparable with those for the diffusion of carbon in ferrite. In order to resolve these difficulties Lement and Cohen⁽³⁾ have recently suggested a dislocation-attraction model.

In the present paper the usual methods will be examined of evaluating the activation energy and the exponent from experimental data, and some weak points will be emphasized. As a result it is suggested that the first stage of tempering can be explained without the help of the dislocation-attraction model and an attempt will be made to do this.

EVALUATION OF THE ACTIVATION ENERGY

It is always possible to define an activation energy for a process on a purely formal basis without any physical model concerning the mechanism of the process. Several different possibilities will be discussed in this paragraph. It should be remembered, however, that such an activation energy may not always have a clear physical significance and the value of comparing it directly with the activation energy for some atomic process, for instance diffusion, may be highly questionable in some cases. Wert⁽⁷⁾ and Birchenall and Mead⁽⁸⁾ have demonstrated this in two actual cases.

VOL.

1959

^{*} Received October 25, 1958.

[†] Swedish Institute for Metal Research, Stockholm,

Furthermore, Zener⁽⁹⁾ has pointed out that a necessary condition is that the activation energy for the process be based on the dimension *time*⁻¹, this being the dimension on which activation energies of atomic processes such as diffusion are based.

In general there is a relationship between the variables f, t and T for a reaction, f being the fraction transformed in time t during an isothermal treatment at the temperature T. This relationship can be represented for instance by a function F

$$1/t = F(f, T) \tag{2a}$$

In a sufficiently narrow temperature range one can represent the temperature dependence of F by an activation energy Q and write equation (2a) in the form

$$1/t = F_0(f) \exp\left[-Q(f)/RT\right] \tag{2b}$$

where, for any degree of transformation $f=f_1,\ Q$ is defined by the relation

$$\frac{Q(f_1)}{R} = -\left(\frac{\partial \ln 1/t}{\partial 1/T}\right)_{f_1} = \left(\frac{\partial \ln t}{\partial 1/T}\right)_{f_2} \tag{3}$$

This relation can be used for evaluating the activation energy from experimental data.

The basic relationship (2a) between f, t and T can also be expressed by means of a rate equation, leading to the definition of another activation energy, which is of a somewhat more fundamental nature.

$$(1/\!\!f)(\partial \!\!f/\partial t) = G(f,\,T) = G_0(f) \exp{[-Q^*(f)/RT]} \quad (4)$$

$$\frac{Q^*(f_1)}{R} = -\left[\frac{\partial \ln(1/f)(\partial f/\partial t)}{\partial 1/T}\right]_{f_1}$$

$$= -\left[\frac{\partial \ln(\partial f/\partial t)}{\partial 1/T}\right]_{f_1}$$
(5)

It is more common to define the rate equation simply by $\partial f/\partial t$, which, however, leads to the same definition of the activation energy. The above method is preferred here because it formally has the correct dimension of $time^{-1}$ and also because it yields a function $G_0(f)$ which is similar to $F_0(f)$. Furthermore it should be noted that the exact nature of F_0 and G_0 is immaterial for the determination of the activation energies since they do not enter into equations (3) and (5).

It can be shown that the two activation energies Q and Q^* are identical when independent of f. Otherwise, for a certain degree of transformation $f = f_1$, equation (3) will yield a value of Q which is equal to some mean value of Q^* given by equation (5) from the beginning of the transformation and up to $f = f_1$.

Equation (5) should therefore be preferred. Sometimes, however, the experimental data may not be accurate enough for an evaluation of $\partial f/\partial t$, and the use of equation (3) is then justified.

Any two of the three variables f, t and T can be considered as independent and the basic equations (2) and (4) can thus as well be written

$$f = H(t, T) = H_0(t) \exp\left[-Q(t)/RT\right] \tag{6}$$

which gives

$$\frac{Q(t_1)}{R} = -\left(\frac{\partial \ln f}{\partial 1/T}\right)_{t_1} \tag{7}$$

and

$$\partial f/\partial t = I(t, T) = I_0(t) \exp\left[-Q^*(t)/RT\right]$$
 (8)

which gives

$$\frac{Q^*(t_1)}{R} = \left[\frac{\partial \ln \left(\partial f/\partial t\right)}{\partial 1/T}\right]_{t_1} \tag{9}$$

The dimension on which these activation energies are based is not $time^{-1}$ but depends on the nature of the functions $H_0(t)$ and $I_0(t)$, which in turn must be evaluated from the experimental data and are thus subject to experimental error. Cohen et al., among others, have tried to compensate for this by the use of an analytical expression instead of the unknown functions $H_0(t)$ and $I_0(t)$. In a series of papers⁽¹⁻³⁾ they have thus arrived at activation energy values for the first stage of tempering of martensite of 8000, 16,000 and 27,000 cal/mole, which in fact were based approximately on the dimensions time-0.3, time-0.6 and $time^{-1}$. In addition to the uncertainty regarding the dimension, the method of substituting analytical expressions for the unknown functions H_0 and I_0 has the limitation of yielding a single activation energy value for the whole process, whereas equations (3) and (5) are capable of revealing a variation of the activation energy during the process.

As a further complication the analytical expressions applied for $I_0(t)$ have sometimes contained the variable f as well as t, a situation brought about by the particular physical model assumed in setting up $I_0(t)$. The activation energy for a process has thus been calculated by means of equations like

$$\frac{Q(t_1)}{R} = \left[\frac{\partial \ln \ln (1-f)}{\partial 1/T}\right]_{t_1} \tag{10}$$

obtained from the Johnson–Mehl equation (1b above) and

$$\frac{Q(t_1)}{R} = \left[\frac{\partial \ln f/(1-f)}{\partial 1/T}\right]_{t_1} \tag{11}$$

obtained from the Austin-Rickett⁽¹⁰⁾ equation.

VOI 7 19 The use of such expressions as (7), (9), (10) and (11) for determining the activation energy of a process seems both unnecessary and inconvenient and it is thus suggested that only equations (2) to (5) be used for this purpose. It is also suggested that the same equations be used for defining and determining the exponent n, especially since a variation of Q with f is shown to affect the value of n. The following discussion on the exponent will thus be based on equation (4) and not on equations (6) and (8), which are usually employed.

EVALUATION OF THE EXPONENT

For the early part of an isothermal process one adopts the relation $f = \text{constant} \cdot t^n$ or $t = \text{constant} \cdot$ $f^{1/n}$, which thus defines the exponent n. This implies that $F_0(f)$ in equations (2b) as well as $G_0(f)$ in equation (4) is proportional to $f^{-1/n}$. The value of n is usually assumed to be determined by the shape of the precipitating particles and is then expected to stay constant during the whole process. However, when applied to experimental data this relation always yields a considerable variation of n with f when f reaches sufficiently high values, one reason being that the fraction of the system which remains to be transformed, (1-f), has then decreased considerably. It is therefore common to introduce a correction factor, the so-called impingement factor, of the form $(1-f)^i$. By a suitable choice of i it is often possible to account for a large portion of a transformation with a constant n value. This procedure will now be discussed and equation (4) is therefore written in the form

1959

$$(1/\!f)(\partial\!f/\partial t) = K \cdot (1-f)^i \cdot f^{-1/n} \cdot \exp\left[-Q^*(f)/RT\right] \tag{12}$$

which can be integrated for certain i values, under the further restrictive assumption that Q^* does not vary with f over the range considered. With the choice of i = 1 + 1/n, for instance, one gets the result

$$1/t = (K/n) \cdot (1 - f)^{1/n} \cdot f^{-1/n} \cdot \exp(-Q/RT) \quad (13)$$

This is identical to the Austin–Rickett equation which says that f/(1-f) is proportional to t^n . The Johnson–Mehl equation (1b above) corresponds approximately to the case $i=\frac{1}{2}(1+1/n)$. It should be noted that these two equations are usually derived from equation (8) assuming $I_0(t)=K\cdot (1-f)^i\cdot t^{n-1}$. The value of i must then be chosen as 2 and 1, respectively, instead of 1+1/n and $\frac{1}{2}(1+1/n)$.

Equation (12) gives the following equation for determining n from experimental data which can be

done by plotting $\ln \left(\partial f/\partial t \right)$ vs. $\ln f$ and reading the slope.

$$\left[\frac{\partial \ln \left(\partial f / \partial t \right)}{\partial \ln f} \right]_T = 1 - \frac{1}{n} - i \cdot \frac{f}{1 - f} - \frac{f}{RT} \frac{dQ^*}{df}$$
 (14)

At the beginning of a process the right-hand side reduces to 1-1/n and the exponent n can thus be evaluated unambiguously. However, as soon as the fraction transformed, f, has reached higher values, the evaluation of n seems rather uncertain in view of the following considerations.

It is often assumed that the activation energy is independent of f and the last term in equation (14) is neglected. However the application of such a low value as $dQ^*/df = 1400$ cal/mole at 350°K and 50 per cent transformation, will, for example, change the calculated n value from 0.33 to 0.50 or from 0.50 to 1. The determination of the activation energy is usually not accurate enough to exclude the possibility of such a variation, especially if one has used a method of calculation involving an analytical expression, since only a mean value of Q for the whole process is then calculated.

The value of i is always chosen rather arbitrarily and is not based on a rigorous physical model. Sometimes a particular value is preferred because it makes a mathematical expression integrable. In other cases one has tried a series of i values and has chosen the value that made n constant in the largest portion of the transformation. It is therefore of interest to examine how sensitive is the calculation of n to the choice of i. If the choice is changed by one unit, the n value obtained would again change from 0.33 to 0.50 or from 0.50 to 1 at 50 per cent transformation, according to equation (14).

When evaluating the exponent from his experimental data on the first stage of tempering of martensite, Krisement⁽⁴⁾ used a plot of $\ln (\partial f/\partial t)$ vs. $\ln t$ and reported a value of n=0.1 assuming that i=0, whereas Cohen $et\ al.$ had reported n=0.3 assuming that i=1. For this method of evaluation one can derive a relation

$$\frac{n(i=0)}{n(i=1)} = 1 - \ln \frac{1}{1-f}$$
 (15)

showing that the discrepancy between the two results is exactly what should be expected at f=0.5. This example clearly demonstrates how sensitive is the result as regards n to variations in the adopted value of i—a value usually based on rather debatable assumptions.

The n values evaluated by Krisement and by Cohen et al. differ already at low f values where the difference

in impingement factor is unimportant. In this range the discrepancy seems to be due mainly to the fact that the kinetic equation employed by Krisement was a rate equation (thus containing $\partial f/\partial t$) whereas Cohen et al. used an integrated form (equation 1b). The integration of equation (la) which yields (lb) is of course only correct if n is really a constant. Already in the discussion on the activation energy it was pointed out that the rate equation (4) is the more fundamental one and that the integrated form (equation 2) gives a correct value of the activation energy only when it does not vary with f. Otherwise this latter form yields a mean value. The same conclusion holds for the exponent, and a calculation shows that the two forms of the kinetic equation may give quite different values of n during a considerable part of a reaction if there is a change of the n value at an early stage, for instance before the measurements were started. This becomes especially serious for low nvalues. As a consequence, it appears advisable to rely on the rate equation as far as possible. Furthermore, it should be noted that the quantity $\partial f/\partial t$ in the rate equation can in principle be expressed as a function of f (equation 4) or as a function of t (equation 8), and these two alternatives will yield different n values when n is not a constant. Again, an important variation of n may have taken place before the measurements were started. It is not immediately clear what alternative should be chosen, but it appears more natural to consider a variation of the exponent during the course of a reaction as an effect of the amount of transformation taken place, f, rather than of the time elapsed, t, It is therefore suggested that the exponent always be defined by a relation like equation (12) and evaluated from a logarithmic plot of $\partial f/\partial t$ vs. f in accordance with equation (14). This is contrary to the generally accepted practice where the exponent is evaluated from a logarithmic plot of $\partial f/\partial t$ or some function of f vs. t.

It should be noted that the evaluation of n is not only dependent on the choice of i but also on the basic assumption that the impingement factor is of the form $(1-f)^i$. If one firmly believes that n is constant during a process, which is not necessarily true, it would perhaps be better to try a series of n values and in each case calculate the impingement factor from

$$K(f) = f^{-1+1/n} \cdot \partial f/\partial t \tag{16}$$

and choose the n value yielding the most reasonable impingement factor.

KINETICS OF TEMPERING OF MARTENSITE

In a recent dilatometric investigation of the first stage of tempering of martensite, Gerdien⁽⁵⁾ has been able to make measurements much earlier during the tempering than Cohen et al.(1-3) Judging from Gerdien's results one appears compelled to infer that more than 10 per cent of the transformation must already have taken place when Cohen et al. made their first length measurement. Gerdien could thus extend the evaluation of Q and n to much smaller f values. He found that the activation energy as function of fappeared to start at about 20,000 cal/mole for very small f, i.e. at the same value that holds for diffusion of carbon in ferrite. With increasing f Gerdien found that Q increased to and even above the value of 27,000 cal/mole, found by Cohen et al. for the whole reaction. It is thus tempting to suggest that ordinary diffusion of carbon is the rate-controlling process at least at the beginning of the first stage of tempering of martensite. Assuming this, one must expect the exponent to have a value of at least 0.5 whereas Cohen's measurements yielded a value of 0.3. The appreciable variation of Q with f, found by Gerdien, and the uncertainty concerning the impingement factor, make this experimental value of the exponent n very uncertain in view of equation (14), however. When evaluated by Cohen's method Gerdien's data also yielded values of the exponent of about 0.3, except at the beginning of the transformation where there was a tendency towards higher values, i.e. values which are in agreement with a Zener type reaction model governed by ordinary diffusion. This may be taken as support for the ordinary-diffusion model. Another test of the suggested mechanism is given by the following calculation of the rate of transformation.

VO

19

Lement et al.⁽¹¹⁾ have reported that ε -carbide forms as a subgrain-boundary film, the subgrain size being of the order of 1000–2000 Å in diameter, according to electron microscopic observations. Accepting this value, and assuming ordinary diffusion of carbon from the matrix of martensite up to this film, one can calculate that it should take 25–100 sec at 56°C to reach a degree of transformation of 10 per cent (f=0.1). This result is in good agreement with Gerdien's experimental data, which give a value of 100 sec.

The above calculation has been based on the diffusion coefficient of carbon in ferrite. It may be argued that carbon is not diffusing through ordinary ferrite but through martensite which may have quite a different diffusion coefficient. This is in fact the argument used by Lement and Cohen⁽³⁾ in explaining their high experimental value for the activation energy of 27,000 cal/mole. However, a theoretical consideration presented in the Appendix yields the result

$$D^{\text{martensite}} = D^{\text{ferrite}} \cdot \exp\left(-1700c/T\right) \tag{17}$$

where c is the weight percentage of carbon in the martensite. The diffusion coefficient thus seems to vary exponentially with the carbon content through the diffusion zone. Wagner⁽¹²⁾, who treated this case theoretically, found that the highest diffusion coefficient in the diffusion zone will dominate the reaction rate. Our use of the diffusion coefficient in ferrite during the first stage of tempering of martensite thus appears justified. Furthermore, Wagner concluded that a precipitation process will appear to be discontinuous if the value of the diffusion coefficient varies with a factor higher than 7 through the diffusion zone. This condition is fulfilled according to equation (17), and the X-ray observation by Kurdjumov and Lyssak(13) and by Werner et al.(14) that the carbon content of martensite adjacent to the growing ε carbide seems to drop discontinuously from its original value to about 0.3 wt. % may thus be explained in terms of the suggested ordinary-diffusion model, lending further support for this model.

Lement and Cohen⁽³⁾ have tried to explain the discontinuous character of the first stage of tempering in terms of their dislocation-attraction model. However, their calculations are based on a solution to a differential equation, containing a quantity C_s which has to be zero in order to satisfy the differential equation and should thus have been left out of the solution. Nevertheless this quantity is assumed by the authors to have a value of about 0.3 wt. %. Furthermore, it should in fact have a very high value in order to satisfy the equilibrium conditions at the end of the first stage of tempering, unless the carbon content of the undisturbed martensitic matrix at a large distance from the ε -carbide is assumed to decrease far below the normal solubility of carbon in ferrite. As a consequence, it is difficult to accept the dislocation model in its present form.

If one accepts that ordinary diffusion of carbon is the rate-controlling mechanism at the beginning of the tempering of martensite, one may draw some conclusion concerning the rest of the first stage of tempering. The apparent decrease of the exponent is the manifestation of a retardation of the reaction. Some mechanism more sluggish than carbon diffusion seems to become more and more important. The fact that the activation energy value is increasing at the same time indicates that the new mechanism has a higher activation energy than diffusion of carbon, and seems to exclude the possibility that some effect of geometry is responsible for lowering the reaction rate. The new rate-controlling mechanism may be of a mechanical nature, for instance plastic deformation of the matrix to provide space for the growing ε-carbide.

A change of the rate-control from one mechanism to another during the course of a transformation, as suggested here, may be quite a common phenomenon and has for instance been discussed in the case of the graphitization of steel and white cast iron.⁽¹⁵⁾

SUMMARY

The methods of calculating the activation energy of a process from kinetic data are discussed and it is suggested that only the expressions

$$\left(\frac{\partial \ln t}{\partial 1/T}\right)_f$$
 and $\left(\frac{\partial \ln \partial f/\partial t}{\partial 1/T}\right)_f$

should be used, and also that a variation of Q with f should be looked for.

The methods for determining the exponent in the kinetic equations are discussed and the uncertainty depending on a variation of Q with f and on the choice of impingement factor are discussed. The discrepancy between the exponents determined by Cohen $et\ al.$ and by Krisement is explained by their different choices of impingement factor. The opposite procedure may sometimes be advantageous, i.e., the impingement factor should be calculated assuming a series of constant values for the exponent.

The values of Q, n and the rate of reaction all seem to indicate that the beginning of the first stage of tempering of martensite is controlled by ordinary diffusion of carbon. The large decrease of the rate of reaction during the transformation is probably caused by a more sluggish process with a higher activation energy.

The diffusion coefficient for carbon in martensite is discussed and its relation to the diffusion coefficient in ferrite is derived theoretically. An exponential variation with the carbon content is found, which may explain why the first stage of tempering of martensite appears to be discontinuous.

APPENDIX

Diffusion Coefficient of Carbon in Martensite

The available sites for carbon atoms in b.c.c. ferrite have tetragonal symmetry and can be divided into three groups with respect to the direction of the tetragonal axis. Nearest-neighbour sites belong to different groups and diffusion is believed always to take place by elementary jumps of carbon atoms, each step involving a change from one group of sites to one of the others. In b.c.t. martensite the majority of the carbon atoms occupy sites of a single group, this fact being the cause of the tetragonality, and martensite may simply be considered as an ordered solution of carbon in ferrite. If the mechanism of the

VOL. 7 1959 diffusion process is the same as in ferrite, a carbon atom must now jump from a preferred site to a "forbidden" site before it can reach another preferred site. From this argument Lement and Cohen concluded that diffusion should be slower in martensite than in ferrite, and an experimental activation energy value of 26,000 cal/mole seemed reasonable. However, it is possible to arrive at a definite estimated value of the activation energy for diffusion of carbon in martensite in the following way.

For a b.c.t. lattice Zener(16) has calculated the energy, U, required to move a carbon atom to one of its nearest-neighbour sites (thus belonging to a different group), due to the tetragonality of the lattice. For martensite with the tetragonality caused by a carbon content of c wt. 0 /₀ his result can be written as NU =6700c cal/mole, N being Avogadro's number. When a carbon atom jumps from one site to another in b.c.c. ferrite it must overcome a certain energy barrier, the height of which determines the jump frequency. It seems reasonable to assume that this barrier has its highest value half-way between two neighbouring sites. The introduction of a certain tetragonality would then increase the difference in energy between a preferred site and the top of the barrier by an amount

approximately $\frac{1}{2}U$. As a consequence, the jump frequency will decrease by a factor $\exp(-NU/2RT)$, where $NU/2R = 1700c \deg$. Since long range diffusion is dominated by the highest energy barrier, the diffusion coefficient in martensite can be estimated as $D^{\mathrm{martensite}} = D^{\mathrm{ferrite}} \cdot \exp{(-NU/2RT)}.$

REFERENCES

- 1. B. L. Averbach and M. Cohen, Trans. Amer. Soc. Metals 41, 1024 (1949).
- 2. C. S. Roberts, B. L. Averbach and M. Cohen, Trans. Amer. Soc. Metals 45, 576 (1953).
- 3. B. S. Lement and M. Cohen, Acta Met. 4, 469 (1956).
- 4. O. Krisement, Arch. Eisenhüttenw. 27, 731 (1956).
- 5. H. O. GERDIEN. To be published in Arch. Eisenhüttenw.
- C. ZENER, J. Appl. Phys. 20, 950 (1949).
 C. WERT, J. Appl. Phys. 20, 943 (1950).
- 8. C. E. BIRCHENALL and H. W. MEAD, J. Metals 8, 1004
- 9. C. Zener, Trans. Amer. Soc. Metals 41, 1057 (1949).
- 10. J. B. Austin and R. L. Rickett, Trans. Amer. Inst. Min. (Metall.) Engrs. 135, 396 (1939).
- 11. B. S. LEMENT, B. L. AVERBACH and M. COHEN, Trans. Amer. Soc. Metals 46, 851 (1954)
- 12. C. WAGNER, J. Metals 4, 91 (1952).
- 13. G. Kurdjumov and L. Lyssak, J. Tech. Phys. 19, 525 (1949).
- 14. F. E. WERNER, B. L. AVERBACH and M. COHEN, Trans. Amer. Soc. Metals 49, 823 (1957)
- M. Hillert, Jernkontor. Ann. 141, 67 (1957).
 C. Zener, Elasticity and Anelasticity of Metals, p. 122. Univ. of Chicago Press (1948).

AN INTERNAL FRICTION PEAK DUE TO SLOW MOVING DISLOCATIONS IN IRON-NITROGEN ALLOYS*

R. RAWLINGS and P. M. ROBINSON+

A small peak in the internal friction–temperature curve has been observed a few degrees above the Snoek peak (due to stress induced ordering) in iron–nitrogen alloys. The peak is produced when specimens are quenched from above the alpha–gamma transformation temperature or when specimens quenched from below the transformation temperature are lightly strained. It is absent in the specimens quenched from below the transformation temperature and not strained. Evidence is given for the belief that this new peak is due to slow moving dislocations.

LE PIC D'AMORTISSEMENT INTERNE DU AUX DISLOCATIONS À DEPLACEMENT LENT DANS LES ALLIAGES FER-AZOTE

Dans des alliages fer-azote, les auteurs ont observé un léger pic d'amortissement interne pour une température de quelques degrés supérieure à celle du pic de Snoek.

Le pic se marque lorsque les échantillons sont trempés à partir d'une température supérieure à celle de la transformation α - γ ou pour des échantillons trempés à partir d'une température inférieure puis légèrement déformés. Il n'existe pas dans ces derniers avant la déformation.

Les auteurs attribuent ce nouveau pic aux dislocations qui se déplacent lentement.

EIN DURCH LANGSAME BEWEGUNG VON VERSETZUNGEN VERURSACHTES MAXIMUM DER INNEREN REIBUNG IN EISEN-STICKSTOFF-LEGIERUNGEN

Einige Grad oberhalb des Snoek–Maximums (das durch spannungsbedingte Ordnungseinstellung verursacht ist) wurde bei Eisen-Stickstoff-Legierungen ein kleines Maximum der inneren Reibung in Abhängigkeit von der Temperatur beobachtet. Das Maximum tritt auf, wenn Proben von Temperaturen oberhalb des $\alpha-\gamma$ -Umwandlungspunktes abgeschreckt werden oder wenn Proben, die von Temperaturen unterhalb dieses Umwandlungspunktes abgeschreckt wurden, leicht verformt werden. Es fehlt bei Proben, die nach Abschrecken von Temperaturen unterhalb des Umwandlungspunktes nicht verformt wurden. Es werden Argumente dafür angeführt, dass dies Maximum auf der langsamen Bewegung von Versetzungen beruht.

1. INTRODUCTION

1959

Slow moving dislocations, i.e. dislocations moving slowly because of the "drag" from accompanying solute atoms, have been suggested as the source of micro-creep⁽¹⁾ and of internal friction effects. (2–3) The evidence for the former is much stronger, being of a quantitative nature, than for the latter. The internal friction peak (2) of an aluminium—copper alloy ascribed by Kê to slow moving dislocations occurred at 1 c/s and at a temperature of 100°C. Apart, however, from the fact that the peak occurred only in the cold worked alloy, the explanation seems to be surmise only.

The investigation arose when it was found that iron-silicon-nitrogen alloys when quenched from the gamma state possessed five internal friction peaks (all of which were absent in iron-silicon alloys similarly quenched). When, however, the same iron-silicon-nitrogen alloys were quenched from the alpha state only three internal friction peaks were found. Further investigation revealed that iron-nitrogen alloys quenched from the gamma state had two peaks, but only one when quenched from the alpha state. It is believed that the peaks found for

alloys (both binary and ternary) quenched from the alpha state are due to the well-known⁽⁴⁾ stress induced ordering of the nitrogen atoms. These we will call Snoek peaks. The additional peak found in iron nitrogen alloys quenched from the gamma state is the subject of this work. It is hoped to discuss the more complicated ternary system in a later paper.

2. EXPERIMENTAL

The iron used in this investigation was kindly supplied by the British Iron & Steel Research Association and was of high purity.

The material was hot rolled to rod 0.25 in. dia. and cold drawn to 0.027 in. dia. wire. The wire specimens were annealed for 3 hr at 900°C in wet hydrogen (dew point room temperature) to remove carbon and nitrogen. This treatment was found sufficient to remove the peaks due to carbon and nitrogen in the internal friction-temperature curve, the internal friction being practically constant (0.002) at temperatures between 18°C and 100°C.

Nitriding was carried out in an atmosphere of 'cracked' ammonia. The ammonia, supplied from a

^{*} Received October 24, 1958.

[†] Department of Metallurgy, University College, Cardiff.
ACTA METALLURGICA, VOL. 7, OCTOBER 1959

 $[\]ddag$ Analysis of B.I.S.R.A. iron A.H.L. (analysis by B.I.S. R.A.) 0.0034% C., 0.0025% Si, 0.005% Mn, 0.005% S, 0.001% P, 0.00005% H, 0.01% Ni, 0.001% Cr, 0.006% Cu, 0.001% Al, 0.0017% O, 0.0035% N.

cylinder, was passed through a steel 'cracker' tube heated to a temperature between 500° and 700°C and thence through two silica tubes in parallel containing the specimens heated to the appropriate temperature. The ammonia was partially 'cracked' in the 'cracker' tube, the degree of dissociation depending on the temperature of the 'cracker' and the flow of gas. Thus at any particular nitriding temperature the nitrogen content of the specimens could be controlled by controlling the temperature of the 'cracker' and the gas flow. The average gas flow was 100 ml/min. The 'cracker' furnace and the nitriding furnace were automatically controlled at constant temperature using chromel-alumel thermocouples. The temperature zone in the nitriding furnace was constant to within $+3^{\circ}$ C over the length of the specimen (2 in.).

The internal friction apparatus consisted of a torsional pendulum similar to that used by $K\hat{e}^{(2)}$. The temperature of the specimen was varied by using a small eureka wire-wound furnace. A specimen only 2 in. in length was used in order to avoid temperature gradients. Measurements were taken at a frequency of vibration of 1.03 c/s. The amplitude of vibration varied from 1 cm to 4 cm at 3 m, corresponding to a shear strain of from 1.125×10^{-5} to 4.5×10^{-5} . All readings were taken at amplitudes within the range in which the internal friction is independent of strain amplitude. The actual measurements of the internal friction could be reproduced to ± 0.0002 . The tensile stress on the specimen was 346 lb/in^2 .

Specimens were nitrided for 3 hr at temperatures of 600° , 700° , 800° and 900° C, the nitriding conditions being adjusted to introduce between 0.015% and 0.025% nitrogen into the specimen. The internal friction of the quenched specimens was determined over the temperature range $16\text{--}100^{\circ}$ C. Other specimens were nitrided at, and quenched from, temperatures in the gamma range. Details are given under Results. Tests were also carried out on decarburised and denitrided specimens.

The internal friction temperature curve was determined after quenching from 1050°C and subsequent ageing at 23°C , 60°C , 80°C , and 115°C , for specimens containing about 0.03% and 0.02% nitrogen.

Other experiments were carried out to elucidate the nature of the second peak. Electrical resistivity measurements were carried out on iron wires (decarburized and denitrided) air cooled from 900°C and 1050°C. Air cooling was used instead of quenching in an effort to avoid quenching strains which would complicate the interpretation of the results. With the wires used (0.027 in. dia.) it was hoped that the

cooling speed would be sufficient to retain some of the high temperature vacancies.

In order to test whether or not the second peak was due in some way to the presence of dislocations, a series of experiments involving straining and ageing was carried out. For the sake of continuity the details are given with the results.

3. RESULTS

A typical internal friction-temperature curve for iron nitrogen wires quenched from the alpha range is shown in Fig. 1. In each case, the experimental curve could be described approximately by a single time of relaxation, i.e.

$$I.F. = C \frac{\omega \tau}{1 + (\omega \tau)^2} \tag{1}$$

195

where C is a constant, $\omega = 2\pi f$, and $\tau (= \tau_0 \exp$ (H/RT)) is the time of relaxation. f is the frequency of vibration, H the activation energy of the process causing the internal friction and T the absolute temperature. For specimens quenched from the gamma range, however, the internal friction at temperatures higher than that of the normal nitrogen peak was greater than that expected from equation (1) (see Fig. 2). The experimental curve could be resolved into one large peak at 21°C and a much smaller one at 29°C. The large peak, although occurring at a slightly different temperature from that in curves for specimens quenched from the alpha range, is obviously identifiable as the normal nitrogen peak. The smaller peak was not observed in curves for decarburized and denitrided specimens quenched from temperatures within the gamma range.

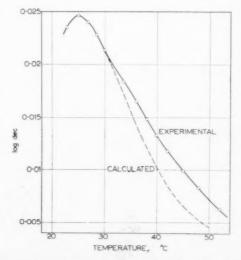


Fig. 1. Iron-nitrogen alloy quenched from the alpha range.

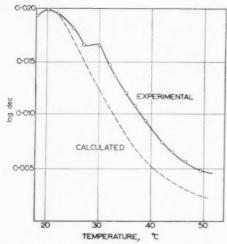


Fig. 2. Iron-nitrogen alloy quenched from the gamma range.

The height of the smaller peak (P_2) was found to vary linearly with the concentration of nitrogen in solution, using the height of the normal peak (P_1) as a measure of the latter (see Fig. 3). The existence of the small peak was thus conclusively shown to require the presence of nitrogen in solution, associated with a quench from the gamma to alpha phase.

3.1. Precipitation results

VOL.

1959

The internal friction-temperature curves after various ageing times were resolved into single time relaxation peaks. The plot of the log time to reach half the original peak is shown, in Fig. 4, against the reciprocal of the absolute ageing temperature. In each case the rate of decrease of the small peak is similar to that of the normal peak. The activation energy is similar to that obtained by Dijkstra⁽⁵⁾ for precipitation in iron–nitrogen solutions.

3.2. Resistivity measurements

A decrease in resistivity at room temperature was found for the wires cooled quickly from the gamma region and for those cooled quickly from the alpha region. The decrease was the same in both cases but in the former case the resistance did not begin to decrease until after 20 hr at room temperature, while

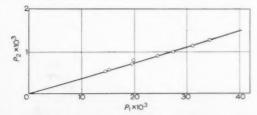


Fig. 3. Variation in height of the anomalous peak (P_2) with nitrogen content.

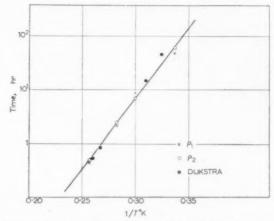


Fig. 4. Time to reach half the original peak height at various ageing temperatures for P_1 and P_2 .

in the latter case, the decrease was observed after only 2 hr. No explanation is offered for these results.

3.3. Strain experiments

These were made in order to check the idea that the small peak was associated with dislocations introduced into the lattice during the gamma to alpha phase transformation. Curve (a) Fig. 5. shows the curve obtained for a specimen quenched from 600° C. After this test the wire was given an oscillation with a maximum shear strain of approximately 2.8×10^{-4} , aged for one hour at room temperature and then tested, with the result shown in curve (b), Fig. 5. A second peak at 29° C, i.e. as in the curves quenched from the gamma, makes its appearance. Repeating the test but using a maximum shear strain of approximately 5.7×10^{-4} caused the normal peak to decrease further and the second peak to

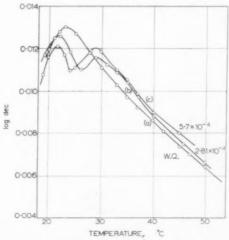


Fig. 5. The effect of strain in producing the anomalous second peak in specimens quenched from the alpha region.

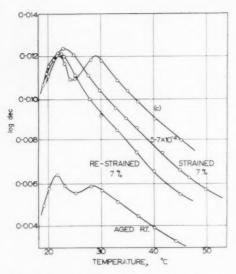


Fig. 6. The effect of increasing amounts of strain and subsequent ageing and straining on the second peak.

increase. This is taken to mean that the second peak is associated with the presence of dislocations in the lattice, and that the height of the peak depends upon the concentration of dislocations present.

The following further test was inspired by a paper by Kunz⁽⁶⁾ dealing with a similar problem. The specimen, now showing two peaks (on analysis), was strained 7 per cent in tension. The second peak disappears and the height of the first peak increases. This suggests that the dislocations have been torn away from the atmospheres, the nitrogen atoms being now mobile and free to take part in stress induced ordering giving rise to the Snoek peak. Ageing at

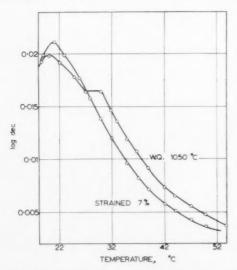


Fig. 7. A specimen quenched from the gamma range and then given a 7 per cent strain (showing the disappearance of the second peak).

room temperature caused a decrease in the height of the first peak and the reappearance of the second peak (See Fig. 6. Note that curve (c) in Fig. 5 is repeated in Fig. 6).

The decrease in the level of both peaks on ageing can be explained if the nitrogen has formed a nitride or has formed condensed atmospheres at dislocations, as well as forming dilute atmospheres. If dilute atmospheres only were formed one would expect a much larger second peak. The question of whether a nitride or a condensed atmosphere was formed on ageing was decided by re-straining the specimen 7 per cent in tension. The height of the first peak then increased almost to the height it had before ageing. This indicates that nitride was not formed on ageing.

A specimen quenched from the gamma region, thus having two peaks, was strained approximately 7 per cent and retested. It can be seen from Fig. 7 that the 7 per cent strain has brought about the disappearance of the second peak—that is, the same results are obtained as for the second peak produced by slightly straining a specimen quenched from the alpha region.

4. DISCUSSION

VOI

195

The second peak in the internal friction-temperature curve for iron nitrogen alloys appears (1) when the alloys are quenched from the gamma range or (2) when alloys quenched from the alpha range are strained by very small amounts $(10^{-4}-10^{-3})$. The evidence then indicates that the presence of both nitrogen and dislocations is necessary for the appearance of the second peak. The nitrogen must be associated with the dislocations as an atmosphere (if it is in solution at normal sites it merely increases the height of the first peak). It is therefore postulated that the second peak is due to the stress induced movement of dislocations whose speed is reduced by their atmospheres of nitrogen. This is analogous to the explanation for a low frequency, low temperature peak in an Al-Cu alloy given by Kê⁽²⁾. A theoretical treatment of slow moving dislocations is discussed by Cottrell⁽⁷⁾. The peak cannot be due to movement of nitrogen atoms in strained sites around dislocations as this movement is believed to be the cause of the peak obtained at about 200°C on testing cold worked iron specimens (the plastic strain being much greater than in the present case).

5. CONCLUSIONS

(1) A second internal friction peak at temperature not far above the Snoek peak is introduced into iron nitrogen alloys either when (a) specimens are quenched from the gamma state or when (b) specimens quenched from the alpha state are given a strain of 2.8×10^{-4} -5.1×10^{-4} .

- (2) The second peak disappears if the specimen is strained 7 per cent and the Snoek peak increases.
 - (3) Both peaks decrease on ageing.
- (4) The second peak is believed to be due to energy losses associated with slow moving dislocations.
- (5) In the case of iron-silicon-nitrogen alloys, two peaks may be obtained due to slow moving dislocations. These will be dealt with later.

ACKNOWLEDGMENTS

Thanks are due to Professor W. R. D. Jones for his encouragement and for providing facilities for this work. One of the authors (P. M. Robinson) is supported by a grant from the Department of Scientific and Industrial Research.

REFERENCES

- 1. A. H. COTTRELL and M. A. JASWON, Proc. Roy. Soc. A 199, 104 (1949)
- T.S.KÉ, Phys. Rev. 78, 420 (1950)
 L. C. WEINER and M. GENSAMER, Acta Met. 5, 692 (1957).
 A. S. NOWICK, Progress in Metal Physics, Vol. IV. Pergamon
- Press, London (1953).
- 5. L. J. Dijkstra, Trans. Amer. Inst. Min. (Metall.) Engrs. 185, 252 (1949).
- 6. F. W. Kunz, Acta Met. 3, 126 (1955).
- 7. A. H. Cottrell, Dislocations and Plastic Flow in Crystals. Oxford University Press (1953).

METALLOGRAPHIC INVESTIGATION OF PRECIPITATION OF SILICON FROM ALUMINUM*:

H. S. ROSENBAUM† and D. TURNBULL†

The precipitation of silicon (diamond cubic) from a supersaturated Al (1% Si) solid solution (f.e.c.) was studied qualitatively by X-ray diffraction and by both light and electron microscopy. This precipitation has the following metallographic features:

1. The precipitated silicon occurs as both plate-like and equi-axed particles.

2. Near grain boundaries there exists a region depleted of precipitate particles. The width of the depleted region increases with slower rates of cooling from the homogenizing temperature (580°C) prior to aging.

3. In specimens that have been water-quenched and then cold worked prior to aging, the precipitate particles are larger and more widely spaced inside slip bands than in unstrained regions. In specimens that have been more slowly cooled from the homogenizing temperature, the effect of cold work prior to aging is to cause nucleation close to grain boundaries, but precipitation along slip bands was not found.

4. In single crystal specimens that were water-quenched from the homogenizing temperature and then aged, the precipitated silicon exhibited strong orientation preferences in the X-ray patterns. However, no exact, or Widmanstätten, orientation relation was found. The orientation preferences diminished as over-aging occurred, and were not found at all in specimens that had been air-cooled instead of water-quenched.

The results are shown to be consistent with the hypothesis that in the quenched alloy precipitation occurs on dislocation loops that result from the coalescence of quenched-in vacancies.

OBSERVATION MÉTALLOGRAPHIQUE DE LA PRÉCIPITATION DU SILICIUM DANS L'ALUMINIUM

Les auteurs étudient qualitativement par diffraction des rayons X et par métallographie optique et électronique, la précipitation du silicium (cubique diamant) dans une solution solide d'aluminium (c.f.c.) sursaturée (1% Si).

VOI

190

La précipitation conduit aux observations métallographiques suivantes:

1. le silicium précipité se présente à la fois sous forme de particules équiaxes et de plaquettes

2. une zone appauvrie en particules précipitées existe aux joints granulaires. Sa largeur croit inversément à la vitesse de refroidissement succédant au traitement d'homogénéisation (580°C) et avant vieillissement.

3. Dans les échantillons trempés à l'eau et écrouis par flexion à la température ambiante et non vieillis, les précipités sont plus gros et plus dispersés dans les bandes de glissement que dans les régions non déformées. Dans les memes conditions, pour les échantillons refroidis plus lentement après homogénéisation, l'écrouissage provoque une germination près des joints, mais on n'observe pas de précipitation dans les bandes de glisssement.

4. Dans les échantillons monocristallins trempés à l'eau après homogénéisation et vieillis, la précipitation du silicium se produit avec orientations préférentielles importantes ainsi que le révèlent les clichés de rayons X. On n'a cependant pas pu établir une relation d'orientation exacte. L'existence des orientations préférentielles diminue lorsque le survieillissement apparait. Dans les échantillons refroidis à l'air, aucune orientation préférentielle ne semble exister.

Les résultats précédents paraissent en accord avec l'hypothèse que dans les échantillons trempés, la précipitation se produit sur les boucles de dislocations formées par la coalescence des lacunes gelées.

METALLOGRAPHISCHE UNTERSUCHUNG DER AUSSCHEIDUNG VON SILIZIUM AUS ALUMINIUM

Die Ausscheidung von Silizium (kubische Diamantstruktur) aus übersättigten Al(1 % Si)-Mischkristallen (kubisch-flächenzentriert) wurde röntgenographisch, licht- und elektronenmikroskopisch untersucht. Diese Ausscheidung hat folgende metallographische Merkmale:

 Das ausgeschiedene Silizium tritt in plattenförmigen Teilchen und in solchen mit allseitig gleicher Ausdehnung auf.

2. In der Nähe von Korngrenzen gibt es ein Gebiet, das von Ausscheidungsteilchen entblösst ist. Die Breite des entblössten Gebiets wächst mit sinkender Geschwindigkeit, mit der die Proben vor dem Auslagern von der Homogenisierungstemperatur $(580^{\circ}\mathrm{C})$ abgekühlt wurden.

3. Bei Proben, die in Wasser abgeschreckt und dann vor dem Auslagern kalt verformt worden waren, sind die ausgeschiedenen Teilchen innerhalb der Gleitbänder grösser und weiter voneinander entfernt als in unverformten Gebieten. Bei Proben, die langsamer von der Homogenisierungstemperatur abgekühlt

^{*}Received November 14, 1958.

General Electic Research Laboratory, Schenectady, New York.

[†] This paper is part of a doctoral dissertation to be presented by H. S. Rosenbaum to the Graduate School of Rensselaer
Polytechnic Institute.

worden waren, verursachte eine Kaltverformung vor dem Auslagern Keimbildung in der Nähe der Korngrenzen, Ausscheidungen entlang Gleitbändern wurden in diesem Fall nicht gefunden.

4. Bei Einkristallen, die von der Homogenisierungstemperatur in Wasser abgeschreckt und dann ausgelagert worden waren, zeigte das ausgeschiedene Silizium röntgenographisch eine starke Vorzugsorientierung. Jedoch ergab sich keine exakte oder Widmanstättensche Orientierungsbeziehung. Die Vorzugsorientierung verschwand bei Überalterung und wurde in allen Proben nicht gefunden, die an Luft abgekühlt anstatt in Wasser abgeschreckt worden waren.

Die Ergebnisse sind, wie gezeigt wird, mit der Hypothese in Einklang, dass in der abgeschreckten Legierung die Ausscheidung an Versetzungsringen stattfindet, die durch Koagulation abgeschreckter Leerstellen entstehen.

INTRODUCTION

Previous investigations^(1,2) have shown that the decomposition of a supersaturated solid solution of silicon in aluminum results in the precipitation of elemental silicon. Recently, it was noticed(3) that the kinetics of the precipitation and the dispersion of the precipitate depend markedly on the thermal history of the alloy. More precisely, if the alloy is cooled at a moderate rate (e.g. air-cooled) to room temperature, only a small number (~106/cm3) of silicon particles appear on aging at 200°-400°C, and the precipitation rate is very slow. However, if the alloy is "inoculated", by which we mean quenched rapidly to room temperature and "pre-aged" for a short time (one to several minutes) between -40°C and 30°C, a large number (~1014/cm3) of silicon particles appear, and precipitation is very rapid. The resistivity of the alloy is not sensibly changed by the inoculation treatment. It was shown that the precipitation rate in the uninoculated alloy, after room temperature cold working, is still far less than that in the inoculated alloy. It was concluded that while cold-work did not appear to increase significantly the number of nuclei, it probably enhances the growth rate of the precipitate particles. The dependence of the reaction rate and of the observed number of particles on the pre-aging treatment led to the conclusion that inoculation results somehow from the annealing-out of quenched-in point defects during the pre-aging treatment.

Two alternative mechanisms for the inoculation in the quenched alloys were discussed. (1) Homogeneous nucleation of silicon occurring at the pre-aging temperatures, the requisite solute mobility being brought about by the transient supersaturation of point defects. (2) Heterogeneous nucleation of silicon at the aging temperature on dislocation loops that may have resulted from the condensation of vacancies at the pre-aging temperature. When these hypotheses were advanced, the supposition that excess vacancies condense to produce dislocation loops was purely speculative. Since then, however, Hirsch et al. (4) have observed such dislocation loops in quenched aluminum by means of electron transmission microscopy. For

an aluminum sample that was quenched into iced brine from 600° C, they observed $\sim 10^{15}$ loops/cm³. These findings lend support to the writers' second hypothesis.

The purpose of this investigation is to obtain a more complete metallographic description of the precipitation. Particularly, we wish to compare the metallographic characteristics of the rapid and the slow precipitations and to observe the effect of cold work on the dispersion of the precipitate particles.

EXPERIMENTAL PROCEDURE

Materials and heat treatments

The materials used in this investigation are the same as those described previously. $^{(3)}$ Briefly, an aluminum alloy containing 1% silicon was made by vacuum melting in alumina and casting in vacuum into graphite. A control alloy was made identically except that no silicon was added. The resulting alloy and control material were found to contain of the order of 0.01% by wt. Cu, 0.01% Fe, and less than 0.001% Mg by a semi-quantitative emission spectrographic analysis. No other impurities were detected.

Heat treatments were done in resistance furnaces in a stream of N_2 for both the homogenization and those aging treatments at temperatures greater than 200°C. The samples were contained in boats of alumina (Norton, R. A. 84 B/p 5733). The aging treatments at 180° – 200° C were carried out either in silicone oil or in a furnace as described above.

In cooling from the homogenization temperature (580°C) four different cooling procedures were used.

- 1. Water quench: The alumina boat was removed from the furnace and quickly over-turned into water at room temperature.
- Alcohol quench: The boat was removed from the furnace and over-turned into denatured alcohol at room temperature.
- 3. Air cool in boat: After removal from the furnace the boat was placed on a large copper block and the sample allowed to cool while in its boat.
- 4. Pack-cool: The boat was packed with granular alumina so that the specimen was buried under

VOL. 7 1959

VOI 7 195

 \sim 1/2 cm of alumina during the homogenization and cooling. The boat was removed from the furnace, placed on a block of transite (pressed asbestos), and allowed to cool to room temperature.

Microscopy

The alloy and control materials were subjected to both light and electron microscopy. The specimens were approximately $0.05 \times 1 \times 4$ cm and were polished electrolytically with a Disa-Pol polisher using the Knuth solution A-2 at 45–50 V. The etchant used here was Vilella's aluminum etch (a mixture of HF, HNO₃, and glycerine). Collodion replicas were used for the electron microscopy; shadows were cast with evaporated chromium at an angle of 30° . A Philips EM-100 electron microscope was used.

Cold work

Some of the metallographic specimens were cold worked while at room temperature subsequent to cooling from the homogenization temperature and immediately prior to aging. The cold work was accomplished by bending the specimen around a 4 in. diameter cylinder and then straightening by hand.

X-ray diffraction

Single crystals of the alloy and control materials were prepared by: (1) plastically stretching well annealed wires of 0.05 or 0.08 cm diameter about 2 per cent; (2) placing these wires into a furnace at room temperature in a stream of N_2 ; (3) raising the temperature of the furnace to $580^{\circ}\mathrm{C}$ in about 4 hr, and (4) allowing the wires to remain at $580^{\circ}\mathrm{C}$ for 2 days. This treatment resulted in crystals 0.3–1 cm long in a "bamboo" structure as revealed by etching in dilute



Fig. 1. Early precipitation as seen in the light microscope. The specimen was quenched from the homogenizing temperature into water at room temperature and then aged at $350^{\circ}\mathrm{C}$ for 2 min.

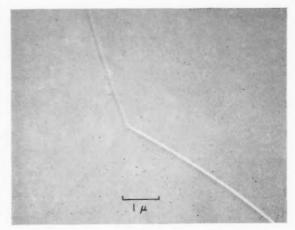


Fig. 2a.

The specimen here was quenched from the homogenizing temperature into water at room temperature. One sees here that no precipitation has occurred during the quench. This is an electron micrograph of a negative collodion replica that was shadowed

with Cr at an angle of 30°.

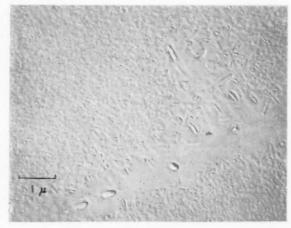


Fig. 2b.

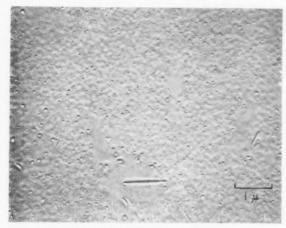
Homogenized and quenched as above and then aged for 2 min at 350°C. The direction of shadowing is approximately from the lower left hand corner of the photograph to the upper right.

HCl. The crystals were cut from the wires and, after suitable precipitation heat treatments as described above, were mounted in a G.E. XRD Universal Mount Goniometer. Unfiltered Cu radiation was used in a cylindrical camera of 10 cm diameter, and a He atmosphere was maintained in the camera to minimize air fluorescence. Exposures were for either 16 or 24 hr.

RESULTS

General appearance of precipitate

Figs. 1 and 2 show the precipitate particles as seen by light and electron microscopy. This series of



 $F_{1G}.\ 2c.$ Homogenized and quenched as in Fig. 2a; then aged 10 min at 350 $^{\circ}$ C. The direction of shadowing is from the bottom to the top of the photograph.

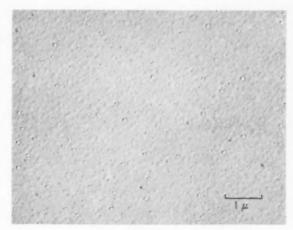


Fig. 2d.

Homogenized and quenched as in Fig. 2a; then aged at 350°C for 39 min. The direction of shadowing is roughly from the lower right to the upper left of the photograph.

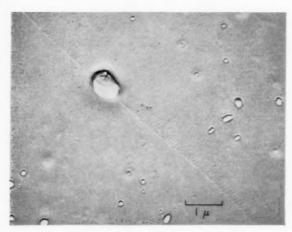


Fig. 2e. Homogenized and quenched as in Fig. 2a; then aged at 350°C for 47 hr. The direction of shadowing is roughly from the bottom to the top of the photograph.

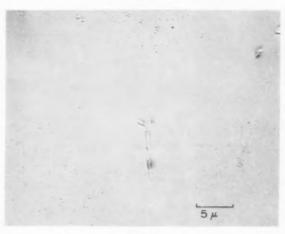


Fig. 3. Electron photomicrograph showing precipitation in an air-cooled specimen. The specimen was air cooled from the homogenizing temperature to room temperature and then aged at 350°C for 4 min. The photomicrograph shows a grain boundary junction. Some particles are aligned on what appear to be portions of low angle boundaries or single dislocations.

photographs illustrates the dispersion of the silicon particles in alloys that were first water quenched to room temperature before aging at 350°C. The light micrograph (Fig. 1) shows large precipitate particles in the grain boundary very early in the aging process. The as-quenched specimens showed no evidence of precipitation. In the electron micrographs (Fig. 2) are seen both plate-like and equi-axed particles. The number of particles is 10^{14} – 10^{15} /cm³, and this number is approximately independent of the aging temperature for temperatures 180° – 370° C. There is a depleted zone near the grain boundaries that is free of particles,

and there are large particles on the grain boundaries. Immediately adjacent to the depleted region the particles are usually larger than those further within the grains (See Figs. 2b and 4).

Fig. 3 shows the dispersion when, instead of quenching into water, the specimen is air-cooled to room temperature before aging. The specimen shown in Fig. 3 differs from those of Fig. 2 only in the way it was cooled from the homogenizing temperature (580°C). In both cases the same length of time was spent at room temperature prior to aging. The particle counts in slowly cooled specimens (air-cooled

VOL. 7 1959

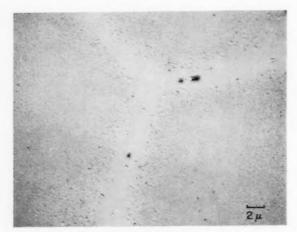


Fig. 4. Electron micrograph of a specimen that was quenched from $580^{\circ}\mathrm{C}$ into alcohol at room temperature and then aged at $350^{\circ}\mathrm{C}$ for 5 min.

or pack-cooled) varied by several orders of magnitude for different specimens and for different grains of the same specimen. Usually, the particles within the grains appear to be randomly dispersed, but often they are aligned in an incomplete network, probably on parts of low-angle boundaries or perhaps along single dislocation lines. Counts of 106-1010 particles/cm3 were observed. In air-cooled specimens no precipitation was detected prior to aging by either the microscopic or X-ray diffraction methods. Previously reported work(3) showed resistometric evidence that no detectable precipitation occurred on air cooling. Thus it can be said that immediately prior to aging, both the air-cooled and the water-quenched specimens were supersaturated to the same extent with respect to the solute.

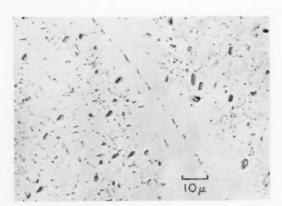


Fig. 5a. Light micrograph of a specimen that was air-cooled from 580° C to room temperature and then aged at 200° C for 72 hr.

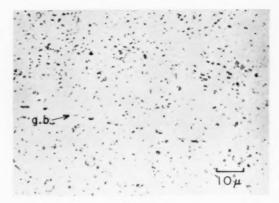


Fig. 5b.

Same as Fig. 5a except that this specimen was cold worked prior to aging. The grain boundary is indicated by an arrow. The depleted region has been eliminated by the cold work.

Grain boundary depletion

The width of the grain boundary depleted region increases as the rate of cooling from the homogenizing temperature decreases. The depleted region, as measured from the boundary toward the interior of one of the grains sharing the boundary, is $\sim\!0.5\,\mu$ for a water-quenched specimen, $\sim\!2\,\mu$ for a specimen quenched into alcohol, $\sim\!10\,\mu$ for a specimen aircooled in its boat, and $\sim\!15\,\mu$ for a specimen cooled while packed in granular alumina. Also the interparticle spacing within the grains is $\sim\!0.1\,\mu$ in the water-quenched specimen and increases with slower cooling rates. Fig. 4 shows the depleted region that resulted from a quench into alcohol. On all of the cooling rates used here no grain boundary precipitation could be seen prior to aging. This implies that the

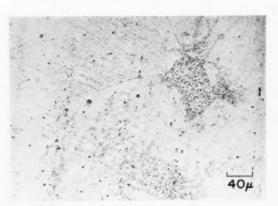


Fig. 6a.

Light photomicrograph showing well developed precipitation along slip bands and in the highly strained grain corners. The specimen was water quenched from 580°C, cold worked at room temperature, and then aged at 350°C for 20 min.

VO 7 19

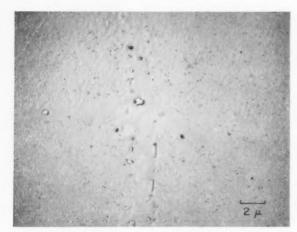


Fig. 6b.

Electron photomicrograph of a specimen treated as in Fig. 6a. A grain boundary junction is seen here; the boundaries emanate from the centre to the top, right, and left of the photograph. A slip band runs vertically from the center to the bottom of the photograph.

grain boundary depletion is not caused by solute segregation to the grain boundary, either during the aging or during the cooling from the homogenizing temperature. As illustrated in Fig. 5, cold work prior to aging causes precipitation to occur close to the grain boundaries, thus tending to eliminate the depleted region.

Depleted regions are sometimes observed within grains (See, for example, Fig. 2b). In these regions there are only a few large particles.

Cold work

1959

In Fig. 6a is seen the microstructure, at low magnification, of a specimen that had been cold worked prior to aging. One sees here well developed precipitation along slip bands and near grain boundary intersections. The small precipitate particles in the unstrained regions cannot be seen. However, with the aid of the electron microscope (Fig. 6b) we see that the slip bands are regions where the particles are fewer in number, but the particles have grown larger than those in the unstrained regions. This effect was not observed in specimens that had been either air-cooled or pack-cooled prior to the cold working and aging. As mentioned earlier, however, cold work tends to eliminate depleted zones adjacent to grain boundaries.

In the earlier resistometric experiments⁽³⁾ we found that cold work did not cause a sensible increase in the rate of precipitation at 200°C in air-cooled specimens. We therefore concluded that cold work did not provide suitable sites for nucleation. However, although this work showed that any cold-work effect must be small

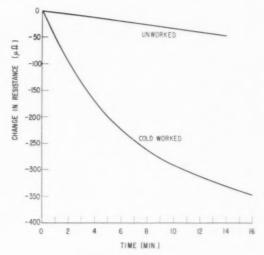


Fig. 7. Change in resistance vs. time at 300°C. These curves show the effect of cold work on the resistance decrease in an uninoculated specimen. In both cases the specimen was air-cooled from 580°C to room temperature and then aged at 300°C. The "cold-worked" curve results when the ribbon specimen is elongated $\sim\!\!2$ per cent and rumpled over its entire length prior to aging. The ribbon is $0.01\times0.2\times3$ cm. The precision of the measurements are $10^{-5}\,\Omega$; the resistance is $0.008\,\Omega$.

in comparison with the inoculation effect, it did not prove that there was no effect. The microscopic evidence shows, in fact, that cold work leads to precipitation in the depleted region. This indicates that, contrary to our earlier conclusion, cold working does produce nuclei. In fact, at higher temperatures, where the precipitation rate in uninoculated specimens is measurable resistometrically, cold work does noticeably increase the rate of precipitation (See Fig. 7). The kinetic experiments do show conclusively that quenching strains cannot account for the very rapid precipitation that was observed in inoculated specimens.

X-ray diffraction

In Fig. 8 is seen an oscillation pattern of a single crystal oriented with its [001] direction vertical. This crystal has been water quenched to room temperature before aging at 234°C for 6 days. The reflections from the silicon particles of the characteristic wavelengths of the X-radiation form incomplete Debye rings. This indicates that there exists certain preferences in the crystallographic orientations of the precipitated particles. These orientation preferences were determined by taking a series of oscillation patterns such as that of Fig. 8 at various positions of the matrix crystal with respect to the X-ray beam. For each position the intense portions of the Debye rings were

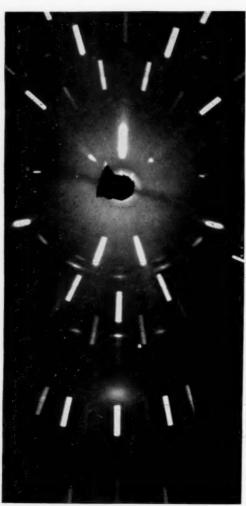


Fig. 8. X-ray pattern of a single crystal that was water-quenched from 580°C and then aged at 234°C for 6 days. The crystal is oriented with a \$\langle 100 \rangle\$ direction nearly vertical, and was oscillated 5° about the vertical axis. The white radiation reflected from the planes of the matrix crystal appears as sharp streaks. This is the transmission portion of the film.

plotted on a stereographic projection (Fig. 9). The resulting pole figures are shown in Fig. 10 for the $\{111\}$ and the $\{220\}$ Si reflections. These are only rough pole figures in that the reflection intensities were plotted as seen by eye on the X-ray films. No attempt was made to grade the intensities of the reflections. The observed reflections can be explained by the following preferences in orientation:

1.	$\{111\}_{\mathrm{Si}}$	$\{100\}_{\alpha};$	$\langle 110 \rangle_{\mathrm{Si}}$	$\langle 100 \rangle_{\rm x}$
2.	$\{111\}_{\mathrm{Si}}$	$\{111\}_{\alpha};$	$\langle 110 \rangle_{\mathrm{Si}}$	$\langle 114 \rangle_z$
3.	$\{1111\}_{Si}$	$\{111\}_{\alpha};$	$\langle 111 \rangle_{\mathrm{Si}}$	$\langle 123 \rangle_{\alpha}$

4.
$$\{111\}_{si} \| \{110\}_{x};$$
 $(112)_{si}^{'} \| (100)_{x}$

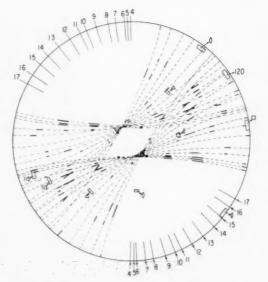


Fig. 9a. Intense portion of the Deybe rings of Cu K_{α} radiation, as reflected from the {111} poles of the silicon precipitate, are plotted stereographically. The numbered arrows on the bottom of the figure indicate the direction of the X-ray beam on the various exposures. The dashed curves are the loci of the {111} reflections for a completely random orientation. Some of the poles of the matrix crystal are plotted; they appear as streaks due to the 5° oscillation of the crystal. The specimen's $\langle 100 \rangle$ direction is perpendicular to the plane of the

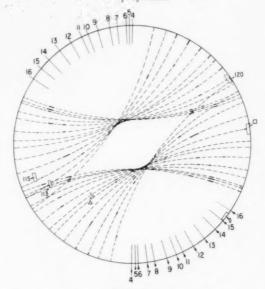


Fig. 9b. Stereographic plot of the $\{220\}$ reflection similar to that of Fig. 9a.

The subscript α refers to the aluminum-rich solid solution. The data do not exclude the orientation $\{111\}_{si} \parallel \{111\}_{\alpha}; \ \langle 110\rangle_{si} \parallel \langle 110\rangle_{\alpha}$ where the silicon phase is oriented nearly identically to the matrix.

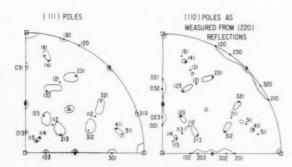


Fig. 10. (111) and (110) pole figures of the silicon precipitate in a single crystal matrix.



Fig.~11a. Stationary X-ray pattern (unfiltered Cu radiation) of a crystal that had been water-quenched from 580° prior to aging 6 days at $232^{\circ}\mathrm{C}.$ Among the Laue spots of the matrix crystal are seen incomplete Debye rings of the silicon precipitate and diffuse streaks emanating radially from the hole of the film.

Such reflections are observed, but they coincide with the reflections of orientation 2.

As over-aging occurs the Debye rings of the precipitated phase become more complete. Those patterns that show a distinct preferred orientation,



Fig. 11b.

Same as Fig. 11a with the crystal in the same orientation. Here, the crystal was aged for an additional 122 hr at 350°C. The Debye rings of the precipitate are more complete, and the radial streaks have sharpened to form shorter streaks and spots.

e.g. Fig. 11a, also have diffuse streaks emanating radially from the transmission portion of the film. As the Debye rings become more complete, the radial streaks become less diffuse and finally are resolved as spots (Fig. 11b). The streaks are interpreted as reflections of white radiation from planes of the precipitate's lattice that are nearly, but not exactly, parallel. These diffuse streaks are ultimately resolved

VOL. 7 1959 into simple Laue spots that are reflections from either large particles or many identically oriented particles in the overaged samples. It must be emphasized that even in the early stages of aging in the quenched specimens no exact, or Widmanstätten, orientation relation is seen. Instead, the data show a preference; that is, precipitate particles whose orientations lie near the preferred orientations collectively reflect higher intensity of the characteristic X-radiation than those particles of other orientations. This means either that more silicon particles are near favorable orientations, or simply that the more favorably oriented particles grow faster and are able to diffract an observable intensity at an earlier stage of precipitation.

In order to compare the results of the X-ray diffraction with that of the microscopy, it should be borne in mind that the aging treatment of 234°C for 6 days should result in roughly the same amount of precipitation as aging at 350°C for 39 min, if one takes as the apparent heat of activation 30,000 cal/g atom, which is a value reported by Köster and Knorr⁽⁵⁾ for this precipitation process. When crystals are aged for shorter times at either 234°C or 350°C the X-ray patterns are the same as that in Fig. 11a, but the precipitate's reflections are less intense.

It is interesting to note that in crystals that were air cooled instead of water quenched, no preference of orientation is noticed. In the air-cooled crystals the Debye rings are fairly complete, and no diffuse streaks appear on the transmission part of the film. However, Laue spots of precipitate particles are present just as in the later stages of aging in quenched specimens. The resolvable Laue spots occur because the particles reach a large size in air-cooled specimens sooner than in the water-quenched specimens.

Morphology

Nishimura et al. (6) have previously reported that in alloys similar to that used here, plate-like silicon particles are precipitated parallel to the {111} and {100} planes of the matrix. From Fig. 6b we can see that some of the silicon platelets lie parallel to the slip traces. Assuming the slip planes of the matrix to be of the type {111}, the findings of Nishimura et al. (6) were confirmed. In all of the photographs where a large number of platelets can be seen there are between four and seven non-parallel sets of platelets in each grain. The normals of the plate traces were plotted stereographically and found to be parallel to the poles of the {111} and {100} planes of the matrix. There is, however, some uncertainty in this operation, arising from the lenticular shape of some of the platelets' traces on the specimen surface. The direction of the

platelet normal in the specimen surface could be obtained to within 5° .

Occasionally one finds a grain where one set of platelets is nearly parallel to the specimen surface. It can then be seen that the platelets have straight edges (the platelets are often triangular or hexagonal in shape) that are parallel to other sets of platelets. This is to be expected because the platelet normals represent directions of slowest growth; crystal faces normal to directions of faster growth tend to disappear. Triangular and hexagonal silicon platelets that were precipitated from an Al(Si) solid solution were also observed by Marburger and Schluchter⁽⁷⁾ using an extraction replication technique.

DISCUSSION

A. Mechanism of inoculation

We now consider the consistency of our results with the two mechanisms of inoculation, (1) homogeneous nucleation, and (2) nucleation on dislocation loops; described in our earlier paper (see also introduction).

The number of silicon particles produced by the inoculation is of the same order of magnitude as the number of dislocation loops seen by Hirsch et al. (4) in their quenched specimens of pure aluminum. This agreement is consistent with the dislocation loop nucleation theory but, of course, does not vindicate it since the effect of dissolved silicon on loop formation is not known. Also we have not enough information to calculate the number of silicon particles that would result from homogeneous nucleation.

19

The precipitate depletion near grain boundaries and in singular areas within the grains, presumably around dislocations, can be attributed to the diffusion of vacancies to the boundary and to dislocations during the cooling just prior to inoculation. In agreement with this idea we have shown that the thickness of the depleted region increases with decreasing rate of cooling. This interpretation implies that the depletion is due to the absence of potential nuclei (formed by vacancies on the basis of either theory) rather than to a lowering of the solute concentration during the quench (e.g. by segregation at grain boundaries). That there is little deficiency of solute in the depleted zone is shown by the result that cold working the uninoculated specimen prior to aging produces many particles in the depleted region. This is shown by Fig. 5b which is the picture of the microstructure of a slowly cooled specimen cold worked prior to aging. There are many particles in the region near the grain boundary which would not have appeared if the specimen had not been cold worked.

Hirsch et al. also observed that there are regions around grain boundaries and within grains (around dislocations) depleted of dislocation loops. The thickness of these regions, $\sim 0.5~\mu$, is about the same as the depth of our precipitate-depleted region for a comparable quenching rate. This agreement again is consistent with the dislocation loop nucleation hypothesis. However, it does not disprove the homogeneous nucleation hypothesis since the vacancy depletion must have occurred during cooling. Therefore the diffusion coefficient might have been large enough for homogeneous nucleation only in the undepleted zones.

We observe that the interparticle spacing increases with decreasing quenching rate. This reflects a greater loss of vacancies during the slower quenches. A smaller concentration of vacancies during the inoculation period would presumably result in fewer dislocation loops and hence, if the dislocation loop nucleation hypothesis is right, fewer silicon nuclei. Of course, fewer nuclei would also be expected to result from a lesser concentration of vacancies on the basis of the homogeneous nucleation hypothesis provided the density of vacancy sinks does not decrease with decreasing vacancy supersaturation.

In our earlier paper we partially discounted the dislocation loop hypothesis because cold-working did not appear to have much effect on the precipitation rate in uninoculated specimens. This argument loses some of its force in view of the present results, which show that cold-work does enhance the precipitation rate in uninoculated specimens and that the failure to detect it in the earlier investigation was due to lack of experimental resolution. However, there is no metallographic evidence that cold working increases the density of nuclei.

In summary the metallographic evidence still does not permit a clear cut choice between the dislocation loop and homogeneous nucleation hypotheses. However, in view of the very close correspondence between the patterns of precipitate particles in inoculated specimens and the dislocation loop patterns observed by Hirsch and his co-workers, the dislocation loop hypothesis now seems to be the most natural and simple explanation for inoculation.

B. Effect of cold work

VOL.

1959

The mechanism of the cold-work effect is not yet clear. Apparently dislocations and low-angle boundaries are preferred sites for nucleation. Yet cold work actually seems to reduce the number of nuclei in strained regions of inoculated specimens while increasing the precipitation rate as measured by resistometric⁽³⁾ or dilatometric⁽⁶⁾ methods. Therefore,

it appears that the growth rate of the particles inside the strained regions must be greater than for those in the unstrained regions. However, we have no conclusive metallographic support for this.

Maddin and Cottrell(8) have observed that quenchhardened (i.e. quenched and aged a short time at room temperature) crystals of aluminum show long, coarse slip lines while crystals that were slowly cooled have short, closely spaced slip lines. Apparently, deformation in crystals that were given the inoculation (quench-hardening) treatment is confined to small regions of the crystal, while in the slowly cooled crystals the deformation is more dispersed. Thus, the fact that well-developed precipitate particles are observed to form along slip bands in the waterquenched (inoculated) specimens, but not in the more slowly cooled specimens, may be associated with the difference in the mechanism of deformation for the material in these two conditions. When the deformation is confined to sharply defined slip bands, the larger precipitate particles are found in these highly deformed regions; but the more dispersed deformation of the slowly cooled specimens leads to a more random dispersion of particles.

C. Orientation and morphology

From our data it is not clear whether the observed preferred orientations in inoculated specimens result from nucleation or subsequent growth. That is, there may be a higher probability for nucleation in certain orientations; on the other hand, nuclei may have formed in random orientations but particles in the observed preferred orientations grow faster. These would then become larger and diffract an observable intensity of the characteristic (K_x and K_β of Cu) X-radiation at an earlier stage of precipitation. When the silicon reflections and the preferred orientations are first detected, the diameters of the equi-axed particles are ~300 Å, as determined by the electron micrographs; and the size of the platelets are 10-100 times greater in their long dimension. In view of the small particle size and the presence of platelets we favor the preferred growth hypothesis. Thus, as over-aging occurs the equi-axed particles grow to a size resolvable by the X-rays resulting in more complete Debve rings.

All of the X-ray patterns of air-cooled specimens resemble those of the over-aged inoculated specimens. This is consistent with the above discussion because the particles of the uninoculated alloys have grown relatively large for equivalent aging times (compare Fig. 3 with Fig. 2). This is because in the inoculated alloy the particles are so closely spaced that their

diffusion fields soon overlap, and their growth rate decreases. The large particle size and the relatively small number of particles cause complete Debve rings as soon as the silicon reflections are visible on the film.

The interesting problem of the morphology of this system is why there exist both equi-axed and plate-like particles. This would be understandable if, as suggested above, there is rapid growth in certain crystallographic directions of the silicon for those particles of particular orientations. However, there is no understanding yet why the existence of directions of rapid growth should depend on the orientation of the particle.

SUMMARY

- 1. Silicon precipitates both in plate-like and equiaxed particles.
- 2. Orientation preferences are observed and can be explained by a random nucleation followed by rapid growth of those particles whose orientations lie near the observed orientation preferences.
- 3. A region depleted of precipitate particles exists near the grain boundaries. This is due to an absence of suitable nucleating agents and is believed to be

associated with the diffusion of quenched-in vacancies to the boundary.

4. At present the simplest and most reasonable explanation of inoculation is nucleation on dislocation loops that result from the annealing of quenched-in vacancies.

ACKNOWLEDGMENTS

The authors are indebted to E. F. Koch and A. Holik for assistance with the electron microscopy, and to Mrs. R. K. DiCerbo for help in obtaining the X-ray diffraction patterns.

REFERENCES

- 1. E. H. DIX, Jr. and A. C. HEATH, Jr., Proc. Inst. Metals
- Div., Amer. Inst. Min. (Metall.) Engrs. 164 (1938). W. L. Fink and K. R. Van Horn, Trans. Amer. Inst. Min. (Metall.) Engrs. 93, 383 (1931).
- 3. H. S. Rosenbaum and D. Turnbull, Acta Met. 6, 653 (1958).
- P. B. Hirsch, J. Silcox, R. E. Smallman and R. K. Westmacott, *Phil. Mag.* 3, 897 (1958).
- W. Köster and W. Knörr, Z. Metallk. 45, 616 (1954). 6. H. Nishimura, Y. Murakami and H. Otzuji, Suiyokwai
- Shi (Wednesday Soc.) 12, 265 (1954). 7. R. E. MARBURGER and A. W. SCHLUCHTER, J. Appl. Phys.
- 29, 184 (1958).
- 8. R. MADDIN and A. H. COTTRELL, Phil. Mag. 46, 735 (1955).

LETTERS TO THE EDITOR

Dispersion hardening*

The effect of the size and spacing of a dispersed second phase on the yield strength of a metal was determined in the iron–mercury system. This system was chosen because the size and spacing of the iron particles in the mercury could be independently varied. The iron was electrodeposited into the liquid mercury, and because of the very small solubility of the iron in the mercury 50 Å particles of iron from in the mercury. These can be grown by heat treatment to 1000 Å, and the spacing between particles can be varied by adding mercury. Tests were performed on extruded specimens at 77°K.

A modified Orowan⁽¹⁾ dependence of yield strength on particle spacing was assumed and as shown in Fig. 1 holds for a given particle diameter. However, it is obvious that the yield strength depends on the particle diameter so we may write:

VOL.

1959

$$\sigma_y = \frac{f(d)}{\Lambda - d} + \sigma_0 \tag{1}$$

where σ_y is the yield strength, Λ is the distance between centers of the particles, d is the particle diameter, σ_0 is the yield strength of the matrix, and f(d) is the slope of the lines and is a function of the particle diameter.

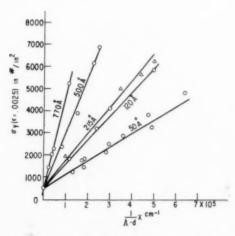


Fig. 1. Yield strength of mercury containing iron particles of the diameters shown on the curves, plotted as a function of the distance between the particles. The tests were performed at 77°K.

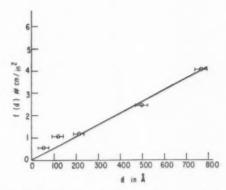


Fig. 2. The slopes of the lines of Fig. 1 are plotted as a function of particle diameter.

Fig. 2 shows a plot of f(d) as a function of d and hence we obtain:

$$f(d) = ad (2)$$

where a is a constant. There is indirect evidence that f(d) for the 50 Å and 100 Å particles is high because of coherency with the mercury lattice. Combining these two equations, we obtain:

$$\sigma_y = ad/(\Lambda - d) + \sigma_0 = a/(\Lambda/d - 1) + \sigma_0$$
 (3)

Equation 3 denies the validity of the Orowan relation in that when $\Lambda \gg d$ the yield strength is proportional to d/Λ , and not $1/\Lambda$. The result shows that the increase in yield strength due to the particles is a function only of Λ/d and since it can be shown that,

$$\Lambda/d = 0.82/f^{1/3} \tag{4}$$

where f is the volume fraction of precipitate, we obtain the result that the increase in yield strength due to the particles is a function only of the volume fraction of precipitate. Substituting equation (4) into equation (3) we obtain:

$$\sigma_y = a f^{1/3} / (0.82 - f^{1/3}) + \sigma_0 \tag{5}$$

These results indicate that the drop in yield strength of overaged material is not due to changes in particle spacing, but rather to a loss in coherency of the particles with the matrix.

We believe that the dependence of the yield strength due to a dispersed phase is given by equations (3) or (5) for the entire range of heat treatment. In the case of coherent particles, the diameter d and the volume fraction f must include the highly stressed

General Electric Research Laboratory Schenectady, New York W. H. Meiklejohn R. E. Skoda

Reference

 E. Orowan, Discussion, Symposium on Internal Stresses, p. 451. Institute of Metals, London (1947).

* Received March 6, 1959.

Comments on the recent paper of Clarebrough, Hargreaves and Loretto*

One finds that in trying to evaluate the many reported values of the energy stored in metals as a result of deformation the magnitude seems most simply related to the true strain; being, in the case of copper, a nearly linear relationship in many cases. If one analyzes the recent data of Clarebrough et al. (1) on the effect of grain size in this fashion one obtains Fig. 1 where each point is the average of three runs which were reported to agree within 5 per cent. From this figure one can draw either of two conclusions: (1) the amount of stored energy is a rather complex function of strain at low strains, a complexity probably not fully elucidated by these results, and it is also a sensitive function of grain size in the same region; or (2) the data are appreciably less accurate in the

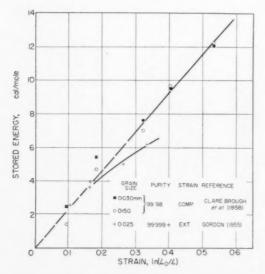


Fig. 1.

region of low strain than believed by the investigators and there is no demonstrated dependence on grain size in terms of actual strain. While intermediate conclusions are possible they seem no more satisfactory than the above. The data of Gordon⁽²⁾ for extension are also shown and are seen to agree very well with the indicated straight line for lower strains. Apart from the direction of cold working the main difference between the two experiments is that Gordon's copper was somewhat purer, probably primarily with respect to insoluble oxygen. Gordon's data would appear to support conclusion (2).

Isothermal kinetics of recrystallization have been well established; in particular, Gordon demonstrated that the energy released during recrystallization was directly proportional to the amount of recrystallization and the results could be expressed fairly accurately by the usual relationship

$$X = 1 - \exp\left[-Yt^k \exp\left(-kQ/RT\right)\right]$$

VOI

195

where X is fraction recrystallized, t is time, k a constant between 3 and 4, Q is an activation energy, T is absolute temperature and Y is a constant. One can substitute T/v for t where v is the velocity of heating (which assumes the sample starts at absolute zero at zero time) and obtain an expression for the kinetics during a constant rate of heating. The resulting expression can be differentiated to give rate. Such calculations were carried out using k as 3.6 and Q as 31,000 (these values were taken from Gordon but are very similar to values obtained on copper by others) and Y is selected to give a maximum rate at the desired temperature. The resulting rate curves are not symmetrical, being steeper and with less tail on the high temperature side but are still similar to those of Clarebrough et al.(1) There are, however, certain differences which are noted: For the calculated curves the widths (at half height) were 9 and 19 degrees for maximum rates at 190° and 400°C respectively while the widths from the above work are greater by a factor up to 4 for the coarse grained material and almost 3 for the fine grained material at the lowest temperatures. This discrepancy decreases with increasing temperatures until the fine grained material is approximately half the calculated width at the highest temperature. It is by no means clear what this means but perhaps the course of recrystallization is quite different for continuous heating as compared to isothermal runs.

It might be noted that even greater widths have been observed in most of the earlier work but not infrequently the material was twisted in torsion and would have a range of recrystallization temperatures; this should lead primarily to a tail on the high temperature side without increasing the widths too much.

It would seem that more work is required to clarify this situation.

R. O. WILLIAMS

Oak Ridge National Laboratories
Oak Ridge, Tennessee
formerly at:
The Cincinnati Milling Machine Co.
Cincinnati, Ohio

References

 L. M. Clarebrough, M. E. Hargreaves and M. H. Loretto, Acta Met. 6, 725 (1958).

 P. GORDON, Trans. Amer. Inst. Min. (Metall.) Engrs. 206, 618 (1956).

* Received March 9, 1959.

VOL.

1959

Further observations on the growth of silver whiskers from silver chloride*

The growth of silver whiskers by the hydrogen reduction of silver chloride was first reported by Kohlschütter⁽¹⁾ in 1932. More recently the present author^(2,3) described the conditions for the growth of a variety of whiskers from their halides including that of silver from AgCl and AgI. Kohlschütter suggested that unlike the silver filaments that grew from solid

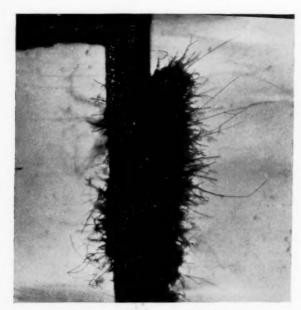


Fig. 1. Silver whiskers grown from AgCl on hot filament in stream of hydrogen.

 $\mathrm{Ag}_2\mathrm{S}$ the silver whiskers from AgCl grow by the condensation of silver vapor according to

2
AgCl (vapor) + H
$$_2$$
 \rightarrow 2
HCl + 2
Ag (vapor) $$\downarrow$$ Ag (whisker)

By visually following the growth of the silver whiskers it is apparent that the whiskers do not grow by a vapor phase mechanism but rather grow out from their base. The growth of the whiskers can easily be observed by heating a bead of AgCl on a hot filament in stream of hydrogen as shown in Fig. 1. The whiskers grow out from the liquid AgCl at temperatures ranging from 460° to 925°C. No whisker growth was observed below the melting point of AgCl. The whiskers continually push out from the chloride surface and then fall over to merge with the liquid. The whiskers appear to remain uniform in diameter during their growth. At temperatures of 700°C and above the whiskers obtain lengths of several millimeters and their growth rate is as high as 100 μ/sec . All of the whiskers that have been cross-sectioned in connection with a separate investigation (4) have been found to be round, with their diameters varying from 2 to 15 u.

The growth velocity of the whiskers can be rationalized by use of the following model (Fig. 2). Suppose a small crystal of Ag that is nucleated on the liquid AgCl surface contains a single dislocation perpendicular to the AgCl surface. If the nucleation of silver in AgCl is difficult and the diffusion of Ag⁺ in AgCl is rapid the silver ions can migrate to the crystal nucleus and attach themselves to it at the emerging dislocation. If the interfacial energy AgCl–Ag is higher than that of Ag–H $_2$ the crystal can rise from the liquid as silver is deposited at the bottom of the crystal. As the crystal grows in length it becomes top-heavy and falls over onto the surface of the halide. The growth velocity, \dot{L} , of the whiskers will then be given by

$$\dot{L} \simeq \frac{D.2\pi R^2}{\pi r^2 \rho} \frac{\Delta c}{R} \simeq \frac{0.2DR \ \Delta C}{r^2} \text{ cm/sec}$$
 (1)

where r = radius of whisker,

 $\rho = \text{density of silver},$

D = diffusivity of Ag+ in AgCl,

 $\Delta c/R = {
m concentration}$ gradient of Ag⁺ in diffusion zone,

R = radius of hemispherical diffusion zone (see Fig. 2).

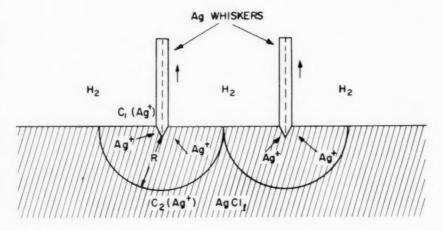


Fig. 2. Model for the growth of silver whiskers from AgCl.

The magnitude of R must be approximately equal to 1/2 the spacing between whiskers. D can be estimated from the conductivity, σ , by means of

$$\sigma/D = Ne^2/kT \tag{2}$$

where N = number of ion pairs per cm³.

Equation (2) assumes that conduction occurs primarily by the movement of the cation. There are indications⁽⁵⁾ that this is true for AgCl.

At 700°C, σ is approximately 4 ohm⁻¹ cm^{-1(5.6)} and D is therefore 2×10^{-4} using $N = 10^{22}$. Using the reasonable values of $10^{-2}\,\mathrm{cm}$ for R and 10^{-3} for Δc (equivalent to a silver excess of 2.4×10^{-2} per cent) \dot{L} is 100 μ/sec for a 4 μ diameter whisker.

That the silver whiskers do not grow by a vapor phase transport mechanism such as Cu from CuI(7) is not unexpected since the vapor pressure of AgCl below 700°C is less than 1/1000 that of CuI. It is clear that high ionic conductivity is not the sole criterion for rapid whisker growth to occur from the base. The ionic conductivity of Ag+ in AgI is nearly as great as in AgCl, vet no whiskers grow at an observable rate on the surface of molten AgI that is being reduced with H2. Such factors as chemical reactivity and excess concentration of cations have to be considered. It is of interest that when AgI is reduced in a porcelain boat at 600°C polygonal silver whiskers grow at a slow rate on the sides of the boat, presumably by the same vapor transport mechanism responsible for the growth of Cu whiskers from CuI. The vapor pressure of AgI is also significantly higher than that of AgCl.

S. S. BRENNER

General Electric Research Laboratory Schenectady, New York

References

- 1. H. W. Kohlschütter, Z. Elektrochemie 38, 345 (1932).
- S. S. BRENNER, Acta Met. 4, 62 (1956).
 S. S. BRENNER, Thesis RPI, May 1957
- S. S. Brenner, J. Appl. Phys. 27, 1484 (1956).
 M. Bloom and E. Heymann, Proc. Roy. Soc. A188, 392 (1946).
- 6. C. Tubant and E. Lorenz, Z. Phys. Chem. 87, 513 (1914).
- 7. S. S. Brenner, Submitted to Acta Met.
- * Received March 25, 1959.

On the orientation of silicon precipitating from an Al-rich solid solution*

19

Recently, it was reported⁽¹⁾ that X-ray diffraction patterns of silicon, as precipitated (in its ordinary diamond cubic structure) from an Al-rich solid solution, revealed certain orientation preferences of the silicon with respect to the Al-rich matrix. Microscopically it was seen that the silicon precipitated in both equi-axed and plate-like particles. The plates were 10-100 times longer in their long dimension than either their thickness or the diameters of the equi-axed particles. The plates were parallel to the {111} and {100} planes of the matrix. It was inferred from the X-ray and microscopic evidence that the nucleation of silicon particles occurred in random orientations, but that this was followed by rapid growth of those particles whose orientations were near the observed preferred orientations. It was then proposed that the X-rays diffracted sharply only from the larger particles, while diffraction from the small, randomly oriented particles was too diffuse to be seen on the film. (The small particles, as seen by a replication technique with the electron miscroscope were ~300 Å diameter).

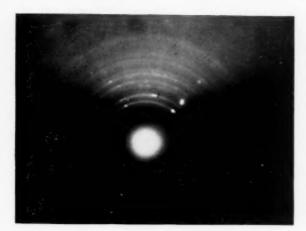


Fig. 1. Reflection electron diffraction pattern showing the rings of the precipitated silicon in a single crystal Al-rich matrix. We see diffraction rings due to the precipitated silicon and two spots of the matrix reciprocal lattice.

We now have direct evidence that this interpretation is correct. Electron diffraction patterns of the precipitated silicon (see Fig. 1) were obtained by a reflection technique with 50 kV electrons. The single crystal specimen of an Al(1% Si) alloy was homogenized for 1 hr at 580°C in a N_2 atmosphere and then quenched in ice-water. After remaining at room temperature for $\sim \frac{1}{2}$ hr, it was aged at 200°C for 18 hr. The specimen was chemically polished in a hot (\sim 85°C) solution of H_3PO_4 (94 parts by vol.) and HNO_3 (6 parts by vol.). The electron diffraction patterns so obtained (e.g. that of Fig. 1) showed no orientation preferences. X-ray diffraction patterns of single crystals with similar heat treatments showed strong orientation preferences.

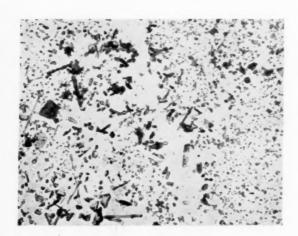


Fig. 2a. Carbon extraction replies showing equi-axed and plate-like silicon particles in the vicinity of a grain boundary.

Additional evidence for a random orientation of silicon particles was obtained by electron diffraction (by transmission) of an extraction replica. A similar specimen was homogenized and quenched as above, and then aged at 200°C for 22½ hr. A direct carbon film was evaporated onto an electro-polished and chemically etched surface, and then etched away from the specimen with a solution of HNO₃ (10 parts by vol.), HCl (5 parts by vol.), and water (85 parts by vol.). The extraction replica and its diffraction pattern are shown in Fig. 2. The pattern is that of silicon and shows no orientation preferences. The photograph and pattern were obtained by E. F. Koch on a Phillips EM-100 electron microscope at 50 kV.

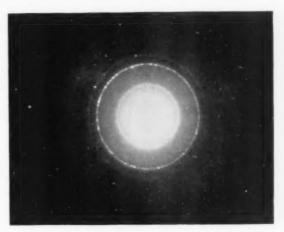


Fig. 2b. Electron transmission diffraction pattern showing no orientation preference. The area of the replica irradiated was immediately to the left of the grain boundary in Fig. 2a.

Since the shorter wavelength electrons ($\lambda \sim 0.05 \text{ Å}$) shows a random distribution of orientations while the X-rays ($\lambda \sim 1.5 \text{ Å}$) show strong orientation preferences, we can conclude that the X-rays diffract only from the larger (presumably the plate-like particles. Thus the previous inference that the silicon is nucleated in random orientations with respect to the matrix is confirmed.

Acknowledgments

The authors gratefully acknowledge the help of E. F. Koch in this work.

H. S. ROSENBAUM

D. TURNBULL

E. I. ALESSANDRINI

Laboratory Schenectady, New York

References

- H. S. ROSENBAUM and D. TURNBULL, G. E. Report 58– RL-2153, also Acta Met., 7, 664 (1959).
 - * Received April 3, 1959.

General Electric Research

VOL. 7 1959

Vacancy precipitation in quenched gold from internal friction measurements*

Very little is known about the nature of the atomic mechanisms involved in the annealing-out of quenched vacancies in metals. The complexity of the observed decay has prevented clear information being obtained about the processes in operation. The decay with time of the quenched-in resistivity⁽¹⁾ and mechanical properties⁽²⁾ in metals was generally assumed to obey a simple exponential decay law, although restrictions were sometimes made that the quench temperature should not exceed a certain limit⁽³⁾ otherwise deviations would be unavoidable. The present investigation is an attempt to follow up experimentally, by internal friction measurements, the kinetics of vacancy precipitation in quenched gold in the initial annealing period.

Pure gold strips (thickness 0.006 cm) were clamped at one end and then electrostatically excited to transverse vibrations at their natural frequencies ($\approx 30 \text{ c/s}$). A micro-vibration pick-up circuit was used to render visible on the screen of a cathode-ray oscilloscope the small amplitudes of vibration (strain amplitude of the order 10^{-7}). By removing the driving force, the vibration decays freely, and low-stress internal friction, Q^{-1} , was measured from the time of half decay of amplitude.

Specimens were rapidly quenched (while clamped in their support) into cold water from high temperatures, then immediately brought to the experimental measuring position. Room temperature internal friction measurements followed immediately. Great care was taken to standardise the initial quenching conditions of every run; also a new sample from the stock was used for each fresh set of observations. The duration of the annealing time was measured from the moment of quenching. Typical quenched-in internal friction decay curves in the initial annealing period are shown in Fig. 1. An initial sharp decay characterizes the curves for samples quenched from higher temperatures (>700°C). The energy of formation of vacancies was found to be 0.96 eV.

Assuming to a first approximation that the disappearance of vacancies is mainly responsible for the observed decay in the quenched-in internal friction, vacancy precipitation curves for different quenches were calculated using the formula:

$$f(t) = 1 - \exp\left[-(t/\tau)^n\right]$$

where f(t) is the fraction of vacancies precipitated after a time t and is here calculated from $[\Delta Q^{-1}(t)/\Delta Q^{-1}(0)]$. Results are represented in Fig. 2. The

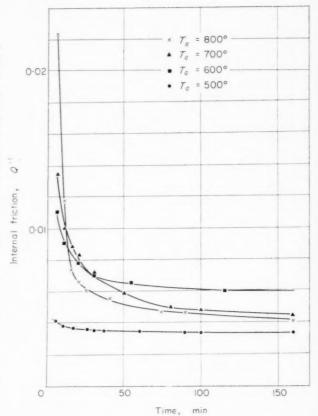


Fig. 1. Initial parts of room temperature annealing curves for gold strips quenched from different temperatures.

195

curves show that for quenches from below 700° C the precipitation follows an exponential decay law, as judged from the corresponding slopes of the precipitation lines which approximate to unity. This result was confirmed by plotting rate of decay of internal friction, dQ^{-1}/dt , vs. annealing time t, and a linear relationship resulted. According to a recent theory⁽⁴⁾ on diffusion-limited precipitation from super-saturated solid solutions, the slope of the precipitation curve was found to be unity only when the majority of sinks were in the form of long thin cylinders. By analogy, it might be envisaged here that stray dislocation lines originally present in the gold matrix form the predominating sinks for vacancies in the case of quenches from below 700° C.

For quenches from temperatures higher than 700°C, the precipitation curves show two distinct stages, indicating two different modes of vacancy precipitation. The high decay rate characterizing the first stage may be attributed to the high concentration of vacancies which generate their own dislocation sinks, namely the Frank sessile rings, by the collapse of

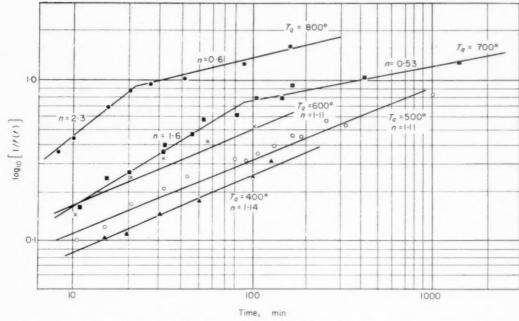


Fig. 2. Precipitation of vacancies after different quenches. The quenching temperature, T_g , and the slopes of the precipitation lines, n, are given on each line.

vacancy clusters condensed on the (111) planes. In the second stage the slopes of the precipitation lines yielded a value of about 0.6, which is less than that obtained in the case of low-temperature quenching. This observed difference in the behaviour of the vacancy precipitation process in the two cases may be attributed to the fact that at the end of the first stage (where $T_q > 700^{\circ}\mathrm{C}$) the crystal becomes enriched with stacking faults⁽⁵⁾ which possibly interact with the remaining vacancies to cause the observed delay in decay rate.

R. KAMEL

Physics Department, Faculty of Science University of Cairo, Egypt

1959

References

- J. W. KAUFFMAN and J. S. KOEHLER, Phys. Rev. 88, 149 (1952); ibid. 97, 555 (1955).
 F. J. BRADSHAW and S. PEARSON, Phil. Mag. 1, 812 (1956); ibid. 2, 379, 570 (1957).
 C. PANSERI, F. GATTO and T. FEDERIGHI, Acta Met. 5,
- 50 (1957).
 2. M. LEVY and M. METZGER, Phil. Mag. 46, (vii) 1021 (1955).
- E. Roswell and A. S. Nowick, Acta Met. 5, 228 (1957).
 J. E. Bauerle, C. E. Klaubunde and J. S. Koehler, Phys. Rev. 102, 1182 (1956).
- F. Seitz, Acta Phys. Hung. 8, 19 (1957).
- F. S. Ham, J. Phys. Chem. Solids 6, 335 (1958).
 H. Kimura, R. Maddin and D. Kuhlmann-Wilsdorf, Acta Met. 7, 145, 154 (1959).
 - * Received April 24, 1959.

Hole model for diffusion in liquids*

The structure and properties of liquid and solid metals are remarkably similar; in fact, the elastic shear modulus is about the only property of a solid metal which undergoes a drastic change upon melting. It is tempting, then, to describe diffusion in liquid metals in terms of the motion of atoms into adjacent vacancies or holes in the liquid structure, the process being similar to vacancy diffusion in crystals. Theories of diffusion and of the viscosity of liquid metals have been developed along these lines by Frenkel(1) and Eyring(2) among others. Nachtrieb(3) has pointed out the following difficulties with a vacancy model of liquid self-diffusion: First, the small size of D_0 obtained from a plot of $\ln D$ vs. 1/T implies that ΔS , the molar entropy of the activated state, must be of the order of -5 E.U. whereas in the erystalline case ΔS is known from both theory and experiment to be always positive. Nachtrieb points out that it is difficult to see how more order could be introduced into the liquid during the jump of an atom into a vacant site. Second, it is observed that the activation volume for self-diffusion is an order of magnitude smaller in liquid metals than in metal crystals. Since the activation volume may be thought of as the molar volume of vacancies at the mid-point of their jump, this seems to argue against a vacancy mechanism. Finally, there is the disturbing fact

that the activation energies for self-diffusion in liquid metals do not correlate with the latent heats of vaporization.

Some experiments on the propagation of sound in liquid metals(4) suggest that it may be useful to describe liquid metal structure in terms of a free volume localized into small holes. It is found that the energy required for the formation of these holes is of the order of a quarter to a third of the activation energy for self-diffusion, implying thus the relatively larger activation energy for atomic jump expected because of the small size of the diffusing holes. On this model the above objections to a hole model of liquid diffusion do not seem so serious: It is easy to imagine that the jump of a small hole involves forcing neighboring atoms into more nearly perfect close packing, thus increasing the amount of order in the liquid and giving a negative ΔS . Also, the small activation volume for liquid self-diffusion seems reasonable for the jump of small holes. It is found that there is no correlation of the energy for hole formation in different metals with their latent heats of vaporization, so that no such correlation should be expected for the diffusion energies. Whether or not a relation between this latent heat and the energy of hole formation should be expected does not seem to be clear at present.

As an alternative to the hole or vacancy model of liquid metal diffusion, Swalin⁽⁵⁾ has developed a theory of diffusion based on the movement of atoms small and variable distances because of local density fluctuations. He calculates the mean square value of the jump distance to be

$$\overline{j^2} = 3Z N_0 kT/16 \; \Delta H_v \alpha^2$$

in terms of the co-ordination number Z, the latent heat of vaporization ΔH_v , Avogadro's number N_0 , and α , a measure of the curvature of the energy vs. j curve. Inserting numerical values into this relation yields mean jump distances of the order of hundredths of an angstrom. In order to find the diffusion coefficient through the relation $D=\frac{1}{6}[\bar{j}^2/\tau]$, Swalin calculates the atomic jump frequency to be

$$1/\tau = kTZ/h$$

Since j is so small, $1/\tau$ must be very large if D is to be appreciable, so large that it is difficult to form a physical picture of the diffusion process being considered. In the Debye model of solids the maximum atomic vibration frequency is

$$v_m = k\Theta_D/h$$

and there is every reason to believe that, if anything, it is lower in liquids. One finds that the ratio

$$rac{v_m}{1/ au} = rac{\Theta_D}{TZ}$$

is of the order of 1/40 for the metals considered by Swalin when T is taken to be the melting temperature. It would not be safe to assume that a complete theory of liquid metal diffusion could be obtained by simply substituting numerous small holes for the vacancies which appear in the theory of diffusion in closed packed crystals. On the other hand, one probably cannot rule out the possibility of the activated jumps of holes as is done in Swalin's theory. An accurate theory of liquid metal diffusion will probably have to take into account atom movements resulting from both activated jumps and local density fluctuations. It may be that these two processes are of comparable importance in liquid metals.

R. B. GORDON

195

Hammond Metallurgical Laboratory Yale University New Haven, Connecticut

References

- J. FRENKEL, Kinetic Theory of Liquids, p. 200ff. Oxford (1946).
- S. GLASSTONE, K. J. LAIDLER and H. EYRING, Theory of Rate Processes. New York (1941).
- N. H. Nachtrieb in Liquid Metals and Solidification. Amer. Soc. Metals, Cleveland (1958).
- 4. R. B. GORDON, Acta Met. 7, 1 (1959).
- 5. R. A. SWALIN, Acta Met. in press.
 - * Received April 29, 1959.

Some observations on the retention of the β -phase in quenched Zr 50 at. % Ti alloys*

It has been reported that the high temperature β -phase can be retained on quenching to room temperature alloys of compositions between Zr-10 at.% Ti and Zr-90 at.% Ti, the maximum amount of retained β occurring in the Zr-50 at.% Ti alloy. This evidence is based on thermal analysis measurements supported by X-ray examination of quenched powders.

In the present work a single crystal of Zr–50 at. % Ti was heated for 1½ hr at 850°C in an evacuated silica tube and quenched by smashing the tube under water. The rate of cooling during the quench was

^{*} This work formed part of a programme carried out for Metallurgy Division, Atomic Energy Research Establishment, Harwell.

estimated to be better than 200°C/see which is faster than the minimum rate quoted as necessary for the retention of β . Single crystal oscillation photographs, however, showed no evidence of β , the lower limit of detection being about 0.5 per cent.

To establish whether this result was due to using a single crystal rather than the (polycrystalline) powder specimens used in the earlier work, a small cylindrical specimen 0.3 cm dia. by 0.7 cm long was heated for $1\frac{1}{2}$ hr at 850°C in a McQuillan type quenching furnace and water quenched. A glancing incidence X-ray pattern from an etched surface again showed no retained β .

A number of specimens of filings and slivers $1.0\times0.05\times0.025$ cm were then examined after quenching into water and liquid nitrogen from temperatures between 850° and $950^\circ\mathrm{C}$. In some of these the β phase was retained, but the results showed inconsistencies. It appeared that these were due to varying amounts of contamination in the specimens. In addition faint diffractions of an extra constituent were observed. This has not been identified but the lines can be indexed on a f.c.c. cell of parameter 4.62 Å. There are a number of hydrides, oxides and earbides of titanium and zirconium having similar crystal structures. Lattice parameter considerations suggest that the extra constituent is a zirconium compound of this form.

The effect of contamination on retention of the β structure has been investigated systematically using a thermal arrest apparatus, and making subsequent X-ray examination of the same solid specimens. A specimen of thin foil (0.01 in. thick) was suspended from a Pt/Pt-Rh thermocouple inside a continuously evacuated tube, the vacuum being $\sim 1 \times 10^{-6}$ mm Hg. The tube was fitted with a valve permitting a jet of argon to be directed over the specimen giving a quenching rate greater than 1000°C/sec. The temperature was recorded automatically on a moving chart. Initially a Zr-50 at. % Ti specimen was tested and no retained β was observed. The specimen was then deliberately contaminated by admitting air until the vacuum fell to ~10⁻³ mm Hg. After re-heating and quenching the β phase was retained. Corresponding to this result a variation in the thermal arrest of the $\beta \rightarrow \alpha$ transformation during comparatively slow cooling $(\sim 20^{\circ}\text{C/sec} \text{ at } \beta \rightarrow \alpha)$ could be observed. Fig. 1 illustrates this smoothening of the thermal analysis curve on successive contaminations of a single specimen. The final condition in this sequence corresponds to about 60% retained β as determined by subsequent room temperature X-ray measurement.

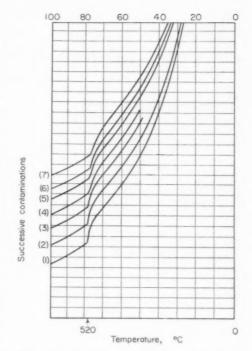


Fig. 1. Effect of air contamination on thermal arrest of Zr 50 at. % Ti. Chart speed 3in./min.

From the observation that β cannot be retained in pure material at the 1000°C/sec quenching rate, it may be concluded that either M_f is above room temperature or complete isothermal transformation occurs in less than 1 sec. The retention of β in the slowly cooled contaminated material implies that the complete isothermal curve for this material cannot lie very close to the temperature axis and furthermore that M_f must certainly lie below room temperature.

On heat treating at 400°C a specimen in which the β -phase had been retained by contamination in this way, it was found, by X-ray examination, that the β structure transforms to α via the metastable ω phase.

Acknowledgment

Thanks are due to the Director, Atomic Energy Research Establishment, Harwell, for permission to publish this letter.

> B. A. HATT G. I. WILLIAMS

Physics Laboratory Fulmer Research Institute Ltd. Stoke Poges, Buckinghamshire

Reference

1. P. Duwez, J. Inst. Met. 80, 525 (1951-52).

Received March 18, 1959.

Mise en évidence d'un microrelief, indice de cisaillement martensitique*

Tandis que les transformations martensitiques vraies—du type Fe/C—s'accompagnent d'un relief de surface couvrant la totalité du grain, indice de cisaillement homogène, les marques de transformation

observables dans le cobalt ne présentent qu'environ 10 pour cent de la surface du métal (Fig. 1).

Cependant, l'analyse dilatométrique et radiocristallographique montrent de façon certaine que le métal subit à chaque cycle de chauffe au delà de 430°C une transformation complète. (1) Comment la transformation s'opère-telle alors dans la plus grande

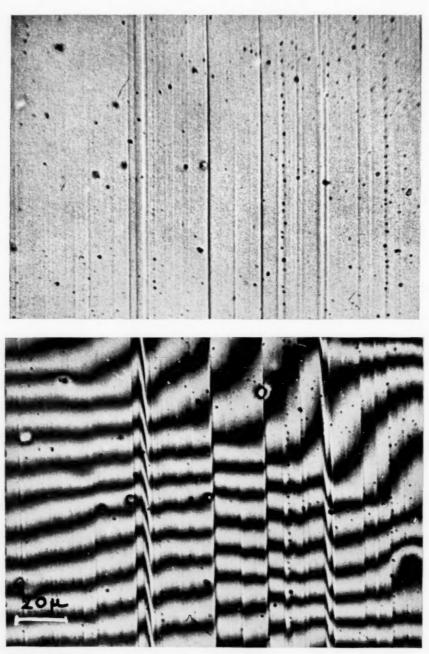


Fig. 1. Echantillon de Co après double transformation hex. \rightarrow c.f.c. \rightarrow hex. (chauffage à 500°C suivi du refroidissement a l'ambiante). La micrographie interférentielle montre des plaquettes de 1–5 μ séparées par des regions apparemment exemptes de relief.

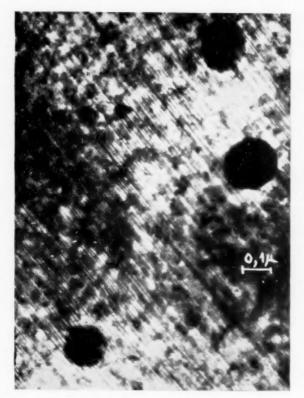


Fig. 2. Echantillon de Co/Ni à 25% de Ni. Micrographie électronique directe sur film minee. G=115~000

partie du cristal? L'absence ou la présence de marques sur la surface fournira un indice précieux dans la recherche du mécanisme de la transformation.

Nous avons déjà avancé l'hypothèse(2) que le cisaillement martensitique dans le Co, bien que non décelable par le relief de surface, serait général. Il ne reste visible, cependant, que dans les seules regions où il s'est effectué de façon coopérative dans un même sens, sur une echelle suffisamment grande pour faire naître des contraintes non négligeables dans le métal. Le glissement dû au relachement des contraintes rend le cisaillement de la transformation inverse dissymétrique ce qui permet d'en apercevoir les traces sur la surface de l'echantillon. Mais dans environ 90 pour cent du métal, la transformation s'effectue par cisaillement à échelle suffisamment fine (de l'ordre de quelques couches atomiques) pour que les contraintes développées par la croissance des plaquettes demeurent dans le domaine élastique. Le cisaillement créé lors de la transformation $\beta \rightarrow \alpha$ s'annule donc au cours de la transformation inverse $\alpha \rightarrow \beta$. Par conséquent, l'observation de l'échantillon à froid, c'est-à-dire après une double transformation $\beta \rightarrow \alpha \rightarrow$ β , ne devrait plus permettre de déceler un quelconque relief de surface. Son absence ne saurait donc servir d'argument contre le cisaillement martensitique.

Pour vérifier cette hypothèse il devient nécessaire d'examiner le métal après une seule transformation, de préférence à chaud, à l'état c.f.c. α . Nous avons d'abord essayé d'obtenir des repliques à chaud; des couches de carbone vaporisé sur la surface du métal porté à 500°C ne nous ont pas donné le résultat escompté.

Nous avons alors procéde à l'examen direct, au microscope électronique, des couches minces des alliages Co/Ni à 25% de Ni (l'addition du Ni a pour effet d'abaisser la température de la transformation). Certains parties isolées du film métallique arrivent effectivement, sous l'impact du faisceau d'électrons, à dépasser la température de transformation $\beta \rightarrow \alpha$ (\sim 265°C). Nous avons pu prendre des clichés montrant un microrelief de surface extrêmement fin (Fig. 2), de l'ordre de 20 Å. Le diagramme de diffraction du même endroit indiquait que le métal était à l'état c.f.c., c'est-à-dire qu'il a subi la seule transformation au chauffage.

Office National d'Etudes et de Hervé Bibring Recherches Aéronautiques Chatillon-sous-Bagneux (Seine)

Bibliographie

- H. Bibring et F. Sebilleau, C.R. Acad. Sci., Paris 238, 1026 (1954).
- 2. J. Inst. Met. 87, 3, 71, (1958).
 - * Received April 17, 1959

The effect of impurities on the strength of silver chloride*†

The recent emphasis on the study of the ductile characteristics of some refractory nonmetallic materials has prompted a general survey of the mechanical properties of materials having the same or similar structures. The objective of these investigations was to determine the effect of small impurity additions on the stress-strain characteristics of a representative ionic material. It has been reported by several investigators^(1,2,3) that ionic materials with the sodium chloride structure exhibit ductility, and also that the ductility is a function of purity and, in some cases, surface condition.

It has been known for some time⁽⁴⁾ that silver chloride exhibits a great deal of plasticity and may

[†] This research was supported by the United States Air Force through the Air Force Office of Scientific Research of the Air Research and Development Command, under contract No. AF49(638)-56. Reproduction in whole or in part is permitted for any purpose of the United States Government.

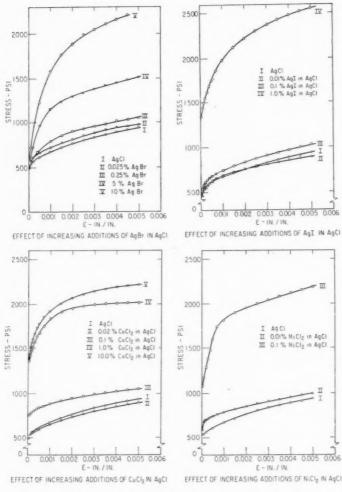


Fig. 1.

be shaped in the same manner as metals by extrusion, rolling, etc. Since AgCl has the same structure as many of the high temperature refractories, it seemed reasonable that the effects of additions on the properties of this material should give some idea as to what to expect from modified high temperature refractories.

Specimens of silver chloride were prepared by chill casting, annealing, rolling, punching to shape, and a final anneal before testing. The specimens used were flat with a reduced gauge section 1 in. long, 5/16 in. wide, and 0·050 in. thick. Varying amounts of impurities were added to the melt before casting. All preparation and testing were done under dark-room conditions. The impurities added were AgBr, AgI, CuCl₂, and NiCl₂. The grain size was maintained at an average of approximately 0·5 mm.

All additions caused AgCl to become more light

sensitive. Therefore, extreme care had to be taken to prevent silver from precipitating before the test was completed. In addition to its light sensitivity, AgCl is very reactive when under stress. All metal parts touching the specimen had to be of nonreactive metal; the parts were protected by gold plating. The stress–strain curves in Fig. 1 show the effect of various additions on the tensile properties of AgCl. Each curve represents an average of five tests. As indicated by the points shown, the scatter was very small and the reproductibility in any one set of tests was very good. The specimens were not strained to fracture, but all showed a great deal of ductility.

195

Silver bromide was easily added to AgCl in any proportion while the other materials, if added in much greater amounts than that indicated, would cause decomposition. The yield point in all cases seemed to vary only slightly, while the strength rose at an

increasing rate with larger amounts of additive. It was seen also that the different addition materials had definitely different effects. One per cent CuCla had a great deal more effect than one percent of AgBr. but the addition of 10% of either had about the same effect. NiCl2 and AgI also had a greater effect for small additions than did AgBr. This difference in properties could be explained if the addition of AgBr truly formed a solid solution while the others formed two-phase systems. However, X-ray examination of the specimens did not indicate that a second structure was present in any of the samples. All samples tested showed the silver chloride lattice and in a very few cases enough silver was present to be detected. Some silver was, of course, reduced during the X-ray determination. Further examination of the X-ray data indicated some rather large changes in lattice parameter in some cases. 10% AgCl showed the greatest change of approximately one per cent. AgI also showed an increase of about 0.13 per cent for the alloy containing 1% AgI. The additions of Cu and Ni chloride did not show a readily measurable change, but there is apparently some slight decrease in parameter. The increased effect of AgI as compared with AgBr may well be due to the increased polarizability of AgI. The decreased parameter and increased effect on strength, by small amounts of Ni and Cu chlorides, are very likely the result of a change in the bond configuration due to the addition of a divalent ion. It is interesting to note that the effect of these additions on the stress-strain curve is similar to that found in metal solid solution systems. These results do not compare with data from the tests on MgO. (5) containing a soluble impurity Fe, where a few (10) parts per million increase the strength up to 50 per cent while also increasing the yield. AgCl seems to be much more closely related to metals, where mechanical properties are concerned, than to its isostructural compounds.

W. J. LUHMAN

A. E. GORUM

Minerals Research Laboratory University of California Berkeley

1959

References

- A. E. GORUM, E. R. PARKER, and J. A. PASK, Effect of Surface Conditions on the Room Temperature Ductility of Ionic Crystals, J. Amer. Ceram. Soc. 41 (5) (May 1958).
 J. J. GILMAN and W. G. JOHNSTON, Observations of Dis-
- J. J. GILMAN and W. G. JOHNSTON, Observations of Dislocation Glide and Climb in Lithium Fluoride Crystals, J. Appl. Phys. 27, (1956).
- A. Joffe, M. W. Kirpitschewa, and M. A. Lewitsky, Deformation and Strength of Crystals, Z. Physik 22, 286 (1924).
- A. V. Stepanovi, Plastic Properties of Single Crystals of Silver and Thallium Halides, Physik Z. Sowjet Union 6 (1934).

- A. E. GORUM, W. J. LUHMAN, and J. A. PASK, Effect of Impurities and Heat Treatment on the Ductility of MgO, in press, Amer. Ceram. Soc. (1959).
 - * Received April 30, 1959.

The escape of hydrogen from iron*

Although a considerable body of literature⁽¹⁾ exists on the effect of hydrogen on the properties of iron and its alloys, most of these data are either qualitative or too fragmentary to serve as the basis for a description of the kinetics of the escape of hydrogen from the metal. It is hoped that the data presented herewith may serve to clarify the mechanism of the process.

Using a flexing method to determine the brittleness caused by hydrogen, Bastien⁽²⁾ showed that the decrease in brittleness is linearly proportional to the amount of gas which has escaped. It was decided, therefore, to use brittleness as a measure of the gas content of the iron.

Hydrogen may be introduced into the metal either by heating at high gas pressures or by making the metal the cathode in a dilute electrolytic bath. The first method has the advantage that the concentration of gas in the metal may be more readily controlled but has the disadvantage that the high temperature may produce changes in the body of the metal which are not characteristic of the annealed metal free of hydrogen. For this reason the electrolytic method of charging with hydrogen was adopted.

Since it is necessary to test a number of samples which have been given identical treatment in hydrogen, a torsion method using cylindrical rods seemed most suitable as a measure of "brittleness" and hence hydrogen content. Rods of cold rolled Armco ingot iron were used. These were annealed at a temperature of 700°-800°F for a period of about 10 hr in a helium atmosphere. An additional annealing time up to 24 hr produced no further change in their torsional characteristics. These rods were 17-18 in. long. Circular grooves of carefully controlled depth were cut in the rods at 2 in. intervals with a 60° Vee threading tool. The tool angle is of no special importance, however, as long as the same tool is used to cut all the grooves in one size of specimen. In fact, for the largest diameter specimens used, a 120° angle tool was used.

The rods were then made the cathode in the 10% H_2SO_4 electrolyte and left in the bath for a time

VOI 7 195

sufficient to cause equilibrium in the concentration of hydrogen. This time was determined for a given diameter rod by leaving successive rods in the bath for increasing times until no further change in the rate of escape of the gas was observed after removal from the bath. The current through the bath was controlled so that the hydrogen concentration in the iron was not so high as to cause permanent embrittlement. The time needed for equilibrium varied from 18 to 48 hr depending on the current and on the diameter of the rods used. It was found that with a given current a sample which reached equilibrium in 36 hr could be left in the bath for a week without any further change in its subsequent behavior.

When saturation had been reached the rod was removed and cut into 2 in. lengths with the grooves at the middle of each piece. These could then be broken in a hand operated torsion tester at definite time intervals after removal from the bath. Thus the decrease in brittleness due to escape of hydrogen as a function of time and temperature could be determined. It was found that if the hydrogen concentration was such that the angle through which a sample could be twisted before fracture was close to one half of the angle for a gas free sample, no difficulty was encountered because of permanent embrittlement.

Samples prepared in the manner just described were placed at room temperature in

a. dry air d. air saturated with water vapor

b. helium e. water

c. hydrogen f. chromic acid cleaning solution

No difference in the time rate of decrease in brittleness could be detected among these various environments. One must, therefore, conclude that the rate of escape of the gas is not determined by surface conditions—with the exception of surface area.

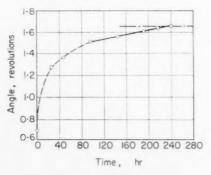


Fig. 1.

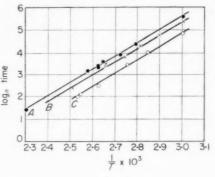


Fig. 2.

Samples saturated with hydrogen as described were placed in mineral oil at fixed temperatures. Fig. 1 gives a plot of the angle of break (measured in revolutions) vs. time for a set of samples kept at 60°C in mineral oil. The dashed horizontal line at the top of the curve gives the angle of break for an annealed specimen before impregnation with the gas. It is to be noted that the upper part of this curve is linear so that the time for complete de-embrittlement can be measured quite accurately. The shape of the dotted portion of the curve is determined in part by the time needed to establish a concentration gradient in the specimen. This time decreases rapidly with increasing temperatures.

Fig. 2 is a plot of the natural log of the time for complete de-embrittlement against the reciprocal of the absolute temperature in °K. The three curves are for specimens of three diameters: (A) 3/32, (B) 3/8, (C) 3/16 in.

These plots can be represented by an equation of the form:

$$t = A \exp(-H/kT)$$

where H may be called the heat of activation for de-embrittlement and is equal to 11,900 cal/mole. A will be a function of diameter of specimen and initial concentration of hydrogen.

Some difficulty was experienced at first at the higher temperatures because a concentration of hydrogen which would not cause permanent embrittlement at lower temperatures would do so at the higher ones. Thus it was found necessary to limit the hydrogen concentration to such a value that no permanent effect was produced when the specimens were suddenly raised to the high temperatures by placing them in the oil bath.

The most obvious explanation of this difference in time between charging and escape is that the hydrogen, moves through the metal as atoms (or protons) and recombines in the metal to form H₂ molecules which remain more or less fixed in position. In order for the gas to escape, the molecules must first be dissociated and the heat of activation mentioned earlier is determined by the heat of dissociation of H, molecules in the metal.

The linear nature of the upper portion of the curve in Fig. 1 can be explained as follows: Since the hydrogen atoms move through the iron rapidly, the diffusion rate may be determined not by the iron but by the probability of the atoms recombining to form molecules. In general one can write that,

$$J = D \cdot \partial c/\partial x$$

where J is the diffusion rate across a boundary, D is the diffusion coefficient and $\partial c/\partial x$ is the concentration gradient of atoms. If D is determined by the probability of recombination to form molecular hydrogen one can write,

$$D = \operatorname{const}/c$$
 or $J = (\operatorname{const}/c)(\partial c/\partial x)$

If one writes,

1959

$$c = f(t)\phi(x)$$

and substitutes this in the expression for J, $\phi(t)$ drops out and J becomes independent of time. The rate of escape would then be a constant.

The fact, as shown by Fig. 2, that the time required for complete de-embrittlement of a 3/16 in. diameter specimen is about one half of the time for a 3/32 in. specimen is of no significance since there is no assurance that the hydrogen concentration in the two sets of specimens of different diameters is the same. With a set of specimens of the same diameter, it is possible, through control of the current in the electrolyte bath and the purity of the bath, to prepare specimens with reasonable uniformity of concentration in successive rods. When the diameter of rods is changed, the hydrogen content would undoubtedly change. The important thing about Fig. 2 is that the lines have the same slopes and therefore show the same heat of activation; which is indicative of a mechanism of de-embrittlement. common to all three sizes.

This work was supported by a grant from the Wisconsin Alumni Research Foundation.

Department of Physics and H. B. WAHLIN Department of Mining and D. J. MACK Metallurgy The University of Wisconsin Madison 6

References

- 1. Bur. of Stand. Circ. No. 511, September, 1951.
- 2. P. Bastien, C.R. Acad. Sci., Paris 220, 883-885 (1945).
 - * Received May 14, 1959.

Plastically deformed steel in a weak magnetic field*

In the course of an experimental investigation of the effects of plastic deformation, in tension and in compression, on the magnetic induction of steel, some unexpected phenomena were noticed. As these are thought to be closely related to the occurrence of brittleness in this material, the results of the experiments are given here together with a brief discussion.

The conditions of the experiments were as follows: Test specimens with 38 mm gauge length and 10 mm in diameter were machined from St. 41 Siemens-Martin steel rods of 1 in. diameter which had been annealed for 2 hr at 900°C. The grain size of the material was ASTM 6, the texture uniform and no obvious preferential directions of the grains were observed. The composition of the material was:

N Cu AI Mn $0.16 \quad 0.003 \quad 0.14 \quad 0.010 \quad 0.031 \quad 0.19 \quad 0.014$ 0.55

in weight percentages.

The mechanical tests were carried out on a 35-ton Losenhausen machine of the hydraulic type. The load was determined by a pendulum pressure balance, and the testing velocity was manually regulated by means of a valve. In this manner the rate of strain was maintained at about $10^{-5} \, \text{sec}^{-1}$. The change in diameter of the tested specimen was measured continuously by means of a dial gauge clamped to it. From the readings the strains were calculated assuming that the volume of the deformed metal remained constant; one division on the dial was then equivalent to about $4/3 \times 0.01$ per cent strain. For the compression tests flanges were screwed on to the heads of the tested specimen before it was placed in the machine. The mechanical tests were interrupted at several points in order to determine the change in magnetic induction.

The magnetic experiments were carried out by placing the specimens in a solenoid, described elsewhere, (1) in which a magnetic field of approximately 0.15 oersted (maximum) oscillated with a frequency of 50 e/s. The output of a sensing coil around the middle of the specimen was fed to a valve voltmeter. The readings were accurate to approximately $+\frac{1}{2}$ per cent, some inaccuracy being caused by fluctuations in the feed current of the solenoid. The plastic deformation always caused a loss of magnetic induction, manifested by a lower reading of the voltmeter. The percentage losses of magnetic induction as given in Figs. 1a, 1b and 1c were calculated from the voltmeter readings. The only

Fig. 1. Strain and loss of magnetic induction of a steel specimen on cycling

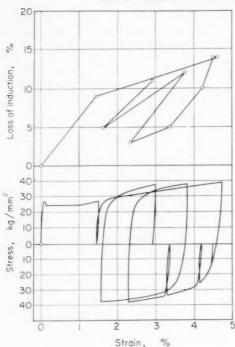


Fig. 1a: between fixed maximum stresses

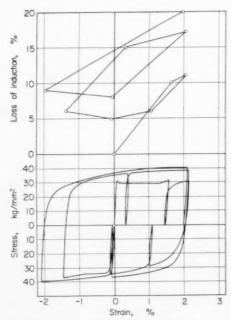


Fig. 1b: between increasing maximum stresses

correction introduced was one for variations in the field strength; the total inaccuracy of the losses is estimated to be ± 1 per cent.

Fig. 1a shows the result of a test in which the specimen was strained alternately to a maximum

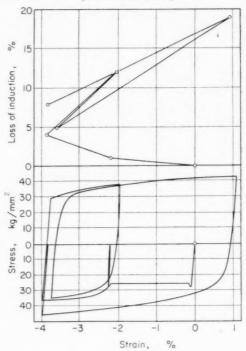


Fig. 1e: starting with compression

load of + or -2900 kg. The result of terminating each successive half-cycle on an increased absolute value of the load is shown in Fig. 1b. Test results of an experiment which commenced with compression are shown in Fig. 1c.

195

Some points of interest in the results of the magnetic tests are:

1. The effect of *tensile* deformation on the virgin material is much more severe than that of *compressive* deformation.

II. The effect of tensile deformation may be partly nullified by subsequent compressive deformation, but the opposite is not true.

III. Cycling a specimen between two limits of load causes the decrease of permeability to remain approximately constant for at least the first few cycles.

IV. Cycling a specimen between limits of load of ever increasing magnitude causes an increase of the loss of induction.

There may be a connection between the features observed and the formation of non-propagating micro-cracks, which phenomenon is known to occur during the early stages of the tensile test in this type of material (Low⁽²⁾, Wessel⁽³⁾, Owen *et al.*⁽⁴⁾). It is known that the magnetization at low field strength takes place by the movement of Bloch walls (Bloch⁽⁵⁾,



Fig. 2. Microcrack formed at 0°C 400 × magnification, negative $3 \times$ enlarged.

Becker⁽⁶⁾). Although a detailed model is lacking, it is conceivable that the micro-cracks created during tensile plastic deformation may act as obstacles to this movement, thus causing a falling-off of magnetic induction. If in addition we assume that a crack formed in tension may be partly closed during subsequent compression, the points enumerated above are seen to be compatible with this concept.

The difference in magnetic behaviour in tension and in compression correlates well with the known mechanical behaviour at temperatures below the ductile-brittle transition temperature in tension. Below that temperature iron breaks in tension without preceding plastic deformation, whereas in compression it shows the usual yield phenomena (Low(7)).

The finding that the decrease of permeability only increases with increasing stress is consistent with the idea of a Griffith crack being opened up. A stable Griffith crack requires more stress if it is to be opened up further (Cottrell⁽⁸⁾).

A few experiments were performed to check the ideas mentioned above. It was initially surmised that creation of vacancies might play the principal rôle in explaining the phenomena. Keeping plastically deformed specimens for 2 months at 120°C did not, however, introduce any change in the magnetic induction.

It was realized that in the literature no mention was thus far made of the occurrence of microcracks at temperatures higher than about -90°C. Fig. 2 is a microphotograph of a crack on the surface of an Armco ingot iron specimen that had been successively electropolished, annealed at 960°C and strained to 4% in tension at 0°C.

A small number of nickel specimens was tested in the same manner as the iron: no restorative effect of compression was noticed. A slight difference between the initial curves in compression and in tension was proved to be due to buckling, to which the nickel specimens were particularly susceptible.

Acknowledgments

The author is much indebted to Professor G. W. Rathenau for his stimulating interest. The composition of the material was determined by Mr. J. Kroonen and his staff of this laboratory. The able assistance of Mr. J. Raadsen, Mr. J. N. Helle and Mr. D. de Graag during the experiments was much appreciated.

A. W. SLEESWYK

Koninklijke Shell-Laboratorium

Amsterdam

(Shell International Research Maatschappij N.V.)

References

- 1. W. HEUKELOM, J. J. BROEDER, and L. L. VAN REIJEN, J. Chim. Phys. 51, 474 (1954).
- 2. J. R. Low, Symposium on Relation of Properties to Microstructure, p. 163. American Society for Metals, Cleveland
- E. T. Wessel, J. Metals 9, 930 (1957).
- 4. W. S. OWEN, B. L. AVERBACH and M. COHEN, Trans. Amer. Soc. Metals 50, 48 (1957)
- 5. F. Bloch, Z. Phys. **74**, 295 (1932). 6. R. Beckeb, Phys. Z. **33**, 905 (1932).
- 7. J. R. Low, IUTAM. Coll. Deformation and Flow of Solids, p. 60. Springer, Berlin (1956).
- 8. A. H. Cottrell, Trans. Amer. Inst. Min. (Metall.) Engrs. 212, 192 (1958).
 - * Received May 21, 1959.

Relation entre la ségrégation des impuretés et l'autodiffusion intergranulaire dans le fer*

Différentes études, théoriques ou expérimentales, ont suggéré que la structure perturbée des joints de grains pouvait déterminer la ségrégation intergranulaire des impuretés. Ainsi McLean et Northcott⁽¹⁾ ont émis l'hypothèse de ségrégations intergranulaires d'atomes de soluté, même aux températures supérieures à la température limite de solubilité. On sait d'autre part que la structure des joints dépend non seulement de l'orientation relative des cristaux contigus, mais aussi de l'orientation du joint par rapport aux réseaux des grains adjacents. En conséquence, plus la structure des joints est perturbée (joints séparant des cristaux de forte désorientation), et plus la tendance à la ségrégation des impuretés doit être prononcée.

Pour obtenir une preuve directe de cette hypothèse, nous avons comparé les phénomènes d'autodiffusion intergranulaire, à ceux de précipitation d'un soluté dissous à une teneur nettement inférieure à la limite de solubilité. Les techniques autoradiographiques

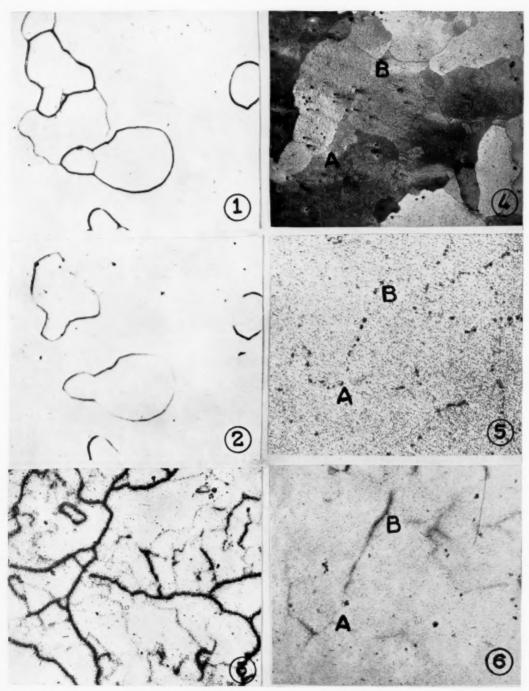


Fig. 1. Diffusion préférentielle de fer radioactif dans un échantillon de fer recuit à 700° C. Autoradiographie obtenue après abrasion de 10μ . G = 50 Fig. 2. Même plage après abrasion de 30μ . G = 50

Fig. 3. Autoradiographie montrant la diffusion préférentiello de ferradioactif dans les sous-joints de polygonisation d'un fer pur (recuit de 66 h à $700\,^{\circ}\text{C}$). G=50

Fig. 4. Micrographie d'une plage de fer contenant 0,005% de soufre radioactif. $\rm G=40$

Fig. 5. Ségrégation du soufre radioactif dans les joints de la même plage observée par autoradiographie. G=40 Fig. 6. Autodiffusion préférentielle du fer radioactif dans les joints de la même plage (recuit de 66 h à 700° C).

permettent seules par leur sensibilité d'aborder l'étude de phénomènes qui intéressent une épaisseur de métal nettement inférieure au pouvoir de résolution des autres techniques expérimentales.

Les autoradiographies (Figs. 1 et 2) montrent en effet l'autodiffusion préférentielle du fer radioactif (mélange de Fe⁵⁵ + Fe⁵⁹) dans les joints de grains d'un échantillon de fer inerte après un recuit de diffusion de 74 h à 700°C. Après dissolution du dépôt initial de fer radioactif, des autoradiographies effectuées à différents niveaux parallèles à l'interface montrent une différence de pénétration intergranulaire fonction à la fois de l'orientation des réseaux contigus et de l'orientation propre du joint. (2) Elle est très faible dans un joint de macle cohérent et très faible aussi dans les sous-joints de polygonisation comme le montre la Fig. 3. (3)

Dans une autre série d'expériences, on ajoute à un fer pur une teneur totale en soufre radioactif (0,005%) nettement inférieure à la limite de solubilité actuellement admise (0,02% à 900°C). Après recuit de 16 h à 750°C, puis de 32 h à 870°C et refroidissement lent jusqu'à 20°C, le soufre primitivement réparti uniformément dans la structure brute de coulée du métal se rassemble dans les joints. La comparaison de la structure micrographique (Fig. 4) et de l'autoradiographie de la même plage (Fig. 5) montre que le soufre ne s'est pas précipité uniformément dans tous les joints de grains.

1959

Lorsque la radioactivité du soufre est devenue indécelable, nous avons sur ce même échantillon déposé du fer radioactif et effectué un recuit de diffusion à basse température (66 h à 700°C) comparable à celui ayant donné les autoradiographies des Figs. 1 et 2. La Fig. 6 montre aussitôt qu'aux joints à plus forte ségrégation en soufre correspondent précisément les joints où l'autodiffusion intergranulaire est la plus

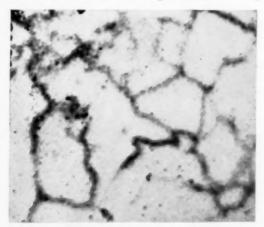


Fig. 7. Autodiffusion préférentielle dans les joints γ d'un fer recuit 100 h à 1000°C. $\rm G=75$

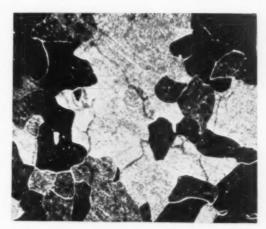


Fig. 8. Même plage, attaquée avec une solution d'acide métanitrobenzène-sulfonique dans l'éthanol. Les traces noires correspondent aux anciens joints. G = 75

prononcée, c'est à dire les joints de grains de plus forte désorientation.

Nous avons enfin étendu ces observations au cas des joints v du fer. Dans la partie inférieure du domaine y, il y a aussi autodiffusion intergranulaire. (4) Après recuit de 100 h à 1000°C effectué sur du fer pur recouvert d'un dépôt de fer radioactif, l'autoradiographie montre la diffusion préférentielle du fer radioactif dans les joints y (Fig. 7). La même plage repolie et attaquée avec un réactif chimique sensible aux traces d'impuretés (solution d'acide métanitrobenzène sulfonique dans l'alcool éthylique) révèle que la réseau des impuretés est surtout localisé dans les joints de grains y où l'autodiffusion a été préférentielle⁽⁵⁾ (Fig. 8). Par contre, les contours de macles qui sont fréquents dans l'austénite n'apparaissent ni sur l'image autoradiographique, ni sur l'image micrographique.

En conclusion, ces expériences apportent une preuve directe de l'influence des paramètres définissant l'orientation des joints et des cristaux contigus sur l'autodiffusion et la ségrégation des impuretés dans les joints de grains. Aux joints de plus forte désorientation en phase α comme en phase γ correspondent les plus fortes concentrations d'impuretés ségrégées.

Centre de Recherches Métallurgiques de l'Ecole des Mines de Paris

- P. COULOMB
- C. LEYMONIE
- P. LACOMBE

Bibliographie

- D. McLean et L. Northcott, J. Inst. Metals 72, 583 (1946).
- 2. C. LEYMONIE et P. LACOMBE, Rev. Mét. 54, 653 (1957).
- P. COULOMB, C. LEYMONIE et P. LACOMBE, C. R. Acad. Sci., Paris 246, 1209 (1958).

VOI 7 19

- S. Z. Bokstein, S. T. Kiskhin et L. M. Moroz, Conférence Internationale sur les Radioisotopes U.N.E.S.C.O. Paris (1957) Mémoire RIC/193.
- 5. P. COULOMB et P. LACOMBE, Rev. Mét. 55, 918 (1958).
 - * Received May 5, 1959.

Cracks due to the piling-up of dislocations on two intersecting slip planes in MgO crystals*

In MgO crystals, two types of crack have been reported. (1,2) One was associated with the Stroh mechanism, (1) and the other with the Cottrell mechanism. (2) The purpose of this communication is to report the observation of a new type of crack in MgO and LiF crystals and to propose a mechanism for the initiation of such a crack.

In 1958 Cottrell⁽³⁾ suggested a mechanism for the nucleation of cleavage cracks on (100) planes in b.c.c. structures due to the coalescence of dislocations on two intersecting slip planes. This type of crack was observed in MgO by Washburn $et\ al.^{(2)}$ in tension tests. The dislocation reaction involved in this process in a structure like MgO is shown schematically in Fig. 1 and can be represented by the following vector equation:

$$\frac{1}{2}a[0\overline{1}1] + \frac{1}{2}a[0\overline{1}\overline{1}] = a[0\overline{1}0]$$
 (1)

However, in contrast with the case of the b.c.c. structure considered by Cottrell, there is no change of elastic energy in the above reaction.

Nevertheless, it can be shown that in crystals like MgO, a different type of dislocation reaction is more favorable than reaction (1) above. If this reaction operates, it will lead to a crack on the slip plane (110) instead of the usual cleavage plane. It is to be noticed that this type of crack is different from that which Stokes *et al.*⁽¹⁾ observed in compression tests, where a piling up of dislocations against a kink band is involved.

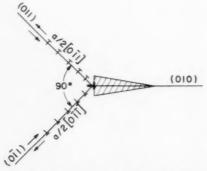


Fig. 1. Crack formation on (010) cleavage plane in MgO crystals.

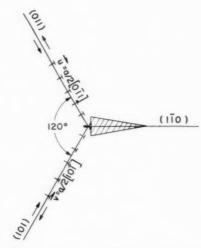


Fig. 2. Crack formation on (110) plane in MgO crystals.

In Fig. 2, two slip planes (011) and (101) intersect along the (111) axis and make an angle of 120° with each other. If we consider a dislocation loop with a slip vector $\mathbf{u}(\mathbf{u} = \frac{1}{2}a[011])$ on the (011) plane and another loop with vector $\mathbf{v}(\mathbf{v} = \frac{1}{2}a[101])$ on the (101) plane, then the sections $\mathbf{O_1P_1}$ and $\mathbf{O_2P_2}$ parallel to the line of intersection combine together and form a new dislocation OP with a Burger's vector $\mathbf{r} = \frac{1}{2}a[110]$. This dislocation reaction can be written as $\mathbf{u} + \mathbf{v} = \mathbf{r}$, or

$$\frac{1}{2}a[0\overline{1}1] + \frac{1}{2}a[10\overline{1}] = \frac{1}{2}a[1\overline{1}0] \tag{2}$$

It is to be noticed that in so combining the two dislocations, half the elastic energy is released. Therefore, this reaction is more favorable than reaction (1). This reaction can probably be better understood by considering the edge and screw components of the individual dislocations:

$$\frac{1}{2}a[0\bar{1}1] = \frac{a}{6}[2\bar{1}1] + \frac{a}{3}[\bar{1}\bar{1}1]$$
 (3)

$$\frac{1}{2}a[10\overline{1}] = \frac{a}{6}[1\overline{2}\overline{1}] + \frac{a}{3}[11\overline{1}] \tag{4}$$

The first term in each reaction is the edge component, and the second term the screw component. As shown in Fig. 3, the two screw components cancel each other and the edge components combine together. This may be represented by the following two equations:

$$\frac{a}{6}[2\overline{1}1] + \frac{a}{6}[1\overline{2}\overline{1}] = \frac{1}{2}a[1\overline{1}0] \tag{5}$$

$$\frac{a}{3}[\Pi 1] + \frac{a}{3}[11\overline{1}] = 0 \tag{6}$$

Therefore the elastic energy due to the coalescence of

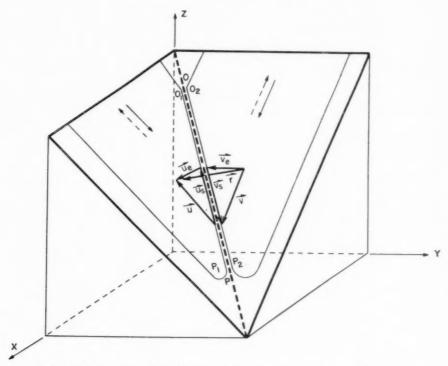


Fig. 3. Interaction of dislocations on two {110} intersecting slip planes.

the screw components is released. The resultant dislocation line OP has a vector $\frac{1}{2}a[1\overline{1}0]$ and lies on the plane (112). It is immobile because of the higher Peierls–Nabarro force as compared to that in the (110) planes. Therefore, the dislocations generated on the two intersecting slip planes (011) and (101) will

1959

Fig. 4. Slip lines and cracks around a microhardness indentation on the (001) cleavage surface of a MgO crystal.

pile up against this immobile dislocation and initiate a crack in the plane $(1\overline{10})$ as shown in Fig. 2.

This type of crack was indeed observed in MgO crystals when micro-hardness indentations were made on two different crystallographic planes. Fig. 4 shows the slip lines and cracks around a microhardness indentation on a (001) cleavage surface. The slip lines are on the (011) and (101) planes, making an angle of 45° with the cleavage plane. The intersections of the cracks with the surface are in the [110] directions. The fact that these cracks do lie in the (110) planes was confirmed by chemically polishing down the surface and examining the cracks underneath. Cracks of the same type were observed in LiF crystals when the indentation was made at a sub-zero temperature.

Fig. 5 shows the slip lines and cracks around an indentation on a chemically polished (110) surface of a MgO crystal. The two cracks, as shown by the black lines in the middle, are parallel to the [001] direction. Subsequent examination of the surfaces underneath indicates that they lie on the (1 $\overline{10}$) plane. This again is in accord with our proposed mechanism of crack formation. The two sets of intersecting slip planes, (011) with (101) and (0 $\overline{11}$) with ($\overline{101}$), upon which the dislocations pile up against their common axes and form cracks, are revealed by the slip lines in Fig. 5.

The authors are grateful to Professor E. R. Parker

Fig. 5. Slip lines and cracks around a microhardness indentation on the (110) surface of a MgO crystal.

for the opportunity to discuss the results of this work with him.

Edgar C. Bain Laboratory for
Fundamental Research, United
States Steel Corporation Research
Center, Monroeville, Pennsylvania

References

- R. J. STOKES, T. L. JOHNSTON and C. H. LI, Phil. Mag. 3, 718 (1958).
- J. WASHBURN, A. E. GORUM and E. R. PARKER, Trans. Amer. Inst. Min. (Metall.) Engrs. 215, 230 (1959).
- A. H. COTTRELL, Trans. Amer. Inst. Min. (Metall.) Engrs. 212, 192 (1958).
- * Received May 28, 1959.

On the mechanism of sulphurization of copper*

The sulphurization of copper in liquid sulphur at $350^{\circ}-444^{\circ}\mathrm{C}$ occurs in accordance with a parabolic law; from this it must be concluded that the scale layer formed on the surface of the metal is compact and that the diffusion of one or both reagents through the scale layer is the slowest step which determines the rate of sulphurization. (1) Using radioactive sulphur as tracer (S³⁵) the authors have demonstrated that under the conditions used the formation of the sulphide scale on copper proceeds exclusively by outward diffusion of the metal. (2)

Since the sulphide scale on copper consists of two distinct layers it must be assumed that the mechanism of formation of these layers is different. The outer layer which forms the main part of the scale is compact, while the inner one is porous and fine-crystalline and can be easily separated (mechanically) from the outer scale layer. The formation of a two-layer scale in this case cannot be explained by

the theory of Wagner.⁽³⁾ In order to obtain further information about the mechanism of this process the kinetics of growth of both sulphide scale layers was investigated.

Metal sheets $4 \times 3 \times 0.5$ cm were sulphurized in liquid sulphur at 444°C varying the time of the experiments from 3 to 60 min. After having separated the scale layer from the metal sheet, parts of scale formed on principal surfaces were cut out. Scale fragments formed at corners could not be investigated because of the decrease of reaction rate there (related to the boundary effect. (4.5) The surface area of scale was graphically integrated and the mass corresponding to the area unit ΔW was calculated. After having separated the porous inner layer its corresponding mass $\Delta W^{(i)}$ was determined. These investigations were carried out in the case of scales formed on both surfaces of the sulphurized preparations. The relative error of the measurements was approximately +5 per cent. It has been stated that after short sulphurization times (which did not exceed 10 min) there was practically no difference between the values of ΔW and $\Delta W^{(i)}$ determined for both surfaces of a given specimen. For longer sulphurization times (exceeding 15 min) the difference amounted sometimes to 20 per cent. The investigations have demonstrated that the scale formation process occurs in accordance with the parabolic law

$$(\Delta W)^2 = kt \tag{1}$$

where k = the parabolic rate constant,

t =time of sulphurization.

This result agrees well with previous investigations carried out by the authors by another method. (1) The relation between $(\Delta W)^2$ and t is shown in Fig. 1 as a straight line.

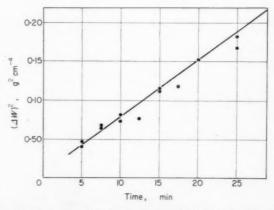


Fig. 1. Sulphurization of copper in liquid sulphur at $444\,^{\circ}\mathrm{C}.$ Parabolic plot.

VOI 7 195

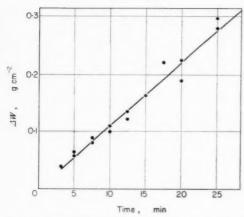


Fig. 2. Formation of inner scale layer at 444 $^{\circ}\mathrm{C}.$ Linear plot.

The growth of the inner layer can however be described by the following linear equation:

$$\Delta W^{(i)} = k^{(i)}t \tag{2}$$

where the index "i" refers to the inner layer.

The plot of the rate of formation of the inner scale layer is shown in Fig. 2.

The ratio $\Delta W^{(i)}/\Delta W$ is therefore not constant but increases with increasing time of experiment and can be described by the following equation

$$\Delta W^{(i)}/\Delta W = (k^{(i)}/\sqrt{k})\sqrt{t} \tag{3}$$

The linear rate of inner sulphide scale layer formation shows that the rate of growth of this layer is determined not by diffusion, but by the chemical reaction occurring at the phase boundary. (6) The process of sulphurization proceeds as a result of the outward diffusion of copper; as a consequence a crack is formed between the metal surface and the growing scale layer. The pressure of sulphur vapour in this space is equal to the dissociation pressure of Cu2-yS. In the case of equilibrium between copper and p-semiconducting cuprous sulphide, (7) the metal deficit, and therefore the dissociation pressure, has the minimum value. This means that on the metal surface the cuprous sulphide can be formed as a product of the reaction occurring between gaseous sulphur and metal

$$(2-x)\operatorname{Cu} + \frac{1}{2}\operatorname{S}_{2}^{(q)} \rightleftharpoons \operatorname{Cu}_{2-x}\operatorname{S} \tag{4}$$

where x < y.

The consumption of sulphur caused by reaction (4) is compensated by the process of decomposition of the cuprous sulphide of the compact outer layer.

According to Rees⁽⁸⁾ this process can be described by the following equation:

$$Cu_{2-y}S \rightleftharpoons (2-2y)Cu^{+1} + yCu^{+2} + 2e^{-1} + \frac{1}{2}S_2^{(q)}$$
 (5)

Cu²⁺ denotes an electron "hole". Copper ions and free electrons formed in the decomposition process diffuse via cation vacancies and electron holes in the direction of the scale surface, where they combine with sulphur. The decomposition process described by equation (5) appears to be the slowest process which determines rate of formation of the inner layer.

Special appreciation is due to Prof. dr. L. Czerski for his help and suggestions.

S. MROWEC T. WERBER

Department of General and Coal Chemistry

School of Mining and Metallurgy

Krakow, Poland

References

- L. CZERSKI, S. MROWEC and T. WERBER, Roczn. Chem. 33, (1959) In press.
- J. Mikulski, S. Mrowec, I. Stronski and T. Werber, Roczn. Chem. 33, (1959) In press.
- C. Wagner, Z. phys. Chem. 21, 25 1933; Ibid. 32, 447 (1936).
- L. CZERSKI and S. PATZAU, Archiw. Górn.-Hutn. Pol. Akad. Nauk. 2, 353 (1954).
- 5. H. ENGELL, Acta Met. 5, 695 (1957).
- K. Hauffe, Oxydation von Metallen und Metallegierungen. Springer, Berlin (1956).
- 7. E. HIRAHARA, J. Phys. Soc. Japan 6, 422 (1951).
- A. Rees, Chemistry of the Defect Solid State. Methuen London (1954).
- * Received May 12, 1959.

Ätzverfahren für Versetzungen in Fe-Ni-Legierungen*

Eine Sichtbarmachung von Versetzungen ist bisher gelungen bei Siliziumeisen (Trafoblech) durch die von Morris⁽¹⁾ entwickelte elektrolytische Ätzung,⁽²⁾ bei Eisen und bei Nickel durch chemische Ätzung^(3,4) und bei Fe-Ni-Legierungen durch thermische Ätzung.⁽⁵⁾ Unseres Wissens ist dagegen in der Literatur noch nicht über elektrolytische oder chemische Ätzung von Versetzungen in Fe-Ni-Legierungen (insbesondere mit 50% Fe, 50% Ni) berichtet worden. Im folgenden werden solche Ätzverfahren mitgeteilt, die Versetzungen in 50/50 Fe-Ni-Legierungen mit verschiedenem Rekristallisationszustand† an 0,1 bzw. 0,15 mm dicken Blechen sichtbar machen.

Kleinwinkelkorngrenzen allein-ohne Subgrenzen

VOL. 7 1959

 $[\]dagger$ Hyperm 50T und 50A der Friedr. Krupp Widia-Fabrik, Essen.

und regellos verteilte Versetzungen—konnten wir mit einem Ni-Polierbad der Zusammensetzung 33% $\rm H_2SO_4$, 33% $\rm Glyzerin$, 34% $\rm H_2O^{(6)}$ im Jenaer Poliermikroskop⁽⁷⁾ elektrolytisch ätzen auf Flächen, die vorher mit dem Elektrolyten A2† in dem handelsüblichen Poliergerät Disa-Electropol $^+$ oder mit Chromsäure–Eisessig nach Morris elektrolytisch poliert worden waren. Proben mit Würfeltextur liessen sich mit diesem Elektrolyten auch polieren.

Kleinwinkelkorngrenzen und Versetzungen in Gleitlinien sowie in einzelnen Fällen in Subgrenzen liessen sich in 50/50 Fe-Ni bei Vorhandensein von Würfeltextur und in sekundär rekristallisiertem Zustand in einer galvanischen Zelle ohne fremde Spannungsquelle ätzen, wobei die mit A2 oder besser mit Chromsäure-Eisessig elektrolytisch polierte Probe nach Auflösung der passivierenden Deckschicht die Anode (also "Minuspol" des galvanischen Elements), V2A-Blech die Kathode bildete und das Element mit einem Spannungsmesser belastet wurde. Der Elektrolyt bestand aus einer Mischung von gebrauchter A2-Lösung und Chromsäure-Eisessig. Mit der A2-Lösung waren vorher zahlreiche Fe-Ni- und Fe-Cu-Legierungen in der üblichen Weise elektrolytisch poliert worden; Chromsäure-Eisessig wurde solange zugesetzt, bis die Lösung auch bei längerer Einwirkung nicht zu einer Kornflächenätzung führte (Mischungsverhältnis 20: 1 bis 5:1. Vorsicht! Chromsäure-Eisessig ist sehr langsam in A2-Lösung einzutropfen, nicht umgekehrt, da A2 Perchlorsäure enthält). Das offene Element hatte eine EMK von 0.3-0.4 V. Bei Belastung mit einem Voltmeter von 3 kΩ Innenwiderstand sank die Spannung auf einen stationären Endwert ab, der von der eintauchenden Fläche des V2A-Blechs abhing. Gute Ergebnisse liessen sich mit 0.05-0.15 V und Stromdichten unter 0.1 mA/cm² bei etwa 2 Std. Ätzzeit erzielen. Ob die Mitwirkung des Stromdurchgangs für den Erfolg notwendig ist oder auch schon chemisches Ätzen mit A2-Lösung, die durch anodische Auflösung von 50/50 Fe-Ni-Material mit Nickel- und Eisen-Ionen angereichert ist, allein zum Ziel führt, wird noch geprüft.

Ähnliche Ergebnisse brachte die Verwendung des oben erwähnten Nickel-Polierbades⁽⁶⁾ als Elektrolyten in der galvanischen Zelle, allerdings hier erst nach mehr als 6 Std. Ätzzeit. Besonders kontrastreiche Ätzungen von Kleinwinkelkorngrenzen, Subgrenzen und regellos verteilten Versetzungen erhält man bei Würfeltextur.

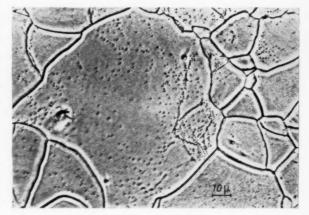


Abb. 1. Versetzungen in einer Fe-Ni-Legierung (50/50) mit Würfeltextur, Mikroskop Ortholux, E. Leitz, Wetzlar. Auflicht-Phasenkontrast.

wenn man nach der erwähnten Politur mit der A2-Lösung im Disa-Electropol die Proben zunächst bei 800° bis 1035°C im gereinigten $\rm H_2$ eine Std. lang glüht. Dabei tritt eine Glättung der Kornflächen und eine leichte thermische Ätzung von Kleinwinkelkorngrenzen auf. Anschliessend wurde wie oben in einer galvanischen Zelle geätzt. Auf den so behandelten Proben des Texturmaterials wurden Versetzungsdichten von etwa $10^7~\rm cm^{-2}$ ausgezählt (Abb. 1). Für primär rekristallisiertes Siliziumeisen sind Versetzungsdichten bei rund $2\cdot10^7~\rm cm^{-2}$ bekannt. (8)

195

Bei Fe-Ni-Material, das nach Sekundärrekristallisation \dagger mit A2 im Disa-Electropol oder mit Chromsäure-Eisessig elektrolytisch poliert worden war, brachte eine Glühung bei 990°C in gereinigtem H_2 eine starke thermische Ätzung von Korngrenzen,

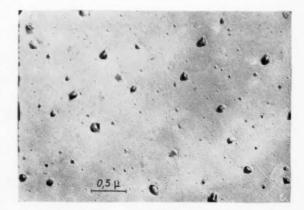


Abb. 2. Versetzungen in einer Fe-Ni-Legierung (50/50) nach Sekundärrekristallisation. Gleitlinien durch plastische Deformation nach Glühen entstanden. Siemens-Elektronenmikroskop (Elmiskop I), Acetobutyratfolie Triafol BW, Schrägbedampfung mit SiO.

 $[\]dagger$ Ein Elektrolyt, der von P. F. Dujardin u. Co., Düsseldorf, geliefert wird.

[‡] Gebaut nach Knuth-Winterfeldt von H. Struers, Kopenhagen.

[†] Hyperm 50A der Friedr. Krupp Widia-Fabrik, Essen.

regellos verteilten Versetzungen sowie von Versetzungen in Gleitlinien. Da die feineren Einzelheiten der lichtmikroskopischen Aufnahmen im Druck verlorengehen, wird hierzu nur ein elektronenmikroskopisches Bild (Abb. 2) wiedergegeben, das eine Stelle mit etwa 2·108 cm⁻² Versetzungsdichte zeigt.

Der Friedr. Krupp Widia-Fabrik, Essen, sind wir zu Dank verpflichtet für die Überlassung der untersuchten Legierungen. Die vorliegende Kurzmitteilung ist ein Teilbericht aus einer noch nicht abgeschlossenen Promotionsarbeit über den Einfluss von Versetzungen auf magnetische Eigenschaften.

W. D. HANNIBAL

Institut für Werkstoffe der Elektrotechnik der Technischen Hochschule Aachen

Literatur

1. C. E. Morris, Metal Progress 56, 696 (1949).

vgl. C. G. Dunn and F. W. Daniels, Trans. Amer. Inst. Min. (Metall.) Engrs. 191, 147 (1951).
 C. G. Dunn and W. R. Hibbard, Acta Met. 4, 306

(1956)

J. C. Suits and J. R. Low Jr., Acta Met. 5, 285 (1957). C. G. Dunn and E. F. Koch, Acta Met. 5, 548 (1957)

3. für Fe vgl. F. W. C. Boswell, Metal Progress 72, (6), 92

4. für Ni vgl. P. Feltham, J. Inst. Met. 86, 237 (1958).

5. H. Suzuki, The thermal etching of dislocations, p. 172 in: Dislocations and Mechanical Properties of Crystals (Eds. J. C. FISHER, W. G. JOHNSTON, R. THOMSON and T. VREELAND, Jr.). Wiley, New York (1957).

6. vgl. W. Machu and A. Ragheb, Z. Metallk. 47, 176 (1956).

R. Zetzsche, Klepzig Fachberichte, Heft 7, S.260 (1957).
 C. G. Dunn and E. F. Koch Acta Met. 5, 548 (1957).

* Received April 1, 1959.

VOL.

1959

Discussion of "Orientation of recrystallized grains in strained aluminum single crystals"(1)*

Yoshida et al.(1) have presented orientation relationships between artificially nucleated grains and the strained aluminum single crystals into which they grew. A preferred orientation relationship consisting of 40° rotations about certain common [111] axes was found, and was interpreted as evidence for the oriented growth theory(2) of recrystallization textures. This interpretation is valid only if recrystallization nuclei in a random distribution of orientations were present in the artificially nucleated region. If there is a texture in such a region, the observed preferred orientation relationship could be the result of oriented nucleation⁽³⁾ as well as oriented growth.

Yoshida et al. presented a Debye-Scherrer photograph of the artificially nucleated region of one of their crystals as evidence for the absence of a preferred orientation of nuclei (their figure 7). However, the

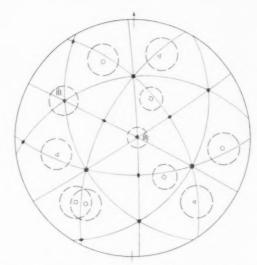


Fig. I. Stereographic projection of Yoshida, Liebmann, and Lücke's crystal B; dotted circles indicate the distribution of {111} poles of the recrystallized grains. Solid symbols, orientation of crystal B.

o ideal orientations of (111) poles after clockwise rotation of 40° about [111].

△ ideal orientations of {111} poles after counter-clockwise rotation of 40° about [111].

ideal orientations of {111} poles after counter-clockwise rotation of 40° about [111].

wire sample was rotated about its axis during the X-ray exposure, presumably to increase the number of diffracting crystals. We wish to point out that this rotation introduces a randomness into the Debye-Scherrer rings, which could have concealed the presence of a texture.

To illustrate this point we assume that the only nuclei which were present in the artificially nucleated region had the same orientations as those grains which grew out of this region. These orientations are indicated by Yoshida et al. in their figure 5. This figure has been redrawn in our Fig. 1 so that the tensile axis of the strained single crystal is vertical: we used the orientation of specimen B, since we deduced that the original Debye-Scherrer photograph was taken with that specimen. The locations of the {111} poles after the ideal 40° [111] rotations are indicated by the same symbols used in the original figure, and the regions of high pole density are approximated by circles of 10° radius.

Rotating the wire about its axis during the X-ray exposure corresponds to rotating Fig. 1 about its vertical axis. The {111} Debye-Scherrer ring which would result from such an exposure can be deduced by noting the points at which the circles of Fig. 1 intersect the {111} reflection circle as the wire is rotated about its vertical axis. Such a constructed

Fig. 2. Constructed {111} Debye-Scherrer ring (CuKα radiation) for the texture of Fig. 1. Wire sample rotated about vertical axis during X-ray exposure.

ring (for CuK_{α} radiation) is shown in Fig. 2. It is apparent that the ring is continuous, even though the original texture was assumed to be quite sharp.

We conclude that rotation of the specimen during the X-ray exposure would have obscured the presence of a texture in the artificially nucleated region of the crystal examined by Yoshida et al. and that the operation of a growth-selection mechanism has consequently not been established in this case.

This conclusion is strengthened by some similar experiments of our own(4) in which artificially nucleated grains were grown into aluminum single crystal strips. A qualitative pole figure obtained from the artificially nucleated region indicated the presence of a texture. It appears that the usual methods of producing artificial nucleation do not give a random distribution of nucleus orientations, and so do not meet the conditions for proving the presence of growth selection.

Institute for the Study of Metals C. S. BARRETT University of Chicago, Ill.

General Electric Research C. D. GRAHAM, JR. Laboratory J. M. LOMMEL

Schenectady, N.Y.

References

- 1. H. YOSHIDA, B. LIEBMANN and K. LÜCKE, Acta Met. 7. 51 (1959).
- P. A. Beck, Acta Met. 1, 230 (1953).
 W. G. Burgers and T. J. Tiedema, Acta Met. 1, 234 (1953). 4. J. M. LOMMEL and C. D. GRAHAM, JR., unpublished work.
 - * Received May 21, 1959.

Twinning in copper electrodeposits*

Recently Orem⁽¹⁾ has found that copper deposits formed from acidified cupric sulphate solution on (111) and (100) single crystal copper substrates occasionally develop by epitaxial twinning. I should like to report briefly some results of similar work.

Deposits on the (111) face, from normal acid copper sulphate solutions at 25°C, are extensions of the base at c.d's below 15 mA/cm2, but at c.d's above this (up to 60 mA/cm²: the maximum studied) the deposit contains material in the twin orientation. The twins form parallel to the {111} plane in the surface. The surface structures are flat and featureless at low c.d's (below 5 mA/cm²) except at regions where developing "platelets" (presumably extending parallel to the surface) have merged. At higher c.d's (e.g. 10-60 mA/cm²) the surface consists of pyramids, which, above 15 mA/cm², develop flat upper surfaces and terraced sides. The deposit above about 40 mA/cm² also contains fine-grained polycrystalline material.

On the (100) face twinning occurs much less readily. and only appears at c.d's above approximately 25 mA/cm². Once growth proceeds in a twin orientation, the deposit tends to become polycrystalline. It is possible, though not yet confirmed, that the development of polycrystallinity is initiated by twinning; successive growth in twin orientation, on many {111} planes giving rise to the polycrystalline deposit.

VOI

195

Similar results are obtained for (111) and (100) surfaces from perchlorate solutions (N:Cu(ClO₄)₉ + N:HClO4 at 35°C), though the current density at which twinning is first observed (on the (111) surface in particular) is different. However, preliminary results indicate that it occurs at a similar cathodic over-potential. This is in accord with the view that cathode polarisation and crystal structure are related.

As in the work of Orem, no twins have been found in (110) deposits. However, only c.d's up to 15 mA/cm², at 25°C, and only acidified sulphate solutions, have been investigated in this case. Deposits on this surface, at both 10 and 15 mA/cm², form in long ridges, aligned in the [110] direction, and with {111} sides, as was found by Pick et al.(2)

Joseph Lucas Laboratory S. C. BARNES Department of Industrial Metallurgy The University Edgbaston, Birmingham 15

References

- 1. T. H. OREM, J. Res. Nat. Bur. Standards 60, 597 (1958). H. J. Pick, G. G. Storey, and T. B. Vaughan. Communicated at (Physical Society) Conference on "Interfacial Held at Cambridge Dec. 1958. To be Phenomena". published elsewhere.
 - * Received May 18, 1959.

THE DIFFUSION OF XENON IN SILVER*

J. M. TOBIN+

Diffusion coefficients for xenon in silver have been determined at temperatures of 500° , 600° , 700° , 735° and 800° C. The activation energy for diffusion is 37.5 kcal/g, atom. The diffusion coefficients can be represented by the equation:

 $D_{\rm Xe} = 0.036 \exp{(-37,500/RT)} \, {\rm cm^2/sec}.$

The diffusion of xenon in silver is attributed to the mobility of *positive* xenon ions from substitutional sites in the lattice to vacant adjacent sites.

LA DIFFUSION DU XENON DANS L'ARGENT

Les coefficients de diffusion du xénon dans l'argent ont été déterminés aux températures de 500° , 600° , 700° , 735° et 800° C. L'énergie d'activation pour la diffusion est 37.5 kçal/atom. Les coefficients de diffusion peuvent être représentés par l'équation:

 $D_{Xe} = 0.036 \text{ exp.} (-37,500/RT) \text{ cm}^2/\text{sec.}$

La diffusion du xénon dans l'árgent est attribuée au déplacement des ions positifs du xénon des sites de substitution vers des sites vacants voisins dans le réseau.

DIE DIFFUSION VON XENON IN SILBER

Die Diffusionskoeffizienten von Xenon in Silber wurden bei 500°, 600°, 700°, 735° und 800°C bestimmt. Die Aktivierungsenergie der Diffusion beträgt 37,5 kcal/Atom. Die Diffusionskoeffizienten können durch die Gleichung $D_{\rm Xe}=0.036~{\rm exp}(-37.500/RT){\rm cm}^2/{\rm sec}$ dargestellt werden.

Die Diffusion von Xenon in Silber wird der Beweglichkeit positiver Xenonionen von substitutionellen Gitterplätzen zu benachbarten leeren Plätzen zugeschrieben.

INTRODUCTION

Normally, the inert gases are insoluble in metals and will not diffuse through them, even at high temperatures and pressures. (1,2,3) Le Claire and Rowe. however, found that argon atoms are quite mobile and will diffuse through silver if the gas is introduced into the metal by an energetic process such as gaseous discharge in a hollow cathode. (4) Two sheets of silver were cold-welded to form a sandwich, with the argonladen faces on the inside. The sandwich was irradiated in a nuclear reactor to form radio-argon. Subsequent heating of the silver caused the radio-argon to diffuse out of the sandwich. The rate of diffusion was followed by counting the gamma activity of the gas which was collected from the sandwich. The diffusion coefficients obtained by LeClaire and Rowe for argon in silver are given by the equation:

 $D_{\rm A} = 0.12 \exp{(-33,600/RT)} \, {\rm cm^2/sec}.$

The diffusion of krypton in silver, under conditions similar to those used by LeClaire and Rowe, has been investigated in this laboratory. (5) The diffusion coefficients may be represented by the equation:

$$D_{\rm Kr} = 1.05 \exp{(-35,000/RT)} \, {\rm cm^2/sec}.$$

A considerable amount of data has been accumulated on the mobility of various other impurity atoms in pure silver. The diffusion coefficients for cadmium, indium, $\sin^{(6)}$ and antimony⁽⁷⁾ have been reported. These elements are immediately to the right of silver in the periodic table, in period V. The basic electronic structure common to each of these elements is the silver ion core, Ag^+ . It is known as a pseudo-inert gas configuration.

A theoretical interpretation of the repulsive potential around impurity atoms in silver has been made by Lazarus. (8) It is successful in confirming the experimentally measured mobility of the four elements to the right of silver in the periodic table. Since xenon is also in period V, it will be possible to use the Lazarus theory to determine the approximate ionic state of the inert gas xenon as it diffuses in silver. The mobility of the xenon in silver is a partial measure of the electrostatic forces between the inert gas atom and the neighboring metal ions.

^{*} Work performed under Contract No. W-31-109-Eng-52 between the Atomic Energy Commission and General Electric Company. Received November 14, 1958.

[†] Fuels Development, Reactor and Fuels Research and Development Operation, Hanford Atomic Products Operation, Richland, Washington. Now at the John Jay Hopkin's Laboratory of General Atomic Division, General Dynamics Corporation, San Diego, California.

The activation energies for diffusion of the inert gases as well as other impurities in silver show a very regular relationship to the "excess valence", as suggested by Lazarus⁽⁸⁾. The relationship is not linear, though, and depends upon the chemical period of the solute atom. Impurity atoms from periods IV and VI are found to have lower activation energies than period V elements having the same "excess valence".

Alternative models for the diffusion mechanism of xenon in silver are presented in which the xenon atom is either electrically neutral as it is in gas form, or ionized with a positive charge. On the basis of comparison of the mobility of each model, it is concluded that the xenon diffuses as a positive ion. Some independent supporting evidence is cited.

EXPERIMENTAL

Silver sheet of high purity (99.99% Ag) was rolled and annealed several times to produce grain coarsening and reduce the grain boundary area of the metal. The thickness was reduced 10 per cent per pass through the rolls. Grain growth occurred during heating at 770°C. The grain size became stable after four to five treatments and was equal to the thickness of the sheet, 0.010 in. Subsequent rolling to 50 per cent reduction and annealing did not noticeably refine the grain size.

Xenon was introduced into the silver by means of a hollow cathode discharge. The silver sheet was rolled into a hollow cylindrical cathode about ½ in. diameter by 2 in. long, and placed in a glow discharge tube containing xenon gas at 1.5–2 mm pressure. A discharge was started at 200 V d.c. and maintained at 450 V for about 2 hr at a current of 30 mA. Two sections of the silver sheets were cut and rolled together with their xenon-laden faces adjacent to form a sandwich.

During subsequent annealing of the sandwich the xenon diffused out of the center of the sandwich into the evacuated furnace tube. Samples of the gas were taken in aliquot portions and transferred to 5 ml quartz ampules. These were irradiated in a reactor to produce xenon-125. The amount of xenon in the sample was determined by the gamma activity of the gas and identified by means of the gamma energy and radioactive half-life.

A detailed description of the techniques and apparatus is given in a previous article⁽⁵⁾ in which the diffusion coefficients of krypton in silver are reported.

The measurements of the gamma activity of the irradiated xenon gas were used to determine the fraction, γ , of xenon which diffused out of the metal in time t.

Results

LeClaire and Rowe⁽⁴⁾ analyzed Fiek's law of diffusion for the diffusion coefficient, D, using the boundary conditions existing in the silver sandwich. They obtained the following relationship between γ and t:

$$\gamma = 1 - \frac{4}{\pi} \sum_{s=1}^{\infty} \frac{(-1)^{s+1}}{2s-1} \exp\left[-(2s-1)^2\right] \pi^2 \frac{Dt}{h^2}$$
 (1)

where h is the sandwich thickness and s is a summation index

Diffusion coefficients were determined with the aid of equation (1) at 500° , 600° , 700° , 735° and 800° C. The values are listed in Table 1.

Table 1. Diffusion coefficients (D_{Xe}) for xenon in silver

Temperature		D (
$^{\circ}\mathrm{C}$	F	$D_{\rm Xe}~({\rm cm^2/sec})$
500	932	6.5×10^{-11}
600	1112	$4.8 imes10^{-10}$
700	1292	2.9×10^{-9}
735	1355	4.9×10^{-9}
800	1472	1.02×10^{-8}

A graph showing log $D_{\rm Xe}$ as a function of the reciprocal temperature is given in Fig. 1. The diffusion coefficients for krypton, $D_{\rm Kr}$, are also shown for comparison. The linear relationship of $D_{\rm Xe}$ with

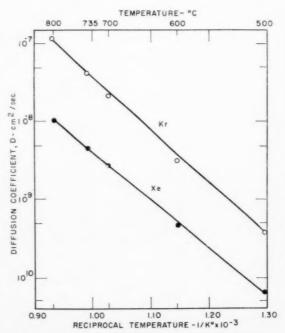


Fig. 1. Log D as a function of reciprocal temperature $(1/{}^{\circ}K)$.

reciprocal temperature is represented by the following equation:

$$D_{\rm Xe} = 0.036 \exp\left(-37,500/RT\right)$$
 (2)

DISCUSSION

The fraction of gas, γ , which diffused out of the sandwich in time t, followed the space-time diffusion relationship in equation (1) for a set of four separate determinations of the diffusion coefficient, D, at each temperature. The same diffusion sample was used for each determination and the time of anneal at that temperature was increased for each determination. The close agreement with the space-time diffusion relationship indicates that xenon diffuses through the bulk of the silver, and under the conditions of this experiment there is very little contribution from structurally sensitive diffusion processes such as grain boundary, crack or void diffusion. Thus, on a macroscopic scale, the xenon diffused essentially by "volume diffusion" in this experiment.

The experimentally measured dependence of the diffusion coefficient, $D_{\rm Xe}$, upon the temperature, T, is given in equation (2). It is of the same functional relationship as the Arrhenius equation which may be derived from Boltzmann statistics. It is usually written as:

VOL.

1959

$$D = D_0 \exp\left(-H/RT\right) \tag{3}$$

where D_0 is the frequency factor and H is the activation energy. Ordinarily, the diffusion coefficients can be expressed in the form where a single activation energy is used for a large temperature range. The interpretation of the diffusion data, for the facecentered cubic lattice of metals such as silver, indicates that the fundamental mechanism of diffusion involves the movement of an atom into a vacant adjacent lattice site. The mobility of the silver and the impurity atoms is controlled by the concentration of vacancies, which depends exponentially upon the temperature. Vacancies are created by thermal agitation of the lattice atoms. The movement of silver atoms and impurity atoms requires the diffusion of vacancies to the atom in question. The atoms may move large distances by individual jumps, each of which requires the movement of a vacancy toward it. The temperature dependence of the diffusion coefficient, D, for xenon and krypton in silver is shown in Fig. 1.

Assuming that the diffusion of vacancies to the xenon is necessary for its mobility, two alternate microscopic diffusion mechanisms are offered for comparison which are based on a positively charged xenon ion and a neutral xenon atom, respectively.

Since the electron distribution for an atom or ion

extends indefinitely, no single characteristic size can be assigned to it. The apparent size depends upon the physical property under discussion, and will differ for different properties. In general, positive ions are much smaller than the neutral atom, and negative ions much larger. The radius of the univalent positive xenon ion as obtained by a method described by Pauling is 0.75 Å. $^{(9)}$ The radius of the neutral xenon atom is 2.15 Å.

A two-dimensional model of each of the mechanisms is given in Fig. 2. Mechanism A involves the movement of the small xenon ion into a neighboring vacancy at position X. The neutral xenon atom occupies 3.4 times the volume of the silver ions. Therefore, in mechanism B, it is represented as occupying four lattice sites simultaneously. In order to occupy four lattice sites, it would have to combine with four vacancies. In order to move one lattice distance in the x direction in the two-dimensional model, the neutral atom must move by the unidirectional movement of two vacancies in the -x direction. This diffusion mechanism is similar to the Kirkendall effect where an insoluble marker or particle moves in a directional flux of vacancies.

If the diffusion mechanism is of the B type, it will require the movement of n vacancies in the same direction before another vacancy approaches from another direction. The probability for jumping in the x direction is $\exp(-n)$ less for the neutral xenon atom than it is for the xenon or silver ions. The mobility of the neutral xenon atom combined with several vacancies is definitely less than the mobility of a silver atom in self-diffusion. The activation energy for the movement of the neutral atom in Fig. 2 is predicted to be twice that for self-diffusion of silver, about 90 kcal/atom.

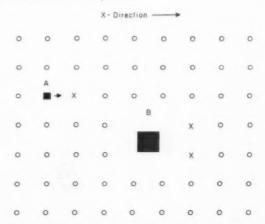


Fig. 2. Two models for diffusion of xenon in silver. A is the positive xenon ion. B is the neutral xenon atom.

A third possible mechanism is the diffusion of a neutral xenon atom occupying a single lattice site. However, the elastic strain energy of the large neutral xenon atom in silver enables it to form a stable combination with the first few vacancies which diffuse toward it.

The measured mobility of xenon in silver is actually greater than the mobility of silver ions by self-diffusion. The activation energy is only 37.5 keal/atom.

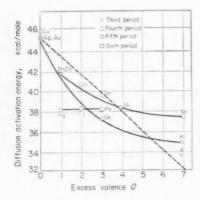


Fig. 3. Activation energies for diffusion of various elements in silver as a function of the "excess valence" (Q).

On the basis of its greater mobility it is concluded that the xenon is not present in the metal lattice as the neutral gas atom, but rather as the positively charged ion. The microscopic diffusion mechanism is the "vacancy" diffusion mechanism in the f.c.e. silver metal lattice, as described by mechanism A above.

Some supporting evidence for this conclusion is provided by activation energies, obtained by radiotracer and radio-analytical techniques, for diffusion of thirteen impurity elements in silver. The diffusion of cadmium, indium and tin in silver were measured by Tomizuka and Slifkin⁽⁶⁾. The diffusion of antimony in silver was measured by Sonder et al.(7) The diffusion of mercury and copper in silver is reported by Sawatsky and Jaumot (10). The same authors made an earlier report of the diffusion of gold in silver(11), and of zinc in silver.(12) The measurement of diffusion of thallium in silver is given by Hoffman(13), germanium in silver by Hoffman(14), and lead in silver by Hoffman et al.(15) The self-diffusion of silver is reported by Sawatsky and Jaumot (12). and by Tomizuka and Sonder(16). The diffusion coefficients of these elements are equal to or greater than that for self-diffusion of silver.

The activation energy for diffusion of each of these

elements is shown in Fig. 3 for comparison. The "excess valence", Q, is defined by Lazarus. (8) He assumes that in the monovalent silver lattice these impurity atoms have 1+Q valence electrons, when Q is positive for elements to the right of silver in the periodic table. The graph shows a definite periodic relationship for the elements in the fourth, fifth and sixth periods. The dashed line is the predicted activation obtained from Lazarus theory. Although the activation energies of Xe and Kr do not follow the Lazarus relationship exactly, there is a regular relationship among each of the three sets of experimental points. The deviations from the Lazarus relationship can be shown to be dependent upon the electrostatic repulsion of the impurity ions. A subsequent article will give a new relationship which accounts for the deviations. From this comparison it seems that the mechanism of diffusion of the inert gases is similar to that for these other elements in silver, and they are thought to diffuse as positive ions.

Further evidence in support of the conclusion that xenon diffuses as a positive ion is the ionization step that is necessary in order to introduce the gas into the metal. This was suggested by LeClaire and Rowe⁽⁴⁾. The validity of the argument was tested by the following experiment. An attempt was made to measure the diffusion of xenon in silver using the method described above, except that no glow discharge was used to introduce the gas. No xenon gas was found by radio-analysis of the gas which diffused out of the silver control sandwich. It is apparently essential to ionize the gas before it can enter the metal.

VOI

195

Calculations of the kinetic energy of the xenon ions in the region of the glow discharge indicate an energy of $10~{\rm eV/ion}$. This may be sufficient energy to displace surface silver ions. Sputtering of the silver definitely occurs during discharge. However, it is insufficient energy to displace an internal atom since this would require a threshold energy of about $25~{\rm eV}$. Still higher energy would be required to force the xenon into the metal as projectile ions.

Sectioning and analysis for xenon gas showed that the xenon was not present in that part of the surface from which the metal had been sputtered, but rather where the sputtered metal had deposited. This effect was previously observed by LeClaire and Rowe⁽⁴⁾. Sputtering, of course, occurs where the ions are striking the cathode with the greatest kinetic energy.

There is sufficient energy for the xenon ions to become attached to the metal surface, and this is probably the mechanism of entry into the metal lattice. Once in a substitutional position on the surface, the xenon atom can compete for the "free" electrons with the silver ions and increase its binding energy in the metal.

Because of the high ionization potential of xenon (12·1 eV), there is the possibility of its recovering an electron once it is introduced into the metal, presumably from the "free" electrons in the metal. However. it would have to compete for possession of the electron with the silver ions which also have a high ionization potential (7.6 eV). Cadmium also has a high ionization potential (9.0 eV) and is believed to diffuse in silver as a positive ion.

Certain metals, when employed as electrodes in discharge tubes containing inert gases, will absorb apparently stoichiometric quantities of these gases, as described by Moeller⁽¹⁷⁾. Spectrographic analysis has shown the presence of compounds formed during gaseous discharge between the metals and the inert gases.(17)

More direct experimental evidence was reported recently by Noyce⁽¹⁸⁾. The chemically clean surface of a germanium crystal was exposed to low-energy gas discharges in several gaseous atmospheres. He found that the discharge in hydrogen and argon introduced p-type impurities into the germanium semi-conductor. The argon apparently moves towards the cathode in germanium, indicating that it is positively charged.

1959

SUMMARY AND CONCLUSIONS

The diffusion coefficients for xenon in silver were determined at 500°, 600°, 700°, 735° and 800°C. The logarithm of the diffusion coefficient is inversely proportional to the absolute temperature. The measured values of the coefficients can be expressed by equation:

 $D_{\rm Xe} = 0.036 \exp{(-37,500/RT)} \, {\rm cm^2/sec}.$

Thus, the activation energy for diffusion of xenon in silver is 37.5 kcal/atom.

The diffusion of xenon follows closely the spacetime diffusion equation analyzed for the boundary conditions in the sandwich. Under the conditions of the experiment there was little contribution from structurally sensitive diffusion processes such as grain boundary diffusion, erack or void diffusion.

ACKNOWLEDGMENT

The author wishes to acknowledge the technical assistance given by the Analytical Chemistry, Glassblowers and Special Irradiations Units at Hanford. He is also grateful to J. J. Hauth for his help in writing this article.

REFERENCES

- W. D. Urrey, J. Amer. Chem. Soc. 55, 3242 (1933).
- 2. F. Henning, Temperaturessung, Handbuch der Physik,
- p. 535. Berlin (1926).
 3. C. J. Smithells and C. E. Ransley, Proc. Roy. Soc. A 150, 172 (1935).
- 4. A. D. LeClaire and A. H. Rowe, Rev. mét. 52, 94 (1955).
- 5. J. M. Tobin, Acta Met. 5, 398 (1957).
- C. T. Tomizuka and L. Slifkin, Phys. Rev. 96, 610 (1954).
 E. Sonder, L. Slifkin and C. T. Tomizuka, Phys. Rev.
- 93, 970 (1954). 8. D. Lazarus, Impurities and Imperfections, p. 107. American Society for Metals, Cleveland, Ohio (1955).
- 9. L. Pauling, The Nature of the Chemical Bond, p. 343. Cornell University Press, Ithaca, New York (1948)
- 10. A. SAWATSKY and F. E. JAUMOT, JR., J. Metals 9, 1207 (1957)
- 11. F. E. Jaumot, Jr. and A. Sawatsky, J. Appl. Phys. 27, 1186 (1956).
- 12. A. SAWATSKY and F. E. JAUMOT, JR., Phys. Rev. 100, 1627 (1955).
- 13. R. E. HOFFMAN, Acta Met. 6, 95 (1958).
- 14. R. E. Hoffman, Self-Diffusion in Dilute Binary Solid Solutions, July 1957, SO-2051 (Unclassified).
- 15. R. E. HOFFMAN, D. TURNBULL, and E. W. HART, Acta Met. 3, 417 (1955).
- 16. C. T. TOMIZUKA and E. SONDER, Phys. Rev. 103, 1182 (1956).
- 17. T. Moeller, Inorganic Chemistry, p. 378. John Wiley, New York (1952).
- R. N. NOYCE, J. Appl. Phys. 27, 843 (1956).

EFFECT OF HYDROGEN ON THE YIELDING OF MILD STEEL*

F. de KAZINCZY†

From measurements of Luder's band-front velocities it is concluded that hydrogen does not affect the activation energy for separating a dislocation and its atmosphere and thereby the delay-time for yielding. Suppression of the upper yield point by hydrogen seems rather to be caused by local stresses surrounding inclusions of molecular hydrogen, which contribute to the stresses at the specimen shoulder, and thus facilitate the initiation of the first Luder's band. Hydrogen raises the flow stress, which seems to be due to dragging of hydrogen along with moving dislocations.

EFFET DE L'HYDROGENE SUR LE CROCHET A LA LIMITE ELASTIQUE DE L'ACIER DOUX

De mesures de vitesses de déplacement du front des bandes de Lüders, l'auteur conclut que l'hydrogène ne modifie pas l'énergie d'activation nécessaire pour séparer une dislocation de son atmosphère, et dès lors que cet élément n'intervient pas sur le temps d'incubation lié l'apparition du crochet à la limite élastique. La disparition du crochet en présence d'hydrogène paraît plutôt être due à des tensions locales autour d'inclusions d'hydrogène moléculaire qui s'ajoutentaux tensions dues au système d'attache de l'éprouvette et facilitent ainsi l'apparition de la première bande de Lüders. L'hydrogène augumente la limite élastique par suite, semble-t-il, de l'entraînement de l'hydrogène par les dislocations en mouvement.

DER EINFLUSS VON WASSERSTOFF AUF DAS FLIESSEN VON FLUSSEISEN

Aus Messungen der Geschwindigkeit einer Lüders-Bandfront folgt, dass Wasserstoff die Aktivierungsenergie zur Trennung einer Versetzung von ihrer Wolke und damit die Verzugszeit des Fliessens nicht beeinflusst. Die Unterdrückung der oberen Streckgrenze durch Wasserstoff scheint vielmehr von lokalen Spannungen in der Umgebung von Einschlüssen molekularen Wasserstoffs herzurühren, die zu den Spannungen an der Probenschulter beitragen und so den Beginn des ersten Lüders-Bands erleichtern. Wasserstoff erhöht die Fliesspannung, dies scheint auf dem Mitschleppen von Wasserstoff mit bewegten Versetzungen zu beruhen.

1. INTRODUCTION

At temperatures below -80°C hydrogen causes an upper yield point to appear in iron, (1.2) the nature of which seems to be closely related to the yield point due to earbon or nitrogen. At room temperature, however, hydrogen suppresses the carbon or nitrogen yield point. This was first observed by Cracknell and Petch⁽³⁾, who attributed it to inhomogenous stresses caused by inclusions of molecular hydrogen of high pressure. According to these authors, yielding would initiate in regions of high stress, and plastic zones would then spread across the specimen. If the whole specimen were to yield in this manner before Luder's bands appeared, the yield point would be completely eliminated. Rogers (4) also observed the yield point suppression above −12°C and suggested two possible mechanisms. First, hydrogen could be bound more tightly to dislocations than carbon and nitrogen and displace them from dislocation sites. As hydrogen diffuses readily at room temperature and has no locking action on dislocations, no yield point should appear. A very similar hypothesis was also proposed by Vaughan and de Morton⁽⁵⁾. Rogers feels,

however, that this mechanism is unlikely to be valid as no increase in internal friction was observed after charging with hydrogen, which would be expected if carbon and nitrogen were expelled from dislocation sites and their lattice concentration thereby increased. According to the second mechanism of Rogers, hydrogen is less tightly bound to dislocations than earbon or nitrogen, but attaches itself to loops of dislocations that are freed from them by thermal fluctuations. This lowers the energy of dislocations to some extent. The activation energy for separating a dislocation from its carbon or nitrogen atmosphere becomes the difference between the energy of a hydrogen-bound and a carbon or nitrogen-bound dislocation, which is smaller than the difference between a free and carbon or nitrogen-bound dislocation.

Further details of the last-mentioned mechanism are obtained from Fisher's⁽⁶⁾ theory. If the activation energy is lowered by lowering the energy per unit length of dislocation free from carbon and nitrogen (γ_0) , the delay-time for yielding will decrease, and the upper yield point will be lowered. Hydrogen would thus affect the upper yield point by its effect on the delay time. If this is true, the Luder's band-front velocity should also be affected. The motion of a band-front can be looked upon as the yielding of many

^{*} Received October 16, 1958.

[†] Department of Metallurgy, Massachusetts Institute of Technology, Cambridge, Massachusetts.

ACTA METALLURGICA, VOL. 7, NOVEMBER 1959

successive small increments along the specimen. The spreading of a Luder's band was treated in this sense by Fisher and Rogers⁽⁷⁾ who showed that the bandfront velocity depends upon stress and temperature as does the reciprocal of the delay time; thus a linear relationship exists between $(\sigma T)^{-1}$ and $\log v$, where σ is the stress, T the temperature, and v the band-front velocity. The slope of this line is a sensitive function of γ_0 . Therefore, by determining the effect of hydrogen on the slope, it should be possible to establish a basis for evaluating the above hypothesis.

2. EXPERIMENTAL

Flat tensile specimens 0.50 in. wide with 3.25 in. gage length were prepared from a hot-rolled strip of SAE-1010 steel having ASTM No. 10.5 grain size. The thickness was ground down from 0.065 in. to 0.050 in., after which the specimens were stress relieved at 620°C for 1 hr. Immediately before hydrogen charging the specimens were lightly ground with 4/0 emery paper to activate the surface. Charging was carried out electrolytically in pure IN H.SO, at a current density of 0.1 A/in2 or in 1N H2SO4 with 100 mg/l Na₂HAsO₄ at 0.025 A/in² during 3 hr, in both cases with moderate stirring of the electrolyte. Neither treatment produced blisters, and no difference in results was obtained with the two charging treatments. If current density was increased to 0.1 A/in² in the second solution, however, blisters were formed.

VOL.

1959

A grid with 5 mm spacing was scratched lightly on the specimens, which then were tested within 3 min after charging in an Instron machine at 20°C. Measurements were made at different crosshead rates: the stress was recorded, and the band-front velocity was determined by measuring the time required for the band to pass between two grid markings. Measurements were only made when the band-front propagated smoothly including a stable angle of 55° with the specimen axis, which greatly increased the accuracy of stress measurements. The results are shown in Fig. 1. It appears, that the slope of the line was not altered by hydrogen, but the flow stress was raised by 300–350 lb/in². The yield elongation, being about 4 per cent, was only slightly affected.

Other specimens, charged at different current densities, were investigated at a strain rate of 0.006 min⁻¹ with regard to their upper yield point. On 20 unblistered specimens, Luder's bands always started at the specimen shoulders, and the upper yield point was partially or (in three cases) totally suppressed after charging at current densities higher than 0.037 A/in² in the pure electrolyte. The degree of

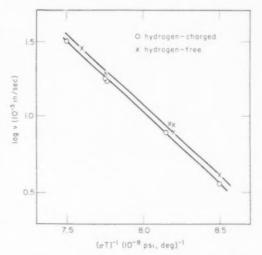


Fig. 1. Effect of hydrogen on Luder's band-front velocity.

suppression, however, was not reproducible, and no clear relationship was found with current density. In cases of total suppression it was always observed that a Luder's band started at one specimen shoulder at a stress lower than the flow stress, and propagated slowly across the width of the specimen. During this period the stress increased and reached its maximum value as the Luder's band reached the other edge of the specimen, then decreased slightly until the bandfront included the stable angle with the specimen axis.

On 5 blistered specimens, Luder's bands often started at blisters and a considerable plastic strain was recorded before the first band could be observed. With one exception the yield-point was totally suppressed.

3. DISCUSSION

Since the slope of the line relating stress and Luder's band-front velocity (Fig. 1) is not altered by hydrogen. it can be concluded that hydrogen does not effect suppression of the upper yield point by interaction with dislocations in the manner that has been suggested by Rogers. (4) The poor reproducibility of the suppression indicates that hydrogen content or activity is not the only responsible factor and that some other uncontrolled factor is of considerable importance. It is suggested that local stresses surrounding inclusions of molecular hydrogen of high pressure contribute to the stress distribution at the specimen shoulder, causing a Luder's band to initiate at a smaller external stress. An important trap for molecular hydrogen seems to exist at the boundary of slag inclusions, because if the pressure of hydrogen is increased sufficiently, internal cracks usually start at such

locations and may then develop into blisters. (8) The spacing of the most effective traps is fairly large, comparable to the spacing of blisters, and as their positions in relation to the specimen shoulder are different in different specimens, the resulting variation of their stress fields might well account for the spread in experimental results. This model does not exclude the possibility of limited plastic deformation around hydrogen traps, which is quite likely to occur, but the plastic zones are apparently too small to spread and initiate gross yielding.

It was also observed, that hydrogen raised the flow stress by 300-350 lb/in2. This might be due to the dragging of a hydrogen atmosphere along with moving dislocations, which originally was proposed by Bastien and Azou⁽⁹⁾. An estimate can be made of the maximum elevation of flow stress due to this mechanism. According to Cottrell and Jaswon⁽¹⁰⁾ it amounts to $\sigma_{\rm max} \simeq 17 U_{\rm max} c_0 N$, where c_0 is the concentration of hydrogen, which is set at 10-4 (corresponding to 2.0 ml/100 g), N the total number of atoms $0.85 \times$ $10^{23} \,\mathrm{cm}^{-3}$, and U the interaction energy between a solute atom and dislocation. U_{max} is proportional to the volume change caused by the solute atom. For carbon in ferrite $\Delta v = 0.78 \times 10^{-23} \, \mathrm{cm}^3$ and $U_{\mathrm{max}} \simeq$ 0.5 eV; for hydrogen in ferrite $\Delta V = 2.0 \text{ cm}^3/\text{g}$, (11) $\Delta v = 0.33 \times 10^{-23} \, \mathrm{cm}^3$ and thus $U_{\mathrm{max}} \simeq 0.2 \, \mathrm{eV}$. It can also be estimated from the relationship $U_{\text{max}} =$ $-kT_0 \ln c_0$, where T_0 is the highest temperature at which the sites of strongest binding still are practically filled with solute atoms. Taking this as the highest temperature at which a hydrogen yield point has been observed, $T_0 = 190^{\circ} \text{K}$, one obtains $U_{\text{max}} = 0.15 \text{ eV}$. Inserting the latter value one obtains $\sigma_{\text{max}} = 500 \text{lb/in}^2$ in shear or 1000 lb/in2 in tension, which is consistent

with the experimental results. An increased flow stress would also be expected if it was assumed that hydrogen atoms are not dragged along with dislocations but remain at their lattice sites, as their stress field would hinder dislocations movement. An equation derived by Cracknell and Petch(12) can be directly applied to this case. The calculated elevation of flow stress is 15 lb/in2, using the above values for the constants, which does not account for the measured difference, however.

If a dislocation is surrounded by a hydrogen atmosphere, which seems probable according to the above calculations, its energy is certainly lowered. However, in the very moment a dislocation breaks away from its carbon or nitrogen atmosphere it is essentially free from solute atoms, some time being required for the hydrogen to diffuse to the newly formed loop. The activation energy for separating a dislocation from its atmosphere is therefore the same as in hydrogen-free steel, which explains why the delay-time is not affected by hydrogen.

ACKNOWLEDGMENT

The author is indebted to Professor W. A. Backofen for helpful discussions.

VOI

195

REFERENCES

- 1. H. C. Rogers, Acta Met. 2, 167 (1954).
- H. C. ROGERS, Acta Met. 5, 112 (1957).
 A. CRACKNELL and N. J. PETCH, Acta Met. 3, 200 (1955).
- H. C. Rogers, Acta Met. 4, 117 (1956).
- 5. H. G. VAUGHAN and M. E. DE MORTON, Brit. Welding J. 4, 40 (1957).
- 6. J. C. Fisher, Trans. Amer. Soc. Metals, 47, 451 (1955).
- 7. J. C. FISHER and H. C. ROGERS, Acta Met. 4, 180 (1956).
- 8. F. DE KAZINCZY, Jernkontor. Ann. 140, 347 (1956).
- 9. P. Bastien and P. Azou, Rev. Met. 49, 837 (1952).
- 10. A. H. COTTRELL and M. A. JASWON, Proc. Roy. Soc. A199, 104 (1949).
- 11. G. Phragmén, Jernkontor. Ann. 128, 537 (1944).
- 12. A. CRACKNELL and N. J. PETCH, Acta Met. 3, 186 (1955).

"SUPERHIGH PLASTICITY" OF COMMERCIAL IRON UNDER CYCLIC FLUCTUATIONS OF TEMPERATURE*

MICHAEL G. LOZINSKY† and IZINA S. SIMEONOVA†

While investigating by high temperature metallography the influence of cyclic fluctuations of temperature on the character of the process of deformation of Armco iron containing 0.03% C, it was found that two necks form on the specimen in the zones with a temperature of about $720^{\circ}-850^{\circ}$ C when a temperature gradient arises along the specimen (under electric heating by the application of a 50 Hz low voltage) and with definite durations of exposure with limiting temperatures. These two necks are located symmetrically on either side of the middle section of the sample, which is raised to a much higher temperature (to $T_{\rm max} = 1000^{\circ}-1100^{\circ}$ C and $T_{\rm min} = 800^{\circ}$ C). The appearance of two necks shows that the development of "superhigh plasticity" takes place under the temperature conditions mentioned. This phenomenon is explained by the irregular distribution of carbon inside the grains and its concentration near the boundaries of grains and blocks. This leads to the process of polymorphous $\alpha-\gamma$ transformation at temperatures of $720-850^{\circ}$ C only in those microregions of the neck zones which are carbon rich. As a result of the transformation the coherency of the crystal lattice is upset. This in its turn is conducive to a sharp reduction of strength which results in an increase of plasticity.

With increase of the maximum temperature value from 900° to 1100°C and retention of the lower limit of 800°C the distance between the necks increases monotonically.

"SUPERPLASTICITE" DU FER PUR SOUS DES FLUCTUATIONS CYCLIQUES DE TEMPERATURE

Les auteurs étudient par métallographie à haute température l'influence de cycles de fluctuations thermiques sur le processus de déformation du fer Armco contenant 0.03%C. Ils observent la formation de deux constrictions dans les zones où la température est de 720–850°C et lorsqu'un gradient thermique existe le long des échantillons (chauffage électrique à basse tension et sous 50 Hz). Ces deux constrictions se disposent symétriquement des deux côtés de la section centrale de l'échantillon, qui se trouve à une température nettement plus élevée (température maximum: 1000-1100°C et température minimum = 800°C). L'apparition de ces deux constrictions montre qu'un phénomène de "superplasticité" prend place dans les conditions thermiques indiquées.

Ce phénomène s'explique par la distribution irrégulière du carbone dans les grains et sa concentration près des frontières. Ce fait conduit à une transformation polymorphique $\alpha-\gamma$ à des températures de $720-850^\circ\mathrm{C}$ seulement dans ces micro-régions riches en carbone. En conséquence, la cohérence du réseau cristallin est perturbée et provoque une réduction importante de résistance qui conduit à une augmentation de la plasticité. A température minimum constante ($800^\circ\mathrm{C}$), lorsque la température maximum croit de 900 à $1100^\circ\mathrm{C}$, la distance entre les deux constrictions augmente de façon monotone.

"SUPERHOHE PLASTIZITAT" VON HANDELSÜBLICHEM EISEN UNTER ZYKLISCHEN SCHWANKUNGEN DER TEMPERATUR

Mit Hilfe von metallographischen Hochtemperatur-Einrichtungen wurde der Einfluss zyklischer Schwankungen der Temperatur auf den Charakter des Verformungsvorgangs von Armco-Eisen mit 0,03% C-Gehalt untersucht. Entsteht entlang der Probe ein Temperaturgradient (durch elektrische Heizung mit 50 Hz Niederspannung), so bilden sich bei bestimmten Einwirkungszeiten zwischen Grenztemperaturen auf der Probe zwei Einschnürungen in den Zonen, die eine Temperatur von etwa 720°–850°C haben. Diese beiden Einschnürungen liegen symmetrisch zu beiden Seiten der Probenmitte, die auf eine viel höhere Temperatur erwärmt wird (auf $T_{\rm max}=1000^\circ-1100^\circ{\rm C}$ und $T_{\rm min}=800^\circ{\rm C}$). Das Auftreten von zwei Einschnürungen zeigt, dass die Entwicklung von "superhoher Plastizität" unter den erwähnten Temperatubedingungen stattfindet. Dieses Phänomen wird durch die unregelmässige Verteilung von Kohlenstoff innerhalb der Körner und esine Anreicherung in der Nähe der Grenzen von Körnern und Blöcken erklärt. Dies führt dazu, dass der Prozess der polymorphen α - γ Umwandlung bei Temperaturen von 720°–850°C nur in jenen Mikroregionen des Einschnürungsgebiets stattfindet, die kohlenstoffreich sind. Als Ergebnis der Umwandlung wird die Kohärenz des Kristallgitters stark gestört. Dies wiederum führt zu einem starken Abfall der Festigkeit, die eine Zunahme der Plastizität zur Folge hat.

Steigert man die Maximaltemperatur von 900° auf 1100° C und hält die untere Grenze bei 800° C fest, so wächst der Abstand der beiden Einschnürungen monoton.

In any modern machines and mechanisms the components of which operate under heating conditions, temperature fluctuations are inevitable. These fluctuations, as will be shown, may produce a sharp reduction of strength under particular temperature cycling rates. Hence it appears important to promote investigations in the field of detailed studies of those factors which bring about the appearance of a peculiar "superplasticity" of metals and alloys under cyclic temperature variations.

We should bear in mind that when designing

VOL.

^{*} Received December 1, 1958.

[†] Institute of Machine Engineering, Academy of Sciences of the USSR.

components working under heating conditions it is usual to depart from the values of permissible stress found while ereep testing the material. These are mostly determined while straining the specimens under isothermal conditions with a high degree of temperature stability. The influence of temperature fluctuations (which always exist in normal service) upon the creep process has so far been very little studied.

Thus, e.g., in a jet engine at the time of starting, rapid heating takes place, followed by cooling to the ambient temperature on stopping. Several hundred such heating-cooling eyeles take place during the "life" of such an engine. Many parts of internal combustion engines and other engineering units undergo cyclic influences of high temperatures during operation. The effect of such temperature variations, which under particular conditions promotes a sharp increase of creep, is not as a rule taken into consideration when designing and operating machines.

The present authors have carried out, by methods of high temperature metallography, investigations into the laws of deformation of commercial iron under conditions of straining with a temperature gradient along samples undergoing symmetrically repeated cycles of heating and cooling (with limiting temperature values in the middle section of the specimen $800^{\circ} \rightleftharpoons 1000^{\circ}$ C).

These investigations have revealed the appearance, in the sections disposed on either side of the "heated zone" (which are at considerably lower temperatures) of a peculiar "superplasticity" characterized by the appearance of two necks in the specimen and by the rapid developing of shear deformation.

Some results of these investigations carried out with samples of commercial iron with 0.03% carbon are given in the present paper. Before starting the experiments the samples were vacuum annealed at 1000°C for 2 hr.

The experiments were carried out on an installation of the type IJMAIII-5M, $^{(1-3)}$ which permitted direct observation of the microstructure of the sample and also the measurement of deformation with a precision of $\pm 2\mu$ on the 10 mm gage length while heating to 1100°C and straining by a stress up to 60 kg/mm².

"Chains" of impressions were made distant about 50μ from one another, by an instrument of the type IIMT-3, to measure microhardness along the length of the specimens of commercial iron under test before placing them in the vacuum working camera of the installation IIMAIII-5M. These impressions were situated in the middle zone of the specimen and also at some distance from it. In Fig. 1 the form of

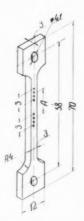


Fig. 1. External view of a specimen used for the study of microstructure in the process of cyclic temperature fluctuations under strain in a vacuum.

specimen used for the tests is shown, its geometrical dimensions are given, and the positions of the impressions of the diamond pyramid are shown. The letter A denotes the distance between the "chains" of impressions disposed in the middle part of the specimen and near the zone of superplasticity which was from 7 to 17.5 mm. This distance was found experimentally during preliminary tests which indicated the possibility of defining the position of dangerous zones under cyclical temperature fluctuations.

19

The specimen was heated by an electric current at low voltage and commercial frequency which was passed through the specimen at the time of the experiment. The current was fed to the specimen by means of flexible copper conductors fitted with clamps. Under such heating conditions a temperature gradient appeared along the specimen, and the highest temperature was developed in its middle region. With an effective cross-section of the sample of 9 mm² and the length of the heated section 46 mm. on heating to 1000°C for example this temperature value remained uniform in the middle part of the specimen over approximately 12 mm, and decreased monotonically as the copper clamps were approached. Fig. 2 illustrates the type of temperature distribution along the specimen of commercial iron when heating the middle zone to 800° and 1000°C respectively (curves 1 and 2).

Thus while heating and cooling the middle zone of the specimen to the above temperatures, a gradually changing scale of temperature developed in the adjacent sections situated on either side of the most intensely heated middle region. In this way a wide range of temperature appeared in one specimen. It

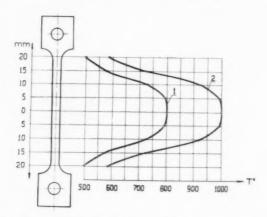


Fig. 2. Temperature distribution along a specimen of commercial iron under electric heating in a vacuum to 800°C (curve 1) and 1000°C (curve 2).

extended from about $400^{\circ}\mathrm{C}$ at the ends near the clamps, to $1000^{\circ}\mathrm{C}$ in the middle section.

While carrying out most of the experiments, the cyclical temperature changes in the specimen took place according to the graph given in Fig. 3. Each cycle consisted of: holding for $t_1=2$ sec at the lower temperature value $T_1=800^{\circ}\mathrm{C}$, followed by heating to $T_2=1000^{\circ}\mathrm{C}$ which was held for $t_2=2$ sec, and then a cooling to $T_1=800^{\circ}\mathrm{C}$. The overall duration of each cycle was $\tau=60$ sec.

While carrying out further investigations to be described concerning the influence of exposure time under limiting temperature values within the range $800-1000^{\circ}\text{C}$, the periods t_1 and t_2 were changed to times up to 60 sec.

1959

Automatic repetition of the required conditions of cyclical heating was secured by means of a special electrical device which was connected within the installation IIMAIII-5M and which controlled the electric heating system. The duration of the exposure under limiting temperature values could be smoothly

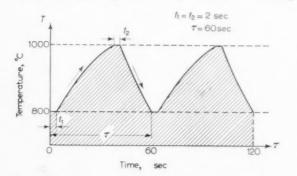


Fig. 3. The character of the temperature change in the middle part of the specimen, during tests to study the influence of cyclic temperature fluctuations on the strength of commercial iron.

regulated, by means of a motor time relay, from zero to 2 min.

Under certain test conditions related to the cyclical temperature fluctuations two necks instead of one appear on the specimen. They are situated symmetrically at the ends of the section heated to a higher temperature.

The anomaly of the appearance of these necks in zones of lower temperature may be explained by the influence of the following factors.

With average carbon contents in commercial iron of 0.03% as determined by chemical analysis, the carbon concentration in some parts of the grains, especially close to their boundaries as well as to the block boundaries, may be considerably greater than this average value. The inevitable appearance of such an irregularity is confirmed by investigations carried out by the method of autoradiography (by introducing radioactive carbon into the iron).

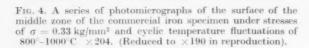
Thus for example the experiments carried out by Lagerberg and Josefsson⁽⁴⁾ have shown convincingly that the solubility of carbon increases with the growth of the total surface of the boundaries of iron grains resulting from reduction of grain size. This proves that the carbon atoms are mainly situated at the grain boundaries.

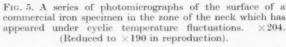
While regarding as established the existence of different carbon concentrations within the boundaries of separate microvolumes, we may suppose that where there exists along the specimen a temperature gradient characterized by the diagram of Fig. 2, the $\alpha \rightleftharpoons \gamma$ transformation will take place only in discrete regions. This may be explained by the fact that with increase of carbon content the temperature of transition of the α -phase into the γ -modification decreases. This temperature, which is 910°C for pure iron, decreases to 721°C if the sample contains 0.83% of carbon.

Under cyclical changes of temperature of the specimen by repeated heating and cooling the appearance and subsequent destruction of α and γ phases take place in the boundary regions of grains and blocks, in separate localised microvolumes in a grain where there is an increased amount of carbon.

As is well known, during the polymorphous $\alpha \rightleftharpoons \gamma$ transformations in iron, changes of structure take place: the body-centred cubic lattice of the α -phases is translated into a face-centred cubic lattice characteristic of the α -phase. At the same time the lattice parameter increases by 12.4% (corrected to 20%C) which gives 2.861 Å for the α -phase and 3.5586 Å for the γ -phase.

With increase of carbon content in austenite the lattice parameter also increases and is, for instance,





with 0.2% C—3.5650 Å, with 0.4% C—3.5714 Å, with 0.6% C—3.5778 Å, with 0.8% C—3.5842 Å and with 1.4% C—3.6034 Å. $^{(5)}$

The influence of the two factors: the irregular distribution of carbon in the microvolumes of the grains as well as of the centres in which the polymorphous $\alpha \rightleftharpoons \gamma$ transformations take place locally in

separate grain sections, causing disturbances in the coherent relationship of atoms in the crystal lattice—it is this that is conducive to the lowering in strength of the iron and the formation of two necks.

Accelerated deformation may be influenced by the "uneven" change in the metal's characteristics at the temperature of polymorphous transformation. During the transition from the α to the γ -phase, strength

measured in terms of hardness, for instance, increases by nearly 50% (6)

One of the reasons which may be conducive to the formation of two zones with low deformation resistance on the specimen is, according to the English investigator P. Feltham,* the influence of dislocation motion due to the temperature gradient which develops in the specimen under conditions of electric heating. This view is also supported by the use of a similar temperature distribution in zone melting, for instance, for the purpose of refining the metal by the migration of impurities.

In the middle region of the specimen which is rapidly heated to 1000°C , the $\alpha \rightleftharpoons \gamma$ transformation proceeds under any carbon concentration in separate microvolumes. In this middle zone therefore there is no sign of the effect of heterogeneity of carbon content on the appearance of superplasticity due to tensile stresses which produce this phenomenon in regions having a definitely "dangerous" temperature gradient.

Now let us analyse the experimental data which were obtained while studying the influence of cyclic temperature fluctuations on strength when straining commercial iron containing 0.03% C.

The microstructure of the middle part of the specimen of this iron under cyclic temperature fluctuations within the limits $800^{\circ} \rightleftharpoons 1000^{\circ} \text{C}$ is shown in Fig. 4. In the photomicrograph of the specimen surface before the beginning of the experiment, as shown in Fig. 4a, arrows denote the direction of the influence of straining stresses. We can also see the "chain" of impressions of the diamond pyramid made with a 20 g load.

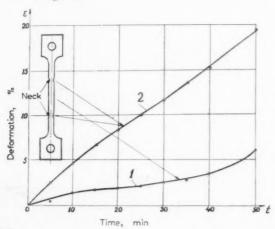


Fig. 6. The deformation diagram of the middle zone and neck of a commercial iron specimen under a stress of $\sigma=0.33~\rm kg/mm^2$ and with cyclic temperature fluctuations in the middle of the specimen within the limits $800 \rightleftarrows 1000 ^{\circ} \rm C.$

The successive surveys of the studied zone which took place after 10, 20, 30, 40, 60 and 70 eycles as seen in Fig. 4, b–g, show the characteristic "Waviness" in separate austenite grains.

Observations of the zone of a neck of the same type formed in the "dangerous temperature" interval reveal some peculiarities of the microstructure. Fig. 5 shows a series of photomicrographs taken during the experiment on one and the same section of the specimen surface of the neck zone. Fig. 5a shows the initial surface, and Fig. 5, b–g, the micrographs taken after the same cyclic treatments as mentioned above in the description of Fig. 4.

It is interesting to note the appearance and gradual development of fissures and zones marked by arrows in Fig. 5g.

Fig. 6 shows a diagram illustrating the deformation laws of a sample of commercial iron in the middle zone, where the temperature varied within the limits $800^{\circ} \rightleftharpoons 1000^{\circ}\text{C}$ (curve 1), as well as in the neck zone which experienced the effect of varying temperatures within the limits $720^{\circ} \rightleftharpoons 850^{\circ}\text{C}$ (curve 2).

Attention should be drawn to the fact that the total deformation in the neck, which is in the cooler zone at any moment of the experiment, is several times greater than that in the middle part of the specimen which is at a higher temperature.

A number of tests was carried out for the purpose of studying the influence of the upper temperature limit of cyclic heating on the disposition of necks on the specimen. The maximum temperatures used were respectively 850°, 900°, 950°, 1000°, 1050° and 1100°C. The lower temperature limit for all the experiments remained constant at 800°C.

In those cases when the upper temperature limit was 850°C, one neck appeared in the middle of the "hot" zone of the specimen; when the temperature limits were higher, between 900° and 1100°C, the distance between the necks ranged from 14 to 35 mm.

In Fig. 7a an external view of the specimen is shown before the experiment. In Fig. 7, b–f, we see the specimens which have undergone cyclic tests under various values of maximum temperature with a minimum temperature of 800°C.

The regulating of the increase of the distance B from specimen edge to middle of the neck under different temperature gradients during cyclic tests is reflected in the graph of Fig. 8. The distance between the specimen edge and the middle part of the neck was taken as basic when plotting this diagram. That was so since the distance between the necks depended on the number of cycles in the experiments conducted. Each point on the graph is the result of five tests.

1959

^{*} Private communication

Fig. 7. The external appearance of commercial iron specimens (a) before the tests, (b-f) after cyclic tests on the installation IIMAIII-5M under different top temperature values and the same lower temperature limit of 800°C;

- (b) 450 cycles; 800° ≥ 850°C;
- (c) 180 cycles; 800° ≈ 900°C;
- (d) 200 cycles; 800° ≥ 950°C;
- (f) 180 cycles; 800° ≈ 1100°C

Strain under constant stress $\sigma = 0.33 \text{ kg/mm}^2$. (Reduced by 20% in reproduction).

As may be seen from Figs. 7 and 8, the distance between the specimen edge and the middle of the neck decreases with rise of the upper temperature limit. This may be explained by the widening of the middle zone with a uniform distribution of temperature above the "dangerous" value. Below this value local processes of polymorphous transformation, leading to the appearance of superplasticity, take place in separate microvolumes as a result of cyclic temperature changes.

Increase of the exposure duration t_1 (Fig. 2) five times (from 2 to 10 sec), as well as ten times and more, established that only one neck is formed in the middle part of the specimen.

These experiments have shown conclusively that for the appearance of two necks on the specimen in zones of lower temperature than that developed in its middle region by electric heating, particular conditions

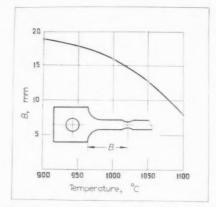


Fig. 8. The influence of maximum temperature in the middle part of the commercial iron specimen on the change in the distance between the middle part of the neck and the edge during cyclic tests.

are necessary not only as to the distribution of the temperature gradient along the specimen, but also as to the strictly limited durations of exposure to those temperatures. Such heat loading conditions may at times appear in some components during different operations which take place under conditions of repeated heating and cooling. These conditions may result in a sharp decrease in strength which may cause accidents by failure.

This circumstance points to the advisability of developing further studies of the strength of metals and alloys under different conditions of cyclic temperature fluctuation.

The experiments carried out by the authors on specimens of iron melted in vacuo with carbon content 0.006%, under cyclic fluctuations of temperature in the middle zone of the specimen in the range 800°
≥ 1000°C, show the appearance of but one neck. This corroborates the hypothesis on the effect of irregular distribution of carbon within the grains of commercial iron with 0.03% C.

CONCLUSIONS

The following conclusions may be drawn as a result of the experiments carried out on specimens of commercial iron:

1. Under conditions of electrical heating of specimens of commercial iron by means of a current passing through them which produces a temperature gradient along the sample, as well as under cyclic temperature variations within the range 1100°-800°C with a 2 sec exposure at limiting temperatures, a sharp decrease of resistance to deformation under the influence of straining stresses appears in the specimens. This results in the formation of two necks situated in the temperature zones $720^{\circ} \gtrsim 850^{\circ}$ C.

195

3. The data obtained during the experiments show that while Armeo iron contains an average of 0.03% carbon, in separate microvolumes near the boundaries of grains and blocks undergoing transformation at temperatures of $720^{\circ} \rightleftharpoons 850^{\circ} \text{C}$ the carbon contents increase scores of times (to about 0.3-0.83% C. i.e. 10-90 times the average value).

4. Increase of the exposure period at limiting temperature values eliminates the appearance of the observed phenomenon.

5. There is a need for developing further the study of the influence of different conditions of cyclic temperature changes on the strength of constructional materials, as well as the study of factors leading to the appearance of "superplasticity" under particular conditions.

REFERENCES

- 1. M. G. Lozinsky, Metallovedenie i obrabotka metallov No. 11
- M. G. Lozinsky, Izvestia Academii Nauk SSSR, OTN, No. 11 (1957).
- 3. M. G. Losinsky, Hutnicke listy, Roc 12, No. 11, Brno (1957)
- 4. G. Lagerberg and A. Josefsson, Acta Met. 3, (1955).
- 5. S. F. Yuriev, Specific phase volumes in martensite trans-
- formations of austenite. Metallurgizdat (1950).
 6. M. G. LOZINSKY and M. B. GUTERMAN, Zavodskaia Laboratoria No. 11 (1956).

THE EFFECT OF QUENCHED-IN VACANCIES ON THE ELASTIC MODULUS OF ALUMINUM*

R. C. FOLWEILER† and F. R. BROTZEN‡

The effect of quenched-in vacancies upon the elastic modulus of aluminum was investigated. Equipment for the dynamic measurement of modulus changes was developed for this purpose. The presence of lattice vacancies was found to reduce the elastic modulus. The change in modulus was investigated during annealing at room temperature subsequent to quenching. The time relation of vacancy concentration observed was analogous to that determined by electrical resistivity measurements.

L'ACTION DES LACUNES GELEES PAR TREMPE SUR LE MODULE ELASTIQUE DE L'ALUMINIUM

Les auteurs ont étudié l'action des lacunes gélées par trempe sur la module élastique de l'aluminium. Dans ce but, ils ont conçu une installation de mesure dynamique des variations de module. La présence de lacunes dans le réseau réduit le module élastique.

Les auteurs étudient les variations du module au cours du revenu à la température ambiante après trempe. La relation obtenue pour la concentration des lacunes au cours du temps est analogue à celle que l'on déduit des mesures de résistivité électrique.

DER EINFLUSS VON ABGESCHRECKTEN LEERSTELLEN AUF DIE ELASTIZITÄTSMODULN VON ALUMINIUM

Der Einfluss von abgeschreckten Leerstellen auf die Elastizitätsmoduln von Aluminium wurde untersucht. Zu diesem Zweck wurde eine Apparatur zur dynamischen Messung von Moduländerungen entwickelt. Es wurde gefunden, dass die Anwesenheit von Gitterleerstellen die Elastizitätsmoduln verkleinert. Die Moduländerungen wurden nach dem Abschrecken während der Erholung bei Raumtemperatur untersucht. Die beobachtete Abhängigkeit der Leerstellenkonzentration von der Zeit war analog zu derjenigen, die durch Messung des elektrischen Widerstands bestimmt wird.

1. INTRODUCTION

When a pure metal is alloyed with soluble elements the elastic modulus is reduced. Köster and Rauscher⁽¹⁾ observed this effect in copper and in gold alloys, using solutes having a wide range of atomic diameters. Zener⁽²⁾ analyzed the above data and concluded that the change in elastic modulus was associated with the elastic strain energy introduced into the lattice by the difference in atomic size. According to the analysis, the change in modulus should decrease linearly with increasing solute concentration. The introduction of strain energy as a basic concept for variation in modulus implies that vacancies should influence the modulus in a manner analogous to solute atoms.

The decrease in modulus as a result of vacancy introduction was predicted also by Dienes⁽³⁾. He reasoned that a number of atomic bonds are disrupted in the immediate vicinity of a vacancy. This changes the repulsive potential and leads to a variation in the modulus of elasticity.

Vacancies can be introduced into a solid material most conveniently by quenching from a high tempera-

ture. In aluminum these quenched-in vacancies anneal out at room temperature. In quenched aluminum the elastic modulus can therefore be expected to increase with time.

195

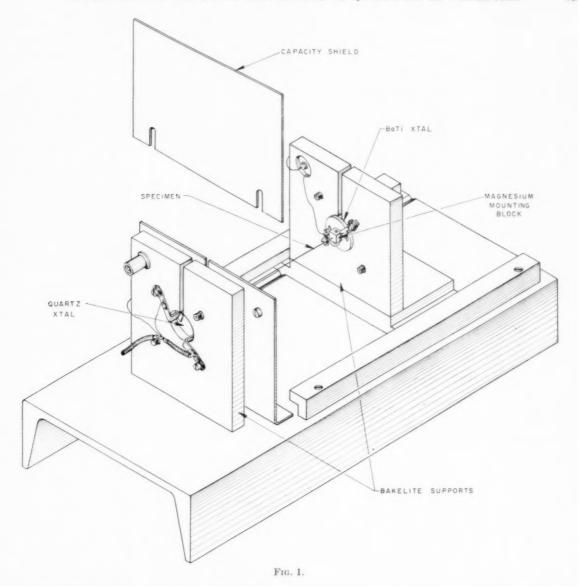
2. EXPERIMENTAL EQUIPMENT AND PROCEDURE

Because only very small changes in the elastic modulus could possibly be caused by the number of vacancies introduced by quenching, the development of an accurate dynamic method for the measurement of the modulus was imperative. For the purpose of this study only measurements of the change in elastic modulus, not its absolute value, were considered essential. The introduction of vacancies by quenching is most suitable because other techniques, such as cold work or irradiation, tend to generate other imperfections in addition to vacancies. In order to obtain a rapid quench the wire specimen must have a very small cross section. Past dynamic techniques for measurement of elastic properties have often made use of comparatively large rods in composite oscillators. Such rods cannot be quenched effectively. The other frequently used technique, the pulse method, was not considered sufficiently accurate for the small changes in modulus anticipated. Therefore,

^{*} Received December 11, 1958.

[†] Formerly at The Rice Institute, Houston, Texas, presently with General Electric Corporation, Schenectady, N.Y.

[†] The Rice Institute, Houston, Texas.



a system similar in idea to the composite oscillator was selected, which could make use of fine wires as specimens.

VOL.

1959

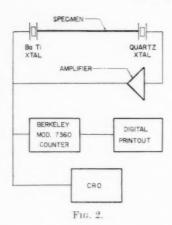
The apparatus used in this investigation consisted of two crystals mounted in counterbored bakelite holders, Fig. 1. Spring-loaded clips held the crystals in place and provided the electrical contact to the plated surface of the crystals. To minimize capacitive transmission between input and output circuits a grounded shield was installed between the crystals. The entire assembly was placed within a lucite box lined with aluminum sheet to reduce further capacitive transmission.

Specimens, about 5 cm long, were made of No. 30 (0.25 mm diameter) aluminum wire of 99.997%

purity.* The wire specimens were fastened to the crystals by means of magnesium blocks of $5\times5\times3$ mm. These blocks were attached to the surface of the crystals with Duco cement. They contained holes and small set screws to hold the wire in place.

The circuit, Fig. 2, was designed as an oscillator whose frequency in part was determined by the physical characteristics of the wire. The output of the receiving crystal (quartz) was amplified and used to drive the transmitting crystal (barium titanate). The latter was operated near its resonant peak, while the former oscillated far off resonance. The frequency of oscillation was measured by means of a Berkeley

 $[\]sp{*}$ Obtained through the courtesy of Alcoa Research Laboratory,



Universal Eput Counter and was recorded by a digital printer.

Specimens, mounted in a holder, were quenched from a temperature of 530°C after heating for 10 min in a helium atmosphere. As the heated specimens with their holders were dropped into water, they passed through a blast of air. This technique produced a quench from 530°C to room temperature within 15 msec, as measured on an oscilloscope. The specimen was then removed from its holder and placed in the mounting blocks on the crystals. The time required for this operation was 4–6 min. Special care was taken to avoid deformation of the wire.

The data thus obtained were in terms of changes of oscillator frequency. The relationship between this frequency change and the change of the elastic modulus was established by utilizing the known temperature dependence of the elastic modulus in aluminum. (4) This was accomplished by warming the entire apparatus a few degrees and then allowing it to cool very slowly. As expected, the frequency varied as a function of temperature. From the temperature–frequency relation a calibration factor was computed, after correction was made for the variation in the barium titanate crystal frequency as a result of temperature changes. (5)

3. RESULTS AND DISCUSSION

The experimental procedure of this investigation was based on the measurement of the change in velocity of sound in the wire specimen. This change causes additional phase shift in the feedback loop of the oscillator and thereby shifts the oscillator frequency. This frequency as a function of time is shown in Fig. 3.

The velocity of transmission of a longitudinal elastic wave, v, is related to the modulus, E, by the equation

$$v^2 = E/d \tag{1}$$

VOI

195

where d is the density. This equation holds for bodies with small ratio of width to length, satisfied in these experiments. For small variations in modulus and for the first harmonic one obtains from equation (1)

$$2\alpha(v) \cdot \delta v/v = \delta E/E + \delta L/L = \delta E/E + \frac{1}{3}\delta V/V$$
 (2)

where ν is the resonant frequency, L is the length, and V is the volume of the wire. $\alpha(\nu)$ is the experimentally determined calibration factor. The variation in length

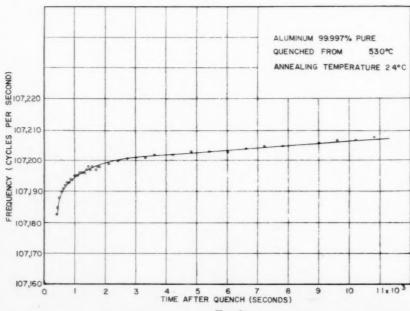
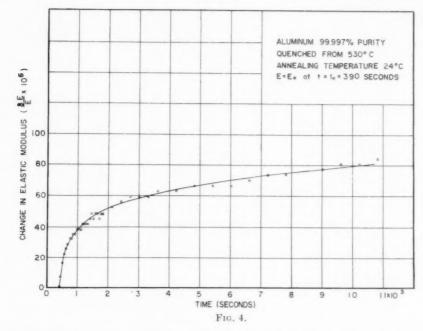


Fig. 3.



of the wire would be due to isotropic volume changes eaused by variation in vacancy concentration.

The relative influence of volume changes and of modulus changes upon the variation in observed resonant frequency must be estimated. Since the aluminum was quenched from 530° C, the vacancy concentration would probably not exceed 15×10^{-6} .* The relative change in volume associated with a given concentration change of vacancies, δc , was estimated for the case of copper by Jongenburger⁽⁷⁾ to be

1959

$$\delta V/V = 0.6 \ \delta c$$
.

This is in very close agreement with recent theoretical results obtained by Terwordt⁽⁸⁾. Applying the data for copper to the present case of aluminum, the second term on the right of equation (2) would be at most 3×10^{-6} . Yet, the corrected term for the left of equation (2) exceeded 100×10^{-6} in all experiments, so that volume changes could be neglected in all computations. The corresponding plot of relative modulus change as a function of time is shown in Fig. 4.

The change of elastic modulus as a function of solute concentration was analyzed by Zener⁽²⁾. He concluded that the change in shear coefficient, μ , with strain energy, U, introduced by the size difference between solute and solvent atoms can be expressed by

$$d\mu/dU = (\frac{3}{2}Nk)^{-1} d\mu/dT \tag{3}$$

where N is the number of atoms, k is Boltzmann's constant, and T is temperature. From elasticity theory the strain energy associated with the introduction of an atom of different size from that of the matrix can be calculated, so that

$$(1/\mu)d\mu/dc = 4(\delta R/R)^2 (Nk)^{-1} d\mu/dT$$
 (4)

where R is the radius of the solute atoms and δR is the difference between solute and solvent radii. The left-hand-side of equation (4) may be considered equivalent to (1/E)dE/dc.

Combining equations (3) and (4)

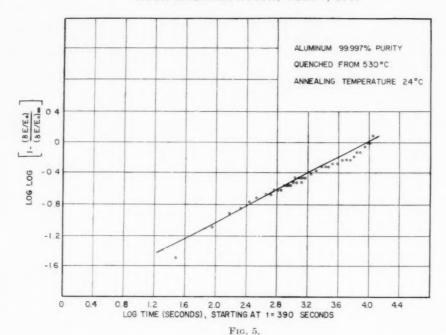
$$(1/E)dE/dc = 6(\delta R/R)^2 d\mu/dU.$$
 (5)

Using Köster's data, ⁽⁴⁾ Zener calculated $d\mu/dU = -10$ for aluminum. The atomic volume change associated with the introduction of a vacancy as computed by Jongenburger⁽⁷⁾ would lead to a value of $\delta R/R = 0.157$ in copper. Introducing these values into equation (5) yields

$$dE/E = -1.5dc \tag{6}$$

This would indicate that the maximum change in elastic modulus for specimens quenched from $530^{\circ}\mathrm{C}$ should be about 23×10^{-6} . This value, though in the proper order of magnitude, is somewhat smaller than the observed one, Fig. 4. This difference may reflect an inaccuracy in the value of 1.5 in equation (6). In general, values obtained by Zener's analysis for modulus changes as a result of solute introduction were found to be lower than experimentally determined

^{*} Estimate based on data by Bradshaw and Pearson, $^{(6)}$ assuming that 1 per cent vacancy concentration causes a change in electrical resistivity of 1.5 \times 10⁻⁶ Ω -cm.



ones. It is therefore likely that the coefficient in equation (6) in reality is greater than 1.5.

Dienes⁽³⁾ estimated that the change of modulus should be in the same order as the change in vacancy concentration. This, again, is in line with experimental evidence presented here.

The rate at which vacancies are eliminated during annealing was discussed by Wintenberger⁽⁹⁾. He used the relation

$$c(t) = c_0 \exp\left(-At^m\right) \tag{7}$$

where c_0 is the vacancy concentration at time t=0, and A and m are constants. Wintenberger's measurements of electrical resistivity revealed that $m=\frac{1}{2}$ for aluminum quenched from 500°C and annealed at room temperature.

One can make use of this analysis in the interpretation of the data of Fig. 4. Equation (6) can be integrated

$$\int_{E_0}^E \!\! d\ln E = -K \int_{c_0}^c \!\! dc$$

or

$$\ln (E/E_0) \simeq \delta E/E_0 = Kc_0(1 - c/c_0)$$
 (8)

Combining equations (7) and (8)

$$\delta E/E_0 = Kc_0[1 - \exp(-At^m)]$$

It follows that $\lim_{t\to\infty} (\delta E/E_0) = Kc_0$ for A>0. This limit can be evaluated from Fig. 4, so that

$$\log \log \left[1 - \frac{\delta E/E_0}{(\delta E/E_0)_{\infty}}\right]^{-1} = \log \frac{A}{2.3} + m \log t \quad (9)$$

A plot in terms of equation (9), given in Fig. 5, demonstrates the linearity anticipated. The slope by computation of least squares from 41 experimental points is 0.51, corroborating Wintenberger's resistivity results. The value of A obtained by this method was $2.0 \times 10^{-2}~{\rm sec}^{-1/2}$. According to Wintenberger,

$$A = \pi \rho_D (2DW_M b^2/kT)^{1/2}$$

where $\rho_D =$ density of dislocations.

D = vacancy diffusion coefficient, estimatedas $10^{-10} \text{ cm}^2/\text{sec.}$

b = magnitude of Burgers Vector.

 $W_M=$ interaction energy between vacancies and dislocation, estimated to be $Gb^3/10$, where G= shear modulus.

k = Boltzmann's constant.

T = absolute temperature of anneal.

The only unknown in this case would be the dislocation density which, from the above data for A, could then be estimated to be

$$\rho_D = 4 \times 10^9 \text{ cm}^{-2}$$
.

This value is reasonably close to accepted values for dislocation densities in annealed metals.

4. CONCLUSIONS

From the above discussion it appears that the study of point-defect migration by means of elastic measurements may be successfully undertaken. From the behaviour of Young's modulus in a quenched

high-purity aluminum wire the following conclusions may be drawn:

- (1) Quenched-in vacancies decrease the elastic modulus.
- (2) The measured change is in the expected order of magnitude, if Zener's analysis for solute atoms is applied to vacancies. Results predicted by Dienes would be equally valid.
- (3) The kinetics of the modulus change are in close agreement with data obtained by Wintenberger by means of electrical resistivity measurements.

ACKNOWLEDGMENT

The authors are indebted to the Aluminum Com-

pany of America, which supplied the research grant under which this work was carried out.

REFERENCES

- 1. W. KÖSTER and W. RAUSCHER, Z. Metallk. 39, 111
- 2. C. ZENER, Acta Cryst. 2, 163 (1949).

- G. J. Dienes, Phys. Rev. 86, 228 (1952).
 W. Köster, Z. Metallk. 39, 1 (1948).
 Piezotronic Technical Data. Brush Electronics, Cleveland (1953).
- 6. F. J. Bradshaw and S. Pearson, Phil. Mag. Ser. 8, 2, 570 (1957)

- P. JONGENBURGER, Phys. Rev. 106, 66 (1957).
 L. TERWORDT, Phys. Rev. 109, 61 (1958).
 M. WINTENBERGER, C. R. Acad. Sci., Paris 242, 128 (1956); Ibid. 244, 2800 (1957).

THE ATTACK OF SOLID ALLOYS BY LIQUID METALS AND SALT MELTS*

J. D. HARRISON† and C. WAGNER‡

If one component of a solid alloy is leached out by a liquid metal or salt melt at elevated temperatures, a plane solid–liquid interface is not stable according to a theoretical analysis. Thus a highly rugged interface may develop. In accord herewith, rapidly advancing liquid penetrations have been observed (1) in solid Cu–Ni alloys involving 18–87 at. % Cu immersed in liquid Ag at 1000°C with preferential dissolution of Cu, (2) in solid Au–Cu alloys involving 67 and 74 at. % Au immersed in liquid Bi at 400°C with preferential dissolution of Au, and (3) in solid Ag–Au alloys involving 12 at. % Au from which Ag was dissolved anodically in molten AgCl at 800°C. In contrast, a plane solid–liquid interface has been found when Cu–Ni alloys were immersed in liquid Bi at 800°C since the solubilities of Cu and Ni in liquid Bi are about equal.

L'ATTAQUE D'ALLIAGES SOLIDES PAR LES METAUX LIQUIDES ET LES SELS FONDUS

Si l'un des constituants d'un alliage solide est dissous sélectivement par un métal liquide ou un sel fondu à haute température, la théorie montre qu'une interface plane solide-liquide ne peut être stable. En conséquence, une interface très irrégulière peut se former. En accord avec ces remarques, des pénétrations rapides de liquides ont été observées:

l dans des alliages Cu-Ni contenant de 18 à 87% atomiques de cuivre immergés dans l'argent liquide à 1000°C (dissolution sélective du cuivre).

2 dans des alliages Au–Cu contenant 67% et 74% at. d'or immergé dans le bismuth liquide à 400% (dissolution sélective de l'or)

3 dans des alliages Ag
–Au à 12% at. d'or dont l'argent a été dissous par voie anodique dans Ag
Cl fondu à 800%C.

Au contraire, une interface solide-liquide plane a été observée lorsque les alliages Cu-Ni ont été immergés dans le bismuth liquide à 800°C car les solubilités du cuivre et du nickel dans le bismuth liquide sont égales.

AUFLÖSUNG FESTER LEGIERUNGEN IN FLÜSSIGEN METALLEN UND SALZSCHMELZEN

Wenn man bei hohen Temperaturen eine Komponente einer festen Legierung durch ein flussiges Metall oder eine Salzschmelze auslaugt, ist nach einer theoretischen Untersuchung eine ebene Grenzfläche fest-flüssig nicht stabil, sondern es entwickeln sich oft sehr zackige Grenzflächen. In Übereinstimmung hiermit wurde ein schnelles Eindringen der Flüssigkeit beobachtet (1) bei festen Cu-Ni-Legierungen mit 18–87 Atom% Cu in flüssigem Ag bei 1000°C, wobei vorzugsweise Cu gelöst wird; (2) bei festen Au-Cu-Legierungen mit 67 und 74 Atom% Au in flüssigem Bi bei 400°C, wobei vorzugsweise Au gelöst wird; (3) bei festen Ag-Au-Legierungen mit 12 Atom% Au, aus denen Ag in geschmolzenem AgCl bei 800°C anodisch gelöst wurde. Dagegen wurde eine ebene Grenzfläche festflüssig gefunden, wenn Cu-Ni-Legierungen in flüssiges Bi von 800°C getaucht wurden, da Cu und Ni in flüssigem Bi etwa gleich gut löslich sind.

INTRODUCTION

When a pure solid is dissolved in a liquid, e.g. NaCl in $\rm H_2O$, the rate of dissolution is, in general, determined by two processes in series, (1) the transition of individual atoms, ions, or molecules from the solid into the liquid phase and (2) diffusion from the solid-

liquid interface toward the bulk liquid, in most cases supported by natural or free convection of the liquid. As a limiting case first considered by Noyes and Whitney⁽¹⁾ and Nernst⁽²⁾, equilibrium at the interface, i.e. exclusive transport control may be assumed. In many instances, e.g. dissolution of NaCl(3) or benzoic acid, (4) observed dissolution rates agree quite satisfactorily with rates calculated from equations derived for exclusive transport control. Eldred⁽⁵⁾ has reviewed available observations on metallic systems. Ward and Taylor⁽⁶⁾ have recently investigated the rate of dissolution of solid Cu in liquid Bi and Pb between 360° and 410°C with both natural and forced convection. They have concluded that the rate is mostly diffusion controlled. Lommel and Chalmers⁽⁷⁾ have found prevailing diffusion control for the dissolution

191

^{*} This investigation was sponsored by the U.S. Atomic Energy Commission under Contract AT(30-1)-1903. The paper is based on a thesis submitted by J. D. Harrison in partial fulfillment of requirements for the degree of D.Sc. in metallurgy, Massachusetts Institute of Technology, Cambridge, Mass. Received October 7, 1958.

bridge, Mass. Received October 7, 1958.

† Department of Metallurgy, Massachusetts Institute of Technology, Cambridge, Massachusetts; present address: Fritz Haber Institut der Max Planck Gesellschaft, Berlin-

Dahlem, Germany.

† Department of Metallurgy, Massachusetts Institute of Technology, Cambridge, Massachusetts; present address: Max Planck Institut für physikalische Chemie, Göttingen, Comment.

of solid Pb in liquid Sn in the absence of natural and forced convection. In experiments involving forced convection, however, the phase boundary reaction was found to be an additional controlling factor. Local variations of the rate of dissolution were attributed to a dependence of the rate of the phase boundary reaction on the orientation of individual grains.

The dissolution of solid alloys in liquid metals is still more complex because in general the solubilities of the components of the solid alloy in the liquid differ. Hence there is the tendency for one component to be dissolved preferentially. The surface of the solid alloy is thereby depleted with respect to the more soluble component, and accordingly diffusion in the solid alloy becomes another important factor in addition to phase boundary reactions and diffusion in the liquid.

A theoretical analysis of diffusion processes occurring during the oxidation of alloys involving noble metals⁽⁸⁾ has shown that a plane alloy-oxide interface is stable if diffusion in the alloy is rapid in comparison to diffusion in the oxide layer. If diffusion in the alloy is slow, there is a tendency to form a rugged alloy-oxide interface and the rate of oxidation may be much higher than for a plane interface. A similar situation prevails when a solid alloy is brought in contact with a liquid phase which dissolves one component of the alloy preferentially. The liquid phase may penetrate the solid alloy along grain boundaries, but attack within grains is also possible.

VOL.

1959

In this paper, experiments and theoretical considerations are confined to elevated temperatures, with volume diffusion rather than grain boundary or surface diffusion as the mechanism for the movement of the constituent atoms in the alloy. The liquid medium in which one component dissolves preferentially may be either a liquid metal or a salt melt. In the latter case, preferential dissolution of the less noble component may be effected either by an applied current with the solid alloy as anode, or by the presence of an oxidizer.

Pronounced localized attack of stainless steel in liquid lead at about 800°C has been reported by Cathcart and Manly^(9–11). Similar observations have been reported by Graf and Klatte^(12,13) for Au–Cu alloys in liquid Hg, though at significantly lower temperatures (70°–170°C) where the mechanism of solid state diffusion is complex. Further complications are due to the occurrence of intermetallic compounds in the system Au–Hg and also, below 96°C. in the system Cu–Hg. Earlier observations on various alloys in liquid metals have been cited in a report by Eldred⁽⁵⁾.

Smith et al. (14-16) have made extensive investigations

on stainless steel in molten sodium hydroxide at 700° – 800° C. In addition, numerous observations have been published on preferential dissolution of the less noble components of alloys in aqueous solution at 0° – 100° C.

A particularly simple case is the attack of solid Cu–Ni alloys by liquid silver since copper and nickel are completely miscible in the solid state and neither copper nor nickel forms an intermetallic compound with silver. At 1000°C liquid silver dissolves up to 89 at.% copper,(17) whereas the solubility of solid nickel in liquid silver is only 0.5 at.%. Thus copper is leached out preferentially from a solid Cu–Ni alloy immersed in liquid silver, and the surface of the solid alloy becomes depleted with respect to copper.

With the help of calculations analogous to those for the oxidation of alloys involving noble metals, (8) it may be shown rigorously that a plane solid-liquid interface is not stable. The salient points may be understood without calculations. Fig. 1 shows a slight perturbation of a plane interface between a solid alloy A-B and liquid metal C in which B is virtually insoluble. Thus only metal A is dissolved. Diffusion of metal A takes place in both the solid and the liquid phases but diffusion in the solid phase is mainly the rate-determining step. The effective length of the path for diffusion of metal A from the bulk solid toward the interface is greater at point I than at point II, as is indicated schematically in Fig. 1 by arrows of different lengths. Thus more metal A is removed at point II than at point I, and accordingly the interface recedes further at point II than at point I. As the amplitude of the perturbation increases with time, it follows that a plane interface is not stable.

After an induction period, deep penetrations of liquid metal may occur between trunks of solid alloy. Two limiting cases shown schematically in Figs. 2 and 3 can be anticipated. Fig. 2 shows widely spaced wedges of penetrating liquid separated by large regions of solid alloy having mainly the original composition.

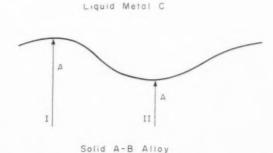


Fig. 1. Leaching of copper (= metal A) from a solid Cu–Ni alloy (= A–B alloy) by liquid Ag (= metal C) saturated with nickel.

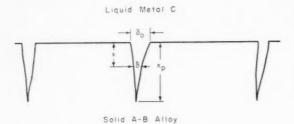


Fig. 2. Wedges filled with liquid metal C in a solid A-B alloy.

Fig. 3 shows a highly rugged penetration zone with very slender solid trunks consisting mainly of the less soluble component B.

According to the foregoing analysis, fluctuations as required by the atomic structure of matter are sufficient to initiate the formation of a highly rugged interface. In addition, irregularities present in real crystals and especially in polycrystalline material may be operative. In particular, wedge-like penetrations of the liquid phase may be initiated by grain boundaries. This follows from considerations by Smith⁽¹⁹⁾ and observations by Ikeuve and Smith (20). Consider the interface between polycrystalline pure metal A and liquid metal C saturated with A. If a grain boundary extends to the solid-liquid interface, and accordingly two grains and the liquid phase meet along a common edge, local equilibrium requires definite dihedral angles between the solid-liquid interfaces and the grain boundary. These angles are determined by the values of the grain boundary free energy and the solid-liquid interfacial free energies. Consequently, by virtue of dissolution and redeposition of metal A in the liquid, small grooves are formed until the dihedral angles have attained their equilibrium values. Robertson and Bakish(21) have pointed out that such grooves are also to be expected in the case of alloys and may initiate the formation of deeper penetrations as shown in Fig. 2. This explains the grain boundary penetrations reported below.

In addition, transgranular penetrations have been

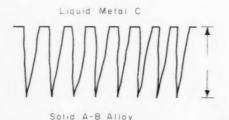


Fig. 3. Penetrations of liquid metal C in a solid A-B alloy with slender trunks of B-rich alloy.

observed in the present research, especially in alloys rich in the more soluble component. Robertson and Bakish⁽²¹⁾ have observed that transgranular attack of Cu–Au alloys in aqueous solutions is initiated by slip clusters and other imperfections inside individual grains. The same may be true for the attack of solid alloys by liquid metal at elevated temperatures. This hypothesis, however, has not yet been tested during the present investigation.

OUTLINE OF INVESTIGATIONS

Although the solubilities of Cu and Ni in liquid Ag at 1000°C, 89 and 0.5 mole % respectively, differ widely, both Cu and Ni dissolve when Cu-Ni alloys are immersed in liquid Ag. However, dissolution of Ni may be completely suppressed by saturating the liquid Ag in advance with Ni. The attack of solid Cu-Ni alloys in liquid Ag saturated with Ni at 1000°C has therefore been investigated, in order to have conditions corresponding to the limiting case of exclusive removal of one component of a solid alloy. These experiments have been supplemented by a study of the somewhat more complex attack of solid Cu-Ni alloys by liquid Ag in which no Ni was present initially. Excessive accumulation of Ni in the liquid Ag was prevented as Ni was continually removed by the displacement reaction:

A similar case is the attack of solid Au–Cu alloys by liquid Bi at 400°C with preferential dissolution of Au, since the solubilities of Au and Cu in liquid Bi at 400°C are about 39 and 2 mole % respectively. (17) Also in this case, there was a complete series of solid solutions in the solid system Au–Cu since samples of the alloys used in these runs were quenched from 500°C in order to prevent the formation of ordered structures, and the immersion experiments lasted only for short times. Neither Au nor Cu forms a solid compound with Bi at 400°C. (17)

As a counterpart, the attack of Cu–Ni alloys in liquid Bi at 800°C has been investigated. In this system, the solubilities of the components of the solid alloy in the liquid solvent are of the same order of magnitude, 40 and 27 mole % Cu and Ni, respectively. (17) Since these solubilities are nearly equal, there is no pronounced tendency for preferential removal of one or the other component from the solid alloy. Thus no instability of a plane solid–liquid interface is anticipated and in accord herewith no rugged interface has been found.

In addition, the behavior of solid Ag-Au alloys as

VOI 7 19 anodes in molten AgCl has been investigated at a constant electrode potential, leading to virtually exclusive dissolution of Ag.

EXPERIMENTAL

Preparation of alloys

VOL.

1959

Cu–Ni alloys: Reagent grade copper and nickel were melted separately under hydrogen in order to remove oxygen. Alloys were prepared in an induction furnace. A charge consisting of about 10% Cu and 90% Ni was melted under vacuum, helium was admitted, and a sample of the alloy was sucked into a 9 mm Vycor tube. Alloys involving more copper were obtained by adding appropriate amounts of copper to the remaining charge and repeating the foregoing procedure. According to electrolytic determinations of the copper content, the synthetic alloys contained 10, 18, 29, 39, 46 and 58 mole % Cu. In addition, two commercial alloys involving 66.7 and 84.2 at. % Cu were investigated.

The synthetic alloys were cold-rolled to a thickness of 0.2–0.3 cm, annealed for 15 hr in purified nitrogen at 1000°C, rolled to a final thickness of about 0.1 cm, and annealed once more for 18 hr at 1000°C. Upon microscopical examination of surfaces etched in acid $\rm K_2Cr_2O_7$ solution, no significant inhomogeneities were detected.

Most of the samples were bright after annealing and were used without abrasion. Samples which had tarnished slightly during annealing were abraded with No. 1 emery paper.

Au–Cu alloys with 10, 33, 61 and 74 at. % Au obtained in the form of plates 2 mm thick* were annealed 116 hr at 800°C for homogenization, quenched in water, and rolled to 1 mm thickness. From this stock, platelets $7\times10\times1$ mm were cut, annealed 30 hr at 500°C, and quenched in water.

Ag–Au alloys involving 88, 65 and 44 at. % Ag were obtained from the same source. Samples $6\times10\times2$ mm were cut and annealed 100 hr at 850°C for homogenization.

General procedures for investigations on the attack of solid Cu–Ni and Au–Cu alloys by liquid metals

To investigate the rate of attack of solid Cu–Ni alloys in liquid Ag, platelets of the alloy $0.7 \times 1.0 \times 0.1$ cm with a hole at one end, held by a slotted 6 mm Vycor tube as shown in Fig. 4, were immersed in liquid metal contained in a 25 mm Vycor tube under nitrogen. In part, samples remained at rest. In part, samples were rotated at 60 rev/min.

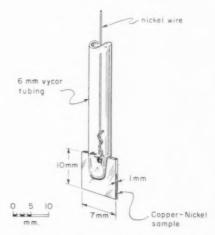


Fig. 4. Sample holder for Cu-Ni alloys.

To saturate the silver with nickel, excess nickel shot was added before the beginning of a run. An atmosphere of purified nitrogen was provided until the silver was melted. To exclude presence of oxygen during a run, molten KCl was placed above the liquid silver.

In order to investigate the attack of Cu–Ni alloys in Ag not saturated with nickel, an amount of 15–30 g molten AgCl was placed above a charge of about 150 g Ag. Accumulation of an excessive concentration of Ni in Ag was prevented as nickel was continually removed by displacement reaction (1).

Preliminary runs showed considerable local differences in the rate of attack of the same sample. Invisible oxide films and other kinds of surface contamination were suspected of preventing contact between the solid and the liquid metal on part of the surface. This situation was remedied by dipping alloy samples in fused Na₂B₄O₇ prior to immersion in liquid Ag. The remaining layer of borax on the surface of the samples was removed when the latter passed the molten KCl or AgCl above the liquid metal.

Cu–Ni alloys were tested similarly in liquid Bi covered by molten KCl at 800°C.

Au–Cu alloys were tested in liquid Bi covered by a ZnCl₂–NaCl melt containing 17 wt. % NaCl at 400°C, without previous dipping in fused borax.

The samples from all tests were sectioned perpendicular to the 7×10 or 6×10 mm face, mounted in bakelite, ground, and polished. Flatness was essential to reveal the details at the edges of the samples. For this reason, a hard thin silk cloth and fine gamma alumina abrasive were used for the final polishing.

Satisfactory flatness was achieved, but some scratching could not be avoided, especially with the soft Ag-Au alloys.

Cu-Ni alloys were etched with a solution consisting

^{*} From Baker and Co., Newark, N.J.

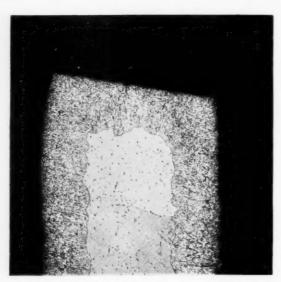


Fig. 5. Section of a Cu–Ni alloy ($N_{\rm Cu}{}'=0.29$) after immersion in liquid Ag saturated with Ni at 1000°C for 12 min. $\times 50$.

of 2 g $\rm K_2Cr_2O_7$, 4 ml saturated NaCl solution, 6 ml $\rm H_2SO_4$, and 100 ml $\rm H_2O^{(22)}$ Grain boundaries were weakly etched. Penetrations of Ag and Bi were darkly stained.

Au–Cu and Ag–Au alloys were etched with a freshly prepared mixture of equal parts of a 10% KCN solution and a 10% (NH₄)₂S₂O₈ solution. Penetrations of Bi or AgCl were readily etched. The same etchant also revealed grain boundaries, but only after much

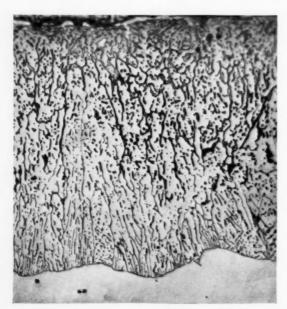


Fig. 6. Section of a Cu–Ni alloy ($N_{\rm Cu}=0.39$) after immersion in liquid Ag saturated with Ni at 1000°C for 4 min. $\times\,250$.

longer application when the penetrations of Bi or AgCl were overetched.

Solid Cu-Ni alloys in liquid silver saturated with nickel

Upon microscopical examination of Cu–Ni alloys immersed in liquid Ag at 1000°C and rotated at 60 rev/min, it was found that liquid silver had penetrated into the samples as shown schematically in Figs. 2 and 3 except for samples involving only 10 at. % Cu.

Fig. 5 shows the photomicrograph of a sample containing 29 at. % Cu sectioned perpendicular to the initial surface. The penetrations of silver appear as fine dark lines owing to etching with dichromate

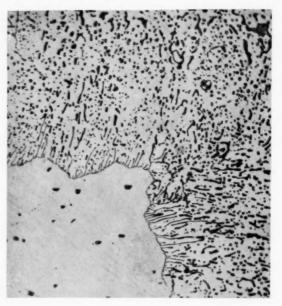


Fig. 7. Section of a Cu–Ni alloy ($N_{\rm Cu}=0.29$) after immersion in liquid Ag saturated with Ni at 1000°C for 12 min. $\times 250$.

solution. The spacing between these penetrations is much smaller than the average grain size of the original alloy. Thus transgranular penetrations do occur. The same general type of attack was observed with all alloys involving copper contents between 29 and 87 at. 0 /₀ Cu.

Fig. 6 is a photomicrograph taken at a higher magnification in order to illustrate details of the structure of the penetration zone. Inasmuch as the photomicrograph represents only a two-dimensional section through a three-dimensional structure, penetrations are not generally revealed in simple repose but rather appear as separate oblique segments. Some penetrations, however, may be traced over fairly long distances or even over almost the entire thickness of the penetration zone. This suggests wedge-like rather than needle-like penetrations. Fig. 6 also reveals

VO: 7 19

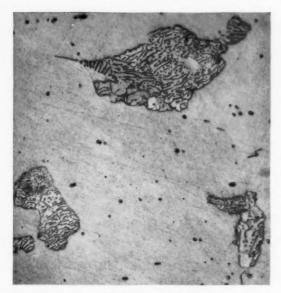


FIG. 8. Section of a Cu–Ni alloy ($N_{\rm Cu}{}'=0.29$) polished parallel to the original surface after immersion in liquid Ag saturated with Ni at 1000°C for 12 min. $\times 250$.

frequent side-branching of penetrations not shown in the schematic drawings in Figs. 2 and 3.

For further clarification, half a sample involving 29 at. % Cu was sectioned perpendicular to the initial surface (see Fig. 7) and the other half was ground and polished parallel to the initial surface until most of the penetration zone had been removed (Fig. 8). The dark patches of silver-rich alloy in Fig. 8 with a pattern similar to that of pearlite show the top view of wedgelike penetrations. Conclusions drawn from Fig. 6 are thereby confirmed.

1959

Fig. 9 shows preferential penetration at grain boundaries in an alloy involving 67 at. % Cu, in which grain boundary attack was most pronounced.



Fig. 9. Section of a Cu–Ni alloy ($N_{\rm Cu}'=0.67$) after immersion in liquid Ag saturated with Ni at 1000 C for 3 min. $\times 250$.

Samples involving 18 at. % Cu showed non-uniform attack. At some spots, a rugged penetration zone formed readily, whereas at other spots the liquid-solid interface remained essentially plane. The longer the time of immersion, the greater was the part of the surface showing penetrations.

On samples involving 10 at. % Cu, no rugged penetration zone was found.

Fig. 10 shows a logarithmic plot of representative values of the depth of penetrations x_p as a function of time t. The results obtained for each alloy may be approximated by straight lines. Except for the alloy involving only 18 at. % Cu, where values of x_p are not very well defined because of large local differences, the slopes of the straight lines are closer to 0.5 than to unity, i.e. the depth of penetration x_p is approximately proportional to the square root of time. This suggests prevailing diffusion control.

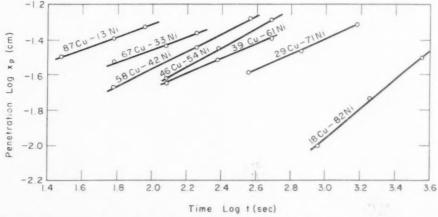


Fig. 10. Logarithmic plot of depth of penetration, x_p , of liquid Ag saturated with Ni in solid Cu–Ni alloys at 1000° C, vs. time t.

Solid Cu-Ni alloys in liquid Ag not saturated with Ni

Solid Cu–Ni alloys in liquid Ag from which Ni was continually removed by a displacement reaction with liquid AgCl, according to equation (1), showed essentially the same type of rugged penetration zones as Cu–Ni alloys in liquid Ag saturated with nickel. Also the depths of penetration were about the same, and the results are therefore not presented in detail.

Solid Cu-Ni alloys in liquid Bi

The attack of solid Cu–Ni alloys in liquid Bi has been investigated as a counterpart to the attack of these alloys in liquid Ag. It has been mentioned above that the solubilities of Cu and Ni in liquid Bi at 800°C, 40 and 27 mole %, respectively, do not differ widely. In view of these high solubilities, Cu–Ni samples were immersed in liquid Bi at 800°C only for 15 and 30 sec in order to prevent complete dissolution. Only static tests were made. In accord with theoretical considerations presented above, microscopical examination of sectioned samples revealed no major irregularities of the liquid–solid interface but only small grooves at grain boundaries similar to those found at the interface between a pure solid metal and another liquid metal according to Smith⁽¹⁹⁾.

Tests on alloys were supplemented by tests with pure Cu and Ni. The decrease in thickness of samples of the pure metals and Cu-Ni alloys after immersion was measured microscopically on sectioned samples. Therefrom the recession of the solid-liquid interface was calculated. The decrease in thickness of individual samples showed local variations of the order of +50per cent. Representative values of the recession of the solid-liquid interface after 15 sec were found to be of the order of 0.01 cm. This is also the order of magnitude calculated for the limiting case of exclusive diffusion control and natural convection of the ambient liquid. (3,4) Thus diffusion of the dissolved atoms away from the surface is an important factor. In view of the local variations of the recession of the solid-liquid interface, however, the dissolution rate seems to be controlled in part also by a phase boundary reaction whose rate depends on the orientation of individual grains, and eventually on other factors such as the density of dislocations and other imperfections.

Further tests were made at lower temperatures, 500° and 340°C, where, however, conditions are more complex because of the occurrence of the solid compounds BiNi and BiNi₃.⁽¹⁷⁾ Liquid solutions Cu–Bi saturated with Cu at 500° and 340°C, respectively, contain about 5 and 1 mole % Cu.⁽¹⁷⁾ Liquid solutions Bi–Ni coexisting with solid NiBi and NiBi₃, respectively, contain about 13 mole % Ni at 500°C and 1 mole

 $^{\circ}$ /_o Ni at 340°C.⁽¹⁷⁾ Thus the maximum concentrations of Cu and Ni in liquid Bi are of the same order of magnitude also at 500° and 340°C. In accord herewith, Cu–Ni samples immersed in liquid Bi at 500° and 340°C and rotated at 60 rev/min did not show rugged penetration zones. Thin intermediate white layers found on sections etched with dichromate may be attributed to the formation of Bi–Ni compounds.

Sclid Au-Cu alloys in liquid Bi

The attack of solid Au–Cu alloys in liquid Bi without rotation was investigated at 400°C. Since the solubilities of pure Au and pure Cu in liquid Bi at 400°C are 39 and 2 at. %, respectively, (17) Au is leached out preferentially. Thus the formation of rugged penetration zones similar to those found on Cu–Ni samples in liquid Ag may be expected. Experimental results are in accord herewith, see Figs. 11–14.

Fig. 15 shows a logarithmic plot of representative values of the depth of penetration as a function of time t. The results obtained for each alloy may be approximated by straight lines. The slopes are closer to 0.5 than to unity. This suggests prevailing diffusion control.

The behaviour of solid Ag-Au anodes in molten AgCl

19

As has been mentioned above, a rugged penetration zone is also expected when a solid alloy is treated as an anode in an electrolyte, under conditions where virtually only the less noble component is dissolved. The behaviour of Ag-Au anodes in aqueous electrolytes investigated by Tischer and Gerischer (23) is in accord, with this conclusion. To test this conclusion further the behaviour of solid Ag-Au alloys involving 88, 65 and 44 at. % Ag has been studied in molten AgCl as electrolyte with a cathode consisting of pure Ag. Preliminary tests were made at 500°C in a Pyrex vessel. Final tests were made at 800°C in a Vycor vessel as shown in Fig. 16. Cathode and anode compartment were separated by a Vycor frit in order to prevent short circuits resulting from dendritic Ag deposition at the cathode.

In the final runs, constant voltages of 0.1, 0.2, 0.3 and 0.4 V, respectively, were supplied from a potentiometer circuit of low resistance. In most runs the resulting current was measured with the help of a galvanometer and an Ayrton shunt in series with the cell. The voltage drop in the meter for the current did not exceed 0.003 V.

Each alloy sample was weighed before the run. After the run it was placed in a solution of Na₂S₂O₃ in order to remove adherent AgCl. After rinsing with water and drying, the final weight of the sample was

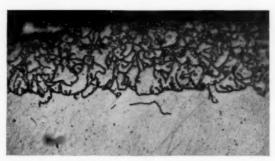
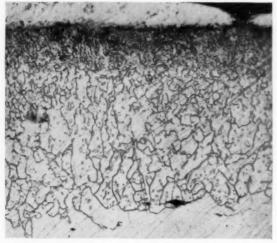


Fig. 11. Section of a Au–Cu alloy $(N_{Au'}=0.74)$ after immersion in liquid Bi at 400°C after 3 min. $\times\,250$.



Fig. 13. Section of a Au–Cu alloy $(N_{Au'}=0.33)$ after immersion in liquid Bi at 400 °C for 60 min. $\times 250$.



1959

Fig. 12. Section of a Au–Cu alloy ($N_{Au'}=0.61$) after immersion in liquid Bi at 400°C for 10 min. $\times 250$.

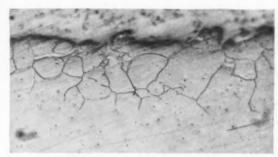


Fig. 14. Section of a Au–Cu alloy $(N_{Au'}=0.10)$ after immersion in liquid Bi at 400°C for 70 min. $\times 250$.

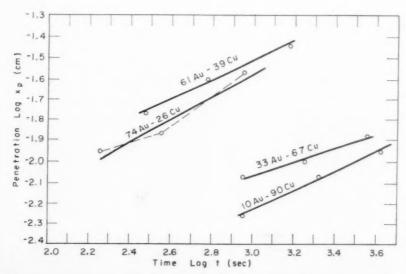


Fig. 15. Logarithmic plot of depth of penetration, x_p , of liquid Bi in solid Au–Cu alloys at 400°C, vs. time t.

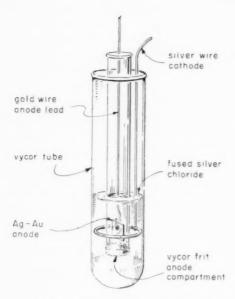


Fig. 16. Vessel for the investigation of anodic attack of solid Ag–Au alloys in molten AgCl at 800°C.

determined. The weight loss was compared with values calculated from the current—time integral and Faraday's law, assuming that the anodic process involves only formation of monovalent silver ions. At an applied voltage of 0.2 V, observed and calculated weight losses did not differ to a large extent. Deviations up to 20 per cent might be ascribed to incomplete removal of AgCl by Na₂S₂O₃. At voltages of 0.3 and 0.4 V, the observed weight losses were in some runs less than half the calculated values. No explanation for this discrepancy can be offered. Therefore, only results for runs with a voltage of 0.2 V will be discussed.

Microscopical examination of sectioned and etched samples showed significant grain boundary penetration of AgCl in all alloys and even in pure Ag.

Samples involving 88 at. % Ag showed the formation of highly rugged penetration zones in addition to more rapidly advancing penetrations along grain boundaries. No definite statement can be made with regard to the behaviour of alloys involving 65 at. % Ag. Samples involving 44 at. % Ag showed only grain boundary penetration but no transgranular penetration.

Although the tests with Ag–Au samples in molten AgCl are rather incomplete, it may be noted that the tendency for the formation of a rugged penetration zone was not very pronounced, especially in comparison with the behaviour of Cu–Ni alloys in liquid Ag and that of Ag–Au alloys in gaseous or liquid sulfur leading to the formation of Ag₂S. (24)

THEORETICAL ANALYSIS

Solid Cu-Ni alloys in liquid silver saturated with nickel

If liquid silver is saturated with nickel, only copper is dissolved. Since the diffusivity of copper in the solid alloy is much lower than in the liquid phase, the rate of copper removal may be assumed to be controlled essentially by diffusion in the solid alloy. In what follows, the rate of recession of the solid–liquid interface for a solid alloy A–B in liquid metal C saturated with metal B is calculated.

In the case of a plane interface, the mole fraction $N_{\rm B}{}'$ in a solid alloy A–B is a function of distance x from the initial solid–liquid interface and time t Thus Fick's second law reads

$$(\partial N_{\rm B}'/\partial t) = D'(\partial^2 N_{\rm B}'/\partial x^2)$$
 at $x > x_i$ (2)

where x_i denotes the distance of the solid-liquid interface at time t from the initial solid-liquid interface and the diffusion coefficient D' in the alloy is assumed to be independent of alloy composition.

If the solubility of A in the liquid phase is high and the concentration of A in the bulk liquid is low, the solid allow at the interface is virtually pure B, i.e.

$$N_{\mathrm{B}}^{'} \cong 1$$
 at $x = x_{i}$, (3)

Since no metal B enters the liquid phase, backward diffusion of B from the solid–liquid interface toward the bulk alloy must keep pace with the rate of recession $u=dx_i/dt$ of the solid–liquid interface. From the principle of the conservation of mass and Fick's first law it follows that

$$N_{\rm B}{'}u = D'(\partial N_{\rm B}{'}/\partial x)$$
 at $x = x_i$ (4)

In addition, there is the initial condition

$$N_{\rm B}{}' = N_{\rm B}^{\prime(0)}$$
 at $x > 0, t = 0$ (5)

where $N_{\rm B}^{\prime(0)}$ is the initial mole fraction of B in the solid alloy.

If the thickness of the alloy sample is sufficiently large, virtually no change in composition takes place in the midplane. Thus the solution for diffusion from a semi-infinite space applies.⁽²⁵⁾ Equations (2)–(5) are found to be satisfied by

$$x_i = 2\alpha (D't)^{1/2} (7)$$

where the dimensionless parameter α is determined by the auxiliary equation

$$\pi^{1/2}\alpha \exp \alpha^2 \operatorname{erfc} \alpha = 1 - N_{\mathrm{R}}^{\prime(0)}$$
 (8)

If the initial mole fraction of the more soluble component A, $N_A^{\prime(0)}=1-N_B^{\prime(0)}$, is low, α is much less than unity. Thus the exponential function and the complementary error function in equation (8) are nearly equal to unity whereupon

$$\alpha \simeq N_A^{\prime(0)}/\pi^{1/2}$$
 if $N_A^{\prime(0)} \ll 1$ (9)

Substitution of equation (9) in equation (7) yields

$$x_i \simeq 2N_A^{\prime(0)}(D't/\pi)^{1/2}$$
 if $N_A^{\prime(0)} \ll 1$ (10)

Actually, however, a plane solid-liquid interface is not stable according to theoretical considerations and experimental results reported above. Therefore, one may try to calculate the rate of attack for conditions involving the formation of deeply penetrating zones of liquid metal between trunks of solid alloy shown schematically in Figs. 2 and 3. If the width of the liquid zones is much smaller than their depth, concentration differences in the liquid in directions parallel to the initial solid-liquid interface are negligible. For a quantitative theoretical analysis, one may, therefore, consider the concentration of A in the liquid phase as a function of time t and distance x alone. Since the diffusivity of A in the solid alloy is much lower than in the liquid, diffusion of A in the solid alloy occurs mainly in the direction perpendicular to the local solid-liquid interface, i.e. from the interior of the solid trunks to the liquid in a direction parallel to the original solid-liquid interface.

Two different limiting cases may be considered.

(1) The penetrating liquid zones are close together as is shown in Fig. 3. Accordingly the trunks of solid alloy are very thin and local equilibrium between the solid and the liquid phase at each distance x is virtually attained. With the help of calculations analogous to those for the rate of oxidation of alloys involving noble metals, $^{(8)}$ the depth of penetration x_p as a function of time t is found to be

$$x_p \simeq 2(KN_A^{\prime(0)}D_A^{"}t)^{1/2} \quad \text{if} \quad N_A^{\prime(0)} \ll 1$$
 (11)

where $D_{\Lambda}^{"}$ is the diffusion coefficient of metal A in the liquid phase and K is the distribution coefficient of A between the liquid and the solid phase for low concentrations of A. Since $D_{\Lambda}^{"}$ for diffusion in the liquid phase is much greater than D' for diffusion in the solid alloy, the depth of penetration x_p according to equation (11) is much greater than the recession of the solid–liquid interface according to equation (10).

(2) The penetrating liquid zones are widely spaced as is shown in Fig. 2. Accordingly the trunks of solid alloy have essentially the initial composition except for small regions adjacent to the penetrating zones of the liquid phase. Under these conditions, diffusion of

A from the solid trunks to the penetrating zones of the liquid phase in a direction parallel to the original solid–liquid interface corresponds virtually to diffusion from a semi-infinite space.

The depth of penetration x_p of a single wedge perpendicular to the initial surface of the alloy may be calculated with the help of an integral method analogous to that used in hydrodynamic boundary layer theory. (26)

Since diffusion control is assumed, one may let

$$x_p = 2\beta (D_A''t)^{1/2} \tag{12}$$

where β is a dimensionless parameter whose value is calculated below.

Next to the surface $(x \simeq 0)$, the recession of the solid-liquid interface from the midplane of the wedge is given by the right-hand member of equation (10). The width $\delta(x=0)=\delta_0$ of the wedge is twice this value,

$$\delta_0 = 4\alpha (D't)^{1/2} \tag{13}$$

where α is determined by equations (8) or (9).

The width of the wedge at any distance x may be expressed as

$$\delta = \delta_0 f(\xi) \tag{14}$$

where

$$\xi = x/x_n \tag{15}$$

and $f(\xi)$ decreases from unity at $\xi = 0$ to zero at $\xi = 1$. At the tip of the wedge, distribution equilibrium of metal A between the liquid phase and the bulk alloy may be assumed as a limiting case. Thus

$$N_{A}''(\xi = 1) = N_{A}''(eq)$$
 (16)

where $N_{\rm A}{''}({\rm eq})$ is the mole fraction of A in the liquid phase in equilibrium with solid alloy of the original composition.

The mole fraction of A in the wedge decreases gradually virtually to zero at x=0 where a much larger cross section for outward diffusion of A is available, and moreover diffusion is supported by convection. Thus

$$N_{\text{A}}'' = N_{\text{A}}''(\text{eq})g(\xi) \tag{17}$$

where $g(\xi)$ varies between zero for $\xi=0$ and unity for $\xi=1$. If the content of metal B in the liquid phase is neglected and the volume change on mixing liquid metals A and C is negligible, the total volume in the wedge must equal the sum of the volumes of metals A and C in the wedge. To simplify the calculation, the molar volumes of metals A and C are assumed to be equal. Thus the volume of metal C in the wedge is equal to the product of the molar volume V'' of the liquid phase and the number of moles of

VOL. 7 1959

VOI 7 195

metal C, diffused from t=0 from the bulk liquid into the wedge. The volume of metal A in the wedge is equal to the integral of the mole fraction of metal A over the volume of the wedge. Hence

$$\begin{split} \int_{0}^{x_{p}} \delta L \, dx &= -V'' \! \int_{0}^{t} \! \delta_{0} L D'' \frac{\partial}{\partial x} \left(\! \frac{N_{\text{C}}''}{V''} \! \right)_{x=0} \! dt \\ &+ \! \int_{0}^{x_{p}} \! \delta L N_{\text{A}}'' \, dx \quad (18) \end{split}$$

where $N_{\rm C}''$ is the mole fraction of metal C as solvent and L is the length of the wedge perpendicular to the cross section shown in Fig. 2.

In view of equations (12)-(17) and the relation

$$N_{\rm A}" + N_{\rm B}" + N_{\rm C}" = 1,$$

equation (18) becomes

$$\beta \int_{0}^{1} f(\xi) d\xi = N_{\Lambda}''(\text{eq}) \left[(1/4\beta)(dg/d\xi)_{\xi=0} + \beta \int_{0}^{1} f(\xi)g(\xi) d\xi \right]$$
(19)

Next, plausible functions for $f(\xi)$ and $g(\xi)$, which satisfy the conditions for $\xi = 0$ and $\xi = 1$ stated above, are introduced

$$f(\xi) = 1 - \xi^2 \tag{20}$$

$$g(\xi) = 1 - (1 - \xi)^2 \tag{21}$$

Upon substituting equations (20) and (21) in equation (19), solving for β , and introducing the latter value in equation (12), it follows that

$$x_p \simeq \left[\frac{3N_A''(\text{eq})}{1 - \frac{11}{20} N_A''(\text{eq})} D_A''t \right]^{1/2}$$
 (22)

Other functions than those suggested in equations (20) and (21) give a similar result. This justifies use of the integral method with arbitrary functions $f(\xi)$ and $g(\xi)$.

For low concentrations of A, Henry's law is supposed to hold. Thus

$$N_{\Lambda}''(\text{eq}) = N_{\Lambda}'^{(0)}K \quad \text{if} \quad N_{\Lambda}'^{(0)} \ll 1$$
 (23)

Substitution of equation (23) in equation (22) yields

$$x_n = (3KN_A^{\prime(0)}D_A^{"t})^{1/2} \text{ if } N_A^{"(0)} \ll 1$$
 (24)

The difference between values of x_p according to equations (11) and (24) is only minor, although the physical situations underlying these equations differ substantially.

The foregoing calculations involve various assumptions which may not hold. The following deviations

seem particularly important. First, equilibrium between liquid and bulk solid alloy at the tip of a wedge may not prevail. It has already been mentioned above that the rate of dissolution of pure solid metals is controlled in part by diffusion and in part by a phase boundary reaction. Moreover, transfer of A from the bulk alloy to the liquid at the tip of a wedge also requires some diffusion in the solid, though only over short distances. So far no estimate of the corresponding "diffusion resistance" has been made. Such an estimate would require a more realistic approximation for the geometry at the tip of a liquid penetration. In particular, in the case of a transgranular penetration, one may expect a rounded tip instead of a sharp edge involving a very small angle according to equations (14) and (20), since in view of the dependence of the local solubility of a solute on the radius of curvature of the interface, metal B is steadily transferred from the lateral faces of the wedge to the tip of a penetration. Under these conditions, the steady-state geometry of the wedge near the tip is determined not only by dissolution of A but also by local dissolution and redeposition of B. In view of these considerations, equation (16) is replaced by the inequality

$$N_{\text{A}}''(\xi = 1) \leqslant N_{\text{A}}''(\text{eq}) \tag{25}$$

Second, in the foregoing calculations side-branching of penetrating wedges of liquid has not been considered. Actually, side-branching does occur according to microscopical observations reported above. This also tends to decrease the depth of penetration but probably only to a minor extent.

Third, the liquid does not penetrate always in a direction perpendicular to the initial surface of the alloy. Thus the actual diffusion path in the liquid filling a wedge is somewhat greater than its projection, i.e. the distance of the tip of the wedge from the surface. Accordingly the rate of transport of A is lowered.

In view of the foregoing three reasons, equations (11) and (22) give upper limiting values of x_p rather than definite values. Hence it is more realistic to rewrite equation (22) as

$$x_p \leqslant \left[\frac{3N_A''(\text{eq})}{1 - \frac{11}{20} N_A''(\text{eq})} D_A''t \right]^{1/2}$$
 (26)

Upon solving equation (26) for t, one obtains a relation which yields the time $t(x_p)$ required for reaching a given depth of penetration,

$$t(x_p) \ge \frac{x_p^2}{3D_{\rm A}"N_{\rm A}"({\rm eq})} \left[1 - \frac{11}{20} N_{\rm A}"({\rm eq})\right]$$
 (27)

To evaluate the right-hand side of equation (27), the value D_{Λ}'' for the diffusivity in the liquid phase has been estimated to be 3×10^{-5} cm²/sec in view of other data for diffusion in liquid alloys. (27)

To obtain the mole fraction $N_A''(eq)$ of copper = metal A in the liquid for a given mole fraction $N_A''^{(0)} = N_{Cu}'$ in the solid, activities of Cu were plotted vs. the mole fraction first in the solid solution Cu–Ni and second in the liquid solution Cu–Ag, using solid copper with unit activity as the reference state. In the case of equilibrium, the activities of copper in both the solid and the liquid phases are equal. Thus one reads first the value of a_{Cu} for given values of N_{Cu}' from the plot a_{Cu} vs. N_{Cu}' for the solid system Cu–Ni, and second the value of $N_{Cu}'' = N_A''(eq)$ corresponding to the activity a_{Cu} from a plot a_{Cu} vs. N_{Cu}'' for the liquid system Cu–Ag.

Activities of Cu in liquid Ag–Cu alloys for liquid copper as the reference state have been deduced by Koros⁽²⁸⁾ from phase diagram data for 1200°C, assuming ideal entropy of mixing. Therefrom values for 1000°C and solid copper as the reference state were calculated.

The activity of Ni in solid Cu–Ni alloys has been derived by Nanis⁽²⁹⁾ from emf measurements on cells involving a borate melt saturated with NiO as electrolyte at 700°C,

$$\log a_{\text{Ni}} \simeq \log N_{\text{Ni}}' + 0.76 (1 - N_{\text{Ni}}')^2$$
 (28)

whereupon in view of the Gibbs-Duhem equation

$$\log a_{\text{Cu}} \simeq \log N_{\text{Cu}}' + 0.76 (1 - N_{\text{Cu}}')^2$$
 (29)

Therefrom the activity of Cu in solid Cu-Ni alloys at 1000°C has been calculated, assuming ideal entropy of mixing. Positive deviations from ideality as indicated by equations (28) and (29) are in accord with positive values for the heat of mixing. (30) Probably, however, deviations from ideality are less than according to equations (28) and (29) because these values suggest a miscibility gap in the system Cu-Ni below 580°C which has not yet been observed. Activities deduced from emf measurements may be in error because of a displacement reaction between alloy and electrolyte. Since the activities calculated from equation (29) are somewhat too high, values of $N_A''(eq)$ deduced from the plots mentioned above are too low. The error, however, is not important because other approximations in the evaluation of equation (27) introduce greater uncertainties.

Values of t for a penetration of $x_p = 0.025$ cm obtained by interpolation or, if necessary, by extrapolation of data shown in Fig. 10, are compared in Table 1 with values calculated from equation (27).

Table 1.—Penetration of liquid silver in solid Cu–Ni alloys at 1000° C

N_{Cu}'	$N_{ m Cu}''(m eq)$	$t(x_p = 0.025 \text{ cm})$		$t(x_i = 0.025 \text{ cm})$ see $\times 10^6$	
		obs.	cale.	cale.	
0.87	0.76	16	≥5	0.8	
0.67	0.56	40	≥8	3	
0.58	0.49	70	≥10	5	
0.46	0.42	125	≥13	11	
0.39	0.38	130	≥14	17	
0.29	0.31	400	≥19	62	
0.18	0.22	1400	≥28	110	

All observed values of $t(x_p=0.025~{\rm cm})$ are higher than the upper limits of the calculated values. For the alloy with the highest copper content $(N_{\rm Cu}'=0.87)$ the observed value is about three times higher than the calculated value. This divergence may be due essentially to the uncertainty in the estimate of $D_{\rm A}''$, to side-branching of penetrations, and to the difference between the length of the actual diffusion path and its projection. The divergence between observed values and the upper limits of the calculated values increases markedly with decreasing copper content. This indicates lack of attainment of equilibrium between the liquid at the front of penetrations and the bulk solid.

The last column of Table 1 shows values of the time $t(x_i=0.025\,\mathrm{cm})$ required for recession of a hypothetical plane solid–liquid interface by $x_i=0.025\,\mathrm{cm}$ according to equation (10), deduced for diffusion of Cu in the solid alloy as the rate determining step with $D'\cong 10^{-10}~\mathrm{cm}^2/\mathrm{sec}$ as the average diffusion coefficient. (31) The values $t(x_i=0.025\,\mathrm{cm})$ in 10^6 sec are much greater than the observed values for the advancement of penetrations. This shows that attack of solid alloys accompanied by penetrations proceeds much faster than under conditions involving a plane solid–liquid interface,

Solid Cu-Ni alloys in liquid silver not saturated with nickel

If a solid Cu–Ni alloy is immersed in liquid silver not saturated with nickel, both Cu and Ni dissolve. Also in this case, a plane solid–liquid interface may not be stable. At the bottom of a valley of a perturbed interface shown in Fig. 1, dissolution of the more soluble component A, i.e. copper, is enhanced since local differences in the rate of dissolution of A are determined mainly by diffusion of A in the solid phase toward the interface, and the effective path of diffusion of A in the solid is smaller at the bottom of a valley

1959

than at the top of a hill. On the other hand, dissolution of the less soluble component B, i.e. nickel, is retarded at the bottom of a valley since local differences in the rate of dissolution of B are determined by diffusion of B from the interface into the liquid, and the effective path of diffusion of B in the liquid is greater at the bottom of a valley than at the top of a hill. In view of these two opposing tendencies, it is not possible to arrive at definite conclusions on the basis of qualitative considerations. The results of calculations not included in this paper may be summarized as follows. If exclusive diffusion control is assumed and the solubility of A is much greater than that of B, as is the case in the system Cu-Ni, a plane interface is unstable if $N_{\rm B}^{\prime(0)} < 0.5$, but a plane interface is stable if $N_{\rm B}^{\prime(0)} > 0.5$. Experiments reported above, however, show that a rugged interface is formed even if the nickel content is as high as 80 at. %. The discrepancy between theory and experiment indicates that one or several of the presuppositions of the theory are not realistic.

The most important point seems to be that dissolution of nickel is controlled in part by diffusion into the liquid phase and in part by a phase boundary reaction. Thus the difference in the local dissolution rates of metal B at points I and II in Fig. 1 is less than predicted by diffusion equations, and accordingly the stabilization of a plane interface due to simultaneous dissolution of A and B becomes effective only at concentrations of B significantly higher than 50 at. %.

Solid Au-Cu alloys in liquid bismuth

Penetration of liquid Bi into solid Au-Cu alloys, due to preferential dissolution of Au at 400°C, may be treated in the same way as penetration of liquid Ag into solid Cu-Ni alloys. To apply equation (27), $D_{\rm A}'' = 3 \times 10^{-5}$ cm²/sec has been assumed. The equilibrium mole fractions of gold in the liquid, $N_{Au}'' = N_{A}''(eq)$, for given compositions of the solid, were obtained with the help of the same general procedure indicated above for Cu-Ni alloys in liquid Ag. For solid Au-Cu alloys, activities deduced from emf measurements by Oriani(32) were used. The activity of Bi in liquid Au-Bi alloys at 700°C is virtually equal to the mole fraction of Bi according to emf measurements by Kleppa⁽³³⁾. Large deviations of the entropy of mixing reported previously (33) have not been confirmed. (34) Thus ideal behavior of the liquid phase in the system Au-Bi at 400°C has been assumed as a fair approximation.

Values of t for a penetration of $x_n = 0.015$ cm read from Fig. 15 are compared in Table 2 with values calculated from equation (27). The divergence

Table 2.—Penetration of liquid bismuth in solid Au-Cu alloys at 400°C

$N_{ m Au'}$	$N_{ m Au}''({ m eq})$		= 0.015 em) sec	
		obs.	eale.	
0.74	0.25	300	≥9	
0.61	0.19	210	≥12	
$0.33 \\ 0.10$	0.03	6000 8000	≥ 82 ≥ 833	

between observed values of t and the upper limits of the calculated values is considerable even for gold-rich alloys. Hence it is concluded that the presupposition of equilibrium between the liquid at the front of the penetration and the bulk solid does not hold.

CONCLUDING REMARKS

The present investigation shows that rapid penetration of a liquid into a solid alloy may be expected whenever one component of a binary solid alloy is much more soluble than the other component. This may result in rapid weakening of structural parts, which is to be avoided as a most undesirable corrosion phenomenon. On the other hand, one may utilize this type of attack in order to produce sponge-like structures useful as porous bearings accommodating lubricants, or as catalysts. To this end, the penetrating liquid is replaced by another volatile liquid which may be vaporized. In particular, Raney nickel as a compact but highly porous catalyst is produced from Ni-Al alloys by dissolving Al with the aid of concentrated NaOH solution and rinsing with water. (35) Since the Ni-Al alloys used for this purpose involve two different metallic phases, details of the attack are somewhat more complex in comparison to systems selected for experiments in this paper.

195

ACKNOWLEDGMENT

The authors are indebted to Dr. J. F. Elliott and Dr. B. D. Lichter for helpful discussions and suggestions. The help of A. P. Bond and F. Haynes during the preparation of Cu-Ni alloys is gratefully acknowledged.

REFERENCES

- 1. W. A. Noyes and W. R. Whitney, Z. phys. Chem. 23,
- W. NERNST, Z. phys. Chem. 47, 52 (1904).
 C. WAGNER, J. Phys. Chem. 53, 1030 (1949)
- 4. C. R. WILKE, M. EISENBERG and C. W. TOBIAS, Chem. Eng. Progress 49, 663 (1953).
- 5. V. W. Eldred, Interaction between Solid and Liquid Metals and Alloys. Atomic Energy Research Establishment (Great Britain) X/R 1806 (1955).

- 6. A. G. WARD and J. W. TAYLOR, J. Inst. Met. 85, 145 (1956); Ibid. 86, 36 (1957)
- 7. J. M. LOMMEL and B. CHALMERS, Trans. Inst. Min. (Metall.) Engrs. 215, 499 (1959).
- 8. C. Wagner, J. Electrochem. Soc. 103, 571 (1956).
- 9. J. V. CATHCART and W. D. MANLY, Corrosion 10, 432t (1954).
- 10. J. V. CATHCART and W. D. MANLY, Corrosion 12, 87t (1956).
- 11. W. D. Manly, Corrosion 12, 336t (1956).
- L. Graf and H. Klatte, Z. phys. Chem. N.F. 10, 306 (1957); Ibid. 11, 342 (1957).
- L. Graf, Acta Met. 6, 116 (1958).
 G. P. Smith, M. E. Steidlitz, and E. E. Hoffman, Corrosion 13, 561t (1957).
- 15. G. P. SMITH and E. E. HOFFMAN, Corrosion 13, 627t (1957).
- 16. G. P. SMITH, M. E. STEIDLITZ and E. E. HOFFMAN, Corrosion 14, 47t (1958).
- M. Hansen and K. Anderko, Constitution of Binary Alloys. McGraw-Hill, New York (1958).
- 18. D. A. Stevenson, to be published.
- 19. C. S. Smith, Trans. Amer. Inst. Min. (Metall.) Engrs. 175, 15 (1948).
- 20. K. K. IKEUYE and C. S. SMITH, Trans. Amer. Inst. Min. (Metall.) Engrs. 185, 762 (1949).
- 21. W. D. Robertson and R. Bakish, Structural Factors Associated with Stress Corrosion Cracking of Homogeneous Alloys, in Stress Corrosion Cracking and Embrittlement,

- edited by W. D. Robertson. John Wiley, New York (1956); R. Bakish and W. D. Robertson, Trans. Amer. Inst. Min. (Metall.) Engrs. 206, 1277 (1956).
- 22. R. F. Kehl, The Principles of Metallographic Laboratory Practice. McGraw-Hill, New York (1949)
- 23. R. P. TISCHER and H. GERISCHER, Z. Elektrochem. 62, 50 (1958).
- 24. B. D. LICHTER and C. WAGNER, to be published.
- 25. J. Crank, The Mathematics of Diffusion. Clarendon Press, Oxford (1956).
- 26. T. von Karman, Z. angew. Math. Mechanik. 1, 233 (1921). 27. W. Seith, Diffusion in Metallen (2nd Ed.) pp. 283-288.
- W. SEITH, Diffusion in Medicine (and Edity pp. 2002).
 Springer-Verlag, Berlin (1955).
 P. J. Koros, The Effect of Carbon and Silicon on the Activity Coefficient of Copper in Liquid Iron at 1600°C.
 M.Sc. Thesis, Course III, M.I.T. (1954).
 L. Nans, Thermodynamic Activity of Nickel in Solid
- Copper-Nickel Alloys. M.Sc. Thesis, Course III, M.I.T. (1954).
- 30. R. A. Oriani, private communication.
- L. C. CORREA DA SILVA and R. F. MEHL, Trans. Amer. Inst. Min. (Metall.) Engrs. 191, 155 (1951).
- 32. R. A. ORIANI, Acta Met. 2, 608 (1954).
- 33. O. J. KLEPPA, J. Amer. Chem. Soc. 73, 385 (1951).
- O. J. Kleppa, J. Phys. Chem. 60, 446 (1956).
 M. Raney, U.S. Patents 1, 563, 581 (1927); 1, 628, 190 (1927); 1, 915, 473 (1933); Ind. Eng. Chem. 32, 1199 (1940).

ON THE THEORY OF SELF-DIFFUSION IN LIQUID METALS*

R. A. SWALIN†

The theory of diffusion in liquids is considered from the standpoint of fluctuation theory. It is postulated that diffusion results from the movement of atoms small and variable distances as a result of local density fluctuations. From geometrical considerations it is deduced that about four atoms besides the diffusing atom are involved in such a fluctuation. The energy of a fluctuation is expressed in terms of the Morse function. The following equation is derived for D, the self-diffusion coefficient

$$D = 1.29 \times 10^{-8} \ T^2/\Delta H_v \alpha^2 \ {
m cm}^2/{
m sec}$$

where ΔH_v is the heat of vaporization and α is related to the curvature of the potential vs. distance curve. The theory results in there being no activation energy for the diffusion process but a plot of log D vs. 1/T yields an apparent straight line over a small temperature interval, the slope of which is not a function of the properties of the element but only a function of the temperature of measurement. The relative value of D for various elements is a function of the properties of the elements, however. The theory is compared with experimental results with the agreement being generally quite good.

It also follows that there is no activation volume in the usual sense but what is measured in pressure experiments, according to the theory, is the effect of pressure on the magnitude of fluctuations.

The theory, if correct, also implies that thermodynamic properties such as the partial molar heat of solution are important in solute diffusion and may be more important than solute atomic size effects.

SUR LA THEORIE DE L'AUTO-DIFFUSION DANS LES METAUX LIQUIDES

La diffusion dans les liquides est considérée du point de vue de la théorie des fluctuations. On postule que cette diffusion résulte du mouvement d'atomes à des distances variables, mais petites sous l'action de fluctuations locales de densité.

A partir de considérations géométriques, on déduit qu'en plus de celui qui diffuse, environ quatre atomes sont impliqués dans une telle fluctuation. L'énergie d'une fluctuation s'exprime à l'aide de la fonction de Morse. On obtient l'équation suivante pour D, coéfficient d'auto-diffusion

 $\hat{D} = 1.29 \times 10^{-8} \, T^2 / \Delta H_v \alpha^2 \, \mathrm{cm}^2 / \mathrm{sec}$

où H_v est la chaleur de vaporisation et α est relié à la courbure de la courbe du potentiel en fonction de la distance.

VOI

105

La théorie conduit à l'absence d'énergie d'activation par le processus de diffusion. Par contre, si l'on porte $\lg D$ en fonction de 1/T, on obtient une ligne droite sur un petit intervalle de température.

La pente ne dépend pas des propriétés de l'élément, mais seulement de la température à laquelle les mesures sont faites. Toutefois, la valeur relative de D pour divers éléments dépend des propriétés de ceux-ci. L'accord entre la théorie et l'expérience s'avère généralement très bon.

Il s'ensuit aussi qu'il n'y a pas de volume d'activation au sens habituel du mot. D'après la théorie, ce qui est mesuré, c'est l'effet de la pression sur la grandeur des fluctuations. Si elle est correcte, la théorie implique que les propriétés thermodynamiques, telles que la chaleur partielle molaire de solution sont importantes dans la diffusion du soluté et peut-être même plus que les effets de taille atomique.

ÜBER DIE THEORIE DER SELBSTDIFFUSION IN FLÜSSIGEN METALLEN

Die Theorie der Diffusion in Flüssigkeiten wird vom Standpunkt einer Fluktuationstheorie aus betrachtet. Es wird postuliert, dass die Diffusion das Ergebnis der Bewegung von Atomen über kleine und variable Entfernungen hinweg ist; sie ist die Folge von lokalen Dichte-Fluktuationen. Aus geometrischen Betrachtungen wird abgeleitet, dass ausser dem diffundierenden Atom etwa vier Atome an einer solchen Fluktuation beteiligt sind. Die Energie einer Fluktuation wird mit Hilfe einer Morse-Funktion ausgedrückt. Für den Selbstdiffusionkoeffizienten D wird folgende Gleichung abgeleitet:

$$D = 1.29 \, \times \, 10^{-8} T^2 / \Delta H_v \alpha^2 {\rm cm}^2 / {\rm sec}$$

wobei ΔH_v die Verdampfungswärme ist und α mit der Krümmung der Potential-Abstandskurve zusammenhängt.

Aus der Theorie folgt, dass es für den Diffusionsvorgang keine Aktivierungsenergie gibt, jedoch ergibt eine Darstellung von log D gegen 1/T über einem kleinen Temperaturintervall eine gerade Linie, deren Anstieg nicht von den Eigenschaften des Elements, sondern nur von der Temperatur der Messung abhängt. Der relative Wert von D für verschiedene Elemente hängt jedoch von den Eigenschaften der Elemente ab. Die Theorie wird mit experimentellen Ergebnissen verglichen; die Übereinstimmung ist im allgemeinen recht gut

Es folgt auch, dass es kein Aktivierungsvolumen im üblichen Sinne gibt; sondern das, was bei Druckversuchen gemessen wird, ist (gemäss der vorliegenden Theorie) der Einfluss des Drucks auf die Grösse der Fluktuationen.

Die Theorie besagt auch, wenn sie richtig ist, dass thermodynamische Eigenschaften wie die partielle molare Lösungswärme bei der Diffusion von Lösungen wichtig sind und wichtiger sein können als Grösseneffekte der gelösten Atome.

^{*} This research has been sponsored in part by the Research Corporation. Received January 5, 1959.

[†] Department of Metallurgy, University of Minnesota, Minneapolis 14, Minn.

INTRODUCTION

The theory of diffusion in liquid metals is in a rather unsatisfactory state compared with the theory for solids and gases. The reason for this is related to the difficulty of quantitatively elucidating the structure of the liquid state. Because of the similarity in many of the properties of liquids and solids, there has been a tendency to obtain a theory of transport properties in liquids such as diffusion by using a quasi-crystalline approach. Diffusion, for example, in liquids has been treated as the thermally activated jump of an atom into a neighboring "hole" thus leading to a diffusion equation very similar to that for diffusion in crystals(1) The "hole", however, is not a vacancy but may have varying dimension. To obtain an activation energy for such a process, Frenkel(2) had to identify this energy barrier with the energy of formation of a "hole" since the atom itself would not be expected to have to surmount an energy barrier in order to move. This meant that a critically sized "hole" had to be postulated, sizes below which did not contribute to diffusion. Thus the activation energy was identified with the surface energy of formation of the critically sized spherical "hole". This view, as recognized by Frenkel⁽²⁾ and Nachtrieb⁽³⁾, also leads to the expectation that the activation energy of diffusion (energy of "hole" formation) be proportional to the heat of vaporization, but experiment shows no correlation between the two quantities.

This paper represents an attempt to consider the process of diffusion from a somewhat different standpoint than heretofore considered, although there are similarities between the view to be presented here and the "hole" theory. The theory will be compared with existing experimental data.

1959

THE MECHANISM OF DIFFUSION

In Fig. 1a is shown a two-dimensional schematic view of a liquid metal as deduced from X-ray results. A given atom is surrounded by Z other atoms (Z=10-12) with a separation of about x_0 between centers. We can expect a certain probability that at a given time a density fluctuation as shown in Fig. 1b will occur next to a given atom. This atom then has the opportunity of moving a distance j into the temporary void. Geometrically a fluctuation suitable for diffusion can occur if the two atoms marked 1 and 2, plus one below the plane of Fig. 1b and one above the plane, move a distance j from our central atom simultaneously. The volume of the void thus formed is given by

$$\Delta V \simeq (1/6)\pi x_0^2 j \tag{1}$$

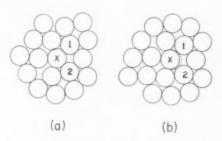


Fig. 1a. Schematic drawing of liquid metals.
Fig. 1b. Schematic drawing of liquid metal showing density fluctuation.

treating the void as a section of a prolate spheroid. Since a continuous distribution of fluctuation sizes is to be expected, the possible distance of a diffusion jump is variable and not a discrete value as in crystals. Consequently the probability of our atom X being adjacent to a fluctuation of any magnitude is equal to one. The problem of evaluating the diffusion coefficient thus involves determining the size distribution of fluctuations.

CALCULATIONS OF THE DIFFUSION CONSTANT

For a random walk process such as the one being considered, $Einstein^{(4)}$ has shown that

$$D = (1/6)\overline{j^2}/\tau \tag{2}$$

where $\overline{j^2}$ is the mean square value of the jump distance or in this case the mean square value of the fluctuation distance, and τ is the mean time of stay of an atom at a particular site.

For simplicity, in order to find j^2 , let us consider voids of volume $(1/6)\pi x_0^2 j$ as though they are distributed in a continuum. Furth⁽⁵⁾ has treated this problem for spherical "holes", and by substituting our particular geometry in place of spheres we find that

$$p(j) dj = Cj^2 \exp\left[-E(j)/kT\right] dj \tag{3}$$

where p(j) dj is the probability of finding a fluctuation in the size range of j and j + dj, C is a constant and E(j) represents the energy needed to cause a fluctuation of magnitude j. Furth's equation had a j^6 term in place of j^2 in equation 3 since the volume of his spherical "holes" depended on the cube of the radius of the hole whereas given in equation 1, the volume considered here depends on j to the first power.

Because of the high coordination number in liquid metals, nearest neighbor interactions need only be considered in calculating E(j). We thus can consider the energy of a fluctuation such as shown in Fig. 1b

included since the entropy involved in a fluctuation of the type considered can be shown to be negligible relative to E(j). Substituting equation 6 into 12 we find that (13)

In this derivation a small entropy term has not been

$$\gamma = 8\Delta H_r \alpha^2 / Z N_0 kT \tag{13}$$

Substitution of this relation into equation 11 and thence equation 11 into 10 yields

$$\overline{j^2} = 3ZN_0kT/16\Delta H_{\nu}\alpha^2 \tag{14}$$

In order to evaluate D, $\bar{\tau}$ is the only term left to consider. Applying the formalism of the absolute reaction rate theory

$$\frac{1}{\tau} = p \, \frac{kT}{h} \cdot \frac{F^*}{F} \tag{15}$$

where p is the number of available paths, h is Planck's constant, F^* is the partition function of an atom in the activated state and F is the partition function in the normal state. In the case of liquid diffusion as represented in Fig. 1b there is very little difference between an atom in the activated state and in the normal state and in fact there is no energy barrier to surmount. We may expect that the ratio F^*/F does not differ very much from unity and the number of paths $p \simeq Z$ therefore

$$1/\bar{\tau} \simeq kTZ/h \tag{16}$$

19

Substitution of equations 14 and 16 into 2 yields

$$D = 3Z^2 N_0 k^2 T^2 / 96h \Delta H_v \alpha^2 \tag{17}$$

Equation 17 shows that there is no unique activation energy for the diffusion process as presented here. There is a continuous size distribution of fluctuations which will change with temperature, but no critically sized fluctuations have been postulated in order to obtain the activation energy. Actually the only basis for postulating a thermally activated process for diffusion in liquids is that a plot of $\log D$ or \log (viscosity) vs. reciprocal of absolute temperature appears to give a straight line relation over a fairly small temperature interval. As will be shown in the next section, equation 17 plotted in this manner yields an apparent straight line over the temperature interval investigated in a normal diffusion study.

It perhaps should be emphasized at this point that $1/\bar{\tau}$ is the average frequency of jumping regardless of the distance an atom travels. Since there is a complete size distribution of fluctuation, every atom has a probability of unity of being adjacent to a density fluctuation and thus most of the atoms in the liquid will be participating in diffusion at a given instant.

to result from the elongation of four nearest neighbor bonds. To evaluate this energy an equation expressing the energy as a function of separation must be used.

Perhaps the best representation of the energy between atoms in a metal crystal as a function of their separation is the Morse function, and since the bonding in liquid metals is similar to that in the crystalline phase we might expect the Morse function to be applicable to liquids also. The energy expended in increasing the distance between two nearest neighbors a value j over their equilibrium spacing is thus

$$\varepsilon = \varepsilon_D [1 + \exp(-2\alpha j) - 2 \exp(-\alpha j)]$$
 (4)

where ε_D represents the energy of dissociation of a bond and α is related to the curvature of the ε vs. jcurve. ε_D can be estimated from the heat of vaporization, ΔH_r , of the liquid from quasi-chemical theory⁽⁶⁾. Thus

$$\varepsilon_D = 2\Delta H_v / Z N_0 \tag{5}$$

where N_0 is Avogadro's number. Since we can consider a fluctuation to result from the elongation of four nearest neighbor bonds, $E(j) = 4\varepsilon$ and therefore

$$E(j) = (8\Delta H_v/ZN_0) [1 + \exp(-2\alpha j) -2 \exp(-\alpha j)]$$
 (6)

The constant C in equation 3 can be evaluated since

$$\int_0^\infty p(j) \, dj = 1 \tag{7}$$

Therefore

$$C = \left(\int_0^\infty j^2 \exp\left[-E(j)/kT\right] dj \right)^{-1} \tag{8}$$

Since

$$\tilde{j}^2 = \int_0^\infty j^2 p(j) \, dj \tag{9}$$

we find that

$$\bar{j}^{2} = \frac{\int_{0}^{\infty} j^{4} \exp\left[-E(j)/kT\right] dj}{\int_{0}^{\infty} j^{2} \exp\left[-E(j)/kT\right] dj}$$
(10)

The term $\exp[-E(j)/kT]$ can be expanded in a Maclaurin's series, and since E(j) would be expected to be quite small, high order terms can be eliminated after Slater(7) and we thus obtain

$$\exp\left[-E(j)/kT\right] = \exp\left[-E(j=0)/kT\right]$$

$$\exp\left[-\gamma j^2\right] \qquad (11)$$

where

$$\gamma = \frac{1}{2kT} \left(\frac{d^2 E(j)}{dj^2} \right)_{i=0} \tag{12}$$

Substitution of Z=10, the average coordination number in liquid metals, into equation 17 and evaluating constants gives

$$D = 1.29 \times 10^{-8} T^2/\Delta H_v \alpha^2 \text{ cm}^2/\text{sec}$$
 (18)

where α has dimensions of reciprocal angstroms and ΔH_v has units of kcal/mole. The slope of a line on a log D vs. reciprocal temperature graph is found to be

$$d \log D/d(1/T) = -0.87T = -Q/2.3R \tag{19}$$

where Q is the quantity listed in tables as an activation energy. Thus

$$Q = 2RT \tag{20}$$

This implies that the higher the temperature of the diffusion measurement, the higher the apparent activation energy will be.

CORRELATION BETWEEN THEORY AND EXPERIMENT

Self-diffusion data have been obtained for five elements, namely Hg, $^{(8,9)}$ Na, $^{(10)}$ In, $^{(11,12,13)}$ Sn $^{(13)}$ and Ga. $^{(14)}$ These experimental results will be compared with the theory. The values of α and ΔH_v used for calculating D are listed in Table 1.

Values of ΔH_v were obtained from reference 15 and values for α were obtained from force constant data of Waser and Pauling. (16) α is found to be related to their force constant k by the relation

1959

$$\alpha = (ZN_0k/4\Delta H_v)^{\frac{1}{2}} \tag{21}$$

In Fig. 2 are shown the curves calculated from the theory and from experiments. The agreement is generally quite satisfactory. The theoretical curve for Na which offers the poorest agreement is still within a factor of 2.

In Table 2 are listed apparent values of Q and D_0 as determined from the slopes of the lines and intercepts at 1/T=0 respectively.

DISCUSSION

The agreement between theory and experiment as compared in Fig. 2 and Table 2 is basically quite satisfactory. The theoretical values of Q listed in

Table 1. Quantities used in calculating D

Element	$\alpha(\mathring{A}^{-1})$	$\Delta H_v({ m kcal/mole})$
Na	0.75	25.7
Hg	2.1	14.7
Hg Ga	1.25	65.1
In	0.88	58.4
Sn	1.30	70.2

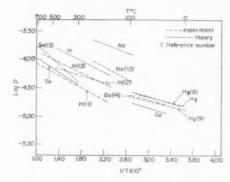


Fig. 2. Comparison between theory and experimental diffusion results.

Table 2 although not in exact numerical agreement show a trend upward from Hg and Ga to Na to In and Sn as found experimentally. The calculated values of D_0 compared with experiment are in surprisingly good agreement particuarly in view of the large extrapolation necessary to obtain these values.

As mentioned earlier, if the theory is correct, there is no activation energy for the process of liquid state diffusion but a plot of $\log D$ vs. 1/T yields a seeming straight line over a small temperature interval. According to the theory the slope of the line is independent of the nature of the element in principle but is only a function of the temperature of measurement. Fig. 2 shows this trend. Hg and Ga were studied at lower temperatures than the other elements under consideration and both were found to have the same activation energy. This value of Q is the smallest of the group. Na was investigated in the next highest temperature range and was found to have a higher value of Q. Sn was studied in the highest temperature range and was found to have the highest value of Q. In, as the data show, is open to question. If Q depended on the properties of the elements one would find it difficult to explain the fact that Ga and Hg

Table 2. Comparison of theoretical and experimental values of Q and D_0

Element	$Q \pmod{\mathrm{mole}}$		D_{θ} (cm ² /sec × 16	
	theor.	expt.	theor.	expt.
Na	1.8	2.4	13	11
Hg Ga	1.3	1.1	1.8	1.0
Ga	1.3	1.1	1.0	1.1
In	2.3	1.3	7.4	1.8
Sn	2.9	4.0	3.9	14

have the same value in view of their considerably different properties.

If the theory of diffusion as discussed here is correct, the activation volume for liquid diffusion needs redefinition. Theoretically the activation volume ΔV_{\pm}^{\pm} is given by

$$\Delta V_{+}^{+} = (\partial \Delta F_{+}^{+}/\partial P)_{T} \tag{22}$$

where P is pressure and ΔF_+^* is the activation free energy. Because of the connection between ΔF_+^* and D for a thermally activated diffusion process, equation 22 is equivalent to

$$\Delta V_{+}^{+} = -RT(\partial \ln D/\partial P)_{T} \tag{23}$$

and in practice ΔV_+^* is determined from equation 23. Since in the theory presented, $\Delta F_+^*=0$ the effect of pressure on D must have a different meaning. Substituting equation 16 into equation 2 and then equation 2 into 23 yields

$$\Delta V_{+}^{+} = -RT[\partial \ln \bar{j}^{2}/\partial P]_{T} \tag{24}$$

and so ΔV_+^* according to the theory represents the effect of pressure on the size distribution of the fluctuations. This definition of ΔV_+^* is considerably different from that for an activated process in which ΔV_+^* represents the excess volume associated with an atom in an activated state and is essentially pressure independent.

It is also interesting to consider solute diffusion in liquids in relation to the theory. Usually, in solute diffusion studies, investigators have used the Stokes-Einstein equation and/or the Eyring equation involving the dependence of the diffusion coefficient on the radius of the diffusing species, and have thereby

attempted to calculate the radius of the diffusing ion. Equation 18 indicates that the binding energy between solute and solvent is important. If D is the solute diffusion coefficient, ΔH_v is closely related to the energy involved in the transfer of the solute atom from liquid solvent to the gas phase. ΔH_v would be large for solutes having a large negative partial molar heat of solution and smaller for solutes having a large positive heat of solution. D would, therefore, be smaller in the former case than in the latter. Some recent solute diffusion data obtained by Ma and Swalin⁽¹⁷⁾ indicate such a dependence on the heats of solution. The theory in relation to solute diffusion will be considered in a later paper in more detail.

REFERENCES

- S. GLASSTONE, K. J. LAIDLER and H. EYRING, The Theory of Rate Processes. McGraw-Hill, New York (1946).
- J. Frenkel, Kinetic Theory of Liquids. Oxford (1946).
 N. H. Nachtrieb, Liquid Metals and Solidification.
- Amer. Soc. Metals, Cleveland (1958).
 4. A. Einstein, An Investigation of the Theory of Brownian
- Movement. Methuen, London (1926). 5. R. Furth, Cambridge Philosophical Soc. 37, 252 (1941).
- C. Wagner, Thermodynamics of Alloys. Addison Wesley, Cambridge (1952).
- J. C. Slater, Introduction to Chemical Physics. McGraw-Hill, New York (1939).
- R. E. Hoffman, J. Chem. Phys. 20, 1567 (1952).
- N. H. Nachtrieb and J. Petit, J. Chem. Phys. 24, 746 (1956).
- R. E. MEYER and N. H. NACHTRIEB, J. Chem. Phys. 23, 1851 (1955).
- 11. A. LODDING, Z. Naturf. 11 A, 200 (1956).
- G. Careri, A. Paoletti and F. L. Salvetti, Nuovo Cimento 11, Series 9, 399 (1954).
- G. CARERI and A. PAOLETTI, Nuovo Cimento 2, Series 10, 574 (1955).
- J. PETIT and N. H. NACHTRIEB, J. Chem. Phys. 24, 1027 (1956).
- O. Kubaschewski and E. Ll. Evans, Metallurgical Thermochemistry, 2nd Ed. Wiley, New York (1956).
- 16. J. Waser and L. Pauling, J. Chem. Phys. 18, 747 (1950).
- 17. C. Ma and R. A. SWALIN, to be published.

7 195

THE ROLE OF VACANCIES IN AN UNUSUAL ANELASTIC PHENOMENON*

B. S. BERRY+

The internal friction results obtained by Entwistle^(1,2) from a number of quench aging Al alloys are re-examined and interpreted. Two transient contributions to the internal friction are observed on aging duralumin near room temperature. The first contribution develops during the initial hardening, and is deduced to be of anelastic origin. It is suggested that this contribution occurs by a stress induced rearrangement of clusters of solute atoms, and at a rate greatly accelerated by the presence of excess vacancies. The second contribution, which develops considerably later in the aging sequence, is also a relaxation phenomenon but with a shorter relaxation time governed by an activation energy of 13.5 kcal/mole and a frequency factor of 10¹⁴ sec⁻¹. This later relaxation is thought to arise from a stress induced rearrangement of small groups of solute atoms containing vacant lattice sites as an integral component of their structure. This model successfully explains the salient experimental results, and leads directly to the interpretation of the activation energy as that for vacancy motion. The observed sequence of changes indicates that the relaxation centers responsible for both contributions occur within the G.P. zones, and that a spontaneous reorganization within the zones is responsible for the changeover from one contribution to the other.

LE ROLE DES LACUNES DANS UN PHENOMENE PARTICULIER D'ANELASTICITE

L'auteur examine et interprète les résultats obtenus par Entwistle à l'aide du frottement interne dans des alliages d'aluminium à vieillissement structural. Le frottement interne résulte de deux phénomènes qui peuvent être observés au cours du vieillissement s'effectuant au voisinage de la température ordinaire. Le premier se déroule au début du durcissement et a une origine anélastique. L'auteur l'attribue à un réarrangement d'amas d'atomes dissous sous l'action d'une tension et à une vitesse qui est fortement accélérée par la présence d'un excès de lacunes. Le second phénomène, qui apparait beaucoup plus tard, est aussi une relaxation mais avec un temps plus court, caractérisée par une énergie d'activation de 13,5 kcal/mole et une fréquence de 10¹⁴ sec⁻¹. L'origine pourrait en être un réarrangement sous tension de petits groupes d'atomes dissous contenant des lacunes comme parties intégrantes de leur structure. Ce modèle est en accord avec les faits expérimentaux et associe l'énergie d'activation du mouvement des lacunes. La séquence observée montre que les contres de relaxation responsables des deux phénomènes se trouvent à l'intérieur des zones de Guinier-Preston. Une réorganisation interne de ces zones fait passer du premier phénomène au second.

DIE ROLLE DER GITTERLÜCKEN BEI EINEM UNGEWÖHNLICHEN ANELASTISCHEN PHÄNOMEN

Die Ergebnisse, die Entwistle $^{(1,2)}$ bei der Untersuchung der inneren Reibung einer Anzahl von abgeschreckten und ausgelagerten Al-Legierungen erhielt, werden kritisch gesichtet und gedeutet. Beim Auslagern in der Nähe der Raumtemperatur werden zwei Beiträge zur inneren Reibung beobachtet, die nicht bleibender Natur sind. Der erste Beitrag tritt während der anfänglichen Härtesteigerung auf, und es wird gezeigt, dass er anelastischen Ursprungs ist. Zur Erklärung wird eine durch die Spannung hervorgerufene Umordnung von Komplexen gelöster Atome vorgeschlagen; die Geschwindigkeit der Umordnung wird dabei durch im Überschuss vorhandene Leerstellen erheblich beschleunigt. Der zweite Beitrag, der in der Reihenfolge der Alterungserscheinungen erheblich später auftritt, ist ebenfalls eine Relaxationserscheinung; die Relaxationszeit ist jedoch erheblich kürzer und wird durch eine Aktivierungsenergie von 13,5 kcal/Mol (ca. 0,59 eV) und einen Frequenzfaktor von 10¹⁴ sec⁻¹ bestimmt. Diese Relaxation beruht vermutlich darauf, dass kleine Komplexe, die aus gelösten Atomen und Leerstellen aufgebaut sind, sieh infolge der Spannung umordnen. Dies Modell vermag die hervorstechenden experimentellen Ergebnisse zu erklären und führt unmittelbar zur Deutung der gemessenen Aktivierungsenergie als derjenigen der Leerstellenwanderung. Die beobachtete Reihenfolge der Eigenschaftsänderungen zeigt, dass die Relaxationszentren, die für die beiden Beiträge verantwortlich sind, innerhalb der G.P.-Zonen auftreten, und dass spontane Veränderungen innerhalb der Zonen zur Ablösung eines Beitrags durch den anderen führen.

INTRODUCTION

VOL.

This paper presents an interpretation of the internal friction results obtained by Entwistle^(1,2) from a variety of quenched Al-rich age hardening alloys. Although unable to explain his findings, Entwistle

concluded that vacancies do not play a direct part in the anelastic relaxation process that he observed in these alloys after prolonged aging near room temperature. The present interpretation, on the other hand, rationalizes much of the experimental information on the basis that the relaxation centers responsible for this phenomenon consist of clusters of solute atoms containing vacant lattice sites. The interpretation will

^{*} Received August 13, 1958; revised version January 14, 1959.

[†] IBM Research Center, Yorktown Heights, N.Y.

ACTA METALLURGICA, VOL. 7, NOVEMBER 1959

drawn from them.

at higher temperatures are simply explained by the greater differences between the peak temperature and the aging temperature. The observation of an internal friction peak as a function of temperature T implies that the relaxation time τ is temperature sensitive according to the relation $\tau^{-1} = \tau_0^{-1} \exp\left(-H/RT\right) \tag{1}$

of this peak, which is located at 25°C for a frequency of 1262 c/s. The lower values of $B_{\rm max}$ for aging runs

SUMMARY OF EXPERIMENTAL RESULTS

be preceded by a brief summary of the experimental

results^(1,2) and the formal conclusions that can be

1. For a frequency of 2 kc/s, the internal friction of solution treated and quenched duralumin, isothermally aged at temperatures between 19° and 63°C, varies with time in the manner shown schematically in Fig. 1. The shape of the experimental curve suggests the development of two partially overlapping transient contributions, marked A and B in Fig. 1. Higher aging temperatures within the range 19°-63°C not only shift A and B to shorter aging times but also profoundly alter their relative magnitudes, Amax increasing and B_{max} decreasing with an increase of aging temperature. (It should be emphasised that A_{max} and B_{max} are defined as the maxima of the dotted aging curves of Fig. 1, and are not the heights of damping peaks). The magnitudes of A_{max} and B_{max} lie within the range 10^{-5} – 2×10^{-4} (expressed as the logarithmic decrement), and at 40° C A_{max} appears after 0.4 hr and B_{max} after 30 hr.

2. Neither the A nor the B contributions were observed in a variety of simpler binary and ternary alloys. The simplest alloys having a behavior similar to duralumin were found to be those of the quaternary Al-Cu-Mg-Si primary solid solution.

3. The B contribution was shown to be due to a transient internal friction peak of anelastic origin. After aging to develop the B contribution, the peak was observed from measurements made on cooling from the aging temperature down to -70° C. The rise and fall of the B contribution with time during isothermal aging merely reflects the growth and decay

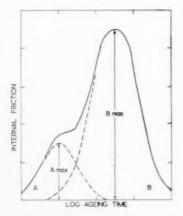


Fig. 1. Schematic representation of the 2 kc/s internal friction of solution treated and quenched duralumin during isothermal aging near room temperature, showing resolution of the experimental (solid) curve into the contributions marked A and B (dotted).

From measurements of the peak at two frequencies the values $10^{14}\,\mathrm{sec^{-1}}$ and $13.5\,\mathrm{kcal/mole}$ were obtained for the frequency factor τ_0^{-1} and the activation energy H, respectively. The observed peak is approximately twice as broad as that calculated for a unique relaxation time.

4. A detailed study established the following important general characteristics of the B internal friction peak:

- (a) The temperature of the peak remains constant throughout the period of existence of the peak. The relaxation time therefore remains constant, and by implication τ₀ and H also remain constant, during aging.
- (b) The temperature of the peak is also unaffected by the temperature from which the alloy was quenched.

195

- (c) The height of the peak does depend on the quenching temperature, insofar as this affects the supersaturation of solute obtained on quenching.
- (d) The height of the peak is strongly dependent on the composition of the alloy.

5. From the evidence given below, it is deduced that the A contribution is also due to a transient anelastic relaxation phenomenon. Accordingly, just as for the B contribution, the A contribution is simply the damping corresponding to some point on the side of an internal friction peak whose height is changing with time. The important difference responsible for the opposite behavior of the A and the B contributions is that the B contribution arises from a peak located below the range of aging temperatures employed, whereas the A contribution is due to a peak located above this range. Consequently, for the same temperature, the relaxation time for the early occurring A relaxation must be considerably longer than that for the later B relaxation.

The evidence for these conclusions is as follows. The aging curves obtained at lower frequencies of vibration were different from that of Fig. 1, which is for 2 kc/s. At the lowest frequencies used (2.8 and 11 c/s) the damping passed through a maximum much

earlier in the aging sequence, and the height of the maximum was larger for the lower frequency. It can be safely concluded that the differences in the aging curves arise because $A_{\rm max}$ increases (and $B_{\rm max}$ decreases) for runs made at lower frequencies.* The frequency dependence of $A_{\rm max}$ revealed by these runs complements the temperature dependence of $A_{\rm max}$ (item 1) in the specific manner characteristic of a relaxation process. This will be taken as sufficient identification of the anelastic origin of the A contribution. Furthermore, the fact that $A_{\rm max}$ becomes larger as the temperature is raised (or as the frequency is lowered) shows that the temperature of the internal friction peak must lie above the range of aging temperatures employed.

INTERPRETATION

There is little doubt that the A and B contributions are due to two different relaxation processes that have a transient existence over different periods of the aging sequence. The fact that the relaxations develop and subsequently disappear only on aging the quenched alloy indicates that relaxation centers of limited lifetime are formed during the spontaneous atomic rearrangements occurring on aging. Disregarding the detailed nature of the relaxation centers, it can be stated quite generally that inasmuch as the existence of the relaxations is intimately related to the distribution of solute atoms in the alloy, the relaxations can be expected to arise from processes of stress-induced ordering.(3) In terms of the usual conception of this mechanism the observed relaxation rate τ^{-1} is to be identified approximately with an appropriate atomic jump rate, as discussed by Nowick(4).

1959

The data available for the B relaxation show, however, as Entwistle has already emphasized, (1) that this expectation does not appear to accord with the extremely short relaxation times and the low activation energy observed experimentally. For example, at 25° C the B relaxation time has a value of 10^{-4} sec, whereas the atomic jump time is estimated to be greater than 1 sec, even after generous allowance is made for the number of quenched-in vacancies remaining in the alloy.

This discrepancy is resolved by postulating that

the relaxation centers giving rise to the B contribution consist of small groupings of atoms containing vacant lattice sites as an integral component of their structure. For anelastic effects to occur, such groupings must produce anisotropic distortion of the surrounding lattice. The relaxation process is pictured as a stressinduced redistribution of the various atoms and vacancies within the groups by the interchange of atoms with vacancies. The simplest case of this general mechanism is the stress-induced reorientation of a solute atom-vacancy bound pair. In this case the vacancy clearly serves the dual purpose of (a) interacting with the solute atom to produce a unit of tetragonal symmetry, and (b) providing a constant source of mobility for the solute atom. It is not implied however that the simple pair model is appropriate to the B relaxation.

The general type of relaxation center described above is characterized by two distinctive features. First, the temperature dependence of the relaxation time is governed only by the mobility of the vacancies, since the number present in a grouping is constant, at least over the temperature range for which the grouping can exist. Consequently the activation energy of the relaxation is to be interpreted as that for motion of a vacancy. The experimental value of 13.5 kcal/mole therefore appears very reasonable in view of the value of 12 kcal/mole inferred for pure aluminum from the resistivity measurements of De Sorbo and Turnbull⁽⁵⁾. The second feature of the model is that the frequency factor τ_0^{-1} for the relaxation will be related to the product of the frequency factor for vacancy motion and the concentration of vacancies in the relaxing group. As the frequency factor for the B relaxation ($10^{14} \, \text{sec}^{-1}$) is the same order of magnitude as that expected theoretically for a specific vacancy jump, it is concluded that the effective vacancy concentration is rather high. This result is consistent with the idea that the relaxation centers consist of a small number of atoms, since a single vacancy could then be a near neighbor to all the atoms in the group.

A further important result of this hypothesis for the B relaxation is that the relaxation time should be independent of the general vacancy concentration in the lattice. Consequently, the temperature of the internal friction peak should be insensitive to both the quenching temperature and the aging time, as observed experimentally. It is therefore considered that there is strong evidence for the view that the B relaxation is a stress-induced ordering phenomenon, with the novel feature that the relaxation centers contain vacant lattice sites.

This hypothesis will now be examined in relation to

^{*} This conclusion is not the same as that stated by Entwistle in reference 1. The correctness of the present conclusion can be proved by the following analysis. A decrease in frequency moves the B internal friction peak further away from the aging temperature, and hence decreases the contribution made at the aging temperature. Knowing H (item 2) the shift can be calculated and the reduced contribution estimated. Subtracting this from the experimental curves leaves only the A contribution, which is clearly seen to increase as the frequency is reduced. Entwistle has also reached this conclusion independently (private communication).

what is known about the aging behavior of duralumin type alloys. The resistivity measurements of Cohen⁽⁶⁾ provide evidence that the atomic rearrangement on aging will not proceed beyond the clustering stage for the times and temperatures required to produce and overage the B contribution. Accordingly, it appears reasonable to assume that the relaxation centers originate from the solute-rich clusters of atoms formed on aging (the G.P. zones). The assumption is compatible with the very small relaxation strengths exhibited (typically 3×10^{-4}), since so small a value is an indication that a relatively small number of atoms are participating in the relaxation process. It should be emphasized that a whole G.P. zone (which may contain 500 atoms or more) is far too large to be considered as an individual relaxation center; it should rather be thought of as a small volume of anelastic material containing many groupings of atoms capable of rearranging under stress (i.e. acting as relaxation centers). Since none of the binary or ternary alloys examined was found to develop either the A or the B contribution, it seems that groupings of the necessary asymmetry occur only in complex alloys.

With reference to the kinetics of clustering, the results of Cohen⁽⁶⁾ and the hardness measurements of Entwistle(1) show that clustering occurs much earlier in the aging sequence than the development of the Bcontribution. In fact it is the growth of the A contribution that appears to parallel the clustering process, while a significant growth of the B contribution does not occur until the hardness and resistivity changes have virtually levelled off and the A contribution starts to fall. Consequently it appears that the clusters as formed initially are responsible for the A contribution, and that the decline of the A and the rise of the B contribution are produced as a result of later changes in the structure of the clusters to which hardness and resistivity measurements are insensitive. The possibility of spontaneous rearrangement within a zone has previously been mentioned by Guinier⁽⁷⁾. A consistent scheme fitting in with the interpretation of the B relaxation given above is that such a reorganization is associated with the appearance of vacant lattice sites in the zones. The vacancies may be generated in the zones by groups of smaller sized solute atoms packing together more closely than the spacing of the parent aluminum lattice. Alternatively the reorganization may not generate vacancies but may turn the zones into traps for wandering lattice vacancies. In either case there is the interesting possibility that the rearrangement may take the form of a slow ordering reaction. Overaging of the B

contribution would then be expected on the grounds that a fully ordered structure is not susceptible to stress-induced ordering, as is expected theoretically and has been shown experimentally for Mg-Cd alloys by Lulay and Wert. (8) It appears possible that the ordering reaction suggested above may be analogous to G.P. [2] formation in the binary Al-4% Cu alloy. If so, it may be detectable by X-ray techniques.

An interpretation of the A contribution, observed first in the aging sequence, is hampered by lack of experimental information, particularly of the values of τ_0 and H. However, the data available appear consistent with a mechanism of stress-induced ordering within the zones as formed initially, i.e., prior to the reorganization discussed above. Since the A relaxation time is considerably longer than that for the Bcontribution (item 4), it seems that the A relaxation occurs in an environment in which the effective vacancy concentration is considerably smaller than that for the B relaxation. Considering the temperatures and frequencies at which the A contribution is detected, it is clear that the effective vacancy concentration is nevertheless many orders of magnitude higher than the equilibrium vacancy concentration. This is almost certainly related to the excess vacancy concentration trapped by quenching from the solution treatment temperature.

Hart⁽⁹⁾ has recently discussed the consequences of strong solute-vacancy interactions in alloys which exhibit clustering after quenching. His suggestion of transient non-equilibrium precipitates containing vacancies as a "chemical" component is very similar to the description given here for the G.P. zones during that stage for which the B relaxation is exhibited. For dilute Al-Cu alloys, Hart supposes that coppervacancy pairs and more complex aggregates form from the start of aging. If such groupings existed and were to give rise to anelasticity, the internal friction peak would be of the B type. However, no anelastic effects whatever were observed by Entwistle in the Al-4% Cu alloy. This result does not necessarily mean that the groupings do not exist, for it is also possible that the distortion around the groupings is not sufficiently asymmetrical to produce a relaxation of detectable strength. Nevertheless the fact that the duralumin type alloys first exhibit the A rather than the B contribution may indicate that the solute atomvacancy interactions present are not as strong as those assumed by Hart.

ACKNOWLEDGMENT

The writer gratefully acknowledges the helpful criticisms offered by Dr. A. S. Nowick.

VOI 7 19

REFERENCES

- K. M. Entwistle, J. Inst. Met. 82, 249 (1953-54).
 K. M. Entwistle, J. Inst. Met. 85, 425 (1956-57).
 A. S. Nowick, Progress in Metal Physics Vol. 4, Chap. 1. Pergamon Press, London (1953).
 A. S. Nowick, Phys. Rev. 88, 925 (1952).
 W. De Sorbo and D. Turnbull, Acta Met. 7, 83 (1959).

VOL. 7 1959

- 6. M. COHEN, Trans. Amer. Inst. Min. (Metall.) Engrs. 133, 95 (1939).
- 7. A. GUINIER, Trans. Amer. Inst. Min. (Metall.) Engrs. 206, 673 (1956).
- J. LULAY and C. WERT, Acta Met. 4, 627 (1956).
 E. W. HART, Acta Met. 6, 553 (1958).

A simplified treatment of surface melting*

The purpose of this note is to present a simplified treatment of the statistical problem that arises in the theory of Burton and Cabrera^(1,2) (hereafter referred to as B.C.) concerning the atomic roughening (surface melting) of a planar crystal face as the temperature rises. We accept their formulation of the problem in terms of a nearest neighbor bond picture for the solid. Then as B.C. have shown, surface melting becomes a cooperative problem in statistical mechanics. The rigorous solution of the problem for more than two levels is unknown and B.C. use a generalization of Bethe's⁽³⁾ method of treating order–disorder to obtain an approximate solution. The procedure is somewhat involved.

Since the representation of most real crystals in terms of a bond picture already involves a considerable degree of approximation, a simpler treatment of the mathematical problem would seem to suffice. Accordingly, we discuss the problem from the point of view of a generalization of the Bragg-Williams theory of order-disorder. The advantages of a simpler treatment are the following: a clear physical picture of the competition between the tendency for a low total bond energy and a high configurational entropy in determining the degree of roughening present; the degree of ease with which the discussion may be extended to cases other than the one considered here that involve (1) the geometries of other crystal planes and other crystal structures, (2) the presence of more than one species of atom and (3) a model entailing more than three geometrical levels for the surface atoms.

We confine the treatment to a $\{100\}$ plane of a simple cubic crystal (i.e. a square lattice). Let this plane contain n lattice sites. Following B.C., we define the surface level to be zero for the flat surface at T=0. For T>0 there will be roughening. Let x_1 be the fraction of surface sites for which the surface level is +1 (units of interplanar spacing) due to the presence of an adsorbed atom, x_{-1} be the fraction of surface sites of level -1 due to a vacancy in the surface layer, and x_0 be the fraction of unaltered surface sites of level 0. Although atoms (or vacancies) may stand two deep or more above (or below) the original surface, we will ignore this complication as it neither alters the qualitative picture nor seems likely to be very probable for $\{100\}$ planes of real crystals below their melting

points. Thus we have a 3-level model for which $x_{-1} + x_0 + x_1 = 1$.

Let ϕ be the energy required to break a bond between two atoms that are nearest neighbors; then $\phi/2$ will be the energy associated with a free bond at the surface. Parallel to a line joining any two surface sites that are nearest neighbors there will be a certain number of free bonds equal to the difference in level of the two sites. The corresponding energy is tabulated in the following self-explanatory table for two nearest neighbor sites A and B.

We proceed to calculate the internal energy U, the entropy S, and the free energy F = U - TS of the surface (all quantities are referred to a site). In calculating U, only that part arising from bonds parallel to the surface need be considered since the number of bonds normal to the surface is unaltered by roughening. The entropy S is assumed to arise solely from the multiplicity of geometrical configurations (the surface vibrational spectrum is assumed independent of surface topography).

Although not necessary, we may avail ourselves of a simplification by noting that Table 1 is symmetric about the dotted diagonal so that U must be unaltered by interchanging all +1 sites with all -1 sites. It follows that in equilibrium (max. S for a given U) $x_{-1} = x_1$. Thus we need work with only one variable $x = x_1 = x_{-1} = (1 - x_0)/2$.

VOI

191

The essential feature of the present approximation is now to ignore the correlation between the levels of adjacent sites. For example, the fraction of pairs of sites in which a 0 level is adjacent to a 1 level is taken to be $4x_0x_1 = 4x(1-2x)$. Proceeding in this way to calculate the fraction of each of the six possible adjacent pairs, multiplying each fraction by the corresponding energy given by the table and adding all

TABLE 1.

		Level of site B		
		-1	0	+1
	1	0	$\phi/2$, 6
Level of Site A	0	$\phi/2$	0	$\phi/2$
	+1	ø	$\phi/2$	0

terms, we easily find the following expression for U,

$$U = 4\phi x (1 - x). \tag{1}$$

Since correlations are assumed absent, the entropy per site is given by $S = (k/n) \ln W$, where W is simply the number of arrangements of the n sites for a fixed x. We have

$$S = (k/n) \ln \frac{n!}{(nx!)^2[(1-2x)n]!}$$

= $-k[2x \ln x + (1-2x) \ln (1-2x)]$ (2)

Equilibrium requires dF/dx = dU/dx - TdS/dx = 0This gives the equation

$$\frac{x}{1-2x} = \exp\left[-\frac{2\phi}{kT}(1-2x)\right]. \tag{3}$$

Instead of plotting x(T) we focus attention on the quantity defined by B.C. as the surface roughness S, given by the number of free bonds parallel to the surface per site. Thus in our case $S = U/(\phi/2) =$ 8x(1-x). Fig. 1 shows a plot (solid line) of S vs. $\tau = kT/\phi$ obtained by assigning values to x and calculating S from the definition and τ from equation 3. For comparison the curve of B.C.(2) is shown as a dotted line. It is seen that the curves are quite similar. The correlations which we have ignored and which B.C. have partially taken into account will tend to make sites of like elevation adjacent. The resulting reduction in the number of free bonds will make the onset of roughening easier but will make the attainment of complete roughening more difficult than we have computed. This difference is evident from Fig. 1.

For an interpretation of the results plotted in Fig. 1, the reader is referred to the discussion given by B.C.^(1,2) We only reiterate their conclusion that the

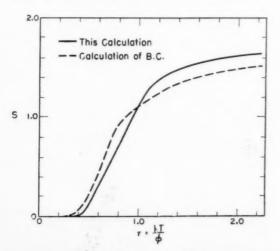


Fig. 1. Surface roughness vs. reduced temperature

melting points of most materials suitably represented by a bond picture occur far enough to the left of Fig. 1 to make appreciable roughening of low index planes unlikely. Higher index planes may roughen before the melting point is reached since the required energies are less.

A discussion of the roughening of a liquid–solid interface has recently been given by Jackson⁽⁴⁾. The treatment resembles that given above but is confined to two levels for which the rigorous solution is known, and is not concerned with the roughness as a function of temperature.

W. W. MULLINS

Metallurgy Department Westinghouse Research Laboratories Pittsburgh 35, Pennsylvania

References

- W. K. Burton and N. Cabrera, Disc. Faraday Soc. 5, 33 (1949).
- W. K. Burton, N. Cabrera and F. C. Frank, Phil. Trans. Roy. Soc. London, Ser. A, 243, 299 (1951).
- H. A. Bethe, Proc. Roy. Soc. A 150, 552 (1935).
 K. A. Jackson, Chapter in Liquid Metals and Solidit
- K. A. Jackson, Chapter in Liquid Metals and Solidification. Amer. Soc. Metals, Cleveland (1958).
- * Received February 16, 1959.

On surface roughness*

Surface melting has been treated by several authors. (1,2,3) There is some confusion about the application of these ideas.

The degree of surface roughness depends on two factors. The first of these is the detailed atomic configuration of the surface layers under consideration. The second factor depends on the binding energy of the solid and on the temperature, in the dimensionless form ϕ/kT ; ϕ being proportional to or equal to the binding energy of the solid, k Boltzmann's constant and T the temperature. It is this factor which has given rise to the confusion.

The original treatment of Burton and Cabrera, (1) and the simplified treatment of Mullins, (3) both assume that the solid surface is in a vacuum. More specifically it is assumed that no atoms leave or join the surface. In this case, the solid surface is in equilibrium with itself and the crystal below it. The binding energy ϕ is specified, and the degree of equilibrium surface roughness can be determined as a function of the temperature T.

Another interpretation is possible. If one assumes that there is another phase present at the crystal surface, then there will be an inter-change of atoms between the two phases. If there is equilibrium

VOL. 7 1959 between the two phases, then the surface will be in equilibrium with the crystal below it, and with the other phase. T thus becomes the equilibrium temperature between the two phases, and ϕ the latent heat or enthalpy change associated with the transformation between the two phases. ϕ is no longer unique for a given crystal, but depends on the other phase present at the interface. The degree of surface roughness depends on both the latent heat and the equilibrium temperature between the crystal and the other phase.

If the two phases are not in equilibrium, then the degree of surface roughness will depend on the departure of the temperature from the equilibrium temperature. The surface roughness in this case will depend on both the equilibrium temperature and on the departure from equilibrium, and not simply on the temperature.

One difficulty which has not yet been resolved is that the rough faces of a crystal retain a sense of the crystal structure of the solid. For example, although all the faces of a metal crystal in contact with its melt are rough, the growth rate depends on orientation, i.e. the solid grows dendritically. This must mean that the surfaces of a crystal are influenced by the structure of the solid, even though they are rough.

K. A. Jackson

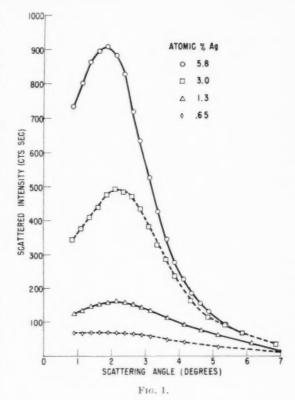
Harvard University Cambridge, Mass.

References

- W. K. Burton and N. Cabrera, Discuss. Faraday Soc. 5, 33 (1949).
- K. A. Jackson, Liquid Metals and Solidification p. 174. Amer. Soc. Metals, Cleveland (1957).
- 3. M. W. Mullins, Acta Met. 7, 746 (1959).
 - * Received April 30, 1959.

The structure of G.P. zones in Al(Ag) alloys*

When dilute Al(Ag) alloys are homogenized and then quenched, the initial precipitation of Ag proceeds rapidly even at room temperature and leads to the formation of G.P. zones. There have been extensive studies of the kinetics of the reaction, $^{(1)}$ and the resulting structure has been investigated by several authors using X-ray techniques. $^{(2)}$ Most recently Walker and Guinier $^{(3,4)}$ have measured the small angle scattering from alloys containing about 5.0 at. 0 / $_{0}$ Ag. The work reported here extends these experiments to alloys with compositions ranging from 0.5 to 5.0 at. 0 / $_{0}$. In addition a somewhat different interpretation of the data is presented.



Alloys† were rolled into foils of nearly optimum thickness for scattering $\mathrm{Cu}K_{\alpha}$ radiation, homogenized at 550°C, and quenched in brine at -50°C. The samples were allowed to warm slowly to room temperature and aged 1 month. Resistivity measurements show this treatment allows the "fast" reaction to go on to completion but no appreciable further changes to occur. The resulting state is referred to as P_1 by Turnbull $\operatorname{et} al.^{(1)}$

19

The small angle X-ray scattering was measured using equipment previously described. $\dot{z}^{(5)}$ The X-ray tube was run at 33 kV and 80 mA with a Cu anode, and the $\mathrm{Cu}K_{\mathrm{x}}$ scattered radiation was detected with a proportional counter and pulse height discriminator. The scattering curves are shown in Fig. 1.

The scattering curves, § for all but the most dilute alloy, show a maximum at approximately h = 3 where $h = (4\pi \sin \theta)/\lambda$. Beyond the maxima, there is a considerable region (the narrowest being

† Samples were prepared by H. N. Treaftis by methods described in reference 1.

[‡] We are indebted to Prof. W. W. Beeman who kindly made the fine facilities of his laboratory available to us for these measurements.

§ These curves are uncorrected for slit height and such correction would change the quantitative interpretation somewhat; however, the slits are not "infinitely high" and so the asymptotic behavior is still h^{-4} instead of h^{-3} .

TABLE 1.

Composition (at. % Ag)	Radius of gyration (Å)	Radius (Å)	No. of atoms per cluster	Surface to volume ratio (Å ⁻¹)	Radius (Å)	Relative No. of clusters
5.8 3.0 1.3 0.65	4.3 3.8 2.8 2.5	5.5 4.8 3.6 3.2	42 29 12 8	1.0 1.2	3.0	0.75 0.88 1.3 1.0

3.4 < h < 6.2 for the 5% alloy) where, within experimental error, the scattering curve is Gaussian in accordance with the Guinier approximation. At the largest angle, the scattering falls as h^{-4} .

Unambiguous interpretation of the scattering from a polydisperse collection of clusters with arbitrary shapes is impossible, but a reasonable and self-consistent interpretation of this data may be made by considering simple Ag-rich clusters with no internal structure. In this case, the decreasing intensity at small angles is attributed to interparticle interference effects. Radii of gyration of the Ag clusters, determined from the Gaussian region of the scattering curves, are given in column 2 of Table 1. Column 3 gives the radii in angstroms, and column 4 the volumes in units of the atomic volume, of spheres having these radii of gyration. For a polydisperse collection of clusters, the radius of gyration determined from the Guinier approximation is given by (6)

$$\overline{R^2} = rac{\Sigma p(m) n^2_{m} R^2_{m}}{\Sigma p(m) n^2_{m}}$$

where p(m) is the number of clusters containing n_m electrons (actually $(n_m-n_0)^2$ for clusters in a medium with n_0 electrons in an equal volume) and having a radius of gyration R_m . Thus this average emphasizes the large clusters.

An idea of the particle size distribution may be obtained as follows. Assuming all the clusters have uniform and equal electron density, the total surface to total volume ratio is given by:

$$rac{\sum p(m)S_m}{\sum p(m)V_m} pprox \int_0^{\infty} h^2I(h) dh$$

evaluated at large angles where the scattered intensity is proportional to h^{-4} . Interparticle interference effects are important only at the smallest angles and make little contribution to the integral because of the h^2 factor. At large angles, the contribution to the integral from the region beyond the range of the data is determined by extending the h^{-4} dependence. The surface to volume ratio measured in this way for

the more concentrated samples, is given in column 5 of the table. Column 6 gives the radius of the spherical cluster which would have this surface to volume ratio. This radius may be considered as an average which emphasizes the small clusters and a comparison with column 3 indicates that the cluster size distribution is quite narrow.

An estimate of the relative number of clusters, assuming each contains n Ag atoms, can be obtained by extrapolating the linear portion of the Guinier plot to h=0 since the intercept is proportional to Nn^2 , where N is the number of clusters in the illuminated volume. This number is given in column 7 of the table. Knowledge of the absolute scattering would allow one to estimate the total amount of Ag precipitated. Attempting that, in this case, gives an amount of Ag precipitated in excess of the amount present by a factor of 2 or 3. However, in view of the difficulties of this measurement and the sensitivity of the result to the necessary assumptions, this discrepancy is not considered to be serious.

The above interpretation makes use of the experimental data only in the angular range beyond the maximum in the scattering curve. In order to show that the shape of the curve at smaller angles may reasonably be explained as an interparticle interference effect, it is assumed that the clusters are spherical and each has a structure factor given by the extrapolation of the linear region of the Guinier plot. The cluster pair distribution function is assumed to be:

$$\begin{split} p\left(r\right) &= \text{Constant for } r > R_0 \\ &= 0 \text{ for } r < R_0 \end{split}$$

Choosing a value of R_0 ranging from 10 to 12 Å for the various alloys, a Zernike–Prins type equation may be fit to the data essentially within the experimental accuracy. Interparticle interference effects in polydisperse systems are very complicated and this treatment is only intended to give qualitative features of the pair distribution function. It is, however, consistent with the above interpretation

1959

since, for each composition, the volume excluded to other particles contains, in the homogenized alloy essentially the number of Ag atoms per cluster.

Thus it is concluded that the "fast reaction" in Al-Ag alloys leads to a state in which all or almost all of the Ag has precipitated into roughly spherical clusters whose average volume is approximately proportional to the initial concentration, and whose size distribution function is quite narrow. The number of clusters is nearly independent of concentration. These clusters are not situated at random, but tend to stay clearly separated from one another.

Walker and Guinier (3,4) have inverted the small angle scattering curves to obtain the Ag atom pair distribution function, which they interpret in terms of independently scattering centers with an internal structure, each consisting of a nearly spherical Ag cluster surrounded by a shell depleted of Ag. However, it cannot be entirely correct to consider such clusters as scattering independently since, as an appreciable fraction of the Ag is precipitated, any depleted shells must have merged. Although Walker and Guinier describe a final state qualitatively similar to that given above, the present interpretation emphasizes that each Ag cluster must not be considered to have its own depleted shell whose exterior surface has any physical significance.

Acknowledgments

The author acknowledges helpful discussions with D. Turnbull and Prof. W. W. Beeman.

M. B. WEBB

General Electric Research Laboratory Schenectady, New York

References

1. For example D. Turnbull, H. S. Rosenbaum and H. N. TREAFTIS, Submitted to Acta Met. and D. TURNBULL, Solid State Physics Vol. 3, pp. 225-306. Academic Press, N.Y. (1956).

2. H. K. HARDY and T. J. HEAL, Progress in Metal Physics Vol. 5, p. 143. Pergamon Press, London (1954).

3. C. B. WALKER and A. GUINIER, Acta Met. 1, 568 (1953). 4. GUINIER, WALKER, FOURNET and YUDOWITCH, Small Angle

Scattering of X-rays. New York, London (1955).

5. R. H. NEYNABER, Ph.D. Thesis, University of Wisconsin (1955) unpublished.

W. W. BEEMAN, P. KAESBERG, J. W. ANDEREGG, and M. B. Webb, Handbuch Der Physik 32, 321 (1957).

* Received April 6, 1959

The mechanism of crack propagation in ductile metals

A recent study of the fracture behavior of ductile metals has shown(1) that the fracture of a cylindrical bar in tension is initiated by the formation of voids

within the bulk of the metal. These voids grow in the central region of the neck to a considerable size, and then coalesce to form a central crack. Under certain testing conditions the final separation of the two fracture halves takes place by a mechanism which produces what has been termed a "double-cup" fracture. (1.2) Two possible mechanisms have been proposed, one being the "alternating slip" mechanism first suggested by Orowan(3) and the second being some sort of "ductile cleavage."(1) The purpose of this note is to present a third mechanism which better fits all the experimental data and which contains less ad hoc assumptions. Since this final phase of the fracture is merely the propagation of an internal "crack" in a very ductile metal, it will be considered from this aspect.

Part of the problem in understanding ductile crack propagation has been a conceptual or semantic one. Brittle cleavage fracture of metals occurs by the separation of crystallographic planes and the breaking of atomic bonds under the action of a normal stress during crack propagation. This type of normal stress failure does not occur in, or at least is only incidental to, the crack propagation in ductile metals. There are two features essential to this process which must be appreciated before the mechanism becomes clear. They are:

- 1. A surface grain can behave as a constrained single crystal.
- 2. A "crack" in a ductile metal is merely a sharp notch.

It is well known that a single crystal of a ductile metal will, when deformed in tension, very frequently exhibit a knife-edge failure. This results from alternate slip on two systems, and the crystal may be said to glide to failure. Rupture of atomic bonds does not occur under the action of a normal stress which is greater than that imposed on the slip plane by the passage of a dislocation. The behavior of grains at a free surface of a polycrystal will be approximately that of single crystals modified by the constraint of having to remain contiguous to the rest of metal which is behaving, on a gross scale, as a typical polycrystalline aggregate. Plastic flow in a notched bar in tension, as well as during necking of a cylindrical bar, is conceived in plasticity theory as taking place by the inhomogeneous deformation of the volume elements constituting the cross-section, which remain constant in number during deformation. This is not valid for real metals since the total number of "volume elements" (i.e., grains) may decrease whenever a surface grain flows apart, exposing what had previously been an internal grain. For sharply

190

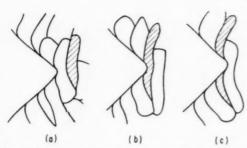


Fig. 1. Schematic behavior of a grain during the propagation of a crack in a ductile metal.

(a) Rapid elongation of the grain as the crack tip approaches it. (b) Slipping apart of the grain as a constrained single crystal when it becomes the surface grain. (c) Two parts of the slipped-apart grain on opposite crack surfaces.

notched or cracked bars this loss of surface grains is the mechanism by which a crack is propagated.

Fried and Sachs⁽⁴⁾ have shown, for notched bars in tension, that when plastic deformation is occurring throughout the transverse section through the notch, there is a larger than average strain occurring at the surface of the bottom of the notch, the ratio of this



FIG. 2. Cross-section through the tip of a crack propagating in fine-grained OFHC copper, showing the large amount of surface flow and bending of the parts of grains on opposite sides of the crack surface. (Oblique illumination) (Copper plated to protect surface). ×1000.

surface strain to the average strain, $\varepsilon_s/\varepsilon_{av}$, increasing as the notch sharpness is increased. The notch sharpness in a circumferentially notched round bar is measured as the ratio of the notch root radius to the radius of the minimum cross-section of the bar through the notch root. When this value is 10, $\varepsilon_s/\varepsilon_{av}=7$. For a much sharper notch the ratio would be much higher, although one would assume that whatever notch was put into the material to start a crack, the actual equilibrium notch sharpness attained during propagation would be a function of the rate of strain hardening, temperature, etc. This is borne out by the data of Fried and Sachs which show that very blunt notches tend to sharpen, while very sharp notches become blunt. Whatever the ratio, however, the primary effect is that while the majority of the grains are gradually elongating in the tension direction, one, or at most a few, grains in a cross-section at the surface of the bottom of the notch are slipping apart under the very high local strain there, thus deepening the notch so that this concentrated strain now occurs in the newly exposed surface grains. Fig. 1 schematically illustrates this crack propagation mechanism. Fig. 2 is a cross-section through a propagating crack in OFHC copper, showing the large amount of surface flow and bending of the grains which have already been parted and now form part of the fracture surface (copper plated for protection). Fig. 3 shows a single grain at the tip of the crack slipping apart as a single erystal would.

Bridgman⁽⁵⁾ found when he subjected metal cylinders to tension under very high hydrostatic stresses that, in addition to the very high local reduction in area which occurred before fracture, the cross-section became non-circular. Although the relatively high degree of preferred orientation that may develop as a result of the large deformation could assist in producing this effect, the primary cause is undoubtedly the substantial reduction in the number of grains remaining in the minimum cross-section. The specimen behavior would then deviate markedly from that of an ideal polycrystal.

Even though the fracture surface of an *ideal* failure of this type should be approximately that of the surface of the necked region of a fractured single crystal, appearing smooth and rippled under the electron microscope, (1) in general one finds on a typical surface the remains of a significant number of extraneous voids. Such voids are formed ahead of the tip of the crack in the region of high triaxial stress, presumably when the grains in this region are oriented unfavorably for slip. If the surface formed by the slipping apart of the crystals crosses one of these voids,

VOL. 7 1959



Fig. 3. A single grain of coarse-grained OFHC copper flowing apart at the tip of a crack. (Oblique illumination) (Copper plated to protect surface). ×500.

part of the void remains on one half of the surface and part of it on the other. When the overall triaxiality is high, the erack prefers to propagate completely by void formation rather than by the process described here. This has been termed the "void sheet" mechanism⁽¹⁾ of crack propagation.

It has previously been shown that the surface of the large internal voids which initiate fracture in ductile metals is the same as that observed for the ductile crack propagation.⁽¹⁾ Thus, small, internal voids, once nucleated, act as little internal cracks or notches and propagate by the same mechanism.

H. C. ROGERS

General Electric Research Laboratory Schenectady, New York

References

- H. C. ROGERS, G.E. Research Laboratory Report 59-RL-2213, submitted to AIME for publication.
 W. I. Pumphrey, Proc. Phys. Soc. 62B, 647 (1949).
- 3. E. Orowan, Reports on Progress in Physics 12, 185 (1948).
 4. M. L. Fried and G. Sachs, ASTM Symposium on Deforma-
- tion of Metals as Related to Forming and Service (1948).

 5. P. W. Bridgman, Studies in Large Plastic Flow and Fracture. McGraw-Hill, New York (1952).

Received June 12, 1959.

Studies of copper targets attacked by shaped charges

Recently, intensive studies have been made $^{(1-6)}$ of the changes in hardness and microstructure in steel samples attacked by jets squirted from high explosives with metal-lined cavities (shaped charges). The present note describes metallographic studies of a face-centred cubic metal (copper) attacked by shaped charges at room temperature (35°C) and at -75°C.

The target, diameter 7.6 cm and length 10.2 cm, was cut from a copper (99.8% purity) bar and annealed. The original grain size was about 0.3 mm. The target was attacked by a metal jet emanating from a 3.8 cm calibre shaped charge, and was then sectioned into quarternary segments of depth 2 cm for metallographic examination.

The segments (plane normal to the axis of the crater) were ground, polished, and etched with ferric chloride. Fig. 1 shows the recrystallized polygonal grains of copper of 2.5-5 μ average size. Annealing twins were not observed in the recrystallized grains. The depth of the region was about 0.1 mm. The presence of fine recrystallized grains and absence of annealing twins indicate that the metal at the profile of the target did not attain sufficiently high temperatures to cause crystal growth. Adjoining this region was a heavily deformed region up to about 1.5 mm from the crater edge. The deformed and elongated grains therein showed etch markings or strain markings parallel to the contour of the crater. These were wavy, curved or branched, and could not be resolved. This region shows signs of very high lattice distortion and fragmentation. From 1.5 mm to 5.5 mm distance from the crater edge, the structure consisted of large polygonal grains with etch markings (Fig. 2), bent annealing twins (Fig. 3), and deformation twins (Fig. 4). Generally the etch markings had a single orientation in each grain, but in a few grains two or three directions were observed. The fact that the deformation twins are generally straight, and

191

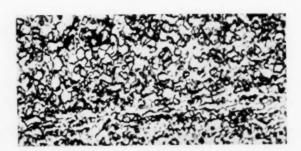


Fig. 1. Photomicrograph showing the recrystallized region very near the crater surface. $\times 1000$.



Fig. 2. Photomicrograph showing the etch markings. $\times 100$.

parallel to each other, and that, when one twin approaches the side of another, there is clear evidence of a tendency to "pinching off", differentiates these effects from etch markings. The deformation twins are very narrow as compared to the annealing twins. Occasionally the grains showed neither etch markings nor deformation twins. It appears that the behaviour of a grain is dependent on its orientation in relation to the shock. The etch markings are possibly due to fragmentation or other localized atomic changes, and the bent annealing twins indicate lattice bending in the region under the transient stresses. Beyond 7 mm, the structure of the target was analogous to that of the original structure.

In another set of experiments, the targets were cooled to $-75^{\circ}\mathrm{C}$ by immersing them in a bath of solid carbon dioxide, and then fired at by shaped

1959

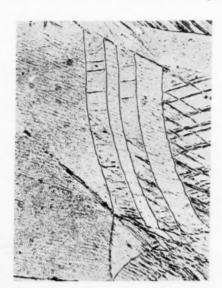


Fig. 3. Photomicrograph showing the bent annealing twins. $\times 200$.

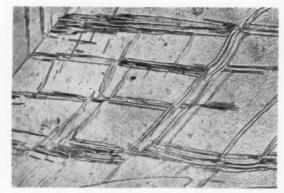


Fig. 4. Photomicrograph showing crossed deformation twins, $\times 600$.

charges. The crater diameter in the cooled target was less than in the room temperature experiment. This is possibly due to the decreased ductility and increased strength at lower temperatures. A microstructural examination of the cooled target showed however identical structures to that attacked at room temperature.

It is of interest to point out that deformation twins were observed by Blewitt et al.⁽⁷⁾ in copper crystals subjected to tensile tests at 4.2°K and also in silver and gold crystals; by Smith⁽⁸⁾ in copper samples subjected to shock pressures of more than 200 kilobars, and by Suzuki and Barrett⁽⁹⁾ in silver–gold alloy crystals under tensile test at low temperatures. The deformation twins reported here in copper samples are analogous to that observed in the copper slug.⁽¹⁰⁾

In most of the segments, shear fractures at approximately 45° to the circumference of the crater were also observed. These fractures are analogous to that observed in iron targets. (2,3)

Microhardness measurements were taken along

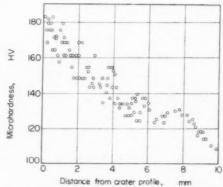


Fig. 5. Typical microhardness (HV = Hardness Vickers, measured with the Leitz Durimet microhardness tester employing a load of 50 gm) curve plotted from data taken along a radius of a circular cross-section of the target.

different radii of the targets impacted both at room temperature and at -75° C. The hardness values showed a large scatter, particularly in the heavily deformed region, and indicated the absence of plateaus along which the hardness remained constant (Fig. 5). The decrease in hardness along any radius is obviously due to the decreasing deformation of the grains.

Acknowledgments

The authors are grateful to Professor D. S. Kothari. Scientific Adviser to the Minister of Defence, for his interest and encouragement and for permission to publish this note. Thanks are also due to Dr. R. C. Deshpande for valuable suggestions and Mr. T. G. Shamanna for assistance in the metallographic work.

Defence Science Laboratory SAMPOORAN SINGHT Research and Development Organisation Ministry of Defence New Delhi, India

Machine Tool Prototype Factory A. Soundraraj Ambarnath, India

References

- 1. W. M. Evans and G. I. Taylor, Research, Lond. 5, 502 (1952).
- 2. S. Singh and P. N. Gandhi, Research, Lond. 9, 55 (1956).
- 3. S. Singh, N. R. Krishnaswamy and A. Soundraraj, J. Appl. Phys. 27, 617 (1956).

4. H. P. Tardif, Research, Lond. 9, S42 (1956).

- S. Singh and A. Soundraraj, Acta Met. 6, 557 (1958).
 A. Soundraraj and S. Singh, J. Sci. Industr. Res. (India) B18, 86 (1959).
- 7. T. H. BLEWITT, R. R. COLTMAN and J. K. REDMAN, J. Appl. Phys. 28, 651 (1957).

- 8. C. S. SMITH, Trans. Met. Soc. 214, 574 (1958). 9. H. Suzuki and C. S. Barrett, Acta Met. 6, 156 (1958). 10. S. Singh, A. Soundraraj and R. C. Deshpande, Trans. Met. Soc. 215, 166 (1959).
 - * Received June 23, 1959.

The plasticity of alkali halide crystals*

Some recent work by Aerts and Dekeyser(1) and by Gorum et al. (2) has suggested a new explanation of the Joffé effect. These authors have found that rocksalt. and indeed a number of ionic crystals having the rocksalt type of structure, are inherently ductile. The apparent brittle behaviour of these materials has been shown to be attributable not to surface microcracks postulated by Joffé but to a reaction of the crystal surface with components of the atmosphere. It is suggested by Gorum et al. that this reaction produces a surface layer through which it is difficult for dis-

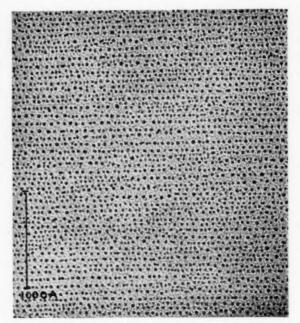


Fig. 1. Slip steps on the surface of potassium bromide crystal decorated with gold. ×240,000.

locations to pass from the interior of the crystal to the surface, although no detailed explanation of how the mechanism operates has been proposed.

VOI

7

19

Some support for the view that it is a reaction between the crystal surface and atmospheric components which influences markedly the motion and generation of dislocations in rocksalt is given by the following observations.

A number of slices approximately $12 \times 2 \times 2$ mm were cleaved from melt grown crystals of various alkali halides. Within about ½ min of the generation of new faces by cleavage, the slices were deformed in bending. Under these conditions it was possible to strain some specimens by several per cent. The tension face of the bent crystals was then examined in an electron microscope by the decoration replica method previously described by Bassett(3). This method of examination is able to reveal surface steps on the crystal down to atomic dimensions, by preferential nucleation of vacuum evaporated gold along step edges.

Closely and uniformly spaced slip steps, as illustrated in the accompanying micrograph, were observed in this way on the bent crystals. The mean spacing of 60 Å of the slip lines, on the particular crystal of potassium bromide illustrated here, was remarkably uniform over the length of the crystal face available for examination in the microscope. Estimates of the strain from the radius of bending, and from the spacing of the slip lines taken to be uniform over the

[†] Now at Armament Research and Development Establishment, Fort Halstead, Kent, England.

gauge length of the crystal, coincide closely, if it is assumed that unit slip has occurred on each operative slip plane.

Crystals which have aged in air after cleavage and show the normal near-brittle behaviour may still be deformed plastically by a small amount generally less than 1 per cent. However a decoration replica of an aged deformed crystal shows no evidence of surface steps associated with this deformation. The few slip steps observed on the aged surface arise from incidental deformation during cleavage. This is consistent with the observations of Pratt⁽⁴⁾ that, at room temperature, slip in rocksalt is unable to break through to the surface to form steps.

It is of interest to inquire into the origin of the large numbers of dislocations producing the uniform deformation before ageing. It may be that surface sources play an important role in the deformation of the freshly cleaved crystal, and that after penetration of the crystal surface by components of the atmosphere these sources are inhibited and the crystal becomes brittle. An alternative explanation, however, is that the plastic deformation leading to bending originates from internal sources, but that the dislocations from these can emerge at the surface only after fresh cleavage. Exposure to the atmosphere in some way develops a hard brittle layer which restricts complete plastic deformation and ultimately breaks down by cracking. As yet, there is insufficient evidence to enable a choice to be made between these two explanations.

Thanks are due to Dr. J. W. Menter and several laboratory colleagues for useful discussion and to the Chairman of Tube Investments Ltd. for permission to publish this note.

G. A. Bassett

Tube Investments Research Laboratories Hinxton Hall, Cambridge, England

References

- 1. E. Aebts and W. Dekeyser, Acta Met. 4, 557 (1956). A. E. GORUM, E. R. PARKER and J. A. PASK, J. Amer. Ceram. Soc. 41, 161 (1958).
- G. A. Bassett, Phil. Mag. 3, 1042 (1958).
 P. L. Pratt, 1953 Discussion, Properties of Metallic Surfaces, p. 346. Institute of Metals, London (1954).
 - * Received June 11, 1959.

1959

On two dimensional nucleation[†]

Classical nucleation theory, (1) in which nuclei of the stable phase of the critical size for stability are assumed to be in equilibrium with the untransformed metastable phase, yields a rate expression for nucleation.

$$J^* = \omega_i^* n_i^*, \tag{1}$$

where ω^*_i is the frequency with which critical nuclei become supercritical and n,* is the concentration of critical nuclei. Zeldovich(2) modified equation (1) to account for depletion of critical nuclei in the nonequilibrium situation obtaining when nucleation proceeds, yielding

$$J^* = Z\omega_i^* n_i^*, \tag{2}$$

where Z is the Zeldovich factor. In the most elegant treatment of homogeneous nucleation of three dimensional particles from the vapor phase, Reiss(3) has shown

$$Z = (\Delta F_i^*/3\pi k T i^{*2})^{1/2} \tag{3}$$

where ΔF_i^* is the free energy of formation of the critical size nucleus, i* is the number of atoms in the critical nucleus, and k and T have their usual meaning. Also Turnbull and Fisher⁽⁴⁾ present a treatment of homogeneous nucleation in condensed phases that vields the same Zeldovich factor, equation (3), as for condensation from the vapor phase (although their work appears to give a different result because of the omission of a factor $i^{*2/3}$ in their final equation).

Now, in the growth of a perfect crystal plane from the vapor, Kossel(5) has shown that condensation takes place by the discontinuous addition of monolayers to the crystal surface; and that two dimensional homogeneous nucleation is required to form such monolayers. However, Frank⁽⁶⁾ has shown that growth can take place without the requirement for monolayer nucleation if the surface is intersected by a dislocation with a screw component normal to the surface. Nevertheless, a kinetic treatment of growth in such a case (7,8) indicates that the condensation coefficient (the ratio of rate of condensation to rate of impingement from the vapor) should change abruptly. as a function of supersaturation, at the supersaturation corresponding to Kossel's two dimensional nucleation. Hence it is interesting to extend the Zeldovich treatment to the case of two dimensional nucleation.

The free energy of formation of a two dimensional nucleus containing i atoms is

$$\Delta Fi = Ai^{1/2} + \Omega \Delta F_v i, \tag{4}$$

where Ω is the atomic volume, ΔF_{e} is the bulk free energy change per unit volume, and A is a factor depending on nucleus geometry. Here a disc shaped nucleus is assumed and $A = 2(\pi a\Omega)^{1/2}\sigma$, where σ is the specific interfacial free energy of the condensed phase

and a is the step height of the monolayer. Classically, using equation (1), one would maximize equation (4) with respect to i to obtain ΔF_i^* which gives

$$n_i^* = n \exp\left(-\Delta F_i^*/kT\right),\tag{5}$$

where n is the concentration of single atoms adsorbed on the crystal surface and is a function of the supersaturation p/p_e , i.e. $(n/n_e) = (p/p_e)$, where p_e is the equilibrium vapor pressure over the surface, p is the actual vapor pressure, and n_e is the concentration of adsorbed atoms on the surface in equilibrium with a disc of infinite radius. Further, nuclei will grow by surface diffusion of atoms adjacent to the critical nucleus so(9)

$$\omega_i = 2\alpha n(\pi\Omega a)^{1/2} i^{1/2} v \exp(-\Delta F_D/kT). \tag{6}$$

where ν is the vibrational frequency of adsorbed surface atoms, $\alpha = 1/4$ is the probability of jumping in the direction of the critical nucleus and ΔF_D is the activation energy for surface diffusion. For the growth of critical nuclei, $\omega_i = \omega_i^*$ and the classical expression obtains:

$$J^* = 2\alpha n^2 (\pi \Omega a)^{1/2} i^{*1/2} \nu \exp{[-(\Delta F_i^* + \Delta F_D)/kT]}. \eqno(7)$$

Now consider the non-equilibrium kinetics. For net transfer from size i to i + 1 the positive flux is

$$J_{\perp} = \omega_i n_i. \tag{8}$$

The negative flux, J_{-} , is difficult to evaluate because of the uncertainty in estimating the activation energy for dissociation of an atom from a disc of size i + 1. However suppose that a population of discs of size i+1 is in equilibrium with an adsorbed atom population n'. Then by the principle of microscopic reversibility the flux of atoms J_{-} will just equal the flux of atoms, $J_{+}' = \omega'_{i+1} n_{i+1}$, condensing onto the dises from the population n'. Referring back to equation (6) it is seen that $\omega'_{i+1} = \omega_{i+1} n'/n$ so

$$J_{-} = J_{+}{}' = \omega_{i+1} n_{i+1} n' / n. \tag{9}$$

From the Gibbs-Thompson equation

$$n = n_e \exp(\sigma \Omega / r^* kT) = n_e \exp(A/2kTi^{*1/2}),$$
 (10)

$$\begin{split} n' &= n_e \exp{(\sigma \Omega / rkT)} = n_e \exp{(A/2kTi^{1/2})} \\ &= n \exp{[A(i^{-1/2} - i^{*-1/2})/2kT]}, \end{split} \tag{11}$$

where r is the radius of a disc of size i. Combining equations (8), (9), (10), and (11) and noting that $n_i + 1 = n_i + (\partial n_i/\partial i)$ and $\omega_i + 1 \simeq \omega_i$, the following differential equation obtains

$$\begin{aligned} (\partial n_i/\partial i) + n_i \{ 1 - \exp\left[A(i^{*-1/2} - i^{-1/2})/2kT\right] \} \\ = -J \exp\left[A(i^{*-1/2} - i^{-1/2})/2kT\right]/\omega_i, \end{aligned} (12)$$

where J is the net flux = $J_{+} - J_{-}$. This differential equation is now in exactly the same form as that treated by Turnbull and Fisher⁽⁴⁾ and is subjected to similar constraints so, referring the details to their paper, the solution to equation (11) is

$$J = J^* = 2\alpha^2 (\pi \Omega a)^{1/2} i^{*1/2} \nu (\Delta F_i^* / 4\pi k T i^{*2})^{1/2}$$
$$\exp\left[-(\Delta F_i^* + \Delta F_D / k T)\right]. \tag{13}$$

Comparing equations (7) and (13) it is evident that the Zeldovich factor for two dimensional homogeneous nucleation is

$$Z = (\Delta F_i^* / 4\pi k T i^{*2})^{1/2}. \tag{14}$$

This factor is typically about 10⁻² and typically increases the calculated value for critical supersaturation by 10 to 15 per cent.

The author would like to thank Dr. G. M. Pound of this laboratory for stimulating discussions. This work was sponsored by the U.S. Office of Naval Research.

J. P. HIRTH

VOI

195

Metals Research Laboratory. Carnegie Institute of Technology. Pittsburgh 13. Pennsylvania

References

- 1. M. Volmer, Kinetic der Phasenbildung, Edwards Brothers, Ann Arbor, Michigan (1945).

- J. B. Zeldovich, Acta Physicochim. U.R.S.S. 18, 1 (1943).
 H. Reiss, J. Chem. Phys. 20, 1216 (1952).
 D. Turnbull and J. C. Fisher, J. Chem. Phys. 17, 71
- 5. W. Kossel, Nachr. Ges. Wiss, Goettingen, 135 (1927).
- F. C. Frank, Disc. Faraday Soc. 5, 48 (1949).
 J. P. Hirth and G. M. Pound, Acta Met. 5, 649 (1957).
- 8. J. P. HIRTH and G. M. POUND. To be published.
- G. M. POUND, M. T. SIMNAD and L. YANG, J. Chem. Phys. 22, 1215 (1954).
 - † Received April 10, 1959; revised version June 15, 1959.

LATTICE PARAMETER AND RESISTIVITY STUDY OF ORDER IN THE ALLOY CuAu₂*

P. WRIGHT† and K. F. GODDARD†‡

Observed changes in lattice parameter and resistivity with degree of order indicate $T_c \simeq 190\,^{\circ}\mathrm{C}$ for the alloy CuAu₃; from Cowley's theory of order this yields $V_1 = 269k$, $V_2 = -26.9k$, $V_3 = 0$, for the ordering interaction energies of pairs of atoms separated by the three shortest distances.

The possibility of a linear relationship between lattice parameter and short-range order parameter or configurational energy is examined.

PARAMETRE CRISTALLIN ET RESISTIVITE DANS L'ALLIAGE CUAU3 ORDONNE

Les modifications observées pour le paramètre réticulaire et pour la résistivité en fonction du degré d'ordre fournissent $T_c \simeq 190\,^{\circ}\mathrm{C}$ por l'alliage $\mathrm{CuAu_3}$. A partir de la théorie de Cowley, ce résultat conduit à $V_1 = 269k$, $V_2 = -26.9k$, $V_3 = 0$ pour les énergies d'interaction de paires d'atomes séparées par les trois distances les plus courtes.

Les auteurs examinent la possibilité d'une relation linéarie entre le paramétre cristallin et le paramètre d'ordre à petite distance (ou l'énergie de configuration).

UNTERSUCHUNG DER ORDNUNGSEINSTELLUNG VON $\mathrm{CuAu_{3}}$ DURCH MESSUNGEN VON GITTERPARAMETER UND WIDERSTAND

Die beobachtete Abhängigkeit von Gitterparameter und Widerstand vom Ordnungsgrad zeigt, dass für die Legierung CuAu₃ $T_c \simeq 190^{\circ}$ C ist; nach der Ordnungstheorie von Cowley ergibt das $V_1 = 269k$, $V_2 = -26.9k$, $V_3 = 0$ für die die Ordnung bestimmenden Wechselwirkungsenergien von Atompaaren, die durch die drei kürzesten Abstände getrennt sind.

Die Möglichkeit einer linearen Beziehung zwischen dem Gitterparameter und dem Nahordnungsparameter oder Konfigurations-Energie wird geprüft.

1. INTRODUCTION

VOL.

1959

Although weak superlattice reflections from Cu-Au alloys near the composition CuAu₃ were first observed in 1936,(1) conclusive evidence of ordering was not obtained until comparatively recently. (2) From observations of the disappearance of superlattice lines as initially ordered alloys were annealed at successively higher temperatures, Batterman⁽³⁾ placed the critical temperature at 199°C for the composition CuAu₂. He also determined some order parameters for this alloy and found them to be qualitatively similar to those for Cu₃Au; unlike Cu₃Au, however, sharp superlattice lines could not be obtained by annealing, and from the width of the lines the maximum size of antiphase domains appeared to be about 50 Å. The existence of small antiphase domains has been postulated by the present writers to account for the anomalous resistivity of ordered CuAu3. (4) The ordered resistivity-temperature curve for the quenched alloy indicated a critical temperature of ≃190°C in agreement with Cowley's prediction. (5) We have since confirmed this result by resistivity measurements "at temperature", and also by studying the change in lattice parameter with degree of order; the results of these investigations are presented herein.

2. RESISTIVITY MEASUREMENTS

In Fig. 1(a), a section of the curve is reproduced. which shows the variation with temperature in the quenched resistivity of a CuAu₃ wire (74.40 at. % Au) in which the equilibrium degree of order had been established by a pulse-annealing process. (4,6) In this process a wire filament of the alloy was heated by an electric current from room temperature to a predetermined annealing temperature in about 20 sec. The temperature was thermostatically controlled during the anneal, the wire was then quenched to room temperature in a few seconds by a jet of cold nitrogen. and its resistivity at 20°C determined from potentiometer measurements near room temperature. Provided the lattice configurations corresponding to different annealing temperatures are retained during quenching, variations in resistivity due to changes in configuration can be studied in the absence of relatively large variations due to temperature.

For the purpose of comparison with Fig. 1(b), where the equilibrium resistivity of a sample of the same wire was measured at the annealing temperature, the ordinates have been chosen to represent percentage changes referred to equilibrium values at 400°C. The curve Fig. 1(b) was determined with the wire in a precisely controlled furnace; the resistivities ρ are the limiting values attained by long annealing at constant temperature.

In obtaining both curves, an annealing period of a few hours was usually sufficient to produce equilibrium

^{*} Received November 26, 1958.

[†] University College of North Wales, Bangor.

^{*} Now at Royal Aeronautical Estab., S. Farnborough,

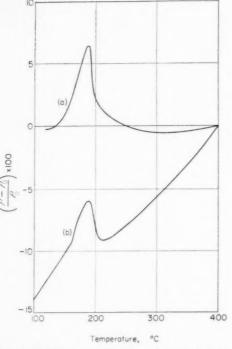


Fig. 1. Equilibrium resistivity of ordered $CuAu_3$ vs. temperature.

Curve (a). Resistivity measured at 20°C after pulseannealing.

Curve (b). Resistivity measured 'at temperature'. $^{o}_{o}$ changes in resistivity (ρ) referred to resistivity (ρ_{0}) at 400°C.

at temperatures above 190°C. The isothermals, Fig. 2, show, however, that annealing periods of over 2000 hr are required at temperatures below 190°C when the alloy is initially in the disordered state. The 167°C isothermal, Fig. 2(a), was obtained by pulse-annealing with the alloy initially in equilibrium at 195°C. After this long anneal, equilibrium was established by annealing for a few days at other temperatures between 190°C and 120°C; below ~120°C the relaxation proceeded too slowly to be profitably followed. The 169°C isothermal, Fig. 2(b), was determined "at temperature" with the alloy initially in equilibrium at 190°C. As may be seen from the form of this curve, equilibrium is not readily established by simple isothermal annealing. A total annealing period of about 6 months was required in determining the part of the equilibrium curve below 190°C, and no isothermal change in resistivity was observed at temperatures below ∼160°C.

The "at temperature" measurements provide general confirmation of the earlier results obtained by pulse-annealing; the implications of these results have already been fully discussed elsewhere. (4) The method of annealing does, however, influence the

rate at which ordering proceeds, as may be seen by comparing the isothermals, Fig. 2. Though the additional ordering produced by a single pulse-anneal is believed to be small, the many pulsing and quenching operations involved in obtaining an equilibrium state at any temperature evidently do, in effect, accelerate the ordering relaxation and thereby extend the lower limit of temperature at which long-range order can be induced in the alloy. It is to be concluded that the ordering process is facilitated by vacancy migrations at some stage or stages in a pulse-annealing operation.

3. LATTICE PARAMETER MEASUREMENTS

Lattice parameter measurements were made using a back-reflection focusing camera, with the powder specimen oscillated to produce smooth spectrum lines. CoK_{π} radiation gave a single doublet reflection at a high Bragg angle from the (331) planes of the CuAu₂ f.c.c. lattice. Powder samples were obtained from small ingots prepared by fusing spectroscopically pure metals in evacuated silica tubes. Each ingot was homogenised by alternate annealing and cold work until the lattice parameters of filings from centre and ends agreed within the limits of accuracy of the parameter measurements. Finally the ingots were powdered, annealed for 15 min at 893°C, and quenched in liquid air: the measured parameters at 21°C ranged from 3.97613 kX to 3.97660 kX, indicating a difference in composition of about 0.1 at. %. The error in our observations of change in parameter with degree of order is represented by the uncertainty in the last figure, i.e. of the order $10^{-5} kX$.

After annealing at 893°C and quenching in liquid air, the powdered material was divided into small portions each of which was sealed into an evacuated Pyrex capsule and annealed at a different temperature. The procedure was essentially one of pulse-annealing since the specimen was inserted in a hole in a copper block which was already at the annealing temperature, and, after annealing, rapidly quenched in water. The lattice parameter of the alloy was then determined and the powder replaced in the furnace for a further period of annealing. Complete isothermals showing the change in lattice parameter, Δa (with respect to the alloy as quenched from 893°C), as a function of time were obtained by this method at several representative temperatures between 300°C and 160°C (see Fig. 3). At other temperatures in this range the limiting values of Δa were determined by sufficiently long annealing.

The time required to reach equilibrium increased with decreasing temperature, but whereas only a few

VOI 7 195



Fig. 2. Resistivity isothermals for $CuAu_3$. Curve (a). Resistivity measured at 20°C after pulse-annealing at 167°C; alloy initially in equilibrium at 195°C. Curve (b). Resistivity measured at annealing temperature 169°C; alloy initially in equilibrium at 190°C. $0'_6$ changes in resistivity (ρ) referred to initial resistivity (ρ_1) .

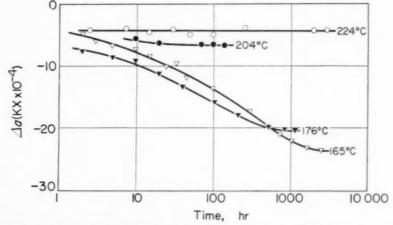


Fig. 3. Lattice parameter isothermals for CuAu₃. \(\Delta a = \text{change in lattice parameter measured at 21°C. Alloy initially as quenched from 893°C.

hours of annealing were required at temperatures above 190°C, upwards of 2000 hr were necessary below 190°C. The variation of lattice parameter with annealing temperature is shown in Fig. 4; all the data refer to the alloy in equilibrium. The curve is seen to descend rapidly below 200°C and to have an inflexion at ~190°C.

 Δa becomes immeasurably small above about 350°C; this supports the view that no significant fraction of the parameter change is to be attributed to annealing-out of defects in excess of the equilibrium value at the anneal temperature.

4. DISCUSSION OF RESULTS

The results of both resistivity and lattice parameter investigations are consistent with the conclusion that the critical temperature T_c for the ordering transition in CuAu₃ is approximately 190°C. From Cowley's theory of order

$$T_c = rac{3}{2k} \left(V_1 - rac{3}{2} V_2 + \cdots
ight)$$

where V_1 , V_2 , etc. are the ordering interaction energies between pairs of atoms separated by the first, second, etc. shortest distances. Cowley obtained good agree-

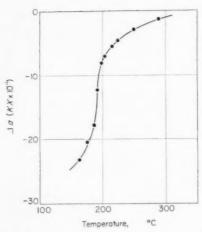


Fig. 4. Variation of lattice parameter of ordered ${\rm CuAu_3}$ with temperature. Equilibrium values of Δa plotted against annealing temperature.

ment between experimental and theoretical values of order parameters for $\mathrm{Cu_3Au}$ by taking $V_2 = -V_1/10$ and ignoring further energy terms. With this same assumption we find from the observed $T_c = 190^{\circ}\mathrm{C}$ for $\mathrm{CuAu_3}$, using the above formula,

$$V_1 = 269k, \quad V_2 = -26.9k$$

From a thermodynamical treatment of relaxation effects arising from local order, Le Claire and Lomer⁽⁷⁾ derived a relation between the changes in energy dV, lattice parameter da, and short-range order parameter $d\sigma$, based upon the assumption that the total configurational energy can be expressed in terms of a

single interaction energy V. For the $\mathrm{CuAu_3}$ f.c.e. lattice the relation reduces to

$$dV/da = 6Ka \cdot da/d\sigma$$

where $\sigma = [q-q \, ({\rm random})]/[q({\rm max})-q({\rm random})], \, q$ being the fraction of unlike nearest-neighbour pairs, and K is the bulk modulus. Assuming K lies between 1 and $2\times 10^{12}\,{\rm dyn}\,{\rm cm}^{-2}$, we find that corresponding to the maximum value of Δa observed in the present experiments, the change in V is 0.5–1 per cent. This is of the same order of magnitude as that calculated on the assumption that V is proportional to a^{-6} .

For the alloy Cu_3Au the $\Delta a: T$ relation corresponding to that of Fig. 4 has been determined experimentally by Betteridge(8). The curve obtained resembles that for CuAu3, and descends sharply at the known critical temperature, 390°C, for Cu₂Au. Betteridge, and more recently Dienes(9), by making certain arbitrary assumptions find that the lattice parameter is linearly related to the short-range order parameter. As there is not sufficient experimental data on order parameters to verify this relation, we have taken Cowley's theoretical values of σ at various temperatures and plotted these against the observed values of the lattice parameter a, for both Cu₂Au and CuAu3. The curves obtained in this way do not support the possibility of a linear relationship between a and σ . This might be taken to indicate that the interaction between an atom and its neighbours is not adequately represented by a single order parameter. We have, therefore, in Fig. 5, plotted the

19

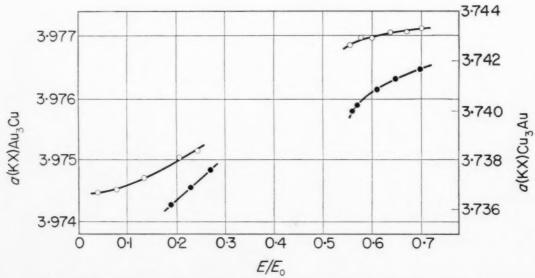


Fig. 5. Variation of lattice parameters of ordered Cu₃Au and CuAu₃ with configurational energy,

O Cu₃Au (Betteridge).

O CuAu₃ (Wright and Goddard).

observed values of a as a function of the total configurational energy E (referred to E_0 the energy difference between perfect order and complete randomness); the E/E_0 are derived from Cowley's theoretical results, the energy contributions from both first and second nearest neighbour pairs being considered.

Since E/E_0 is largely determined by the order parameter for the first shell of nearest neighbours the E/E_0 : a curves exhibit the same general characteristics as the σ : a curves. Below T_c there is some indication that a is approximately linear in E/E_0 , but there is clearly no simple relation covering the whole range of the ordering transformation.

A possible explanation of the non-linearity may be found in the early work of Jones and Sykes(10) in which they showed that the lattice parameter of CuAu₃ varied with the size of the antiphase nuclei present. Nuclei of various sizes having the same degree of local order were produced by annealing for different periods at a constant temperature below T_c . It was established that the value of the lattice parameter was proportional to the relative amounts of ordered and disordered material, and that the parameter did not attain its true or final value until the nuclei had grown to a size comparable with the grain size of the alloy. If, as appears probable from

1959

the accumulated evidence, nuclei of local order already exist in alloys at temperatures above T_c , the growth of these nuclei in size and number as T_c is approached from higher temperatures introduces a factor affecting lattice parameter which is not taken into consideration in the theoretical treatments mentioned above. Some support for this argument is given by the marked departure from linearity in the E/E_0 : a relation above T_c in the case of CuAu₃, since for this alloy resistivity measurements show that nucleation is a dominant feature of the ordering process.

ACKNOWLEDGMENT

It is a pleasure to record our thanks to the Royal Society for financial assistance.

REFERENCES

- 1. C. H. Johansson and J. O. Linde, Ann. Phys. 28, 1 (1936).
- M. HIRABAYASHI, J. Japan Inst. Metals 16, 67 (1952).
 B. W. BATTERMAN, J. Appl. Phys. 28, 556 (1957).
 P. WRIGHT and K. F. GODDARD, Proc. Phys. Soc. 71,
- 506 (1958).
- J. M. COWLEY, Phys. Rev. 77, 669 (1950).
 P. WRIGHT and K. THOMAS, Brit. J. Appl. Phys. 9, 330 (1958).
- 7. A. D. LE CLAIRE and W. M. LOMER, Acta Met. 2, 731 (1954).
- W. Betteridge, J. Inst. Met. 75, 559 (1949).
- 9. G. J. DIENES, Acta Met. 6, 278 (1958).
- 10. F. W. Jones and C. Sykes, Proc. Roy. Soc. A 166, 376 (1938).

THE LATTICE SPACINGS AND THE STABILITY OF CLOSE-PACKED HEXAGONAL Cu-Ga, Cu-Ge AND Ag-Al ALLOYS*

T. B. MASSALSKI† AND B. COCKAYNE†

The lattice spacings of close-packed hexagonal ζ -phases in the systems Cu–Ge, Cu–Ga and Ag–Al have been determined as a function of composition and electron: atom ratio, using alloys quenched from 550°C. The results how that overlap of occupied states across the {1010} faces of the Brillouin zone occurs at the electron: atom ratio of 1.415 in Cu–Ge alloys, 1.43 in Cu–Ga alloys and at 1.47 in Ag–Al alloys. In all three systems the relative distortion of the a lattice spacings due to overlap increases linearly at higher values of overlap at a rate of 3.5 × 10⁻³ Å per 0.1 increase in the electron: atom ratio.

In the system Ag–Al the change of slope in the c lattice spacings near the electron : atom value of 1.62 may be interpreted in terms of interaction of the Fermi surface with the $\{1010\}$ faces of the Brillouin zone before contact.

LES DIMENSIONS DU RÉSEAU ET LA STABILITÉ DE LA PHASE HEXAGONALE COMPACTE DANS LES ALLIAGES Cu-Ga, Cu-Ge et Ag-Al

Les auteurs ont trempé à partir de $550\,^{\circ}\mathrm{C}$ des alliages de Cu–Ga, Cu–Ge et Ag–Al et déterminé les dimensions du réseau de la phase ζ hexagonale compacte en fonction de la composition et du rapport électrons : atomes. Les résultats révèlent qu'il y a un chevauchement des états occupés sur les plans $\{1010\}$ des zones de Brillouin pour les rapports électrons : atomes de 1,415 pour les alliages de Cu–Ge, de 1,43 pour ceuse de Cu–Ga et de 1,7 pour les alliages de Ag–Al. Ce chevauchement entraîne dans les trois systèmes une distorsion relative du paramètre "a" du réseau qui augmente d'une façon linéaire à raison de $3.5 \times 10^{-3}\,\mathrm{\mathring{A}}$ pour un accroissement de 0,1 des rapports électrons : atomes.

Dans le système Ag-Al, le changement de la pente du paramètre c du réseau aux environs d'un rapport électrons : atomes de 1,62 peut être interprété comme une interaction des surfaces de Fermi avec les plans $\{10\overline{10}\}$ des zones de Brillouin avant contact.

GITTERKONSTANTEN UND STABILITÄT DER HEXAGONAL DICHTGEPACKTEN LEGIERUNGEN Cu–Ga, Cu–Ge und Ag–Al

Die Gitterkonstanten der ζ -Phasen (hexagonale dichteste Kugelpackung) in den Systemen Cu–Ga, Cu–Ge und Ag–Al wurden als Funktion der Zusammensetzung und des Verhältnisses Elektronen : Atome bestimmt. Dazu wurden die Legierungen von 550° C abgeschreckt. Das Verhältnis Elektronen : Atome, bei dem die besetzten Zustände die $\{1010\}$ -Flächen der Brillouin-Zone überlappen, beträgt 1,415 für Cu–Ge-, 1,43 für Cu–Ga-Legierungen, dagegen 1,47 für Ag–Al-Legierungen. In allen drei Systemen steigt die relative Änderung der Gitterkonstanten a infolge der Überlappung linar, und zwar um 3.5×10^{-3} , wenn das Verhältnis Elektronen : Atome um 0,1 steight.

Beim System Ag–Al ändert sich beim Verhältnis Elektronen: Atome 1,62 die Neigu der Kurven für die Gitterkonstante c. Das lässt sich verstehen, wenn man eine Wechselwirkung der Fermi-Oberfläche und der {1011}-Flächen de Brillouin-Zone bereits vor ihrer Berührung annimmt.

1. INTRODUCTION

Intermediate phases with the close-packed hexagonal structure (c.p. hex.) are often stable in the systems which copper, silver and gold form with the elements of the B-subgroups of the periodic table. When such phases are present the ranges of their homogeneity lie within the broad region of electron concentration values between approximately 1.3 and 1.8, and they are often referred to as electron compounds. (1–3) The term electron concentration (e/a) usually denotes the ratio of all valency electrons to the number of atoms.

Previous investigations⁽¹⁻³⁾ have shown that although the positions, and widths, of individual phases in different equilibrium diagrams show quite

considerable scatter when expressed in terms of values of e/a, the most frequently observed values are in the region either of 3/2 or 7/4. Nevertheless almost all such phases can be classified as electron compounds, and they are believed to be stabilized by interaction of the Fermi surface and certain faces of the Brillouin zone. (3,4) Information about the nature of such interaction can usually be obtained from the study of the variation of lattice spacings with composition, and e/a. All the c.p. hex. phases so far examined show remarkably consistent trends.

If, as a result of the increase in the electron concentration, the $\{10\overline{1}0\}$ faces of the Brillouin zone are about to be touched by the Fermi surface, or if they are overlapped, the a lattice spacings, extending in the direction at right angles to the $\{10\overline{1}0\}$ faces, expand, and the axial ratio decreases; (2.3) if the interaction takes place between the Fermi surface and the $\{0002\}$ faces of the zone the c lattice spacings expand and the

^{*} Received December 12, 1958.

[†] Dept. of Physical Metallurgy, University of Birmingham, Edgbaston, Birmingham 15, England.

^{*} Now at Mellon Institute Pittsburgh 13, Pa., U.S.A.

ACTA METALLURGICA, VOL. 7, DECEMBER 1959

axial ratio increases. The mechanisms for such axial ratio distortions have been discussed by Jones⁽⁵⁾, Goodenough⁽⁶⁾, Schubert⁽⁷⁾ and others,

Previous investigations have also shown that the e/a is the major controlling factor which influences the systematic changes of the lattice spacings and of the axial ratio observed in e.p. hex. electron compounds. If the composition of alloys in a ternary system is adjusted so that no change of e/a occurs the axial ratio remains strikingly constant.⁽⁴⁾

The present investigation is an extension of lattice spacing measurements already made on other systems based upon copper, silver and gold. Changes in lattice spacing have been accurately measured in the systems copper–gallium, copper–germanium, and silver–aluminium, at values of e/a between 1.36 and 1.8. The interpretation of the data so obtained provides new information about the onset, and influence, of overlap across the $\{10\overline{1}0\}$ faces of the Brillouin zone in all three systems, and the nature of interactions between the approaching Fermi surface and the $\{10\overline{1}1\}$ zone faces in the system silver–aluminium.

2. MATERIALS AND EXPERIMENTAL METHODS

1959

Alloys were prepared from oxygen-free, high conductivity copper,* and from spectroscopically standardized gallium, germanium, silver and aluminium.† Weighed quantities of the pure metals were melted under reduced pressure of argon in small, sealed silica capsules with vigorous shaking; details of this technique have been published earlier. (8) Alloys containing aluminium were melted in graphite crucibles, under argon, by means of a high-frequency induction technique. Details of homogenization, heat-treatment, metallographic examination, chemical analysis, and preparation of X-ray specimens were the same as in earlier investigations. (8.9)

In order to obtain accurate values of the lattice spacings the last eight high-angle X-ray lines, resolved into doublets, were plotted against the Nelson and Riley function $^{(10)}$ and the a spacings were then evaluated by extrapolation to $\theta=90^{\circ}$. To obtain a straight-line plot the axial ratio was first adjusted by a trial and error method. The c lattice spacings were then calculated from the evaluated a and c/a values. All values are reported in Ångstrom units, based upon the following values assumed for the $\mathrm{Cu} K_{\alpha}$ radiation:

$$\mathrm{Cu}K_{lpha_1} = 1.5405006~\mathrm{\AA}$$

 $\mathrm{Cu}K_{lpha_2} = 1.5443412~\mathrm{\AA}$

The approximate temperature at which measurements were recorded was $26^{\circ} + 2^{\circ}$ C.

3. EXPERIMENTAL RESULTS

3.1 The system silver-aluminium

The values of axial ratio and a and c lattice spacings obtained for the c.p. hex. alloys quenched from 550°C are plotted as a function of e/a in Fig. 1. The a spacing varies linearly with e/a, but the curves for the axial ratio and the c spacings show a distinct

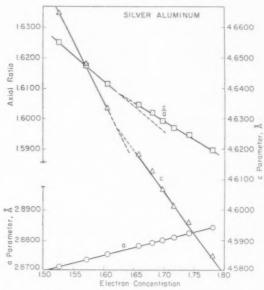


Fig. 1. Variation of lattice spacings with electron concentration in the system silver-aluminium.

change of slope between the e/a values of 1.62 and 1.63. The general tendency for the axial ratio to decrease has already been shown by the work of Westgren and Bradley in $1928^{(11)}$ but their data lacks the precision necessary for revealing the finer details now observed.

3.2 The system copper-germanium

The present lattice spacing values for the c.p. hex. alloys quenched from $550^{\circ}\mathrm{C}$ are shown in Fig. 2, plotted again as a function of e/a. It can be seen from the figure that the c spacing curve shows a general decrease with increasing e/a. The curves for axial ratio, and a spacing, however, show a change of slope as the electron to atom ratio increases from 1.36 to 1.45. At values of electron concentration greater than 1.45, axial ratio and a spacing increase linearly as e/a is increased.

^{*} Supplied by Imperial Chemical Industries Limited.

[†] Supplied by Messrs. Johnson, Matthey and Co., Ltd.



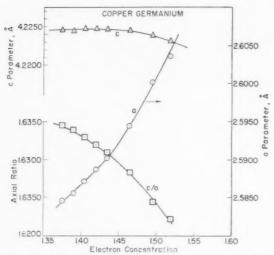


Fig. 2. Variation lattice spacings with electron concentration in the system copper–germanium.

The present results differ considerably from those reported by Schubert and Brandauer⁽¹²⁾ whose data are however insufficiently critical for a direct comparison.

3.3 The system copper-gallium

The previous accurate work on the e.p. hex. phases in this system was done by Raynor and Massalski⁽⁴⁾ who determined the lattice spacings of the ζ_1 and ζ_2 phases shown in the upper portion of Fig. 3. The

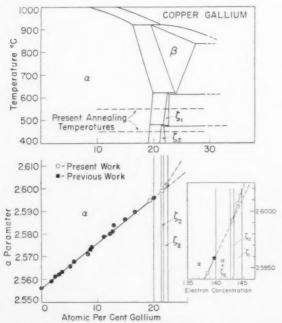


Fig. 3. Variation of lattice spacings with composition and electron concentration in the system coppergallium.

present results for two alloys in the ζ_1 phase, quenched from 550°C and one alloy in the ζ_2 phase, quenched from 450°C are listed in Table 1 together with one alloy in the α phase, quenched from 550°C. These results are plotted in the lower portion of Fig. 3.

TABLE 1. Composition a c.p c c.p. of alloy a f.c.c. Phase hex. hex. c/aela (at. %) (A) (A) (A) Cu Ga 80.7 19.3 3.6991 (2.5946)1.386 78.521.52.5992 4.2442 1.632950 1.430 78.022.0 2.6007 4.2433 1.6316 1.440 22.2 2.6013 4.24351.6313 1.444

The result for the primary solid solution (z) agrees well with previous work, $^{(13.14)}$ but the a spacings of the c.p. hex. phases are slightly higher than those previously reported by Raynor and Massalski⁽⁴⁾. This discrepancy is however consistent with the different temperatures at which the lattice spacings were measured; the present work was carried out at a temperature of $26^{\circ} \pm 2^{\circ}$ C, whilst the earlier work was at $18^{\circ} \pm 3^{\circ}$ C.

4. DISCUSSION

4.1 Overlap of the Fermi surface across the $\{10\overline{1}0\}$ faces of the Brillouin zone

The present results confirm the trend already observed in all c.p. hex. phases of systems based upon Cu, Ag and Au for the axial ratio to decrease with increase in e/a if the value of e/a is approximately between 1.36 and 1.85. In addition certain interesting comparisons can be made between the three systems studied if the a spacings available for the primary solid solutions and the a spacings obtained in the present work for the c.p. hex. phases are plotted as functions of composition as shown in Figs. 3, 4 and 5. Since the face-centred cubic structure and the close-packed hexagonal structure possess the same arrangement of atoms in their closest packed planes, {111} and {0001} respectively, it is convenient to compare the two structures by referring to the lattice spacings in these planes.* It may be seen from Figs. 3 and 4 that the $a/\sqrt{2}$ spacing of the primary solid solutions of copper with gallium, and copper with germanium, increases as alloving element is added. This is in contrast to the primary solid solution of silver with aluminium, see

^{*} For that purpose the following correspondence is valid: spacing along the cube edge = $\sqrt{2} \times$ spacing in the cubic {111} planes = spacing in the c.p. hex. {0001} basal planes. Therefore cubic a spacings must be divided by $\sqrt{2}$ for direct comparison with the c.p. hex a spacings.

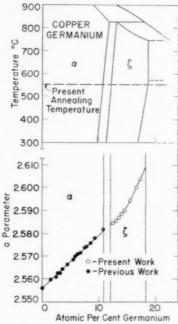


Fig. 4. Variation of lattice spacings with composition in the system copper-germanium.

Fig 5, where the $a/\sqrt{2}$ spacing decreases with increasing aluminium content. According to Raynor⁽¹⁷⁾ such lattice spacing changes may be interpreted in terms of the size and valencies of the component atoms.

It appears from Fig. 3, that these size and valency effects continue with the hexagonal ζ_2 phase of the copper–gallium system, but that in the ζ_1 phase the

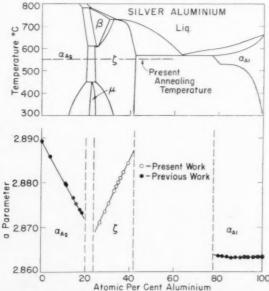


Fig. 5. Variation of lattice spacings with composition in the system silver-aluminium.

a spacing/composition curve has an increased slope.* The size and valency effects also continue in the c.p. hex. phase of the copper–germanium system up to about 14 at. % germanium; at greater germanium contents the a spacing curve increases in slope. In the silver–aluminium system, however, there is no change of slope within the c.p. hex. phase, but a marked change of slope, with a reversal of trend, exists between the curves for the primary solid solution and the c.p. hex. phase, as is evident from Fig. 5.

If the lattice spacing changes are plotted in terms of e/a it becomes apparent that a change of slope in the

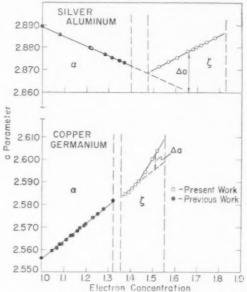


Fig. 6. Variation of lattice spacings with electron concentration in the systems copper–germanium and silver–aluminium. Δa shows the lattice distortion due to overlap.

a spacing occurs in all three systems at approximately the same value of electron concentration. This is illustrated in Fig. 6 for the systems copper–germanium and silver–aluminium. In the former case the change of slope occurs within the ζ phase, and in the latter case it falls into the two-phase region between the α and ζ phases. Similarly, in the system copper–gallium the change of slope occurs in the e/a region between the ζ_2 and ζ_1 phases. This is shown in Fig. 3.

It is suggested that the observed change of slope is the result of an overlap of the Fermi surface across

VOL. 7 1959

^{*} In order to confirm this point great care was taken to obtain high accuracy in lattice spacing measurements. The width of the phase fields ζ_1 and ζ_2 is very narrow and only one alloy was studied in the ζ_2 range, and two alloys in the ζ_1 range. Nevertheless we believe that the accuracy of the present measurements establishes the change of slope beyond any doubt.

the {10I0} faces of the Brillouin zone (see Fig. 7). According to Jones (5), overlaps tend to distort the Brillouin zone so that the overlapped zone face moves towards the origin of the K-space, thus causing an expansion of the corresponding lattice spacing in real space. It has been proposed earlier⁽⁴⁾ that all c.p. hex. 3/2 and 7/4 electron compounds are stabilized by an overlap across the {1010} faces of the zone which therefore causes the a spacings to increase and the axial ratio to decrease. The present work suggests that such an overlap actually begins at values of e/ain the vicinity of 1.42 in copper based alloys and 1.47 in silver based alloys, and is superimposed upon the continued decrease, in the system silver-aluminium, or increase, in the systems copper-germanium and copper-gallium of the a lattice spacing curve, which would still take place had there been no overlap.

For convenience, the distortion due to overlap within the c.p. hex. phases at any particular value of e/a may be defined as Δa , the difference between the observed a lattice spacings and that value obtained by extrapolation of the curves for the primary solid solution. This is indicated in Fig. 6. If now the fractional distortions $\Delta a/a$ (where a is the extrapolated value) are plotted for each system as a function of electron concentration, as shown in Fig. 8, a set of straight lines is obtained showing that distortions due to overlap are nearly the same in the three systems, and that the rates of distortion are nearly identical. The extrapolation of the $\Delta a/a$ vs. e/a plot to the point where $\Delta a/a$ is equal to zero, see Fig. 8, permits the establishment of the point where overlap actually begins. The values obtained are 1.43, 1.415

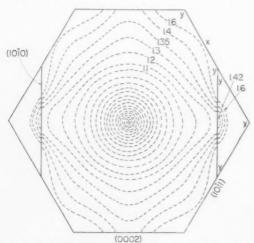


Fig. 7. Vertical section through the first Brillouin zone for the close packed hexagonal structure, proposed by Jones⁽⁵⁾. The contours inside the zone outline the most likely distortion of the Fermi surface at various values of the electron concentration.

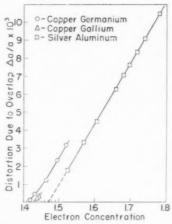


Fig. 8. Variation of the relative distortion of the a lattice spacings ($\triangle a/a$) with electron concentration in the systems copper–gallium, copper–germanium and silver–aluminium.

and 1.47 respectively for the three systems coppergallium, copper–germanium and silver–aluminium. Since these values are very nearly the same in the binary alloys the method of accurate lattice spacing measurements could be fruitfully extended to the study of ternary c.p. hex. electron compounds. For example one could determine the valency contribution from a transition element by assuming that the points where $\Delta a/a=0$ in a ternary system based on copper and silver as solvents correspond with the values of e/a equal to 1.42 for copper based alloys, and 1.47 for silver based alloys. Work of this kind is now in progress in the authors' laboratory.

19

In the system copper-gallium the point of overlap falls between the two e.p. hex. phases ζ_2 and ζ_1 . The greatly restricted homogeneity ranges of these phases have been previously discussed by Raynor and Massalski⁽⁴⁾ who proposed that they are a result of a borderline size factor* of gallium with respect to copper. The present work now suggests that the ζ_1 phase differs from the ζ_2 phase by the onset of overlap across the {1010} faces of the Brillouin zone, and following it a different rate of change of the lattice spacings with composition. In the system coppergermanium, where the size-factor is favourable (4) the overlap is accommodated within the wide c.p. hex. phase, but in the system copper-gallium more critical size conditions result in the existence of a two-phase field between the ζ_2 and ζ_1 phases at temperatures near 475°C. This is in close analogy to the two-phase field existing between the ϵ and η phases in the system

^{*} Size factor may be defined as $\frac{d \text{ solute} - d \text{ solute}}{d \text{ solute}} \times 100$ where d values denote the closest distance of approach in the structure of the pure element.

Cu–Zn.⁽⁵⁾ In the former case the ζ_2 and ζ_1 phases are separated by the $\{10\overline{10}\}$ overlap and in the latter case the ϵ and η phases are separated by the $\{0002\}$ overlap.

4.2 The interaction between the Fermi surface and the $\{10\Pi1\}$ faces of the Brillouin zone

The change of slope which occurs in the axial ratio and the c spacing curves of the silver–aluminium c.p. hex. alloys, as shown in Fig. 1, can be related to the interaction effect, proposed by Goodenough⁽⁶⁾, between the Fermi surface and the $\{10\overline{1}1\}$ faces of the Brillouin zone. Such an interaction should tend to move the $\{10\overline{1}0\}$ faces towards the origin of the zone. For a c.p. hex. structure with an ideal axial ratio, the interaction should occur at an electron concentration of 1.67 provided the Fermi surface is assumed to possess a spherical shape.

The present work shows that in the system silveraluminium a change of slope occurs in the c and c/acurves at values of e/a between 1.61 and 1.64. However, the axial ratio in the region where the interaction occurs is nearly 1.61, which is substantially below the ideal value of 1.63. Consequently, the zone will be extended in the direction of the {0002} faces and such an extension presumably affects the {1011} faces in such a way that the Fermi surface approaches them at values of e/a somewhat lower than 1.67. In addition it is reasonable to expect that the Fermi surface will be considerably distorted from the spherical shape because of the nearness of the zone discontinuities. The most probable contours for the Fermi surface, for various indicated values of e/a, are shown in Fig. 7. Fig. 7 also shows that because of the presence of the {10I0} discontinuities within the Brillouin zone, the Fermi surface will most likely interact only with a portion of each {1011} face, in the vicinity of the point marked X. The presently obtained lattice spacings in the silver-aluminium alloys show a significant change of slope in the c lattice spacings in the range of e/a values where an interaction is expected between the approaching Fermi surface and a portion of the {1011} faces of the zone. Such a change of slope would be expected if, as a result of interaction, the {1011} faces of the Brillouin zone were to undergo a twist with the accompanying displacement of the {0002} faces towards the origin of the zone. As a result of such a distortion the c spacings should show an increase while the a spacings may remain relatively unaffected.

1959

After the upper portions of the $\{10\Pi\}$ faces are touched the remaining portions of the Brillouin zone to be filled, as e/a increases above the values of

approximately 1.62, are the areas marked y in Fig. 7. Wittig⁽¹⁸⁾ has recently determined the heat of formation of c.p. hex. silver-aluminium alloys and his data indicate a minimum in the heat of formation/composition curve, which coincides with the change of slope in the c lattice spacings observed in the present work. Following the minimum there is a steep rise of the values of the heats of formation, indicating a decreasing stability of the c.p. hex. phase. If the thermodynamic data are correlated with the presently discussed picture of the Brillouin zone it appears that the rise in the values of the heats of formation when e/a increases above 1.62 is associated with the filling of the relatively unfavourable states (marked y) within the zone.

CONCLUSIONS

The experimental results presented and discussed above show that it is possible by means of accurate measurements of the lattice spacings to detect the onset of overlap across the $\{1010\}$ faces of the Brillouin zone in the c.p. hex. electron compounds based upon copper and silver. The value of e/a at which overlap occurs in the three systems studied varies from 1.415 to 1.47, and the relative rate of lattice spacing distortion due to overlap appears at higher values of overlap to be almost identical in the three systems, amounting to a relative change of approximately 3.5×10^{-3} in the a lattice spacing per 0.1 change in e/a.

It is suggested that the presence of two closely related c.p. hex. ζ_2 and ζ_1 phases in the system coppergallium may be a result of a combination of borderline size effects discussed earlier⁽⁴⁾ and the overlap effect within the ζ_2 phase discussed in the present work.

Evidence is discussed which suggests that the observed change of slope in the c lattice spacing/composition curve of silver–aluminium alloys is the result of an interaction between the Fermi surface and portions of $\{10\overline{1}1\}$ Brillouin zone faces, before they are touched.

ACKNOWLEDGMENTS

This work was done under the general direction of Professor G. V. Raynor to whom we are grateful for the provision of facilities for research and for many stimulating discussions. One of us (B. C.) wishes to thank the University of Birmingham for the provision of financial support in the form of the William Gibbons Research Scholarship.

REFERENCES

 W. Hume-Rothery and G. V. Raynor, The structure of metals and alloys. Institute of Metals (Monograph and Report series No. 1) London (1954).

- 2. T. B. Massalski, 1955 Symposium on the theory of alloy
- J. B. Massalski, 1955 Symposium on the theory of duoy phases. Amer. Soc. Metals, Cleveland (1956).
 T. B. Massalski, The lattice spacing relationships in alloys Metallurgical Reviews 3, 45 (1958).
 G. V. RAYNOB and T. B. Massalski, Acta Met. 3, 480
- (1955).
- 5. H. Jones, Proc. Roy. Soc. A147, 396 (1934); Phil. Mag. 41, 663 (1950).
- 6. J. GOODENOUGH, Phys. Rev. 89, 282 (1953).
- 7. K. Schubert, Z. Metallk. 43, 1 (1952).
- 8. T. B. Massalski and G. V. Raynor, J. Inst. Met. 82, 539 (1954).
- 9. T. B. Massalski, Acta Met. 5, 541 (1957).
- 10. J. B. NELSON and D. P. RILEY, Proc. Phys. Soc. A57, 160 (1945).

- 11. A. WESTGREN and A. J. BRADLEY, Phil. Mag. 6, 280
- 12. K. SCHUBERT and G. BRANDAUER, Z. Metallk. 43, 262 (1952).
- 13. E. A. OWEN and E. W. ROBERTS, Phil. Mag. 27, 294 (1939).
- R. J. Hodgkinson, Phil. Mag. 46, 410 (1955).
 W. Hume-Rothery, G. F. Lewis and P. W. Reynolds, Proc. Roy. Soc. A157, 167 (1936).
 F. Foote and E. R. Jette, Trans. Amer. Inst. Min. (Metall.) Engrs. 143, 151 (1941).

- (A. C. C. RAYNOR, Trans. Faraday Soc. 45, 698 (1949).
 18. F. E. WITTIG, N.P.L. Symposium on Physical Chemistry of Metallic Solutions and Intermetallic Compounds. London (1958) to be published.

LATTICE PARAMETERS AND ZONE OVERLAP IN SOLID SOLUTIONS OF LEAD IN MAGNESIUM*

C. B. WALKER† and M. MAREZIO† ±

Lattice parameters have been measured as a function of composition for solid solutions of lead in magnesium with a relative precision of 1:25,000. Both parameters vary smoothly with composition, with no sign of a break or rapid change in slope, and thus give no evidence of any onset of electron overlap across faces of the Brillouin zone, contrary to the results of Raynor. Further consideration of the various lattice parameter data in the literature for five other dilute solid solutions in magnesium suggests that in none of these particular solid solutions do the lattice parameter data give satisfactory evidence of the onset of overlap.

PARAMETRES RETICULAIRES ET RECOUVREMENT DE ZONES DANS LES SOLUTIONS SOLIDES DE PLOMB DANS LE MAGNESIUM

Les auteurs ont mesuré les paramètres réticulaires en fonction de la composition de solutions solides de plomb dans le magnésium avec une précision relative de 1 : 25,000. Les deux paramètres varient lentement avec la composition et l'on n'a pas observé une variation abrupte dans leur évolution. Contrairement aux résultats de Raynor, il ne semble pas qu'il se produise une interférence d'électrons au travers des faces de la zone de Brillouin. Un examen plus poussé des déterminations de différents paramètres réticulaires tels qu'on les trouve dans la litérature pour cinq autres solutions solides diluées dans le magnésium ne permet pas de conclure à une telle interférence électronique.

GITTERPARAMETER UND DAS ÜBERRAGEN DER BRILLOUIN-ZONEN BEI MAGNESIUM-BLEI-MISCHKRISTALLEN

Die Gitterparameter von festen Lösungen von Blei in Magnesium wurden mit einer relativen Genauigkeit von 1:25 000 als Funktion der Zusammensetzung gemessen. Beide Parameter ändern sich stetig mit der Zusammensetzung ohne Anzeichen einer Unstetigkeit oder raschen Änderung des Anstiegs. Sie geben also keinen Hinweis darauf, daß die Fermi-Oberfläche über die Grenzfläche der Brillouin-Zone hinwegzureichen anfängt; im Gegensatz zu der Ergebnissen von Raynor. Weitere Betrachtungen verschiedener Gitterparameterdaten aus der Literatur von fünf anderen verdünnten festen Lösungen in Magnesium führen zu der Annahme, daß in keinem dieser besonderen Mischkristalle die Gitterparameter befriedigende Hinweise auf den Beginn einer Zonenüberragung geben.

1. INTRODUCTION

In 1940 Raynor⁽¹⁾, and Hume-Rotherv and Raynor⁽²⁾, investigated the lattice parameters of the primary solid solutions in magnesium of various solute metals. The results for the alloys with trivalent aluminum and indium, the two alloying elements with a higher valence than magnesium, were unusual: while the a parameter curves were the usual smooth functions of composition, the c parameter curves showed abrupt changes in slope at approximately 0.75 at. % solute. Interpreting these breaks as electronic effects explicable in terms of the Jones electron overlap theory, (3) Hume-Rothery and Raynor proposed that in magnesium solid solutions at an electron concentration of 2.0075 electrons/atom there is an onset of overlap of the conduction electrons across the faces of the second Brillouin zone perpendicular to the c axis, the overlap causing a contraction of the zone in this direction and hence an expansion of the real lattice c parameter. Raynor⁽⁴⁾ then extended the measurements to solid solutions with two other trivalent metals, gallium and thallium, and two tetravalent metals, tin and lead, and his results gave further support to this interpretation; the a parameter curves varied smoothly, but all c parameter curves showed abrupt breaks in slope at compositions corresponding approximately to electron concentrations of 2.0075 electrons/atom. In view of this confirmation, these measurements and their interpretation have since been incorporated in several texts and reviews on the structure of metals and alloys. (5-7)

Different evidence of this overlap was sought by Salkovitz and Schindler(8), who with Kammer(9) investigated electron transport properties of several magnesium alloys. Their Hall coefficient and thermoelectric power measurements for the solid solutions with aluminum, indium, tin and lead showed effects that could be attributed to such an overlap. However the electron concentrations at which these overlap

^{*} Research supported partly by the Office of Ordnance Research, U.S. Army. Received January 8, 1959.

† Institute for the Study of Metals, University of Chicago,

Chicago 37, Illinois.

On leave from Istituto di Chimica Generale, Universita di Roma.

effects were found varied widely, depending both on the particular alloy system and on the particular transport property, and only in one instance was there agreement with the electron concentration given by the lattice parameter breaks.

The few independent lattice parameter measurements that have been made for these solid solutions either conflict with the reported lattice parameter breaks or else cannot be used to support them. Foote and Jette⁽¹⁰⁾ had measured the lattice parameters of solid solutions of lead in magnesium and had reported a smooth variation of the c parameter with composition, with no indication of a break at 0.375 at. % lead. Raynor⁽⁴⁾, noting that they had examined no alloys with less than 0.51 at. % lead, stated that their experimental points were not inconsistent with the break he reported. Busk⁽¹¹⁾ measured lattice parameters for all six of these solid solutions, but the data show too much scatter to serve as a check on the lattice parameter breaks*. Von Batchelder and Raeuchle⁽¹²⁾, in a recent re-examination of the solid solutions with aluminum and indium, obtained results conflicting with the data of Raynor and Hume-Rothery: the magnesium-aluminum lattice parameter curves did not show a break, and the magnesium-indium lattice parameter curves showed a departure from linearity which, while considered significant, was much less than that previously reported and occurred at a different electron concentration.

The experimental observations thus show several discrepancies and disagreements. There has also been criticism of the theory of the effect of overlap on lattice parameters, several authors (13) modifying the Jones treatment in various ways and discussing the difficulties and inadequacies of such theories. However, despite these factors, the concept that the lattice parameter breaks found by Raynor and Hume-Rothery signify the onset of electron overlap in these magnesium-base alloys still has wide acceptance, perhaps partially because of the marked effects that have been found in other hexagonal and cubic alloy phases. (14,15)

In the present investigation we have remeasured the lattice parameters of solid solutions of lead in magnesium. The series of alloys studied included several in the region of low lead content, and the precision of measurement was sufficiently high to reveal effects of the type under discussion. Since the results differ markedly from those of Raynor, the experimental procedure will be described in some detail.

2. EXPERIMENTAL DETAILS

Alloys were prepared in two sets, one including compositions of nominal 2, 4, 6 and 8 wt. % lead and the other including compositions of nominal 10, 15, 20, 25 and 30 wt. % lead. The magnesium for the first set was 99.94% pure, the major impurity being iron, and the magnesium for the second set was 99.97% pure, with sodium and zinc the major impurities. The lead for all alloys was 99.9+% pure, the primary impurity being tellurium.

Alloys of the set with higher lead content were melted by induction heating in graphite crucibles and bottom poured into graphite molds under streaming argon. Alloys in the set with small lead content were melted by induction heating in graphite crucibles under argon in a closed furnace and solidified by withdrawal of the crucible from the hot zone. All alloy ingots, 7 in. in diameter, were hot extruded to in. diameter rods at approximately 300°C and then swaged to 0.237 in. diameter rods at room temperature. After being etched clean the rods were cut to 6 in. lengths, wrapped in bundles with high purity iron wire placed to prevent contact of the alloys with any other material, sealed in Vycor under a reduced pressure of argon or helium, and given a homogenization anneal of 1 week at 450°C. The surfaces of the annealed rods were scraped to remove slight traces of tarnishing, and then filings were made by hand filing in air of moderate humidity. The filings passed by a 250 mesh screen were kept in a dessicator until needed.

195

Filings to be used were put in thin walled iron containers with loose-fitting lids and placed in soda glass tubing; these were alternately evacuated and flushed with purified helium for periods of approximately 16 hr and then sealed under a reduced pressure of helium. These samples were annealed at 450°C for 2 hr and then rapidly quenched in dried, distilled kerosene,* the glass shattering on contact with the liquid. The filings recovered by filtering were used both as samples for the X-ray patterns and as specimens for the chemical analyses to determine the composition. The six alloys with the higher lead content were analyzed for both constituents, each analysis being accurate to a relative precision of

^{*} See, for example, Busk's data for Mg-Pb solid solutions plotted in Fig. 2 of this paper.

^{*} In preliminary work water quenches were used, but the alloys reacted quickly with the water even at room temperature. Foote and Jette⁽¹⁹⁾ have reported the same effect. The reports of Raynor⁽⁴⁾ and Busk⁽¹¹⁾ do not make clear whether or not water actually came in contact with the specimens during their water quenches.

0.2%. The sum of the two measured weight percentages varied between 99.99% and 98.98%, the average being 99.55%. The remainder is attributed primarily to glass fragments unavoidably mixed with the filings during recovery from the quench, a conclusion supported by the silicon contents reported by spectroscopic analyses. The alloys with nominal 2, 4 and 6 wt. % lead were thus analyzed only for lead, magnesium being assumed to make up the difference. The homogeneity of all alloys was demonstrated by the sharpness of the X-ray diffraction lines.

X-ray diffraction patterns were made with a 10 cm diameter symmetrical back-reflection focusing camera, using cobalt radiation ($CoK\alpha_1 = 1.78892 \text{ Å}$; $CoK\alpha_2 = 1.79278$ Å) and single emulsion film. The camera temperature was held constant at $33.0^{\circ} \pm 0.1^{\circ}$ C during exposures by a simple constant temperature enclosure, and film development and reading procedures were uniform for all films. Lattice parameters were determined from measurements of seven high angle lines by the least squares method of Cohen^(16,17). The highest angle line occurred at a Bragg angle of 84.3°-85.6°, so reasonable precision could be expected. Several samples were prepared of each alloy, and often two films were made of each sample. The observed standard deviation of the mean value of the c parameter was less than 1:50,000 for all alloys, and the observed standard deviation of the mean value of the a parameter was in all cases less than 1:80,000. As a conservative estimate of limits of error, we then consider the mean values of all parameters to be accurate to within a relative precision of 1:25,000.

1959

All lattice parameters have been corrected for the wavelength change due to refraction⁽¹⁸⁾ and adjusted to a temperature of 25°C using the thermal expansion coefficients for pure magnesium given by Goens and Schmid⁽¹⁹⁾.

3. RESULTS

The average values of the lattice parameters of the solid solutions at 25°C are listed in Table 1, together with the number of films on which each average is based. For ease of inspection the parameters are also presented graphically in Fig. 1.

Within the relative precision of 1:25,000, all parameters vary smoothly with increasing lead content, with no sign of a sharp break or rapid change in slope.

A comparison of these results with those of other investigations shows discrepancies both in absolute magnitudes and in the variation with lead content. The differences in absolute magnitude are illustrated

Table 1. Lattice parameters of solid solutions of lead in magnesium at $25\,^{\circ}\mathrm{C}$

At. % lead	Number of films	$a_0 (\mathring{\mathbb{A}})$	c_0 (Å)	c/a
0.000	12	3.20022	5.21067	1.62366
0.246	6	3.20947	5.21165	1.62384
0.506	4	3.20969	5.21260	1.62402
0.746	6	3.20996	5.21363	1.62420
1.009	4	3.21027	5.21484	1.62442
1.294	3	3.21050	5.21620	1.62473
1.992	9	3.21123	5.21918	1.62529
2.820	3	3.21184	5.22316	1.62622
3.721	8	3.21254	5.22766	1.62727
4.823	3	3.21320	5.23368	1.62881

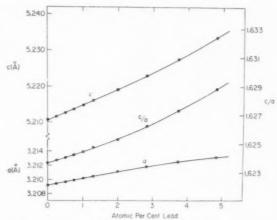


Fig. 1. Lattice parameters of solid solutions of lead in magnesium at 25°C determined in the present investigation.

by comparing the data for pure magnesium. Lattice parameters of high purity magnesium have been reported with relatively small limits of error by Jette and Foote⁽¹⁷⁾, Ievins et al.⁽²⁰⁾ Raynor and

Table 2. Lattice parameters of magnesium at 25°C

Reference	$a_n(\mathbf{\hat{A}})$	$c_{0}\left(\mathring{\mathbf{A}}\right)$
17	3.20947	5.21071
20	3.20927	5.21033
21	3.20949	5.21124
4	3.20945	5.21090
4 12	3.20956	5.21071
12	3.20938	5,21069
Average	3.20944	5.21076

Hume-Rothery⁽²¹⁾, Raynor⁽⁴⁾, and von Batchelder and Raeuchle⁽¹²⁾. These values, adjusted to 25°C and converted to Angstrom units,* are given in Table 2. The present measurement of the c parameter

^{*} Thermal expansion coefficients were those of Goens and Schmid;⁽¹⁹⁾ the kX-to-Angstrom conversion was made with the factor 1.00202.

is in rather good agreement with the average of these values, but the present value for the a parameter is lower by approximately 1:15,000. The origin of this discrepancy has not been found; its magnitude can serve as a measure of the absolute accuracy of the present measurements.

To facilitate comparison of the various solid solution lattice parameter data, we have redrawn our lattice parameter curves in Fig. 2 and have plotted there the data of Foote and Jette⁽¹⁰⁾ (circles), Raynor⁽⁴⁾ (triangles) and Busk⁽¹¹⁾ (squares), all adjusted to Angstrom units at 25°C. The present a parameter curve lies consistently below the data of Foote and Jette by approximately 1:15,000, while Raynor's data are still higher. The relative changes with composition of all three seem in reasonable agreement. The data of Busk for both parameters show appreciable scatter.

The present c parameter curve is in excellent agreement with the data of Foote and Jette. Raynor's measurements differ markedly, not only suggesting a break at low lead content but also diverging somewhat systematically over the entire composition range. The break in slope, the important factor for the electron overlap arguments, seems to be required only by his measurement for one alloy, that with 0.30 at. % lead. The present measurements include data for alloys with 0.246 at. % lead (two films for each of three separate samples) and 0.506 at. % lead (two films for each of two separate samples), and the mean c parameters all fall on a smooth curve that also fits well with the data of Foote and Jette. We

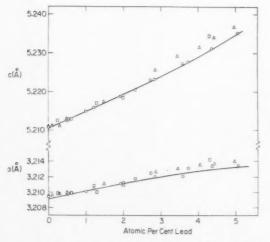


Fig. 2. Lattice parameter data for solid solutions of lead in magnesium reported by Foote and Jette⁽¹⁰⁾ (circles), Raynor⁽⁴⁾ (triangles), and Busk⁽¹¹⁾ (squares), together with the smooth lattice parameter curves determined in the present investigation. All data are in Angstrom units at 25°C.

conclude that the break is not real, but that instead Raynor's measurement for the 0.30 at. % lead alloy is incorrect.

The systematic divergence between Raynor's c parameter data and those of Foote and Jette and the authors is more difficult to understand. The effect is quite large; at the higher lead compositions the difference between the lattice parameters for a given composition is greater than 1:2500, over four times the error usually expected with that X-ray technique. An interpretation in terms of errors in chemical analyses would require mistakes of over 10% in the lead determination. We can offer no explanation for this systematic divergence. The observed reproducibility of our own lattice parameter determinations and chemical analyses, added to the excellent agreement with the data of Foote and Jette, suggests strongly that the error lies in the measurements of Raynor.

4. DISCUSSION

The present measurements have shown that the lattice parameters of the solid solutions of lead in magnesium vary smoothly with composition, with no sign of a sharp break or rapid change in slope. If then there is an onset of electron overlap across faces of the Brillouin zone at some electron concentration in this solid solution, such an overlap does not produce an observable abrupt change in these lattice parameters. There is of course the possibility that overlap may produce only a gradual change in the lattice parameters, as was suggested by Marcus⁽¹³⁾ on theoretical grounds. However, the many examples of departures from Vegard's law make difficult any clear interpretation of such a gradual change. We must conclude that the lattice parameter measurements of this solid solution give no evidence of any onset of overlap.

The primary evidence that has been interpreted to mean the onset of overlap in the magnesium-base solid solutions has been the abrupt breaks in slope of the c parameter curves reported by Raynor and Hume-Rothery for six such alloy systems. Three of these have now been remeasured in independent investigations, and the original lattice parameter measurements have not been confirmed: in two cases (Mg-Pb and Mg-Al) no break has been found, and in the third (Mg-In) an effect was found which, though considered significant, was much smaller and occurred at a different composition. In two of the remaining three solid solutions (Mg-Sn and Mg-Tl) the existence of a sharp break in the c parameter curves again seems to be required by only one measurement in each series (the alloys with respectively, 0.18 at. % tin

VOI 7 19

and 0.75 at. % thallium), and in the third system (Mg-Ga) the reported change in slope is quite small, approximately the same as was originally given for the Mg-Al alloys. Until there has been independent confirmation of these data by other investigations, we suggest that none of the lattice parameter data on these particular magnesium-base solid solutions can serve as satisfactory evidence of the onset of electron overlap.

ACKNOWLEDGMENT

We acknowledge with many thanks the help of Miss M. Bachelder, who carried out the chemical analyses necessary for this research.

REFERENCES

- G. V. RAYNOR, Proc. Roy. Soc. A174, 457 (1940).
 W. HUME-ROTHERY and G. V. RAYNOR, Proc. Roy. Soc. A177, 27 (1940).
- H. JONES, Proc. Roy. Soc. A147, 400 (1934); see also Physica 15, 13 (1949) and Phil. Mag. 41, 663 (1950).
- G. V. RAYNOR, Proc. Roy. Soc. A180, 107 (1942).
- 5. G. V. RAYNOR, Progress in Metal Physics Vol. 1, p. 1. Butterworths, London (1949).
- 6. W. Hume-Rothery and G. V. Raynor, The Structure of Metals and Alloys (3rd Ed.). Institute of Metals, London

- 7. W. B. Pearson, A Handbook of Lattice Spacings and Structures of Metals and Alloys. Pergamon Press, New York (1958).
- 8. E. I. SALKOVITZ and A. I. SCHINDLER, Phys. Rev. 91, 234(A) and 1320 (1953); Ibid. 98, 543 (1955)
- 9. E. I. SALKOVITZ, A. I. SCHINDLER and E. W. KAMMER, Phys. Rev. 105, 887 (1957); Ibid. 107, 1549 (1957).
- 10. F. FOOTE and E. R. JETTE, Trans. Amer. Inst. Min. (Metall.) Engrs. 143, 124 (1941).
- 11. R. S. Busk, Trans. Amer. Inst. Min. (Metall.) Engrs. 188, 1460 (1950).
- 12. F. W. von Batchelder and R. F. Raeuchle, Phys. Rev. 105, 59 (1957).
- 13. J. B. GOODENOUGH, Phys. Rev. 89, 282 (1953); J. W. McClure, Phys. Rev. **98**, 449 (1955); P. M. Marcus, Phys. Rev. **98**, 1552(A) (1955); J. C. Slater, Band Theory of Bonding in Metals, chapter in Theory of Alloy Phases. Amer. Soc. Metals, Cleveland (1956).
- T. B. Massalski, Metallurg. Rev. 3, 45 (1958).
- 15. C. Kittel, Introduction to Solid State Physics, (2nd Ed.). Wiley, New York (1956).
- 16. M. U. COHEN, Rev. Sci. Instrum. 6, 68 (1935).
- 17. E. R. JETTE and F. FOOTE, J. Chem. Phys. 3, 605
- 18. A. J. C. Wilson, Proc. Camb. Phil. Soc. 36, 485 (1940).
- 19. E. Goens and E. Schmid, Phys. Z. 37, 385 (1936).
- 20. A. IEVINS, M. STRAUMANIS and K. KARLSONS, Z. Phys. Chem. B40, 347 (1938).
- 21. G. V. RAYNOR and W. HUME-ROTHERY, J. Inst. Met. 65, 379 (1939).

INFLUENCE DE FAIBLES OUANTITÉS DE NICKEL SUR L'OXYDATION DU CUIVRE*

F. BOUILLON† et J. STEVENS†‡

Les auteurs étudient l'influence de la présence de faibles quantités de nickel sur l'oxydation du cuivre aux températures inférieures ou égale à 200° C et à pression atmosphèrique d'oxygène pur. Dans ces conditions, il existe toujours un large domaine où il ne se forme qu'un seul oxyde: Cu₂O. Cette étude montre que.

(1) les alliages Cu–Ni à 5 et 10% de Ni s'oxydent moins vite que le cuivre pur pendant toute la période étudiée.

(2) les alliages Cu–Ni à 0.5 et 1% de Ni s'oxydent plus rapidement pendant une période initiale dont la durée est inversement proportionnelle à la concentration en Ni,

(3) l'alliage à 0,1% s'oxyde plus rapidement dans tout le domaine étudié,

(4) l'oxyde cuivrique CuO apparait toujours plus tôt sur les alliages.

INFLUENCE OF SMALL QUANTITIES OF NICKEL ON THE OXIDATION OF COPPER

The authors have studied the influence of small quantities of nickel on the oxidation in pure oxygen at atmospheric pressure, of copper at temperatures equal to and below 200°C.

Under these conditions, there always exists a large region where only Cu₂O is formed.

This study shows that:

(1) the alloys of Cu-Ni containing 5 and 10% nickel oxidize less rapidly than pure copper during the period studied.

(2) alloys containing 0.5 and 1% nickel oxidize more rapidly during an initial period, the length of which varies inversely with the nickel content.

(3) the alloys containing 0,1 per cent oxidizes the most rapidly during the period investigated.

(4) the oxide CuO always appears sooner on these alloys.

EINFLUSS GERINGER NICKELZUSÄTZE AUF DIE OXYDATION VON KUPFER

Es wird untersucht, wie der Zusatz von geringen Nickelmengen die Oxydation von Kupfer bei Temperaturen bis 200° C in reinem Sauerstoff von Atmosphärendruck beeinflusst. Unter diesen Bedingungen gibt es stets einen längeren Zeitraum, in dem als einziges Oxyd Cu₂O entsteht. Es zeigtsich, dass

(1) bei Cu–Ni Legierungen mit 5 und 10% Ni die Oxydation im ganzen untersuchten Zeitraum langsamer verläuft als bei reinem Kupfer,

(2) bei Cu-Ni Legierungen mit 0,5 und 1% Ni die Oxydation während einer Anfangsperiode schneller verläuft; die Länge dieser Periode ist der Ni-Konzentration umgekehrt proportional;

(3) bei der Legierung mit 0.1% Ni im ganzen untersuchten Zeitraum die Oxydation schneller verläuft

(4) das Oxyd CuO in allen Fällen bei den Legierungen früher erscheint,

Le mécanisme de la croissance sur les métaux de films minces et continus d'oxyde dont les épaisseurs sont comprises entre 20 et 1000 Å est encore mal connu.

Ces films, qui présentent des teintes d'interférences caractéristiques, se forment sur le cuivre aux températures modérées ($\leq 200^{\circ}$ C) et aux pressions élevées (1 à 760 mm). Ils ont fait l'objet de peu de travaux expérimentaux, et les modèles théoriques destinés à interpréter les résultats sont peu précis. (1)

Tout au plus, peut-on admettre que le champ établi par la présence d'ions oxygène chimisorbés⁽²⁾ à la surface de la couche d'oxyde est responsable de la migration des ions métalliques vers l'interface oxyde-gaz. La nature des sites par lesquels se fait cette diffusion n'est pas clairement établie. VOI

195

C'est pour cette raison qu'il nous semble utile d'étudier le rôle de quelques paramètres susceptibles de modifier le phénomène.

Dans cette note, nous examinerons l'influence de la présence de quantités croissantes de nickel dans le réseau de cuivre. La similitude des propriétés du nickel et du cuivre permet en effet d'espérer, au moins pour les faibles concentrations en nickel, la formation d'oxydes mixtes.

Les mesures préliminaires que nous décrivons ici, portent sur cinq alliages, respectivement à 0.1%, 0.5%, 1%, 5% et 10% de nickel en poids.

Ces alliages ont été préparés à partir de métaux purs, homogénéisés et finalement polis électrolytiquement.

^{*} Received January 16, 1959

[†] Laboratorie de Chimie Analytique et Minérale, Université libre de Bruxelles.

[‡] Titulaire d'une bourse de spécialisation de l'IRSIA. Thèse de doctorat.

L'évolution de la réaction a été suivie grâce à la méthode électrométrique de Miley, dont nous avons préalablement démontré la validité. (3) La méthode ne permet de doser que les seuls oxydes de cuivre. Ceci nous permet donc de rapporter l'ensemble de nos mesures à la formation de l'oxyde de cuivre.

Ils expriment donc l'influence de nickel dans le réseau du cuivre sur la formation des oxydes de cuivre.

La morphologie des films d'oxydes a été étudiée aux microscopes optiques et électroniques, et leur nature a été analysée par diffraction électronique et de rayons X.

RÉSULTATS EXPÉRIMENTAUX

Nature des oxydes (150, 185 et 200°C)

Aux températures envisagées, on ne détecte d'oxyde de nickel par aucun des moyens utilisés. Il se forme toujours essentiellement $\mathrm{Cu_2O}$. L'oxyde cuivrique n'apparait qu'ultérieurement, et toujours plus tôt sur les alliages que sur le cuivre pur.

Etudes cinétiques

1959

Les résultats fondamentaux de cette étude sont les suivants:

(1) les alliages Cu–Ni à 5% et à 10% de Ni s'oxydent moins vite que le cuivre pur pendant toute la période étudiée.

(2) les alliages Cu–Ni à 0,5% et à 1% s'oxydent plus vite que le cuivre pur pendant une période initiale dont la durée est inversement proportionnelle à la concentration en Ni. Cet effet se manifeste pour des alliages dont les teneurs en nickel varient depuis 1% jusqu'à 0,1%.

Il se produit ensuite un ralentissement et l'alliage s'oxyde plus lentement que le métal pur après un temps déterminé.

(3) l'alliage à 0.1% de Ni est accélérateur sur la totalité de la période envisagée (4 h).

Nous présentons, dans la Figure 1, l'ensemble des résultats obtenus à $200\,^{\circ}$ C, et à pression atmosphérique d'oxygène pur.

(4) les alliages s'oxydent tous selon deux lois paraboliques successives à partir de 200°C. La constante cinétique de la première loi est toujours nettement plus grande.

A 185°C, les alliages 0,1% et 0,5% s'oxydent suivant une seule loi parabolique; aux concentrations plus élevées, nous obtenons toujours deux droites dans le graphique

$$\xi^2(\mu \mathbf{g}^2 \ \mathbf{O_2} \cdot \mathbf{cm^{-4}}) = \mathit{F}(t_{\mathrm{minutes}})$$

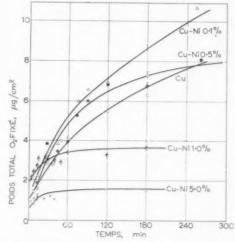


Fig. 1. Oxydation à pression atmosphérique dans O_2 pur, à 200 °C.

T: Ce signe mentionne la détection de CuO en surface par diffraction électronique en réflexion. Le diagramme de transmission montre que même quand CuO est détecté en surface, la grosse majorité du film d'oxyde est constituée par Cu₂O.

A $150\,^{\circ}$ C, les alliages $1\,^{\circ}$ /₀ et $5\,^{\circ}$ /₀ s'oxydent également suivant deux lois paraboliques. Dans tout ce domaine, le cuivre pur s'oxyde suivant une loi parabolique simple.

Nous avons rassemblé les valeurs des constantes paraboliques calculées à l'aide de la relation $\xi^2=\xi_0{}^2+k_vt$ où

 ξ = poids total d'oxygène fixé par cm². (µg $O_2 \cdot \text{cm}^{-2}$).

 $\xi_0=$ poids de ${\rm O}_2$ à partir duquel la loi parabolique est valable.

t = minutes.

dans le tableau suivant.

Nous n'avons pas pu détecter d'oxyde de Ni aux températures envisagées ici. Sa présence a pu être démontrée à partir de 250°C, pour une durée d'oxydation de 60 min. Cet oxyde de nickel adhère à la phase métallique et se trouve donc dans les parties profondes de la couche d'oxydation.

CONCLUSIONS

Ces mesures préliminaires semblent donc démontrer que l'augmentation du désorde provoqué par la présence d'ions nickel dans le réseau de $\mathrm{Cu}_2\mathrm{O}$ se manifeste de la même manière que dans le cas des couches épaisses formées à haute température, c'est à dire par une accélération du phénomène d'oxydation.

D'autre part, l'augmentation de la durée d'oxydation, de la concentration en nickel et de la température d'oxydation paraissent favoriser la ségrégation

Température	Conc en Ni (% poids)	Ctes paraboliques (μg^2 . cm ⁻⁴ . min ⁻¹)		6
		Valeur	Domaine de validité (min)	$\xi_0 = \mu g^2$. cm
$150^{\circ}\mathrm{C}$	0 1 5	$\begin{array}{c} 0,040 \\ 0,0344 \\ 0,0240 \\ 0,0360 \\ 0,0204 \end{array}$	$\begin{array}{c} 0-240 \\ 0-60 \\ 60-240 \\ 0-50 \\ 50-240 \end{array}$	$\begin{array}{c} 0,540 \\ 0,720 \\ 1,280 \\ 0,12 \\ 0,720 \end{array}$
185°C	0 0,1 0,5 1	$\begin{array}{c} 0.332 \\ 0.956 \\ 1.108 \\ 0.528 \\ 0.080 \\ 0.084 \\ 0.010 \end{array}$	0-240 $0-240$ $0-240$ $0-240$ $0-60$ $60-240$ $0-50$ $50-240$	1,280 0 0 5,00 30,80 0,40 4,00
200°C	0 0,1 0,5 1 5	1,140 2,220 1,264 1,956 0,520 0,472 0,1144 0,240 0,0308	0-180 $0-130$ $130-240$ $0-110$ $110-240$ $0-45$ $45-180$ $0-20$ $20-180$	$\begin{array}{c} 2.4 \\ 0 \\ 74.8 \\ 0 \\ 114.0 \\ 22.60 \\ 35.2 \\ 1.60 \\ 5.10 \\ \end{array}$

de NiO et provoquent donc un ralentissement de l'oxydation.

Des expériences sont en cours pour vérifier ces hypothèses.

ACKNOWLEDGEMENTS

Ce travail a été effectué sous la direction de Mademoiselle de Brouckère, que nous tenons à remercier ici.

L'Union Minière du Haut Katanga a mérité notre reconnaissance pour les subsides qu'elle a accordé au laboratoire.

BIBLIOGRAPHIE

- 1. voir par exemple:
 - F. BOUILLON, Bull. Soc. Chim. Belges 60, 337-56, 451-8

VOI

195

- W. W. Harris, F. L. Ball et A. T. Gwathmey, Acta Met. 5, 574-81 (1957).
 T. N. Rhodin, J. Chim. phys. 54, 72-88 (1957).
 N. Cabrera et N. F. Mott, Rep. Progr. Phys. 12, 163-84 (1957).

 - (1948-49).
 - K. Hauffe, Reaktionen in und an festen Stoffen p. 555.
- Springer Verlag.
 3. F. BOUILLON, M. OFFERGELD-JARDINIER, J. PIRON, J. STÉVENS et G. VAN DER SCHRICK, Bull. Soc. Chim. Belges (1959) sous presse.

REACTION RATE AND GROWTH FORMS OF REACTION PRODUCT IN THE SYSTEM Ag-H₂S*

H. FISCHMEISTER† and J. DROTT‡

In the system ${\rm Ag-H_2S}$ at room temperature, the growth form of the reaction product is found to exert a decisive influence on the kinetics of the reaction. The initial stage is characterized by a cubic rate law and by the nucleation and growth of irregularly distributed mounds of sulfide on the silver surface. In the next stage, there is a sudden increase of the reaction rate, accompanied by the appearance of needles perpendicular to the metal surface. During the third stage, the reaction rate decreases again while fewer and fewer needles continue to grow.

The length of the largest needles observed in this study was about 20μ , corresponding to ca. twenty times the maximum possible thickness of a compact bottom layer. Although their volume accounts for only a fraction of the total amount of sulfide formed, the needles are thought to be decisive in determining the reaction rate after the initial stage.

VITESSE DE REACTION ET FORMES DE CROISSANCE DU PRODUIT DE REACTION DANS LE SYSTEME $Ag-H_2S$

Dans le système $Ag-H_2S$ à la température ambiante, la forme de croissance du produit de réaction exerce une influence décisive sur la cinétique de réaction. Le stade initial est caractérisé par une loi de vitesse cubique, ainsi que par la nucléation et croissance de "collines" de sulfure sur la surface d'argent. Au stade suivant, la vitesse de réaction subit une augmentation soudaine, accompagnée de l'apparition d'aiguilles perpendiculaires à la surface du métal. Pendant le troisième stade, la vitesse de réaction décroît de nouveau tandis que de moins en moins d'aiguilles poursuivent leur croissance. La longueur des plus grandes aiguilles observées dans ce travail est d'environ $20~\mu$, correspondant à peu près à vingt fois l'épaisseur maximum possible d'une couche de base compacte. Bien que leur volume ne corresponde qu'à une fraction du sulfure formé, les aiguilles sont considérées comme un facteur essentiel pour la vitesse de réaction intervenant après le stade initial.

REAKTIONSGESCHWINDIGKEIR UND WACHSTUMSFORMEN DES REAKTIONS-PRODUKTS BEIM SYSTEM Ag-H.,S.

Im System Ag–H₂S wird bei Zimmertemperatur ein entscheidender Einfluss der Wachstumsform des Reaktionsproduktes auf die Kinetik der Reaktion festgestellt. Das Anfangsstadium der Reaktion ist gekennzeichnet durch Bildung und Wachstum unregelmässig verteilter "Hügel" von Sulfide auf der Silberoberfläche, bei gleichzeitiger Gültigkeit eines kubischen Anlaufgesetzes. Im nächsten Stadium folgt ein plötzlicher Anstieg der Reaktionsgeschwindigkeit, begleitet vom Auftreten von Nadeln senkrecht zur Metalloberfläche. Im dritten Stadium fällt die Reaktionsgeschwindigkeit wieder ab, während immer weniger Nadeln ihr Wachstum fortsetzen.

Die Länge der grössten Nadeln betrug etwa $20~\mu$, ungefähr das Zwanzigfache der grösstmöglichen Dicke einer kompakten Grundschicht im betreffenden Reaktionsstadium. Obwohl die Nadeln volumensmässig nur einen kleinen Bruchteil der gesamten Sulfidmenge ausmachen, dürften sie entscheidend für die Reaktionsgeschwindigkeit im zweiten und dritten Stadium der Reaktion sein.

Since the discovery, by Pfefferkorn⁽¹⁾ and Cowley⁽²⁾, of spikelike crystal growth of CuO during air oxidation of copper at temperatures of about 400°C, many instances of similar crystal growth have been reported in studies of oxidation and related reactions. In fact, the range of conditions and reaction systems for which whisker, columnar or lamellar growth of reaction products has been observed^(3–15) is great enough to raise suspicion that these might be quite normal features of certain stages of most oxidation

reactions. An equally impressive number of observations exists concerning nucleation phenomena and other non-continuous oxide growth. (16-21)

Although Pfefferkorn^(3,4) called attention to the possible kinetic implications of such growth forms as early as 1954, the question seems to have attracted no experimental research. Yet it appears to be one of fundamental importance, since all established theories of oxidation kinetics are based on the assumption of a plane parallel oxide film. The initial tendency, to discard the observations of oxide needle growth as either exceptional or unessential to the course of the reaction, becomes dubious in the face of the increasing number of observations.

^{*} Received February 3, 1959.

[†] Institute of Chemistry, University of Uppsala, and Swedish Institute of Metal Research, Stockholm 26.

[‡] Institute of Chemistry, University of Uppsala.

It has been suggested⁽²²⁾ that oxide needles invariably grow on top of comparatively thick layers, so that the rate-determining step is still diffusion through an essentially plane-parallel layer. Though true in many cases—e.g. where oxide spikes have been observed on surfaces of fractured samples by light microscopy^(13,14)—this does not appear to be the general rule: Pfefferkorn⁽³⁾ reports oxide whiskers on copper after 5 see at 400°C in air, with a tarnishing colour of first order purple.

The purpose of this paper is to report some preliminary results of a current investigation into the relation between growth morphology and kinetics for the reaction between silver and hydrogen sulfide.

EXPERIMENTAL

Samples were in the form of wires of 0.9 mm diameter and ca. 70 mm length. Hard drawn wire was chosen because the heavy cold work provided an easy means of securing constant—although admittedly unsatisfactorily defined—surface conditions. The influence of the degree of deformation of the metal is being investigated at present. According to spectroscopic analysis by the supplier,* the impurity level of the material was below 15 ppm, the most important impurities being 5 p.p.m Cu, 3 p.p.m Cd, 2 p.p.m Fe, 1 p.p.m Pb.

The samples were degreased in ethyl alcohol in a Soxhlet-type apparatus, electrolytically polished in an alkaline evanide bath and slightly etched in 0.1 M HNO2, after which they were washed in distilled water and again in ethyl alcohol. They were then placed in a polythene holder inside a glass vessel that was filled with an atmosphere of H₂O-saturated air, containing 2% H₂S by volume. All experiments were carried out at room temperature (18-21°C). Ordinary tank hydrogen sulfide was used, except for one experiment which was conducted with extremely purified HoS and non-laboratory air. Despite these precautions, the same kind of needle growth was observed as in the other experiments. Variation of degreasing agent, time of etching and concentration of etchant did not significantly affect the rate of tarnishing, which is taken as an indication that the cleansing process adopted gave metallic surfaces of reproducible properties and that any surface films formed during the electropolishing step were effectively removed by the etching.

Fig. 1 shows a replica electron micrograph of the surface of a sample prepared in this way and illustrates the grain size of the material. (This and the other replicas were, in fact, taken from a ribbon cold

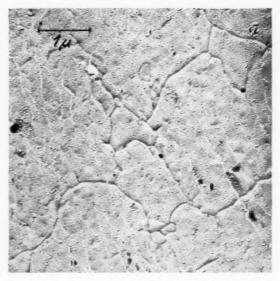


Fig. 1. Formvar replica of electropolished and etched silver sample after standard pretreatment for tarnishing experiments. Shadowed.

rolled from the wire ordinarily employed. Owing to the high degree of cold work of the wire, it is believed that the rolling introduced no significant changes.)

VOI

195

The amount of reaction product formed on the surface of the samples was determined by coulometric reduction $^{(23)}$ in a closed cell $^{(24)}$ under oxygen-free N₂, using deoxygenated 0·1 M KCl as electrolyte. $^{(25)}$ Short lengths of most of the wire samples were saved for electron microscopic study. The sample holder of the microscope could accommodate them without further preparation. The growth forms on the cylindrical surface of the wire were studied directly in silhouette at low magnification (usually $\times 2500$). Only for very slightly tarnished samples were replicatechniques and higher magnifications found necessary.

RESULTS

The results of the kinetic study are presented in Fig. 2. During an initial stage the reaction proceeds according to a rate law of the cubic type,

$$(\Delta m)^3 = \text{const. } t$$

(The data collected in Fig. 2 place the exponent between 2.72 and 3.53, the best fit being obtained with the value 3.0). At the end of the initial stage, just before the sudden increase of the reaction rate, the amount of sulfide per unit area would correspond to a film thickness of ca. 160 Å if it were present in the form of a compact, plane-parallel layer. Films in this thickness range are expected to grow according to the thin film mechanism proposed by Cabrera and Mott⁽²⁶⁾ and by Hauffe⁽²²⁾. Ag₂S being an n-type

^{*} Messrs. Johnson, Matthey and Co. of London.

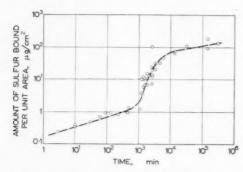


Fig. 2. Reaction kinetics for the system Ag-H₂S.

conductor, $^{(27,28)}$ the rate law ought to be of the parabolic rather than of the cubic type, although the possibility of a p-type surface zone $^{(29)}$ has to be kept in mind.

Electron microscopic study, however, shows that the tarnish film is certainly not a plane-parallel layer. Fig. 3a shows the silhouette electron micrograph of an untarnished wire, and Fig. 3b that of a surface after 500 min corrosion. It is seen that the reaction product has built up small mounds on the originally fairly smooth surface. Replica studies on ribbon samples cold rolled from the same wire (Fig. 4) indicate that the mounds are equally spaced and have a diameter of ca. 0.5μ , a figure that agrees well with the average of the silhouette micrographs. As the reaction proceeds, the mounds increase in diameter and (as indicated by silhouette studies) in height, but apparently not so much in number. A statistical study of the population density of the mounds has been deferred to a later stage of the investigation. It may be noted that their distribution appears to be entirely unrelated to the grain structure of the metal.

In the next stage, from ca. 1000 to 5000 min, the reaction proceeds at a considerably greater rate and the values of Δm , the amount of sulfide per unit area, suddenly begin to scatter considerably. Simultaneously, a drastic change in growth form occurs. Fig. 5, a silhouette micrograph of the reaction product formed after 5290 min, shows a multitude of small needles. This growth form continues to be typical throughout the subsequent stages of the reaction, the needles growing chiefly in length, but also in diameter. Fig. 6 shows the largest needles observed in our study. Compared with Fig. 5, the population density of prominent needles has been much reduced. Obviously, progressively fewer individuals continue to grow during the third stage of the reaction, where the reaction rate again decreases to approximately its initial value.

It is interesting to estimate the possible thickness of a hypothetical, compact bottom layer in relation to the dimensions of the needle crystals. If all the sulfide formed after a reaction period corresponding to Fig. 6 were present in the form of a plane-parallel layer, its thickness would be ca. 1.02 μ . A statistical study of the average thickness of the needles and of their length above the apparent bottom level, keeping in mind the partial shielding of needles below and above the equatorial plane of the cylindrical sample, reveals that the volume of the needles accounts for approximately 3 per cent of the total amount of sulfide present. This puts the thickness of the bottom layer at about 1 µ—which is still only one tenth to one twentieth of the length of the prominent needles. (Similar proportions between needle length and thickness of the bottom layer prevail at the beginning of needle growth).

The growth history illustrated by Figs. 5 and 6 suggests that the bottom layer should be envisaged not as a homogeneous plane parallel film but rather as a thick undergrowth of smaller needles, arrested earlier in their growth, and perhaps with interstices filled in by subsequent sulfide deposition. This will give a columnar structure with very many "easy diffusion paths" perpendicular to the surface. If diffusion through this undergrowth layer should become rate determining at a later stage of the reaction, one would expect the ordinary parabolic rate law (though with a higher rate constant than for a film grown in the manner usually imagined). It is tempting to make such a mechanism responsible for the decrease of the reaction rate during the third stage of the reaction, but the data collected so far would favour a higher value than two for the exponent in the rate law.

Sulfide needles on silver can become extremely large. Terem⁽¹⁵⁾ has produced needles of a few millimeters length by reaction at elevated temperatures. Needles big enough to be visible to the naked eye are sometimes observed on electrical contacts of silver after very long exposure to town atmospheres, ⁽³⁰⁾ Although such exceptionally large spikes may be encountered only under unusual conditions, the ease and reproducibility with which needles of the size range demonstrated in this paper were obtained indicates that they do indeed represent the normal growth form of the reaction product under these circumstances.

It appears premature, at the present juncture, to speculate on the mechanism involved in the appearance—notably first in an advanced stage of the reaction—and the subsequent growth of the needles.

VOL. 7 1959

Fig. 3a. Silhouette electron micrograph of electropolished wire sample before tarnishing treatment.



Fig. 3b. Same, after 500 min exposure to tarnishing atmosphere.

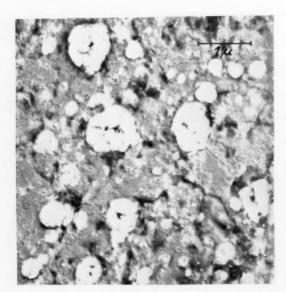


Fig. 4. Formvar replica of ribbon sample after 500 min exposure to tarnishing atmosphere.



Fig. 5. Silhouette electron micrograph of wire sample after $2590\,\mathrm{min}$ exposure to tarnishing atmosphere.

The study is being continued with respect to the system $Ag-H_2S$ and to other systems, in the first place, $Cu-O_2$. Obviously, a more thorough phenomenological study of the growth and nucleation of the sulfide is needed, as well as an examination of the influence of conditions such as the dislocation density in the metal surface, the temperature, and the pressure

of the reacting and auxiliary gases. It is felt, however, that already the present results indicate that the morphology of the reaction product plays a decisive role in the kinetics of the reaction studied here. Further experimental work may help to decide whether this is a general feature of metal—gas reactions, or an exception.



Fig. 6. Silhouette electron micrograph of wire sample after 142.560 min exposure to tarnishing atmosphere.

ACKNOWLEDGMENTS

VOL.

1959

The authors wish to record their sincere gratitude to Prof. G. Hägg for his interest and his generosity in placing at their disposal the facilities of the Institute of Chemistry at Uppsala. The electron micrographs reproduced in Figs. 1 and 4 were made at the Swedish Institute of Metal Research. The authors are grateful to Prof. E. Rudberg and Mr. S. Modin for the use of the electron microscope. Interest in the problems treated here was first aroused during a study of the technical corrosion behaviour of silver alloys for electrical contacts, carried out for Telefon-AB L. M. Ericsson, Stockholm, and by discussions between one of us (H. F.) and Prof. E. Justi (Braunschweig) and Prof. G. Pfefferkorn (Münster). Telefon-AB L. M. Ericsson has furthered our work in several ways, i.e. by donating the spectroscopically pure silver wire. Since January, 1958, the work has been supported jointly by Statens Naturvetenskapliga Forskningsråd and Statens Tekniska Forskningsråd (The Swedish Natural Science and Technical Research Councils, resp.).

REFERENCES

- G. Pfefferkorn, Naturwiss. 40, 551 (1953).
- J. M. Cowley, J. Electrochem. Soc. 101, 277 (1954).
- G. PFEFFERKORN, Z. wiss. Mikroskopie 62, 109 (1954).
 G. PFEFFERKORN, Z. Metallk. 46, 204 (1955).
- 5. S. M. ARNOLD and S. E. KOONC J. Appl. Phys. 27, 964 (1956)
- 6. A. F. Moodie, Acta Cryst. 9, 995 (1956).
- 7. H. Hashimato, and K. Tanaka, Proc. 1st Regional Conf. Electron Microscopy in Asia and Oceania, Tokyo 1956, p. 292.

- R. Takagi, J. Electron Microscopy 3, 18 (1955)
- 9. H. Hashimoto, K. Tanaka, E. Yoda and H. Araki, Acta Met. 6, 557 (1958).
- 10. E. A. GULBRANSEN and T. COPAN, J. Appl. Phys. 28, 1374 (1957); Westinghouse Res. Rept. 6-94602-1-R5 (Sept. 18, 1957) (privately communicated manuscript)
- 11. J. Markali, Research 10, 367 (1957)
- 12. T. HURLEN, H. KJØLLESDAL and J. MARKALI, Proc. 2nd Scandinavian Corrosion Meeting, Stockholm (1958).
- 13. J. Paidassi, Trans. Amer. Inst. Min. (Metall.) Engrs. 197, 1570 (1953).
- R. F. TYLECOTE, J. Inst. Met. 81, 681 (1953).
- 15. H. N. TEREM, Rev. Fac. Sci. Univ. Istanbul 18, A 81 (1953).
- J. BARDOLLE and J. BÉNARD, Rev. mét. 49, 613 (1952).
- J. BARDOLLE, J. chim. phys. 639 (1956).
- F. GRØNLUND, J. chim. phys. 660 (1956).
 E. A. GULBRANSEN, W. R. McMILLAN and K. F. ANDREW, J. Metals, N.Y. 6, 3 (1954).
- 20. W. W. HARRIS, F. L. BALL and A. T. GWATHMEY, Acta Met. 5, 574 (1957).
- 21. E. Menzel, W. Stössel and C. Menzel-Kopp, Z. Naturf. 12a, 404 (1957).
- 22. K. Hauffe, Oxydation von Metallen und Metallegierungen. Springer Verlag, Berlin (1956).
- 23. L. E. PRICE and G. J. THOMAS, Trans. Electrochem. Soc. 76, 329 (1939).
- 24. W. E. Campbell and U. B. Thomas, Trans. Electrochem. Soc. 76, 303 (1939).
- J. A. Allen, Trans. Faraday Soc. 48, 273 (1951).
- 26. N. Cabrera and N. F. Mott, Rep. Progr. Phys. 12, 163 (1949).
- 27. F. KLAIBER, Ann. Physik 3, 229 (1929).
- C. Wagner, J. Chem. Phys. 21, 1819 (1953).
- 29. F. S. Stone, Proc. 3rd Intern. Congr. Reactivity of Solids, Madrid 1956, p. 641.
- C. Ringström, communicated in discussion of this paper at 2nd Scandinavian Corrosion Meeting, Stockholm 1958. Similar observations have been reported by Mr. G. Hasselbohm of Telefon-AB L. M. Ericsson, Stockholm.

THE EFFECT OF PLASTIC DEFORMATION ON THE DIFFUSION OF HYDROGEN IN NICKEL*

H. H. GRIMES†

The diffusion of hydrogen in elastically and plastically strained nickel has been measured by a permeability experiment with the result that no significant change of the diffusion coefficient was observed for deformations up to 10 per cent. These results are in agreement with a recent theoretical analysis of interstitial diffusion in strained systems based upon considerations of interatomic forces and strain gradients.

The diffusion coefficient calculated for hydrogen through unstrained nickel can be represented by the equation:

 $D = 0.0095 \exp(-10.300/RT) \text{ cm}^2/\text{sec}$

in the temperature interval $430^{\circ} - 850^{\circ}\mathrm{C}.$

L'EFFET DE LA DEFORMATION PLASTIQUE SUR LA DIFFUSION DE L'HYDROGENE DANS LE NICKEL

L'auteur a mesuré, par des essais de perméabilité, la diffusion de l'hydrogène dans le nickel déformé élastiquement et plastiquement. Il n'a pas obtenu une modification appréciable du coefficient de diffusion pour des déformations allant jusqu'à 10 pour cent.

Ces résultats sont en accord avec une analyse théorique récente de la diffusion interstitielle dans les systèmes déformés qui s'appuie sur des considérations de forces inter-atomiques et de gradients de déformations. Le coefficient de diffusion calculé pour l'hydrogène dans le nickel non déformé, peut être représenté par l'équation:

 $D = 0.0095 \exp(-10.300/RT) \text{ cm}^2/\text{sec}$

pour un intervalle de température de 430 à 850°C.

DER EINFLUSS PLASTISCHER VERFORMUNG AUF DIE DIFFUSION VON WASSERSTOFF IN NICKEL

Durch Messung der Durchlässigkeit wurde die Diffusion von Wasserstoff in elastisch und plastisch verformtem Nickel untersucht. Für Deformationen bis 10 Prozent ergab sich keine wesentliche Änderung des Diffusions-Koeffizienten. Das stimmt überein mit einer kürzlich gemachten theoretischen Untersuchung der Zwischengitter-Diffusion in verformten Systemen, die sich auf Betrachtungen der zwischenatomaren Kräfte und des Gradienten der Verzerrung stützt.

Der Diffusions-Koeffizient für Wasserstoff in unverformtem Nickel lässt sich im Temperaturgebiet $430^{\circ}-850^{\circ}$ C darstellen durch: D=0.0095 exp (-10300/RT)cm²/sec.

INTRODUCTION

The results of recent experiments have clarified the effect of plastic and elastic strains on the diffusion coefficient for materials in which diffusion proceeds by a vacancy mechanism. Plastic strains increase the diffusion coefficients by an order of magnitude⁽¹⁻³⁾ and large elastic compressive strains produce relatively smaller decreases in the self-diffusion of several substances.⁽⁴⁻⁷⁾

It is well known, however that many important solid diffusion systems involve interstitial transport mechanisms. Unfortunately, very little discussion of the effects of strain on these systems has appeared in the literature. It is of interest, therefore, to determine whether a pronounced enhancement of diffusion occurs when a metal containing interstitially diffusing hydrogen undergoes a plastic or elastic strain. This system is of particular practical importance because

of the prominent role hydrogen plays in various metal treatments and in embrittlement.

19

The experiment was designed to measure the interstitial diffusion in a system subjected to both elastic and plastic strains up to 10 per cent total strain at temperatures between 430° and 850°C. Specifically, this involved determining the rate of permeation of hydrogen through tubular nickel specimens pulled elastically in tension at constant load or plastically at constant strain rate.

The system hydrogen in nickel was chosen for this permeability study because the diffusion process is known to be rate determining for the temperatures and pressures employed. (8) In addition this system is fortunate in its freedom from complicating factors: (1) the absence of compound formation, (2) the absence of phase changes in the experimental range, and (3) the known high rate of diffusion permitting accurate experimental measurements.

A recent extension of the theory of diffusion in solids treats the influence of strain on the diffusion rate.⁽⁹⁾ For elastic strains, the extended theory states

^{*} Received December 1, 1958; revised version February 13, 1959.

[†] Lewis Research Center, National Aeronautics and Space Administration, Cleveland, Ohio.

that the effect of strain on both vacancy and interstitial diffusion arises principally from changes in the free energy of activation for diffusion resulting from the lattice strains. The approximate magnitude of this effect can be obtained from considerations of the lattice strains and interatomic forces.

In crystals undergoing plastic deformation a second and somewhat greater effect of strain on vacancy diffusion has been shown to be associated with the production of additional lattice vacancies, thereby increasing the probability of a diffusion jump into a vacant site. For interstitial diffusion, however, due to the large number of available diffusion sites already present, any increase in interstitial sites or vacancies resulting from plastic deformation would be negligible, so that any change in the coefficient will be ascribed to the first effect; viz., the change in the free energy of activation.

The approximate magnitude of this effect can be calculated from the equation given in reference 9 for the change in the coefficient in an interstitial diffusion system subjected to a homogeneous linear strain.

$$\frac{D_s}{D_u} = (1+\varepsilon)^2 \exp\left[\frac{\varepsilon}{kT} \left(\frac{\partial \Phi}{\partial \varepsilon}\right)_{z,0} (2\mu - 1)\right] \quad (1)$$

Here D_s/D_u is the ratio of the interstitial diffusion coefficient in the strained system to that in the

unstrained case. ε is the strain in the direction of the applied stress, μ is the Poisson ratio, k is the Boltzmann constant, and T is the absolute temperature. $(\partial \Phi/\partial \varepsilon)_{\frac{1}{\varepsilon},0}$ is the rate of change of the potential energy with strain when the diffusing particle is at the saddle point of the activated state.

EXPERIMENTAL

The apparatus used in these permeability experiments is shown schematically in Fig. 1. The apparatus consisted basically of a supply of hydrogen which diffused laterally through a heated, tubular nickel specimen and was measured by the pressure increase in a low-pressure manifold.

Three-inch long test specimens were fabricated from "L" nickel tubing (99.4% Ni) of 1/4 in. diameter with a wall thickness of 1/32 in.

After the entire system was degassed to about 10^{-5} mm of Hg, pure dry hydrogen was introduced and contained at 1 atmosphere pressure in a gastight chamber surrounding the specimen. The diffusion chamber was designed to allow the specimens to be pulled in tension during the runs.

The plastically strained specimens were pulled in tension at strain rates from 0.02 to $0.4~\rm hr^{-1}$ to a total strain of 10 per cent. The elastically strained specimens were loaded to a maximum of $325~\rm lb/in.^2$

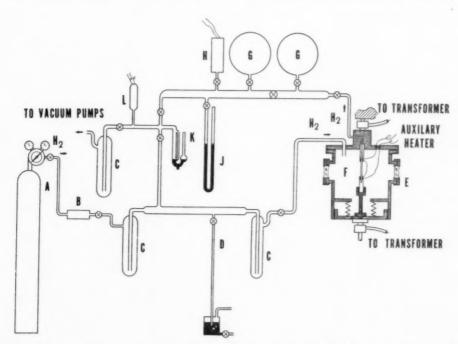


Fig. 1. Gas permeability apparatus: A, hydrogen cylinder; B, Deoxo-deoxidizer; C, liquid nitrogen traps; D, gas bubbler pressure regulator; E, diffusion chamber (mounted in tensile testing machine); F, test specimen; G, gas reservoirs; H, Alphatron pressure gage; J, mercury manometer; K, McLeod gage; L, ionization gage (used in degassing procedure).

The nickel specimen was heated by passing an electric current through the tube itself. Thick-walled, 3/4 in. diameter cylindrical sections were brazed to the ends of the specimens and served to limit the diffusion to a central 3 in. test section by decreasing the concentration gradient and lowering the electric resistive heating beyond this region. Furthermore, when the specimens were pulled in tension, these end pieces restricted the deformation to the central test portion.

End heaters were used to obtain a uniform temperature distribution over the test length of the specimen. With this procedure the temperature was found to vary less than 10°C over the central 2 in. portion.

The temperature profile was determined both with fine chromel–alumel thermocouples spot welded onto the specimens and also, whenever possible, with an optical pyrometer.

Corrections to the diffusion coefficient were made for the effects of end cooling by calculating the small flux through the cooler end portions of the tube and subtracting this value from the total flux. The flux then used in calculating the diffusion coefficient was that through the central uniform temperature region.

Pressure increases due to hydrogen diffusion into the evacuated manifold of known volume were continuously displayed on an Alphatron pressure gage with a relative error estimated to be less than 3 per cent of the total internal pressure. In no determination was the pressure in the low pressure manifold allowed to exceed 40 mm, so that the pressure gradient was closely given by the gas pressure on the high pressure side of the diffusion specimen.

The specimens were all fabricated from a single length of nickel tubing and all received an identical heat treatment before the diffusion runs (30 min in vacuum at 1135° C). The purpose of this anneal was to insure greater uniformity of sample history, and also to increase the grain size of the material and thus reduce the effects of grain boundary diffusion. The average grain size before and after diffusion was about $200~\mu$. Volume diffusion was also favored by the high temperatures used in the experiments.

The specimen diameter, wall thickness, and extension were determined radiographically before and after diffusion. The specimens were also examined metallographically to determine the presence of voids or cracks. In none of the experiments was any evidence of void formation, cracking, or channeling noted.

The experimental diffusion coefficients were calculated from the equation

$$D = (J/S) (100/\rho) (\ln R/r)/2\pi l$$
 (2)

where

J measured flux in cm³ STP/sec

R outside radius of the tube

r inside radius of the tube

ρ density of the metal

l specimen test length in cm

and S the gas solubility in cm3 STP/100 gm of metal

Within the temperature range 300°–1450°C the solubility S may be calculated from the equation of Armbruster⁽¹⁰⁾

$$\log_{10} (S/p^{\frac{1}{2}}) = -A/T + B.$$

where

A is a constant = 645

B is a constant = 0.082

T is the absolute temperature

and p is the pressure gradient of the diffusing gas in mm of Hg.

RESULTS AND DISCUSSION

Table 1 lists the measured diffusion coefficients for hydrogen in nickel for strained and unstrained conditions calculated from equation (2). A plot of

Table 1. Diffusion coefficient (D . $10^6~\rm{cm^2/sec}$) as a function of temperature and strain rate

Type of strain	T (°K)	Strain rate (hr^{-1})			
	, 12/	0	0.02	0.2	0.4
Elastic	804 807 1072 1097	*14.8(325 lb/in²) *13.7(325 lb/in²) *77.6(140 lb/in²) *81.8(140 lb/in²)			
Plastic	690 708 927	,	$\frac{5.64}{6.73}$	31.9	
	$\frac{1072}{1077}$				77.6 68.8
	$\frac{1097}{1150}$				81.8
Unstrained	724	7.71			101
	750	9.67			
	798	16.2			
	803	13.2			
	811	14.6			
	816	16.0			
	825	18.6			
	851	19.2			
	881	23.8			
	917	38.1			
	920	32.9			
	952	46.5			
	981	49.3			
	1066	67.4			
	$\frac{1066}{1090}$., 86.5			
	1119	79.1			
	1119	110			

^{*} Constant load applied during run.

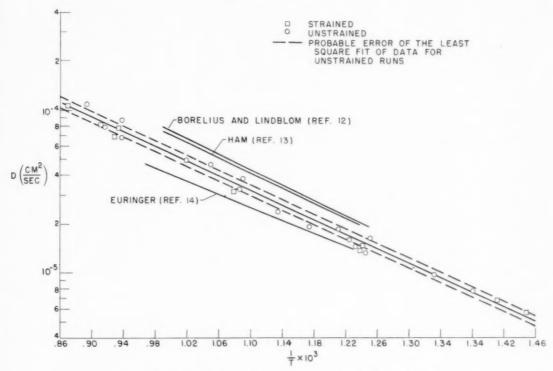


Fig. 2. Temperature dependence of the diffusion coefficient.

log D against 1/T is shown in Fig. 2 for all of the diffusion data obtained in these experiments. A least-square fit of the data for the diffusion coefficient in the unstrained metal is given by the equation

1959

$$D = 0.0095 \exp(-10.300/RT) \text{ cm}^2/\text{sec}$$

which, as seen in Fig. 2, is in good agreement with values obtained by other experimenters. The probable error in D is ± 6 per cent.

All the values of the diffusion coefficient for strained nickel lie well within the scatter band for the unstrained material. Thus, the data indicate no pronounced enhancement of diffusion due either to plastic or elastic strains attained in the experiment.

A theoretical calculation of D_s/D_u was made from equation (1) using simple potential theory, considering only nearest neighbors interactions in calculating the energy difference in $(\partial\Phi/\partial\varepsilon)_{z=0}$.

The lattice strains were estimated from the experimentally measured strains at the yield point. In a crystal undergoing plastic deformation it seems reasonable to postulate that plastic flow occurs by the displacement of large blocks of material as a result of dislocation movement, so that the microscopic strains defining the relative atomic positions are very much smaller than the macroscopic strains. In fact it is highly probable that the microscopic strains are

always below the elastic limit of the materials. On this basis it was estimated that the microstrains in this experiment never exceeded the 0.1 per cent elastic strain at the yield point even during plastic deformation.

The calculated ratio of the diffusion coefficients, (D_s/D_u) , differed from unity by less than 1 per cent. This result is in agreement with the experimental findings and is representative of many interstitial diffusion systems having similar interaction energies.

It should be noted that this conclusion does not imply that the permeability of the diffusing species is unaffected by plastic or elastic strains. The permeability (P) is related to the diffusion coefficient by

$$P = DS \tag{3}$$

where S is the solubility of the gas in the metal. Thus, an applied strain may alter the solubility of a material and thereby change the permeability even for a constant diffusion coefficient. For the determinations made on strained samples, the coefficients calculated from the data are based on solubilities available only for unstrained material. It is significant, however, that the permeability showed an imperceptible variation with strain in the experiments. It follows from equation (3) that for a constant permeability the product of diffusion coefficient and solubility must

remain unchanged. In the presence of a tensile strain it is not expected that either the diffusion coefficient or the solubility increases at the expense of the other, so that within the experimental error both solubility and diffusion coefficient must remain unchanged. This result for the diffusion coefficient is in agreement with the previous theoretical calculations.

The absence of an experimentally significant strain dependence of the solubility in either elastically or plastically strained nickel undoubtedly reflects the relatively small increases in lattice volume resulting from the strains. In the experiment the interstitial atoms occupy only about 1/2500 of the available lattice volume (1 atom per 2500 sites). The small increase in volume resulting from elastic lattice strains in the experiment would produce a solubility increase below the sensitivity of the experiment. At lower temperatures, where larger elastic strains are possible, de Kazinczy⁽¹¹⁾ has shown that elastic deformation of iron containing dissolved hydrogen does increase the hydrogen permeability slightly. The author shows that the effect can be ascribed entirely to increased lattice solubility.

The lattice volume increase due to the excess vacancies produced in plastic deformation is also insignificantly small compared to the total available volume. For nickel at the temperatures and strain rates attained in this experiment the solubility increases due to the excess vacancies produced (about

1 vacancy per 10⁶ sites) are well below the precision of the experimental measurements. The excess vacancy concentration, however, is appreciable compared to the equilibrium vacancy concentration. It is for this reason that plastic strains have such a profound effect on the vacancy diffusion coefficient.

It is significant, then, that this experiment indicates that plastic strains, capable of increasing vacancy diffusion by orders of magnitude, (3) have relatively little effect on the interstitial diffusion coefficient. This result, however, has been shown to be in accord with theoretical predictions based on interatomic force considerations and transport mechanism.

REFERENCES

- 1. F. S. Buffington and M. Cohen, Trans. Amer. Inst. Min. (Metall.) Engrs. 194, 859 (1952)
- 2. N. UJIIYE, B. L. AVERBACH, M. COHEN and V. GRIFFITHS, Acta Met. 6, 68 (1958)
- 3. A. F. Forestieri and L. A. Girifalco, J. Phys. Chem. Solids 10, 99 (1959).
- 4. T. LIU and H. G. DRICKAMER, J. Chem. Phys. 22, 312 (1954).
- 5. N. H. NACHTRIEB, WADC Tech. Rep. 55-68 (1954).
- 6. J. Petit and N. H. Nachtrieb, J. Chem. Phys. 24, 1027 (1956)
- W. Jost and G. Nehlep, Z. Phys. Chem. 34, 348 (1936).
- C. T. SMITHELLS and C. E. RANSLEY, Proc. Roy. Soc. Lond. A157, 292 (1936).
- 9. L. A. GIRIFALCO and H. H. GRIMES, NACA Tech. Note No-4408.
- 10. M. Armbruster, J. Amer. Chem. Soc. 65, 1043 (1943).
- F. DE KAZINCZY, Jernkont. Ann. 139, 885 (1955).
 G. BORELIUS and J. LINDBLOM, Ann. Phys. 82, 201 (1927).

19

- 13. W. R. Ham, J. Chem. Phys. 1, 476 (1932).
- 14. G. EURINGER, Z. Phys. 96, 37 (1935).

THE NUCLEATION OF NICKEL WHISKERS*

R. E. CECH†

The nucleation step in the formation of nickel whiskers by hydrogen reduction of halide salts was examined. The finding of Gorsuch that whiskers were nucleated on an oxide were confirmed and it was demonstrated that the nucleation step for whisker formation was the hydrogen reduction of nickel oxide to metal.

LA GERMINATION DES BARBES DE NICKEL

L'auteur a examiné la germination de barbes de nickel lors de la réduction par l'hydrogène de sels halogènes. Les résultats obtenus confirment ceux de Gorsuch, selon lesquels les barbes naissent sur un oxyde. L'auteur démontre en outre que la germination des barbes est due à la réduction par l'hydrogène de l'oxyde de nickel en métal.

KEIMBILDUNG BEI NICKEL-WHISKERS

Bei der Bildung von Nickel-Haarkristallen (Whiskers), die durch Reduktion von Halogeniden mittels Wasserstoff erfolgte, wurde die Keimbildungsstufe untersucht. Die Beobachtung von Gorsuch, dass die Keimbildung auf einem Oxyd stattfindet, wurde bestätigt. Ferner liess sich zeigen, dass der für die Keimbildung bei der Entstehung der Whiskers entscheidende Schritt die Reduktion von Nickeloxyd durch Wasserstoff zum Metall ist.

1. INTRODUCTION

VOL.

1959

Metallic crystals of filamentary shape are extremely useful in studies of the fundamental properties of solids. Frequently these studies are seriously hampered by an inability to produce crystals of uniform quality and in large numbers. The present investigation was undertaken in the hope that a better understanding of the mechanism of formation of filamentary crystals would lead to improved techniques of preparation for scientific or other applications.

The preparation techniques for crystals of the metals of most widespread interest, copper, iron, nickel, and cobalt have centered largely about the hydrogen reduction of halide salts. This technique was first used by Kohlschütter⁽¹⁾ in preparing silver and copper filaments from their respective chlorides. Later, Fullman and Gatti⁽²⁾ found that iron crystals of filamentary form could be produced by reduction of a mixture of ammonium chloride and iron oxide. Doremus and Sears⁽³⁾ demonstrated that the active ingredient in the Fullman–Gatti method of iron crystal preparation was an iron chloride. Brenner⁽⁴⁾ extended the technique to the preparation of "whiskers" of copper, silver, iron, nickel, cobalt, platinum, and gold. Gorsuch⁽⁵⁾, in an intensive

investigation of the growth of cube-oriented iron whiskers demonstrated that the presence of iron oxide was necessary for whisker growth to occur. He did not seek to establish the mechanism by which the oxide brought about whisker nucleation.

The present investigation is concerned with the mechanism by which a whisker is nucleated by an oxide. "Nucleation" here refers to the formation of the first layer of metal upon which growth occurs to form a whisker.

One can envisage three ways by which the nucleation of a whisker can occur on an oxide substrate. An accidental foreign particle in the oxide may promote a metal halide—hydrogen reaction so as to deposit metal on (or near to) the impurity. Alternatively, the metal halide and hydrogen may react in the vapor or on the oxide surface and deposit metal in a manner analogous to low-pressure vapor deposition. In a third alternative mechanism, hydrogen may attack the oxide to produce the first layer of metal. The metal halide—hydrogen reaction could then be catalyzed on the metal surface to produce a whisker. In this investigation it is demonstrated that whisker nucleation proceeds by the last of the three mechanisms.

2. EXPERIMENTAL TECHNIQUE

Nickel oxide single crystals were grown by decomposing Amend C.P. nickel bromide with watervapor on magnesium oxide crystals. The technique

^{*} Received February 18, 1959.

[†] General Electric Research Laboratory, Schenectady, New York.

and apparatus have been described in detail elsewhere. (6) In one experiment, described later, nickel chloride was used in place of nickel bromide. Nickel whiskers were grown upon the surface of the oxide crystals in the same apparatus immediately following the preparation of the oxide. The system temperature was constant throughout the oxide preparation and whisker growing portions of the runs. In all cases oxide crystals and nickel whiskers were grown at a temperature of 650°C.

Two techniques were used for growing nickel whiskers. In the first technique the atmosphere, which was oxidizing during the preparation of the oxide crystals, was made slightly reducing by admitting an argon-hydrogen-water vapor mixture to the system at a very low flow rate. The atmosphere change was made while a small amount of nickel bromide remained in the system. Whisker growth occurred on the oxide crystals following the change from oxidizing to reducing conditions.

The second whisker growing technique consisted of simply growing the nickel oxide crystals in a sealed reaction chamber under a water vapor pressure of 25 mm/Hg. A large reservoir of water was maintained at room temperature at one end of the reaction chamber. It is believed that because nickel oxide forms with slight oxygen excess, hydrogen is generated from decomposition of water vapor. This eventually causes the chamber atmosphere to become sufficiently reducing to produce a growth of whiskers of nickel.

Specimens of nickel oxide with whiskers grown upon them were examined microscopically to determine the oxide surface characteristics and internal structure at points where whiskers were formed. Where large numbers of fine crystals or whiskers were found the angular position of the metal crystals with respect to the known crystallographic directions in the oxide were measured. In other specimens where a few large whiskers were found, back-reflection Laue X-ray photographs were taken. These photos recorded on the same film both the whisker and the oxide substrate orientations. Whisker-oxide orientation relationships were obtained from an analysis of the films.

3. RESULTS

The whisker growing technique which involved the direct introduction of a reducing gas resulted in large numbers of small crystals forming along occasional cracks in the oxide. Because of extensive overlapping, these crystals could not be analyzed.

The crack-free areas of oxide contained large numbers of whiskers and growth crystals dispersed

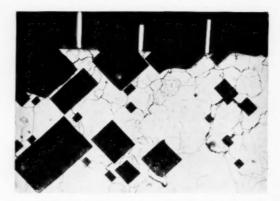


Fig. 1. Nickel whiskers grown near a cube edge of a nickel oxide crystal. $\times 500$.

uniformly over the surface. A few of these whiskers growing nearly perpendicular to the oxide substrate are shown in Fig. 1. The rectangular black areas are pyramidal overgrowths of nickel oxide.

Measurements were made of the angle subtended between a side face of a nickel whisker and a cube edge of the oxide crystal substrate. The results for 650 whiskers are plotted in a histogram of number of whiskers vs. the angle (α) , Fig. 2. It is clear that whatever the crystal orientation of the nickel whiskers may be, they are not random with respect to the oxide substrate. This result contradicts the hypothesis that whisker nucleation occurs on accidental dirt particles.

It is worthy of note that many other growth

191

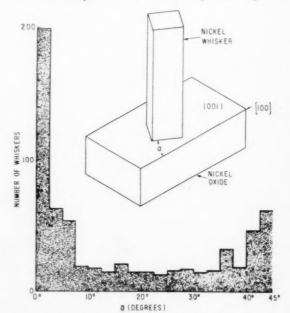


Fig. 2. Histogram of number of whiskers vs. α . The angle α was measured between a side face of the whisker and a cube edge of the nickel oxide crystal.

crystals in addition to whiskers were found on the oxide crystals. Whiskers comprised 66 per cent of the total number of crystals while the remainder consisted of 11 per cent cube-on-edge crystals, 8 per cent triangular pyramid crystals and 15 per cent non-definable form crystals. The cube-on-edge crystals were preferentially oriented in much the same manner as the whiskers. A histogram of number of cube-on-edge crystals which form an angle β between the metal–oxide intersection and the oxide cube edge, had peaks where β is \sim 0° and 45°.

All whiskers formed by deliberate addition of hydrogen to the system were too small to obtain satisfactory X-ray photographs for orientation analysis. The latter described technique of allowing the system to produce its own hydrogen was therefore used to grow larger whiskers. A total of eight whiskers were subsequently analyzed by means of back-reflection Laue X-ray photographs which simultaneously recorded both the whisker and the substrate orientation.

The cube poles of five whiskers are plotted in sterographic projection in Fig. 3. On the same projection the cube poles of four closely related low temperature hydrogen reduction orientations are plotted as shaded regions. The correspondences of

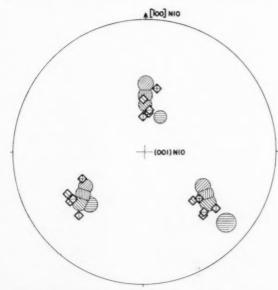


Fig. 3. The cube poles of five nickel whiskers are plotted in stereographic projection. The reference plane is the cubic surface of the nickel oxide substrate. Shaded areas represent the orientations of crystals of nickel formed by hydrogen reduction of the oxide at 550°* and 650°°C.

*(531)[105]Ni//(001)[110]NiO
(112)[110]Ni//(001)[100]NiO
(1188)[10 77]Ni//(001)[100]NiO
(111)[110]Ni//(001)[100]NiO

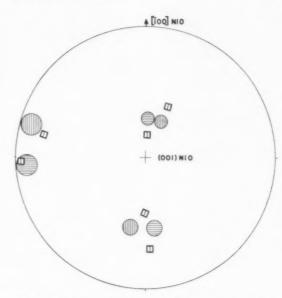


Fig. 4. The cube poles of two nickel whiskers are plotted in stereographic projection. The reference plane is the cubic surface of the nickel oxide substrate. Shaded areas represent the irrational index orientations of crystals of nickel formed by hydrogen reduction of the oxide at $550^{\circ}\mathrm{C}.$

Orientation Relationship No. 3 of reference 8.

Orientation Relationship No. 4 of reference 8.

whisker-oxide orientation relationships and reduction crystal-oxide orientation relationships are clear.

In Fig. 4 are plotted the cube poles of two whiskers which had irrational orientation relationships closely approximating another two low temperature hydrogen reduction orientation relationships. One whisker had an orientation which did not approximate any of the fourteen orientations found on direct reduction of oxide. The whisker could have been disturbed in handling.

All nickel whiskers analyzed had [110] fiber axes and side surfaces made up of alternate (100) and (110) planes. In one specimen it was found that two whiskers grew parallel from opposite sides of a thick portion of a nickel oxide crystal, as shown in Fig. 5. The whiskers nucleated on the side surfaces of the thicker region of oxide crystal running diagonally through the photomicrograph. The orientations of both whiskers were determined from back-reflection Laue photographs, using an indexing camera which allowed no possibility of error in determining the relationship between the two whisker orientations. The cube poles of the two whiskers are plotted in sterographic projection in Fig. 6. The two whiskers exist in two different permutations of the same orientation relationship. These whiskers therefore nucleated independently of one another.

The internal structure of the nickel oxide substrate.

VOL.

1959



Fig. 5. Two nickel whiskers are shown growing parallel to the cube face of a nickel oxide crystal. Oblique illumination. $\times 50$.

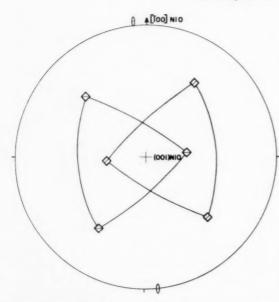


Fig. 6. The cube poles of the two whiskers shown in Fig. 5 are plotted in stereographic projection. The [110] whisker axes are also plotted. The cube face of the nickel oxide substrate crystal is in the plane of projection.

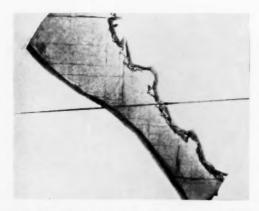


Fig. 7. Same area as shown in Fig. 5, transmitted light. $\times 50$.

upon which the nickel whiskers grew, is shown by transmitted light in Fig. 7. A thick line of precipitation is seen joining the two whiskers. This observation suggests that a structural singularity exists in the oxide beneath the whiskers. Some precipitation has also occurred in what appear to be slip planes within the oxide crystal.

The presence of a precipitate "tail" in the oxide beneath whiskers had also been found in the case of whiskers grown from nickel chloride. In Fig. 8 is shown a whisker growing from a point near the center of a subgrain of the oxide crystal. The same area as viewed by transmitted light is shown in Fig. 9. A line of precipitate can be noted beneath the whisker. This whisker "tail" terminates on a foreign particle. This observation suggests that the tail is a structural singularity formed when the oxide crystal deposited around the foreign particle.

195

There was a marked tendency for whiskers to form near the center of subgrains in the nickel oxide crystals. This is the case for the whisker shown in Figs. 8 and 9 although the subgrain boundaries are difficult to see. In Fig. 10 are shown whiskers which clearly originate from the growth centers of the oxide subgrains. The concentric rings on the oxide surface are growth steps.

4. DISCUSSION

The measurements of the angle between a side surface of a whisker and the cube directions in the substrate oxide crystal show that whiskers are crystallographically related in some way to the oxide crystal. Therefore, the hypothesis of nucleation on accidental dirt particles can be ruled out. The remaining two possible mechanisms for nucleation of the whiskers are:

1. The deposition of nickel from vapor-phase halide reduction, and,

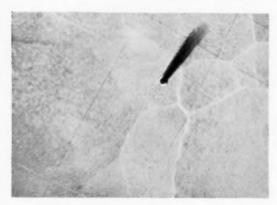


Fig. 8. Nickel whisker growing up from cube surface of a nickel oxide crystal. Bright field illumination. $\times\,2000$.

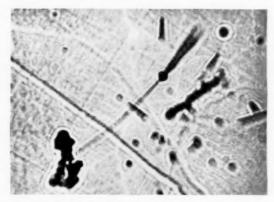


Fig. 9. Same area as Fig. 8, transmitted light. ×2000.

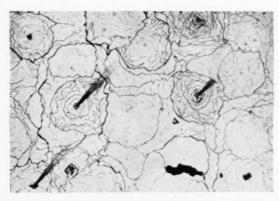


Fig. 10. Nickel whiskers growing from centers of nickel oxide subgrains which have prominent growth steps on the surface. $\times 500$.

2. Hydrogen reduction of nickel oxide followed by nickel halide reduction on the small patch of metal formed by hydrogen reduction.

The differentiation of mechanisms 1 and 2 may be made principally on the basis of a comparison of whisker-oxide crystallographic orientation relationships with metal-oxide orientation relationships for vapor deposition and for hydrogen reduction.

There appears to have been no determination of the orientation of nickel crystals formed by vapor deposition of nickel on nickel oxide. However, such vapor deposition experiments have been performed using a sodium chloride crystal substrate. Sodium chloride has the same structure, cubic (NaCl), as nickel oxide. Nickel films deposited from the vapor on cube-surface NaCl crystals were found to have the identical orientation i.e. (001) [100] Ni//(001) [100] NaCl. Since the Ni–NaCl lattice parameter mismatch is much greater than the Ni–NiO lattice parameter mismatch, (37.4 per cent vs. 15.6 per cent) it is reasonable to expect that nickel should also deposit on nickel oxide cube surfaces with the identical orientation.

A comparison of whisker orientations with the "identical orientation" disclosed that all eight whiskers analyzed had orientations greatly different from the identical orientation. This finding suggests that whisker nucleation is not a vapor deposition process.

The orientations of nickel grains formed by hydrogen reduction of the oxide are listed in a separate publication. (8) Reduction in a near-equilibrium atmosphere at 650°C yields the identical orientation and five other orientations which are unique to the reduction process. They are:

- 1. (111)[T10]Ni//(001)[T00]NiO
- 2. ~(11 88)[T0 77]Ni//(001)[T00]NiO
- 3. (112)[Ī10]Ni//(001)[Ī00]NiO
- 4. (001)[T00]Ni//(001)[T10]NiO
- 5. (111)[T10]Ni//(001)[T10]NiO (not certain)

The orientations of five out of eight whiskers corresponded closely to the related series of reduction orientations numbered 1, 2 and 3. The cube poles of orientations Nos. 1, 2, and 3 together with the principle orientation found on reduction at 550°C are plotted as shaded patches in Fig. 3. Two whiskers had orientations close to two other irrational index hydrogen reduction orientations which were found in nickel specimens reduced at 550°C. The cube poles of these orientations are shown as shaded patches in Fig. 4.

This strong correspondence of whisker orientations to reduction orientations provides conclusive evidence that the nucleation step for nickel whiskers in this investigation is hydrogen reduction of oxide.

Further evidence in support of this conclusion is provided by the observations concerning the characteristics of the oxide crystals at points where whiskers are generated. It was noted that whisker or crystal growth occurred primarily along cracks in the oxide when these were present. Similar observations were noted regarding the preferred sites for nucleation of reduction crystallites. In the absence of cracks, whiskers formed at random on the surface of the oxide crystal. In some cases precipitate "tails" beneath the whiskers suggested that a structural singularity existed in the oxide beneath the whiskers. Visual observations on nucleating sites for reduction crystallites resulted in a similar conclusion that reduction began at points where a structural singularity intersected the surface of the oxide crystal. It is quite probable that these structural singularities are dislocations. It is, therefore, evident that whiskers form at the same type of sites on the oxide as do the hydrogen reduction crystallites.

The correspondence of nucleating sites and of orientation relationships for whisker formation and for hydrogen reduction of oxide lead one to suggest that whiskers may be utilized in studies of oxide reduction literally to pinpoint both the site and the orientation of initial reduction crystallites.

In any system where whiskers are formed the nucleation mechanism which operates will be that

one having the lowest free-energy barrier to nucleation. The presently described mechanism can operate only in those cases where a metal halide and oxide co-exist in an atmosphere capable of reducing these compounds to metal. Even in those cases, nucleation of whiskers will not necessarily proceed by the mechanism described here. It will be necessary to examine other systems before drawing general conclusions regarding nucleation of whiskers grown from decomposition of metal halides.

5. CONCLUSION

The nucleation of nickel whiskers formed from reduction of the halide is brought about by a hydrogen reduction of nickel oxide.

ACKNOWLEDGMENTS

The author benefited from many valued discussions with P. D. Gorsuch. Mrs. R. K. DeCerbo performed the orientation analyses on nickel whiskers.

REFERENCES

- H. W. Kohlschütter, Z. Elektrochem. 38, 345 (1932).
 R. L. Fullman and A. Gatti, U.S. Pat. 2 842 469 (July 1958).
- 3. R. M. Doremus and G. W. Sears, unpublished research.
- 4. S. S. BRENNER. Acta Met. 4, 62 (1956).
- P. D. Gorsuch, The Growth of Iron Whiskers by the Hydrogen Reduction of Iron Halide Salts, R. L. Report No. 57-RL-1840. To be published as part of Int. Symp. on Phys. Chem. of Proc. Metallurgy, Pittsburgh, Pa. (Apri 1959) AIME.
- R. E. Cech and E. Allessandrini, Trans. Amer. Soc. Metals 51, 150 (1959).

195

- L. E. COLLINS and O. S. HEAVENS, Proc. Phys. Soc. Lond. B 70, 265 (1957).
- R. E. CECH. The Reduction of Nickel Oxide, R. L. Report No. 58-RL-2078; Trans. Amer. Inst. Min. (Metall.) Engrs., to be published.

ON THE THEORY OF MARTENSITIC TRANSFORMATIONS. THE GENERALIZED LATTICE INVARIANT SHEAR AND THE DEGENERACY OF SOLUTIONS FOR THE CUBIC TO TETRAGONAL TRANSFORMATION*

M. S. WECHSLER+

The theory of the crystallography of martensitic transformations is extended in terms of generalized elements for the lattice invariant shear. The degeneracy of solutions for the undistorted plane, the orientation relation, and the macroscopic change of shape is examined analytically for the cubic to tetragonal transformation. The criteria for K-degeneracy and g-degeneracy are developed and compared with those given by Christian as a result of a geometrical treatment. Existence conditions for real solutions are also developed in terms of the generalized theory.

SUR LA TÆFORIE DES TRANSFORMATIONS MARTENSITIQUES-ELEMENTS GENERALISES DU CISAILLEMENT INVARIANT DU RESEAU ET DEGENERESCENCE DES SOLUTIONS POUR LA TRANSFORMATION DU SYSTEME CUBIQUE EN SYSTEME TETRAGONAL

L'auteur étend la théorie cristallographique des transformations martensitiques en fonction des éléments généralisés pour le cisaillement invariant du réseau. La dégénérescence des solutions pour le plan non déformé, la relation d'orientation et la modification macroscopique de forme est examinée analytiquement pour la transformation du système cubique en système tétragonal. Les critères de dégénérescence K et g sont développés et comparés avec ceux de Christian, à la suite d'une étude géométrique. Les conditions d'existence de solutions reélles sont également développées en relation avec la théorie généralisée.

ZUR THEORIE MARTENSITISCHER UMWANDLUNGEN. DIE VERALLGEMEINEKTE GITTERINVARIANTE SCHERUNG UND DIE ENTARTUNG DER LÖSUNGEN FÜR DIE UMWANDLUNG KUBISCH-TETRAGONAL

Die Theorie der Kristallographie martensitischer Umwandlungen wird erweitert durch Hinzunahme verallgemeinerter Elemente für die gitterinvariante Scherung. Für die Umwandlung kubischtetragonal wird die Entartung der Lösungen für die unverzerte Ebene, die Orientierungsbeziehung und die makroskopische Formänderung analytisch untersucht. Die Kriterien für K-Entartung und g-Entartung werden hergeleitet und mit denen verglichen, die Christian auf Grund einer geometrischen Behandlung angegeben hat. Schliesslich werden die Existenzbedingungen für reelle Lösungen im Rahmen der verallgemeinerten Theorie entwickelt.

1. INTRODUCTION

The phenomenological theories of the crystallography of martensitic transformations have been discussed by Christian⁽¹⁾. It was pointed out that the theories of Bowles and Mackenzie⁽²⁻⁴⁾ and of Wechsler, Lieberman, and Read^(5,6) are essentially equivalent, although they differ in mathematical formulation. In this paper, the latter formulation is used.

The fundamental idea on which the theory is based is that the total transformation distortion is such that at least one plane is undistorted and unrotated. Since the transformed part of the crystal is in contact with the remaining undeformed part, the undistorted plane is taken to be the interface plane (or habit plane) that separates the two phases. It has been shown^(5,7) that a necessary and sufficient condition that a plane of zero distortion exist is that one of the principal values of the total transformation distortion be unity and that, of the other two principal values, one be less than unity and the other greater than unity. It is

usually possible to specify the most reasonable pure distortion that brings about the essential change in erystal structure. In the case of the austenite (f.c.c.) \rightarrow martensite (b.c.t.) transformation, (5) this pure distortion is given by a contraction along one of the cube edges of the austenite and an isotropic expansion in the plane perpendicular to this direction. But, in general, the pure lattice distortion does not contain a unity principal value. Therefore, an undistorted plane is not produced if the total distortion consists solely of the pure lattice distortion. However, the pure lattice distortion may be combined with a distortion. which does not affect the lattice structure, but which. nevertheless, produces a macroscopic change in shape. Such an additional distortion is a slip shear or a twinning shear over a fraction of the crystal. This shear has been called the "inhomogeneous" or "lattice invariant" shear. In the theory, a critical amount of lattice invariant shear is determined such that the combined result of the pure lattice distortion and the lattice invariant shear produces a plane of zero distortion.

In the previous analysis of the austenite-martensite

^{*} Received February 26, 1959.

[†] Solid State Division, Oak Ridge National Laboratory, Oak Ridge, Tennessee.

 $\mathbf{T}[A] = \begin{pmatrix} \eta_1 & 0 & 0 \\ 0 & \eta_2 & 0 \\ 0 & 0 & n \end{pmatrix}$

elements of the lattice invariant shear. An interesting aspect of the theory of martensitic transformations, and one that may help to establish the relationship between the theoretical and experimental results, is the degeneracy of solutions. Christian⁽¹⁾ has considered the degeneracy of solutions from a geometrical point of view. It was pointed out that, in general, there are four solutions that are not crystallographically equivalent. The criteria were discussed whereby the number of solutions is reduced to two or even to one. These criteria are examined here from the analytical point of view. Agreement is obtained with the criterion given by Christian for one of the two types of degeneracy (K-degeneracy), but the analysis given here indicates that Christian's criterion for the other type of degeneracy (gdegeneracy) is based on a premise that is not quite general.

transformation(5) the elements of the lattice invariant

shear were taken to be those characteristic of twinning

in the product structure. It was pointed out that

identical results are obtained if the critical amount of

lattice invariant shear is considered to result from a

critical amount of slip or from the twinning of a

critical fraction of the crystal. In this case, it was

possible to express the habit plane normal and the macroscopic change of shape as explicit functions of

the lattice parameters of the two phases. When the

lattice parameters appropriate to the austenite-

martensite transformation in steels were substituted

in the expressions derived on the basis of this choice

of lattice invariant shear, the derived habit plane, macroscopic distortion, and orientation relation

between crystal axes in the two phases were found to agree quite closely with experimental results on an Fe-Ni-C alloy. (8) However, quite different habit

planes have been observed for other steels. (7,9)

Distinctly different sets of habit planes have also been

observed in other alloy systems. (7) If the lattice

invariant shear is regarded as being the result of a

slip distortion, a variety of solutions for a plane of

zero distortion may be obtained, corresponding to

different choices of the plane and direction of the shear.

The possibility presents itself that the different sets of observed habit planes for a given material are the

result of the operation of different systems of lattice

invariant shear. Accordingly, in this paper, the theory is extended in terms of a general specification of the

2. THE PRINCIPAL VALUES AND VECTORS

If the transformation distortion, E, consists of a pure lattice distortion, T, combined with a lattice invariant shear, G, then there is, in general, a critical

amount of shear such that a plane of zero distortion is established. This plane will be rotated, and a rigid body rotation, Φ , is included in the total transformation distortion to rotate the plane of zero distortion back to its original orientation. The total transformation distortion is written, in matrix notation, * as

$$\mathbf{E} = \mathbf{\Phi} \mathbf{T} \mathbf{G} \tag{1}$$

where Φ is the rotation, T is the pure lattice distortion and G is the lattice invariant shear. For the f.c.c. \rightarrow b.c.t. (austenite -> martensite) transformation, the pure lattice distortion (Bain distortion), T, is given by †

$$\mathbf{T}[A] = \begin{pmatrix} \eta_1 & 0 & 0 \\ 0 & \eta_2 & 0 \\ 0 & 0 & \eta_1 \end{pmatrix} \tag{2}$$

where $\eta_1 = \sqrt{2a/a_0}$, $\eta_2 = c/a_0$, where a and c are the tetragonal lattice parameters and a_0 is the cubic lattice parameter. The lattice invariant shear is most conveniently expressed with respect to the shear axis system \mathbf{i}_g , \mathbf{j}_g , \mathbf{k}_g , where \mathbf{i}_g and \mathbf{j}_g are unit vectors along the shear direction and the shear plane normal respectively and \mathbf{k}_a is the direction mutually perpendicular to \mathbf{i}_{q} and \mathbf{j}_{q} . In this system

$$\mathbf{G}[g] = \begin{pmatrix} 1 & g & 0 \\ 0 & 1 & 0 \\ 0 & 0 & 1 \end{pmatrix} \tag{3}$$

VOL

195

where g is the amount of shear. The matrix \mathbf{F} is defined by the relation

$$\mathbf{F} = \mathbf{TG} \tag{4}$$

If the shear axes are given by

$$\mathbf{i}_{\boldsymbol{g}}[A] = \begin{pmatrix} u_1 \\ u_2 \\ u_3 \end{pmatrix}, \ \ \mathbf{j}_{\boldsymbol{g}}[A] = \begin{pmatrix} v_1 \\ v_2 \\ v_3 \end{pmatrix}, \ \ \text{and} \ \ \mathbf{k}_{\boldsymbol{g}}[A] = \begin{pmatrix} w_1 \\ w_2 \\ w_3 \end{pmatrix}$$

The order of the distortions in equation (1) is arbitrary. For purposes of mathematical manipulation, the shear G is considered to precede T, although in Reference (5) the order of these two distortions was reversed.

† Throughout this paper, the unique axis of T is arbitrarily taken to be [010].

^{*} Matrices are represented by boldface, upper case letters, with Greek letters reserved for rotation matrices. When it is convenient to indicate the reference system with respect to which the components of a matrix or vector are expressed, this is done by placing a symbol in square brackets following the matrix or vector symbol. Thus, T[A] indicates the pure lattice distortion with respect to f.c.c. (austenite) axes. In addition, [g] and [d] are used to denote the shear axis system (based on the shear direction and shear plane normal) and the principal axis system (based on the principal vectors, as defined below), respectively. Indices of planes and directions are with respect to cubic axes unless otherwise specified.

then in the shear system

$$\mathbf{F}[g] = \mathbf{T}[g]\mathbf{G}[g] = \phi_{1} = \text{trace } \mathbf{P} = \eta_{1}^{2}[2 - 2gu_{2}v_{2} + g^{2}(1 + 2gu_{2}v_{2})] + \eta_{2}^{2}[1 + 2gu_{2}v_{2}] + \eta_{2}^{2}[1 + 2gu_{2}v_{2}] + \eta_{1}^{2}[1 + 2gu_{2}v_{2}] + \eta_{1}^{2}[1 + 2gu_{2}v_{2} + g^{2}(1 + 2gu_{2}v_{2})] + \eta_{1}^{2}[1 + 2gu_{2}v_{2}] + \eta_$$

where $\beta = \eta_1 - \eta_2$ and $\gamma = (u_2 g + v_2)$. **F** is not symmetric, but the symmetric matrix $P = F^*F$ may be formed,† which may be diagonalized to give

$$\mathbf{P} = \mathbf{F}^* \mathbf{F} = \mathbf{\Gamma} \mathbf{F}^2 \mathbf{\Gamma}^* \tag{6}$$

where

$$\mathbf{F}_{d}^{2} = \begin{pmatrix} \lambda_{1}^{2} & 0 & 0 \\ 0 & \lambda_{2}^{2} & 0 \\ 0 & 0 & \lambda_{3}^{2} \end{pmatrix} \tag{7}$$

and the λ_i^2 are the principal values. † It is convenient to express equation (6) in the shear system, in which case the columns of the rotation matrix Γ give the components of the principal directions; with respect to the axes \mathbf{i}_{q} , \mathbf{j}_{q} , \mathbf{k}_{q} . From equation (5), it is found that the elements of P[g] are

$$\begin{split} \mathbf{P}[g]_{11} &= \eta_1^{\ 2} - u_2^{\ 2}(\eta_1^{\ 2} - \eta_2^{\ 2}) \\ \mathbf{P}[g]_{22} &= \eta_1^{\ 2}(1+g^2) - (\eta_1^2 - \eta_2^2)\gamma^2 \\ \mathbf{P}[g]_{33} &= \eta_1^{\ 2} - w_2^{\ 2}(\eta_1^{\ 2} - \eta_2^{\ 2}) \\ \mathbf{P}[g]_{12} &= \mathbf{P}[g]_{21} = \eta_1^{\ 2}g - u_2(\eta_1^{\ 2} - \eta_2^{\ 2})\gamma \\ \mathbf{P}[g]_{23} &= \mathbf{P}[g]_{32} = -w_2(\eta_1^{\ 2} - \eta_2^{\ 2})\gamma \\ \mathbf{P}[g]_{31} &= \mathbf{P}[g]_{13} = -u_2w_2(\eta_1^{\ 2} - \eta_2^{\ 2}) \end{split}$$

The characteristic function $f(\lambda^2)$ is given by

$$f(\lambda^2) = \det \left(\mathbf{P} - \lambda^2 \mathbf{I} \right) = -\lambda^6 + \phi_1 \lambda^4 - \phi_2 \lambda^2 + \phi_3 \quad (9)$$

where I is the unit matrix and ϕ_1 , ϕ_2 , and ϕ_3 are the scalar invariants of P, which from (8) are found to be given by

$$\begin{split} \phi_1 &= \text{trace } \mathbf{P} = \eta_1^{\ 2} [2 - 2gu_2v_2 + g^2(1-u_2^{\ 2})] \\ &+ \eta_2^{\ 2} [1 + 2gu_2v_2 + g^2u_2^{\ 2}] \end{split} \ (10) \end{split}$$

$$\phi_2 = \eta_1^4 [1 - 2gu_2v_2 + g^2v_2^2] + \eta_1^2\eta_2^2 \times [2 + 2gu_3v_2 + g^2(1 - v_3^2)]$$
(11)

$$\phi_3 = \det \mathbf{P} = \eta_1^4 \eta_2^2 \tag{12}$$

The characteristic equation is

$$f(\lambda^2) = 0 \tag{13}$$

and the critical amount of shear, g, is determined from the condition that one of the principal values must be unity, in order that a plane of zero distortion exist. The equation f(1) = 0 gives a quadratic equation in g

$$Ag^2 + Bg + C = 0 (14)$$

where

$$A = (\eta_1^2 - \eta_2^2)(u_2^2 + v_2^2\eta_1^2) - \eta_1^2(1 - \eta_2^2) \quad (15)$$

$$B = -2(\eta_1^2 - \eta_2^2)(\eta_1^2 - 1)u_2v_2 \tag{16}$$

$$C = (1 - \eta_2^2)(\eta_1^2 - 1)^2 \tag{17}$$

which gives the result

$$g = \frac{{{\eta _1}^2} - 1}{A}\left[{{u_2}{v_2}({\eta _1}^2 - {\eta _2}^2) + {\delta _g}{H^{\frac{1}{2}}}} \right] \tag{18}$$

$$\begin{split} H = [\eta_1^{\ 2}(1-{\eta_2}^2) - (\eta_1^{\ 2}-{\eta_2}^2)u_2^{\ 2}][(1-{\eta_2}^2) \\ - (\eta_1^{\ 2}-{\eta_2}^2)v_2^{\ 2}] \end{split}$$

We shall let $g = g_1$ for $\delta_g = 1$ and $g = g_2$ for $\delta_g = -1$. The unity principal value is designated as λ_1^2 . The other two principal values, λ_2^2 and λ_3^2 , are then given by

$$\lambda_i^4 + (1 - \phi_1)\lambda_i^2 + \phi_3 = 0 \tag{19}$$

where ϕ_1 and ϕ_3 are given by (10) and (12), with ggiven by (18).

The principal directions, $\mathbf{r}^{(i)}$, are determined by the equations

$$(\mathbf{P} - \lambda_i^2 \mathbf{I}) \cdot \mathbf{r}^{(i)} = 0 \tag{20}$$

The principal direction corresponding to the unity principal value is called the "undistorted principal direction." It is seen from (8) that P[g] becomes partly diagonal, viz. $P[g]_{23} = P[g]_{31} = 0$, when $w_2 = 0$ or when $u_2 = v_2 = 0$ $(w_2 = 1)$. Therefore, it is convenient to give expressions for the components of

 $[\]mathbf{F}^*$ is the transpose of \mathbf{F} , where $(\mathbf{F}^*)_{pq} = \mathbf{F}_{qp}$. The principal values and vectors referred to are those of the matrix $\mathbf{E}^*\mathbf{E} = \mathbf{F}^*\mathbf{F}$. \mathbf{F} is non-symmetric, but may be represented by $\mathbf{F} = \mathbf{\Psi}\mathbf{F}_s$, where $\mathbf{\Psi}$ is a rotation and \mathbf{F}_s is a represented by $\mathbf{F} = \mathbf{\Psi}\mathbf{F}_s$, where $\mathbf{\Psi}$ is a rotation and \mathbf{F}_s is a symmetric matrix. Thus, $\mathbf{E} = \mathbf{\Phi}\mathbf{\Psi}\mathbf{F}_s$. \mathbf{F}_s may then be diagonalized to give $\mathbf{F}_s = \mathbf{\Gamma}\mathbf{F}_d\mathbf{\Gamma}^*$, where the non-zero elements of the diagonal matrix \mathbf{F}_d are λ_1 , λ_2 , and λ_3 . Thus, the principal values of $\mathbf{F}^*\mathbf{F}$ are the squares of the principal values of the symmetric part (\mathbf{F}_s) of the total transformation matrix, and the principal vectors of $\mathbf{F}^*\mathbf{F}$ are identical with the principal vectors of Fs. Since Fd represents only the symmetric part of \mathbf{F} in the principal axis system, the symbol \mathbf{F}_d is used instead of $\mathbf{F}[d]$. Also, the locus of points \mathbf{r} transformed to a unit sphere is $|\mathbf{E}\mathbf{r}|^2 = \mathbf{r}\mathbf{F}^*\mathbf{F}\mathbf{r} = 1$. Therefore, the principal directions are identical with the axes of the reciprocal shape ellipsoid discussed by Christian(1).

(a)
$$w_2 \neq 0, w_2 \neq 1$$
:

$$\begin{split} x^{(i)}[g] &= \frac{w_2(\eta_1^2 - \eta_2^2)}{N^{(i)}} [u_2(\eta_1^2 - \lambda_i^2) \\ &- v_2\eta_1^2 g], \, i = 1, \, 2, \, 3 \\ y^{(i)}[g] &= \frac{w_2(\eta_1^2 - \eta_2^2)}{N^{(i)}} [v_2(\eta_1^2 - \lambda_i^2) \\ &- u_2\lambda_i^2 g], \, i = 1, \, 2, \, 3 \\ \\ z^{(i)}[g] &= \begin{cases} \frac{1}{N^{(i)}} \{(\eta_1^2 - 1)^2 - \eta_1^2 g^2 \\ &+ (\eta_1^2 - \eta_2^2)[u_2^2 g^2 + 2u_2 v_2 g \\ &- (\eta_1^2 - 1)(1 - w_2^2)]\}, \, i = 1 \\ \frac{1}{N^{(i)}} \{(\lambda_i^2 - \eta_1^2 \eta_2^2)(\eta_1^2 - 1) + w_2^2 \\ &\times (\eta_1^2 - \eta_2^2)(\eta_1^2 - \lambda_i^2)\}, \, i = 2, \, 3 \end{split} \end{split}$$

where the $N^{(i)}$ are normalization factors.

(b) $w_2 = 0$:

From (19), it is found that the principal values are $\lambda_1^2 = 1$, $\lambda_2^2 = \eta_1^2$, and $\lambda_3^2 = \eta_1^2 \eta_2^2$. The components of the corresponding principal directions are

$$\begin{split} x^{(1)}[g] &= \frac{1}{N}[u_2v_2(\eta_1^2 - \eta_2^2) - (v_2^2\eta_1^2 + u_2^2\eta_2^2)g] \\ y^{(1)}[g] &= \frac{1}{N}[\eta_1^2 - 1 - u_2^2(\eta_1^2 - \eta_2^2)], z^{(1)}[g] = 0 \\ x^{(2)}[g] &= 0, \ y^{(2)}[g] = 0, \ z^{(2)}[g] = 1 \\ x^{(3)}[g] &= -y^{(1)}[g], \ y^{(3)}[g] = x^{(1)}[g], z^{(3)}[g] = 0 \end{split} \right\} (22)$$

where $N^2=(1-\eta_1^2\eta_2^2)[u_2^2(\eta_1^2-\eta_2^2)-(\eta_1^2-1)].$ Thus, when $w_2=0$, one of the principal vectors is along the \mathbf{k}_a direction.

(c)
$$w_9 = 1$$
:

For this case, the principal values are $\lambda_1^2 = 1$, $\lambda_2^2 = \eta_1^4$ and $\lambda_3^2 = \eta_2^2$. The components of the corresponding principal directions are

$$x^{(1)}[g] = -\delta_g \eta_1 / M, \ y^{(1)}[g] = 1 / M, \ z^{(1)}[g] = 0$$

$$x^{(2)}[g] = -1 / M, \ y^{(2)}[g] = -\delta_g \eta_1 / M, \ z^{(2)}[g] = 0$$

$$x^{(3)}[g] = 0, \ y^{(3)}[g] = 0, \ z^{(3)}[g] = 1$$

$$(23)$$

where δ_g originates from (18) and $M^2 = \eta_1^2 + 1$. Therefore, when $w_2 = 1$, i.e., when both the shear direction and the shear plane normal are perpendicular to the unique axis of the pure lattice distortion, one of the principal directions is along \mathbf{k}_g , as in the case for $w_2 = 0$.

3. THE DEGENERACY OF THE UNDISTORTED PLANES

The total transformation distortion \mathbf{E} may be written from (1) and (4)

$$\mathbf{E} = \mathbf{\Phi} \mathbf{F}$$

and if the vector \mathbf{v} lies in the plane of zero distortion

$$|\mathbf{E}\mathbf{v}|^2 = \mathbf{v}\mathbf{F}^*\mathbf{F}\mathbf{v} = v^2$$

Therefore, as has been shown previously, ⁽⁵⁾ it follows from (6) and (7) that the undistorted directions must satisfy the equation

$$(\lambda_1^2 - 1)x^2 + (\lambda_2^2 - 1)y^2 + (\lambda_3^2 - 1)z^2 = 0$$

where x, y, and z are the components of \mathbf{v} in the principal axis system. Setting $\lambda_1^2 = 1$, we find as undistorted directions, the undistorted principal axis, $\mathbf{r}^{(1)}[d] = [100]_d$ and the two directions

$$\mathbf{v}[d] = \frac{1}{(1+K^2)^{\frac{1}{2}}} \begin{pmatrix} 0\\ \delta_K K \end{pmatrix} \tag{24}$$

where

$$K = \left(\frac{1-\lambda_3^2}{\lambda_2^2-1}\right)^{\frac{1}{4}}$$
 and $\delta_K = \pm 1$

There are two undistorted planes for each value of g in equation (18). The first contains $\mathbf{r}^{(1)}$ and \mathbf{v} corresponding to $\delta_K = 1$. The second contains $\mathbf{r}^{(1)}$ and \mathbf{v} corresponding to $\delta_K = -1$. Hence, the normals to the undistorted planes are given by^(1,5)

$$\mathbf{n}[d] = \frac{1}{(1+K^2)^{\frac{1}{2}}} \begin{pmatrix} 0\\1\\\delta_K K \end{pmatrix}$$
 (25)

Thus, as was deduced from geometrical considerations, (1) in the absence of any degeneracy, there are four crystallographically non-equivalent solutions for the undistorted plane corresponding to $\delta_K = \pm 1$ in (25) and $\delta_g = \pm 1$ in (18).

(a) K-degeneracy

The degeneracy that results when the **n**'s corresponding to $\delta_K=\pm 1$ in equation (25) are crystallographically equivalent in the cubic system is referred to as "K-degeneracy." The conditions on the shear elements that lead to K-degeneracy may be analyzed by considering the graphical method.

The graphical method⁽¹⁰⁻¹²⁾ can be used to determine undistorted planes, when specific values are used for the lattice parameters. In this method, the loci of undistorted directions from the lattice invariant shear **G** and for the pure lattice distortion **T** are plotted separately on a stereographic projection. The direc-

7 195

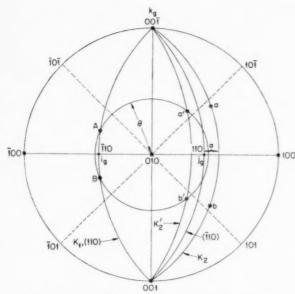


Fig. 1. The transformation geometry for the case of (110)[110] shear. The lattice parameters correspond to axial ratio c/a=1 and a volume ratio $V=\eta_1{}^2\eta_2=1.04$. The larger of the two shears in equation (18) is used. One undistorted plane contains directions A and b and the other contains B and a. The indices shown are with respect to cubic axes.

VOL.

1959

tions undistorted by both **G** and **T** are given by the intersections of the two loci. For a simple shear such as **G**, the undistorted directions lie in two planes, the shear plane K_1 and the K_2 plane which contains \mathbf{k}_g . The K_1 plane is not rotated by **G**, but the K_2 plane is rotated from K_2 to K_2' , Fig. 1. The figure shows the transformation geometry for the case of $(110)[\bar{1}10]$, which are the shear elements in the cubic (austenite) corresponding to $(121)_M[1\bar{1}1]_M$ in the tetragonal phase (martensite). This is the case previously treated by the theory. (5) The angle 2α through which the K_2 plane is rotated is related to g in (3) by

$$g=2\tan\alpha$$

The locus of undistorted directions for T is a right circular cone whose axis is [010] and whose semi-vertex angle is given by

$$\theta = \tan^{-1} \left(\frac{1 - \eta_2^2}{\eta_1^2 - 1} \right)^{1/2} \tag{26}$$

Therefore, the directions A and B in the figure are undistorted. Also undistorted are the directions a' and b', whose directions before the shear are a and b. Thus, the undistorted planes are the planes Ab (containing A and b) and Ba. The planes Ab and Ba correspond to the solutions that result from $\delta_K = \pm 1$ in (25). The planes corresponding to Aa and Bb are

the undistorted planes for the other shear. It can be seen in the figure that plane Ab is crystallographically equivalent to Ba.

In order that the undistorted planes such as Ab and Ba in the figure be crystallographically equivalent, directions a and b must be related by the same symmetry operation (reflection in the (001) plane in the case shown in the figure) as A and B. Furthermore, the criteria that are sought for K-degeneracy must be independent of the lattice parameters, i.e. independent of η_1 and η_2 . Therefore, the crystallographic equivalence of directions a and b must be independent of the angle through which K_2 is rotated. Thus, only those shear elements that preserve the symmetry relation between a and b in rotating them to a' and b' will lead to K-degeneracy that is not accidental. It follows from this that the k, direction must be a two-fold axis* of symmetry for K-degeneracy to result. More specifically, it must be a direction of the type $\mathbf{k}_{a}[A] =$ (100) or it must be either $\mathbf{k}_a[A] = [101]$ or $\mathbf{k}_a[A] =$ $[10\overline{1}]$, when [010] is the unique axis of the pure lattice distortion. In the case where \mathbf{k}_a is in a cube edge direction, the K-degeneracy involves a change in the signs of components of the normal to the undistorted plane. On the other hand, when $k_a[A] = [101]$ or [$\overline{101}$], the magnitudes of the x and z components are interchanged.

The above considerations lead to the conclusion that K-degeneracy occurs when \mathbf{k}_a is a two-fold axis and the shear elements are characterized by $w_2 = 0$ or $w_2 = 1$. This result may be correlated with the equations for the principal axis directions. Equations (22) show that, when $w_2 = 0$, the principal direction $\mathbf{r}^{(2)}$ corresponding to λ_2^2 is along \mathbf{k}_g . Similarly, equations (23) show that, when $w_2 = 1$, the principal direction $\mathbf{r}^{(3)}$ corresponding to λ_3^2 is along \mathbf{k}_a . Therefore, in these cases, if \mathbf{k}_a is a two-fold axis, $\mathbf{r}^{(2)}$ or $\mathbf{r}^{(3)}$ is also. But from equation (25) the normals to the undistorted planes for $\delta_K = \pm 1$ lie in the \mathbf{j}_d , \mathbf{k}_d plane and make equal angles with $\mathbf{j}_d (= \mathbf{r}^{(2)})$ and $\mathbf{k}_d (= \mathbf{r}^{(3)})$. Therefore, if $\mathbf{r}^{(2)}$ or $\mathbf{r}^{(3)}$ is a two-fold axis, the undistorted planes are crystallographically equivalent. (1) As a result, the criterion for K-degeneracy may be stated as follows. Provided solutions exist at all (i.e. provided H in equation (18) and K in equation (24) are real), K-degeneracy results when \mathbf{k}_a is a two-fold axis and is either parallel or perpendicular to the unique axis of the pure lattice distortion. The conditions for K-degeneracy are summarized in Table 1.

^{*} As is true throughout, the conclusions that follow from the condition of two-fold symmetry are also valid for four-fold symmetry.

Table 1. Summary of degeneracy conditions for the undistorted planes

Type of degeneracy	Conditions on the shear elements	Symmetry conditions
(A) K-degeneracy	$\begin{array}{ll} (1) & w_2 = 0 \\ (2) & u_2 = v_2 = 0, w_2 = 1 \end{array}$	\mathbf{k}_g a two-fold axis \mathbf{k}_g a two-fold axis
(B) g-degeneracy	$\begin{array}{ll} (1) & u_2=0, v_2\neq 0, w_2\neq 0\\ (2) & u_2\neq 0, v_2=0, w_2\neq 0\\ (3) & u_2\neq 0, v_2\neq 0, w_2=0\\ (4) & u_2=v_2=0, w_3=1 \end{array}$	i, a two-fold axis j, a two-fold axis either i, or j, a two-fold axis either i, or j, a two-fold axis

(b) g-degeneracy

In this section, the conditions under which the two values of g in equation (18) lead to crystallographically equivalent solutions ("g-degeneracy") are examined. The discussion of g-degeneracy in Christian's paper⁽¹⁾ is based on the proposition that the principal values are the same for g_1 and g_2 and the principal directions are related by a rotation of 180° about the shear plane normal, \mathbf{j}_a . From this it would follow that intrinsic degeneracy occurs only when \mathbf{j}_q is a two-fold axis of symmetry in the cubic phase. However, the expressions derived above can be used to show that this proposition is not valid in general, although it does apply in certain special cases. It can be seen that the principal values are not the same, in general, for g_1 and g_2 from an examination of equation (19), which gives λ_2^2 and λ_3^2 in terms of ϕ_1 and ϕ_3 . Since ϕ_3 is given by ${\eta_1}^4{\eta_2}^2$ for both g_1 and g_2 , all the dependence on g resides in ϕ_1 . From equations (10) and (14) it is found that

$$\begin{split} \phi_1(g_1) - \phi_1(g_2) &= \frac{2}{A^2} (B^2 - 4AC)^{1/2} \\ &\times (\eta_1^2 - \eta_2^2)^2 \eta_1^2 u_2 v_2 w_2^2 \end{split} \tag{27}$$

Therefore, λ_2^2 and λ_3^2 are the same for g_1 and g_2 for general values of η_1 and η_2 only if at least one of the quantities u_2 , v_2 , and w_2 is zero. In cases where the λ_i^2 are not the same for g_1 and g_2 , there can be no g-degeneracy.

It is helpful to analyze the conditions for g-degeneracy by considering various sets of values of u_2 , v_2 , and w_3 :

- (1) u_2, v_2, w_2 all not zero: no g-degeneracy.
- (2) $u_9 = 0, v_9 \neq 0, w_9 \neq 0$:

The components of the principal directions, equations (21), are now given by

$$x^{(i)}[g] = -\frac{1}{N^{(i)}} \, v_2 w_2 \eta_1{}^2 (\eta_1{}^2 - \eta_2{}^2) g, \qquad \quad i = 1, \, 2, \, 3$$

$$y^{(i)}[g] = \frac{1}{N^{(i)}} v_2 w_2 (\eta_1^{\ 2} - \eta_2^{\ 2}) (\eta_1^{\ 2} - \lambda_i^{\ 2}), \quad \ i = 1, \, 2, \, 3$$

$$z^{(i)}[g] = \begin{cases} \frac{1}{N^{(i)}} [(\eta_1{}^2 - 1)^2 - \eta_1{}^2 g \\ - (\eta_1{}^2 - \eta_2{}^2)(\eta_1{}^2 - 1) v_2{}^2], \, i = 1 \\ \frac{1}{N^{(i)}} [(\lambda_i{}^2 - \eta_1{}^2 \eta_2{}^2)(\eta_1{}^2 - 1) \\ + w_2{}^2 (\eta_1{}^2 - \eta_2{}^2)(\eta_1{}^2 - \lambda_i{}^2)], \, i = 2, 3 \end{cases}$$

Equation (18) shows that $g_1 = -g_2$, and equations (19) and (27) show that $\lambda_i^2(g_1) = \lambda_i^2(g_2)$. Therefore*,

$$\begin{split} x^{(i)}(g_1) &= -x^{(i)}(g_2) \\ y^{(i)}(g_1) &= y^{(i)}(g_2) \\ z^{(i)}(g_1) &= z^{(i)}(g_2) \end{split}$$

The principal vectors for g_1 and g_2 are related by a rotation of 180° about the shear direction, \mathbf{i}_g (plus inversion through the origin). Therefore, g-degeneracy occurs if \mathbf{i}_g is a two-fold axis of symmetry in the cubic phase. An example of this case is $(111)[\bar{1}01]$ shear, for which the habit planes for lattice parameters appropriate to the austenite–martensite transformation in steels have been determined by the graphical method. (12)

(3)
$$u_2 \neq 0$$
, $v_2 = 0$, $w_2 \neq 0$:

Equations (21) now become

$$x^{(i)}[g] = \frac{1}{N^{(i)}} \, u_2 w_2 (\eta_1{}^2 - \eta_2{}^2) (\eta_1{}^2 - \hat{\lambda}_i{}^2), \quad i = 1, \, 2, \, 3$$

$$y^{(i)}[g] = -\frac{1}{N^{(i)}} \, u_2 w_2 (\eta_1{}^2 - \eta_2{}^2) \lambda_{\iota}{}^2 g, \qquad \quad i = 1, \, 2, \, 3$$

^{*} The symbol "g" in square brackets, indicating that the components of the principal vectors are with respect to the shear system, is omitted here and in some of the equations that follow.

$$z^{(i)}[g] = \begin{cases} \frac{1}{N^{(i)}} \{ (\eta_1{}^2 - 1)^2 - \eta_1{}^2 g^2 + (\eta_1{}^2 - \eta_2{}^2) u_2{}^2 \\ & \times [g^2 - (\eta_1{}^2 - 1)] \}, \, i = 1 \\ \\ \frac{1}{N^{(i)}} [(\lambda_i{}^2 - \eta_1{}^2 \eta_2{}^2) (\eta_1{}^2 - 1) + w_2{}^2 \\ & (\eta_1{}^2 - \eta_2{}^2) (\eta_1{}^2 - \lambda_i{}^2)], \, i = 2, \, 3 \end{cases}$$

As in the previous case, $\lambda_i^2(g_1)=\lambda_i^2(g_2)$ and $g_1=-g_2$. The above equations yield the result that

$$\begin{split} x^{(i)}(g_1) &= x^{(i)}(g_2) \\ y^{(i)}(g_1) &= -y^{(i)}(g_2) \\ z^{(i)}(g_1) &= z^{(i)}(g_2) \end{split}$$

Therefore, the principal vectors are related by a 180° rotation about the \mathbf{j}_{g} direction (plus an inversion through the origin). Thus, in this case g-degeneracy occurs when \mathbf{j}_{g} is a two-fold axis of symmetry.

(4)
$$u_2 \neq 0$$
, $v_2 \neq 0$, $w_2 = 0$:

In this case, equations (22) apply. The equation for $x^{(1)}[g]$ may be written

$$x^{(1)} = -\frac{Ag + \frac{1}{2}B}{N(\eta_1^2 - 1)}$$

Since $Ag_1 + B/2 = -(Ag_2 + B/2)$, it is seen that

$$x^{(1)}(g_1) = -x^{(1)}(g_2) \tag{28}$$

$$y^{(1)}(g_1) = y^{(1)}(g_2) \tag{29}$$

$$z^{(1)}(g_1) = z^{(1)}(g_2) = 0$$
 (30)

and similarly for $\mathbf{r}^{(3)}$. Therefore, the principal directions for g_1 and g_2 are related by a rotation of 180° about either \mathbf{i}_g or \mathbf{j}_g and g-degeneracy results if either of these directions is a two-fold axis. The case of $(110)[\overline{110}]$ shear originally treated by the theory (5) is an example of this type of g-degeneracy.

(5)
$$u_2 = v_2 = 0$$
, $w_2 = 1$:

Equations (23) apply here. As in the previous case, g-degeneracy occurs if either \mathbf{i}_g or \mathbf{j}_g is a two-fold axis (although, in this case, if either of \mathbf{i}_g or \mathbf{j}_g is a two-fold axis, the other is also). The possible cases are (101)[10 $\overline{1}$] shear and (100)[001] shear.

Thus, as is summarized in Table 1, g-degeneracy may result if \mathbf{i}_g or \mathbf{j}_g is a two-fold axis of symmetry, depending upon the values for the components of the shear elements in the shear system.

4. THE DEGENERACY OF THE ORIENTATION RELATIONS AND MACROSCOPIC CHANGE OF SHAPE

When one of the principal values of the total transformation distortion is unity, an undistorted plane

exists such that no line in the plane is extended or contracted. This plane is rotated, however, by the action of the lattice invariant shear, G, and the pure lattice distortion, T. Therefore, the rotation Φ is included in the expression for the total transformation distortion, equation (1), so that the undistorted plane may be rotated back to its original orientation. The orientation relations between crystal axes in the two phases depend intimately on the rotation Φ . This can be seen as follows. Since the lattice invariant shear, G, is considered to arise from microscopic slip, it has no effect on crystallographic directions. Furthermore, in the case of the austenite-martensite transformation, the correspondence between crystal axes is such that the tetragonal axis of the martensite is derived from the unique axis of the pure lattice distortion, T, and the other two martensite axes are derived from the two (110) directions perpendicular to the contraction axis (see Fig. 1, Ref. 5). It can be seen from the form of T in equation (2) that the directions [101], [101], and [010] are not rotated by T. Therefore, the directions of the martensite axes are given simply by the action of Φ on these three directions. As a result, the degeneracy of the orientation relations depends upon whether the Φ 's for $\delta_K = \pm 1$ in (24) and $\delta_g = \pm 1$ in (18) are crystallographically equivalent. It should be mentioned that the conditions for the crystallographic equivalence of Φ are not necessarily the same as for the normal to the undistorted plane. Indeed, in one case, we shall find that although the undistorted planes are g-degenerate, the orientation relations are not.

Two directions in the undistorted plane are given by the invariant principal axis, $\mathbf{r}^{(1)}$, and the direction \mathbf{v} , equation (24). These vectors are changed in direction to $\mathbf{r}_F^{(1)} = \mathbf{F}\mathbf{r}^{(1)}$ and $\mathbf{v}_F = \mathbf{F}\mathbf{v}$ by the action of \mathbf{F} . Since $\mathbf{\Phi}$ rotates $\mathbf{r}_F^{(1)}$ back to $\mathbf{r}^{(1)}$ and \mathbf{v}_F back to \mathbf{v} , the axis of rotation \mathbf{p} , and the amount of rotation, φ , are given by $\mathbf{r}^{(13)}$

$${f p} an rac{arphi}{2} = rac{({f r}_F{}^{(1)} - {f r}^{(1)}) imes ({f v}_F - {f v})}{({f v}_F - {f v}) \cdot ({f r}_F{}^{(1)} + {f r}^{(1)})}$$

It is clear that, since $\mathbf{r}^{(1)}$ and \mathbf{v} lie in the undistorted in its unrotated orientation, the orientation relation cannot be degenerate unless the corresponding undistorted plane is degenerate. However, in order that the orientation relation be degenerate, the vectors $\mathbf{r}_F^{(1)}$ and \mathbf{v}_F must also be degenerate, i.e. $\mathbf{r}_F^{(1)}$ must change to a crystallographically equivalent orientation when the sign of δ_K or δ_g is changed, and similarly for \mathbf{v}_F . Let us consider the case of K-degeneracy first, in which case Table 1 shows that either $w_2=0$ or $w_2=1$. In the case of $w_2=0$, the

00

rotation Γ , which connects the [d] and [g] systems, is of the form

$$\mathbf{F} = egin{pmatrix} x^{(1)} & 0 & -y^{(1)} \ y^{(1)} & 0 & x^{(1)} \ 0 & 1 & 0 \end{pmatrix}$$

where $x^{(1)}$ and $y^{(1)}$ are given in (22) and $\mathbf{F}[g]$ is of the form

$$\mathbf{F}[g] = \begin{pmatrix} F_{11} & F_{21} & 0 \\ F_{12} & F_{22} & 0 \\ 0 & 0 & F_{23} \end{pmatrix}$$

where the non-zero elements are given in (5). With the use of these expressions, one finds that

$$\mathbf{r}_{F}^{(1)}[g] = \begin{pmatrix} F_{11}x^{(1)} + F_{12}y^{(1)} \\ F_{21}x^{(1)} + F_{22}z^{(1)} \\ 0 \end{pmatrix}$$
and
$$\mathbf{v}_{F}[g] = \begin{pmatrix} -F_{11}y^{(1)} + F_{12}x^{(1)} \\ -F_{21}y^{(1)} + F_{22}x^{(1)} \\ \delta_{K}KF_{33} \end{pmatrix}$$
(31)

The vectors $\mathbf{r}_F^{(1)}$ and \mathbf{v}_F are rotated 180° about \mathbf{k}_q and inverted in the origin upon changing the sign of δ_K . Since the undistorted plane undergoes the same symmetry operation upon change of sign of δ_K . the orientation relation is K-degenerate in the same way as the undistorted plane. The same is true of the K-degeneracy when $w_2 = 1$. In the case of gdegeneracy, for the cases of B-1 and B-2 in Table 1, the orientation relations are degenerate by the same symmetry operation as the undistorted plane. However, in the case B-3 ($u_2 \neq 0$, $v_2 \neq 0$, $w_2 = 0$), the situation is different. With regard to equations (31), it is found that the magnitude of F_{12} is not the same for g_1 and g_2 and similarly for F_{22} . As a result, when the relations (28), (29), and (30) are taken into account, the conclusion is reached that $\mathbf{r}_{F}^{(1)}$ for g_{1} is not crystallographically equivalent to $\mathbf{r}_{F}^{(1)}$ for g_2 and similarly for \mathbf{v}_{F} . Thus, the orientation relations are not g-degenerate in this case, although the undistorted planes are. Finally, for g-degeneracy of type B-4 in Table 1, the orientation relations are g-degenerate when \mathbf{j}_a is a two-fold axis but not when i, is a two-fold axis. This is a trivial matter since, in this special case, if either of \mathbf{i}_a and \mathbf{j}_a is a two-fold axis, the other is also.

The macroscopic change in shape that accompanies the transformation may be described as a simple shear on the undistorted plane, combined with an extension or contraction perpendicular to the undistorted plane to account for the change in volume. The macroscopic distortion is planar and takes place in the plane perpendicular to the invariant principal axis, $\mathbf{r}^{(1)}$. Since the direction of the simple shear, \mathbf{s} , is perpendicular to both the normal to the undistorted plane, \mathbf{n} , and the undistorted principal axis, $\mathbf{r}^{(1)}$, it must be coincident with \mathbf{v} , equation (24). Therefore, the direction of the simple shear will obey the same degeneracy conditions that govern \mathbf{n} . The amount of simple shear is given by $^{(5)}$

$$S = [(\lambda_2^2 - 1)(1 - \lambda_3^2)]^{1/2}$$

S is always invariant to change of sign of δ_K . Also, it is invariant to change of sign of δ_g , whenever one of the quantities u_2 , v_2 , and w_2 is zero (equation 27). The direction of macroscopic motion is⁽⁵⁾

$$\mathbf{s}'' = \frac{1}{\mathcal{S}''}[S\mathbf{s} + (\lambda_2\lambda_3 - 1)\mathbf{n}]$$

where $S'' = \lambda_2 - \lambda_3$. Thus, this quantity also follows the degeneracy conditions that govern **n**, as given in Table 1.

5. THE EXISTENCE CONDITIONS

195

It has been pointed out for the special case previously treated $^{(1,5)}$ that certain relations developed in the theory may be used to derive conditions that must be satisfied in order that real solutions exist. In terms of the generalized theory, the existence conditions are $H \geq 0$ and $K \geq 0$, where H and K are given in (18) and (24), respectively. It may be seen with the aid of (19) that the condition on K is equivalent to $\phi_1 - \phi_3 - 2 \geq 0$. Therefore, the two existence conditions are designated as the "H-condition" and the " ϕ -condition." It is of interest to examine the relations between the shear elements and the lattice parameters that must be satisfied for the special cases considered above.

(a)
$$u_2 = 0$$
, $v_2 \neq 0$, $w_2 \neq 0$:

The ϕ -condition yields the result that $(1-\eta_2^2)$ and $(\eta_1^2-\eta_2^2)$ must be of the same sign.* The H-condition then yields the more restrictive result that

$$(\eta_1^2 - 1)(1 - \eta_2^2) > 0 (32)$$

It is seen from (26) that this condition is necessary in order that a cone of undistorted directions exist as a

^{*} In what follows, the special cases where either η_1 or η_2 is unity are excluded from consideration. The analysis is redundant for these cases. However, such transformations are expected to be rare, if they exist at all.

result of the pure lattice distortion. Furthermore, it is found from the H-condition that

$$v_2^2 < (1 - \eta_2^2)/(\eta_1^2 - \eta_2^2) \tag{33}$$

This inequality is the relation to be satisfied in order that the shear plane intersect the cone of undistorted directions. A similar, though somewhat more complicated condition on v_2^2 results from the ϕ -condition, but this is found to be implicit in (33).

(b)
$$u_9 \neq 0$$
, $v_9 = 0$, $w_9 \neq 0$:

The imposition of the H-condition and the ϕ -condition in this case yields results similar to those in (a) above. The condition that u_2^2 must satisfy is

$$u_2^2 < \eta_1^2 (1 - \eta_2^2)/(\eta_1^2 - \eta_2^2)$$

(c)
$$u_2 \neq 0$$
, $v_2 \neq 0$, $w_2 = 0$:

The ϕ -condition is independent of the shear elements and results in the relation

$$(\eta_1^2 - 1)(1 - \eta_1^2 \eta_2^2) > 0 \tag{34}$$

which is more restrictive than (32). When the two factors in (34) are positive, the two factors in H, equation (18), are also positive and, similarly, when the two factors in (34) are negative. In either case, however, the H-condition leads to the requirement that

$$\frac{{\eta_2}^2({\eta_1}^2-1)}{{\eta_1}^2-{\eta_2}^2} < {v_2}^2 < \frac{1-{\eta_2}^2}{{\eta_1}^2-{\eta_2}^2} \tag{35}$$

The previously treated case $^{(1,5)}$ corresponds to $v_2^2=1/2$, in which case (35) becomes

$$2\eta_1^2\eta_2^2 < (\eta_1^2 + \eta_2^2) < 2 \tag{36}$$

when the two factors in (34) are positive. When the two factors in (34) are negative, the inequality signs in (36) are reversed. Furthermore, it may be shown that the left-hand inequality in (36) is implicit in the right-hand inequality, as has been pointed out.⁽¹⁾

(d)
$$u_2 = v_2 = 0, w_2 = 1$$
:

The *H*-condition specifies that $\eta_1^2(1-\eta_2^2)^2>0$, which is always satisfied for real values of the η 's. The ϕ -condition yields the result that

$$(\eta_1^4 - 1)(1 - \eta_2^2) > 0$$

(e)
$$u_2 = w_2 = 0$$
, $v_2 = 1$ and $v_2 = w_2 = 0$, $u_2 = 1$:

In both these cases, the ϕ -condition gives the relation (34). But

$$H = -\eta_1^2(1 - \eta_2^2)(\eta_1^2 - 1)$$
, for $v_2 = 1$

and

VOL.

1959

7

$$H = -\eta_2^2(1 - \eta_2^2)(\eta_1^2 - 1)$$
, for $u_2 = 1$

Therefore, the H-condition cannot be satisfied in either of these cases, and no solutions exist.

6. SUMMARY

The theory of the crystallography of martensitic transformations is extended in terms of generalized elements for the lattice invariant shear. Expressions for the principal values and directions of the transformation distortion are derived as functions of the shear elements. These expressions are used to examine the conditions under which the solutions for the undistorted plane, orientation relations, and macroscopic change of shape are degenerate. In the nondegenerate case, four solutions are obtained that exhibit no crystallographical equivalence.(1) Two types of degeneracy are discussed, each of which divides the number of crystallographically non-equivalent solutions in half: K-degeneracy corresponding to δ_K = ± 1 in equation (25) and g-degeneracy corresponding to $\delta_q = \pm 1$ in equation (18). The results for the undistorted plane are summarized in Table 1. It is seen that K-degeneracy depends upon the presence of a two-fold axis in the cubic phase along the direction \mathbf{k}_{q} , whereas g-symmetry requires that the shear direction, \mathbf{i}_{a} , or the shear plane normal, \mathbf{j}_{a} , be a twofold axis. It is to be noted that double degeneracy, where only one solution appears, is rather rare, since it requires that all three shear axes be two-fold axes of symmetry. This is true for the (110)[110] case previously treated(5) and is responsible for the fact that the analytical expressions were sufficiently tractable to allow the undistorted plane normal to be expressed as an explicit function of the lattice parameters of the two phases. The cases of (100)[001] and (101)[101] shear also lead to doubly degenerate solutions for the undistorted plane. The degeneracy of the orientation relations and macroscopic change of shape is also considered. The degeneracy of the macroscopic change of shape is of the same type as for the undistorted plane, but this is not necessarily true for the orientation relations. A case is discussed for which the orientation relation is not degenerate, although the normal to the undistorted planes is degenerate. The results in the present paper concerning K-degeneracy are in agreement with the conclusions of Christian⁽¹⁾. However, Christian's remarks concerning q-degeneracy are based on the premise that the principal axes for the two values of g are related by a rotation of 180° about the shear plane normal. The present analytical treatment indicates that this is not always the case. Therefore, cases arise, such as (111)[121] shear, for which the undistorted plane is g-degenerate, even though the

shear plane does not possess mirror symmetry. The general conditions that must be satisfied in order that real solutions exist are derived and expressions are given for the special cases under consideration.

ACKNOWLEDGMENTS

Thanks are due to H. M. Otte and H. C. Schweinler, who read the manuscript and made valuable suggestions.

REFERENCES

- 1. J. W. Christian, J. Inst. Met. 84, 386 (1955).
- 2. J. S. Bowles and J. K. Mackenzie, Acta Met. 2, 129 (1954).

- 3. J. K. Mackenzie and J. S. Bowles, Acta Met. 2, 138
- 4. J. S. Bowles and J. K. Mackenzie, Acta Met. 2, 224 (1954).
- 5. M. S. WECHSLER, D. S. LIEBERMAN and T. A. READ,
- M. S. WECHSLER, D. S. LIEBERMAN RIGG I. A. READ, Trans. Amer. Inst. Min. (Metall.) Engrs. 197, 1503 (1953).
 D. S. LIEBERMAN, M. S. WECHSLER and T. A. READ, J. Appl. Phys. 26, 473 (1955).
 B. A. BILBY and J. W. CHRISTIAN, Martensitic Trans-tics of the Action of the Action of the Conference of the
- B. A. Bilby and J. W. Christian, Mariensitic Transformations, Monogr. Ser. Inst. Metals No. 18 (1955).
 A. B. Greeinger and A. R. Troiano, Trans. Amer. Inst. Min. (Metall.) Engrs. 185, 590 (1949).
 A. B. Greeinger and A. R. Troiano, Trans. Amer. Inst. Metall. Engrs. 140, 2022 (1949).
- Min. (Metall.) Engrs. 140, 307 (1940).
 10. D. S. Lieberman, T. A. Read and M. S. Wechsler, J. Appl. Phys. 28, 532 (1957).
 11. D. S. Lieberman, Acta Met. 6, 680 (1958).

- 12. M. S. WECHSLEB and T. A. READ, unpublished work.
 13. C. J. Coe, Theoretical Mechanics. Macmillan, London (1938).

X-RAY STUDY OF THE KINETICS OF ORDERING IN AuCu*

J. L. O'BRIEN† and G. C. KUCZYNSKI‡

The kinetics of the disorder-to-order transformation in AuCu has been studied by means of X-ray powder patterns. It has been found that the transformation occurs by the nucleation and growth of ordered domains in the disordered matrix. The degree of order in the newly formed domains is close to but less than the equilibrium value.

ETUDE AUX RAYONS X DE LA CINETIQUE DE LA FORMATION DE L'ORDRE DANS AuCu.

La cinétique de la transformation ordre-désordre dans l'alliage AuCu est étudiée au moyen des rayons X par la méthode des poudres.

Les auteurs trouvent que la transformation a lieu par germination et croissance de domaines ordonnés dans une matrice désordonnée.

 $\label{lem:lemma$

RÖNTGEN-UNTERSUCHUNG DER KINETIK DER ORDNUNGSEINSTELLUNG BEI Aucu

Die Kinetik der Umwandlung Unordnung-Ordnung von AuCu wurde mit Hilfe von Röntgen-Beugungsaufnahmen an Pulvern untersucht. Die Umwandlung vollzieht sich durch Keimbildung und Wachstum von geordneten Bezirken in der ungeordneten Matrix. Der Grad der Ordnung in den neugebildeten Bezirken liegt nahe, aber unter dem Gleichgewichtswert.

The investigations reported in this paper were initiated in order to resolve an apparent inconsistency in the results obtained by two groups of researchers working on the problem of the kinetics of ordering in AuCu.

1959

The ordering transformation in this alloy is complicated by the existence of two different ordered phases. According to Johansson and Linde⁽¹⁾, the superlattice formed between 408 and 375°C consists of a large unit cell made up, approximately, of 10 cells of the disordered face-centered-cubic lattice. The structure is orthorhombic with two axes nearly equal and the third approximately ten times as long. Below 375°C, the ordered alloy assumes a tetragonal structure.

There are two possible ways in which we can envisage the occurrence of the ordering transformation. First, within the disordered matrix nuclei of the ordered structure might form and grow, gradually converting the whole crystal into a mosaic of more or less perfectly ordered domains. Second, the ordering might proceed uniformly throughout the whole crystal. The former process would be evidenced by a

gradual increase in the intensities of the tetragonal or orthorhombic superlattice lines, with only minor changes in their positions due to the completion of ordering within the domains. The latter mechanism would be evidenced by a gradual splitting and shifting of the fundamental lines to the positions corresponding to the tetragonal or orthorhombic structure, and also by a gradual shift of the superlattice lines, such as (001), from the position corresponding to a c/a ratio near unity towards the position corresponding to the equilibrium value of this quotient, about 0.925.

Borelius^(2,3) has found that both effects occur. At temperatures lower than 350°C the (311) fundamental line changed gradually through intermediate positions from disorder to order. Above that temperature the change was found to be discontinuous. He claims that this proves the existence of a potential barrier between the ordered and disordered states at higher temperatures, forcing the nucleation type of transformation. At lower temperatures this barrier disappears. It should be noted that in the course of his experiments Borelius never examined the behaviour of the superlattice lines.

On the other hand, Kuczynski et al. (4), studying the rate of ordering by measuring electrical resistance, have found well defined induction periods, indicating a nucleated transformation, throughout the whole range of temperature. They also found that the transformation is accompanied by a twin-like structure which, at temperatures above 360°C,

^{*} Sponsored by the Office of Naval Research. This paper represents part of a thesis by J. L. O'Brien submitted in partial fulfillment of the requirements for the degree of Master of Science to the Graduate School of the University of Notre Dame. Received April 24, 1958; revised version March 11, 1959.

[†] Department of Metallurgy, University of Notre Dame. Notre Dame, Indiana. Now at: Gordon McKay Laboratory, Harvard University, Cambridge, Mass.

^{*} Department of Metallurgy, University of Notre Dame, Notre Dame, Indiana.

appears simultaneously with the inception of order; below that temperature ordering begins before the twin-like structure appears. To explain these effects it was assumed that below 300°C the critical nucleus size for "twinning" is larger than that for order and therefore the ordered domains grow coherently within the disordered matrix. Above that temperature the reverse is true. The ordered nuclei "twin" as soon as they are formed and grow incoherently. In the former case large broadening of X-ray lines should be expected due to the coherency strains. broadening was indeed observed by Hirabayashi and Ogawa⁽⁵⁾, who studied Laue patterns of single crystals of AuCu during the early stages of ordering at 100° and 200°C. They found internal lattice strains in (110) directions. These were attributed to coherency strains from small particles of the ordered phase growing on (110) planes of the disordered matrix. Similar strains have also been found in single crystals of CoPt upon ordering. (6)

Thus there seems to be a contradiction as to the mechanism of ordering below 360°C. The results of Borelius seem to indicate a uniform ordering throughout the whole crystal, while those of Kuczynski suggest nucleation. In order to resolve this discrepancy, a careful study of X-ray diffraction lines was undertaken during the early stages of ordering in AuCu.

EXPERIMENTAL RESULTS

The alloy used in these experiments was made by melting gold of 99.986% and copper of 99.99% purity, in evacuated quartz tubes. The resulting ingot contained 75.63 wt. % gold and 24.37 wt. % copper, corresponding very closely to the AuCu composition. Subsequently the ingot was cold swaged and homogenized for 12 hr at 800°C. The minus 325 mesh powder prepared from this alloy by filing was cold pressed at 40 ton/in² and sintered at 700°C for 1 hr to give it handling strength. This treatment also secured a fine grained specimen for the X-ray studies. The powder compact was finally disordered for 20 hr at 425°C in vacuum. Subsequent ordering treatments were carried out, also in vacuum, at 300, 320, 350, 360 and 370°C for periods of time ranging from 20 sec to several hours.

A General Electric XRD-3 diffractometer and filtered copper radiation were employed to follow the progress of ordering in the compact. The diffracted intensity at any value of the angle 2θ was obtained by scaling. Both the (311) and (200) fundamental lines, and the (001) and (110) superlattice lines, were investigated. The ordering kinetics at 300°C, which were followed by measuring the change of angle 2θ of

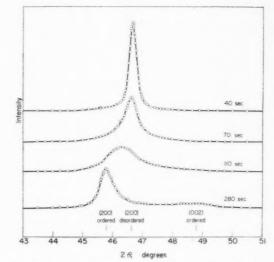


Fig. 1. Diffraction curves of the (200) lines from AuCu, ordered at 300°C for the times indicated.

the (311) line with time, seemed to verify Borelius' results. However, later in the work it was decided to use the (200) line since the (200) peak, occurring at a lower 2θ angle than the (311) peak, is sharper because of less resolution of the $K\alpha$ doublet. In addition, two superlattice lines, (001) and (110), were also examined. The diffractometer was used with a 1° defining slit and 0.1° or 0.2° receiving slits.

190

Fig. 1 represents the (200) diffraction curves for a specimen ordered at 300°C for the times indicated, and Fig. 2 similar curves for the (001) and (110) reflections. These curves are representative of those found for ordering temperatures up to and including 360°C. It should be noted that the angles corresponding to the maxima of the (001) and (110) lines change very little, if at all, with time of ordering. The (200) curves as a function of time for the specimen ordered at 370°C are represented in Fig. 3. It was impossible to use the diffraction method to determine the volume fraction of the ordered phase as a function of time. To do so would require a sample composed of randomly oriented grains. Unfortunately, the compact used in this investigation had a high degree of preferred orientation, as indicated by the fact that the measured ratio of integrated intensities I_{110}/I_{001} was only 0.6 of the calculated value. Also, as can be seen from Fig. 2, it would be difficult to determine the integrated intensities of the superlattice lines. Thus the present work must of necessity remain qualitative.

DISCUSSION

The results described in the previous section confirmed the observations of Borelius⁽³⁾ that the

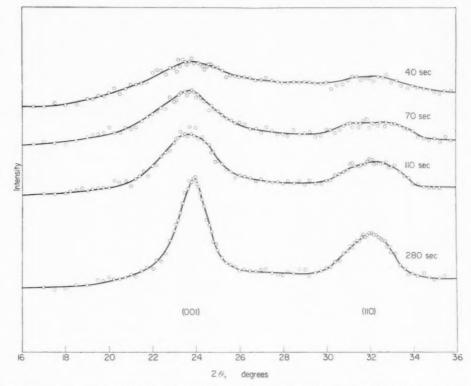


Fig. 2. Diffraction curves of the (001) and (110) lines from AuCu ordered at 300°C for the times indicated.

fundamental lines, such as (200) or (311), of alloys ordered below 360°C shift continuously (Fig. 1) and those of alloys ordered above that temperature split into three lines (Fig. 3). However, the fact that the superlattice lines (001) and (110) (Fig. 2) appear early during the ordering process, at an angle very near to that corresponding to a completely ordered alloy, suggests an interpretation entirely different from that put forward by Borelius. Moreover, a comparison of Figs. 1 and 2 reveals that the superlattice lines appear well before the (200) line begins to shift, indicating that the specimen is already partially ordered before any shift in the fundamental lines can be detected. This seems to be strong evidence against the homogeneous mechanism of ordering.

The alternative mechanism, the nucleation of almost perfectly ordered domains (as indicated by the position of superlattice lines) and their subsequent growth, can readily explain the observed facts. The fundamental line is composed of three lines, the (200) "ordered", the (200) "disordered" and the (002) "ordered". These lines would not be necessarily distinct, if they were broad. The positions of the "ordered" peaks, as calculated from the positions of the (001) and (110) lines, are indicated in Fig. 1. The apparent shift of the composite peak is attributed to

the increase in intensity of the "ordered" (200) line and the decrease in intensity of the "disordered" line, as the amount of the ordered phase increases. If this is true, then the angle $2\theta_{mh}$, corresponding to the

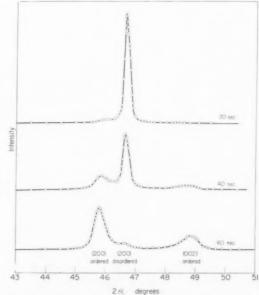


Fig. 3. Diffraction curves of the (200) lines from AuCu ordered at 370°C for the times indicated.

Table 1. The times, angles, and resistivities corresponding to maximimum (200) line breadth as a function of ordering

Ordering	tm.b.	20	$\rho_{m,b}$.
temperature (°C)	(sec)	$2\theta_{m,b}$.	$(\mu\Omega\text{-em})$
300	110	46.30°	11.3
320	70	46.25	10.9
350	20	46.35	11.1

peak of the (200) line exhibiting maximum breadth, should depend only on the ratio of the intensities of the ordered and disordered peaks, I_0/I_d , provided that the angles of these peaks are not changed. Indeed, Table 1 seems to indicate that this angle remains reasonably constant with the temperature of ordering. The ratio I_0/I_d is proportional to the ratio V_0/V_d , where V_0 is the volume of ordered and V_d the volume of disordered phase, and the latter ratio in turn is a unique function of electrical resistivity. Therefore, the resistivities $\rho_{m,b}$ of the samples ordered at various temperatures to the state yielding the angle of maximum breadth should be the same. The figures in Table 1 seem to indicate that this is so. The resistivities were measured on wires of the same composition and heated together with the X-ray samples.

In addition, the fundamental line (200) becomes asymmetrical with time of ordering. First, even before it begins to shift, there is more intensity on

the low-angle side than on the high-angle side. This would be due to the addition of the intensity of the (200) "ordered" peak to the intensity of the low-angle side of the (200) "disordered" peak. When the apparent peak is near the position of the (200) "ordered" peak, there is more intensity on the high-angle side of the line, due to the remnant of the (200) disordered peak (See Fig. 1). Similar behavior was observed in the specimens ordered at 320, 350 and 360°C. The broadening of the tetragonal lines, as already mentioned in the introduction, seems to support the hypothesis advanced elsewhere (4) that below 365°C the ordered nuclei are coherent with the disordered lattice and therefore strained. They are also very small. Above 365°C the coherency stresses are relieved by "twinning".

ACKNOWLEDGMENT

The authors express their gratitude to Dr. B. D. Cullity for numerous illuminating discussions and to the Office of Naval Research for financial support.

REFERENCES

- 1. C. H. Johansson and T. O. Linde, Ann. Phys. 25, 1 (1936).
- G. Borelius, J. Inst. Met. 74, 17 (1948).
- O. Kallback, J. Nystrom and G. Borelius, Ingen-Vetensk Akad. Handl. 157, 1 (1941).
- G. C. KUCZYNSKI, R. F. HOCHMAN and M. DOYAMA, J. Appl. Phys. 26, 871 (1955).
- M. Hirabayashi and S. Ogawa, J. Phys. Soc. Japan 11, No. 9 (1956).

195

J. B. Newkirk, A. H. Geisler, D. L. Martin and R. Smoluchowski, Trans. Amer. Inst. Min. (Metall.) Engrs. 188, 1249 (1950); Acta Cryst., Camb. 4, 507 (1951).

LETTERS TO THE EDITOR

Existence de plusieurs stades de précipitation pour les alliages à base de cuivre durcis par le titane*

Le durcissement des alliages cuivre-titane riches en cuivre, est attribué à la précipitation de la phase Cu₃Ti. Cette phase a été étudiée par différents auteurs, ⁽¹⁾ en particulier par Karlsson⁽²⁾, qui lui attribue une maille orthorhombique ordonnée à basse température, peu

chacun des noeuds (200) et (400) et non homothétique comme cela aurait été le cas pour des variations de paramètre de régions incohérentes. Les noeuds satellites sont alors de faible intensité et symétriques par rapport à la tache centrale; ils se rapprochent ultérieurement, deviennent plus intenses et dissymétriques en intensité et position. Nous avons déjà signalé ce résultat. (5) Une telle disposition dans



Fig. 1. Alliage 3,5%, vieilli 500 h à 300°C après trempe, diagramme Debye–Scherrer.

différente d'une maille hexagonale. L'objet de cette étude a été de suivre l'évolution de la structure, lorsque la phase Cu₃Ti est susceptible de précipiter à partir de la solution solide sursaturée cubique à faces centrées. Nous avons choisi des alliages de teneur comprise entre 1,5 et 5% de titane en poids. Ces alliages ont été coulés sous vide à partir de constituants de haute pureté. L'homogénéisation a été effectuée à 900° C pendant 64 heures, sur des bandes de $4 \times 10 \text{ mm}$ de section. Les échantillons pour les diagrammes de rayons X ont été obtenus par laminages et recuits successifs. Des tôles à grains de 0,5 mm de diamètre environ, ont été préparées par un écrouissage de 3% suivi d'un recuit. Les traitements thermiques de vieillissement après trempe à l'eau étaient isothermes. aux températures de 300, 400, 450 et 550°C pendant des durées allant jusqu'à mille heures.

L'évolution pour ces températures est d'autant plus lente que la température est plus basse, mais pour toutes, le début de la décomposition est caractérisé par de la diffusion anormale sur les diagrammes de ravons X. Cette diffusion avait la forme de raies satellites sur les diagrammes Debye-Scherrer (Fig. 1) correspondant à la même disposition dans l'espace réciproque que pour les alliages Ni-Al, Ni-Cu-Si(3) et Ni-Ti⁽⁴⁾, soit: une paire de noeuds satellités pour (h00), deux paires pour (hk0) et trois paires pour (hkl). Ces noeuds pour chaque paire sont de part et d'autre de la tache de Bragg correspondant à la matrice sursaturée et suivant les directions (100) de l'espace réciproque. Nous avons pu vérifier au début de ce stade de préprécipitation, que l'écartement des satellites est sensiblement constant, dans l'espace réciproque, pour ACTA METALLURGICA, VOL. 7, DECEMBER 1959

l'espace réciproque et une telle évolution indiquent une forme plane du complexe de pré-précipitation. Les déplacements des plans {100} par rapport à la position moyenne du réseau de la matrice sursaturée donnent la diffusion principale, les facteurs de structure atomique du cuivre et du titane n'étant pas très différents. La dissymétrie des satellites apparaît parce que, les déplacements des plans atomiques étant relativement importants, l'épaisseur du complexe est grande. (5)

Ici le passage de la diffusion anormale à la diffraction se fait progressivement. Nous ne savons pas s'il y a continuité, dans cette éventualité chaque partie du complexe aurait alors acquis une épaisseur suffisante pour donner en propre des taches de diffraction. Il peut s'y ajouter une rupture de cohérence sur les interfaces où les contraintes de cisaillement deviennent trop importantes.

A la fin de ce deuxième stade, les diagrammes comportent les raies de la matrice appauvrie et celle d'une phase transitoire à structure quadratique peu différente d'une structure cubique à faces centrées; le rapport c/a est égal à 0,982 pour l'alliage à 3,5% de titane après un vieillissement de 600 heures à 400°C. Les raies sont larges et cette valeur correspond au maximum d'intensité évalué. La matrice est ellemême légèrement quadratique mais les raies ne sont pas distinctes. La cohérence est vraisemblablement maintenue suivant les directions [100] perpendiculaires aux plans des plaquettes du précipité transitoire. C'est ce qui ressort des raies du diagramme Debye-Scherrer Fig. 2 et de la disposition des noeuds (220) Fig. 3. Sur cette dernière figure la tache la plus

Fig. 2. Alliage 3,5% vieilli 600 h à 400°C après trempe.

intense correspond au réseau de la matrice, peu déformé, les trois autres aux trois positions possibles du précipité sur les plans {100}. La tache la plus éloignée située dans la direction du centre correspond au plan (110) parallèle à la direction de cohérence.

Cette phase quadratique transitoire se maintient



Fig. 3. Taches (220) pour le même alliage vieilli 1 h à 550°C après trempe.

longtemps si la température est basse. Cependant pour l'alliage à 3,5% de titane par exemple et après un vieillissement de 2 heures à 550°C, les raies de la phase d'équilibre Cu₃Ti apparaissent. La précipitation de cette phase est discontinue avec un aspect perlitique. Ce dernier résultat a été signalé par Doi⁽⁶⁾. La recristallisation part des joints de grains, et les nouveaux cristaux envahissent la totalité de l'échantillon. La phase transitoire quadratique disparaît alors et ses raies ne sont plus visibles sur les diagrammes de rayons X.

Ces résultats sont intéressants à deux points de vue: pour la connaissance du mode de précipitation dans ce groupe d'alliages, mais aussi parce qu'ils apportent un exemple supplémentaire de cette forme de décomposition rencontrée dans d'autres familles d'alliages tels que les alliages à base de nickel.

O.N.E.R.A.

J. MANENC

Chatillon, France

Bibliographie

- V. N. VIGDOROVICH, A. N. KRESTOVNIKOV, et M. V. MALTSEV, *Iz vest. Akad. Nauk U.R.S.S.* 2, 145 (1958);
 W. GRUHL et H. CORDIER, *Metall.* 11, 928 (1957);

 K.
- Dies, Metall. 11, 933 (1957).

 2. N. Karlsson, J. Inst. Met. 18, 391 (1951).

 3. J. Manenc, Acta Met. 7, 124 (1959).

 4. C. Buckle, B. Genty et J. Manenc, Rev. Met. 56, No. 3,
- 247 (1959). 5. J. Manenc, C.R. Acad. Sci., Paris 248, 1914 (1959).
- 6. T. Doi, Acta Met. 7, 291 (1959).
 - *Received June 3, 1959.

Heats of formation of liquid Na-Cs alloys*

The enthalpies of formation of liquid solutions of the alkali metals in one another represent very important data from the point of view of the future development of the theory of alloys. This is because the alkali metals are the simplest for the theoretician to deal with, so that it may be expected that their binary solutions will prove most amenable to theoretical treatment. Therefore, when it was necessary to make sodium-cesium alloys in connection with other work, it was decided to accomplish the mixing within a simple calorimeter in order to obtain the heats of mixing with moderate accuracy.

Liquid cesium of 99.9% purity was added to liquid sodium of the same nominal purity in a Pyrex apparatus immersed in a well-stirred oil bath at 112°C. Each metal was introduced into the previously wellbaked-out apparatus by well-known though tedious procedures, the cesium being kept from dropping into the sodium by means of a solenoid-operated steel tapered plug fitted into a glass seat. The liquid metals were exposed only to vacuum or argon, both of which were sufficiently good for no observable oxidation to take place. When both metals were at constant and uniform temperature (about 112°C), both being immersed in the same oil bath, the cesium was allowed to drop into the sodium by energizing the solenoid; the resulting heat effect was followed by recording the amplified signal from a four-junction thermocouple within the oil bath. The observed temperature drop was translated into a heat effect by using the calibration factor of the calorimeter; this was obtained by supplying metered electrical energy to a heating cilo in the oil bath when the contents and the geometry within the oil bath were identical with those in the mixing experiment. The raw heat effect was converted to the basis of one gram-atom of alloy by the knowledge of the total amount of alloy, obtained by acid titration of an alcohol-water solution of the alloy, and after the chemical analysis of the alloy by Dr. D. H. Wilkins of this Laboratory. The experimental results are given in Table 1; the accuracy of the ΔH is estimated as ± 5 per cent.

195

From these data and from the Bragg-Williams approximation one can estimate that the liquid alloy would decompose into two liquid phases at about -70°C if the solid phases did not intervene. The only

Table 1. Heat of formation of liquid Na–Cs alloys at 112° C, referred to the pure liquid metals

At. % Cs	$\frac{\Delta H}{\text{(eal/g atom)}}$
1.6	24.7
2.1	22.0
22.4	184
65.0	182

other data on alkali metal binaries with which the present work can be compared are those of McKisson and Bromley^(1,2), who found similar positive numbers for three compositions of liquid sodium–potassium alloys. It is very interesting and quite significant that the liquid alkali metal binaries are characterized by sizeable positive enthalpies of formation, despite the fact that there is no ion-core repulsion in these systems. Crudely speaking, the positive ΔH probably reflects the difficulty of matching of the electronic wave functions and their radial derivatives at the boundaries of contiguous atomic cells of disparate sizes.

R. A. ORIANI†

General Electric Research Laboratory Schenectady, New York

References

- R. L. McKisson and L. A. Bromley, J. Amer. Chem. Soc. 73, 314 (1951).
- O. Kubaschewski and J. A. Catterall, Thermochemical Data of Alloys. Pergamon Press, London (1956).
 - * Received June 12, 1959.
- † Now at Laboratory for Fundamental Research, U.S. Steel Corporation, Monroeville, Pennsylvania.

The growth of precipitates from solid solutions*

The growth of particles of a second phase from a homogeneous, supersaturated solid solution was discussed by Zener⁽¹⁾ and Wert^(2,3), and their results have since been widely applied to various precipitation processes. The purpose of the present note is to present a further refinement which is based upon a model more closely representing real conditions.

Zener⁽¹⁾ showed that if the rate of growth of an isolated particle is limited only the diffusion of solute through the parent solution

$$X = \alpha (Dt)^{\frac{1}{2}} \tag{1}$$

where X is some characteristic dimension of the particle (e.g. the radius of sphere or cylinder or the half-thickness of a plate), D is the diffusion coefficient, t is the time of growth and α is a constant. Values

of α were given. The rate of transformation follows directly, provided that the shape of the particle is known or assumed and that all particles in the sample start to grow at the same time. The result is

$$y = 1 - \exp[-(t/k)^n]$$
 (2)

where y is the fraction transformed at the time t, k is a parameter which is a function of α , D, the number of particles and various concentration terms. n is a constant depending solely on the shape of the precipitate; it is the index of t in the expression for the volume of a single particle as a function of time. For spheres the volume is proportional to R^3 and thus to $t^{3/2}$; then n=3/2. For cylinders it was assumed⁽²⁾ that the rate of increase of length, L, is constant since the concentration conditions around the ends do not change as the end advances. The volume is proportional to $L \times R^2$ and thus n=2. For discs it was assumed that the radial growth is constant, whilst the thickness grows according to equation (1); thus n=5/2.

In calculating the volume of cylinders and discs it was implicitly assumed that the ends of the cylinders and edges of the discs remain plane. Since radial and axial growth proceed concurrently, the end of a cylinder will be rounded unless radial growth is very much more rapid than the rate of axial extension. This tendency will be further increased by surface tension considerations.

The necessary modification to the rate equations for cylinders and discs is obtained as follows:—

Volume of cylinder,

$$v = 2\pi R^2 L + (4/3)\pi R^3 \tag{3}$$

Where L, the half-length, is given by

$$L = \beta t$$

and R by equation (1)

Thus.

$$v = 2\pi\alpha^2 Dt^2\beta + (4/3)\pi\alpha^3 (Dt)^{3/2} \tag{4}$$

Following the usual procedure and allowing for the impingement of regions depleted in solute by the factor $(1-y)^{(1,2)}$ gives,

$$\ln(1-y) = -k_1(3t^2\beta + 2\alpha D^{\frac{1}{2}}t^{3/2}) \tag{5}$$

 k_1 is a parameter similar to k in equation (2). Without the second term equation (5) is the rate equation for growth with plane ends.

For disc-like particles growing with rounded edges

$$v = 2\pi R^2 X + \pi^2 R X^2 \tag{6}$$

X is the half-thickness given by equation (1) and $R^{(1,2)}$ is given by

$$R = \gamma t \tag{7}$$

then

$$\ln(1-y) = -k_2(2\gamma t^{5/2} + \pi \alpha D^{\frac{1}{2}}t^2) \tag{8}$$

The second term expresses the modification to the growth rate due to the development of rounded edge.

If β and γ in equations (5) and (8) are very large compared with αD^{1} the rate equations are approximated by equation (2). Physically this corresponds to long, narrow cylinders growing predominantly axially and to thin discs growing mainly radially; the result is intuitively obvious. When the rates of growth in three dimensions are comparable there is a substantial difference between equations (2) and (5) or (8); in such cases conclusions obtained by fitting data to equation (2) are of doubtful significance.

Department of Metallurgy
The University, Liverpool 3

J. BURKE

References

- C. Zener, J. Appl. Phys. 20, 950 (1949).
- C. A. Wert, J. Appl. Phys. 20, 943 (1949).
 C. A. Wert, Thermodynamics in Physical Metallurgy. Amer. Soc. Metals, Cleveland, Ohio (1950).
- * Received July 6, 1959.

Bismuth at low temperatures*

Experiments have recently been reported that are interpreted as evidence for a strain-induced phase change in bismuth.(1) The data consisted of irregularities in the force measured by a mechanical testing machine (held, apparently, at a constant strain after prior plastic uniaxial compression) while the specimen warmed up from about 78°K. Since the interpretation of such readings involves the differential expansion of specimen and testing equipment, and the unknown dependence of the flow stress with temperature, it is not clear that the method could provide a reliable test of transformation characteristics; however, the authors report that the method yielded results on lithium and sodium that were in reasonable agreement with X-ray results.(2-5) On the other hand their suggestion that all the other alkali metals also undergo strain transformation is not in accord with available X-ray information. (5)

Tests for transformation on simple cooling to 78°K and to 4.2°K, using filed powders in the annealed state and also using single crystal slabs with reflection from the (0001) plane (hexagonal indices) in the first

twelve orders, has failed to disclose any evidence for a transformation although contraction of the lattice and alteration of the atomic parameter was observed. (6) But since plastic strain can initiate some transformations that are suppressed on simple cooling, further tests were made in which a slab of bismuth was peened severely while maintained in vacuo in a cryostat at liquid helium temperature, and then X-rayed without warming above the operating temperature which was about 5°K, using a cryostat designed for this type of experiment. (5) The tool used for the purpose causes extremely severe cold work, especially in the layers near the surface that are penetrated by the CuK, radiation that was used. The bismuth sample, supplied by D. H. Reneker, had been zone refined by fifteen or twenty passes of a molten zone; spectroscopic analysis showed only a trace of Cu and Ag, estimated at less than one part per million, and no other spectroscopically detected impurities.(7)

No X-ray reflections from a new phase were found in the rate meter recordings of any of the tests, even though the samples were at lower temperatures and the cold work was more intense than in the Russian tests. But since the Russian work⁽¹⁾ had involved cold work near 78°K rather than 5°K the test was repeated with liquid nitrogen cooling. In these tests, cold working at 78°K was immediately followed by X-raying at 78°K. Again the diffraction pattern was entirely accounted for by the R3m rhombohedral structure of bismuth, the phase that is normal at ordinary temperatures (Structurbericht Type A7).

195

An important implication of the present results concerns the suggestion⁽¹⁾ that the superconductivity of films of bismuth deposited at helium temperatures⁽⁸⁾ might be due to the existence of a new crystal structure in the deposit. We were forced to conclude from our diffraction studies that a new crystalline phase did not exist either in the severely deformed metal or in the cooled powders and either at 78°K or 5°K, in quantities sufficient to be recorded in our diffraction patterns, which would have shown a phase constituting roughly 5 per cent of the whole; but the possibility remained that cold work might produce enough local amorphous or semi-amorphous material in the sample, or enough defects, to yield detectable superconductivity of the type exhibited by bismuth films.

To test this possibility a bar of large grained polycrystalline bismuth of the purity mentioned above, having the dimensions $3\times3\times20\,\mathrm{mm}$ was inlaid in a groove of an insulating block in the specimen holder of the X-ray cryostat and equipped with current and potential leads pressed into holes drilled in the bar. After cooling to liquid helium temperature,

the bar was peened by a chisel-shaped tool in vacuo until it was reduced to about half thickness by spalling from the surface under the intense cold work of this hammering.

Tests for traces of superconductivity were then conducted, using galvanometer currents small enough to avoid danger of loss of superconductivity through magnetic fields accompanying the testing current. (1) An electromagnet near the specimen was energized, but no change in the resistance of the specimen was detected. (2) When the specimen was warmed above the temperature of 6°K, which Buckel and Hilsch⁽⁸⁾ found was the superconducting critical temperature for thin bismuth deposits, no abrupt increase in resistance was noted. (3) No evidence was found for the prominent lack of reversibility in resistance such as has been observed(8) in deposited bismuth films when heated above 15°K and subsequently cooled. None of these tests, therefore, indicated a detectable trace of superconductivity. The only anomalies observed were abrupt changes in resistance during hammering, particularly in the early stages of hammering, which were attributed to the changing preferred orientation in the sample due to the hammering. Such changes are to be expected in this material since it has a large anisotropy of resistivity and is subject to reorientation by the formation of mechanical twins during deformation.

Thanks are due Drs. J. R. Schrieffer and B. W. Roberts for stimulating discussions. The work was supported in part by ONR Contract Nonr-2121(11).

C. S. BARRETT

Institute for the Study of Metals University of Chicago, Chicago, Ill.

VOL.

References

 A. GRINDIN, B. G. LAZAREV, I. D. SLARODUBOV, and V. I. KHOTKEVICH, Soviet Phys. JETP 8, 556 (1959).

 C. S. Barrett and O. Trautz, Trans. Amer. Inst. Min. (Metall.) Engrs. 175, 579 (1948).

3. C. S. Barrett, in *Phase Transformation in Solids*. Wiley, New York (1951).

V. I. KHOTKEVICH, J. Tech. Phys., U.S.S.R. 22, 477 (1952).
 C. S. BARRETT, Acta Cryst., Camb. 9, 621 (1956).

C. S. BARRETT, The Structure of Bismuth at Low Temperatures, Conference on Solid State Physics, Australian Branch of the Institute of Physics, August 27, 1958 (to be published).

D. H. RENEKER, Phys. Rev. 115, 303 (1959).

8. W. Buckel and R. Hilsch, Z. Phys. 138, 109-120 (1954).

* Received August 3, 1959.

The temperature dependence of the flow stress of an age-hardened alloy*

In a recent paper⁽¹⁾ measurements were described of the temperature dependence of the plastic properties

of single crystals of Al-4.23 wt. % Cu aged to contain Guinier-Preston zones of the first kind (GPI). The temperature dependence of the critical resolved shear stress (CRSS), and of the flow stress during deformation, was found to be small at temperatures above about 160°K but at lower temperatures rose rapidly. In the discussion of these results it was concluded that this large increase in flow stress at low temperatures could not be due to a very high density of "forest" dislocations and it was suggested that thermally activated cross-slip might be responsible for the temperature dependence, enabling dislocations to avoid passing through the zones at high temperature. At low temperatures it was suggested that either the stress necessary to produce cross-slip or that to force dislocations through the GP zones should be identified with the flow stress.

The object of this note is to consider these processes in a little more detail and to show that the large increase in flow stress at low temperatures must arise from a short range interaction between zones and dislocations.

Examination of electron micrographs (2) of crystals aged in an identical manner to those used by Kelly and Chou⁽¹⁾ show the separation of the zones along a line to be ~70 Å. This is consistent with the calculated average separation of zone centres of 150 Å deduced from the X-ray results. (3) The CRSS of these crystals at room temperature is 8.0 kg/mm² or less than $3 \times 10^{-3}G$, where G is the shear modulus. This means that any dislocation cannot be bent to a radius of curvature of less than 160b, where b is the Burgers vector, i.e. to a radius of curvature of <450 Å. It should be noted that stresses of G/30, the theoretical strength of a perfect crystal, would be required to bend a dislocation to a radius of curvature of 70 Å. Since a radius of curvature of <70 Å would be necessary for a dislocation to avoid an appreciable number of precipitates, we conclude from this that even if cross-slip occurs at a minimum stress, i.e. the dislocations are undissociated, motion of a dislocation cannot occur under these stresses without shearing of the zones. Hence cross-slip cannot lead to dislocations avoiding the zones, and hence dislocations must pass through the zones at all temperatures of deformation.

The earlier results $^{(1)}$ were plotted as a ratio of the flow stress during deformation at temperature T, σ_T , to that at 273°K, σ_{273} . It was found that the ratio σ_{77}/σ_{273} depended on deformation, falling rapidly in the first few per cent of deformation and then reaching an approximately constant value. The final value depended on the orientation of the crystal, varying

over the range 1.25-1.33. If, however, instead of the ratio σ_{77}/σ_{273} we form the quantity $\sigma_{77}-\sigma_{273}$, we find this to be constant during deformation as illustrated in Table 1, for crystal 8. We see that $\sigma_{77} - \sigma_{273}$ is equal to 3.2 kg/mm² throughout the deformation. The decrease in the ratio σ_{77}/σ_{273} is thus due to work hardening of the crystal. The quantity $\sigma_{77}-\sigma_{273}$ shows the same behaviour for the other crystals examined and the values (Crystal 9. 3.0 kg/mm²; Crystal 3, 2.8 kg/mm²) are closely similar. The variation in the ratio σ_{77}/σ_{273} with crystal orientation thus arises because of the different rates of work hardening of crystals of varying orientation.

For crystal 32 of lower copper content the behaviour is the same but the value of $\sigma_{77} - \sigma_{273}$ is smaller, being 2.45 kg/mm². The value of 3.0 kg/mm² is exactly the change in CRSS of these crystals between 77°K and 273°K, as can be seen from Fig. 2 of Reference (1).

We are thus led to the conclusion that there is present, from the start of deformation, a barrier to dislocation motion which provides a completely thermally reversible component of the flow stress of a constant magnitude. This must be identified with a short range interaction between dislocations and zones. The interaction must be short ranged because it can be shown quite generally(4) that thermal fluctuations at room temperature cannot lead to dislocation motion through an obstacle which extends more than a few interatomic distances in the slip plane.

It has been pointed out⁽³⁾ that, when a dislocation passes through a zone, a change in the number of Al-Cu near neighbours occurs across the slip plane. This tends to reverse the process of clustering and hence additional work must be done by the applied stress to bring this about. This process then provides a short range interaction between dislocations and precipitates, and furthermore, for these precipitates lying parallel to the Burgers vector of a dislocation, the barrier is a thin one and hence could be overcome

TABLE 1.

$(\mathrm{kg/mm^2})$	$\begin{array}{c} \sigma_{77} - \sigma_{273} \\ (\mathrm{kg/mm^2}) \end{array}$
8.05	_
8.53	3.15
8.68	3.17
9.30	3.18
9.35	3.21
9.75	3.26
9.82	3.24
10.35	3.20
10.40	3.22

by thermal fluctuations at room temperature. We conclude that the increase in flow stress at low temperatures in these crystals must be associated with at least part of the stress required to force the dislocations through the zones.

Department of Metallurgy University of Cambridge England

A. KELLY

195

References

- A. Kelly and C. Chiou, Acta Met. 6, 565 (1958).
 R. B. Nicholson and J. Nutting, Phil. Mag. 3, 531 (1958).
- 3. A. KELLY and M. E. FINE, Acta Met. 5, 365 (1957).
- 4. G. Leibfried, in Dislocations and Mechanical Properties of Crystals, p. 495. Wiley, New York. (1956).
- * Received September 11, 1959.

On the orientation dependence of surface free energy*

Herring(1,2) has pointed out that the equations describing the local equilibrium of three interfaces, having a common line of intersection, should contain terms which depend on the orientation of the interfaces when solid phases are present in the system. In particular, he demonstrated from theoretical considerations, that the variation of specific surface energy γ of a solid/vapor interface with orientation α, near a specific orientation α_0 that corresponds to a plane of low Miller indices, should have a cusp shape as shown in Fig. 1. The quantity $\partial \gamma/\partial \alpha$, which has been termed variously as a torque term or an orientation derivative, serves as a convenient measure of the anisotropy of the surface energy, and moreover, is the form in which the orientation dependence appears in the equations of equilibrium.

The purpose of this note is to point out the difficulty that has been encountered in the past in estimating $\partial y/\partial \alpha$, for a single interface, and to show that a minimum value of the orientation derivative, for a solid/vapor interface of known orientation, can be determined with considerably less uncertainty than in the past, from some recent findings of Moore(3). These minimal values are found to be appreciably larger than the estimates that have been reported previously.



Fig. 1. The variation of specific surface free energy orientation near a low index plane.

The literature⁽⁴⁻⁷⁾ contains some estimates of torque terms that have been obtained from the equilibrium of two solid/vapor interfaces and a grain boundary. Measurements of this type, however, are limited by the fact that, in order to obtain a value for the sum of the orientation derivatives, it is necessary to assume that, for each side of the thermal groove, the interfaces (a) have equal surface energies and (b) have the same magnitude and sign for the orientation derivatives. With these assumptions, Brooks⁽⁴⁾ was able to show that a discrepancy in the copper twin energy, as determined by two different methods, could be accounted for if

$$\frac{2}{\gamma} \left| \frac{\partial \gamma}{\partial \alpha} \right| = 0.01 \text{ rad}^{-1}$$

Buttner et al.⁽⁵⁾ found that in thermally grooved gold wires, having a bamboo structure, a given grain boundary exhibited decided variations in dihedral angle as measured around the circumference of the wire. Mykura⁽⁶⁾ claims that these results can be taken to mean that

$$\left| rac{2}{\gamma} \left| rac{\partial \gamma}{\partial lpha}
ight| = 0.12 \; \mathrm{rad^{-1}}$$

VOL.

1959

At some points along the circumference, however, the dihedral angle approached 180°; this can mean that the sum of the orientation derivatives is as large as 0.30 rad⁻¹. On the other hand, it should be recalled that these measurements were taken from wires that have been reported⁽⁷⁾ to exhibit such phenomena as kinking, offsetting, and bulging due to the effects of a stress applied during the annealing. These effects could result in a distortion of the dihedral angle.

On subjecting nickel twin boundaries to a thermal grooving treatment, Mykura⁽⁶⁾ observed that, for a given pair of twin boundaries, one showed a dihedral angle greater than 180° and the other less than 180° , by nearly equal amounts. Such a configuration is clearly impossible unless the torque terms have a finite value. He found that the sum of the orientation derivatives for both planes (unidentified) present in the groove was in one case $0.105 \; \mathrm{rad}^{-1}$ and in another $0.036 \; \mathrm{rad}^{-1}$.

It can be seen from the points reviewed above that equilibria involving three interfaces have been able only to supply information concerning the *sum* of two orientation derivatives; the individual derivatives may actually differ in magnitude and sign. Recently Moore⁽³⁾ has investigated the case of an equilibrium of two interfaces, and it will be shown below that an analysis of this type of equilibrium leads to an

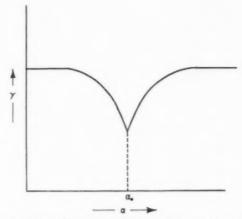


Fig. 2. Schematic profile of the surface configuration of silver or copper specimens after thermal etching in an oxygenbearing atmosphere.

expression for the orientation derivative of a low index plane.

Moore's results show that the surface striations, produced by thermally etching silver in air, represent a surface composed of simple (111) or (100) planes, and complex planes, which when viewed in profile, appear as shown in Fig. 2. This equilibrium is described by two equations that can be derived by the method of virtual displacements, as pointed out by Herring⁽¹⁾. Taking an infinitesimal displacement along the simple plane, the first order change in the total surface free energy ΔF will be

$$\Delta F = \Delta \sum\limits_{i=s,c} (\gamma_i A_i) = \sum\limits_{i=s,c} A_i \, \Delta \gamma_i + \sum\limits_{i=s,c} \gamma_i \, \Delta A_i$$
 (1)

where A_i is the area of the *i*th interface, and where the summation is carried out over both the simple and complex planes. The first term on the right hand side of equation (1) will be zero since it is assumed that γ_c is isotropic, while the second term leads to the expression

$$\gamma_s = \gamma_c \cos{(\alpha + \beta)} \tag{2}$$

when ΔF is set equal to zero. Moore⁽³⁾ obtained this result by a different method.

Consider now the displacement along the complex plane. Here the assumption is made that the simple plane is initially in the cusp position α_0 . The only displacement that need be considered is that in which α decreases, since only in this case will the terms of equation (1) be of opposite sign. If equation (1) is developed for this case, and the substitution of equation (2) carried out, the final result is given by

$$\frac{\Delta F}{\gamma_c \, \Delta A_c \sin{(\alpha + \beta)}} = - \sin{(\alpha + \beta)} - \frac{1}{\gamma_c} \left[\frac{\partial \gamma_s}{\partial \alpha} \right]_{\alpha_0} \, (3)$$

where $\partial \gamma_s/\partial \alpha$ is a negative quantity and is evaluated at α_0 .

Experimentally, Moore(3) found that simple planes (111) and (100) were located very near the cusp position α_0 (most of them were within 5°, the experimental error in measuring the angles being $\pm 2^{\circ}$ at best). Thus, the simple plane appears to be constrained to cusp position. This will be true if, in equation (3), $\Delta F > 0$, which in turn requires that

$$\frac{1}{\gamma_c} \left| \left[\frac{\partial \gamma_s}{\partial \alpha} \right]_{\alpha_0} \right| > \sin \left(\alpha + \beta \right) \tag{4}$$

Under these conditions, then, $\gamma_c \sin{(\alpha + \beta)}$ represents a minimum value for the orientation derivative at the root of the cusp.

It is of interest to examine the magnitude of the torque terms, given in Table 1 for silver and copper, because it is believed that they represent the only available values for a single interface of known orientation. In the case of silver, $(\alpha + \beta)$ was measured optically by Moore⁽³⁾. In this laboratory, faceting on a copper bicrystal due to (100)—or (110)†—planes has been observed on annealing in a hydrogen atmosphere which had been contaminated with oxygen. In this work a Zeiss Interference Microscope was used to determine $(\alpha + \beta)$.

TABLE 1.

Plane	Metal	VolVe	$\sin (\alpha + \beta)$	Limiting angle
(111)	Ag	0.838	0.55	33° 04′
(100)	Ag	0.907	0.42	24° 57′
(100) or (110)	Cu	0.91	0.41	24° 30′

It is interesting to note that these minimal values are significantly larger than the estimates that were reported by other workers. This discrepancy could stem from the fact that the sum of the orientation derivatives may include terms of the opposite sign. On the other hand, it is quite likely that the magnitude of the orientation derivatives depends on the concentration of chemisorbed oxygen atoms on the surface, particularly since the appearance of faceting during annealing seems to depend on the presence of a proper amount of oxygen in the atmosphere. This latter factor would undoubtedly make it difficult to compare values obtained under different experimental conditions, as has been the case thus far. A comparison of the ratio of grain boundary to surface free energy, which for most metals is in the range 0.3-0.4, with the torque terms given in Table 1, suggests that under proper conditions it would be

possible to suppress thermal grooving at the intersection of a large angle grain boundary and a planar facet. This effect seemingly was observed by Buttner et al. (5) on gold wires. However, it is not clear whether this finding can be attributed to faceting or some factor such as kinking, offsetting, and bulging(6) that occurred during the annealing of the wires under stress. As stated above, Mykura (6) has found dihedral angles greater than 180°, a phenomenon that also would be expected from this comparison.

The author is indebted to Dr. P. G. Shewmon for many helpful discussions.

N. A. GJOSTEIN Materials Research Department Thompson Ramo Wooldridge, Inc. Cleveland, Ohio

References

- 1. C. Herring, Structure and Properties of Surfaces, p.5.
- University of Chicago Press (1952).
 2. C. Herring, The Physics of Powder Metallurgy, p.143. McGraw-Hill, New York (1951).
- 3. A. J. W. MOORE, Acta Met. 6, 293 (1958).
- 4. H. Brooks, Metal Interfaces, p.20. Amer. Soc. Metals, Cleveland (1959).
- 5. F. H. BUTTNER, H. UDIN, and J. WULFF, Trans. Amer. Inst. Min. (Metall.) Engrs. 197, 313 (1953).
- 6. H. MYKURA, Acta Met. 5, 346 (1957).
- F. H. BUTTNER, H. UDIN, and J. WULFF, J. Metals, N.Y. 3, 1209 (1951).
- * Received August 24, 1959.

The role of austenitizing temperature in the nucleation of pearlite*

The nucleation rate of the austenite-to-pearlite reaction is known to decrease with increasing austenitizing temperature, (1) even though the variations of this temperature are kept entirely within the singlephase austenitic region of the equilibrium diagram. Two obvious factors may contribute to this effect: (a) residual concentration gradients from the solution of ferrite or carbide in the austenite may be dissipated by raising the austenitizing temperature, and (b) the increase in grain size of the austenite may reduce the number of preferred nucleation sites at grain boundaries. Both of these possible contributions are irreversible in the sense that the dispersal of residual concentration gradients and the growth of the austenitic grains do not undergo reversal if the austenitizing temperature is lowered from a higher level. The purpose of this communication is to describe some experiments which show that the low rate of pearlite nucleation characteristic of a high austenitizing temperature may be progressively increased as that temperature is lowered.

[†] The uncertainty here stems from a lack of knowledge concerning association of the facets with one particular grain of the bicrystal.

High-purity iron-earbon alloys, ranging in earbon content from 0.62 to 1.04% were used in this investigation; the findings on the 0.78% carbon alloy are typical and are presented here. The austenitizing temperature, T_A , was varied from 870° to 1095°C (45 min in each instance), and the pearlitic transformation was studied by hot quenching specimens to 680°C. Transformation curves were obtained by lineal analysis, and the time for a certain fraction of transformation (10 or 50 percent) was introduced into the Johnson-Mehl⁽²⁾ equation to compute the product N_nG^3 :

$$f=1-\exp\left(-\frac{\pi}{3}\,\dot{N}_vG^3t^4_{\ T}\right) \eqno(1)$$

where:

f =fraction transformed to pearlite

 $\dot{N}_{v} = \text{volume nuclealion rate in nuclei/cm}^{3}/\text{sec.}$

G = growth rate in cm/sec.

 $t_T =$ time of transformation in sec.

The rate of growth, G, was measured separately in the usual way⁽¹⁾ and N_n could then be calculated. While this procedure gives only a rough measure of the rate of nucleation because the assumptions implicit in equation (1) do not necessarily prevail, the resulting N_c values are undoubtedly indicative of the trend to be discussed.

If pearlite nucleation occurs at austenite grain boundaries, (3) then a surface nucleation rate, $\dot{N}_{\rm s}$, can be calculated:

$$\dot{N}_s = \dot{N}_v / (S/V) \tag{2}$$

where:

 $\dot{N}_s = \text{surface nucleation rate in nuclei/cm}^2/\text{sec.}$

S/V = surface to volume ratio of austenite grains,

The volume and surface nucleation rates determined thus are listed against austenitizing temperature in Table 1.

In confirmation of the results of Hull et al., (1) N. decreases with increasing austenitizing temperature, and the decrease cannot be accounted for on the basis of the increase in grain size because \dot{N}_s is also sensitive to austenitizing temperature. In contrast to the earlier work, metallographic examination showed that

Table 1. Pearlite-nucleation rate at 680° C in iron-0.78 carbon alloy

Austeni- tizing temp. °C	Time in sec. for $f = 0.1$ in pearlite reaction	\hat{N}_{v} (eq. (1)) nuclei cm ⁻³ sec ⁻¹	ASTM grain size	S/V cm ⁻¹	\dot{N}_s (eq. (2) nuclei cm ⁻² sec ⁻¹
870	17	110	6	5.4	2.1
980	36	5.9	4	2.7	0.22
1095	100	0.094	0	0.67	0.014

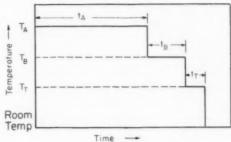


Fig. 1. Heat Treatment Cycle

TA = Temperature of Austenitizing
TB = Temperature of Second Austenitizing

 $T_{\rm T} = {
m Temperature of Transformation}$

ta = Time of Austenitizing

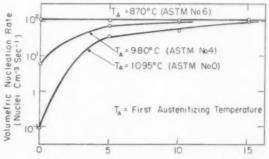
tB = Time at Second Austenitizing Temperature

 $t_{\rm T} = {\rm Time~of~Transformation}$

nucleation does not occur preferentially along austenite grain boundaries.

To study the reversal of this trend with decreasing austenitizing temperature, another austenitizing treatment was inserted between T_A and the pearlite reaction temperature, as indicated in Fig. 1. The second austenitizing temperature, T_B , was maintained within the all-austenite field, below the initial austenitizing temperature, T_A . Inasmuch as the grain size was fixed by the austenitizing treatment at T_A , the effect of time at the second temperature could be studied at a constant grain size.

Fig. 2 shows the effect of time at 870°C (T_B) after prior austenitizing at (T₄) 870°, 980°, and 1095°C for 45 min. Heating at 870°C after 45 min at 870°C $(T_A = T_B)$ does not influence the rate of pearlite nucleation. On the other hand, when $T_A > T_B$, there is a progressive increase in the rate of pearlite nucleation as a function of time at T_R . Furthermore, the values seem to approach the nucleation rate characteristic of direct austenitizing at T_B . Accordingly, the



Time at Second Austenitizing Temperature (T_e=870°C)
(Min)

Fig. 2. Volumetric nucleation rate of pearlite at 680° Cvs. time at second austenitizing temperature for a 0.78% iron–earbon alloy. Time at first austenitizing temperature was 45 min. Nucleation rate values were determined by substitution of time for 10 per cent transformation in equation (1).

reduction in nucleation rate due to raising the austenitizing temperature (Table 1) is reversed by further holding at a lower austenitizing temperature (Fig. 2). A phenomenologically similar effect of austenitizing temperature on the bainitic transformation has recently been reported by Graham and Axon(4).

These results indicate that there is a reversible phenomenon at play in the austenitizing treatment, over and above any possible effect of austenite grain growth or dissipation of macroscopic concentration gradients. The reversible phenomenon may be related to the formation of transformation sites or embryos which are stabilized by the presence of imperfections in the parent phase, and which tend to decrease reversibly in size or potency with increasing temperature. A model of this type has been proposed for the nucleation of martensite (5) from austenite in iron-nickel alloys. Another possibility is that a metastable clustering of carbon atoms may occur about lattice imperfections in the parent phase, it being these imperfections that participate in the pearlite-nucleation process. Studies are under way to distinguish between these two alternatives.

Department of Metallurgy Massachusetts Institute of Technology, Cambridge Massachusetts

M. H. RICHMAN

D. A. THOMAS

M. COHEN

References

1. F. C. Hull, F. C. Colton and R. F. Mehl, Trans. Amer. Inst. Min. (Metall.) Engrs. 150, 185 (1942).
 W. A. Johnson and R. F. Mehl, Trans. Amer. Inst. Min.

(Metall.) Engrs. 135, 416 (1939).
3. R. F. Mehl and W. C. Hagel, in Progress in Metal Physics, Vol. 6. Pergamon Press, New York (1956). 4. L. W. Graham and H. J. Axon, J. Iron St. Inst. 191,

Part 4, 361 (1959).

5. M. Cohen, Trans. Amer. Inst. Min. (Metall.) Engrs. 212, 171 (1958).

* Part of a thesis submitted June 1957 to the Department of Metallurgy, Massachusetts Institute of Technology, by M. H. Richman, in partial fulfillment of the requirements for the SB degree. Received June 29, 1959.

Dislocation barriers and cross slip*

One of the current theories for the deformation of face-centered cubic crystals(1) assumes cross slip by screw dislocations to avoid Lomer-Cottrell barriers (2.3) which have been formed by the reaction of parallel dislocations from different slip planes. The most likely Lomer-Cottrell reaction involves a dislocation from the most stressed (primary) slip system, but the barriers produced by this reaction are not parallel to screws on the primary system.

Therefore cross slip is difficult. (4) However, motion of dislocations on a single slip system can give rise to Lomer-Cottrell type barriers which are parallel to primary screw dislocations and which therefore can cause screw dislocations to cross slip.

Kocks⁽⁵⁾ has considered the cutting of stationary dislocations of [101] slip vector, by primary [101] (111) dislocations moving across their slip plane. When [101] dislocations are cut by a number of primary dislocations, long jogs will be produced in them. Since these jogs have a [101] vector and lie in a [101] direction, they have (010) slip planes. Kocks supposed that these long jogs would not move easily because of a high Peierls force. (6) There is, however, special reason to expect these jogs to be highly sessile. A [101] (010) dislocation is of precisely the type which Cottrell⁽³⁾ showed could dissociate to become what is now termed a Lomer-Cottrell barrier. Since these barriers are in the [101] direction, they parallel screw dislocations. A [10I] dislocation containing such a barrier is shown in Fig. 1.

Unit jogs produced by the cutting can not dissociate⁽⁷⁾ and so may be free to run along the [101] dislocation. Such unit jogs would tend to combine, forming long jogs, thereby lowering the total constriction energy. Sufficiently long jogs may dissociate into barriers. Therefore if long jogs are not formed during the cutting process itself, they should form as a result of it.

An interesting statement may be made concerning [110] (001) slip: Such slip is highly unlikely. Consider a [110] (001) dislocation of a part-edge, part-screw

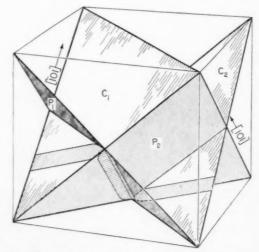


Fig. 1. Barrier formed on a primary plane $(p_1 \text{ or } p_2)$ and its cross slip plane $(p_2 \text{ or } p_1)$ as a result of primary slip across a dislocation originally on a critical plane $(c_1 \text{ or } c_2)$. Here $p_1 = (1\Pi)$; $p_2 = (1\Pi)$; and $c_1 = c_2 = (1\Pi)$.

orientation. If it acquires a screw orientation, it will dissociate into partials and glide on an octahedral plane; if it acquires an edge orientation, it will dissociate into a barrier and become sessile. This reasoning is in agreement with the failures to observe slip on cube planes in highly favorable stress situations.(8-10)

The authors are grateful to the Atomic Energy Commission for financial support.

Metals Processing Laboratory W. F. Hosford[†] Department of Metallurgy R. L. Fleischer† Massachusetts Institute of Technology

References

I. A. SEEGER, J. DIEHL, S. MADER, and H. REBSTOCK, Phil. Mag. 2, 323 (1957).

2. W. M. LOMER, Phil. Mag. 42, 1327 (1951). 3. A. H. COTTRELL, Phil. Mag. 43, 645 (1952).

R. L. Fleischer, Acta Met. 6, 553 (1958). 5. U. F. Kocks, Ph.D. Thesis, Harvard, (1959); to be published in Acta Met.

6. R. E. Peierls, Proc. Phys. Scc. 52, 23 (1940).

7. N. Thompson, Conference on Defects in Crystalline Solids, p. 153. Physical Society, London (1955).

8. H. Wilsdorf and D. Kuhlman-Wilsdorf, Trans. Amer. Inst. Min. (Metall.) Engrs. 194, 527 (1952).
9. J. D. Livingston, Ph.D. Thesis, Harvard, (1956).
10. Y. A. Rocher, L. A. Shepard, and J. E. Dorn, Trans.

Amer. Inst. Min. (Metall.) Engrs. 215 316 (1959).

* Received August 21, 1959.

† Assistant Professor, Metals Processing Laboratory, Department of Metallurgy, Massachusetts Institute of Technology

Absolute grain boundary energies in copper*

Recently Gjostein and Rhines(1) presented measurements of grain boundary energies relative to surface energies in copper which had been annealed at 1065°C. By use of the measurements of Udin et al.(2) on absolute surface energies, absolute grain boundary energies could be found and compared with the Read-Shockley formula(3)

$$\varepsilon = E_0 \theta (A - \ln \theta). \tag{1}$$

Here ε is the boundary energy, θ the angular disorientation, A a constant, and E_0 is $G\mathbf{b}/4\pi(1-\nu)$ for a simple tilt boundary (G = shear modulus; v = Poisson's ratio; $\mathbf{b} = \text{slip vector}$). For (100) tilt boundaries Gjostein and Rhines separated their results into two ranges of angles each of which could be described by equation (1) by choosing E_0 appropriately. On an ε/θ vs. In θ plot this corresponded to two regions of constant slope. Using elastic parameters reduced 15 per cent to allow for the temperature change between room temperature and 1065°C, the theoretical slope of the curve agreed with the

experimental values for small angles, while it was a factor of about 2 too large for higher angles (3° < $\theta < 53^{\circ}$). They concluded therefore that only for small values of θ was the theoretical calculation appropriate.

It is desired in this note to show that theory and experiment do agree for larger angles and that the presence of a twist component in the tilt boundary can account for disagreement which exists for θ less than 3°. An approximate value for the 1065°C elastic constants may be obtained by a 100°C extrapolation of Köster's measurements of Young's modulus.(4) His data indicate that the ratio of the value at 1065°C to that at room temperature is about 0.41 as compared with the assumed value⁽¹⁾ of 0.85. Hence, the factor of 2 discrepancy is shifted to very small values of θ , where the energy will be most strongly affected by the presence of a small twist component, whose constant average value would be specified by the experimental accuracy.

For a tilt boundary containing a small twist component the energy is assumed to be separable into tilt and twist components, denoted by subscripts E and S:

$$\varepsilon = \varepsilon_E + \varepsilon_S,$$
 (2)

where
$$\varepsilon_E = E_0 \theta_E (A - \ln \theta_E)$$

The slope on an ε/θ vs. In θ plot, where the tilt disorientation θ_E is varied, is then

$$\begin{split} \frac{d(\varepsilon/\theta_E)}{d \ln \theta_E} &= \frac{d}{d \ln \theta_E} [E_0(A - \ln \theta_E) \\ &+ \varepsilon_S/\theta_E] = -E_0 - \varepsilon_S/\theta_E, \end{split} \tag{3}$$

so that for small θ_E the magnitude of the slope increases, as was observed. (1) Equation (3) indicates that the slope should double when $\theta_E = \varepsilon_S/E_0$. Taking E_0 from the results for angles $>3^{\circ}$ and ε_S as the extrapolated value for a twist boundary with a twist of 0.15° (typical values were reported to be less than 0.2), it is found that $\theta_E \approx 0.9^{\circ}$. This value checks within experimental scatter with Gjostein and Rhines' results.

Another uncertainty in a measurement of boundary energy arises from solute atoms lowering the observed energy of a boundary relative to the Read-Shockley formula by segregating to edge dislocations in a tilt boundary. An estimate of the effect is now made assuming arbitrarily that the change in dilation due to the solute atoms equals that due to the dislocations

^{*} Good agreement is also obtained between theory and experiment for E_0 values in twist boundaries, the measured value of E_0 being 725 ergs/cm² as compared with a calculated

composing the boundary. The number n of solute atoms per unit area of boundary to equal the dilation of one sign is given by Webb $^{(5)}$ as

$$(1-2v)/(1-v)4\pi b^2\epsilon$$
,

where ϵ is a strain parameter (r'-r)/r, r and r' being the radii of solvent and solute atoms. The energy change \bar{U} in moving a solute atom from perfect crystal to a distance b from the dislocation is given by Bilby's refinement⁽⁶⁾ of Cottrell's calculation⁽⁷⁾ as $Gb^3\epsilon/2$. Hence the total energy change $\Delta \epsilon$ is $2n\bar{U}$, assuming that dilation of both signs has been released. Therefore

$$\Delta \varepsilon = Gb(1 - 2\nu)/4\pi(1 - \nu). \tag{4}$$

Since Cottrell's calculation of \tilde{U} is not valid very close to a dislocation or for solute atoms close to one another, this result must be considered as an estimate only and hence should be multiplied by some correction factor. This factor, to be called a, is probably of the order of 1/4. Combining (4) with (1):

$$\varepsilon - \Delta \varepsilon = \frac{Gb}{4\pi(1-v)} \left[\theta(A - \ln \theta) - a(1-2v) \right] \quad (5)$$

In addition, Webb has shown that, geometrically, only for $\theta > (1-2\nu)/4\pi^2\epsilon(1-\nu)$ can all the impurity atoms needed be accommodated as close to a dislocation as was assumed here. Hence, for very small θ , $\Delta\varepsilon$ becomes a function of θ . With these limitations in mind it would appear from (5) that solute atoms could lower the boundary energy by as much as 80 ergs/cm² and would cause deviations from equation (1) at angles of about one or two degrees.

Of critical importance for the effect just considered, as well as for the appropriate value of E_0 , is the cooling schedule after annealing a boundary. For ideally rapid cooling the elastic constants at the annealing temperature are appropriate; for less rapid cooling, readjustment of the boundary during cooling may occur, so that the effective temperature of the experiment may be lowered. Similarly the impurity atmosphere is controlled by the annealing temperature (5) and the subsequent thermal history.

The author is pleased to give thanks to the Atomic Energy Commission for financial support.

R. L. Fleischer

Department of Metallurgy Massachusetts Institute of Technology Cambridge 39, Massachusetts

References

- N. A. GJOSTEIN and F. N. RHINES, Acta Met. 7, 319 (1959).
 H. UDIN, A. J. SHALER and J. WULFF, Amer. Inst. Min.
- (Metall.) Engrs. 185, 186 (1949).
 W. T. Read and W. Shockley, Phys. Rev. 78, 275 (1950).

- 4. W. KÖSTER, Z. Metallk. 39, 1 (1948).
- W. W. Webb, Acta Met. 5, 89 (1957).
 B. A. Bilby, Proc. Phys. Soc. A 63, 191 (1950).
- A. H. COTTRELL, Report on the Conference on Strength of Solids, p. 30. Physical Society, London (1948).
 - * Received July 9, 1959.

The production of vacancy clusters during cold work*

Recent calculations^(1,2) and experiments^(3,4) on the activation energy for the motion of vacancies in copper indicate strongly a value of 1.1 to 1.3 eV. One expects, therefore, that vacancies in copper will become mobile only above room temperature. These results do not fit in very well with suggested annealing mechanisms for cold-worked copper.⁽⁵⁾ It would be helpful in the interpretation if it could be demonstrated that appreciable concentrations of fast moving defects, such as divacancies, can be built up during cold work. The purpose of this note is to speculate about such a mechanism.

Some of the mechanisms⁽⁶⁾ for the generation of vacancies during cold work require that rows of vacancies be formed. A chain of vacancies (i.e. a row of vacancies where each vacancy is a nearest neighbor of the next one) is presumably unstable and will tend to break up into smaller clusters and isolated vacancies. A semiquantitative argument indicates that the rate of evaporation of divacancies from such a chain is much higher than that for single vacancies.

195

Let the vacancies in the chain in a face centered cubic crystal be at the coordinates (in units of a/2 where a is the lattice parameter) (0,0,0), (1,1,0), (2,2,0), etc. The jump of any nearest neighbor of (0,0,0) (i.e. at the end of a chain), which is not a nearest neighbor of (1,1,0), into (0,0,0) detaches a single vacancy from the chain. The activation energy for this jump is very nearly that for the motion of a single vacancy, i.e. about $1.2 \, \mathrm{eV}$, increased by the breaking of a vacancy–vacancy bond, which is about $0.3 \, \mathrm{eV}$. $^{(7,8)}$ The overall activation energy is, therefore, about $1.5 \, \mathrm{eV}$.

The jump of an atom from (1,0,1) (or equivalent positions) into (1,1,0) splits off a divacancy from the chain (jump of (1,0,1) into (0,0,0) produces only a kink in the original chain). The overall activation energy in this case is the sum of the migration energy for divacancies, about $0.2 \, {\rm eV},^{(2)}$ and the energy to break a vacancy–vacancy bond, about $0.3 \, {\rm eV}$, giving a final value of about $0.5 \, {\rm eV}$. The energy difference

between these two processes is therefore about 1 eV in favor of the divacancy formation. Thus, the rate of evaporation of divacancies is expected to be several orders of magnitude higher than that for single vacancies. This easy "divacancy type" jump can occur anywhere along the chain creating new chain ends which, in turn, also split off divacancies in the manner already described.

A precise calculation is difficult to make because of our inaccurate knowledge of the various quantities involved (particularly the effects of electronic rearrangement). The real situation is further complicated by the formation of trivacancies, which are probably very stable, (2) and higher clusters whose properties are not known. Nevertheless, the above crude estimates suggest strongly that divacancies may play an important role in the low temperature annealing of cold work in copper.

A. C. Damask†

Brookhaven National Laboratory G. J. Dienes Upton, New York

References

1. F. G. Fumi, Phil. Mag. 46, 1007 (1955).

VOL.

1959

 A. C. Damask, G. J. Dienes and V. G. Weizer, Phys. Rev. 113, 781 (1959).

 A. Granato, A. Hikata and K. Lücke, Phys. Rev. 108, 1344 (1957).

 G. Airoldi, G. J. Bacchella and B. Germagnoli, Phys. Rev. Letters 2, 145 (1959).

 For a recent review see T. Broom and B. K. Ham, in Vacancies and Other Point Defects in Metals and Alloys, pp. 41-79, The Institute of Metals, London (1958).

 See for example A. H. COTTRELL, in Vacancies and Other Point Defects in Metals and Alloys, pp. 26-29. The Institute of Metals, London (1958); J. FRIEDEL, Les Dislocations, pp. 75-79, Gauthier-Villars, Paris (1956).

 J. H. Bartlett and G. J. Dienes, Phys. Rev. 89, 848 (1953).

8. A. SEEGER and H. Bross, Z. Phys. 145, 161 (1956).

* Supported in part by the U.S. Atomic Energy Commission, Received August 10, 1959.

† Supported by a Secretary of the Army Fellowship.

Experimental evidence for martensitic embryos *

Recent theories^(1,2) concerning the athermal and isothermal kinetics of martensitic transformations require the presence of pre-existing embryos of appreciable size, as "frozen-in" during the cooling from the austenitizing treatment. These embryos are not of the classical (steady-state) type, but are presumed to be stabilized in the parent phase by dislocations which associate themselves with the interface. If the structure of the embryo is taken to be that of the martensitic phase (which forms spontaneously at the M_* temperature), it is possible to calculate, at

least in the case of iron–nickel alloys, the embryo size that becomes critical for cataclysmic growth at the M_s temperature. (1.2)

The shape of the embryos should be approximately ellipsoidal or lenticular in order to minimize the sum of the interfacial and strain energies for a given size. $^{(3.4)}$ On this basis, the calculations show that the largest embryos should be of the order of 1000 Å in diameter and 100 Å in thickness in the iron–nickel alloys to be discussed here. There is also a distribution of smaller-size embryos which become active only at temperatures below M_s .

The recently-developed method of thin-foil (transmission) electron microscopy (5.6) provides an excellent opportunity for detecting these embryos. To this end, iron-nickel foils in the austenitic state were prepared by electrolytic thinning at room temperature, using the method of Wilsdorf et al. (7) The M, for each alloy was below room temperature. Fig. 1 presents a typical area in the austenitic matrix, with plate-like markings which are interpreted as martensitic embryos. Other possible explanations for these manifestations, such as stacking faults, mechanical twins, or artifacts, have been ruled out. Moreover, electron diffraction patterns from these areas revealed the presence of b.c.c. (martensite) as well as f.c.c. (austenite) structures, and the diffraction pattern of the b.c.c. structure disappears if the electron beam is confined to regions not containing the plate-shaped markings.

The quantitative measurements and calculations of the maximum embryo sizes are compared in Table 1. Considering the assumptions that enter into the calculations, the trend indicated in Table 1 offers further evidence in favor of the interpretation given here. The electron micrographs also disclose a distribution



Fig. 1. Austenite matrix showing martensitic embryos. A transmission electron micrograph of Fe–29.3 at, % Ni. $\times 27,000$.

Table 1. Comparison of observed and calculated maximum embryo sizes in iron-nickel alloys

At, % Ni	M_{*}	Embryo di	ameter (Å)	Embryo th	ickness (Å)
	(°C)	Observed	Calculated	Observed	Calculated
28.0	+7	15,000	2,300	130	66
29.3 30.7	$-30 \\ -72$	$\frac{4,700}{2,500}$	$\frac{2,150}{2,080}$	55 35	67 62

of embryo sizes, as required by the theory. (1.2)

The decrease in embryo size with increasing nickel content arises, in the calculations, from the decrease in driving force for the f.c.c. \rightarrow b.c.c. reaction. That the corresponding embryos are "frozen-in" is demonstrated by the fact that, in any given iron-nickel alloy, the embryo size does not change as M_s is approached. For example, the embryo size observed at room temperature remains fixed in each alloy on subcooling to within 5°C of the respective M_s temperatures.

Cooling experiments are now in progress to correlate these observations with the actual initiation of the martensitic transformation.

Acknowledgments

The authors would like to express their appreciation to the following: the Office of Naval Research for providing financial support for this investigation;

the Franklin Institute Laboratories, through its Technical Director, Dr. Raymond Smith, for providing the laboratory facilities; Mr. Charles Varker for his assistance in establishing the proper polishing and microscope procedures, and the Physics of Metals Branch for the lively discussion and interest manifested toward this study.

Department of Metallurgy	M. H. RICHMAN
Massachusetts Institute of	M. COHEN

Technology	
Cambridge.	Massachusetts

Philadelphia, Pennsylvania

- References 1. M. COHEN, Trans. Amer. Inst. Min. (Metall.) Engrs. 212, No. 2, 171 (April 1958).
- L. KAUFMAN and M. COHEN, Progress in Metal Physics, Vol. 8, Chap. 7. Pergamon Press, London (1958).
 J. C. FISHER, J. H. HOLLOMON and D. TURNBULL, Trans.
- Amer. Inst. Min. (Metall.) Engrs. 185, 691 (1949).
- 4. H. KNAPP and U. DEHLINGER, Acta Met. 4, 289 (1956). W. Bollmann, Phys. Rev. 103, 1588 (1956).
- 6. P. B. HIRSCH, R. W. HORNE and M. J. WHELAN, Phil. Mag.
- 7. H. G. F. WILSDORF, L. CINQUINA and C. J. VARKER, Proc. Fourth International Congress for Electron Microscopy, Berlin (1958). In press.

19

^{*} This work is part of a thesis being conducted by Marc Richman for the degree of Doctor of Science at the Massachusetts Institute of Technology. The overall program is sponsored by the Office of Naval Research under Contract No. Nomr-1841 (35). Received August 24, 1959.